fg

Development of a Molecular Toolbox for Multifunctional Lanthanide-based Supramolecular Materials

A thesis presented in partial fulfilment of the requirements for the degree of

Doctor of Philosophy
in
Chemistry

at Massey University, Albany, New Zealand.

Alex Thomas O'Neil
2022

Abstract

Using simple building blocks to develop functional supramolecular materials is an active area of research. To this extent the use of lanthanide ions (Ln^{3+}) to direct supramolecular self-assembly with organic ligands has become a popularised method whereby the interesting photophysical properties of Ln^{3+} can be manipulated by simple modification of the organic architecture. Applications of such systems vary from solar waveguides, OLEDS, molecular sensors, contrast agents, bio-probes, security inks and barcodes. Herein, a synthetic strategy has been developed and investigated to readily functionalise the organic scaffolds 2,6-pyridinedicarboxamide (PDA) and 6-carbamoylpyridine-2-carboxcylic acid (PDC), using 1,2,3-triazole "click" chemistry.

Using this approach, we have synthesised and assessed the *f*-directed self-assembly ability of some novel PDA-based and PDC-based assemblies. Initial studies focused on symmetrical incorporation of the 1,2,3-triazole linker into the PDA motif *via* side carbonyls. This resulted in the development of four ligand architectures (**1**-**4**), which in the presence of Eu^{3+} and Tb^{3+} self-assemble into $Ln(\mathbf{L})_3(CF_3SO_3)_3$ (where **L** = **1**-**3**) luminescent assemblies. While results of the PDA systems were promising, the systems were relatively unstable in competitive solvents, and as a result subsequent systems focused on the unsymmetrical modification of the PDC motif. Incorporation of our synthetic strategy into the PDC motif was straightforward and additionally improved both Ln^{3+} complex stability and emission intensity. Using this approach, amphiphilic ligand **5** and visibly emissive amphiphilic complexes $Ln(\mathbf{5})_3$ (where Ln = Eu^{3+}, Tb^{3+}, Sm^{3+} and Dy^{3+}) were synthesised. The incorporation of a long alkane chain *via* the 1,2,3-triazole in ligand **5** allowed for the fabrication of ultra-thin luminescent films by Langmuir-Blodgett (LB) technique resulting in bright visibly emissive monolayer films. Furthermore, mixing of the emissive $Ln(\mathbf{5})_3$ complexes resulted in tunable emission dependent on the composition in both solution and monolayer film. Following this, single component dual emissive systems $Ln(\mathbf{6})_3$, $[Ln(\mathbf{7})_3](CF_3SO_3)_3$ and $Ln(\mathbf{8})_3$ were developed. This entailed the incorporation of blue emissive 1,8-naphthalimide (**6** & **7**) and pyrene (**8**) *via* the 1,2,3-triazole linker. When complexed with Eu^{3+} it resulted in dual emissive systems which were colour-tunable, changing colour dependent on the excitation wavelength, and in the case of $Eu(\mathbf{6})_3$ and $Eu(\mathbf{8})_3$ it results in white emissive solids and solutions. These properties were transferable to thin films, by spin coating techniques. Finally, the synthetic strategy was used in the initial development of multi-nuclear assemblies forming three multitopic ligands (**9**-**11**) and initial complexation studies were undertaken.

Acknowledgements

I am extremely grateful for my supervisor Associate Professor Jonathan Kitchen and co-supervisor Associate Professor John Harrison. Both have been instrumental throughout the undertaking of my research. They have provided me with the skills and knowledge that was required to carry out this research and have always been available to assist in problem solving, paper writing and encouragement for future endeavours. I would like to specifically thank Associate Professor Jonathan Kitchen for giving me this opportunity, taking me on as an honours student and then pushing for me to undertake a Ph.D at Massey University. Throughout these four years he has taught me so much and I would not have been able to achieve what I have without his teachings and assistance. I would like to specifically thank my co-supervisor Associate Professor John Harrison; he has taught me throughout my academic life and has always been a solid support through the difficulties of COVID and issues with Massey University.

I am deeply indebted to Jade Pope and Erin Moffet, technical members of the Massey Albany chemistry department; without them it would have been impossible to finish my research. Both have always been willing to help in any way possible, ordering chemicals, finding equipment, and assisting with instrumentation. I would like to specifically thank Erin Moffet, who was always willing to drop everything to help me capture a picture or solve an instrument issue. She has kept me sane throughout the years and has always been available to discuss issues, ideas and initially help me with methodology for analytical techniques, and always made the department a friendly and inviting environment. I am especially thankful for her baking. I would like to also specifically thank Jade Pope for her help over the last 7 years. She has always been a supportive co-worker and friend, and without her I would have never been pressured to do an honours degree which led to this Ph.D. I would like to thank her for the many hours she spent with me editing my papers, posters, talks, and thesis, and without her this thesis and many other projects would have taken much longer without her expert skills at proof reading. Both have truly become close friends throughout my years of study and will continue to be.

I would also like to thank the remaining members of the Massey Albany chemistry department: Professor Al Nielson, Dr Marie-Anne Thelen, and Dr Debbie Jordan. Although they have not been directly involved in this thesis, it is from their teaching that I was able to get to this stage. I would like to specifically thank Professor Al Nielson and Dr Marie-Anne Thelen, who have always been willing to discuss my research and have offered their wisdom.

I would like to acknowledge Massey University for funding my research by awarding me the Massey Vice-Chancellor's Doctoral scholarship and Massey Scholarship of Sciences which have allowed me to undertake these studies. I would also like to thank the New Zealand Ministry of Business, Innovation and Employment, and the Royal Society Te Apārangi, for a catalyst: seeding fund which helped fund some of the research which was undertaken in this thesis and allowed me to travel to England to visit Southampton University.

I am also grateful to Dr Jack Chen from Auckland University of Technology for allowing me access to their Agilent Technologies Cary Eclipse spectrophotometer; without this I would not have been able to fully investigate my systems; and Professor Stephen Goldup for allowing me to visit his lab and experience working with a large research group.

I would like to thank my friends Adam Mago, Andrew Sheu, Jonathan Ramsay, Josh Snoad, Junn Foo and Natrell Wicks. Over the last 8 years of study they have kept me sane and driven me to achieve my goals. Without them I would never have been able to do what I have done.

Lastly this endeavour would not have been possible without my family. Without the support of my parents Joseph and Elaine O'Neil and my brother Joe O'Neil, I would never have been able to achieve this let alone my bachelors and honours degrees. It is to them that I am eternally indebted to for the support throughout all my studies and life.

Declaration of Authorship

I, Alex O'Neil, declare that this thesis, titled "Development of a Molecular Toolbox for Multifunctional Lanthanide-based Supramolecular Materials" and the work presented in it are my own.

I confirm that:

- All work presented in this thesis was carried out by the author unless otherwise stated in the acknowledgements.
- This work has solely been carried during the author's Ph.D. candidacy at Massey University.
- Where I have consulted published work of others, ownership has always been clearly attributed.
- I certify that I have made all reasonable efforts to secure copyright permissions for third-party content included in this thesis and have not knowingly added copyright content to my work without the owner's permission.

Table of Contents

Abstract i
Acknowledgements ii
Declaration of Authorship iv
Table of Contents vi
List of Abbreviations viii
List of Figures ix
List of Tables xxiv
List of Publications xxvi
1. Introduction 1
1.1 Project Overview *1*
1.2 Lanthanide Fundamentals *7*
1.2.1 Electronic Structure 9
1.3 Lanthanide Photophysics *12*
1.3.1 Direct Excitation and Absorption of Ln^{3+} 13
1.3.2 Indirect Excitation or Sensitisation 15
1.3.3 Emission Spectra 18
1.3.4 Efficient Sensitisation 20
1.4 References *24*
2. Literature Review 27
2.1 Introduction *27*
2.2 2,6-Pyridinedicarboxamide (PDA) *28*
2.2.1 Tris-Mononuclear $[Ln(L)_3]^{3+}$ Assemblies 29
2.2.2 Multitopic Ligand Architectures 33
2.3 6-Carbamoylpyridine-2-carboxcylic (PDC) *39*
2.4 References *43*
3. Luminescent Molecular Bundles 45
3.1 Introduction *45*
3.2 Results and Discussion *47*
3.2.1 Ligand Synthesis and Characterisation 47
3.2.2 Ligand Molecular Structures 49
3.2.3 Complex Synthesis and Characterisation 51
3.2.4 Photophysical Studies 55
3.2.5 Self-Assembly Investigation 61
3.2.6 Computational Studies 77
3.3 Conclusion *79*
3.4 Experimental *80*
3.4.1 General Experimental Details 80
3.4.2 Photophysical Measurements 80
3.4.3 Ligand Synthesis 82
3.4.4 Lanthanide Complexation 85
3.5 Acknowledgements *87*
3.6 References *87*
4. Mixed Lanthanide Langmuir Blodgett Films 90
4.1 Introduction *90*
4.2 Results and Discussion *97*
4.2.1 Ligand Synthesis and Characterisation 97
4.2.2 Ligand Molecular Structure 103
4.2.3 Self-Assembly Studies 105
4.2.4 Complexation Studies 108
4.2.5 Photophysical Properties of Lanthanide Complexes 113
4.2.6 Langmuir-Blodgett Studies 120
4.2.7 Mixed Lanthanide Studies 131
4.3 Conclusion *141*

4.3.1 Future Work 144
4.4 Experimental *145*
4.4.1 General Experimental Details 145
4.4.2 Langmuir-Blodgett Technique 145
4.4.3 Photophysical Measurements 145
4.4.4 X-ray Photoelectron Spectroscopy (XPS) 146
4.4.5 Ligand Synthesis 147
4.4.6 Lanthanide Complexation 149
4.5 Acknowledgements *151*
4.6 References *151*
5. Dual Emissive Spin Coated Films 155
5.1 Introduction *155*
5.2 Results and Discussion *164*
5.2.1 Ligand Synthesis and Characterisation 164
5.2.2 Ligand Molecular Structures 171
5.2.3 Ligand Photophysical Properties 179
5.2.4 Self-Assembly Studies 182
5.2.5 Complex Synthesis and Characterisation 194
5.2.6 Lanthanide Photophysical Properties 200
5.2.7 Spin Coating and Film Formation 215
5.3 Conclusion *224*
5.3.1 Oxygen Sensing 225
5.4 Experimental *226*
5.4.1 General Experimental Details 226
5.4.2 Photophysical Measurements 226
5.4.3 Spin Coating 227
5.4.4 Ligand Synthesis 228
5.4.5 Lanthanide Complexation 233
5.5 Acknowledgements *236*
5.6 References *236*
6. Larger Assemblies 239
6.1 Introduction *239*
6.2 Results and Discussion *244*
6.2.1 Ligand Synthesis and Characterisation 244
6.2.2 Initial Complexation Results 247
6.3 Conclusion *258*
6.4 Experimental *260*
6.4.1 General Experimental Details 260
6.4.2 Ligand Synthesis 261
6.5 References *263*
7. Conclusion 265
7.1 Future Studies *267*
7.1.1 Future Applications and Improvements for Current Systems 267
7.1.2 Improved Ligand Scaffold 270
7.2 References *271*
8. Appendices 273

List of Abbreviations

Ra	Average Roughness	**MRI**	Magnetic Resonance Imaging
BT	Back Transfer	**Nap**	Naphthalene
Bn	Benzyl	**NIR**	Near Infrared
CT	Charge Transfer	**nr**	Non-radiative
CPL	Circular Polarized Emission	**NMR**	Nuclear Magnetic Resonance
CIE	Commission Internationale de l'Eclairage	τ_{obs}	Observed Lifetime
CuAAC	Copper-Catalysed Azide-Alkyne Cycloaddition	**OLED**	Organic Light Emitting Diode
DPA	Dipicolinic acid	Φ_{Ln}^{L}	Overall Quantum Yield
d	Doublet	**ppm**	Parts Per Million
dd	Doublet of doublets	**PYR**	Pyrene
DC	Down Conversion	**py**	Pyridine
Z_{eff}	Effective Nuclear Charge	**Φ**	Quantum Yield
ED	Electric Dipole	**q**	Quartet
λ_{em}	Emission Wavelength	τ^{rad}	Radiative Lifetime
ET	Energy Transfer	**RASSS**	Rapid Annealing Self-Solution-Shearing
λ_{ex}	Excitation Wavelength	k_{obs}	Rate of Depopulation of Excited States
T^*	Excited Triplet State	k^{rad}	Rate of Radiative Emission
FTIR	Fourier Transform Infrared Spectroscopy	**rpm**	Revolutions Per Minute
HRMS	High Resolution Mass Spectroscopy	**RCM**	Ring Closing Metathesis
IEDT	Induced Electric Dipole Transition	**r.t**	Room Temperature
ISC	Intersystem Crossing	**s**	Singlet
ILCT	Intra Ligand Charge Transfer	S_0	Singlet Ground State
Φ^{Ln}	Intrinsic Quantum Yield	**TR**	Transfer Ratio
LB	Langmuir-Blodgett	Ln^{3+}	Trivalent Lanthanide Ion
LMCT	Ligand to Metal Charge Transfer	**TMAO**	Trimethylamine N-oxide
LRMS	Low Resolution Mass Spectrometry	**t**	Triplet
T_1	Lowest Excited Triplet State	**UV**	Ultraviolet
MD	Magnetic Dipole	**UC**	Up Conversion
MS	Mass Spectroscopy	**PDC**	6-Carbamoylpyridine-2-carboxcylic acid
m/z	Mass to Charge Ratio	**NI**	1,8-Naphthalimide
m	Multiplet	**PDA**	2,6-Pyridinedicarboxamide

List of Figures

Figure 1.1. Standard periodic table showing the f block separate from the rest of the elements. Lanthanide elements have been coloured to represent the colour that their Ln^{3+} state is commonly known to emit. Near-infrared red emissive lanthanides Ce, Nd, Ho and Yb shown in dark red, visibly emissive lanthanides Pr, Pm, Sm, Eu, Tb, Dy, Er and Tm shown in their dominant visible emission colour, ultra-violet emissive Gd shown in violet and non-emissive La and Lu are shown in grey. 1

Figure 1.2. Images of lanthanide applications, with the initial incandescent gas mantle in the centre, surrounded by more modern applications. Image adapted with permission from J.-C. G. Bünzli, Eur. J. Inorg. Chem., **2017**, 5058-5063. Copyright 2022 European Chemical Society. 2

Figure 1.3. DPA ligand motif, forming the 1:3 M:L species with tricapped trigonal prismatic geometry. Crystal structure adapted with permission from V. Legrand, F. Aubert, A. D'Aléo, P. Rabiller and O. Maury, Acta Cryst. E, Structure reports online, 2008, **64**, 1280-1281. 4

Figure 1.4. DPA and similar pyridine centred tridentate ligand motifs. 4

Figure 1.5. CuAAC 1,2,3-triazole formation proposed mechanism from reference 58. 5

Figure 1.6. Representation of potential "molecular toolbox" synthetic strategy. 6

Figure 1.7. Simplified radial distribution function vs radius of a range of orbitals, showing the internal nature of 4f orbitals within the xenon core. Image adapted from open access and CC-BY article, Y. Hasegawa, Y. Kitagawa and T. Nakanishi, NPG Asia Mater., 2018, **10**, 52-70..... 7

Figure 1.8. Diagram shows the 4f microstate energy levels that trivalent lanthanides are capable of. These states were determined for LaF_3 by W. T. Carnall, G. L. Goodman, K. Rajnak and R. S. Rana, J. Chem. Phys., 1989, **90**, 3443-3457 and image adapted from open access and CC-BY article: Y. Hasegawa, Y. Kitagawa and T. Nakanishi, NPG Asia Materials, 2018, **10**, 52-70. .. 9

Figure 1.9. Different microstate energy levels of Eu^{3+} as a result of the different interactions, showing the different energy significance of each interaction. Image adapted with permission from M. H. V. Werts, Sci. Prog., 2005, **88**, 101-131. Copyright 2022, SAGE publications. 11

Figure 1.10. Ln^{3+} emission spectra. Image adapted with permission from J.-C. G. Bünzli, in Handbook on the Physics and Chemistry of Rare Earths, eds. J.-C. G. Bünzli and V. K. Pecharsky, Elsevier, 2016, vol. 50, pp. 141-176. Copyright 2022, Elsevier Books. 12

Figure 1.11. Pictorial representation of the antenna effect. Abbreviations EX for the excitation source and EM for emission. 15

Figure 1.12. Jablonski diagram showing the $S_1 \rightarrow T_1 \rightarrow Ln^{3+}$ and $S_1 \rightarrow Ln^{3+}$ excitation pathways and competing energy pathways. 16

Figure 1.13. Potential energy transfer mechanism, starting from already populated triplet states. Image based off potential energy transfer mechanism in C. G. Bünzli, in Spectroscopic Properties of Rare Earths in Optical Materials, eds. R. Hull, J. Parisi, R. M. Osgood, H. Warlimont, G. Liu and B. Jacquier, Springer Berlin Heidelberg, Berlin, Heidelberg, 2005. 17

Figure 1.14. Example of how Ln^{3+} (specifically in this case Eu^{3+}) microstate band gap results in different wavelengths of light, with the common transitions of Eu^{3+} on the left and the corresponding emission spectrum on the right. 18

Figure 1.15. Example of Eu^{3+} organic complex emission and excitation profile demonstrating the Richardson shift. 19

Figure 1.16. Shows the Jablonski diagram for energy transfer to Tb^{3+} from a triplet state. In this case, energy levels of the triplet state and excited state of Tb^{3+} are close enough that BT can take place. Additionally, we see that the Tb^{3+} excited state is being quenched by vibrational energy transfer with O-H vibrations, suggested to require four phonons to quench the energy where it can be seen that Er^{3+} is more susceptible as it only requires two phonons. This diagram is not to scale and number of phonons were taken from reference 7. 21

Figure 1.17. Jablonski diagram depicting the two types of Φ for Ln^{3+}. Equation 7 is the equation used to determine sensitisation efficiency from overall and intrinsic quantum yields. Abbreviation stands for: I_{Ln} – intensity or photons absorbed (A) or emitted (E) by Ln^{3+}, $I_L(A)$ – photons absorbed (A) ligand or antenna. Diagram is based off a figure in reference 33 and has been redrawn with permission from C. G. Bünzli, Coord. Chem. Rev., 2015, **293-294**, 19-47. Copyright 2022, Elsevir. 23

Figure 2.1. Different motifs used as building blocks for Ln^{3+} assemblies. 27
Figure 2.2. Soundararajan and Jagannathan **L[1,2]** ligand architectures, **L[1]** later adapted by Bünzli, Piguet and co-workers. 28
Figure 2.3. Fu and co-workers **L[3]** and Gunnlaugsson and co-workers **L[4,5]** ligand architectures for $[Ln(\mathbf{L_3})_3]^{3+}$assemblies. Φ_{Ln}^{L} of $[Eu(\mathbf{L^{4,5}})_3]^{3+}$ in MeOH and MeCN, values taken from reference 53. 29
Figure 2.4. Muller and co-workers **L[6]** ligand architectures for $[Ln(\mathbf{L^6})_3]^{3+}$ assemblies. Φ_{Ln}^{L} of $[Eu(\mathbf{L^{4,5}})_3]^{3+}$ in MeCN, values taken from reference 38. Crystal structure of helicate assembly adapted with permission from T. Hua, J. Xu, E. E. Quiroz, S. Lopez, A. J. Ingram, V. A. Johnson, A. R. Tisch, A. de Bettencourt-Dias, D. A. Straus and G. Muller, Inorg. Chem., 2012, **51**, 647-660. Copyright 2022 American Chemical Society. 30
Figure 2.5. (Left) Gunnlaugsson and co-workers **L[7]** ligand architectures for $[Ln(\mathbf{L^7})_3]^{3+}$ assemblies and catenane formation post RCM. Image adapted with permission from C. Lincheneau, B. Jean-Denis and T. Gunnlaugsson, Chem. Commun., 2014, **50**, 2857-2860. Copyright 2022 Royal Society of Chemistry. (Right) Leigh and co-workers **L[8,9]** ligand architectures for $Ln(\mathbf{L^{8,9}})_3$ assemblies and knot formation post RCM. Image adapted from open access and CC-BY article, J.-F. Ayme, G. Gil-Ramírez, D. A. Leigh, J.-F. Lemonnier, A. Markevicius, C. A. Muryn and G. Zhang, J. Am. Chem. Soc, 2014, **136**, 13142-13145. 31
Figure 2.6. Gunnlaugsson and co-workers **L[10]** ligand architectures for $[Ln(\mathbf{L^{10}})_3]^{3+}$ assemblies. Φ_{Ln}^{L} of $[Eu(\mathbf{L^{10}})_3]^{3+}$and $[Tb(\mathbf{L^{10}})_3]^{3+}$ in MeOH, values taken from reference 58. Additional 0.5 equivalents of Ln^{3+} results in "cross-linked" supramolecular self-assemblies (Left). (Right) Luminescent gels formation of $[Ln(\mathbf{L^{10}})_3{:}Ln(CH_3COO)_3]^{3+}$, shown under ambient light (A), under UV irradiation (B) and gels spread on quartz plates (C) (Ln = Eu^{3+} (red), Tb^{3+} (green) and Eu^{3+}:Tb^{3+}(1:1, orange)). Image adapted with permission from M. Martínez-Calvo, O. Kotova, M. E. Möbius, A. P. Bell, T. McCabe, J. J. Boland and T. Gunnlaugsson, J. Am. Chem. Soc., 2015, **137**, 1983-1992. Copyright 2022 American Chemical Society. 32
Figure 2.7. **L[11]** ligand architecture is utilized to form $[Ln(\mathbf{L^{11}})_3]^{3+}$ and subject to the sol-gel method, for a range of different films and gels. Gunnlaugsson and co-workers **L[12]** ligand architectures for $[Ln(\mathbf{L^{12}})_3]^{3+}$ assemblies are used to form luminescent LB films. It is worth noting that there is also a version of **L[12]** similar to **L[5]** but is only investigated for Eu^{3+} complexes and LB films. 34
Figure 2.8. (Top) Bünzli, Piguet and co-workers triethylamine linker **L**[13] which forms $[Ln(\mathbf{L^{13}})]^{3+}$ encapsulating mononuclear tripodal podates assemblies. (Bottom) Lacour and co-workers tripodal **L[14]** PDA ligand and model encapsulating mononuclear tripodal podates $[Eu(\mathbf{L^{14}})]^{3+}$. Image adapted with permission from J. Hamacek, C. Besnard, N. Mehanna and J. Lacour, Dalton Trans., 2012, **41**, 6777-6782. Copyright 2022 Royal Society of Chemisty Publishing. 33
Figure 2.9. (Left) Tripodal PDA ligand: **L[15]** and **L[16]** by Hamacek and co-worker, and **L[17]** by Sun and co-workers. (Right) Tetrahedral $[Ln_4\mathbf{L}_4]^{12+}$ cage assemblies which ligands **L[15-17]** form in the presence of 1 equivalent of Ln^{3+}. 34
Figure 2.10. Leigh and co-workers single molecular strand **L[18]** for knot formation of $[Ln(\mathbf{L^{18}})]^{3+}$. Image adapted from open access and CC-BY article, G. Gil-Ramírez, S. Hoekman, M. O. Kitching, D. A. Leigh, I. J. Vitorica-Yrezabal and G. Zhang, J. Am. Chem. Soc., 2016, **138**, 13159-13162. 34
Figure 2.11. a) Leigh and co-workers single molecular strand, connected to an axle (orange) via a 1,2,3-triazole linker forming **L[19]**. It can be seen in the image that the macrocycle can thread the untied **L[19]** which is then closed by the presence of Ln^{3+} forming the knot stopper. Following this the knot can be untied and the macrocycle unthreaded. Image adapted from open access and CC-BY article, D. A. Leigh, L. Pirvu, F. Schaufelberger, D. J. Tetlow and L. Zhang, Angew. Chem. Int. Ed., 2018, **57**, 10484-10488. b) Leigh and co-workers single molecular strand with different terminal ends **L[20]** for the formation of granny and square knots (shown on the left) by 1,2,3-triazole "click" chemistry and RCM. Image adapted from open access and CC-BY article. D. A. Leigh, L. Pirvu and F. Schaufelberger, J. Am. Chem. Soc. 2019, **141**, 6054-6059. 35
Figure 2.12. Gunnlaugsson and co-workers **L[21,22]** and Law and co-workers **L[23,24]** forming $Ln_2\mathbf{L}_3$ helicate assemblies. Below is a crystal structure of $[Eu_2(\mathbf{L^{23}})_3]^{6+}$ (ΛΛ) helicate assembly. Crystal structure of helicate assembly adapted with permission from J C.-T. Yeung, W. T. K. Chan,

S.-C. Yan, K.-L. Yu, K.-H. Yim, W.-T. Wong and G.-L. Law, Chem. Commun., 2015, **51**, 592-595. Copyright 2022 Royal Society of Chemistry Publishing. 36

Figure 2.13. (Top) Ligand architectures which have been used to form helicate assemblies $[Ln_2L_3]^{6+}$ ($L^{25, 26,28 \& 29}$), tetrahedral cages $[Ln_4L_6]^{12+}$ ($L^{27,28}$) and cubic cages $[Ln_8L_{12}]^{24+}$ (L^{29}). (Bottom) Crystal structure of the tetrahedral cage assembly of $[Eu_4(L^{28})_6]^{12+}$ and a cartoon representation of cubic cage arrangement. Crystal structure of the tetrahedral cage adapted with permission from X.-Z. Li, L.-P. Zhou, L.-L. Yan, D.-Q. Yuan, C.-S. Lin and Q.-F. Sun, J. Am. Chem. Soc., 2017, **139**, 8237-8244. Copyright 2022 American Chemical Society. 37

Figure 2.14. Hamacek and co-workers larger assemblies with their initial pentanuclear assemblies $[Ln_5(L^{30})_3(L^{15})]^{15+}$ formed with L^{30} (Top) and their octanuclear assemblies $[Ln_8(L^{31})_4]^{24+}$ formed with L^{31}. On the left of each ligand structure is their calculated complex structure with Ln^{3+}. Images adapted with permission from B. E. Aroussi, S. Zebret, C. Besnard, P. Perrottet and J. Hamacek, J. Am. Chem. Soc., 2011, **133**, 10764-10767 and S. Zebret, E. Vögele, T. Klumpler and J. Hamacek, Chem. Eur. J., 2015, **21**, 6695-6699 respectively. Copyright 2022, American Chemical Society and John Wiley and Sons Publishing, respectively. 38

Figure 2.15. Horrocks and Lessmann's ligand architectures L^{32}, L^{33} and L^{34}. 39

Figure 2.16. Bünzli, Piguet and co-workers L^{35} ligand architecture and corresponding Tb(L^{35}) crystal structure. Φ_{Ln}^{L} for Ln(L^{35}) (measured in H_2O) and $[Ln(L^{35})]^{3+}$ (measured in MeCN:H_2O, 4:1), values taken from reference 86. Crystal structure of Tb(L^{35}) encapsulating mononuclear tripodal podate assembly adapted with permission from J.-M. Senegas, G. Bernardinelli, D. Imbert, J.-C. G. Bünzli, P.-Y. Morgantini, J. Weber and C. Piguet, Inorg. Chem., 2003, **42**, 4680-4695. Copyright 2022 American Chemical Society. 40

Figure 2.17. (Top) An and co-workers L^{36}, L^{37} and L^{38} ligand architectures, along with Φ_{Ln}^{L} for Ln(**L**)$_3$ (measured in EtOH) values taken from reference 89 and 90. (Bottom) Crystal structure of Sm(L^{36}), with carbonyl of the carboxylates highlighted in red, adapted with permission from B.-L. An, M.-L. Gong, M.-X. Li and J.-M. Zhang, J. Mol. Struct., 2004, **687**, 1-6. Copyright 2022 ELSEVIER. 40

Figure 2.18. Gunnlaugsson and co-workers L^{39} and L^{40} ligand architectures, with Φ_{Ln}^{L} for Ln(**L**)$_3$ values taken from reference 93. 41

Figure 2.19. Bünzli and co-workers L^{41} ligand architecture for formation of Ln^{3+} luminescent resins. 41

Figure 3.1. (Left) Ligand **2** coordinating to Ln^{3+} to form a 1:3 metal:ligand species. (Right) Solid Eu(**2**)$_3$(CF$_3$SO$_3$)$_3$ and Tb(**2**)$_3$(CF$_3$SO$_3$)$_3$ crystalline complexes under a microscope, first under ambient light and then shortwave UV irradiation (λ_{ex} = 254 nm). 45

Figure 3.2. Piguet and co-workers PDA ligand system, which is unable to form the 1:3 M:L species due to bulkiness. Obtained from reference 8. 46

Figure 3.3. Ligands **1**-**4**. 46

Figure 3.4. (Top) ^{1}H NMR of intermediate **B** and ligands **1**, **2**, **3** and **4** (300 MHz, DMSO-d$_6$). (Bottom) ^{13}C NMR of intermediate **B** and ligands **1**, **2**, **3** and **4** (75 MHz, DMSO-d$_6$) Abbreviations stand for: py - central pyridyl ring, t - 1,2,3-triazole ring, Bn - benzyl ring, Nap - naphthalene ring, and 4py - 4-pyridine. 48

Figure 3.5. Ball and stick representation of the molecular structures of **1**, **2** and **3**. 49

Figure 3.6. Hydrogen bonding interactions which are occurring between stacked ligands, shown in ball and stick representation. Only one of the crystallographically independent molecules of **2** is shown here. 50

Figure 3.7. Mass spectrum of [Eu(**1**)$_3$](CF$_3$SO$_3$)$_3$ in MeOH (0.01 mM). Insert: experimental isotopic distribution of [Eu(**1**)$_3$](CF$_3$SO$_3$)$^{2+}$ vs calculated. 52

Figure 3.8. Infrared spectra of **1** and Ln(**1**)(CF$_3$SO$_3$)$_3$, where Ln = Eu^{3+}, Tb^{3+} and La^{3+}. Insert: zoom in of carbonyl region, showing shift observed in C=O from ligand to complex alongside the triflate ion frequencies. 53

Figure 3.9. ^{1}H NMR of **1** and La(**1**)$_3$ (Top), **2** and La(**2**)$_3$ (Middle) and **3** and La(**3**)$_3$ (Bottom) done in CDCl$_3$ and MeOD (9:1). Abbreviations: py for central pyridyl ring with P for *para* and M for *meta* positions, t for 1,2,3-triazole ring, Bn for benzyl ring, Nap for naphthalene and x-CH$_2$ indicates the CH$_2$ coordination to an identifiable group x. 54

Figure 3.10. (Top left) UV-visible absorbance spectra of ligands **1** (0.01 mM), **2** (0.01 mM) and **3** (0.005 mM) in MeCN. UV-visible absorbance spectra of ligand **1** (Top right), **2** (Bottom left), and **3** (Bottom right) in MeCN (0.001 mM) and their lanthanide complexes. Insert: zoom in of

absorbance range 240-300 nm associated with the pyridyl unit showing the small red shift upon complexation. 55
Figure 3.11. UV-visible absorption spectrum of hydroxymethyl-1,2,3-triazolylhexadecane (abbreviated to 1,2,3-triazole) (0.01 mM, MeCN). Insert: absorption spectra of **1**, **2**, **3** and hydroxymethyl-1,2,3-triazolylhexadecane (all are 0.01 mM, in MeCN). 56
Figure 3.12. Fluorescence emission and excitation spectra of Eu(**L**)$_3$(CF$_3$SO$_3$)$_3$ (**L** = **1** and **2**) (0.01 mM, MeCN). Inserts: zoom in of 581 nm ($^5D_0 \rightarrow {}^7F_0$) transition and Eu(**1**)$_3$(CF$_3$SO$_3$)$_3$ solid and solution under shortwave UV irradiation (λ_{ex} = 254 nm). 57
Figure 3.13. Fluorescence emission and excitation spectra of Tb(**L**)$_3$(CF$_3$SO$_3$)$_3$ (**L** = **1** and **2**) (0.01 mM, MeCN). Inserts: Tb(**1**)$_3$(CF$_3$SO$_3$)$_3$ solid and liquid under shortwave UV irradiation (λ_{ex} = 254 nm) 57
Figure 3.14. Fluorescence emission and excitation spectra of Tb(**L**)$_3$(CF$_3$SO$_3$)$_3$ (**L** = **1** and **2**) (0.01 mM, MeCN). Insert: La(**3**)$_3$(CF$_3$SO$_3$)$_3$ solution under shortwave UV irradiation (λ_{ex} = 254 nm). 60
Figure 3.15. Eu(**L**)$_3$(CF$_3$SO$_3$)$_3$ and Tb(**L**)$_3$(CF$_3$SO$_3$)$_3$ solids under shortwave UV irradiation (λex = 254 nm) (**L** = **1** in (a) and **2** in (b) and (c)). Image (b) is under a microscope, under ambient light (Left) and under short wave irradiation (Right). 58
Figure 3.16. PDA based ligands with known overall quantum yields from references 16, 17, 23, 33-36. 59
Figure 3.17. Jablonski energy diagram, showing the energy transfer process likely occurring between ligands **1**-**3** with Eu^{3+} and Tb^{3+}. The energy levels are not exact but show relative position in terms of height between one another. This gives a visual insight into the energy level difference between the triplet of the ligand and excited states of the Ln^{3+} and why the BT is so more likely to occur in **3**. Abbreviations: ISC for intersystem crossing and ET for energy transfer. 60
Figure 3.18. UV-visible absorption titration of **1** (0.02 M, MeCN) with Eu(CF$_3$SO$_3$)$_3$·6H$_2$O 0 to 4.5 equivalents, done in triplicate. Insert: monitoring changes in absorbance vs Eu^{3+} equivalents, at λ = 193, 208, 220 and 274 nm 61
Figure 3.19. UV-visible absorption titration of **2** (0.02 M, MeCN) with Eu(CF$_3$SO$_3$)$_3$·6H$_2$O 0 to 4.5 equivalents, done in triplicate. Insert: monitoring changes in absorbance vs Eu^{3+} equivalents, at λ = 207, 274 and 283 nm. 62
Figure 3.20. UV-visible absorption titration of **3** (0.005 M, MeCN) with Eu(CF$_3$SO$_3$)$_3$·6H$_2$O 0 to 4.5 equivalents, done in triplicate. Insert: Monitoring changes in absorbance vs Eu^{3+} equivalents at λ = 204, 274 and 283 nm. 63
Figure 3.21. UV-visible absorption titration of **3** (0.005 M, MeCN) with Eu(CF$_3$SO$_3$)$_3$·6H$_2$O 0 to 4.5 equivalents, monitoring changes in absorbance vs Eu^{3+} equivalents at λ = 225 nm. 63
Figure 3.22. Fluorescence titration of **1** (Top) and **2** (Bottom) (0.02 M, MeCN) with Eu(CF$_3$SO$_3$)$_3$·6H$_2$O 0 to 4.5 equivalents, done in triplicate. Insert: monitoring changes in intensity vs Ln^{3+} equivalents, at λ = 594, 616, 651 and 697 nm. 64
Figure 3.23. Fluorescence titration of **1** (Top) and **2** (Bottom) (0.02 M, MeCN) with Tb(CF$_3$SO$_3$)$_3$·5H$_2$O 0 to 4.5 equivalents, done in triplicate. Insert: monitoring changes in intensity vs Ln^{3+} equivalents, at λ = 490, 545, 587 and 621 nm. 65
Figure 3.24. Fluorescence titration of **3** (0.02 M, MeCN) with Tb(CF$_3$SO$_3$)$_3$·5H$_2$O 0 to 4.5 equivalents, done in triplicate. Insert: monitoring changes in intensity vs Ln^{3+} equivalents, at λ = 336 and 545 nm. 66
Figure 3.25. Fluorescence titration of **3** (0.02 M, MeCN) with Eu(CF$_3$SO$_3$)$_3$·6H$_2$O 0 to 4.5 equivalents, done in triplicate. Insert: monitoring changes in intensity vs Ln^{3+} equivalents, at λ = 336 and 616 nm. 67
Figure 3.26. Fluorescence titration of **3** (0.02 M, MeCN) with La(CF$_3$SO$_3$)$_3$·9H$_2$O 0 to 4.5 equivalents, done in triplicate. Insert: Monitoring changes in intensity vs Ln^{3+} equivalents, at λ = 336 nm. 68
Figure 3.27. Speciation plots of fitted data from UV-visible absorption titrations with **1**, Eu^{3+}, Tb^{3+} and La^{3+}. 71
Figure 3.28. Speciation plots of fitted data from UV-visible absorption titrations with **2**, Eu^{3+}, Tb^{3+} and La^{3+}. 72
Figure 3.29. Speciation plots of fitted data from UV-visible absorption titrations with **3**, Eu^{3+}, Tb^{3+} and La^{3+}. 73
Figure 3.30. Protons of interest in ^{1}H NMR titrations. 74

Figure 3.31. Overall changes in the ^{1}H NMR spectra of **1** (0.001 M, 300 MHz) upon titrating with $La(CF_3SO_3)_3$ (0 – 2 equivalents). 74
Figure 3.32. Overall changes in the ^{1}H NMR spectra of **2** (0.001 M, 300 MHz) upon titrating with $La(CF_3SO_3)_3$ (0 – 2 equivalents). 75
Figure 3.33. Overall changes in the ^{1}H NMR spectra of **3** (0.001 M, 300 MHz) upon titrating with $La(CF_3SO_3)_3$ (0 – 2 equivalents), zoomed in to better see the 1,2,3-triazole position. 76
Figure 3.34. Calculated structure of $[La(\mathbf{1})_3]^{3+}$. 77
Figure 3.35. Calculated structures of $[La(\mathbf{2})_3]^{3+}$ (Left) and $[La(\mathbf{3})_3]^{3+}$ (Right). 78
Figure 3.36. PDC side arms, where sensors or structure directing groups can be simply "clicked" onto the scaffold. 79
Figure 4.1. PDA and PDC motif with 1,2,3-triazole linker. 90
Figure 4.2. Diagram showing the formation of Langmuir films in a Langmuir trough. Initially the barriers are widespread and the area available to the deposited amphiphilic molecules is large enough such that molecular interactions are sparse and in a surface gaseous arrangement. Barrier compression causes the molecules to aggregate into a liquid like phase, forcing interactions between the alkyl chains. Upon enough barrier compression the amphiphilic molecules form an orderly monolayer Langmuir film on top of the subphase, with Van der Waals force interactions between the alkyl chains. 91
Figure 4.3. Kibron G2 Microtrough in which Langmuir isotherms and stabilities were measured on. . 91
Figure 4.4. An example of a surface pressure – area per molecule isotherm measured on a Langmuir trough. Initially the surface pressure is low with minimal interaction between amphiphilic molecules in a gaseous phase. Upon barrier compression associated with the reduction in area per molecule, the amphiphiles are compressed into a liquid compressed or expanded phase. Further compression results in the formation of the orderly Langmuir film, in a solid or compressed phase, with chains orientated in the same direction. Finally additional barrier compression results in a collapse of the Langmuir film. It is worth pointing out that there are two zones where surface pressure has plateaued; this indicates the phase change, but is uncommon to see with long chain amphiphilic molecules and will not be seen in this study's Langmuir isotherms. 92
Figure 4.5. Example of a stability measurement, in which the barrier compression has stopped, in this case at ≈ 30 mN/m. The stable film (of $Eu(\mathbf{5})_3$) is seen to remain at the same surface pressure for an extended period, while the unstable film is seen to drop indicating the film has collapsed. 93
Figure 4.6. Diagram shows how **Z-** and **X**- type mono and multilayer films are deposited onto a solid substrate by emersion or immersion respectively, changing the orientation of the molecules. **Y**-type deposition can be seen in Figure 4.47. 94
Figure 4.7. Luminescent spectrum of multilayer (54 layers) LB film of $Eu(Bh)_3$:$Tb(Bh)_3$ (1:1). Image adapted with permission from V. I. Belyi, A. A. Rastorguev, A. A. Remova, I. A. Badmaeva, S. M. Repinsky and L. L. Sveshnikova, Thin Solid Films, 2002, **419**, 189-193. Copyright 2022, ELSEVIER. 95
Figure 4.8. Pungsheng and co-workers LB isotherms of (A) $Gd(DPM)_3$:AA (1:2), (B) $Eu(DPM)_3$:$Gd(DPM)_3$:AA (2:1:6) and (C) $Eu(DPM)_3$:AA (1:2) measured on an air water interface. Abbreviations: AA - arachidic acid and DPM - 2,2,6,6-tetramethyl-3,5-heptanedionate. Image adapted with permission from Z. Gang, Z. Yanze and H. Pingsheng, Thin Solid Films, 2004, **468**, 268-272. Copyright 2022, ELSEVIER. 96
Figure 4.9. Molecular structure of ligand **5.** 96
Figure 4.10. ^{1}H NMR of mono "clicked" benzyl, with either workup in NH_4OH resulting in amide (Top) or NaOH resulting in protecting group remaining present (Bottom) (300 MHz, $CDCl_3$ & DMSO-d_6). 98
Figure 4.11. Shows the π,σ-bis(copper) acetylide formed in solution with intermediate **B** before the addition of 1-azidohexadecane resulting in a yellow solution colour. After the addition of the azide the solution darkens to a brown colour and potential "click" intermediates are forming; finally, it results in a grey precipitate, which is commonly suspended in a blue copper solution. Click intermediates and π,σ-bis(copper) acetylide are based off those suggested in H. Ben El Ayouchia, L. Bahsis, H. Anane, L. R. Domingo and S.-E. Stiriba, RSC Advances, 2018, **8**, 7670-7678 and round bottom flasks are generated in chemix, https://chemix.org. 100

Figure 4.12. ^{1}H NMR spectra following the synthetic pathway from intermediates **C**, **D**, **E** and 1-azidohexadecane and ligand **5**. Abbreviations: NH for amide protons, M-py for *meta* protons on pyridine ring, P-py for *para* proton on pyridine ring, t for 1,2,3-triazole ring proton, Bn for benzyl ring protons (300 MHz, $CDCl_3$). 101
Figure 4.13. ^{13}C NMR spectra, following the synthetic pathway from intermediates **C**, **D**, **E** and 1-azidohexadecane and ligand **5**. Abbreviations: CO(py) for carbonyl carbons on pyridyl unit, CN(Py) and CH(py) for carbons on pyridyl ring, C(Bn) and CH(Bn) for carbons on benzyl ring, C(t) and CH(t) for carbons on 1,2,3-triazole ring, C(A) and CH(A) for alkyne and a dash (–) indicates it is the carbon attached to the distinguishing feature (75 MHz, $CDCl_3$). 102
Figure 4.14. UV-visible absorption spectrum of **5** in MeCN (0.01 mM). 102
Figure 4.15. Image of crystals of **5** and pipette reactor from which they were grown in. 103
Figure 4.16. The crystallographically independent molecule of **5** in the asymmetric unit and associated hydrogen bonding with the singular DMSO solvent molecule, 50 % ellipsoid representation. 103
Figure 4.17. The overall result of the aforementioned interactions is the formation of sheet-like packing along the crystallographic a-axis. 104
Figure 4.18. Crystal packing along a-axis, representative of potential packing of **Z**-type LB film of **5** deposited on quartz. 104
Figure 4.19. UV-visible titration of **5** (0.02 mM, MeCN) with $Eu(CF_3SO_3)_3{\cdot}6H_2O$ from 0 to 4.5 equivalents. 105
Figure 4.20. Fluorescence titration of **5** (0.02 mM, MeCN) with $Eu(CF_3SO_3)_3{\cdot}6H_2O$ from 0 to 4.5 equivalents. Excitation wavelength 275 nm. 106
Figure 4.21. ReactLab^{TM} Equilibrium generated speciation plot from fluorescence titration in Figure 4.20. 106
Figure 4.22. (Top) HRMS m/z = 1564.8694 $[Eu(\mathbf{5})_3 + H]^+$. (Bottom) Calc. for $(C_{78}H_{121}N_{15}O_9Eu)^+$, 1564.8678. 109
Figure 4.23. FTIR spectrum of **5** and $Eu(\mathbf{5})_3$ showing shift in carbonyl stretches upon complexation and disappearance of the N-H stretch. 109
Figure 4.24. ^{1}H NMR spectrum of $La(\mathbf{5})_3$ (Top) and **5** (Bottom) (300 MHz, $CDCl_3$ & CD_3OD). Abbreviation py for central pyridyl ring with P for *para* and M for *meta* positions, t for 1,2,3-triazole ring and x-CH_2 indicates the CH_2 coordination to an identifiable group x. 110
Figure 4.25. Zoom in of ^{1}H NMR spectrum of $La(\mathbf{5})_3$ (Top) and **5** (Bottom) (300 MHz, DMSO-d_6) with insert showing splitting of pyridyl peaks. 1,2,3-triazole proton does shift upfield in DMSO-d_6 but is an indication of electron density increase, potentially from interaction with solvent; an interaction with La^{3+} would likely result in a downfield shift, as discussed. Abbreviation py for central pyridyl ring with P for para and M for meta positions, t for 1,2,3-triazole ring and x-CH_2 indicates the CH_2 coordination to an identifiable group x. 111
Figure 4.26. $\mathbf{L^{36}}$ and $Sm(\mathbf{L^{36}})_3$ complex (CIF of $Tb(\mathbf{L^{36}})_3$ complex unavailable). Adapted with permission from B.-L. An, M.-L. Gong, M.-X. Li and J.-M. Zhang, J. Mol. Struct., 2004, **687**, 1-6. Copyright 2022 ELSEVIER. 111
Figure 4.27. Calculated $Tb(\mathbf{5})_3$ complex structure with C_3 symmetry. 112
Figure 4.28. Lanthanide complexes $Ln(\mathbf{5})_3$ (a) under ambient light and (b) under shortwave UV irradiation (λ_{ex} = 254 nm): left to right - $Sm(\mathbf{5})_3$, $Dy(\mathbf{5})_3$, $Tb(\mathbf{5})_3$ and $Eu(\mathbf{5})_3$. 113
Figure 4.29. UV-visible absorption of **5**, and $Ln(\mathbf{5})_3$ where Ln = Eu^{3+}, Tb^{3+}, Dy^{3+}, Sm^{3+}, Tm^{3+}, and La^{3+} (0.01 mM, MeCN). 113
Figure 4.30. Fluorescence spectra of $Eu(\mathbf{5})_3$ (Top) and $Tb(\mathbf{5})_3$ (Bottom), with inserts of phosphorescence emission spectra (0.01 mM, MeCN). Excitation wavelength of 275 nm and monitoring wavelengths for excitation spectra 616 nm and 545 nm respectively 114
Figure 4.31. Fluorescence spectra of $Sm(\mathbf{5})_3$ (0.01 mM, MeCN). Excitation wavelength of 275 nm and monitoring wavelengths for excitation spectrum 602 nm. 115
Figure 4.32. Fluorescence spectra of $Dy(\mathbf{5})_3$ (0.01 mM, MeCN). Excitation wavelength of 275 nm and monitoring wavelengths for excitation spectra 480 and 574 nm. 116
Figure 4.33. (Left) CIE 1931 chromaticity diagram with calculated CIE coordinates for emissions of $Ln(\mathbf{5})_3$ complexes (where Ln = Eu^{3+}, Tb^{3+}, Dy^{3+} and Sm^{3+}) in 0.01 mM MeCN. $Eu(\mathbf{5})_3$ x,y = 0.66, 0.34; $Tb(\mathbf{5})_3$ x,y = 0.30, 0.56; $Dy(\mathbf{5})_3$ x,y = 0.33, 0.38 and $Sm(\mathbf{5})_3$ x,y = 0.62, 0.38. (Top right) CIE diagram showing colour of different coordinates. Image and caption are adapted with permission from E. F. Schubert, Light-Emitting Diodes, Cambridge University Press,

Cambridge, 2 edn., 2006. (Bottom right) White light region of the CIE 1931 chromaticity diagram; not all points within this region give "pure-white", but are still considered as white. Image and caption adapted from open access and CC-BY article from D. N. Anwar and A. Srivastava, IEEE Access, 2020, **8**, 159609-159621. 116
Figure 4.34. Molecular structure of **L^{44}** from reference 105. 118
Figure 4.35. Lanthanide complexes Ln(**5**)$_3$ under shortwave UV irradiation (λ_{ex} = 254 nm): left to right - Sm(**5**)$_3$, Dy(**5**)$_3$, Eu(**5**)$_3$ and Tb(**5**)$_3$ 119
Figure 4.36. Surface area – pressure isotherms of **5**. 120
Figure 4.37. Surface area – pressure isotherms of Ln(**5**)$_3$ (where Ln = Eu^{3+}, Tb^{3+}, Dy^{3+}, Sm^{3+} and La^{3+}). Insert: Stability measurements held at 30 mN m^{-1} for over 60 minutes. 121
Figure 4.38. LB deposition plot of area of trough (between barriers) (mm) vs time (s), showing trough area decrease of approximately 1300 mm during deposition. (a) Eu(**5**)$_3$, (b) Tb(**5**)$_3$, (c) Dy(**5**)$_3$, and (d) Sm(**5**)$_3$. 122
Figure 4.39. LB films of Ln(**5**)$_3$, (where Ln = Eu^{3+}, Tb^{3+}, Dy^{3+} and Sm^{3+}) shown under shortwave UV irradiation (a, λ_{ex} = 254 nm) and ambient light (b). From left to right LB films are Eu(**5**)$_3$, Sm(**5**)$_3$, Dy(**5**)$_3$, Tb(**5**)$_3$, and a blank slide. 123
Figure 4.40. UV-visible absorption spectra of LB film. 123
Figure 4.41. Phosphorescence emission and excitation plots of Eu(**5**)$_3$ (Top) and Tb(**5**)$_3$ (Bottom) of both LB films (solid lines) and in solution MeCN (0.01 mM) (dashed line). Inserts: images of the monolayer LB films of Eu(**5**)$_3$ (Top) and Tb(**5**)$_3$ (Bottom). 124
Figure 4.42. Phosphorescence emission and excitation plots of Sm(**5**)$_3$ (Top) and Dy(**5**)$_3$ (Bottom) of both LB films (solid lines except for an excitation plot of Dy(**5**)$_3$ at 574 nm for visibility) and in solution MeCN (0.01 mM) (dashed line). Inserts: images of the monolayer LB films of Sm(**5**)$_3$ (Top) and Dy(**5**)$_3$ (Bottom). 125
Figure 4.43. CIE 1931 chromaticity diagram with calculated CIE coordinates for both LB film and solutions (abbreviated to Sol) emissions of Ln(**5**)$_3$ complexes (where Ln = Eu^{3+}, Tb^{3+}, Dy^{3+} and Sm^{3+}). Eu(**5**)$_3$ LB film x,y = 0.66, 0.34 and solution x,y = 0.66, 0.34; Tb(**5**)$_3$ LB film x,y = 0.30, 0.57 and solution x,y = 0.30, 0.56; Dy(**5**)$_3$ LB film x,y = 0.34, 0.39 and solution x,y = 0.33, 0.38 and Sm(**5**)$_3$ LB film x,y = 0.60, 0.40 and solution x,y = 0.62, 0.38. 125
Figure 4.44. XPS vacuum chamber window showing LB slides inside. 126
Figure 4.45. Survey scan XPS spectrum of Eu(**5**)$_3$ monolayer LB film. Insert: Core level scans. 127
Figure 4.46. (Top) LB films fresh after deposition and (Bottom) LB films 6 months after initial deposition. 127
Figure 4.47. Diagram shows Eu(**5**)$_3$ as an amphiphilic molecule, which has formed a **Y**-type LB film, by emersion and immersion Blodgett deposition of the Langmuir film, all shown in the diagram. 128
Figure 4.48. Image of monolayer and multilayered LB films of Eu(**5**)$_3$ with 1, 3, 5, and 7 layers from left to right. 128
Figure 4.49. Deposition plots of multilayer Eu(**5**)$_3$ (Top, left) 3 layered film, (Top right) 5 layered film and (Bottom) 7 layered film. 129
Figure 4.50. UV-visible absorption (Left) and phosphorescence emission spectra (Right) of multilayered Eu(**5**)$_3$ films. 130
Figure 4.51. (Left) FTIR spectrum of 8 layered Eu(**5**)$_3$ LB film on CaF_2 slide. (Right) 8 layered Eu(**5**)$_3$ LB film on CaF_2 slide. 130
Figure 4.52. Diagram shows the multilayering **Z**-type mixed LB film, with an example of an initial Eu(**5**)$_3$ emersion followed by a 2nd emersion of Tb(**5**)$_3$ resulting in the Eu(**5**)$_3$: Tb(**5**)$_3$ multilayer film. 131
Figure 4.53. Mixed multilayered Eu(**5**)$_3$:Tb(**5**)$_3$ LB film fluorescence spectrum showing both Ln^{3+} distinct emission transitions. Insert: image is Eu(**5**)$_3$:Tb(**5**)$_3$ mixed multilayered film in the centre with a monolayer Eu(**5**)$_3$ film on the left and Tb(**5**)$_3$ on the right under shortwave UV irradiation (λ_{ex} = 254 nm). 132
Figure 4.54. Mixed multilayered Eu(**5**)$_3$:Dy(**5**)$_3$ LB film fluorescence spectrum showing both Ln^{3+} distinct emission transitions. Insert: image is Eu(**5**)$_3$:Dy(**5**)$_3$ mixed multilayered film in the centre with a monolayer Dy(**5**)$_3$ film on the left and Eu(**5**)$_3$ on the right under shortwave UV irradiation (λ_{ex} = 254 nm). 133
Figure 4.55. Eu(**5**)$_3$:Tb(**5**)$_3$:Dy(**5**)$_3$ mixed multilayered film on the right end, with monolayer Eu(**5**)$_3$, Tb(**5**)$_3$ and Dy(**5**)$_3$ films from left to right. Under shortwave UV irradiation (λ_{ex} = 254 nm) 133

Figure 4.56. Mixed multilayered Eu(**5**)$_3$:Tb(**5**)$_3$:Dy(**5**)$_3$ LB film fluorescence spectrum showing most of the Ln^{3+} distinct emission transitions. 134
Figure 4.57. CIE 1931 chromaticity diagram with calculated CIE coordinates for emissions of Ln(**5**)$_3$ complexes (where Ln = Eu^{3+}, Tb^{3+}, Dy^{3+} and Sm^{3+}) of monolayer LB films and mixed multilayer LB films. Eu(**5**)$_3$ x,y = 0.66, 0.34; Tb(**5**)$_3$ x,y = 0.30, 0.56; Dy(**5**)$_3$ x,y = 0.33, 0.38; Sm(**5**)$_3$ x,y = 0.62, 0.38; Eu(**5**)$_3$:Tb(**5**)$_3$ x,y = 0.47, 0.45; Eu(**5**)$_3$:Dy(**5**)$_3$ x,y =0.56, 0.36 and Eu(**5**)$_3$:Tb(**5**)$_3$:Dy(**5**)$_3$ x,y = 0.42, 0.47. 134
Figure 4.58. (Left) 0.1 mM solution of Eu(**5**)$_3$, Eu(**5**)$_3$:Tb(**5**)$_3$ (1:1) and Tb(**5**)$_3$ in MeOH under shortwave UV irradiation (λ_{ex} =254 nm). (Right) CIE chromaticity diagram with calculated CIE 1931 coordinates of 0.01 mM solution of Eu(**5**)$_3$ (x,y = 0.66, 0.34), Eu(**5**)$_3$:Tb(**5**)$_3$ (1:1) (x,y = 0.45, 0.48) and Tb(**5**)$_3$ (x,y = 0.3, 0.56) in MeOH 135
Figure 4.59. Surface area – pressure isotherms of Eu(**5**)$_3$ and different complex combinations. Insert: Stability measurements held at ≈ 30 mN/m for over 60 minutes. 136
Figure 4.60. Fluorescence spectra of the different variations of Eu(**5**)$_3$:Tb(**5**)$_3$ in solution and as LB films both multilayered and monolayered. Insert: Image shows the different variations of Eu(**5**)$_3$:Tb(**5**)$_3$ including: 0.1 mM MeOH solution, mixed multilayered film, and mixed monolayer film (left to right) under shortwave UV irradiation. 136
Figure 4.61. (Left) CIE 1931 chromaticity diagram with calculated CIE coordinates of Eu(**5**)$_3$:Dy(**5**)$_3$ ratios: (0:1) x,y = 0.33, 0.38, (1:0) x,y = 0.67, 0.34, (1:1), x,y = 0.60, 0.35, (1:3) x,y = 0.48, 0.37, (1:10) x,y = 0.44, 0.38, and (1:20) x,y =0.38, 0.38. (Right) CIE 1931 chromaticity diagram with calculated CIE coordinates of Sm(**5**)$_3$:Dy(**5**)$_3$ ratios: (0:1) x,y = 0.33, 0.38, (1:0) x,y = 0.6, 0.38, (1:1), x,y = 0.48, 0.48, (1:10) x,y = 0.40, 0.38, and (1:20) x,y =0.35, 0.38. 137
Figure 4.62. Fluorescence emission spectra of Eu(**5**)$_3$:Dy(**5**)$_3$ (1:10) in solution (0.01 mM MeOH) and as a monolayer film. Insert: image of Eu(**5**)$_3$:Dy(**5**)$_3$ (1:10) film in the centre with Eu(**5**)$_3$ (left) and Dy(**5**)$_3$ (right) under shortwave UV irradiation (λ_{ex} = 254 nm). 138
Figure 4.63. Fluorescence emission spectra of Eu(**5**)$_3$:Dy(**5**)$_3$ (1:1) in solution (0.01 mM MeOH), as a monolayer and multilayer film. 138
Figure 4.64. Image of three monolayer LB films of Ln(**5**)$_3$ (where Ln^{3+} = Eu^{3+}, $Tb^{3+}$and Dy^{3+} respectively) and the final triple mixed monolayer LB film of Eu(**5**)$_3$:Tb(**5**)$_3$:Dy(**5**)$_3$ (1:1:10) on the right, all under shortwave UV irradiation (λ_{ex} = 254 nm). 139
Figure 4.65. (Top) Image of all four monolayer LB films of Ln(**5**)$_3$ (where Ln = Eu^{3+}, Sm^{3+}, Dy^{3+} and Tb^{3+} respectively) and the final quadruple mixed monolayer LB film of Eu(**5**)$_3$:Tb(**5**)$_3$:Dy(**5**)$_3$:Sm(**5**)$_3$ (1:1:1:10) on the right, all under shortwave UV irradiation. (Bottom) Fluorescence spectrum of Eu(**5**)$_3$:Tb(**5**)$_3$:Dy(**5**)$_3$:Sm(**5**)$_3$ (1:1:1:10) showing distinct transition from all four Ln(**5**)$_3$ complexes (where Ln = Eu^{3+}, Sm^{3+}, Dy^{3+} and Tb^{3+}). The assigned major emission is listed first if there are multiple emissions for the region. 140
Figure 4.66. Enclosed window scan of Eu(**5**)$_3$:Tb(**5**)$_3$:Dy(**5**)$_3$:Sm(**5**)$_3$ (1:1:1:1) monolayer LB film (a total of 10 scans). With Eu^{3+} $3d_{3/2}$ = 1164 and $3d_{5/2}$ = 1134 eV, expected being 1136 and 1166 eV, Tb^{3+} $3d_{3/2}$ = 1175 and $3d_{5/2}$ = 1141 eV, expected being 1176 and 1141 eV, Dy^{3+} $3d_{3/2}$ = 1334 and $3d_{5/2}$ = 1295 eV, expected being 1333 and 1296 eV and with Sm^{3+} $3d_{3/2}$ = 1108 and $3d_{5/2}$ = 1082 eV, expected being 1108 and 1281 eV. 140
Figure 4.67. CIE 1931 chromaticity diagram with calculated CIE coordinates for emissions of Ln(**5**)$_3$ complexes (where Ln = Eu^{3+}, Tb^{3+}, Dy^{3+} and Sm^{3+}) of monolayer LB films and mixed monolayer LB films. Eu(**5**)$_3$ x,y = 0.66, 0.34; Tb(**5**)$_3$ x,y = 0.30, 0.56; Dy(**5**)$_3$ x,y = 0.33, 0.38; Sm(**5**)$_3$ x,y = 0.62, 0.38; Eu(**5**)$_3$:Tb(**5**)$_3$ (1:1) x,y = 0.46, 0.46; Eu(**5**)$_3$:Dy(**5**)$_3$ (1:1) x,y = 0.56, 035 and (1:10) x,y = 0.41, 0.37; Eu(**5**)$_3$:Tb(**5**)$_3$:Dy(**5**)$_3$ (1:1:1) x,y = 0.44, 0.42 and (1:1:10) x,y = 0.39, 0.48; Eu(**5**)$_3$:Tb(**5**)$_3$:Dy(**5**)$_3$:Sm(**5**)$_3$ (1:1:1:1) x,y = 0.43, 0.48, (1:1:10:10) x,y = 0.41, 0.45 and (1:1:10:50) x,y = 0.44, 0.41. 142
Figure 4.68. Potential colour-tunable emission regions with combinations of different ratios of Ln(**5**)$_3$ (where Ln = Eu^{3+}, Tb^{3+}, Dy^{3+} and Sm^{3+}) 143
Figure 4.69. Potential modification avenue for **5** from the back para position of the PDC scaffold unit. 144
Figure 5.1. CIE 1931 chromaticity diagram showing the potential of emission ranges of colour-tunable emission when combined with red emission from Eu^{3+}, green emission from Tb^{3+} and blue emission from organic aromatic 1,8-naphthalimide and pyrene. Position and lines are not accurate but are in a reasonable location as to what is expected. 155

Figure 5.2. Examples of potential 1,8-naphthalimide based chromophores with different dominant emission which could be coupled with Ln^{3+} to form a range of dual emissive complexes. Green emissive 1,8-naphthalimide from J. E. Elbert, S. Paulsen, L. Robinson, S. Elzey and K. Klein, J. Photochem. Photbiol, 2005, **169**, 9-19; Red emissive 1,8-naphthalimide C. J. Christopherson, D. M. Mayder, J. Poisson, N. R. Paisley, C. M. Tonge and Z. M. Hudson, ACS Appl. Mater. Interfaces, 2020, **12**, 20000-20011; Yellow emissive 1,8-naphthalimide from Y. Yin, Z. Chen, C. Fan, G. Liu and S. Pu, ACS Omega, 2019, **4**, 14324-14332. 156

Figure 5.3. Simplistic diagram showing the stages of spin coating, with the initial **deposition**, followed by **spin up/off** and the final **evaporation** stage leaving a molecular film. 157

Figure 5.4. Aromatic "clicked" PDA (**7**) and PDC (**6** and **8**) ligands. It is worth noting that a bis clicked **NI** PDA system has also been synthesised - this was made in case the blue emission from a single **NI** was not emissive enough for white emission, but as results will show this was unnecessary and further showcases the benefits of the PDC motif. 158

Figure 5.5. Examples of monomer and aggregation induced excimer emission from ligand **6** when titrated with $Eu(CF_3SO_3)_3$, further discussed in detail in later sections. 159

Figure 5.6. Jablonski energy diagram, showing the potential pathway of the absorbed UV energy to either emit through monomer or excimer chromophore emission, or to undergo intersystem crossing (ISC) and energy transfer (ET) to the Ln^{3+}. The energy levels are not accurate but have height positions based off **NI** and Eu^{3+}. Reference D. W. Cho and D. W. Cho, New J. Chem., 2014, **38**, 2233-2236 is used as a guide for excimer energy level positioning on the diagram. 160

Figure 5.7. Ward and co-workers' DOTA based **NI** antenna system capable of white light emission in MeCN. Image adapted with permission from A. H. Shelton, I. V. Sazanovich, J. A. Weinstein and M. D. Ward, Chem. Commun., 2012, **48**, 2749-2751. Copyright 2022 Royal Society of Chemistry. 160

Figure 5.8. Yan and co-workers' simplistic **NI** based complexes, in which overall emission is tunable by increasing or decreasing the alkyl linker chain to modify the ISC effects of the **NI** antenna, resulting in the drastic change from overall red emission to extremely close to white emission. Image adapted with permission from J. Zhang, H. Li, P. Chen, W. Sun, T. Gao and P. Yan, J. Mater. Chem. C, 2015, **3**, 1799-1806. Copyright 2022 Royal Society of Chemistry. 161

Figure 5.9. Prasad and co-workers' white emissive gel, made from poly(arylether)dendron, coordinated to a mixture of Eu^{3+} and Tb^{3+} as well as forming donor-acceptor pairs with **PYR** donor, suggested to be associated with the benzyl ester motif. Images adapted with permission from reference P. Kumar, S. Soumya and E. Prasad, ACS Appl. Mater. Interfaces, 2016, **8**, 8068-8075. Copyright American Chemical Society. 162

Figure 5.10. (Top) Oh and co-worker MOF structure and components utilized to form white emissive crystals. (Bottom) Oh and co-worker MOF structure with a Eu^{3+}:Tb^{3+} (0.1:0.9) ratio and H_2L and H_2BDC (0.025:0.975) ratio in order to achieve close to white solid emission which is also colour-tunable. (A) Shows the fluorescence emission changes as excitation wavelength changes and (B) shows corresponding overall emission colour on a CIE 1931 chromaticity diagram. Images adapted with permission from J. Park and M. Oh, CrystEngComm, 2016, 18, 8372-8376. Copyright 2022 Royal Society of Chemistry. 163

Figure 5.11. Aromatic "clicked" PDA (**7**) and PDC (**6** and **8**) ligands. 164

Figure 5.12. ^1H NMR of **6** via different deprotection methods. (Top/green) The resulting product when intermediate **I** is "deprotected" with 1 eq. NaOH, resulting in only suspected starting material 1,8-naphthalic anhydride. (Middle/blue) The initial result when intermediate **I** is deprotected via LiOH, showing presence of cleaved 1,8-naphthalic anhydride, which is not present in **I** (see Figure 5.13). (Bottom/black) Resulting product **6** after washing with acetone. 167

Figure 5.13. ^1H NMR of **6** and its corresponding starting materials and intermediate **I**. Abbreviations: Nap-a for ortho and para protons of **NI**, Nap-b for meta protons of **NI**, py for pyridine ring, t for 1,2,3-triazole, and Bn for benzyl ring. Dash (-) indicates the group that the CH_2 (which is associated with this signal) is bonded to. 169

Figure 5.14. ^1H NMR of ligand **8** and its corresponding starting materials and intermediate **L**. Abbreviations: py for pyridine ring, **PYR** for pyrene ring, t for 1,2,3-triazole, and Bn for benzyl

ring. Dash (-) indicates the group that the CH_2 (which is associated with this signal) is bonded to. 169
Figure 5.15. ^{1}H NMR of **7** and its corresponding starting materials. Abbreviations: Nap-a for ortho and para protons of **NI**, Nap-b for meta protons of **NI**, py for pyridine ring, t for 1,2,3-triazole, and Bn for benzyl ring. Dash (-) indicates the group that the CH_2 (which is associated with this signal) is bonded to. 170
Figure 5.16. ^{13}C NMR of **6** and its corresponding starting materials and intermediate **I**. Abbreviation: Nap for **NI** carbons, py for pyridine carbons, t for 1,2,3-triazole carbons, CN for non-saturated carbons of the pyridine ring, and Bn for benzyl carbons. 170
Figure 5.17. Ball and stick representation of **7** showing hydrogen bonding occurring between ligand and solvent DMF. 171
Figure 5.18. Acute angles δ and Θ between the centroid-centroid vector (line distance) and the aromatic plane which have been measured**.** Image adapted with permission from Y. Zhao, J. Li, H. Gu, D. Wei, Y. C. Xu, W. Fu and Z. Yu, Interdiscip Sci, 2015, **7**, 211-220. Copyright 2022 SpringerLink. 171
Figure 5.19. OLEX2 generated image, showing planes which were formed to find all π-π stacking interactions. Labels are used to indicate the individual ring which π-π stacking is occurring with. 172
Figure 5.20. (Top) π - π stacking interactions found by OLEX2 software and given centroid-centroid distances. For context, the central pyridyl ring π - π stacking is occurring mainly in the centre of the image, the N7 **NI** ring offset π - π stacking with itself is occurring on the right, and N11 **NI** system's extensive π - π stacking interactions is seen on the left. (Bottom) The overall resulting chain generated by the unique π - π stacking interactions. 172
Figure 5.21. Weak hydrogen bonding interactions occurring between 1,2,3-triazole rings and carbonyl, likely due to the close interaction brought about from π - π stacking interactions. 173
Figure 5.22. Overall packing of **8**, looking down the different axes. 173
Figure 5.23. (Left) Ball and stick representation of intermediate **I**. (Right) Hydrogen bonding occurring between the PDC pocket and naphthalimide CH ring proton. 174
Figure 5.24. π - π stacking and hydrogen bonding found within **7**, calculated by OLEX2. Insert: **I** with label used to define centroids. 175
Figure 5.25. Stacked sheets of **I** when viewed down the b-axis. When crystal packing is viewed down the c-axis it shows the zig zag π- π stacking interactions 175
Figure 5.26. Ball and stick representation of intermediate **L.** 176
Figure 5.27. Hydrogen bonding interactions occurring between **L** and water. 176
Figure 5.28. Weak π - π stacking occurring between **PYR** rings. 177
Figure 5.29. (Left) Shows the π - π stacked interactions viewed down the a-axis. (Right) Sheet like packing observed down the b-axis. 177
Figure 5.30. (Top) Ball and stick representation of **8.** (Bottom) CH/π interactions observed between two molecules of **8**. 179
Figure 5.31. UV-visable absorption spectra of **6** and **7** (0.01 mM, MeOH). 179
Figure 5.32. Fluorescence emission and excitation spectra of **6** and **7** (0.01 mM, MeOH). Insert: CIE chromaticity diagram, with CIE 1931 coordinates of the resulting emission of **6** x,y = 0.16, 0.05 and **7** x,y = 0.17, 0.25. 180
Figure 5.33. Solid powders of Ligands **6** (Left) and **7** (Right) under longwave UV irradiation (λ_{ex} = 365nm). 180
Figure 5.34. UV-visible absorption spectra of **8** and **K** (0.01 mM, MeOH) to show similarity between ligand and precursor. 181
Figure 5.35. Fluorescence emission and excitation spectra of **8** (0.01 mM, MeOH) **-** other excitation wavelengths were tested, and all resulted in similar emission profiles. Inserts: CIE chromaticity diagram, with CIE 1931 coordinates of the resulting emission of **8** x, y = 0.15, 0.03 and image of solid powder **8** under longwave UV irradiation (λ_{ex} = 365 nm). 181
Figure 5.36. UV-visible absorption of **6** (0.02 mM, MeOH) titrated with $Eu(CF_3SO_3)\cdot 6H_2O$ in MeOH. 182
Figure 5.37. Monitoring changes in UV-visible absorption at 232, 274 and 333 nm of **6** (0.02 mM, MeOH) titrated with $Eu(CF_3SO_3)\cdot 6H_2O$ in MeOH from 0 to 1 equivalents (Top) and from 0 to 4.5 equivalents (Bottom). 183
Figure 5.38. Fluorescence of **6** (0.02 mM, MeOH) titrated with $Eu(CF_3SO_3)\cdot 6H_2O$ in MeOH. 184

Figure 5.39. Monitoring changes of fluorescence emission of **6** (0.02 mM, MeOH) titrated with $Eu(CF_3SO_3)\cdot 6H_2O$ in MeOH at a specific point of interest. 185
Figure 5.40. Speciation plot of fluorescence titration of **6** with $Eu(CF_3SO_3)_3$ 186
Figure 5.41. (Top) UV-visible absorption of **7** (0.02 mM, MeOH) titrated with $Eu(CF_3SO_3)\cdot 6H_2O$ in MeOH. Insert: monitoring changes at 278 nm. (Bottom) UV-visible absorption of **7** (0.02 mM, MeOH) titrated with $Eu(CF_3SO_3)\cdot 6H_2O$ in MeOH monitoring changes at 232 and 332 nm. 187
Figure 5.42. (Top) Fluorescence of **7** (0.02 mM, MeOH) titrated with $Eu(CF_3SO_3)\cdot 6H_2O$ in MeOH. (Bottom) Monitoring changes at 380, 480, and 616 nm. Insert: Monitoring changes at 380 and 480 nm between 0 to 1 equivalents. 188
Figure 5.43. Speciation plot of fluorescence titration of **7** with $Eu(CF_3SO_3)_3$ 189
Figure 5.44. UV-visible absorption of **8** (0.02 mM, MeOH) titrated with $Eu(CF_3SO_3)\cdot 6H_2O$ in MeOH. Inserts: monitoring changes at 283 and 242 nm. 190
Figure 5.45. Fluorescence of **8** (0.02 mM, MeOH) titrated with $Eu(CF_3SO_3)\cdot 6H_2O$ in MeOH. 191
Figure 5.46. Fluorescence of **3** (0.02 mM, MeOH) titrated with $Eu(CF_3SO_3)\cdot 6H_2O$ in MeOH, monitoring changes at 395, 475, and 616 nm. 191
Figure 5.47. Speciation plot of fluorescence titration of **8** with $Eu(CF_3SO_3)_3$ 192
Figure 5.48. IR spectrum of **6** vs Eu(**6**)$_3$. Insert: zoom in of the carbonyl region, seeing visible shifts and disappearances noted in the text. 195
Figure 5.49. ^{1}H NMR of **6** and La(**6**)$_3$. Abbreviations: Nap for **NI**, t for 1,2,3-triazole ring and x-CH_2 indicates the CH_2 coordination to an identifiable group (DMSO-d_6). 196
Figure 5.50. ^{1}H NMR of **8** and La(**8**)$_3$. Abbreviations: py for pyridyl, **PYR** for pyrene, t for 1,2,3-triazole ring and x-CH_2 indicates the CH_2 coordination to an identifiable group (DMSO-d_6). 196
Figure 5.51. ^{1}H NMR of **7** and La(**7**)$_3$. Abbreviations: py for pyridyl ring, Nap for **NI**, t for 1,2,3-triazole ring, o - *ortho*, m - *meta* and p - *para* (3:1, $CDCl_3$:CD_3OD). 197
Figure 5.52. Ligands used in complexes, for bond length comparison. 198
Figure 5.53. Calculated Eu(**6**)$_3$ complex structure with C_3 symmetry. 198
Figure 5.54. Calculated $[Eu(\mathbf{7})_3]^{3+}$complex structure with C_3 symmetry. 199
Figure 5.55. Calculated Eu(**8**)$_3$ complex structure with C_3 symmetry. 199
Figure 5.56. Fluorescence spectra of Eu(**6**)$_3$ (0.01 mM, MeOH). 200
Figure 5.57. Fluorescence spectra of $[Eu(\mathbf{7})_3](CF_3SO_3)_3$ (0.01 mM, MeCN). 201
Figure 5.58. Fluorescence spectra of Eu(**8**)$_3$ (0.01 mM, MeOH). 201
Figure 5.59. Fluorescence spectra of Eu(**6**)$_3$ (0.01 mM, MeCN). 203
Figure 5.60. Eu(**6**)$_3$ solid powder, under ambient light, shortwave UV irradiation (λ_{ex} = 254 nm) and longwave UV irradiation (λ_{ex} = 365 nm), from left to right. 204
Figure 5.61. Fluorescence profiles of Eu(**6**)$_3$ solid, showing change in monomer, excimer and Eu^{3+} emission as excitation wavelength changes. 204
Figure 5.62. CIE 1931 chromaticity diagram with different overall colours capable of Eu(**6**)$_3$ dependent on λ_{ex}. Calculated CIE coordinates: 250 nm x,y = 0.21, 0.25; 251 nm x,y = 0.23 ,0.25; 253 nm x,y = 0.24, 0.27; 255 nm x,y = 0.26, 0.28; 260 nm x,y = 0.28, 0.29; 265 nm x,y = 0.29, 0.29; 270 nm x,y = 0.31 ,0.29; 271-272 nm x,y = 0.31, 0.29 ; 273-278 nm x,y = 0.32, 0.29; 278-280 nm x,y = 0.31, 0.29 ; 281-286 nm x,y = 0.30, 0.29; 287 nm x,y = 0.29, 0.29; 288 nm x,y = 0.28, 0.29; 289 nm x,y = 0.26, 0.29; 290 nm x,y = 0.24, 0.28; 295 nm x,y = 0.20, 0.28; 300 nm x,y = 0.19, 0.27; 310 nm x,y = 0.18, 0.26 and 350 nm x,y = 0.18, 0.26. 205
Figure 5.63. Eu(**6**)$_3$ solid and 0.01 mM MeCN solution under longwave irradiation (Left, λ_{ex} = 254 nm) and shortwave irradiation (Right, λ_{ex} = 365 nm). 205
Figure 5.64. CIE 1931 chromaticity diagram with different overall colours capable of Eu(**6**)$_3$ in 0.01 mM MeOH solution dependent on λ_{ex} and fluorescence spectra of important λ_{ex}. Calculated CIE coordinates: 235 nm x,y = 0.25, 0.21; 240 nm x,y = 0.28 ,0.23; 255 nm x,y = 0.47, 0.29; 260 nm x,y = 0.50, 0.29; 275 nm x,y = 0.54, 0.30; 280 nm x,y = 0.50, 0.30; 270 nm x,y = 0.31 ,0.29; 271-272 nm x,y = 0.31, 0.29 ; 273-278 nm x,y = 0.32, 0.29; 278-280 nm x,y = 0.31, 0.29 ; 286 nm x,y = 0.45, 0.29; 287 nm x,y = 0.42, 0.28; 288 nm x,y = 0.38, 0.27; 289 nm x,y = 0.34, 0.27; 290 nm x,y = 0.34, 0.27; 291 nm x,y = 0.27, 0.23; 293 nm x,y = 0.20, 0.22; 296 nm x,y = 0.20, 0.22 and 330 nm x,y = 0.18, 0.20. 206
Figure 5.65. CIE 1931 chromaticity diagram with different overall colours capable of Eu(**6**)$_3$ in 0.01 mM MeCN solution dependent on λ_{ex} and fluorescence spectra of important λ_{ex}. Calculated CIE coordinates: 230 nm x,y = 0.23, 0.24; 240 nm x,y = 0.24 ,0.25; 250 nm x,y = 0.35, 0.27; 255

nm x,y = 0.38, 0.28; 260 nm x,y = 0.41, 0.29; 265 nm x,y = 0.50, 0.30; 270 nm x,y = 0.31 ,0.29; 271-272 nm x,y = 0.31, 0.29 ; 273-278 nm x,y = 0.32, 0.29; 278-280 nm x,y = 0.43, 0.29 ; 270 nm x,y = 0.44, 0.30; 275 nm x,y = 0.44, 0.30; 280 nm x,y = 0.41, 0.29; 285 nm x,y = 0.40, 0.29; 290 nm x,y = 0.29, 0.27; 295 nm x,y = 0.21, 0.25 and 300 nm x,y = 0.19, 0.25. 207

Figure 5.66. Eu(**6**)$_3$ in MeOH solutions with 10, 5, 1, 0.01 mM concentrations left to right, under shortwave UV irradiation (white and red) and under longwave UV irradiation (blue). 207

Figure 5.67. CIE 1931 chromaticity diagram with different overall colours capable of Eu(**6**)$_3$ in a 10 mM MeOH solution dependent on λ_{ex} and fluorescence spectra of important λ_{ex}. Calculated CIE coordinates: 230 nm x,y = 0.19, 0.23; 240 nm x,y = 0.19 ,0.23; 250 nm x,y = 0.21, 0.24; 255 nm x,y = 0.24, 0.25; 260 nm x,y = 0.25, 0.25; 265nm x,y = 0.27, 0.26; 270 nm x,y = 0.28 ,0.26; 275 nm x,y = 0.26, 0.26 ; 280 nm x,y = 0.26, 0.28; 290 nm x,y = 0.20, 0.24 and 300 nm x,y = 0.17, 0.23. 208

Figure 5.68. CIE 1931 chromaticity diagram with different overall colours capable of Eu(**6**)$_3$ in a 5 mM MeOH solution dependent on λ_{ex} and fluorescence spectra of important λ_{ex}. Calculated CIE coordinates: 230 nm x,y = 0.20, 0.25; 240 nm x,y = 0.20 ,0.25; 250 nm x,y = 0.24, 0.27; 260 nm x,y = 0.28, 0.27; 261 nm x,y = 0.28, 0.27; 261 nm x,y = 0.29, 0.27; 262-273 nm x,y = 0.30, 0.27; 275 nm x,y = 0.30, 0.26; 277 nm x,y = 0.29 ,0.26; 280 nm x,y = 0.28, 0.26 ; 285 nm x,y = 0.25, 0.25; 290 nm x,y = 0.20, 0.23 and 300 nm x,y = 0.18, 0.23. 208

Figure 5.69. CIE 1931 chromaticity diagram with different overall colours capable of Eu(**6**)$_3$ in 1 mM MeOH solution dependent on λ_{ex} and fluorescence spectra of important λ_{ex}. Calculated CIE coordinates: 230 nm x,y = 0.22, 0.24; 240 nm x,y = 0.23 ,0.25; 250 nm x,y = 0.33, 0.28; 251 nm x,y = 0.34, 0.28; 252 nm x,y = 0.35, 0.28; 253 nm x,y = 0.36, 0.28; 254 nm x,y = 0.37, 0.28; 255 nm x,y = 0.37, 0.29; 256 nm x,y = 0.38, 0.29; 257 nm x,y = 0.39, 0.29; 258-260 nm x,y = 0.40, 0.9; 261-264 nm x,y = 0.42, 0.29; 265-266 nm x,y = 0.43, 0.29; 267-275 nm x,y = 0.44, 0.29; 277 nm x,y = 0.42, 0.28; 280 nm x,y = 0.41, 0.28; 285 nm x,y = 0.34, 0.27; 290 nm x,y = 0.24, 0.24 and 300 nm x,y =0.18, 0.22. 209

Figure 5.70. Solid powder of [Eu(**7**)$_3$](CF$_3$SO$_3$)$_3$, under ambient light, longwave irradiation (λ_{ex} = 365 nm), and shortwave irradiation (λ_{ex} = 254 nm), from left to right. 209

Figure 5.71. CIE 1931 chromaticity diagram with different overall colours capable of [Eu(**7**)$_3$](CF$_3$SO$_3$)$_3$ in 0.01 mM MeCN solution dependent on λ_{ex} and fluorescence spectrum of important λ_{ex}. Calculated CIE coordinates: 240 nm x,y = 0.15, 0.24; 250 nm x,y = 0.19, 0.22; 270 nm x,y = 0.22, 0.23; 290 nm x,y = 0.20, 0.22 and 300 nm x,y = 0.17, 0.21. 210

Figure 5.72. Solid powder of Eu(**8**)$_3$ under ambient light, longwave irradiation (λ_{ex} = 365 nm), and shortwave irradiation (λ_{ex} = 254 nm), from left to right. 210

Figure 5.73. CIE 1931 chromaticity diagram with different overall colours capable of Eu(**8**)$_3$ in 0.01 mM MeOH solution dependent on λ_{ex} and fluorescence spectra of important λ_{ex}. Calculated CIE coordinates: 240 nm x,y = 0.19, 0.16; 245 nm x,y = 0.22, 0.19; 250nm x,y = 0.30, 0.22; 270 nm x,y = 0.31, 0.24; 280 nm x,y = 0.37, 0.26; 285 nm x,y = 0.41, 0.27; 290 nm x,y = 0.25, 0.29. 211

Figure 5.74. CIE 1931 chromaticity diagram with different overall colours capable of Eu(**8**)$_3$ in 5 mM MeOH solution dependent on λ_{ex} and fluorescence spectra of important λ_{ex}. Calculated CIE coordinates: 240 nm x,y = 0.26, 0.33; 250 nm x,y = 0.30, 0.32; 270 nm x,y = 0.32, 0.33; 280 nm x,y = 0.33, 0.32; 281 nm x,y = 0.35, 0.32; 282 nm x,y = 0.36, 0.32; 283 nm x,y = 0.37, 0.31; 284 nm x,y = 0.36, 0.31; 285 nm x,y = 0.32, 0.30; 286 nm x,y = 0.33, 0.30; 287 nm x,y = 0.31, 0.29; 288 nm x,y = 0.29, 0.29; 282 nm x,y = 0.27, 0.28; 290 nm x,y = 0.26, 0.29; 295 nm x,y = 0.23, 0.30; 300 nm x,y = 0.22, 0.33; and 340 nm x,y = 0.21, 0.32. 211

Figure 5.75. Fluorescence spectrum of Tb(**6**)$_3$ (0.01 mM, MeOH). 212

Figure 5.76. Phosphorescence spectrum of Tb(**6**)$_3$ (0.01 mM, MeOH). 213

Figure 5.77. Fluorescence spectrum of Dy(**6**)$_3$ (0.01 mM, MeOH). 213

Figure 5.78. (Left) Ossila spin coater, with white chuck in the centre of the spin coater. (Right) Initial spin coated film of Eu(**6**)$_3$ from DCM:MeOH (1:1) solution, max spin rate of 4000 rpm. 215

Figure 5.79. Spin coated films of Eu(**6**)$_3$ (under longwave irradiation), fabricated from DMF solution. The spin coated film is made from Eu(**6**)$_3$ in a 10 mg/mL DMF solution, spun at 4000 rpm. 216

Figure 5.80. (Top) Shows the brightness of the spin coated film under shortwave irradiation. The spin coated film is made from Eu(**6**)$_3$ in a 10 mg/mL DMF solution, spun at 4000 rpm. (Bottom) Spin coated film deposited on a quartz slide and shown under short- (A, λ_{ex} = 254 nm) and

long- (C, λ_{ex} = 365 nm) wave UV irradiation (≈10 x 10 mm) (B) is a blank under shortwave UV light. 217
Figure 5.81. (Top) UV-visible absorption spectrum of spin coated Eu(**6**)$_3$ film and 0.01 mM MeOH solution. (Bottom left) Fluorescence spectrum of Eu(**6**)$_3$, spin coated slide. (Bottom right) CIE 1931 chromaticity diagram with calculated CIE coordinates: 340 nm x,y = 0.19, 0.20; 240 nm x,y = 0.19 ,0.26 and 280 nm x,y = 0.34, 0.28. 217
Figure 5.82. Microscope images of 10 mg/mL (2000 rpm) spin coated slides on silica wafers under short (A, λ_{ex} = 254 nm) and long wave (B, λ_{ex} = 365 nm) UV irradiation (≈10 x 10 mm) (C) is a 4x magnification into the centre of the film showing film smoothness to the eye in areas not affected by dust particles. 218
Figure 5.83. AFM measurement of spin coated film of Eu(**6**)$_3$ fabricated from 10mg/mL DMF solution (2000 rpm) used to determine surface roughness. (Left) Shows the area (white squares) from which the roughness was measured from, Ra ≈ 8.083 $\pm$ 2.117 nm over the whole film (large square), 5.211 $\pm$ 2.019 nm in areas without large spots (small square). (Right) Shows 3D representation of the films surface showing that the film is not uniform over a wide region. 218
Figure 5.84. (A) microscope image of scraped film, showing a clear step visible to the eye (even without a microscope). (B) AFM map of scratch, showing clear surface difference of scratched step and the region which height has been measured in C. (C) 3D AFM image showing height difference of step and film, below being the average height over the region in B, with the wafer height being measured to 14.81 nm, wafer + film = 25.40 nm, therefore average film height = 10.60 nm. 219
Figure 5.85. Different spin coated films of Eu(**6**)$_3$ on 15 x 20 mm glass slides. Bottom row is 100 µL and top row is 50 µL deposition volumes. From left to right solvents used to dissolve Eu(**6**)$_3$ into a 10 mg/ml solution are DMF, MeOH:DCM (1:1), MeOH:DCM:DMF (3.5:3.5:3), MeOH:DCM:DMF (4.5:4.5:1) and MeOH:DCM:DMF (4:4:2), all spun up to 2000 rpm..... 220
Figure 5.86. Eu(**6**)$_3$ spin coated film (10 mg/ml, 5000 rpm) on 15 x 20 mm glass substrates. Left under longwave (λ_{ex} = 365 nm) and right under shortwave (λ_{ex} = 254 nm) irradiation. 221
Figure 5.87. Eu(**6**)$_3$ spin coated films at different spin rates, from left to right 2000, 3000, 4000 and 5000 rpm. Top image is under shortwave UV irradiation (λ_{ex} = 254 nm), bottom image is under longwave (λ_{ex} = 365 nm). 221
Figure 5.88. CIE 1931 chromaticity diagram with different overall colours capable of Eu(**6**)$_3$ in 2000 (Top) and 3000 (Bottom) rpm spin coated films dependent on λ_{ex} and fluorescence spectra of important λ_{ex}. Calculated CIE coordinates for 2000 rpm: 240 nm x,y = 0.21, 0.24; 250 nm x,y = 0.20, 0.24; 260 nm x,y = 0.25, 0.25; 261 nm x,y = 0.29, 0.27; 264 nm x,y = 0.25, 0.26; 265-267 nm x,y = 0.31, 0.28; 267-270 nm x,y = 0.32, 0.28; 271-277 nm x,y = 0.33, 0.28; 279-281 nm x,y = 0.32, 0.28; 283 nm x,y = 0.31, 0.28; 285 nm x,y = 0.29, 0.28; 287 nm x,y = 0.27, 0.27; 289 nm x,y = 0.24, 0.27; 290 nm x,y = 0.23, 0.26; 295 nm x,y = 0.19, 0.26 and 300 nm x,y = 0.18, 0.25. Calculated CIE coordinates for 3000 rpm: 240 nm x,y = 0.22, 0.23; 260 nm x,y = 0.28, 0.26; 261 nm x,y = 0.29, 0.26; 263 nm x,y = 0.30, 0.27; 265 nm x,y = 0.31, 0.27; 266-267 nm x,y = 0.32, 0.28; 268-274 nm x,y = 0.33, 0.28; 272-278 nm x,y = 0.33, 0.28; 279-282 nm x,y = 0.33, 0.28; 283 nm x,y = 0.32, 0.28; 284nm x,y = 0.32, 0.28; 285 nm x,y = 0.30, 0.28; 286 nm x,y = 0.29, 0.27; 287 nm x,y = 0.28, 0.27; 288 nm x,y = 0.26, 0.27; 289 nm x,y = 0.25, 0.27; 290 nm x,y = 0.19, 0.27 and 300 nm x,y = 0.19, 0.26. 222
Figure 5.89. CIE 1931 chromaticity diagram with different overall colours capable of Eu(**6**)$_3$ in 4000 (Top) and 5000 (Bottom) rpm spin coated films dependent on λ_{ex} and fluorescence spectra of important λ_{ex}. Calculated CIE coordinates for 4000 rpm: 240 nm x,y = 0.19, 0.21; 260 nm x,y = 0.28, 0.26; 261 nm x,y = 0.29, 0.26; 262-263 nm x,y = 0.30, 0.27; 264 nm x,y = 0.31, 0.27; 265-266 nm x,y = 0.32, 0.28; 267-273 nm x,y = 0.33, 0.28; 274-278 nm x,y = 0.34, 0.28; 279-283 nm x,y = 0.33, 0.28; 284-285 nm x,y = 0.32, 0.28; 286 nm x,y = 0.30, 0.28; 287 nm x,y = 0.29, 0.27; 289nm x,y = 0.26, 0.27; 290 nm x,y = 0.25, 0.27; 295 nm x,y = 0.20, 0.26 and 300 nm x,y = 0.19, 0. Calculated CIE coordinates for 5000 rpm: 240 nm x,y = 0.20, 0.21; 250 nm x,y = 0.22, 0.21; 260 nm x,y = 0.26, 0.25; 261 nm x,y = 0.27, 0.26; 264 nm x,y = 0.28, 0.26; 267-270 nm x,y = 0.30, 0.27; 271 nm x,y = 0.31, 0.27; 272-273 nm x,y = 0.31, 0.28; 27 4nm x,y = 0.31, 0.27; 275 nm x,y = 0.32, 0.27; 276 nm x,y = 0.32, 0.28; 277 nm x,y = 0.33, 0.28; 278 nm x,y = 0.31, 0.28; 279nm x,y = 0.32, 0.28; 280 nm x,y = 0.30, 0.28; 281 nm x,y = 0.32, 0.28; 281 nm x,y = 0.30, 0.28; 282 -283 nm x,y = 0.32, 0.28; 284 nm x,y = 0.30, 0.28; 285 nm

x,y = 0.32, 0.28; 286 nm x,y = 0.30, 0.28; 286 nm x,y = 0.32, 0.28; 288 nm x,y = 0.28, 0.27; 290 nm x,y = 0.25, 0.27; 295 nm x,y = 0.19, 0.25 and 300 nm x,y = 0.18, 0.25. 223
Figure 5.90. Eu(**6**)$_3$ in 0.01 mM MeOH solution, pre and post bubbling with oxygen or nitrogen gas (λ_{ex} = 340 nm). 225
Figure 5.91. Ln(**6**)$_3$ 233
Figure 5.92. [Ln(**7**)$_3$]$^{3+}$ 233
Figure 5.93. Ln(**8**)$_3$ 233
Figure 6.1. Ligands **9**, **10** and **11.** 239
Figure 6.2. Bis-PDA based ligands which in the presence of Ln^{3+} can form helicate assemblies (Ln_2**L**$_3$), complex tetrahedral (Ln_4**L**$_6$) and cubic (Ln_8**L**$_{12}$) cages. 240
Figure 6.3. De Cola and co-workers Ir^{3+} and Eu^{3+} complex capable of dual Ln^{3+} and d-block metal emission resulting in overall close to white emission. 241
Figure 6.4. Piguet and co-workers Cr^{3+} l Er^{3+} l Cr^{3+} tri-metal triple stranded helicate capable of UC. Image adapted with permission from L. Aboshyan-Sorgho, C. Besnard, P. Pattison, K. R. Kittilstved, A. Aebischer, J.-C. G. Bünzli, A. Hauser and C. Piguet, Angew. Chem. Int. Ed., 2011, **50**, 4108-4112. Copyright 2022 John Wiley and Sons. 241
Figure 6.5. (Top) Sun and co-workers' 3D trigonal bipyramidal cages. Image adapted with permission from Z. Wang, L.-P. Zhou, T.-H. Zhao, L.-X. Cai, X.-Q. Guo, P.-F. Duan and Q.-F. Sun, Inorg. Chem., 2018, **57**, 7982-7992. Copyright 2022 American Chemical Society. (Bottom) Sun and co-workers square like macrocycle. Image adapted with permission from Q.-Y. Zhu, L.-P. Zhou and Q.-F. Sun, Dalton Transactions, 2019, **48**, 4479-4483. Copyright 2022 Royal Sosciety of Chemistry. 242
Figure 6.6. **9** tridentate binding pockets in which would ideally form a triple stranded helicate. 243
Figure 6.7. Potential complex formations of **10** and **11**. 243
Figure 6.8. ^{1}H NMR of **9** and Bis-alkyne (**B**). Abbreviations: Py for PDA pyridine ring, 2Py for 2-pyridylmethyl and t for 1,2,3-triazole. 245
Figure 6.9. ^{1}H NMR of **10**, **11** and mono-alkyne (**D**). Abbreviations: Py for PDA pyridine ring, Bn for benzyl ring and t for 1,2,3-triazole. 246
Figure 6.10. ^{13}C NMR of **9-11.** Abbreviations: Py for PDA pyridine ring, 2Py for 2-pyridylmethyl, Bn for benzyl ring and t for 1,2,3-triazole. 246
Figure 6.11. Spartan model of [Eu(**9**)$_3$(Zn)$_2$]$^{7+}$. 247
Figure 6.12. Mechanically optimized structure of [Eu(**9**)$_3$(Zn)$_2$]$^{7+}$. 248
Figure 6.13. Protons of interest in ^{1}H NMR titrations. 249
Figure 6.14. ^{1}H NMR spectra of **9** (0.001 M in CD_3CN, 300 MHz) upon titrating with La(CF_3SO_3)$_3$ (0 – 2 equivalents). 249
Figure 6.15. ^{1}H NMR spectra of **9** (0.001 M in CD_3CN, 300 MHz) upon titrating with Zn(CF_3SO_3)$_2$ (0 – 2 equivalents). 250
Figure 6.16. ^{1}H NMR spectra of **9** (0.001 M in CD_3CN, 300 MHz) upon titrating with 0.3 equivalents La(CF_3SO_3)$_3$ and then Zn(CF_3SO_3)$_2$ (0 – 2 equivalents). 251
Figure 6.17. Fluorescence titration of **9** (0.02 M) with Eu(CF_3SO_3)$_3$·6H_2O (Left) and Tb(CF_3SO_3)$_3$·5H_2O (Right) from 0 to 4.5 equivalents, monitoring changes in intensity vs Ln^{3+} equivalents, at λ = 616 and 545 nm respectively. 252
Figure 6.18. Fluorescence titration of **9** (0.02 M) with initial 0.35 equivalents of Eu(CF_3SO_3)$_3$·6H_2O (Left) and Tb(CF_3SO_3)$_3$·5H_2O (Right) and then Zn(CF_3SO_3)$_2$ from 0 to 3 equivalents, monitoring changes in intensity vs Ln^{3+} equivalents, at λ = 616 and 545 nm respectively. 252
Figure 6.19. (Top) Ball and stick representation of the metal coordination polymer crystal structure. (Bottom) Drawn scheme of the polymer which is not 100 % accurate but does show how **9** are linked by Zn^{2+} and the two different octahedral coordination which form the polymer like chain. 253
Figure 6.20. Asymmetric unit of Zn-**9** polymer network (ball and stick representation). 254
Figure 6.21. (Top) The unit cell "monomer" crystal structure, ball and stick representation. (Bottom) Drawn scheme of the unit cell, which is not 100 % accurate but does show how **9** are coordinated to Zn^{2+} and the two different octahedral coordinations which form the polymer like chain. 255
Figure 6.22. (Top) Zn(**9$_b$**)$_2$(H_2O)$_2$ linking two Zn(**9$_a$**)$_2$(**9$_b$**)$_2$, ball and stick representation. (Bottom) Drawn scheme of the unit cell which is not 100 % accurate but does show how **9** are coordinated

to Zn^{2+} and the two different octahedral coordinations which form the polymer like chain. 256
Figure 6.23. Eu(**10**)$_x$ solid shown under ambient light, shortwave, and longwave irradiation from left to right. (Bottom) Eu(**11**)$_x$ solid, under ambient light and shortwave irradiation from left to right. 257
Figure 6.24. Infrared spectra of **10** and Eu(**10**)$_x$(CF_3SO_3)$_x$. 257
Figure 6.25. Updated ligand design for mixed metal complexes. 258
Figure 6.26. Updated ligand design for multidentate complexes. 259
Figure 7.1. Solar spectrum showing the fractions which can be collected by silicon cells (green), and regions which DC and UC could take place. Image adapted with permission from J. C. G. Bünzli and S. V. Eliseeva, in Comprehensive Inorganic Chemistry II (Second Edition), eds. J. Reedijk and K. Poeppelmeier, Elsevier, Amsterdam, 2013, pp. 339-398 and B. S. Richards, Sol. Energy Mater. Sol. Cells, 2006, **90**, 2329-2337. Copyright 2022, Elsevir. 267
Figure 7.2. Potential ligand design for mixed d-block metal and Ln^{3+} for UC or DC with Eu^{3+} and Zn^{3+}. It should be noted coordination spheres are not drawn to accuracy and are only there to give insight into how coordination may occur. 268
Figure 7.3. Potential OLED fabrication design. It is worth noting that a hole blocking layer with a high LUMO level to block electrons from going from EML to HTL would likely be required. HOMO LUMO energy levels obtained from Y. He, L. Liu, G. Fu, W. Li, X. Lü, H. He and W.-Y. Wong, J. Mate. Chem. C, 2019, **7**, 4800-4807. 269
Figure 7.4. PDC side arms, where sensors or structure directing groups can be simply “clicked” onto the scaffold. 270
Figure 7.5. The future PDC motif with dual modification allowing for multiple substituents with different properties to be attached to the binding pocket. 270

List of Tables

Table 1.1. Ionization energies (kJ/mole) for lanthanide ions formation. Table contents were adapted with permission from S. Cotton, in Lanthanide and Actinide Chemistry, John Wiley & Sons Ltd, ch. 2, pp. 9-22. 8

Table 1.2. Selection rules for "allowed" and "forbidden" transitions. 13

Table 3.1. Hydrogen bonding interactions 50

Table 3.2. All peaks found in mass spectra associated with the 1:3 M:L species. 52

Table 3.3. Experimental measured overall quantum yields (Φ_{Ln}^{L}), observed lifetimes (τ_{obs}), calculated radiative lifetimes (τ^{rad}), intrinsic quantum yields (Φ_{Ln}^{Ln}), and sensitisation efficiency (n_{sens}) of Eu^{3+} and Tb^{3+} complexes. 59

Table 3.4. Overall quantum yields and lifetimes, measurements done in MeCN expect for **L[10]**. Values obtained from references 16, 17, 23, 33-36. 59

Table 3.5. Binding constants from fitted data of both UV-visible absorption and fluorescence titration. In the case of the fluorescence titrations with Tb^{3+} and ligand **2**, it required one of the binding coefficients to be fixed to a value to be fitted. This was achieved by fitting the data three times, each time changing the fixed coefficient such that each value has been fitted in conjunction with one another, ending with the Log $\beta_{1:2}$ as the fixed coefficient. 69

Table 3.6. Binding constants from fitted data of both UV-visible absorption and fluorescence titration from other PDA based ligands done in MeCN. Values obtained from references 16, 17, 23, 33 and 45. 70

Table 3.7. Species formation percentages of fitted data from both UV-visible absorption and fluorescence emission titration with **1**, Eu^{3+}, Tb^{3+} and La^{3+} at specific equivalents (0, 0.3, 0.6 and 1 equivalent). 71

Table 3.8. Species formation percentages of fitted data from both UV-visible absorption, and fluorescence emission titration with **2**, Eu^{3+}, Tb^{3+} and La^{3+} at specific equivalents (0, 0.3, 0.6 and 1 equivalent). 72

Table 3.9. Species formation percentages of fitted data from both UV-visible absorption, and fluorescence emission titration with **3**, Eu^{3+}, Tb^{3+} and La^{3+} at specific equivalents (0, 0.3, 0.6 and 1 equivalent). 73

Table 3.10. Bond lengths of $[La(\mathbf{L})_3]^{3+}$ in comparison to $La(\mathbf{L^1})_3$. 78

Table 4.1. Mass peaks observed for ligands and intermediates vs calculated values. 100

Table 4.2. Binding constants from fitted experimental data of both UV-visible absorption or fluorescence titration of **5** vs ligands **1**, **2** and **3**, literature PDC ligands **L[39]**, **L[41]** (from reference 58 and 65) and DPA (from reference 73). Solvent which experiments were carried out in are shown in superscript. 107

Table 4.3. All peaks found in mass spectra associated with the 1:3 M:L species. 109

Table 4.4. Bond length of $Tb(\mathbf{5})_3$ in comparison to $Tb(\mathbf{L^{36}})_3$, values obtained from reference 81. 112

Table 4.5. Experimental measured overall quantum yields (Φ_{Ln}^{L}), observed lifetimes (τ_{obs}), calculated radiative lifetimes (τ^{rad}), intrinsic quantum yields (Φ_{Ln}^{Ln}), and sensitisation efficiency (n_{sens}) of $Ln(\mathbf{5})_3$ complexes. 117

Table 4.6. Experimental measured overall quantum yields $\left(\Phi_{Ln}^{L}\right)$ and observed lifetimes (τ_{obs}) of other PDC and DPA based Eu^{3+} and Tb^{3+} complexes. Values obtained from references 5, 58, 75 and 106. 118

Table 4.7. Experimental measured overall quantum yields (Φ_{Ln}^{L}). Values obtained from references 81, 80 and 107. 118

Table 4.8. XPS binding energies measured from monolayer films compared to expected literature values from reference 110-112. 126

Table 4.9. IR stretches observed in LB film of $Eu(\mathbf{5})_3$ compared to IR stretches of solid **5** and $Eu(\mathbf{5})_3$ complex. 130

Table 4.10. Transfer ratios of mixed multilayer LB films. 132

Table 5.1. Mass peaks observed for ligands and intermediates vs calculated values. 168

Table 5.2. Hydrogen bonding interactions between **7** and DMF. 171

Table 5.3. π - π Stacking interactions occurring between **NI** and pyridine in **7**. 173

Table 5.4. Hydrogen bonding interactions within **I**. 174

Table 5.5. π - π Stacking and hydrogen bonding interactions occurring between **NI** and py of **I**. 175
Table 5.6. Hydrogen bonding interactions with **L** and H_2O. 177
Table 5.7. Binding constants from fitted data of fluorescence titration from other PDC based ligands **6** and **5**. Solvent which the titrations were carried out in are shown in superscript. 186
Table 5.8. Binding constants from fitted data of fluorescence titration from other PDA based ligands **7**, **2** and **3**. Solvent which the titrations were carried out in are shown in superscript. 189
Table 5.9. Binding constants from fitted data of fluorescence titration from other PDC based ligands **8**, **6** and **5**. Solvent which the titrations were carried out in are shown in superscript. 192
Table 5.10. Mass peaks of complexes observed. HRMS reported to 4 decimal places and LRMS to 2 decimal places. 194
Table 5.11. Bond length of Eu(**6**)$_3$ in comparison to Eu(**L^{40}-R**)$_3$, values obtained from reference 70... 198
Table 5.12. Bond length of [Eu(**7**)$_3$]$^{3+}$ in comparison to [Eu(**L^{6}-R,R**)$_3$]$^{3+}$, values obtained from reference 80. 199
Table 5.13. Bond length of Eu(**8**)$_3$ in comparison to Eu(**L^{40}-R**)$_3$, values obtained from reference 70... 199
Table 5.14. Lanthanide centred emission, overall quantum yields (Φ_{Ln}^{L}), observed lifetimes (τ_{obs}), radiative lifetime (τ^{rad}), intrinsic quantum yield (Φ_{Ln}^{Ln}) and sensitisation efficiency (n_{sens}). 202
Table 5.15. Chromophore centred emission quantum yields when excited at 366 nm (values also include lanthanide emission when present). 203
Table 5.16. λ_{ex} which result in the closest to "pure-white" emission from the different spin coated films of Eu(**6**)$_3$. 221
Table 6.1. Important bond lengths and angles of calculated [Eu(**9**)$_3$(Zn)$_2$]$^{7+}$ compared to calculated [Eu(**7**)$_3$]$^{3+}$. 248

List of Publications

Chapters 3 and 4 of this thesis have content that has been published in a peer reviewed journal and in case of chapter 4 an additional paper is ready for submission. Chapter 5 has two papers which are ready for submission.

Chapter 3.

A. T. O'Neil, N. Zhang, J. A. Harrison, S. M. Goldup and J. A. Kitchen, Synthesis, photophysical and assembly studies of novel luminescent lanthanide(III) complexes of 1,2,3-triazolyl-pyridine-2,6-dicarboxamide-based ligands, Supramol. Chem., 2021, **33**, 160-173.

Chapter 4.

A. T. O'Neil, J. A. Harrison and J. A. Kitchen, Ultra-thin films of amphiphilic lanthanide complexes: multi-colour emission from molecular monolayers, Chem. Commun., 2021, **57**, 8067-8070.

Manuscripts for submission:

A. T. O'Neil, and J. A. Kitchen, Lanthanide-based Langmuir-Blodgett Multilayers: Multi-Emissive, Temperature Dependent Thin Films.

Chapter 5.

Manuscripts for submission:

A. T. O'Neil, A. Chalard, J. Malmström and J. A. Kitchen, Single Component White Light Emission from a Europium-1,8-Naphthalimide Thin Film.

A. T. O'Neil, J. Pope, J. A. Harrison and J. A. Kitchen, Single-Component White Emission from a Pyrene Containing Europium Coordination Complex,

Beside the aforementioned papers, I contributed to two other papers during my Ph.D. study.

A. T. O'Neil, K. J. Kilpin, and J. A. Kitchen, Towards functional surfaces using Langmuir-Blodgett deposition techniques, CiNZ., 2019, **3**, 108-112

D. Preston, K. M. Patil, **A. T. O'Neil**, R. A. S. Vasdev, J. A. Kitchen, P. E. Kruger, Long-cavity $[Pd_2L_4]^{4+}$ cages and designer 1,8-naphthalimide sulfonate guests: rich variation in affinity and differentiated binding stoichiometry, Inorg, Chem., Front. 2020, **7**, 2990-300

1. Introduction

1.1 Project Overview

The *4f* elements, correctly referred to as lanthanoids,[1, 2] are elements from lanthanum (La, 57) to lutetium (Lu, 71), found within the 4*f* block of the periodic table (Figure 1.1). This group of elements are more commonly referred to as lanthanides or as rare earth elements, a term which is inclusive of non-lanthanide elements scandium (Sc) and yttrium (Y).[3] Rare earth elements have a rich history with their initial discovery in 1751 as a collective in a black mineral found in Ytterby, Sweden, a mineral which was slowly separated into its individual "rare earth" elements over the course of more than a century, eventually yielding 16 unique rare earth elements by 1901 and the elusive final lanthanide, radioactive promethium (Pm), identified in 1947.[3]

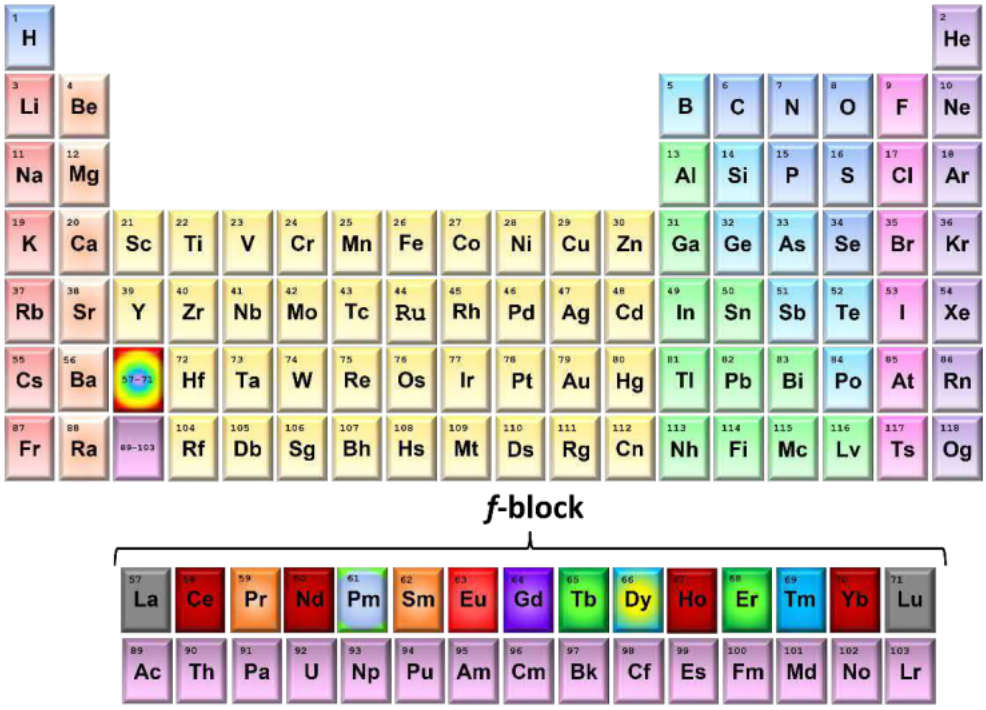

Figure 1.1. Standard periodic table showing the f block separate from the rest of the elements. Lanthanide elements have been coloured to represent the colour that their Ln^{3+} state is commonly known to emit. Near-infrared red emissive lanthanides Ce, Nd, Ho and Yb shown in dark red, visibly emissive lanthanides Pr, Pm, Sm, Eu, Tb, Dy, Er and Tm shown in their dominant visible emission colour, ultra-violet emissive Gd shown in violet and non-emissive La and Lu are shown in grey.

Since their discovery, trivalent lanthanide ions (Ln^{3+}) have developed into a rich vein of research, resulting in a wide variety of real-world applications which predominantly utilize the unique photophysical properties of the Ln^{3+}. Many of these applications were, or still are, used in everyday society without people realizing it. In the very early 20th century, Ln^{3+} found their initial application in the form of incandescent gas mantles, used to light up homes and streets (Figure 1.2).[4] Whilst in more recent times the Ln^{3+} based lighting applications continue with Ln^{3+} being

found in fluorescent lamps, cathode ray televisions which commonly utilized the red emission of europium (Eu), and more modern LED and new OLED technology.[4-8] The world's telecommunications systems which transfer information around the globe could not work without Ln^{3+}, specifically erbium (Er).[4, 5, 9] Modern telecommunications systems utilize silica optical fibres, where signals weaken over 100 km, and it is erbium-doped fibre amplifiers which strengthens the signals allowing information to traverse the globe.[4, 5, 9]

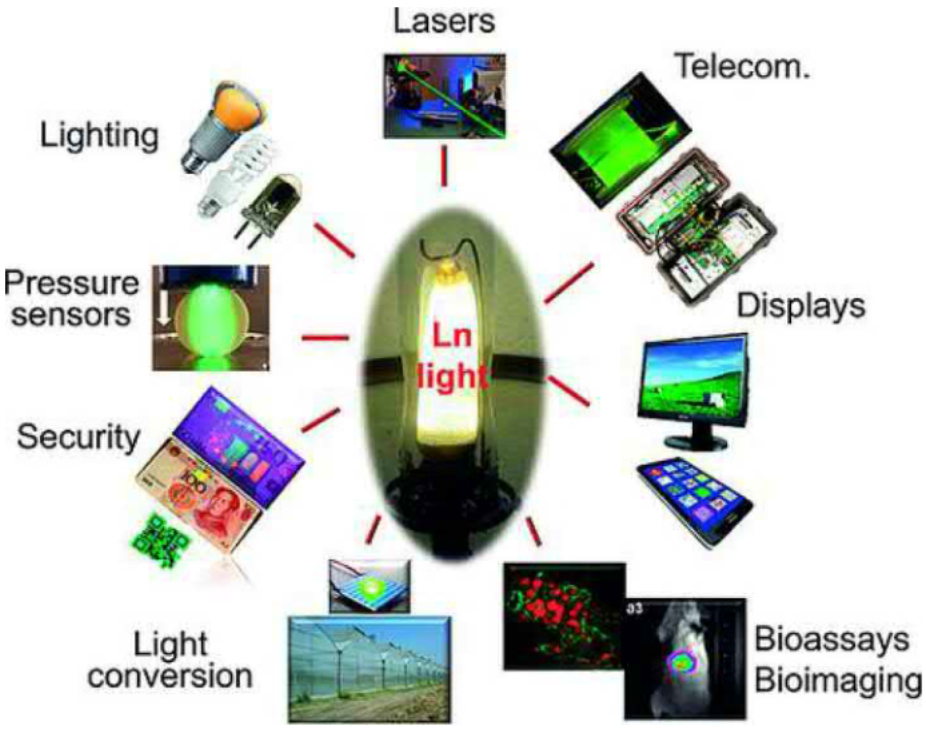

Figure. 1.2.. Images. of. lanthanide. applications,. with. the. initial. incandescent. gas. mantle. in. the. centre,. surrounded. by. more. modern. applications.. Image. adapted. with. permission. from. J.-C.. G.. Bünzli,. Eur. J. Inorg. Chem.,. ***2017***,. *5058-5063.. Copyright. 2022. European Chemical. Society..*

Other key examples of Ln^{3+} applications are their use in lasers;[4, 8] security inks used in modern day bank notes;[8] molecular sensors for temperature,[10] oxygen,[11] and various analytes;[12] bioimaging and immunoassays;[5, 6, 10, 13] magnetic resonance imaging (MRI) contrast agents;[13] and solar waveguides, which are capable of capturing ultraviolet (UV) or near infrared (NIR) light which is not utilized by the silicon cells and is converted to visible light which the solar cell can absorb, increasing solar cell efficiency.[4, 6, 14] It is worth noting that Ln^{3+} also possess interesting magnetic properties which have been used in single molecule magnets; however, magnetic properties of Ln^{3+} will not be discussed as it is beyond the scope of this study.[4]

Directly accessing the Ln^{3+} photophysical properties utilized in the aforementioned applications is relatively difficult and inefficient for most real-world applications (see Section 1.3). To overcome this Ln^{3+} are commonly incorporated into a "host" material, such as being doped within glass[15] or nanoparticles,[16] or are incorporated within inorganic phosphors[17] or metal-

organic assemblies.[18, 19] For the purpose of this research, the focus is on the development of metal-organic architectures or more appropriately supramolecular lanthanide directed self-assembling architectures.[20] The metal-organic approach can indirectly access the Ln^{3+} photophysical properties, *via* the organic chromophore, resulting in luminescent materials (see Section 1.3.2).[6] Although the organic chromophore can induce non-radiative pathways reducing Ln^{3+} emission, the metal-organic approach allows for easy modification of the ligand motif, allowing for the antenna to be better tuned for a specific Ln^{3+} and for the incorporation of additional functionality such as the inclusion of structure directing groups, application or materials formation substituents.[18] Additionally, this approach allows for easy in solution complexation by simply mixing components in solution. Ln^{3+} are highly labile, their interactions are more ionic in nature and do not form covalent bonds with the organic chromophore due to the 4*f* electrons being shielded (see Section 1.2).[1, 21] As a result, Ln^{3+} complexes can form multiple species with the same ligand system but will often self-assemble into the optimal arrangement when given enough time. This self-assembly process can be monitored by various techniques, giving insight into the speciation occurring, including calculating binding constants, which can be used to compare ligand architectures and solvent effects.[22] It is because of these factors that the metal-organic approach is in a constant state of development and research due to a wide range of different organic antennae which can be utilized and applications which they can be tailored to.[4-6, 13, 19, 20, 23-25]

The coordination sphere of Ln^{3+} can be relatively unpredictable in contrast to transition metals, where the coordination sphere is generally predictable and commonly dependent on the oxidation state of the metal.[21, 26] The large radius of Ln^{3+} allows for coordination numbers ranging as high as 12 but also as low as 2, although due to 4*f* electrons not taking part in coordination, Ln^{3+} coordination is generally similar across the table when complexed with the same ligand motif.[21, 27] The coordination number is dependent on how crowded the coordination sphere is, governed by first- and second-order steric crowding effects, the former being the repulsion between groups which are directly coordinated to the Ln^{3+}, and the latter dependent on the crowding and bulkiness of the overall coordinated motif.[21, 26, 28] This means that Ln^{3+} complex geometry largely depends on the ligand design, with predictability possible when appropriate ligand design is taken. Ln^{3+} are hard Lewis acids, favouring hard Lewis bases such as O and N meaning systems incorporating Ln^{3+} generally include carbonyls, aromatic nitrogen, and alcohols.[20] Ligand architectures are also commonly designed to be chelating in order to form a predictable coordination pocket for the Ln^{3+}.[20] Such ligand design can lead to the predictable self-assembly of lanthanide based supramolecular architectures when in the presence of Ln^{3+}.

One such ligand filling these criteria is dipicolinic acid (DPA), seen in Figure 1.3, a ligand motif which has been extensively explored for lanthanide studies.[20] DPA has been shown in general to have a predictable coordination in the NO_2 pocket and can form an enclosed 1:3 M:L species with a tricapped trigonal prismatic geometry (Figure 1.3).[29-34] Additionally the DPA motif is a proven effective antenna for a range of visibly emissive Ln^{3+} (Sm^{3+}, Eu^{3+}, Tb^{3+}, Dy^{3+} and Tm^{3+}).[29, 30, 35] However, the DPA motif is relatively simple and lacks an easily accessible pathway to add additional complexity.[36] Because of this, various DPA derivatives[5, 20, 24] have been explored retaining the central pyridine ring binding motif but modifying either the carboxy substituent or modifying off the back of the pyridyl ring, as seen in Figure 1.4.[20]

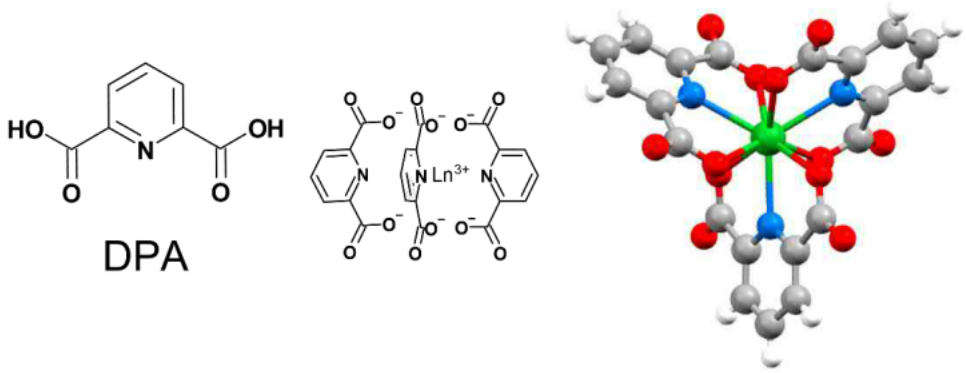

Figure 1.3.. DPA ligand motif,. forming the 1:3 M:L species with tricapped trigonal prismatic geometry.. Crystal structure adapted with permission from V.. Legrand,. F.. Aubert,. A.. D'Aléo,. P.. Rabiller and O.. Maury,. Acta Cryst. E,. *2008,.* ***64****,. 1280-1281..*

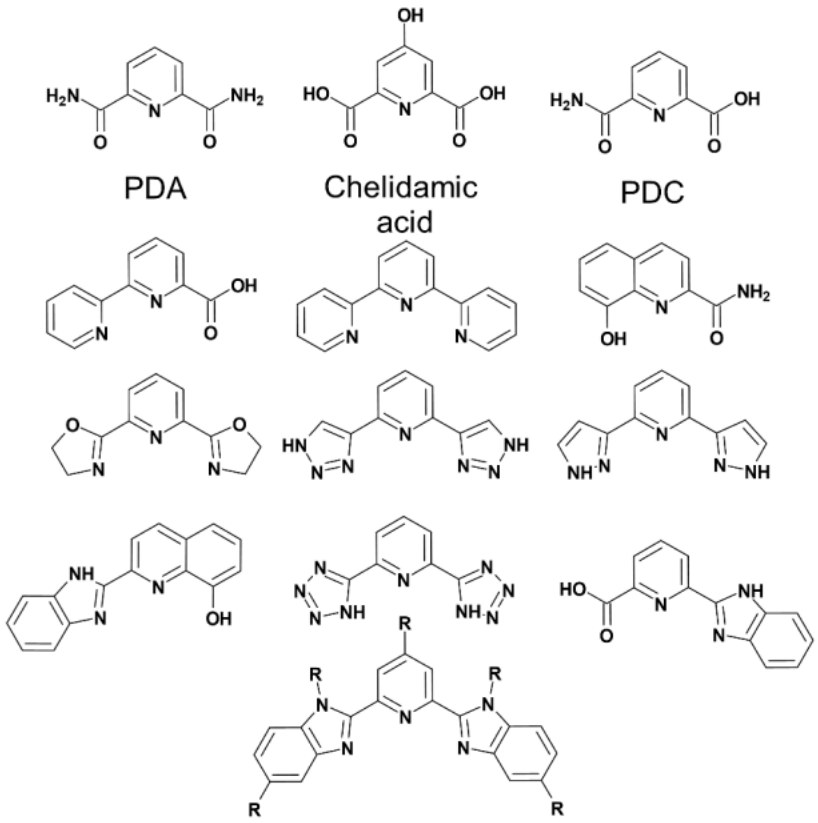

Figure 1.4.. Similar pyridine centred tridentate ligand motifs..

Two such systems are 2,6-pyridinedicarboxamide (PDA) and 6-carbamoylpyridine-2-carboxylic acid (PDC), which substitutes both or a single carboxylic acid binding unit for an amide allowing for additional substituents to be added to the organic motif, as seen in chapter 2. In comparison to other organic motifs used for Ln^{3+} assemblies like the β-diketonates,[1, 19, 37] both the PDA[24] motif and especially PDC[38-52] motifs are relatively underutilized ligand motifs for Ln^{3+} assemblies. Both have only become popularised in the last two decades, however the systems developed do show how the additional modification through the amide can add complexity to the Ln^{3+} systems formed, while mostly retaining a predictive coordination and are an effective antenna for population of a range of Ln^{3+} (see chapter 2).[24, 39-48, 53] In most cases of the PDA and PDC motif, substituents are directly attached to the NO_2 pocket via the amide carbonyl, which can create a steric issue around the NO_2 pocket hindering the formation of the 1:3 M:L species.[54] Attaching bulky substituents via a 1,2,3-triazole linker would move any potential bulky aromatics away from the central pocket, helping maintain the 1:3 M:L species formation by minimising crowding (it should be noted here that inclusion of the 1,2,3-triazole linker could potentially be too bulky itself and could potentially coordinate with the Ln^{3+}, an issue explored in the initial studies of chapter 3). Using a 1,2,3-triazole motif as linker would mean that any aryl or alkyl halides could ideally be "clicked" in a one-pot reaction with sodium azide (NaN_3) and a terminal alkyne appended PDA or PDC motif with relatively similar conditions, allowing for rapid synthesis of a range of individually distinct ligand architectures.[55] Additionally, using copper-catalysed azide-alkyne cycloaddition (CuAAC) to form the 1,2,3-triazole as the "click" name suggests should result in reactions which are relatively high yielding, generating no offensive by-products meaning the product should be easily purified without the need for column chromatography.[56] The CuAAC mechanism is not fully understood, but current understanding provided by Fokin, seen in Figure 1.5, suggests a cooperative dual Cu(I) intermediate, where a σ-Cu(I)-acetylide is additionally interacting with a second π bound Cu(I), reacting with the NaN_3 forming initial C-N covalent bond intermediate, with the reaction carrying on to close the ring.[57-59]

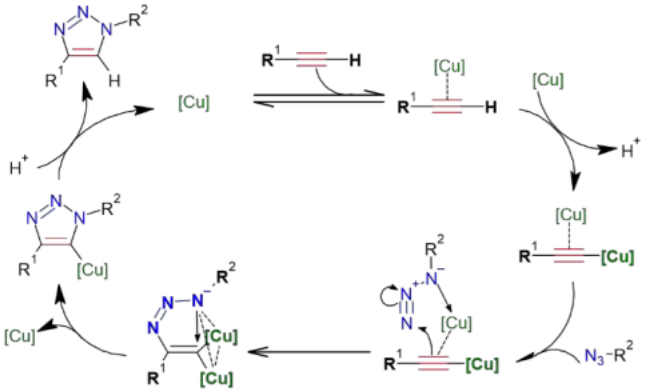

Figure. 1.5.. CuAAC. 1,2,3-triazole. formation. proposed. mechanism. from. reference. 57..

To this end, our approach or "synthetic strategy" for designing Ln^{3+} assemblies and materials is to utilize simple building blocks to synthesise a range of similar but distinct assemblies. In essence this approach is referred to as our "molecular toolbox" (Figure 1.6), in which a fixed set of "tools" or "building blocks" are used in ligand and complex design, streamlining the design and synthetic process.

The Synthetic Strategy Incorporates

- Ln^{3+} for their photophysical properties which can be tuned towards a wide array of applications.
- PDA and PDC motifs act as a scaffold for ligand architectures. It maintains a predictable coordination with Ln^{3+}, acts as base antenna for population of Ln^{3+} excited states and allows for additional complexity to be added *via* the carbonyl.
- 1,2,3-triazole "click" chemistry which should streamline synthesis of ligand architectures while removing bulky substituents from the NO_2 pocket.

Overall, the synthetic strategy should allow for a range of individually distinct but similar ligand architectures to be quickly synthesised and characterised, allowing the ideal candidate to be quickly moved into materials formation or application stages. Having said this the aim of this research was to investigate the synthetic strategy's potential for development of luminescent lanthanide complexes and to specifically target ligand architectures that would allow the luminescent lanthanide complexes to further develop into material assemblies.

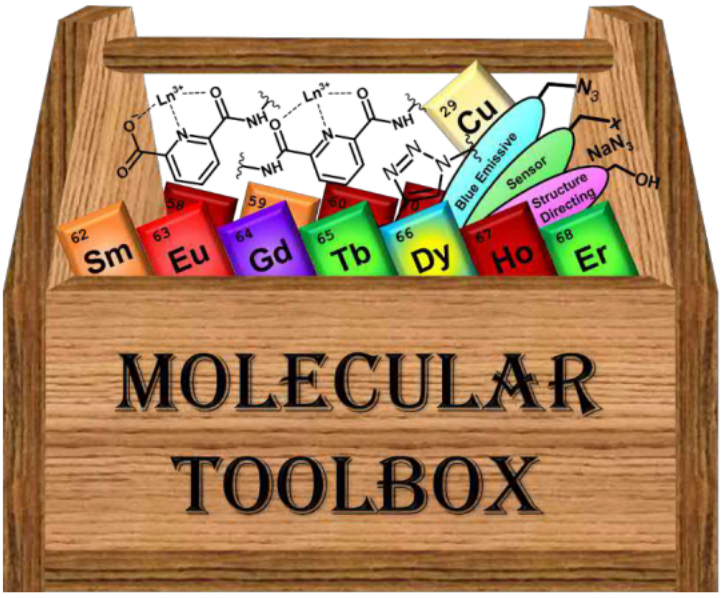

Figure 1.6.. Representation of potential.. "molecular toolbox". synthetic strategy..

1.2 Lanthanide Fundamentals

The fundamental properties of lanthanides can largely be associated with the fact that the 4*f* orbitals are shielded by the xenon core, with the 5s and 5p orbitals extending beyond the 4*f* orbitals (Figure 1.7).[60-63] This causes the valence 4*f* electrons to act as if they are inner core electrons and helps explain why the Ln^{3+} are relatively ignorant of their external environment.[60, 63] This also causes what is commonly known as lanthanide contraction, since the 4*f* orbitals are within the xenon core, they are poorly shielded from the nuclear charge, thus as the effective nuclear charge (Z_{eff}) increases along the sequence, it causes a relatively steady decrease in the radius of Ln^{3+} (also caused by some relativistic effects).[61]

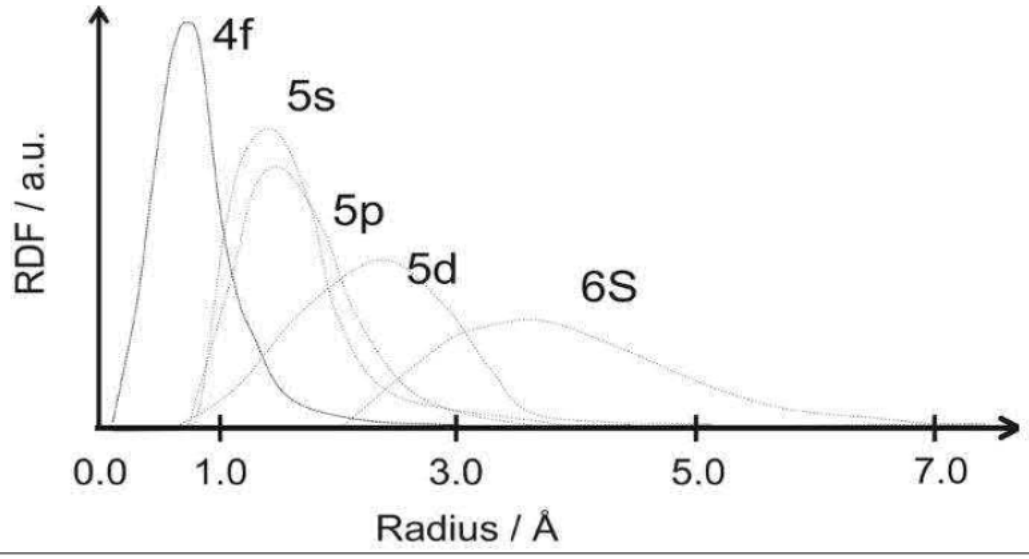

*Figure 1.7. Simplified radial distribution function vs radius of a range of orbitals, showing the internal nature of 4f orbitals within the xenon core. Image adapted from open access and CC-BY article, Y. Hasegawa, Y. Kitagawa and T. Nakanishi, NPG Asia Mater., 2018, **10**, 52-70.*

Lanthanides generally are found in a trivalent oxidation state Ln^{3+}, described by the electron configuration [Xe]$4f^n$ (n = 0-14).[60, 61, 64] This can be explained when observing the individual ionization energies as electrons are removed from the outer shells (6*s* or 5*d*) and then the single electron from the 4*f* orbital. As each electron is removed the Z_{eff} experienced on individual electrons increases, thus increasing 4*f* orbital contraction, requiring more energy to remove each electron.[60, 61] Removal of a second electron from the 4*f* orbital becomes more difficult, as the electrons are contracted closer to the nucleus, which is clearly visible in the ionization energy associated with the removal of a fourth electron, with its value being larger than the combination of the previous three energies (Table 1.1).[60, 61]

Table 1.1. Ionization energies (kJ/mole) for lanthanide ions formation. Table contents were adapted with permission from S. Cotton, in Lanthanide and Actinide Chemistry, *John Wiley & Sons Ltd, ch. 2, pp. 9-22.*

Ln	I_1	I_2	I_3	I_4	$I_1+I_2+I_3$	$I_1+I_2+I_3+I_4$
La	538	1067	1850	4819	3455	8274
Ce	527	1047	1949	3547	3523	7070
Pr	523	1018	2086	3761	3627	7388
Nd	529	1035	2130	3899	3694	7593
Pm	536	1052	2150	3970	3738	7708
Sm	543	1068	2260	3990	3871	7861
Eu	546	1085	2404	4110	4035	8145
Gd	593	1167	1990	4250	3750	8000
Tb	564	1112	2114	3839	3790	7629
Dy	572	1126	2200	4001	3898	7899
Ho	581	1139	2204	4110	3924	8034
Er	589	1151	2194	4115	3934	8049
Tm	597	1163	2285	4119	4045	8164
Yb	603	1176	2415	4220	4194	8414
Lu	523	1340	2033	4360	3896	8256

There are of course a few exceptions to this rule, with examples of Ln^{2+} (e.g. Nd^{2+}, Sm^{2+}, Eu^{2+}, Tm^{2+} and Yb^{2+}) and Ln^{4+} oxidation states (e.g. Ce^{4+}, Pr^{4+}, Nd^{4+}, Tb^{4+} and Dy^{4+}) being observed.[61, 64] These states are possible due to a combination of factors, such as the stability effects of half-filled and fully filled shells, common examples being Eu^{2+} [Xe]$4f^7$ and Yb^{2+} [Xe]$4f^{14}$.[61, 64] Where Ln^{4+} oxidation states are commonly observed in the early lanthanides, this is because the effect of lanthanide contraction is minimal, and consequently the energy difference between the 4*f* and 5*d* orbitals is reduced and an electron can more easily populate the valence orbitals and be lost.[61, 64]

1.2.1 Electronic Structure

Apart from La^{3+} and Lu^{3+}, lanthanides have an exceptionally large number of energy levels that electrons can occupy (Figure 1.8). When just taking into consideration the number of electrons (**n**) present within the seven 4*f* orbitals and the spin associated with them, the combination can generate tens to thousands of different energy levels.[6, 65, 66] For example using the given equation 14!/**n**!(14-**n**)! (n= 0-14), for Gd^{3+} **n** = 7 or Eu^{3+} **n** = 6 there are 3432 and 3003 different energy levels respectively.[6, 60, 65, 67, 68]

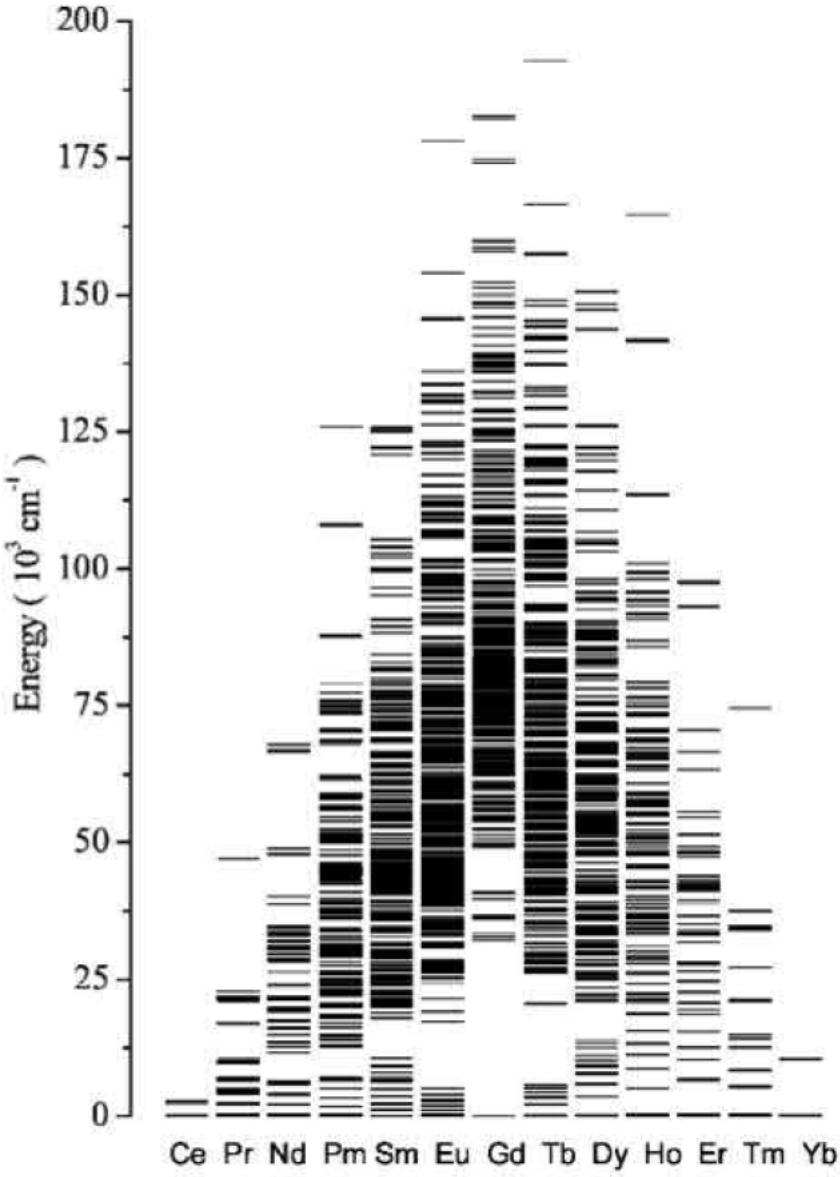

Figure. 1.8.. Diagram. shows. the. 4f. microstate. energy. levels. that. trivalent. lanthanides. are. capable. of.. These. states. were. determined. for. LnF_3 by. W.. T.. Carnall,. G.. L.. Goodman,. K.. Rajnak and. R.. S.. Rana,. J. Chem. Phys.,. *1989,.* **90**,. *3443-3457. and. image. adapted. from. open access. and. CC-BY. article:. Y.. Hasegawa,. Y.. Kitagawa. and. T.. Nakanishi,. NPG. Asia. Materials,. 2018,.* ***10***,. *52-70.*

These states are considered relatively non-degenerate, due to coulomb repulsion and spin-orbit coupling causing these states to have different energy levels.[6, 60, 65, 69] These energy levels remain well defined and are relatively unaffected by changes in the external chemical environment, and unlike transition metals, Ln^{3+} experience minimal crystal field or Stark effects, once again due to the shielding of the 4*f* orbitals.[68, 70]

$$^{(2S+1)}L_J \Rightarrow Eu^{3+} \approx {}^7F_o$$

Hund's Rules

1. The maximum spin multiplicity (2S + 1)
2. The largest L-value is the ground state

$$< 7e^- \; J = |L - S| = J_{min}$$
$$> 7e^- \; J = |L + S| = J_{max}$$
$$= 7e^- \; J = |L - S|$$

Scheme 1.1.. Russell-Saunders coupling term utilized for ground state of Eu^{3+} and Hund's rules for Russell-Saunders coupling terms.

The Russell-Saunders coupling scheme seen in Scheme 1.1 is commonly used to define these energy levels.[6, 18, 60, 70, 71] These terms are built upon the general quantum term symbols (n, l, m_l & m_s) which are used to identify electronic states. In the case of the 4*f* electrons, two of these terms remain relatively constant, this being the principal quantum number n = 4 (shell number) and the orbital angular momentum l = 3 (orbital shape).[70, 72] The determining factors of Russell-Saunders coupling terms is largely based on the electron momentum in terms of spin and orbital. These factors are the total spin angular momentum (S) which is the vectoral sum of the electron spin m_s where $m_s = \pm\frac{1}{2}$, and the total orbital angular momentum (L), which is determined from the maximized vectoral sum of the magnetic quantum number m_l, where m_l = l, l-1, l-2, ..., 0, l+2, l+1; a value which is then assigned to a state symbol (0 to 7 corresponding to S, P, D, F, G, H, I and K), seen in Scheme 1.2.[6, 60, 68, 70]

$$L = \sum_{i=1}^{n} (m_l)_i \qquad S = \sum_{i=1}^{n} (m_s)_i \qquad J = (L+S), (L+S-1), .. |L-S|$$

Scheme 1.2.. Russell-Saunders coupling term equations..

These two quantum numbers can be used to generate the term symbol $^{2S+1}$L which summarizes the quantum number information of the different energy levels as a result of coulomb or electron-electron repulsion occurring within the 4*f* orbital, the largest factor of energy level split between energy levels as seen in Figure 1.9.[18, 60, 68, 73] However, in lanthanides the Russell-Saunders coupling terms incorporate an additional quantum number, J, for total angular momentum, as spin-orbit coupling is relatively significant due to the heavy nuclei of the Ln^{3+} as

seen in Figure 1.9. As a result of this, $^{2S+1}L_J$ term symbols are used to describe the energy levels.[6, 18, 68, 70] Determination of individual states can be relatively difficult except for the ground state, which is able to be determined following Hund's rules, shown in scheme 1.1.[6, 18, 68, 70]

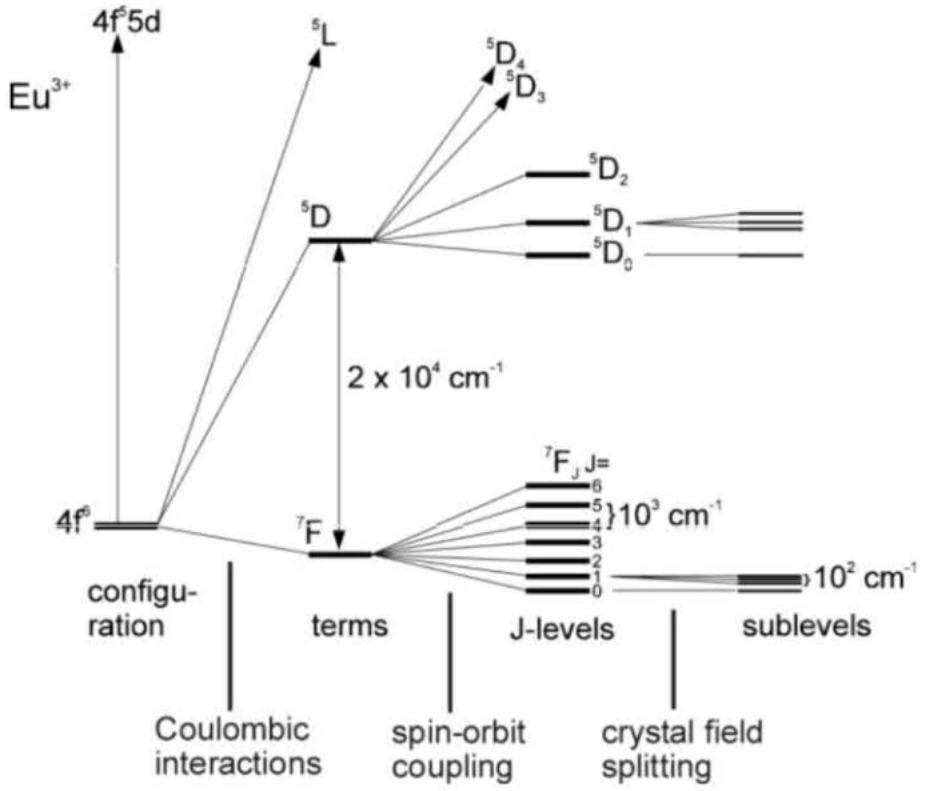

*Figure 1.9.. Different microstate energy levels of Eu^{3+} as a result of the different interactions,. showing the different energy significance of each interaction.. Image adapted with permission from M.. H.. V.. Werts,. Sci.. Prog.,. 2005,. **88**,. 101-131.. Copyright 2022,. SAGE publications..*

The $^{2S+1}L_J$ term symbols account for the energy levels of the free uncoordinated Ln^{3+}, which largely stay the same when coordinated as the 4*f* electrons are shielded from interaction with coordinating ligands.[18, 70] However, Ln^{3+} do experience a weak crystal field or Stark effect caused by being incorporated within a new chemical environment, destroying spherical symmetry, and causing a loss of degeneracy of J values which are split into individual (2J + 1) values, as seen in Figure 1.9.[18, 70, 73] As stated this effect is minuscule for lanthanides, and as a result the colour of solid lanthanides remain relatively similar when complexed, unlike transition metals which are significantly affected by crystal field splitting. However, as discussed later, crystal field splitting does play an important role in allowing certain $f - f$ transitions to occur, some of which can be hypersensitive transitions, which can be used to determine the symmetry of the Ln^{3+} external environment.[70] Further splitting of the energy levels is possible but for description of the photophysical properties of Ln^{3+} the $^{2S+1}L_J$ term symbols are sufficient.[19, 68, 73]

1.3 Lanthanide Photophysics

This extensive collection of energy levels the Ln^{3+} have access to allows them to emit through a significant part of the electromagnetic spectrum, as seen in Figure 1.10. Gd^{3+} emits in the UV region ($^6P_{7/2} \rightarrow {}^8S_{7/2}$), Pr^{3+} (orange, $^3P_0 \rightarrow {}^3H_{4\text{-}6}$), Sm^{3+} (orange, $^4G_{5/2} \rightarrow {}^6H_{5/2\text{-}15/2}$), Eu^{3+} (red, $^5D_0 \rightarrow {}^7F_{0\text{-}6}$), Tb^{3+} (green, $^5D_4 \rightarrow {}^7F_{6\text{-}0}$), Dy^{3+} (yellow and blue, $^4F_{9/2} \rightarrow {}^6H_{15/2\text{-}5/2}$), Ho^{3+} (green $^5S_2 \rightarrow {}^5I_{8\text{-}4}$) and Tm^{3+} (blue, $^1G_4 \rightarrow {}^3H_{6\text{-}4}$) are all visible emissive, whilst Pr^{3+} ($^1G_4 \rightarrow {}^3H_{4\text{-}6}$ or $^1D_2 \rightarrow {}^3F_{2\text{-}4}$), Nd^{3+} ($^4F_{3/2} \rightarrow {}^4I_{9/2\text{-}15/2}$), Ho^{3+} ($^5F_5 \rightarrow {}^5I_{8\text{-}4}$), Er^{3+} ($^4I_{13/2} \rightarrow {}^4I_{15/2}$) and Yb^{3+} ($^2F_{5/2} \rightarrow {}^2F_{7/2}$) emit in the NIR.[20, 23] Emission (and absorption bands) can be assigned to individual energy levels transitions as the bands are relatively sharp and narrow, which is once again because of the 4*f* electrons being shielded within the xenon core, meaning they are experiencing limited vibronic coupling. The challenge is reliably populating the correct excited states and obtaining the desired emission, which is not as simple as it seems, with many processes needing to be optimised for the desired output.

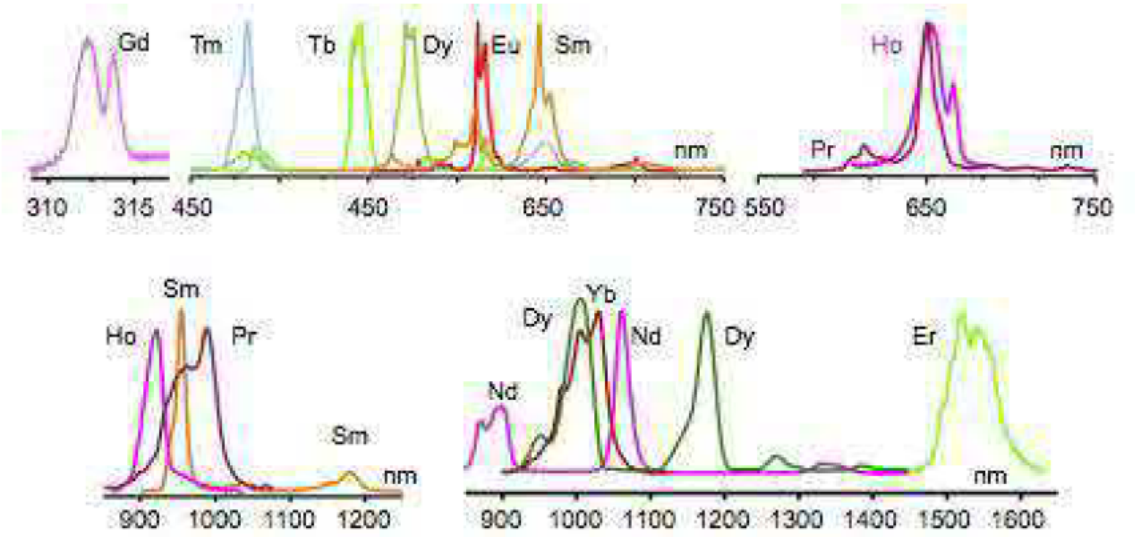

Figure 1.10. Ln^{3+} emission spectra. Image adapted with permission from J.-C. G. Bünzli, in Handbook on the Physics and Chemistry of Rare Earths, eds. J.-C. G. Bünzli and V. K. Pecharsky, Elsevier, 2016, vol. 50, pp. 141-176. Copyright 2022, ELSEVIER.

1.3.1 Direct Excitation and Absorption of Ln^{3+}

In order to obtain these photophysical emission properties of Ln^{3+}, the appropriate excited states must be first populated. This is most often achieved by absorption of light resulting in photoluminescence or by electrical current, electroluminescence.[19, 74, 75] Absorption of light results in two major transitions, either an electric dipole (ED) or magnetic dipole (MD) transition, dependent on the absorption of either the electronic or magnetic field components of the electromagnetic wave.[6, 60, 68, 76, 77] Ln^{3+} absorption of the electromagnetic wave results in predominately 4*f*-4*f* transitions (4*f*-5*d* transitions can also occur but are rare as they are higher energy transitions).[6, 60] As previously mentioned, populating the excited states of Ln^{3+} directly is relatively inefficient because most of the 4*f*-4*f* transitions are largely "forbidden" (better referred to as improbable). As a result, Ln^{3+} molar absorptivities are very low and require a strong excitation source (laser) to overcome the "forbidden" nature to directly excite Ln^{3+}.[6, 60, 68, 77]

Table 1.2. Selection rules for "allowed" and "forbidden" transitions.

Transition	Parity	ΔS	ΔL	ΔJ
ED	ungerade	0	≤ 6	≤ 6 (2, 4, 6 if J or J' = 0)
MD	gerade	0	0	0, ±1

Whether the transitions are "forbidden" or "allowed" is governed by the selection rules seen in Table 1.2. The rule of importance for the 4*f*-4*f* transition is the Laporte parity, in which the transition must result in the total angular momentum changing in parity by an odd integer.[6, 60, 68, 77] Since 4*f* orbitals are ungerade (odd, antisymmetric) it means that when the selection rules are strictly followed for the 4*f*-4*f* transition only the weaker MD (gerade, even) transitions are "allowed" as they are Laporte allowed.[6, 60, 68, 77, 78] However, this results in very few 4*f*-4*f* transitions as they are also restricted to the selection rule ΔJ = 0 or ± 1, meaning that only few Ln^{3+} transitions such as Eu^{3+} $^5D_0 \rightarrow {}^7F_1$ have a high probability of taking place.[6, 60, 68, 77] The majority of 4*f*-4*f* transitions are ED transitions but are "forbidden" according to the Laporte selection rule; yet, as literature shows there are many instances in which transitions are "forbidden" but still take place.[6, 60, 68, 77] In terms of the rule of spin, in which spin must remain the same (ΔS=0), the rule is relaxed and the spin quantum number is no longer strictly valid due to the large spin-orbit coupling experienced by the heavy Ln^{3+}, causing mixing of spin states.[68, 79-81] Similar to this, the Laporte selection rule is only true for free Ln^{3+} in a centrosymmetric environment. Inserting a Ln^{3+} into a host material can break down this symmetry from a combination of crystal field effects and asymmetric vibronic coupling, allowing a mixing of electronic states with different parity.[60, 68, 80-82] The Laporte selection rule in the host

matrix is no longer as strict and allows for what are known as Induced Electric Dipole Transitions (IEDT).[60, 68, 80, 81] These transitions can be heavily dependent on the external environment, with some IEDT transitions only appearing in certain symmetry (like, Eu^{3+} $^5D_0 \rightarrow {}^7F_0$ transition) and others which are hypersensitive, and intensity changes depending on the external environment.[60, 68, 77, 81, 83] Overall, direct excitation is not a commonly used method when developing highly luminescent Ln^{3+} materials.

1.3.2 Indirect Excitation or Sensitisation

Although these transitions are partially allowed, direct excitation is still not favoured because of the "forbidden" nature, and the transitions are still unlikely and result in a very low molar absorptivity. This can be overcome by incorporating the Ln^{3+} within a "host" material, in which the Ln^{3+} excited states are populated indirectly via an external source, either charge transfer (CT) processes (commonly utilized in inorganic compounds) or energy transfers (ET) from near-by organic chromophores (often in the form of coordinated ligands).[6, 60] Focusing on the latter, this is known as lanthanide sensitisation or the antenna effect (Figure 1.11), where an organic chromophore acts as a light or energy harvester. With its much higher molar absorptivity, it can effectively populate the excited states of Ln^{3+}.

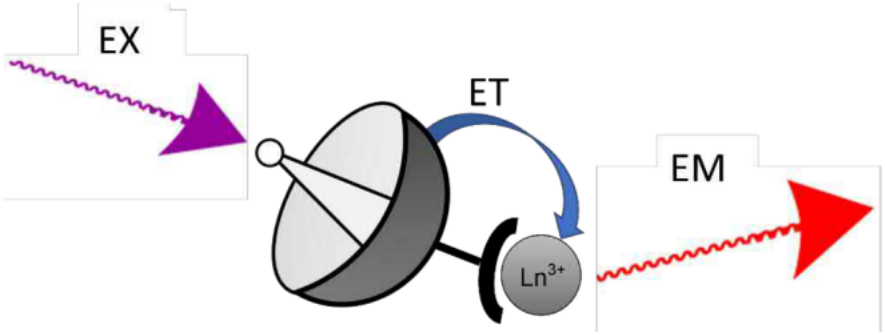

Figure 1.11. Pictorial representation of the antenna effect. Abbreviations EX for the excitation source and EM for emission.

Since there are minimal interactions between the 4*f* electrons and coordinating ligands, the energy process can be considered as two separate entities, as seen in the Jablonski diagram (Figure 1.12).[60] The Jablonski diagram shows that the organic chromophore absorbs electromagnetic radiation (via Laporte and spin allowed transitions such as $\pi \rightarrow \pi^*$) which excites an electron from the singlet ground state (S_0) into an excited singlet state, from which it relaxes through internal conversion and intramolecular vibration relaxation to the lowest excited energy level (S_1).[6, 60, 84] From here the energy can be either expelled in the form of a photon, resulting in fluorescent emission, or by a non-radiative decay (nr) pathway lacking emission, both pathways resulting in relaxation back to the ground state.[84] The third option is to undergo "forbidden" ($\Delta S \neq 0$) intersystem crossing (ISC) from S_1 to an excited triplet state (T^*). This is facilitated by overlapping energy levels and is heavily dependent on spin orbit coupling, so coordination complexes with heavy, paramagnetic Ln^{3+} strongly increases the probability of this crossing (heavy atom effect).[68, 75, 84] Similar to before, the excited state can relax to the lowest excited triplet state (T_1), where it can further relax to the ground state by nr or by a spin "forbidden" transition from $T_1 \rightarrow S_0$ resulting in phosphorescent emission.[84] However as the T_1 is long lasting due to the "forbidden" nature of the transition it makes the state more accessible

to undergo ET to the excited state of Ln^{3+} ($T_1 \rightarrow Ln^{3+}$), from which the Ln^{3+} can emit (see Section 1.3.3).[23, 85] This $S_1 \rightarrow T_1 \rightarrow Ln^{3+}$ energy pathway is considered the main pathway for populating the Ln^{3+} excited states, but there are also instances where Ln^{3+} excited states have been populated via the S_1 state (Figure 1.12), however this is considered less likely due to their short lifetime.[23, 85, 86] Additionally, Ln^{3+} can be excited by CT states such as intra ligand CT (ILCT), ligand to metal CT (LMCT) and metal to ligand CT (MLCT) but these are not utilized in this study.[81]

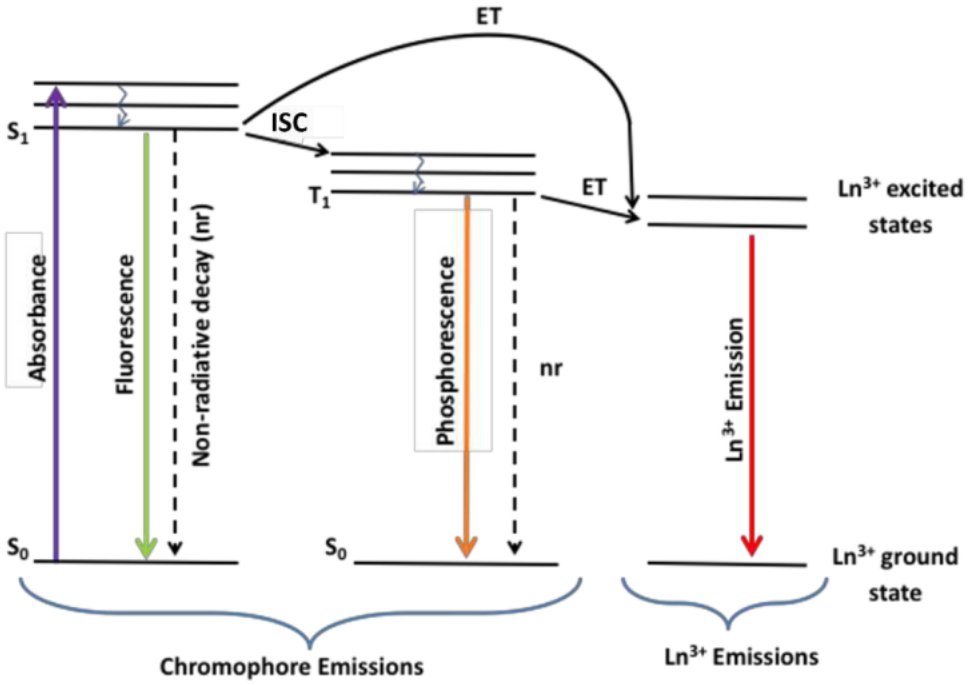

Figure 1.12. Jablonski diagram showing the $S_1 \rightarrow T_1 \rightarrow Ln^{3+}$ and $S_1 \rightarrow Ln^{3+}$ excitation pathways and competing energy pathways.

The $T_1 \rightarrow Ln^{3+}$ ET process can occur via two mechanisms, Förster's dipole-dipole mechanism[71] or Dexter's electron exchange[87] (Figure 1.13). Dexter's electron exchange, as the name insinuates, is the swapping of electrons between the antenna and Ln^{3+}. This consists of the excited electron in the triplet state populating the excited state of the Ln^{3+}, in exchange an electron from the highest occupied energy level of the Ln^{3+} populates S_0 state of the antenna.[20, 23, 82] This mechanism is generally considered to be unlikely for ET ($T_1 \rightarrow Ln^{3+}$) as it requires good orbital overlap, however *4f* orbitals are shielded within the xenon core.[20, 23, 82] Because of this the Förster's dipole-dipole mechanism is generally considered the main ET process. It is a through space mechanism, in which dipole moment relaxation of T_1 couples with the dipole moment of the *4f* orbitals, which causes the *4f* electron to populate the excited state.[20, 23, 82] The lack of electron exchange means Förster's dipole-dipole mechanism allows the mechanism to be long range and is dependent on an emission and absorption overlap of the antenna and Ln^{3+} respectively.[20, 23, 82]

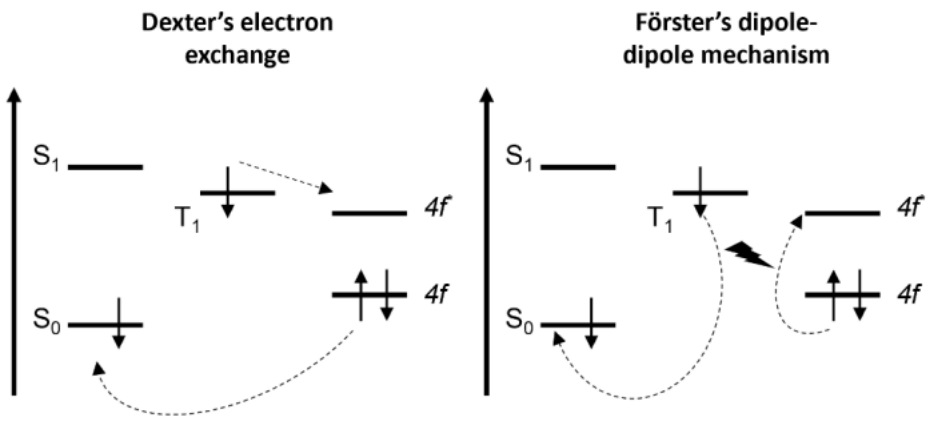

Figure. 1.13.. Potential. energy. transfer. mechanism,. starting. from. already. populated. triplet. states.. Image. based. off. potential. energy. transfer. mechanism. in. C.. G.. Bünzli,. in. Spectroscopic Properties of Rare Earths in Optical Materials*,. eds.. R.. Hull,. J.. Parisi,. R.. M.. Osgood,. H.. Warlimont,. G.. Liu. and. B.. Jacquier,. Springer. Berlin. Heidelberg,. Berlin,. Heidelberg,. 2005..*

1.3.3 Emission Spectra

With the effective population of Ln^{3+} excited states via the antenna effect, lanthanide emission is more feasible and exploitable. Similar to organic chromophores, the electrons that occupy the excited energy state of the Ln^{3+} can relax through either nr decay processes (discussed in Section 1.3.4) or by emitting a photon. As stated, the wide variety of electronic states available to Ln^{3+} allow for different Ln^{3+} to emit in the UV, visible or NIR regions, with the wavelength of the emitting photon inversely proportional to the energy gap between the excited state and final or resting state, given by the Planck-Einstein relation $E = \frac{hc}{\lambda}$ (where h = Planck's constant and c = speed of light) as seen in Figure 1.14.[83]

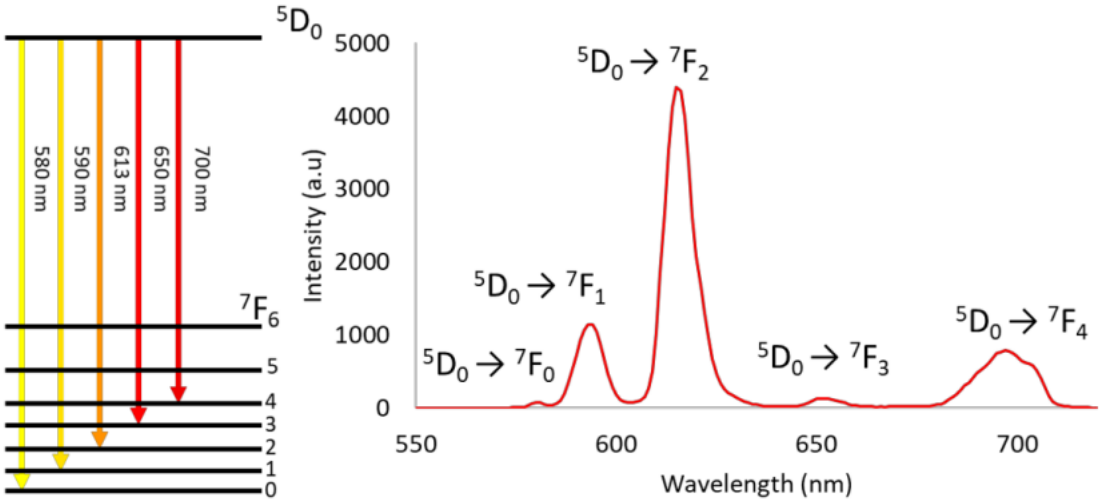

Figure. 1.14.. Example. of. how. Ln^{3+}. (specifically. in. this. case. Eu^{3+}). microstate. band. gap. results. in. different. wavelengths. of. light,. with. the. common. transitions. of. Eu^{3+}. on. the. left. and. the. corresponding. emission. spectrum. on. the. right..

Lanthanide *4f-4f* emission can be fluorescent (ΔS=0) or phosphorescent (ΔS≠0). The emission bands are very narrow and line like, once again because of the limited vibronic coupling experienced by 4*f* orbitals due to shielding, which, as seen in Figure 1.14, allows for the individual transitions to be identified.[5, 6, 60, 68] The limited vibronic coupling also aids in the long-lived lifetimes of Ln^{3+} emission, which coupled with the fact that the population process involves "forbidden" T_1 formation and "forbidden" *4f-4f* transitions results in emission lifetimes in the millisecond range.[5, 6, 60, 68]

Additionally by population via the antenna effect, aside from the more effective population of Ln^{3+} excited states, gives the process a large induced Stokes shift (better referred to as a Richardson shift – when absorption and emission occur from different chromophores).[78, 85] In direct excitation Ln^{3+} emission there is a significantly small Stokes shift (once again from shielding observed by 4*f* orbitals and limited vibronic coupling) where emission is very close to the absorbed wavelength.[6, 60] Whilst in a coordinated complex the Richardson shift can be significantly bigger (Figure 1.15), with the organic chromophore absorption and subsequent Ln^{3+} emission occurring in a different section of the electromagnetic spectrum. For example, the organic chromophore can absorb in the UV region which the Ln^{3+} then emits in the visible region (Figure 1.15).

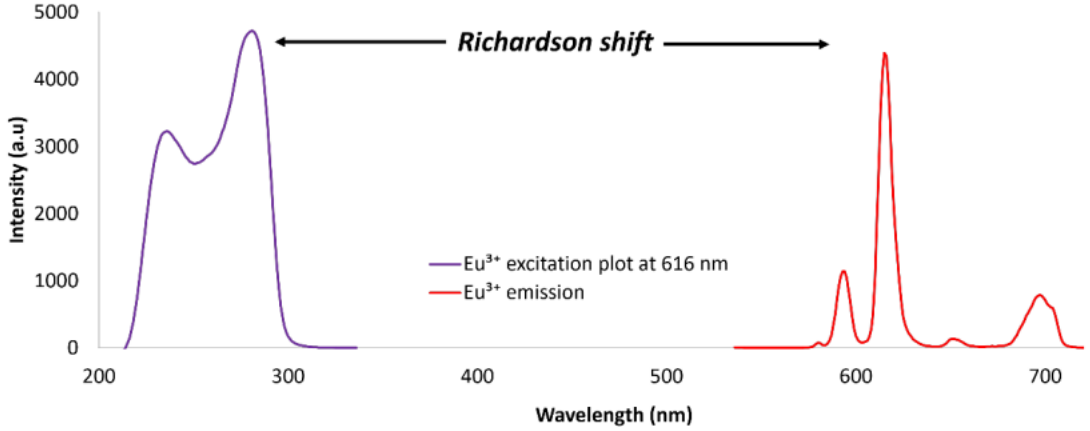

Figure 1.15. Example of Eu^{3+} organic complex emission and excitation profile demonstrating the Richardson shift.

1.3.4 Efficient Sensitisation

Ln^{3+} excited states can be effectively populated via the antenna effect, however indirect excitation is a complicated kinetic puzzle, dependent on various individual pathways and their rates. Focusing on the "main" sensitisation pathway, being $S_0 \rightarrow S_1 \rightarrow T_1 \rightarrow Ln^{3+}$, there are multiple competitive and unwanted pathways, such as organic fluorescence or phosphorescence and nr decay, all of which can reduce Ln^{3+} centred emission. These are all occurring before Ln^{3+} excited states are even populated. Once the 4*f* orbital excited states have effectively been populated, *f-f* transitions can be out-competed by nr decay processes available to the Ln^{3+} excited state such as excited state quenching from energy back transfer (BT), and vibrational deactivation or multiphonon quenching.[6, 60, 85] Indirect excitation, although very useful, is a complicated puzzle which is not simply one antenna fits all Ln^{3+}. Thankfully the metal-organic approach allows for simple modifications of the ligands' antennas to better tune antenna properties for certain Ln^{3+} or overcome some possible nr decay pathways.

1.3.4.1 Singlet State and Triplet State Importance

Firstly for successful population of the Ln^{3+} excited states via the sensitisation pathway $S_0 \rightarrow S_1 \rightarrow T_1 \rightarrow Ln^{3+}$, appropriate singlet state and triplet state energy levels are required to both facilitate the process and to mitigate negative depopulation of the Ln^{3+} excited states.[6, 85, 88] Population of the S_1 can result in fluorescent emission or nr decay from the organic chromophore rather than undergoing spin "forbidden" ISC, the presence of heavy atoms such as the Ln^{3+} can facilitate ISC, but it also known to be favoured when the energy difference between $S_1 \rightarrow T^*$ is $\Delta E \approx 5{,}000\ cm^{-1}$.[20, 27, 60] Similarly, ET processes are dependent on the organic chromophore's lowest lying triplet state energy level. The lowest lying triplet state energy plays a vital role in populating the Ln^{3+} excited states, but it is a balancing act. If the lowest lying triplet state energy is below or much higher than the excited state of the Ln^{3+}, ET is unlikely. Additionally, if it is too close the BT process (Figure 1.16) can occur in which energy from the excited state Ln^{3+} reverts to the triplet state of the organic antenna, all situations which would result in unwanted nr processes or phosphorescent emission from the organic antenna.[6, 20, 82] To optimize the ET process, it is suggested that the triplet state should lie $2000\ cm^{-1}$ above the accepting lanthanide energy state to avoid BT, but for optimal ET the triplet state should be around $2500\ cm^{-1}$ to $3500\ cm^{-1}$ above the Ln^{3+} excited state.[6, 20, 60, 82]

1.3.4.2 Multiphonon Relaxation

Now that the Ln^{3+} excited states are successfully populated they can be relaxed, either by emission or by unwanted nr processes. As stated, the shielding of 4*f* orbitals of lanthanides means they experience weak or limited vibronic coupling from the coordinated ligands, however the Ln^{3+} excited states can still be relaxed by energy transfer to other vibronic oscillators, commonly referred to as multiphonon relaxation, which requires high energy vibration and anharmonic oscillators such as O-H ($\boldsymbol{\nu}$ ≈ 3,600 cm^{-1}) N-H ($\boldsymbol{\nu}$ ≈ 3,300 cm^{-1}), and C-H ($\boldsymbol{\nu}$ ≈ 2,900 cm^{-1}).[67, 82, 89, 90] Depending on the Ln^{3+} energy gap between the excited state and ground state, the Ln^{3+} can be very susceptible to vibrational deactivation processes, through either the bound ligands or from interactions with solvents like H_2O.[67, 82, 89, 90] The basic principle is the larger the gap the more resistant they are to undergoing multiphonon relaxation. Larger energy gaps like Gd^{3+} (ΔE = 32,100 cm^{-1}), Tb^{3+} (ΔE = 14,800 cm^{-1}) and Eu^{3+} (ΔE = 12,300 cm^{-1}) are more resistant to deactivation, while NIR emitting Er^{3+} (ΔE = 6,600 cm^{-1}), Nd^{3+} (ΔE = 5,450 cm^{-1}), and Ho^{3+} (ΔE = 2,840 cm^{-1}) are more susceptible, as they require less phonons to bridge the gap (Figure 1.16).[6, 67, 82, 89-91] Multiphonon relaxation can be minimized by either filling in the Ln^{3+} coordination sphere so solvent interaction is minimised or by avoiding functional groups with the higher energy vibrations such as O-H and N-H. This is not as simple for C-H vibronic oscillations ($C\text{-}H_{\text{aromatic}}$ ΔE = 3,161 cm^{-1}) as these are commonly found in aromatics which are often used as antenna groups. This is inconsequential for Ln^{3+} with large energy gaps, but for the NIR emitting ions such Nd^{3+}, luminescence is more easily quenched.[6, 67, 82, 89-91]

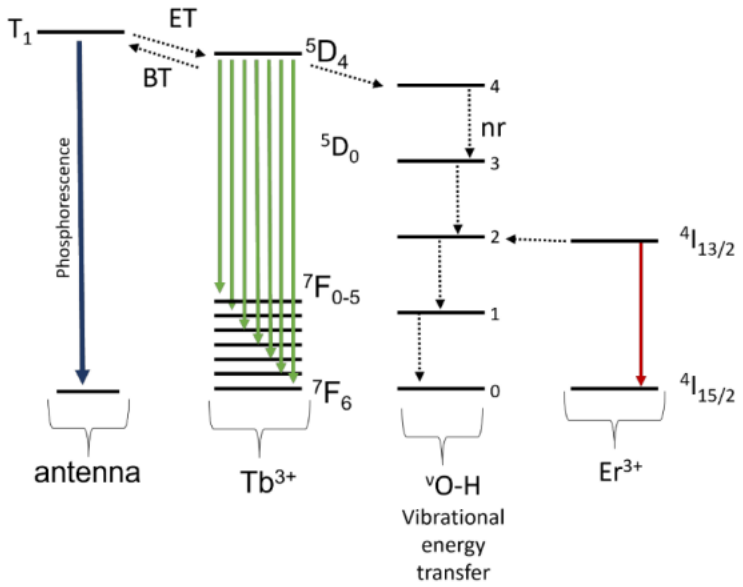

Figure 1.16.. Shows the Jablonski diagram for energy transfer to Tb^{3+} from a triplet state.. In this case energy levels of the triplet state and excited state of Tb^{3+} are close enough that BT can take place.. Additionally,. we see that the Tb^{3+} excited state is being quenched by vibrational energy transfer with O-H vibrations,. suggested to require four phonons to quench the energy where it can be seen that Er^{3+} is more susceptible as it only requires two phonons.. This diagram is not to scale and number of phonons were taken from reference 6.

1.3.4.3 Quantification

Finally, with these potential competitive pathways the efficiency of the indirect excitation processes can be analysed by measuring and calculating the quantum yield (Φ) of Ln^{3+} centred emission. This can be thought of as measuring the ratio of photons emitted vs photons absorbed as shown by equation 1. In reality it is a complex process, where competing kinetic pathways are present (Figure 1.17).[67, 85] For Ln^{3+} there are two types of Φ: firstly there is the intrinsic quantum yield (Φ_{Ln}^{Ln}), which is the Φ for when the Ln^{3+} is directly excited.[92]

Quantum yield

$$\Phi = \frac{Photons\ emitted}{Photons\ absorbed} \quad (1)$$

Intrinsic quantum yield (direct excitation)

$$\Phi_{Ln}^{Ln} = \frac{k^{rad}}{k_{obs}} = \frac{\tau_{obs}}{\tau^{rad}} \quad (2)$$

Rate of depopulation of the excited states

$$k_{obs} = k^{rad} + \sum_i k_{nr}^i \quad (3)$$

Scheme 1.3.. Equation 1 is a simple view of Φ in which they are the ratio of photons emitted versus total photons aborbed. Equation 2 is the intrinsic quantum yield.. Equation 3 is the rate of depopulation of the excited state which is equal to the sum of rates including the rate of radiative decay and the rate of nr decay,. which can be separated into different processes.

Φ_{Ln}^{Ln} is dependent on the ratio of rate of radiative emission (k^{rad}) and the rate of depopulation of the excited states (k_{obs}), as seen in equation 2.[6, 67, 85] k_{obs} (equation 3) is the sum of rates for radiative emission and any nr emission process taking place. As a result theoretically if no nr process is present Φ_{Ln}^{Ln} should be equal to 100 % or 1.[6] Experimental determination of Φ_{Ln}^{Ln} is relatively difficult due to the weak molar absorptivity of Ln^{3+} and thus are commonly estimated by using the observed lifetimes ($\tau_{obs} = \frac{1}{k_{obs}}$) which can be experimentally measured and compared to calculated radiative lifetimes ($\tau^{rad} = \frac{1}{k^{rad}}$). Unfortunately the calculation of τ^{rad} is no easier than the experimental measurement of Φ_{Ln}^{Ln}.[6, 85, 92] There are two exceptions which simplify the calculation of τ^{rad}. If the absorption spectrum and resulting emission spectrum is known, it can be used to simplify equation 4. In the specific case of Eu^{3+} the purely magnetic dipole transition $^5D_0 \rightarrow {}^7F_1$ is completely independent of the Eu^{3+} external environment, allowing simplification of equation 4 to equation 5. This equation is commonly used to determine Φ_{Ln}^{Ln}, and as discussed below is needed to determine the antenna indirect excitation efficiency.[6, 85, 92]

Determination of τ^{rad}

$$\frac{1}{\tau^{rad}} = \frac{64\pi^4\tilde{\nu}^3}{3h(2J+1)}\left[\frac{n(n^2+2)^2}{9} D_{ED} + n^3 D_{MD}\right] \quad (4)$$

Determination of τ^{rad} for Eu^{3+} $^5D_0 \rightarrow {}^7F_1$

$$\frac{1}{\tau^{rad}} = A_{MD,0} n^3 \left(\frac{I_{tot}}{I_{MD}}\right) \quad (5)$$

Scheme 1.4.. Equation 4 is the complex equation which is used to determine the radiative lifetime.. Equation 5 is the equation used to determine radiative lifetime of the specific magnetic dipole transition $^5D_0 \rightarrow {}^7F_1$.. Abbreviations for equation 5 are,. n for refractive index of the solution,. A_{MD} spontaneous emission probability of the Eu ($^5D_0 \rightarrow {}^7F_1$) transition,. a constant equal to 14.65 s^{-1} and finally the ratio between the total integrated emission of Eu $^5D_0 \rightarrow {}^7F_{0\text{-}6}$ (I_{tot}),. over just the $^5D_0 \rightarrow {}^7F_1$ (I_{MD}).

The second type, and more relevant Φ for Ln^{3+}, is the overall quantum yield Φ_{Ln}^{L}, which is much easier to determine experimentally. This can be done by either using an integrating sphere resulting in the absolute Φ_{Ln}^{L} [93] or by comparing the emission to a known standard,[94] using the optically dilute comparison method, and calculated by equation 6.[30]

$$\Phi_{Ln}^{L} = \Phi_x = \frac{E_x}{E_r} \times \frac{A_r(\lambda_r)}{A_x(\lambda_x)} \times \frac{I_r(\lambda_r)}{I_x(\lambda_x)} \times \frac{\eta_x^2}{\eta_r^2} \times \Phi_r \quad (6)$$

Scheme 1.5.. Equation 6 is the equation used for the optically dilute comparison method.. Abbreviations E for integrated luminescence intensity;. A for absorbance at the excitation wavelength;. I for intensity of the excitation light at the same wavelength;. n for refractive index of the solution and Φ is quantum yields with subscript of r for reference and x for sample..

Φ_{Ln}^{L} is the Φ resulting from the indirect excitation process, which means it is dependent on the sensitisation efficiency (n_{sens}, which includes the efficiency of ISC and ET processes) of the antenna and Φ_{Ln}^{Ln} (which in this instance can be thought of as the efficiency of Ln^{3+} excited states resulting in emission vs nr decay), as seen in equation 7.[6, 85] This means that the organic ligand antenna efficiency can also be deduced by rearranging equation 7, meaning once the experimental determination of Φ_{Ln}^{L} and τ_{obs} is carried out and Φ_{Ln}^{Ln} is calculated, n_{sens} can be determined. [6, 85]

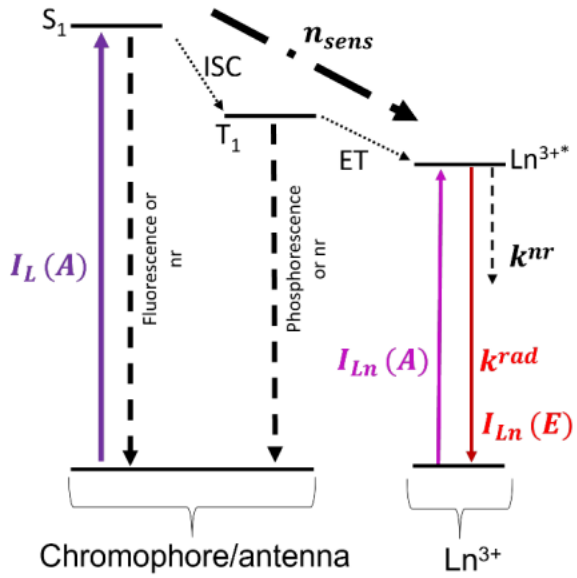

$$\Phi_{Ln}^{L} = \frac{I_{Ln}(E)}{I_L(A)} = n_{sens}\Phi_{Ln}^{Ln} \quad (7)$$

$$\Phi_{Ln}^{Ln} = \frac{I_{Ln}(E)}{I_{Ln}(A)} = \frac{k^{rad}}{k^{rad} + \sum_i k^{nr}}$$

*Figure 1.17.. Jablonski diagram depicting the two types of Φ for Ln^{3+}.. Equation 7 is the equation used to determine the overall.. quantum yield from sensitisation efficiency and the intrinsic quantum yields.. Abbreviation stands for: I_{Ln} - intensity or photons absorbed (A) or emitted (E) by Ln^{3+}, $I_L(A)$ - photons absorbed (A) ligand or antenna.. Diagram has been redrawn with permission from C.. G.. Bünzli,. Coord. Chem.. Rev.,. 2015,. **293-294**,. 19-47.. Copyright 2022,. Elsevir..*

Determination of these Φ values and n_{sens} value is important as it gives researchers insight into the antenna efficiency and potential negative quenching effects that may be occurring due to the ligand design. This allows for the comparison of different antenna designs, which is essential if the antenna is to be tuned and improved upon.

1.4 References

1. J.-C. G. Bünzli, *J. Coord. Chem.*, 2014, **67**, 3706-3733.
2. *Nomenclature of Inorganic Chemistry, IUPAC Recommendations 2005*, RSC Publishing, 2005.
3. P. Thyssen and K. Binnemans, in *Handbook on the Physics and Chemistry of Rare Earths*, eds. K. A. Gschneidner, J.-C. G. Bünzli and V. K. Pecharsky, Elsevier, 2011, vol. 41, pp. 1-93.
4. S. V. Eliseeva and J.-C. G. Bünzli, *New J. Chem.*, 2011, **35**, 1165-1176.
5. S. V. Eliseeva and J.-C. G. Bünzli, *Chem. Soc. Rev.*, 2010, **39**, 189-227.
6. J. C. G. Bünzli and S. V. Eliseeva, in *Comprehensive Inorganic Chemistry II (Second Edition)*, eds. J. Reedijk and K. Poeppelmeier, Elsevier, Amsterdam, 2013, vol. 8, pp. 339-398.
7. J.-C. G. Bünzli, *Eur. J. Inorg. Chem.*, 2017, **2017**, 5058-5063.
8. J.-C. G. Bünzli, *Trends Chem*, 2019, **1**, 751-762.
9. J.-C. G. Bünzli and S. V. Eliseeva, *J. Rare Earths*, 2010, **28**, 824-842.
10. C. J. Salas-Juárez, R. E. Navarro, A. Pérez-Rodríguez, U. Orozco-Valencia and R. Aceves, *Sens. Actuator A Phys.*, 2020, **315**, 112293.
11. K. Iman and M. Shahid, *New J. Chem.*, 2019, **43**, 1094-1116.
12. M. L. Aulsebrook, B. Graham, M. R. Grace and K. L. Tuck, *Coord. Chem. Rev.*, 2018, **375**, 191-220.
13. A. J. Amoroso and S. J. A. Pope, *Chem. Soc. Rev.*, 2015, **44**, 4723-4742.
14. J.-C. G. Bünzli and A.-S. Chauvin, in *Handbook on the Physics and Chemistry of Rare Earths*, eds. J.-C. G. Bünzli and V. K. Pecharsky, Elsevier, 2014, vol. 44, pp. 169-281.
15. E. Erol, N. Vahedigharehchopogh, O. Kıbrıslı, M. Ç. Ersundu and A. E. Ersundu, *J. Phys.: Condens. Matter*, 2021, **33**, 483001.
16. H. Wen and F. Wang, in *Nanocrystalline Materials (Second Edition)*, ed. S.-C. Tjong, Elsevier, Oxford, 2014, pp. 121-160.
17. X. Qin, X. Liu, W. Huang, M. Bettinelli and X. Liu, *Chem. Rev.*, 2017, **117**, 4488-4527.
18. M. H. V. Werts, *Sci. Prog.*, 2005, **88**, 101-131.
19. K. Binnemans, *Chem. Rev.*, 2009, **109**, 4283-4374.
20. D. E. Barry, D. F. Caffrey and T. Gunnlaugsson, *Chem. Soc. Rev.*, 2016, **45**, 3244-3274.
21. S. A. Cotton, in *Lanthanide and Actinide Chemistry*, ed. S. A. Cotton, John Wiley & Sons Ltd, 2006, pp. 35-60.
22. M. Martínez-Calvo, O. Kotova, M. E. Möbius, A. P. Bell, T. McCabe, J. J. Boland and T. Gunnlaugsson, *J. Am. Chem. Soc.*, 2015, **137**, 1983-1992.
23. J.-C. G. Bünzli and C. Piguet, *Chem. Soc. Rev.*, 2005, **34**, 1048-1077.
24. J. A. Kitchen, *Coord. Chem. Rev.*, 2017, **340**, 232-246.
25. O. Kotova, S. J. Bradberry, A. J. Savyasachi and T. Gunnlaugsson, *Dalton Trans.*, 2018, **47**, 16377-16387.
26. S. A. Cotton, *Comptes Rendus Chimie*, 2005, **8**, 129-145.
27. K. T. Hua, J. Xu, E. E. Quiroz, S. Lopez, A. J. Ingram, V. A. Johnson, A. R. Tisch, A. de Bettencourt-Dias, D. A. Straus and G. Muller, *Inorg. Chem.*, 2012, **51**, 647-660.
28. K. W. Bagnall and L. Xing-fu, *J. Chem. Soc., Dalton Trans.*, 1982, 1365-1369.
29. A. D'Aléo, L. Toupet, S. Rigaut, C. Andraud and O. Maury, *Opt. Mater.*, 2008, **30**, 1682-1688.
30. A. S. Chauvin, F. Gumy, D. Imbert and J. C. G. Bünzli, *Spectrosc. Lett.*, 2004, **37**, 517-532.
31. N. Tancrez, C. Feuvrie, I. Ledoux, J. Zyss, L. Toupet, H. Le Bozec and O. Maury, *J. Am. Chem. Soc.*, 2005, **127**, 13474-13475.
32. P. A. Brayshaw, J.-C. G. Buenzli, P. Froidevaux, J. M. Harrowfield, Y. Kim and A. N. Sobolev, *Inorg. Chem.*, 1995, **34**, 2068-2076.
33. J. Harrowfield, Y. Kim, B. Skelton and A. White, *Aust. J. Chem.*, 1995, **48**, 807-823.

34. V. Legrand, F. Aubert, A. D'Aléo, P. Rabiller and O. Maury, *Acta Cryst. E*, 2008, **64**, 1280-1281.
35. J. Andres and A.-S. Chauvin, *Molecules*, 2020, **25**, 4022.
36. F. Renaud, C. Piguet, G. Bernardinelli, J.-C. G. Bünzli and G. Hopfgartner, *Chem. Eur. J.*, 1997, **3**, 1646-1659.
37. K. Binnemans, in *Handbook on the Physics and Chemistry of Rare Earths*, eds. K. A. Gschneidner, J.-C. G. Bünzli and V. K. Pecharsky, Elsevier, 2005, vol. 35, pp. 107-272.
38. R. M. Abdelhameed, D. Ananias, A. M. S. Silva and J. Rocha, *ChemistrySelect*, 2017, **2**, 136-139.
39. B.-L. An, M.-L. Gong, K.-W. Cheah, W.-K. Wong and J.-M. Zhang, *J. Alloys Compd.*, 2004, **368**, 326-332.
40. B.-L. An, M.-L. Gong, K.-W. Cheah, J.-M. Zhang and K.-F. Li, *Chem. Phys. Lett.*, 2004, **385**, 345-350.
41. B.-L. An, M.-L. Gong, M.-X. Li and J.-M. Zhang, *J. Mol. Struct.*, 2004, **687**, 1-6.
42. B.-L. An, M.-L. Gong, M.-X. Li, J.-M. Zhang and Z.-X. Cheng, *J. Fluoresc.*, 2005, **15**, 613-617.
43. B.-L. An, M.-L. Gong, J.-M. Zhang and S.-L. Zheng, *Polyhedron*, 2003, **22**, 2719-2724.
44. B.-L. An, J. Song, K.-W. Cheah, Y.-Y. Ren and Z.-X. Cheng, *Inorg. Chim. Acta*, 2009, **362**, 3196-3200.
45. A.-S. Chauvin, J.-C. G. Bünzli, F. Bochud, R. Scopelliti and P. Froidevaux, *Chem. Eur. J.*, 2006, **12**, 6852-6864.
46. O. Kotova, S. Blasco, B. Twamley, J. O'Brien, R. D. Peacock, J. A. Kitchen, M. Martínez-Calvo and T. Gunnlaugsson, *Chem. Sci.*, 2015, **6**, 457-471.
47. J. J. Lessmann and W. D. Horrocks, *Inorg. Chem.*, 2000, **39**, 3114-3124.
48. J.-M. Senegas, G. Bernardinelli, D. Imbert, J.-C. G. Bünzli, P.-Y. Morgantini, J. Weber and C. Piguet, *Inorg. Chem.*, 2003, **42**, 4680-4695.
49. S. M. Vithanarachchi, D. Kovacs and K. E. Borbas, *Inorg. Chim. Acta*, 2017, **460**, 148-158.
50. S. Zebret, N. Dupont, G. Bernardinelli and J. Hamacek, *Chem. Eur. J.*, 2009, **15**, 3355-3358.
51. S. Zebret, E. Torres, E. Terreno, L. Guénée, C. Senatore and J. Hamacek, *Dalton Trans.*, 2011, **40**, 4284-4290.
52. H. Hou, Y. Wei, Y. Song, Y. Fan and Y. Zhu, *Inorg. Chem.*, 2004, **43**, 1323-1327.
53. C. Lincheneau, C. Destribats, D. E. Barry, J. A. Kitchen, R. D. Peacock and T. Gunnlaugsson, *Dalton Trans.*, 2011, **40**, 12056-12059.
54. T. Le Borgne, J.-M. Bénech, S. Floquet, G. Bernardinelli, C. Aliprandini, P. Bettens and C. Piguet, *Dalton Trans.*, 2003, 3856-3868.
55. J. D. Crowley, P. H. Bandeen and L. R. Hanton, *Polyhedron*, 2010, **29**, 70-83.
56. H. C. Kolb, M. G. Finn and K. B. Sharpless, *Angew. Chem. Int. Ed.*, 2001, **40**, 2004-2021.
57. B. T. Worrell, J. A. Malik and V. V. Fokin, *Science*, 2013, **340**, 457-460.
58. L. Jin, D. R. Tolentino, M. Melaimi and G. Bertrand, *Sci. Adv.*, 2015, **1**, 1500304.
59. H. Ben El Ayouchia, L. Bahsis, H. Anane, L. R. Domingo and S.-E. Stiriba, *RSC Adv.*, 2018, **8**, 7670-7678.
60. J.-C. Bünzli and S. Eliseeva, in *Lanthanide Luminescence*, ed. P. Hänninen, Härmä, Harri, Springer, Berlin, Heidelberg, 2010, vol. 7, pp. 1-45.
61. S. Cotton, in *Lanthanide and Actinide Chemistry*, ed. S. Cotton, John Wiley & Sons Ltd, ch. 2, pp. 9-22.
62. A. J. Freeman and R. E. Watson, *Phys. Rev.*, 1962, **127**, 2058-2075.
63. H. G. Friedman, G. R. Choppin and D. G. Feuerbacher, *J. Chem. Educ.*, 1964, **41**, 354.
64. G. R. Choppin and E. N. Rizkalla, in *Handbook on the Physics and Chemistry of Rare Earths*, Elsevier, 1994, vol. 18, pp. 559-590.
65. A. Y. Freidzon, I. A. Kurbatov and V. I. Vovna, *Phys. Chem. Chem. Phys.*, 2018, **20**, 14564-14577.
66. W. T. Carnall, G. L. Goodman, K. Rajnak and R. S. Rana, *Chem. Phys.*, 1989, **90**, 3443-3457.
67. J.-C. G. Bünzli, *Chem. Rev.*, 2010, **110**, 2729-2755.

68. A. de Bettencourt-Dias, in *Luminescence of Lanthanide Ions in Coordination Compounds and Nanomaterials*, ed. A. d. Bettencourt-Dias, 2014, pp. 1-48.
69. P. S. Peijzel, A. Meijerink, R. T. Wegh, M. F. Reid and G. W. Burdick, *J. Solid State Chem.*, 2005, **178**, 448-453.
70. S. A. Cotton, in *Lanthanide and Actinide Chemistry*, ed. S. A. Cotton, 2006, pp. 61-87.
71. T. Förster, *Annalen der Physik*, 1948, **437**, 55-75.
72. G. Liu, in *Spectroscopic Properties of Rare Earths in Optical Materials*, eds. R. Hull, J. Parisi, R. M. Osgood, H. Warlimont, G. Liu and B. Jacquier, Springer Berlin Heidelberg, Berlin, Heidelberg, 2005, pp. 1-94.
73. E. Bartolomé, A. Arauzo, J. Luzón, J. Bartolomé and F. Bartolomé, in *Handbook of Magnetic Materials*, ed. E. Brück, Elsevier, 2017, vol. 26, pp. 1-289.
74. J. Kido and Y. Okamoto, *Chem. Rev.*, 2002, **102**, 2357-2368.
75. S. Omagari, in *Energy Transfer Processes in Polynuclear Lanthanide Complexes*, Springer Singapore, Singapore, 2019, pp. 1-23.
76. J.-C. G. Bünzli and S. V. Eliseeva, *Chem. Sci.*, 2013, **4**, 1939-1949.
77. C. Görller-Walrand and K. Binnemans, in *Handbook on the Physics and Chemistry of Rare Earths*, Elsevier, 1998, vol. 25, pp. 101-264.
78. P. A. Tanner, *Chem. Soc. Rev.*, 2013, **42**, 5090-5101.
79. M. C. Downer, G. W. Burdick and D. K. Sardar, *Chem. Phys.*, 1988, **89**, 1787-1797.
80. B. Walsh, in *Advances in Spectroscopy for Lasers and Sensing*, Springer, Dordrecht, 2005, pp. 403-433.
81. J.-C. G. Bünzli, in *Handbook on the Physics and Chemistry of Rare Earths*, eds. J.-C. G. Bünzli and V. K. Pecharsky, Elsevier, 2016, vol. 50, pp. 141-176.
82. J.-C. G. Bünzli, in *Spectroscopic Properties of Rare Earths in Optical Materials*, eds. R. Hull, J. Parisi, R. M. Osgood, H. Warlimont, G. Liu and B. Jacquier, Springer Berlin Heidelberg, Berlin, Heidelberg, 2005, pp. 462-499.
83. K. Binnemans, *Coord. Chem. Rev.*, 2015, **295**, 1-45.
84. J. Lichtman and J. Conchello, *Nat. Methods*, 2006, **2**, 910-919.
85. J.-C. G. Bünzli, *Coord. Chem. Rev.*, 2015, **293-294**, 19-47.
86. M. Kleinerman, *Chem. Phys.*, 1969, **51**, 2370-2381.
87. D. L. Dexter, *Chem. Phys.*, 1953, **21**, 836-850.
88. C. Lincheneau, R. D. Peacock and T. Gunnlaugsson, *Chem. Asian J.*, 2010, **5**, 500-504.
89. A. Beeby, I. M. Clarkson, R. S. Dickins, S. Faulkner, D. Parker, L. Royle, A. S. de Sousa, J. A. Gareth Williams and M. Woods, *J. Chem. Soc., Perkin Trans. 2*, 1999, 493-504.
90. E. Kreidt, C. Kruck and M. Seitz, in *Handbook on the Physics and Chemistry of Rare Earths*, eds. J.-C. G. Bünzli and V. K. Pecharsky, Elsevier, 2018, vol. 53, pp. 35-79.
91. I. Hernández and W. P. Gillin, in *Handbook on the Physics and Chemistry of Rare Earths*, eds. J.-C. Bünzli and V. K. Pecharsky, Elsevier, 2015, vol. 47, pp. 1-100.
92. A. Aebischer, F. Gumy and J.-C. G. Bünzli, *Phys. Chem. Chem. Phys.*, 2009, **11**, 1346-1353.
93. J. C. de Mello, H. F. Wittmann and R. H. Friend, *Adv. Mater.*, 1997, **9**, 230-232.
94. G. A. Crosby and J. N. Demas, *J. Phys. Chem.*, 1971, **75**, 991-1024.

2. Literature Review

2.1 Introduction

As stated, both the PDA and PDC ligand scaffolds are ideal building block materials to develop simple ligand architectures. Both motifs are relatively underutilized for Ln^{3+} assemblies in comparison to other motifs like β-diketonates.[1] PDA motifs have only recently become popularised for Ln^{3+} assemblies in the last two decades,[2] while the PDC motif is still relatively novel.

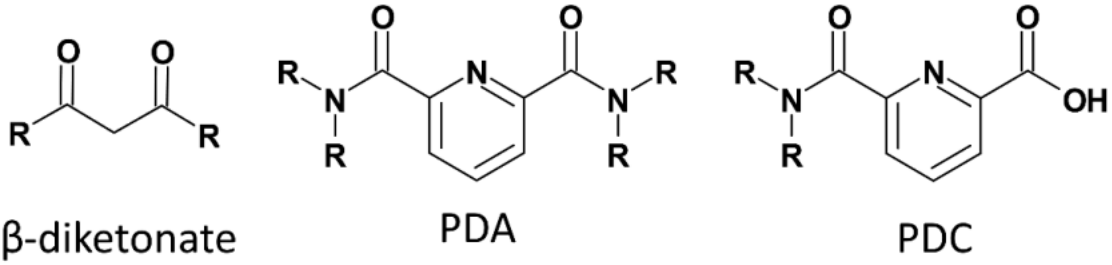

Figure 2.1. Different motifs used as building blocks for Ln^{3+} assemblies.

PDA and PDC motifs are ideal candidates for Ln^{3+} assemblies, as they retain the predictable NO_2 coordination, predominantly form 1:3 M:L species, and are effective antenna for a range of visible and some NIR emitting Ln^{3+}.[3] Herein is a review on the PDA and PDC ligand architectures which in the presence of Ln^{3+} form a 1:3 M:L coordination sphere. The review is focused on Ln^{3+} assemblies that were investigated for their photophysical properties, whereas systems developed for magnetic properties are not discussed as they are beyond the scope of this study.

2.2 2,6-Pyridinedicarboxamide (PDA)

The PDA scaffold was first utilized for Ln^{3+} coordination by Soundararajan and Jagannathan in 1979 with two PDA based ligands N,N,N',N'-tetraethylpyridine-2,6-dicarboxamide (**L¹**),[4] and N,N,N',N'-tetramethylpyridine-2,6-dicarboxamide (**L²**) (Figure 2.2).[5] Complexation was carried out with a range of Ln^{3+}, forming tris-mononuclear, 1:3 M:L species with Ln^{3+} coordination occurring within the NO_2 pocket.

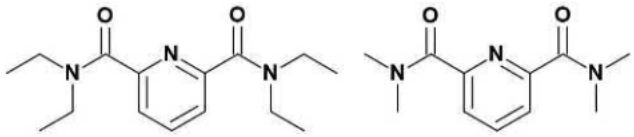

L¹ L²

Figure 2.2.. Soundararajan and Jagannathan L¹,² ligand architectures, L¹ later adapted by Bünzli, Piguet and co-workers..

It took another two decades until the PDA ligand motif, specifically **L¹**, was revisited by Bünzli, Piguet and co-workers (in 1997) for an in-depth study into PDA coordination and more importantly potential antenna properties.[6] This study confirmed the $[Ln(\mathbf{L^1})_3]^{3+}$ species formation and Ln^{3+} coordination within the NO_2 pocket, in both solid and solution state. Crystal structures of $[La(\mathbf{L^1})_3]^{3+}$ and $[Eu(\mathbf{L^1})_3]^{3+}$ showed a pseudo-tricapped trigonal prismatic geometry with a C_3 axis, while ^1H NMR and mass spectrometry (MS) results indicated the 1:3 assemblies formation in solution. From in solution self-assembly titrations, (by monitoring changes in MS and UV-visible absorption spectra) the $[Ln(\mathbf{L^1})_3]^{3+}$ species formation was indicated for all Ln^{3+} (La^{3+} to Lu^{3+}) and gave the first indication that the 1:3 M:L species was not the only assembly available to the PDA motif. At higher concentrations of Ln^{3+} the formation of 1:2 and 1:1 M:L species was observed. Fundamentally this study, to the best of our knowledge, was the first instance of PDA being used as an antenna for both Eu^{3+} and Tb^{3+}. The study showed that PDA could effectively populate Eu^{3+} and Tb^{3+}, with $[Eu(\mathbf{L^1})_3]^{3+}$ and $[Tb(\mathbf{L^1})_3]^{3+}$ resulting in Ln^{3+} centred emission with expected transitions of $^5D_0 \rightarrow {}^7F_{J=1,2\,\&\,4}$ and $^5D_4 \rightarrow {}^7F_{J=6\text{-}3}$ respectively. Quantum yield measurements indicated that the antenna was better suited for Tb^{3+} population with Φ_{Ln}^{L} = 3.5 % and 0.009 % for $[Tb(\mathbf{L^1})_3]^{3+}$ and $[Eu(\mathbf{L^1})_3]^{3+}$ respectively.[7] Although Φ_{Ln}^{L} were low in comparison to the DPA motif ($Cs_3[Eu(DPA)_3]$ and $Cs_3[Tb(DPA)_3]$ Φ_{Ln}^{L} = 24 % and 22 % respectively),[8] Bünzli and Piguet's publication established PDA as a new antenna for Ln^{3+} which allowed for further modification. This publication is clearly associated with the increased frequency of publications involving PDA based Ln^{3+} complexes. Over the last two decades a range of PDA based ligand architectures have been developed for the formation of tris-mononuclear $[Ln(\mathbf{L})_3]^{3+}$ assemblies ranging from discrete mononuclear ligand architectures or Ln^{3+} assemblies such as encapsulating podates, helicates, cages and larger assemblies from ligand architectures which contain multiple PDA binding pockets.

2.2.1 Tris-Mononuclear $[Ln(L)_3]^{3+}$ Assemblies

The PDA ligand architectures which are used in the formation of $[Ln(\mathbf{L})_3]^{3+}$ assemblies are commonly symmetrical (such as $\mathbf{L^1}$ and $\mathbf{L^2}$), the simplest of which is Fu and co-workers $\mathbf{L^3}$ system (Figure 2.3) which formed luminescent solids $[Eu(\mathbf{L^3})_3]^{3+}$ and $[Tb(\mathbf{L^3})_3]^{3+}$ in the presence of Eu^{3+} and Tb^{3+}.[9]

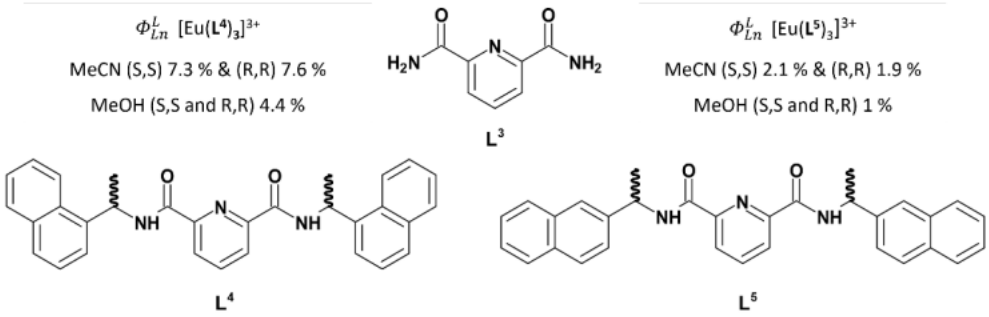

Figure 2.3.. Fu and co-workers $\mathbf{L^3}$ and Gunnlaugsson and co-workers $\mathbf{L^{4,5}}$ ligand architectures for $[Ln(\mathbf{L})_3]^{3+}$ assemblies.. Φ_{Ln}^{L} of $[Eu(\mathbf{L^{4,5}})_3]^{3+}$ in MeOH and MeCN,. values taken from reference 11..

Fu and co-workers $Ln(\mathbf{L^3})_3$ represents the simplest PDA based Ln^{3+} assemblies, lacking any additional functional groups. In comparison, Gunnlaugsson and co-workers $\mathbf{L^4}$ ligand architecture, developed a year later than Fu and co-workers, incorporated chirality into the PDA ligand architectures. Enantiomeric Ln^{3+} centres have potential applications as biological and pharmaceutical chiral sensing probes.[10] As a result, it has become popular to incorporate chirality into ligand architectures used for Ln^{3+} assemblies.[10] Gunnlaugsson and co-workers $\mathbf{L^4}$ system was the first to introduce chirality into the PDA motif by amide coupling chiral (R)- or (S)-1-(1-naphthyl)-ethylamine to form chiral (S,S) and (R,R) $\mathbf{L^4}$ ligands.[11] When complexed with Ln^{3+} the chirality of the ligands is transferred to the metal centre forming enantioselective tris-mononuclear complexes (Δ for R,R and Λ for S,S), resulting in circular dichroism (CD) absorption and circular polarized emission (CPL) properties, exhibited by $[Eu(\mathbf{L^4})_3]^{3+}$ and $[Sm(\mathbf{L^4})_3]^{3+}$. Their follow up study on the similar chiral $\mathbf{L^5}$ ligands also resulted in CD and CPL properties of $[Eu(\mathbf{L^5})_3]^{3+}$.[12] Importantly this study also examined the Φ_{Ln}^{L} of the $[Eu(\mathbf{L^4})_3]^{3+}$ and $[Eu(\mathbf{L^5})_3]^{3+}$ showing a much improved upon Φ_{Ln}^{L} (Figure 2.3) in comparison to $[Eu(\mathbf{L^1})_3]^{3+}$, and a n_{sens} of up to 51 % specifically for $[Eu(\mathbf{L^{4(S,S)}})_3]^{3+}$, demonstrating that the PDA antenna properties can be improved by substituent addition.

Following the results of Gunnlaugsson and co-workers $\mathbf{L^4}$ system, it has become relatively common to see chirality in PDA ligand architectures. Muller and co-workers developed a similar $\mathbf{L^6}$ (Figure 2.4) chiral PDA ligand, replacing the naphthalene motif for a benzyl ring.[3] Similar to previous PDA ligands, $\mathbf{L^6}$ was found to readily form the $[Ln(\mathbf{L^6})_3]^{3+}$ with a range of Ln^{3+}, with crystal

structures of $[Ln(\mathbf{L^6})_3]^{3+}$ (where Ln^{3+} = Eu^{3+}, Gd^{3+}, Tb^{3+} and Yb^{3+}) retaining chirality upon complexation and $[Eu(\mathbf{L^6})_3]^{3+}$ displaying CPL emission.[3, 13] Additionally Muller and co-workers carried out extensive photophysical investigations of $\mathbf{L^6}$ with a range of visible and NIR emitting Ln^{3+}. Similar to previous systems $[Eu(\mathbf{L^6})_3]^{3+}$ and $[Tb(\mathbf{L^6})_3]^{3+}$ resulted in expected Eu^{3+} and Tb^{3+} centred emission when excited into the pyridyl antenna. Φ_{Ln}^{L} are again observed to be significantly better than those reported for $\mathbf{L^1}$ and Tb^{3+} emission continues to be significantly better than Eu^{3+} (Figure 2.4). Muller and co-workers were able to justify the large difference in Φ_{Ln}^{L} from the measured triplet states of $\mathbf{L^6}$ ($^3\pi\pi^*$), determined to be 27,025 cm^{-1}, an energy level much more optimally matched to Tb^{3+} (20,500 cm^{-1}) than Eu^{3+} (17,293 cm^{-1}) excited state.[14] To the best of our knowledge, they also reported the first instance of Pr^{3+}, Dy^{3+}, Tm^{3+}, Yb^{3+} and Er^{3+} visible and NIR emissions by indirect population *via* the PDA antenna, demonstrating that the PDA motif could be used for all major visibly emissive Ln^{3+} and for NIR emitting Ln^{3+} ($[Sm(\mathbf{L^4})_3]^{3+}$ was the first example of Sm^{3+} emission from a PDA antenna).

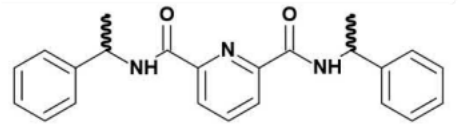

$\mathbf{L^6}$

Complex	MeCN Φ_{Ln}^{L}
$Eu(\mathbf{L^6})_3$	1 %
$Tb(\mathbf{L^6})_3$	8.6 %
$Sm(\mathbf{L^6})_3$	0.024 %
$Dy(\mathbf{L^6})_3$	0.1 %

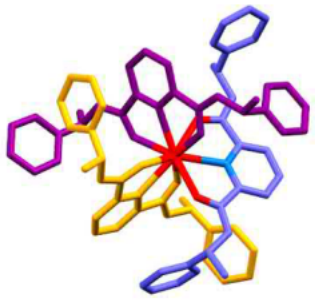

$[Eu(\mathbf{L^6})_3]^{3+}$

*Figure. 2.4.. Muller. and. co-workers. $\mathbf{L^6}$. ligand. architectures. for. $[Ln(\mathbf{L^6})_3]^{3+}$. assemblies.. Φ_{Ln}^{L}. of. $[Eu(\mathbf{L^6})_3]^{3+}$. in. MeCN,. values. taken. from. reference. 3.. Crystal. structure. of. helicate. assembly. adapted. with. permission. from. T.. Hua,. J.. Xu,. E.. E.. Quiroz,. S.. Lopez,. A.. J.. Ingram,. V.. A.. Johnson,. A.. R.. Tisch,. A.. de. Bettencourt-Dias,. D.. A.. Straus. and. G.. Muller,. Inorg.. Chem.,. 2012,. **51**,. 647-660.. Copyright. 2022. American Chemical. Society..*

With the established predictable self-assembly of the PDA forming tris-mononuclear complexes, research moved towards more complex, inter-locked architectures, materials formation, and large assemblies (Section 2.2.2). Around the same time two groups published larger inter-locking architectures, an inter-locked [3] catenane by Gunnlaugsson and co-workers ($\mathbf{L^7}$, Figure 2.5)[15] and tri-folded knot assemblies by Leigh and co-workers ($\mathbf{L^8}$, Figure 2.5).[16] Both groups employed a relatively similar strategy - the symmetrical PDA motifs were modified with terminal allyl ethers which were used for olefin ring closing metathesis (RCM), closing the catenanes or tying the knot. Gunnlaugsson and co-workers catenane formation was the result of the more flexible ethoxy chain linkers which connected the allyl ether to the PDA motif allowing for RCM to occur within the same $\mathbf{L^7}$ ligand, while Leigh and co-workers were able to facilitate knot formation instead by using the rigid naphthalene linkers which, from a combination of π stacking and rigidity, forces RCM to take place between different molecules of

$\mathbf{L^8}$ forming the knot structure (Figure 2.5). Leigh and co-workers follow up ligand architecture ($\mathbf{L^9}$)[17] incorporated the chiral centre previously utilized by the Gunnlaugsson group, forming enantiomeric knot assemblies and confirmed knot formation by crystal structure unlike the previous studies.

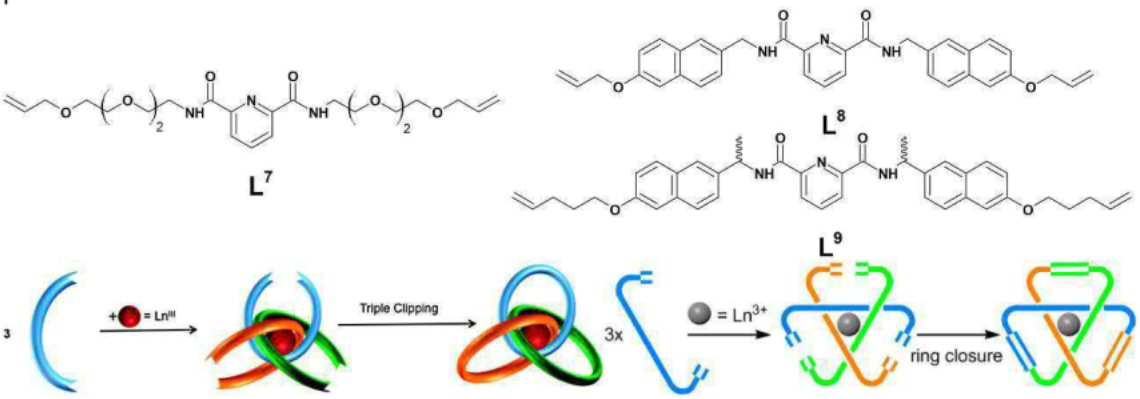

*Figure. 2.5.. (Left). Gunnlaugsson. and. co-workers. $\mathbf{L^7}$. ligand. architectures. for. $[Ln(\mathbf{L^7})_3]^{3+}$. assemblies. and. catenane. formation. post. RCM. Image. adapted. with. permission. from. C.. Lincheneau,. B.. Jean-Denis. and. T.. Gunnlaugsson,. Chem.. Commun.,. 2014,. **50**,. 2857-2860. Copyright. 2022. Royal. Society. of. Chemistry.. (Right). Leigh. and. co-workers. $\mathbf{L^{8,9}}$ ligand. architectures. for. $[Ln(\mathbf{L^{8,9}})_3]^{3+}$.. assemblies. and. knot formation. post. RCM.. Image. adapted. from. open. access. and. CC-BY. article,. J.-F.. Ayme,. G.. Gil-Ramírez,. D.. A.. Leigh,. J.-F.. Lemonnier,. A. Markevicius,. C.. A.. Muryn. and. G.. Zhang,. J.. Am.. Chem.. Soc,. 2014,. **136**,. 13142-13145..*

The Gunnlaugsson group continued to be on the forefront of research involving the tris-mononuclear $[Ln(PDA)_3]^{3+}$ assemblies, taking the luminescent self-assemblies from simple solid powders and solutions to more industry friendly materials like gels (Figure 2.6). They foresaw that by incorporation of a secondary Ln^{3+} binding pocket (benzoic acid, to form $\mathbf{L^{10}}$),[18] in the presence of excess Ln^{3+} "cross-linked" supramolecular self-assembling gels could form. Initially, in the presence of Ln^{3+}, $\mathbf{L^{10}}$ forms the standard $[Eu(\mathbf{L^{10}})_3]^{3+}$ and $[Tb(\mathbf{L^{10}})_3]^{3+}$ luminescent assemblies. When additional Ln^{3+} (0.5 equivalents) were added post 1:3 M:L species formation, coordination occurred within the benzoic acid binding pockets resulting in $[Ln(\mathbf{L^{10}})_3{:}Ln(CH_3COO)_3]^{3+}$ assemblies. This additional coordination results in cross-linked polymeric systems, forming a luminescent gel-like soft material (Figure 2.6). Similar thin films and "gel" like materials have also been formed with the $[Ln(PDA)_3]^{3+}$ assemblies by utilizing the sol-gel method which encompasses hydrolysis and condensation of organoalkylsilanes, used by a range of different research groups.[19-22] Terminal triethoxysilanes are incorporated into the PDA motif ($\mathbf{L^{11}}$, Figure 2.7) and undergo hydrolysis and condensation with tetraethyl orthosilicate forming Si-O-Si matrices. In the presence of Eu^{3+} both Wang and coworkers[19] and Barja and coworkers[20] used this to form luminescent $[Eu(\mathbf{L^{11}})_3]^{3+}$ "gel" assemblies, while Zink and co-workers[22] instead formed thin films of $[Tb(\mathbf{L^{11}})_3]^{3+}$ by depositing the gel onto a silicon strip.

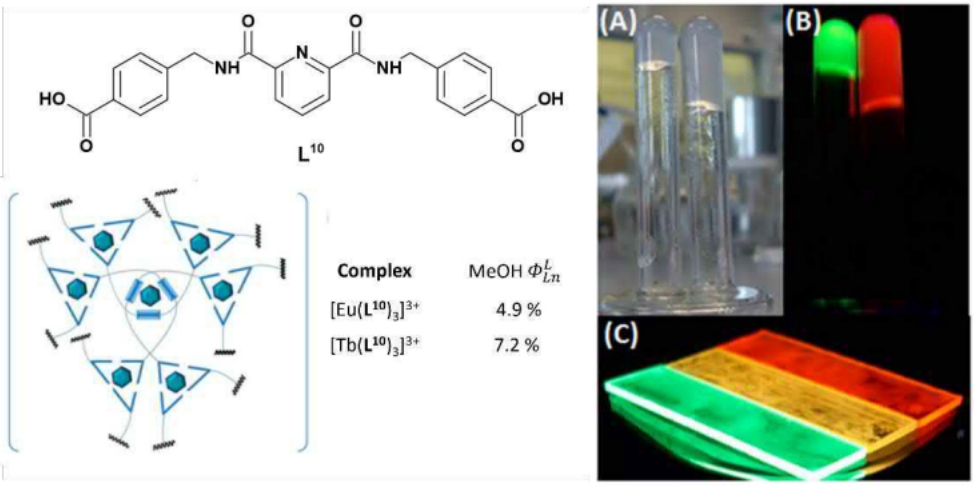

Figure 2.6.. Gunnlaugsson and co-workers L^{10} ligand architectures for $[Ln(L^{10})_3]^{3+}$ assemblies.. Φ_{Ln}^{L} of $[Eu(L^{10})_3]^{3+}$ and $[Tb(L^{10})_3]^{3+}$ in MeOH, values taken from reference 18.. Additional 0.5 equivalents of Ln^{3+} results in "cross-linked" supramolecular self-assemblies (Left).. (Right) Luminescent gels formation of $[Ln(L^{10})_3:Ln(CH_3COO)_3]^{3+}$,. shown under ambient light (A),. under UV irradiation (B) and gels spread on quartz plates (C). (Ln = Eu^{3+} (red),. Tb^{3+} (green) and $Eu^{3+}:Tb^{3+}$ (1:1,. orange)).. Image adapted with permission from M. Martínez-Calvo, O. Kotova, M. E. Möbius, A. P. Bell, T. McCabe, J. J. Boland and T. Gunnlaugsson, J. Am. Chem. Soc., 2015, **137**, 1983-1992. *Copyright 2022 American Chemical Society..*

The Gunnlaugsson group also developed lanthanide based luminescent thin films by the Langmuir-Blodgett (LB) technique.[23-26] Unsymmetrically modifying the PDA motif is relatively common when multiple PDA binding pockets are present in the ligand architecture. To the best of our knowledge L^{12} is the only example of an unsymmetric singular PDA ligand motif. The unsymmetric approach clearly allows for the increase in functionality in which different substituents can focus on different functions. Gunnlaugsson and co-workers L^{12} (Figure 2.7) demonstrates this, in which the chiral naphthalene is present for CD and CPL applications, while the long alkyl chain is present for LB film formation (see Section 4.1 for details of LB formation). When complexed with Ln^{3+} (where Ln^{3+} = Eu^{3+}, Tb^{3+}, Sm^{3+}, Dy^{3+}, Nd^{3+} and Lu^{3+}), the tris-mononuclear $[Ln(L^{12})_3]^{3+}$ are again formed, in most cases forming visible emissive complexes except for $[Dy(L^{12})_3]^{3+}$ and $[Lu(L^{12})_3]^{3+}$ which were non emissive and $[Nd(L^{12})_3]^{3+}$ which is NIR emitting. These luminescent complexes successfully retain the luminescent properties after LB deposition, resulting in luminescent LB films, including CPL emission properties in the case of $[Eu(L^{12})_3]^{3+}$ (in $[Sm(L^{10})_3]^{3+}$ and $[Tb(L^{10})_3]^{3+}$ CPL is present in solution but lost upon deposition).

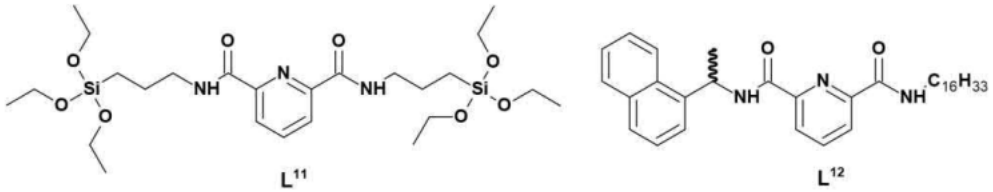

Figure 2.7.. L^{11} ligand architecture is utilized to form $[Ln(L^{11})_3]^{3+}$ and subject to the sol-gel method,. for a range of different films and gels.. Gunnlaugsson and co-workers L^{12} ligand architectures for $[Ln(L^{12})_3]^{3+}$.. assemblies are used to form luminescent LB films.. It is worth noting that there is also a version of L^{12} similar to L^{5} but is only investigated for Eu^{3+} complexes and LB films..

2.2.2 Multitopic Ligand Architectures

With PDA retaining a relatively predictable 1:3 M:L assembly with Ln^{3+}, larger ligand architectures which contain multiple PDA binding pockets have been designed such that in the presence of Ln^{3+}, complex lanthanide assemblies form. These included encapsulating mononuclear assemblies such as tripodal podates[27-29] and knots,[30-32] or multinuclear assemblies such as helicates,[33-38] cages[38-42] and larger assemblies.[43, 44] The first example of a ligand architecture containing multiple PDA binding pockets was designed by Bünzli, Piguet and co-workers as a follow up to their **L**[1] system, linking three PDA motifs by a triethylamine linker **L**[13] (Figure 2.8).[27, 28] In the presence of Ln^{3+}, **L**[13] forms $[Ln(\mathbf{L^{13}})]^{3+}$ encapsulating mononuclear tripodal podates assemblies (Figure 2.8), which were found to slightly improve Φ_{Ln}^{L} and kinetic stability over the discrete assemblies with **L**[1].[27, 28]

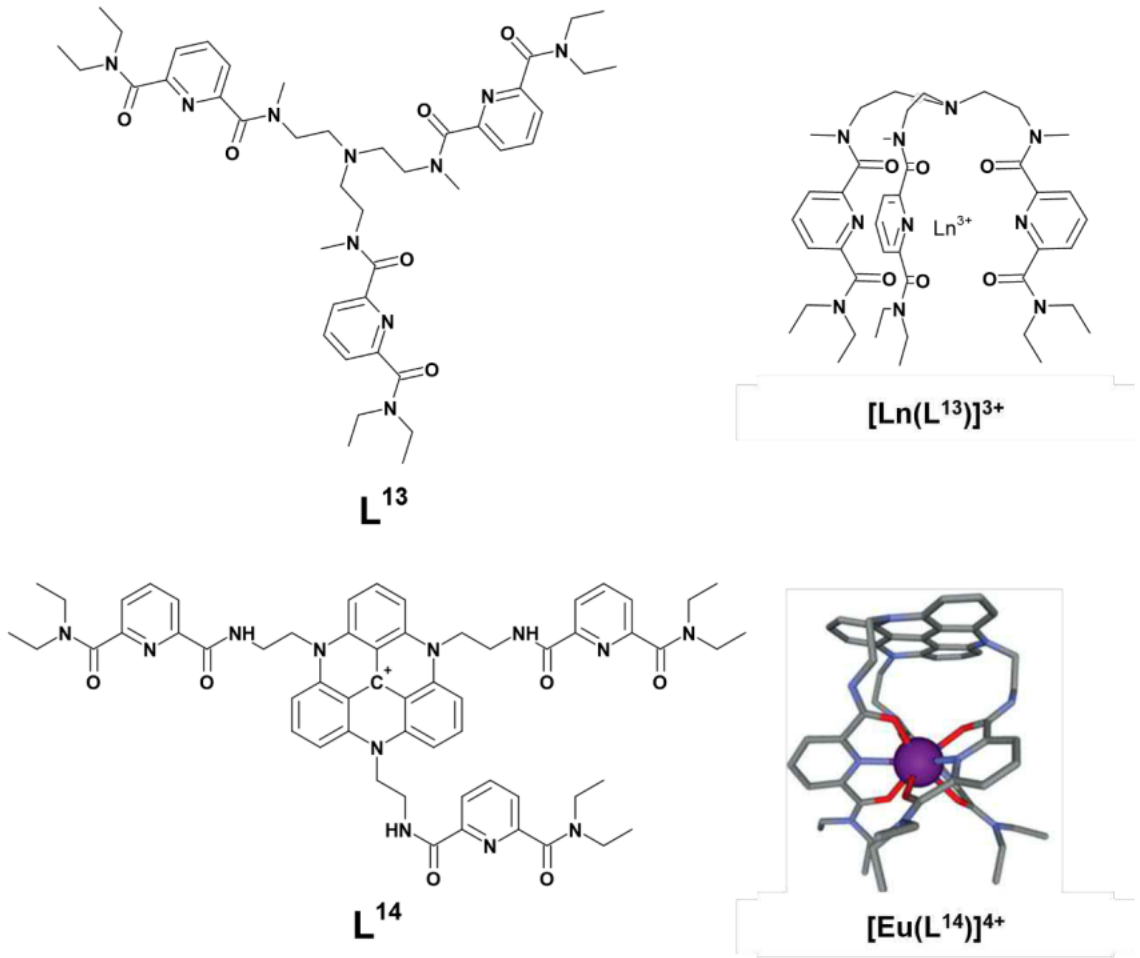

*Figure. 2.8.. (Top). Bünzli,. Piguet. and. co-workers. triethylamine. linker. **L**[13] which. forms. [Ln(**L**[13])]$^{3+}$. encapsulating. mononuclear. tripodal podates. assemblies.. (Bottom). Lacour. and. co-workers. tripodal. **L**[14] PDA. ligand. and. model. encapsulating. mononuclear. tripodal. podates. [Eu(**L**[14])]$^{4+}$.. Image. adapted. with. permission. from. J.. Hamacek,. C.. Besnard,. N.. Mehanna. and. J.. Lacour,.* Dalton Trans.*,. 2012,. **41**,. 6777-6782.. Copyright. 2022. Royal. Society. of. Chemistry..*

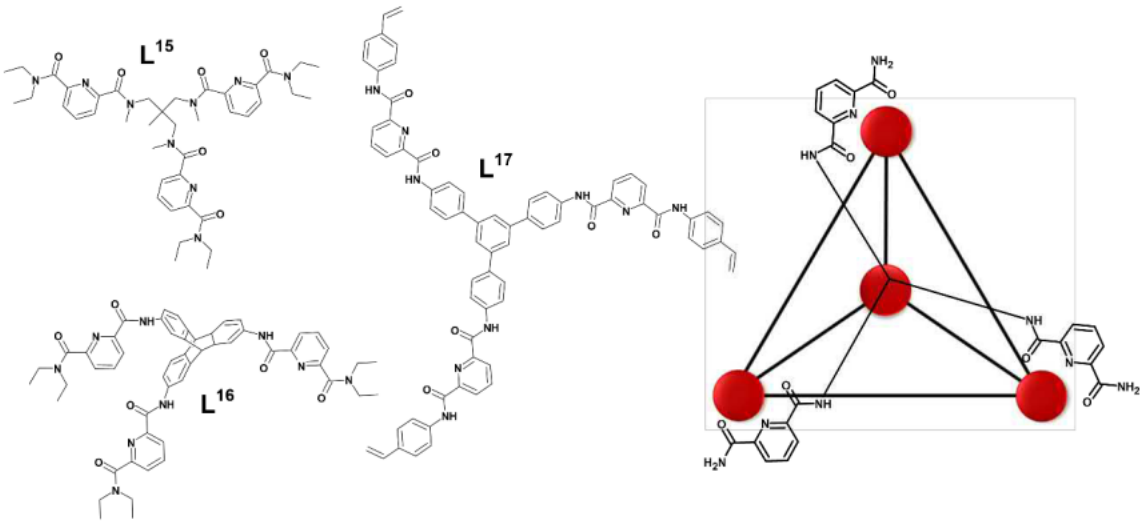

*Figure 2.9.. (Left). Tripodal PDA ligand:. **L15**. and. **L16**. by. Hamacek. and. co-worker,. and. **L17**. by. Sun. and. co-workers.. (Right). Tetrahedral [Ln4L4]12+. cage. assemblies. which. ligands. **L15-17**. form. in. the. presence. of. 1. equivalent. of. Ln3+..*

Since then, similar tripodal ligand architectures have been developed, which also form encapsulating mononuclear tripodal podates in the case of **L14** (Figure 2.8)[29] or tetrahedral $[Ln_4L_4]^{12+}$ cage assemblies in the cases of **L15**, **L16** and **L17** (Figure 2.9),[39-41] both of which occur when in a 1:1 ratio of Ln^{3+}:**L**. The defining factor between cage formation over podate formation is largely to do with the tripodal anchor design, which links the PDA motifs. The tripodal anchors of **L16** and **L17** are rigid triptycene[40] or 1,3,5-triphenylbenzene[41] respectively, not allowing for podate formation and thus favouring the tetrahedral $[Ln_4L_4]^{12+}$ cage assemblies. While **L14** may also contain a rigid triazatriangulenium, the PDA binding pockets are connected by a flexible ethane chain, facilitating the encapsulating mononuclear tripodal podates. Similarly, Hamacek and co-workers **L15** ligand design, although very close to Bünzli, Piguet and co-workers **L13** system, forms tetrahedral $[Ln_4L_4]^{12+}$ cage assemblies over the encapsulating geometry. A subtle difference in the chain length connecting the PDA motif to the tripodal anchor reduces the flexibility of the PDA binder, favouring the cage formation.

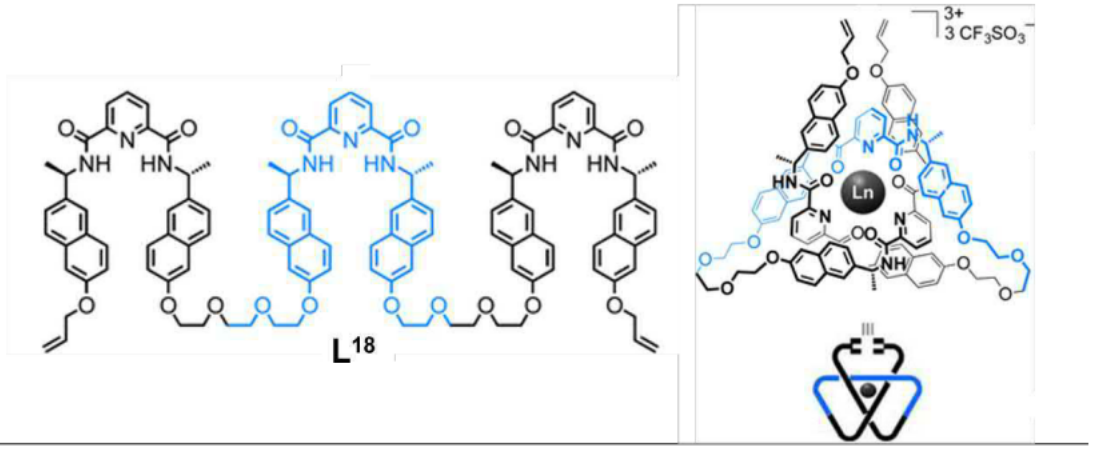

*Figure 2.10.. Leigh. and. co-workers. single. molecular. strand **L18**. for. knot. formation. of. [Ln(**L18**)]3+.. Image. adapted. from. open. access. and CC-BY. article,. G.. Gil-Ramírez,. S.. Hoekman,. M.. O.. Kitching,. D.. A.. Leigh,. I.. J.. Vitorica-Yrezabal. and. G.. Zhang,. J. Am. Chem. Soc.,. 2016, **138**,. 13159-13162...*

Ligand architectures that contain three PDA binding pockets are not only tripodal assemblies. Carrying on from their use of discrete molecules for the formation of knot assemblies, Leigh and co-workers moved towards using a single molecular stranded ligand architecture **L**[18] (Figure 2.10) for knot formation.[32] In the presence of Ln^{3+}, **L**[18] self-assembles into a knot with both terminal allyl groups found in close proximity (Figure 2.10), allowing for the knot to be closed by RCM. Leigh and co-workers knot formation by a single molecular strand (**L**[18]) rather than from three discrete molecules (**L**[8,9]) allows for the terminal ends to be used for other applications. Initially Leigh and co-workers used this new single molecular strand knot as a stopper knot for a rotaxane assembly **L**[19] (Figure 2.11). They demonstrated the self-assembling knot could act as a molecular "switch" in which the knot "stopper" could be untied or tied, unlocking or locking the macrocycle onto the axle. Under the right conditions threading of the macrocycle through **L**[19] onto the axle could be facilitated and knot formation in the presence of Ln^{3+} would lock the

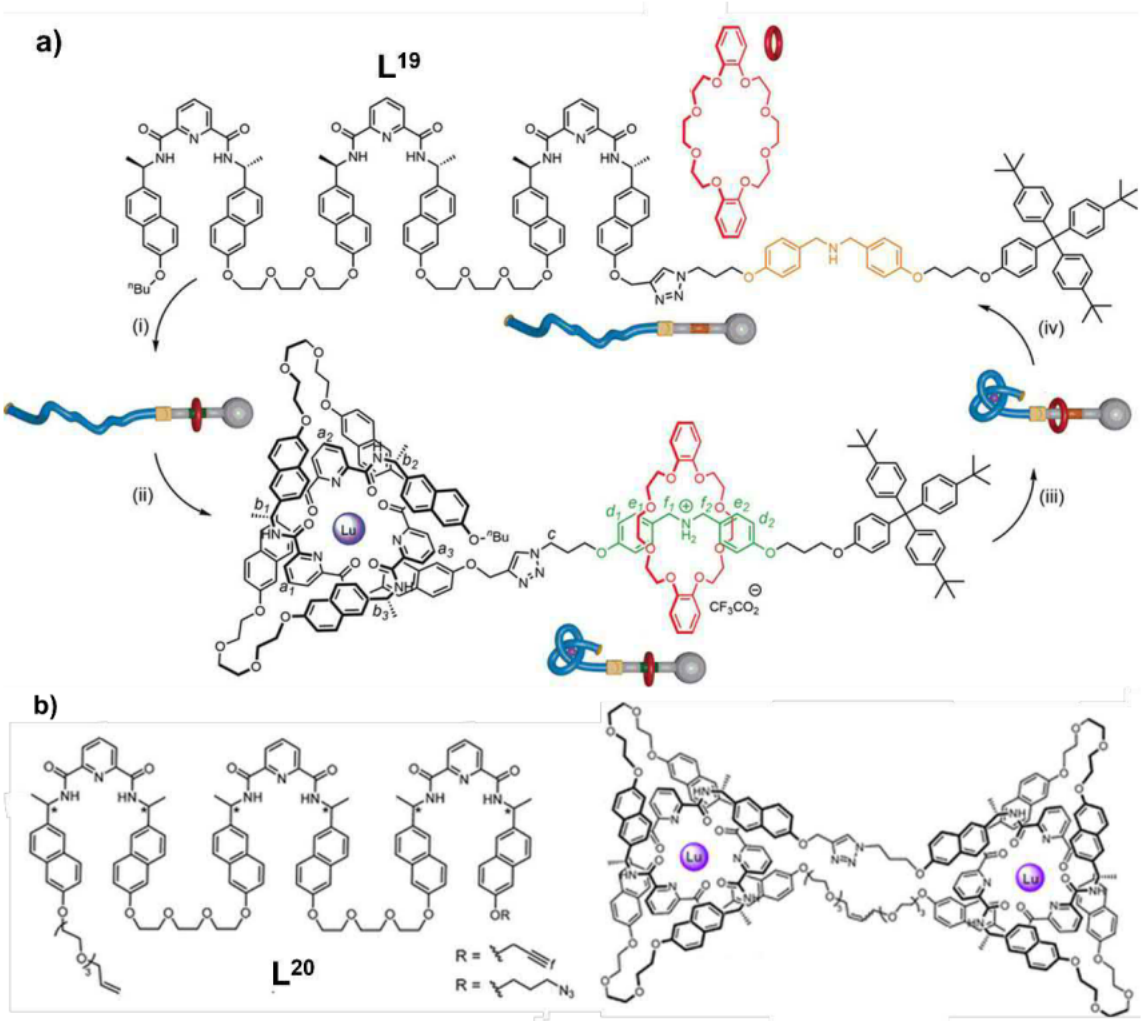

Figure. 2.11.. a). Leigh. and. co-workers. single. molecular. strand,. connected. to. an. axle. (orange). via. a. 1,2,3-triazole. linker. forming. ***L*[19]***.. It. can. be. seen. in. the. image. that. the. macrocycle. can. thread. the. untied.* ***L*[19]** *which. is. then. closed. by. the. presence. of. Ln^{3+}. forming. the. knot stopper.. Following. this. the. knot. can. be. untied. and. the. macrocycle. unthreaded.. Image. adapted. from. open. access. and. CC-BY. article,. D.. A.. Leigh,. L.. Pirvu,. F.. Schaufelberger,. D.. J.. Tetlow. and. L.. Zhang,. Angew.. Chem.. Int.. Ed.,. 2018,.* ***57***,*. 10484-10488.. b). Leigh. and. co-workers. single. molecular. strand. with. different. terminal. ends.* ***L*[20]** *for. the. formation. of. granny. and. square. knots. (right). by. 1,2,3-triazole. "click". chemistry. and. RCM.. Image. adapted. from. open. access. and. CC-BY. article.. D.. A.. Leigh,. L.. Pirvu. and. F.. Schaufelberger,. J.. Am.. Chem.. Soc. 2019,.* ***141***,*. 6054-6059..*

macrocycle in place, while removal of Ln^{3+} would result in untying of the knot and thus unthreading of the macrocycle. Following this Leigh and co-workers have used the now free terminal ends of **L**[20] to connect two different knots to form granny and square knots (Figure 2.11).[30] In reality this entails connecting knots of the same chirality (granny) or different chirality (square) by initially 1,2,3-triazole "click" chemistry and then RCM to close the new knots. It is worth mentioning both the stopper knot and granny/square knots as it is to the best of our knowledge the only instance in which 1,2,3-triazole "click" chemistry has been used on the side substituents of PDA molecules used in lanthanide assemblies.

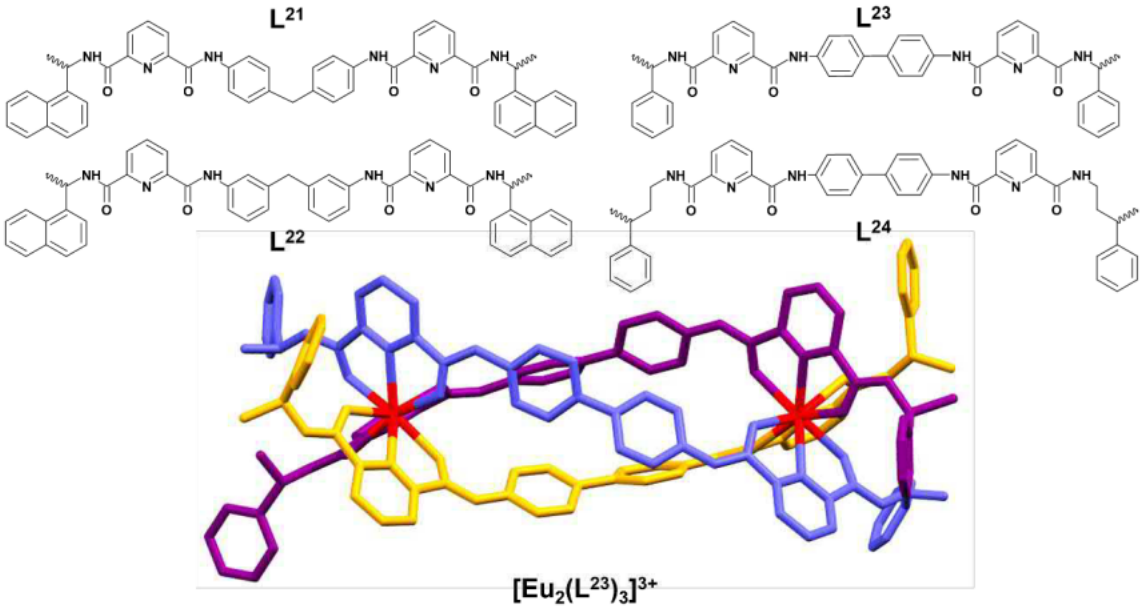

Figure. 2.12.. Gunnlaugsson. and. co-workers. ***L*** *[21,22]. and. Law. and. co-workers.* ***L*** *[23,24]. forming. Ln_2L_3 helicate. assemblies.. Below. is. a. crystal structure. of. $[Eu_2(L^{23})_3]^{6+}$. (ΛΛ). helicate. assembly.. Crystal. structure. of. helicate. assembly. adapted. with. permission. from. J. C.-T.. Yeung,. W. T.. K.. Chan,. S.-C.. Yan,. K.-L.. Yu,. K.-H.. Yim,. W.-T.. Wong. and. G.-L.. Law,. Chem.. Commun.,. 2015,.* ***51*** *,. 592-595.. Copyright. 2022. Royal. Society of. Chemistry...*

The predictable coordination of the PDA motif has also led to the design of ligand architectures containing two PDA binding pockets, predominantly self-assembling into chiral helicate assemblies ($[Ln_2L_3]^{6+}$) but also cage assemblies ($[Ln_4L_6]^{12+}$ and $[Ln_8L_{12}]^{24+}$) in the presence of Ln^{3+}. PDA based helical assemblies were first investigated by Gunnlaugsson and co-workers continuing their use of their PDA appended chiral naphthalene substituents (**L**[4]), now linking two unsymmetrical PDA appended motifs (**L**[39,40]) to form **L**[21,22] (Figure 2.12). In the presence of Eu^{3+} they formed enantiomeric helicate assemblies ($[Eu_2(L^{21,22})_3]^{6+}$, ΔΔ for R,R and ΛΛ for S,S) capable of CPL emission.[35, 36] Since then, similar chiral helicate assemblies have been developed, now building off Muller and co-workers chiral centre benzyl substituent motif (**L**[6]). Law and co-workers demonstrated that the chiral centre must be close to the PDA coordination pocket, otherwise chirality is not transferred to Eu^{3+} as in the case of **L**[24],[37] while Sun and co-workers formed similar chiral helicates, modifying the linking substituent to add functionality to the helicate assembly. **L**[25] forms dual emissive helicate assemblies by the incorporation of a pyrene

linker,[34] whereas **L**[26] contains a photochromic linker able to increase (ring closed) or decrease (ring open) Eu^{3+} centred emission dependent on the linker state (Figure 2.13).[33] Additionally, in Sun and co-workers investigation of different linking motifs, they demonstrated that ligand architectures containing two PDA binding pockets could preferably self-assemble into tetrahedral cages ($[Ln_4\mathbf{L_6}]^{12+}$) in the case of **L**[27],[42] or simultaneously form cages and helicate assemblies, with **L**[28] forming a tetrahedral cage and **L**[29] forming a cubic cage ($[Ln_8\mathbf{L_{12}}]^{24+}$) alongside their helicate assemblies (Figure 2.13).[38]

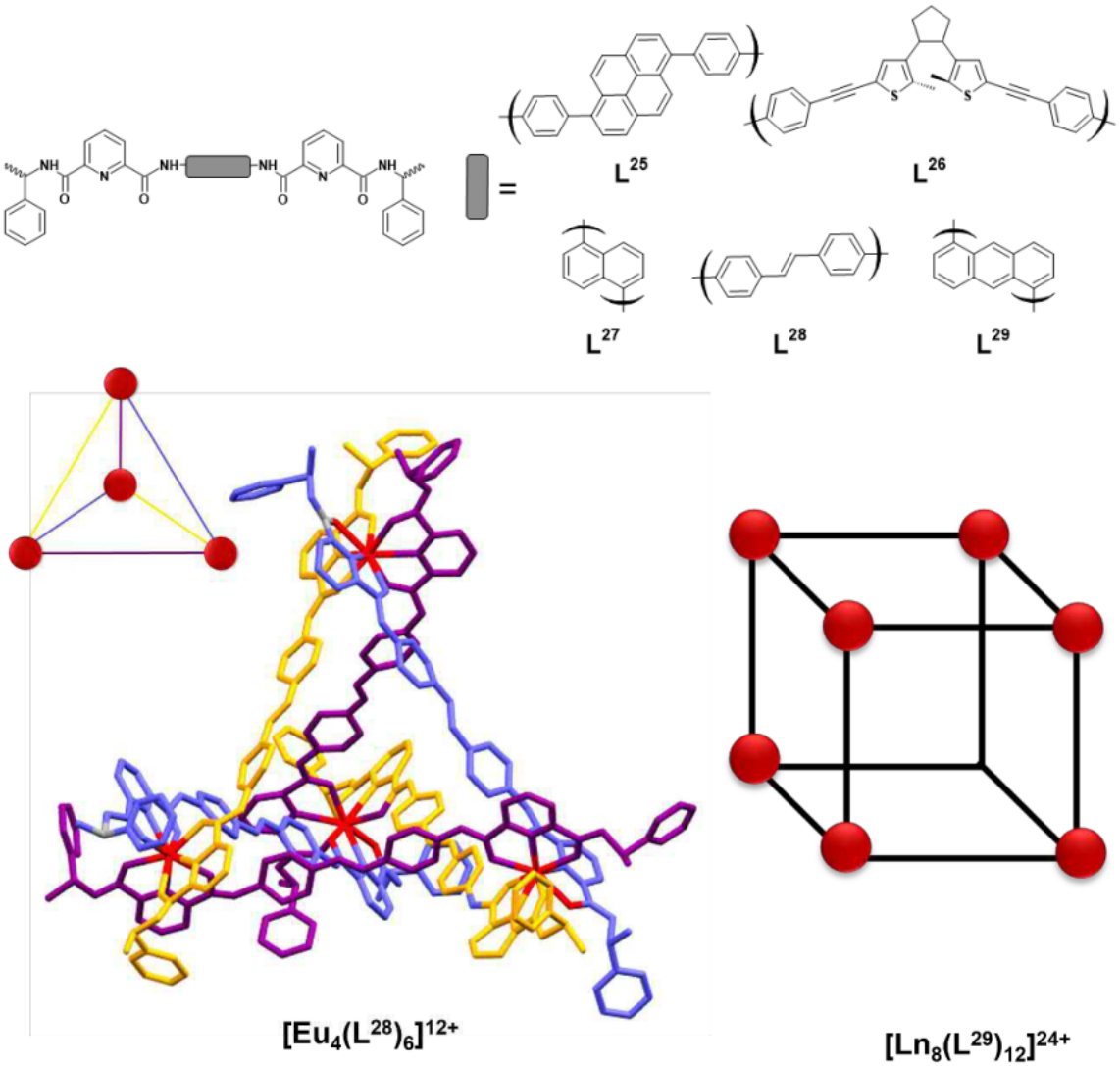

*Figure. 2.13.. (Top). Ligand. architectures. which. have. been. used. to. form. helicate. assemblies. $[Ln_2\mathbf{L_3}]^{6+}$. (**L**[25, 26, 28 & 29])*,*. tetrahedral. cages $[Ln_4\mathbf{L_6}]^{12+}$. (**L**[27,28]). and. cubic. cages. $[Ln_8\mathbf{L_{12}}]^{24+}$. (**L**[29])*.. (Bottom). Crystal. structure. of. the. tetrahedral. cage. assembly. of. $[Eu_4(\mathbf{L^{28}})_6]^{12+}$ and. a cartoon. representation. of. cubic. cage. arrangement.. Crystal. structure. of. the. tetrahedral. cage. adapted. with. permission. from. X.-Z.. Li,. L.-P.. Zhou,. L.-L.. Yan,. D.-Q.. Yuan,. C.-S.. Lin. and. Q.-F.. Sun,. J.. Am.. Chem.. Soc.,. 2017,. **139**,. 8237-8244.. Copyright. 2022. American. Chemical Society..*

Finally, larger multinuclear assemblies have been developed utilizing the predictable coordination of the PDA motif. Following on from their tripodal $\mathbf{L^{15}}$ ligand architecture, which formed tetrahedral cages, Hamacek and co-workers modified $\mathbf{L^{15}}$, extending the structure to include an additional PDA binding unit at a single side of the tripodal ligand ($\mathbf{L^{30}}$)[43] and at all three ends ($\mathbf{L^{31}}$)[44] (Figure 2.14). In the presence of Ln^{3+} (and 1 equivalent of $\mathbf{L^{15}}$), $\mathbf{L^{30}}$ forms pentanuclear assemblies $[Ln_5(\mathbf{L^{30}})_3(\mathbf{L^{15}})]^{15+}$ as confirmed by MS. Although crystal structures of the pentanuclear assemblies were elusive, molecular calculations of $[Ln_5(\mathbf{L^{30}})_3(\mathbf{L^{15}})]^{15+}$ showed a tetrahedral cage assembly ($Ln_4(\mathbf{L^{30}})_3(\mathbf{L^{15}})$) topped with a helicate tower ($Ln_2(\mathbf{L^{30}})_3$). Hamacek and co-workers follow up $\mathbf{L^{31}}$ system in the presence of Ln^{3+} forms octanuclear assemblies $[Ln_8(\mathbf{L^{31}})_4]^{24+}$ confirmed by MS. Again, the crystal structure could not be obtained, although with molecular calculations reveals a T-shaped tripodal triple stranded helicate formation, which overall results in a tetrahedral shaped assembly (Figure 2.14).

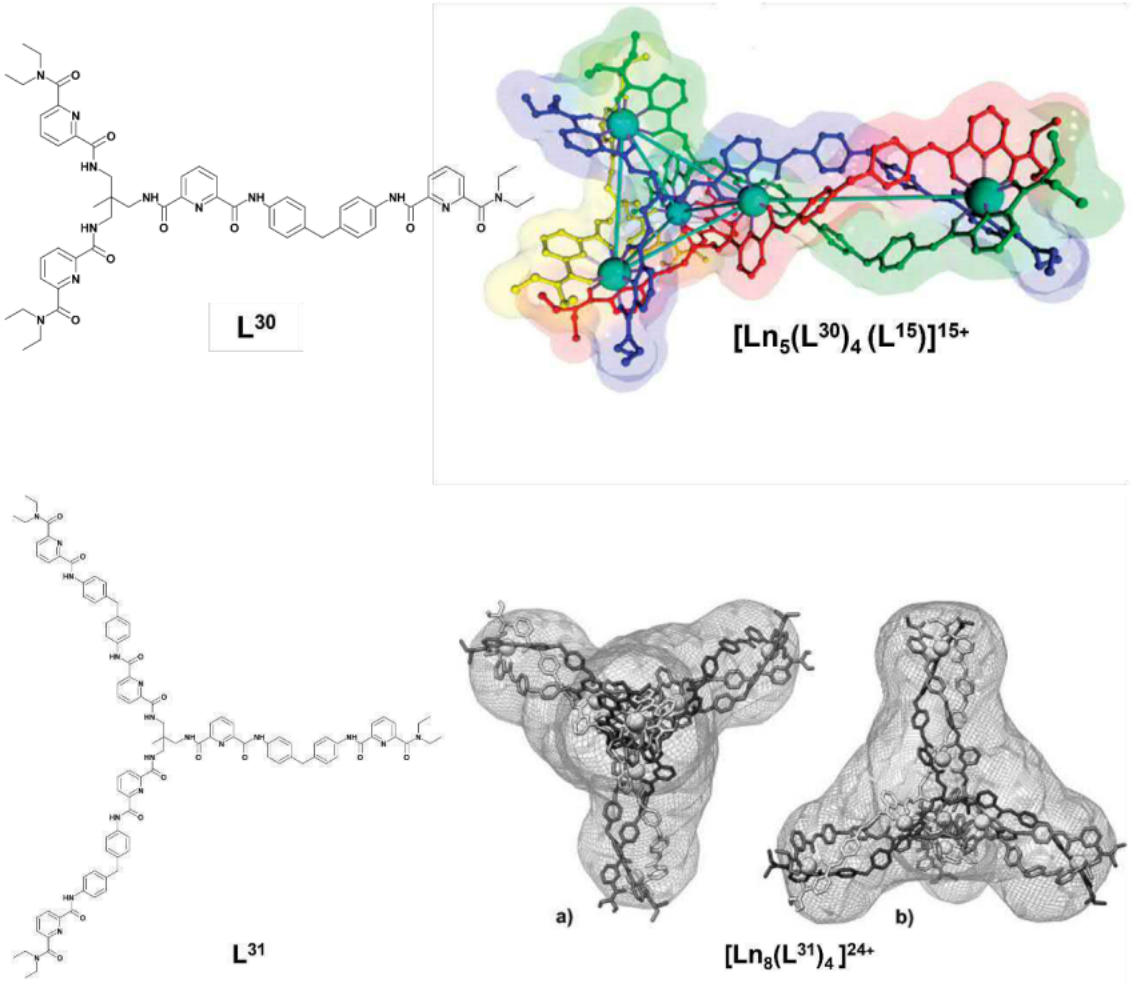

*Figure. 2.14.. Hamacek. and. co-workers. larger. assemblies. with. their. initial. pentanuclear. assemblies. $[Ln_5(\mathbf{L^{30}})_3(\mathbf{L^{15}})]^{15+}$. formed. with. $\mathbf{L^{30}}$ (Top). and. their. octanuclear. assemblies. $[Ln_8(\mathbf{L^{31}})_4]^{24+}$. formed. with. $\mathbf{L^{31}}$.. On. the. right. of. each. ligand. structure. is. their. calculated. complex structure. with. Ln^{3+}.. Images. adapted. with. permission. from. B.. E.. Aroussi,. S.. Zebret,. C.. Besnard,. P.. Perrottet. and. J.. Hamacek,. J.. Am.. Chem. Soc.,. 2011,. **133**,. 10764-10767.. Copyright. 2022,. American. Chemical. Society,. and. S.. Zebret,. E.. Vögele,. T.. Klumpler. and. J.. Hamacek, Chem.. Eur.. J.,. 2015,. **21**,. 6695-6699. respectively.. Copyright. 2022,. John. Wiley. and. Sons. Publishing,. respectively..*

2.3 6-Carbamoylpyridine-2-carboxcylic (PDC)

In comparison publications on PDC ligand architectures used in lanthanide assemblies are relatively scarce. The first use of the PDC motif for lanthanide assemblies was by Horrocks and Lessmann, in which three PDC based ligand architectures **L**[32], **L**[33] and **L**[34] (Figure 2.15) were synthesised for their expected formation of neutral helicate assemblies (Ln_2**L**$_3$) and tris-mononuclear Ln(**L**)$_3$ assemblies.[45] The investigation into the lanthanide complexes formed in the presence of said ligands is very limited, as lanthanide complexes were not isolated and all reported photophysical measurements are taken from solution mixtures of ligand and Ln^{3+}. As a result, lanthanide coordination into the NO_2 pocket and lanthanide species formation are not confirmed in this study. However, Horrocks and Lessmann demonstrate that from fluorescent titration measurements in water, the PDC antenna can effectively populate both Eu^{3+} and Tb^{3+} excited states resulting in Ln^{3+} centred emission and that the systems self-assembled into the Ln_2(**L**)$_3$ and Ln(**L**)$_3$ assemblies. Importantly this study alludes to the additional complex stability that the anionic carboxylate adds, with their more labile PDA counterparts unlikely to be able to form Ln(**L**)$_3$ assemblies in such a competitive solvent.

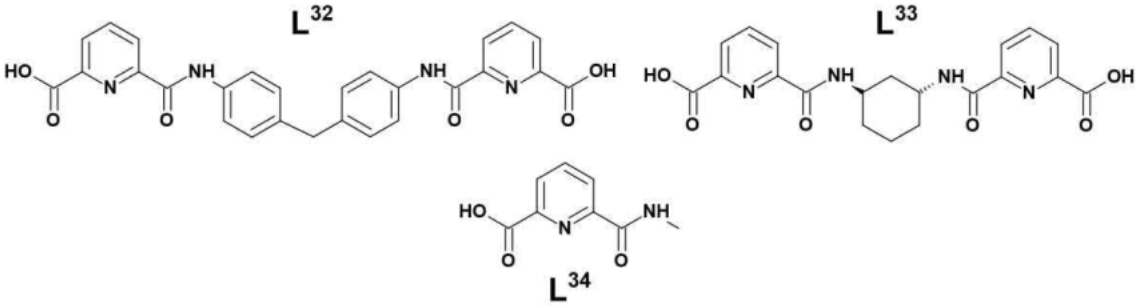

Figure 2.15. Horrocks and Lessmann's ligand architectures ***L*[32], *L*[33] *and* *L*[34].**

This improved stability is confirmed in Bünzli, Piguet and co-workers follow up study from their **L**[13] system, replacing the terminal amides for an anionic carboxylate **L**[35].[46] Firstly, akin to its predecessor in the presence of Ln^{3+}, **L**[35] does predictably coordinate with Ln^{3+} forming the expected encapsulating mononuclear tripodal podates Ln(**L**[35]) confirmed by crystal structure (Figure 2.16). However, unlike [Ln(**L**[13])]$^{3+}$ which dissociates in the presence of water, Ln(**L**[35]) with the added anionic carboxylate was found to be very stable in the competitive solvent. The improvement continues with photophysical measurements of Ln(**L**[35]), increasing Φ_{Ln}^{L} for both Eu^{3+} and Tb^{3+}, while the antenna n_{sens} specifically for Eu^{3+} is calculated to have improved 10-fold (see Figure 2.16 for values). However, with the improved stability and photophysical properties, the inclusion of the three anionic carboxylates results in a significantly insoluble complex.

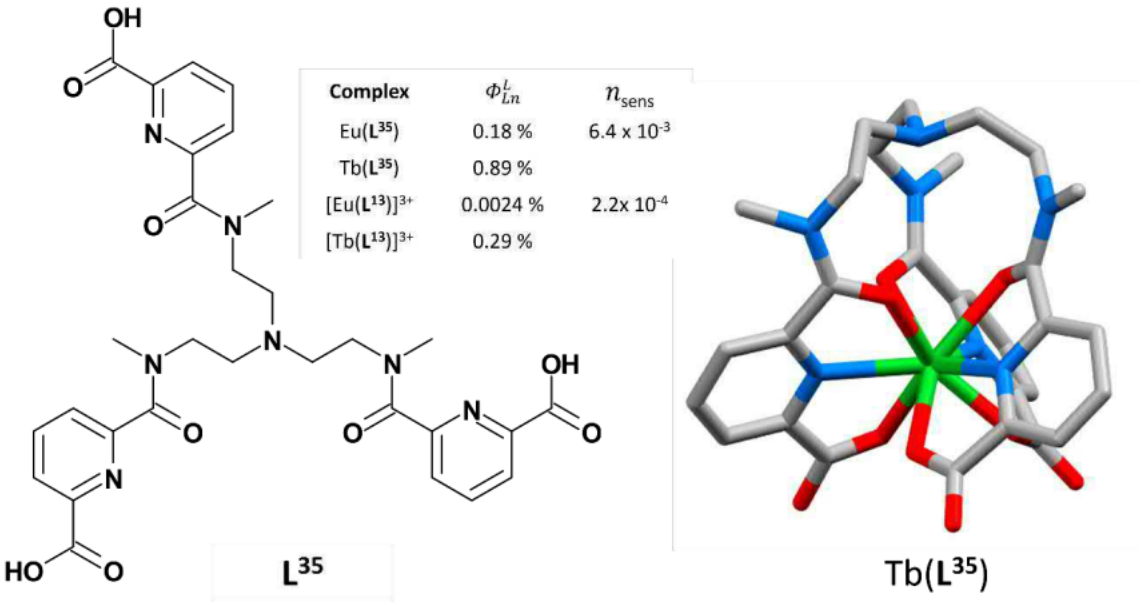

Complex	Φ_{Ln}^{L}	n_{sens}
Eu(L^{35})	0.18 %	6.4 x 10^{-3}
Tb(L^{35})	0.89 %	
$[Eu(L^{13})]^{3+}$	0.0024 %	2.2x 10^{-4}
$[Tb(L^{13})]^{3+}$	0.29 %	

*Figure 2.16. Bünzli, Piguet and co-workers L^{35} ligand architecture and corresponding Tb(L^{35}) crystal structure. Φ_{Ln}^{L} for Ln(L^{35}) (measured in H_2O) and $[Ln(L^{35})]^{3+}$ (measured in MeCN:H_2O, 4:1), values taken from reference 46. Crystal structure of Tb(L^{35}) encapsulating mononuclear tripodal podate assembly adapted with permission from J.-M. Senegas, G. Bernardinelli, D. Imbert, J.-C. G. Bünzli, P.-Y. Morgantini, J. Weber and C. Piguet, Inorg. Chem., 2003, **42**, 4680-4695. Copyright 2022, American Chemical Society.*

The solubility issues noted for L^{35} were overcome in other PDC based assemblies, where ligand architectures are discrete, forming tris-mononuclear Ln(**L**)$_3$ assemblies.[47-49] An and co-workers L^{36} ligand architecture was the first discrete PDC motif to be fully investigated for tris-mononuclear Ln(**L**)$_3$ assemblies. L^{36} was complexed with a range of visible emissive Ln^{3+} (Eu^{3+}, Tb^{3+}, Dy^{3+} and Sm^{3+}) and UV emissive Gd^{3+}, with Ln(**L**)$_3$ formation confirmed by elemental analyses and crystal structures (Figure 2.17) which indicated for all complexes that the assemblies are symmetric with anionic carboxylates on one side of the complex. Photophysical measurements were carried out in ethanol and resulted in the expected Ln^{3+} transitions in the visible region for Eu^{3+}, Tb^{3+} and Sm^{3+} and UV region for Gd^{3+}. Again Φ_{Ln}^{L} of the PDC antenna are

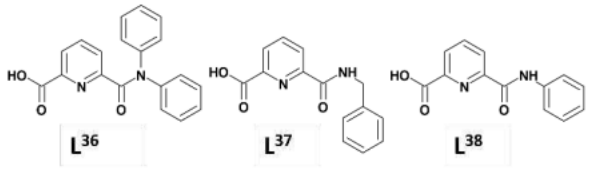

Complex	Φ_{Ln}^{L}
Eu(L^{36})$_3$	12 %
Eu(L^{37})$_3$	15 %
Tb(L^{38})$_3$	34 %

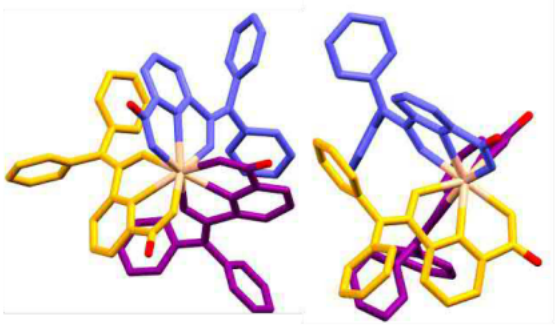

$Sm(L^{36})_3^{+}$

*Figure 2.17. (Top) An and co-workers L^{36}, L^{37} and L^{38} ligand architectures, along with Φ_{Ln}^{L} for Ln(**L**)$_3$ (measured in EtOH) values taken from reference 47 and 48. (Bottom) Crystal structure of Sm(L^{36})$_3$ with carbonyl of the carboxylates highlighted in red, adapted with permission from B.-L. An, M.-L. Gong, M.-X. Li and J.-M. Zhang, J. Mol. Struct., 2004, **687**, 1-6. Copyright 2022, ELSEVIER.*

observed to be significantly higher than PDA based assemblies (Figure 2.17), which from the measured triplet state energy level can be associated with **L**[36] much closer triplet state energy level match (**L**[36], T_1 = 20,477 cm^{-1})[47] to that of Eu^{3+} and Tb^{3+} compared to PDA antennae. Improved Φ_{Ln}^{L} are further observed by An and co-workers **L**[37] system, where tris-mononuclear Eu(**L**[37])$_3$ and Tb(**L**[37])$_3$ assemblies recorded, to the best of our knowledge, the highest Φ_{Ln}^{L} for discrete PDC tris-mononuclear assemblies to date.[50] Furthermore An and co-workers investigated **L**[38] for Ln^{3+} coordination, which also formed tris-mononuclear Eu(**L**[38])$_3$ and Tb(**L**[38])$_3$ complexes, although Φ_{Ln}^{L} were not reported.[51]

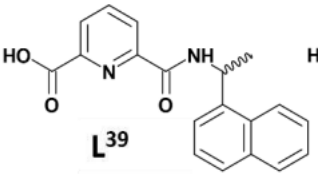

L[39]

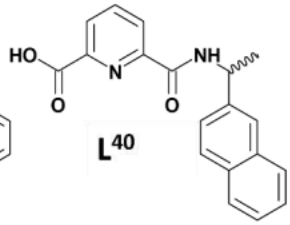

L[40]

Complex	Φ_{Ln}^{L} MeCN	Φ_{Ln}^{L} MeOH
Eu(**L**[39])$_3$ (R)	8.2 %	2.2 %
Eu(**L**[39])$_3$ (S)	8.4 %	2.3 %
Eu(**L**[40])$_3$ (R)	2.1 %	0.6 %
Eu(**L**[40])$_3$ (S)	1.6 %	0.5 %

*Figure 2.18.. Gunnlaugsson and co-workers **L**[39] and **L**[40] ligand architectures, with Φ_{Ln}^{L} for Ln(**L**)$_3$ values taken from reference 53..*

Gunnlaugsson and co-workers continued their trend of incorporating chirality into the ligand architecture by investigating ligands **L**[39] and **L**[40] for enantiomeric tris-mononuclear Ln(**L**)$_3$ assemblies (Figure 2.18).[52, 53] Similar to other PDC systems, in the presence of Eu^{3+} both ligands form Eu(**L**)$_3$ assemblies. Photophysical measurements of the Eu(**L**)$_3$ were able to be done in MeCN and MeOH, again demonstrating Eu^{3+} emission and CPL emission. Surprisingly, contrary to previous PDC based antenna, Φ_{Ln}^{L} are found to be relatively similar to their PDA predecessors **L**[4] and **L**[5] in MeCN, while in MeOH Φ_{Ln}^{L} are much weaker. This significant decrease observed in MeOH is potentially associated with the better shielding that the bulkier PDA ligands (**L**[4], **L**[5]) provide the complex, protecting Ln^{3+} from solvent interaction, however, without Φ_{Ln}^{Ln}, this can only be speculated.

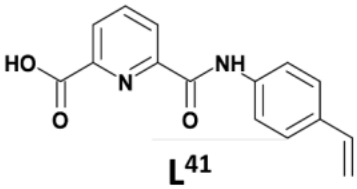

L[41]

*Figure 2.19.. Bünzli and co-workers **L**[41] ligand architecture for formation of Ln^{3+} luminescent resins..*

Finally, to the best of our knowledge the only example for which the PDC motif has been used for materials formation was developed by Bünzli and co-workers. They developed PDC based resins for the purpose of extraction of Ln^{3+} and the rare earth Y^{3+}. This entailed utilizing the PDC motif to form the predictable Ln(**L**)$_3$ assemblies which would then be polymerised by incorporating a terminal styrene within the ligand architecture (**L**[41], Figure 2.19).[54] Firstly, as with

previous PDC motifs **L^{41}** was observed to form Ln(**L^{41}**)$_3$ assemblies (where Ln = Eu^{3+}, Tb^{3+} and La^{3+}), which in the case of Eu(**L^{41}**)$_3$ and Tb(**L^{41}**)$_3$ are found to be luminescent. They then utilized rare earth Y^{3+} to form Y(**L^{41}**)$_3$ assemblies. The Y(**L^{41}**)$_3$ complex is subjected to polymerisation with divinylbenzene, resulting in polymer resins. The Y^{3+} was then removed, resulting in polymer resins which retain the ion coordination cavities, which then was refilled with other Ln^{3+} such as Eu^{3+} to form luminescent polymer resins.

The PDA motif is clearly the more popular motif in comparison to PDC, with a variety of ligand architectures being developed over the last few decades while the PDC motif remains relatively novel. However, in both instances the motifs have been rarely utilized in materials formation, with only a few examples of either motif being used in the formation of luminescent films, gels, or polymer materials. This review highlights the coordination that the PDA and PDC motifs retain with Ln^{3+} even after modification to the carbonyl side arms. This predictability allows researchers to focus on ligand modification for applications, material formation, or the formation of large assemblies without having to be concerned with impacting the formation of the 1:3 M:L coordination sphere. Additionally, both motifs have demonstrated that they can indirectly populate a range of Ln^{3+}, meaning the motif can be employed for various applications which may require certain Ln^{3+}. It is for these reasons that both motifs are ideal for base scaffolds used in the "molecular toolbox" synthetic strategy as they allow for modifications which are in most cases unlikely to impact Ln^{3+} coordination, and a range of Ln^{3+} can be used for different applications if desired. While the PDA motif allows for both sides of the ligand to be modified, the unsymmetrical approach shows promise as it allows for different substituents with different properties (*i.e* materials formation and sensor) to be incorporated into the same ligand architecture. The PDC motif in most cases demonstrates improved kinetic stability and overall quantum yields, but only allows for functionality to be added on one side of the motif, meaning functionality is limited or multiple properties must be encompassed in a single substituent. It is because of this that both motifs will be investigated for the "molecular toolbox" synthetic strategy, as depending on the desired application, both motifs have drawbacks and benefits that can manipulated.

2.4 References

1. K. Binnemans, *Chem. Rev.*, 2009, **109**, 4283-4374.
2. J. A. Kitchen, *Coord. Chem. Rev.*, 2017, **340**, 232-246.
3. K. T. Hua, J. Xu, E. E. Quiroz, S. Lopez, A. J. Ingram, V. A. Johnson, A. R. Tisch, A. de Bettencourt-Dias, D. A. Straus and G. Muller, *Inorg. Chem.*, 2012, **51**, 647-660.
4. R. Jagannathan and S. Soundararajan, *Indian J. Chem.*, 1979, **18A**, 319-321.
5. R. Jagannathan and S. Soundararajan, *J. Coord. Chem.*, 1979, **9**, 31-35.
6. F. Renaud, C. Piguet, G. Bernardinelli, J.-C. G. Bünzli and G. Hopfgartner, *Chem. Eur. J.*, 1997, **3**, 1646-1659.
7. T. Le Borgne, J.-M. Bénech, S. Floquet, G. Bernardinelli, C. Aliprandini, P. Bettens and C. Piguet, *Dalton Trans.*, 2003, 3856-3868.
8. A. S. Chauvin, F. Gumy, D. Imbert and J. C. G. Bünzli, *Spectrosc. Lett.*, 2004, **37**, 517-532.
9. S. Tanase, P. M. Gallego, R. de Gelder and W. T. Fu, *Inorg. Chim. Acta*, 2007, **360**, 102-108.
10. D. E. Barry, D. F. Caffrey and T. Gunnlaugsson, *Chem. Soc. Rev.*, 2016, **45**, 3244-3274.
11. J. P. Leonard, P. Jensen, T. McCabe, J. E. O'Brien, R. D. Peacock, P. E. Kruger and T. Gunnlaugsson, *J. Am. Chem. Soc.*, 2007, **129**, 10986-10987.
12. O. Kotova, J. A. Kitchen, C. Lincheneau, R. D. Peacock and T. Gunnlaugsson, *Chem. Eur. J.*, 2013, **19**, 16181-16186.
13. S. D. Bonsall, M. Houcheime, D. A. Straus and G. Muller, *Chem. Commun.*, 2007, 3676-3678.
14. Y. Hasegawa, Y. Kitagawa and T. Nakanishi, *NPG Asia Mater.*, 2018, **10**, 52-70.
15. C. Lincheneau, B. Jean-Denis and T. Gunnlaugsson, *Chem. Commun.*, 2014, **50**, 2857-2860.
16. J.-F. Ayme, G. Gil-Ramírez, D. A. Leigh, J.-F. Lemonnier, A. Markevicius, C. A. Muryn and G. Zhang, *J. Am. Chem. Soc.*, 2014, **136**, 13142-13145.
17. G. Zhang, G. Gil-Ramírez, A. Markevicius, C. Browne, I. J. Vitorica-Yrezabal and D. A. Leigh, *J. Am. Chem. Soc.*, 2015, **137**, 10437-10442.
18. M. Martínez-Calvo, O. Kotova, M. E. Möbius, A. P. Bell, T. McCabe, J. J. Boland and T. Gunnlaugsson, *J. Am. Chem. Soc.*, 2015, **137**, 1983-1992.
19. Y. Li, W. Chian, X. Wang, W. Sha, Y. Zhang and W. Jiang, *Photochem. Photobiol.*, 2011, **87**, 618-625.
20. B. C. Barja and P. F. Aramendía, *Photochem. Photobiol. Sci.*, 2008, **7**, 1391-1399.
21. Z. Li, S. Zuo, J. Zhou, X. Yuan, Y. Song and H. Zhang, *Chin. J. Chem.*, 2015, **33**, 292-297.
22. P. N. Minoofar, B. S. Dunn and J. I. Zink, *J. Am. Chem. Soc.*, 2005, **127**, 2656-2665.
23. J. A. Kitchen, D. E. Barry, L. Mercs, M. Albrecht, R. D. Peacock and T. Gunnlaugsson, *Angew. Chem. Int. Ed.*, 2012, **51**, 704-708.
24. D. E. Barry, J. A. Kitchen, M. Albrecht, S. Faulkner and T. Gunnlaugsson, *Langmuir*, 2013, **29**, 11506-11515.
25. D. E. Barry, J. A. Kitchen, L. Mercs, R. D. Peacock, M. Albrecht and T. Gunnlaugsson, *Dalton Trans.*, 2019, **48**, 11317-11325.
26. A. Galanti, O. Kotova, S. Blasco, C. J. Johnson, R. D. Peacock, S. Mills, J. J. Boland, M. Albrecht and T. Gunnlaugsson, *Chem. Eur. J.*, 2016, **22**, 9709-9723.
27. F. Renaud, C. Piguet, G. Bernardinelli, J.-C. G. Bünzli and G. Hopfgartner, *J. Am. Chem. Soc.*, 1999, **121**, 9326-9342.
28. F. Renaud, C. Piguet, G. Bernardinelli, G. Hopfgartner and J.-C. G. Bünzli, *Chem. Commun.*, 1999, 457-458.
29. J. Hamacek, C. Besnard, N. Mehanna and J. Lacour, *Dalton Trans.*, 2012, **41**, 6777-6782.
30. D. A. Leigh, L. Pirvu and F. Schaufelberger, *J. Am. Chem. Soc.*, 2019, **141**, 6054-6059.

31. D. A. Leigh, L. Pirvu, F. Schaufelberger, D. J. Tetlow and L. Zhang, *Angew. Chem. Int. Ed.*, 2018, **57**, 10484-10488.
32. G. Gil-Ramírez, S. Hoekman, M. O. Kitching, D. A. Leigh, I. J. Vitorica-Yrezabal and G. Zhang, *J. Am. Chem. Soc.*, 2016, **138**, 13159-13162.
33. L.-X. Cai, L.-L. Yan, S.-C. Li, L.-P. Zhou and Q.-F. Sun, *Dalton Trans.*, 2018, **47**, 14204-14210.
34. T. Zhang, G.-L. Zhang, L.-P. Zhou, X.-Q. Guo and Q.-F. Sun, *Tetrahedron: Asymmetry*, 2017, **28**, 550-554.
35. C. Lincheneau, R. D. Peacock and T. Gunnlaugsson, *Chem. Asian J.*, 2010, **5**, 500-504.
36. F. Stomeo, C. Lincheneau, J. P. Leonard, J. E. O'Brien, R. D. Peacock, C. P. McCoy and T. Gunnlaugsson, *J. Am. Chem. Soc.*, 2009, **131**, 9636-9637.
37. C.-T. Yeung, W. T. K. Chan, S.-C. Yan, K.-L. Yu, K.-H. Yim, W.-T. Wong and G.-L. Law, *Chem. Commun.*, 2015, **51**, 592-595.
38. X.-Z. Li, L.-P. Zhou, L.-L. Yan, D.-Q. Yuan, C.-S. Lin and Q.-F. Sun, *J. Am. Chem. Soc.*, 2017, **139**, 8237-8244.
39. J. Hamacek, C. Besnard, T. Penhouet and P.-Y. Morgantini, *Chemistry*, 2011, **17**, 6753-6764.
40. J. Hamacek, A. Vuillamy, L. Peterhans, A. Homberg, D. Poggiali, M. W. Schneider and M. Mastalerz, *New J. Chem.*, 2018, **42**, 7803-7809.
41. Q.-Q. Yan, L.-P. Zhou, H.-Y. Zhou, Z. Wang, L.-X. Cai, X.-Q. Guo, X.-Q. Sun and Q.-F. Sun, *Dalton Trans.*, 2019, **48**, 7080-7084.
42. L.-L. Yan, C.-H. Tan, G.-L. Zhang, L.-P. Zhou, J.-C. Bünzli and Q.-F. Sun, *J. Am. Chem. Soc.*, 2015, **137**, 8550-8555.
43. B. E. Aroussi, S. Zebret, C. Besnard, P. Perrottet and J. Hamacek, *J. Am. Chem. Soc.*, 2011, **133**, 10764-10767.
44. S. Zebret, E. Vögele, T. Klumpler and J. Hamacek, *Chem. Eur. J.*, 2015, **21**, 6695-6699.
45. J. J. Lessmann and W. D. Horrocks, *Inorg. Chem.*, 2000, **39**, 3114-3124.
46. J.-M. Senegas, G. Bernardinelli, D. Imbert, J.-C. G. Bünzli, P.-Y. Morgantini, J. Weber and C. Piguet, *Inorg. Chem.*, 2003, **42**, 4680-4695.
47. B.-L. An, M.-L. Gong, K.-W. Cheah, W.-K. Wong and J.-M. Zhang, *J. Alloys Compd.*, 2004, **368**, 326-332.
48. B.-L. An, M.-L. Gong, M.-X. Li and J.-M. Zhang, *J. Mol. Struct.*, 2004, **687**, 1-6.
49. B.-L. An, M.-L. Gong, J.-M. Zhang and S.-L. Zheng, *Polyhedron*, 2003, **22**, 2719-2724.
50. B.-L. An, M.-L. Gong, K.-W. Cheah, J.-M. Zhang and K.-F. Li, *Chem. Phys. Lett.*, 2004, **385**, 345-350.
51. B. L. An, M. L. Gong, M. X. Li, J. M. Zhang and Z. X. Cheng, *J. Fluoresc.*, 2005, **15**, 613-617.
52. C. Lincheneau, C. Destribats, D. E. Barry, J. A. Kitchen, R. D. Peacock and T. Gunnlaugsson, *Dalton Trans.*, 2011, **40**, 12056-12059.
53. O. Kotova, S. Blasco, B. Twamley, J. O'Brien, R. D. Peacock, J. A. Kitchen, M. Martínez-Calvo and T. Gunnlaugsson, *Chem. Sci.*, 2015, **6**, 457-471.
54. A.-S. Chauvin, J.-C. G. Bünzli, F. Bochud, R. Scopelliti and P. Froidevaux, *Chem. Eur. J.*, 2006, **12**, 6852-6864.

3. Luminescent Molecular Bundles

These results have been published in A. T. O'Neil, N. Zhang, J. A. Harrison, S. M. Goldup and J. A. Kitchen, Synthesis, photophysical and assembly studies of novel luminescent lanthanide(III) complexes of 1,2,3-triazolyl-pyridine-2,6-dicarboxamide-based ligands, Supramol. Chem., 2021, **33**, 160-173.

3.1 Introduction

As stated in chapter 1, the overarching goal of this research was to develop a synthetic strategy or "molecular toolbox" which combined the predictable coordination of the PDA/PDC ligand with the versatile CuAAC "click" chemistry in order to predesign, optimize, and rapidly synthesise a range of different ligand architectures. These ligands in the presence of Ln^{3+} retain predictive coordination forming tricapped trigonal prismatic 1:3 metal to ligand species, and maintain the capability to populate lanthanide excited states. Utilizing our synthetic strategy, we can develop a large range of different luminescent lanthanide complexes for rapid materials discovery. With this goal in mind, a preliminary study to investigate the ability to incorporate CuAAC "click" chemistry into the PDA motif and how the incorporation of the 1,2-3-triazole may compromise the coordination ability of the ligand, was initially carried out.

*Figure 3.1. (Left) Ligand **2** coordinating to Ln^{3+} to form a 1:3 metal:ligand species. (Right) Solid $Eu(\mathbf{2})_3(CF_3SO_3)_3$ and $Tb(\mathbf{2})_3(CF_3SO_3)_3$ crystalline complexes under a microscope, firstly under ambient light and then under shortwave UV irradiation (λ_{ex} = 254 nm).*

The decision was made to append the alkyne directly to PDA motif at the 2- or 6- amide position, such that it could be easily "clicked" to a range of aryl or alkyl halides, or alcohols (which are easily converted to halides). A small group of similar motifs (Intermediate **B**, Scheme 3.1) have been designed and are largely used for biological or [1-5] anion binding[6, 7] applications. To the best of our knowledge this is the first example of such a motif which incorporates CuAAC "click" chemistry on the side 2- or 6- amide position of the PDC unit, forming a 1,2,3-triazole linked motif for the goal of rapid ligand synthesis and formation of lanthanide complexes.

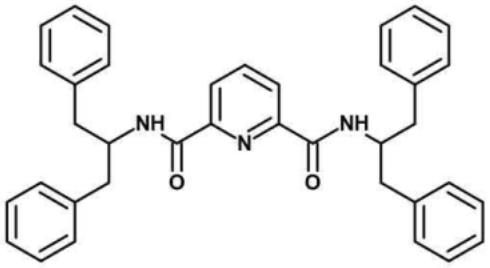

Figure. 3.2.. Piguet. and. co-workers. PDA. ligand. system. which. is. unable. to. form. the. 1:3. M:L. species. due. to. bulkiness.. Obtained. from reference.8..

Because of the lack of previous 1,2,3-triazole appended PDC units (at the 2- or 6- amide position) utilized in lanthanide studies, an important aspect of this initial investigation was to monitor Ln^{3+} coordination. With the introduction of the 1,2,3-triazole motif, the potential for a competitive coordinating pocket is introduced, alongside potentially causing the overall ligand architecture to be too bulky to form the 1:3 M:L species. This has been previously noted by Piguet and co-workers, whose ligand system was too bulky and would not form 1:3 species, favouring formation of lesser species 1:2 and 1:1 (Figure 3.2).[8] In order to monitor the maximum effects of the introduction of the 1,2,3-triazole motif into the PDC unit and its effect on lanthanide coordination, a range of symmetric bis-"clicked" ligands were synthesized (Figure 3.3).

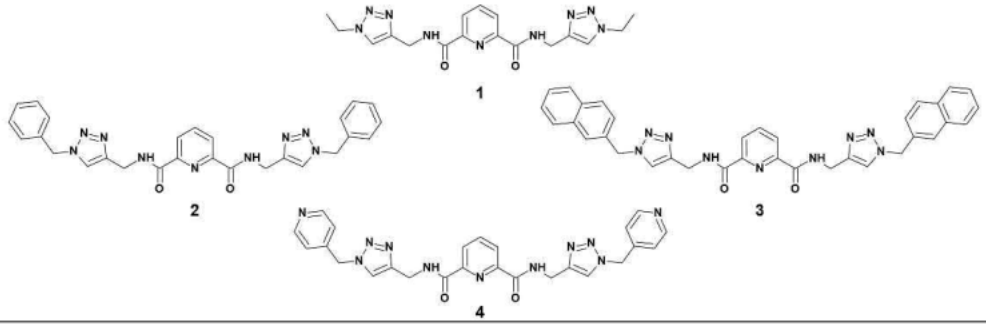

*Figure. 3.3.. Ligands.**1**-**4**..*

Herein, an initial study has been undertaken into the synthetic formation of symmetric bis-"clicked" ligands **1 – 4**, with substituents (**1** = ethyl, **2** = benzyl, **3** = naphthalene, **4** = 4-pyridine) selected to investigate how the different levels of substituent bulkiness and aromaticity may alter the lanthanide complexes formation and photophysical properties. Ligands **1 – 3**, in the presence of Ln^{3+} formed luminescent lanthanide complexes ($[Ln(\mathbf{L})_3](CF_3SO_3)_3$) and photophysical properties have been analysed. Due to ligand **4**'s lack of solubility in non-competitive solvents, lanthanide complexes with **4** were not obtained. Importantly, a detailed study into the self-assembly behaviour of ligands **1** – **3** with lanthanides has been carried out by monitoring changes in physical and photophysical properties alongside DFT calculations using the Gaussian 16[9] software suite to give further insight into coordinated structures.

3.2 Results and Discussion

3.2.1 Ligand Synthesis and Characterisation

Ligands **1**-**4** were synthesised in three steps starting from commercially available dipicolinic acid (DPA) (Scheme 3.1). Firstly, DPA was converted to the acid chloride by refluxing with thionyl chloride in CH_2Cl_2 for 5 hours under a nitrogen atmosphere. The solvent and excess thionyl chloride were removed by evaporation under a stream of nitrogen, giving **A** as a pale-yellow solid.[2] Compound **A** was then immediately dissolved in CH_2Cl_2 and added dropwise to a cooled CH_2Cl_2 solution of propargylamine and triethylamine.[2] Acid-base workup of the resulting red solution gave **B** as a pale brown solid in good yield (84 %). Ligands **1**-**4** were then obtained via a one-pot multi-component CuAAC reaction, where bis-alkyne **B** underwent a $CuSO_4{\cdot}5H_2O$ catalysed cyclization in a DMF:H_2O (4:1) solvent mixture with selected alkyl bromides (**1** = ethyl bromide, **2** = benzyl bromide, **3** = 2-(bromomethyl)naphthalene and **4** = 4-(bromomethyl)pyridine hydrobromide) that formed their respective azides *in situ* (reacting with NaN_3). The resulting mixtures were stirred for 24 hours before (0.1 M) EDTA:NH_4OH was added causing the precipitation of pale solids that, on filtration and washing with 50 mL of H_2O followed by 50 mL of diethyl ether, gave the desired products as off-white solids in good yields (82 - 95 %).

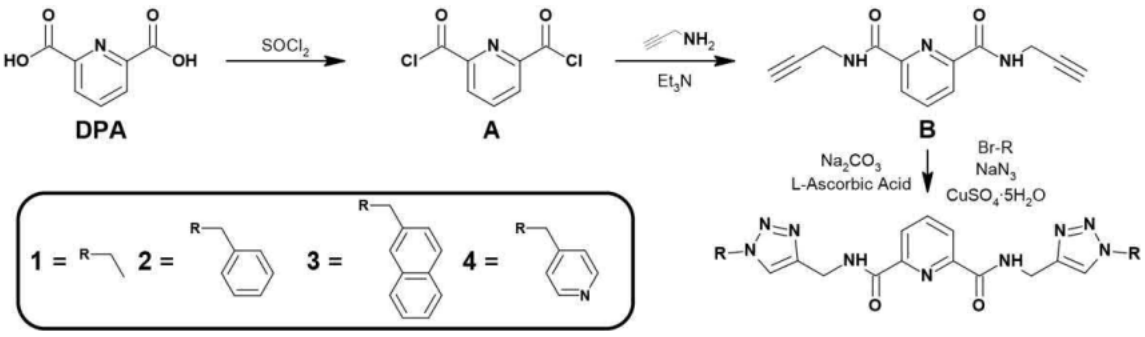

*Scheme 3.1. Synthetic pathway for the formation of ligands **1**, **2**, **3**, and **4** from starting DPA material.*

Ligands **1**-**4** were characterised by ^{1}H NMR, ^{13}C NMR, low-resolution mass spectrometry (LRMS), Fourier transform infrared spectroscopy (FTIR) and UV-visible absorption spectroscopy. ^{1}H NMR and ^{13}C NMR spectra (Figure 3.4) indicated the successful formation of all four ligands. This was evident from the disappearance of the terminal alkyne proton at 3.23 ppm (and in ^{13}C-NMR at 81.1 (C) and 72.3 (CH) ppm), and the introduction of the singlet resonance present at 8.00 - 8.10 ppm assigned to the 1,2,3-triazole protons. There was also a noticeable downfield shift of the alkyne CH_2 linker (4.20 to 4.60 ppm) associated with the formation of the electron withdrawing 1,2,3-triazole ring as well as the introduction of a new signal for the CH_2 linker at 5.50 – 5.70

ppm (4.22 ppm for **1**) and additional proton signals associated with the individual substituents. ^{13}C-NMR also confirmed formation of ligands **1 – 4** with the correct number of carbon environments and the presence of 1,2,3-triazole ring signals at 145 and 123 ppm. Finally, LRMS further confirmed the successful synthesis of all four ligands with *m/z* values of 348.05 for **1**, 508.15 for **2** and 510.1 for **4** corresponding to $[M + H]^+$, and 630.15 for **3** corresponding to $[M + Na]^+$ (see Section 8.1.1).

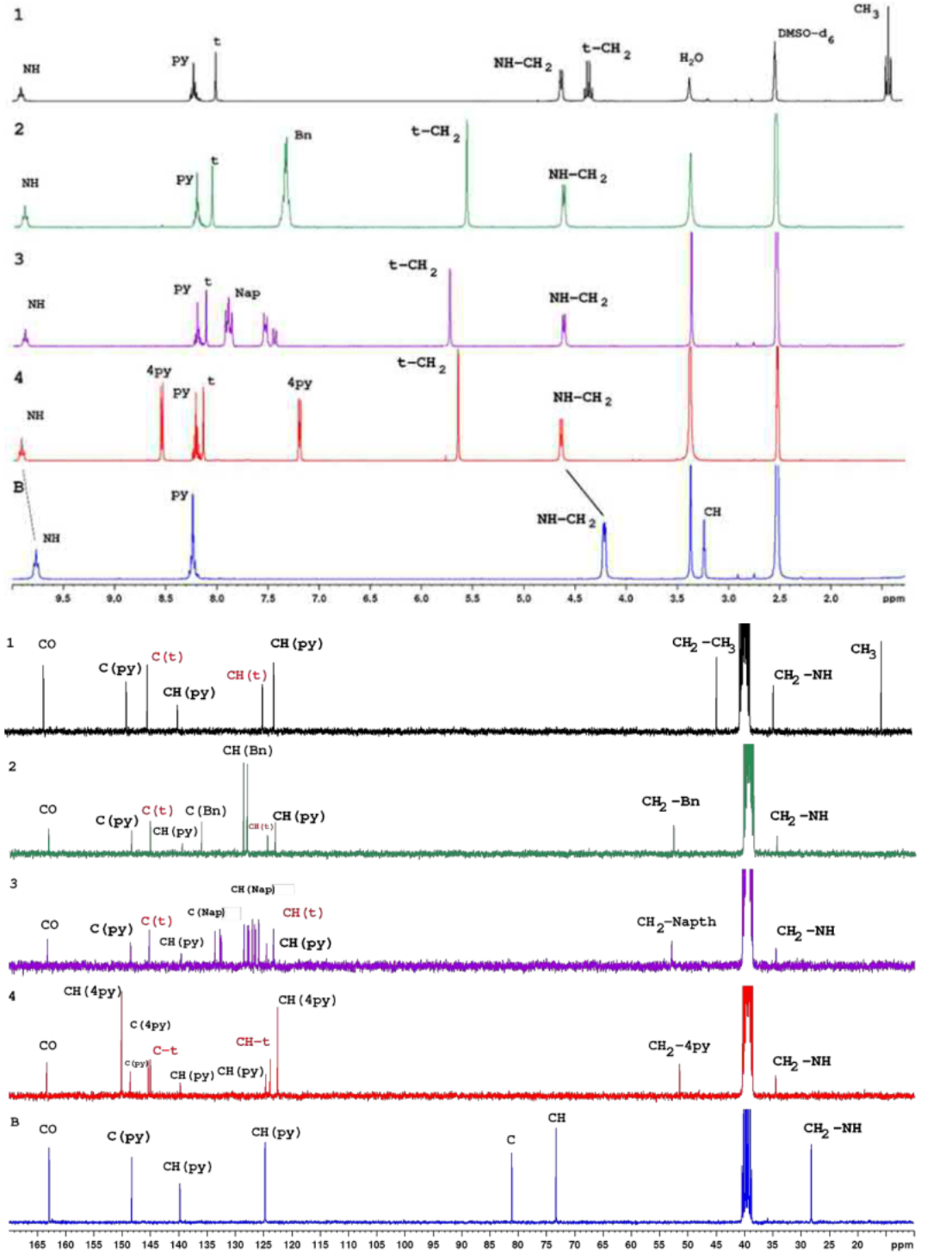

*Figure 3.4.. (Top). ^{1}H NMR of intermediate **B** and ligands **1**, **2**, **3** and **4** (300 MHz, DMSO-d_6).. (Bottom). ^{13}C NMR of intermediate **B** and ligands **1**, **2**, **3** and **4**.. (75 MHz, DMSO-d_6).. Abbreviations stand for: py for central pyridyl ring, t for 1,2,3-triazole ring, Bn for benzyl ring, Nap for naphthalene ring, and 4py for 4-pyridine.. Dash (-) indicates the group that the CH_2 is bonded to..*

3.2.2 Ligand Molecular Structures

Single crystals suitable for X-ray diffraction studies of **1** - **3** were successfully grown either by slow evaporation or vapour diffusion of diethyl ether and low temperature (≈ 100 K) structures were collected, with all three ligands showing the expected connectivity (Figure 3.5). Ligands **1** and **3** both crystallised in the monoclinic space group $P2_1/c$ with both containing a single molecule in the asymmetric unit alongside an interstitial H_2O molecule. **2** crystallised in the chiral orthorhombic space group $Pca2_1$ and contained two crystallographically independent molecules of **2** in the asymmetric unit.

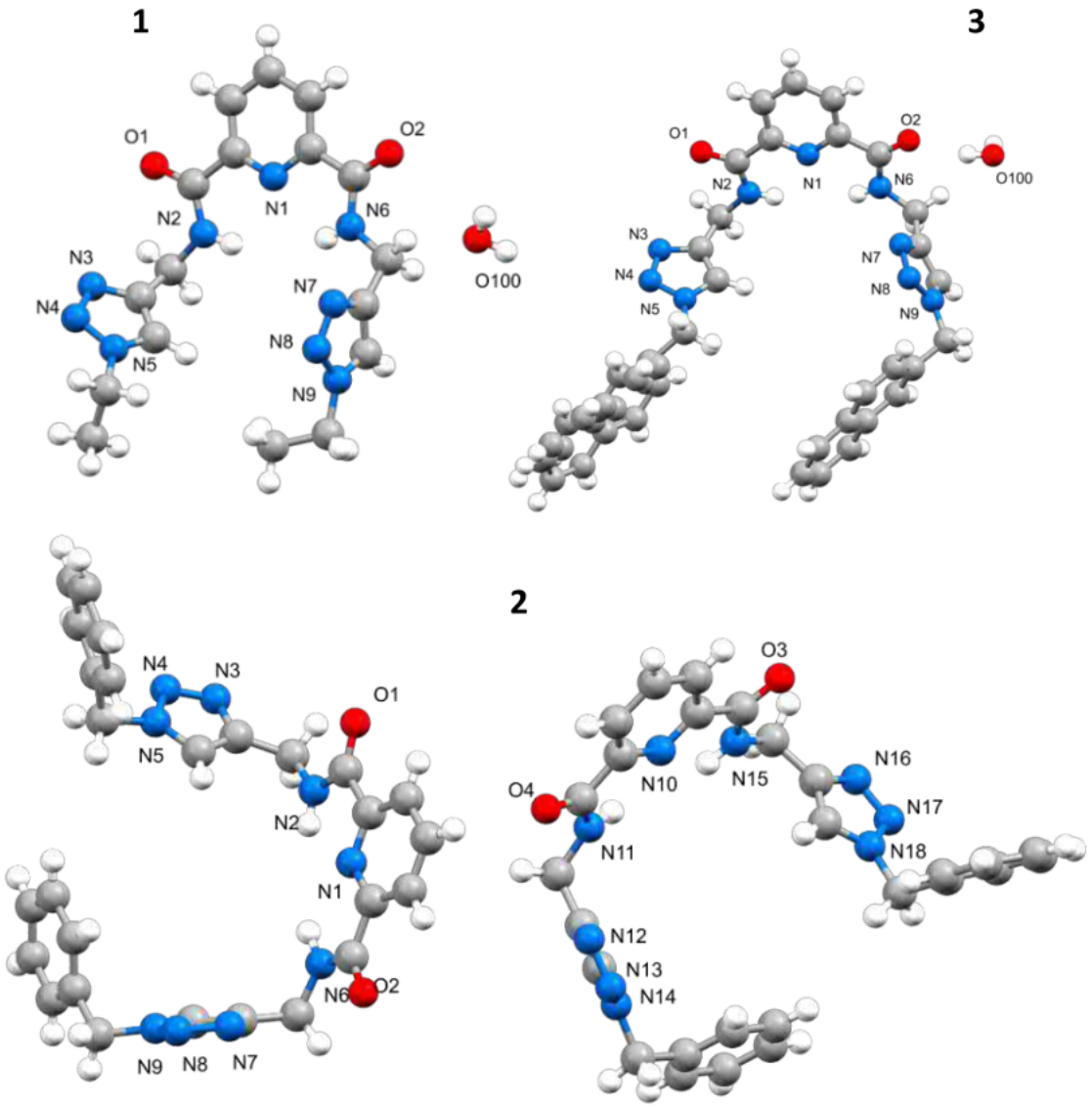

*Figure 3.5.. Ball and stick representation of the molecular structures of **1**, **2** and **3**..*

The crystal packing is relatively similar for **1**-**3**. All ligands have amide bonds oriented such that the NH groups point towards the central pyridyl nitrogen atom (Figure 3.6). This permits moderate hydrogen bonding[10] to occur between amide NH and the neighbouring 1,2,3-triazole nitrogen atoms for all three ligands (Table 3.1). Moderate hydrogen bonding is also seen to occur between the carbonyl group and water in **1** and **3**, while **2** contains an additional non-classical CH hydrogen bonding between the 1,2,3-triazole ring CH group and neighbouring 1,2,3-triazole ring.[10] No appreciable π-π stacking was observed.[11]

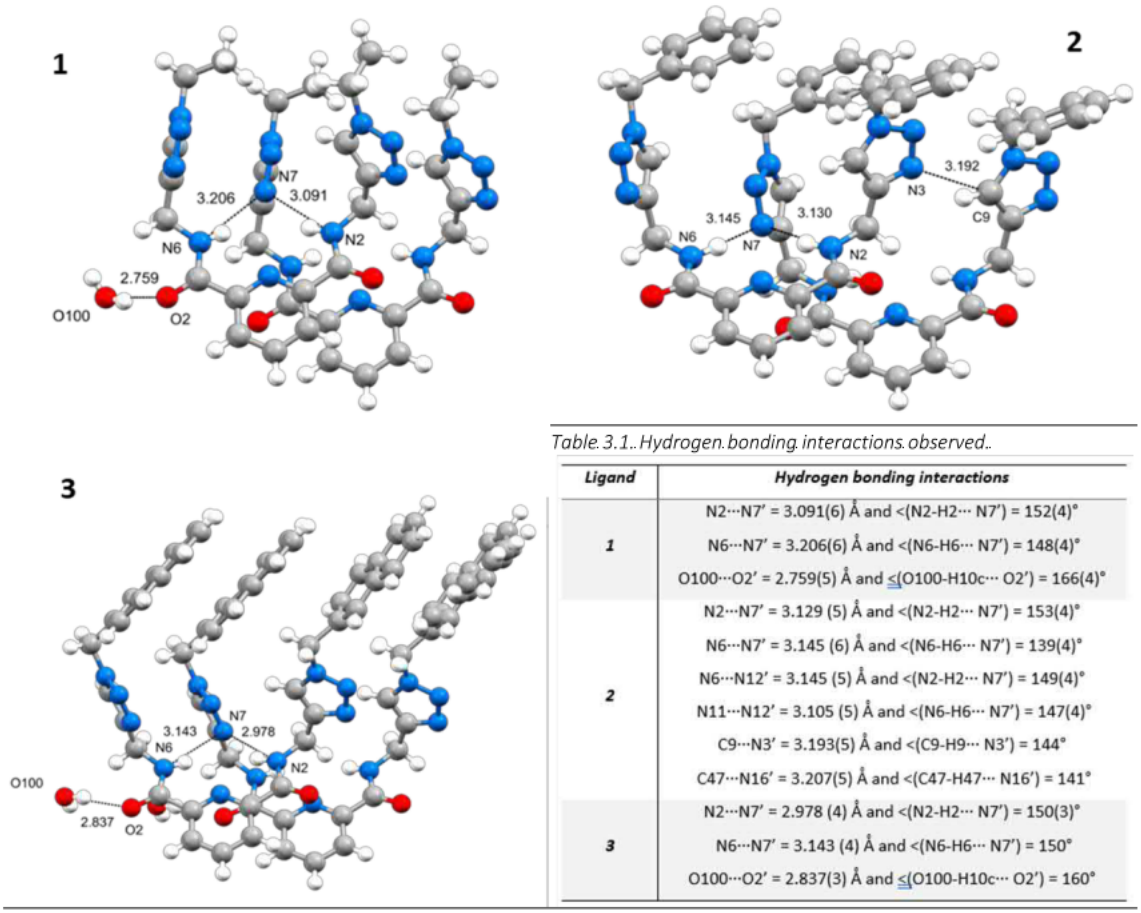

Table 3.1.. Hydrogen bonding interactions observed..

Ligand	Hydrogen bonding interactions
1	N2···N7′ = 3.091(6) Å and <(N2-H2··· N7′) = 152(4)°
	N6···N7′ = 3.206(6) Å and <(N6-H6··· N7′) = 148(4)°
	O100···O2′ = 2.759(5) Å and ≤(O100-H10c··· O2′) = 166(4)°
2	N2···N7′ = 3.129 (5) Å and <(N2-H2··· N7′) = 153(4)°
	N6···N7′ = 3.145 (6) Å and <(N6-H6··· N7′) = 139(4)°
	N6···N12′ = 3.145 (5) Å and <(N2-H2··· N7′) = 149(4)°
	N11···N12′ = 3.105 (5) Å and <(N6-H6··· N7′) = 147(4)°
	C9···N3′ = 3.193(5) Å and <(C9-H9··· N3′) = 144°
	C47···N16′ = 3.207(5) Å and <(C47-H47··· N16′) = 141°
3	N2···N7′ = 2.978 (4) Å and <(N2-H2··· N7′) = 150(3)°
	N6···N7′ = 3.143 (4) Å and <(N6-H6··· N7′) = 150°
	O100···O2′ = 2.837(3) Å and ≤(O100-H10c··· O2′) = 160°

*Figure 3.6.. Hydrogen bonding interactions which are occurring between stacked ligands, shown in ball and stick representation.. Only one of the crystallographically independent molecules of **2** is shown here..*

3.2.3 Complex Synthesis and Characterisation

As stated in the introduction (Section 3.1), lanthanide complexation focused on ligands **1**-**3** as ligand **4** was insoluble in all non-competitive solvents that were investigated. In terms of lanthanide ions, the visibly emissive Eu^{3+} (red) and Tb^{3+} (green) were selected as they are known to be effectively populated by the PDA antenna giving visibly emissive solids[12] and are commonly the more emissive of the lanthanide ions.[13] This gives an indication of lanthanide complexation just from luminescent emissions but also insight into species symmetry from Eu^{3+} centred emission.[14] Alongside these two visibly emissive lanthanides the non-emissive diamagnetic La^{3+} was also coordinated to **1**-**3**, predominantly for ^{1}H NMR studies.

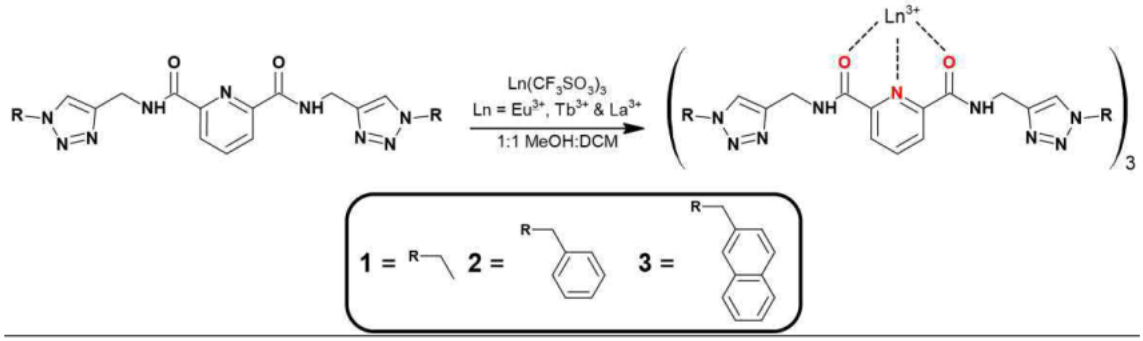

*Scheme 3.2.. Synthetic pathway for the formation of lanthanide complexes. [Ln(**L**)$_3$](CF$_3$SO$_3$)$_3$;. (where Ln. = .Eu^{3+},. Tb^{3+}; and La^{3+},. and **L** = **1**, **2**,. and **3**)..*

[Ln(**L**)$_3$](CF$_3$SO$_3$)$_3$ complexes (where Ln = Eu^{3+}, Tb^{3+}, and La^{3+}, and L = **1**, **2**, and **3**) were prepared by refluxing the appropriate ligand with the selected Ln(CF$_3$SO$_3$)$_3$·xH$_2$O in a 1:3 stoichiometric M:L ratio in MeOH:CH$_2$Cl$_2$ (1:1) for 30 mins under microwave irradiation (Scheme 3.2). The solutions were then subjected to vapour diffusion of diethyl ether which yielded the products as white solids in ≈ 40 - 90 % yields. Lanthanide triflate salts were selected as the anions are expected to not interfere with the complexation self-assembly studies.[15] Complexation of the desired [Ln(**L**)$_3$]$^{3+}$ for all nine complexes was confirmed by high resolution mass spectroscopy (HRMS). Various ions have been identified in the mass spectra with observed peak position and isotopic distribution patterns in agreement with the calculated values. For example, [Eu(**1**)$_3$](CF$_3$SO$_3$)$^{2+}$, [Eu(**1**)$_3$](CF$_3$SO$_3$)$_2^+$ and [Eu(**1**)$_3$]$^{3+}$ show corresponding m/z values of 1600.3621, 725.7048 and 434.1526 respectively (Table 3.2), indicative of the 1:3 (M:L) formation. Other ions for lesser species such as 1:2 and 1:1 (M:L) were present in the mass spectra a likely result of species fragmentation in the mass spectrometer or species dissociation in low concentration solutions which is common in PDA based systems.[16] Although a mixture of species cannot be completely ruled out, from the self-assembly investigation below we believe the 1:3 M:L species is the predominate species when the correct ratio of Ln^{3+} to ligand is used in complexation.

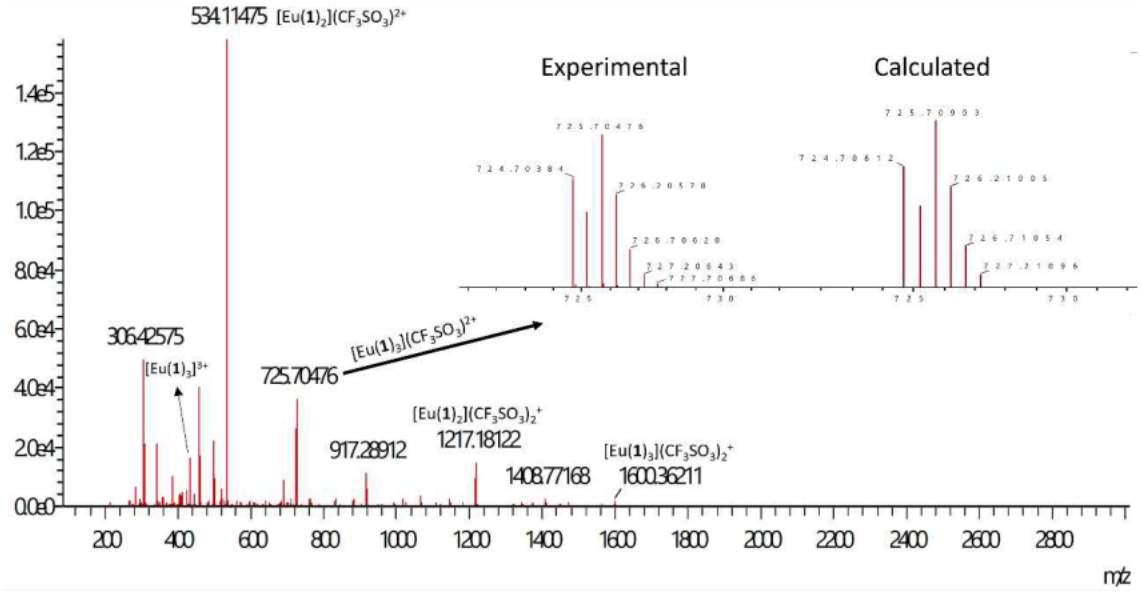

*Figure. 3.7.. Mass. spectrum. of. [Eu(**1**)$_3$](CF$_3$SO$_3$)$_3$ in. MeOH. (0.01. mM).. Insert:. experimental. isotopic. distribution. of. [Eu(**1**)$_3$](CF$_3$SO$_3$)$^{2+}$ vs calculated..*

Table. 3.2.. All. peaks. found. in. mass. spectra. associated. with. the. 1:3. M:L. species..

Complex	Calculated *m/z*	Experimental *m/z*
[Eu(**1**)$_3$(CF$_3$SO$_3$)$_2$]$^+$	1600.3705	1600.3621
[Eu(**1**)$_3$(CF$_3$SO$_3$)]$^{2+}$	725.7090	725.7048
[Eu(**1**)$_3$]$^{3+}$	434.1552	434.1526
[Tb(**1**)$_3$(CF$_3$SO$_3$)$_2$]$^+$	1606.3743	1606.3745
[Tb(**1**)$_3$(CF$_3$SO$_3$)]$^{2+}$	728.7109	728.7109
[Tb(**1**)$_3$]$^{3+}$	436.1564	436.1565
[La(**1**)$_3$(CF$_3$SO$_3$)$_2$]$^+$	1586.3553	1586.3327
[La(**1**)$_3$(CF$_3$SO$_3$)]$^{2+}$	718.7014	718.6913
[Eu(**2**)$_3$(CF$_3$SO$_3$)$_2$]$^+$	1972.4651	1972.4652
[Eu(**2**)$_3$(CF$_3$SO$_3$)]$^{2+}$	911.7563	911.7564
[Eu(**2**)$_3$]$^{3+}$	558.1867	558.1869
[Tb(**2**)$_3$(CF$_3$SO$_3$)$_2$]$^+$	1978.4688	1978.4705
[Tb(**2**)$_3$(CF$_3$SO$_3$)]$^{2+}$	915.7578	915.7536
[Tb(**2**)$_3$]$^{3+}$	560.1877	560.1851
[La(**2**)$_3$(CF$_3$SO$_3$)$_2$]$^+$	1958.4492	1958.4223
[La(**2**)$_3$(CF$_3$SO$_3$)]$^{2+}$	904.7483	904.7362
[Eu(**3**)$_3$(CF$_3$SO$_3$)$_2$]$^+$	2273.5614	2273.5604
[Eu(**3**)$_3$(CF$_3$SO$_3$)]$^{2+}$	1062.3045	1062.3053
[Eu(**3**)$_3$]$^{3+}$	658.5522	658.5528
[Tb(**3**)$_3$(CF$_3$SO$_3$)$_2$]$^+$	2279.5655	2279.5354
[Tb(**3**)$_3$(CF$_3$SO$_3$)]$^{2+}$	1065.3062	1065.2920
[Tb(**3**)$_3$]$^{3+}$	660.5533	660.5445
[La(**3**)$_3$(CF$_3$SO$_3$)$_2$]$^+$	2259.5465	2259.5155
[La(**3**)$_3$(CF$_3$SO$_3$)]$^{2+}$	1055.2967	1055.2858
[La(**3**)$_3$]$^{3+}$	653.8803	653.8715

Lanthanide ion coordination into the NO_2 pocket was indicated from the significant shifts in FTIR spectra (see Figure 3.8 and Section 8.1.3), where the amide C=O frequencies (≈ 1650 cm^{-1}) shifted to lower energies upon coordination (Δν = -20 cm^{-1} for **1** and **2** and -32 cm^{-1} for **3**) due to electron density being withdrawn by Ln^{3+} as observed for similar Ln^{3+} systems.[17, 18] Assigning frequencies directly to the 1,2,3-triazole ring proved difficult. To gain insight into the 1,2,3-triazole ring contribution a simple (hydroxymethyl-1,2,3-triazol-4-yl)hexadecane was synthesised using methodology developed in chapter 4 (see Section 8.1.5). From this, bands at 1468, 1026, and 860 cm^{-1} are suspected to be associated with the two 1,2,3-triazole rings.[19-21] All three peaks remain unshifted upon coordination as expected.

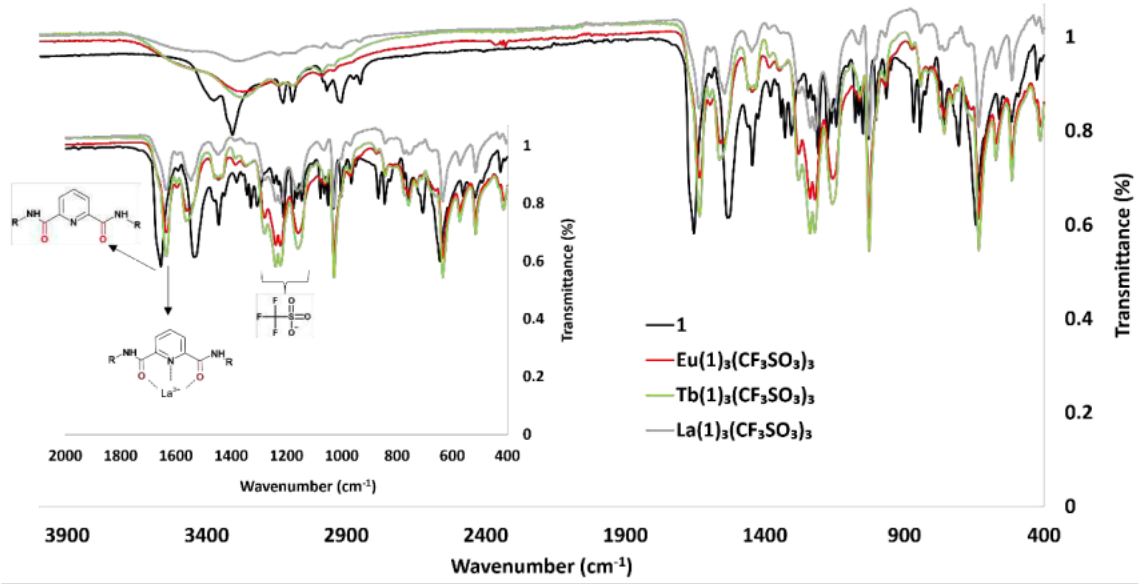

*Figure 3.8. Infrared spectra of **1** and Ln(**1**)$(CF_3SO_3)_3$, where Ln = Eu^{3+}, Tb^{3+} and La^{3+}. Insert: zoom in of the carbonyl region, showing shift observed in C=O from ligand to complex alongside the triflate ion frequencies.*

^{1}H NMR of lanthanum complexes and ligands **1**, **2** and **3** (Figure 3.9) were run in a mixture of $CDCl_3$ and MeOD (9:1), this combination is required for solubility and it is worth noting that attempts to run in DMSO-d_6 resulted in near identical spectra to the ligands, suggesting that the competitive solvent completely dissociated the complex in solution. All three complexes showed similar proton shifts and broadening of the pyridyl proton signals, indicative of La^{3+} coordination.[22] Significant downfield shift and broadening was observed in the pyridyl *para* proton signal indicative of coordination occurring in the NO_2 pocket, caused by La^{3+} removing electron density, previously noted in other PDA systems.[16] Alongside this a similar signal decrease and likely downfield shift of NH proton signal was observed, also indicative of La^{3+} coordination within the NO_2 pocket.[22] Other shifts of note were the minor downfield shifts observed in the *meta* proton of the pyridyl and 1,2,3-triazole ring along with an associated upfield shift observed in both Bn-CH_2 and Nap-CH_2. Proton signals associated with ethane, benzyl and naphthalene substituents remained unshifted. It is worth noting that these shifts are in line

for what is observed in the ^{1}H-NMR titration of **1**, **2** and **3** with La^{3+} when the 1:3 M:L chemical environment is reached (Section 3.2.5.2).

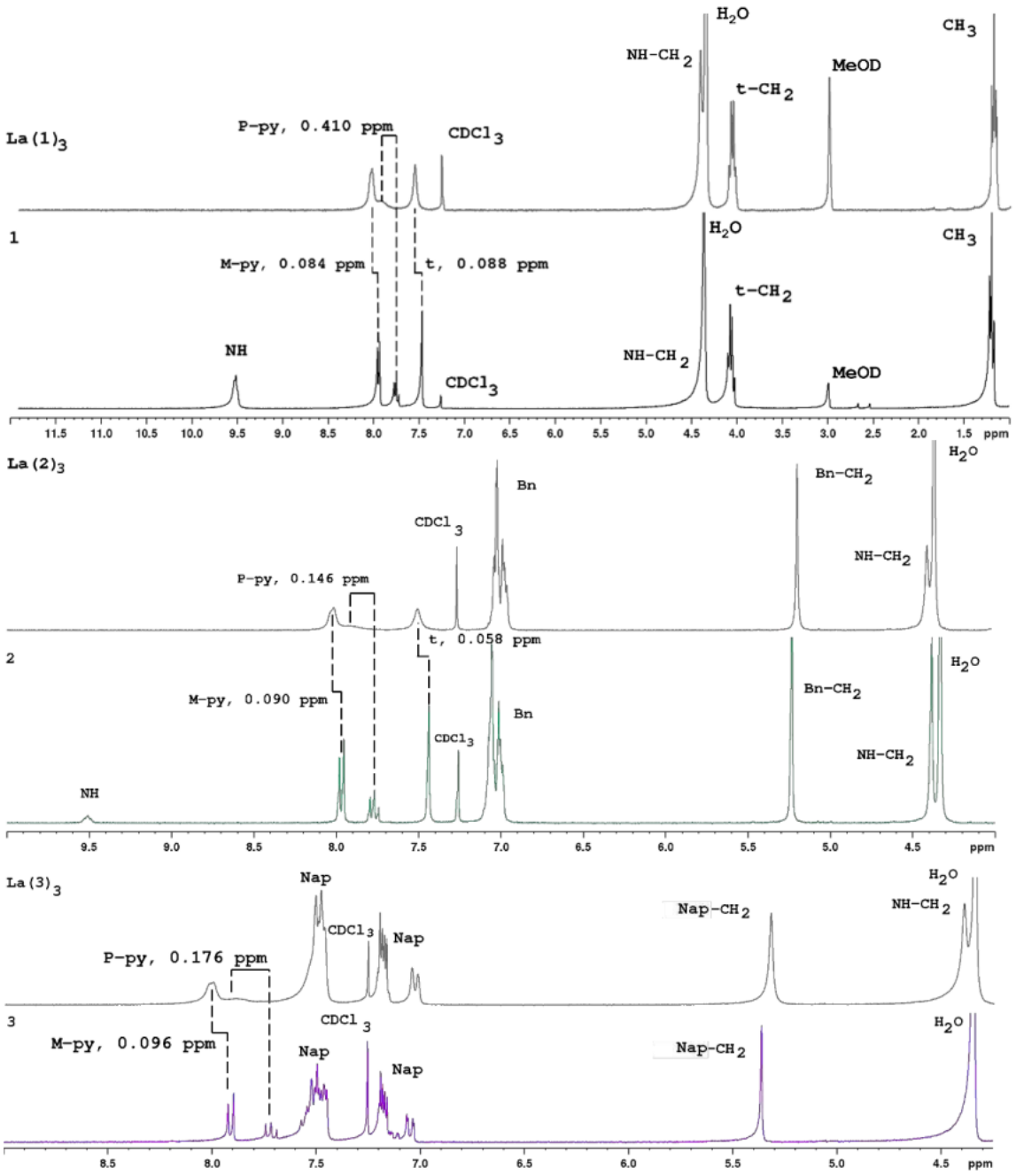

*Figure 3.9. ^{1}H NMR of **1** and La(**1**)$_3$ (Top), **2** and La(**2**)$_3$ (Middle) and **3** and La(**3**)$_3$ (Bottom) done in $CDCl_3$ and MeOD (9:1). Abbreviations: py for central pyridyl ring with P for para and M for meta positions, t for 1,2,3-triazole ring, Bn for benzyl ring, Nap for naphthalene and dash (-) indicates the group that the CH_2 is bonded to.*

3.2.4 Photophysical Studies

For characterisation of lanthanide complexes, it is important to assign the photophysical transitions and note any changes observed in both the ligands and corresponding complexes, primarily to give insight into the active antenna but also to show additional signs of coordination. The photophysical properties of ligands **1 – 3** and all $[Ln(\mathbf{L})_3](CF_3SO_3)_3$ complexes were evaluated in MeCN solutions (0.01 mM or 0.001 mM).

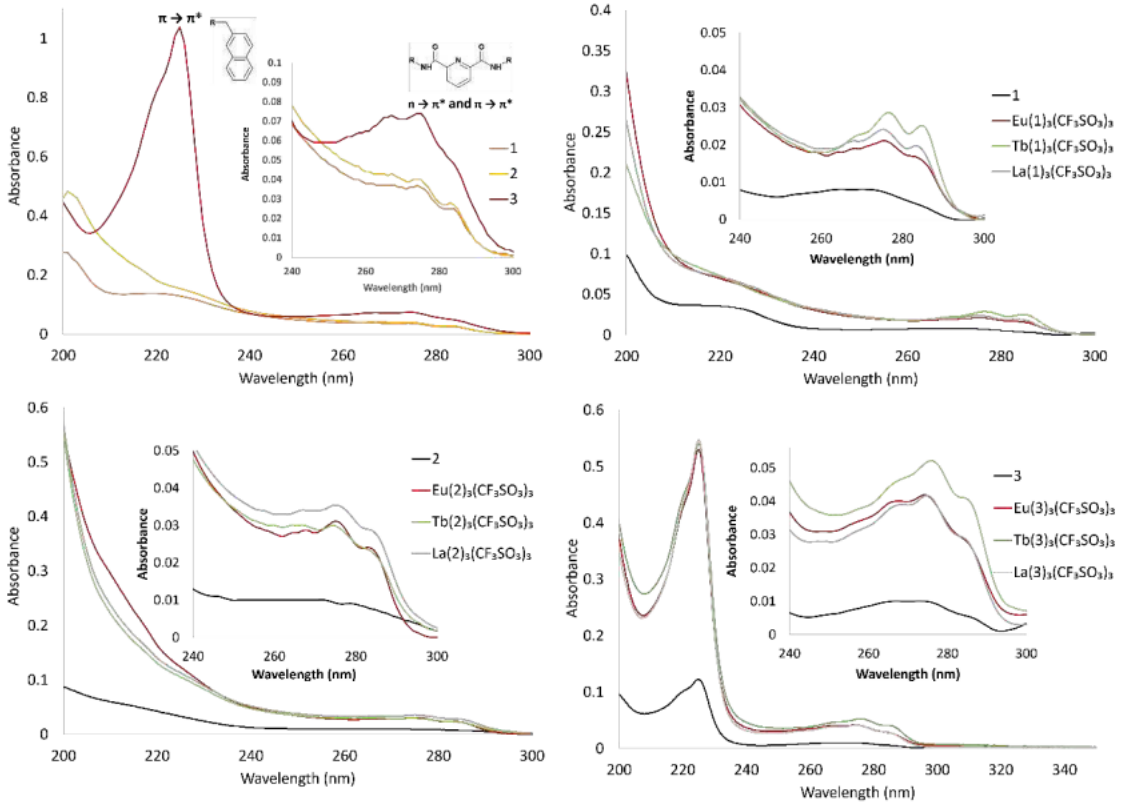

*Figure 3.10.. (Top left) UV-visible absorbance spectra of ligands **1** (0.01 mM),, **2** (0.01 mM) and **3** (0.005 mM) in MeCN.. Insert:: zoom in of absorbance range 240-300 nm associated with the pyridyl unit.. UV-visible absorbance spectra of ligand **1** (Top right)),, **2** (Bottom left),, and **3** (Bottom right) in MeCN (0.001 mM) and their lanthanide complexes.. Inserts:: zoom in of absorbance range 240-300 nm associated with the pyridyl unit showing the small red shift upon complexation..*

UV-visible absorption spectra for all ligands and complexes exhibited broad absorption bands ranging from 200 to 300 nm, with a characteristic major absorption broad band located at 281 nm, which showed three shoulders at 268, 274, and 283 nm (Figure 3.10). These have previously been assigned to the n → π* and π → π* transitions from the central 2,6-pyridinedicarboxamide.[8, 16, 17, 23] In the case of **3** the absorption in this region is increased as it contains contributions from both the 2,6-pyridinedicarboxamide and the 2-naphthalene side arm.[24-26] On complexation these three shoulder bands red shifted to 269 nm, 277 nm and 285 nm, as seen in similar systems.[23, 25, 27] **3** contained an additional absorption at 225 nm, assigned to the π → π* transitions of the 2-naphthalene, but also likely contains small contributions associated with the carbonyl of the central pyridyl ring.[24-26, 28] Other bands of note in this region

were at 193, 220 (for **1**) and 207 nm (for **2**) but were significantly weaker than that of **3** and were only associated with a n → π* transition of the central pyridyl ring.[23, 24] The 1,2,3-triazole rings gave a small contribution to the absorption band ranging from 200 to 240 nm associated with π → π* transitions. To gain insight into the 1,2,3-triazole rings contribution (hydroxymethyl-1,2,3-triazolyl)hexadecane was again used. As seen in the absorption spectrum in Figure 3.11, there was a weak absorbance from 200 nm to 240 nm, which has been previously observed and assigned to a π → π* transition.[29] This absorbance is weak in comparison to those of the central PDC and naphthalene absorptions in the same region (experiment conducted in the same solvent and with the same concentration). However, it will have a small contribution to the overall absorption in this region.

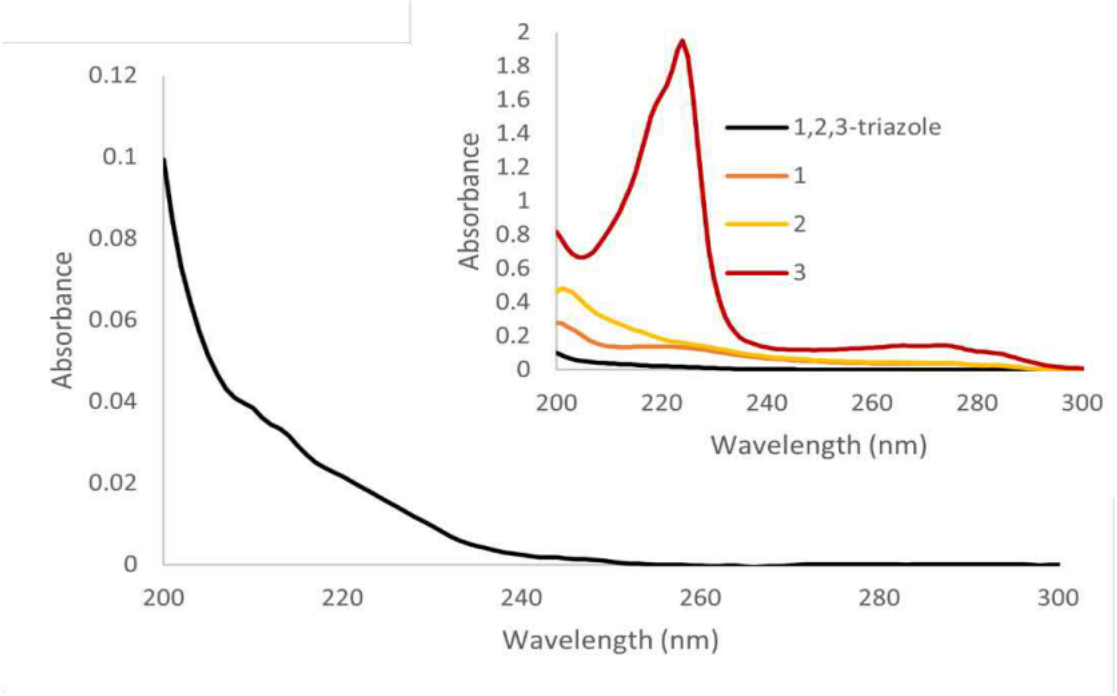

Figure. 3.11.. UV-visible. absorption. spectrum. of. (hydroxymethyl-1,2,3-triazolyl)hexadecane. (abbreviated. to. 1,2,3-triazole). (0.01. mM, MeCN).. Insert:. absorption. spectra. of. ***1****,.* ***2****,.* ***3****. and. (hydroxymethyl-1,2,3-triazolyl)hexadecane. (0.01. mM,. MeCN)..*

Fluorescent and phosphorescent emission measurements were recorded for $[Eu(\mathbf{L})_3](CF_3SO_3)_3$ and $[Tb(\mathbf{L})_3](CF_3SO_3)_3$ (L = **1** - **3**) with an excitation wavelength of λ_{max} = 274 nm. All complexes gave rise to the characteristic red (Eu^{3+}) and green (Tb^{3+}) emission profiles (Figures 3.12-14). In the case of Eu^{3+}, population of the $^5D_0$ excited state and the subsequent depopulation to the ^7F_J (J = 0 – 4) states gave sharp emission bands centred at λ = 594 nm ($^5D_0 \rightarrow {}^7F_1$), 616 nm ($^5D_0 \rightarrow {}^7F_2$), 651 nm ($^5D_0 \rightarrow {}^7F_3$) and 697 nm ($^5D_0 \rightarrow {}^7F_4$). The Eu^{3+} complexes also displayed a weak peak at λ = 581 nm ($^5D_0 \rightarrow {}^7F_0$) which indicated the Eu^{3+} occupies a site with a symmetry of C_{nv}, C_n or C_s, which in our system indicated that the complexes likely contain an overall symmetry of C_3.[14, 30]

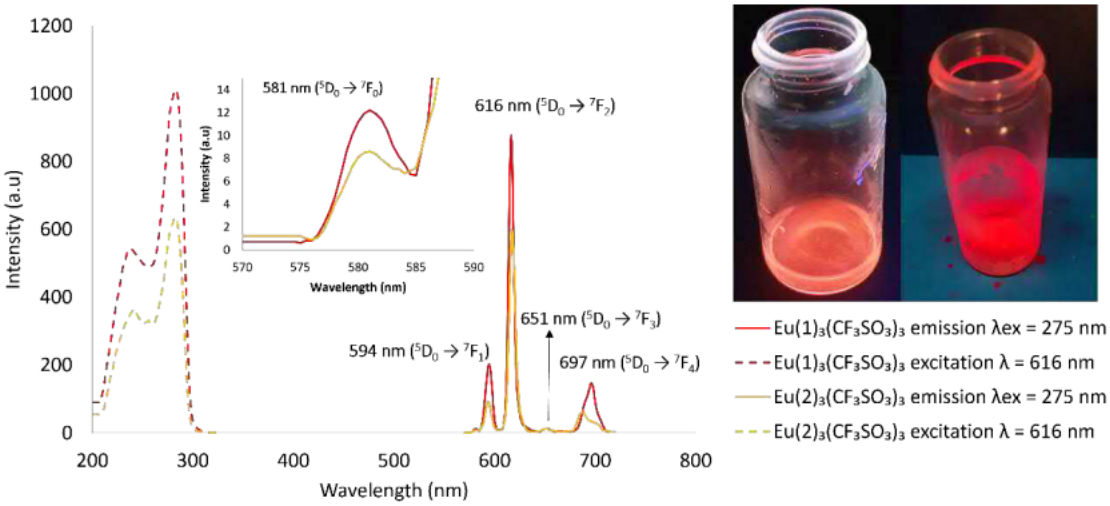

*Figure 3.12.. Fluorescence emission and excitation spectra of Eu(**L**)$_3$(CF$_3$SO$_3$)$_3$ (**L** = **1** and **2**) (0.01 mM, MeCN).. Inserts: zoom in of 581 nm ($^5D_0 \rightarrow {}^7F_0$) transition and Eu(**1**)$_3$(CF$_3$SO$_3$)$_3$ solid and solution under shortwave UV irradiation (λ_{ex} = 254 nm)..*

For Tb^{3+} complexes effective population of the $^5D_4$ state and the subsequent deactivation to the ^7F_J (J = 3 – 6) states was observed, forming sharp emission bands centred at 490 nm ($^5D_4 \rightarrow {}^7F_6$), 545 nm ($^5D_4 \rightarrow {}^7F_5$), 587 nm ($^5D_4 \rightarrow {}^7F_4$) and 621 nm ($^5D_4 \rightarrow {}^7F_3$). Excitation spectra of [Eu(**L**)$_3$](CF$_3$SO$_3$)$_3$ and [Tb(**L**)$_3$](CF$_3$SO$_3$)$_3$ were also measured (λ_{em} = 616 nm (Eu^{3+}) and 545 nm (Tb^{3+})), showing a similar spectral range to the corresponding absorption spectra (200 – 300 nm), indicative of the population of lanthanide excited states through indirect excitation from the ligand antenna as seen in Figures 3.12-13.

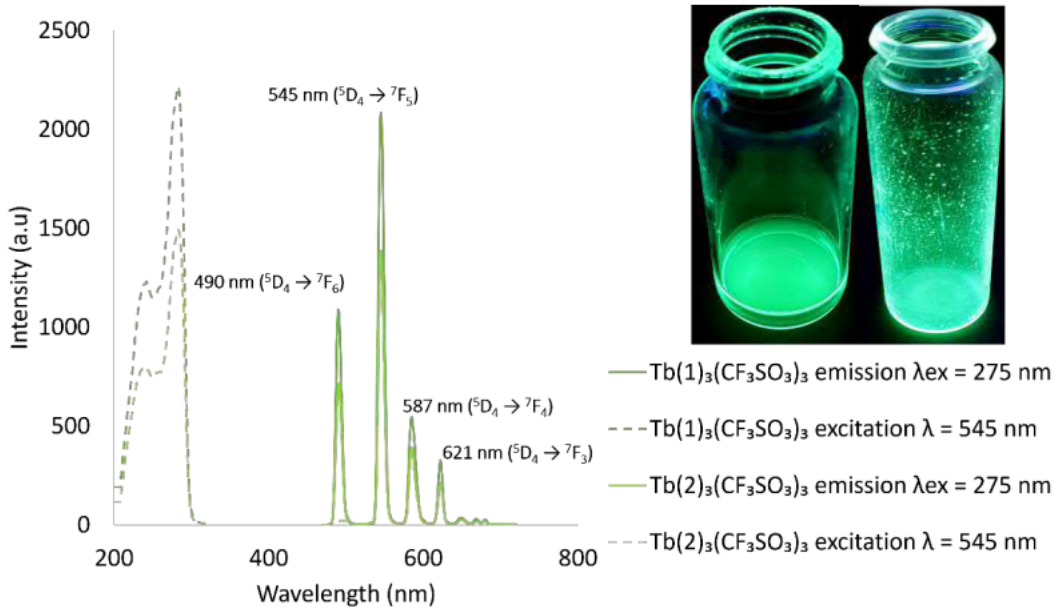

*Figure 3.13.. Fluorescence emission and excitation spectra of Tb(**L**)$_3$(CF$_3$SO$_3$)$_3$ (**L** = **1** and **2**) (0.01 mM, MeCN).. Insert: Tb(**1**)$_3$(CF$_3$SO$_3$)$_3$ solid and liquid under shortwave UV irradiation (λ_{ex} = 254 nm).*

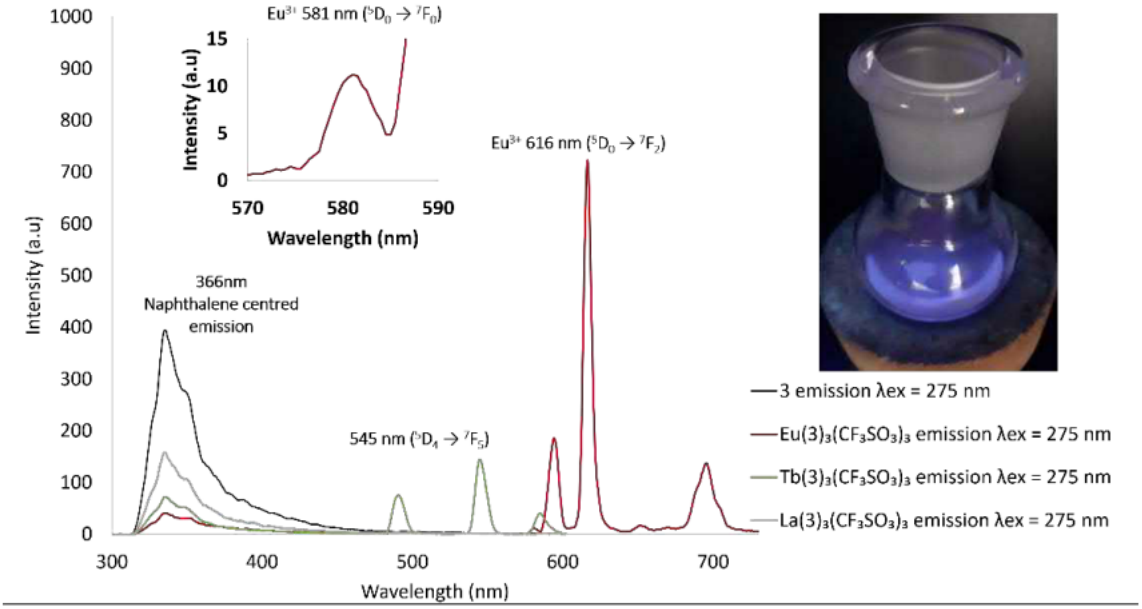

*Figure 3.14.. Fluorescence emission spectra of 3 and Ln(**3**)$_3$(CF$_3$SO$_3$)$_3$ (Ln = Eu^{3+}, Tb^{3+} and La^{3+}) (0.01 mM, MeCN).. Insert: zoom in of 581 nm ($^5D_0 \rightarrow {}^7F_0$) transition and image of La(**3**)$_3$(CF$_3$SO$_3$)$_3$ in solution under shortwave UV irradiation (λ_{ex} = 254 nm)..*

In terms of ligand-centred emission only ligand **3** was observed to be fluorescent, with a broad emission from 310 to 450 nm associated with the 2-naphthalene. The excitation spectrum indicated population occurs both at 230 nm and 280 nm, which are associated with the naphthalene absorption. Upon coordination to Eu^{3+}, Tb^{3+} and La^{3+} ligand centred emission was seen to decrease. This could be associated with a combination of both the coordination causing ISC to become more favoured from heavy atom effects,[31] resulting in nr decay from the triplet state in the case of La^{3+}, but also with population of the excited states of Eu^{3+} and Tb^{3+} resulting in an overall less ligand centred emission, but overall still results in dual emissive species.

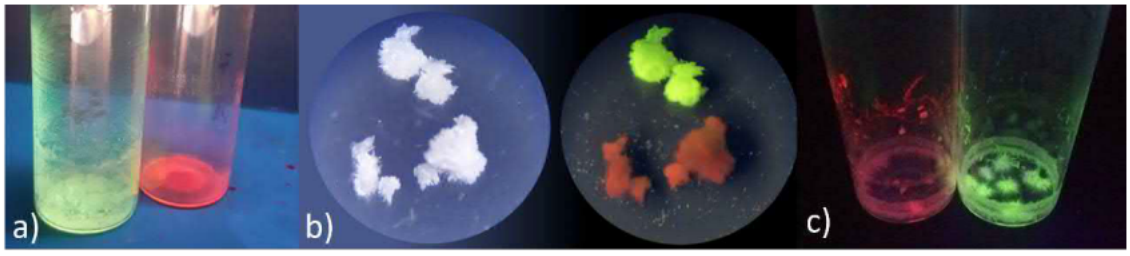

*Figure 3.15.. Eu(**L**)$_3$(CF$_3$SO$_3$)$_3$ and Tb(**L**)$_3$(CF$_3$SO$_3$)$_3$.. solids under shortwave UV irradiation (λ_{ex} = 254 nm). (**L** = **1** in (a) and **2** in (b) and (c)). Image (b) is under a microscope,. under ambient light (Left) and under short wave irradiation (Right)..*

Luminescent lifetimes of Eu^{3+} (616 nm $^5D_0 \rightarrow {}^7F_2$) and Tb^{3+} (545 nm $^5D_4 \rightarrow {}^7F_5$) were best fit to single exponential decay functions indicative of a single emissive species present in solution. Excited state lifetimes for [Eu(**L**)$_3$](CF$_3$SO$_3$)$_3$ complexes are relatively short lived compared to those of similar PDA systems, with lifetimes of 0.46 ms, 0.58 ms, and 0.68 ms for ligands **1**, **2**, and **3** respectively, where other PDA systems can range from 1 to 2 ms (see Table 3.4).[23, 32] This is suggestive of a nr pathway being favoured and depopulating the Eu^{3+} excited state. Interestingly the overall quantum yields (Φ_{Ln}^{L}) of [Eu(**1**)$_3$](CF$_3$SO$_3$)$_3$ and [Eu(**2**)$_3$](CF$_3$SO$_3$)$_3$, are 4.3 % and 2.7 % respectively, which are within range of similar PDA systems, see Figure 3.16 and

Table 3.3 for values.[16, 17, 23, 33-36] The large difference in Φ_{Ln}^{L} between ligands **1** and **2** compared to that of **3** can be rationalised from calculated sensitisation efficiencies, as shown in Table. The sensitisation efficiency of ligand **3** is significantly less than that of **1** and **2**. This is potentially due to the naphthalene absorption overlap with the central pyridyl antenna competing for the same excitation wavelength, reducing the overall energy received by the Eu^{3+} excited state.

Table. 3.3.. Experimental. measured. overall. quantum. yields. (Φ_{Ln}^{L}), observed. lifetimes. (τ_{obs}),. calculated. radiative. lifetimes. (τ^{rad}), intrinsic. quantum. yields. (Φ_{Ln}^{Ln}),. and. sensitisation. efficiency. (n_{sens}). of. Eu^{3+}. and. Tb^{3+}. complexes..

Complex	Φ_{Ln}^{L} (%)	τ_{obs} (ms)	τ^{rad} (ms)	Φ_{Ln}^{Ln} (%)	n_{sens} (%)
Eu(**1**)$_3$(CF$_3$SO$_3$)$_3$	4.3	0.46	5.2	11.4	37.7
Eu(**2**)$_3$(CF$_3$SO$_3$)$_3$	2.7	0.58	4.9	8.5	32.1
Eu(**3**)$_3$(CF$_3$SO$_3$)$_3$	0.5	0.68	5.5	8.2	6.4
Tb(**1**)$_3$(CF$_3$SO$_3$)$_3$	13	1.38	-	-	-
Tb(**2**)$_3$(CF$_3$SO$_3$)$_3$	12	1.44	-	-	-
Tb(**3**)$_3$(CF$_3$SO$_3$)$_3$	0.1	0.09	-	-	-

In the case of the [Tb(**L**)$_3$](CF$_3$SO$_3$)$_3$ complexes, ligands **1** and **2** gave lifetimes that were significantly higher than their Eu^{3+} counterparts, averaging 1.38 ms and 1.44 ms respectively, although in the case of [Tb(**3**)$_3$](CF$_3$SO$_3$)$_3$ the lifetime is dramatically lower at 0.09 ms. This coincides with the much better overall quantum yields of [Tb(**L**)$_3$](CF$_3$SO$_3$)$_3$ with complexes of ligands **1** and **2** $\Phi_{Ln}^{L} = 13$ % and 12 % (similar to that of other PDA based systems, see Table 3.4), while **3** ($\Phi_{Ln}^{L} = 0.1$ %) is very low. This significant drop in quantum yields and lifetimes of [Tb(**3**)$_3$](CF$_3$SO$_3$)$_3$ is likely associated with the naphthalene absorption overlap and poor energy match between the triplet state of naphthalene (21,250 cm^{-1}) to the Tb^{3+} excited state $^5D_4$ (20,500 cm^{-1}), which is close enough for BT to occur.[37]

*Table. 3.4.. Overall. quantum. yields. and. lifetimes,. measurements. done. in. MeCN. except. for. **L10**. .. Values. obtained. from. references. 16,. 17, 23,. 33-36..*

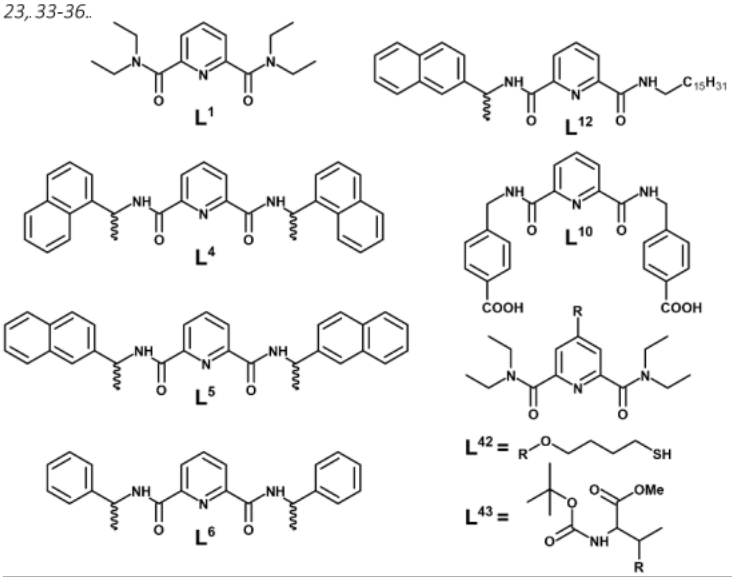

Complex	Φ_{Ln}^{L} (%)	τ_{obs} (ms)
[Eu(**L^1**)$_3$]$^{3+}$	0.009	2.42
[Eu(**L^4**)$_3$]$^{3+}$	7.3-7.6	1.84-1.85
[Eu(**L^5**)$_3$]$^{3+}$	1.9-2.1	1.79-1.81
[Eu(**L^6**)$_3$]$^{3+}$	1	1.84-1.95
[Eu(**L^{10}**)$_3$]$^{3+}$	4.9	-
[Eu(**L^{12}**)$_3$]$^{3+}$	2.6-3.1	1.61-16.5
[Tb(**L^1**)$_3$]$^{3+}$	3.5	1.85
[Tb(**L^4**)$_3$]$^{3+}$	8.6	1.75-1.89
[Tb(**L^{10}**)$_3$]$^{3+}$	7.2	-
[Tb(**L^{42}**)$_3$]$^{3+}$	11.6	1.13
[Tb(**L^{43}**)$_3$]$^{3+}$	1.2	1.55

Figure. 3.16.. PDA. based. ligands. with. known. overall. quantum. yields. from. references. 16,. 17,. 23,. 33-36..

The much higher quantum yields observed in the Tb^{3+} systems compared to Eu^{3+} is seen in most other PDA based ligands where both Eu^{3+} and Tb^{3+} complexes were prepared. Muller and co-workers suggest this is likely due to the better triplet state energy level match of the PDA antenna to the Tb^{3+} $^5D_4$ excited state, with Eu^{3+} $^5D_0$ excited state being further away.[23] To obtain the triplet state energy level of **1**-**3**, DFT optimization and frequency calculations of ground state and triplet state were carried out on the base ligand structures obtained from crystal structures. Although it would be more informative to do this on the lanthanide complexes as the ions would likely affect the energy state, it was found that it would require a TD-DFT calculation, which was too computationally intensive. Using a B3LYP[38-41] functional with a cc-pVTZ[42, 43] basis set as parameterized in the Gaussian 16 software suite,[9] the triplet state energies of the ligands were obtained, with **1** = 26,628 cm^{-1} , **2** = 26,579 cm^{-1} and **3** = 20,520 cm^{-1}. This clearly explains why Tb^{3+} systems with **1** and **2** have an overall better quantum yield, as their triplet state energy is much more suited for excitation of the $^5D_4$ (20,500 cm^{-1}) of Tb^{3+} than the $^5D_0$ (17,293 cm^{-1}) of Eu^{3+},[37] and furthermore indicates the BT likely occurring between ligand **3** and the Tb^{3+} excited state (Figure 3.17).

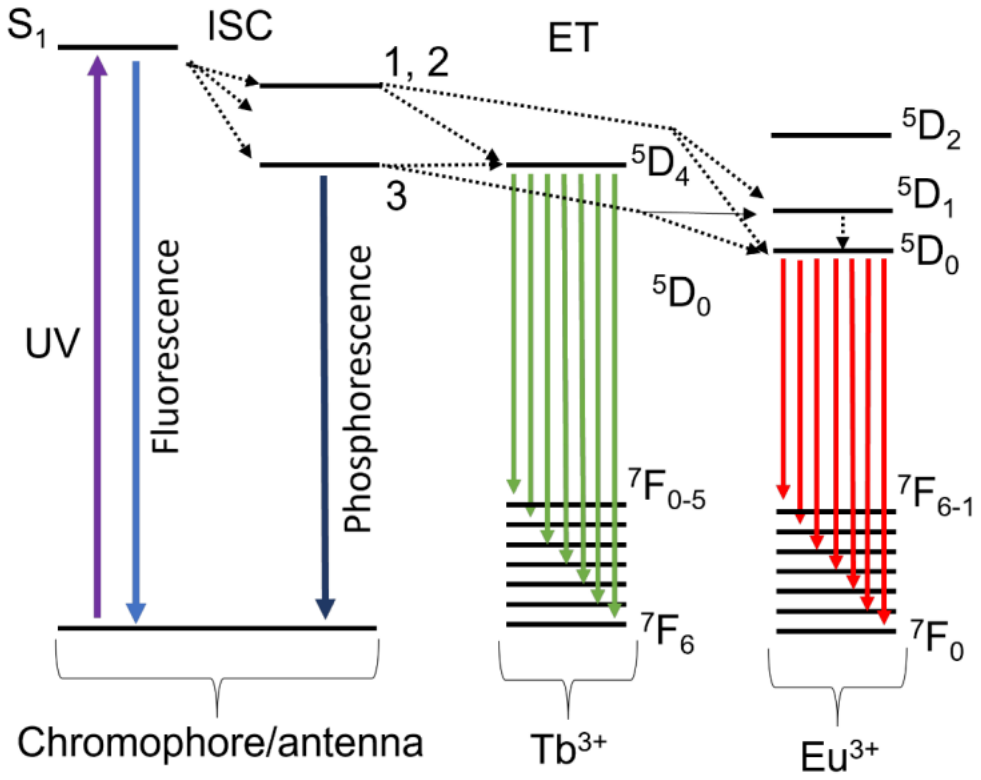

Figure. 3.17.. Jablonski. energy. diagram,. showing. the. energy. transfer. process. likely. occurring. between. ligands. ***1-3*** *with. Eu^{3+}. and. Tb^{3+}. The. energy. levels. are. not. exact. but. show. relative. position. in. terms. of. height. between. one. another.. This. gives. a. visual. insight. into. the energy. level. difference. between. the. triplet. of. the. ligand. and. excited. states. of. the. Ln^{3+}. and. why. the. BT. is. more. likely. to. occur. in.* ***3****. Abbreviations:. ISC for. intersystem. crossing. and. ET. for. energy. transfer...*

3.2.5 Self-Assembly Investigation

The solution self-assembly process that ligands **1**, **2**, and **3** undergo in the presence of lanthanide ions was studied *in situ* by monitoring changes in UV-visible absorption, fluorescence emission, and ^{1}H NMR spectra (La^{3+}) at room temperature. Utilizing species identified in MS and previous PDA based studies,[23, 25, 27, 33, 36, 44, 45] changes were reasonably assigned to the formation of 1:3, 1:2 and 1:1 M:L species.

3.2.5.1 Photophysical Self-Assembly Investigation

Formation of 1:1, 1:2 and 1:3 (M:L) species was monitored by measuring changes in the UV-visible absorption and fluorescence spectra of ligands in MeCN solutions (solutions were made from a 0.010 M ligand stock solution in DCM:MeOH (1:1) to make either 2.0×10^{-5} M or 5.0×10^{-6} M for **3** UV-visible absorption in MeCN) when titrated with specific aliquots of lanthanide $Ln(CF_3SO_3)_3 \cdot xH_2O$ from a 1 mM MeCN solution (where Ln = Eu^{3+}, Tb^{3+}, and La^{3+}). Additions were 0 to 4.5 equivalents, with 3 µL aliquots for 0 to 1 equivalent, 6 µL aliquots for 1 to 2 equivalents, and 30 µL aliquots for 2 to 4.5 equivalents. Care was taken to remain below a 10 % volume addition to avoid dilution effects, and experiments were carried out in triplicate to observe repeatable trends.

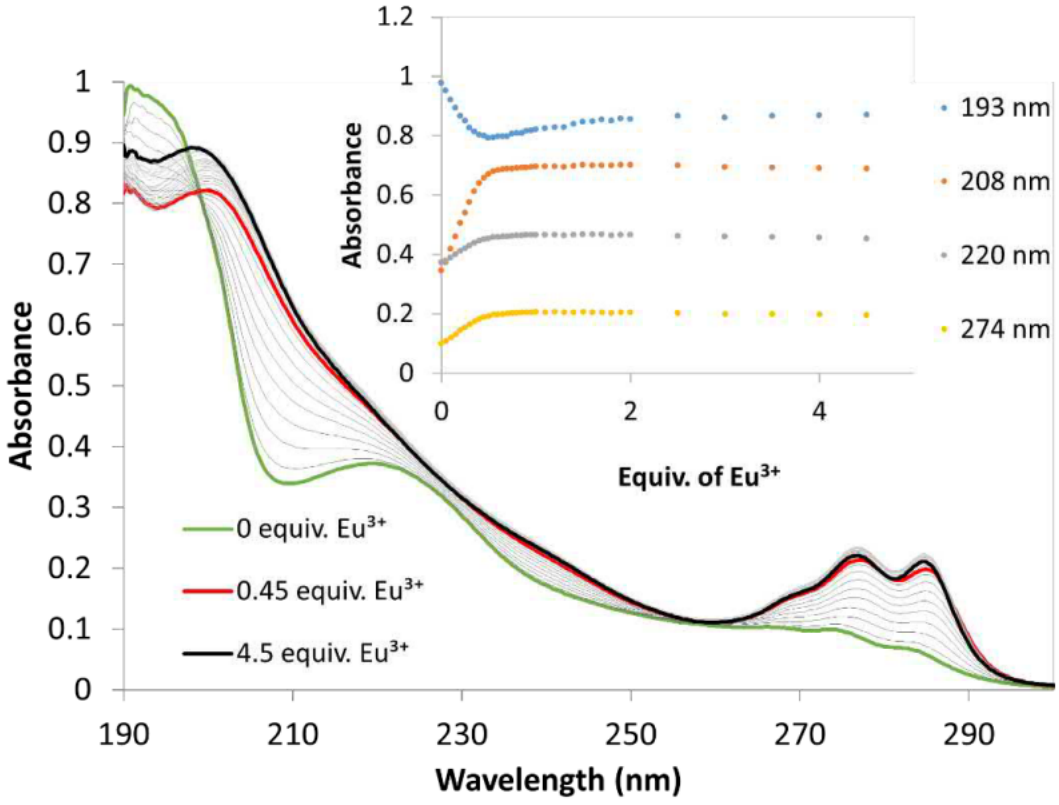

Figure 3.18.. UV-visible absorption titration of **1** *(0.02 M,. MeCN) with Eu(CF₃SO₃)₃·6H₂O 0 to 4.5 equivalents,. done in triplicate.. Insert:. monitoring changes in absorbance vs Eu³⁺ equivalents,. at λ = 193,. 208,. 220 and 274 nm..*

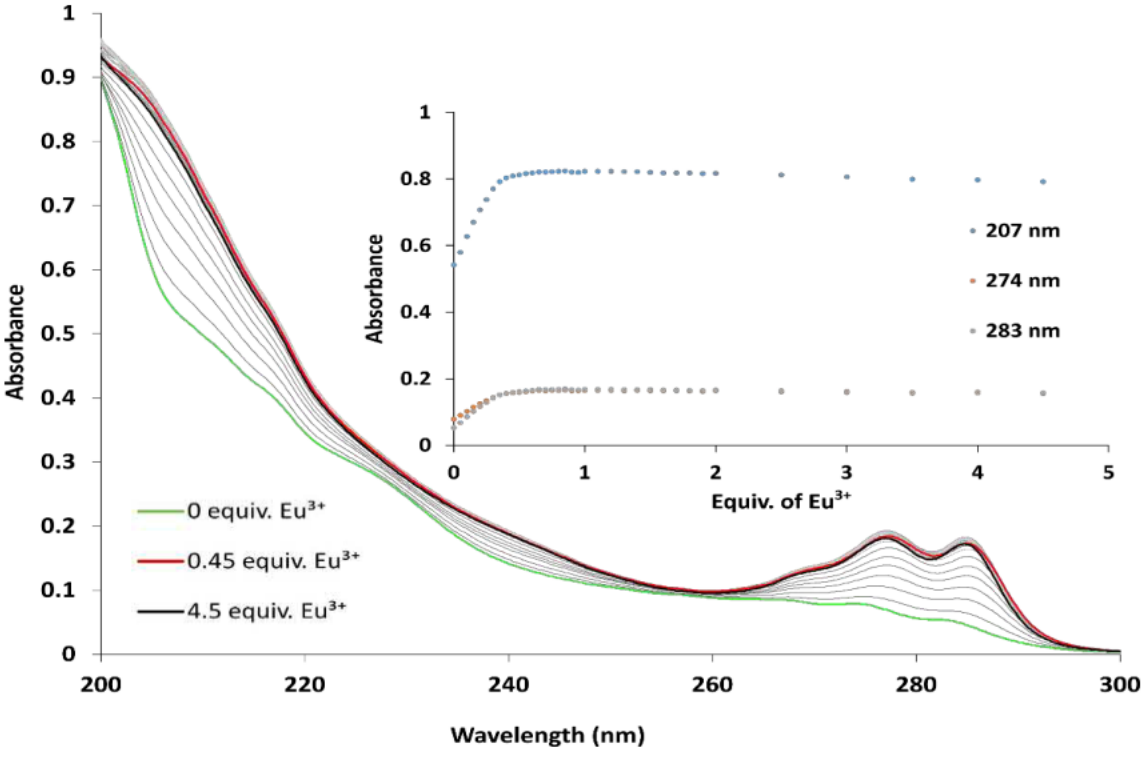

*Figure 3.19.. UV-visible absorption titration of **2** (0.02 M,. MeCN) with $Eu(CF_3SO_3)_3 \cdot 6H_2O$ 0 to 4.5 equivalents,. done in triplicate.. Insert: monitoring changes in absorbance vs Eu^{3+} equivalents,. at λ =. 207,. 274 and 283 nm..*

General trends between different ligands and Ln^{3+} were found to be practically identical in the UV-visible spectra (see Figures 3.19-21 and Section 8.14). All three ligands were observed to experience the most significant changes between 0 to 0.45 equivalents of Ln^{3+}. The primary shoulder bands at 274 nm and 283 nm associated with the central pyridyl unit (assigned to the n → π* and π → π* transitions) undergo large hyperchromic shifts, signifying the formation of the M:L assemblies, specifically 1:3 species. Upon further addition of Ln^{3+}, changes in absorption values begin to plateau and remain practically unchanged, however the peaks continue to undergo a red shift until approximately 1 equivalent where it stops. For example, in the case of **1** absorption is seen to change by a significant ≈ 0.9 absorbance units from 0 to 0.45 equivalents; upon further addition, until 1 equivalent is reached, only a small change of 0.1 absorbance units were observed, despite a larger range of additions, with further addition from 1 to 4.5 equivalents seen to plateau. Such changes are indicative of assembly/disassembly of complexes as metal concentration increases and complex formation evolves from M:L ratios of 1:3 through to 1:1,[22, 25, 44] with clear signs of formation of 1:3 M:L species. A similar trend was also observed for the peaks at 207 nm in **2** and 208 nm in **1** and 220 nm for both, all associated with the pyridyl unit. The unique peak at 225 nm (Figure 3.21), specific to ligand **3** experiences a hypochromic effect from 0 to approximately 0.35 equivalents (highlighting the 1:3 M:L formation) after which it undergoes a significant absorption enhancement until 1 equivalent, which leads to an eventual plateau. This is also observed in other naphthalene containing PDC systems, indicative of the

initial 1:3 M:L formation up to 0.35 equiv. before the increased metal concentration favours the formation of other M:L species (1:2 and 1:1).[25, 33, 44] A similar effect was observed in **1** where the band at 193 nm experienced a similar hypochromic effect from 0 to approximately 0.45 equivalents, which upon further addition we see a similar absorption enhancement which leads to a plateau (Figure 3.18).

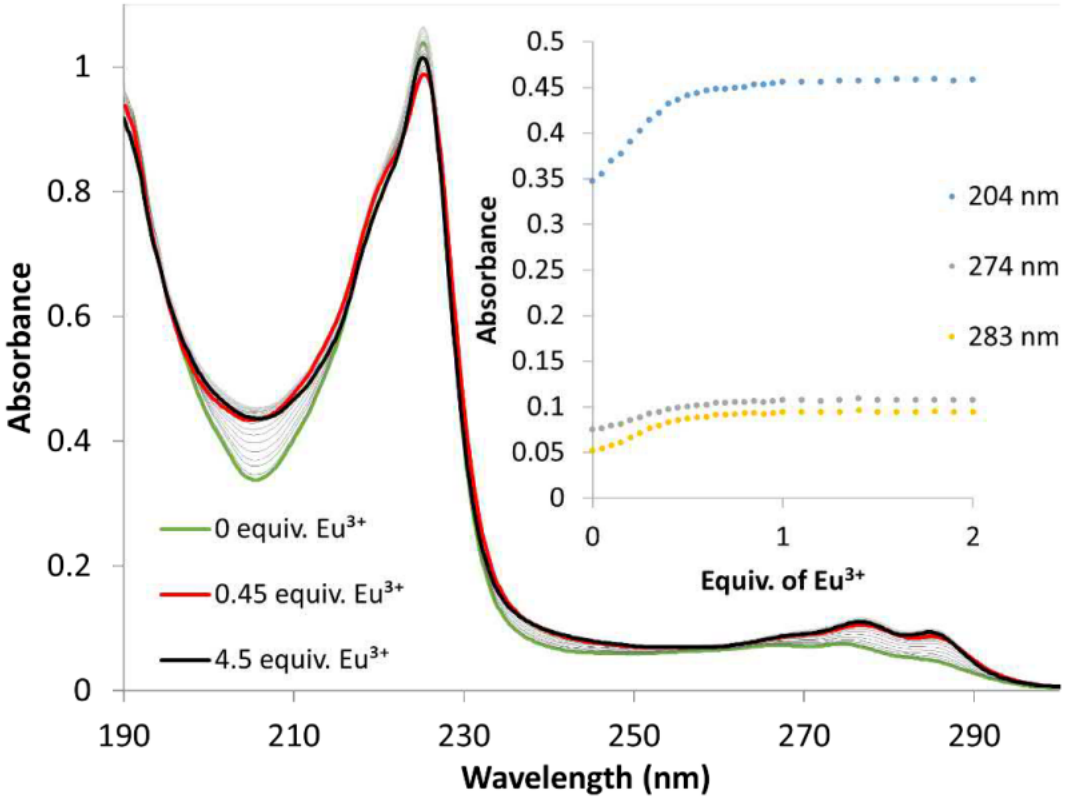

*Figure 3.20.. UV-visible absorption titration of **3** (0.005 M,. MeCN) with $Eu(CF_3SO_3)_3 \cdot 6H_2O$ 0 to 4.5 equivalents,. done in triplicate.. Insert: Monitoring changes in absorbance vs Eu^{3+} equivalents at λ = 204,. 274 and 283 nm..*

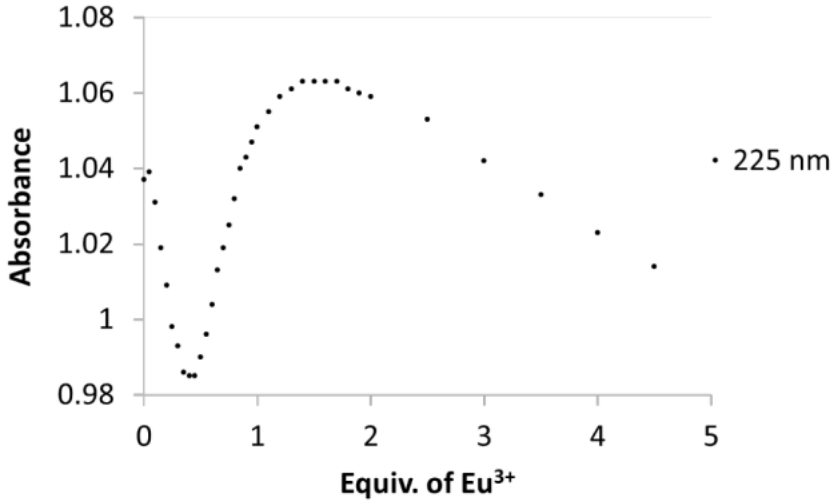

*Figure 3.21.. UV-visible absorption titration of **3** (0.005 M,. MeCN) with $Eu(CF_3SO_3)_3 \cdot 6H_2O$ 0 to 4.5 equivalents,. monitoring changes in absorbance vs Eu^{3+} equivalents at λ = 225 nm..*

Monitoring species formation by changes in fluorescent emission of Eu^{3+}, Tb^{3+} and ligand centred emission gave a much clearer insight into the speciation processes occurring during titrations. The observed changes were again similar between different ligands. When using Eu^{3+} an initially steady increase of the characteristic sharp emission bands at 594 nm ($^5D_0 \rightarrow {}^7F_1$), 616 nm ($^5D_0 \rightarrow {}^7F_2$), 651 nm ($^5D_0 \rightarrow {}^7F_3$), and 697 nm ($^5D_0 \rightarrow {}^7F_4$) until 0.3 equivalents was observed. Upon further additions of Eu^{3+} the emission significantly decreased before reaching a plateau at 1 equivalent (Figure 3.22 and 3.25). This indicated that the most emissive species is the 1:3 Eu:**L** system forming at 0.3 equivalents, as can be expected when the maximum number of ligand antennas are coordinated. The sharp decrease and plateau upon addition of excess metal indicated formation of other M:L species in solution, specifically the 1:2 and 1:1 as these should be less emissive (as fewer antenna groups are coordinated).

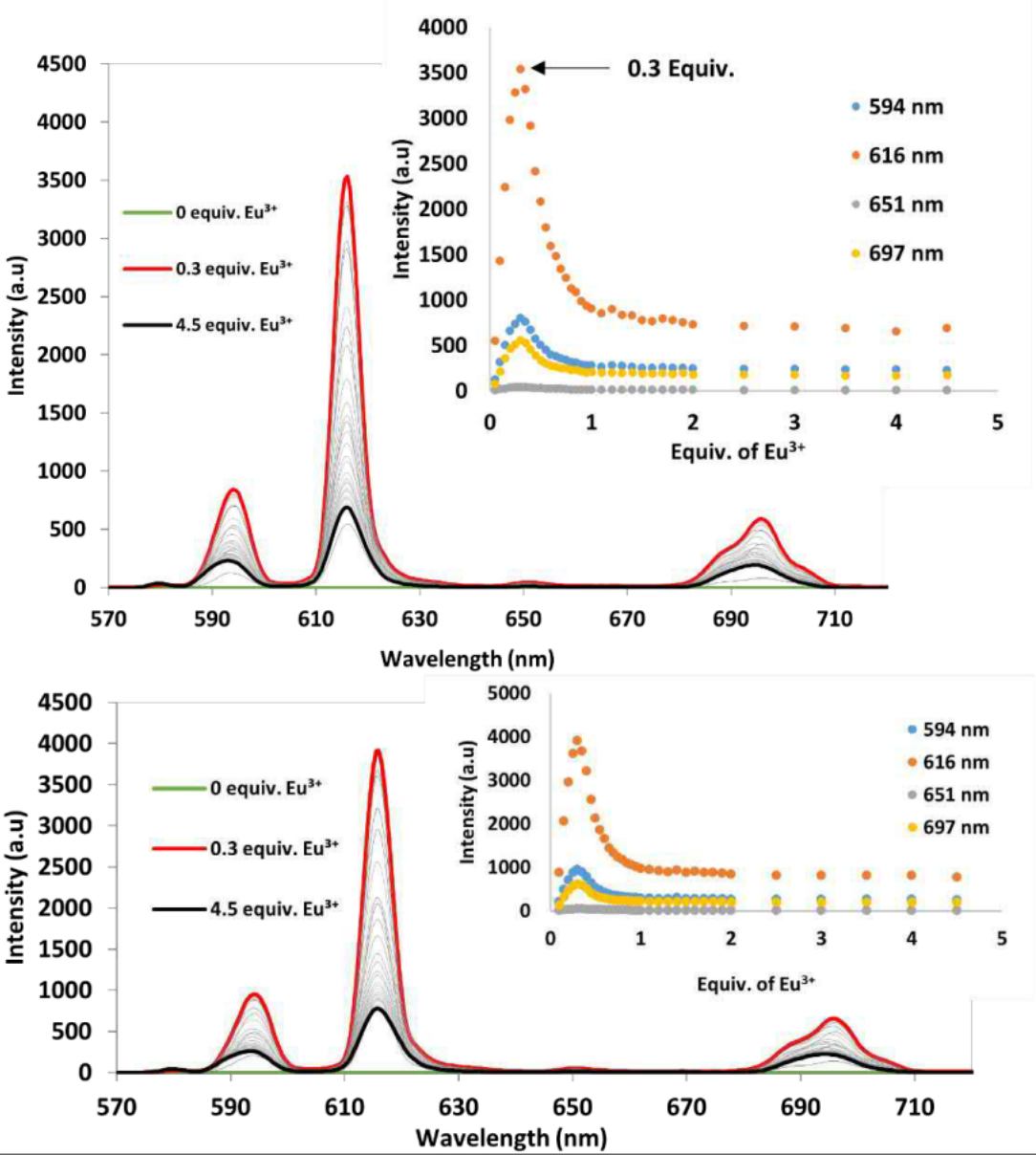

*Figure 3.22.. Fluorescence titration of **1** (Top) and **2** (Bottom) (0.02 M, MeCN) with $Eu(CF_3SO_3)_3{\cdot}6H_2O$ 0 to 4.5 equivalents, done in triplicate. Insert: monitoring changes in intensity vs Ln^{3+} equivalents, at λ = 594, 616, 651 and 697 nm.*

Similar changes were observed when carrying out the same titrations with Tb^{3+} and monitoring the Tb^{3+} centred emission. Titrations using ligands **1** and **2** show the characteristic sharp Tb^{3+} emission bands at 490 nm ($^5D_4 \rightarrow {}^7F_6$), 545 nm ($^5D_4 \rightarrow {}^7F_5$), 587 nm ($^5D_4 \rightarrow {}^7F_4$), and 621 nm ($^5D_4 \rightarrow {}^7F_3$) increasing until 0.3 equivalents, where it then underwent a gradual decrease in intensity until the eventual plateau at 1 equivalent (Figure 3.23), showing the same evolutionary process as observed in the Eu^{3+} titrations with **1** and **2**.

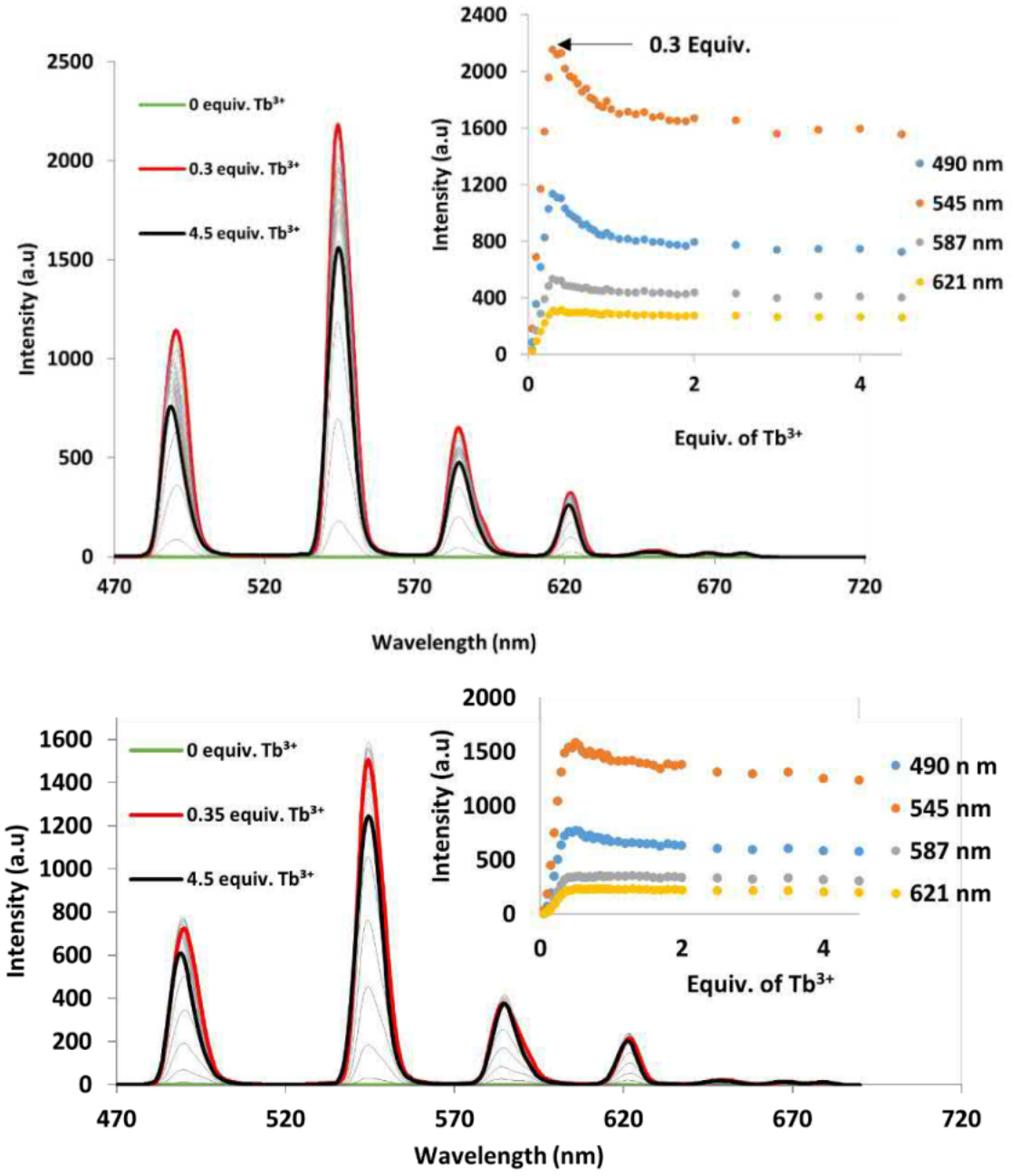

*Figure. 3.23.. Fluorescence. titration. of. **1**. (Top). and. **2**. (Bottom). (0.02. M,. MeCN). with. $Tb(CF_3SO_3)_3{\cdot}5H_2O$. 0. to. 4.5. equivalents,. done. in. triplicate.. Insert:. monitoring. changes. in. intensity. vs. Ln^{3+}. equivalents,. at. λ =. 490,. 545,. 587. and. 621. nm..*

Unexpectedly, titrations between **3** and Tb^{3+} did not follow the same profile. The expected sharp emission bands associated with Tb^{3+} were observed throughout the titration, however, the emission intensity gradually increased up to 1 equivalent before a plateau was reached and maintained up to 4.5 equivalents (Figure 3.24). This behaviour was noted in the literature for PDA-based ligands that contain naphthalene substituents and was attributed to a BT process likely occurring between the triplet state of the ligand and the excited state of Tb^{3+}, as previously noted in our system as well.[25]

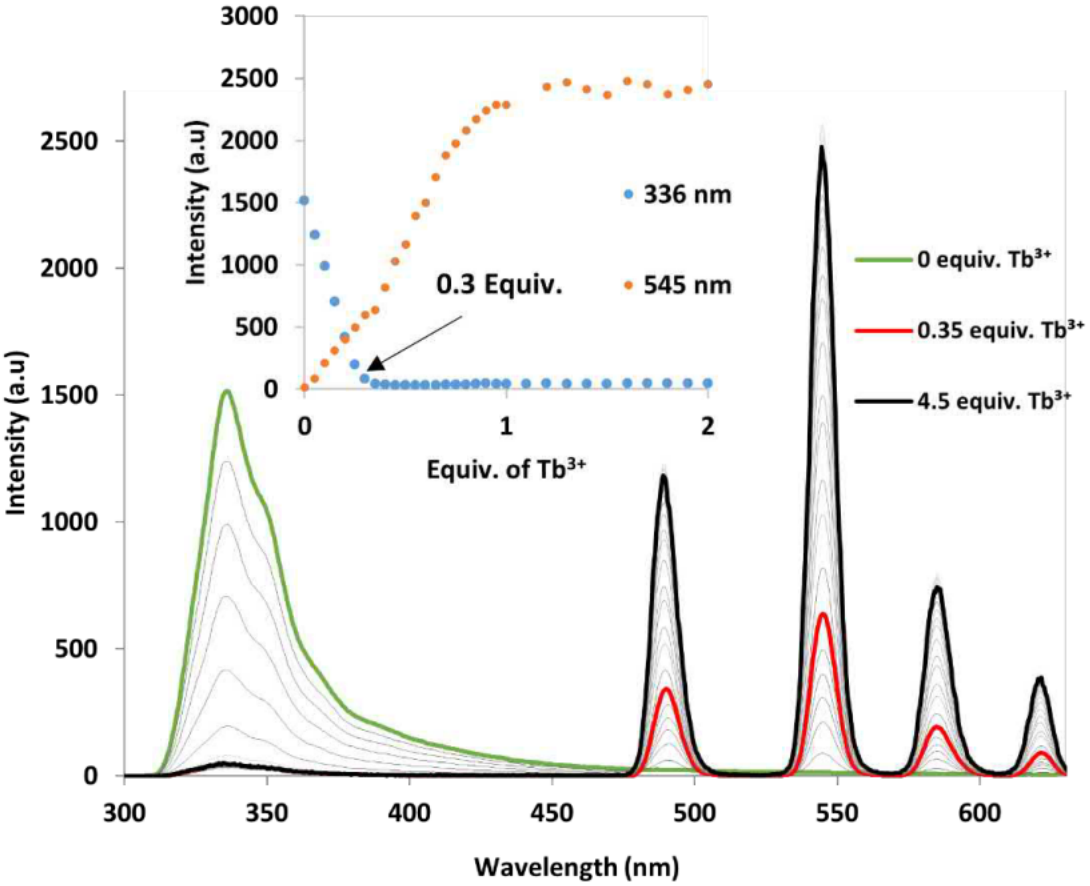

*Figure 3.24. Fluorescence titration of **3** (0.02 M, MeCN) with $Tb(CF_3SO_3)_3 \cdot 5H_2O$ 0 to 4.5 equivalents, done in triplicate. Insert: monitoring changes in intensity vs Ln^{3+} equivalents, at λ = 336 and 545 nm.*

Lastly, in terms of ligand centred emission of **3** at 336 nm, all Ln^{3+} resulted in significant quenching of ligand centred emission from 0 to 0.3-0.4 equivalents, with titrations of both Eu^{3+} and Tb^{3+} reaching a plateau of practically no emission at 0.45 and 0.35 equivalents respectively, indicative of the 1:3 species formation (Figure 3.24-25). This was likely a result of the energy transfer from the naphthalene to the excited state of the Ln^{3+}. The fact that Tb^{3+} results in an early plateau may be a result of the better matched energy states, but as stated prior this does not improve the complex's Tb^{3+} centred emission, as it leads to BT.

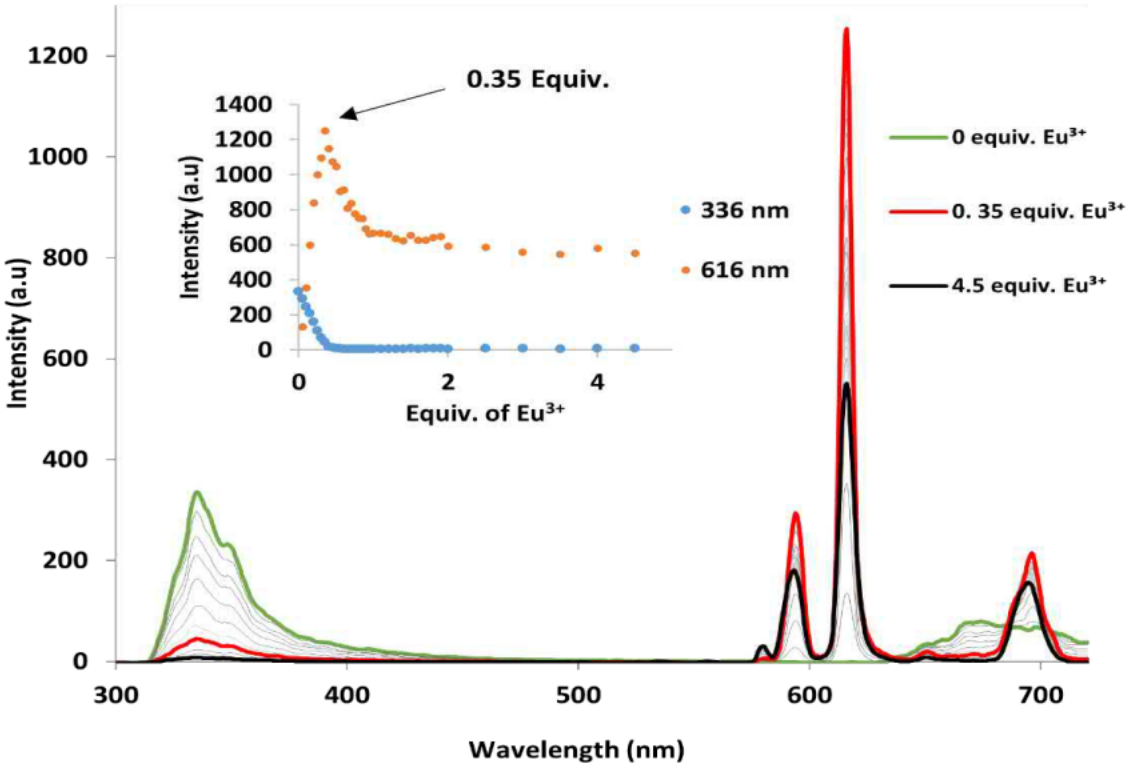

*Figure 3.25. Fluorescence titration of **3** (0.02 M, MeCN) with $Eu(CF_3SO_3)_3 \cdot 6H_2O$ 0 to 4.5 equivalents, done in triplicate. Insert: monitoring changes in intensity vs Ln^{3+} equivalents, at λ = 336 and 616 nm.*

Similar quenching was observed with La^{3+} with significant changes occurring between 0 to 0.4 equivalents, indicating the formation of the 1:3 species (Figure 3.26). As previously stated, the ligand centred emission decrease was likely due to ISC becoming favoured from heavy atom effects, increasing nr decay from the T_1 to ground state. Unlike Eu^{3+} and Tb^{3+}, emission decay was seen to continue and did not reach a plateau until 1 equivalent, indicative of the evolution to 1:2 and 1:1 species, although decreases are much less significant after 0.4 equivalents. From 0 to 0.4 equivalents the intensity changes by ≈ 1270 a.u, whereas from 0.4 to 1 equivalent it changes by ≈ 146 a.u which is significantly more compared to titrations with Eu^{3+} or Tb^{3+}, where changes from their plateau points (of 0.45 and 0.35 equivalents respectively) to 1 equivalent are 7.9 and 1.7 a.u respectively. This was put down to the ISC likely becoming slightly more effective as the species evolve from the 1:3, 1:2, and finally 1:1 species, where in the case of Eu^{3+} and Tb^{3+} the fact that a plateau was reached much earlier suggests that energy from both the naphthalene triplet state and singlet state are being transferred to the excited state of the Ln^{3+}.

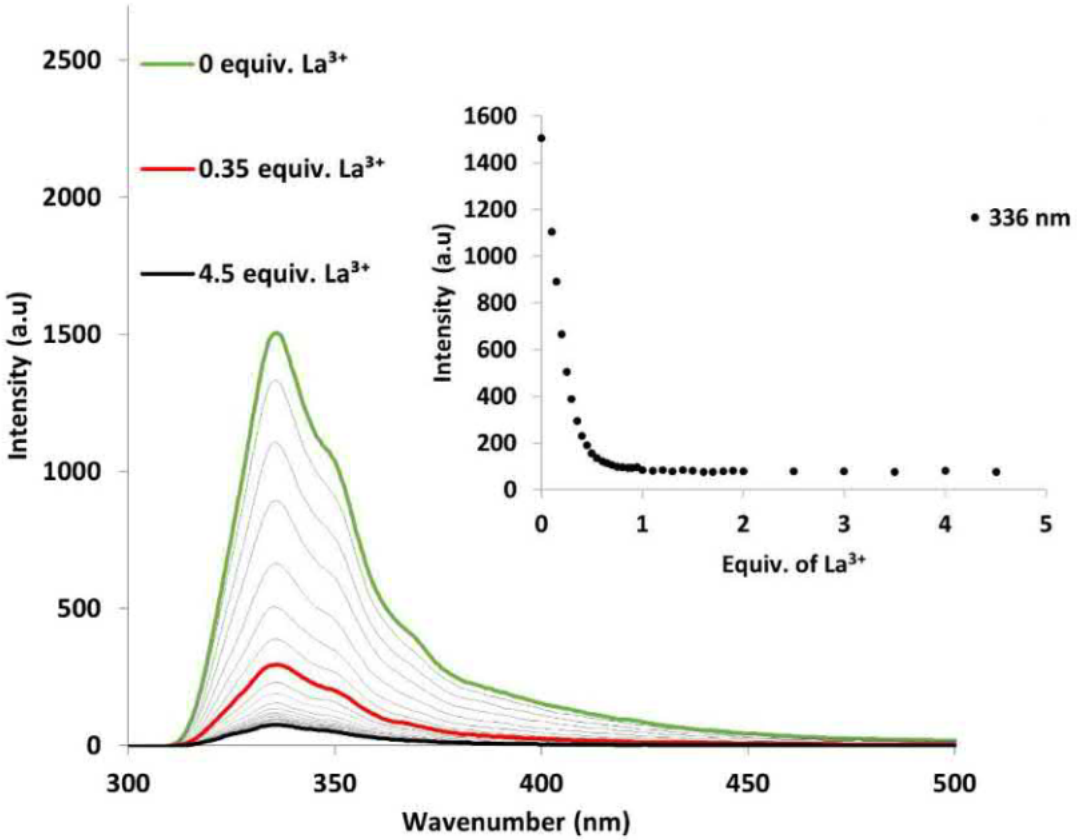

*Figure 3.26. Fluorescence titration of **3** (0.02 M, MeCN) with $La(CF_3SO_3)_3 \cdot 9H_2O$ 0 to 4.5 equivalents, done in triplicate. Insert: monitoring changes in intensity vs Ln^{3+} equivalents, at $\lambda = 336$ nm.*

From a combination of the results of monitoring both UV-visible absorption and fluorescence emission changes it is apparent that the 1:3 M:L species is forming in solution for all ligands and Ln^{3+}. Furthermore an evolutionary change is occurring into the lesser species, likely 1:2 and 1:1, upon additional Ln^{3+} as seen in previous PDA systems.[23, 25, 27, 33, 36, 44, 45]

3.2.5.2 Non-linear Regression Analysis

To gain further insight into species formation, the global changes in the UV-visible absorption (ground state) and fluorescence (excited state) titrations were analysed by fitting the data to 1:3, 1:2, and 1:1 M:L species (anions and solvent molecules were excluded for simplicity, and ions used are justified by ions identified in mass spectra and other PDA based systems)[23, 25, 27, 33, 36, 44, 45] using the non-linear regression analysis program ReactLab™ equilibria.[46] This gave speciation distribution plots with insight into species percentage formation and binding constants (Log $\beta_{1:x}$ where x = 3, 2 and 1). In most cases data was fitted from 0 to 4.5 equivalents, with the whole spectrum of absorbance or fluorescence, with a few cases requiring a lower maximum equivalent to obtain a good fit. In the case of titrations of **3** with Tb^{3+} the data could not be fitted, due to the complex processes occurring (back-transfer), similar to that which occurred in literature for other naphthalene containing ligands.[25]

$$\mathbf{Ln + L} \leftrightarrow [\mathbf{Ln(L)}]^{3+} \quad \text{Log } \beta_{1:1} \qquad (1)$$

$$\mathbf{Ln + 2L} \leftrightarrow [\mathbf{Ln(L)_2}]^{3+} \quad \text{Log } \beta_{1:2} \qquad (2)$$

$$\mathbf{Ln + 3L} \leftrightarrow [\mathbf{Ln(L)_3}]^{3+} \quad \text{Log } \beta_{1:3} \qquad (3)$$

Equations 3.1. Equilibrium equations used in ReactLab™ equilibria for which the titration data has been fit with.

Similar to the general changes observed in titrations between different ligands and Ln^{3+}, the speciation distribution plots obtained also followed the same general trend, independent of the ligand or Ln^{3+} used. Alongside this in most cases data fitted from UV-visible absorption and fluorescence titrations resulted in similar speciation processes with near identical binding constants (Table 3.5) showing good agreement between observed changes in each titration.

*Table 3.5. Binding constants from fitted data of both UV-visible absorption and fluorescence titration. In the case of the fluorescence titrations with Tb^{3+} and ligand **2**, it required one of the binding coefficients to be fixed to a value to be fitted. This was achieved by fitting the data three times, each time changing the fixed coefficient such that each value has been fitted in conjunction with one another, ending with the Log $\beta_{1:2}$ as the fixed coefficient.*

Ln(L)	UV-visible absorption			Fluorescent emission		
	Log $\beta_{1:1}$	Log $\beta_{1:2}$	Log $\beta_{1:3}$	Log $\beta_{1:1}$	Log $\beta_{1:2}$	Log $\beta_{1:3}$
Eu(**1**)	6.4 ± 0.02	13.1 ± 0.03	18.8 ± 0.05	6.6 ± 0.01	13.1 ± 0.01	18.9 ± 0.01
Eu(**2**)	7.1 ± 0.02	14.4 ± 0.02	21.5 ± 0.02	8.0 ± 0.04	15.3 ± 0.06	22.0 ± 0.08
Eu(**3**)	8.2 ± 0.03	15.3 ± 0.06	22.0. ± 0.10	8.4 ± 0.06	15.5 ± 0.10	21.8 ± 0.10
Tb(**1**)	6.6 ± 0.03	13.4 ± 0.06	19.8 ± 0.08	6.0 ± 0.03	12.6 ± 0.04	19.4 ± 0.03
Tb(**2**)	7.2 ± 0.08	14.7 ± 0.06	21.8 ± 0.24	8.2 ± 0.04	14.8 (fixed)	22.3 ± 0.03
Tb(**3**)	7.7 ± 0.05	15.1 ± 0.10	22.6 ± 0.15	-	-	-
La(**1**)	5.8 ± 0.02	11.5 ± 0.02	17.1 ± 0.02	-	-	-
La(**2**)	6.6 ± 0.03	13.0 ± 0.05	18.2 ± 0.06	-	-	-
La(**3**)	6.7 ± 0.02	12.6 ± 0.03	18.8 ± 0.06	7.5 ± 0.09	12.8 ± 0.09	18.8 ± 0.09

Examination of binding constants of different Ln^{3+} and ligands gave rise to some interesting trends. Ligands **2** and **3** in all cases experienced higher binding constants than ligand **1**, with log $\beta_{1:3}$ ranging from 21.5 – 22.6 for both Eu(**L**)$_3$ and Tb(**L**)$_3$, and 18.2 - 18.8 for La(**L**)$_3$, in both absorption and emission titrations. In comparison log $\beta_{1:3}$ for Eu(**1**)$_3$ = 18.8-18.9, Tb(**1**)$_3$ = 19.8-19.4 and La(**1**)$_3$ = 17.1, indicated that the aromatic substituents may aid in stabilizing or favouring the formation of the 1:3 species, potentially through π – π stacking interactions, which are not viable for ligand **1**. There was also a clear trend of binding constant increasing from $La^{3+} < Eu^{3+} < Tb^{3+}$ associated with the decrease in ionic radius, as noted previously in Bünzli and co-workers PDA based ligand **L^1** (Figure 3.16).[16] This was associated with the species formation percentages of [La(**L**)$_3$] (24 % – 39 %) being significantly lower compared to those of Eu^{3+} or Tb^{3+} (42 % – 81%). Importantly, the values of log $\beta_{1:3}$ are in good agreement to other PDA-based systems (Table 3.6) with values of log $\beta_{1:3}$ ranging from 23.8 to 17.0 with Eu^{3+}, as well as similar values for the other Ln^{3+}.[16, 17, 23, 33, 45]

Table 3.6.. Binding constants from fitted data of both UV-visible absorption and fluorescence titration from other PDA based ligands done in MeCN.. Values obtained from references 16,. 17,. 23,. 33 and 45..

Ln(L)	Log $\beta_{1:1}$	Log $\beta_{1:2}$	Log $\beta_{1:3}$
La(**L^1**)	7.4 ± 0.3	14.8 ± 0.3	21.0 ± 0.3
Tb(**L^1**)	8.2 ± 0.3	14.5 ± 0.4	22.9 ± 0.4
Eu(**L^1**)	8.3 ± 0.3	15.3 ± 0.3	22.3 ± 0.3
Eu(**L^4 - S,S**)	6.0 ± 0.1	13.1 ± 0.2	19.0 ± 0.3
Eu(**L^5 - S,S**)	5.3 ± 0.2	11.4 ± 0.1	17.0 ± 0.3
Eu(**L^6**)	8.0 ± 0.2	15.9 ± 0.2	23.8 ± 0.2
Eu(**L^{12} - S,S**)	6.7 ± 0.2	14.3 ± 0.3	21.9 ± 0.4
La(**L^{43}**)	7.4 ± 0.4	13.9 ± 0.5	19.0 ± 0.5
Eu(**L^{43}**)	8.2 ± 0.0	14.6 ± 0.5	19.7 ± 0.5

The general speciation trend can be split into three major events occurring between 0 to 0.35, 0.4 to 0.65, and 0.7 to 1 equivalent (Figures 3.27-29 and Tables 3.7-9). Firstly, upon the addition of Ln^{3+}, the system undergoes a rapid formation of the 1:3 M:L species which coincides with a rapid depopulation of free ligand. At 0.3 equivalents, the 1:3 M:L species becomes the dominant species with most of the free ligand coordinated and lesser species (1:1 and 1:2) largely not present. Upon an additional 0.05 equivalent (0.35 total equiv.), in most cases the peak formation of the 1:3 species occurs, ranging from Eu(**L**)$_3$ 42 - 77 %, Tb(**L**)$_3$ 69 - 81 % and La(**L**)$_3$ 24 – 30 %. This coincides with initial formation of the 1:2 species with formation ranging from 17 – 40 %; see Tables 3.7-9 for more details.

In all cases, further addition leads to instant rapid loss of the 1:3 species, with the evolutionary formation of the subsequent 1:2 species, which becomes the dominant species at 0.4 equivalents reaching a maximum around 0.6 - 0.65 equivalents. In some cases (**3** with La^{3+} and Tb^{3+}), the dominant formation of the 1:2 species is skipped, favouring the 1:1 species (Figure 3.29 and Table 3.9).

*Table 3.7.. Species formation percentages from fitted data of both UV-visible absorption and fluorescence emission titrations with **1**, Eu^{3+}, Tb^{3+} and La^{3+} at specific equivalents, (0, 0.3, 0.6 and 1 equivalent)..*

	UV-visible Absorption Fitted Data				Fluorescent Emission Fitted Data			
Species Formation with x Equiv. Eu^{3+}	0 Equiv.	0.3 Equiv.	0.6 Equiv.	1 Equiv.	0 Equiv.	0.3 Equiv.	0.6 Equiv.	1 Equiv.
1	100 %	34 %	1 %	0 %	100 %	40 %	4 %	3 %
Eu(**1**)	0 %	6 %	20 %	37 %	0 %	1 %	28 %	49 %
$Eu(\mathbf{1})_2$	0 %	14 %	65 %	57 %	0 %	17 %	52 %	42 %
$Eu(\mathbf{1})_3$	0 %	56 %	14 %	6 %	0 %	42 %	16 %	6 %
Species Formation with x Equiv. Tb^{3+}	0 Equiv.	0.3 Equiv.	0.6 Equiv.	1 Equiv.	0 Equiv.	0.3 Equiv.	0.6 Equiv.	1 Equiv.
1	100 %	32 %	2 %	1 %	100 %	29 %	4 %	3 %
Tb(**1**)	0 %	1 %	24 %	42 %	0 %	1 %	15 %	26 %
$Tb(\mathbf{1})_2$	0 %	9 %	45 %	42 %	0 %	4 %	24 %	27 %
$Tb(\mathbf{1})_3$	0 %	58 %	29 %	15 %	0 %	66 %	57 %	44 %
Species Formation with x Equiv. La^{3+}	0 Equiv.	0.3 Equiv.	0.6 Equiv.	1 Equiv.				
1	100 %	49 %	17 %	9 %				
La(**1**)	0 %	5 %	30 %	48 %				
$La(\mathbf{1})_2$	0 %	15 %	30 %	29 %				
$La(\mathbf{1})_3$	0 %	31 %	23 %	13 %				

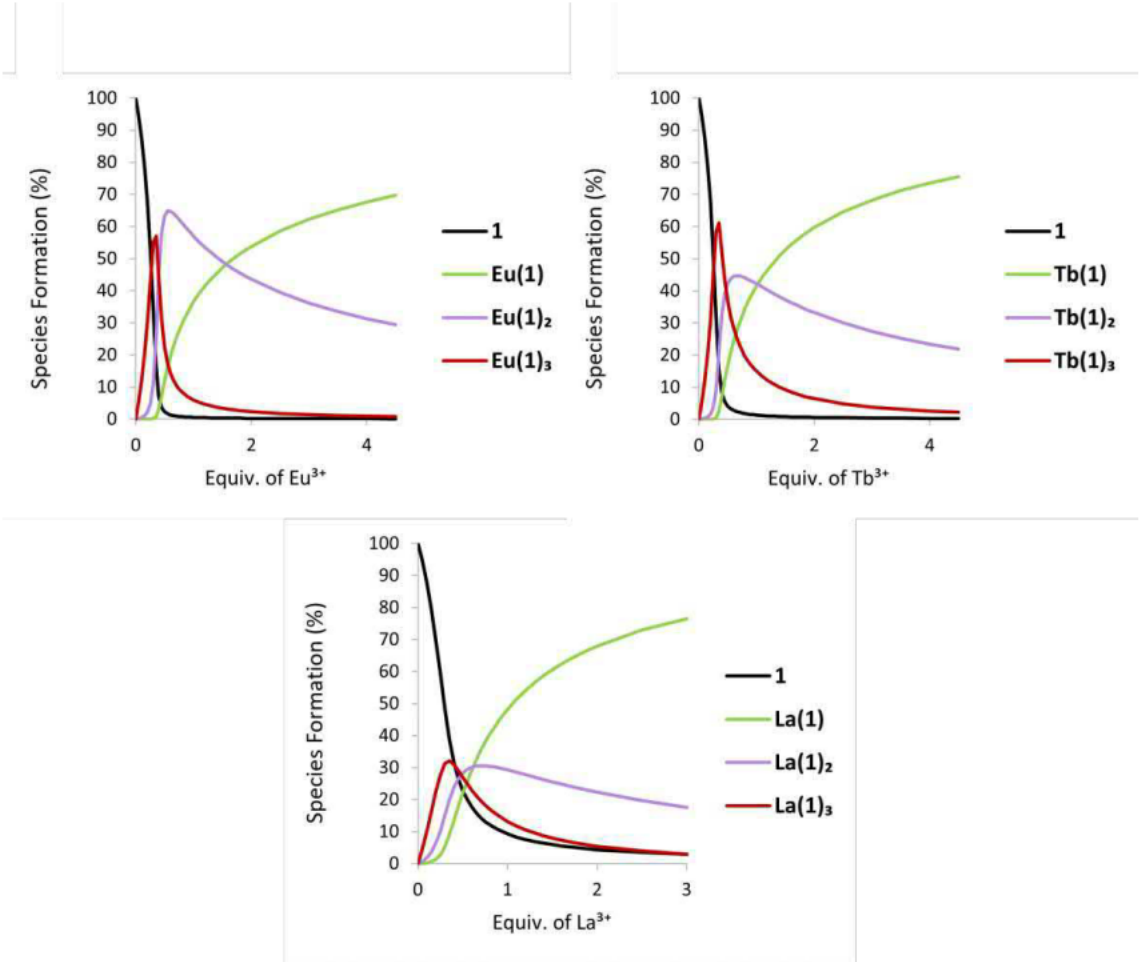

*Figure 3.27.. Speciation plots of fitted data from UV-visible absorption titrations with **1**, Eu^{3+}, Tb^{3+} and La^{3+}..*

In all systems, further additions from 0.65 - 1.2 equivalents resulted in the loss of the 1:2 species and the formation of the 1:1, becoming more dominant as more Ln^{3+} was added. This evolutionary trend observed throughout these titrations is commonly seen in other PDA-based ligand titrations with $Ln(CF_3SO_3)_3$.[22, 25, 33, 44]

Table. 3.8.. Species. formation. percentages. of. fitted. data. from. both. UV-visible. absorption,. and. fluorescence. emission. titration. with. ***2****, Eu^{3+},. Tb^{3+}. and. La^{3+}. at. specific. equivalents. (0,. 0.3,. 0.6. and. 1. equivalent)..*

	UV-visible Absorption Fitted Data				Fluorescent Emission Fitted Data			
Species Formation with x Equiv. Eu^{3+}	0 Equiv.	0.3 Equiv.	0.6 Equiv.	1 Equiv.	0 Equiv.	0.3 Equiv.	0.6 Equiv.	1 Equiv.
2	100 %	27 %	1 %	0 %	100 %	11 %	1 %	0 %
Eu(**2**)	0 %	0 %	23 %	40 %	0 %	2 %	39 %	60 %
$Eu(\mathbf{2})_2$	0 %	3 %	42 %	41 %	0 %	20 %	44 %	34 %
$Eu(\mathbf{2})_3$	0 %	70 %	34 %	19 %	0 %	68 %	16 %	6 %
Species Formation with x Equiv. Tb^{3+}	0 Equiv.	0.3 Equiv.	0.6 Equiv.	1 Equiv.	0 Equiv.	0.3 Equiv.	0.6 Equiv.	1 Equiv.
2	100 %	27 %	1 %	0 %	100 %	26 %	0 %	0 %
Tb(**2**)	0 %	0 %	23 %	42 %	0 %	0 %	52 %	84 %
$Tb(\mathbf{2})_2$	0 %	3 %	47 %	43 %	0 %	2 %	23 %	12 %
$Tb(\mathbf{2})_3$	0 %	70 %	29 %	15 %	0 %	72 %	25 %	4 %
Species Formation with x Equiv. La^{3+}	0 Equiv.	0.3 Equiv.	0.6 Equiv.	1 Equiv.				
2	100 %	48 %	6 %	3 %				
La(**2**)	0 %	2 %	29 %	54 %				
$La(\mathbf{2})_2$	0 %	26 %	57 %	41 %				
$La(\mathbf{2})_3$	0 %	24 %	8 %	2 %				

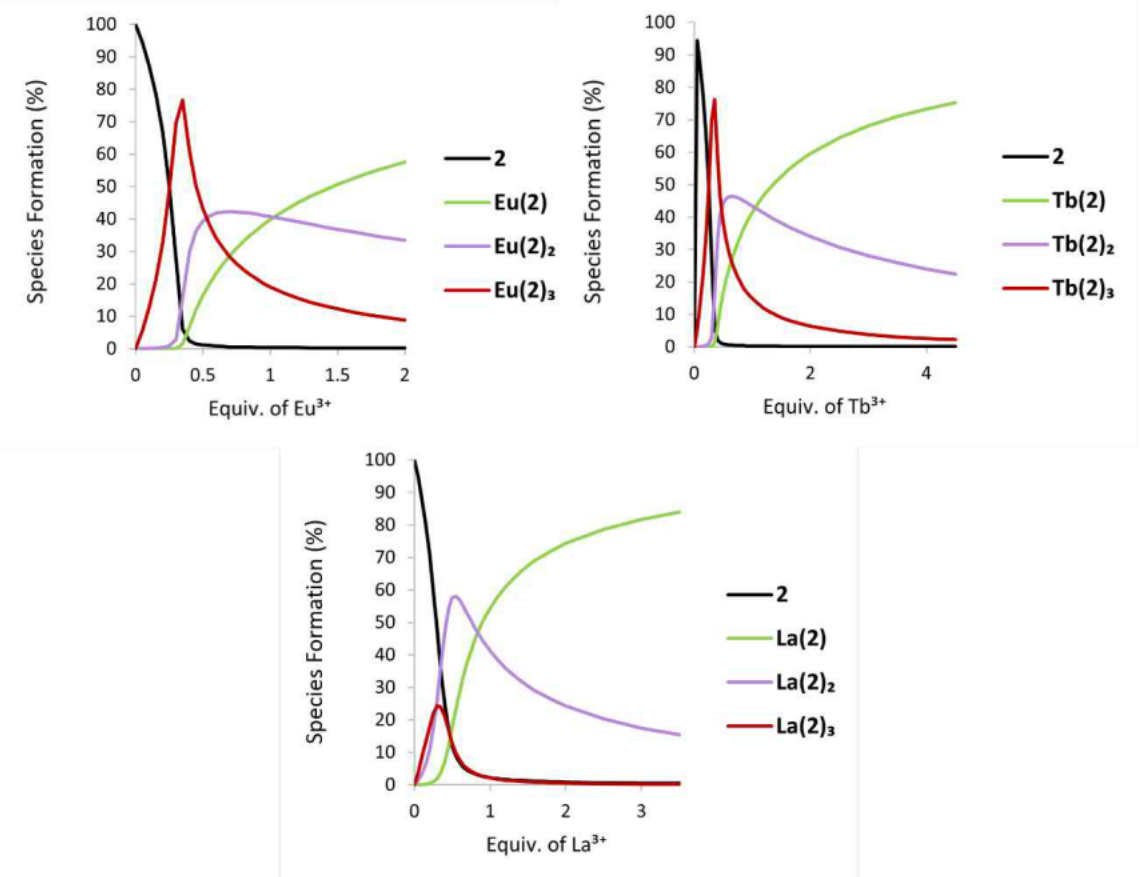

Figure. 3.28.. Speciation. plots. of. fitted. data. from. UV-visible. absorption. titrations. with. ***2****,. Eu^{3+},. Tb^{3+}. and. La^{3+}..*

*Table 3.9.. Species formation percentages of fitted data from both UV-visible absorption, and fluorescence emission titration with **3**, Eu^{3+}, Tb^{3+} and La^{3+} at specific equivalents (0, 0.3, 0.6 and 1 equivalent).*

	UV-visible absorption Fitted Data				Fluorescent emission Fitted Data			
Species Formation with x Equiv. Eu^{3+}	0 Equiv.	0.3 Equiv.	0.6 Equiv.	1 Equiv.	0 Equiv.	0.3 Equiv.	0.6 Equiv.	1 Equiv.
3	100 %	36 %	3 %	1 %	100 %	33 %	1 %	0 %
Eu(**3**)	0 %	1 %	43 %	77 %	0 %	0 %	41 %	83 %
$Eu(\mathbf{3})_2$	0 %	13 %	41 %	21 %	0 %	10 %	49 %	16 %
$Eu(\mathbf{3})_3$	0 %	50 %	14 %	2 %	0 %	57 %	9 %	1 %
Species Formation with x Equiv. Tb^{3+}	0 Equiv.	0.3 Equiv.	0.6 Equiv.	1 Equiv.				
3	100 %	29 %	1 %	0 %				
Tb(**3**)	0 %	0 %	35 %	57 %				
$Tb(\mathbf{3})_2$	0 %	4 %	33 %	28 %				
$Tb(\mathbf{3})_3$	0 %	67 %	31 %	15 %				
Species Formation with x Equiv. La^{3+}	0 Equiv.	0.3 Equiv.	0.6 Equiv.	1 Equiv.	0 Equiv.	0.3 Equiv.	0.6 Equiv.	1 Equiv.
3	100 %	51 %	20 %	8 %	100 %	44 %	9 %	2 %
La(**3**)	0 %	10 %	41 %	66 %	0 %	8 %	56 %	92 %
$La(\mathbf{3})_2$	0 %	11 %	20 %	17 %	0 %	9 %	16 %	4 %
$La(\mathbf{3})_3$	0 %	28 %	19 %	9 %	0 %	39 %	19 %	2 %

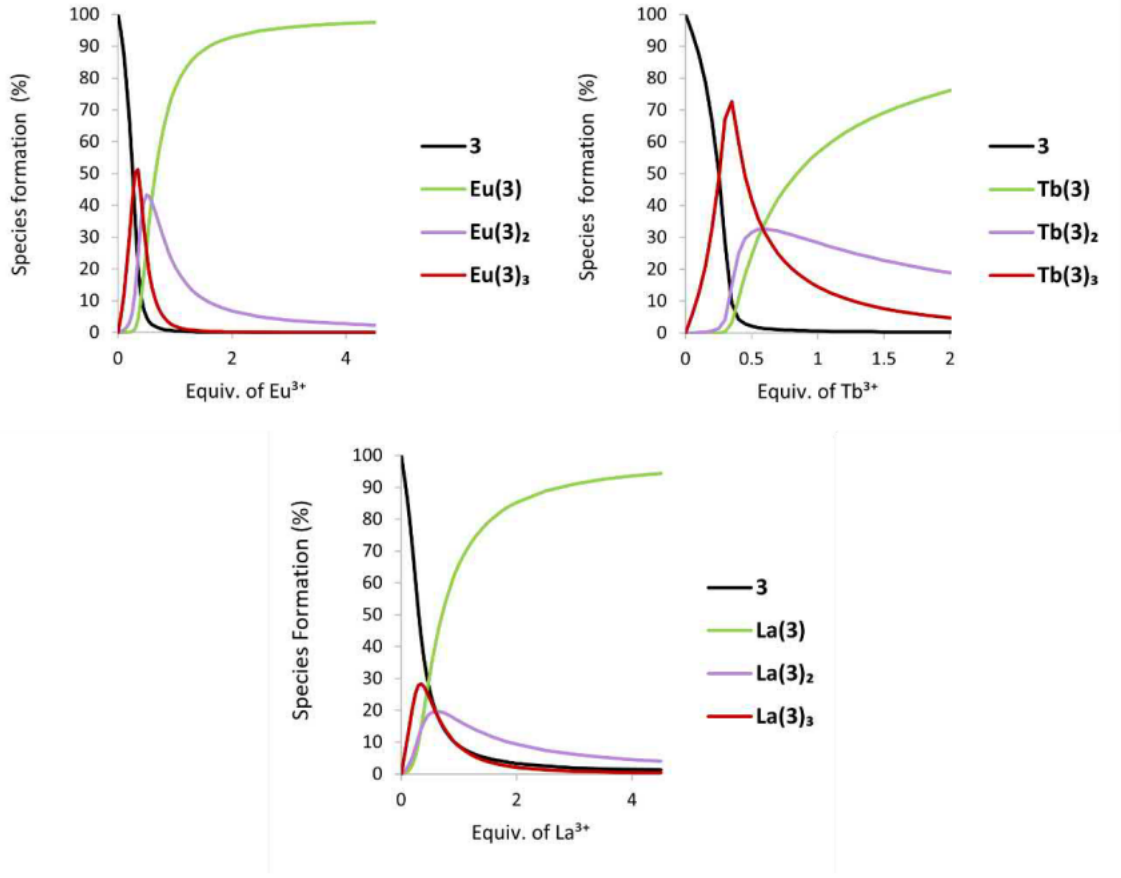

*Figure 3.29.. Speciation plots of fitted data from UV-visible absorption titrations with **3** Eu^{3+}, Tb^{3+} and La^{3+}.*

3.2.5.2 Physical (^{1}H NMR) Self-Assembly Investigation

Finally, the Ln^{3+} directed self-assemblies and binding with ligands **1**, **2**, and **3** were also studied *in situ* by analysing the changes in ^{1}H NMR spectra at r.t. This was carried out in a 1 mM ligand solution in CD_3CN:CD_3OD:$CDCl_3$ (9.99:0.005:0.005, 1 mM) with additions from 0 to 2 equivalents of $La(CF_3SO_3)_3 \cdot 9H_2O$ taking a 250 scan (30 minute) spectrum between each addition. Spectra were calibrated to the CD_3CN peak at 1.94 ppm. It is worth noting that titrations were originally attempted in DMSO-d_6, but no visible changes were observed likely due to competitive interaction of the DMSO-d_6 with the PDA pocket and coordination to the lanthanide ion itself.[47]

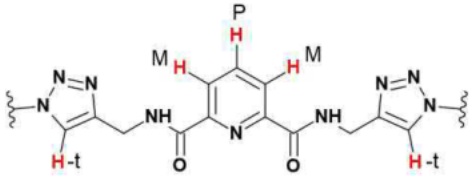

Figure 3.30.. Protons of interest in ^{1}H NMR titrations..

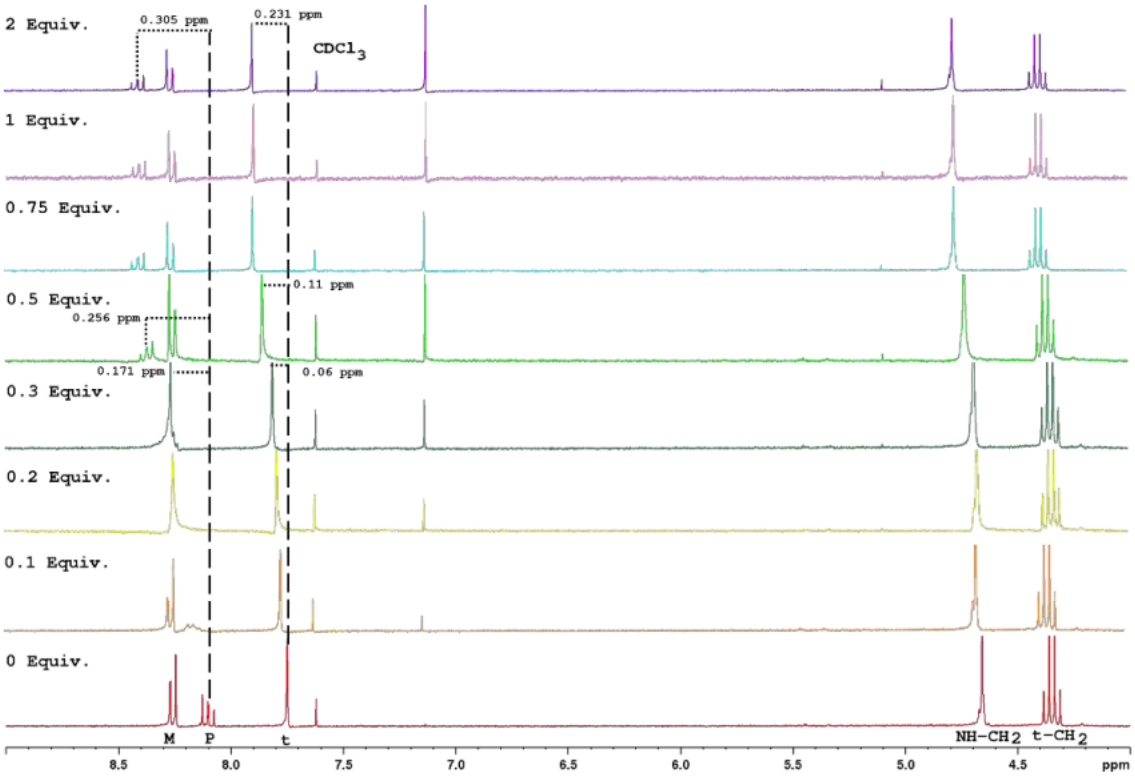

*Figure 3.31.. Overall changes in the ^{1}H NMR spectra of **1** (CD_3CN:CD_3OD:$CDCl_3$ (9.99:0.005:0.005),. 0.001 M,. 300 MHz) upon titrating with $La(CF_3SO_3)_3$ (0 – 2 equivalents)..*

Once again titrations between the different ligands experience the same general trend, as seen in Figures 3.31-33, indicating that the "click" substituents appear to have no major effect on the binding of the pyridyl unit. In the case of all ligands, upon the addition of 0.1 equivalent of La^{3+} the overall spectrum remains relatively the same, aside from the peaks associated with the *meta*-protons (***M***) on the pyridyl unit broadening and the peaks associated with the *para*-proton

(***P***) nearly disappearing and undergoing a downfield shift. This downfield shift is characteristic of the La^{3+} pulling electron density out from the pyridine ring and is suggestive of coordination occurring in the NO_2 binding pocket as expected and as observed in other PDA systems.[8, 16] The downfield shift is seen to continue as more La^{3+} is added, and at 0.3 equivalents it appears that the **P** and **M** protons merge with a total shift of around 0.15 – 0.17 ppm observed on the **P** proton. The reduced number of signals observed at 0.3 equivalents was indicative of the formation of the 1:3 species and was also an indication of higher symmetry in the **M** proton as seen in previous systems.[8]

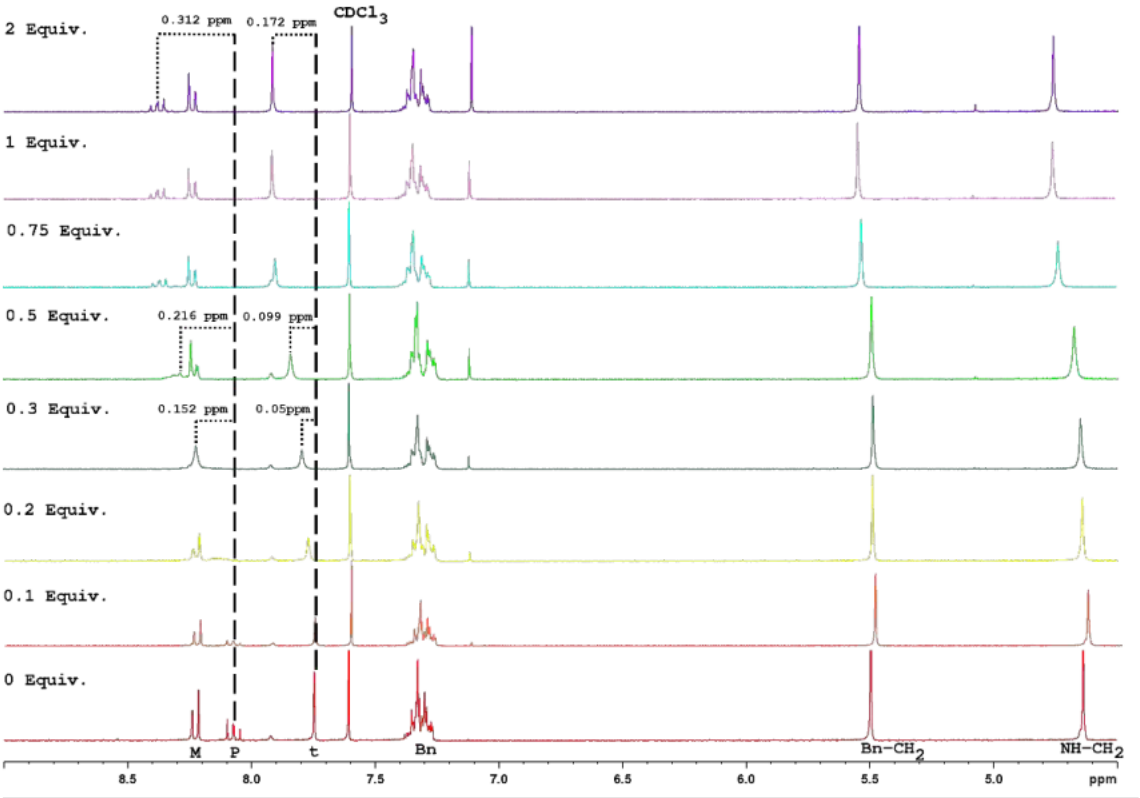

Figure. 3.32.. Overall. changes. in. the. ^{1}H. NMR. spectra. of. ***2*** *(CD$_3$CN:CD$_3$OD:CDCl$_3$ (9.99:0.005:0.005),. 0.001. M,. 300. MHz). upon. titrating with. La(CF$_3$SO$_3$)$_3$ (0.–.2. equivalents)..*

The downfield shift was seen to continue, and at 0.5 equivalents **P** can be seen to separate from **M**, and the two distinct peaks associated with the **M** signal swap position; at 0.75 equivalents the **P** peak reappears with sharp splitting. The downfield shifts continue until 1 equivalent is reached, where the addition of a second equivalent results in no change, further indication of the evolutionary formation of 1:3, 1:2 and 1:1 (M:L) species. Electron density withdrawal becomes more concentrated on the singular central pyridyl ring as the ligands associated with the La^{3+} decreases, thus upon an additional second equivalent, no shift occurs as the minimum association (1:1) is reached. Minor shifts in the alkyl chains and aromatics are observed but are insignificant, indicating they do not interact with La^{3+}. There is however a downfield shift observed in the 1,2,3-triazole ring (**t**): initially from 0 to 0.3 equivalents the changes are minor

with a small shift of 0.03 - 0.06 ppm; it is upon additional La^{3+} that this shift becomes more significant, doubling in size to approximately 0.10 ppm at 0.5 equivalents and again becoming much larger at 0.75 and 1 equivalent (≈ 0.13 - 0.23 ppm). There are two potential causes for this shift, either the 1,2,3-triazole ring CH proton was interacting with the triflate ion, as seen previously with a similar system to that of **2** with Cl^- , Br^- and I^-,[6] or potential coordination is occurring between the 1,2,3-triazole ring and the La^{3+}. At early stages this interaction is insignificant, but at larger equivalents of La^{3+} (0.5 - 1) the interaction becomes more prominent and causes larger shifts, suggesting that this interaction likely occurs more in the 1:2 and 1:1 species, potentially wrapping around the Ln^{3+}. It also worth noting that the shifts observed between different ligands are relatively similar for the **P** proton, suggestive of similar bonding, whereas the shifts of the **t** proton are large in **1** and get smaller with **2** and **3**, potentially due to the bulky aromatics of **2** and **3** hindering or weakening this secondary coordination.

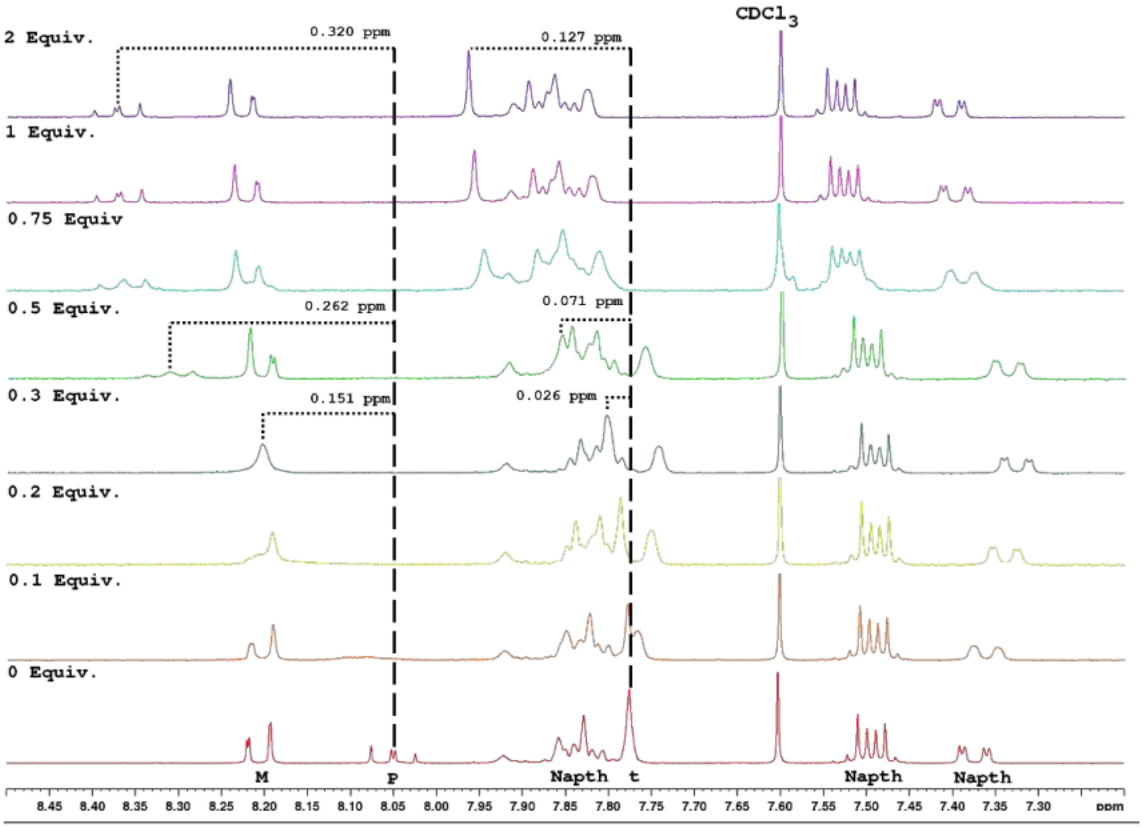

Figure 3.33.. Overall changes in the ^{1}H NMR spectra of ***3*** *(CD_3CN:CD_3OD:$CDCl_3$ (9.99:0.005:0.005), 0.001 M, 300 MHz) upon titrating with $La(CF_3SO_3)_3$ (0 – 2 equivalents), zoomed in to better see the 1,2,3-triazole position.*

From these titrations it becomes apparent that the La^{3+} are coordinating in the NO_2 binding pocket and further indicates a clear evolutionary process is taking place from 0 to 1 equivalent, which suggests the deformation and formation of 1:1, 1:2 and 1:3 (M:L) species.

3.2.6 Computational Studies

Attempts to obtain X-ray quality crystals of the lanthanide complexes were unsuccessful despite trying a range of different crystallising attempts (vapour diffusion, evaporation, pipette reactors, and MOF conditions). The limiting factor of these systems was the solvent in which they would remain soluble. MeOH:DCM mixtures and DMF and DMSO were the best solvents, however the latter two appeared to result in dissociation of the complexes (based on ^{1}H NMR studies).To gain insight into the coordination and structural characteristics of these complexes, ground state calculations were run on the La^{3+} systems $[La(\mathbf{1})_3]^{3+}$, $[La(\mathbf{2})_3]^{3+}$ and $[La(\mathbf{3})_3]^{3+}$. Lanthanum was chosen due to its diamagnetic electron configuration, and anions were excluded, making the calculations less computationally taxing. In later chapters other lanthanides are used as computational knowledge had improved. The starting geometry of the complexes are based on available crystallographic data[32] and the predicted coordination of PDC units *i.e.* three PDC ligands forming an N_3O_6 coordination around the La^{3+}, with a tricapped trigonal prismatic geometry. The substituents were attached in such a manner as to have an overall starting geometry close to C_3. The La^{3+} complexes were subjected to a DFT geometry optimisation using the PBEPBE[48, 49] functional with a mixed basis set of cc-pVDZ[50] for N, H, O, C and Def2SVPP[51] with corresponding effective core potential[52, 53] for La^{3+} as parameterised in the Gaussian 16 software suite.[9]

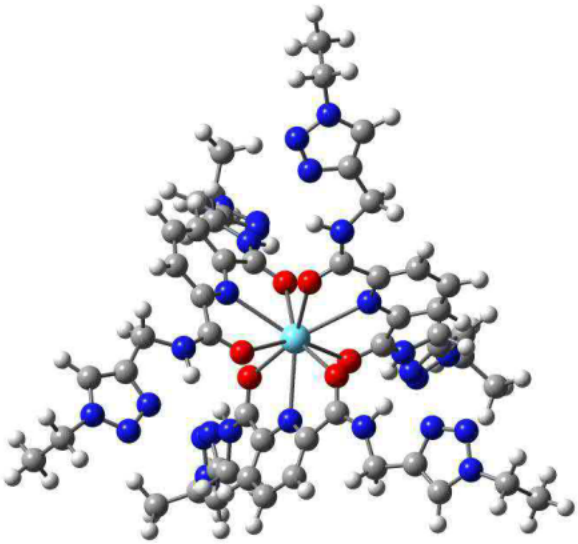

Figure 3.34.. Calculated structure of $[La(\mathbf{1})_3]^{3+}$..

Subsequent frequency calculations yielded all real frequencies as appropriate for a minimum energy structure. The complex models of $[La(\mathbf{1})_3]^{3+}$, $[La(\mathbf{2})_3]^{3+}$ and $[La(\mathbf{3})_3]^{3+}$ (Figures 3.34-35) appear to maintain the tricapped trigonal prismatic geometry and expected N_3O_6 coordination sphere with C_3 symmetry. To verify the calculated structures the bond lengths of La-N and La-O

have been compared to available crystallographic data [16] of a similar PDA system (**L**^{1}, see Figure 3.16) and showed good comparisons, with the largest difference between calculated and experimental bond lengths being 0.095 Å (Table 3.10). From calculations we were able to view a potential coordination structure of the complexes, further confirming that the ligands were not too bulky to form the 1:3 M:L species.

Table 3.10.. Bond lengths of calculated $[La(\mathbf{L})_3]^{3+}$ in comparison to X-ray crystallographic data of $La(\mathbf{L}^1)_3$..

Bond length	$[La(\mathbf{1})_3]^{3+}$	$[La(\mathbf{2})_3]^{3+}$	$[La(\mathbf{3})_3]^{3+}$	$[La(\mathbf{L}^1)_3]^{3+}$
La-N (Å)	2.774	2.773	2.772	2.679 (7), 2.731 (7) & 2.696 (7)
La-O (Å)	2.542	2.542	2.542	2.525 (5), 2.501 (5) & 2.501 (6)
La-O (Å)	2.544	2.544	2.543	2.470 (5), 2.496 (6) & 2.527 (6)

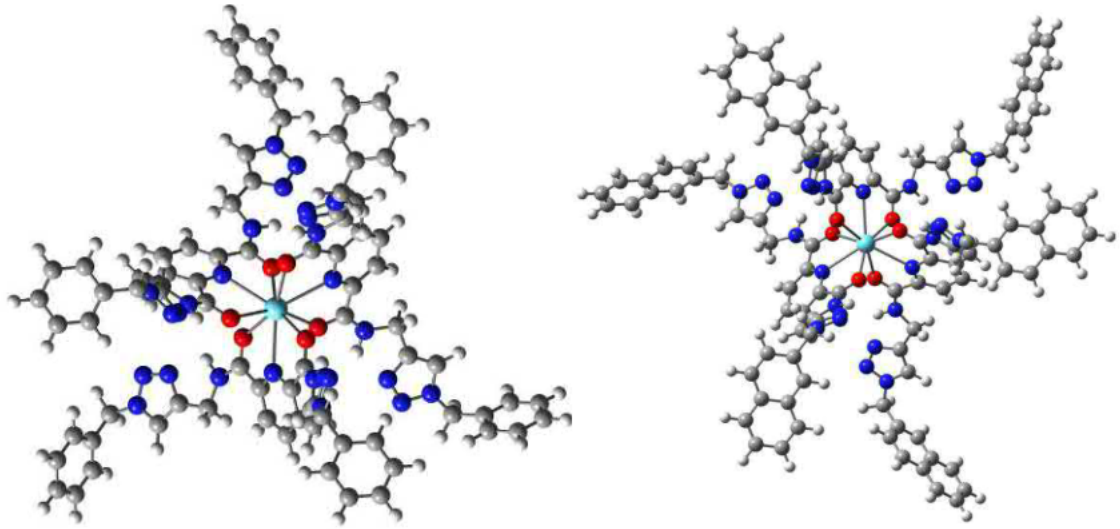

Figure 3.35.. Calculated structures of $[La(\mathbf{2})_3]^{3+}$ (Left) and $[La(\mathbf{3})_3]^{3+}$ (Right)..

3.3 Conclusion

The main objective of this study was to combine the versatility of "click" chemistry with the predictable coordination of the PDA scaffold with the intent to form a range of new and easily functionalised ligands for developing luminescent lanthanide systems. Herein it was demonstrated that these ligands are readily and reliably synthesised in a one-pot synthesis with high yields, and coordinate to lanthanide ions forming $[Ln(\mathbf{L})_3](CF_3SO_3)_3$ (where Ln = Eu^{3+}, Tb^{3+} and La^{3+}). The exception to this was ligand **4** which due to solubility issues was excluded from coordination studies. All complexes of Eu^{3+} and Tb^{3+} displayed sensitised emission within the range of previous PDA based antenna. In the unique case of ligand **3**, the inclusion of the naphthalene substituent allowed for the formation of a dual emissive system but is suspected to be the cause of the much lower quantum yields for both Tb^{3+} and Eu^{3+} centred emission. From solution based self-assembly investigations, HRMS, FTIR and ^{1}H NMR, it is apparent that all three ligands form the predicted 1:3 M:L species in a similar fashion to previous PDA based antenna. It is also clear that the coordination is occurring at the NO_2 tridentate binding pocket and an evolutionary process forming the 1:2 and 1:1 species upon addition of increasing amounts of lanthanide ion is occurring as previously seen. ^{1}H NMR suggested potential for the 1,2,3-triazole to interact in the 1:2 and 1:1 M:L species, not in the desired 1:3 M:L species.

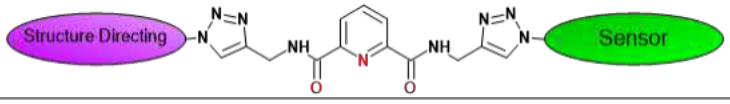

Figure 3.36.. PDC side arms,. where sensors or structure directing groups can be simply "clicked" onto the scaffold..

Through the thorough investigation of these 1,2,3-triazole incorporated PDA based systems, some issues were encountered. These included poor solubility, 1,2,3-triazole potential anion coordination and very mobile coordination. Because of this the decision was made to move to mono "clicked" PDC systems in the hope to improve Ln^{3+} stability. Even so, this study still demonstrated the ability of the synthetic strategy to develop new ligands for lanthanide assemblies, an area of significant interest for the preparation of new luminescent supramolecular materials. The inclusion of the 1,2,3-triazole "click" functionalisation strategy opens access to an incredibly large range of ligands with many different properties that can be simply introduced through the CuAAC methodologies. This should allow for straightforward ligand architecture predesign by simply changing the "clicked" substituents to include functional groups such as long chains, $\pi - \pi$ stacking aromatics, additional metal coordinating groups for multi-metallic assemblies (*e.g* MOF like structures), or other luminescent groups for a range of different applications. Future work of these bis-"clicked" systems would ideally focus on the formation of unsymmetrical bis-clicked ligand structures, such that one substituent focuses on material formation and the other on applications (Figure 3.36).

3.4 Experimental

3.4.1 General Experimental Details

All reagents, solvents and starting materials were purchased from Sigma-Aldrich. NMR spectra were recorded using a Bruker Ultrashield 300, with chemical shifts recorded in parts per million (ppm) downfield from the standard. Mass spectrometry of ligands was carried out in HPLC grade solvents, on a Shimadzu LCMS-2020 for ligands and a Shimadzu LCMS-9030 for complexes. IR spectra were recorded on a Bruker Alpha platinum-ATR. Melting points were obtained on an Electrothermal IA9000 Series Melting Point Apparatus. UV-visible spectra were recorded on a Shimadzu UV-1800 using MeCN, $CHCl_3$ and MeOH solvents in a 3 mL quartz cuvette with a 1 cm path length. Steady-state fluorescence measurements were recorded on a Shimadzu RF-6000 Spectrofluorophotometer with a ZJB380 UV filter, measured in MeCN, $CHCl_3$ and MeOH solvents in a capped 3.5 mL quartz cuvette with a 1 cm path length. Time-resolved phosphorescence measurements were carried out using an Agilent Technologies Cary Eclipse fluorescence spectrophotometer with internal UV filters. Single crystal X-ray diffraction data were collected at 100 K on either a Bruker D8 Venture equipped with an IμS DIAMOND microfocus with a Cu-Kα (λ = 1.54178) X-ray source, with a PHOTON III detector or a Rigaku AFC12 goniometer equipped with an enhanced sensitivity (HG) Saturn 724+ detector mounted at the window of an FR-E+ Superbright Mo–Kα rotating anode generator (λ = 0.71075 Å). HF unit cell parameters were refined against all data[54] and an empirical absorption correction applied in either CrystalClear[55] or APEX3. Structures were solved by direct methods using SHELXS-2013[56] and refined on Fo^2 by SHELXL-2013[56] using Olex2.[57] CSD entries: 2004994, 2042361 and 2042362. Gas Phase DFT geometry optimisation and frequency calculations were carried out using the B3LYP[38-41] functional with a cc-pVTZ[42, 43] basis set for ligand ground state and triplet state calculations, and with the PBEPBE[48, 49] functional with a mixed basis set of cc-pVDZ[50] for N, H, O, C and Def2SVPP[51] with corresponding effective core potential[52, 53] for La^{3+} for complex calculations as parameterised in the Gaussian 16 software suite.[9] Safety Note: low molecular weight organic azides are potential explosives, and care must be taken during their handling; however, no issues were encountered here.

3.4.2 Photophysical Measurements

Unless otherwise stated, all measurements were performed at r.t in MeCN (HPLC grade). The stock solutions of ligand or complex were prepared using 1:1 ratio of CH_2Cl_2 and MeOH (spectroscopic grade). UV–visable absorption spectra were measured in 1 cm quartz cuvettes. Phosphorescence lifetimes of the Eu^{3+} and Tb^{3+} excited states were measured in MeCN in time-resolved mode, by monitoring the emission decay at 616 and 543 nm; these were carried out in triplicate and averaged.

3.4.2.1 Photophysical Self-Assembly Titrations

The formation of 1:1, 1:2 and 1:3 (M:L) species was monitored by measuring changes in the UV-visible absorption and fluorescence spectra of a solution of **l**igand (2×10^{-5} M or 5×10^{-6} M for **3** UV-visible absorption, in 3 mL volume) in MeOH:DCM:MeCN (0.005:0.005:9.99) when titrated with $Ln(CF_3SO_3)_3 \cdot xH_2O$ solution in MeCN (1 mM, 0 → 4.5 equivalents, with 3 μL additions for 0 to 1 equivalents, 6 μL additions for 1 to 2 equivalents, and 30 μL additions for 2 to 4.5 equivalents). Data was then fitted with ReactLab™ Equilibrium[46] for non-linear regression analysis.

3.4.2.2 ^{1}H NMR Self-Assembly Titrations

The M:L species formation was monitored by measuring changes in the ^{1}H NMR of a solution of ligand (1×10^{-3} M, ≈ 2 mL) in MeOD:$CDCl_3$:CD_3CN (0.005:0.005:9.99) when titrated with $Ln(CF_3SO_3)_3 \cdot xH_2O$ solution in CD_3CN (10 mM, 0 → 2 equivalents) taking 250 scans for each ^{1}H NMR.

3.4.2.3 Quantum Yield Measurements

Quantum yields were measured by optically dilute method[58] using $Cs_3[Eu(DPA)_3]\cdot 8H_2O$ and $Cs_3[Tb(DPA)_3]\cdot 8H_2O$ complex in 0.1 M Tris buffer (pH = 7.45) as references with known quantum yields of $\Phi_r = 24 \pm 2.5$ % for Eu^{3+} complex and $\Phi_r = 22 \pm 2.5$ % for Tb^{3+} complex.[59, 60] Estimated overall quantum yields (Φ_{Ln}^{L}) were calculated according to the following equation 4. The abbreviations are E for integrated luminescence intensity; A for absorbance at the excitation wavelength; I for intensity of the excitation light at the same wavelength; n for refractive index of the solution and subscripts are r for reference and x for sample.

$$\Phi_{Ln}^{L} = \Phi_x = \frac{E_x}{E_r} \times \frac{A_r(\lambda_r)}{A_x(\lambda_x)} \times \frac{I_r(\lambda_r)}{I_x(\lambda_x)} \times \frac{\eta_x^2}{\eta_r^2} \times \Phi_r (4)$$

Radiative lifetime (τ_{rad}) of Eu^{3+} complexes was calculated by equation 5. The abbreviations are: $\frac{I_{MD}}{I_{tot}}$ is the ratio of area under the Eu($^5D_0 \rightarrow {}^7F_1$) to the integrated total emission (J=0-6), $A_{MD,0}$ is the spontaneous emission probability of the Eu($^5D_0 \rightarrow {}^7F_1$) transition (14.65 s^{-1}).[59]

$$\tau_{rad} = \frac{1}{A_{MD,0} n^3} \left(\frac{I_{MD}}{I_{tot}}\right) (5)$$

From this the intrinsic quantum yield (Φ_{Ln}^{Ln}) was estimated from the ratio of observed lifetime (τ_{obs}) to the estimated radiative lifetime (τ^{rad}) seen in equation 6, which in turn was used to find the sensitisation efficiency (n_{sens}) with equation 7.

$$\Phi_{Ln}^{Ln} = \frac{\tau_{obs}}{\tau^{rad}} (6)$$

$$n_{sens} = \frac{\Phi_{L}^{Ln}}{\Phi_{Ln}^{Ln}} (7)$$

$Cs_3[Eu(DPA)_3]\cdot 8H_2O$ and $Cs_3[Tb(DPA)_3]\cdot 8H_2O$ were synthesised following literature procedures and were confirmed by elemental analysis.[61]

Elemental analysis for $C_{21}H_9N_3O_{12}EuCs_3\cdot 8H_2O$ (1190.1162 $gmol^{-1}$) Calculated: C 21.19, H 2.12, N 3.53 %. Found C 21.19, H 2.13, N 3.72 %

Elemental analysis for $C_{21}H_9N_3O_{12}TbCs_3\cdot 8H_2O$ (1197.0792 $gmol^{-1}$) Calculated: C 21.07, H 2.10, N 3.51 %. Found C 21.00, H 2.00, N 3.65 %.

3.4.3 Ligand Synthesis

3.4.3.1 Synthesis of N_2,N_6 -di(prop-2-ynyl)pyridine-2,6-dicarboxamide (B)

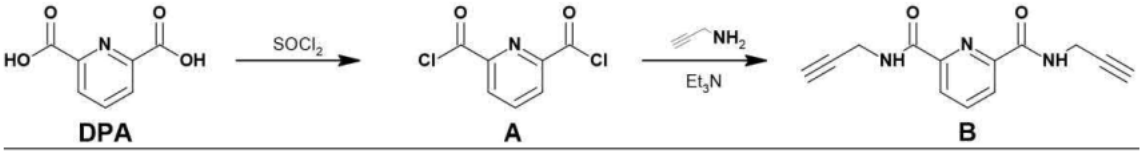

Scheme. 3.3.. Synthesis. of. intermediates. ***A*** *and* ***B****.*

DPA (1.25 g, 7.5 mmol, 1 equivalent) was dissolved in 20 mL of dry CH_2Cl_2 and was placed under nitrogen. Following this 1.2 mL of thionyl chloride (16.5 mmol, 2.2 equivalents) was added and the solution was then refluxed for 5 hours under nitrogen. The solution turned from clear to a yellow tinge during refluxing. The solution was cooled, and a stream of nitrogen was placed over the solution removing the excess thionyl chloride and CH_2Cl_2, yielding **A** as a light brown solid. This solid was dissolved in 10 mL of dried CH_2Cl_2 (giving a pale-yellow solution) and added dropwise to a cooled (bright green) solution of CH_2Cl_2 (10 mL) containing 0.96 mL of propargyl amine (0.015 mol, 2 equivalents) and 5.50 mL of NEt_3. This caused the pale green propargyl amine solution to develop a dark red colour. The solution was left to stir overnight and then 100 mL of 1 M HCl was added and stirred. This caused a white solid to precipitate which was then filtered and left to dry yielding intermediate **B** as a white solid (1.53 g, 85 %). Melting point = 188.5 °C. LRMS *m/z* = 241.95 [**B** + H]$^+$ (calc. for $C_{13}H_{12}N_3O_2^+$, 242.09) and *m/z* = 263.95 [**B** + Na]$^+$ (calc. for $C_{13}H_{11}N_3O_2Na^+$, 264.07). ^{1}H NMR (300 MHz, DMSO-d_6, ppm), δ = 9.74 (m, 2H, NH), 8.21 (m, 3H, py-H), 4.20 (d, J = 6.0 Hz, 2H, CH_2), 3.19 (m, CH); ^{13}C NMR (75 MHz, DMSO-d_6, ppm): δ = 162.9 (CO), 148.3 (C-py), 139.7 (CH-py), 124.7 (CH-py), 81.1 (C), 73.2 (CH), 28.1 (CH_2). FTIR (cm^{-1}) 3216, 2972, 2934, 2497, 2164, 2119, 1928, 1855, 1751, 1679, 1659, 1524, 1444, 1428, 1417, 1348, 1315, 1305, 1271, 1259, 1231, 1170, 1076, 1053, 1019, 999, 924, 826, 842, 800, 753, 726, 708, 676, 655, 680, 520, 427, 405.

3.4.3.2 General procedure for synthesis of N_2,N_6-bis((1-(R)-1H-1,2,3-triazol-4-yl)methyl)pyridine-2,6-dicarboxamide (1, 2, and 3)

B (1 equivalent) was combined with NaN_3 (2.4 equivalents), $CuSO_4{\cdot}5H_2O$ (0.4 equivalents), ascorbic acid (2 equivalents), Na_2CO_3 (6 equivalents) and the appropriate alkyl bromide (2 equivalents) in 30 mL of DMF:H_2O (4:1). The solution was stirred for 24 hours at r.t under an inert atmosphere of nitrogen gas before being mixed with 60 mL of (0.1 M) EDTA:NH_4OH and left to stand for 30 minutes to allow for precipitation. The precipitate was filtered and washed with 50 mL of H_2O and 50 mL of diethyl ether and left to air dry.[62]

3.4.3.3 Synthesis of N_2,N_6 -bis((1-(ethyl)-1H-1,2,3-triazol-4-yl)methyl)pyridine-2,6-dicarboxamide (1)

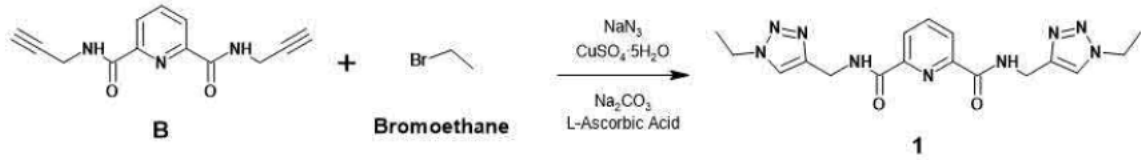

Scheme. 3.4.. Synthesis. of. ligand. ***1****.*

B (0.206 g, 0.85 mmol) was combined with NaN_3 (0.133 g, 2.04 mmol), $CuSO_4{\cdot}5H_2O$ (0.085 g, 0.34 mmol), ascorbic acid (0.300 g, 1.70 mmol), Na_2CO_3 (0.543 g, 5.10 mmol) and 0.127 mL of bromoethane (1.70 mmol) in 30 mL of DMF:H_2O (4:1). The yellow solution turned orange and over the course of 24 hours became brown with an orange precipitate. Upon addition to (0.1 M) EDTA:NH_4OH the solution turned light orange and over the course of 24 hours became cloudy with a fine precipitate. An orange solid was collected and after water and diethyl ether washes **1** was isolated as an off-white powder (0.289 g, 89 %). Melting point = 179.3 °C. LRMS *m/z* = 384.05 [**1** + H]$^+$ (calc. for $C_{17}H_{22}N_3O_2^+$, 384.19), *m/z* = 406.05 [**1** + Na]$^+$ (calc. for $C_{17}H_{21}N_9O_2Na^+$, 406.17) and *m/z* = 422.05 [**1** + K]$^+$ (calc. for $C_{17}H_{21}N_9O_2K^+$, 422.15). ^{1}H NMR (300 MHz, DMSO-d_6, ppm), δ = 9.91 (m, 2H, NH), 8.21 (m, 3H, py-H), 8.00 (s, 2H, t), 4.60 (d, J = 6.0 Hz, 4H, -CH_2-NH), 4.33 (q, J = 7.0 Hz, 4H, CH_2), 1.39 (t, J = 7.0 Hz, 6H, CH_3); ^{13}C NMR (75 MHz, DMSO-d_6, ppm): δ = 163.1 (CO), 148.5 (C-py), 144.8 (C-t), 139.5 (CH-py), 124.4 (CH-py), 122.4 (CH-t), 44.4 (**CH_2**-CH_3), 34.4(**CH_2**-NH), 15.4 (CH_3). FTIR (cm^{-1}) 3371, 3306, 3126, 3094, 2970, 2929, 2875, 1730, 1657, 1592, 1535, 1461, 1445, 1424, 1380, 1358, 1343, 1329, 1307, 1243, 1229, 1209, 1174, 1161, 1145, 1104, 1077, 1064, 1050, 1038, 1002, 965, 950, 868, 844, 824, 798, 773, 760, 707, 645, 561, 517, 426.

3.4.3.4 Synthesis of N_2,N_6 -bis((1-(benzyl)-1H-1,2,3-triazol-4-yl)methyl)pyridine-2,6-dicarboxamide (2)

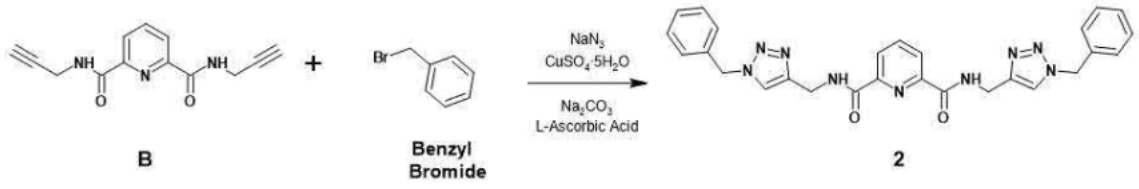

*Scheme.3.5.. Synthesis.of.ligand.**2.***

B (0.493 g, 2.04 mmol) was combined with NaN_3 (0.319 g, 4.9 mmol), $CuSO_4{\cdot}5H_2O$ (0.204 g, 0.817 mmol), ascorbic acid (0.720 g, 4.09 mmol), Na_2CO_3 (1.299 g, 12.26 mmol) and 0.486 mL of benzyl bromide (4.09 mmol) in 30 mL of DMF:H_2O (4:1). The solution turned from cloudy white to yellow and finally to a light green over the course of 24 hours. Upon addition to (0.1 M) EDTA:NH_4OH solution an orange solid precipitate formed and after water and diethyl ether washes **2** was isolated as an off-white powder (0.986 g, 95 %). Melting point = 211.6 °C. LRMS *m/z* = 508.15 [2 + H]$^+$ (calc. for $C_{27}H_{26}N_9O_2^+$, 508.22), *m/z* = 530.15 [2 + Na]$^+$ (calc. for $C_{27}H_{25}N_9O_2Na^+$, 530.20) and *m/z* = 546.15 [2 + K]$^+$ (calc. for $C_{27}H_{25}N_9O_2K^+$, 546.18). ^{1}H NMR (300 MHz, DMSO-d_6, ppm), δ = 9.89 (m, 2H, NH), 8.21 (m 3H, py-H), 8.05 (s, 2H, t), 7.33 (m, 10H, Bn-H), 5.54 (s, 4H, CH_2), 4.60 (d, J = 6.0 Hz, 4H, -**CH_2**-NH); ^{13}C NMR (75 MHz, DMSO-d_6, ppm): δ = 163.2 (CO), 148.5 (C -py), 145.2 (C-t), 139.6 (CH-py), 136.1 (C-Bn), 128.7 (CH-Bn), 128.1 (CH-Bn), 128.0 (CH-Bn), 124.5 (CH-py), 123.1 (CH -t), 52.7(CH_2-Bn), 34.5 (**CH_2**-NH). FTIR (cm^{-1}) 3341, 3300, 3146, 3053, 2931, 1670, 1532 1493, 1434, 1423, 1425, 1332, 1330, 1242, 1211, 1215, 1121, 1058, 1026, 1022, 846, 762, 713, 642, 611, 516.

3.4.3.5 N_2,N_6-bis((1-(2-naphthalenemethyl)-1H-1,2,3-triazol-4-yl)methyl)pyridine-2,6-dicarboxamide (3)

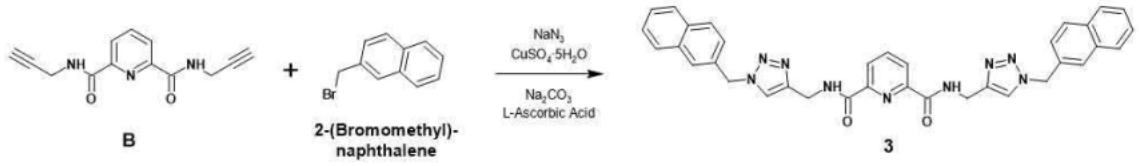

*Scheme.3.6.. Synthesis.of.ligand.**3.***

B (0.198 g, 0.82 mmol) was combined with NaN_3 (0.123 g, 1.97 mmol), $CuSO_4{\cdot}5H_2O$ (0.082 g, 0.33 mmol), ascorbic acid (0.289 g, 1.64 mmol), Na_2CO_3 (0.522 g, 4.92 mmol) and 2-(bromomethyl)naphthalene (0.363 g, 1.64 mmol) in 30 mL of DMF:H_2O (4:1). The clear solution turned yellow and over the course of 24 hours a white precipitate formed. Upon addition to (0.1 M) EDTA:NH_4OH the solution became cloudy and a fine white precipitate formed. A white solid was collected and after water and diethyl ether washes **3** was isolated as an off-white powder (0.411 g, 83 %). Melting point = 132.8 °C. LRMS *m/z* = 630.15 [**3** + Na]$^+$ (calc. for $C_{27}H_{25}N_9O_2Na^+$, 630.23) and *m/z* = 646.20 [**3** + K]$^+$ (calc. for $C_{27}H_{25}N_9O_2K^+$, 646.21). ^{1}H NMR (300 MHz, DMSO-d_6, ppm), δ= 9.87 (m, 2H, NH), 8.18 (m, 3H, py-H), 8.10 (s, 2H, t), 7.88 (m, 8H, Nap), 7.52 (m, 4H, Nap), 7.41 (d, J = 8.5, 1.5 Hz, 2H, Nap), 5.71 (s, 2H, CH_3), 4.59 (d, J = 6.0 Hz, 2H, -CH_2-NH); ^{13}C NMR (75 MHz, DMSO-d_6, ppm): δ = 163.1 (CO), 148.5 (C-py), 145.2 (C-t), 139.5 (CH-py), 133.6 (C-Nap), 132.7 (C-Nap), 132.4 (C-Nap), 128.4(CH-Nap), 127.8 (CH-Nap), 127.6 (CH-Nap), 127.0 (CH-Nap), 126.5 (CH-Nap), 126.4 (CH-Nap), 125.8 (CH-Nap), 124.4 (CH-py), 123.2 (CH-t), 52.9 (**CH_2**-Nap), 34.4 (**CH_2**-NH). FTIR (cm^{-1}) 3625, 3461, 3373, 3269, 3155, 3128, 3078, 3055, 2954, 2337, 2318, 1932, 1669, 1629, 1601, 1536, 1462, 1444, 1428, 1373, 13304, 1253, 1242, 1213, 1176, 1143, 1126, 11076, 1054, 1019, 1000, 982, 947, 900, 888, 838, 829, 812, 787, 766, 746, 731, 701, 677, 646, 639, 568, 543, 532, 518, 511, 471, 425, 412.

3.4.3.6 N_2,N_6-bis((1-(4-pyridylmethyl)-1H-1,2,3-triazol-4-yl)methyl)pyridine-2,6-dicarboxamide (4)

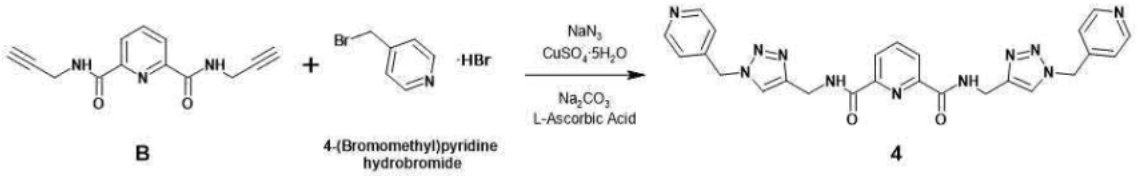

*Scheme.3.7.. Synthesis.of.ligand.***4.**

B (0.500 g, 2.07 mmol) was combined with NaN_3 (0.323 g, 4.97 mmol), $CuSO_4 \cdot 5H_2O$ (0.207 g , 0.83 mmol), ascorbic acid (0.730 g, 4.14 mmol,), Na_2CO_3 (1.318 g, 12.4 mmol) and 4-(bromomethyl)pyridine hydrobromide (1.048 g, 4.14 mmol) in 30 mL of DMF:H_2O (4:1). The red solution slowly turned brown over the course of 24 hours. Upon addition to 0.1 M EDTA:NH_4OH a brown precipitate formed; this was filtered and washed with water and diethyl ether yielding **4** as a white solid (0.935 g, 89 %). Melting point 255.4 °C. LRMS *m/z* = 510.1 [**4** + H]$^+$ (calc. for $C_{35}H_{30}N_9O_2^+$, 510.2), *m/z* = 532.1 [**4** + Na]$^+$ (calc. for $C_{35}H_{29}N_9O_2\,Na^+$, 532.2) and *m/z* = 548.1 (calc. for $C_{35}H_{29}N_9O_2K^+$, 548.2). ^{1}H NMR (300 MHz, DMSO-d_6, ppm), δ = 9.91 (m, 2H, NH), 8.53 (d, J = 6.0 Hz, 4H, 4py-H), 8.18 (m, 3H, py-H), 8.12 (s, 2H, t), 7.19 (d, J = 6.0 Hz, 4H, 4py-H), 5.63 (s, 2H, **CH$_2$**-4py), 4.62 (d, J = 6.0 Hz, 2H, **CH$_2$**-NH); ^{13}C NMR (75 MHz, DMSO-d_6, ppm): δ =163.3 (CO), 150.1 (CH-py), 148.5 (C-py), 145.4 (C-4py), 145.0 (C-t), 139.7 (CH-py), 124.6 (CH-py), 123.8 (CH-t), 122.5 (CH-4py), 51.5 (**CH$_2$**-4py), 34.5 (**CH$_2$**-NH). FTIR (cm^{-1}) 3392, 3235, 3131, 3035, 2955, 1658, 1656, 1601, 1597, 1515, 1413, 1368, 1364, 1211, 1117, 1073, 1046, 1042, 989, 824, 771, 724, 656, 577.

3.4.4 Lanthanide Complexation

3.4.4.1 General Procedure for Complexation of Ligands 1, 2, and 3 with Ln^{3+}

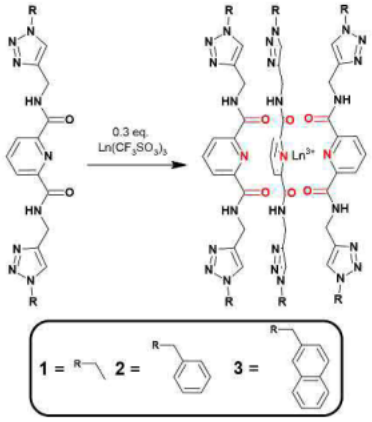

Scheme 3.8.. Complexation of ligands ***1***, ***2***, *and* ***3***..

40 - 50 mg of selected ligand was combined with selected $Ln(CF_3SO_3)_3 \cdot xH_2O$ (Ln = La^{3+}, Eu^{3+}, and Tb^{3+}, 0.3 equivalent) in 10 mL of MeOH or MeOH:CH_2Cl_2 (1:1). The solution was sonicated until the solids were dissolved. The solution was irradiated with microwaves for 30 minutes, cooled and subjected to vapour diffusion of diethyl ether, until a solid formed. The solution was then decanted and the solid was left to dry under vacuum.

3.4.4.2 $[Eu(1)_3](CF_3SO_3)_3$

1 (0.042 g, 0.11 mmol) was combined with $Eu(CF_3SO_3)_3 \cdot 6H_2O$ (0.023 g, 0.03 mmol) in 10 mL of MeOH. This complex formed a colourless film around the vial after vapour diffusion of diethyl ether affording $[Eu(\mathbf{1})_3](CF_3SO_3)_3$ as a white solid after drying (red emissive under short wave UV light) (0.047 g, 73 %). HRMS *m/z* = 1600.3621 $[Eu(\mathbf{1})_3](CF_3SO_3)_2^+$ (calc. for $(C_{53}H_{63}N_{27}O_{12}S_2F_6Eu)^+$, 1600.3705), *m/z* = 725.7048 $[Eu(\mathbf{1})_3](CF_3SO_3)^{2+}$ (calc. for $(C_{52}H_{63}N_{27}O_9SF_3Eu)^{2+}$, 725.7090) and *m/z* = 434.1526 $[Eu(\mathbf{1})_3]^{3+}$ (calc. for $(C_{51}H_{63}N_{27}O_6Eu)^{3+}$, 434.1552). FTIR ($cm^{-1}$) 3458, 3371, 3271, 3128, 1639, 1601, 1535, 1511, 1460, 1428, 1380, 1225, 1169, 1127, 1076, 1053, 1511, 1460, 1428, 1380, 1225, 1169, 1127, 1075, 1053, 1028, 981, 967, 901, 838, 815, 787, 751, 731, 678, 635, 573, 515, 472, 413.

3.4.4.3 $[Tb(1)_3](CF_3SO_3)_3$

1 (0.041 g, 0.11 mmol) was combined with $Tb(CF_3SO_3)_3 \cdot 5H_2O$ (0.023 g, 0.03 mmol) in 10 mL of MeOH. This complex formed a colourless film around the vial after vapour diffusion of diethyl ether affording $[Tb(\mathbf{1})_3](CF_3SO_3)_3$ as a white solid (green emissive under short wave UV light) (0.053 g, 85 %). HRMS *m/z* = 1606.3745 $[Tb(\mathbf{1})_3](CF_3SO_3)_2^+$ (calc. for $(C_{53}H_{63}N_{27}O_{12}S_2F_6Tb)^+$, 1606.3743), *m/z* = 728.7109 $[Tb(\mathbf{1})_3](CF_3SO_3)^{2+}$ (calc. for $(C_{52}H_{63}N_{27}O_9SF_3Tb)^{2+}$, 728.7109) and *m/z* = 436.1565 $[Tb(\mathbf{1})_3]^{3+}$ (calc. for $(C_{51}H_{63}N_{27}O_6Tb)^{3+}$, 436.1564). FTIR ($cm^{-1}$) 3271, 3143, 3093, 2988, 1634, 1598, 1563, 1461, 1447, 1433, 1384, 1345, 1279, 1239, 1222, 1158, 1060, 1027, 969, 873, 842, 814, 758, 729, 709, 658, 634, 573, 515, 414.

3.4.4.4 $[La(1)_3](CF_3SO_3)_3$

1 (0.047 g, 0.12 mmol) was combined with $La(CF_3SO_3)_3 \cdot 9H_2O$ (0.028 g, 0.04 mmol) in 10 mL of MeOH. This complex formed a colourless film around the vial after vapour diffusion of diethyl ether affording $[La(\mathbf{1})_3](CF_3SO_3)_3$ as a white solid once dried (0.059 g, 82 %). HRMS *m/z* = 1586.3327 $[La(\mathbf{1})_3](CF_3SO_3)_2^+$ (calc. for $(C_{53}H_{63}N_{27}O_{12}S_2F_6La)^+$, 1586.3553) and *m/z* = 718.6913 $[La(\mathbf{1})_3](CF_3SO_3)^{2+}$ (calc. for $(C_{52}H_{63}N_{27}O_9SF_3La)^{2+}$, 718.7014). FTIR ($cm^{-1}$) 3292, 3140, 2990, 2921, 2851, 2132, 2031, 2020, 1955, 1637, 1595, 1544, 1448, 1386, 1278, 1238, 1221, 1160, 1063, 1027, 1002, 969, 842, 774, 758, 671, 634, 572, 515, 429.

3.4.4.5 $[Eu(2)_3](CF_3SO_3)_3$

2 (0.043 g, 0.01 mmol) was combined with $Eu(CF_3SO_3)_3{\cdot}6H_2O$ (0.018 g, 0.03 mmol) in 10 mL of MeOH:CH_2Cl_2 (1:1). This complex formed a colourless film around the vial after vapour diffusion of diethyl ether affording $[Eu(\mathbf{2})_3](CF_3SO_3)_3$ as a white solid once dried (red emissive under short wave UV light), (0.024 g, 40 %). HRMS *m/z* = 1972.4652 $[Eu(\mathbf{2})_3](CF_3SO_3)_2^+$ (calc. for $(C_{83}H_{75}N_{27}O_{12}S_2F_6Eu)^+$, 1972.4651), *m/z* = 911.7564 $[Eu(\mathbf{2})_3](CF_3SO_3)^{2+}$ (calc. for $(C_{82}H_{75}N_{27}O_9SF_3Eu)^{2+}$, 911.7563) and *m/z* = 558.1869 $[Eu(\mathbf{2})_3]^{3+}$ (calc. for $(C_{81}H_{75}N_{27}O_6Eu)^{3+}$, 558.1867). FTIR ($cm^{-1}$) 3553, 3341, 1638, 1544, 1521, 1456, 1340, 1279, 1223, 1162, 1117, 1028, 1011, 842, 758, 720, 634, 618, 622, 520, 461.

3.4.4.6 $[Tb(2)_3](CF_3SO_3)_3$

2 (0.046 g, 0.09 mmol) was combined with $Tb(CF_3SO_3)_3{\cdot}5H_2O$ (0.019 g, 0.03 mmol) in 10 mL of MeOH:CH_2Cl_2 (1:1). This complex formed a colourless film around the vial after vapour diffusion of diethyl ether affording $[Tb(\mathbf{2})_3](CF_3SO_3)_3$ as a white solid once dried (green emissive when irradiated with short wave UV light) (0.037 g, 58 %). HRMS *m/z* = 1978.4705 $[Tb(\mathbf{2})_3](CF_3SO_3)_2^+$ (calc. for $(C_{83}H_{75}N_{27}O_{12}S_2F_6Tb)^+$, 1978.4688), *m/z* = 915.7536 $[Tb(\mathbf{2})_3](CF_3SO_3)^{2+}$ (calc. for $(C_{82}H_{75}N_{27}O_9SF_3Tb)^{2+}$, 915.7578) and *m/z* = 560.1851 $[Tb(\mathbf{2})_3]^{3+}$ (calc. for $(C_{81}H_{75}N_{27}O_6Tb)^{3+}$, 560.1877). FTIR ($cm^{-1}$) 3374, 3294, 3129, 2964, 1638, 1536, 1456, 1432, 1281, 1226, 1211, 1028, 840, 797, 762, 724, 634, 614, 516, 505, 416.

3.4.4.7 $[La(2)_3](CF_3SO_3)_3$

2 (0.045 g, 0.09 mmol) was combined with $La(CF_3SO_3)_3{\cdot}9H_2O$ (0.020 g, 0.03 mmol) in 10 mL of MeOH:CH_2Cl_2 (1:1). This complex formed a colourless film around the vial after vapour diffusion of diethyl ether affording $[La(\mathbf{2})_3](CF_3SO_3)_3$ as a white solid once dried (0.053 g, 85 %). HRMS *m/z* = 1958.4223 $[La(\mathbf{2})_3](CF_3SO_3)_2^+$ (calc. for $(C_{83}H_{75}N_{27}O_{12}S_2F_6La)^+$, 1958.4492 and *m/z* = 904.7362 [La(**2**)3]$(CF_3SO_3)^{2+}$ (calc. for $(C_{82}H_{75}N_{27}O_9SF_3La)^{2+}$, 904.7483). FTIR ($cm^{-1}$) 3308, 2923, 2851, 1638, 1546, 1456, 1450, 1423, 1279, 1223, 1215, 1028, 842, 760, 724, 634, 616, 516, 501.

3.4.4.8 $[Eu(3)_3](CF_3SO_3)_3$

3 (0.051 g, 0.11 mmol) was combined with $Eu(CF_3SO_3)_3{\cdot}6H_2O$ (0.018 g, 0.033 mmol) in 10 mL of MeOH:CH_2Cl_2 (1:1). This complex formed a colourless film around the vial after vapour diffusion of diethyl ether affording $[Eu(\mathbf{3})_3](CF_3SO_3)_3$ as a white solid once dried (0.056 g, 82 %). HRMS *m/z* = 2273.5604 $[Eu(\mathbf{3})_3](CF_3SO_3)_2^+$ (calc. for $(C_{107}H_{87}N_{27}O_{12}S_2F_6Eu)^+$, 2273.5614), *m/z* = 1062.3053 $[Eu(\mathbf{3})_3](CF_3SO_3)^{2+}$ (calc. for $(C_{106}H_{87}N_{27}O_9SF_3Eu)^{2+}$, 1062.3045) and *m/z* = 658.5528 $[Eu(\mathbf{3})_3]^{3+}$ (calc. for $(C_{105}H_{87}N_{27}O_6Eu)^{3+}$, 658.5522). FTIR ($cm^{-1}$) 3458, 3371, 3271, 3128, 2100, 1639, 1601, 1535, 1511, 1460, 1428, 1380, 1225, 1169, 1127, 1075, 1053, 1028, 981, 967, 901, 838, 815, 787, 751, 731, 678, 573, 515, 472, 413.

3.4.4.9 $[Tb(3)_3](CF_3SO_3)_3$

3 (0.050 g, 0.08 mmol) was combined with $Tb(CF_3SO_3)_3{\cdot}5H_2O$ (0.017 g, 0.02 mmol) in 10 mL of MeOH:CH_2Cl_2 (1:1). This complex formed a colourless film around the vial after vapour diffusion of diethyl ether affording $[Tb(\mathbf{3})_3](CF_3SO_3)_3$ as a white solid once dried (0.061 g, 91 %). HRMS *m/z* = 2279.5354 $[Tb(\mathbf{3})_3](CF_3SO_3)_2^+$ (calc. for $(C_{107}H_{87}N_{27}O_{12}S_2F_6Tb)^+$, 2279.5655), *m/z* = 1065.2920 $[Tb(\mathbf{3})_3](CF_3SO_3)^{2+}$ (calc. for $(C_{106}H_{87}N_{27}O_9SF_3Tb)^{2+}$, 1065.3062) and *m/z* = 660.5445 $[Tb(\mathbf{3})_3]^{3+}$ (calc. for $(C_{105}H_{87}N_{27}O_6Tb)^{3+}$, 660.5533). FTIR ($cm^{-1}$) 3271, 3086, 2342, 2330, 1934, 1635, 1600, 1556, 1512, 1460, 1431, 1371, 1336, 1280, 1235, 1223, 1161, 1055, 1028, 967, 900, 860, 841, 817, 785, 754, 635, 573, 516, 473, 415.

3.4.4.10 $[La(3)_3](CF_3SO_3)_3$

3 (0.040 g, 0.66 mmol) was combined with $La(CF_3SO_3)_3{\cdot}9H_2O$ (0.016 g, 0.02 mmol) in 10 mL of MeOH:CH_2Cl_2 (1:1). This complex formed a colourless film around the vial after vapour diffusion of diethyl ether affording $[La(\mathbf{3})_3](CF_3SO_3)_3$ as a white solid once dried (0.042 g, 79 %). HRMS *m/z* = 2259.5155 $[La(\mathbf{3})_3](CF_3SO_3)_2^+$ (calc. for $(C_{107}H_{87}N_{27}O_{12}S_2F_6La)^+$, 2259.5465), *m/z* = 1055.2858 $[La(\mathbf{3})_3](CF_3SO_3)^{2+}$ (calc. for $(C_{106}H_{87}N_{27}O_9SF_3La)^{2+}$, 1055.2967) and *m/z* = 653.8715 $[La(\mathbf{3})_3]^{3+}$ (calc. for $(C_{105}H_{87}N_{27}O_6La)^{3+}$, 653.8803). FTIR ($cm^{-1}$) 3742, 3271, 3096, 2881, 2802, 2301, 2134, 1991, 1920, 1633, 1601, 1547, 1511, 1448, 1433, 1373, 1336, 1279, 1223, 1161, 1064, 1027, 966, 901, 861, 841, 816, 786, 687, 635, 573, 515, 473, 427, 406.

3.5 Acknowledgements

I would like to thank Ian Stewart from Otago University for collecting HRMS of the lanthanide complexes; Ningjin Zhang from Southampton University for collecting crystal structure data of **1**; Dr Jack Chen from Auckland University of Technology for allowing me access to the Agilent Technologies Cary Eclipse spectrophotometer and Professor Stephen Goldup from Southampton University, for allowing me to work in his laboratory and access to Agilent Technologies Cary Eclipse spectrophotometer.

3.6 References

1. T. Ziegler and C. Hermann, *Tetrahedron Lett.*, 2008, **49**, 2166-2169.
2. A. Chauhan, S. Paladhi, M. Debnath, S. Mandal, R. N. Das, S. Bhowmik and J. Dash, *Bioorg. Med. Chem.*, 2014, **22**, 4422-4429.
3. K. Lal, C. P. Kaushik, K. Kumar, A. Kumar, A. K. Qazi, A. Hamid and S. Jaglan, *Med. Chem. Res.*, 2014, **23**, 4761-4770.
4. K. Lal, C. P. Kaushik and A. Kumar, *Med. Chem. Res.*, 2015, **24**, 3258-3271.
5. L. Faour, C. Adam, C. Gautier, S. Goeb, M. Allain, E. Levillain, D. Canevet and M. Sallé, *Chem. Commun.*, 2019, **55**, 5743-5746.
6. S.-L. Yim, H.-F. Chow and M.-C. Chan, *Chem. Commun.*, 2014, **50**, 3064-3066.
7. C. Adam, L. Faour, V. Bonnin, T. Breton, E. Levillain, M. Sallé, C. Gautier and D. Canevet, *Chem. Commun.*, 2019, **55**, 8426-8429.
8. T. Le Borgne, J.-M. Bénech, S. Floquet, G. Bernardinelli, C. Aliprandini, P. Bettens and C. Piguet, *Dalton Trans.*, 2003, 3856-3868.
9. *Gaussian 16, Revision C.01,* Frisch, M. J.; Trucks, G. W.; Schlegel, H. B.; Scuseria, G. E.; Robb, M. A.; Cheeseman, J. R.; Scalmani, G.; Barone, V.; Petersson, G. A.; Nakatsuji, H.; Li, X.; Caricato, M.; Marenich, A. V.; Bloino, J.; Janesko, B. G.; Gomperts, R.; Mennucci, B.; Hratchian, H. P.; Ortiz, J. V.; Izmaylov, A. F.; Sonnenberg, J. L.; Williams-Young, D.; Ding, F.; Lipparini, F.; Egidi, F.; Goings, J.; Peng, B.; Petrone, A.; Henderson, T.; Ranasinghe, D.; Zakrzewski, V. G.; Gao, J.; Rega, N.; Zheng, G.; Liang, W.; Hada, M.; Ehara, M.; Toyota, K.; Fukuda, R.; Hasegawa, J.; Ishida, M.; Nakajima, T.; Honda, Y.; Kitao, O.; Nakai, H.; Vreven, T.; Throssell, K.; Montgomery, J. A., Jr.; Peralta, J. E.; Ogliaro, F.; Bearpark, M. J.; Heyd, J. J.; Brothers, E. N.; Kudin, K. N.; Staroverov, V. N.; Keith, T. A.; Kobayashi, R.; Normand, J.; Raghavachari, K.; Rendell, A. P.; Burant, J. C.; Iyengar, S. S.; Tomasi, J.; Cossi, M.; Millam, J. M.; Klene, M.; Adamo, C.; Cammi, R.; Ochterski, J. W.; Martin, R. L.; Morokuma, K.; Farkas, O.; Foresman, J. B.; Fox, D. J. *Gaussian, Inc., Wallingford CT, 2016.*
10. J. J. Dannenberg, *J. Am. Chem. Soc.*, 1998, **120**, 5604-5604.
11. M. Shibata, Y. Sakai and D. Yokoyama, *J. Mater. Chem. C*, 2015, **3**, 11178-11191.
12. J. A. Kitchen, *Coord. Chem. Rev.*, 2017, **340**, 232-246.
13. N. T. Kalyani, H. Swart and S. J. Dhoble, in *Principles and Applications of Organic Light Emitting Diodes (OLEDs)*, eds. N. T. Kalyani, H. Swart and S. J. Dhoble, Woodhead Publishing, 2017, pp. 1-37.
14. K. Binnemans, *Coord. Chem. Rev.*, 2015, **295**, 1-45.
15. C. Lincheneau, B. Jean-Denis and T. Gunnlaugsson, *Chem. Commun.*, 2014, **50**, 2857-2860.

16. F. Renaud, C. Piguet, G. Bernardinelli, J.-C. G. Bünzli and G. Hopfgartner, *Chem. Eur. J.*, 1997, **3**, 1646-1659.
17. G. Muller, B. Schmidt, J. Jiricek, G. Hopfgartner, J. P. Riehl, J.-C. G. Bünzli and C. Piguet, *J. Chem. Soc., Dalton Trans.*, 2001, 2655-2662.
18. R. Jagannathan and S. Soundararajan, *J. Coord. Chem.*, 1979, **9**, 31-35.
19. E. Borello, A. Zecchina and E. Guglielminotti, *J. Chem. Soc. B*, 1966, 1243-1245.
20. E. Borello and A. Zecchina, *Spectrochim. Acta*, 1963, **19**, 1703-1715.
21. F. Billes, H. Endrédi and G. Keresztury, *J. Mol. Strucut. THEOCHEM*, 2000, **530**, 183-200.
22. O. Kotova, S. Blasco, B. Twamley, J. O'Brien, R. D. Peacock, J. A. Kitchen, M. Martínez-Calvo and T. Gunnlaugsson, *Chem. Sci.*, 2015, **6**, 457-471.
23. K. T. Hua, J. Xu, E. E. Quiroz, S. Lopez, A. J. Ingram, V. A. Johnson, A. R. Tisch, A. de Bettencourt-Dias, D. A. Straus and G. Muller, *Inorg. Chem.*, 2012, **51**, 647-660.
24. D. E. Barry, J. A. Kitchen, M. Albrecht, S. Faulkner and T. Gunnlaugsson, *Langmuir*, 2013, **29**, 11506-11515.
25. D. E. Barry, J. A. Kitchen, L. Mercs, R. D. Peacock, M. Albrecht and T. Gunnlaugsson, *Dalton Trans.*, 2019, **48**, 11317-11325.
26. E. S. Da Silva, P. Wong-Wah-Chung, M. Sarakha and H. D. Burrows, *J. Photochem. Photobiol. A*, 2013, **265**, 29-40.
27. F. Renaud, C. Piguet, G. Bernardinelli, J.-C. G. Bünzli and G. Hopfgartner, *J. Am. Chem. Soc.*, 1999, **121**, 9326-9342.
28. A.-S. Chauvin, J.-C. G. Bünzli, F. Bochud, R. Scopelliti and P. Froidevaux, *Chem. Eur. J.*, 2006, **12**, 6852-6864.
29. G. A. King, T. A. A. Oliver, M. G. D. Nix and M. N. R. Ashfold, *Chem. Phys.*, 2010, **132**, 064305.
30. C.-T. Yeung, W. T. K. Chan, S.-C. Yan, K.-L. Yu, K.-H. Yim, W.-T. Wong and G.-L. Law, *Chem. Commun.*, 2015, **51**, 592-595.
31. A. de Bettencourt-Dias, in *Luminescence of Lanthanide Ions in Coordination Compounds and Nanomaterials*, ed. A. d. Bettencourt-Dias, 2014, pp. 1-48.
32. J. P. Leonard, P. Jensen, T. McCabe, J. E. O'Brien, R. D. Peacock, P. E. Kruger and T. Gunnlaugsson, *J. Am. Chem. Soc.*, 2007, **129**, 10986-10987.
33. O. Kotova, J. A. Kitchen, C. Lincheneau, R. D. Peacock and T. Gunnlaugsson, *Chem. Eur. J.*, 2013, **19**, 16181-16186.
34. A. Galanti, O. Kotova, S. Blasco, C. J. Johnson, R. D. Peacock, S. Mills, J. J. Boland, M. Albrecht and T. Gunnlaugsson, *Chem. Eur. J.*, 2016, **22**, 9709-9723.
35. M. Martínez-Calvo, O. Kotova, M. E. Möbius, A. P. Bell, T. McCabe, J. J. Boland and T. Gunnlaugsson, *J. Am. Chem. Soc.*, 2015, **137**, 1983-1992.
36. R. A. Tigaa, G. J. Lucas and A. de Bettencourt-Dias, *Inorg. Chem.*, 2017, **56**, 3260-3268.
37. Y. Hasegawa, Y. Kitagawa and T. Nakanishi, *NPG Asia Mater.*, 2018, **10**, 52-70.
38. P. J. Stephens, F. J. Devlin, C. F. Chabalowski and M. J. Frisch, *Phys. Chem.*, 1994, **98**, 11623-11627.
39. A. D. Becke, *Chem. Phys.*, 1993, **98**, 5648-5652.
40. C. Lee, W. Yang and R. G. Parr, *Phys. Rev. B Condens. Matter*, 1988, **37**, 785-789.
41. R. Krishnan, J. S. Binkley, R. Seeger and J. A. Pople, *Chem. Phys.*, 1980, **72**, 650-654.
42. R. A. Kendall, T. H. D. Jr. and R. J. Harrison, *Chem. Phys.*, 1992, **96**, 6796-6806.
43. E. R. Davidson, *Chem. Phys. Lett.*, 1996, **260**, 514-518.
44. A. Galanti, O. Kotova, S. Blasco, C. J. Johnson, R. D. Peacock, S. Mills, J. J. Boland, M. Albrecht and T. Gunnlaugsson, *Chem. Eur. J*, 2016, **22**, 9709-9723.
45. J. A. Kitchen, D. E. Barry, L. Mercs, M. Albrecht, R. D. Peacock and T. Gunnlaugsson, *Angew. Chem. Int. Ed.*, 2012, **51**, 704-708.
46. *ReactLabTM EQUILIBRIA (1.1), Jplus Consulting Multivariate Analytical Technologies, Kilaben Bay, Australia, 2022*.
47. R. Díaz-Torres and S. Alvarez, *Dalton Trans.*, 2011, **40**, 10742-10750.

48. J. P. Perdew, K. Burke and M. Ernzerhof, *Phys. Rev. Lett.*, 1997, **78**, 1396-1396.
49. J. P. Perdew, K. Burke and M. Ernzerhof, *Phys. Rev. Lett.*, 1996, **77**, 3865-3868.
50. T. H. D. Jr., *J. Chem. Phys.*, 1989, **90**, 1007-1023.
51. F. Weigend and R. Ahlrichs, *Phys. Chem. Chem. Phys.*, 2005, **7**, 3297-3305.
52. M. Dolg, H. Stoll, A. Savin and H. Preuss, *Theor. Chim. Acta.*, 1989, **75**, 173-194.
53. M. Dolg, H. Stoll and H. Preuss, *Theor. Chem. Acta.*, 1993, **85**, 441-450.
54. S. J. Coles and P. A. Gale, *Chem. Sci.*, 2012, **3**, 683-689.
55. *Rigaku, CystalClear-SM Expert (3.1), Rigaku Corporation., Tokyo, Japan, 2012.*
56. G. Sheldrick, *Acta Crystallogr., Sect. A.*, 2008, **64**, 112-122.
57. O. V. Dolomanov, L. J. Bourhis, R. J. Gildea, J. A. K. Howard and H. Puschmann, *J. Appl. Crystallogr*, 2009, **42**, 339-341.
58. G. A. Crosby and J. N. Demas, *J. Phys. Chem. A.*, 1971, **75**, 991-1024.
59. A. S. Chauvin, F. Gumy, D. Imbert and J. C. G. Bünzli, *Spectrosc. Lett*, 2004, **37**, 517-532.
60. A. S. Chauvin, F. Gumy, D. Imbert and J. C. G. Bünzli, *Spectrosc. Lett.*, 2007, **40**, 193-193.
61. P. A. Brayshaw, J.-C. G. Buenzli, P. Froidevaux, J. M. Harrowfield, Y. Kim and A. N. Sobolev, *Inorg. Chem.*, 1995, **34**, 2068-2076.
62. J. D. Crowley, P. H. Bandeen and L. R. Hanton, *Polyhedron*, 2010, **29**, 70-83.

4. Mixed Lanthanide Langmuir Blodgett Films

These results have been published in A. T. O'Neil, J. A. Harrison and J. A. Kitchen, Ultra-thin films of amphiphilic lanthanide complexes: multi-colour emission from molecular monolayers, Chem. Commun., 2021, 57, 8067-8070.

4.1 Introduction

The study in chapter 3 established the overall synthetic strategy for developing a range of new lanthanide-based complexes. This encompassed the introduction of the 1,2,3-triazole linker into the PDA scaffold and indicated that even with the formation of the new bulky ligands and the addition of the potentially competitive 1,2,3-triazole ring, Ln^{3+} coordination was still occurring in the desired NO_2 pocket giving 1:3 M:L complexes.[1] However the decision was made to move away from the PDA motif to focus on the PDC motif (Figure 4.1). The switch to the PDC motif was expected to overcome some drawbacks of the PDA scaffold, namely improving stability and potentially the antenna properties.[2] The stability of the complexes is suspected to be improved with the inclusion of the anionic carbonyl, a group that strongly binds to Ln^{3+}.[2, 3] This should make characterisation of the lanthanide complexes less complicated by removing the need for cold injection in mass spectrometry and additionally avoiding the speciation observed in the labile chapter 3 PDA systems. Although the PDC motif is rare for lanthanide complexes, with only 11 reported to date, the few examples which have measured overall quantum yields of Eu^{3+} or Tb^{3+} were higher compared to the PDA based counter parts (see Section 2.3).[2, 4, 5]

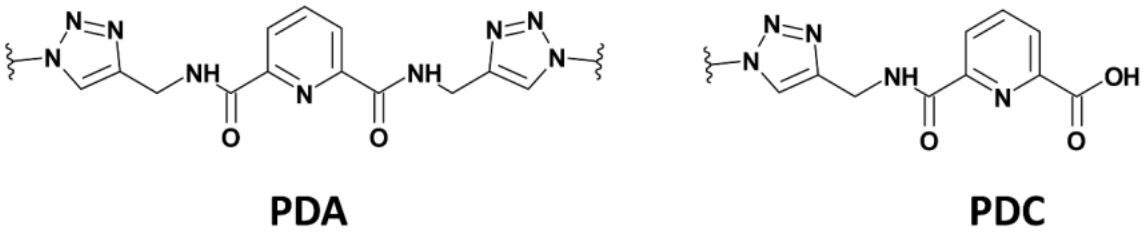

Figure 4.1.. PDA and PDC motif with 1,2,3-triazole linker..

The main focus of this study was to move onto systems for materials-based discovery, specifically Langmuir-Blodgett (LB) films. LB films, developed by Irving Langmuir[6] and Katharine Blodgett,[6-8] are the self-assembly of molecules commonly on a water-air interface into orderly molecular thin films known as Langmuir films (Figure 4.2). These are commonly made of amphiphilic molecules which self-orientate on the liquid-gas plane and can form strong Van der Waals force interactions between the alkyl chains and hydrogen bonds between hydrophilic heads. The Langmuir film formed on the water subphase can be deposited or transferred from the subphase onto a substrate surface by, in this case, Blodgett deposition to form LB films.[9-11]

The specific interest of LB films over other surface immobilization techniques available such as spin coating, dip coating, rapid annealing self-solution-shearing (RASSS) and vapour deposition, is due to the precision that the LB technique allows over film formation. As discussed below the LB technique allows for direct monitoring of monolayer film formation, film stability, and film deposition.[9, 10] It offers large surface homogeneity across the film and allows for control over film thickness through multiple depositions, forming multilayered films (unlike self-assembled monolayers (SAMs)).[12] LB also allows for control over film orientation and uses very little material for each monolayer, coinciding with significantly less waste than other techniques. Whilst the LB technique is commonly used on small substrates it can be upscaled for industrial use if required with roll-to-roll deposition.[13-15]

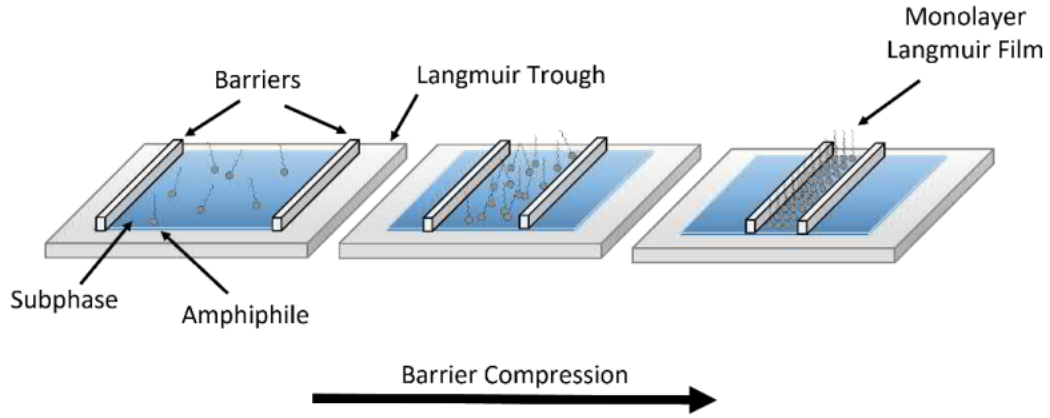

Figure 4.2.. Diagram showing the formation of Langmuir films in a Langmuir trough.. Initially the barriers are widespread and the area available to the deposited amphiphilic molecules is large enough such that molecular interactions are sparse and in a surface gaseous arrangement.. Barrier compression causes the molecules to aggregate into a liquid like phase,. forcing interactions between the alkyl chains.. Upon enough barrier compression the amphiphilic molecules form an orderly monolayer. Langmuir film on top of the subphase, with Van der Waals force interactions between the alkyl chains..

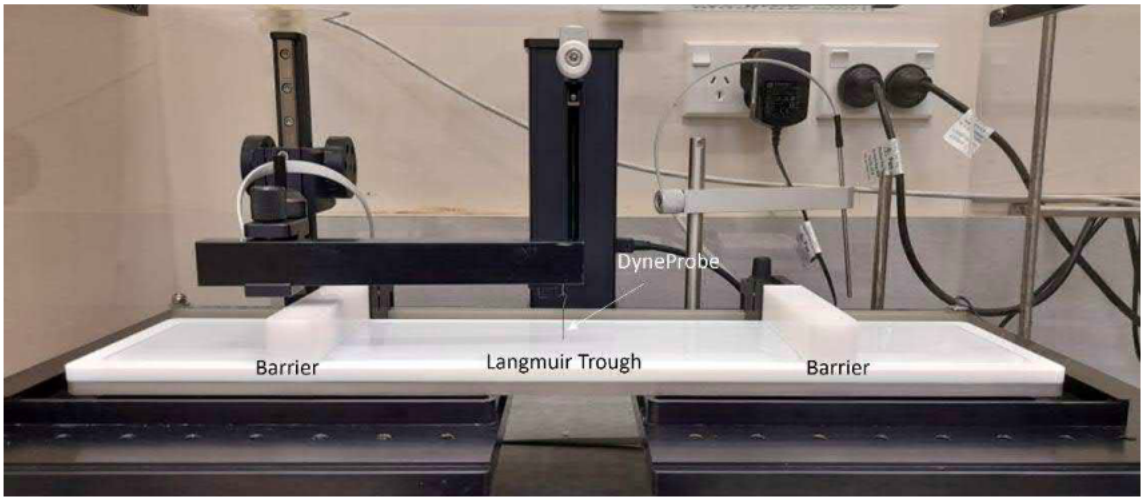

Figure 4.3.. Kibron G2 Microtrough in which Langmuir isotherms and stabilities were measured on..

As stated, the LB technique commonly utilizes amphiphilic molecules which are deposited on top of the water subphase (which is contained in the Langmuir trough, seen in Figure 4.3). Amphiphiles are typically dissolved in a highly volatile organic solvent, which evaporates on the subphase, leaving behind the amphiphilic molecules on the water surface.[9, 10] The molecules are considered to be in a two-dimensional gaseous (G) like phase where there are minimal interactions between the molecules (Figure 4.4).[10] From here, a barrier (single or dual) compresses the molecules by reducing the surface area of the water subphase, causing the molecules to interact. The resulting surface area decrease causes the molecules to undergo phase changes - similar to a gas on a pressure-volume 3D isotherm, as the volume decreases, the pressure exerted on the gas increases, causing the molecules to undergo phase changes to a liquid and subsequent solid.[10] On a Langmuir trough, this is occurring on a two-dimensional scale, and as surface area decreases the molecules are compressed resulting in aggregations of the amphiphilic molecules and subsequent phase transitions.[9, 10]

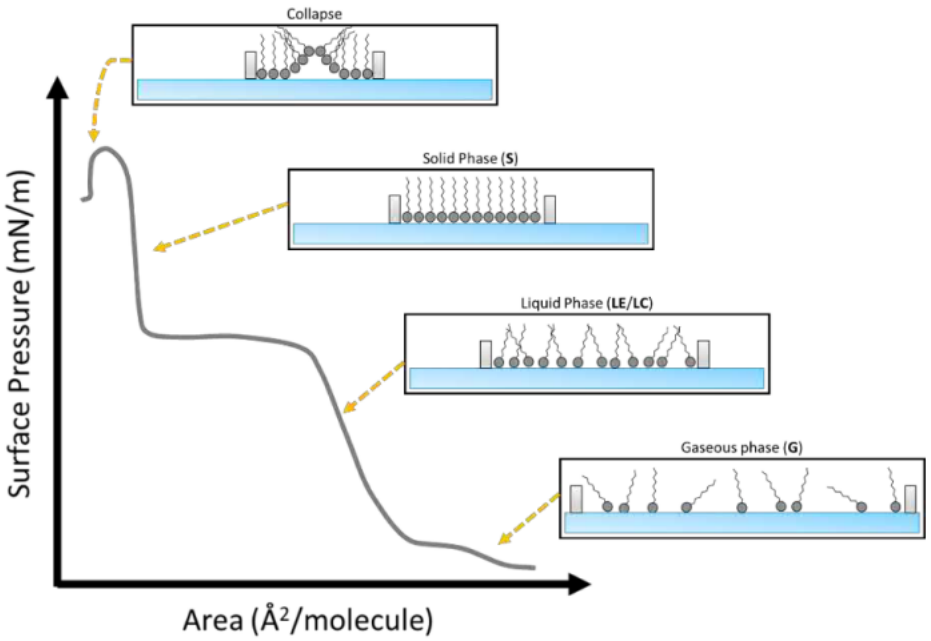

Figure. 4.4.. An. example. of. a. surface. pressure. –. area. per. molecule. isotherm. measured. on. a. Langmuir. trough.. Initially. the. surface pressure.is.low.with.minimal.interaction.between.amphiphilic.molecules.in.a.gaseous.phase.. Upon.barrier.compression.associated.with. the.reduction.in.area.per.molecule,.the.amphiphiles.are.compressed.into.a.liquid.compressed.or.expanded.phase.. Further.compression results. in. the. formation. of. the. orderly. Langmuir. film,. in. a. solid. or. compressed. phase,. with. chains. orientated. in. the. same. direction. Finally.additional.barrier.compression.results.in.a.collapse.of.the.Langmuir.film.. It.is.worth.pointing.out.that.there.are.two.zones.where surface. pressure. has. plateaued;. this. indicates. the. phase. change,. but. is. uncommon. to. see. with. long. chain. amphiphilic. molecules. and will.not.be.seen.in.this.study's.Langmuir.isotherms..

These changes can be monitored and plotted as surface pressure-area isotherms (π - A) by measuring the surface pressure (π) of the subphase (commonly with a platinum Wilhelmy plate or Dyne probe) and plotting against the area per molecule (calculated from surface area of the trough occupied by material divided by number of amphiphilic molecules).[9, 10] As the monolayer undergoes barrier compression, phase transition from a G to liquid-expanded (LE) or liquid condensed (LC) phase occurs. Alkyl chains start to have some interaction between one another

but are irregular in this liquid-like phase, indicated by the initial increase in π on the Langmuir isotherm.[9, 10] Occasionally additional compression leads to a plateau indicating the condensed monolayer phase transition as seen in Figure 4.4, but this is uncommon for simple alkyl chain systems.[10] Further barrier compression results in the solid (S) or compressed phase (C) where molecular interactions form orderly thin monolayer films indicated by rapid increase in π, until an eventual collapse where film rupture occurs, displacing molecules out of the monolayer, potentially forming multilayers or micelles due to excess barrier compression.[10] Once the Langmuir films are formed it is important that they are stable on the subphase under high surface pressures, as this ensures that the films are deposited evenly. Also, if multiple depositions are required the film must remain stable over a long period of time.[9] Stability can easily be tested by stopping barrier compression at a surface pressure deemed to be in the S phase and monitoring π over time.[9] A stable film will remain unchanged over an extended period, while unstable films will be indicated by drops in π over time, indicating the collapse of the film, as shown in Figure 4.5.[9]

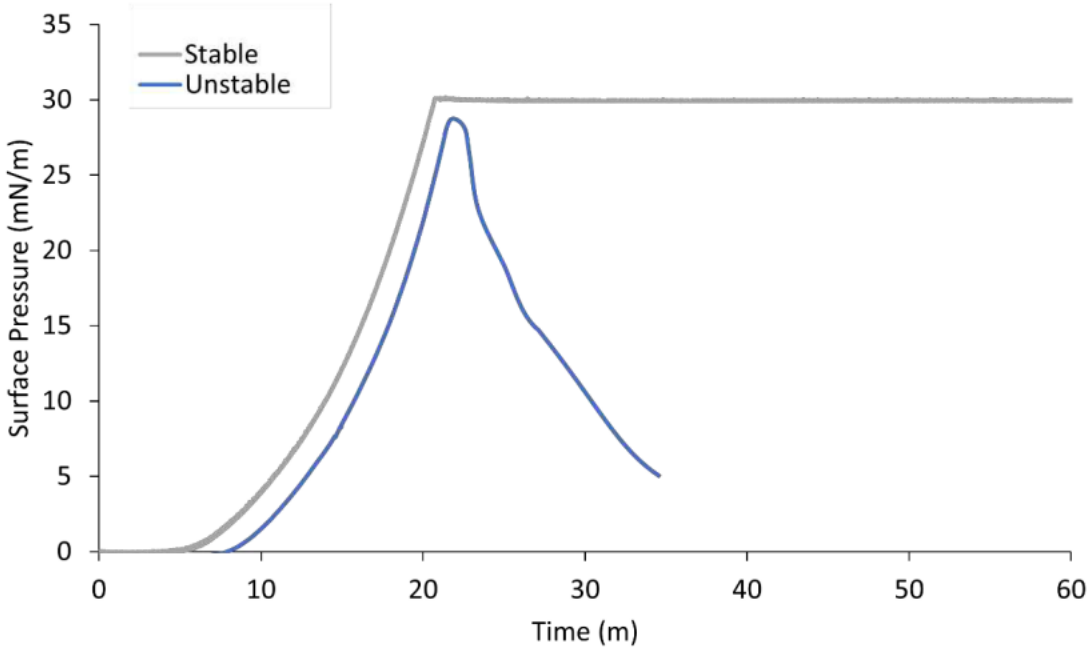

*Figure 4.5.. Example of a stability measurement,. in which the barrier compression has stopped,. in this case at ≈ 30 mN/m.. The stable film (of Eu(**5**)$_3$) is seen to remain at the same surface pressure for an extended period,. while the unstable film is seen to drop indicating the film has collapsed..*

Finally, as stated there are multiple ways these films can be deposited onto a substrate by Blodgett deposition, fabricating a range of films. Blodgett deposition can be done by ***emersion*** (upstroke) or ***immersion*** (downstroke) of the substrate through the subphase resulting in differently orientated film types; **X**-type and **Z**-type respectively (Figure 4.6).[10] Additionally, a **Y**-type multilayered film is achievable by alternating ***emersion*** and ***immersion*** deposition resulting in a head-to-head and a tail-to-tail film (Figure 4.47).[10] The film transfer ratio (TR) or

transfer percentage can be easily measured by monitoring the change in area of the trough occupied by the monolayer film as the deposition is occurring, divided by the area of the substrate that the film is being deposited on.[10]

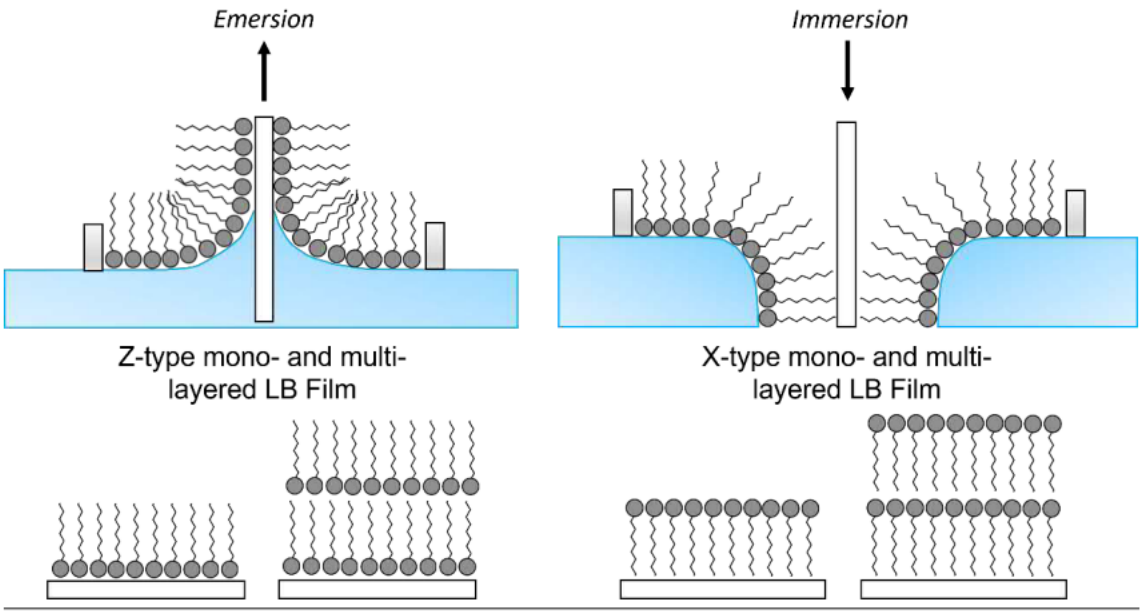

*Figure 4.6. Diagram shows how **Z**- and **X**- type mono and multilayer films are deposited onto a solid substrate by emersion or immersion respectively, changing the orientation of the molecules. **Y**-type deposition can be seen in Figure 4.47.*

The LB technique has been used to form a variety of material films for different applications such as membrane like filters,[16, 17] molecular sensors,[11] molecular electronic devices[18] , OLEDS,[19] and mechanical capture of analytes in water.[20, 21] With the combination of lanthanides and the LB technique, a range of similar applications are possible,[22, 23] most applications mainly focused on molecular sensors;[24-28] but there are also examples of OLEDS[29, 30] and some more unique properties like magnetism[31] and CPL from the LB film's emission.[32, 33] There are very few reports of systems with mixed lanthanide emissions[34, 35] or just mixed lanthanides[36-39] on a LB film. Mixed lanthanide emission systems have a wide variety of applications,[40] such as tunable emission including white-light generation,[41, 42] luminescent bar codes,[43] molecular logic gates,[44] ratiometric sensors (for temperature,[45] analytes[46] and solvents[47]), OLEDS[48] and solar waveguides using either up conversion (UC) or down conversion (DC).[49] These applications would benefit from moving from simple solution-based systems to more industrial friendly coatings if this not the case already.

To the best of our knowledge, in the very few cases where Ln^{3+} have been mixed in LB films, mixed Ln^{3+} emission does not occur. In most cases Ln^{3+} are mixed in LB films to improve only a single Ln^{3+} centred emission. This is done either by pre-mixed nanoparticle LB film containing a mixture of Ln^{3+} ($Yb^{3+}$and Er^{3+})[39] or by forming mixed Ln^{3+} complex LB films with an emissive Eu^{3+}

complex and a non-emissive lanthanide complex (non-emissive either due to a non-optimized antenna energy level or use of a Ln^{3+} that is non-visibly emissive). The non-emissive lanthanide complexes improve Eu^{3+} centred emission by transferring energy to the Eu^{3+} complex in the LB film.[36-38] Mixed emissive LB films have however been achieved by Sveshnikova and co-workers where both Tb^{3+} and Eu^{3+} have been complexed with behenic acid (Bh, $C_{21}H_{43}COOH$), forming $Eu(Bh)_3$ and $Tb(Bh)_3$.[34] The individual multilayer LB films of each $Ln(Bh)_3$ complex show Ln^{3+} emission, but is extremely weak and the organic Bh broad emission dominates the overall emission profile. This is the same in the case of the mixed $Eu(Bh)_3$ and $Tb(Bh)_3$ (1:1) LB multilayer film, as although it shows the presence of both Eu^{3+} and Tb^{3+} centred emission, the Ln^{3+} emission is extremely weak and the broad Bh emission obscures the Tb^{3+} centred emission, as seen in Figure 4.7.

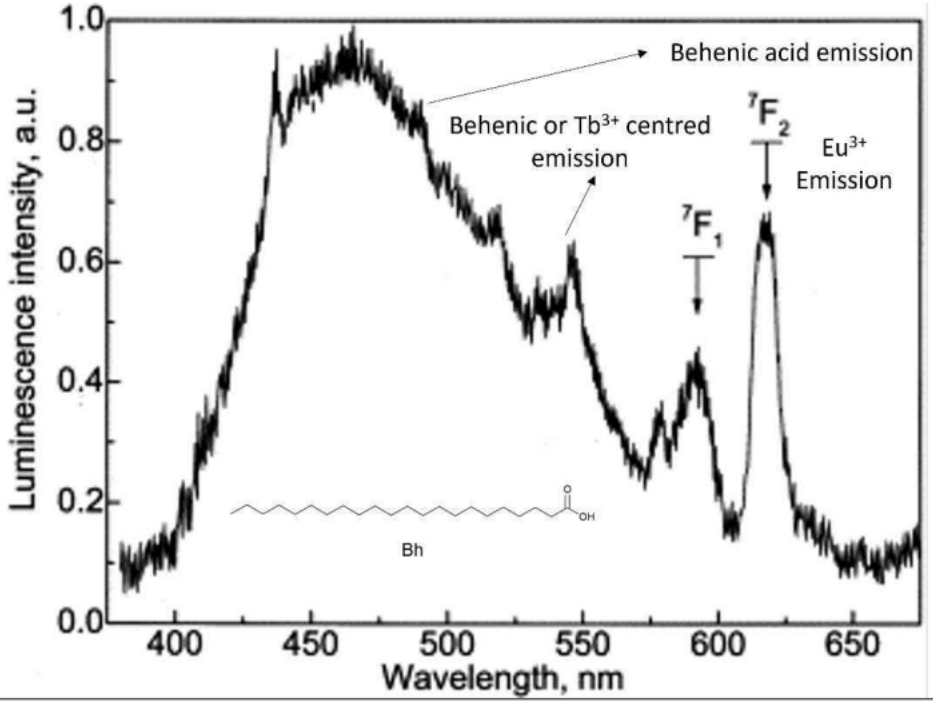

*Figure 4.7. Luminescent spectrum of multilayer (54 layers) LB film of $Eu(Bh)_3$:$Tb(Bh)_3$ (1:1). Image adapted with permission from V. I. Belyi, A. A. Rastorguev, A. A. Remova, I. A. Badmaeva, S. M. Repinsky and L. L. Sveshnikova, Thin Solid Films, 2002, **419**, 189-193. Copyright 2022, ELSEVIER.*

It is worth noting there are also examples of dual emissive LB films, where Ln^{3+} centred emission has been combined with either organic[34] or inorganic emission.[50-53] However, these commonly have emission profiles dominated by non-lanthanide emission, with only very weak signs of Ln^{3+} centred emission. Mixed lanthanide emission is preferred as it allows for the lanthanides' sharp and narrow emission bands to dominate the emission spectra and potentially be used for the above applications. In order to achieve this, a mixture of visible-emitting lanthanide complexes were synthesised, characterised, and then deposited as either mixed multilayer or mixed monolayer LB films. Mixing different components in LB films is not an uncommon occurrence, with the common example of stearic acid being mixed in the LB film material to improve film

formation and stability.[54] With the atomic size of Ln^{3+} being similar, different complexes can be expected to have similar sizes, resulting in similar isotherms,[36, 55, 56] (Figure 4.8), which should make mixed-amphiphile multi- and mono- layer deposition occur smoothly.

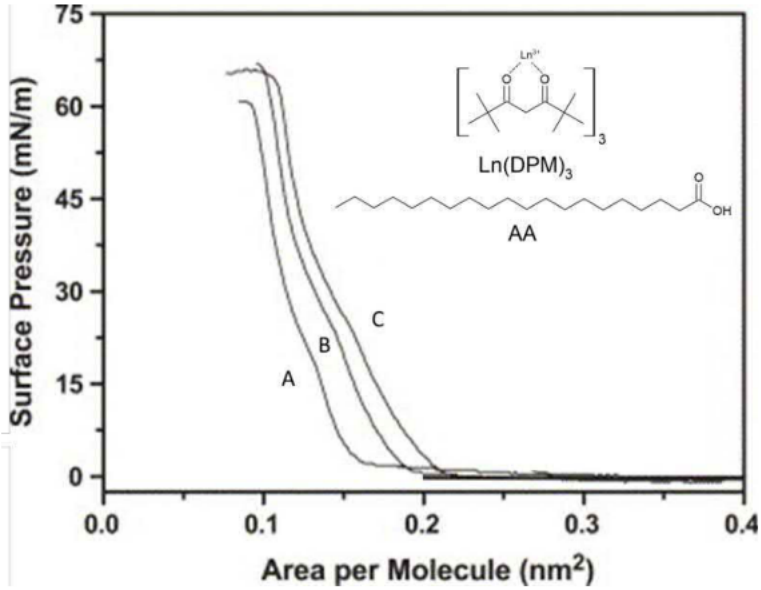

Figure 4.8.. Pungsheng and co-workers LB isotherms of (A) $Gd(DPM)_3$:AA (1:2), (B).. $Eu(DPM)_3$:$Gd(DPM)_3$:AA (2:1:6) and (C) $Eu(DPM)_3$:AA (1:2) measured on an air water interface.. Abbreviations: AA - arachidic acid and DPM - 2,2,6,6-tetramethyl-3,5-heptanedionate.. Image adapted with permission from Z.. Gang, Z.. Yanze and H.. Pingsheng,. Thin Solid Films, *2004, **468**, 268-272.. Copyright 2022, ELSEVIER..*

With the desire to make mixed emissive LB films, a simplistic amphiphilic ligand **5** (Figure 4.9) was designed and complexed with a range of visible emissive Ln^{3+}. The relatively simple ligand design was chosen as the anionic carboxylate group should enhance complex stability, while also resulting in overall neutral complexes ideal for LB films. Ligand antenna properties (triplet energy) should both be better matched as noted in Section 2.3 and the ligands lack any competing aromatic group which could result in less emissive Ln^{3+} complexes as observed in chapter 3. With this system we aimed to develop mixed-amphiphile LB films with tunable overall photoemission. Such mixed LB films could be used for applications such as multi-ratiometric sensors, up and down solar converters/waveguides, and molecular barcodes, to name a few. It is worth noting that to the best of our knowledge there are no examples of PDC lanthanide-based LB films, although there is a PDA based system by Gunnlaugsson and co-workers (Figure 2.7) which due to the similar structure, LB fabrication conditions were based off of this study.

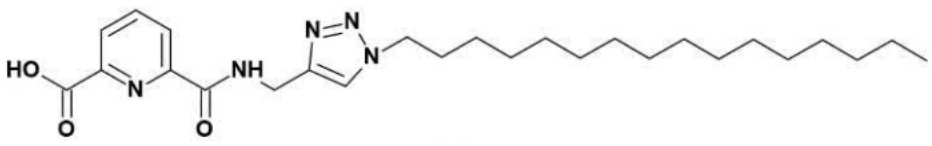

5

*Figure 4.9.. Molecular structure of ligand **5**..*

4.2 Results and Discussion

4.2.1 Ligand Synthesis and Characterisation

Before synthesising the new amphiphilic ligand **5,** a mono-click trial study was carried out with benzyl bromide, as the initial synthesis of intermediate **D** was low yielding (< 10 %) and benzyl bromide was known to easily click under our conditions (whereas the long chain conditions were unknown). Initially, the DPA starting material was protected at a single carboxylate unit following a literature procedure,[57] by reacting DPA with benzyl bromide to give intermediate **C**. Unfortunately, this reaction is commonly low yielding, with yields ranging as low as 40 % to as high as 72 % under the same conditions. The low yields are a result of the large byproduct of bis protected DPA units (Scheme 4.1).

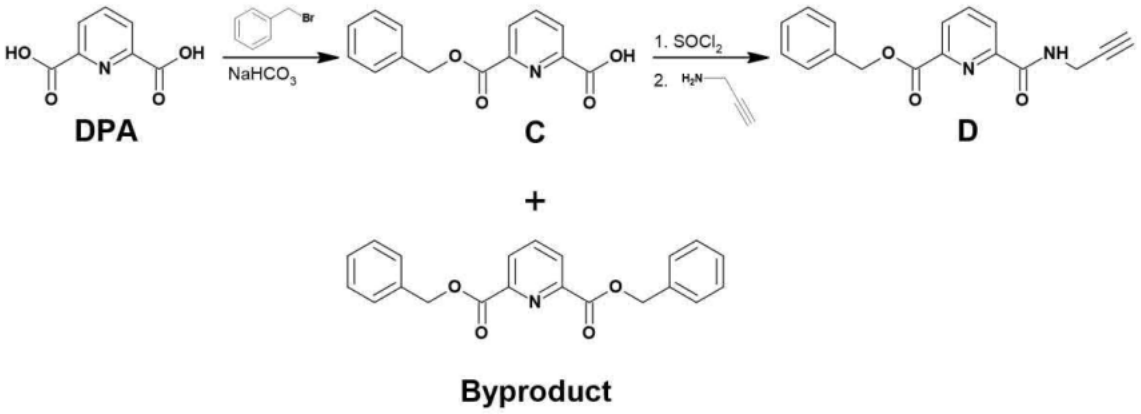

*Scheme 4.1.. Synthetic route to intermediates **C** and **D**..*

The next stage was to append the alkyne. This was carried out in a similar fashion to the bis-alkyne (**B**) intermediate from chapter 3, dissolving intermediate **C** in freshly dried DCM and then refluxing with thionyl chloride to form the acid chloride and then reacting that with propargyl amine. Although it was evident this was working, the initial yields were extremely poor, taking several iterations (done under a N_2 atmosphere, large excess of propargyl amine, complete removal of all solvent to maximize removal of thionyl chloride) to fully optimize the conditions to achieve high yields of around 70 - 90 %.

Because of the initial rarity of this intermediate due to poor yields from both stages, it was opted to click benzyl bromide first as a proof of concept. ^{1}H NMR spectra (Figure 4.10) confirmed the successful formation of the 1,2,3-triazole linker, evident from the singlet assigned to the 1,2,3-triazole proton (t – 8.1 ppm). However, the benzyl (Bn) ester protecting group was also removed, as evident by NH_2 signals (8.9 and 7.8 ppm) and reduction in number of protons for Bn and Bn-CH_2 signals, replacing the protected carboxylate with an amide group. This was suspected to

occur during workup with NH_4OH forming an amide, which agrees with literature.[58] The discovery of the amide formation was both serendipitous and unwanted, as it opened a pathway to another set of ligands, but for this study the carboxylate was desired. Fortunately, this deprotection did not occur during the click and by simply replacing the NH_4OH with NaOH, a mono-clicked benzyl PDC retaining the ester protecting group as seen in Figure 4.10 was synthesised.

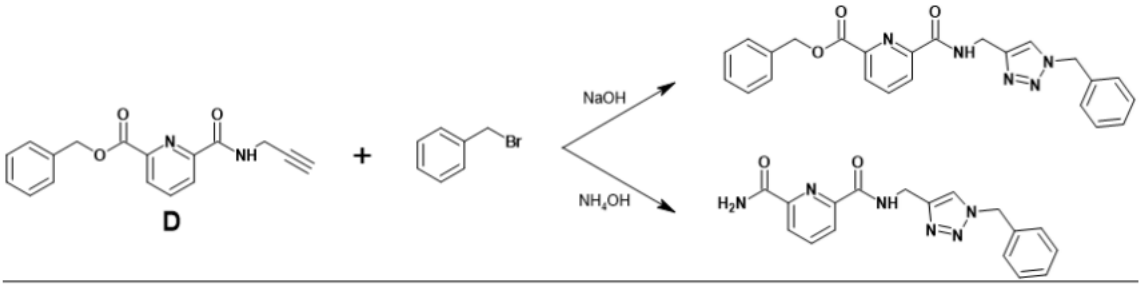

Scheme 4.2.. Synthetic pathway of mono-clicked benzyl ligand resulting in either the wanted protected carboxylate or the unwanted amide dependent on workup solvent..

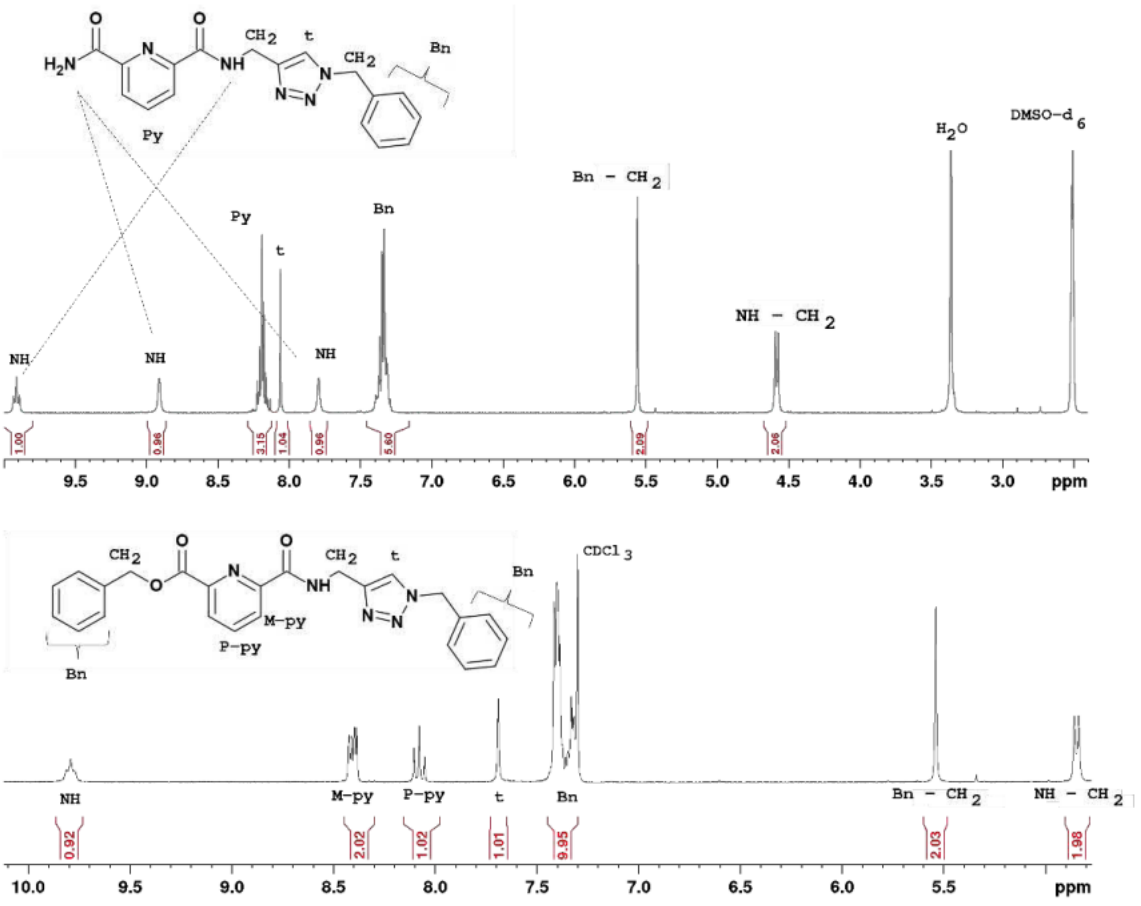

Figure 4.10.: ^{1}H NMR of mono "clicked" benzyl, with either workup in NH_4OH resulting in amide (Top) or NaOH resulting in protecting group remaining present (Bottom) (300 MHz, $CDCl_3$ & DMSO-d_6)..

Based on this trial study, the synthesis of **5** was relatively straight forward, with a six-step process as seen in Scheme 4.3, starting from commercially available DPA and 1-bromohexadecane. Initially DPA was combined with $NaHCO_3$ in dry DMF and the solution was heated to 60 °C for 30 minutes under a N_2 atmosphere. Benzyl bromide was then added, and

the solution was further heated for 24 hours, where the off-white solution turned pale yellow. Acid-base workup yielded an off-white solid of monoester protected **C** (40 - 72 %). **C** was then dissolved in dry DCM under a nitrogen atmosphere and thionyl chloride was then added to the solution, which was left to reflux for 5 hours. Solvent was removed by a stream of nitrogen yielding a pale-yellow solid containing the acid chloride. This was immediately dissolved in dry DCM and added dropwise to a cooled solution of propargyl amine and triethylamine in dry DCM. The resulting solution turned from a lime green to a dark burgundy and was left to stir for 24 hours. Acid-base workup resulted in a dark brown oil which eventually solidified to a light brown solid, containing mono-alkyne **D** (72 %).

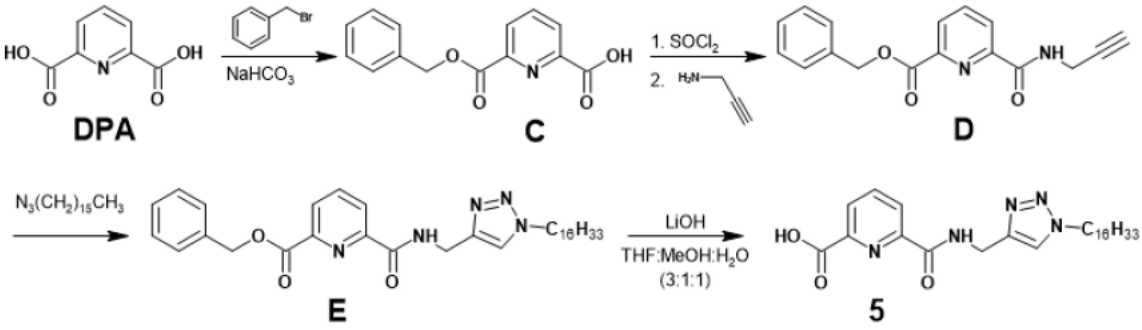

*Scheme 4.3. Synthetic pathway for synthesis of intermediates **C** – **D** and ligand **5**.*

Initially, using the same conditions as in chapter 3, intermediate **D** was "clicked" in a one-pot reaction with 1-bromohexadecane making the azide *in situ*; unfortunately, this resulted in either no "click" occurring or small signals for the 1,2,3-triazole proton. Instead of a one-pot multi-component CuAAC reaction, it was found that the reaction proceeded more favourably when the azide was synthesised and isolated prior to the click reactions. 1-Azidohexadecane was easily obtained by refluxing 1-bromohexadecane with NaN_3 in dry DMF for 24 hours. Water was added to stop the reaction, resulting in a white precipitate, and the product was then extracted into ethyl acetate. The solvent was removed, resulting in a clear oil (88 %). The azide formation and isolation was deemed to be relatively safe with the desired product having a carbon to nitrogen ratio of 5.33 (N_c/N_N= 5.33), which is within the safe ratio to synthesise and store azides at r.t ($N_c/N_N \leq 3$ are deemed unsafe).[59, 60]

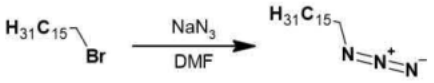

Scheme 4.4. Synthesis of 1-azidohexadecane from 1-bromohexadecane.

Further, the "click" reaction was found to be more favourable when time was given for the $CuSO_4 \cdot 5H_2O$ Cu(II) to convert to catalytic Cu(I) by the new pre-formed sodium ascorbate, as well as the potential to form the Cu(I)-acetylide or π,σ-bis(Cu) intermediates, prior to addition of azide, [61] see Figure 4.11 (solution would turn a pale yellow colour indicative of this formation). To this end **D** was combined with sodium ascorbate and the $CuSO_4 \cdot 5H_2O$ catalyst in DMF:H_2O

(4:1) and heated to 60 °C until the solid had dissolved. 1-Azidohexadecane was then added dropwise to the yellow solution, which over the course of 24 hours turned brown, then to a light grey with visible solid precipitation. The solid precipitate was filtered, yielding a light green solid which was then washed with (1 M) NaOH:(0.5 M) EDTA solution yielding an off-white solid **E** (75 %). **E** was then deprotected by stirring in a 3:1:1 solution of THF:MeOH:H_2O with LiOH, in which the solid slowly dissolved and the clear solution turned yellow. The solvent was removed until a yellow residue remained before 1 M HCl was added causing an off-white precipitate to form. This was filtered and washed with H_2O, yielding **5** as an off-white solid (89 %).

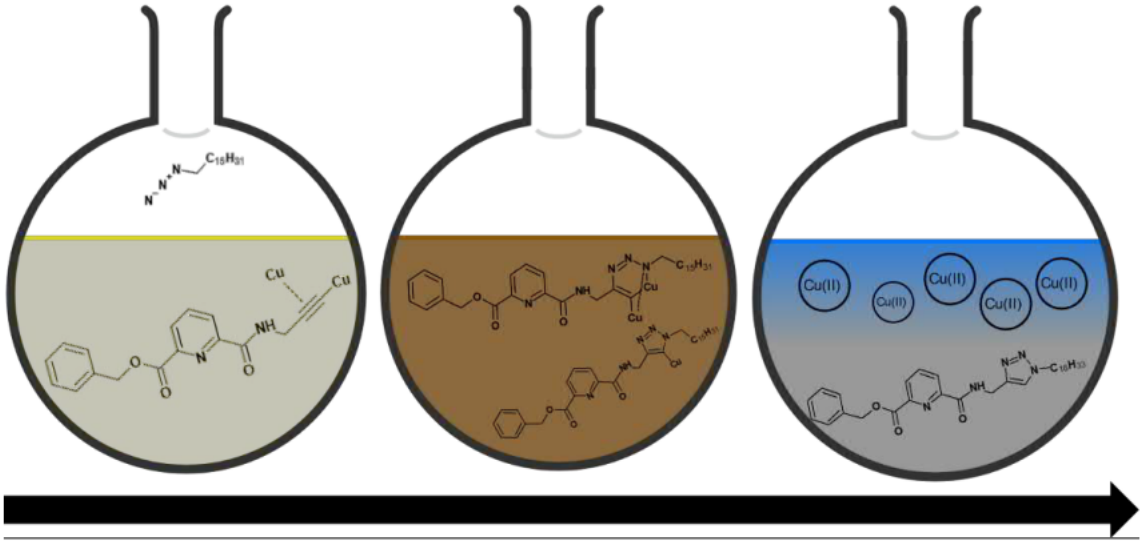

*Figure 4.11. Shows the π,σ-bis(Cu) acetylide formed in solution with intermediate **D** before the addition of 1-azidohexadecane resulting in a yellow solution colour. After the addition of the azide the solution darkens to a brown colour and potential "click" intermediates are forming; finally, it results in a grey precipitate, which is commonly suspended in a blue copper solution. Click intermediates and π,σ-bis(copper) acetylide are based off those suggested in H. Ben El Ayouchia, L. Bahsis, H. Anane, L. R. Domingo and S.-E. Stiriba, RSC Advances, 2018, **8**, 7670-7678 and round bottom flasks are generated in chemix, https://chemix.org.*

The successful synthesis of ligands **5**, intermediates **C, D** and **E**, and precursor 1-azidohexadecane, was confirmed and characterised by ^{1}H NMR, ^{13}C NMR, and LRMS. Ligands were also characterised by FTIR and UV-visible spectroscopy. LRMS confirmed the successful synthesis of ligands and intermediates with observed peaks matching the calculated value (Table 4.1 and Section 8.2.1).

Table 4.1. Mass peaks observed for ligands and intermediates vs calculated values.

Ligands and Intermediates	Calculated *m/z*	Experimental *m/z*
[**5** + H]$^+$	472.33, $C_{26}H_{42}N_5O_3^+$	472.25
[**C** + H]$^+$	258.25, $C_{14}H_{12}NO_4^+$	258.00
[**D** + H]$^+$	295.11, $C_{17}H_{15}N_2O_3^+$	294.95
[**E** + H]$^+$	575.20 , $C_{33}H_{47}N_5O_3^+$	575.15

^{1}H NMR spectra seen in Figure 4.12 shows the stepwise successful synthesis of **5** starting from the initial intermediates **C** and **D**, the latter reacting with 1-azidohexadecane to form intermediate **E**. The successful "click" between intermediate **D** and 1-azidohexadecane is clear with the appearance of the singlet resonance peak (t) at ≈ 7.8 - 7.6 ppm, assigned to the single 1,2,3-triazole proton. This also coincides with the disappearance of the terminal alkyne (CH) proton of **D** at 2.3 ppm, and downfield shifts of the linking methylene groups connected to the 1,2,3-triazole ring (NH-CH_2), (t-CH_2) and the amide (NH) protons from 4.3 to 4.8, 3.3 to 4.3, and 8.3 to 8.6 ppm respectively. Deprotection of the benzyl ester protecting group to final ligand product **5** is clearly indicated by the loss of benzyl aromatic protons (Bn) at ≈ 7.4 ppm and the CH_2-O linker at 5.5 ppm, seen when comparing ^{1}H NMR spectra of **E** to **5**. The only other change of note is the much more significant downfield shift of 8.6 - 9.9 ppm observed in the amide (NH) signals.

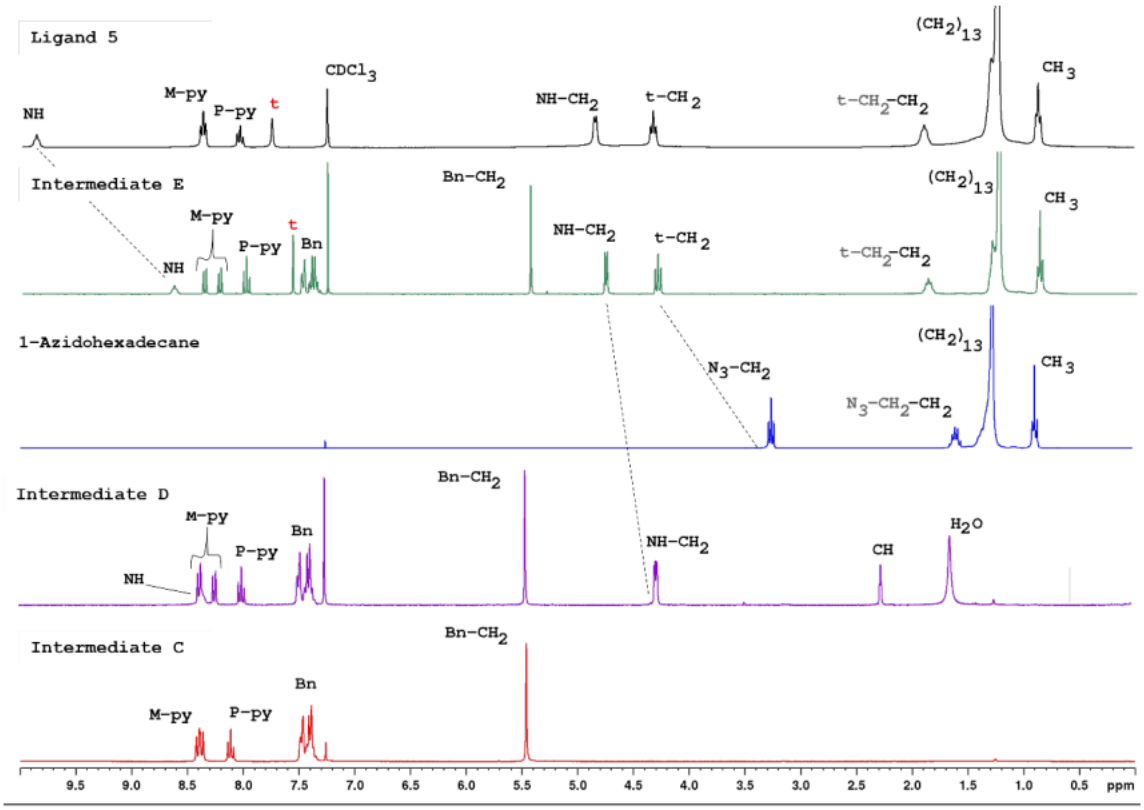

*Figure. 4.12.. ^{1}H. NMR. spectra. following. the. synthetic. pathway. from. intermediates. **C**,. **D**,. **E**. and. 1-azidohexadecane. and. ligand. **5**. Abbreviations:. NH. for. for. amide. protons,. M-py. for. meta. protons. on. pyridine. ring,. P-py.. for. para. proton. on. pyridine. ring,. t for. 1,2,3-triazole. ring. proton,. Bn. for. benzyl. ring. protons. (300. MHz,. $CDCl_3$).. Dash. (-). indicates. the. group. that. the. CH_2 is. bonded. to..*

^{13}C NMR also confirmed formation of **5** (Figure 4.13) and previous intermediates with the correct number of carbon environments being present. Important peaks of interest are the appearance of associated 1,2,3-triazole ring ^{13}C signals at ≈ 144.2 (C) and 123.2 (CH) ppm, alongside the disappearance of the alkyne 79.4 (C) and 71.8 (CH) ppm and benzyl ester motif 135.5 (C-Bn), 128.8 - 128.6 (CH-Bn), 67.9 ppm (CH_2-Bn), indicating successful "click" and subsequent deprotection of the benzyl ester motif.

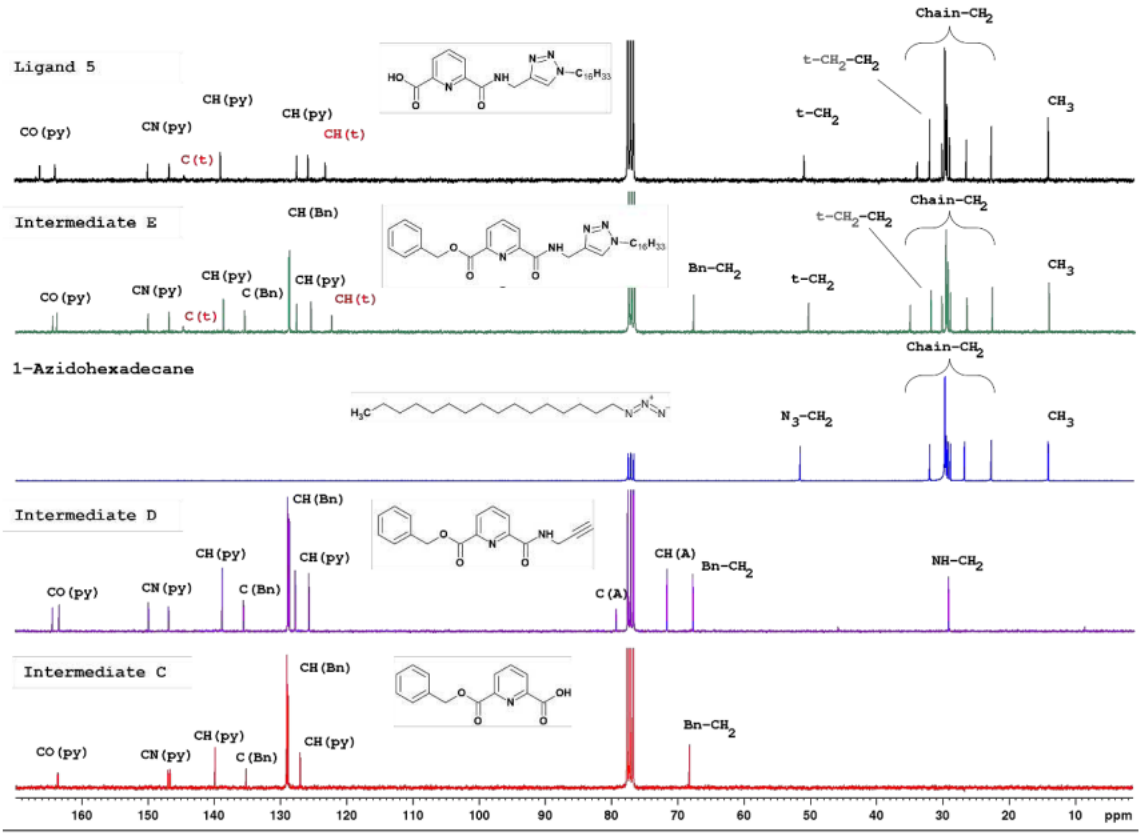

Figure. 4.13.. ^{13}C NMR. spectra,. following. the. synthetic. pathway. from. intermediates. ***C,. D,. E*** *and. 1-azidohexadecane. and. ligand.* ***5****. Abbreviations:. CO(py). for. carbonyl. carbons. on. pyridyl. unit,. CN(py). and. CH(py). for. carbons. on. pyridyl. ring,. C(Bn). and. CH(Bn). for. carbons. on. benzyl. ring,. C(t). and. CH(t). for. carbons. on. 1,2,3-triazole. ring,. C(A). and. CH(A). for. alkyne. and. a. dash. (–). indicates. it. the. carbon. attached. to. the. distinguishing. feature. (75. MHz,. $CDCl_3$).·*

The UV-visible spectrum of **5** (Figure 4.14), is similar to the PDA systems in chapter 3, with the ligand exhibiting broad absorptions ranging from 200 to 300 nm, with the characteristic major bands at 200, 220 nm and three bands at 264, 270 and 279 nm, the latter associated with the previously assigned n → π* and π → π* transitions from the central 2,6-pyridinedicarbonyl unit and with the higher energy bands associated with the carbonyl groups and 1,2,3-triazole ring.[62]

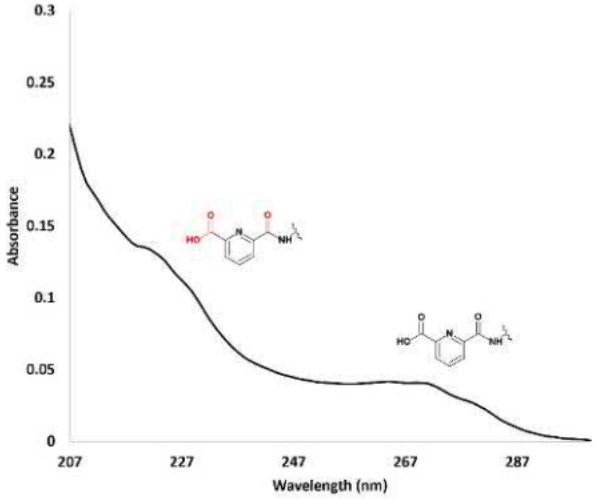

Figure. 4.14.. UV-visible. absorption. spectrum. of. ***5*** *in. MeCN. (0.01. mM)..*

4.2.2 Ligand Molecular Structure

Single crystals suitable for X-ray diffraction studies of **5** were successfully grown by heating a sealed pipette reactor of a solution of **5** in DMSO (≈ 10 mg/mL) (Figure 4.15). The solution was heated to ≈ 100 °C for 24 hours and then slowly cooled down over the course of 24 hours in an oven.

*Figure 4.15.. Image of crystals of **5** and pipette reactor from which they were grown in..*

A low temperature (≈ 123 K) structure was collected. **5** crystallised in the triclinic space group *P*-1 and contained one molecule and an associated DMSO solvent molecule in the asymmetric unit (Figure 4.16). The structure showed the expected connectivity, with both the amide and carboxylate bonds oriented such that the NH and OH groups are pointing towards the central pyridyl nitrogen atom, forming a moderate strength hydrogen bonding pocket that contains the solvent DMSO molecule [N2-H2···O100' = 2.996(4) Å and <(N2-H2···O100') = 165(3)°]; [O1-H1···O100' = 2.696 (4) and <(O3-H3a···O100')= 153(4)°].

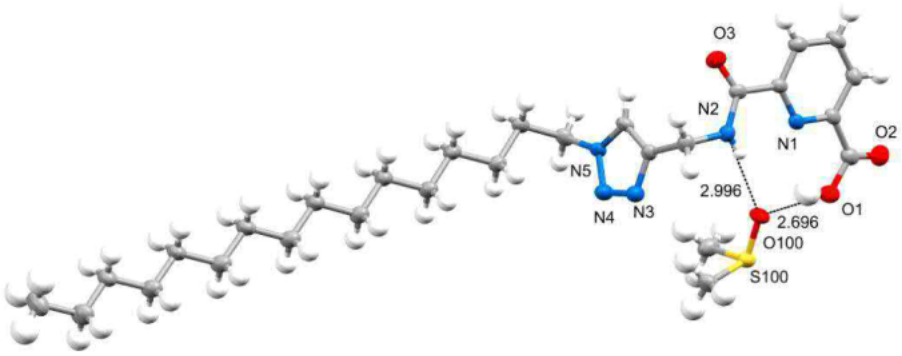

*Figure 4.16.. The crystallographically independent molecule of **5** in the asymmetric unit and associated hydrogen bonding with the singular DMSO solvent molecule,. 50 % ellipsoid representation..*

Importantly the long-range ordering observed (Figure 4.17-18) is strongly controlled by the amphiphilic nature of **5**. The alkyl chains are interdigitated, forming a hydrophobic section showing Van der Waals interaction between long chains, whereas the pyridyl unit forms a hydrophilic section with the DMSO molecules. This results in an almost "membrane" like bilayer packing.

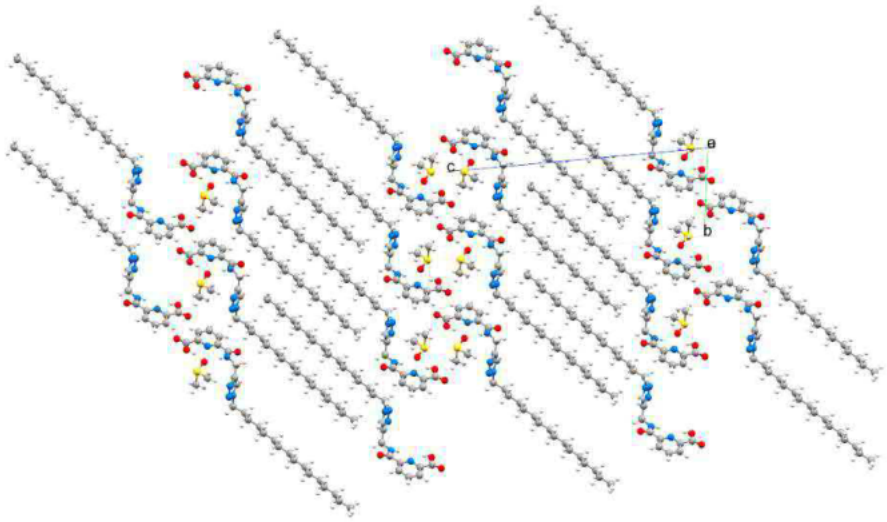

Figure. 4.17.. The. overall. result. of. the. aforementioned. interactions. is. the. formation. of. sheet-like. packing. along. the. crystallographic. a-axis..

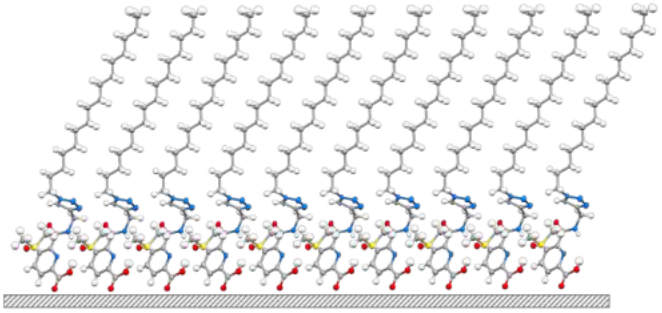

Figure. 4.18.. Crystal. packing. along. the. a-axis,. representative. of. potential. packing. of. ***Z****-type. LB. film. of.* ***5****. deposited. on. quartz...*

4.2.3 Self-Assembly Studies

Photophysical solution based self-assembly studies were once again carried out on **5**, following the same procedure as described in chapter 3, although scaled down from the previous studies to a single lanthanide ion (Eu^{3+}). This was carried out to firstly confirm that the relatively unexplored motif would still predictably self-assemble in solution and favour the formation of the 1:3 M:L species, along with any signs of coordination enhancement from the free carboxylate. Eu^{3+} was selected due to extensive prior studies indicating that PDC is an effective antenna for Eu^{3+} centred emission.[5, 57, 63-66] As stated titrations were carried out after deprotonation of the carboxylic acid with 1 equivalent of tetra methylammonium hydroxide (TMAO, selected for its lack of photophysical characteristics).

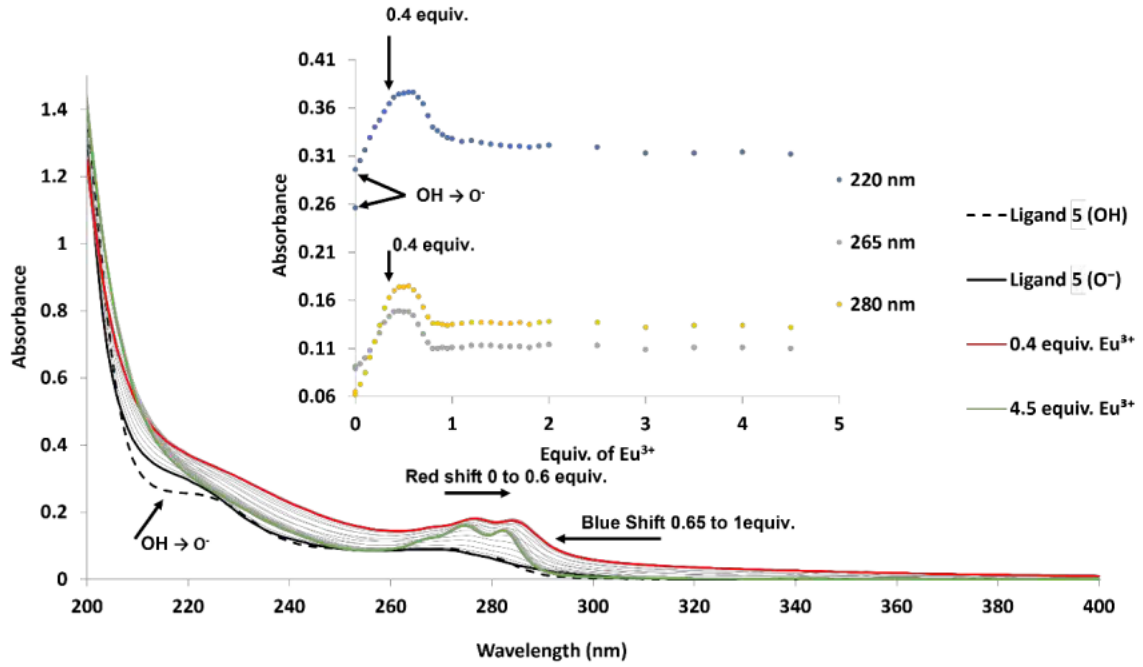

*Figure 4.19.. UV-visible titration of **5** (0.02 mM, MeCN) with $Eu(CF_3SO_3)_3 \cdot 6H_2O$ from 0 to 4.5 equivalents..*

The absorption titration of **5** with $Eu(CF_3SO_3)_3 \cdot 6H_2O$ resulted in similar general trends upon the addition of Eu^{3+} as previously seen with chapter 3 PDA based ligands (Figure 4.19). However, prior to Eu^{3+} addition, the addition of 1 equivalent of TMAO base resulted in an absorbance enhancement in the 210 - 220 nm region, associated with the carbonyl absorption and indicative of the deprotonation occurring. Other bands remained relatively unchanged. Upon the addition of Eu^{3+}, significant increases (hyperchromic shifts) were observed from 0 to 0.4 equivalents in the major band at 220 nm and the smaller bands at 265, 270, and 280 nm, accompanied by a significant red shift, associated with coordination of the electron withdrawing lanthanide and the formation of the 1:3 M:L species. Further addition of Eu^{3+} from 0.45 to 0.6 equivalents resulted in a brief plateau. Upon the addition of 0.65 to 1 equivalent, a reverse blue shift and

hypochromic shift was observed until either 0.8 or 1 equivalent (in 265 - 280 and 220 nm bands respectively). Further addition resulted in a complete plateau. The overall aforementioned changes once again indicated the evolutionary self-assembly process was taking place, initially forming the desired 1:3 M:L species, and then into the lesser 1:1 M:L species.

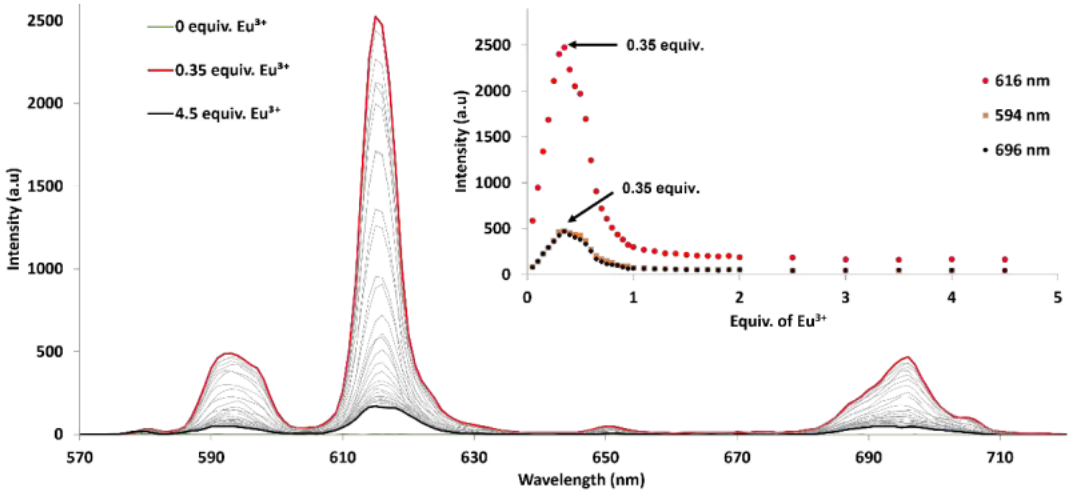

*Figure 4.20.. Fluorescence titration of **5** (0.02 mM, MeCN) with $Eu(CF_3SO_3)_3 \cdot 6H_2O$ from 0 to 4.5 equivalents.. Excitation wavelength 275 nm..*

Fluorescence titrations of **5** with $Eu(CF_3SO_3)_3 \cdot 6H_2O$ are nearly identical to the PDA based ligands in chapter 3. It can be seen in Figure 4.20 that upon the addition of 0 to 0.3 – 0.35 equivalents, there was a significant increase in the Eu^{3+} centred emission ($^5D_0$ to $^7F_{J=0\text{-}4}$), associated with the three antennae surrounding the Eu^{3+}. Upon the further addition of Eu^{3+}, the emission decreased until 1 equivalent, resulting in a plateau, again indicating the predominant formation of the 1:3 M:L species, which upon further addition of Ln^{3+} evolves into lesser species.

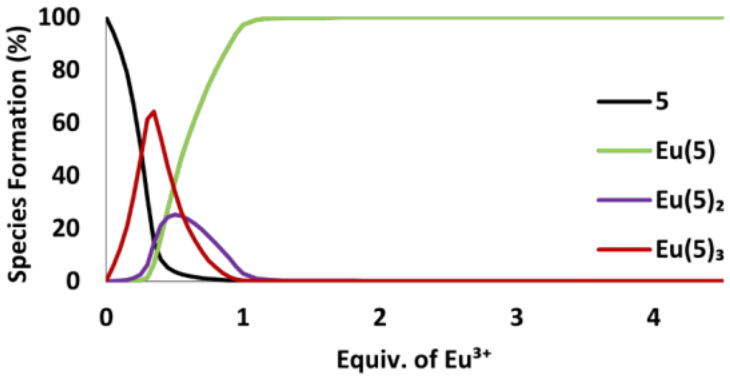

Figure 4.21.. ReactLab™ Equilibrium generated speciation plot from fluorescence titration from Figure 4.20..

The titrations were fitted with ReactLab™ Equilibrium[67] for non-linear regression analysis using the same equation and conditions as the previous chapter. Unfortunately, only fluorescence data was able to be fitted (Figure 4.21), with absorption titrations not converging. Similar fitting issues were also observed in **L**[39], initially struggling to get their titration data to converge.[57] From the speciation formation plot it is evident that the Eu(**5**)$_3$ species formation was the dominant

species formed from 0 to 0.3 equivalents, with Eu(**5**)$_3$ formation maximizing at 0.35 equivalents with 65 % species formation, a percentage which is on the higher end of formation observed by the PDA systems in chapter 3. Upon further addition the Eu(**5**)$_3$ was deformed into lesser species. Unlike previous Eu^{3+} titrations with PDA systems, formation of the Eu(**5**)$_2$ was unfavoured, with Eu(**5**) becoming the dominant species at 0.55 equivalents (46 %), skipping the expected formation of Eu(**5**)$_2$ at ≈ 0.66 equivalents. Eu(**5**) remains the dominant species and was practically the only species at 1 equivalent with 97 % formation. This was also evident by the lack of change observed in the absorption titration from 0.45 - 0.6 equivalents.

Binding constants obtained from the fitting of the fluorescence titration of **5** are similar, although slightly larger than previous PDA systems (**1-3**) (Table 4.2) for all three binding constants. Comparison to similar PDC systems is limited, with only **L^{39}** and **L^{41}** (Figures 2.29-30) having reported values.[57, 62] Both **L^{39}** and **L^{41}** have smaller binding constants than **5**, although the latter **L^{41}** was carried out in water which can impede ligand coordination due to its competitive nature.[68] While in comparison to DPA,[69] binding constants are very similar (although once again carried out in water), indicating a similar binding capacity, even with one less anionic carboxylate.

*Table 4.2.. Binding constants from fitted experimental data for both UV-visible absorption and.. fluorescence titration of **5** vs ligands **1**,**2** and **3**,. literature PDC ligands **L^{39}**, **L^{41}** (from reference 57 and 62) and **DPA** (from reference 67).. Solvent which experiments were carried out in are shown in superscript...*

Ln(L)	UV-visible absorption			Fluorescent emission		
	Log $\beta_{1:1}$	Log $\beta_{1:2}$	Log $\beta_{1:3}$	Log $\beta_{1:1}$	Log $\beta_{1:2}$	Log $\beta_{1:3}$
^{MeCN}Eu(5)	-	-	-	9.7 ± 0.03	16.0 ± 0.03	22.6 ± 0.30
^{MeCN}Eu(1)	6.4 ± 0.02	13.1 ± 0.03	18.8 ± 0.05	6.6 ± 0.01	13.1 ± 0.01	18.9 ± 0.01
^{MeCN}Eu(2)	7.1 ± 0.02	14.4 ± 0.02	21.5 ± 0.02	8.0 ± 0.04	15.3 ± 0.06	22.0 ± 0.08
^{MeCN}Eu(3)	8.2 ± 0.03	15.3 ± 0.06	22.0. ± 0.10	8.4 ± 0.06	15.5 ± 0.10	21.8 ± 0.10
^{MeCN}Eu(L^{39}-S)	5.4 ± 0.30	11.1 ± 0.60	17.3 ± 0.4	6.2 ± 0.10	12.5 ± 0.10	17.9 ± 0.2
^{water}Eu(L^{41})	7.9 ± 0.60	14.0 ± 0.70	19.9 ± 0.70	-	-	-
^{water}Eu(DPA)	8.7± 0.30	16.8 ± 0.30	22.4 ± 0.30	-	-	-

Overall, titrations showed that the self-assembly process was retained in solution, with the 1:3 M:L species retaining its dominant formation. The binding constants of **5** compared to chapter 3 PDA based ligands are slightly larger and potentially suggests a stronger binding. However, the difference is too small to explicitly say that binding is improved from titration data, although lack of formation of the Eu(**5**)$_2$ species does indicate some resistance to deformation of the Eu(**5**)$_3$ species not previously seen. It is worth noting that titrations with no base were tested but resulted in absorption increasing upon every addition of Ln^{3+}.

4.2.4 Complexation Studies

With the confirmation that **5** still favours formation of the 1:3 M:L species, **5** was then complexed with a range of visible emissive Ln^{3+}. The selected Ln^{3+} for this purpose were Eu^{3+} (red), Tb^{3+} (green), Dy^{3+} (yellow, blue, or white dependent on antenna) and Sm^{3+} (orange), as they are known to be populated by the PDC antenna, resulting in visible Ln^{3+} centred emission.[70-73] Additionally, **5** was complexed and fully characterised with La^{3+} for the purpose of NMR studies and Tm^{3+} which was used in hope of obtaining a more definitive blue emission source, which would be useful for later mixed emission studies. Tm^{3+} emission is more commonly studied with inorganic antennas[74], but has been successful with organic antennas including the similar DPA motif[75, 76] and PDA motif,[77] although emission is very weak. [78, 79] To the best of our knowledge Tm^{3+} has not been tested with the PDC antenna. However knowing that the DPA antenna has previously worked, and the close excited energy level match of Tm^{3+} (21, 200 cm^{-1}) and Tb^{3+} (20,400 cm^{-1}), it was worth investigation.[70] The remaining two potentially visible emissive lanthanides Ho^{3+} and Pr^{3+} were not examined as their emission is typically much weaker.[73, 80]

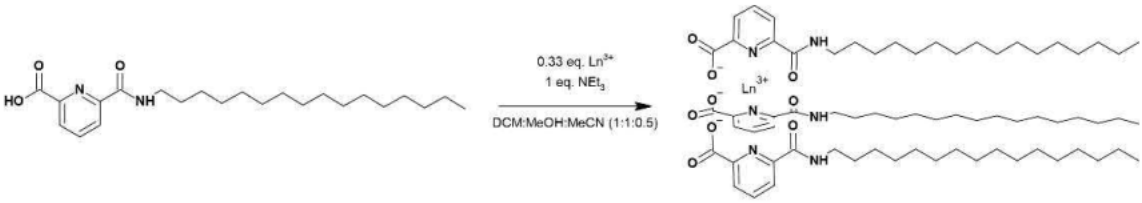

*Scheme 4.5.. Synthesis of lanthanide complexes with **5**.*

Complexes of Ln(**5**)$_3$ (where Ln = Eu^{3+}, Tb^{3+}, Dy^{3+}, Sm^{3+}, La^{3+} and Tm^{3+}) were prepared by refluxing **5** with 0.33 equivalents of lanthanide salt (either $Ln(Cl)_3 \cdot xH_2O$ or $Ln(CF_3SO_3) \cdot xH_2O$) and 1 equivalent of triethylamine in DCM:MeOH:MeCN (1:1:0.5) under microwave irradiation. The resulting clear yellow solutions were subjected to vapour diffusion of diethyl ether which resulted in off-white precipitates. Decanting off the solvent and air drying the precipitates yielded off-white solids in good yields (51 - 77%). Complex formation was confirmed by elemental analysis, HRMS, FTIR, UV-visible absorption and ^{1}H NMR (see Section 8.2.4). HRMS revealed various H and Na adducts for the 1:3 M:L species, with peak positions matching calculated peaks and isotopic distributions, as seen in Figure 4.22, Table 4.3 and Section 8.2.4.

Table 4.3. All peaks found in mass spectra associated with the 1:3 M:L species.

Complex	Calculated *m/z*	Experimental *m/z*
[Eu(**5**)$_3$ + H]$^+$	1564.8694	1564.8678
[Tb(**5**)$_3$ + H]$^+$	1570.8715	1570.8720
[Dy(**5**)$_3$ + H]$^+$	1575.8769	1575.8769
[Sm(**5**)$_3$ + H]$^+$	1606.3743	1606.3745
[Tm(**5**)$_3$ + H]$^+$	1581.8762	1581.8839
[La(**5**)$_3$ + H]$^+$	1550.8528	1550.8530

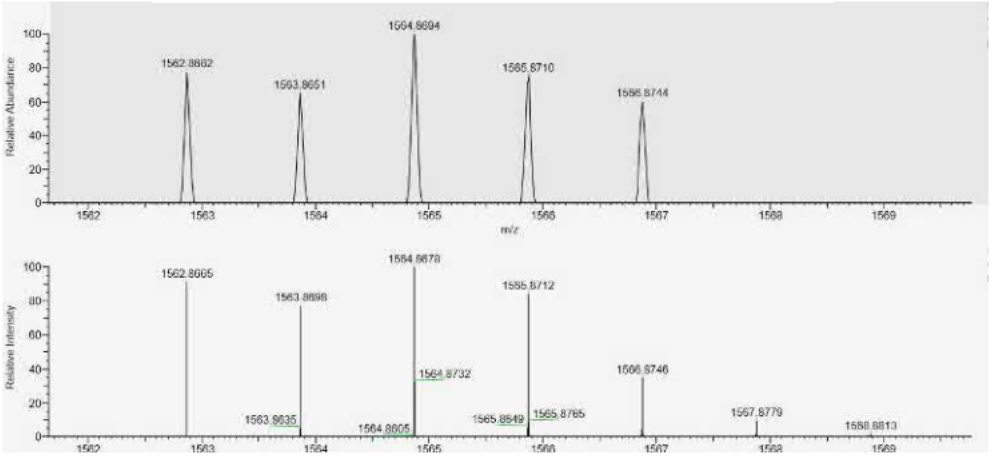

Figure 4.22. (Top) HRMS m/z = 1564.8694 [Eu(**5**)$_3$ + H]$^+$. (Bottom) Calc. for ($C_{78}H_{121}N_{15}O_9Eu$)$^+$, 1564.8678.

FTIR spectra indicated lanthanide coordination within the NO_2 pocket by the notable shift to lower energy for both the C=O stretches from 1744 cm^{-1} (carboxyl) and 1668 cm^{-1} (amide) to a merged peak at 1631 cm^{-1}, a shift commonly associated with coordination to Ln^{3+},[81] as well as a N-H band at 3345 cm^{-1} which disappears (Figure 4.23).

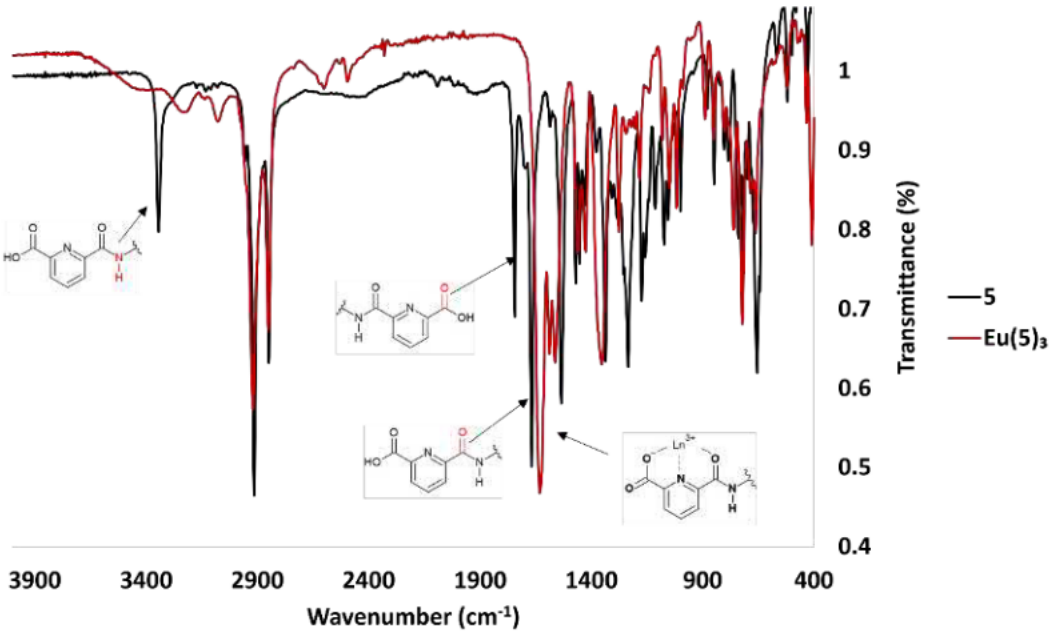

Figure 4.23. FTIR spectrum of **5** and Eu(**5**)$_3$ showing shift in carbonyl stretches upon complexation and disappearance of the N-H stretch.

^{1}H NMR of **5** and La(**5**)$_3$ shown in Figure 4.24-25 were collected in both DMSO-d_6 and $CDCl_3$:CD_3OD (9:1). Unlike previous systems in chapter 3, the competitive DMSO-d_6 solvent did not appear to dissociate the complex, an indication of the stronger binding of the PDC unit. ^{1}H NMR of La(**5**)$_3$ in both cases remains relatively sharp upon coordination to the La^{3+} and retains the same number of proton environments as present in the ligand, indicating that there is likely only one species present in the solution. ^{1}H NMR of La(**5**)$_3$ in $CDCl_3$:CD_3OD (9:1) shows downfield shifts in the NH amide and pyridyl *para* proton, shifted approximately 0.3 ppm (0.6 ppm in DMSO-d_6) and 0.07 ppm respectively, characteristic of the La^{3+} removing electron density from the pyridine ring. This is suggestive of coordination occurring in the NO_2 binding pocket as expected and as seen in previous PDA systems.[82, 83] Furthermore no major shift is noted in the remaining peaks (bar the NH-CH_2 upfield shift associated with the downfield shift of the NH) especially the 1,2,3-triazole proton, indicating La^{3+} coordination is likely only occurring within the NO_2 pocket. It is worth noting that the downfield shifts caused by coordination to La^{3+} and likely upfield shifts from deprotonation of the carbonyl result in the separation of the pyridyl proton into three distinct signals in the case of La(**5**)$_3$ in DMSO-d_6 as seen in Figure 4.25 (where in $CDCl_3$:CD_3OD (9:1) they remain separate distinct signals before complexation). This is suggestive of potential overall C_3 symmetry within the La^{3+} coordination sphere.

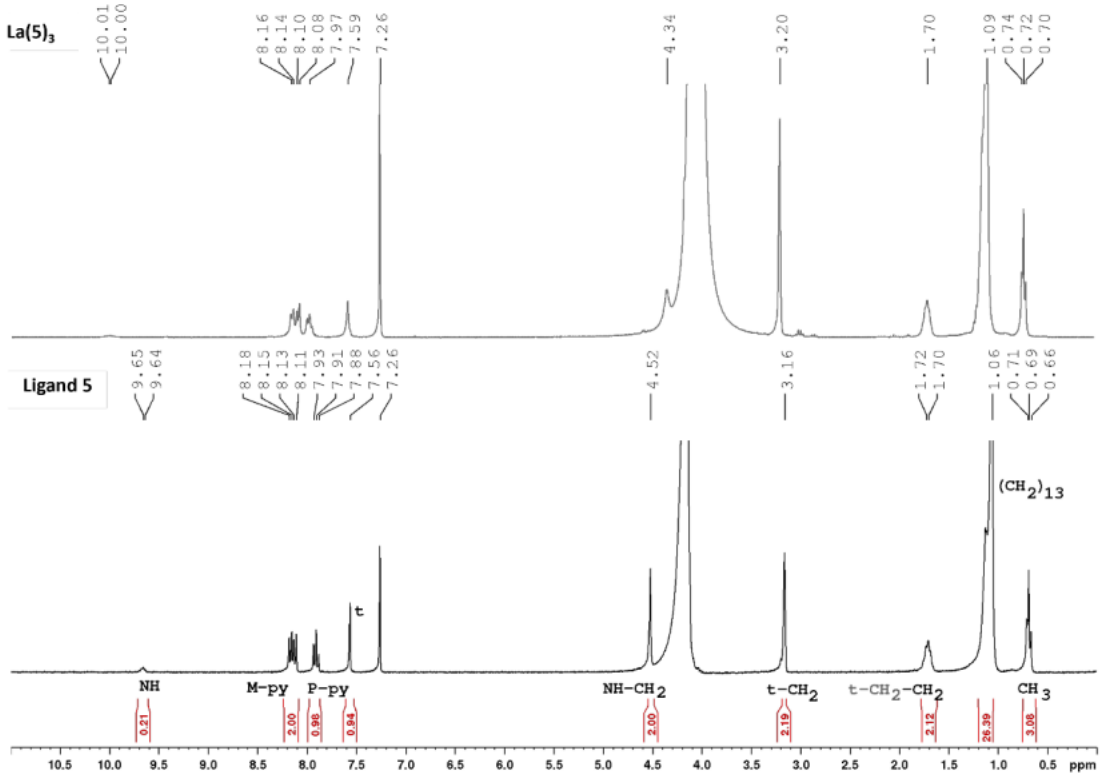

*Figure.4.24.. ^{1}H.NMR.spectrum.of.La(**5**)$_3$.(Top).and.**5**.(Bottom).(300.MHz,.$CDCl_3$.&.CD_3OD)..Abbreviation.py.for.central.pyridyl.ring.with P.for.para.and.M.for.meta.positions,.t.for.1,2,3-triazole.ring.and.x-CH_2.indicates.the.CH_2.coordination.to.an.identifiable.group.x..*

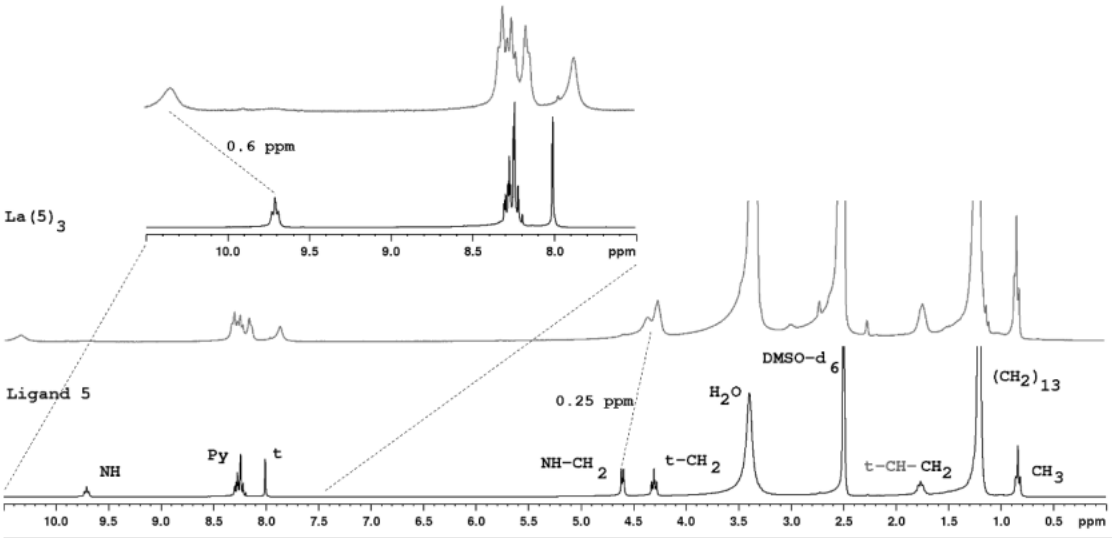

*Figure 4.25. Zoom in of ^{1}H NMR spectrum of La(**5**)$_3$ (Top) and **5** (Bottom) (300 MHz, DMSO-d_6) with insert showing splitting of pyridyl peaks. 1,2,3-triazole proton does shift upfield in DMSO-d_6 but is an indication of electron density increase, potentially from interaction with solvent; an interaction with La^{3+} would likely result in a downfield shift, as discussed. Abbreviation py for central pyridyl ring with P for para and M for meta positions, t for 1,2,3-triazole ring and x-CH_2 indicates the CH_2 coordination to an identifiable group x.*

Attempts to obtain X-ray quality crystals of the lanthanide complexes were unsuccessful, with a range of different crystallisation attempts being made. These included vapour diffusion, evaporation, pipette reactors, and recrystallisation. Since attempts to obtain X-ray quality crystals of lanthanide complexes remained elusive, ground state calculations were carried out on Tb(**5**)$_3$. The preoptimized structure of Tb(**5**)$_3$ was made based on literature crystal structures of Ln(**L^{36}**)$_3$ (where Ln = Eu^{3+}, Tb^{3+}, Gd^{3+}, Sm^{3+} and Dy^{3+}, Figure 4.26).[5, 70, 72] The resulting structure was subjected to a DFT geometry optimisation using the B3LYP[84-87] functional with a mixed basis set of 6-311G+[88] for N, H, O, C and ECP54MBW-II[89-91] with corresponding effective core potential[89, 92] for Tb^{3+} (specific to Tb^{3+}) as parameterised in Gaussian 16 software suite.[93]

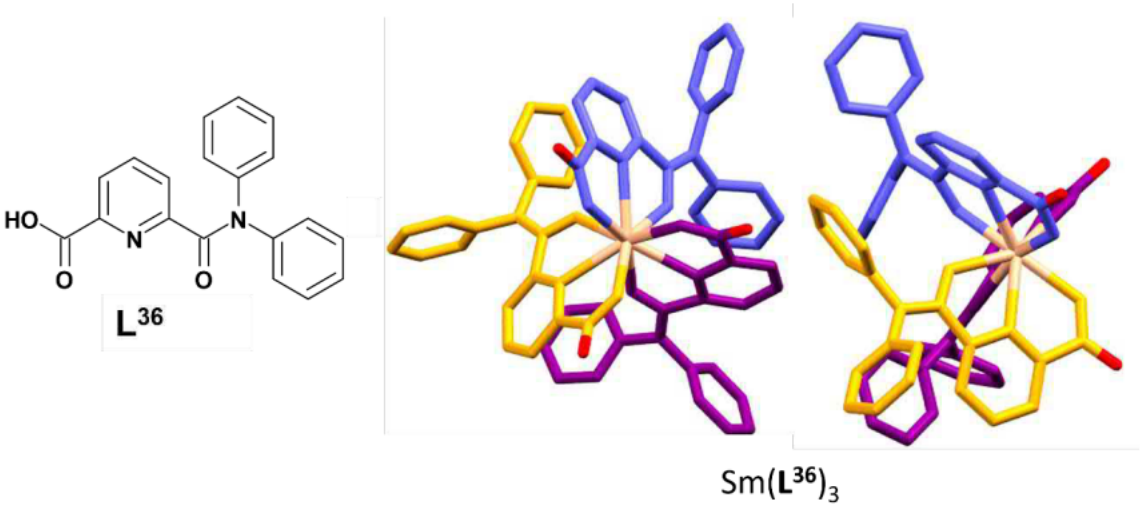

*Figure 4.26. **L^{36}** and Sm(**L^{36}**)$_3$ complex (CIF of Tb(**L^{36}**)$_3$ complex unavailable). Adapted with permission from B.-L. An, M.-L. Gong, M.-X. Li and J.-M. Zhang, J. Mol. Struct., 2004, **687**, 1-6. Copyright 2022 ELSEVIER.*

The complex calculated structures were found to maintain the tricapped trigonal prismatic geometry with an overall C_3 symmetry, and the chains remain oriented in the same direction. The Tb^{3+} was found to stay within the expected N_3O_6 coordination sphere. To verify the calculated structures the coordination lengths of Tb-N and Tb-O have been compared to available crystallographic data of a similar complex $Tb(\mathbf{L^{36}})_3$ (Figure 4.27). As seen in Table 4.4, the calculated coordination lengths and N-Ln-N angle are close to that found experimentally. It is worth noting the significant coordination length decrease in the O^- - Tb compared to =O - Tb which is to be expected, and was evidence of the improved binding of the free carboxylate.

Table 4.4.. Bond length of $Tb(\mathbf{5})_3$ in comparison to $Tb(\mathbf{L^{36}})_3$.. values obtained from reference 70..

Bond/Angle	**Calculated -** $Tb(\mathbf{5})_3$	**Experimental -** $Tb(\mathbf{L^{36}})_3$
=O - Tb^{3+}	2.617 Å	2.453 (5)
O^- - Tb^{3+}	2.307 Å	2.381 (6)
N – Tb^{3+}	2.600 Å	2.577 (6)
N-Tb^{3+}-N	120°	118.6° (5)

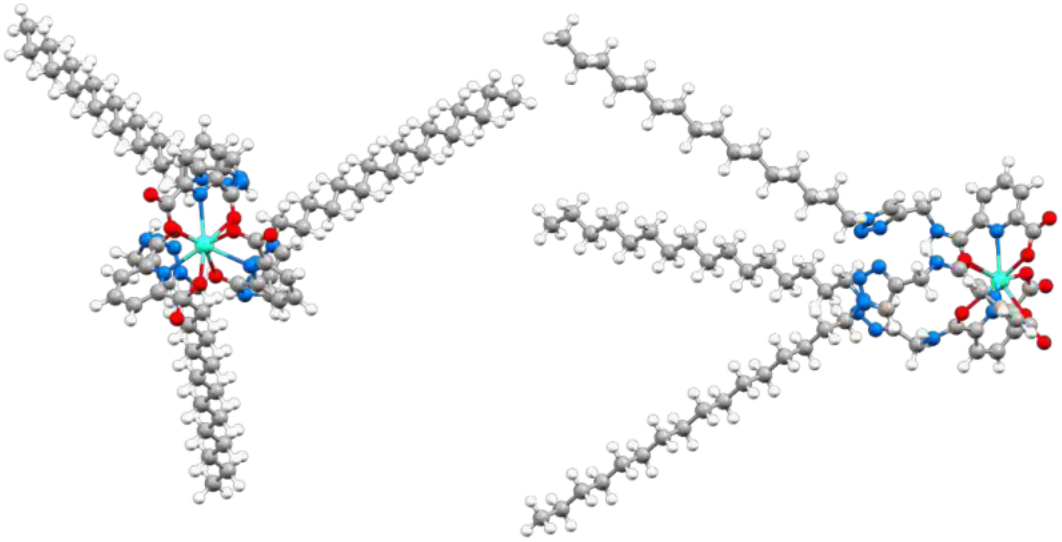

Figure 4.27.. Calculated $Tb(\mathbf{5})_3$ complex structure with C_3 symmetry..

4.2.5 Photophysical Properties of Lanthanide Complexes

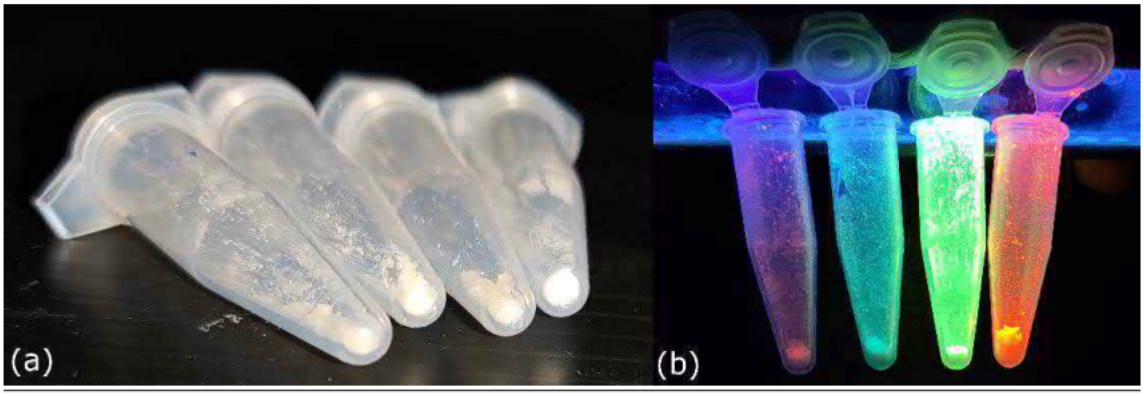

*Figure 4.28. Lanthanide complexes Ln(**5**)$_3$ (a) under ambient light and (b) under shortwave UV irradiation (λ_{ex} = 254 nm): left to right - Sm(**5**)$_3$, Dy(**5**)$_3$, Tb(**5**)$_3$ and Eu(**5**)$_3$.*

The solid lanthanide complexes exhibit strong classical lanthanide emission, as seen in Figure 4.28. The solid complexes of Eu(**5**)$_3$ (red), Tb(**5**)$_3$ (green), Dy(**5**)$_3$ (blue) and Sm(**5**)$_3$ (orange/deep red) are white powders, but in the presence of short-wave UV irradiation ($\lambda_{ex} \approx 255$ nm) are seen as bright emissive solids. As to be expected the non-emissive La(**5**)$_3$ showed no emission, and unfortunately Tm(**5**)$_3$, although had the potential to be emissive, showed no signs of emission in solid or solution-based studies.

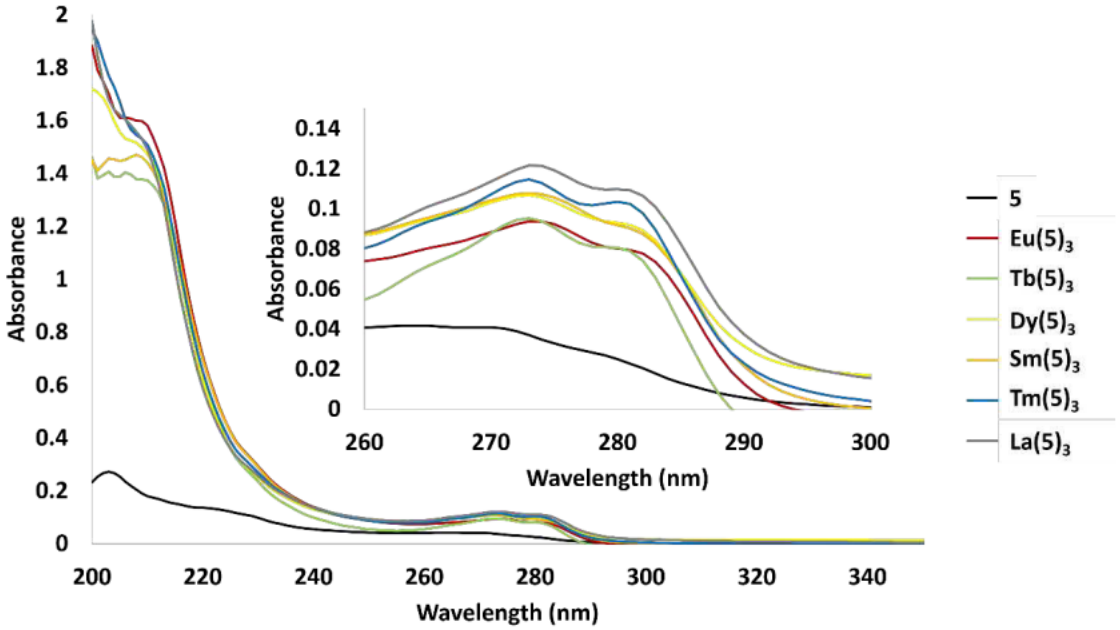

*Figure 4.29. UV-visible absorption of **5** and Ln(**5**)$_3$ where Ln = Eu^{3+}, Tb^{3+}, Dy^{3+}, Sm^{3+}, Tm^{3+}, and La^{3+} (0.01 mM, MeCN).*

Photophysical properties of **5** and all Ln(**5**)$_3$ complexes were evaluated in MeOH and MeCN solutions (0.01 mM). UV-visible absorption data is similar to results noted in chapter 3, with significant increases in absorption and a clear red shift in the pyridyl and carbonyl associated bands (shifting from 272 to 274 nm and 280 to 283 nm, Figure 4.29). Excitation spectra of all complexes were similar with two major bands at approximately 230 nm and 275 nm, as seen in

Figures 4.32-33, matching the pyridyl antenna's major absorbance regions, indicating the successful population of lanthanide excited states *via* indirect transfer process from the pyridyl antenna. Photoluminescence studies were carried out on all emissive complexes with an excitation wavelength of 275 nm. Eu(**5**)$_3$ and Tb(**5**)$_3$ both showed strong fluorescent and phosphorescent emission from Eu^{3+} with $^5D_0 \longrightarrow {}^7F_J$ (J = 0-4) and Tb^{3+} $^5D_4 \longrightarrow {}^7F_J$ (J = 6-3) transitions (Figure 4.30), both giving the overall expected deep red (CIE, x,y = 0.66, 0.34) and light green (CIE x,y = 0.30, 0.56) emission respectively (Figure 4.33). The 581 nm emission associated with the Eu^{3+} $^5D_0 \longrightarrow {}^7F_0$ transition indicates the overall symmetry of the Eu^{3+} environment is C_n or C_{nv}. For Eu(**5**)$_3$ to have an Eu^{3+} environment with C_3 or C_{3v} symmetry, the different coordinating oxygens (carbonyl and deprotonated carboxylate, which have different coordination lengths and thus strengths, Figures 4.26-47 and Table 4.4) would be required to be oriented on one side of the Eu^{3+} complex for all three ligands, further suggesting that the long chains are likely orientated in the same direction.

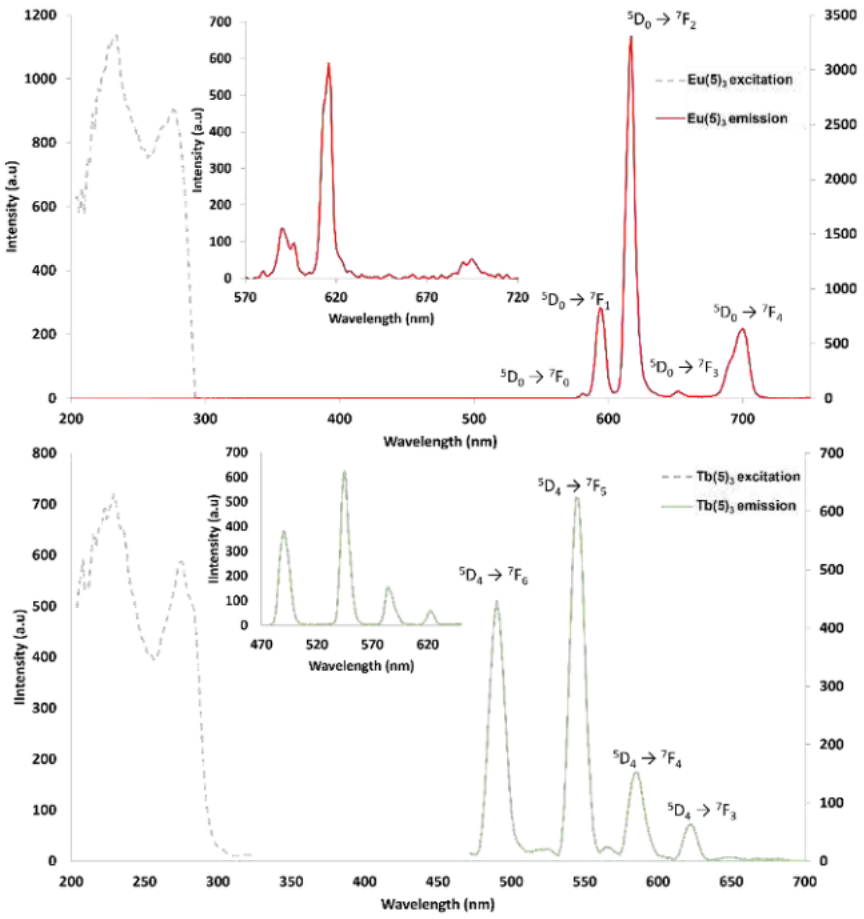

*Figure. 4.30.. Fluorescence. spectra. of. Eu(**5**)$_3$ (Top). and. Tb(**5**)$_3$ (Bottom),. with. inserts. of. phosphorescence. emission. spectra. (0.01. mM,. MeCN).. Excitation. wavelength. of. 275. nm. and. monitoring. wavelengths. for. excitation. spectra. 616. nm. and. 545. nm. respectively.*

In the case Sm(**5**)$_3$ and Dy(**5**)$_3$, fluorescent emission exhibits characteristic sharp bands assigned to the individual transitions unique to the Ln^{3+}. Unfortunately phosphorescent emission was not observable, likely associated with the much shorter lifetimes of these Ln^{3+} being in the microseconds and not the milliseconds that Eu^{3+} and Tb^{3+} exhibit.[23] The Sm(**5**)$_3$ fluorescence spectrum (Figure 4.31), showed effective population of the $^4G_{5/2}$ excited state and subsequent depopulation to ^6H_J (J = 5/2-11/2), with bands at 566 nm ($^4G_{5/2}\rightarrow{}^6H_J$), 602 nm ($^4G_{5/2}\rightarrow{}^6H_J$), 646 nm ($^4G_{5/2}\rightarrow{}^6H_J$), and 718 nm ($^4G_{5/2}\rightarrow{}^6H_J$), resulting in an overall lighter orange colour (CIE, x,y = 0.62, 0.38) (Figure 4.33).

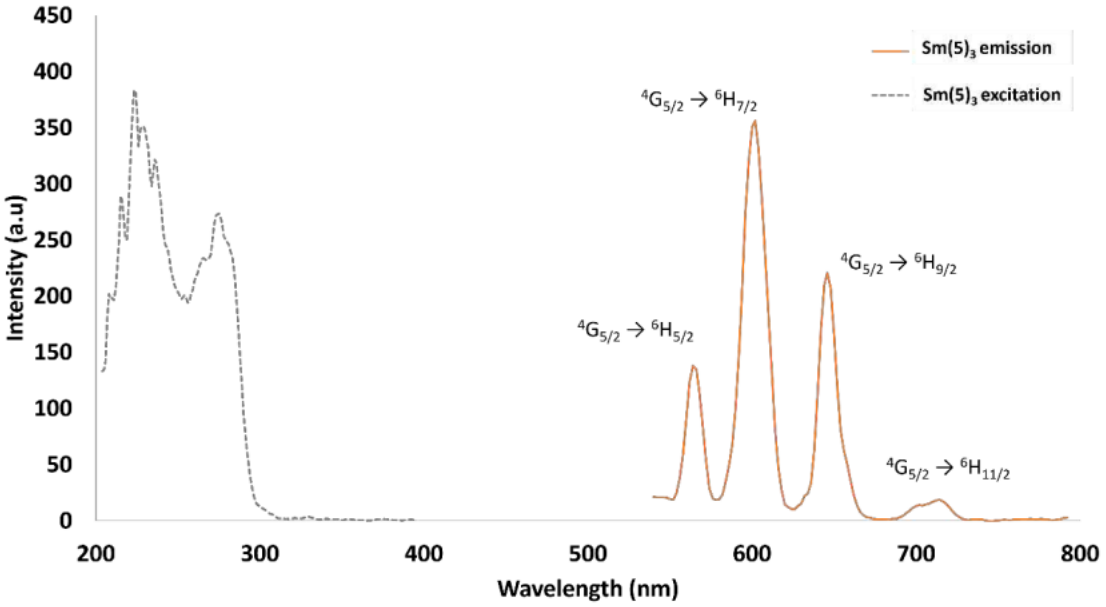

*Figure. 4.31.. Fluorescence. spectra. of. Sm(**5**)$_3$. (0.01. mM,. MeCN).. Excitation. wavelength. of. 275. nm. and. monitoring. wavelengths. for. excitation. spectrum. 602. nm..*

The Dy(**5**)$_3$ fluorescence spectrum (Figure 4.32) showed effective population of the $^4F_{9/2}$ excited state and subsequent depopulation to ^6H_J (J = 15/2 - 9/2), with bands at 480 nm ($^4G_{5/2}\rightarrow{}^6H_{15/2}$), 574 nm ($^4G_{5/2}\rightarrow{}^6H_{11/2}$), 566 nm ($^4G_{5/2}\rightarrow{}^6H_{11/2}$) and 602 nm ($^4G_{5/2}\rightarrow{}^6H_{9/2}$). Surprisingly the Dy(**5**)$_3$ complex overall emission resulted in ***single component, white*** emission. Meaning that the combination of emitting bands results in overall emission with CIE coordinates of x,y = 0.33, 0.38, which is within the white region ("pure-white" emission x,y = 0.33) of the CIE coordinate diagram (Figure 4.33).[94-96] The fact that this is achieved as a single molecule or component is impressive, as most white emission systems need either a combination of emitting components, or in most cases of single component emission, would still normally require a combination of Ln^{3+} and organic emission from the same species. This is solely achieved from the Dy^{3+} centred emission and requires no balancing of other components to achieve the single component white emission .[94]

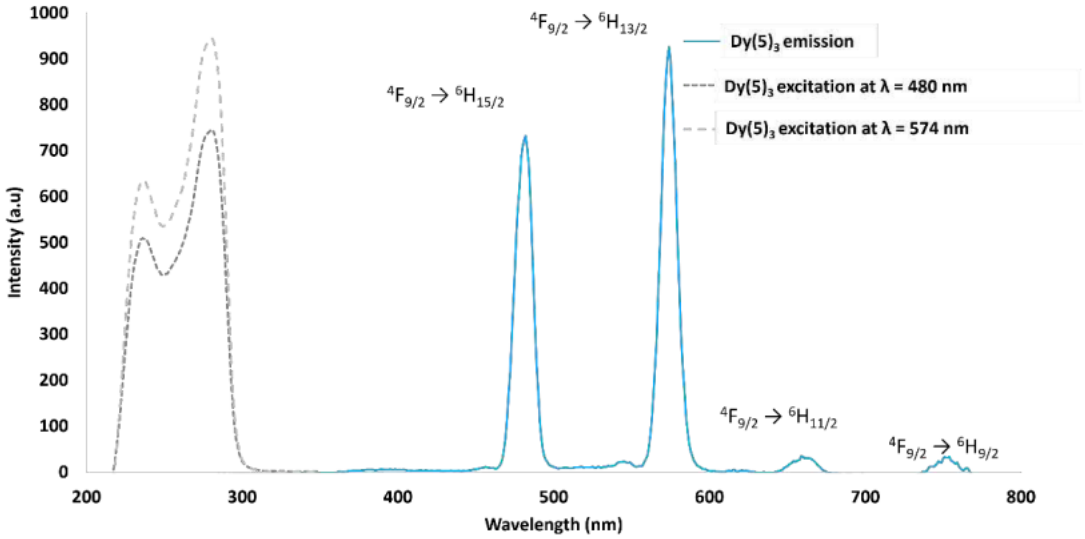

*Figure. 4.32.. Fluorescence. spectra. of. Dy(**5**)$_3$ (0.01. mM,. MeCN).. Excitation. wavelength. of. 275. nm. and. monitoring. wavelengths. for excitation. spectra. 480. and. 574. nm..*

This is not often the case with Dy^{3+} emission, however it has been previously observed.[97, 98] Through a combination of its more intense emission transitions at 480 nm (blue emissive $^4F_{9/2} \rightarrow {}^6H_{15/2}$) and 574 nm (yellow emissive $^4F_{9/2} \rightarrow {}^6H_{13/2}$) and much weaker emissions at 660 and 752 nm (red emissive $^4F_{9/2} \rightarrow {}^6H_{11/2 \text{ and } 9/2}$), close to white emission is achievable depending on the relative intensity of transitions to one another, which can be modified by the Dy^{3+} hypersensitive $^4F_{9/2} \rightarrow {}^6H_{13/2}$ (yellow) transition.[97, 98]

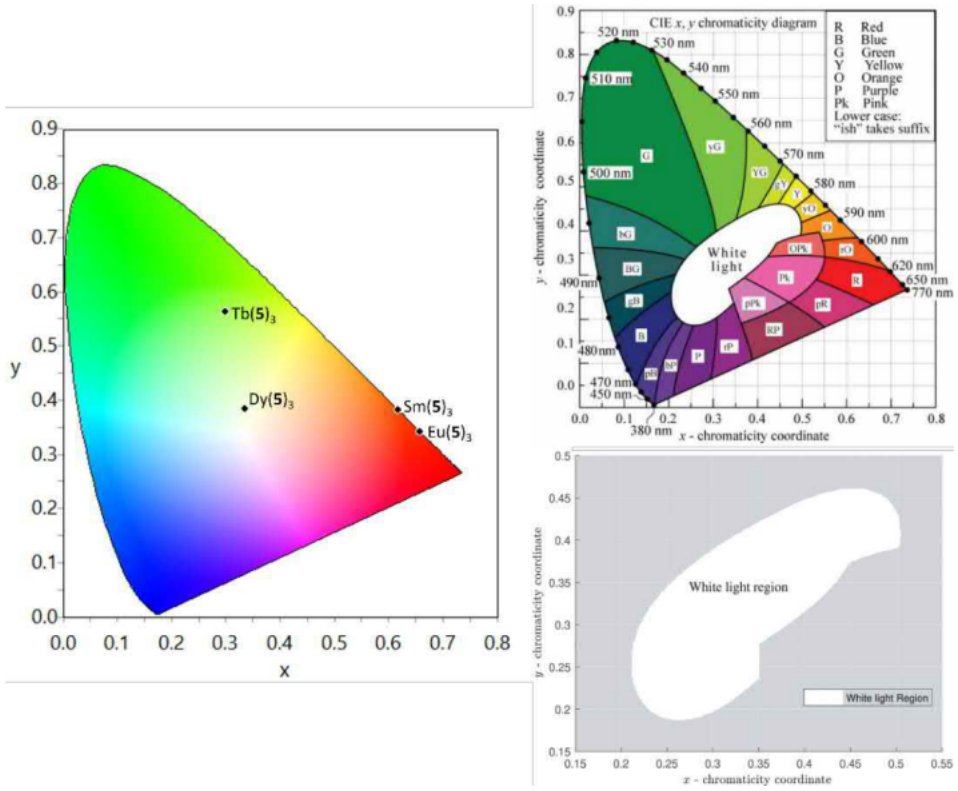

*Figure. 4.33.. (Left). CIE. 1931. chromaticity. diagram. with. calculated. CIE. coordinates. for. emissions. of. Ln(**5**)$_3$ complexes. (where. Ln. =. Eu^{3+}, Tb^{3+},. Dy^{3+}. and. Sm^{3+}). in. 0.01. mM. MeCN.. Eu(**5**)$_3$ x,y. =. 0.66,. 0.34;. Tb(**5**)$_3$ x,y. =. 0.30,. 0.56;. Dy(**5**)$_3$ x,y. =. 0.33,. 0.38. and. Sm(**5**)$_3$ x,y. =. 0.62, 0.38.. (Top. right). CIE. diagram. showing. colour. of. different. coordinates.. Image. and. caption. are. adapted. with. permission. from. E.. F. Schubert,.* Light-Emitting Diodes,. *Cambridge. University. Press,. Cambridge,. 2. edn.,. 2006.. (Bottom. right). White. light. region. of. the. CIE 1931. chromaticity. diagram;. not. all. points. within. this. region. give. "pure-white",. but. are. still. considered. as. white.. Image. and. caption adapted. from. open. access. and. CC-BY. article. from. D.. N.. Anwar. and. A.. Srivastava,.* IEEE Access,. *2020,. **8**,. 159609-159621..*

These lanthanide complexes were much more emissive than the PDA based ligands of chapter 3. The overall quantum yields (Φ_{Ln}^{L}) of the emissive lanthanide complexes were calculated by the "dilute method"[99] in MeOH by comparing to $Cs_3[Eu(dpa)_3]\cdot 8H_2O$ and $Cs_3[Tb(dpa)_3]\cdot 8H_2O$ standards and excited at 279 nm. Eu(**5**)$_3$ and Tb(**5**)$_3$ were compared to their own lanthanide standard, whereas Dy(**5**)$_3$ and Sm(**5**)$_3$ were compared to both and averaged.[100] Eu(**5**)$_3$ was initially measured in both MeOH and MeCN to determine the best solvent to use. Surprisingly Eu(**5**)$_3$ in MeOH was found to be more emissive than in MeCN, 22 % vs 12 %. This was rather surprising as this is normally reversed, due to the vibronic relaxation which the O-H bond of MeOH can exert on the Ln^{3+}. This can be seen in the observed lifetimes (τ_{obs}) with Eu(**5**)$_3$ having a slightly shorter lifetime in MeOH (1.442 ms) than in MeCN (1.888 ms). Calculation of the radiative lifetimes (τ^{rad}) in both solvents resulted in similar values as expected, but there is a large difference in the sensitisation efficiency (n_{sens}). This correlates with the much better Φ_{Ln}^{L} observed in MeOH. This large difference is likely from Eu(**5**)$_3$ being less soluble in MeCN, with the complex likely precipitating out during measurements which would cause the yields to decrease by light scattering resulting in re-absorption processes.[101] Because of this, the remainder of the complexes were only measured in MeOH giving Φ_{Ln}^{L} of 14 %, 2.9 %, and 0.32 % for Tb(**5**)$_3$, Dy(**5**)$_3$ and Sm(**5**)$_3$ respectively.

*Table 4.5. Overall quantum yields (Φ_{Ln}^{L}), observed lifetimes (τ_{obs}), calculated radiative lifetimes (τ^{rad}), intrinsic quantum yields (Φ_{Ln}^{Ln}), and sensitisation efficiency (n_{sens}) of Ln(**5**)$_3$ complexes. Solvent which measurements were run in are shown in superscript.*

Complex	Φ_{Ln}^{L} (%)	τ_{obs} (ms)	τ^{rad} (ms)	Φ_{Ln}^{Ln} (%)	n_{sens} (%)
^{MeOH}Eu(**5**)$_3$	22	1.442	4.570	31.55	71
^{MeCN}Eu(**5**)$_3$	12	1.888	4.402	42.89	28
^{MeOH}Tb(**5**)$_3$ ($^5D_4 \rightarrow {}^7F_5$)	14	0.984	-	-	-
^{MeOH}Dy(**5**)$_3$ ($^4F_{9/2} \rightarrow {}^6H_{13/2}$)	2.9	-	-	-	-
^{MeOH}Sm(**5**)$_3$ ($^4G_{5/2} \rightarrow {}^6H_{7/2}$)	0.32	-	-	-	-

Comparing Eu(**5**)$_3$ and Tb(**5**)$_3$ to previous PDA ligands in chapter 3, it is clear that the PDC based antenna is a better suited antenna for both Ln^{3+}, although it is significantly better for Eu^{3+} with Eu(**5**)$_3$ having an approximately 5 times larger quantum yield than the largest observed in chapter 3 (Φ_{Ln}^{L} = 4.3 % for [Eu(**1**)$_3$](CF$_3$SO$_3$)$_3$). In the case of Tb^{3+}, quantum yields are slightly improved with an increase to 14 % from previous highest value (Φ_{Ln}^{L} = 13 % for [Tb(**1**)$_3$](CF$_3$SO$_3$)$_3$), although lifetimes are slightly shorter. The large difference between Eu(**5**)$_3$ and Tb(**5**)$_3$ indicates that the triplet state of the ligand is much more suited for Eu^{3+} centred emission. DFT calculations of **5** using the same conditions as in chapter 3 further confirm this with a calculated triplet energy level of 22,698 cm^{-1} (close to that of measured triplet of **L^{36}**, being 20,477 cm^{-1}), which is within range for potential BT from Tb^{3+} (20,500 cm^{-}), potentially reducing Tb(**5**)$_3$ Φ_{Ln}^{L}.

Table 4.6.. Overall quantum yields (Φ_{Ln}^{L}) and observed lifetimes (τ_{obs}) of other PDC and DPA based Eu^{3+} and Tb^{3+} complexes.. Values obtained from references 5,. 57,. 71 and 102.. Solvent which measurements were run in are shown in superscript..

Complex	Φ_{L}^{Ln} (%)	τ_{obs} (ms)
$^{EtOH}Eu(\mathbf{L^{36}})_3$	12	0.69 ± 0.01
$^{EtOH}Eu(\mathbf{L^{37}})_3$	15	1.67 ± 0.01
$^{MeCN}Eu(\mathbf{L^{39}})_3$ **R**	8.2	1.94 ± 0.01
$^{MeCN}Eu(\mathbf{L^{39}})_3$ **R**	8.4	1.94 ± 0.01
^{MeCN} $Eu(\mathbf{L^{40}})_3$ **R**	2.1 ± 0.1	1.86 ± 0.02
$^{MeCN}Eu(\mathbf{L^{40}})_3$ **S**	1.6 ± 0.3	1.94 ± 0.01
$^{Water}Cs_3Eu(\mathbf{DPA})_3 \cdot 8H_2O$	24 ± 2.5	-
$^{EtOH}Tb(\mathbf{L^{37}})_3 \cdot 4H_2O$	34	1.31
$^{Water}Cs_3Tb(\mathbf{DPA})_3 \cdot 8H_2O$	22 ± 2.5	-

Comparing overall quantum yields of Ln(**5**)$_3$ to previous PDC[5, 57, 71] and DPA[102] based antennas, Eu(**5**)$_3$ is found to have a larger Φ_{Ln}^{L} than all previous $[Eu(PDC)_3]^{3+}$ complexes and is close to the Φ_{Ln}^{L} of $Cs_3[Eu(\mathbf{DPA})_3]$[102] while Tb(**5**)$_3$ Φ_{Ln}^{L} are found to be less (Table 4.6). There appears to be no reported PDC ligands with quantum yields of Dy^{3+} or Sm^{3+} emission and only one for the PDA motif (**L^6**, Figure 2.4),[77] which has reported quantum yields for both Dy^{3+} and Sm^{3+} complexes (Table 4.7). Comparing the PDC based antenna of **5** to PDA based **L^6**, it can be seen that Dy(**5**)$_3$ has a much better Φ_{Ln}^{L} than $[Dy(\mathbf{L^6})]^{3+}$, while Sm(**5**)$_3$ is only slightly better than $[Sm(\mathbf{L^6})]^{3+}$, although still poor overall. Compared to DPA based antennas, Dy(**5**)$_3$ Φ_{Ln}^{L} is found to be nearly the same as $[Dy(\mathbf{DPA})_3]^{3+}$.[76] While an example of $[Sm(\mathbf{DPA})_3]^{3+}$ could not be found, a similar Sm(**L^{44}**)$_3$ (Figure 4.34)[103] results in a similar rather low quantum yield (0.05 %) suggesting Sm(**5**)$_3$ Φ_{Ln}^{L} may be relatively high for a DPA derivative. It should be noted that Sm(**5**)$_3$ Φ_{Ln}^{L} is not out of the range of Φ_{Ln}^{L} that Sm^{3+} complexes are capable of. With Φ_{L}^{Ln} ranging around 10 to 0.01 % with a range of organic based antenna.[104] Sm(**5**)$_3$ is on the lower end of this scale, potentially due to a poor triplet state energy match with **5** (22,698 cm^{-1}) and Sm^{3+} excited state (17,800 cm^{-1}).[105]

Table 4.7.. Overall quantum yields (Φ_{Ln}^{L}) of other PDA and DPA based Dy^{3+} and Sm^{3+} complexes. Values obtained from references 76, 77 and 103.. Solvent which measurements were run in are shown in superscript..

Complex	Φ_{Ln}^{L} (%)
$^{MeCN}[Dy(\mathbf{L^6})_3]^{3+}$	0.1
$^{water}[Dy(\mathbf{DPA})_3]^{3-}$	2.9
$^{MeCN}[Sm(\mathbf{L^6})_3]^{3+}$	0.024
$^{water}[Sm(\mathbf{L^{44}})_3]^{3-}$	0.05

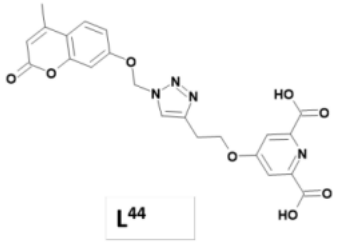

L^{44}

*Figure 4.34.. Molecular structure of **L^{44}** from reference 103..*

Overall, **5** is an impressive antenna which can populate the excited state of four different Ln^{3+} resulting in impressive visible emission in both solution and solid state (Figure 4.35). With high quantum yields for most Ln^{3+}, and the knowledge that the system is definitely forming the 1:3 M:L species and the orientation of the chains are likely in sync, these systems looked promising for the next step of materials formation by LB deposition.

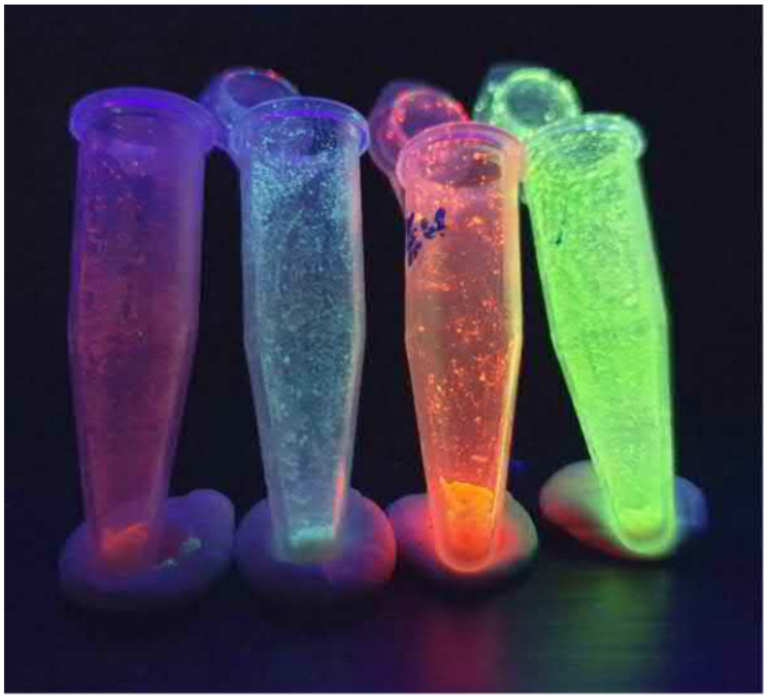

Figure 4.35. Lanthanide complexes $Ln(\mathbf{5})_3$ under shortwave UV irradiation (λ_{ex} = 254 nm): left to right - $Sm(\mathbf{5})_3$, $Dy(\mathbf{5})_3$, $Eu(\mathbf{5})_3$ and $Tb(\mathbf{5})_3$

4.2.6 Langmuir-Blodgett Studies

Next, the ability of **5** and the Ln(**5**)$_3$ complexes to self-assemble at an air-water interface and form Langmuir films was investigated. Initially an isotherm of **5** was measured by depositing 20 mL of a 1 mg/mL solution in $CHCl_3$:MeOH (20:1), onto the surface of a water sub-phase on the Langmuir trough, at r.t. A compression (surface-pressure vs area) isotherm of **5** was run three times. **5** can be seen to form a classic Langmuir isotherm shape close to other single alkyl chain molecules. The isotherms experience an exponential increase in surface pressure upon decrease of the trough area as expected. In this case, the Langmuir film of **5** collapses at a surface pressure of 53 mN m^{-1} and at ≈ 20 Å^2/molecule, which is the expected area for a single alkyl chain.[32, 106, 107] Unlike the example shown in the introduction (Section 4.1), distinction between phase changes is a little bit more difficult to accurately assign, but there is a clear difference in the stages from gas (G) to liquid (L) starting at ≈ 30 Å^2/molecule and from liquid (L) to solid (S) state with a gradient change at ≈ 25 Å^2/molecule as seen in Figure 4.36.

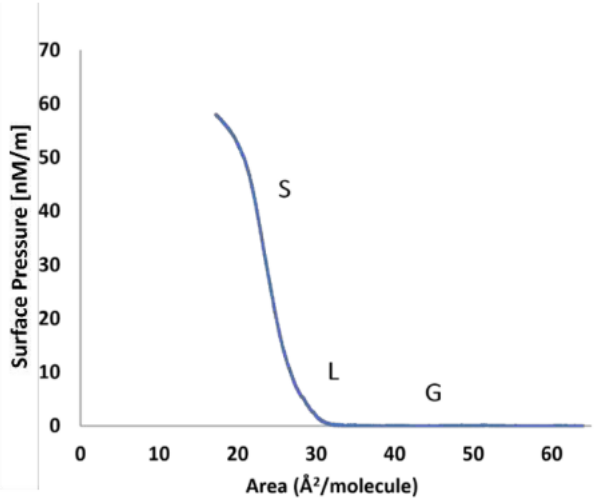

*Figure 4.36.. Surface area – pressure isotherms of **5**..*

Compression isotherms of Ln(**5**)$_3$ complexes were run under the same conditions as **5**. Compression isotherms between complexes are near identical as seen in Figure 4.37, indicating that the complexes are similar, despite the difference in Ln^{3+}. The films collapsed at 53 – 59 mN m^{-1} with molecular areas of 75 – 81 Å^2. The stability of the Langmuir films was also evaluated by keeping the monolayers at a fixed area (the liquid-condensed phase, 30 mN m^{-1}) for prolonged periods of time (> 60 min) while monitoring the surface pressure. All complexes displayed excellent stability profiles with insignificant change occurring over the course of more than an hour, giving the ideal situation for film deposition.

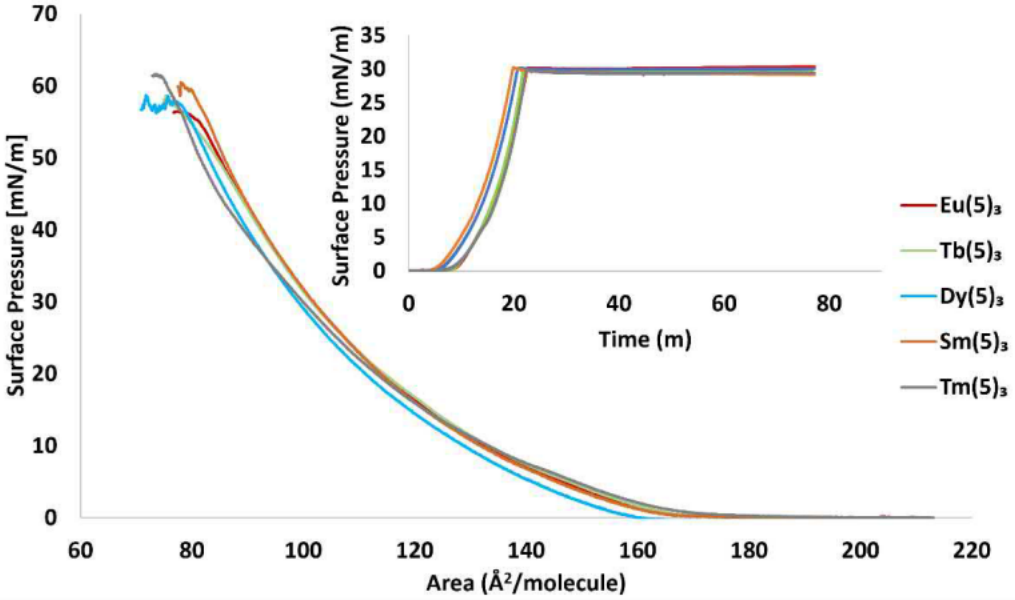

*Figure 4.37.. Surface area – pressure isotherms of Ln(**5**)$_3$ (where Ln. = Eu^{3+}, Tb^{3+}, Dy^{3+}, Sm^{3+} and La^{3+}).. Insert:: stability measurements held at 30 mN.m^{-1} for over 60 minutes..*

4.2.6.1 Monolayer Film Deposition

Langmuir-Blodgett deposition was then carried out using the four emissive lanthanide complexes, Ln(**5**)$_3$ (where Ln^{3+} = Eu^{3+}, Tb^{3+}, Dy^{3+} and Sm^{3+}), on a square quartz slide (30 mm x 30 mm, 1 mm thick) which had been cleaned by nitric acid, piranha solution, and milli-Q water, before being placed 20 mm into the subphase. Monolayer Langmuir films were formed at the air-water interface by performing a compression isotherm until a surface pressure of 30 mN m^{-1} was reached. The monolayer Langmuir films were then deposited onto the quartz slide by ***emersion*** of the slides from the water sub-phase, resulting in **Z**-type deposition as seen in Figure 4.6.[10] Successful transfer of the molecular units was monitored by measuring the change in trough area (between barriers) as the quartz substrate was removed from the water subphase (Figure 4.38). TR values have been calculated taking into account the transfer onto both sides of the substrate and the edges of the slide, giving an overall area to cover of 1270 mm^2, for all monolayer films this has resulted in ≈ 1 TR (for example, TR = 1335 mm^2 /1270 mm^2 = 1.05 for Eu(**5**)$_3$, 1.04 for Tb(**5**)$_3$, and 1.01 for both Dy(**5**)$_3$ and Sm(**5**)$_3$).

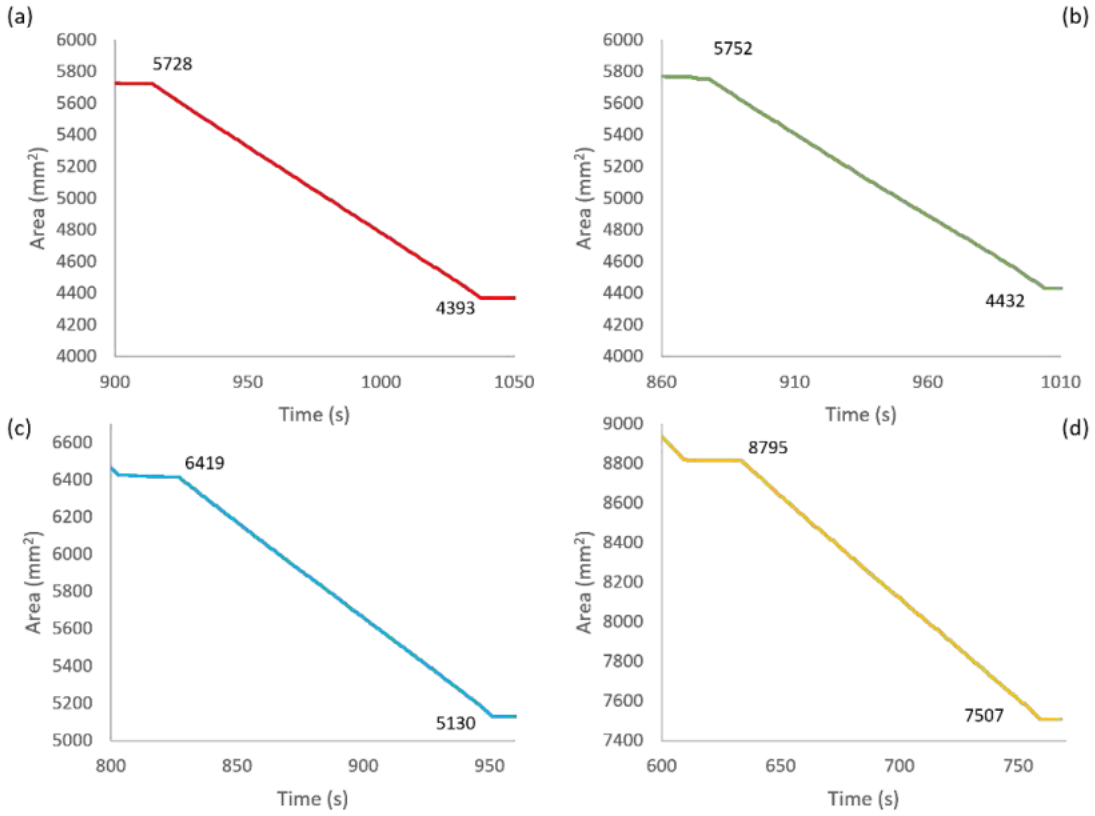

*Figure 4.38.. LB deposition plot of area of trough (between barriers) (mm) vs time (s),, showing trough area decrease of approximately 1300 mm during deposition.. (a) Eu(**5**)$_3$,. (b) Tb(**5**)$_3$,. (c) Dy(**5**)$_3$,. and (d) Sm(**5**)$_3$..*

Successful transfer was also confirmed and characterised by photophysical measurements including UV-visible absorption, emission studies and X-ray photoelectron spectroscopy (XPS) (see Section 8.2.6 and 8.2.7). However, the most obvious confirmation of successful deposition was by placing the substrates under a UV-lamp (Figure 4.39). When viewing the films, in the absence of UV there appears to be no film present on the surface of the substrate, but when subjected to short wave irradiation (λ_{ex} = 254 nm) all four films can be seen to give bright visible emission from a **single monolayer** of the complexes.

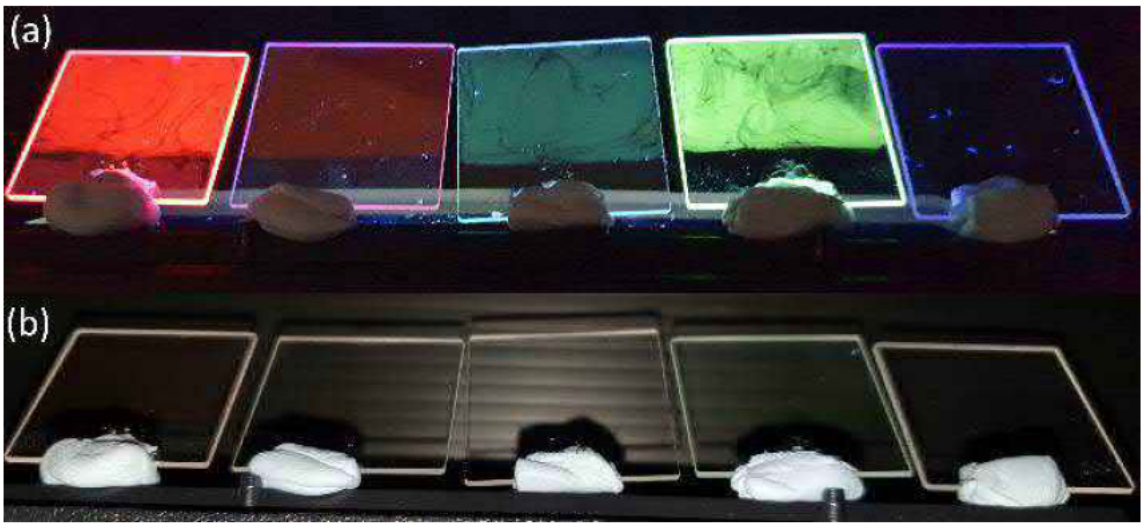

*Figure 4.39.. LB films of Ln(**5**)$_3$. (where Ln = Eu^{3+}, Tb^{3+}, Dy^{3+} and Sm^{3+}) shown under shortwave UV irradiation (a, λ_{ex} = 254 nm) and ambient light (b).. From left to right LB films are Eu(**5**)$_3$, Sm(**5**)$_3$, Dy(**5**)$_3$, Tb(**5**)$_3$ and a blank slide..*

Photophysical properties of the LB films were found to be similar or near identical in terms of photophysical features as solution measurements. UV-visible absorption spectra of the monolayer films (Figure 4.40) show distinct absorption bands ranging from 260 to 280 nm, associated with the pyridyl centre, and the 220 nm band associated with the carbonyl groups. Furthermore, UV-visible absorption intensity is similar for each film, which is to be expected if all films have the same monolayer character.

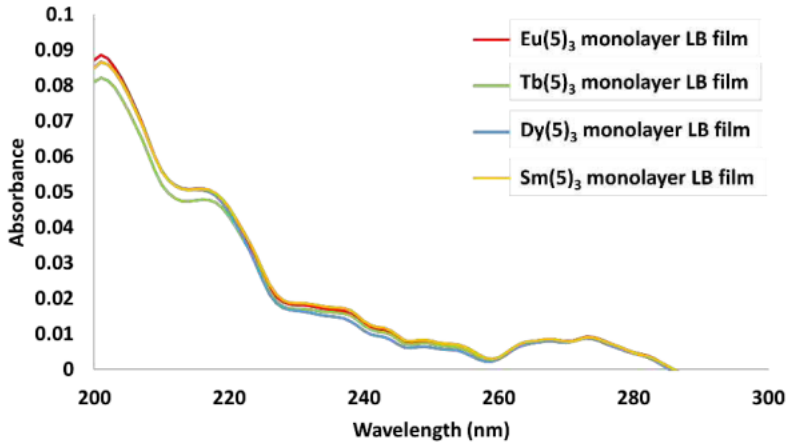

Figure 4.40.. UV-visible absorption spectra of LB films..

Fluorescence and phosphorescence (for Eu(**5**)$_3$ and Tb(**5**)$_3$) spectra are practically identical to that of the measured emissions in solution as seen in Figures 4.41-42, with Eu(**5**)$_3$ ($^5D_0$ -^7F_J, J=1-4), Tb(**5**)$_3$ ($^5D_4$ -^7F_J, J = 6-3), Dy(**5**)$_3$ ($^4F_{9/2}$ -^6H_J, J = 5/2-11/2), and Sm(**5**)$_3$ ($^4G_{5/2}$ -^6H_J, J = 5/2-11/2) exhibiting the expected emission bands. This also results in the overall emission being similar to solution studies (Figure 4.43). It is worth noting that Dy(**5**)$_3$ retains its **single component, white** emission on the surface as a **LB film**, with CIE coordinates of x,y =0.34, 0.39. Excitation spectra of all LB films are similar to in solution and indicated population of the Ln^{3+} via the pyridyl antennas as expected. Lifetimes of the Eu(**5**)$_3$ and Tb(**5**)$_3$ monolayer LB films have also been measured, with averaged lifetimes of 1.396 ms and 1.552 ms respectively. Both emission decays are best fit to a single exponential decay, indicative of only one emissive species present on the single monolayer LB film indicating that the Ln^{3+} are all found in the same chemical environment. These conclusions are supported by XPS measurements discussed below.

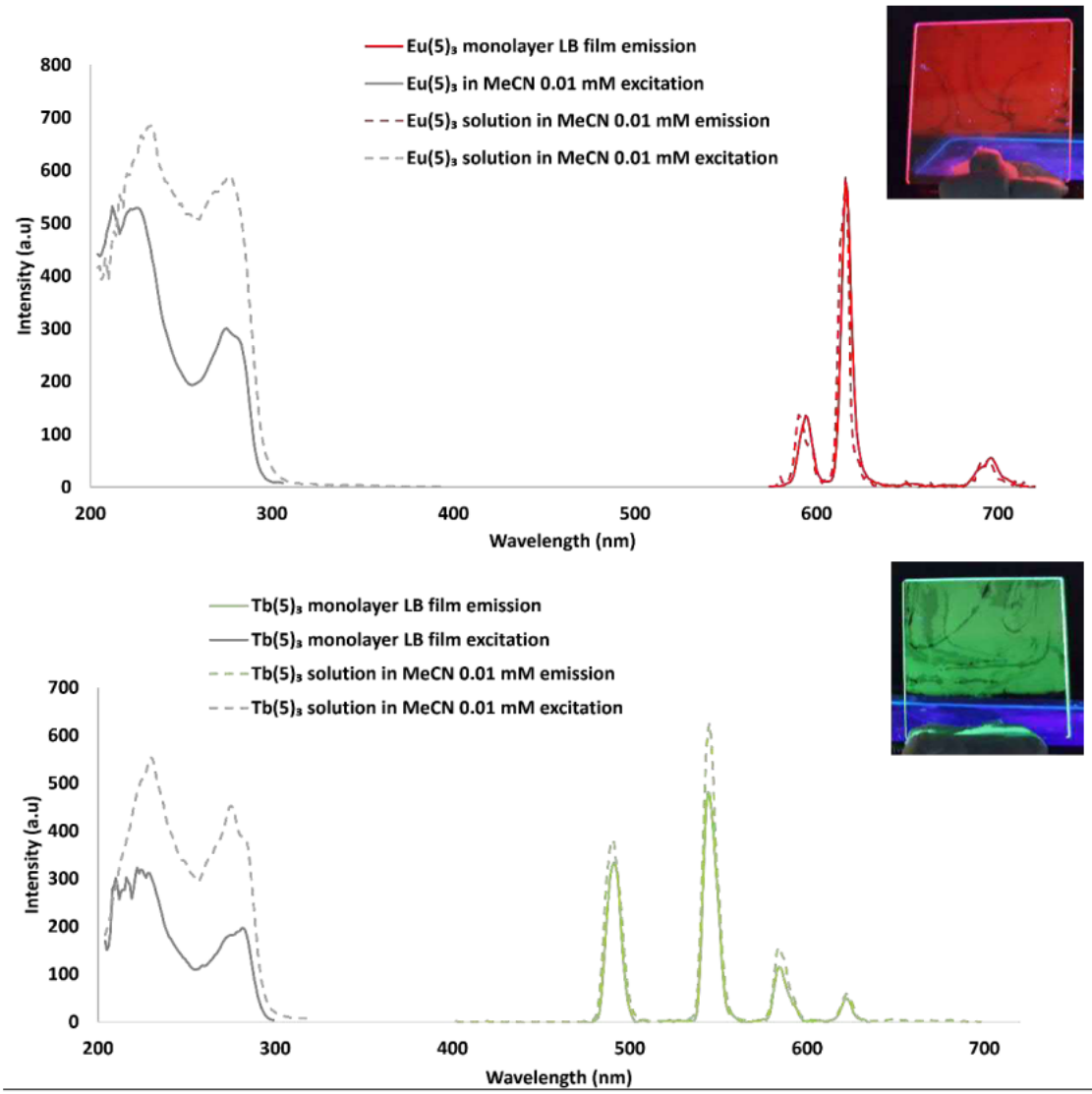

*Figure 4.41.. Phosphorescence emission and excitation plots of Eu(**5**)$_3$ (Top) and Tb(**5**)$_3$ (Bottom) of both LB films (solid lines) and in solution MeCN (0.01 mM) (dashed line).. Inserts:: images of the monolayer LB films of Eu(**5**)$_3$ (Top) and Tb(**5**)$_3$ (Bottom)..*

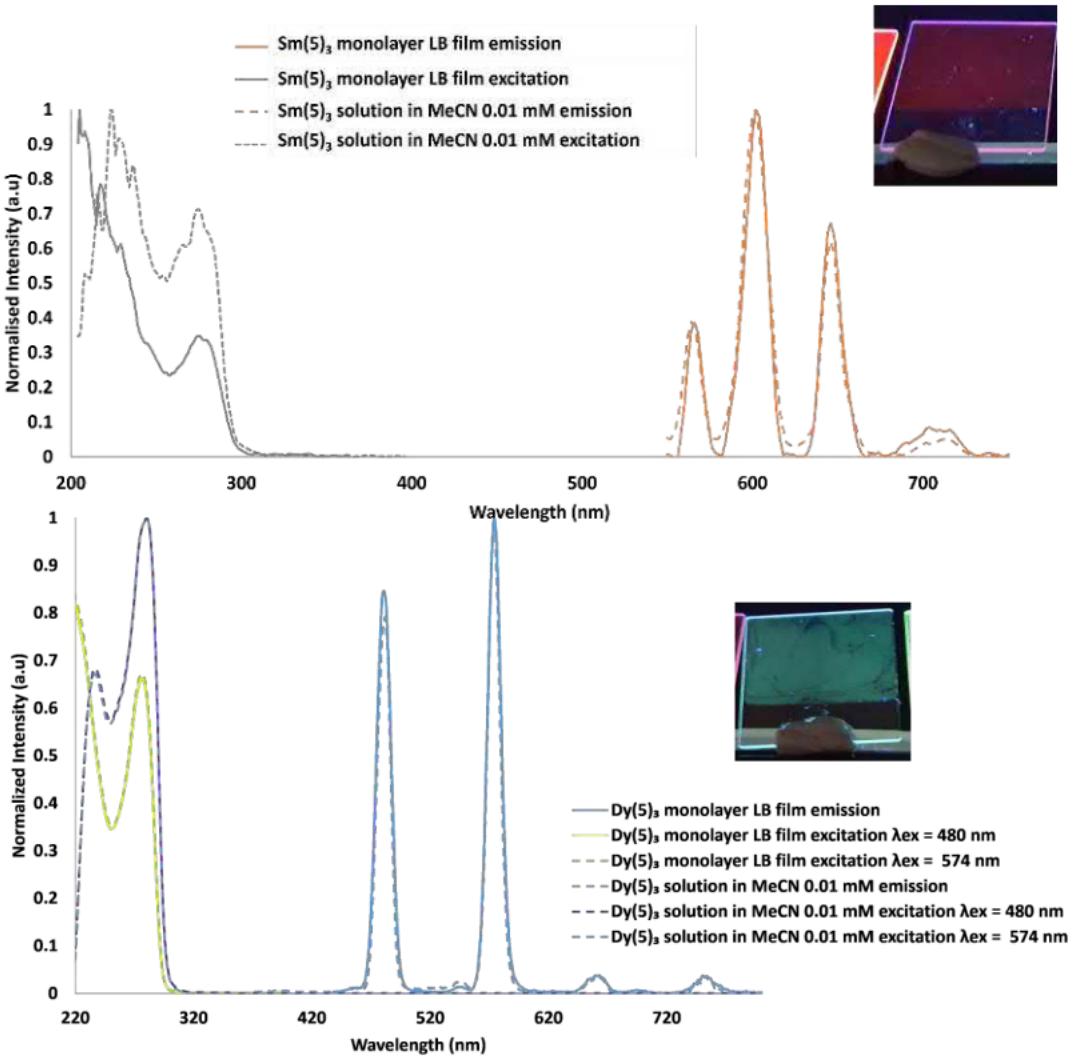

*Figure 4.42.. Phosphorescence emission and excitation plots of Sm(**5**)$_3$ (Top) and Dy(**5**)$_3$ (Bottom) of both LB films (solid lines except for an excitation plot of Dy(**5**)$_3$ at 574 nm for visibility) and in solution MeCN (0.01 mM) (dashed line).. Inserts:: images of the monolayer LB films of Sm(**5**)$_3$ (Top) and Dy(**5**)$_3$ (Bottom)..*

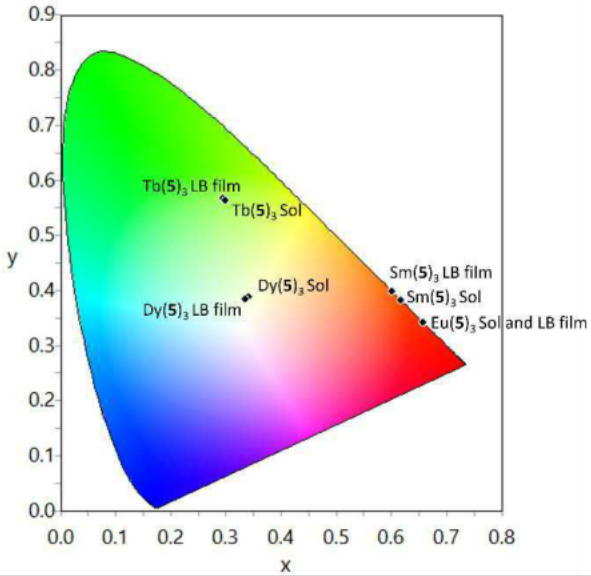

*Figure 4.43.. CIE 1931 chromaticity diagram with calculated CIE coordinates for both LB film and solutions (abbreviated to Sol) emissions of Ln(**5**)$_3$ complexes (where Ln = Eu^{3+}, Tb^{3+}, Dy^{3+} and Sm^{3+}).. Eu(**5**)$_3$ LB film x,y = 0.66, 0.34 and solution x,y = 0.66, 0.34; Tb(**5**)$_3$ LB film x,y = 0.30, 0.57 and solution x,y = 0.30, 0.56; Dy(**5**)$_3$ LB film x,y = 0.34, 0.39 and solution x,y = 0.33, 0.38 and Sm(**5**)$_3$ LB film x,y = 0.60, 0.40 and solution x,y = 0.62, 0.38...*

To confirm the atomic composition of the LB films, XPS measurements were performed. Survey scans revealed the presence of O, N and C on all films associated to the presence of **5** on the surface. Importantly for all monolayer films, distinct peaks associated with the $3d_{3/2}$ and $3d_{5/2}$ binding energy bands for all four individual Ln^{3+} were identified and matched to literature energy levels,[108-110] seen in Table 4.8, Figure 4.45 and Section 8.2.7. Core level scans were carried out for all lanthanide bands regions, resulting in definitive and clear sharp peaks associated with the $3d_{3/2}$ and $3d_{5/2}$, as seen in the inserts in Figures 4.45 and 8.2.79-82. The only other significant peaks observable in the survey scans were Si associated with the quartz substrates. In the case of Eu(**5**)$_3$, Tb(**5**)$_3$ and Sm(**5**)$_3$ monolayer films, by comparing relative signal area of the $3d_{5/2}$ peak associated with the Ln^{3+} to N 1s peak, and accounting for differences in photoelectron escape depths, a ratio of approximately 1:15 (Ln^{3+}: N) was obtained (0.781:15 Eu^{3+}:N, 0.845:15 Tb^{3+}:N and 0.939:15 Sm^{3+}:N). This indicates the presence of the 1:3 M:L species on the surface of the LB films, as **5** contains 5 N atoms so the 1:3 complex is expected to contain a 1:15 (Ln^{3+}: N) ratio (Figures 8.2.87-89). Unfortunately, this was unable to be carried out with Dy(**5**)$_3$, as the CasaXPS library was unable to assign the Dy^{3+} peaks.

Table 4.8.. XPS binding energies measured from monolayer films compared to expected literature values from references 108-110..

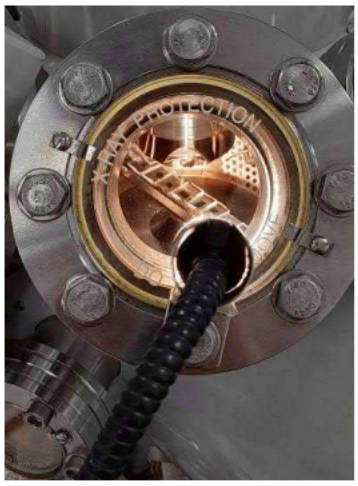

Monolayer LB Film	Binding energy observed (eV)	Binding energy expected (eV)
Eu(**5**)$_3$	$3d_{3/2}$ = 1165 $3d_{5/2}$ = 1135	$3d_{3/2}$ = 1166 $3d_{5/2}$ = 1135
Tb(**5**)$_3$	$3d_{3/2}$ = 1177 $3d_{5/2}$ = 1142	$3d_{3/2}$ = 1176 $3d_{5/2}$ = 1141
Dy(**5**)$_3$	$3d_{3/2}$ = 1334 $3d_{5/2}$ = 1297	$3d_{3/2}$ = 1333 $3d_{5/2}$ = 1296
Sm(**5**)$_3$	$3d_{3/2}$ = 1107 $3d_{5/2}$ = 1080	$3d_{3/2}$ = 1108 $3d_{5/2}$ = 1081

Figure 4.44.. XPS vacuum chamber window showing LB slides inside..

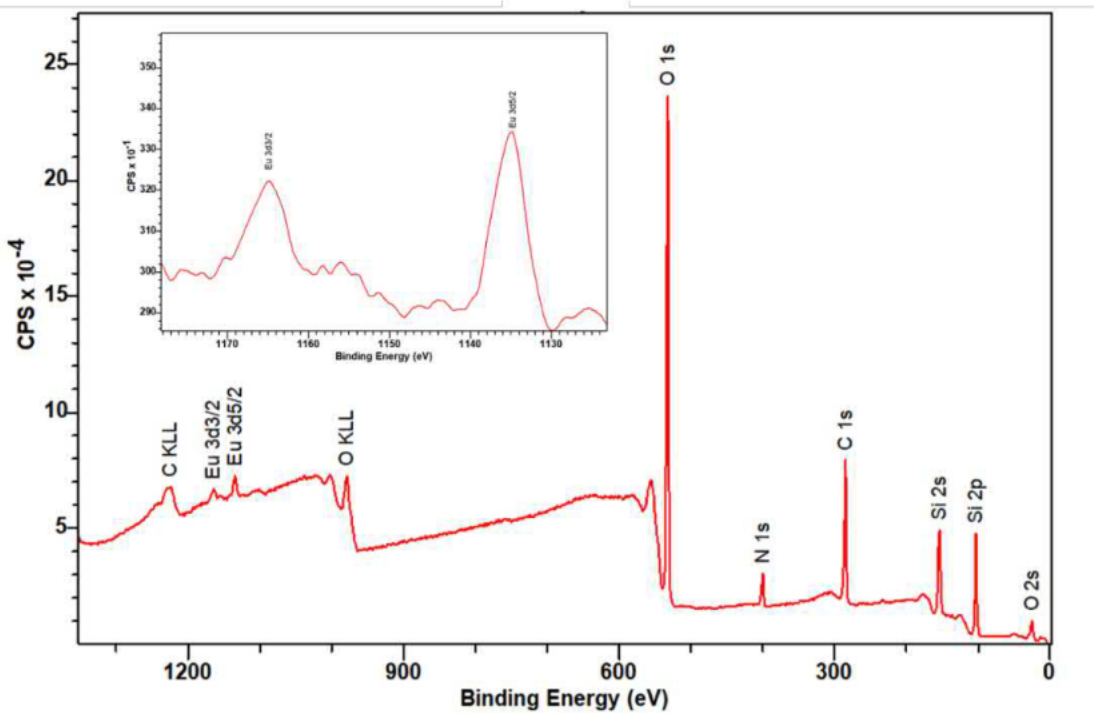

*Figure 4.45.. Survey scan XPS spectrum of Eu(**5**)$_3$ monolayer LB film.. Insert:. core level scans..*

It is also worth noting that due to COVID lockdowns pausing the study, the stability of the LB films was able to be investigated. LB monolayer films were found to remain relatively unchanged after 6 months following deposition as seen in Figure 4.46. The films appear to be nearly identical with no major signs of the film being removed and they retain emissive properties with no sign of quenching.

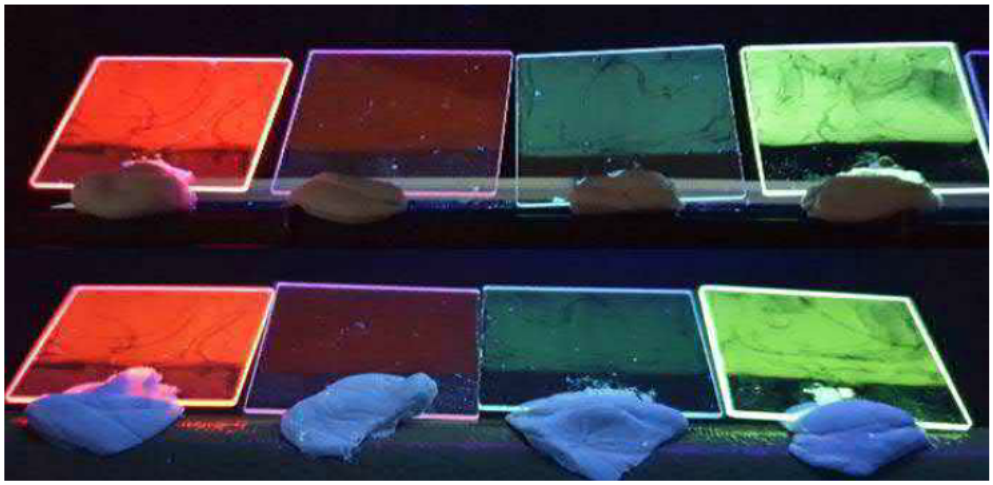

Figure 4.46.. (Top) LB films fresh after deposition and (Bottom) LB films 6 months after initial deposition..

4.2.6.2 Multilayer Film Deposition

The ability for the complexes to form multilayer LB films was investigated to see if multilayer deposition was possible with this system, but also whether this resulted in a significant enhancement of emission intensity. This was carried out only with Eu(**5**)$_3$ as it had the best emission properties.

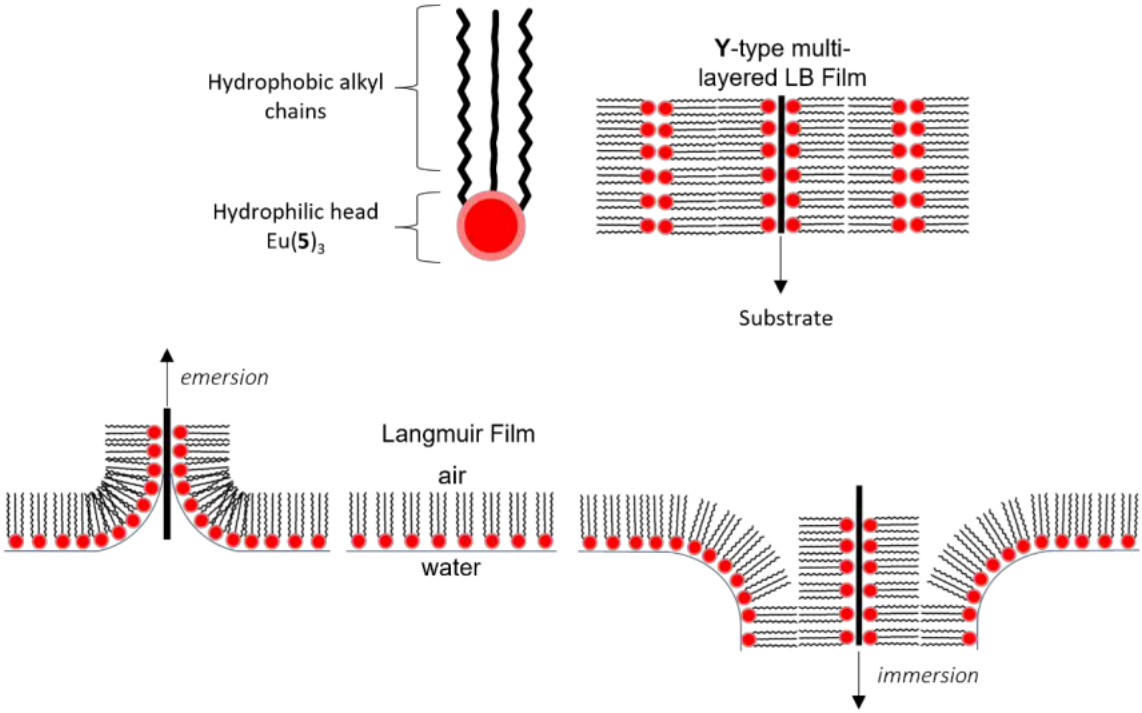

*Figure 4.47. Diagram shows Eu(**5**)$_3$ as an amphiphilic molecule, which has formed a **Y**-type LB film, by emersion and immersion Blodgett deposition of the Langmuir film.*

Multilayer LB deposition was carried out such that formation of **Y**-type multilayer films were formed,[10] which entails deposition occurring during ***emersion*** (*E*) and ***immersion*** (*I*) of the substrate, giving films with a tail-tail, head-head orientation as seen in Figure 4.47. Four Eu(**5**)$_3$ based LB films were produced with this method, starting with an ***emersion*** deposition like the **Z**-type monolayer films. A monolayer film 1 (1:0, *E:I,)* along with multilayered films of 3 (2:1, *E:I)*, 5 (3:2, *E:I)* and 7 (4:3, *E:I)* layers were produced, seen in Figure 4.48, and have been characterised by UV-visible absorption and fluorescent and phosphorescent emission.

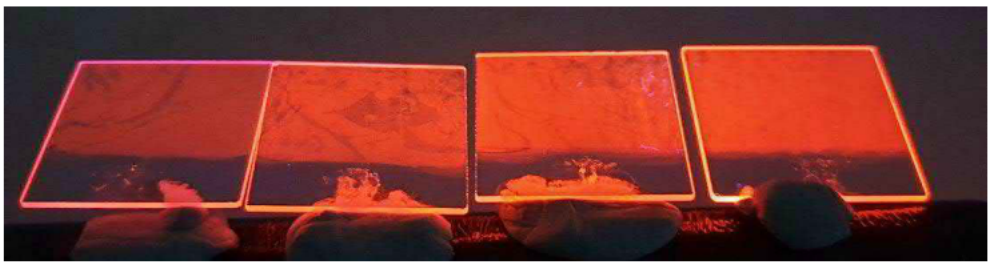

*Figure 4.48. Image of monolayer and multilayered LB films of Eu(**5**)$_3$ with 1, 3, 5, and 7 layers from left to right.*

The multilayered slides in Figure 4.48 appear to be more uniform across the film as more layers are added, but when looking at the deposition plots this is found to be untrue. All LB films showed deposition by ***emersion*** resulting in TR of approximately 1, which was unaffected by whether it was the first or last ***emersion*** of the substrate; whereas deposition by ***immersion*** resulted in lower TR of approximately 0.5, which slightly increased to approximately 0.7 as more layers were added to the substrate. This results in the multilayered films being relatively non-uniform **Y**-type LB films.

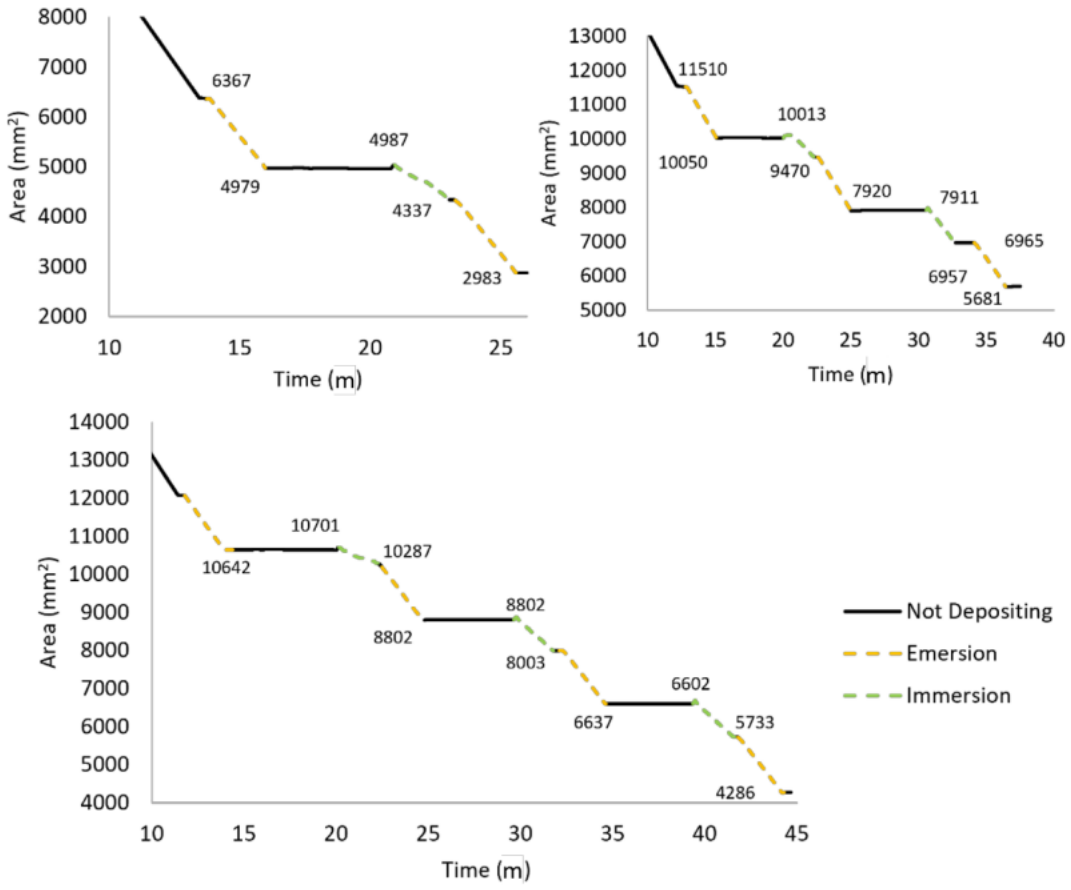

*Figure 4.49.. Deposition plots of multilayer Eu(**5**)$_3$ (Top, left). 3 layered film, (Top right). 5 layered film and (Bottom). 7 layered film..*

LB films of Eu(**5**)$_3$ are strongly emissive as a single monolayer film, but as to be expected, both fluorescent (Figure 8.2.63) and phosphorescent emissions, and UV-visible absorption (Figure 4.50) are observed to increase as more layers are added. Additionally, FTIR measurements were now possible on the multilayered films, which was not possible on the monolayered films (as the LB films were not thick enough). An additional multilayer Eu(**5**)$_3$ film (8 layers, **Y**-type) was deposited onto a CaF_2 slide for the specific purpose of FTIR characterisation. The FTIR spectrum of the film seen in Figure 4.51 showed distinct bands associated with the C=O stretch at 1638 cm^{-1}, notably in the region associated with the complex and not the base ligand, further indicating that the complex remains intact on deposition (Table 4.9).

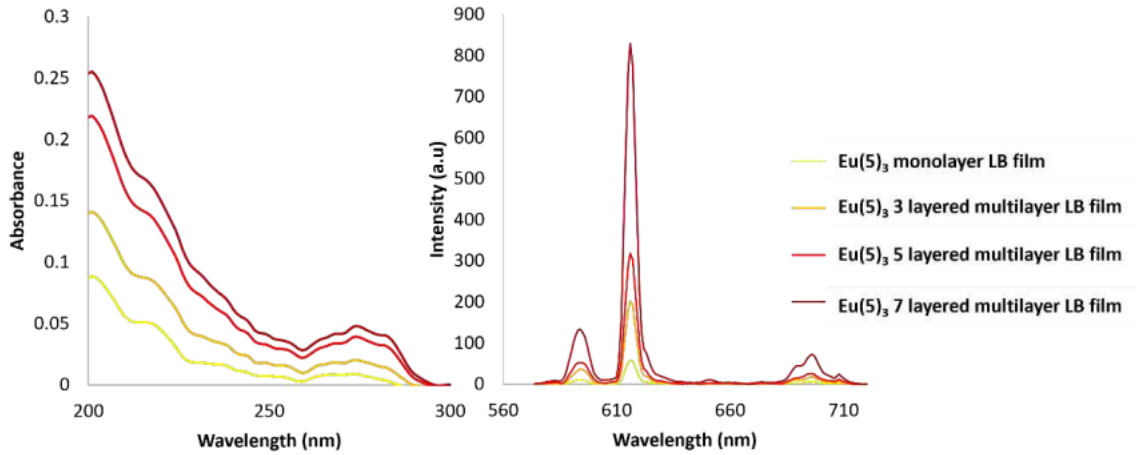

*Figure 4.50.. UV-visible absorption (Left) and phosphorescence emission spectra (Right) of multilayered Eu(**5**)$_3$ films..*

*Table 4.9.. IR stretches observed in LB film of Eu(**5**)$_3$ compared to IR stretches of solid **5** and Eu(**5**)$_3$ complex..*

IR stretch	Solid 5	Solid Eu(5)$_3$	LB Film Eu(5)$_3$
CH_2 (cm^{-1})	2919 and 2849	2919 and 2849	2919 and 2850
C=O (cm^{-1})	1744 and 1668	1631	1638

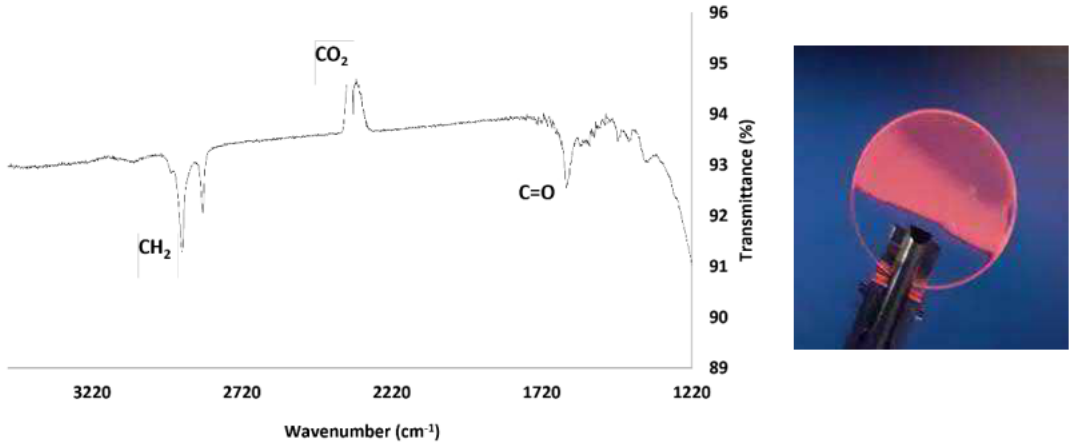

*Figure 4.51.. (Left) FTIR spectrum of 8 layered Eu(**5**)$_3$ LB film on CaF_2 slide.. (Right) 8 layered Eu(**5**)$_3$ LB film on CaF_2 slide..*

4.2.7 Mixed Lanthanide Studies

The results from initial investigation of these amphiphilic Ln(**5**)$_3$ complexes have shown both promising lanthanide based photoluminescence properties with high overall quantum yields, and impressive visible emission both in solution and in solid state. Moreover, the complexes are able to easily form uniform monolayer LB films that have high transfer ratios and retain their impressive photoluminescence properties. The next stage of this study was to look into the potential to form mixed LB films that might result in multi-emissive films, with the potential for tunable emission dependent on the ratio of different lanthanide emissions. As stated in the introduction (Section 4.1) this is a relatively novel and unexplored property in lanthanide-based LB films.

4.2.7.1 Mixed Multilayer Film Deposition

Initially mixed LB films were produced by multilayering LB films as it was thought to maximise emission intensity. From multilayering of the Eu(**5**)$_3$ complex it was clear that **Y**-type multilayering would not result in uniform films, but **Z**-type multilayering (Figure 4.52) from only ***emersion*** deposition had potential for uniform films in terms of higher TR.[10] This would require a full trough reset between deposition (unlike **Y**-type films), but as seen in Table 4.10, this additional step resulted in TR values which are suggestive of a complete film transfer independent of which layer is being deposited and indicates an overall more uniform multilayer film.

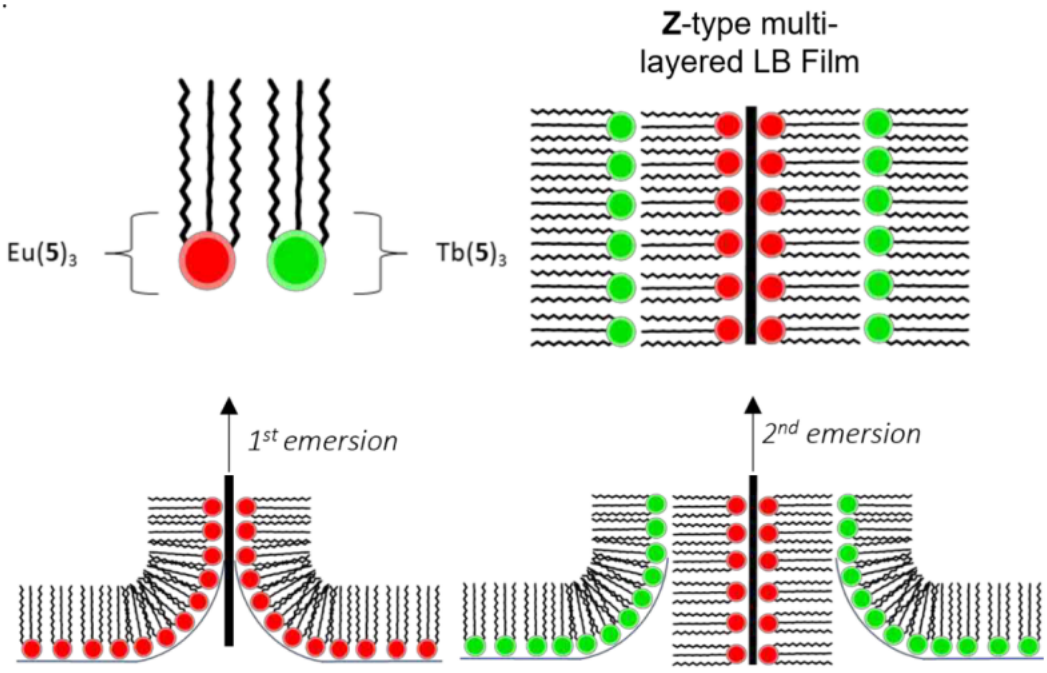

*Figure. 4.52.. Diagram. shows. the. multilayering. **Z**-type. mixed. LB. film,. with. an. example. of. an. initial. Eu(**5**)$_3$ emersion. followed. by. a. 2nd emersion. of. Tb(**5**)$_3$ resulting. in. the. Eu(**5**)$_3$:. Tb(**5**)$_3$ multilayer. film..*

As seen in Table 4.10, only three multilayered mixed LB films were produced, these being Eu(**5**)$_3$:Tb(**5**)$_3$ and Eu(**5**)$_3$:Dy(**5**)$_3$, with a total of 2 layers and Eu(**5**)$_3$:Tb(**5**)$_3$:Dy(**5**)$_3$ with a total of 3 layers. Deposition order was determined by emission intensity, in order to maximise the emission from the less emissive Ln(**5**)$_3$ complexes, minimizing any potential inner filter effect or re-absorption that could occur in the encompassed lower layers. The resulting multilayered **Z**-type LB films as expected show bright emission when excited by shortwave UV irradiation and showed a new overall emission colour, as a result of the combination of different Ln^{3+} emissions as seen in Figures 4.57.

Table 4.10.. Transfer ratios of mixed multilayer LB films..

LB film	1st emersion TR	2nd emersion TR	3rd emersion TR
Eu(**5**)$_3$:Tb(**5**)$_3$	1.07	1.16	
Eu(**5**)$_3$:Dy(**5**)$_3$	1.01	1.03	
Eu(**5**)$_3$:Tb(**5**)$_3$:Dy(**5**)$_3$	1.05	1.09	1.13

The Eu(**5**)$_3$:Tb(**5**)$_3$ multilayered film as seen in Figure 4.53 resulted in overall yellow emission as a result of the Eu^{3+} red and Tb^{3+} green emissions. Such combinations have previously given yellow colours when these Ln^{3+} are combined.[111] The fluorescence spectrum revealed that indeed both Ln^{3+} emit from the same slide, showing all expected transitions: Eu^{3+} ($^5D_0 \rightarrow {}^7F_{1\text{-}4}$) and Tb^{3+} ($^5D_4 \rightarrow {}^7F_{6\text{-}3}$), with the weaker Tb^{3+} ($^5D_4 \rightarrow {}^7F_{4\text{-}3}$) merging with more emissive Eu^{3+} ($^5D_0 \rightarrow {}^7F_{1\text{-}2}$). It is also worth noting Eu(**5**)$_3$ emission is slightly stronger than Tb(**5**)$_3$ as expected from quantum yield results (see Section 4.2.5).

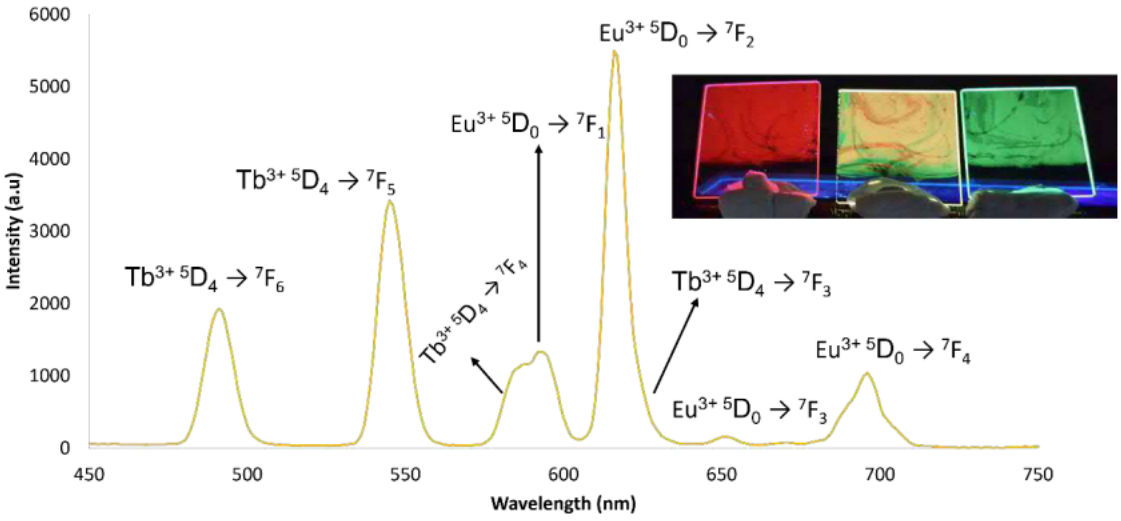

*Figure 4.53.. Mixed multilayered Eu(**5**)$_3$:Tb(**5**)$_3$ LB film fluorescence spectrum showing both Ln^{3+} distinct emission transitions.. Insert: image is Eu(**5**)$_3$:Tb(**5**)$_3$ mixed multilayered film in the centre with a monolayer Eu(**5**)$_3$ film on the left and Tb(**5**)$_3$ on the right under shortwave UV irradiation (λ_{ex} = 254 nm)..*

The Eu(**5**)$_3$:Dy(**5**)$_3$ multilayered film showed a similar result with the overall film emission tuned to a lighter red from the combination of emitting Ln^{3+}. The fluorescence spectrum showed the expected distinct peaks for Ln^{3+} as seen in Figure 4.54 showing emission from both complexes on the slide, but this time it is heavily dominated by the much stronger emitting Eu(**5**)$_3$ complex with Dy(**5**)$_3$ weaker transitions ($^4F_{9/2} \rightarrow {}^6H_{11/2\ \&\ 9/2}$) being nearly undetectable.

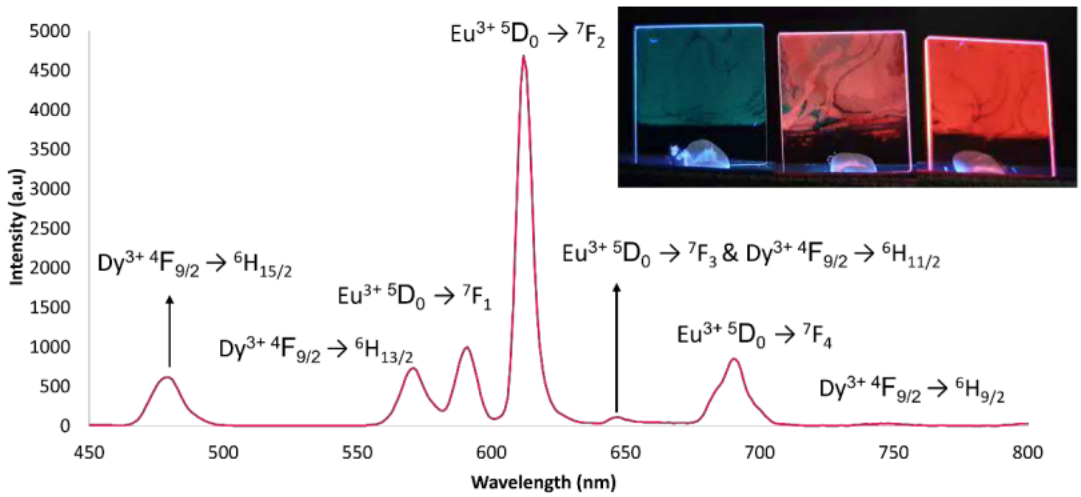

*Figure. 4.54.. Mixed. multilayered. Eu(**5**)$_3$:Dy(**5**)$_3$ LB. film. fluorescence. spectrum. showing. both. Ln^{3+}. distinct. emission. transitions.. Insert: image. is. Eu(**5**)$_3$:Dy(**5**)$_3$ mixed. multilayered. film. in. the. centre. with. a. monolayer. Dy(**5**)$_3$ film. on. the. left. and. Eu(**5**)$_3$ on. the. right. under shortwave. UV. irradiation. (λ_{ex} =. 254. nm)..*

Finally, the triple layered Eu(**5**)$_3$:Tb(**5**)$_3$:Dy(**5**)$_3$ film continued the same trend, with the overall film emission tuned to a similar overall yellow as seen for Eu(**5**)$_3$:Tb(**5**)$_3$ (Figures 4.53 and 4.55). The fluorescence spectrum (Figure 4.56) showed the presence of all three lanthanide complexes emissions on the single substrate, but Dy^{3+} emission was mixed within both Tb^{3+} and Eu^{3+} centred emission and was significantly less emissive. This was likely the cause of the insignificant difference between Eu(**5**)$_3$:Tb(**5**)$_3$ and Eu(**5**)$_3$:Tb(**5**)$_3$:Dy(**5**)$_3$ film's overall emission appearances.

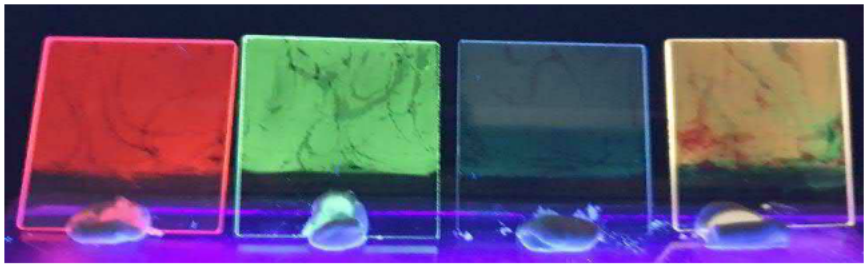

*Figure. 4.55.. Eu(**5**)$_3$:Tb(**5**)$_3$:Dy(**5**)$_3$ mixed. multilayered. film. on. the. right,. with. monolayer. Eu(**5**)$_3$,. Tb(**5**)$_3$ and. Dy(**5**)$_3$ films. from. left. to. right. Under. shortwave. UV. irradiation. (λ_{ex} =. 254. nm)..*

Whilst these results showed that these complexes form multilayered mixed lanthanide LB films, with the overall colour tuned by different Ln^{3+} combinations, there are still significant drawbacks to doing this in a multilayered film. Firstly, as can be seen in Figures 4.53-55, although the TR values suggest a much more uniform film, the overall emission can clearly be seen to have imperfections in the films, with regions having distinct mono-colour emission. Furthermore, even though Dy(**5**)$_3$ is deposited last, the emission is still heavily dominated by the more emissive

Eu(**5**)$_3$ and Tb(**5**)$_3$ complexes. To overcome this with the multilayering method, multiple layers would be required for weaker Ln^{3+} complexes. This could affect the thickness of the film leading to further imperfections in the **Z**-type multilayered films or reach a maximum layer limit. Because of this the next step was to test mixed lanthanide monolayer LB films. Although multilayered films may be slightly more emissive due to the extra material, monolayer LB films have been shown to be brightly emissive themselves. Monolayering also would allow for overall emission control to be much more precise by altering the concentration of each Ln^{3+} in solution.

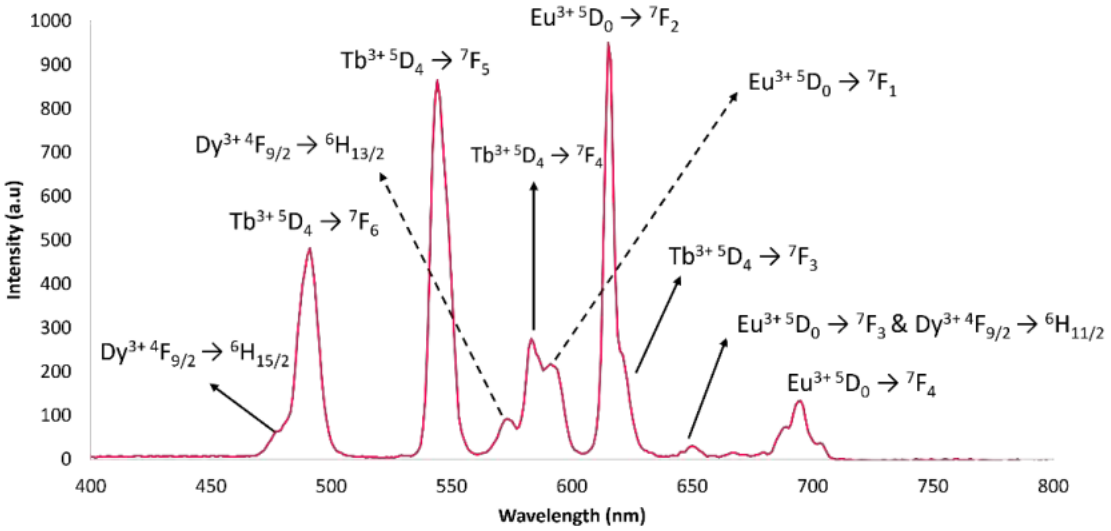

*Figure. 4.56.. Mixed. multilayered. Eu(**5**)$_3$:Tb(**5**)$_3$:Dy(**5**)$_3$ LB. film. fluorescence. spectrum. showing. most. of. the. Ln^{3+}. distinct. emission. transitions..*

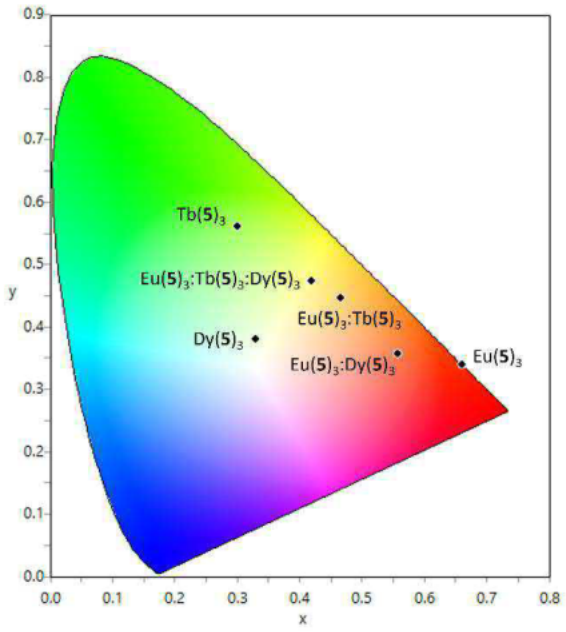

*Figure. 4.57.. CIE. 1931. chromaticity. diagram. with. calculated. CIE. coordinates. for. emissions. of. Ln(**5**)$_3$ complexes. (where. Ln. =. Eu^{3+},. Tb^{3+} and. Dy^{3+}). of. monolayer. LB. films. and. mixed. multilayer. LB. films.. Eu(**5**)$_3$ x,y. =. 0.66,. 0.34;. Tb(**5**)$_3$ x,y. =. 0.30,. 0.56;. Dy(**5**)$_3$ x,y. =. 0.33,. 0.38; Eu(**5**)$_3$:Tb(**5**)$_3$ x,y. =. 0.47,. 0.45;. Eu(**5**)$_3$:Dy(**5**)$_3$ x,y. =0.56,. 0.36. and. Eu(**5**)$_3$:Tb(**5**)$_3$:Dy(**5**)$_3$ x,y. =. 0.42,. 0.47..*

4.2.7.2 Mixed Monolayer Film Deposition

With the near identical Langmuir isotherms and stability profiles of the amphiphilic complexes, the potential for mixed monolayer LB films appeared feasible. However, before undertaking mixed monolayer LB film formation, a small study was carried out in solution to see the difference in relative intensity when the lanthanide complexes are mixed. Initially a solution of Eu(**5**)$_3$:Tb(**5**)$_3$ (1:1) was prepared in MeOH, and as seen in Figure 4.58, the solution appears a very bright yellow similar to that of the previous multilayered Eu(**5**)$_3$:Tb(**5**)$_3$ film. From fluorescence spectra the similarities are further indicated with the solution and film having near identical emission profiles (Figure 4.59).

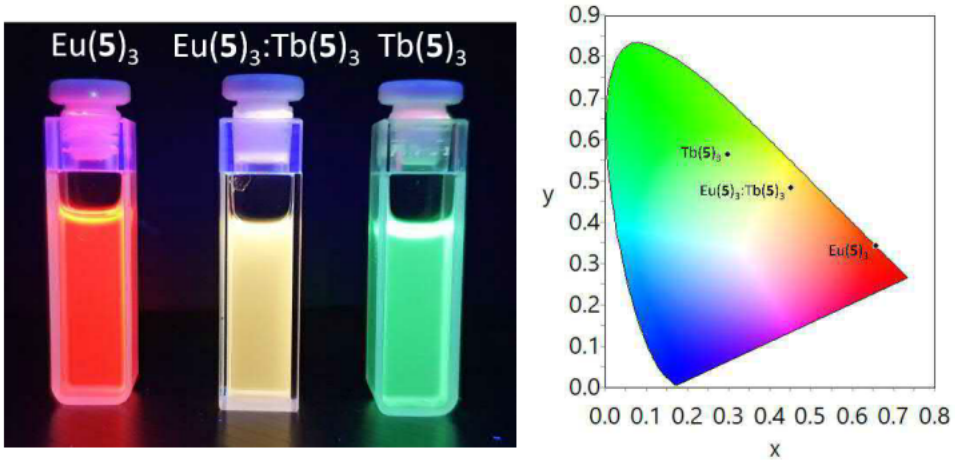

*Figure. 4.58.. (Left). 0.1. mM. solution. of. Eu(**5**)$_3$,.Eu(**5**)$_3$:Tb(**5**)$_3$ (1:1). and. Tb(**5**)$_3$ in. MeOH. under. shortwave. UV. irradiation. (λ_{ex} =. 254. nm). (Right). CIE. 1931. chromaticity. diagram. with. calculated. CIE. coordinates. of. Eu(**5**)$_3$ (x,y. =. 0.66,. 0.34),. Eu(**5**)$_3$:Tb(**5**)$_3$ (1:1). (x,y. =. 0.45,. 0.48) and. Tb(**5**)$_3$ (x,y. =. 0.3,. 0.56). in. MeOH,. 0.01. mM..*

With the easily achievable tunable emission from mixed lanthanide solutions, rather than multilayering, the next step was to test the ability to form monolayer Langmuir films at the air-water interface of mixed Ln^{3+} solutions. As seen in Figure 4.59 the mixture of lanthanide complexes does not affect the Langmuir isotherm profiles. Films still collapsed at 56 – 59 mN m^{-1} with molecular areas of 78– 82 Å^2 within the same region as single complex isotherm. Stability profiles also retain fairly similar profiles as the single component films. Langmuir-Blodgett deposition was then carried out on the Eu(**5**)$_3$:Tb(**5**)$_3$ (1:1) solution (using the same deposition conditions as for the monolayered films) with a single ***emersion*** deposition, resulting in a high TR of 1.12 for the Eu(**5**)$_3$:Tb(**5**)$_3$ film. As seen in Figure 4.60, the film is clearly more uniform in emission profile than the previous multilayered Eu(**5**)$_3$:Tb(**5**)$_3$ film, with overall yellow emission throughout the film and no signs of individual Eu^{3+} or Tb^{3+} emission. The fluorescence spectrum is similar to both the solution and multilayered film, suggesting that the emission can be tuned in solution prior to deposition. Time delayed phosphorescence emission was also recorded, showing a similar emission profile with both Ln^{3+} emissions present

(Figure 8.2.54). Furthermore, the presence of both Ln^{3+} on top of the substrate was also confirmed by XPS, which contained the distinct $3d_{3/2}$ and $3d_{5/2}$ peaks for both Ln^{3+} (Figure 8.2.83).

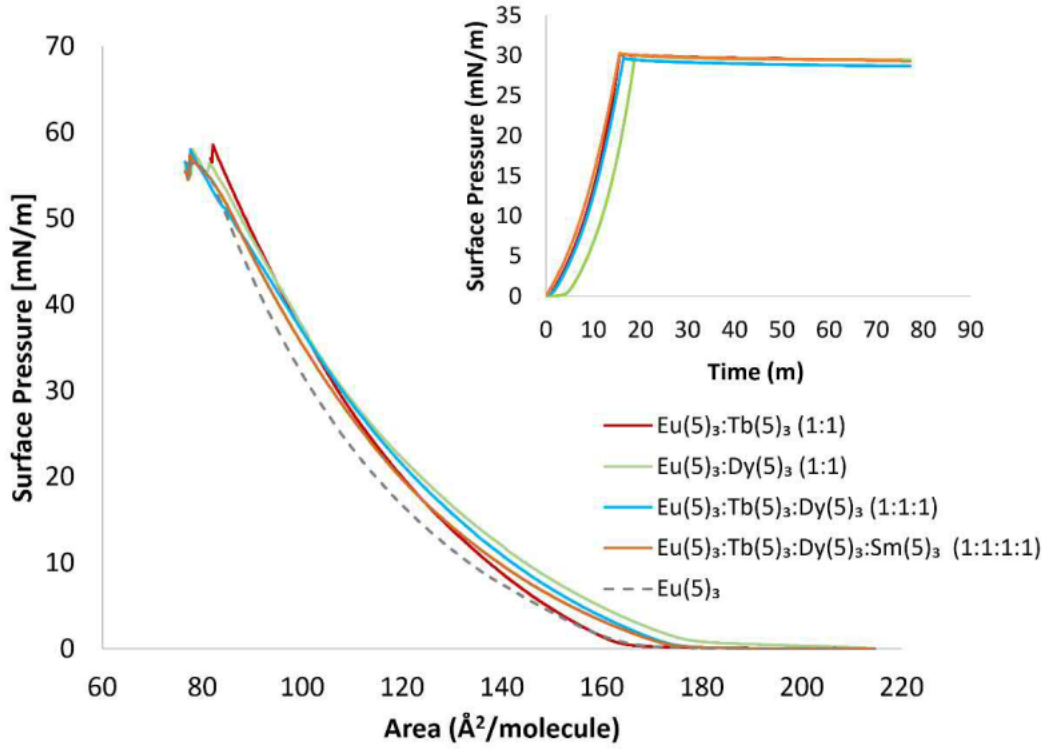

*Figure. 4.59.. Surface. area. – pressure. isotherms. of. Eu(**5**)₃ and. different. complex. combinations.. Insert:. Stability. measurements. held. at. ≈ 30. mN/m. for. over. 60. minutes..*

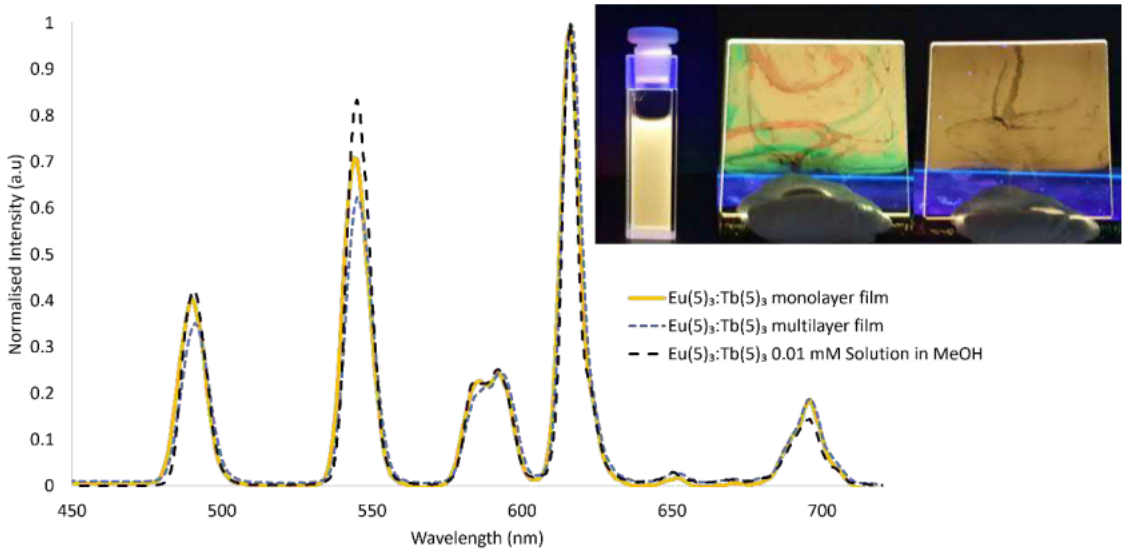

*Figure. 4.60.. Fluorescence. spectra. of. the. different. variations. of. Eu(**5**)₃:Tb(**5**)₃ in. solution. and. as. LB. films. both. multilayered. and. monolayered.. Insert:.. Image. shows. the. different. variations. of. Eu(**5**)₃:Tb(**5**)₃ including:. 0.1. mM. MeOH. solution,. mixed. multilayered. film,. and. mixed. monolayer. film. (left. to. right). under. shortwave. UV. irradiation. (λ$_{ex.}$ =. 254. nm)..*

The promising results of the initial monolayer LB film containing mixed lanthanide complexes Eu(**5**)$_3$:Tb(**5**)$_3$ shows both improvement in emission uniformity across the LB film and the ability to potentially tune the overall emission in solution prior to LB deposition. With these promising results in hand, several more films were fabricated with different Ln^{3+} combinations. Initially the in-solution tuning was utilized in an attempt to tune Dy(**5**)$_3$ overall emission. As stated previously, in both solution and as a LB film Dy(**5**)$_3$ resulted in an unexpected overall emission within the "white region" (CIE x,y = 0.33, 0.38). In a previous study by Sun and co-workers Dy^{3+} emission was able to be tuned closer to "pure-white" emission (CIE, x,y = 0.33) by co-doping Sm^{3+} or Eu^{3+} with Dy^{3+} in a MOF structure achieving CIE coordinates of x,y = 0.36, 0.31 with Eu^{3+}/Dy^{3+} and x,y = 0.33, 0.32 with Sm^{3+}/Dy^{3+}.[112] In an attempt to obtain a similar result, Dy(**5**)$_3$ was mixed with different ratios of Eu(**5**)$_3$ and Sm(**5**)$_3$ with emission being measured in a 0.01 mM solution of MeOH. Unfortunately, as seen in Figure 4.61, unlike Sun and co-workers system, it was clear that addition of either Eu^{3+} or Sm^{3+} resulted in the overall emission becoming less "white". In hindsight this is because of the difference between Dy^{3+} emission in Dy(**5**)$_3$ than Dy^{3+} emission in Sun and co-workers system. In Sun and co-workers system the blue emissive 480 nm ($^4F_{9/2} \rightarrow {}^6H_{15/2}$) transition is stronger than the hypersensitive yellow emissive 574 nm ($^4F_{9/2} \rightarrow {}^6H_{13/2}$) transition, however in Dy(**5**)$_3$ this is reversed. The addition of the orange/red emission from Eu^{3+} or Sm^{3+} moved the overall emission towards the red region, increasing the x- axis of the CIE coordinate, but for Dy(**5**)$_3$ (CIE x,y = 0.33, 0.38) to improve upon its "white" emission, the addition of a blue emissive species would be needed. Unfortunately, Tm(**5**)$_3$ showed no signs of blue emission. This prevented further Dy(**5**)$_3$ tuning and meant a three component Eu(**5**)$_3$:Tb(**5**)$_3$:Tm(**5**)$_3$ (red, green, and blue) "white" emissive combination was not possible using **5** as the ligand/antenna.

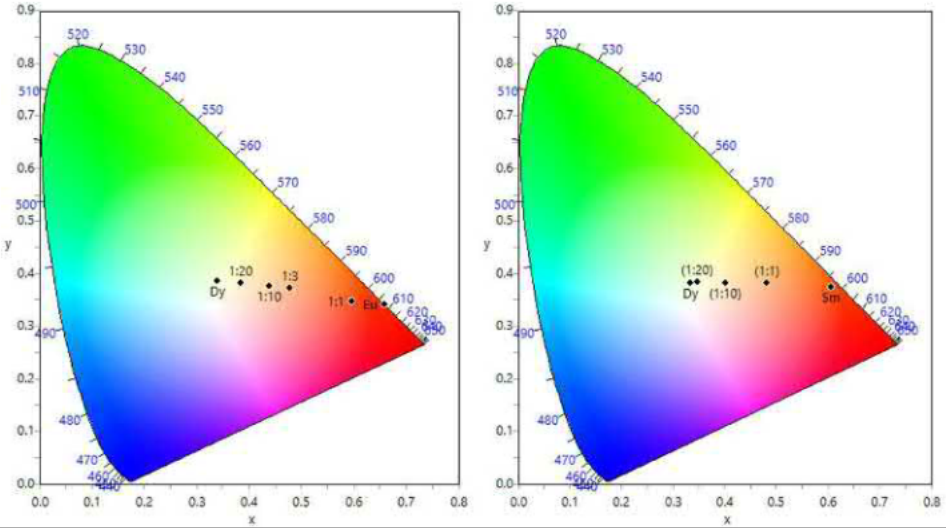

*Figure 4.61.. (Left) CIE 1931 chromaticity diagram with calculated CIE coordinates of Eu(**5**)$_3$:Dy(**5**)$_3$ ratios:. (0:1) x,y = 0.33,. 0.38,. (1:0) x,y = 0.67,. 0.34,. (1:1),. x,y = 0.60,. 0.35,. (1:3) x,y = 0.48,. 0.37,. (1:10) x,y = 0.44,. 0.38,. and (1:20) x,y =0.38,. 0.38.. (Right) CIE 1931 chromaticity diagram with calculated CIE coordinates of Sm(**5**)$_3$:Dy(**5**)$_3$ ratios:. (0:1) x,y = 0.33,. 0.38,. (1:0) x,y = 0.6,. 0.38,. (1:1),. x,y = 0.48,. 0.48,. (1:10) x,y = 0.40,. 0.38,. and (1:20) x,y =0.35,. 0.38..*

Although the combination of Eu(**5**)$_3$:Dy(**5**)$_3$ or Sm(**5**)$_3$:Dy(**5**)$_3$ did not improve upon the "white" emission observed with Dy(**5**)$_3$, the different ratios of the two lanthanides in solution showed that for Dy(**5**)$_3$ to have a similar peak intensity to Eu(**5**)$_3$ it would require a 1:10 ratio of Eu(**5**)$_3$:Dy(**5**)$_3$ (similarly a 1:20 ratio of Sm(**5**)$_3$:Dy(**5**)$_3$ is needed). Because of this, two mixed LB films of Eu(**5**)$_3$:Dy(**5**)$_3$ were fabricated at 1:1 to compare against the prior multilayered film and at 1:10 to be able to clearly see distinct emission from both Ln^{3+}. Deposition of both was carried out resulting in TR 0.93 and 0.99 for 1:1 and 1:10 respectively and uniform emission across the film (Figure 4.62). Fluorescence emission profiles contained distinct transitions from both Ln^{3+} and XPS measurements of the 1:1 film also confirmed the presence of both Ln^{3+} (Figure 8.2.84).

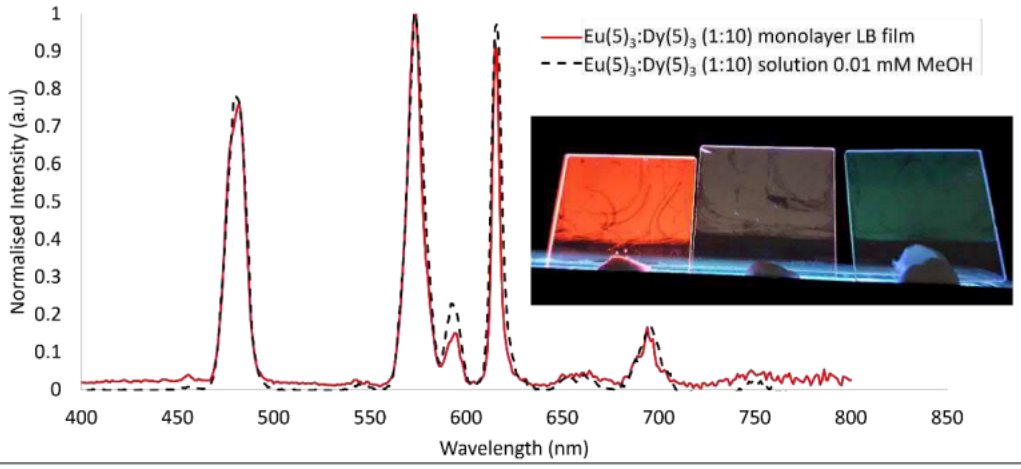

*Figure 4.62.. Fluorescence emission spectra of Eu(**5**)$_3$:Dy(**5**)$_3$ (1:10) in solution (0.01 mM, MeOH) and as a monolayer film.. Insert:: image of Eu(**5**)$_3$:Dy(**5**)$_3$ (1:10) film in the centre with Eu(**5**)$_3$ (left) and Dy(**5**)$_3$ (right) under shortwave UV irradiation (λ_{ex} = 254 nm)...*

Similar to the previous mixed Eu(**5**)$_3$:Tb(**5**) LB monolayer film, Eu(**5**)$_3$:Dy(**5**)$_3$ (1:1 and 1:10) emission profiles closely matched that of the solution and multilayered (1:1) emission profiles (Figures 4.62-63). However, unlike the Eu(**5**)$_3$:Tb(**5**) LB films, time delayed phosphorescence emission was not similar to the fluorescence emission. This was put down to the lifetime difference between Eu^{3+} (ms) and Dy^{3+} (µs), resulting in an unexpected phosphorescence spectrum, where only Eu^{3+} emission was present (Figure 8.2.56).

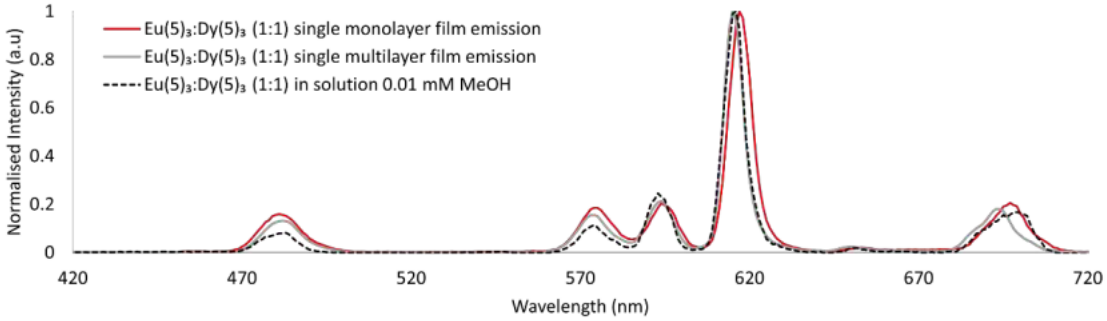

*Figure 4.63.. Fluorescence emission spectra of Eu(**5**)$_3$:Dy(**5**)$_3$ (1:1) in solution (0.01 mM MeOH),. as a monolayer and multilayer film..*

To the best of our knowledge, it is relatively novel for two strong Ln^{3+} emissions to be mixed on a single monolayer LB film for emission tuning. The obvious next step was to see if three or four lanthanide complexes and their corresponding emissions could be mixed on a single monolayer surface. Initially the three most emissive lanthanides were combined on a single monolayer. Two variations were fabricated: Eu(**5**)$_3$:Tb(**5**)$_3$:Dy(**5**)$_3$ in a 1:1:1 and 1:1:10 ratio. Like the dual mixed monolayer films, the triple mixed monolayer films have a high transfer ratio (TR = 1.01 and 1.02 respectively) and emission appeared uniform across the films (Figure 4.64). Fluorescence emission showed clear signs of all three Ln^{3+}, while time delayed phosphorescence again missing Dy^{3+} emission with only Eu^{3+} and Tb^{3+} emission present (Figures 8.2.57-58).

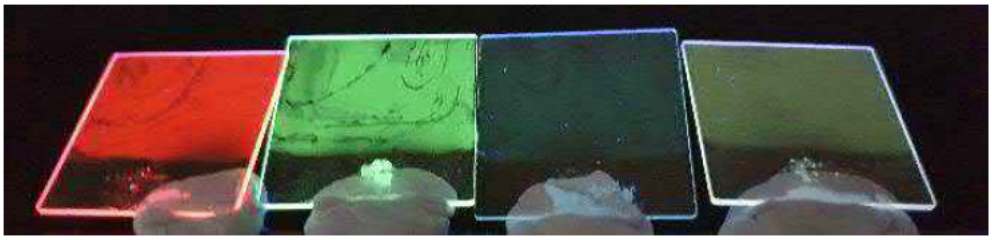

*Figure. 4.64.. Image. of. three. monolayer. LB. films. of. Ln(**5**)$_3$. (where. Ln^{3+}. =. Eu^{3+},. $Tb^{3+}$and. Dy^{3+}. respectively). and. the. final. triple. mixed monolayer. LB. film. of. Eu(**5**)$_3$:Tb(**5**)$_3$:Dy(**5**)$_3$ (1:1:10). on. the. right,. all. under. shortwave. UV. irradiation. (λ_{ex} =. 254. nm)..*

The final step was to incorporate all four visibly emitting lanthanide complexes into a single monolayer film. Three films were fabricated, Eu(**5**)$_3$:Tb(**5**)$_3$:Dy(**5**)$_3$:Sm(**5**)$_3$ (1:1:1:1), (1:1:10:10) and (1:1:10:50). All films retain their high transfer ratios of 1.08, 1.06, and 1.02 respectively. Based on the previous emission intensity study with Dy^{3+}, Eu^{3+} and Sm^{3+} it was no surprise that the initial (1:1:1:1) film only showed strong signs of emissions from Eu(**5**)$_3$ and Tb(**5**)$_3$ (Figure 8.2.59). The (1:1:10:10) showed clear peaks from Eu(**5**)$_3$,Tb(**5**)$_3$ and Dy(**5**)$_3$, but only weak signals from Sm(**5**)$_3$ (Figure 8.2.59). It required a large excess of Sm(**5**)$_3$ due to its much lower quantum yield to be able to easily assign a transition to the Sm^{3+}. The (1:1:10:50) film showed a clear Sm^{3+} centred emission when compared to previous (1:1:1:1) and (1:1:10:10) films (Figure 4.65). Emission at 600 nm and 645 nm was very weak in both previous films, but the (1:1:10:50) film had strong emission at both these regions associated with Sm^{3+} (602 nm, $^4G_{5/2} \rightarrow {}^6H_{7/2}$ and 645 nm, $^4G_{5/2} \rightarrow {}^6H_{5/2}$). Phosphorescence once again only showed the long-lived emission transitions of Eu^{3+} and Tb^{3+} and showed no signs of Dy^{3+} or Sm^{3+} emission (Figure 8.2.60). Finally, XPS once again confirms the existence of all four Ln^{3+} on the surface of the monolayer (1:1:1:1) film (Figure 4.66)

Interestingly the (1:1:10:50) film emission was still strongly dominated by both Eu(**5**)$_3$ and Tb(**5**)$_3$ even though it was calculated that only approximately 3 x 10^{-8} g of each complex was deposited into the Langmuir trough compared to 15 x 10^{-6} g of Sm(**5**)$_3$ complex (only some of which is deposited onto the slide). This shows both the impressive emission of these complexes with

such small amounts giving strong emission and also the LB technique's ability to use such small amounts to form uniform films. This contrasts with other techniques such as spin coating, RASSS, evaporation deposition, and dip coating which are costly in material.

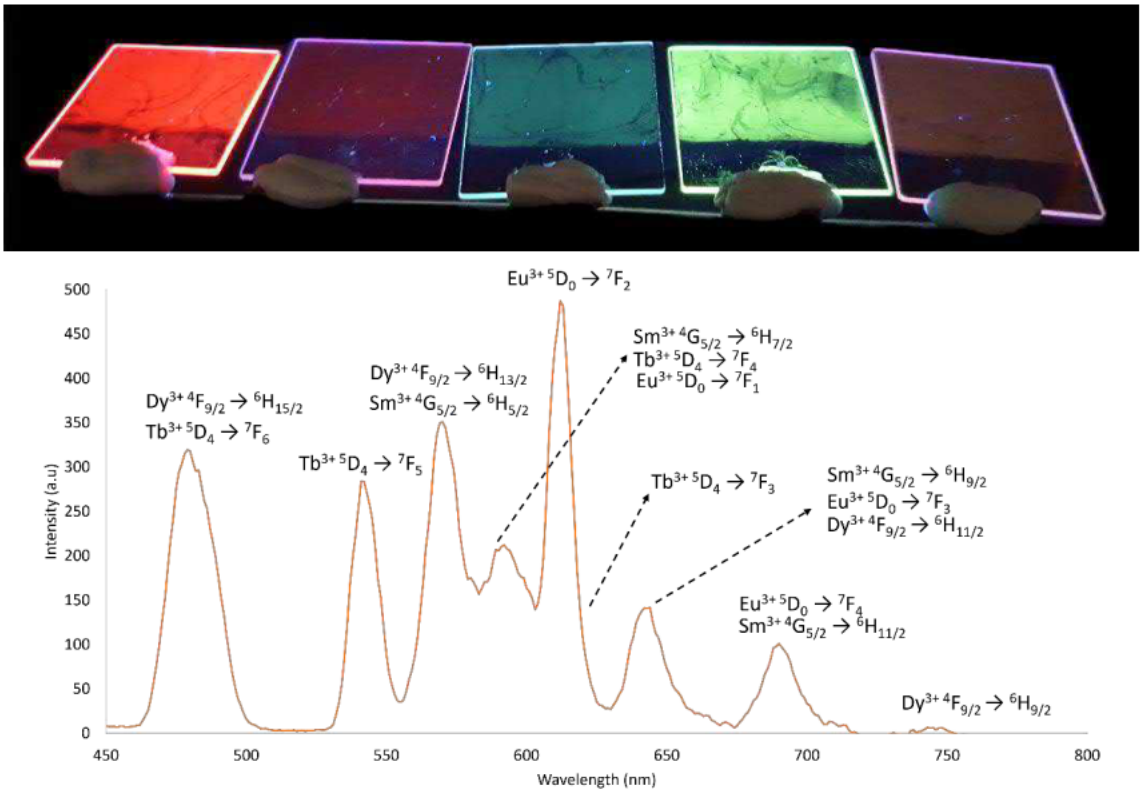

*Figure. 4.65.(Top). Image. of. all. four. monolayer. LB. films. of. Ln(**5**)$_3$ (where. Ln. =. Eu^{3+},. Sm^{3+},. Dy^{3+}. and. Tb^{3+}. respectively). and. the. final quadruple. mixed. monolayer. LB. film. of. Eu(**5**)$_3$:Tb(**5**)$_3$:Dy(**5**)$_3$:Sm(**5**)$_3$ (1:1:1:10). on. the. right,. all. under. shortwave. UV. irradiation.. (Bottom). Fluorescence. spectrum. of. Eu(**5**)$_3$:Tb(**5**)$_3$:Dy(**5**)$_3$:Sm(**5**)$_3$ (1:1:1:10). showing. distinct. transition. from. all. four. Ln(**5**)$_3$. complexes. (where. Ln. = Eu^{3+},. Sm^{3+},. Dy^{3+}. and. Tb^{3+}).. The. assigned. major. emission. is. listed. first. if. there. are. multiple. emissions. for. the. region..*

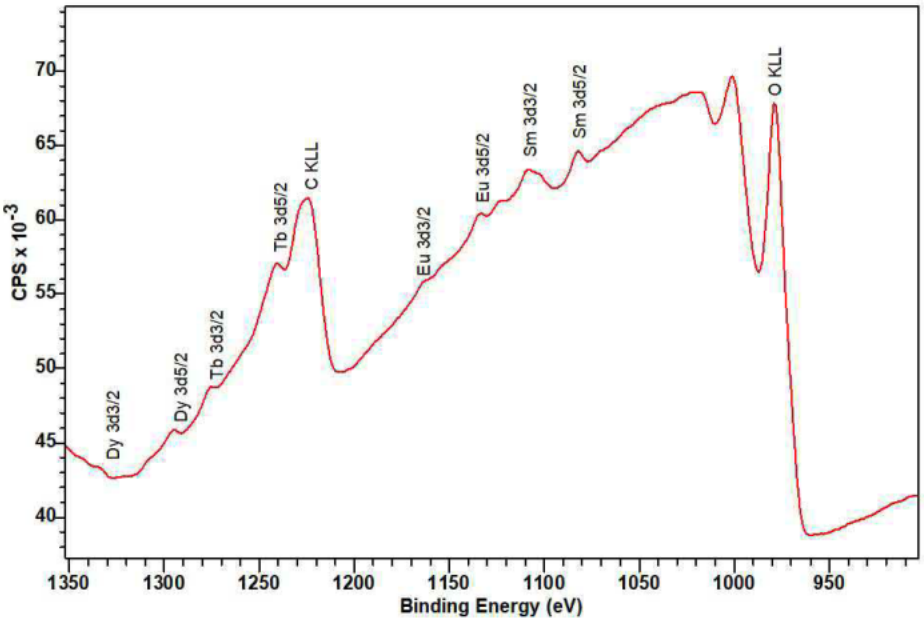

*Figure. 4.66.. Enclosed. window. scan. of. Eu(**5**)$_3$:Tb(**5**)$_3$:Dy(**5**)$_3$:Sm(**5**)$_3$ (1:1:1:1). monolayer. LB. film. (a. total. of. 10. scans).. With. Eu^{3+}. $3d_{3/2}$ = 1164. and. $3d_{5/2}$ =. 1134. eV,. expected. being. 1136. and. 1166. eV,. Tb^{3+}. $3d_{3/2}$ =. 1175. and. $3d_{5/2}$ =. 1141. eV,. expected. being. 1176. and. 1141. eV, Dy^{3+}. $3d_{3/2}$ =. 1334. and. $3d_{5/2}$ =. 1295. eV,. expected. being. 1333. and. 1296. eV. and. with. Sm^{3+} $3d_{3/2}$ =. 1108. and. $3d_{5/2}$ =. 1082. eV,. expected being. 1108. and. 1281. eV..*

4.3 Conclusion

The synthetic strategy has been incorporated into the PDC motif with ease. The 5-step synthesis of **5** occurred in good overall yield of 42 % (when disregarding the initial protection). **5** was easily complexed with a wide range of Ln^{3+}, resulting in visibly emissive solids of Eu(**5**)$_3$, Tb(**5**)$_3$, Dy(**5**)$_3$ and Sm(**5**)$_3$. Characterisation of **5** and the corresponding complexes showed that the PDC binding motif retained the benefits of modification of the side arm, favouring the 1:3 M:L complex formation and again occurring in the NO_2 pocket. Improved stability was also observed in competitive solvents, indicated by lack of dissociation in DMSO-d_6, and improved Ln^{3+} centred emission compared to previous PDA systems.

Langmuir films of **5** and Ln(**5**)$_3$ were easily formed at the air-water interface and remained stable over long periods of time. LB deposition of the complexes was also straightforward, with Langmuir films easily being transferred to solid substrates, forming monolayer **Z**-type films with high TR. Deposition was confirmed by luminescent emission, UV-visible absorption and XPS measurements, which indicated the retention of a 1:3 complex on the surface. The monolayer films retained their impressive emission properties as single monolayer films, with visible emission seen with the naked eye when excited. Dy(**5**)$_3$ exhibited white emission from a single component in solution and as a monolayer LB film. **Y**-type multilayer films of Eu(**5**)$_3$ as expected resulted in stronger emissive films with more layers and FTIR characterisation was possible, also suggestive of complex retention on LB films. Multilayering was however found to be relatively non-uniform when considering TR values. Mixed lanthanide LB films were initially tried with **Z**-type multilayering, with three LB films being fabricated: Eu(**5**)$_3$:Tb(**5**)$_3$, Eu(**5**)$_3$:Dy(**5**)$_3$ and Eu(**5**)$_3$:Tb(**5**)$_3$:Dy(**5**)$_3$. Mixed lanthanide multilayer LB films were dual or triple emissive, showing distinct transitions from each Ln^{3+} and overall emissions of the film were tuned to a new distinct emission as seen in Figure 4.57. However, multilayered films had major flaws, as although the resulting **Z**-type multilayering improved TR values, films were non-uniform to the eye. Along with this if tunable emission was desired, Dy(**5**)$_3$ in mixed films was heavily dominated by Eu(**5**)$_3$ and Tb(**5**)$_3$ emission and would require extensive layering to achieve equal intensity, which would be worse in the case of Sm(**5**)$_3$.

Mixed lanthanide complex monolayer LB films were fabricated, and results were much more promising. Initially in solution emission tuning was tested with Eu(**5**)$_3$ and Tb(**5**)$_3$ in a 1:1 ratio resulting in an overall bright yellow emission. Langmuir isotherms of the mixture resulted in similar profiles to those of the single complex isotherms along with similar stabilities. Deposition of the mixed solution resulted in a uniform monolayer LB film, which retained the overall yellow emission, with similar emission profiles to that of the multilayered LB film and solution measurements. This indicated that the emission profiles could be measured in solution and tuned prior to deposition. In attempts to tune Dy(**5**)$_3$ emission to a more "pure-white" emission, different ratios of Eu(**5**)$_3$ and Sm(**5**)$_3$ were tested in solution, although this resulted in only worsening the overall "white" emission. However, it did show that it would require a 1:10 ratio of Eu(**5**)$_3$:Dy(**5**)$_3$ and a 1:20 ratio of Dy(**5**)$_3$:Sm(**5**)$_3$ to have relatively similar emission intensities. With the promising result of the mixed monolayer Eu(**5**)$_3$:Tb(**5**)$_3$ (1:1) film, two dual emissive Eu(**5**)$_3$:Dy(**5**)$_3$ (1:1 and 1:10) monolayer LB films were produced. Once again both films appeared uniform, with the 1:1 film retaining the same emission profile as the previous multilayered film and solution measurements. The 1:10 film's emission profile showed similar intensities for both Ln^{3+} emissions, on the monolayer film. The mixed monolayer method therefore allowed for ease of emission tuning when compared to multilayered films.

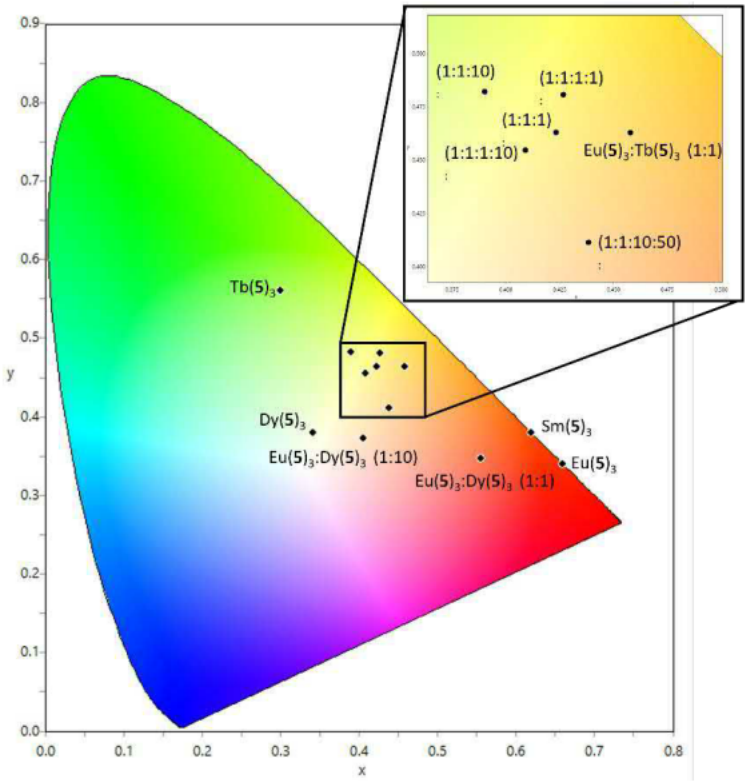

*Figure 4.67.. CIE 1931 chromaticity diagram with calculated CIE coordinates for emissions of Ln(**5**)$_3$ complexes (where Ln = Eu^{3+}, Tb^{3+}, Dy^{3+} and Sm^{3+}) of monolayer LB films and mixed monolayer LB films.. Eu(**5**)$_3$ x,y = 0.66, 0.34; Tb(**5**)$_3$ x,y = 0.30, 0.56; Dy(**5**)$_3$ x,y = 0.33, 0.38; Sm(**5**)$_3$ x,y = 0.62, 0.38; Eu(**5**)$_3$:Tb(**5**)$_3$ (1:1) x,y = 0.46, 0.46; Eu(**5**)$_3$:Dy(**5**)$_3$ (1:1) x,y = 0.56, 035 and (1:10) x,y . = 0.41, 0.37; Eu(**5**)$_3$:Tb(**5**)$_3$:Dy(**5**)$_3$ (1:1:1) x,y = 0.44, 0.42 and (1:1:10) x,y = 0.39, 0.48; Eu(**5**)$_3$:Tb(**5**)$_3$:Dy(**5**)$_3$:Sm(**5**)$_3$ (1:1:1:1) x,y = 0.43, 0.48, (1:1:10:10) x,y = 0.41, 0.45 and (1:1:10:50) x,y = 0.44, 0.41..*

Finally, triple and quadruple emissive monolayer LB films were fabricated. Triple emissive films of Eu(**5**)$_3$:Tb(**5**)$_3$:Dy(**5**)$_3$ with ratios of 1:1:1 and 1:1:10 were formed, which showed distinct emission from each Ln^{3+}, but this time the 1:1:10 film showed clear transitions from Dy^{3+}. Similarly quadruple emissive monolayer LB films of Eu(**5**)$_3$:Tb(**5**)$_3$:Dy(**5**)$_3$:Sm(**5**)$_3$ with ratios of 1:1:1:1, 1:1:10:10 and 1:1:10:50 were produced. The initial two films showed emission from the first three most emissive Ln^{3+} and no sign of Sm(**5**)$_3$. A large excess of Sm(**5**)$_3$ was required for distinct Sm^{3+} emission to be observed on the LB films. To the best of our knowledge this is the first example of clear dual, triple, and quadruple lanthanide emission on monolayer LB films.

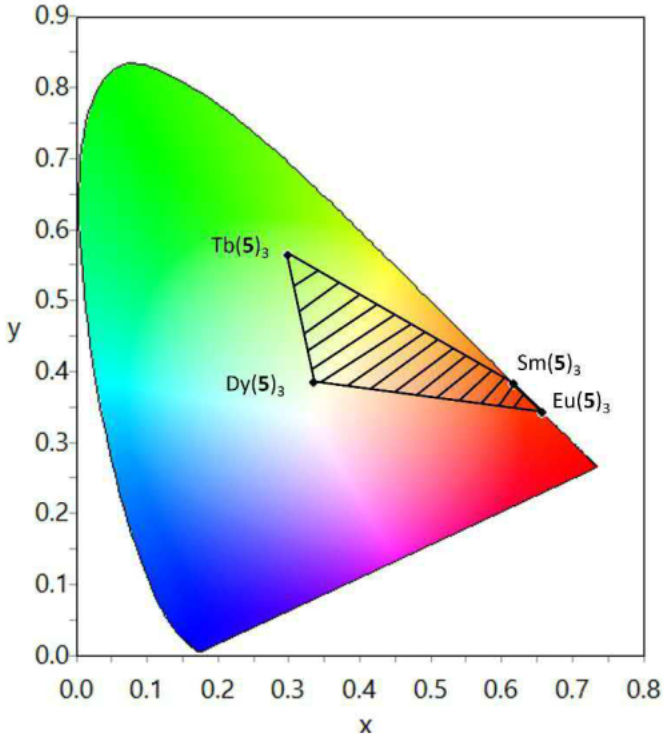

*Figure 4.68.. Potential colour tunable emission regions with combinations of different ratios of Ln(**5**)$_3$ (where Ln = Eu^{3+}, Tb^{3+}, Dy^{3+} and Sm^{3+}).*

4.3.1 Future Work

This system has shown that multiple Ln^{3+} complexes and their distinct emissions can form stable Langmuir films which can be deposited on a solid substrate forming brightly emissive uniform monolayer LB films. These LB films can have their overall emission profile tuned in solution for a range of specific emissions ranging from red, orange, yellow and "close to white" prior to LB fabrication, as seen in Figures 4.67-68. Currently the systems have potential applications as invisible molecular barcodes, with different emission intensities used as an identification tool. But simple modification off the back of the PDC motif could allow for formation of much more complex application-based systems (Figure 4.69). If each lanthanide complex had their own receptors for specific analytes, it would result in a quadruple emission sensor, with four distinct emission changes for four different analytes. Furthermore, the antennas could be modified such that different wavelengths are used to excite certain Ln^{3+} emission making a colour-tunable film or making it possible to excite other visible emissive lanthanides (allowing for potentially improved "white" emission from RGB tuning as described prior) but also UV and NIR emission from other Ln^{3+}. Finally, there is potential for mixed monolayer films which are capable of both up and down conversion as waveguides for solar cells. As stated, this is just the initial study of mixed Ln^{3+} emissive LB films and opens the door for an array of ultra-thin LB films with a variety of applications.

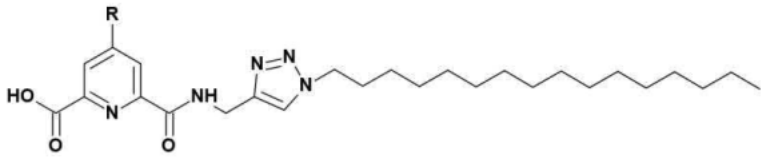

*Figure 4.69.. Potential modification avenue for **5** from the back para position of the PDC scaffold unit..*

4.4 Experimental

4.4.1 General Experimental Details

All reagents, solvents and starting materials were purchased from Sigma-Aldrich. NMR spectra were recorded using a Bruker Ultrashield 300, with chemical shifts recorded in parts per million (ppm) downfield from the standard. MS of ligands was carried out in HPLC grade solvents, on a Shimadzu LCMS-2020 for ligands and a ThermoFisher QExactive Focus coupled to an Ultimate™ 3000 RSLC or a Bruker Daltonics MicrOTOF™ Spectrometer for complexes. FTIR of solids were recorded on a Bruker Alpha platinum-ATR and FTIR of LB films spectra were recorded on a ThermoFisher Scientific Nicolet iS50. Melting points were obtained on an Electrothermal IA9000 Series Melting Point Apparatus. UV-visible spectra were recorded on a Shimadzu UV-1800 or Shimadzu UV-2700 (for quantum measurements), steady-state fluorescence measurements were recorded on a Shimadzu RF-6000 Spectrofluorophotometer with a ZJB380 UV filter 360 nm and time-resolved fluorescence measurements were carried out using an Agilent Technologies Cary Eclipse spectrophotometer, all recorded in MeCN, $CHCl_3$ and MeOH solvents in a capped 3.5 mL quartz cuvette with a 1 cm path length. Refractive index measurements were carried out on a Bellingham + Stanley Abbe 5 optical refractometer. Single crystal X-ray diffraction data were collected at 123 K on a Bruker D8 Venture equipped with an IμS DIAMOND microfocus with a Cu-Kα (λ = 1.54178) X-ray source with a PHOTON III detector. Unit cell parameters were refined against all data and an empirical absorption correction applied in APEX3. Structures were solved by direct methods using SHELXS-2013[113] and refined on Fo2 by SHELXL-2013[113] using Olex2. CIE plots were generated in OSRAM LED ColorCalculator software.[114] Safety Note: low molecular weight organic azides are potential explosives, and care must be taken during their handling; however no issues were encountered here.

4.4.2 Langmuir-Blodgett Technique

Langmuir-Blodgett measurements and film formation were measured on a Kibron G2 Microtrough. Initially the Langmuir trough and barriers were cleaned with $CHCl_3$, EtOH, milli-Q water and dried by suction, before filling the trough with milli-Q water to the level of the trough edge. The DyneProbes were cleaned by a blow torch to remove any potential organic residue, and then washed with EtOH and milli-Q water before being calibrated in air and on the water interface. A barrier compression isotherm was run monitoring the surface pressure. If pressure remained unchanged over the course of the isotherm, the trough was deemed clean, otherwise if surface pressure increased indicating contamination, the top layer of the water surface would be suctioned off and the isotherm repeated until no sign of contamination. 1 mg/mL solution in $CHCl_3$:MeOH (20:1) of ligand or complex was prepared and 20 μL aliquots of the solution were deposited on the edge of the trough in four additions of 5 μL aliquots each, twice on each side of the trough onto the surface of a milli-Q water sub-phase at r.t for isotherm, stability, and deposition measurements. Substrates for deposition were cleaned with nitric acid, piranha solution, and milli-q water before deposition.

4.4.3 Photophysical Measurements

Unless otherwise stated, all measurements were performed at r.t in MeCN (HPLC grade). The stock solutions of ligand or complex were prepared using a (1:1) ratio of CH_2Cl_2 and MeOH (spectroscopic grade). Excitation wavelength unless otherwise stated was 274 nm. Phosphorescence lifetimes of the Eu^{3+} and Tb^{3+} excited states were measured in time-resolved mode by monitoring the emission decay at 616 and 543 nm; these were carried out in triplicate and averaged.

4.4.3.1 Photophysical Self-Assembly Titrations

The formation of 1:1, 1:2 and 1:3 (M:L) species was monitored by measuring changes in the UV-visible absorption and fluorescence spectra of a solution of ligand **5** (2×10^{-5} M MeOH:DCM:MeCN (0.005:0.005:9.99)) when titrated with $Eu(CF_3SO_3)_3.6H_2O$ solution in MeCN (0 → 4.5 equivalents) after being deprotonated by 1 equivalent of tetramethylammonium hydroxide. Titrations were carried out in triplicate and then fitted with ReactLab™ Equilibrium[67] for non-linear regression analysis, however only steady-state data could be fit.

4.4.3.2 Quantum Yield

Quantum yield measurements were determined by the dilute comparison method[115] using relative standards of $Cs_3[Eu(DPA)_3]\cdot 8H_2O$ and $Cs_3[Tb(DPA)_3]\cdot 8H_2O$ complex in a 0.1 M Tris-HCl buffer solution (pH ≈ 7.45), with known quantum yields of Φ_{ref} = 24 ± 2.5 % and Φ_{ref} = 22 ± 2.5 % respectively.[102, 116] $Cs_3[Eu(DPA)_3]\cdot 9H_2O$ was used for Eu(**5**)$_3$ and $Cs_3[Tb(DPA)_3]\cdot 9H_2O$ for Tb(**5**)$_3$, where Sm(**5**)$_3$ and Dy(**5**)$_3$ were averaged from comparisons to both standards. Instrument slit widths remained the same between measurements for different compounds with either 1.5, 3 nm excitation and emission widths (except for Sm which required 3, 3 nm slit widths to have observable emission, which in turn the standard was also measured with). Excitation wavelength of 279 nm was the same for all measurements. Standards were initially cross calibrated with one another to be within the range of error before being compared to lanthanide complexes. Complexes were dissolved in a 1:1 MeOH:CH_2Cl_2 stock solution and then diluted into MeOH to the appropriate concentration for quantum yield studies. MeCN was also used for Eu(**5**)$_3$ but showed a lower quantum yield which was put down to the complex notably slowly precipitating out over time.

Estimated overall quantum yields $\Phi_{Ln}^{L} = \Phi_x$ were calculated according to the following equation 1. Here grad refer to the slope of plotted emission area vs absorbance (emission area was taken from specific emission peaks, Eu(**5**)$_3$ ($^5D_0 \rightarrow {}^7F_2$), Tb(**5**)$_3$ ($^5D_4 \rightarrow {}^7F_5$), Dy(**5**)$_3$ ($^4F_{9/2} \rightarrow {}^6H_{13/2}$) and Sm(**5**)$_3$ ($^4G_{5/2} \rightarrow {}^6H_{7/2}$)), n refers to refractive index of the solution (a refractive index of n = 1.3295 was found for MeOH:CH_2Cl_2 solution and n = 1.3355 for MeCN solution), and subscripts are r for reference and x for sample.[116]

$$\boldsymbol{\Phi_x = \Phi_r\left(\frac{grad_x}{grad_r} \times \left(\frac{n_x{}^2}{n_r{}^2}\right)\right)} \quad \mathbf{(1)}$$

Other values such as observed lifetime (τ_{obs}), radiative lifetime (τ^{rad}), sensitisation efficiency (n_{sens}) and intrinsic quantum yield (Φ_{Ln}^{Ln}) were determined in the same manner as in chapter 3.

4.4.4 X-ray Photoelectron Spectroscopy (XPS)

The XPS data were collected on a Kratos Axis UltraDLD equipped with a hemispherical electron energy analyser. Spectra were excited using monochromatic Al Kα X-rays (1486.69 eV) with the X-ray source operating at 150W. This instrument illuminates a large area on the surface and then using hybrid magnetic and electrostatic lenses collects photoelectrons from a desired location on the surface. In this case the analysis area was a 300 by 700 micron spot (=hybrid/slot). The measurements were carried out in a normal emission geometry. A charge neutralisation system was used to alleviate sample charge buildup, resulting in a shift of approximately 3 eV to lower binding energy. Survey scans were collected with a 160 eV pass energy, whilst core level scans were collected with a pass energy of 20 eV. The analysis chamber was at pressures in the 10^{-9} Torr range throughout the data collection. Data analysis was performed using CasaXPS (www.casaXPS.com). The binding energy scale was corrected for the neutraliser shift by using the C 1s signal from saturated hydrocarbon at 285.0 eV as an internal standard.

4.4.5 Ligand Synthesis

4.4.5.1 Synthesis of 6-((benzyloxy)carbonyl)pyridine-2-carboxylic acid (C)

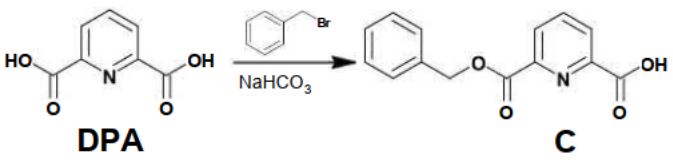

DPA **C**

*Scheme 4.6.. Synthesis of intermediate **C**.*

DPA (2.00 g, 11.97 mmol) was combined with dried $NaHCO_3$ (1.00 g, 11.90 mmol) in 100 mL of dried DMF. The solution was heated to 60 °C for 30 minutes under a N_2 atmosphere resulting in a cloudy, off-white solution. Benzyl bromide (1.4 mL, 12.61 mmol) was added to the solution and left stirring for 48 hours at 60 °C. The resulting pale-yellow solution was then diluted with 100 mL of H_2O and neutralised with a saturated solution of $NaHCO_3$ (pH ≈ 7). The diester side product was extracted by diethyl ether and then the aqueous layer was acidified to a pH ≈ 1. **C** was then extracted into ethyl acetate. The organic layer was dried with $MgSO_4$, filtered and solvent was removed by reduced pressure. This resulted in an off-white cloudy slurry which was dissolved in DCM and the organic layer was washed with H_2O and brine removing residue DMF. The organic layer was then dried with $MgSO_4$, filtered and then solvent was removed under reduced pressure resulting in an off-white solid (1.683 g, 6.54 mmol, 55 %).[57] Melting point = 134.9 °C. LRMS *m/z* = 258.00 [**C** + H]$^+$ (calc. for $C_{14}H_{12}NO_4^+$, 258.25). ^{1}H NMR (300 MHz, $CDCl_3$, ppm), δ = 8.40 (dd, J =10.0, 8.0 Hz , 2H, *meta* py-H), 8.12 (t, J = 8.0 Hz, 1H, *para* py-H), 7.44 (m, 5H, Bn), 5.47 (S, 2H, CH_2); ^{13}C NMR (75 MHz, $CDCl_3$, ppm): δ = 163.6 (C=O), 163.5 (C=O), 146.9 (CN), 146.6 (CN), 139.9 (CH-py), 135.2 (C-Bn), 129.1-128.8 (3x CH-Bn), 127.0 (CH-py), 68.25 (Bn-CH_2). FTIR (cm^{-1}) 2879 -2615 (OH), 1737 (COOR), 1694 (COOH), 1575, 1499, 1467, 1416, 1376, 1329, 1288, 1242, 1151, 1083, 1006, 994, 955, 939, 855, 796, 753, 728, 710, 690, 648, 554, 510, 457, 421.

4.4.5.2 Synthesis of N_2-(prop-2-ynyl)-O_6-((benzyloxy)carbonyl)pyridine-2-carboxamide-6-carboxylate (D)

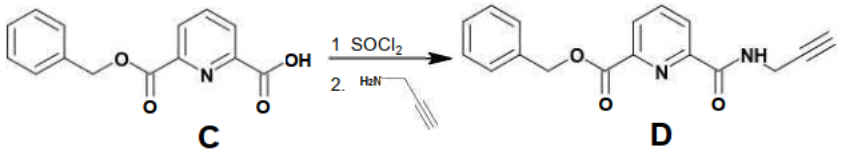

C **D**

*Scheme 4.7.. Synthesis of intermediate **D**.*

C (2.00 g, 7.78 mmol) was dissolved in 20 mL of freshly dried DCM and placed under a nitrogen atmosphere. Thionyl chloride (1.5 mL, 20.56 mmol) was added to the clear solution, causing an off-white precipitate to form. The solution was then heated to 80 °C for 5 hours. The resulting yellow solution, solvent and excess thionyl chloride was removed by a stream of nitrogen resulting in a pale yellow solid (acid chloride product). Once the solid was dry it was then dissolved in 10 mL freshly dried DCM. A separate solution of propargyl amine (0.996 mL, 15.55 mmol) and triethylamine (5.746 mL, 41.23 mmol) in 30 mL of freshly dried DCM was cooled in an ice bath. While stirring the acid chloride solution was added dropwise to the (lime green) propargyl amine containing solution turning the solution a dark red with smoke extruding from the round bottom flask. The solution was left to stir overnight for 24 hours at r.t. The organic layer was washed with 1 M HCl and saturated $NaHCO_3$, then dried with $MgSO_4$, filtered and then solvent was removed by reduced pressure resulting in a brown oil which solidified into a light brown solid (1.640 g, 5.57 mmol, 72 %). Melting point = 75.4 °C. LRMS *m/z* = 294.95 [**D** + H]$^+$ (calc. for $C_{17}H_{15}N_2O_3^+$, 295.11), *m/z* = 316.95 [**D** + H]$^+$ (calc. for $C_{17}H_{15}N_2O_3^+$, 317.19). ^{1}H NMR (300 MHz, $CDCl_3$, ppm), δ = 8.39 (dd, J= 7.79, 1.14 Hz, 1H, *meta* py-H), 8.30 (m, 1H, NH), 8.25 (dd, J= 8.0, 1.0 Hz, 1H, *meta* py-H), 8.00 (t, J= 8.0 Hz, 1H, *para* py-H), 7.44 (m, 5H, Bn), 5.45 (s, 2H, CH_2-O), 4.28 (dd, J = 6.0, 2.5 Hz, 2H, CH_2-NH), 2.26 (t, J= 2.5 Hz, 1H, CH); ^{13}C NMR (75 MHz, $CDCl_3$, ppm): δ = 164.3 (C=O), 163.4 (C=O), 149.9 (CN), 146.8 (CN), 138.8 (CH-py), 135.5 (C-Bn), 128.8-128.6 (3x CH-Bn), 127.8 (CH-py), 125.7(CH-py), 79.4 (C-alkyne), 71.8 (CH-alkyne), 67.9 (Bn-CH_2), 29.3 (NH-CH_2). FTIR (cm^{-1}) 3384, 3212, 1737 (COOR), 1682 (CONH), 1514, 1446, 1418, 1373, 1286, 1256, 1228, 1161, 1082, 1050, 1012, 998, 983, 912, 901, 842, 747, 729, 692, 647, 617, 582, 546, 455, 421.

4.4.5.3 Synthesis of N_2-((1-(hexadecane)-1H-1,2,3-triazol-4-yl)methyl)-O_6-((benzyloxy)carbonyl)pyridine-2-carboxamide-6-carboxylate (E)

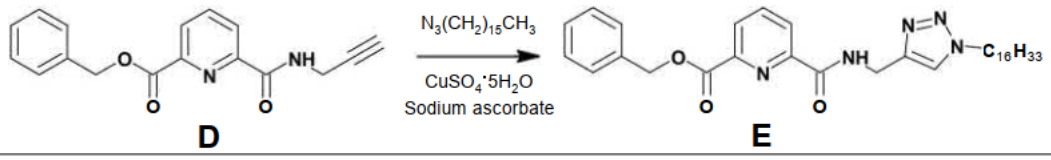

*Scheme 4.8.. Synthesis of intermediate **E**.*

D (0.354 g, 1.20 mmol) was combined with sodium ascorbate (0.217 g, 1.10 mmol) and $CuSO_4 \cdot 5H_2O$ (0.137 g, 0.55 mmol) in 20 mL of DMF:H_2O (4:1) and heated to 60 °C for 30 minutes resulting in pale yellow solution. 1-Azidohexadecane (0.373 g, 1.09 mmol) was added to 4 mL DMF:H_2O (4:1) and then added dropwise to the alkyne solution, which was left to stir at 60 °C for 24 hours. The resulting brown solution formed a grey precipitate overnight, which was filtered and dissolved in DCM. The organic layer was then washed with (1 M) NaOH:(0.5 M) EDTA solution, H_2O and brine before being dried by $MgSO_4$,, filtered and then solvent was removed by reduced pressure resulting in white solid (0.507 g, 0.89 mmol, 75 %). Melting point = 128.4 °C. LRMS *m/z* = 562.35 [**E** + H]$^+$ (calc. for $C_{33}H_{48}N_5O_3^+$, 562.38), *m/z* = 584.25 [**E** + Na]$^+$ (calc. for $C_{33}H_{47}N_5O_3Na^+$, 584.36), *m/z* = 600.25 [**E** + K]$^+$ (calc. for $C_{33}H_{47}N_5O_3K^+$, 600.20). ^{1}H NMR (300 MHz, $CDCl_3$, ppm), δ= 8.62 (t, 1H, NH), 8.36 (dd, J = 8.0, 1.0 Hz, 1H, *meta* py-H), 8.22 (dd, J = 8.0, 1.0 Hz, 1H, *meta* py-H), 7.98 (t, J = 8.0 Hz, 1H, *para* py-H), 7.56 (s, 1H, t), 7.41 (m, 5H, Bn), 5.43 (s, 2H, CH_2-O), 4.75 (d, J = 6.0 Hz, 2H, CH_2-NH), 4.29 (t, J= 7.0 Hz, 2H, t-CH_2), 1.86 (m, 2H, t-CH_2-**CH_2**), 1.27 (m, 26H, 13 x CH_2), 0.86 (t, J = 7.0 Hz, 3H, CH_3); ^{13}C NMR (75 MHz, $CDCl_3$, ppm): δ =164.3 (CO), 163.7 (CO), 150.0 (CN), 146.8 (CN), 144.7 (C-t), 138.6 (CH-py), 135.4 (C-Bn), 128.8-128.7 (3x CH), 127.6 (CH-py), 125.5 (CH-py), 122.3 (CH-t), 67.8 (Bn-CH_2), 50.5 (t-CH_2), 35.2 (NH-CH_2), 32.0 (CH_2), 30.4 (t-CH_2-**CH_2**), 29.8-6 (CH_2 x 9), 29.5 (CH_2), 26.6 (CH_2), 22.8 (CH_2), 14.2 (CH_3). FTIR (cm^{-1}) 3263, 3065, 2955 (CH), 2915 (CH), 2848 (CH), 1740 (COOR), 1635 (CONH), 1587, 1537, 1499, 1470, 1456, 1422, 1373, 1344, 1287, 1248, 1220, 1153, 1089, 1049, 1029, 1009, 992, 971, 849, 830, 775, 756, 728, 717, 692, 665, 641, 588, 517, 458, 421.

4.4.5.4 Synthesis of N_2-(1-(hexadecane)-1H-1,2,3-triazol-4-yl)methyl)-2-carboxamide-6-carboxylic acid (5)

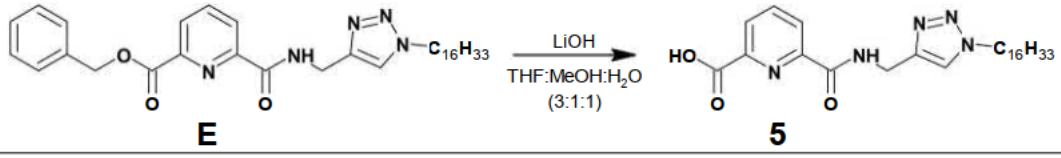

*Scheme 4.9.. Synthesis of ligand **5**.*

E (1.116 g, 1.98 mmol) was combined with LiOH (0.190 g, 7.95 mmol) in 30 mL of THF:MeOH:H_2O (3:1:1) and was stirred at room temperature under a nitrogen atmosphere overnight. The solid slowly dissolved resulting in a clear yellow solution over the course of 24 hours. 50 mL of H_2O was added to the solution causing a white precipitate to form, which was filtered and washed with H_2O, yielding an off-white solid (0.834 g, 89 %). Melting point = 94.3 °C; LRMS *m/z* = 472.25 [**5** + H]$^+$ (calc. for $C_{26}H_{42}N_5O_3^+$, 472.33), *m/z* = 494.20 [**5** + Na]$^+$ (calc. for $C_{26}H_{41}N_5O_3Na^+$, 494.31) and *m/z* = 510.20 [**5** + K]+ (calc. for $C_{26}H_{41}N_5O_3K^+$, 510.28). ^{1}H NMR (300 MHz, $CDCl_3$, ppm), δ= 9.83 (t, 1H, NH), 8.38 (t, J = 7.0 Hz, 2H, *meta* py-H), 8.04 (t, J = 8.0 Hz, 1H, *para* py-H), 7.73 (s, 1H, t), 4.85 (d, J= 5.0 Hz, 2H, **CH_2**-NH), 4.32 (t, J= 7.0 Hz, 2H, t-**CH_2**), 1.87 (m, 2H, t-CH_2-**CH_2**), 1.23 (m, 26H, 13 x CH2), 0.87 (t, J= 7.0, 3H, CH_3) ; ^{13}C NMR (75 MHz, $CDCl_3$, ppm): δ =166.2 (CO), 163.9 (CO), 149.9 (CN), 146.7 (CN), 144.5 (C-t), 139.0 (CH-py), 127.4 (CH-py), 125 (CH-py), 123.2 (CH-t), 51.0 (t-CH_2), 34.0 (NH-CH_2), 32.0 (CH_2), 30.2 (t-CH_2-**CH_2**), 29.8-5(10x CH_2), 26.6 (CH_2), 22.8 (CH_2), 14.2(CH_3). FTIR (cm^{-1}) 3345, 2915 (CH), 2849 (CH), 1745 (COOH), 1669 (CONH), 1536, 1471, 1453, 1430, 1337, 1235, 1174, 1114, 1073, 1056, 999, 879, 849, 804, 785, 739, 716, 699, 659, 568, 520, 428.

4.4.5.5 Synthesis of 1-azidohexadecane

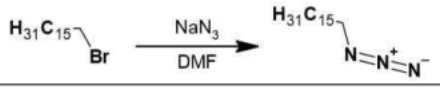

Scheme 4.10.. Synthesis of 1-azidohexadecane.

1-Bromohexadecane (2 mL, 6.54 mmol) combined with NaN_3 (0.638 g, 2.39 mmol) was dissolved in 25 mL DMSO and heated to 60 °C for 24 hours. Ethyl acetate was added to the solution and the organic layer was then washed with 6x 100 mL H_2O followed by brine and then dried with $MgSO_4$, filtered and then solvent was removed by reduced pressure resulting in a clear oil (1.542 g, 5.77 mmol, 88 %).[117] ^{1}H NMR (300 MHz, $CDCl_3$, ppm), δ= 3.25 (t, J = 7.00 Hz, 2H, CH_2-N_3), 1.59 (m, 2H, CH_2-CH_2N_3), 1.26 (m, 26H, 13 x CH_3), 0.88 (d, J= 6.70 Hz, 3H, CH_3); ^{13}C NMR (75 MHz, $CDCl_3$, ppm): δ = 51.6, 32.0, 29.8-29.6, 29.5, 29.3, 29.0, 26.8, 14.2. FTIR (cm−1) 2921 (CH), 2852 (CH), 2092 (N_3), 1465, 1348, 1256, 1063, 895, 720, 557

4.4.6 Lanthanide Complexation

4.4.6.1 General Procedure for Complexation of 5 with Ln^{3+}

Ligand **5** was combined with 0.33 equivalents of selected Ln^{3+} (with either triflate or chloride anion) and 1 equivalent of triethylamine in 5 mL of DCM:MeOH:MeCN (1:1:0.5). The solution was refluxed under microwave irradiation for 30 minutes and then subjected to vapour diffusion of diethyl ether at r.t until precipitation occurred and was then filtered.

4.4.6.2 Synthesis of $Eu(5)_3$

5 (0.0336 g, 0.071 mmol) was combined with $Eu(Cl)_3{\cdot}6H_2O$ (0.0078 g, 0.022 mmol) and 1 equivalent of triethylamine in 5 mL of DCM:MeOH:MeCN. The complex precipitated as a white powder, which was filtered giving $Eu(\mathbf{5})_3$ as a white solid (red emissive under shortwave UV light) (0.0258 g, 77 %). HRMS *m/z* = 1564.8694 $[Eu(\mathbf{5})_3 + H]^+$ (calc. for $(C_{78}H_{121}N_{15}O_9Eu)^+$, 1564.8678), *m/z* = 1586.8340 $[Eu(\mathbf{5})_3 + Na]^+$ (calc. for $(C_{78}H_{120}N_{15}O_9EuNa)^+$, 15686.8511) and m/z = 804.9050 $[Eu(\mathbf{5})_3 + 2Na]^{2+}$ (calc. for $(C_{78}H_{120}N_{15}O_9EuNa)^+$, 1564.8678). FTIR ($cm^{-1}$) 2920, 2851, 1632, 1588, 1461, 1426, 1353, 1183, 1081, 1049, 1017, 889, 852, 802, 760, 722, 661, 521, 434, 409. Elemental analysis for $C_{78}H_{120}N_{15}O_9Eu{\cdot}2H_2O{\cdot}0.5MeCN$ (1616.92 $gmol^{-1}$) Calculated: C 58.52, H 7.80, N 13.39 %. Found C 58.31, H 7.97, N 13.29 %.

4.4.6.3 Synthesis of $Tb(5)_3$

5 (0.0355 g, 0.071 mmol) was combined with $Tb(CF_3SO_3)_3{\cdot}5H_2O$ (0.0157 g, 0.023 mmol) and 1 equivalent of triethylamine in 5 mL of DCM:MeOH:MeCN. The complex precipitated as a white powder, which was filtered giving $Tb(\mathbf{5})_3$ as a white solid (green emissive under shortwave UV light) (0.0235 g, 66 %). HRMS *m/z* = 1570.8715 $[Tb(\mathbf{5})_3 + H]^+$ (calc. for $(C_{78}H_{121}N_{15}O_9Tb)^+$, 1570.8720), *m/z* = 1592.8646 $[Tb(\mathbf{5})_3 + Na]^+$ (calc. for $(C_{78}H_{120}N_{15}O_9TbNa)^+$, 1592.8539 and *m/z* = 807.9306 $[Tb(\mathbf{5})_3 + 2Na]^{2+}$ (calc. for $(C_{78}H_{120}N_{15}O_9TbNa_2)^{2+}$, 807.9216). FTIR ($cm^{-1}$) 2920, 2851, 1032, 1592, 1567, 1464, 1430, 374, 1280, 1240, 1164, 1082, 1029, 889, 852, 760, 723, 661, 636, 574, 518, 437, 414. Elemental analysis for $C_{78}H_{120}N_{15}O_9Tb{\cdot}H_2O{\cdot}2MeCN{\cdot}2.5CH_2Cl_2$ (1883.28 $gmol^{-1}$) Calculated: C 53.90, H 7.34, N 12.78 %. Found C 53.95, H 7.08, N 12.81 %.

4.4.6.4 Synthesis of $Dy(5)_3$

5 (0.0356 g, 0.076 mmol) was combined with $Dy(CF_3SO_3)_3{\cdot}8H_2O$ (0.0158 g, 0.023 mmol) and 1 equivalent of triethylamine in 5 mL of DCM:MeOH:MeCN. The complex precipitated as a white powder, which was filtered giving $Dy(\mathbf{5})_3$ as a white solid (yellow emissive under shortwave UV light) (0.0210 g, 57 %). HRMS *m/z* = 1575.8769 $[Dy(\mathbf{5})_3 + H]^+$ (calc. for $(C_{78}H_{121}N_{15}O_9Dy)^+$, 1575.8769) and *m/z* = 810.4346 $[Dy(\mathbf{5})_3 + 2Na]^{2+}$ (calc. for $(C_{78}H_{120}N_{15}O_9DyNa_2)^{2+}$, 810.4244). FTIR ($cm^{-1}$) 2920, 2851, 1636, 1590, 1562, 1461, 1428, 1375, 1278, 1244, 185, 1160, 1081, 1049, 1029, 891, 852, 761, 724, 661, 637, 573, 518, 460, 436, 414. Elemental analysis for $C_{78}H_{120}N_{15}O_9Dy{\cdot}4.5H_2O$ (1655.47 $gmol^{-1}$) Calculated: C 56.59, H 7.85, N 12.69 %. Found C 56.73, H 7.76, N 12.62 %.

4.4.6.5 Synthesis of $Sm(5)_3$

5 (0.0359 g, 0.076 mmol) was combined with $Sm(Cl)_3{\cdot}6H_2O$ (0.0083 g, 0.023 mmol) and 1 equivalent of triethylamine in 5 mL of DCM:MeOH:MeCN. This complex precipitated as a white powder, which was filtered giving $Sm(\mathbf{5})_3$ as a white solid (dim red/orange emissive under shortwave UV light) (0.0204 g, 56 %). HRMS *m/z* = 1563.8838 $[Sm(\mathbf{5})_3 + H]^+$ (calc. for $(C_{78}H_{121}N_{15}O_9Sm)^+$, 1563.8672), *m/z* = 1585.8727 $[Sm(\mathbf{5})_3 + Na]^+$ (calc. for $(C_{78}H_{120}N_{15}O_9SmNa)^+$, 1585.8491) and *m/z* = 804.4482 $[Sm(\mathbf{5})_3 + 2Na]^{2+}$ (calc. for $(C_{78}H_{120}N_{15}O_9SmNa_2)^{2+}$, 804.4192). FTIR ($cm^{-1}$) 2919, 2850, 1631, 1587, 1562, 1460, 1426, 1350, 1276, 1182, 1080, 1050, 1016, 890, 852, 760, 721, 661, 520, 463, 433, 409. Elemental analysis for $C_{78}H_{120}N_{15}O_9Sm{\cdot}2H_2O$ (1598.30 $gmol^{-1}$) Calculated: C 58.62, H 7.82, N 13.15 %. Found C 58.43, H 7.89, N 13.38 %.

4.4.6.6 Synthesis of La(5)$_3$

5 (0.0285 g, 0.060 mmol) was combined with La(Cl)$_3$·7H$_2$O (0.0067 g, 0.018 mmol) and 1 equivalent of triethylamine in 5 mL of DCM:MeOH:MeCN. This complex precipitated as a white powder; this was filtered giving La(**5**)$_3$ as a white solid (0.0157 g, 51 %). HRMS *m/z* = 1550.8528 [La(**5**)$_3$ + H]$^+$ (calc. for ($C_{78}H_{121}N_{15}O_9La$)$^+$, 1550.8530) and *m/z* = 1572.8352 [La(**5**)$_3$ + Na]$^+$ (calc. for ($C_{78}H_{120}N_{15}O_9LaNa$)$^+$, 1572.8349). FTIR (cm^{-1}) 2920, 2851, 1627, 1586, 1563, 1463, 1425, 1371, 1276, 1183, 1051, 1030, 1014, 887, 853, 759, 721, 689, 659, 638, 517. ^{1}H NMR (300 MHz, $CDCl_3$ & CD_3OD, ppm), δ= 8.20 (m, 2H, py-H), 8.04 (m, 1H, py-H), 7.66 (s, H, t-H), 0.88 (d, J= 6.70 Hz, 3H, CH_3), 1.77 (m, 2H, CH_2-CH_2N), 1.167 (m, 26H, 13 x CH2), 0.80 (t, 3H, CH_3).

4.4.6.7 Synthesis of Tm(5)$_3$

5 (0.0271 g, 0.057 mmol) was combined with Tm(Cl)$_3$·H$_2$O (0.0047 g, 0.017 mmol) and 1 equivalent of triethylamine in 5 mL of DCM:MeOH:MeCN. This complex precipitated as white powder, this was filtered giving Tm(**5**)$_3$ as a white powder (0.0174 g, 65 %). HRMS *m/z* = 1581.8762 [Tm(**5**)$_3$ + H]$^+$ (calc. for ($C_{78}H_{121}N_{15}O_9Tm$)$^+$, 1581.8839). FTIR (cm^{-1}) 2920, 2851, 1634, 1591, 1566, 1462, 1428, 1359, 1279, 1207, 1186, 1138, 1080, 1050, 1020, 892, 852, 764, 723, 683, 662, 527, 471. Elemental analysis for $C_{78}H_{120}N_{15}O_9Sm$·3MeOH·2MeCN (1759.0716 gmol^{-1}) Calculated: C 58.04, H 7.91, N 13.54 %. Found C 57.80, H 8.10, N 13.45 %.

4.5 Acknowledgements

I would like to thank Associate Professor John Harrison for measuring the FTIR of the 8 layer Eu(**5**)$_3$ film; Jade Pope and Erin Moffet for assisting in photography of captured images; Dr Jack Chen from Auckland University of Technology for allowing access to the Agilent Technologies Cary Eclipse spectrophotometer for phosphorescent measurements; Trever Loo (from Massey University, Palmerston North), Jenny Stockdell (from Waikato University) and Catherine Hobbis (Auckland University) for training and allowing access to use the ThermoFisher QExactive Focus coupled to an Ultimate™ 3000 RSLC or Bruker Daltonics MicrOTOF™ Spectrometer for HRMS and Kratos Axis UltraDLD for XPS measurements respectively.

4.6 References

1. J. A. Kitchen, *Coord. Chem. Rev.*, 2017, **340**, 232-246.
2. J.-M. Senegas, G. Bernardinelli, D. Imbert, J.-C. G. Bünzli, P.-Y. Morgantini, J. Weber and C. Piguet, *Inorg. Chem.*, 2003, **42**, 4680-4695.
3. S. Cotton, in *Lanthanide and Actinide Chemistry*, ed. S. Cotton, John Wiley & Sons Ltd, ch. 1, pp. 1-7.
4. Y. Yang, J. Li, X. Liu, S. Zhang, K. Driesen, P. Nockemann and K. Binnemans, *Chemphyschem*, 2008, **9**, 600-606.
5. B.-L. An, M.-L. Gong, J.-M. Zhang and S.-L. Zheng, *Polyhedron*, 2003, **22**, 2719-2724.
6. K. B. Blodgett and I. Langmuir, *Phys. Rev.*, 1937, **51**, 964-982.
7. K. B. Blodgett, *J. Am. Chem. Soc.*, 1935, **57**, 1007-1022.
8. K. B. Blodgett, *J. Am. Chem. Soc.*, 1934, **56**, 495-495.
9. K.-i. Iimura and T. Kato, in *Organized Organic Ultrathin Films*, ed. A. Katsuhiko, Wiley-VCH, pp. 43-105.
10. M. C. Petty, *Langmuir-Blodgett Films: An Introduction*, Cambridge University Press, Cambridge, 1996.
11. K. Ariga, Y. Yamauchi, T. Mori and J. P. Hill, *Adv. Mater.*, 2013, **25**, 6477-6512.
12. D. J. Wales and J. A. Kitchen, *Chem Cent J*, 2016, **10**, 72.
13. M. Parchine, J. McGrath, M. Bardosova and M. E. Pemble, *Langmuir*, 2016, **32**, 5862-5869.
14. M. Parchine, T. Kohoutek, M. Bardosova and M. E. Pemble, *Sol. Energy Mater. Sol. Cells*, 2018, **185**, 158-165.
15. F. Dumur, S. Reculusa, M. Mruczkiewicz, M. Perrin, L. Vignau and S. Fasquel, *Opt. Express*, 2016, **24**, 27184-27198.
16. I. I. I. D. H. McCullough and S. L. Regen, *Chem. Commun.*, 2004, 2787-2791.
17. C. Lin, Q. Chen, S. Yi, M. Wang and S. L. Regen, *Langmuir*, 2014, **30**, 687-691.
18. S. Sangiao, S. Martín, A. González-Orive, C. Magén, P. J. Low, J. M. De Teresa and P. Cea, *Small*, 2017, **13**, 1603207.
19. H. J. Bolink, E. Baranoff, M. Clemente-León, E. Coronado, N. Lardiés, A. López-Muñoz, D. Repetto and M. K. Nazeeruddin, *Langmuir*, 2010, **26**, 11461-11468.
20. K. Ariga, Y. Terasaka, D. Sakai, H. Tsuji and J.-i. Kikuchi, *J. Am. Chem. Soc.*, 2000, **122**, 7835-7836.
21. T. Michinobu, S. Shinoda, T. Nakanishi, J. P. Hill, K. Fujii, T. N. Player, H. Tsukube and K. Ariga, *Phys. Chem. Chem. Phys.*, 2011, **13**, 4895-4900.

22. R. Zhang, J. Shang, J. Xin, B. Xie, Y. Li and H. Möhwald, *Adv. Colloid Interface Sci.*, 2014, **207**, 361-375.
23. D. E. Barry, D. F. Caffrey and T. Gunnlaugsson, *Chem. Soc. Rev.*, 2016, **45**, 3244-3274.
24. M. L. Rodríguez-Méndez, Y. Khoussed, J. Souto, J. Sarabia, R. Aroca and J. A. de Saja, *Actuators B Chem.*, 1994, **18**, 89-92.
25. O. A. Serra, I. L. V. Rosa, C. L. Medeiros and M. E. D. Zaniquelli, *J. Lumin.*, 1994, **60-61**, 112-114.
26. D. J. Wales and J. A. Kitchen, *Chem. Cent. J.*, 2016, **10**, 72.
27. B. Liang, C. Yuan, Y. Wei, Y. Zhang, D. Jiang, S. Zhang and A. Lu, *Synth. Met.*, 1997, **88**, 219-223.
28. M. Mitsuishi, S. Kikuchi, T. Miyashita and Y. Amao, *J. Mater. Chem.*, 2003, **13**, 2875-2879.
29. J.-M. Ouyang, W.-H. Ling, C. Yang, Y. Li and G. Yu, *MSEB*, 2001, **85**, 247-250.
30. M. L. Rodriguez-Mendez, R. Aroca and J. A. DeSaja, *Chem. Mater.*, 1992, **4**, 1017-1020.
31. J. Rozbořil, Y. Rechkemmer, D. Bloos, F. Münz, C. N. Wang, P. Neugebauer, J. Čechal, J. Novák and J. van Slageren, *Dalton Trans.*, 2016, **45**, 7555-7558.
32. J. A. Kitchen, D. E. Barry, L. Mercs, M. Albrecht, R. D. Peacock and T. Gunnlaugsson, *Angew. Chem. Int. Ed.*, 2012, **51**, 704-708.
33. A. Galanti, O. Kotova, S. Blasco, C. J. Johnson, R. D. Peacock, S. Mills, J. J. Boland, M. Albrecht and T. Gunnlaugsson, *Chemistry*, 2016, **22**, 9709-9723.
34. V. I. Belyi, A. A. Rastorguev, A. A. Remova, I. A. Badmaeva, S. M. Repinsky and L. L. Sveshnikova, *Thin Solid Films*, 2002, **419**, 189-193.
35. Q. Dong-Jin and Y. Kong-Zhang, *Acta Phys. -Chim. Sin.*, 1993, **9**, 148-154.
36. Z. Gang, Z. Yanze and H. Pingsheng, *Thin Solid Films*, 2004, **468**, 268-272.
37. G.-L. Zhong, Y.-H. Wang, C.-K. Wang and K.-Z. Yang, *Thin Solid Films*, 2001, **385**, 234-238.
38. G. Zhong, Y. Feng, K. Yang and G. Zhu, *Chem. Lett.*, 1996, **1996**, 775-776.
39. H.-P. Zhou, C. Zhang and C.-H. Yan, *Langmuir*, 2009, **25**, 12914-12925.
40. S. K. Behera, S. Y. Park and J. Gierschner, *Angew. Chem. Int. Ed.*, **60**, 22624-22638.
41. A. R. Ramya, S. Varughese and M. L. P. Reddy, *Dalton Trans.*, 2014, **43**, 10940-10946.
42. Y. Gai, Q. Guo, K. Xiong, F. Jiang, C. Li, X. Li, Y. Chen, C. Zhu, Q. Huang, R. Yao and M. Hong, *Cryst. Growth Des.*, 2017, **17**, 940-944.
43. J. Wang, Y. Suffren, C. Daiguebonne, S. Freslon, K. Bernot, G. Calvez, L. Le Pollès, C. Roiland and O. Guillou, *Inorg. Chem.*, 2019, **58**, 2659-2668.
44. M. A. Hernández-Rodríguez, C. D. S. Brites, G. Antorrena, R. Piñol, R. Cases, L. Pérez-García, M. Rodrigues, J. A. Plaza, N. Torras, I. Díez, A. Millán and L. D. Carlos, *Adv. Opt. Mater.*, 2020, **8**, 2000312.
45. I. N'Dala-Louika, D. Ananias, C. Latouche, R. Dessapt, L. D. Carlos and H. Serier-Brault, *J. Mater. Chem. C*, 2017, **5**, 10933-10937.
46. L. Li, J. Cheng, Z. Liu, L. Song, Y. You, X. Zhou and W. Huang, *ACS Appl. Mater. Interfaces*, 2018, **10**, 44109-44115.
47. S. G. Dunning, A. J. Nuñez, M. D. Moore, A. Steiner, V. M. Lynch, J. L. Sessler, B. J. Holliday and S. M. Humphrey, *Chem*, 2017, **2**, 579-589.
48. D. Zhao, W. Li, Z. Hong, X. Liu, C. Liang and D. Zhao, *J. Lumin.*, 1999, **82**, 105-109.
49. W. Liu, W. Zhang, R. Liu and G. Li, *New J. Chem.*, 2021, **45**, 17377-17383.
50. Q.-M. Fu, H. Fu, L. Hu, L. Liu, S.-Z. Liu, Z.-L. Du and W.-Y. Wong, *J. Inorg. Organomet. Polym. Mater*, 2012, **22**, 97-104.
51. M. Clemente-León, E. Coronado, Á. López-Muñoz, D. Repetto, T. Ito, T. Konya, T. Yamase, E. C. Constable, C. E. Housecroft, K. Doyle and S. Graber, *Langmuir*, 2010, **26**, 1316-1324.
52. L. Liu, M. Chen, J. Yang, S.-Z. Liu, Z.-L. Du and W.-Y. Wong, *J. Polym. Sci., Part A: Polym. Chem.*, 2010, **48**, 879-888.
53. L. H. Gao, K. Z. Wang, L. Cai, H. X. Zhang, L. P. Jin, C. H. Huang and H. J. Gao, *J. Phys. Chem. B*, 2006, **110**, 7402-7408.
54. S. Sundaresan, J. A. Kitchen and S. Brooker, *Inorg. Chem. Front.*, 2020, **7**, 2050-2059.

55. B. Xu and B. Yan, *Colloids Surf.*, 2008, **329**, 7-11.
56. B. Yan and B. Xu, *Appl. Surf. Sci.*, 2008, **254**, 7237-7242.
57. O. Kotova, S. Blasco, B. Twamley, J. O'Brien, R. D. Peacock, J. A. Kitchen, M. Martínez-Calvo and T. Gunnlaugsson, *Chem. Sci.*, 2015, **6**, 457-471.
58. O. B. Shen Tao, Zhou Shaodong, Qian Chao, Chen Xinzhi, *Chin. J. Org. Chem.*, 2019, **39**, 873-877.
59. S. Bräse, C. Gil, K. Knepper and V. Zimmermann, *Angew. Chem. Int. Ed.*, 2005, **44**, 5188-5240.
60. J. D. Crowley, P. H. Bandeen and L. R. Hanton, *Polyhedron*, 2010, **29**, 70-83.
61. H. Ben El Ayouchia, L. Bahsis, H. Anane, L. R. Domingo and S.-E. Stiriba, *RSC Adv.*, 2018, **8**, 7670-7678.
62. A.-S. Chauvin, J.-C. G. Bünzli, F. Bochud, R. Scopelliti and P. Froidevaux, *Chem. Eur. J.*, 2006, **12**, 6852-6864.
63. K. Binnemans, *Coord. Chem. Rev.*, 2015, **295**, 1-45.
64. S. Zebret, E. Torres, E. Terreno, L. Guénée, C. Senatore and J. Hamacek, *Dalton Trans.*, 2011, **40**, 4284-4290.
65. S. Zebret, N. Dupont, G. Bernardinelli and J. Hamacek, *Chem. Eur. J.*, 2009, **15**, 3355-3358.
66. B.-L. An, M.-L. Gong, M.-X. Li, J.-M. Zhang and Z.-X. Cheng, *J. Fluoresc.*, 2005, **15**, 613-617.
67. *ReactLabTM. EQUILIBRIA. (1.1),. Jplus. Consulting. Multivariate. Analytical. Technologies,. Kilaben. Bay,. Australia,. 2022.*.
68. O. Kotova, J. A. Kitchen, C. Lincheneau, R. D. Peacock and T. Gunnlaugsson, *Chem. Eur. J.*, 2013, **19**, 16181-16186.
69. J. Andres and A.-S. Chauvin, *Inorg. Chem.*, 2011, **50**, 10082-10090.
70. B.-L. An, M.-L. Gong, K.-W. Cheah, W.-K. Wong and J.-M. Zhang, *J. Alloys Compd.*, 2004, **368**, 326-332.
71. B.-L. An, M.-L. Gong, K.-W. Cheah, J.-M. Zhang and K.-F. Li, *Chem. Phys. Lett.*, 2004, **385**, 345-350.
72. B.-L. An, M.-L. Gong, M.-X. Li and J.-M. Zhang, *J. Mol. Struct.*, 2004, **687**, 1-6.
73. J.-C. G. Bünzli and C. Piguet, *Chem. Soc. Rev.*, 2005, **34**, 1048-1077.
74. J. Kido and Y. Okamoto, *Chem. Rev.*, 2002, **102**, 2357-2368.
75. P. K. Sharma, A. R. van Doorn and A. G. J. Staring, *J. Lumin.*, 1994, **62**, 219-225.
76. A. D'Aléo, L. Toupet, S. Rigaut, C. Andraud and O. Maury, *Opt. Mater.*, 2008, **30**, 1682-1688.
77. K. T. Hua, J. Xu, E. E. Quiroz, S. Lopez, A. J. Ingram, V. A. Johnson, A. R. Tisch, A. de Bettencourt-Dias, D. A. Straus and G. Muller, *Inorg. Chem.*, 2012, **51**, 647-660.
78. O. A. Serra, E. J. Nassar, P. S. Calefi and I. L. V. Rosa, *J. Alloys Compd.*, 1998, **275-277**, 838-840.
79. O. A. Blackburn, M. Tropiano, T. J. Sørensen, J. Thom, A. Beeby, L. M. Bushby, D. Parker, L. S. Natrajan and S. Faulkner, *Phys. Chem. Chem. Phys.*, 2012, **14**, 13378-13384.
80. A. I. Voloshin, N. M. Shavaleev and V. P. Kazakov, *J. Lumin.*, 2001, **93**, 199-204.
81. R. Jagannathan and S. Soundararajan, *J. Coord. Chem.*, 1979, **9**, 31-35.
82. F. Renaud, C. Piguet, G. Bernardinelli, J.-C. G. Bünzli and G. Hopfgartner, *Chem. Eur. J.*, 1997, **3**, 1646-1659.
83. T. Le Borgne, J.-M. Bénech, S. Floquet, G. Bernardinelli, C. Aliprandini, P. Bettens and C. Piguet, *Dalton Trans.*, 2003, 3856-3868.
84. A. D. Becke, *Chem. Phys.*, 1993, **98**, 5648-5652.
85. C. Lee, W. Yang and R. G. Parr, *Phys. Rev. B Condens. Matter*, 1988, **37**, 785-789.
86. P. J. Stephens, F. J. Devlin, C. F. Chabalowski and M. J. Frisch, *Phys. Chem.*, 1994, **98**, 11623-11627.
87. S. H. Vosko, L. Wilk and M. Nusair, *Can. J. Phys.*, 1980, **58**, 1200-1211.
88. R. Krishnan, J. S. Binkley, R. Seeger and J. A. Pople, *Chem. Phys.*, 1980, **72**, 650-654.
89. M. Dolg, H. Stoll, A. Savin and H. Preuss, *Theor. Chim. Acta*, 1989, **75**, 173-194.

90. J. Yang and M. Dolg, *Theor. Chem. Acc.*, 2005, **113**, 212-224.
91. A. Weigand, X. Cao, J. Yang and M. Dolg, *Theor. Chem. Acc.*, 2010, **126**, 117-127.
92. M. Dolg, H. Stoll and H. Preuss, *Theor. Chim. Acta*, 1993, **85**, 441-450.
93. *Gaussian 16, Revision C.01,* Frisch, M. J.; Trucks, G. W.; Schlegel, H. B.; Scuseria, G. E.; Robb, M. A.; Cheeseman, J. R.; Scalmani, G.; Barone, V.; Petersson, G. A.; Nakatsuji, H.; Li, X.; Caricato, M.; Marenich, A. V.; Bloino, J.; Janesko, B. G.; Gomperts, R.; Mennucci, B.; Hratchian, H. P.; Ortiz, J. V.; Izmaylov, A. F.; Sonnenberg, J. L.; Williams-Young, D.; Ding, F.; Lipparini, F.; Egidi, F.; Goings, J.; Peng, B.; Petrone, A.; Henderson, T.; Ranasinghe, D.; Zakrzewski, V. G.; Gao, J.; Rega, N.; Zheng, G.; Liang, W.; Hada, M.; Ehara, M.; Toyota, K.; Fukuda, R.; Hasegawa, J.; Ishida, M.; Nakajima, T.; Honda, Y.; Kitao, O.; Nakai, H.; Vreven, T.; Throssell, K.; Montgomery, J. A., Jr.; Peralta, J. E.; Ogliaro, F.; Bearpark, M. J.; Heyd, J. J.; Brothers, E. N.; Kudin, K. N.; Staroverov, V. N.; Keith, T. A.; Kobayashi, R.; Normand, J.; Raghavachari, K.; Rendell, A. P.; Burant, J. C.; Iyengar, S. S.; Tomasi, J.; Cossi, M.; Millam, J. M.; Klene, M.; Adamo, C.; Cammi, R.; Ochterski, J. W.; Martin, R. L.; Morokuma, K.; Farkas, O.; Foresman, J. B.; Fox, D. J. *Gaussian, Inc., Wallingford CT, 2016.*
94. S. SeethaLekshmi, A. R. Ramya, M. L. P. Reddy and S. Varughese, *J. Photchem. Photobiol.*, 2017, **33**, 109-131.
95. D. N. Anwar and A. Srivastava, *IEEE Access*, 2020, **8**, 159609-159621.
96. E. F. Schubert, *Light-Emitting Diodes*, Cambridge University Press, Cambridge, 2 edn., 2006.
97. M. Vijayakumar, K. Mahesvaran, D. K. Patel, S. Arunkumar and K. Marimuthu, *Opt. Mater.*, 2014, **37**, 695-705.
98. I. E. Kolesnikov, A. A. Kalinichev, M. A. Kurochkin, E. V. Golyeva, A. S. Terentyeva, E. Y. Kolesnikov and E. Lähderanta, *Sci. Rep.*, 2019, **9**, 2043.
99. G. A. Crosby and J. N. Demas, *J. Phys. Chem.*, 1971, **75**, 991-1024.
100. A. S. Chauvin, F. Gumy, D. Imbert and J. C. G. Bünzli, *Spectrosc. Lett.*, 2004, **37**, 517-532.
101. M. G. Lagorio and E. San Román, *J. Chem. Educ.*, 2002, **79**, 1362.
102. A. S. Chauvin, F. Gumy, D. Imbert and J. C. G. Bünzli, *Spectrosc. Lett.*, 2007, **40**, 193-193.
103. J. Andres and K. E. Borbas, *Inorg. Chem.*, 2015, **54**, 8174-8176.
104. L. L. L. S. Melo, G. P. Castro and S. M. C. Gonçalves, *Inorg. Chem.*, 2019, **58**, 3265-3270.
105. M. Tsvetkov, D. Elenkova and M. Milanova, *Crystals*, 2022, **12**, 120.
106. D. K. Chattoraj, E. Halder, K. P. Das and A. Mitra, *Adv. Colloid Interface Sci.*, 2006, **123-126**, 151-161.
107. R. Johann and D. Vollhardt, *Mater. Sci. Eng.*, 1999, **8-9**, 35-42.
108. K. Myhre, H. Meyer and M. Du, *Surf. Sci. Spectra*, 2016, **23**, 102-111.
109. A. Kurachi, M. Matsumiya, K. Tsunashima and S. Kodama, *J. Appl. Electrochem.*, 2012, **42**, 961-968.
110. J. F. Moulder and J. Chastain, *Handbook of X-ray Photoelectron Spectroscopy: A Reference Book of Standard Spectra for Identification and Interpretation of XPS Data*, Physical Electronics Division, Perkin-Elmer Corporation, 1992.
111. M. Martínez-Calvo, O. Kotova, M. E. Möbius, A. P. Bell, T. McCabe, J. J. Boland and T. Gunnlaugsson, *J. Am. Chem. Soc.*, 2015, **137**, 1983-1992.
112. S. Dang, J.-H. Zhang and Z.-M. Sun, *J. Mater. Chem.*, 2012, **22**, 8868-8873.
113. G. Sheldrick, *Acta Crystallogr., Sect. A.*, 2008, **64**, 112-122.
114. *LED ColorCalculator (7.77), OSRAM SYLVANIA Inc., 2022*.
115. G. A. Crosby and J. N. Demas, *J. Phys. Chem. A.*, 1971, **75**, 991-1024.
116. A. S. Chauvin, F. Gumy, D. Imbert and J. C. G. Bünzli, *Spectrosc. Lett*, 2004, **37**, 517-532.
117. S. B. L. Vollrath, D. Fürniss, U. Schepers and S. Bräse, *Org. Biomol. Chem.*, 2013, **11**, 8197-8201.

5. Dual Emissive Spin Coated Films

5.1 Introduction

The overarching goal of this thesis was to demonstrate the versatility of our synthetic strategy for developing a range of different ligands and thus lanthanide complexes by clicking different substituents to the PDC unit. Because of this, research moved away from the amphiphilic systems (although much more could have been developed with the system) to the development of single component dual-emissive complexes with the intent of forming thicker luminescent coatings by using spin coating. The previous systems in chapter 4 demonstrated tunable emission by mixing different Ln^{3+} emissions but was hampered by the lack of blue emissive Ln^{3+}, reducing the overall region for which emission could be tuned to. Along with this, all emissions resulted from the same excitation wavelength, which meant that the overall emission was controlled by composition of the films.

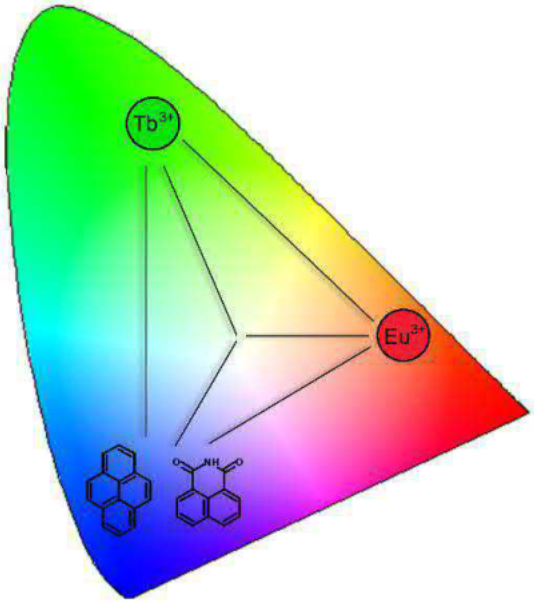

Figure 5.1. CIE 1931 chromaticity diagram showing the potential of emission ranges of colour-tunable emission when combined with red emission from Eu^{3+}, green emission from Tb^{3+} and blue emission from organic aromatic 1,8-naphthalimide or pyrene. Position and lines are not accurate but representative.

The aim of this chapter was to achieve dual emission in a single component system unlike the multiple component dual emissive systems of chapter 4. This entailed the incorporation of brightly emissive chromophores connected *via* the 1,2,3-triazole linker akin to the naphthalene system (**3**) of chapter 3. Ideally the chromophore emission should remain strong once complexed (unlike the naphthalene system of chapter 3) and it should be excited at wavelengths different to that required for Ln^{3+} centred emission. This should result in dual emissive systems where emission is generated from both Ln^{3+} and organic chromophore. The overall emission

could therefore be controlled by the excitation wavelength forming colour-tunable materials, and with the inclusion of a blue emissive chromophore improve upon the "white" emission achieved in chapter 4.

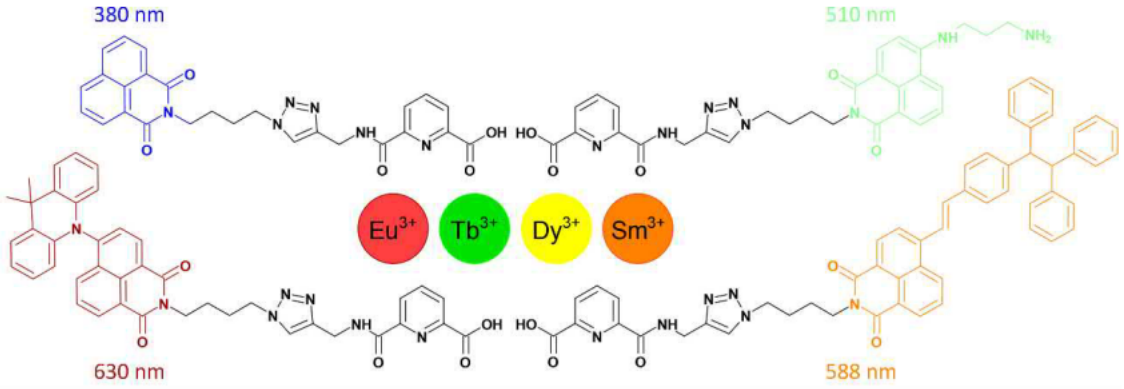

*Figure 5.2.. Examples of potential 1,8-naphthalimide based chromophores with different dominant emission which could be coupled with Ln^{3+} to form a range of dual emissive complexes.. Green emissive 1,8-naphthalimide from J.. E.. Elbert,. S.. Paulsen,. L.. Robinson,. S. Elzey and K.. Klein,. J.. Photochem.. Photbiol,. 2005,. **169**,. 9-19;. Red emissive 1,8-naphthalimide C.. J.. Christopherson,. D.. M.. Mayder,. J. Poisson,. N.. R.. Paisley,. C.. M.. Tonge and Z.. M.. Hudson,. ACS Appl.. Mater.. Interfaces,. 2020,. **12**,. 20000-20011;. Yellow emissive 1,8-naphthalimide from Y.. Yin,. Z.. Chen,. C.. Fan,. G.. Liu and S.. Pu,. ACS Omega,. 2019,. **4**,. 14324-14332..*

With our synthetic strategy, it should be easy to develop a wide variety of dual emissive systems by simply selecting different Ln^{3+} or organic chromophores with known emissions to get a new overall emission,[1] which could be targeted to different applications. Dual emissive systems, some of which were described in chapter 4, have a wide array of applications[2] such as ratiometric sensors (for oxygen,[3] temperature,[4] DNA,[5] or analytes[6]), molecular barcodes[7, 8] or logic gates,[9] multicolour cell imaging[10], white light generation (single component or mixed),[11-13] super-resolution fluorescence microscopy,[10] and OLEDS,[14, 15] applications which can obviously become more complex and potentially improved upon when the emission is also colour-tunable. As stated in previous chapters, ideally our systems should make the fundamental step from simple solutions or solid powders into more complex materials like films, gels, or glasses to make them more industrially friendly and thus more likely to make it to application testing stages. Furthermore, some applications such as OLEDs, molecular barcodes,[7] and logic gates[9] cannot remain as simple solutions or powders and must be in the form of materials like thin films to be incorporated into devices. Thus, to keep the PDC motif, which was found to be more stable and have better antenna properties than its PDA counterpart, the incorporated chromophore would also need structure directing properties for material formation (*e.g.* π-stacking, hydrogen bonding networks or Van der Waals force). In this instance the aim was to develop molecular films using the spin coating method.

Spin coating deposition is a widely used technique for the formation of molecular thin films for applications such as microelectronics (organic semiconductors, OLEDS, and solar cells)[16-18] and biomedical systems (wound dressings, cell culture substrates, and drug delivery devices)[16,19]. The methodology of spin coating can be broken down into four stages but the technique becomes complex in the finer details.[16, 19, 20] The initial ***deposition*** stage involves the solution being deposited onto the substrate. During this stage the solution pools or spreads, covering the substrate (deposition can either occur during substrate rotation known as dynamic deposition or when the substrate is static, called static deposition).[19, 20] Once the solution is deposited, the next stage is referred to as the ***spin up***, in which the substrate reaches the maximum spin rotation speed and the bulk of the solution is lost, leaving a thin film of liquid. It then reaches the third stage of ***spin off*** in which the substrate remains spinning at a constant rate; film thickness becomes more uniform with a gradual film thinning, dependent predominantly on solvent viscosity.[19-21] Finally, the thin film is no longer affected by the centrifugal forces, and the film is now in the ***evaporation*** stage where film thickness is dependent on solvent loss.[19-21] The last two stages predominately control film thickness and are dependent mainly on solution viscosity and spin rate, but also on solution volatility and concentration.[19] The spin coating technique is not the current dominant deposition method used in industry for the formation of thin films, this being thermal evaporation deposition as it gives much more precise control over film thickness.[22, 23] However, spin coating has advantages which make it a more prominent technique in research, this being a combination of spin coating equipment being much more accessible alongside the technique's methodology being much easier and more transferrable to a wide array of systems, as well as allowing more control over film composition.[21-24] Because of these two main factors and the desire to move towards potential OLED fabrication, spin coating was used in these studies for the formation of thicker molecular thin films.

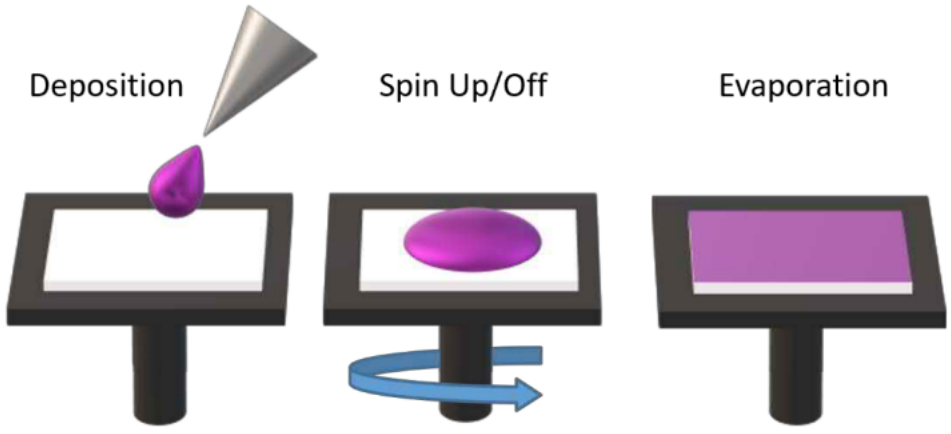

Figure. 5.3.. Simplistic. diagram. showing. the. stages. of. spin. coating,. with. the. initial. ***deposition****,. followed. by.* ***spin. up/off****. and. the. final* ***evaporation****. stage. leaving. a. molecular. film..*

In order to form dual emissive films via the spin coating technique, two different aromatic groups were chosen for incorporation into the PDC unit: 1,8-naphthalimide (**NI**) and pyrene (**PYR**) (Figure 5.4). These large aromatic groups were selected for their combination of emission and structure directing properties. Both systems are known for $\pi - \pi$ stacking interactions, which in this instance is the main intermolecular interaction for coating formation in place of alkane chains (which were used to form LB films previously). Both exhibit similar emission (emitting at 390 and 380 nm respectively) giving an overall blue emission. Combining this with Eu^{3+} red emission it was hoped not only to obtain dual emission but also single component white emission (as seen in Figure 5.1),[11] which has been noted in other previous **NI** and **PYR** lanthanide systems (see below). Additionally, as seen in Figure 5.2, **NI** is a very versatile chromophore with an emission profile that can be easily changed by modification of the aromatic rings, allowing for access to a range of emission profiles.[25-28]

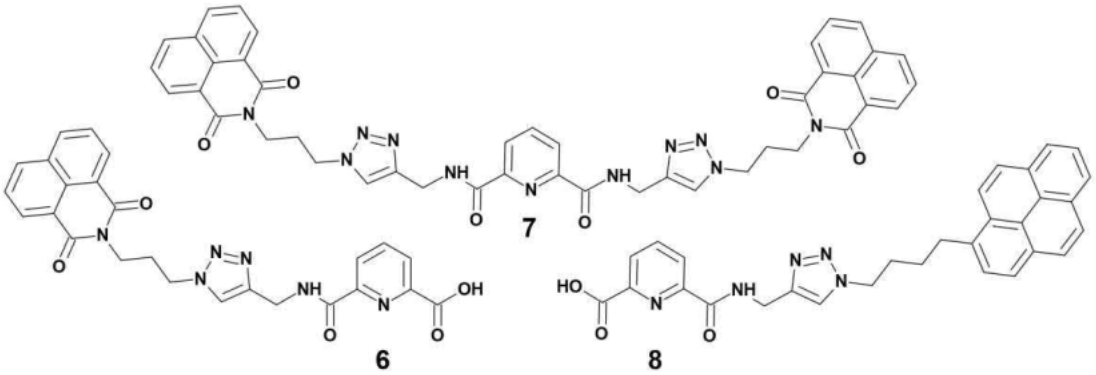

*Figure 5.4.. Aromatic "clicked" PDA (**7**) and PDC (**6** and **8**) ligands.. It is worth noting that a bis clicked **NI** PDA system has also been synthesised - this was made in case the blue emission from a single **NI** was not emissive enough for white emission..*

Previous lanthanide-based **NI** systems are scarce in the literature,[28-40] yet the few systems developed show promising results for what the **NI** based lanthanide systems can achieve. **NI** based lanthanide systems have been utilized for structure directing properties for MOF formation[34, 35] to more photophysical applications such as imaging agents,[29] logic gates or oxygen sensors,[40] white light emission,[36, 39] and $^1O_2$ generation.[32] **NI** based lanthanide systems focus mainly on the incorporation of Eu^{3+}, because alongside the potential of white emission, **NI** contains an ideal triplet state energy (18,500 cm^{-1}) to that of Eu^{3+} (17,500 cm^{-1}), making energy transfer from T_1 to $^5D_0$ favoured (although it may allow back transfer as the energy level is close to the $^5D_0$ excited state of Eu^{3+}).[36] This combined with **NI**'s excellent intersystem crossing efficiency (Φ_{ISC} = 95 %) makes the **NI** antenna appear ideal, at least on paper, for lanthanide excitation.[36] In most of the **NI** based lanthanide systems, all but a few have **NI** as the only antenna for lanthanide excitation.[28, 30, 31, 33, 34, 36, 37, 39] Because of this, in most systems emission is dominated by **NI** emission, where Eu^{3+} emission - as well as other lanthanides - is quite weak and practically hidden.[28, 30-35, 37]

Only a few examples show Eu^{3+} emission as dominant or on par with the **NI** chromophore emission. Yan and co-workers system was able to create Eu^{3+} dominant emission by utilizing a separate β-diketonate molecule as their main antenna, where the **NI** is acting as an ancillary antenna/chromophore. This resulted in improved Eu^{3+} emission, with the overall quantum yield improving 10 fold on introduction of the **NI** secondary antenna; however, this is attributed more to solvent removal than introduction of the **NI** antenna directly exciting the Ln^{3+}.[38] In comparison, the remaining two cases discussed below utilized only the **NI** antenna and were able to achieve strong Eu^{3+} centred emission and also "white" emission. This was achieved by balancing the overall emission of both organic chromophore and Ln^{3+} and taking advantage of excimer emission.

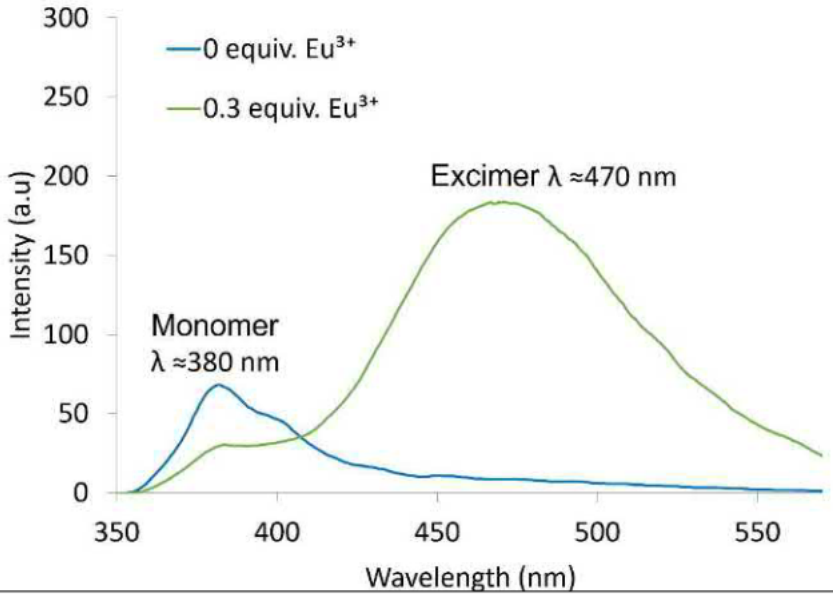

*Figure 5.5.. Examples of monomer and aggregation induced excimer emission from ligand **6** when titrated with $Eu(CF_3SO_3)_3$..*

Excimer emission is a result of π - π interaction between **NI** (or **PYR**) rings forming an "excited state dimer" which is populated from the singlet state, as if it was a triplet state in the phosphorescence process. However, the singlet state monomer emission subsequently is reduced due to the new competing pathway (Figures 5.5 and 5.6).[41-43] Because of this interaction, both **NI** and **PYR** can contain a second simultaneously emitting broad cyan emission peak centred at 480 or 490 nm respectively, alongside their now weaker monomer emission. Excimer emission can be induced by **NI**s which are covalently bonded, but also by intermolecular interactions between molecules, known as aggregation induced emission.[41] Molecules like **NI**s are generally less soluble in more non-polar solvents like MeCN, which causes the molecules to aggregate, allowing for enhanced π - π interactions between molecules (or complexes), leading to excimer emission and thus decreased monomer emission. In MeOH, this effect is reversed and excimer emission, unless present from intramolecular interactions, is missing.[41]

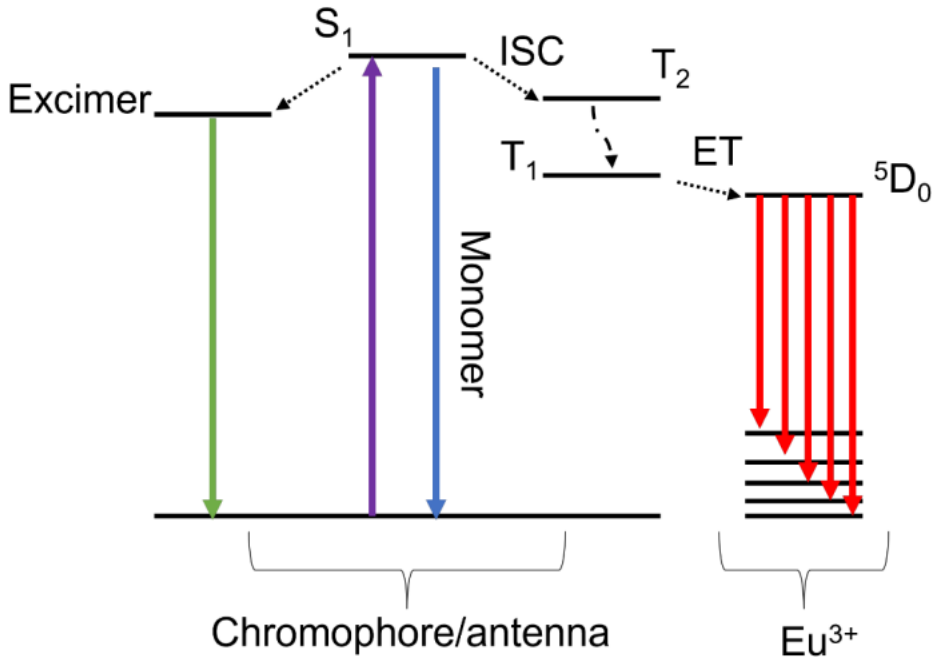

*Figure 5.6.. Jablonski energy diagram,. showing the potential pathway of the absorbed UV energy to either emit through monomer or excimer chromophore emission,. or to undergo intersystem crossing (ISC) and energy transfer (ET) to the Ln^{3+}.. The energy levels are not accurate but have height positions based off **NI** and Eu^{3+}.. Reference D.. W.. Cho and D.. W.. Cho,. New J.. Chem.,. 2014,. **38**,. 2233-2236 is used as a guide for excimer energy level positioning on the diagram..*

Ward and co-workers utilized aggregation induced emission to balance the overall monomer, excimer, and Eu^{3+} emission to achieve white emission in MeCN solution with CIE coordinates of x,y = 0.27, 0.25 ("pure-white" x,y=0.33)[11] using DOTA based **NI** antenna systems (Figure 5.7).[36] In MeOH, the Eu^{3+} emission is significantly weaker than **NI** monomer emission resulting in overall blue emission. Ward and co-workers attempted to prepare white emissive films of the complex but the strong excimer formed in the solid state caused the film to appear blue emissive.[36]

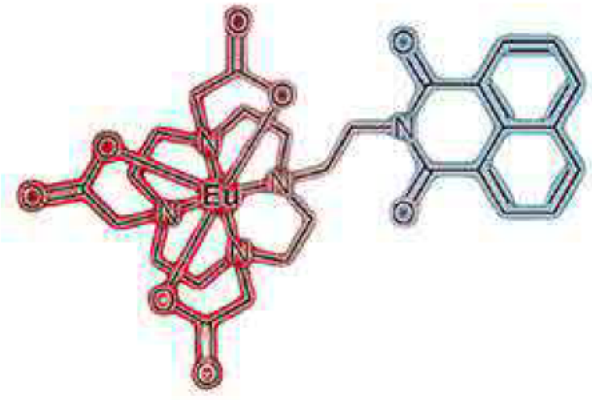

*Figure 5.7.. Ward and co-workers DOTA based **NI** antenna system capable of white light emission in MeCN.. Image adapted with permission from A.. H.. Shelton,. I.. V.. Sazanovich,. J.. A.. Weinstein and M.. D.. Ward,. Chem. Commun.,. 2012,. **48**,. 2749-2751.. Copyright 2022 Royal Society of Chemistry..*

In comparison, Yan and co-workers achieved extremely close to "pure-white" emission with CIE coordinates of x,y = 0.34, 0.31 in solid state (Figure 5.8).[39] Because the emission is in the solid state, the excimer emission is dominated by **NI** chromophore emission, yet the Eu^{3+} centred emission is still as strong as the **NI**. It was suggested by Yan that instead of the common population route of the excited $^5D_0$ of Eu^{3+} *via* the T_1, it was instead being populated from the S_1 of the **NI** chromophore, which has an energy level better matched for both population of Ln^{3+} excited state and mitigation of BT processes.[39] Yan states that they achieved this by making ISC unfavourable (thus reducing the population of the triplet state) by coordinating the **NI** away from the Ln^{3+} centre by an alkyl chain linker (Figure 5.8). Depending on the length of the alkyl chain linker Eu^{3+} centred emission intensity was controlled.[39] With this they could simply increase or decrease the chain length to balance out the overall emissions to achieve close to white emission.[39]

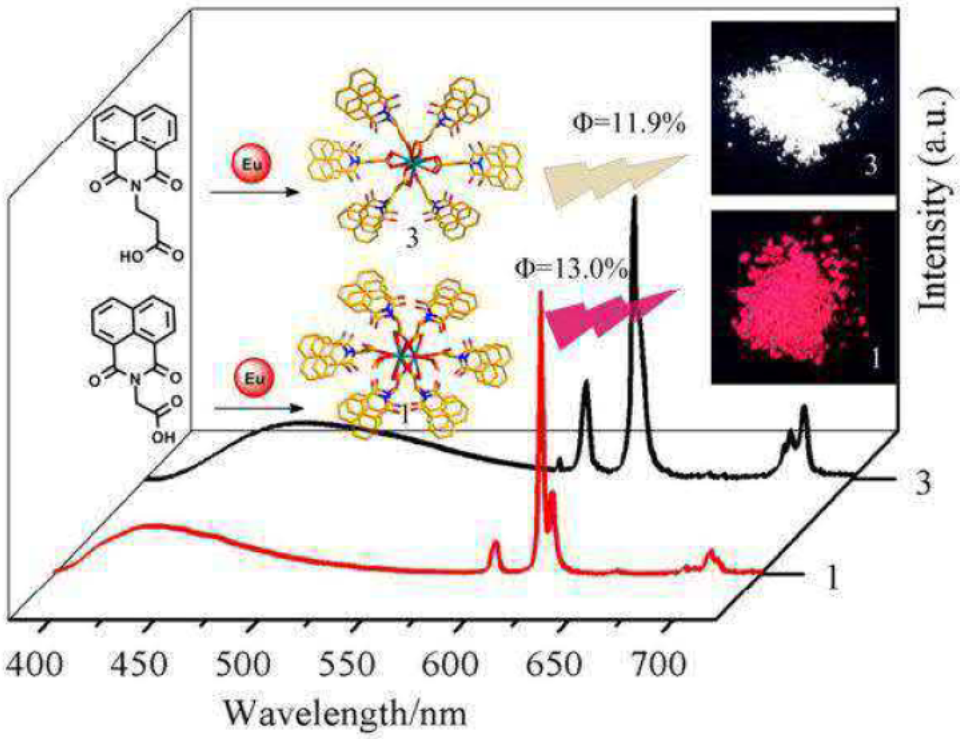

*Figure 5.8. Yan and co-workers simplistic **NI** based complexes, in which overall emission is tunable by increasing or decreasing the alkyl linker chain to modify the ISC effects of the **NI** antenna, resulting in the drastic change from overall red emission to extremely close to white emission. Image adapted with permission from J. Zhang, H. Li, P. Chen, W. Sun, T. Gao and P. Yan, J. Mater. Chem. C, 2015, **3**, 1799-1806. Copyright 2022, Royal Society of Chemistry.*

Similar to **NI**-lanthanide based assemblies, the incorporation of a **PYR** motif is also relatively uncommon.[44-59] Incorporation of a **PYR** motif in lanthanide based assemblies was initially done as an antenna for Eu^{3+} excited states by Fages and co-workers.[56] Similar to **NI**, the **PYR** is not an optimal lanthanide antenna, with a triplet state 16,890 cm^{-1} being below that of the $^5D_0$ excited state of Eu^{3+}.[48, 55, 56] Although the energy level is below that of $^5D_0$, population is still mainly

considered to occur through the triplet state, although there are indications that S_1 population can occur. Since the T_1 is so close in energy to that of the $^5D_0$ state, lanthanide emission is weak with overall quantum yields of 0.86 % being reported.[48, 55, 56] Because of this, **PYR** is more commonly used as an antenna for NIR emitting lanthanides such as Nd^{3+}, Er^{3+} and Yb^{3+} [46, 47, 52] or not used for photophysical properties but rather for materials formation such as gels[58] or drop-cast films.[50] Applications of these **PYR** systems are varied, ranging from MRI contrasting agents,[46] luminescent phospholipid vesicles,[53] oxygen sensing/$^1O_2$ generation[48, 55-57] and white emissive or dual emissive systems.[46, 49, 51, 59] Focusing on the more relevant dual and white emissive systems, Prasad and co-workers were able to achieve white emission within a two component system by utilizing a poly(arylether)dendron molecule which acted as both lanthanide coordinator and gelator (Figure 5.9). It also forms donor-acceptor pairs with the **PYR** molecule which allows resonance energy transfer from the **PYR** to the Ln^{3+} to take place.[49] By modifying a ratio of both Eu^{3+}, Tb^{3+}, and **PYR** in the gel they are able to achieve a white emission with CIE coordinates x,y = 0.35, 0.33 from the combination of emissions.

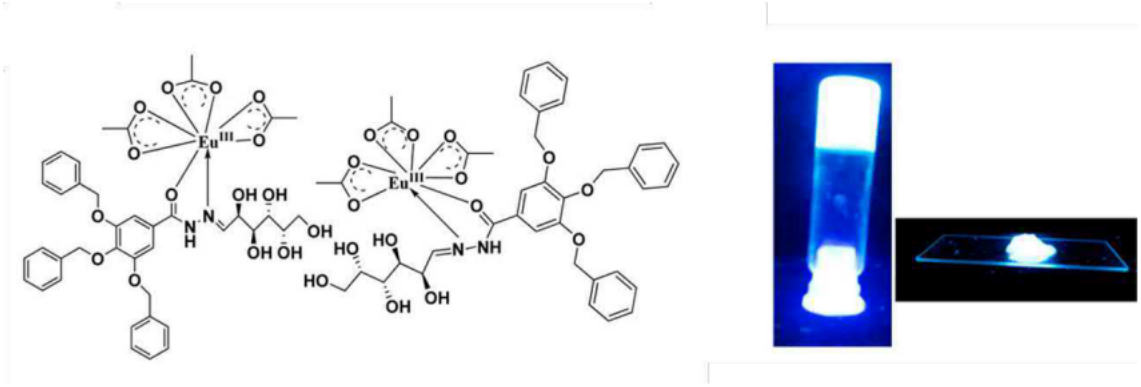

*Figure. 5.9.. Prasad. and. co-workers'. white. emissive. gel,. made. from. poly(arylether)dendron,. coordinated. to. a. mixture. of. Eu^{3+}. and. Tb^{3+} as. well. as. forming. donor-acceptor. pairs. with. **PYR** donor,. suggested. to. be. associated. with. the. benzyl. ester. motif.. Images. adapted. with permission. from. reference. P.. Kumar,. S.. Soumya. and. E.. Prasad,.* ACS Appl. Mater. Interfaces,. *2016,. **8**,. 8068-8075.. Copyright. 2022, American. Chemical. Society..*

Similarly, Oh and co-worker developed a multicomponent MOF architecture in order to achieve white emission at x,y = 0.30, 0.34 (λ_{ex} = 304 nm) (Figure 5.10).[51] Oh and co-worker achieve this by first balancing the ratio of 1,4-benzenedicarboxylic acid and 1-(**pyrene**-1-carboxamidoterephthalic acid) to (0.975:0.025). By doing so they are able to control the **PYR** emission to overall blue (monomer emissive) by reducing (green) excimer formation, then by controlling the ratio of both Eu^{3+} and Tb^{3+} (0.1:0.9), they can achieve an overall yellow emission. As a result, by combining the emission of the organic and Ln^{3+} chromophores, the MOF achieves colour-tunable emission over a very short wavelength range of 10 nm, switching between light green to blue and crossing over the "white" emissive region (Figure 5.10).[51]

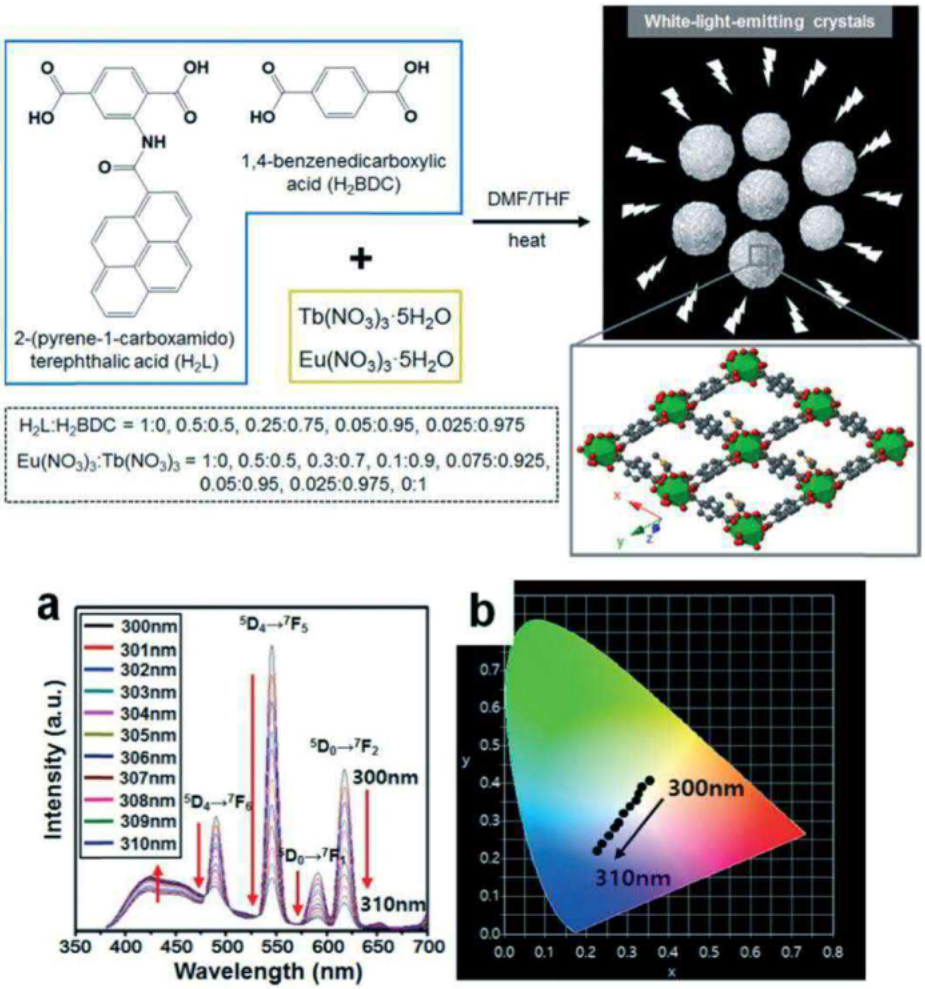

Figure. 5.10.. (Top). Oh. and. co-workers. MOF. structure. and. components. utilized. to. form. white. emissive. crystals.. (Bottom). Oh. and. co-worker. MOF. structure. with. a. Eu^{3+}:Tb^{3+}. (0.1:0.9). ratio. and. H_2L. and. H_2BDC. (0.025:0.975). ratio. in. order. to. achieve. close. to. white. solid. emission. which. is. also. colour-tunable.. (a). Shows. the. fluorescent. emission. changes. as. excitation. wavelength. changes. and. (b). shows corresponding. overall. emission. colour. on. a. CIE. 1931. chromaticity. diagram.. Images. adapted. with. permission. from. J.. Park. and. M.. Oh, CrystEngComm,. *2016,.* ***18****,. 8372-8376.. Copyright. 2022,. Royal. Society. of. Chemistry..*

In comparison to most previous **NI** and **PYR** lanthanide-based systems (the exception being Oh and co-worker's MOF assembly),[51] our systems incorporate two lanthanide antennas in the same ligand. By design this means both the blue chromophore and lanthanide centred emission are separate with Ln^{3+} populated predominately from our central pyridyl antenna. While **NI** and **PYR** may act as a secondary antenna, they are predominately focused on their own emission. This approach, unlike previous systems, should allow for dual emission in a single component system. Additionally, if absorption spectra contain regions of both overlap and no overlap between the different antennae, the systems will ideally be colour-tunable. With this, unlike all but Oh's system[51], the emission will ideally be tuned by the excitation wavelength it is excited by, not by changing the composition of the material. Alongside this, to the best of our knowledge there is no example of **NI** or **PYR** lanthanide-based systems that show both solution, solid state, and molecular films which are colour-tunable and have white emissive properties retained in all forms.

5.2 Results and Discussion

5.2.1 Ligand Synthesis and Characterisation

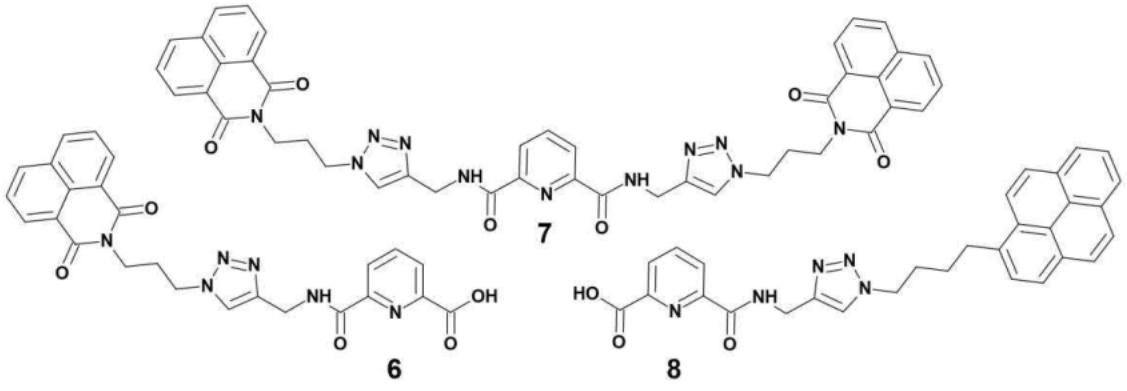

*Figure 5.11.. Aromatic "clicked" PDA (**7**) and PDC (**6** and **8**) ligands..*

Ligands **6**, **7,** and **8** (see Figure 5.11) were all synthesised starting from commercially available DPA. Ligands **6** and **8** were synthesised using the mono-protected alkyne (**D**) prepared in chapter 4, whereas **7** was synthesised from bis-alkyne (**B**) using the procedure developed in chapter 3.

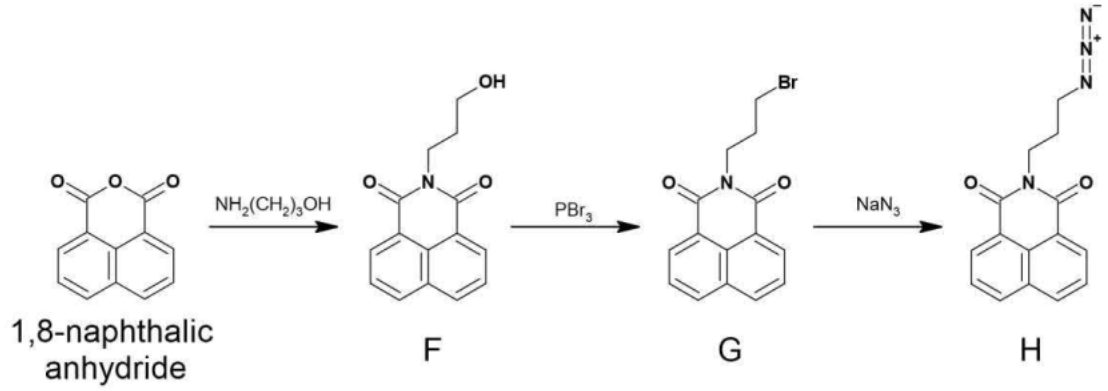

*Scheme 5.1.. Synthetic pathway from starting compound 1,8-naphthalic anhydride to azide reactant **H** used to synthesise both **6** and **7**..*

Focusing initially on **6** and **7**, synthesis of the appropriate halide and subsequent azide was required from commercially available 1,8-naphthalic anhydride (Scheme 5.1). 1,8-Naphthalic anhydride was first refluxed in EtOH in the presence of 1 equivalent of 3-aminopropan-1-ol for 24 hours. The solution was recrystalised yielding N-(2-hydroxypropyl)-1,8-naphthalimide (**F**, 63 %) as a light-yellow crystalline solid.[60] **F** was redissolved in dry ethyl acetate, to which excess phosphorus tribromide was added dropwise. The solution was refluxed for 5 hours, then allowed to cool to r.t before adding cold water until a white solid precipitate formed, which was filtered yielding N-(3-bromopropyl)-1,8-naphthalimide (**G**, 81 %) as a white solid.[60] **G** was then initially used in a one-pot "click" reaction for synthesis of both **6** and **7**, but product formation was poor yielding. Because of this, the decision was made to further convert the bromide to an azide to improve the "click" procedure, even though this lost the one-pot procedure developed in chapter 3. Azide formation was straight forward and relatively

safe with the desired product having a Carbon + Oxygen to Nitrogen ratio of 3.75 (N_O+N_c/N_N= 3.75), which is within the safe ratio to synthesise and store azides at r.t. To do this **G** was dissolved in 30 mL of DMF with 2.2 equivalents of NaN_3 and was heated to 80 °C for 24 hours. The solution was then cooled, to which water was then added to stop the reaction and ethyl acetate added to extract the product. Following this the organic layer was separated and washed with water and brine, yielding N-(3-azidopropyl)-1,8-naphthalimide (**H**, 82 %) as a bright green solid once solvent was removed.

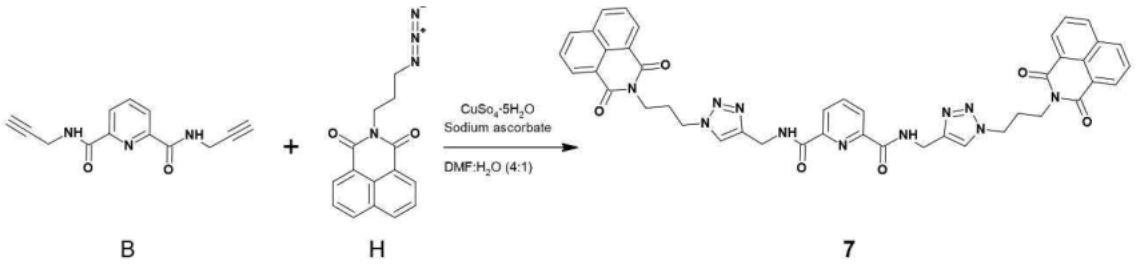

Scheme 5.2. Synthesis of ***7****.*

Synthesis of **7** was then relatively straightforward (Scheme 5.2), following the same procedure in chapter 3 via a multi-component CuAAC reaction, where bis-alkyne (**B**) underwent a $CuSO_4.5H_2O$ catalysed cyclization with **H** in DMF:H_2O (4:1). The solution changed from a bright yellow to a dark green, and addition of water caused a cloudy precipitate to form, which was filtered and washed with (0.1 M) NaOH:(0.5 M) EDTA solution, yielding **7** as an off-white solid. This was further purified by redissolving the product in a hot solution of EtOH:DCE (1:1) and filtering. The solvent was then left to slowly evaporate, yielding **7** as an off-white solid (70 %).

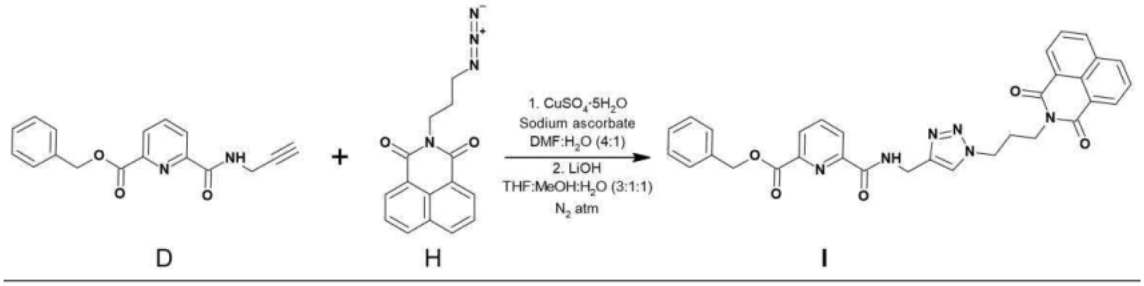

Scheme 5.3. Synthesis of ***I*** *via a multi-component CuAAC reaction.*

Synthesis of **6** was not as straightforward (Scheme 5.3). Initially, intermediate **I** was obtained *via* the same CuAAC reaction method used in chapter 4. Instead of carrying out the click as a one-pot multi-component CuAAC reaction, it was found that the reaction proceeded more favourably when the Cu(I)-acetylide (or π,σ-bis(copper) acetylide, see Figure 4.11 for details) was formed prior to addition of azide.[61] This was achieved by mixing mono-alkyne (**D**) with $CuSO_4.5H_2O$ and sodium ascorbate in DMF:H_2O (4:1) at 80 °C for ≈ 10 minutes before adding **H** to allow formation of the Cu(I)-acetylide, normally indicated by a solution colour change to a deeper orange. Following this **H** was added, and the solution was left for 24 hours, stirring and

heating at 80 °C, during which the solution changed from orange to green overnight. Water was then added to the solution to induce product precipitation, which was then filtered and washed with (1 M) NaOH:(0.5) M EDTA to remove the copper, yielding **I** (71 %) as an off-white solid. If precipitation did not occur upon water addition, the product could then be extracted with a DCM:MeOH solution, which was washed with the (0.1 M) NaOH:(0.5 M) EDTA solution, followed by several water washes. The solvent was then removed until a residue/oil remained which solidified or occasionally crystallised.

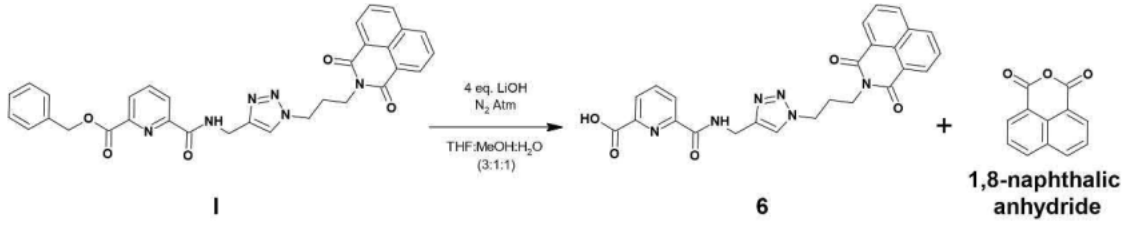

*Scheme 5.4. Synthesis of **6**.*

The final stage of this synthesis was the deprotection of the benzyl ester protecting group (Scheme 5.4). Initially the same method was used as in chapter 4. Intermediate **I** was suspended in a mixture of THF:MeOH:H_2O (3:1:1) with 4 equivalents of LiOH and stirred under a nitrogen atmosphere for 24 hours. The solvent was then evaporated until a residue remained, to which 1 M HCl was added to cause a white precipitate to form alongside a brown sticky residue. From ^{1}H NMR studies (see Figure 5.12) it was clear that the benzyl protecting group was removed but there was also evidence of a byproduct of cleaved 1,8-naphthalimide. In order to remove this, the solid was rinsed with acetone, which dissolved the byproduct leaving behind **6** as an off-white solid (59 %). Methods to circumvent this undesirable cleavage were investigated, one of which was stirring in 1 equivalent of NaOH until product dissolved, then re-acidifying until precipitation. Unfortunately, this resulted in complete cleavage of **NI** (see Figure 5.12). Pd/C catalysed benzyl ester hydrogenolysis was attempted, in which 10 w% of Pd/C was combined with **I** in MeOH and put under 6 atmospheres of H_2 for 24 hours. This solution was then filtered through celite, and solvent was removed, yielding **6**; however, this method was found to be inconsistent, in some cases resulting in an unknown product. Because of the results obtained from these later attempts, the LiOH method was maintained as the main method even though product is lost through some secondary cleavage.

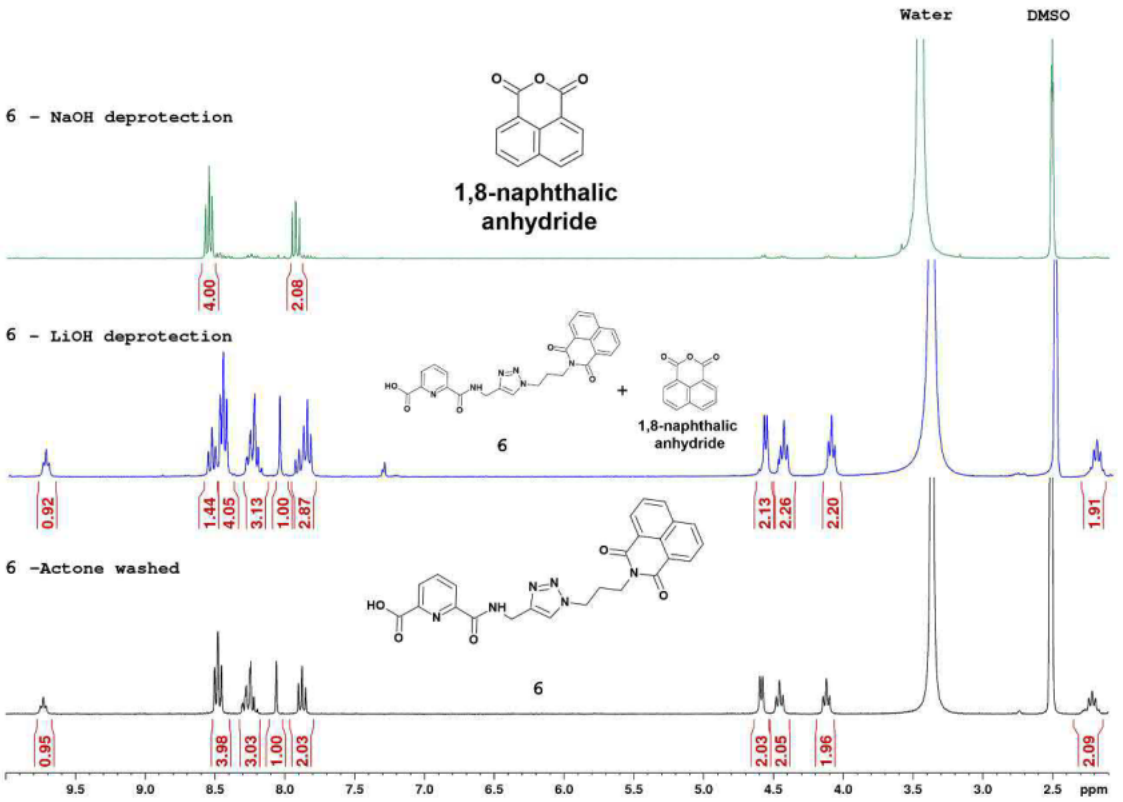

*Figure 5.12: ^{1}H NMR of **6** via different deprotection methods (300 MHz, DMSO-d_6). (Top/green) The resulting product when intermediate **I** is "deprotected" with 1 eq. NaOH, resulting in only suspected starting material 1,8-nahpthalic anhydride. (Middle/blue) The initial result when intermediate **I** is deprotected via LiOH, showing presence of cleaved 1,8-naphthalic anhydride, which is not present in **I** (see Figure 5.13). (Bottom/black) Resulting product **6** after washing with acetone.*

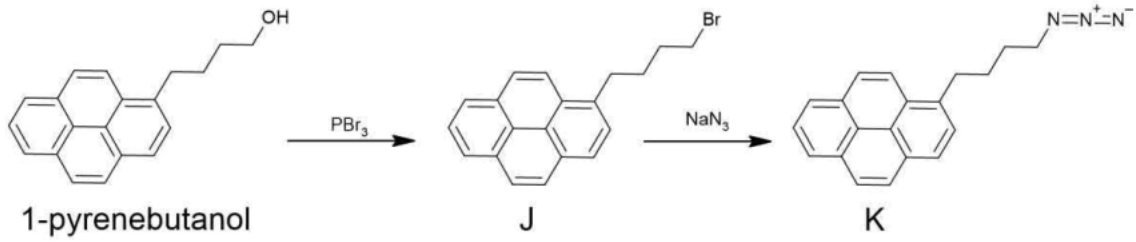

*Scheme 5.5. Synthetic pathway starting from 1-pyrenebutanol to intermediates **J** and **K**.*

For the synthesis of **8**, the appropriate halide and subsequent azide was also required, this time starting from commercially available 1-pyrenebutanol (Scheme 5.5). Converting this to the bromide and subsequent azide (N_O+N_c/N_N= 6.3) was achieved in the same manner as the previous system. Conversion of the alcohol to the bromide was carried out by reacting 1-pyrenebutanol in excess phosphorus bromide in dry ethyl acetate for 5 hours. Cooled water was added slowly to stop the reaction and left in the refrigerator for 24 hours to induce precipitation, yielding 1-(4-bromobutane)pyrene as white crystalline material (**J**, 92 %).[60] **J** was then converted to the azide by heating in DMF with 2.2 equivalents of NaN_3 for 24 hours. This was worked up using the same method as for **K**, yielding 1-(azidobutane)pyrene as a pale pink solid (88 %).

The intermediate **L** was then obtained via the same CuAAC reaction conditions and workup used in the synthesis of **D**, yielding **L** as a brown crystalline solid (44 %) (Scheme 5.6). Similarly, **L** was deprotected using LiOH to obtain **8** as a brown solid (86 %).

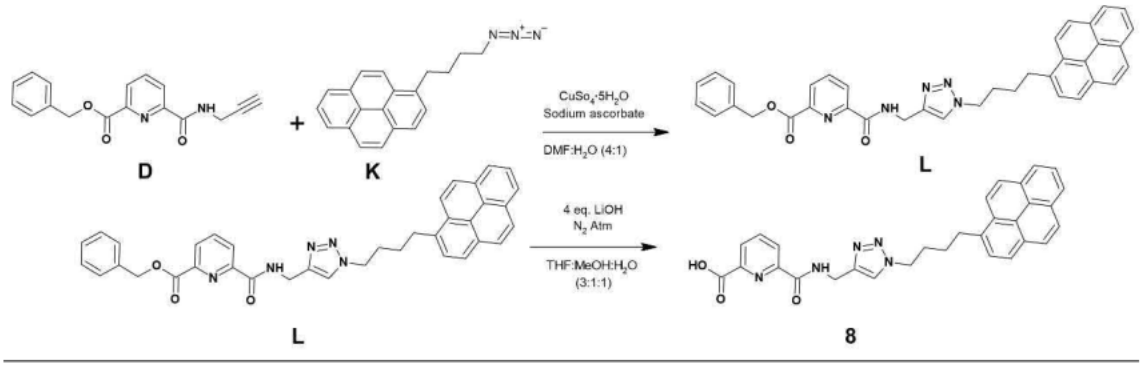

*Scheme 5.6.. Synthetic pathway for synthesis of intermediate **L** and ligand **8**.*

The successful synthesis of ligands **6**-**8** was confirmed by ^{1}H NMR, ^{13}C NMR, and LRMS. Ligands were also characterised by FTIR and UV-visible absorption spectroscopy (see Section 8.3.1 for more details). LRMS confirmed the successful synthesis of ligands and intermediates with observed peaks matching the calculated values (Table 5.1 and Section 8.3.1).

Table 5.1.. Mass peaks observed for ligands and intermediates vs calculated values..

Ligands and Intermediates	Calculated *m/z*	Experimental *m/z*
[**6** + H]$^{+}$	485.16, $C_{25}H_{21}N_6O_5^{+}$	485.10
[**7** + Na]$^{+}$	824.40, $C_{43}H_{35}N_{11}O_6^{+}$	824.40
[**8** - H]$^{-}$	502.54, $C_{30}H_{24}N_5O_3^{-}$	502.10
[**I** + H]$^{+}$	575.10 , $C_{32}H_{27}N_5O_5^{+}$	575.15
[**L** + H]$^{+}$	594.68 , $C_{37}H_{32}N_5O_3^{+}$	594.68

^{1}H NMR spectra (Figures 5.13-15) indicated the successful formation of all three ligands and their intermediate species. Click formation is clear in the synthesis of **7**, **I** and **L** with the appearance of the singlet resonance peak (t) at ≈ 8 ppm assigned to the single or dual 1,2,3-triazole protons. These changes also coincide with the disappearance of the terminal alkyne (CH) protons at 4.1 (mono-alkyne, **D**) and 4.2 (bis-alkyne, **B**) ppm, and the corresponding significant downfield shift of the linking methylene group (CH_2-NH) 4.6 ppm (for **7**, I and **L**) and amide proton (NH) 8.9 - 9.0 ppm for **I** and **L**; 9.7 - 9.9 ppm for **7.** Additionally, the azide reactants disappearance in **H** and **K** is indicated by the disappearance of the CH_2-N_3 (≈ 3.5 ppm) peak which corresponds with a downfield shifted CH_2-t peak (≈ 4.4 ppm). In the case of intermediates **I** and **L** the deprotection of the benzyl ester protecting group is clearly indicated by the loss of benzyl aromatic proton signals (Bn ≈ 7.4 ppm) and the CH_2-O linker (5.4 ppm). The only other change of note is the much more significant downfield shift observed in the NH amide than previously, with 9.0 - 9.7 ppm for both formation of **6** and **8**.

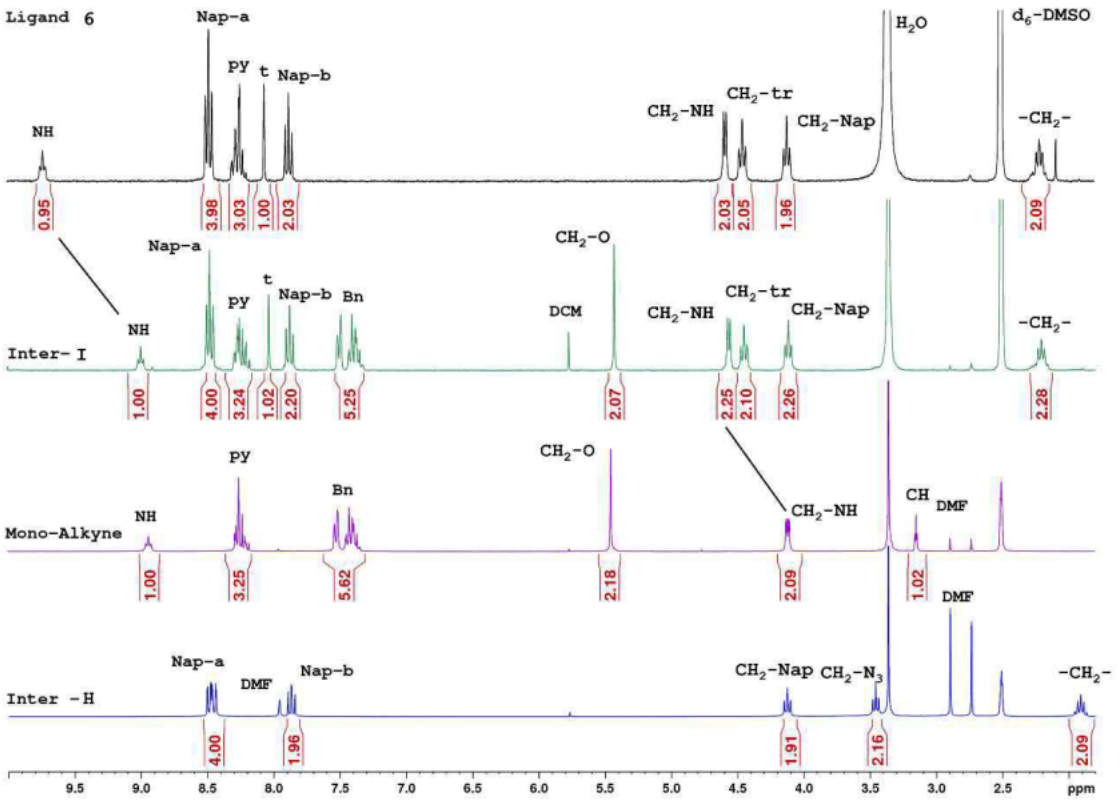

*Figure. 5.13. ^{1}H. NMR. of. **6**. and. its. corresponding. starting. materials. and. intermediate. **I**. (300. MHz,. DMSO-d_6).. Abbreviations:. Nap-a. for ortho. and. para. protons. of. **NI**,. Nap-b. for. meta. protons. of. **NI**,. py. for. pyridine. ring,. t. for. 1,2,3-triazole,. and. Bn. for. benzyl. ring.. Dash. (-) indicates. the. group. that. the. CH_2 (which. is. associated. with. this. signal). is. bonded..*

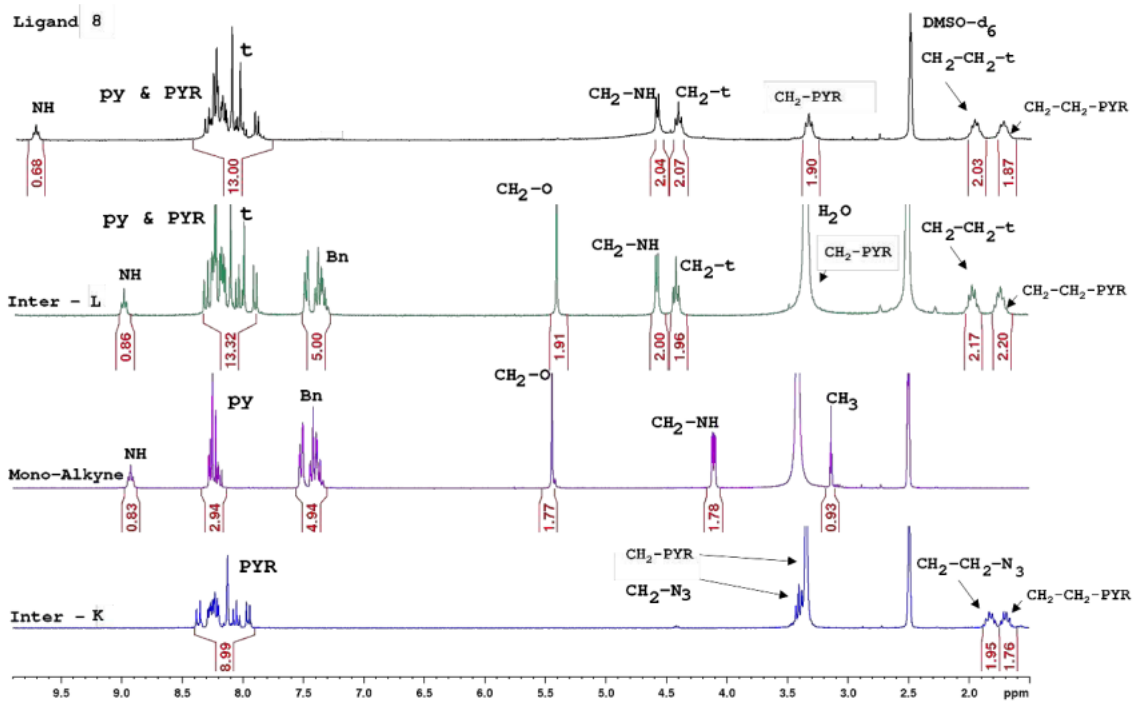

*Figure. 5.14.. ^{1}H. NMR. of. **8**. and. its. corresponding. starting. materials. and. intermediate. **L**. (300. MHz,. DMSO-d_6).. Abbreviations:. py. for pyridine. ring,. **PYR**. for. pyrene. ring,. t. for. 1,2,3-triazole,. and. Bn. for. benzyl. ring.. Dash. (-). indicates. the. group. that. the. CH_2 (which. is associated. with. this. signal). is. bonded. to..*

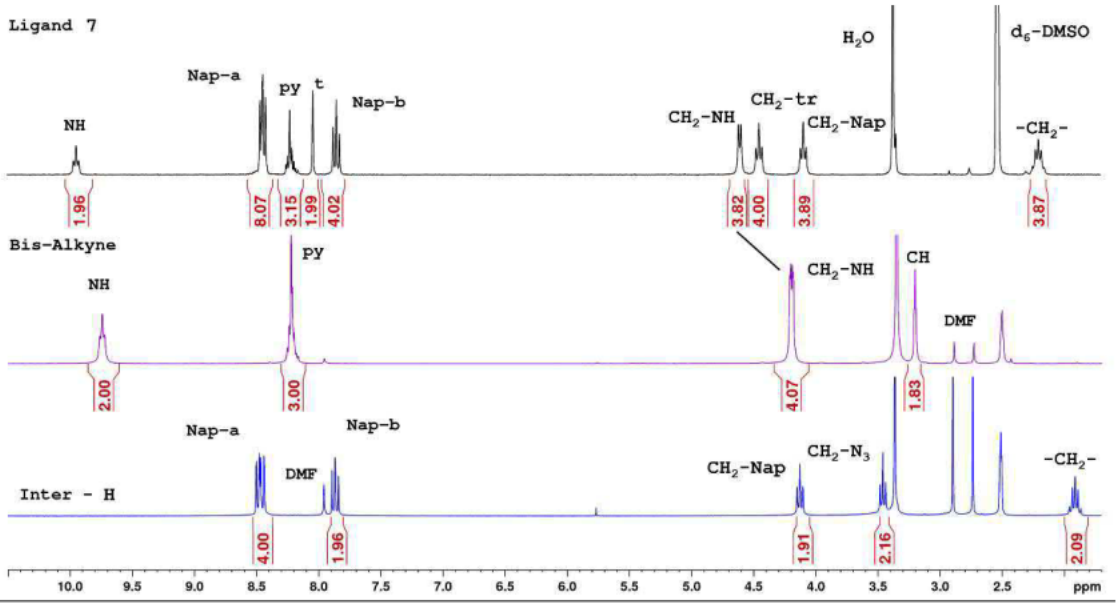

*Figure 5.15.. ^{1}H NMR of **7** and its corresponding starting materials (300 MHz,. DMSO-d_6).. Abbreviations:. Nap-a for ortho and para protons of **NI**,. Nap-b for meta protons of **NI**,. py for pyridine ring,. t for 1,2,3-triazole,. and Bn for benzyl ring.. Dash (-) indicates the group that the CH_2 (which is associated with this signal) is bonded.*

^{13}C NMR also confirmed formation of ligands **6 – 8** with the correct number of carbon environments being present. Important peaks of interest are the appearance of associated 1,2,3-triazole ring signals which at ≈ 144.8 (C) and 123.5 (CH) ppm. In the case of ligands **6** and **8**, the benzyl protecting group peaks disappearance at 129 - 128 (CH-Bn), 136 (C-Bn) and 67 ppm (CH_2-Bn) also indicates the successful deprotection of the intermediates **I** and **L** to final ligand products. See Figure 5.16 for ^{13}C spectrum characterising **6**; details for **7** and **8** can be seen in Section 8.3.1.

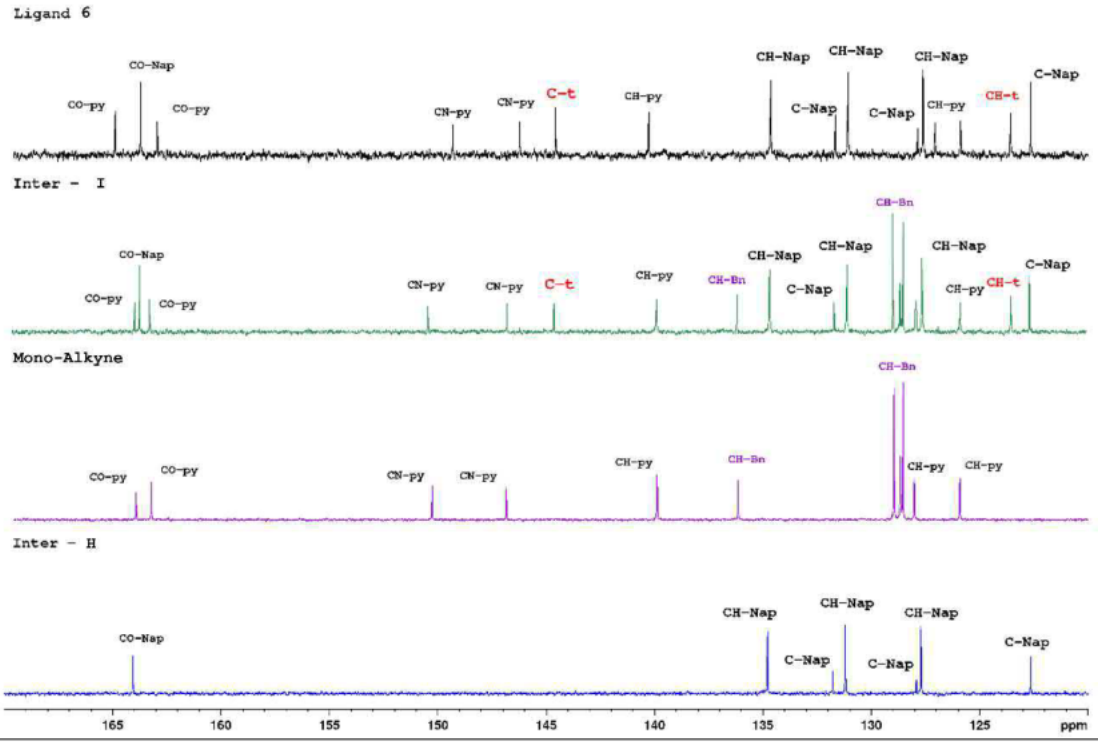

*Figure 5.16: ^{13}C NMR of **6** and its corresponding starting materials and intermediate **I** (75 MHz,. DMSO-d_6).. Abbreviation:. Nap for **NI** carbons,. py for pyridine carbons,. t for 1,2,3-triazole carbons,. CN for.. non-saturated carbons of the pyridine ring,. and Bn for benzyl ring carbons.*

5.2.2 Ligand Molecular Structures

5.2.2.1 Molecular Structure of 7

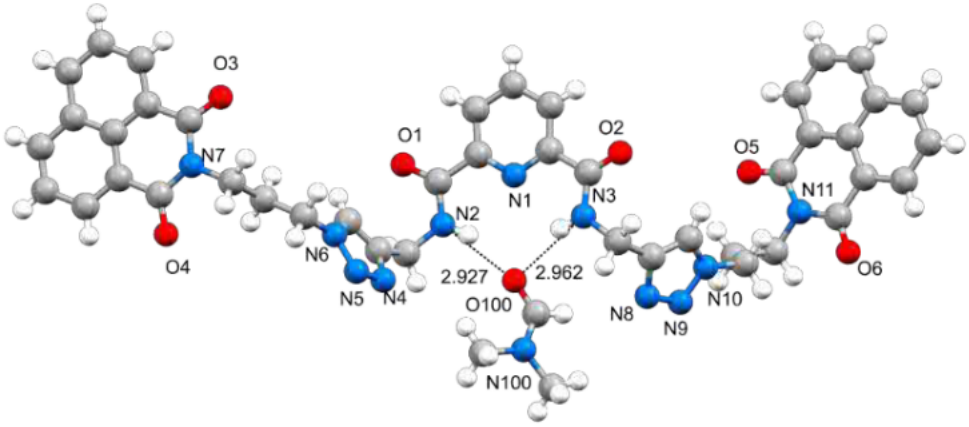

*Figure 5.17. Ball and stick representation of **7** showing hydrogen bonding occurring between ligand and solvent DMF.*

Single crystals suitable for X-ray diffraction studies of **7** were grown by slow evaporation of a concentrated DMF solution and a r.t structure was collected. **7** crystallised in the monoclinic space group $P2_1/n$ and contained one molecule of **7** and an associated DMSO solvent molecule in the asymmetric unit (Figure 5.17). Hydrogen bonding interactions between the PDA central pyridyl amides NH and the DMF carbonyl (CO) form two instances of moderate strength hydrogen bonding (Table 5.2)

*Table 5.2. Hydrogen bonding interactions between **7** and DMF.*

Interaction	Hydrogen bonding Interactions
7 - DMF	N2···O100' = 2.927(11) Å and <(N2-H2··· N7') = 156° N3···O100' = 2.962(11) Å and <(N3-H3··· O100') = 157(7)°
C28 - O2	C28···O2' = 3.193(12) Å and <(C28-H28··· O2') = 137.3°

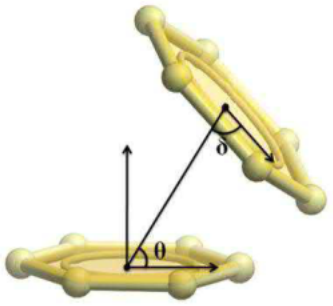

*Figure 5.18. Acute angles δ and Θ between the centroid-centroid vector (line distance) and the aromatic plane which have been measured. Image adapted with permission from Y. Zhao, J. Li, H. Gu, D. Wei, Y. C. Xu, W. Fu and Z. Yu, Interdiscip Sci, 2015, **7**, 211-220. Copyright 2022 SpringerLink.*

As expected, significant π - π stacking exists in **7**, involving the **NI** rings (Figure 5.19). In all cases π - π stacking was either off-set (face to face) or (aligned) face to face interactions. In order to distinguish between the two interactions, both acute angles δ and Θ between the centroid-centroid vector (line distance) and the aromatic plane have been measured (Figure 5.18). If either were larger than 80° it indicates the stacking interactions are (aligned) face to face.[62] For simplicity's sake, centroids of aromatic rings have been labelled either with their nitrogen atom (N1, N7 and N11) or the *para*-carbon of the **NI** ring (C18, C20, C36, and C38) as seen in Figure 5.19, such that N7 or C20 is referring to the centroid of that ring. All π - π stacking interactions and values can be found in Table 5.3.

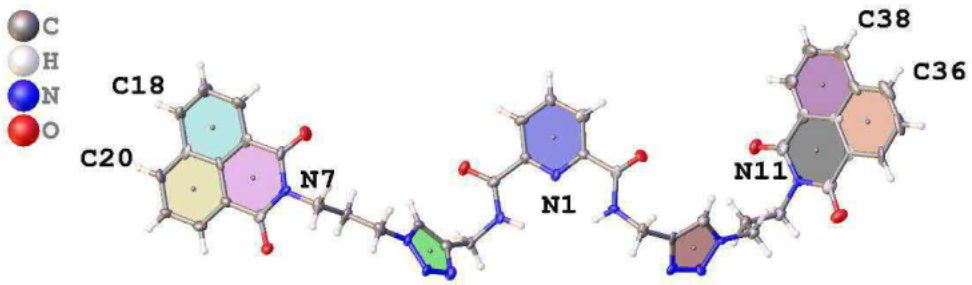

Figure. 5.19.. OLEX2. generated. image,. showing. planes. which. were. formed. to. find. all. π-π. stacking. interactions.. Labels. are. used. to. indicate. the. individual. ring. which. π-π. stacking. is. occurring. with..

π - π Stacking occurs between **NI** rings in a head-to-tail fashion.[63] These π - π stacking interactions are only occurring between the same **NI** rings (on neighbouring molecules) with no π - π stacking between different sides (N7 does not interact with N11, Figure 5.19). The **NI** ring containing centroids N11, C38, and C36 forms an in line head to tail stacking with another **NI** (N11, C38, and C36) system, forming multiple stacking interactions between two **NI**. There is an offset π - π stacking interaction between (N11 ··· N11') with a centroid distance of 3.962 Å, which coincides with two instances of face-to-face stacking (N11 ··· C36) with a centroid distance of 3.443 Å and two instances of offset π - π stacking between (N11 ··· C38) with a centroid distance of 3.889 Å. In comparison the other **NI** ring containing the N7 centroid is much more offset resulting in only one instance of π - π stacking interaction between N7 centroids, forming an offset stacking interaction (N7 ··· N7') with a centroid distance of 3.644 Å.

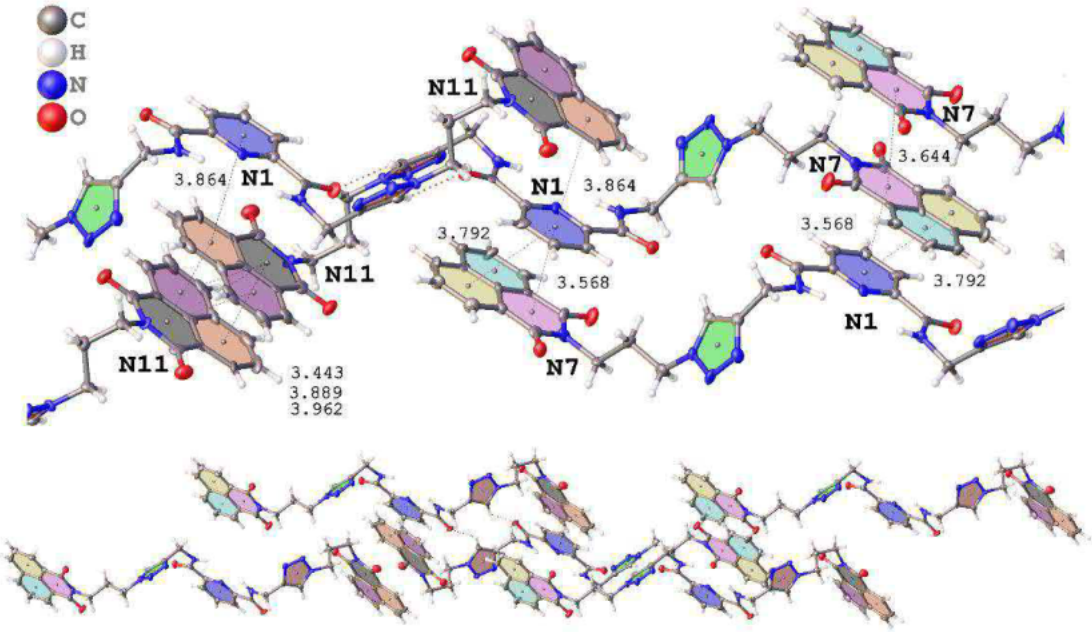

*Figure. 5.20.. (Top). π. -. π. stacking. interactions. found. by. OLEX2. software. and. given. centroid-centroid. distances.. For. context,. the. central. pyridyl. ring. π. -. π. stacking. is. occurring. mainly. in. the. centre. of. the. image,. the. N7. **NI**. ring. offset. π. -. π. stacking. with. itself. is. occurring. on. the. right,. and. N11. **NI**. system's. extensive. π. -. π. stacking. interactions. are. seen. on. the. left.. (Bottom). The. overall. resulting. chain. generated. by. the. unique. π. -. π. stacking. interactions..*

*Table 5.3.. π - π Stacking interactions occurring between **NI** and pyridine in **7**..*

π - π stacking Interaction	Centroid distance	Shift distance	δ	ɵ
Offset N7···N7	3.644 Å	1.429 Å	66.60°	66.60°
Offset N11···N11	3.962 Å	1.980 Å	61.58°	61.58°
face-to-face N11··· C36	3.443 Å	0.498 Å	93.94°	84.26°
Offset N11··· C38	3.889 Å	1.811 Å	64.25°	64.61°
face-to-face N1···N7	3.568 Å	0.696 Å	86.15°	95.22°
Offset N1···C20	3.792 Å	1.596 Å	71.30°	65.81°
Offset N1···C36	3.864 Å	2.259 Å	54.73°	59.93°

There are three other instances of π - π stacking, occurring between the central pyridyl centroid (N1) and **NI** centroids: a moderate face-to-face π - π stacking with centroid N7, (N1 ··· N7) with centroid distance of 3.568 Å, which coincides with an offset π - π stacking interaction occurring within the **NI** ring C20, (N1 ··· C20) with centroid distance of 3.792 Å seen in Figure 5.20. On the other side of the pyridyl ring there is another weaker offset π - π stacking interaction with **NI** ring C36 (N1 ··· C36) with centroid distance of 3.864 Å. A result of these π - π stacking interactions is an unusual, weak hydrogen bonding interaction between the 1,2,3-triazole ring C28 and the carbonyl of the amide O2, details seen in Table 5.2 and Figure 5.21.

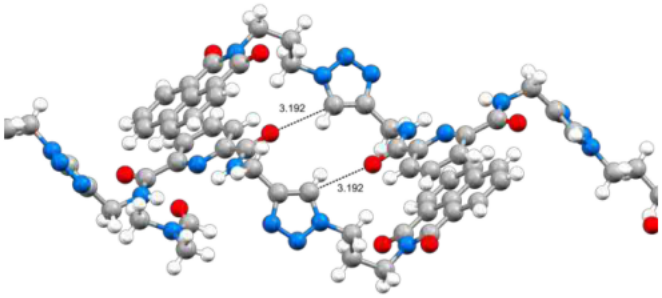

Figure 5.21.. Weak hydrogen bonding interactions occurring between 1,2,3-triazole rings and carbonyl, likely due to the close interaction brought about from π - π stacking interactions..

The aforementioned π - π stacking interactions lead to the formation of sheet like stacks when viewed along the a-axis. When viewed along the c- or b-axis the π - π stacking interactions which form these sheet like stacks can be observed but are difficult to discern from a static image (Figure 5.22).

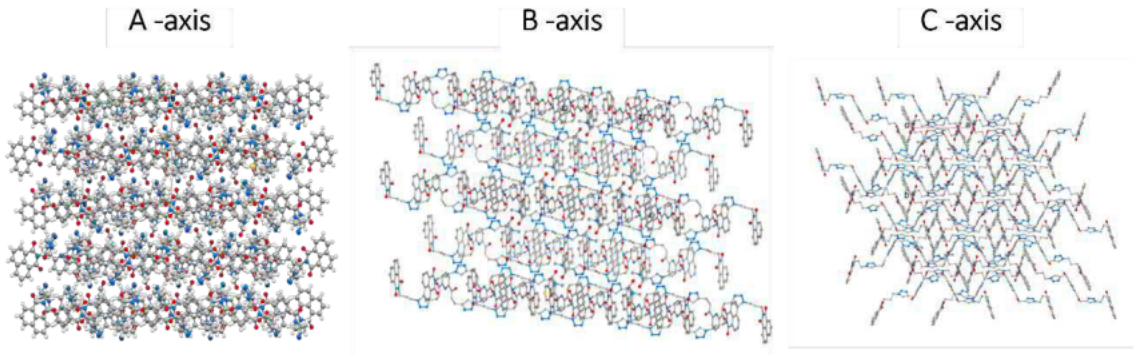

*Figure 5.22.. Overall packing of **8**, looking down the different axes..*

5.2.2.2 Molecular Structure of I

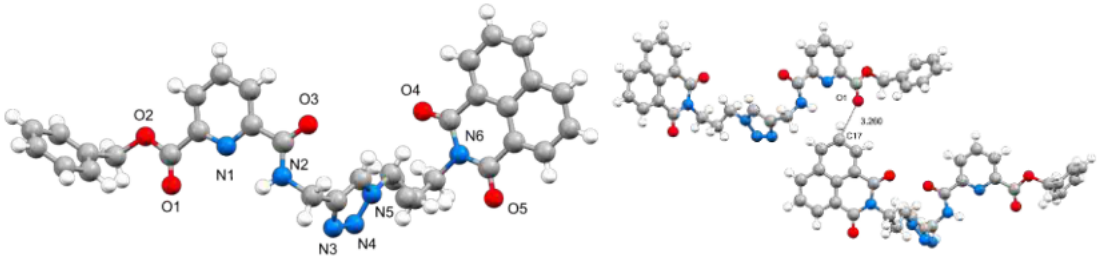

*Figure 5.23. (Left) Ball and stick representation of intermediate **I**. (Right) Hydrogen bonding occurring between the PDC pocket and naphthalimide CH ring proton.*

Single crystals suitable for X-ray diffraction studies of **I** were grown by slow evaporation from DCM:MeOH and a low temperature (123 K) structure was collected. **I** crystallised in the monoclinic space group $P2_1/n$ and contained one molecule of **I** in the asymmetric unit (Figure 5.23). Disorder is present in the propane linker connecting the 1,8-naphthalimide and 1,2,3-triazole ring and has been modelled, split over two sites with relative occupancies of 0.8 (C11 to C12) and 0.2 (C11A to C12A).The lack of solvent present in the crystal leads to an unusual and very weak hydrogen bonding interaction between the carbonyl O1 and the proton (H17-C17) from **NI** ring, causing the **NI** ring to fill the hydrogen bonding pocket of the PDC unit, seen in Figure 5.23 and details in Table 5.4.

*Table 5.4. Hydrogen bonding interactions within **I**.*

Interaction	Hydrogen bonding interactions
Ester - NI	C17···O1′ = 3.261(13) Å and <(C17-H17··· O1′) = 142.8°
Amide - 1,2,3-triazole	C10···O3′ = 3.309(13) Å and <(C10-H10··· O3′) = 106.6° C11···O3′ = 3.190(2) Å and <(C11-H3··· O3′) = 147.7°

Akin to the crystal packing of **8**, **I** crystal packing is also heavily governed by π - π stacking interactions (a similar method has been used to label the centroids as previous system, see Figure 5.24). There are two instances of face-to-face π - π stacking interactions occurring between **NI** (N6 or N19 centroid) and the central pyridyl ring (N1 centroid), with one **NI** stacking above and one below, "sandwiching" the pyridyl ring, seen in Figure 5.24 and Table 5.5 for details. These interactions lead to an unusual weak hydrogen bonding interaction between the amide carbonyl (O3) and 1,2,3-triazole ring (C10-H10 and the C11-H11(B)) methylene group, see Table 5.4 for details. This combination of intermolecular interactions leads to a similar crystal packing as is observed in **I**. Sheet like stacks are seen when viewed down the b-axis, and when viewed along the c-axis the π - π stacking interactions which form these sheets can be seen, but are difficult to discern from a static image (Figure 5.25).

Table 5.5. π - π Stacking and hydrogen bonding interactions occurring between **NI** and py of **I**.

Interaction	Centroid	Shift distance	δ	ϴ
Face-to-face N1···N6	3.448 Å	0.593 Å	80.11°	98.83°
Face-to-face N1···C19	3.544 Å	0.694 Å	103.35°	78.31°

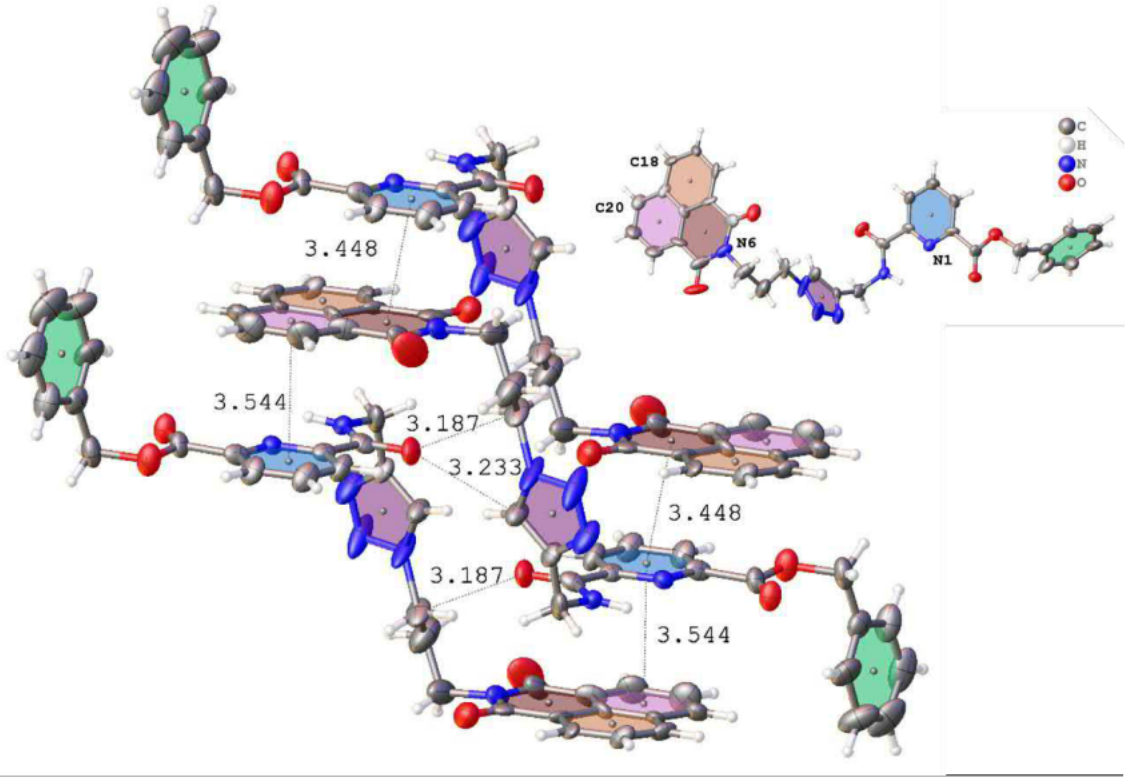

Figure 5.24. π - π stacking and hydrogen bonding found within **7**, calculated by OLEX2. Insert: **I** with label used to define centroids.

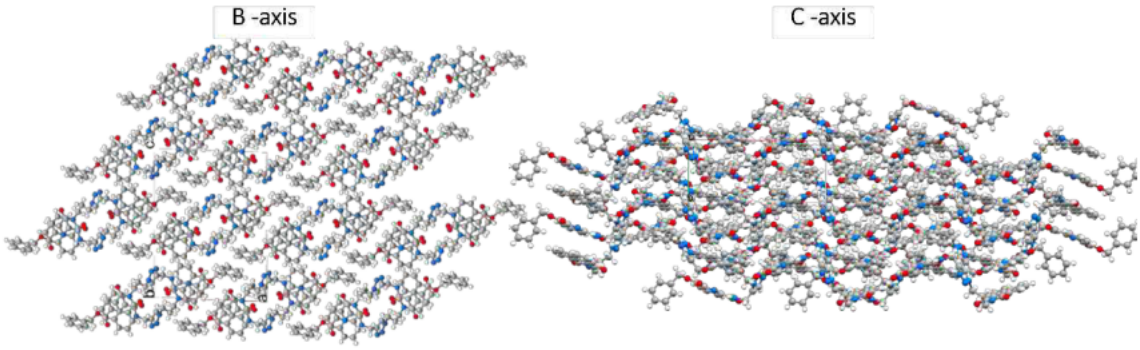

Figure 5.25. Stacked sheets of **I** when viewed down the b-axis. When crystal packing is viewed down the c-axis, it shows the zig-zag π-π stacking interactions.

5.2.2.3 Molecular Structure of L

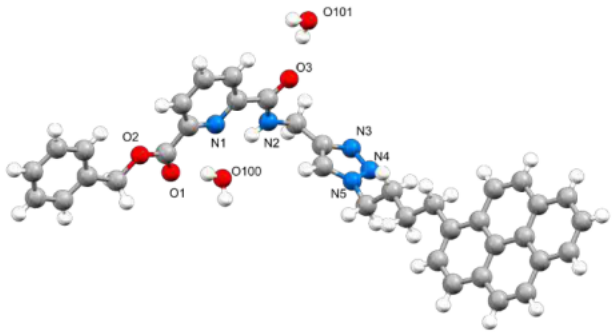

*Figure 5.26.. Ball and stick representation of intermediate **L**..*

Single crystals suitable for X-ray diffraction studies of **L** were grown by slow evaporation from DCM:MeOH and a low temperature (150 K) structure was collected. **L** crystallised in the monoclinic space group $P2_1/c$ and contained one molecule of **L** in the asymmetric unit alongside two water molecules (Figure 5.26). There are multiple hydrogen bonding interactions occurring between **L** and the solvent molecules. Moderate hydrogen bonding interactions were observed between the ester carbonyl (O1) of **L** and a water molecule (O100-H100), alongside this a weaker hydrogen bonding interaction is occuring between the amide (N2-H2) and oxygen (O100) of the same water molecule (Figure 5.27). Additionally, moderate hydrogen bonding interactions occur between the amide carbonyl (O3) with a second water (O101-H101A), which itself is hydrogen bonded to another water (O101-H101B), linking two molecules of **L**, seen in Figure 5.27.

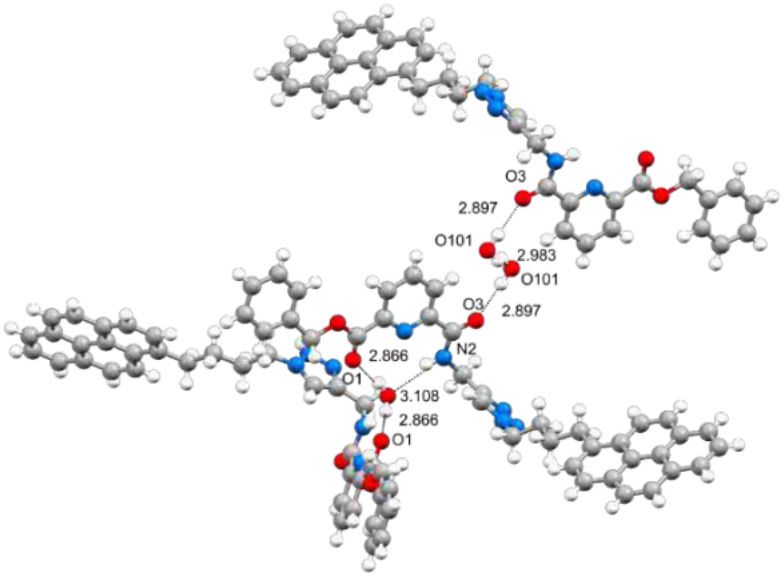

*Figure 5.27.. Hydrogen bonding interactions occurring between **L** and water..*

Table 5.6.. Hydrogen bonding interactions with **L** and H_2O..

Interaction	Hydrogen bonding interactions
Ester carbonyl - H_2O	O100···O1' = 2.866(19) Å and <(O100-H100··· O1') = 169.3°
Amide - H_2O	N2···O100' = 3.108(18) Å and <(N2-H2··· O100') = 158.8°
Amide carbonyl - H_2O	O101···O3' = 2.897(2) Å and <(O101-H101A··· O3') = 171.0°
H_2O - H_2O	O101···O101' = 2.983(4) Å and <(O101-H101B··· O101') = 147.8°

As expected, **L** also exhibits π - π stacking interactions, with a weak offset π - π stacking interaction observed between **PYR** ring centroids C18 and C25 (with a centroid distance of 3.963 Å, shift distance 2.154 Å, δ = 57.18° and Θ = 57.13°). This interaction resulted in a packing dominated by π - π stacked sheets with hydrogen bonding interactions with solvent, seen to connect the stacked sheets. When viewed viewing down the a-axis the π – π interactions between stacked sheets (seen along the b-axis) can clearly be observed, as seen in Figure 5.29.

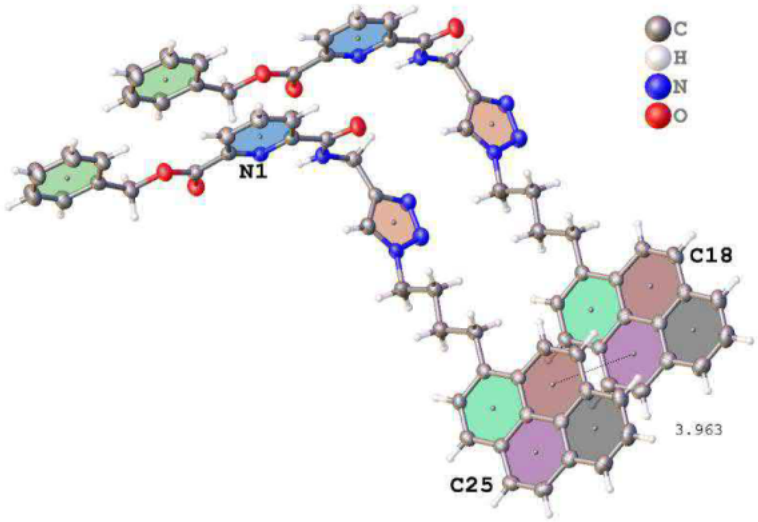

Figure 5.28.. Weak π - π stacking occurring between **PYR** rings..

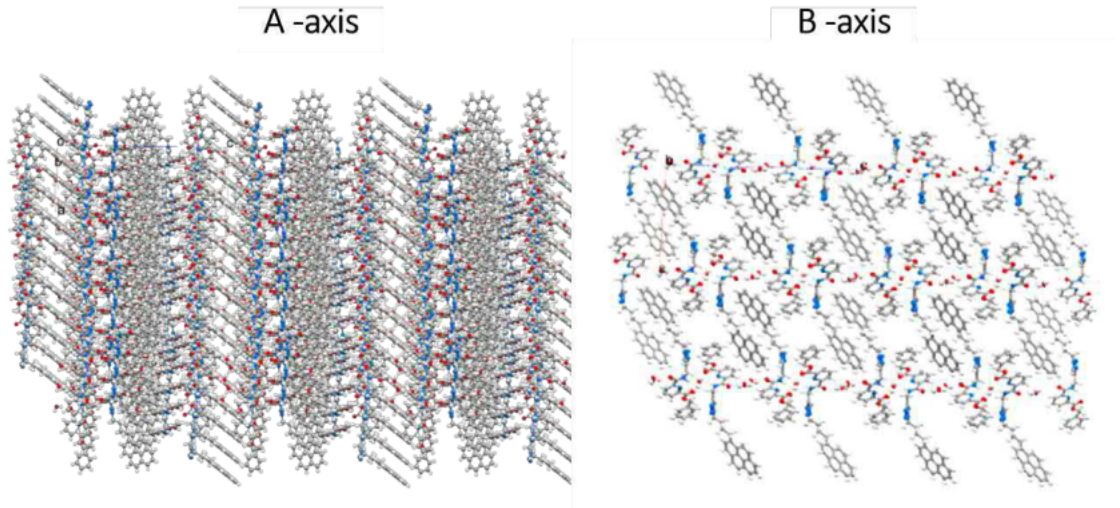

Figure 5.29.. (Left) Shows the π - π stacked interactions viewed down the a-axis.. (Right) Sheet like packing observed down the b-axis..

It is worth noting that single crystals suitable for X-ray diffraction studies of **8** were also successfully grown from slow evaporation of (DCM:MeOH):DMF (4:1) and a r.t structure was collected. A single crystallographically independent molecule of **8** is in the asymmetric unit, showing the expected connectivity as seen in Figure 5.30. Unfortunately, the structure could only be refined to a high R_1 (20.34) so intermolecular interactions are not fully discussed, but it is worth noting that surprisingly the expected π - π interactions are switched for CH/π interactions[64] between the pyrene and alkyl chain linker (with H – centroid distance of 2.6, 2 x 2.9 & 3.1 Å) as seen in Figure 5.30, also leading to sheet like packing.

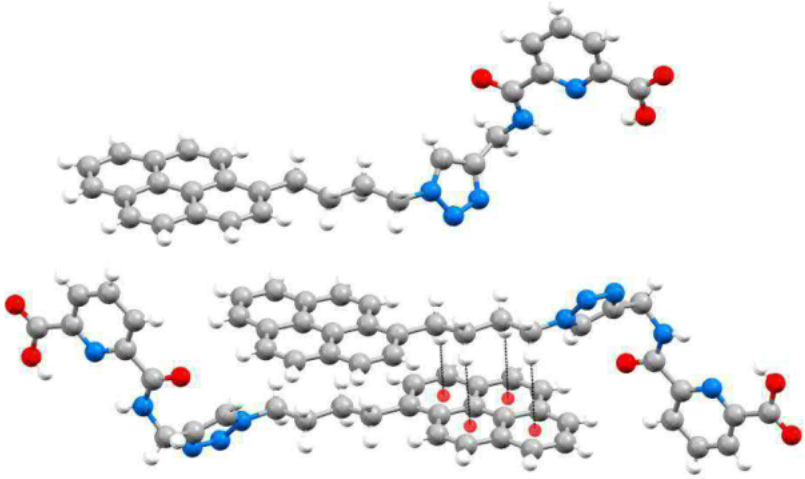

*Figure 5.30. (Top) Ball and stick representation of **8**. (Bottom) CH/π interactions observed between two molecules of **8**.*

5.2.2.4 Ligand Molecular Structures Summary

All four systems show the expected molecular structure, and importantly both **NI** and **PYR** motifs in all four systems are observed to interact *via* π - π stacking interactions (or in the unique case of **8** CH/π). These interactions form sheet like stacks in the overall crystal packing, which is exactly what was desired with the introduction of the larger aromatic substituents into the ligand structure and should aid in the formation of molecular thin films.

5.2.3 Ligand Photophysical Properties

As stated in the introduction (Section 5.1), the large aromatic rings were added for multiple reasons, one being their own fundamental photophysical properties. Both the **NI** and **PYR** systems are fluorescent chromophores with overall blue emission. This coupled with lanthanide emission makes the systems potentially both dual and white emissive. Before lanthanide incorporation, it is important to understand the photophysical properties of **6**-**8** prior to complexation. Photophysical properties of complexes were measured primarily using 0.01 mM solutions in MeOH (diluted from a stock solution of 1:1 DCM:MeOH) for solubility purposes, unless otherwise stated.

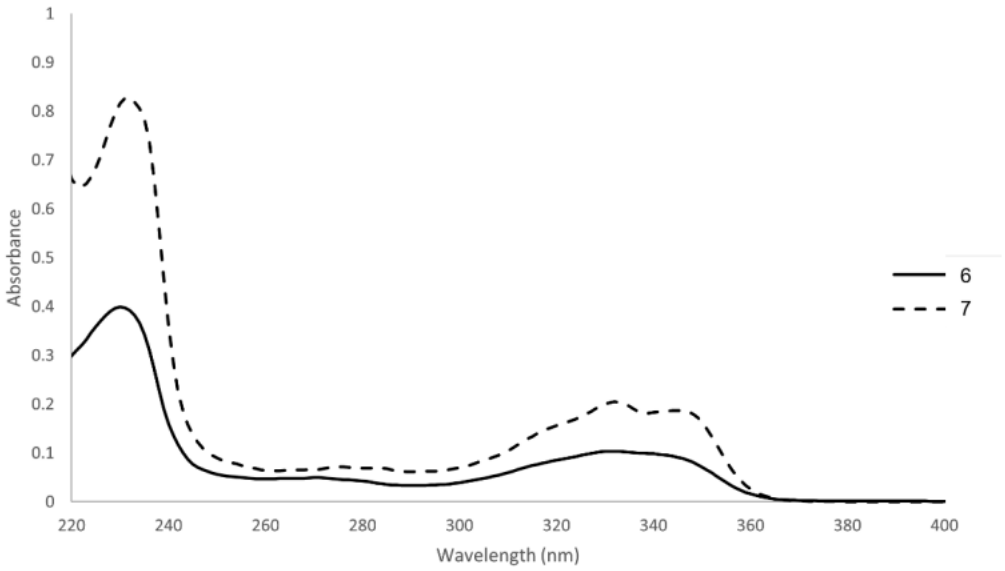

*Figure 5.31. UV-visible absorption spectra of **6** and **7** (0.01 mM, MeOH).*

The **NI** chromophores incorporated into **6** and **7** displayed similar absorption spectra with a broad absorption range from 220 to 370 nm (see Figure 5.31). Both **6** and **7** have intense peaks at 232 nm and a broad peak at 310 – 370 nm with two major bands at 333 nm and 347 nm associated with the combination of mainly π → π* transitions and n → π* transitions of the **NI** rings.[65] Similar to previous PDA/PDC systems in other chapters, **6** and **7** contain a weak absorption band located at 281 nm, assigned to the n → π* and π → π* transitions from the central pyridyl unit. There are also likely contributions to the 232 nm band from the pyridyl unit as seen in previous ligands.

Although **6** and **7** have similar absorption spectra in a 0.01 M solution, they surprisingly result in different emission profiles. **6** appeared as a dark blue where **7** was a lighter blue (Figure 5.32). The emission spectrum of **6** is broad, ranging from 350 – 450 nm with a major peak at 390 nm associated with the π → π* transition known as monomer emission.[36, 41] In the case of **7** there

is another broad peak from 400 - 600 nm, with maximum emission at 480 nm attributed to excimer emission. This additional excimer emission is likely associated with intramolecular π - π interactions between the two **NI**s within **7**. It is worth noting that **6** is also capable of excimer emission. However, this only occurs at higher concentrations (≥ 1 mM) and is caused by intermolecular π - π interactions between **NI**s (Figure 8.3.72). Both systems still retain similar excitation spectra with major peaks at 238 and 340 nm, in line with the absorption spectra, confirming that both emissions are from the **NI** chromophore.

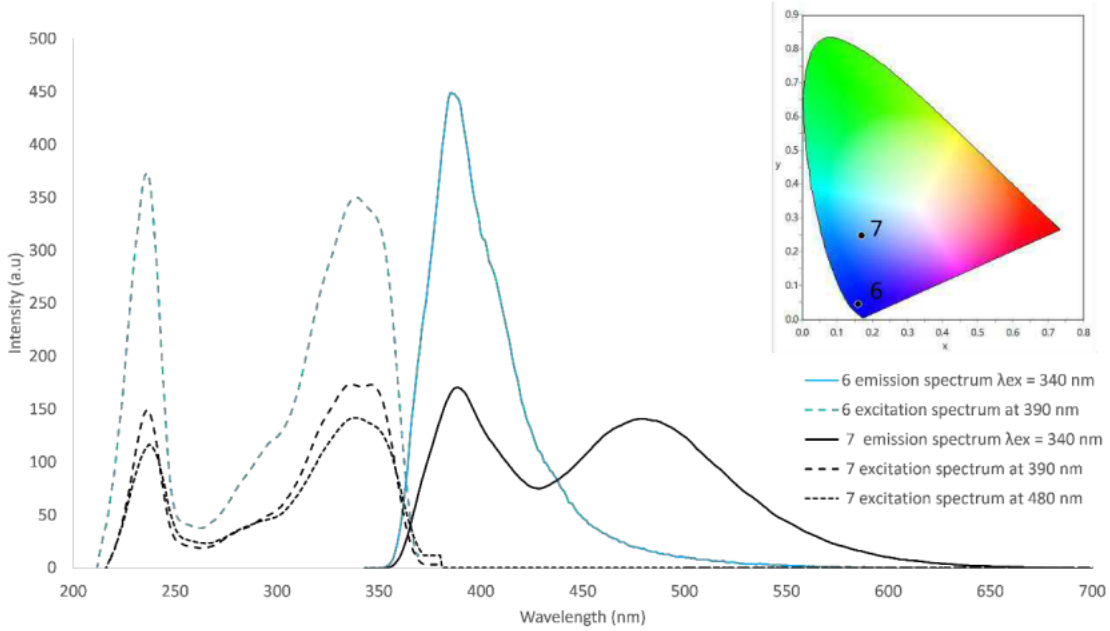

*Figure 5.32.. Fluorescence emission and excitation spectra of **6** and **7** (0.01 mM,. MeOH).. Insert:. CIE 1931 chromaticity diagram,. with CIE coordinates of the resulting emission of **6** x,y. =. 0.16,. 0.05. and **7** x,y. =. 0.17,. 0.25..*

Fluorescent quantum yields (Φ_f) of the two ligand systems were measured and calculated by the dilute comparison method in MeOH and compared against quinine sulfate in 0.5 M H_2SO_4. This resulted in quantum yields of 12 % for **6** and 16 % for **7** which are similar to other **NI** systems.[28, 32, 33, 39] **7** logically has a larger value due to the additional **NI** ring.

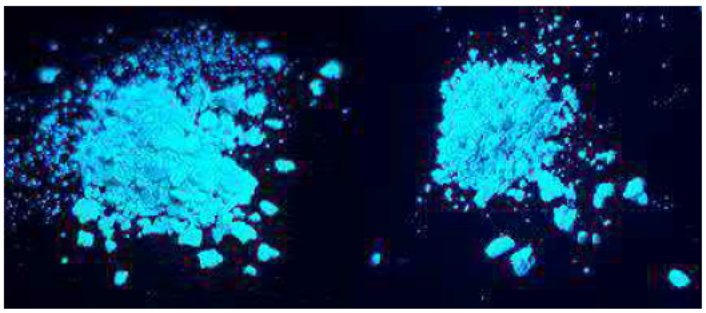

*Figure 5.33.. Solid powders of ligands **6** (Left). and **7** (Right). under longwave UV irradiation. (λ_{ex} =. 365. nm)..*

The incorporation of the **PYR** motif into **8** dominates the absorption spectrum displaying typical pyrene bands. **8** contains a broad absorption spectrum ranging from 200 - 360 nm, which is separated into three major absorption transition regions: $S_0 \rightarrow S_4$ (214 - 250 nm), $S_0 \rightarrow S_3$ (256 - 280 nm) and $S_0 \rightarrow S_2$ (303 - 356 nm), along with a very weak $S_0 \rightarrow S_1$ transition (370 nm),

seen in Figure 5.34.[66] As stated these absorption transitions can easily be assigned to the **PYR** motif, as previously noted in literature **PYR** systems and precursors (**J**-**K**) (see Figure 5.34 and Section 8.3.1). With absorption of **8** being dominated by **PYR** absorption, it is hard to justifiably assign any major contributions from the pyridyl or 1,2,3-triazole unit.

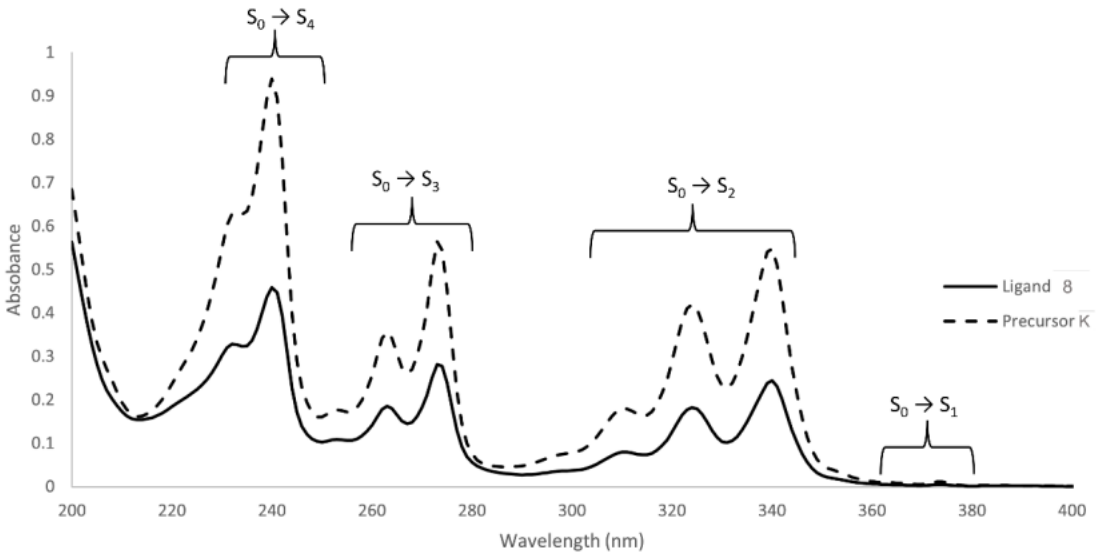

*Figure 5.34.. UV-visible absorption spectra of **8** and **K** (0.01 mM,. MeOH) to show similarity between ligand and precursor..*

The emission spectrum of **8** shows classical **PYR** emission when excited into any of the major absorption transitions. Emission ranges from 365 - 440 nm, containing three major peaks at 378 nm, 397 nm, and 419 nm, giving an overall colour of dark blue (Figure 5.35). The excitation plot of **8** showed near identical spectral shape to the absorption spectrum, indicating that the emission originates from the **PYR** ring. Fluorescent quantum yields of **PYR** centred emission was measured using the same method as **NI** systems. Φ_f were found to be relatively weak (Φ_f = 2.6 %) compared to **NI** systems but this is not uncommon for pyrene systems.[67]

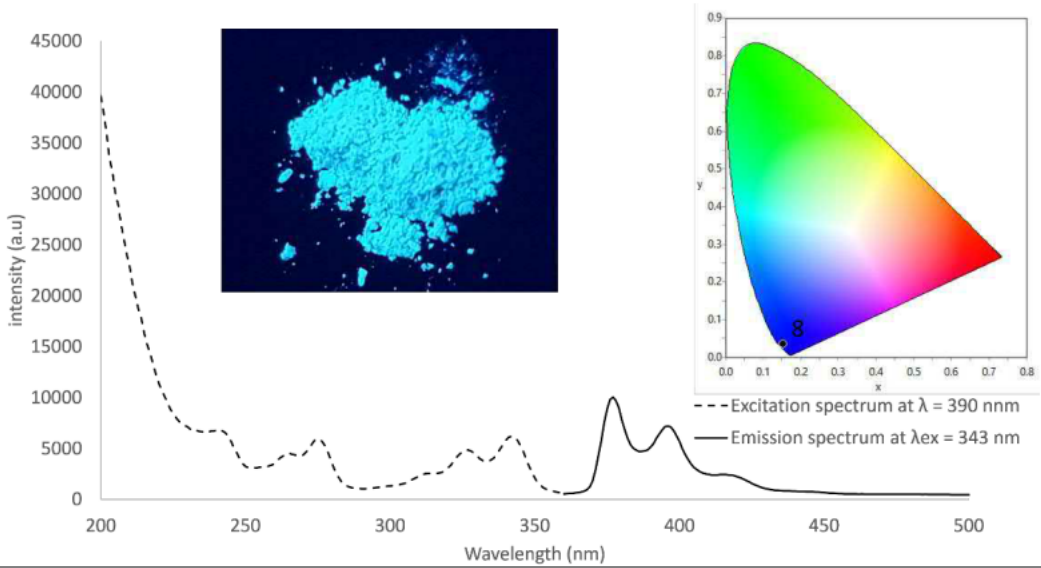

*Figure 5.35.. Fluorescence emission and excitation spectra of **8** (0.01 mM MeOH). - other excitation wavelengths were tested,. and all resulted in similar emission profiles.. Inserts:. CIE 1931 chromaticity diagram,. with CIE coordinates of the resulting emission of **8** x,. y. = 0.15,. 0.03 and image of solid powder **8** under longwave UV irradiation. ($\lambda_{ex.}$ = 365 nm)..*

5.2.4 Self-Assembly Studies

Photophysical solution based self-assembly titrations were once again carried out (in triplicate) by monitoring changes in both the UV-visible absorption and fluorescence emission (λ_{ex} = 274 nm). These were carried out to observe the M:L species formation and importantly to determine whether the desired 1:3 species would still form with the bulky aromatic substituents. Titrations of **6** and **7** followed the same general method utilized for PDA and PDC systems in chapters 3 and 4, while methodology for **8** has been slightly altered and is discussed later. It should be noted that all titrations were carried out in MeOH, due to precipitation during titrations in MeCN. Titration data where possible have also been fitted by ReactLab™ equilibria,[68] giving speciation plots and binding constants.

5.2.4.1 Lanthanide Self-Assembly Studies of 6

Titration results of **6** were found to be quite complex compared to previous systems. Upon the initial addition of 1 equivalent of TMAO base, the only change of note in the absorbance spectra is the distinctive shoulder peaks associated with the central pyridine unit merging to a broad peak ranging from 260 - 290 nm, whereas the fluorescence monomer emission slightly decreased (for simplicity, this has been removed from Figures 5.37 - 39).

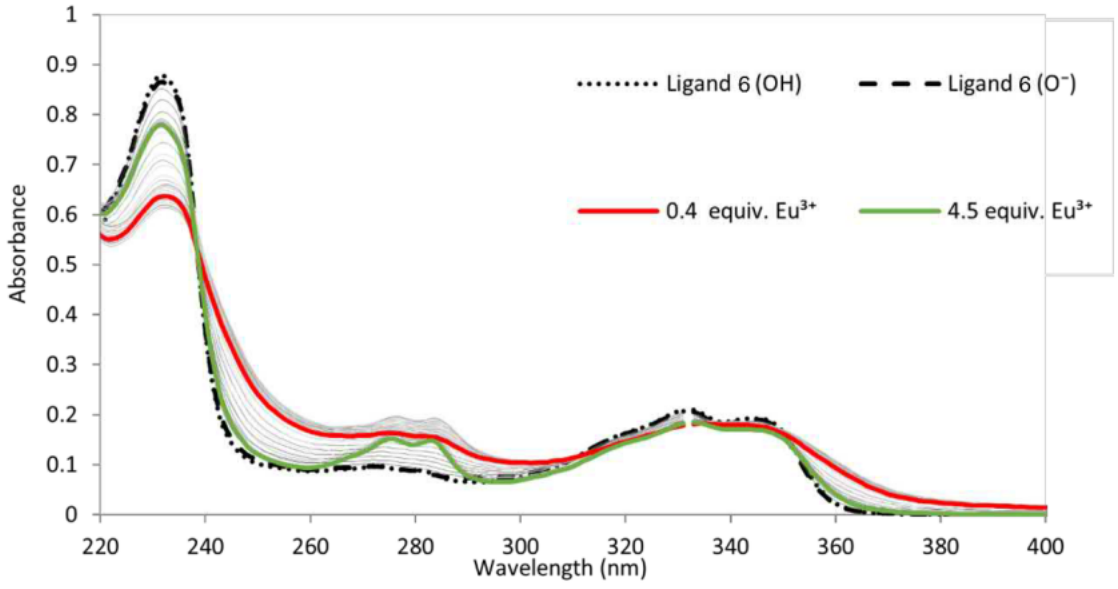

*Figure 5.36.. UV-visible absorption of **6** (0.02 mM,. MeOH) titrated with $Eu(CF_3SO_3)\cdot 6H_2O$ in MeOH..*

Focusing on the changes in the UV-visible spectra upon addition of $Eu(CF_3SO_3)_3$ we can see that the three major bands undergo significant absorbance changes between 0 - 0.45 equivalents. The band associated with the pyridyl unit (274 nm) undergoes a hyperchromic shift, while the bands associated with the **NI** (232 nm and 333 nm) undergo a hypochromic shift, seen in Figure

5.37. This is indicative of the formation of Eu(**6**)$_3$, as seen in previous systems. Upon further addition, until 1 equivalent is reached the absorbance changes are less significant, akin to a plateau but there was a small hyperchromic shift indicative of other species formation. The spectra was also noted to undergo a significant red shift from 0 to 1 equivalent, previously seen in other systems and can be easily seen when comparing **6** (O^-) absorbance to 0.4 equiv. in Figure 5.36.

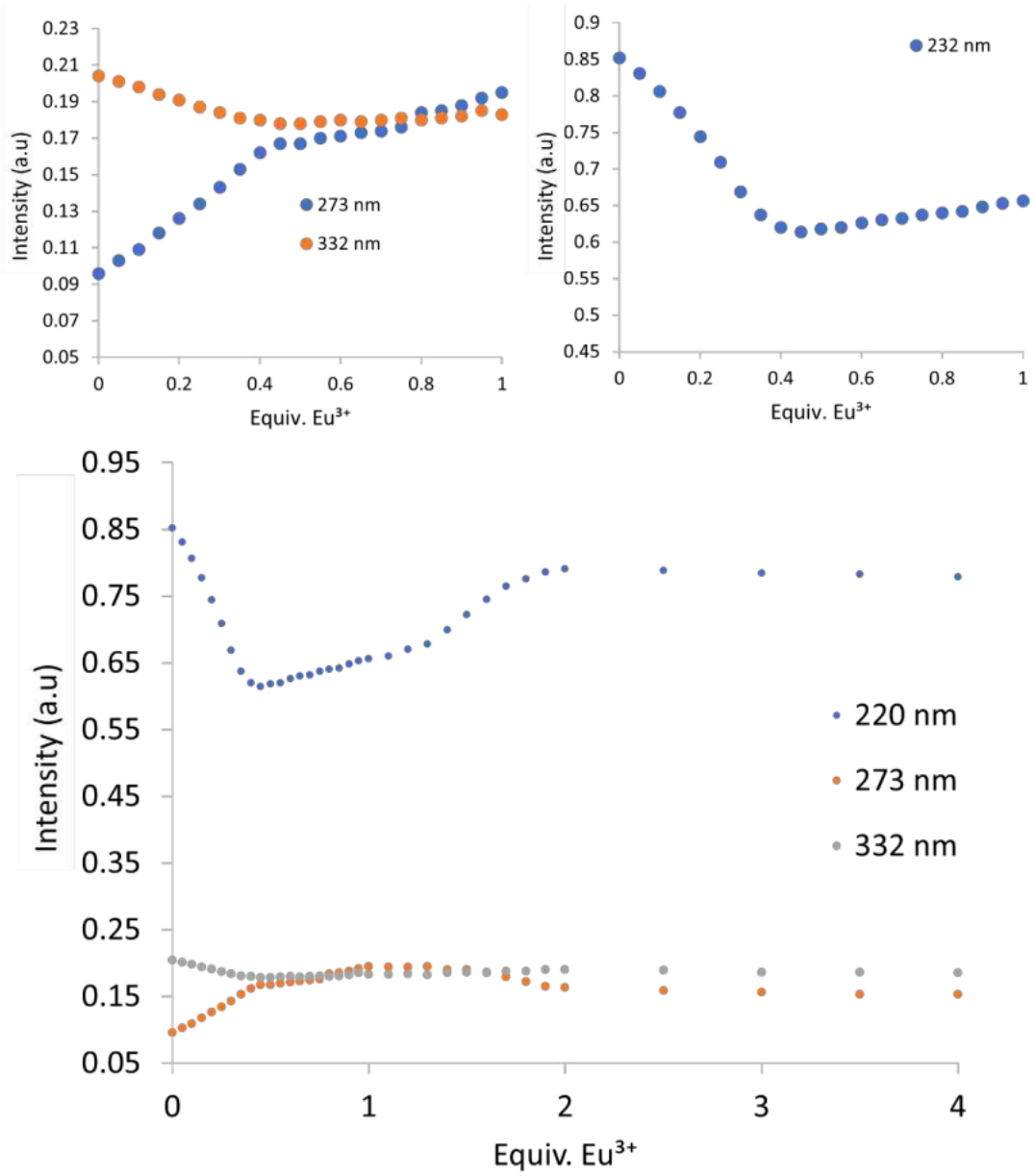

*Figure 5.37. Monitoring changes in UV-visible absorption at 232, 274 and 333 nm of **6** (0.02 mM, MeOH) titrated with Eu(CF_3SO_3)·6H_2O in MeOH from 0 to 1 equivalents (Top) and from 0 to 4.5 equivalents (Bottom).*

Unlike all previous systems the significant changes do not stop at 1 equivalent. After addition of excess Ln^{3+} (1-2 equivalents), as seen in Figure 5.36, the red shift was nearly completely reversed and undergoes a blue shift. All significant peaks invert their original changes (Figure 5.37), with the pyridyl peak (274 nm) undergoing a hypochromic shift, and the **NI** peaks (232 and 333 nm) undergoing a significant hyperchromic shift, a change which was seen with the naphthalene

associated absorbance in chapter 3 but now occurring at a much later stage. Such changes at excess Ln^{3+} concentration have not been present in previous systems, yet identical titration additions and concentrations have been used, ruling out dilution effects. This suggests that under such an excess Ln^{3+} concentration, speciation was still occurring.

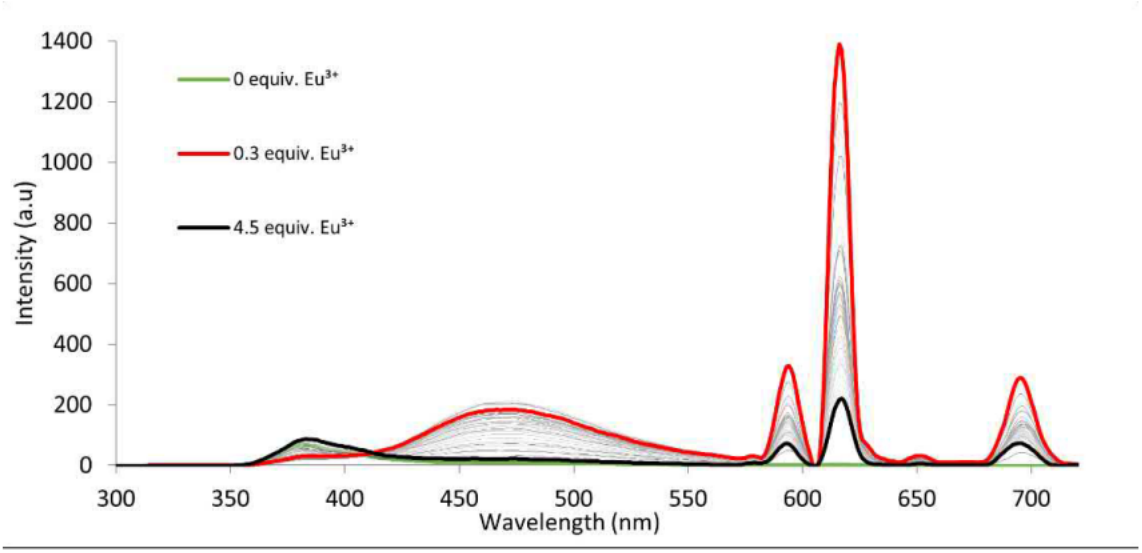

*Figure 5.38.. Fluorescence of **6** (0.02 mM, MeOH) titrated with $Eu(CF_3SO_3)\cdot 6H_2O$ in MeOH..*

Although these changes in absorbance can be used to suggest species formation and evolution, as with previous systems it cannot alone be used to justify or definitively confirm the species formation. However, in combination with changes observed in fluorescence spectra and fitted data, a well-informed argument can be made. Changes observed in fluorescence spectra gave a much clearer insight into species formation. Similar to other systems, a clear significant increase in the Eu^{3+} centred emission at all peaks occurs from 0 to 0.3 - 0.35 equivalents where it reached a maximum intensity as seen in Figure 5.38-39. Intuitively, this indicated the formation of $Eu(\mathbf{6})_3$ as it contains maximum emission intensity, associated with the 3 antennae populating the excited state of the Ln^{3+}. Coinciding with this, a significant disappearance of the **NI** monomer emission alongside the appearance of the excimer emission at 480 nm was seen to significantly increase from 0 to 0.35 equivalents where it reached a maximum emission intensity. The appearance of excimer emission is associated with intramolecular **NI** π - π interactions occurring within the molecule, as previously seen in literature.[43] This corroborates the formation of $Eu(\mathbf{6})_3$ as π π interactions are expected to be maximised when all three ligands are coordinated to the Ln^{3+}. This is also suggestive of the C_3 symmetry with all **NI** aligned on one side, along with the Eu^{3+} $^5D_0 \longrightarrow {}^7F_0$ transition at 581 nm.

Upon further addition of Eu^{3+}, Eu^{3+} centred emission was observed to significantly decrease until 0.6 equivalents was reached, with similar changes observed in **NI** excimer emission. Interestingly, unlike previous systems, the Eu^{3+} centred emission does not continue the significant decrease until 1 equivalent, nor does it reach a plateau; rather, a slow decrease of the Eu^{3+} centred emission is observed until 4.5 equivalents as seen in Figure 5.39. This is rather unique to this system and, along with the lack of a plateau in the UV-visible absorption, indicated, unlike other systems, further addition of Ln^{3+} (0.6-1 equivalent) does not indicate the definite formation of Eu(**6**). Rather, it indicated unfavourable change from Eu(**6**)$_2$ to Eu(**6**) until a large excess is present. This idea is further corroborated by changes in monomer and excimer emission. Monomer emission is observed to reach a minimum intensity at 0.6 equivalents, with further addition plateauing until 1. Additions between 1 - 3 equivalents have significant increases again observed. This coincided with small decreases in excimer emission across 0.6 - 1 equivalent, which become more significant from 1 - 3 equivalents. Such increase and decrease in monomer and excimer emission have previously been noted in the evolution from 1:3 to 1:2 to 1:1 for other **NI** complexes.[43] The fact that all three emissions do not plateau at 1 equivalent but rather at 3 equivalents indicated the species evolution from Eu(**6**)$_2$ to Eu(**6**) is only favoured in an excess of Ln^{3+}. This is suspected to be due to π π interactions occurring in the Eu(**6**)$_3$ and Eu(**6**)$_2$ species **NI** substituents, potentially stabilizing and out-favouring formation of lesser Eu(**6**) species. However, more importantly, from this we can determine that **6** is forming our desired Eu(**6**)$_3$ in the correct chemical environment.

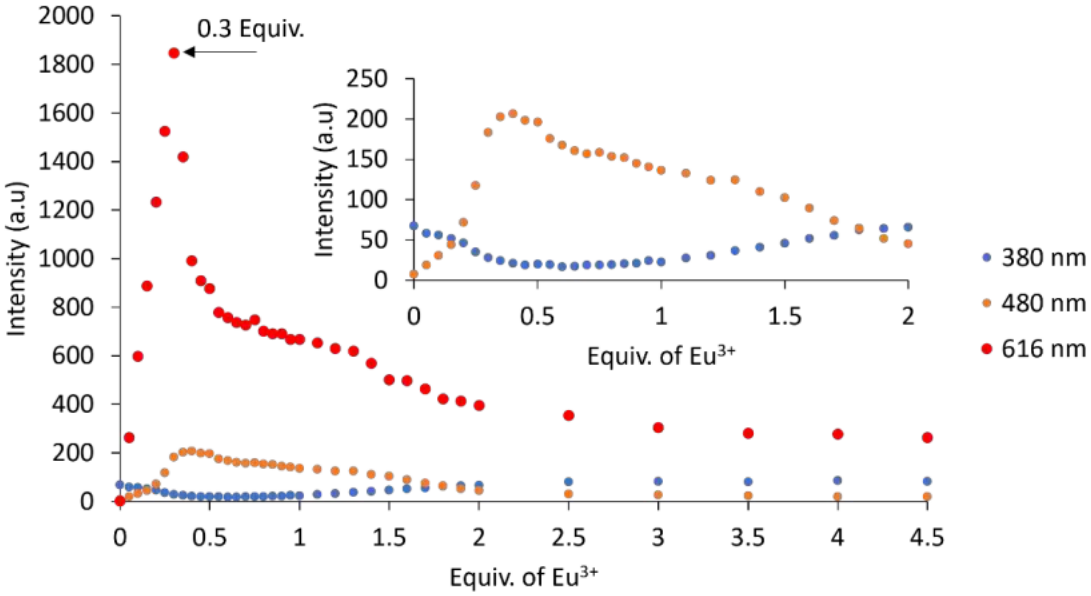

*Figure 5.39.. Monitoring changes of fluorescence emission of **6** (0.02 mM, MeOH) titrated with $Eu(CF_3SO_3)\cdot 6H_2O$ in MeOH at a specific point of interest..*

Similar to the chapter 4 ligand **5** system, only fluorescence data was able to be fitted (Figure 5.40). The speciation plot further corroborates the dominant formation of Eu(**6**)$_3$ at 0.3 equivalents with 53 % formation with peak formation at 0.35 equivalents (55 %). However, unlike the previous PDC system (where Eu(**5**)$_2$ formation was skipped in favour of Eu(**5**), see Figure 4.21) **6** is seen to undergo the evolutionary formation more akin with PDA systems of chapter 3, with deformation of Eu(**6**)$_3$ to Eu(**6**)$_2$ and finally Eu(**6**). Eu(**6**)$_2$ becomes the dominant species at 0.45 equivalents (57%) peaking at 0.55 equivalents (59 %). Upon further additions Eu(**6**)$_2$ is slowly converted to Eu(**6**), with around 64 % Eu(**6**) and 36 % Eu(**6**)$_2$ at 1 equivalent. In comparison to **5**, at 0.45 equivalents Eu(**5**)$_3$ remains the dominant species and at 1 equivalent, Eu(**5**) is practically the only species with 94 % species formation. This further corroborated the idea that Eu(**6**) is not totally favoured over Eu(**6**)$_2$, with Eu(**6**) only reaching 83 % at 2 equivalents. In terms of binding constant, they remain within the expected regions (Table 5.7), and were slightly lower than **5**, which can be expected in the more competitive solvent.

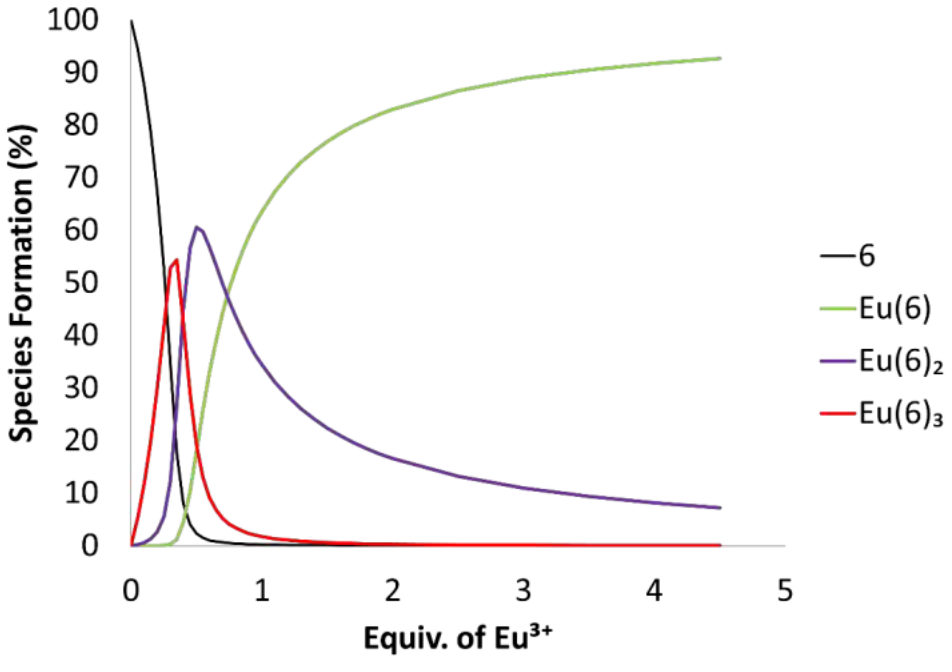

*Figure 5.40.. Speciation plot of fluorescence titration of **6** with Eu(CF$_3$SO$_3$)$_3$..*

*Table 5.7.. Binding constants from fitted data of fluorescence titration from other PDC based ligands **6** and **5**. Solvent which the titrations were carried out in are shown in superscript..*

Ln(L)	Fluorescent emission		
	Log $\beta_{1:1}$	Log $\beta_{1:2}$	Log $\beta_{1:3}$
^{MeOH}Eu(6)	7.7 ± 0.01	14.8 ± 0.03	20.9 ± 0.30
^{MeCN}Eu(5)	9.7 ± 0.03	16.0 ± 0.03	22.6 ± 0.30

5.2.4.2 Lanthanide Self-Assembly Studies of 7

7 is seen to undergo a similar process observed with other PDA based ligands in chapter 3. UV-visible absorption (Figure 5.41) showed the significant changes from 0 to 0.3 - 0.35 equivalents, with similar hypochromic shift for the pyridyl peak (274 nm) and hyperchromic shift for **NI** peaks (232 and 333 nm). Unlike **6**, the pyridyl peak is seen to completely plateau for the remainder of the titration, whereas the **NI** peaks undergo a reverse hypochromic shift early on from 0.4 - 1 equivalent, then reaching a plateau from 1 - 2 equivalents, identical to what is observed for the naphthalene system in chapter 3.

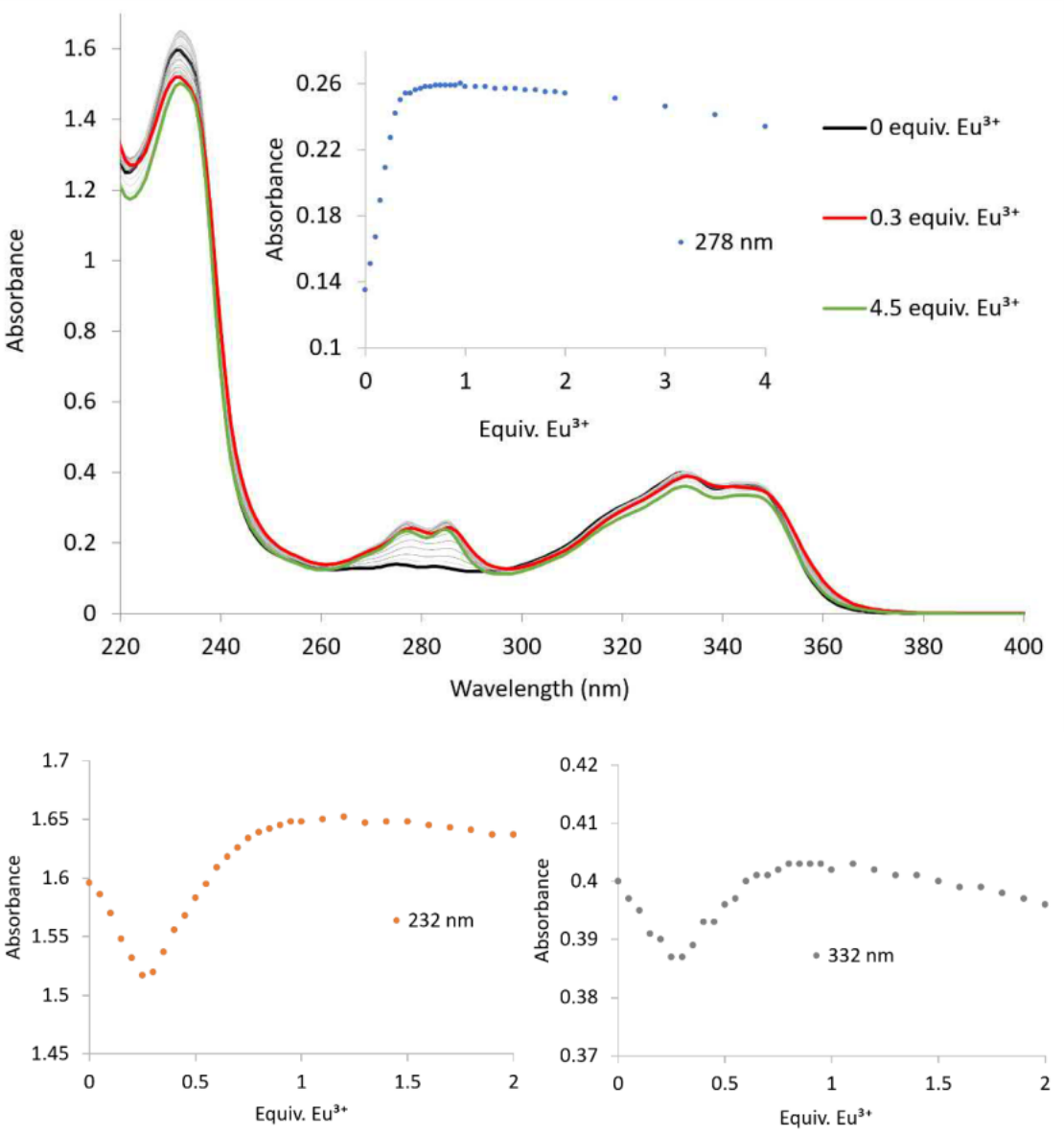

*Figure 5.41.. (Top). UV-visible absorption of **7** (0.02 mM,. MeOH) titrated with $Eu(CF_3SO_3)\cdot 6H_2O$ in MeOH.. Insert:. monitoring changes at 278 nm.. (Bottom). UV-visible absorption of **7** (0.02 mM,. MeOH) titrated with $Eu(CF_3SO_3)\cdot 6H_2O$ in MeOH. monitoring changes at 232 and 332 nm..*

Changes in the fluorescence spectrum (Figure 5.42) further corroborate the more simplistic and consistent changes occurring for this system. Eu^{3+} centred emission and ligand excimer emission is seen to significantly increase from 0 - 0.35 equivalents reaching a maximum, where monomer emission is seen to significantly decrease to a minimum, consistent with the formation of the Eu(**7**)$_3$. Further addition of Eu^{3+} from 0.4 - 1 equivalents reverse these results, with both Eu^{3+} centred emission and ligand excimer emission decreasing until 1 equivalent, and monomer emission increasing until 1 equivalent, with all three peaks then plateauing upon any further addition. The fact that excimer emission is lower and monomer emission is larger than in the free ligand (initial state) indicated that the two **NI** rings contained within **7** are likely now separate from one another in Eu(**7**), (similar to what is observed in the crystal structure Figure 5.17) reducing excimer emission. Both changes in UV-visible and fluorescence spectra are clearly indicative of the initial dominant formation of Eu(**7**)$_3$ and then quickly changing from Eu(**7**)$_3$ to Eu(**7**)$_2$ and Eu(**7**), unlike **6**.

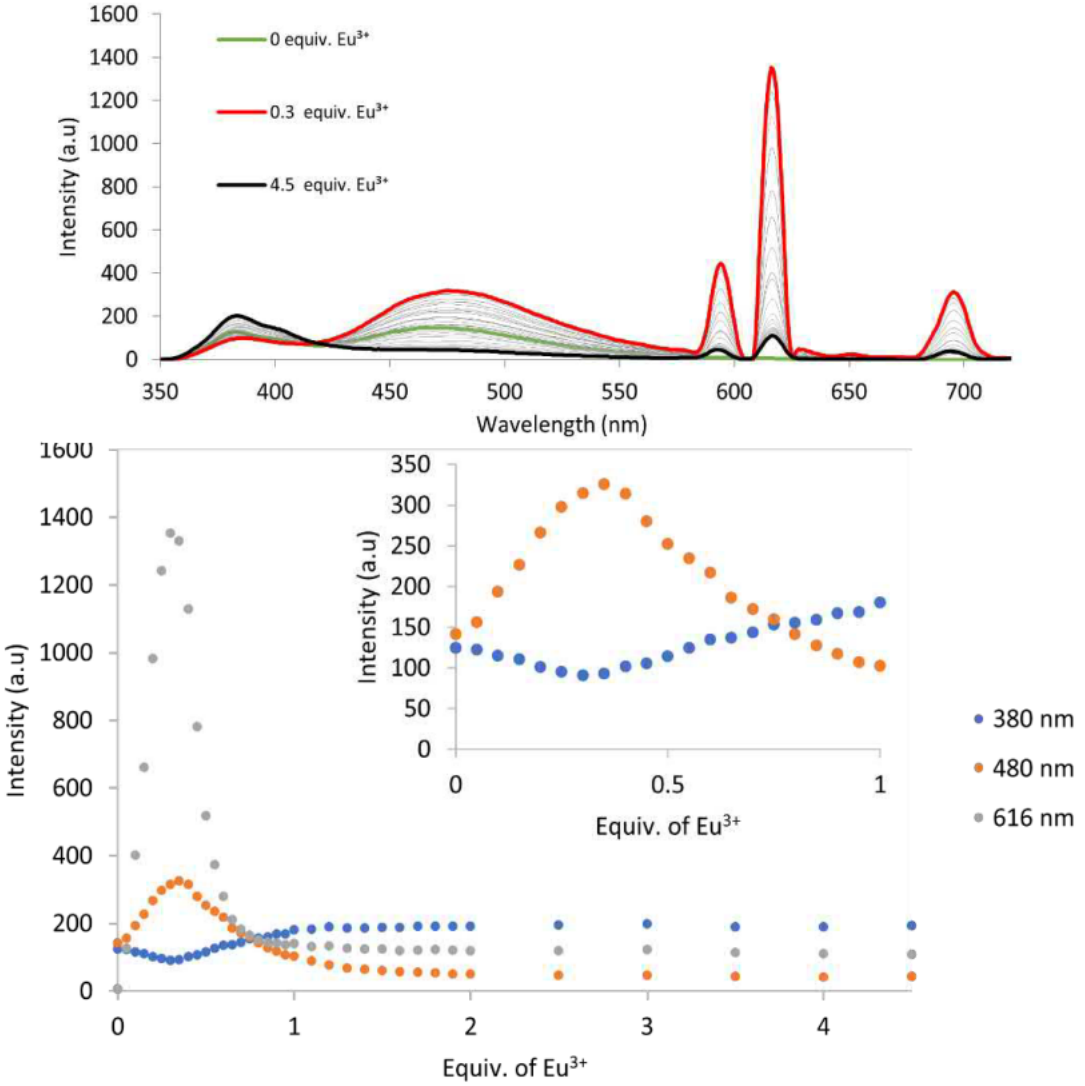

Figure 5.42.. (Top). Fluorescence of **7** *(0.02 mM,. MeOH) titrated with $Eu(CF_3SO_3)\cdot 6H_2O$ in MeOH.. (Bottom). Monitoring changes at 380, 480,. and 616 nm.. Insert:. monitoring changes at 380 and 480 nm between 0 to 1 equivalents..*

Once again only fluorescence data was able to be fitted but had to be restricted to only Eu^{3+} centred emission. The speciation plot further corroborated the evolutionary process noted from changes observed during titrations, following the same general trend as previous PDA based ligands from chapter 3 (Figure 5.43). Importantly once again initially Eu(**7**)$_3$ is the dominant species at 0.3 equivalents (55 %), with additional Eu^{3+} inducing the dominant formation of Eu(**7**)$_2$ at 0.4 equivalents (0.46 %) and Eu(**7**) at 0.9 equivalents. Binding constants were found to be relatively similar to ligands **2** and **3** of chapter 3, which contain similar bulky aromatic groups (see Table 5.8).

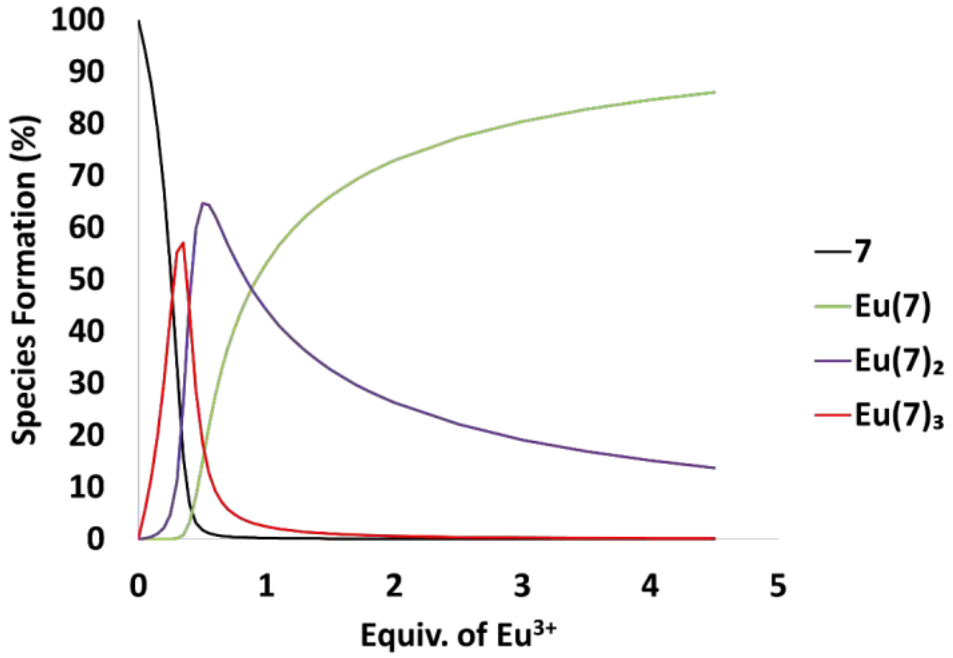

*Figure 5.43.. Speciation plot of fluorescence titration of **7** with $Eu(CF_3SO_3)_3$..*

*Table 5.8.. Binding constants from fitted data of fluorescence titration from other PDA based ligands **7**, **2** and **3**. Solvent which the titrations were carried out in are shown in superscript..*

Ln(L)	Fluorescent emission		
	Log $\beta_{1:1}$	Log $\beta_{1:2}$	Log $\beta_{1:3}$
^{MeOH}Eu(**7**)	7.5 ± 0.01	14.9 ± 0.01	21.1 ± 0.03
^{MecN}Eu(**2**)	8.0 ± 0.04	15.3 ± 0.06	22.0 ± 0.08
^{MeCN}Eu(**3**)	8.4 ± 0.06	15.5 ± 0.10	21.8 ± 0.10

5.2.4.3 Lanthanide Self-Assembly Studies of 8

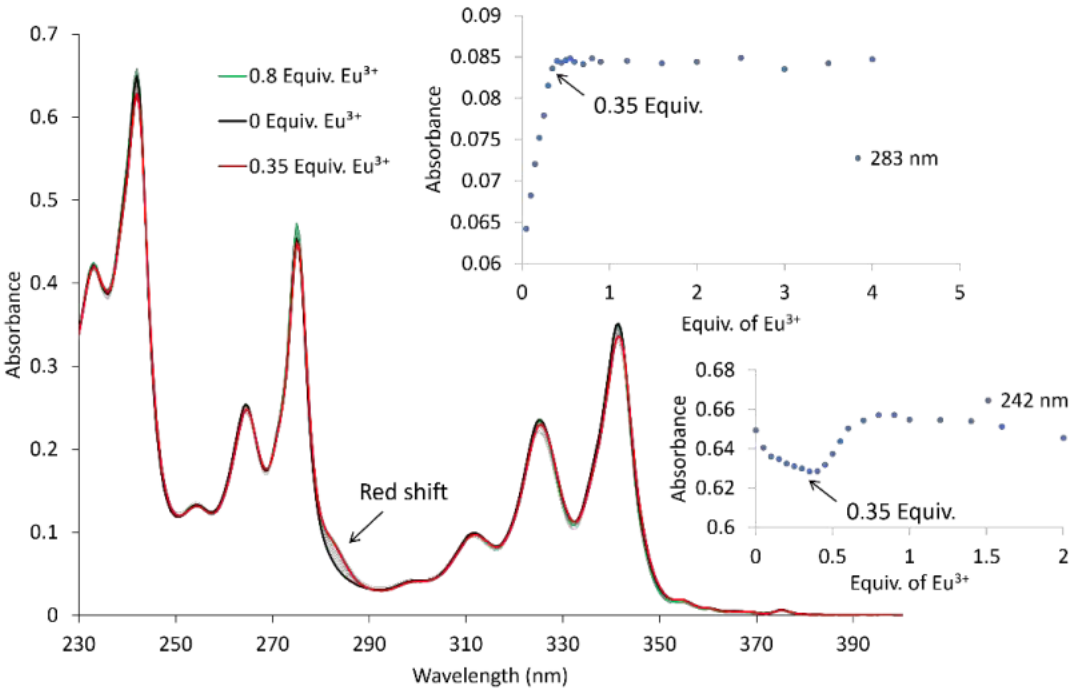

Figure 5.44.. UV-visible absorption of ***8*** *(0.02 mM,. MeOH) titrated with Eu(CF₃SO₃)·6H₂O in MeOH.. Inserts:. monitoring changes at 283 and 242 nm.*

With the absorption spectra of **8** dominated by **PYR**, titrations with Eu(CF$_3$SO$_3$)·6H$_2$O show very little change upon the addition of 0 - 4 equivalents. Because of this the titrations have been slightly simplified by reducing the number of additions (see Section 5.4.2.1 for details). The largest change of note occurs between 0 – 0.35 equivalents, with a red shift occurring between 280 and 290 nm as seen in Figure 5.44. Further addition does not significantly increase the red shift or undergo any major blue shift. Monitoring points between this range, it can be seen the absorbance undergoes a small but significant hyperchromic shift between 0 – 0.35 equivalents, with further additions resulting in a plateau (insert of Figure 5.44). This red and hyperchromic shift leading to a plateau has been seen in most other systems and can be likely associated with the initial formation of the Eu(**8**)$_3$ coordinating into the NO_2 pocket. The only other change of note is that most major bands (242, 275 , 325 and 341 nm) associated with the **PYR** absorption undergo a similar change observed in naphthalene and **NI** absorption bands, with an initially small hypochromic shift from 0 - 0.35 equivalents which then upon further addition between 0.45 – 0.8/0.9 results in a reverse hyperchromic shift, indicative of the evolutionary speciation process forming Eu(**8**)$_3$, Eu(**8**)$_2$ and Eu(**8**).

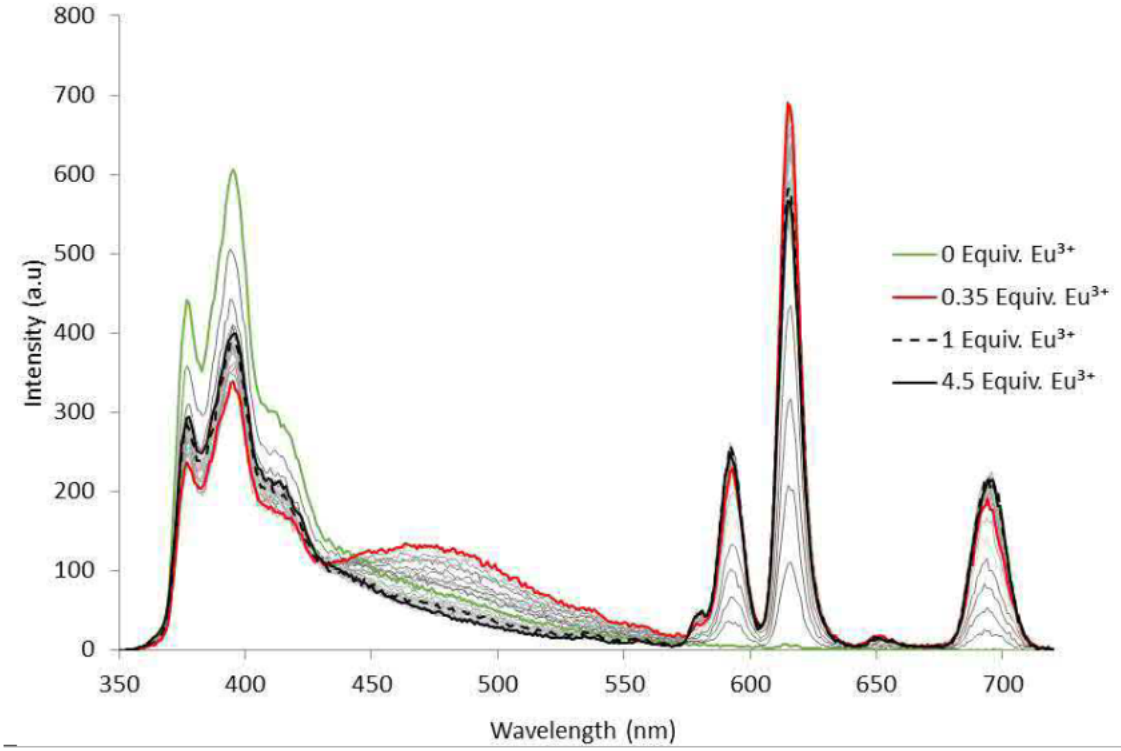

*Figure 5.45.. Fluorescence of **8** (0.02 mM,. MeOH) titrated with Eu(CF$_3$SO$_3$)·6H$_2$O in MeOH..*

Fluorescence titrations of **8** show more significant changes and are very similar to that of **6** (Figure 5.45-46). Initially only **PYR** monomer emission at 395 nm is present. Upon additions of 0 - 0.35 equivalents Eu^{3+}, monomer emission is seen to decrease, along with the steady increase in excimer emission at 476 nm and Eu^{3+} centred emission at 616 nm both reaching a maximum at 0.35 equivalents, while monomer emission reaches a minimum. Again, this is associated with the formation of Eu(**8**)$_3$, which will have maximum emission from three antennae populating the Eu^{3+} excited states, along with maximum π - π interaction, reducing monomer emission while increasing excimer emission. As seen with **6**, further addition of Eu^{3+} from 0.4 - 1 equivalent

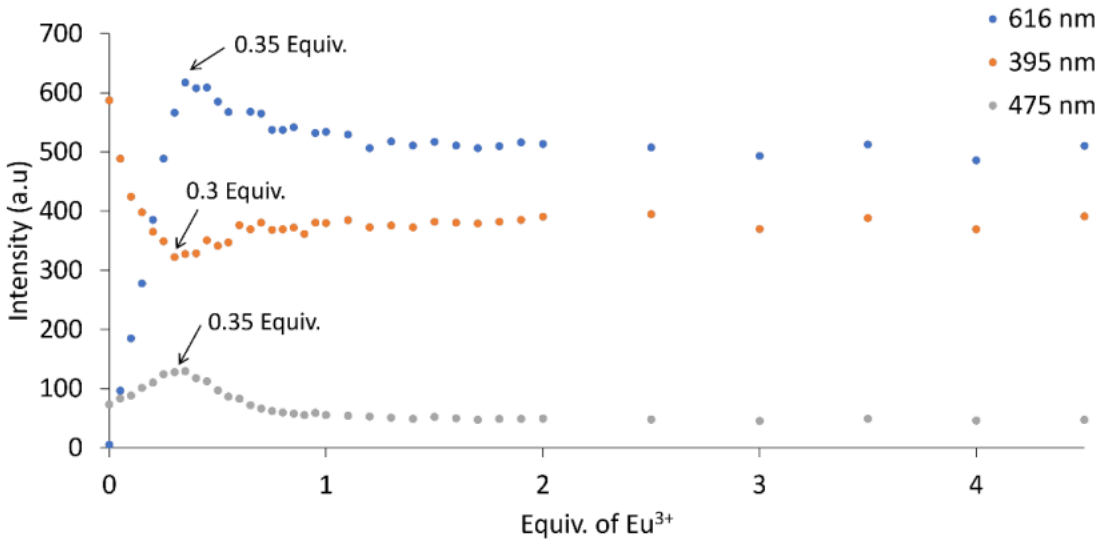

*Figure 5.46.. Fluorescence of **8** (0.02 mM,. MeOH) titrated with Eu(CF$_3$SO$_3$)·6H$_2$O in MeOH, monitoring changes at 395, 475, and 616 nm..*

causes Eu^{3+} and excimer emission to decrease, while monomer emission is slightly restored, indicative of the lesser species formation. Further additions result in no significant changes. It is worth noting that when comparing emission profiles at 0 and 1 equivalents the excimer emission profile is relatively the same as to be expected if only Eu(**8**) is present.

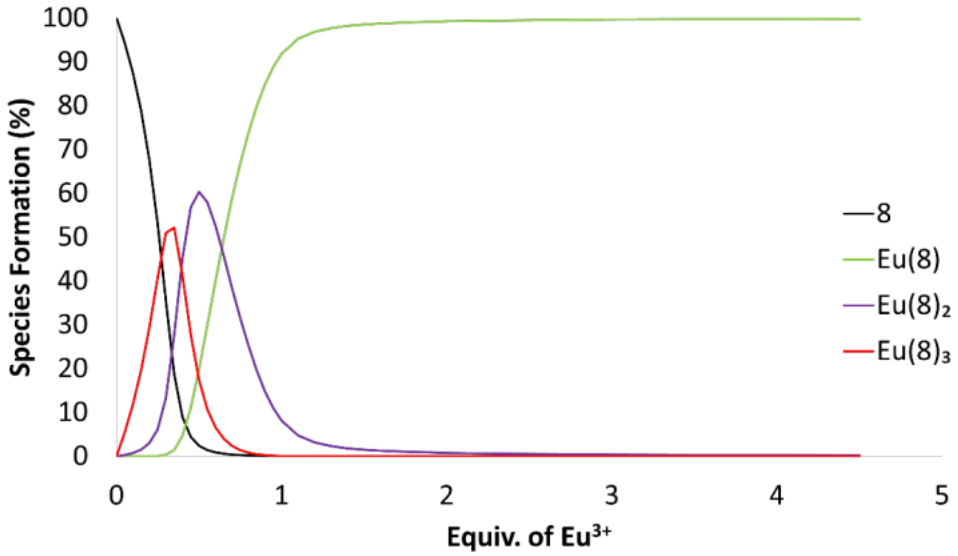

*Figure 5.47. Speciation plot of fluorescence titration of **8** with $Eu(CF_3SO_3)_3$.*

Similar to **7** data could only be fitted with fluorescence titrations when restricted to only the Eu^{3+} centred emission. As indicated by changes observed in titrations, the same evolutionary speciation process is occurring, with initial dominant formation of Eu(**8**)$_3$ at 0.3 equivalents (51%), followed by Eu(**8**)$_2$ at 0.45 equivalents (57%) and finally Eu(**8**) at 0.7 equivalents (59%), as seen in Figure 5.47. It is worth noting that the speciation plot obtained is much more akin to PDC ligand **5** than **6.** Unlike **6** there is no slow formation of the 1:1 M:L species, rather at 1 equivalent it is 90 % formed. This is further indicated by the relatively similar binding constants to **5** obtained for **8** (Table 5.9).

*Table 5.9. Binding constants from fitted data of fluorescence titration from other PDC based ligands **8**, **6** and **5**. C*

Ln(L)	Fluorescent emission		
	Log $\beta_{1:1}$	Log $\beta_{1:2}$	Log $\beta_{1:3}$
^{MeOH}Eu(**8**)	9.2 ± 0.04	16.3 ± 0.05	22.4 ± 0.06
^{MeOH}Eu(**6**)	7.7 ± 0.01	14.8 ± 0.03	20.9 ± 0.30
^{MeCN}Eu(**5**)	9.7 ± 0.03	16.0 ± 0.03	22.6 ± 0.30

5.2.4.4 Lanthanide Self-Assembly Studies Closing Remarks

These self-assembly studies have importantly shown that the 1:3 M:L species is the dominant species for all three ligands when in the correct chemical environment. Additionally, it gives insight into the potential emission profiles of complexes with the dual emissive species, and importantly it shows that all three chromophores should remain strongly emissive when complexed unlike the naphthalene PDA ligand in chapter 3. Furthermore, it showed that complexation in all cases will modify the chromophore emission and induce intramolecular excimer emission, which in some cases nearly completely quenched monomer emission.

5.2.5 Complex Synthesis and Characterisation

Ligands **6** and **7** were both complexed with a range of visible emissive lanthanides (Ln = Eu^{3+}, Tb^{3+}, Dy^{3+}, and La^{3+}) whereas **8** was only complexed with Eu^{3+} and La^{3+}.

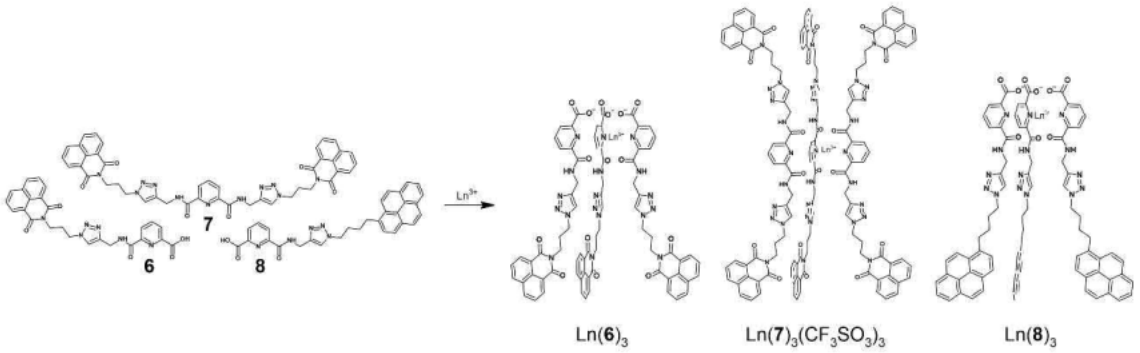

*Scheme 5.7. Complexation of ligands **6**, **7** and **8** with Ln^{3+}.*

Complexation was relatively similar between ligands, the major difference being the solvent mixtures used, which were different for ligand solubility (see Section 5.4.5). In order to form either Ln(**L**)$_3$ (L = **6** and **8**) or [Ln(**7**)$_3$](CF$_3$SO$_3$)$_3$ complexes, both **6** and **8** were first dissolved in ≈ 10 mL of solvent (typically 40 mg of ligand) without the need for heat, whereas ligand **7** required heating until the solid dissolved and was then allowed to cool. 0.33 Equivalents of selected lanthanide were added from a stock solution of the lanthanide salt (either Ln(CF$_3$SO$_3$)$_3$·xH_2O or Ln(Cl)$_3$·xH_2O) dissolved in the appropriate solvent. In the case of **6** and **8**, 1 equivalent of triethylamine was also added. The solutions were refluxed for 30 minutes under microwave irradiation. Once cooled, the solutions were subjected to vapour diffusion of diethyl ether, resulting in white or brown precipitates that were isolated by filtration giving the desired products as white or brown solids in ≈ 50 - 83 % yields.

Table 5.10. Mass peaks of complexes observed. HRMS reported to 4 decimal places and LRMS to 2 decimal places.

Complex	Calculated *m/z*	Experimental *m/z*
[Eu(**6**)$_3$ + 2Na]$^{2+}$	824.1630	824.1980
[Tb(**6**)$_3$ + 2Na]$^{2+}$	827.1644	827.1873
[Dy(**6**)$_3$ + 2Na]$^{2+}$	824.15	824.16
[La(**6**)$_3$ + 2Na]$^{2+}$	817.1549	817.1818
[Eu(**8**)$_3$ + 2Na]$^{2+}$	852.80	825.90
[La(**8**)$_3$ + Na]$^{+}$	1669.65	1669.52

Complex formation of PDC systems was confirmed by HRMS or LRMS, with peaks matching expected *m/z* values and calculated isotopic distributions (see Table 5.10), as well as by elemental analysis for Ln(**6**)$_3$ complexes (see Section 5.4.5). Confirmation of complexation and coordination occurring in the PDC/PDA pocket was also analysed by FTIR, with the classic shifts observed in both the COOH and CONH associated carbonyls of the respective ligands

(see Figure 5.48 and Section 8.3.4). In the case of **6** and **8** both experience a complete disappearance of the COOH IR stretches from 1739 and 1742 cm^{-1}, likely shifted as in previous systems. Similarly, all ligands experience a shift in the carbonyl CONH peak (**6** = 1656 to 1632 cm^{-1}, **7** = 1652 to 1638 cm^{-1} and **8** = 1672 to 1643 cm^{-1}). This indicates that the Ln^{3+} coordination is still occurring in the PDC/PDA pocket, further indicated by the **NI** associated C=O at **6** = 1695 cm^{-1} and at **7** = 1697 cm^{-1}, which is maintained after complexation with no visible shift. Stretches associated with the triflate anion are also present in complexes of **7**, 1281 cm^{-1} assigned to SO_3 and 1168 cm^{-1} assigned to CF_3. In UV-visible absorption spectra, complex absorbance undergoes a visible red shift and increases approximately 3-fold for all complexes compared to their ligands (see Figures 8.3.68-70).

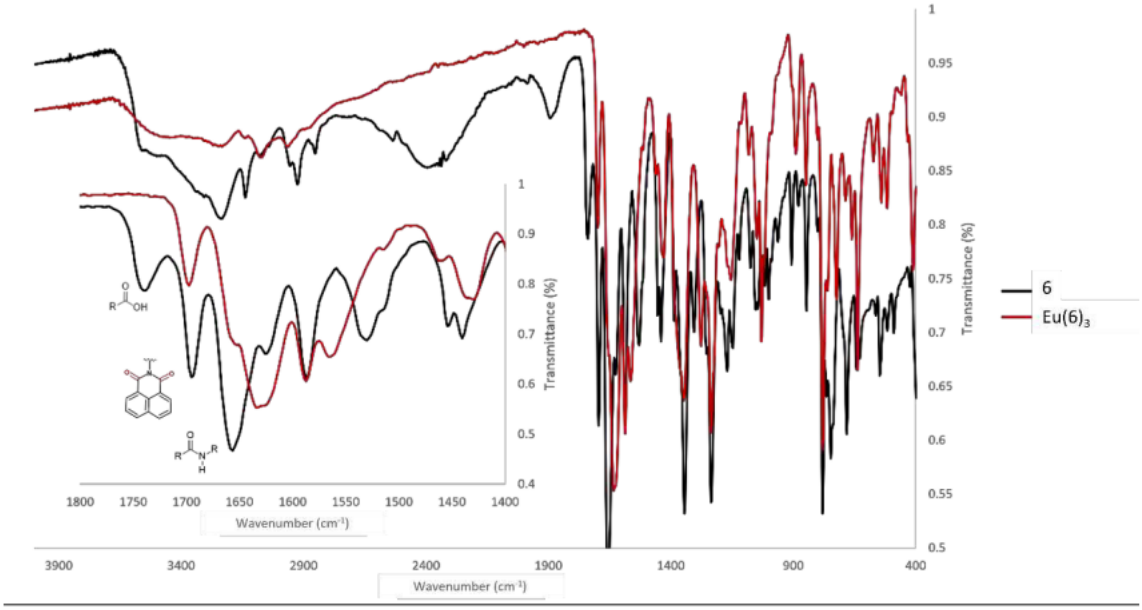

*Figure 5.48.. IR spectra of **6** vs Eu(**6**)$_3$.. Insert:: zoom in of the carbonyl region,. seeing visible shifts and disappearances noted in the text..*

^{1}H NMR of La(**6**)$_3$ and La(**8**)$_3$ was able to be run in DMSO-d_6 while [La(**7**)$_3$](CF$_3$SO$_3$)$_3$ required a 3:1 $CDCl_3$:CD_3OD mixture for solubility. All show clear signs of La^{3+} coordination in the NO_2 pocket from shifts in the pyridyl proton signals. It is worth noting that [La(**7**)$_3$](CF$_3$SO$_3$)$_3$ was also run in DMSO-d_6 and showed signs of dissociation, further showcasing the PDC motif is a more stable coordinating pocket over the PDA motif. ^{1}H NMR of La(**6**)$_3$ and La(**8**)$_3$ show relatively similar shifts from ligand to complex. Both show a strong downfield shift (≈ 0.7 ppm) experienced by the amide (NH) and associated weaker upfield shift experienced by the methylene linker directly bonded to the amide (CH_2-NH), as seen in Figures 5.49-51, indicative of La^{3+} in the NO_2 pocket.[69] Signals associated with the other methylene linker, **NI**, **PYR** and 1,2,3-triazole protons can be seen to undergo very small and insignificant shifts (≈ 0.03 ppm) indicative of La^{3+} coordination occurring away from these regions. The pyridyl PDC ring of **6** where coordination is expected to be occurring has a broad proton signal when in ligand form, whereas in La(**6**)$_3$ this can be seen

to split into three distinct peaks, as previously seen with La(**5**)$_3$, and is indicative of C_3 symmetry (Figure 5.49). The *para*-pyridyl proton is relatively unshifted, while the other two signals undergo a downfield and upfield shift due to La^{3+} coordination and deprotonation of the COOH. Unfortunately for La(**8**)$_3$ this is also likely occurring but is obscured as it is occurring within the **PYR** proton region, so most shifts cannot be observed although there are signs of upfield shifted pyridyl protons as seen in Figure 5.50.

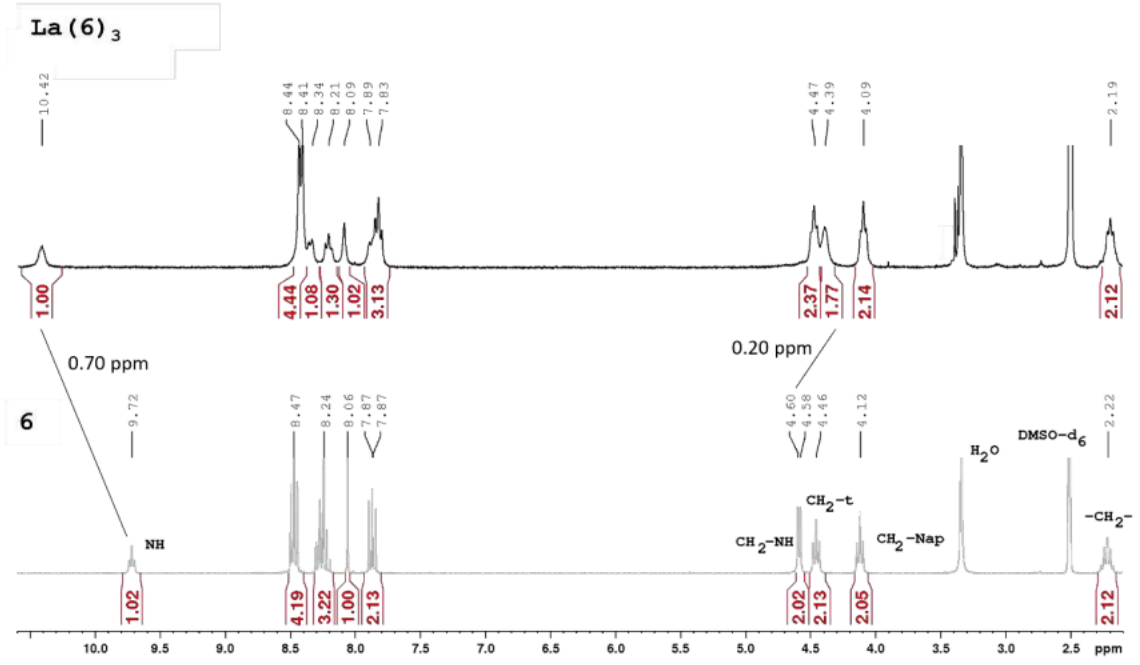

*Figure 5.49. ^{1}H NMR of **6** and La(**6**)$_3$. Abbreviations: Nap for **Nl**, t for 1,2,3-triazole ring and x-CH_2 indicates the CH_2 coordination to an identifiable group (300 MHz, DMSO-d_6):*

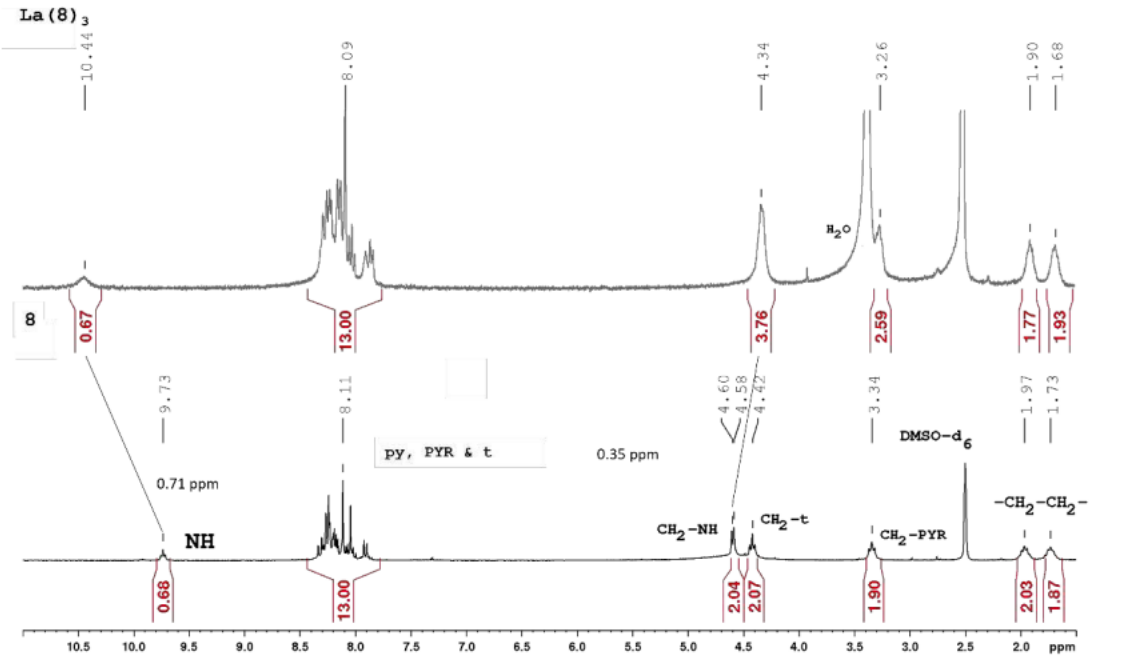

*Figure 5.50. ^{1}H NMR of **8** and La(**8**)$_3$. Abbreviations: py for pyridyl, **PYR** for pyrene, t for 1,2,3-triazole ring and x-CH_2 indicates the CH_2 coordination to an identifiable group (300 MHz, DMSO-d_6).*

^{1}H NMR of [La(**7**)$_3$](CF$_3$SO$_3$)$_3$ shows changes similar to those observed in previous [La(PDA)$_3$]$^{3+}$ complexes in chapter 3, with the significant downfield shift (0.29 ppm) in the pyridyl *para* proton merging/disappearing within the *meta* proton signals, indicative of La^{3+} coordination in the NO_2 pocket and formation of the 1:3 species (see Figure 5.51). Other than the slight downfield shift noted in the 1,2,3-triazole proton, there are no other significant shifts with the methylene linkers and **NI** protons remaining relatively unshifted as expected.

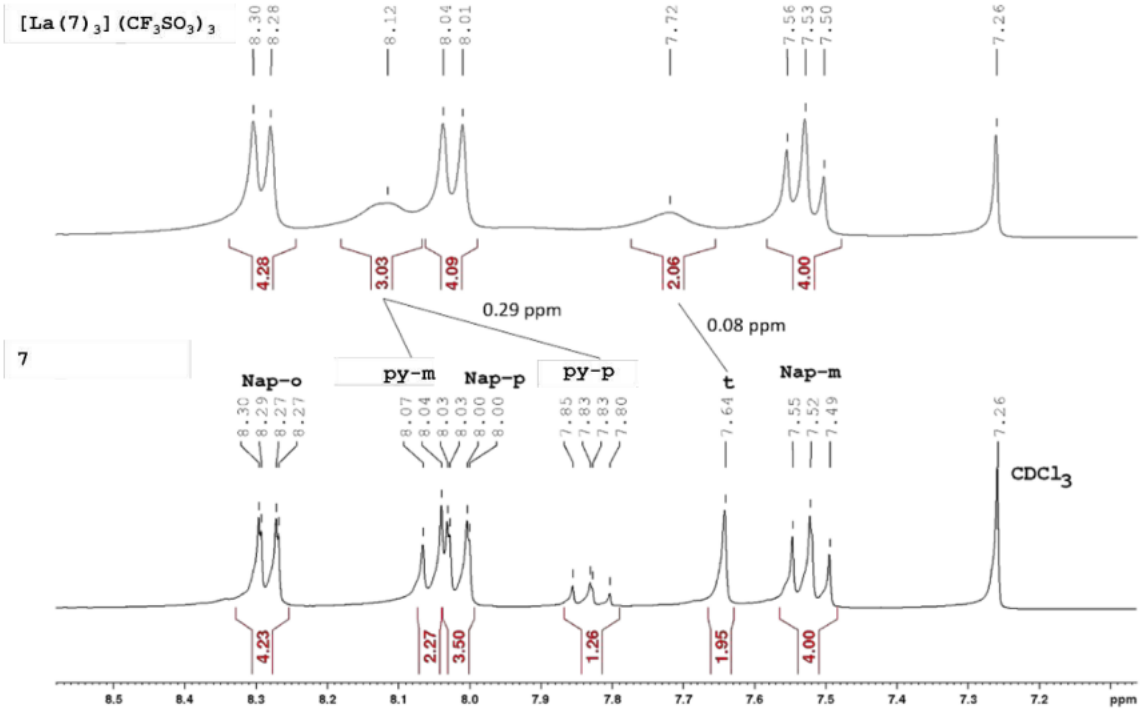

*Figure 5.51.. ^{1}H NMR of **7** and [La(**7**)$_3$](CF$_3$SO$_3$)$_3$.. Abbreviations:. py. for. pyridyl. ring,. Nap. for. **NI**,. t. for. 1,2,3-triazole. ring,. o. -. ortho,. m. - meta. and. p. -. para. (300. MHz,. 3:1,. CDCl$_3$:CD$_3$OD)..*

Attempts to crystallize these systems were unsuccessful. A range of crystallisation methods were attempted, including r.t. vapour diffusion and low temperature vapour diffusion in a refrigerator or freezer, with solvents such as diethyl ether, petroleum spirits, hexane, acetone, methanol, chloroform, and ethyl acetate. Slow evaporation was attempted from DMF and DMSO, which was only viable with **6** and **8** as both solvents would cause dissociation of complexes with **7**. Closed pipette vial and MOF type crystallisations were also attempted, but no single crystals were obtained.

Since attempts to obtain X-ray quality crystals of lanthanide complexes remained elusive, ground state calculations were carried out for Eu(**6**)$_3$, [Eu(**7**)$_3$]$^{3+}$ and Eu(**8**)$_3$ (Figures 5.53-55). The starting structures were based off the previously calculated structures in chapters 3 and 4, with trigonal tricapped prismatic coordination geometries and C_3 symmetry. Calculations to determine HOMO and LUMO energy levels were also carried out for potential OLED design, discussed in the chapter 7 (see Section 8.3.6). The Eu^{3+} complexes were subjected to a DFT

geometry optimisation using the B3LYP[70-72] functional with a mixed basis set of 6-311G+[73] for N, H, O, C and ECP52MBW-II[74-76] with corresponding effective core potential for Eu^{3+} as parameterised in the Gaussian 16 software suite.[77] All calculated structures for the complexes maintain the tricapped trigonal prismatic geometry, with the Ln^{3+} staying within the expected N_3O_6 coordination sphere. To verify the calculated structures the bond lengths of Eu-N and Eu-O have been compared to available crystallographic data of a similar complex: Eu(**6**)$_3$ and Eu(**8**)$_3$ were compared to Eu(**L**^{40}-**R**)$_3$,[69] and [Eu(**7**)$_3$]$^{3+}$ was compared to [Eu(**L**^{6}-**R**,**R**)$_3$]$^{3+}$ (Figure 5.52).[78] As seen in Tables 5.11-13, the calculated bonds are close to those found experimentally, with all bonds (but one type) having differences smaller than 0.1 Å, and the N-Ln-N angle between ligands' (120° as expected) being near identical to those of the crystal structures. The biggest discrepancy is found in Eu(**6**)$_3$ and Eu(**8**)$_3$ O – Eu^{3+} bond, having a difference of ≈ 0.2 Å.

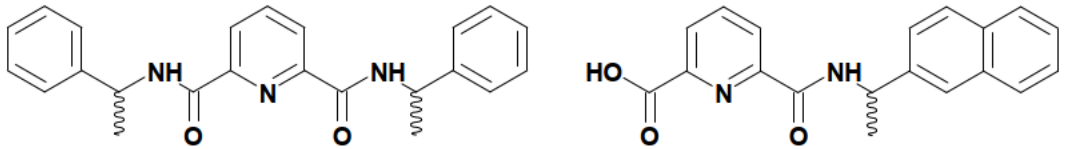

L^{6} **L**^{40}

Figure 5.52.. Ligands used in complexes,. for bond length comparison..

*Table 5.11.. Bond length of Eu(**6**)$_3$ in comparison to Eu(**L**^{40}-**R**)$_3$,. values obtained from reference 69..*

Bond/Angle	Calculated- Eu(6)$_3$	Experimental - Eu(L^{40}-R)$_3$
O – Eu^{3+}	2.616 Å	2.432 (12), 2.415 (15), 2.469 (12)
O^{-} - Eu^{3+}	2.336 Å	2.389 (14), 2.294 (15), 2.423 (12)
N – Eu^{3+}	2.623 Å	2.542 (15), 2.564 (18), 2.596 (17)
N-Ln-N	120°	121.6°, 120.9°, 117.5°

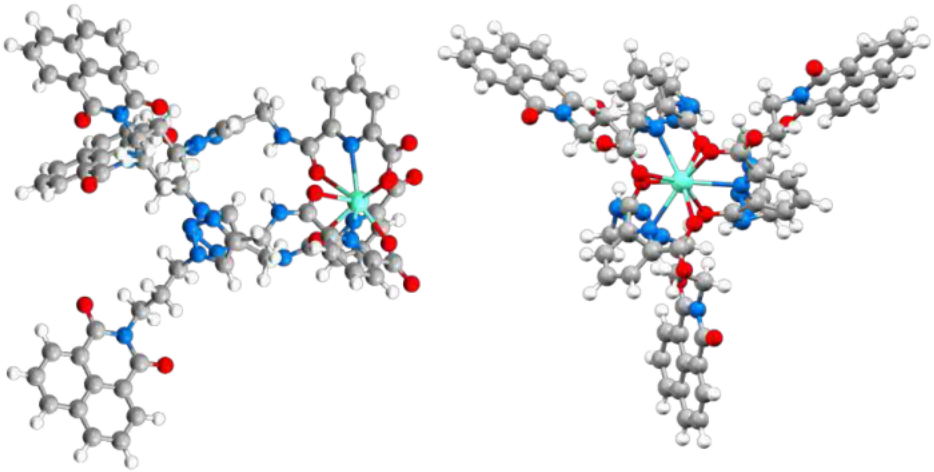

*Figure 5.53.. Calculated Eu(**6**)$_3$ complex structure with C_3 symmetry..*

Table 5.12.. Bond length of $[Eu(\mathbf{7})_3]^{3+}$ in comparison to $[Eu(\mathbf{L^6\text{-}R,R})_3]^{3+}$,. values obtained from reference 78..

Bond/Angle	Calculated – $[Eu(7)_3]^{3+}$	Experimental - $[Eu(L^6\text{-}R,R)_3]^{3+}$
O – Eu^{3+}	2.417 Å, 2.416 Å	2.397 (2)
N – Eu^{3+}	2.652 Å	2.564(2)
N-Ln-N	120 °	119.9°

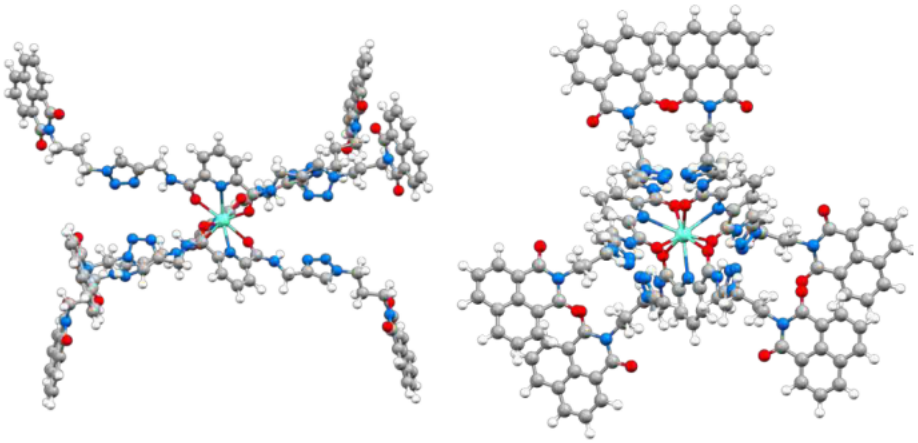

Figure 5.54.. Calculated $[Eu(\mathbf{7})_3]^{3+}$ complex structure with C_3 symmetry..

Table 5.13.. Bond length of $Eu(\mathbf{8})_3$ in comparison to $Eu(\mathbf{L^{40}\text{-}R})_3$,. values obtained from reference 69..

Bond/Angle	Calculated- $Eu(8)_3$	Experimental - $Eu(L^{40}\text{-}R)_3$
O - Eu^{3+}	2.643 Å	2.432 (12), 2.415 (15) , 2.469 (12)
O^- - Eu^{3+}	2.329 Å	2.389 (14), 2.294 (15) , 2.423 (12)
N - Eu^{3+}	2.631 Å	2.542 (15), 2.564 (18) , 2.596 (17)
N-Ln-N	120°	121.6°, 120.9°, 117.5°

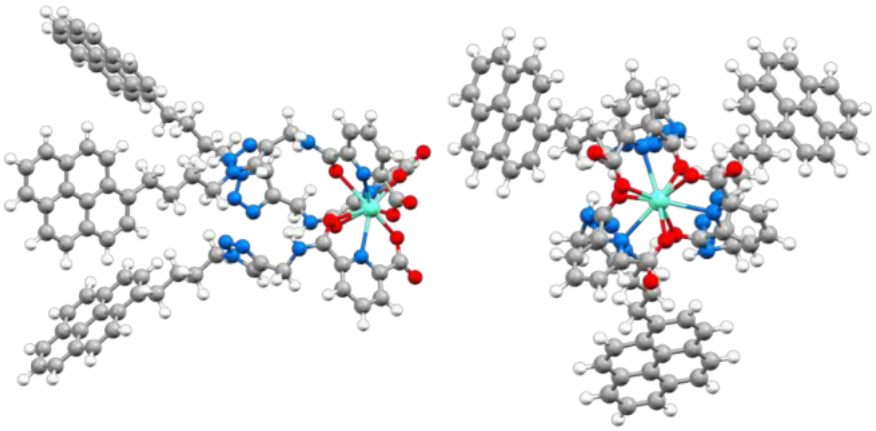

Figure 5.55.. Calculated $Eu(\mathbf{8})_3$ complex structure with C_3 symmetry..

5.2.6 Lanthanide Photophysical Properties

The photophysical properties of Ln(**6**)$_3$, [Ln(**7**)$_3$](CF$_3$SO$_3$)$_3$ and Ln(**8**)$_3$ complexes were evaluated mainly in MeOH, diluted from a mixed stock solution of DCM:MeOH (1:1) for solubility purposes. Occasionally, solutions in MeCN were also evaluated, diluted from a stock solution of MeCN:DCM (1:1), but MeCN was not favoured as precipitation commonly occur.

5.2.6.1 Europium Complexes

Europium complexes from this study (Eu(**6**)$_3$, [Eu(**7**)$_3$](CF$_3$SO$_3$)$_3$ and Eu(**8**)$_3$) were shown to be the best candidates for dual emission compared to other Ln^{3+} explored (Figures 5.56-58). All three Eu^{3+} complexes are clearly dual emissive, with organic chromophore (**PYR** and **NI**) emission visible alongside Eu^{3+} centred emission in fluorescence spectra while in phosphorescence spectra only the long-lasting emission of Eu^{3+} remains. Before a more detailed description of the dual emission observed, it is easier to firstly discuss Eu^{3+} and chromophore centred emission separately.

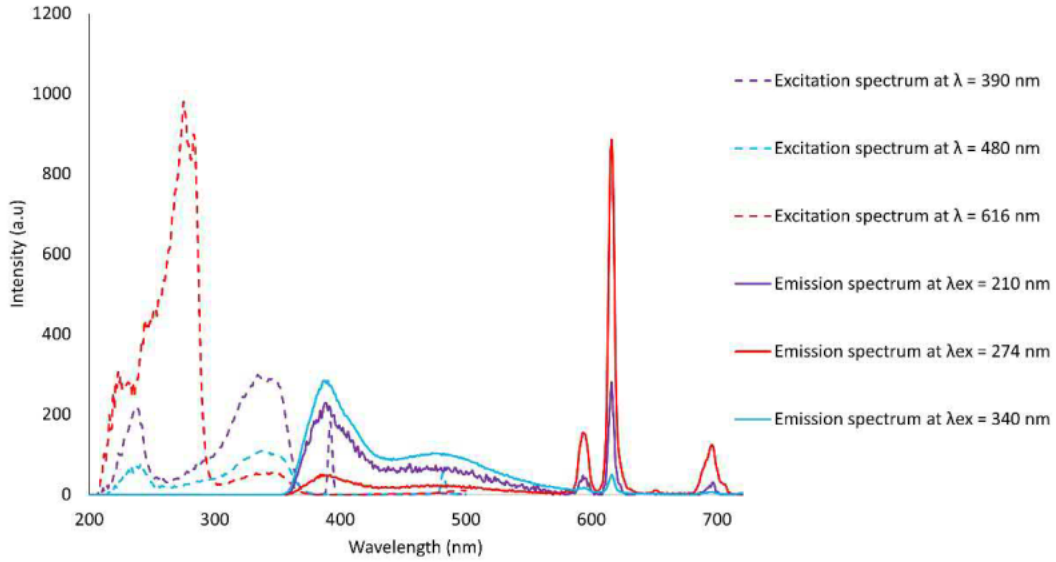

*Figure 5.56.. Fluorescence spectra of Eu(**6**)$_3$ (0.01 mM,. MeOH)..*

All three ligands showed effective population of the $^5D_0$ excited state of Eu^{3+}. The subsequent deactivation to the ^7F_J (J = 0 – 4) states gave the expected sharp emission bands centred at λ = 594 nm ($^5D_0 \rightarrow {}^7F_1$), 616 nm ($^5D_0 \rightarrow {}^7F_2$), 651 nm ($^5D_0 \rightarrow {}^7F_3$), and 697 nm ($^5D_0 \rightarrow {}^7F_4$). The Eu^{3+} complexes also displayed a weak signal at λ = 581 nm ($^5D_0 \rightarrow {}^7F_0$), indicative of the overall symmetry of the complex being C_3.[79] Lifetimes of the Eu^{3+} centred emission ($^5D_0 \rightarrow {}^7F_2$) transition were also measured (except Eu(**8**)$_3$) and fitted to single exponential decays indicative of single species in solution, with average lifetimes of 1.175 and 0.363 ms for Eu(**6**)$_3$ and [Eu(**7**)$_3$](CF$_3$SO$_3$)$_3$.

Time delayed emission studies were not collected for Eu(**8**)$_3$ as COVID lockdowns prevented access to the spectrophotometer.

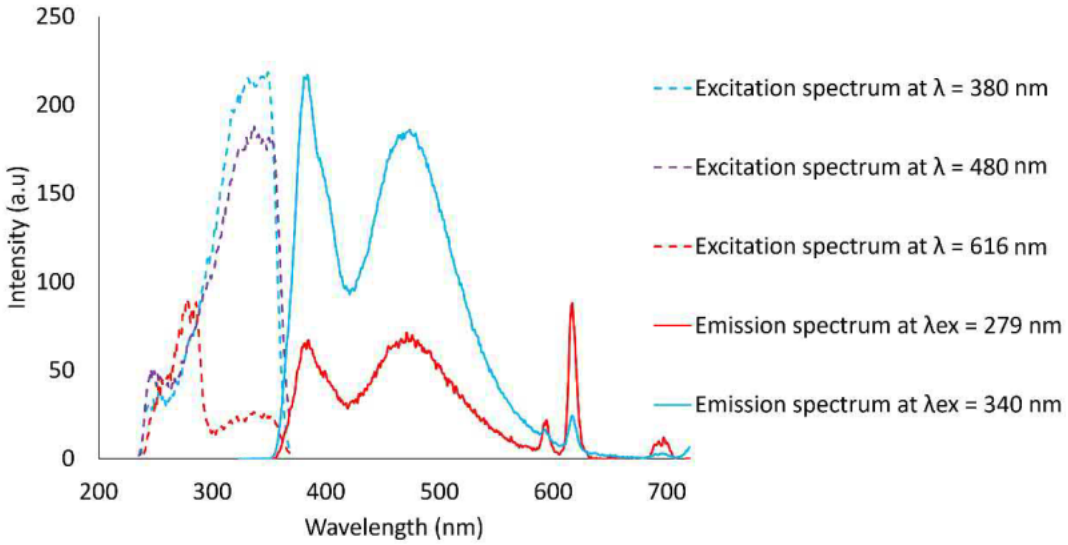

*Figure 5.57.. Fluorescence spectra of [Eu(**7**)$_3$](CF$_3$SO$_3$)$_3$ (0.01 mM, MeCN)..*

Population of Eu^{3+} excited states from excitation spectra showed maximum emission intensity at 270 - 280 nm for all complexes, indicating that the pyridyl unit remains the main antenna for lanthanide excitation for all complexes. In the case of Eu(**6**)$_3$ and [Eu(**7**)$_3$](CF$_3$SO$_3$), there are clear signs of Eu^{3+} population also occurring from **NI**, with the excitation spectra also containing a band ranging 300 - 350 nm only associated with the **NI** ring (Figures 5.56-57). In the case of Eu(**8**)$_3$, there was no clear evidence from the excitation plot and emission to indicate that Eu^{3+} centred emission was populated *via* the **PYR** unit (Figure 5.58), potentially a result of the additional methylene linker making the antenna too distant for this interaction.

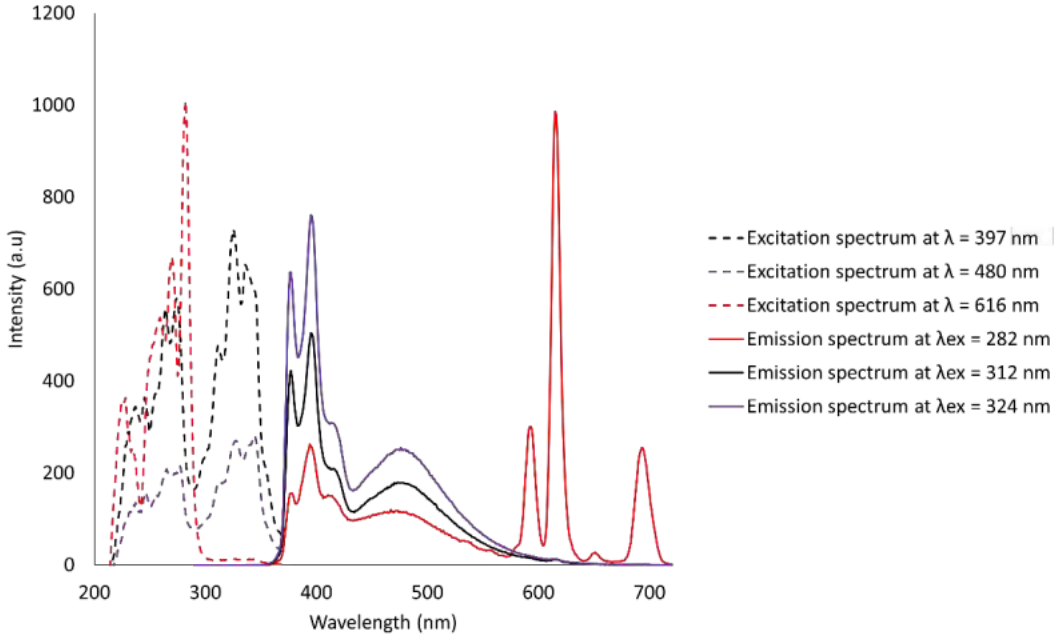

*Figure 5.58.. Fluorescence spectra of Eu(**8**)$_3$ (0.01 mM, MeOH)..*

Eu^{3+} centred emission overall quantum yields (Φ_{Ln}^{L}) were measured using the same method described in chapter 4. Both MeCN and MeOH were evaluated, however, in most cases only one solvent is reported, as either the complex was insoluble (MeCN-Eu(**8**)$_3$) or Eu^{3+} centred emission was quenched in that solvent (MeOH-[Eu(**7**)$_3$](CF_3SO_3)$_3$)). Although Eu^{3+} centred emission was visible in all complexes, Eu(**6**)$_3$ had significantly better Φ_{Ln}^{L} as seen in Table 5.14. The large discrepancies between Eu(**6**)$_3$ and [Eu(**7**)$_3$](CF_3SO_3)$_3$ are associated with the mono PDC being a better antenna for lanthanide excitation as seen in chapter 4. For Eu(**8**)$_3$ the extremely low quantum yield is associated with the strong **PYR** absorbance over the pyridyl unit range, resulting in significantly weaker emission. It is because of this extremely low Φ_{Ln}^{L} that it was deemed unnecessary to complex **8** with other visibly emissive Ln^{3+}.

Table 5.14.. Lanthanide centred emission,. overall quantum yields. (Φ_{Ln}^{L}),. observed lifetimes. (τ_{osb}),. radiative lifetime. (τ^{rad}),. intrinsic quantum yield.(Φ_{Ln}^{Ln}). and sensitisation efficiency. (n_{sens})..

Complex	Φ_{Ln}^{L} (%)	τ_{osb} (ms)	τ^{rad} (ms)	Φ_{Ln}^{Ln} (%)	n_{sens} (%)
MeOH Eu(**6**)$_3$	7.6	1.059	4.998	21.2	35.9
MeCN Eu(**6**)$_3$	7.5	-	-	-	-
MeCN [Eu(**7**)$_3$](CF_3SO_3)$_3$	2.8	-	-	-	-
MeOH Eu(**8**)$_3$	0.19	-	-	-	-

In terms of organic chromophore emission, complexation of both Eu(**6**)$_3$ and Eu(**8**)$_3$ led to intramolecular excimer bands at 480 and 490 nm respectively, while [Eu(**7**)$_3$](CF_3SO_3)$_3$ retained the already present excimer emission as seen in Figures 5.56-58. The appearance of excimer emission in both Eu(**6**)$_3$ and Eu(**8**)$_3$, as seen in self-assembly studies, indicated that the aromatic chromophores within the complex were brought into close enough proximity to form π - π intramolecular interactions. In the case of the more promising dual emissive complex Eu(**6**)$_3$, this was further investigated and found to be affected by both the polarity of the solvent and concentration (discussed later). Eu(**6**)$_3$ fluorescence emission measured in MeCN (Figure 5.59) resulted in **NI** excimer emission becoming significantly more dominant than monomer emission, which is reversed in MeOH (Figure 5.56). This is likely due to aggregation induced emission. Since Eu(**6**)$_3$ and **NI** in general are less soluble in non-polar solvents like MeCN, it causes the molecules to aggregate, which allows for more π - π intermolecular interactions between complexes, leading to stronger excimer emission. As stated in the introduction (Section 5.1), this effect has previously been used by Ward and co-workers to achieve close to “white” light emission in solution.[36]

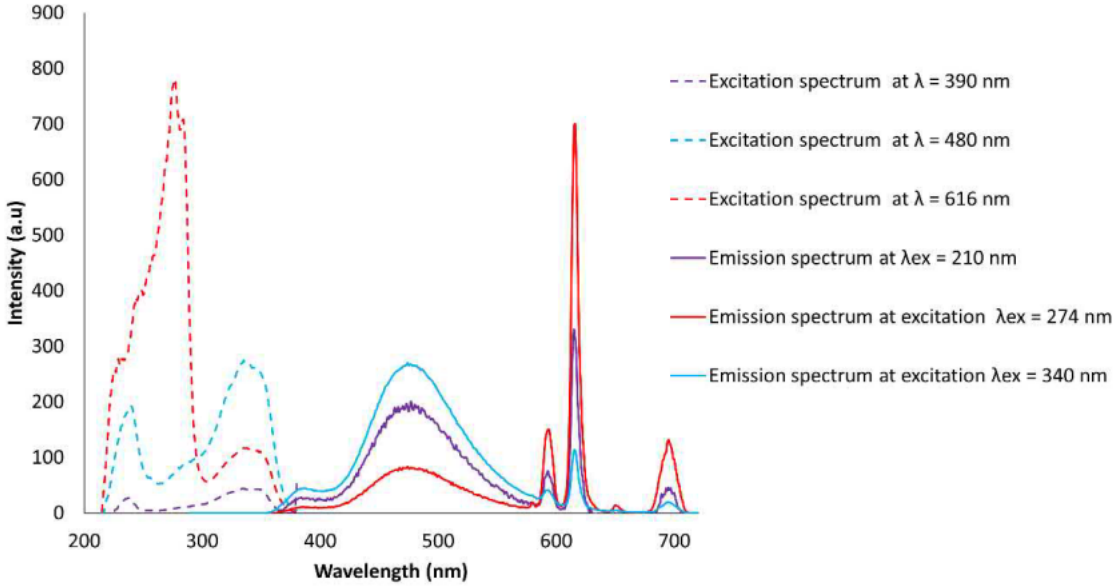

*Figure 5.59. Fluorescence spectra of Eu(**6**)$_3$ (0.01 mM, MeCN).*

Fluorescent quantum yields (Φ_f) of the organic chromophore emission (these include some Ln^{3+} centred emission as in most cases it is too difficult to separate from organic chromophore emission) were also measured as seen in Table 5.15. Fluorescent quantum yields for organic emission were again measured against quinine sulfate with a λ_{ex} = 366 nm. It was found that Eu(**6**)$_3$ also has the strongest organic emission. However, it is important to note that although the Eu^{3+} centred emission is very weak when the excitation wavelength is 366 nm, it is still present, and this is contributing to Eu(**6**)$_3$ quantum yields (see Figure 5.56 with an λ_{ex} = 340 nm).

Table 5.15. Organic emission quantum yields when excited at 366 nm (values also include lanthanide emission when present).

6 and corresponding Complexes	**Φ_f (%)**	**7 and corresponding Complexes**	**Φ_f (%)**	**8 and corresponding Complexes**	**Φ_f (%)**
6	12	**7** ligand emission	16	**8**	2.6
Eu(**6**)$_3$ MeOH	15. 0	[Eu(**7**)$_3$](CF$_3$SO$_3$)$_3$	14	Eu(**8**)$_3$	1.5
Eu(**6**)$_3$ MeCN	17	[Dy(**7**)$_3$](CF$_3$SO$_3$)$_3$	16	La(**8**)$_3$	1.7
Dy(**6**)$_3$	15	[Tb(**7**)$_3$](CF$_3$SO$_3$)$_3$	16		
Tb(**6**)$_3$	11	[La(**7**)$_3$](CF$_3$SO$_3$)$_3$	17		
La(**6**)$_3$	15				

5.2.6.2 Dual Emission of Europium Complexes

All three complexes not only exhibit dual emission but also colour-tunable emission, meaning that depending on the excitation wavelength the overall perceived emission colour changed, and furthermore both Eu(**6**)$_3$ and Eu(**8**)$_3$ showed that they were able to achieve white emission.

*Figure 5.60. Eu(**6**)$_3$ solid powder, under ambient light, shortwave UV irradiation (λ_{ex} = 254 nm) and longwave UV irradiation (λ_{ex} = 365 nm), from left to right.*

This property was most apparent for Eu(**6**)$_3$, with the effect being clearly visible to the naked eye under a UV lamp. As seen in Figures 5.60-62, the solid appeared either blue under longwave irradiation (365 nm) or white under shortwave irradiation (254 nm). This effect is caused by the different excitation wavelengths favouring either Eu^{3+} centred emission (shortwave) or organic chromophore centred emission (longwave). Solid fluorescence spectra showed that at λ_{ex} below 265 nm and above 286 nm result in an overall blue emission, but as seen in Figures 5.61-62, there is a slight difference between short and long wavelengths, the latter having a stronger excimer emission and appearing a slightly lighter blue in the CIE diagram while the shortwave still contains some monomer emission causing a slightly darker blue.

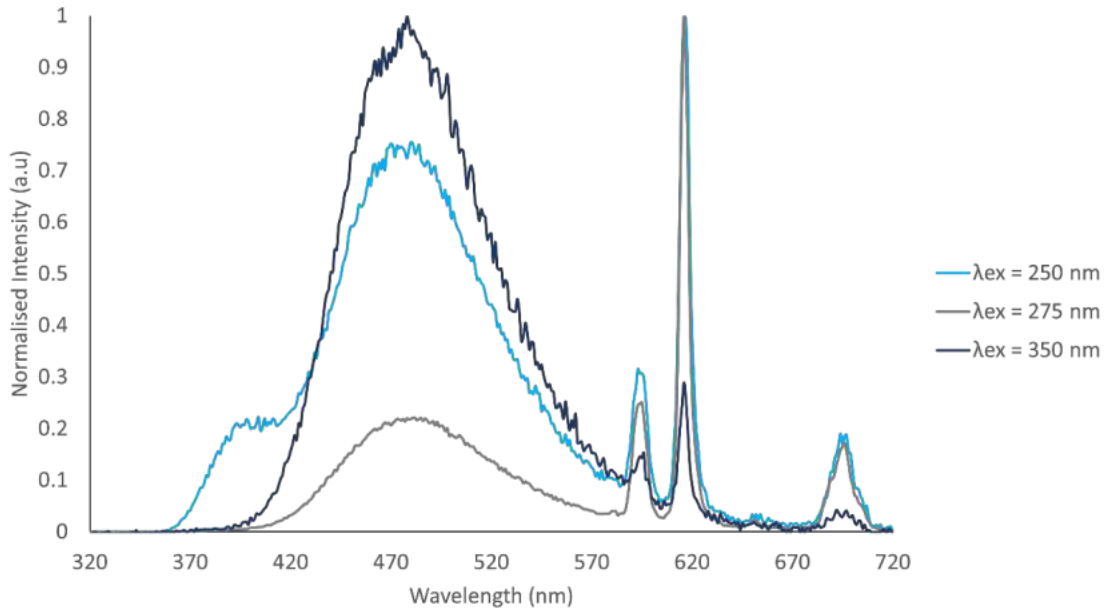

*Figure 5.61. Fluorescence profiles of Eu(**6**)$_3$ solid, showing change in monomer, excimer and Eu^{3+} emission as excitation wavelength changes.*

At λ_{ex} between 265 nm and 286 nm, Eu^{3+} centred emission changes significantly and becomes strong, causing the overall emission to move within the "white" region, with CIE coordinates ranging within x = 0.29 - 0.30 and y = 0.29 - 0.32 (Figure 5.62). The closest to "pure-white" emission occurs at λ_{ex} = 275 nm, with CIE coordinates x,y = 0.32, 0.29, much closer than Ward and co-workers white (x,y = 0.27, 0.25) but not as good as Yan and co-workers "pure-white" (x,y = 0.34, 0.31). It is worth noting that the emission profiles from the solid Eu(**6**)$_3$ complex are very similar to that observed in MeCN, due to the aggregation the nonpolar solvent causes.

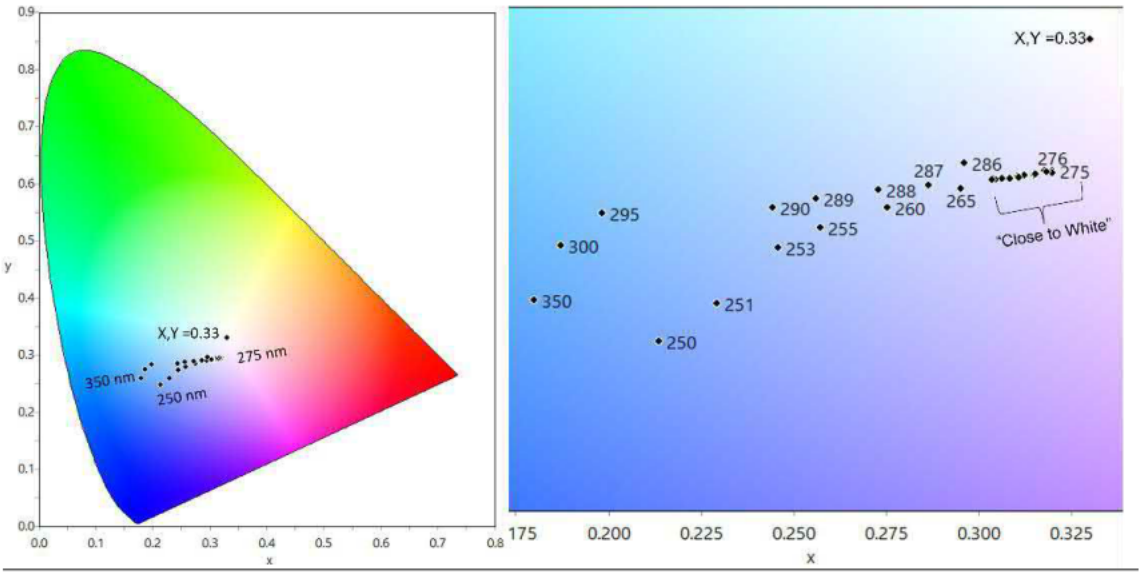

*Figure. 5.62.. CIE. 1931. chromaticity. diagram. with. different. overall. colours. capable. of. Eu(**6**)$_3$. dependent. on. λ_{ex}.. Calculated. CIE coordinates:. 250. nm. x,y. =. 0.21,. 0.25;. 251. nm. x,y. =. 0.23. ,0.25;. 253. nm. x,y. =. 0.24,. 0.27;. 255. nm. x,y. =. 0.26,. 0.28;. 260. nm. x,y. =. 0.28,. 0.29;. 265. nm. x,y. =. 0.29,. 0.29;. 270. nm. x,y. =. 0.31. ,0.29;. 271-272. nm. x,y. =. 0.31,. 0.29. ;. 273-278. nm. x,y. =. 0.32,. 0.29;. 278-280. nm. x,y. =. 0.31,. 0.29. ;. 281-286. nm. x,y. =. 0.30,. 0.29;. 287. nm. x,y. =. 0.29,. 0.29;. 288. nm. x,y. =. 0.28,. 0.29;. 289. nm. x,y. =. 0.26,. 0.29;. 290. nm. x,y. =. 0.24,. 0.28;. 295. nm. x,y. =. 0.20,. 0.28;. 300. nm. x,y. =. 0.19,. 0.27;. 310. nm. x,y. =. 0.18,. 0.26. and. 350. nm. x,y. =. 0.18,. 0.26..*

The overall emission in Eu(**6**)$_3$ (Figures 5.63-65) is quite complex and able to achieve a range of emission colours from dark blue through to white as a solid. The colour-tunable emission and white emissive properties of Eu(**6**)$_3$ are retained in solution, but as expected are dependent on both solvent and concentration, which as previously discussed is associated with the level of excimer emission from aggregation in solution.

*Figure. 5.63.. Eu(**6**)$_3$ solid. and. 0.01. mM. MeCN. solution. under. longwave. irradiation. (Left,. λ_{ex} =. 254. nm). and. shortwave. irradiation. (Right, λ_{ex} =. 365. nm)..*

Eu(**6**)$_3$ emission in 0.01 mM solutions is not limited to only white and blue emission but is able to achieve bright red emission in both MeOH and MeCN as seen in Figures 5.64-65. The colour-tunable emission of Eu(**6**)$_3$ again occurs over an excitation range of λ_{ex} = 230 - 300 nm. As previously seen in solid fluorescence, at longwave λ_{ex} = 300 - 360 nm or shortwave $\lambda_{ex} \geq$ 245 nm, the overall emission from both solutions is blue from the dominant **NI** emission. Major changes occur when the pyridyl unit starts to be excited beginning at $\lambda_{ex} \approx$ 245 nm. From here the overall emission moves towards the red region of the CIE chromaticity diagram as Eu^{3+} centred emission becomes stronger. Eu(**6**)$_3$ in both MeCN and MeOH emission is within the "white region" (see Figure 4.33) when $^{MeOH}\lambda_{ex}$ = 288 nm x,y = 0.38, 0.27 or $^{MeCN}\lambda_{ex}$ = 250 nm x,y = 0.35, 0.27. Closer to "pure-white" emission occurs in MeCN due to stronger excimer emission (Figure 5.64-65). At longer λ_{ex} = 255 - 287 nm, the emission turns to overall red until a maximum is reached at $^{MeOH}\lambda_{ex}$ = 275 nm x,y =0.54, 0.31 and $^{MeCN}\lambda_{ex}$ = 275 nm x,y = 0.44, 0.30. With the weak excimer emission in MeOH, Eu(**6**)$_3$ is able to achieve much deeper reds than in MeCN (Figures 5.64-65).

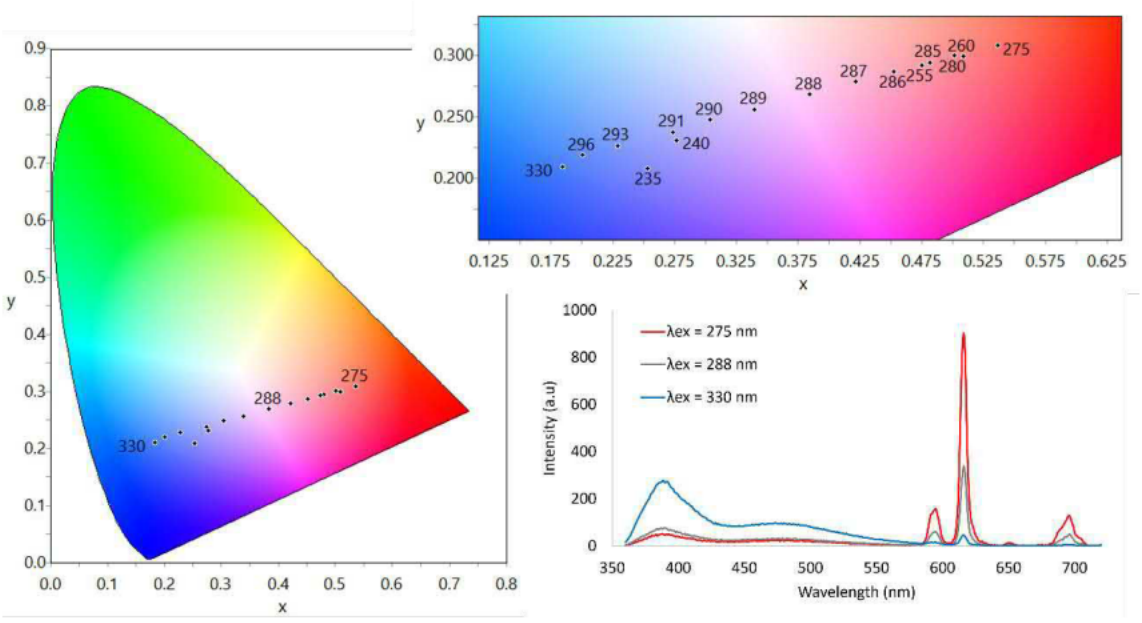

*Figure 5.64.. CIE 1931 chromaticity diagram with different overall colours capable of Eu(**6**)$_3$ in 0.01 mM MeOH solution dependent on λ_{ex} and fluorescence spectra of important λ_{ex}.. Calculated CIE coordinates:. 235 nm x,y = 0.25,. 0.21;. 240 nm x,y = 0.28 ,0.23;. 255 nm x,y = 0.47,. 0.29;. 260 nm x,y = 0.50,. 0.29;. 275 nm x,y = 0.54,. 0.30;. 280 nm x,y = 0.50,. 0.30;. 270 nm x,y = 0.31 .,0.29;. 271-272 nm x,y = 0.31,. 0.29 .;. 273-278 nm x,y = 0.32,. 0.29;. 278-280 nm x,y = 0.31,. 0.29 .;. 286 nm x,y = 0.45,. 0.29;. 287 nm x,y = 0.42,. 0.28;. 288 nm x,y = 0.38, 0.27;. 289 nm x,y = 0.34,. 0.27;. 290 nm x,y = 0.34,. 0.27;. 291 nm x,y = 0.27,. 0.23;. 293 nm x,y = 0.20,. 0.22;. 296 nm x,y = 0.20,. 0.22 and 330 nm x,y = 0.18,. 0.20..*

Increasing the λ_{ex} causes the Eu^{3+} emission to decrease and thus reverts the overall emission back to blue at $\lambda_{ex} \approx$ 300 nm. As seen in Figures 5.64-65 the solvent plays an important role in the overall emission observed, with Eu(**6**)$_3$ in MeCN having a much smaller range than Eu(**6**)$_3$ in MeOH, not being able to achieve as deep a red or blue but achieving much closer to "pure-white" emission. It is worth noting that not as many data points were able to be collected for 0.01 mM MeCN as the complex would precipitate over a short period of time affecting the overall emission.

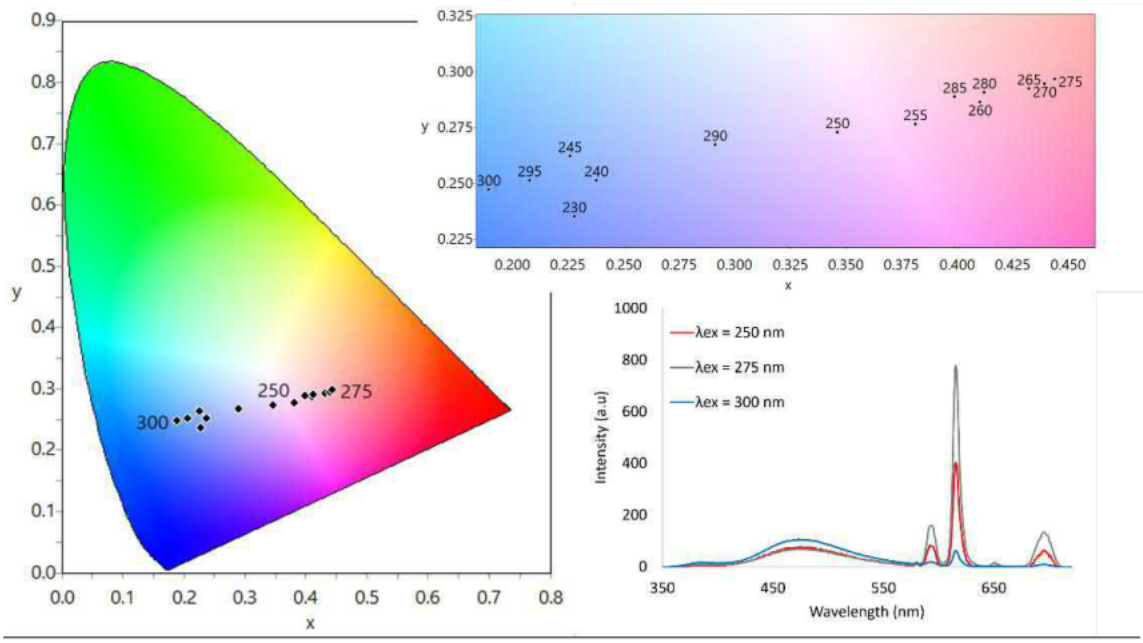

*Figure 5.65.. CIE 1931 chromaticity diagram with different overall colours capable of Eu(**6**)$_3$ in 0.01 mM MeCN solution dependent on λ_{ex} and fluorescence spectra of important λ_{ex}.. Calculated CIE coordinates:: 230 nm x,y = 0.23,.0.24;: 240 nm x,y = 0.24.,0.25;: 250 nm x,y = 0.35,.0.27;: 255 nm x,y = 0.38,.0.28;: 260 nm x,y = 0.41,.0.29;: 265 nm x,y = 0.50,.0.30;: 270 nm x,y = 0.31.,0.29;: 271-272 nm x,y = 0.31,.0.29.;: 273-278 nm x,y = 0.32,.0.29;: 278-280 nm x,y = 0.43,.0.29.;: 270 nm x,y = 0.44,.0.30;: 275 nm x,y = 0.44,.0.30;: 280 nm x,y = 0.41,.0.29;: 285 nm x,y = 0.40,.0.29;: 290 nm x,y = 0.29,.0.27;: 295 nm x,y = 0.21,.0.25 and 300 nm x,y = 0.19,.0.25..*

A range of different concentrations of Eu(**6**)$_3$ from 10 mM to 0.001 mM were measured in MeOH. At higher concentrations (10 mM and 5 mM), excimer emission is strongly present at all wavelengths, which causes the solution's overall emission to appear white (5 mM) or blue-white (10 mM) when excited with shortwave irradiation, while lower concentrations (1 mM and 0.01 mM) appear a light pink and dark red respectively (Figure 5.66). With longwave irradiation, the emission remains relatively similar with blue emission throughout. Comparing fluorescence spectra and resulting CIE coordinates of the different solutions, all achieved some degree of emission within the white region. At the high concentration of 10 mM the colour-tunable window is heavily reduced (Figure 5.67). Overall emission largely remains blue, although at λ_{ex} = 275 nm CIE coordinates are x,y = 0.28, 0.25, within the white region but very much a blue-white.

*Figure 5.66.. Eu(**6**)$_3$ in MeOH solutions with 10,.5,.1,.0.01 mM concentrations left to right,.under shortwave UV irradiation (white and red).and under longwave UV irradiation (blue)..*

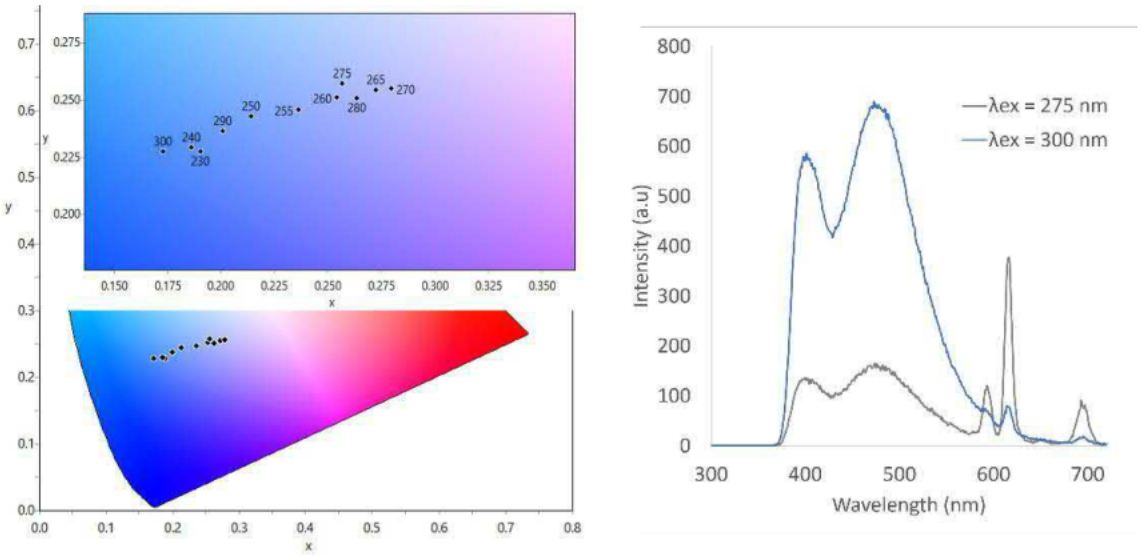

*Figure. 5.67.. CIE. 1931. chromaticity. diagram. with. different. overall. colours. capable. of. Eu(**6**)$_3$ in. a. 10. mM. MeOH. solution. dependent. on. λ_{ex} and. fluorescence. spectra. of. important. λ_{ex}.. Calculated. CIE. coordinates:. 230. nm. x,y. =. 0.19,. 0.23;. 240. nm. x,y. =. 0.19. ,0.23;. 250. nm. x,y. =. 0.21,. 0.24;. 255. nm. x,y. =. 0.24,. 0.25;. 260. nm. x,y. =. 0.25,. 0.25;. 265nm. x,y. =. 0.27,. 0.26;. 270. nm. x,y. =. 0.28. ,0.26;. 275. nm. x,y. =. 0.26,. 0.26 ;. 280. nm. x,y. =. 0.26,. 0.28;. 290. nm. x,y. =. 0.20,. 0.24. and. 300. nm. x,y. =. 0.17,. 0.23..*

At the lower concentration of 5 mM, red emission is still not achievable, but the colour-tunable window is slightly larger and "white" emission is achieved over multiple λ_{ex} (260 to 280 nm) where CIE coordinates are within x = 0.30 - 0.31 and y = 0.25 – 0.27 (Figure 5.68), with the closest to "pure-white" occurring at λ_{ex} = 271 nm (x,y = 0.31, 0.27). Fluorescence profiles showed excimer emission still heavily present, but Eu^{3+} emission becomes more prominent in the more dilute solution as expected.

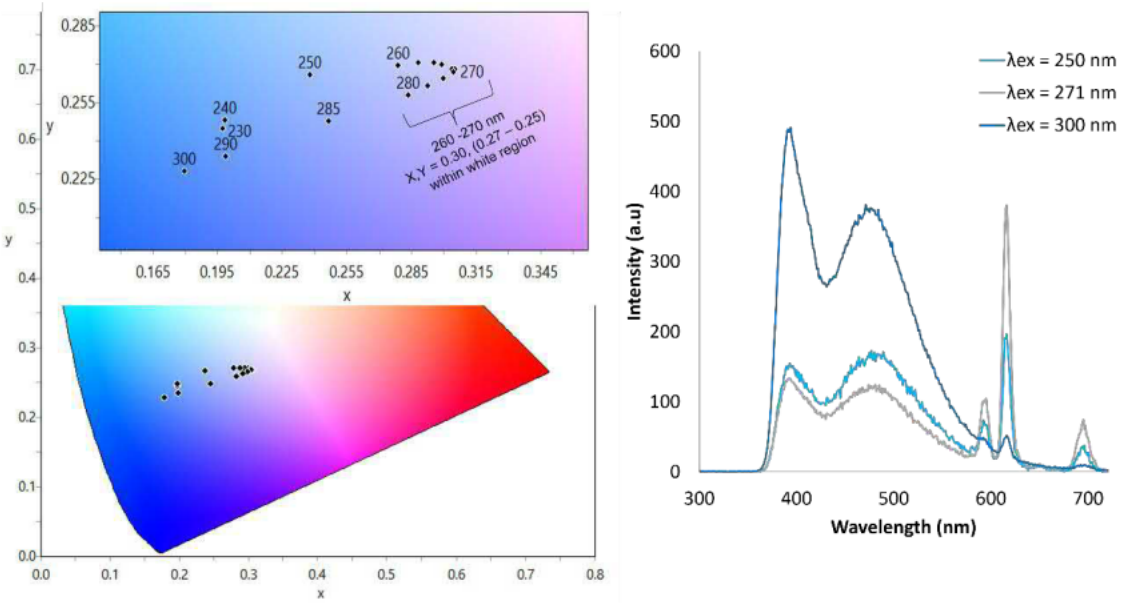

*Figure. 5.. 68.. CIE. 1931. chromaticity. diagram. with. different. overall. colours. capable. of. Eu(**6**)$_3$ in. a. 5. mM. MeOH. solution. dependent. on. λ_{ex} and. fluorescence. spectra. of. important. λ_{ex}.. Calculated. CIE. coordinates:. 230. nm. x,y. =. 0.20,. 0.25;. 240. nm. x,y. =. 0.20. ,0.25;. 250. nm. x,y =. 0.24,. 0.27;. 260. nm. x,y. =. 0.28,. 0.27;. 261. nm. x,y. =. 0.28,. 0.27;. 261. nm. x,y. =. 0.29,. 0.27;. 262-273. nm. x,y. =. 0.30,. 0.27;. 275. nm. x,y. =. 0.30, 0.26;. 277. nm. x,y. =. 0.29. ,0.26;. 280. nm. x,y. =. 0.28,. 0.26 ;. 285. nm. x,y. =. 0.25,. 0.25;. 290. nm. x,y. =. 0.20,. 0.23. and. 300. nm. x,y. =. 0.18,. 0.23..*

At concentrations of 1 mM, the colour-tunable emission significantly opens up (Figure 5.69), as previously observed with the 0.01 mM solution (Figure 5.64). Emission ranges from blue through the "white region" to light red/pink. Multiple λ_{ex} result in emission within the "white region", but the closest to "pure-white" observed in any solution measured occurs at λ_{ex} = 250 nm with CIE coordinates of x,y = 0.33 , 0.28. Fluorescence spectra showed this was a result of the Eu^{3+} emission becoming significantly stronger at certain λ_{ex} as previously seen in the 0.01 mM MeOH solution.

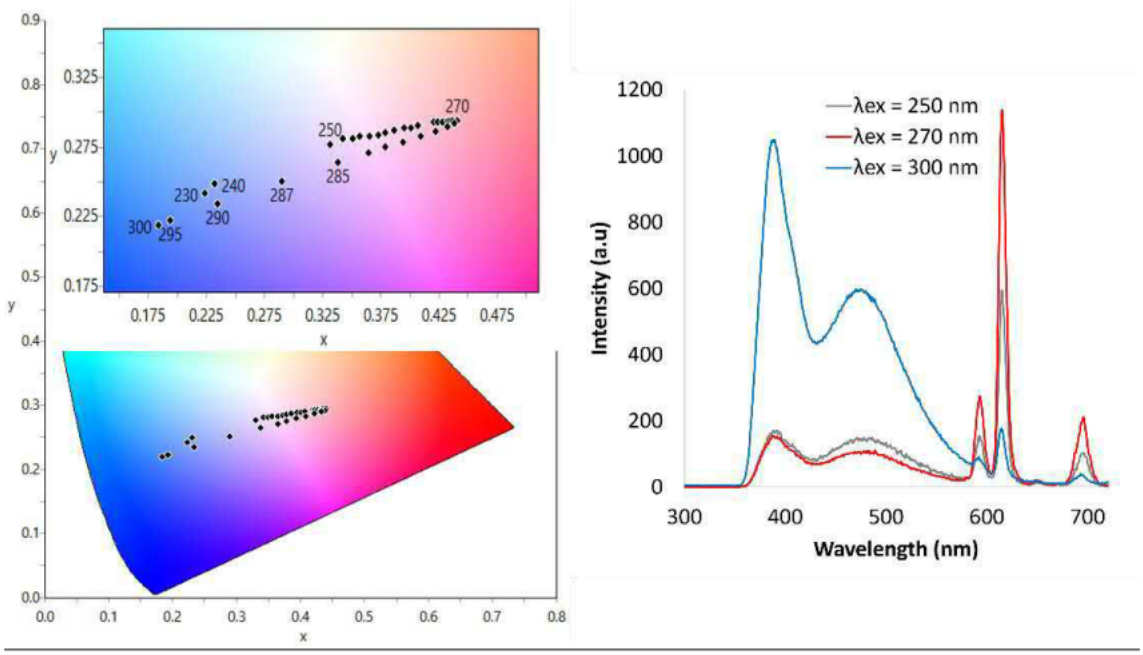

*Figure 5.69.. CIE 1931 chromaticity diagram with different overall colours capable of Eu(**6**)$_3$ in 1 mM MeOH solution dependent on λ_{ex} and fluorescence spectra of important λ_{ex}.. Calculated CIE coordinates:: 230 nm x,y = 0.22,.0.24;: 240 nm x,y = 0.23.,0.25;: 250 nm x,y = 0.33,.0.28;: 251 nm x,y = 0.34,.0.28;: 252 nm x,y = 0.35,.0.28;: 253 nm x,y = 0.36,.0.28;: 254 nm x,y = 0.37,.0.28;: 255 nm x,y = 0.37,.0.29;: 256 nm x,y = 0.38,.0.29;: 257 nm x,y = 0.39,.0.29;: 258-260 nm x,y = 0.40,.0.9;: 261-264 nm x,y = 0.42,.0.29;: 265-266 nm x,y = 0.43,.0.29;: 267-275 nm x,y = 0.44,.0.29;: 277 nm x,y = 0.42,.0.28;: 280 nm x,y = 0.41,.0.28;: 285 nm x,y = 0.34,.0.27;: 290 nm x,y = 0.24,.0.24 and 300 nm x,y =0.18,.0.22..*

Colour-tunable emission was also observed in the case of $[Eu(\mathbf{7})_3](CF_3SO_3)_3$, however the effect was much weaker, with the colour-tunable emission remaining in the blue region and only changing from dark blue (λ_{ex} = 365 nm) to a lighter blue (λ_{ex} = 254 nm) as seen in Figures 5.70-71. The much smaller colour-tunable region (in comparison to Eu(**6**)$_3$) is likely associated with the **NI** chromophore centred emission being significantly stronger than Eu^{3+} centred emission.

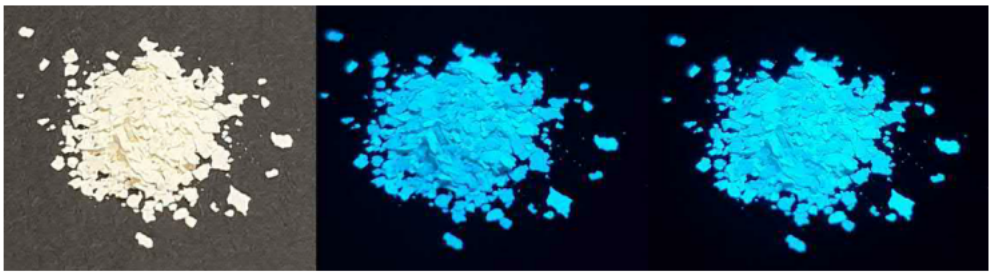

Figure 5.70.. Solid powder of $[Eu(\mathbf{7})_3](CF_3SO_3)_3$, under ambient light, longwave irradiation (λ_{ex} = 365 nm), and shortwave irradiation (λ_{ex} = 254 nm), from left to right

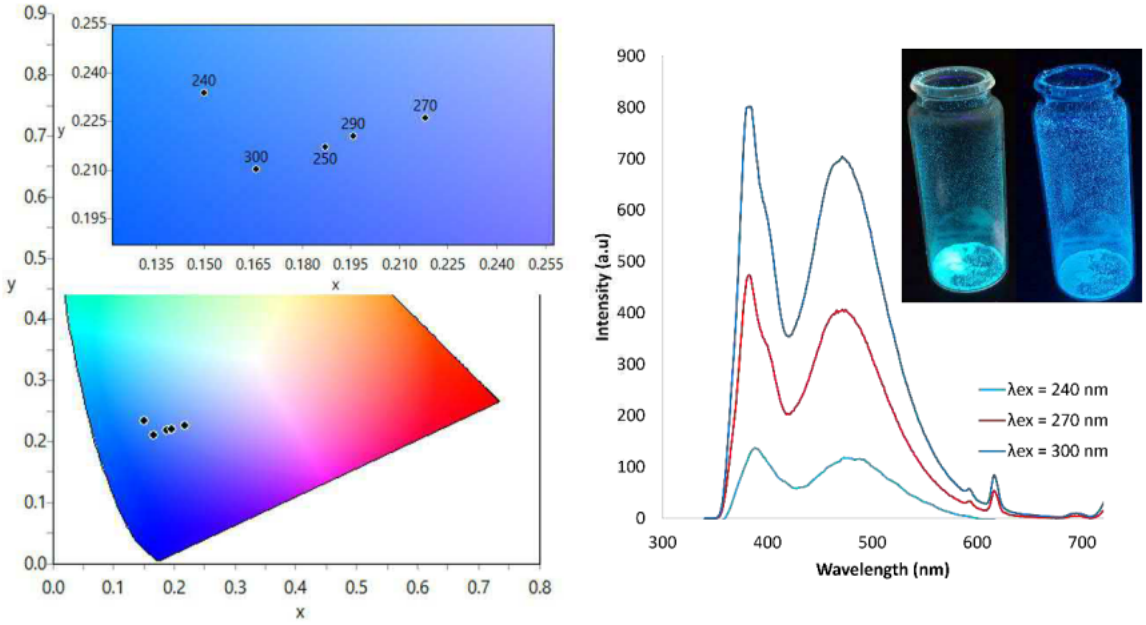

*Figure. 5.71.. CIE. 1931. chromaticity. diagram. with. different. overall. colours. capable. of. [Eu(**7**)$_3$](CF$_3$SO$_3$)$_3$. in. 0.01. mM. MeCN. solution dependent. on. λ_{ex} and. fluorescence. spectra. of. important. λ_{ex}.. Calculated. CIE. coordinates:. 240. nm. x,y. =. 0.15,. 0.24;. 250. nm. x,y. =. 0.19, 0.22;. 270. nm. x,y. =. 0.22,. 0.23;. 290. nm. x,y. =. 0.20,. 0.22. and. 300. nm. x,y. =. 0.17,. 0.21.. Insert:. solid. powder. of. [Eu(**7**)$_3$](CF$_3$SO$_3$)$_3$,. under shortwave. irradiation. (λ_{ex} =. 254. nm),. and. longwave. irradiation. (λ_{ex} =. 365. nm),. from. left. to. right..*

In comparison, solid Eu(**8**)$_3$ exhibits similar colour-tunable properties to solid Eu(**6**)$_3$ changing from blue to a bluish-white with similar λ_{ex} (Figure 5.72), although the "white" emissive solid was not as intense as Eu(**6**)$_3$. This is associated with the much weaker quantum yields of both **PYR** and Eu^{3+} centred emission of Eu(**8**)$_3$ (see Table 5.14-15).

*Figure. 5.72.. Solid. powder. of. Eu(**8**)$_3$ under. ambient. light,. longwave. irradiation. (λ_{ex} =. 365. nm),. and. shortwave. irradiation. (λ_{ex} =. 254. nm), from. left. to. right..*

The fluorescence spectra of Eu(**8**)$_3$ in 0.01 mM MeOH solution exhibits similar colour-tunable properties. The overall emission is blue at λ_{ex} = 300 - 360 nm and $\lambda_{ex} \geq$ 250 nm (**PRY** emission dominated), while between $\lambda_{ex} \approx$ 260 - 285 nm, strong Eu^{3+} emission is present, resulting in light red emission, with a maximum intensity at λ_{ex} = 285 nm (CIE x,y = 0.41, 0.26). Emission within the white region occurs with λ_{ex} = 270 nm (CIE x,y = 0.31, 0.24) as seen in Figure 5.73. Similar to Eu(**6**)$_3$ the white emission is significantly improved by inducing intermolecular interactions between Eu(**8**)$_3$, thus increasing the overall excimer emission by increasing the concentration. As seen in Figure 5.74, when increasing the concentration to 5 mM, excimer emission dominates. As a result, overall emission stays within the centre of the white emission region when both **PYR** and Eu^{3+} emission are present ($\lambda_{ex} \approx$ 240 – 290 nm) and achieves a very close to

"pure-white" emission with λ_{ex} = 270 nm and 280 nm resulting in CIE coordinates of x,y = 0.32, 0.33 and x,y = 0.33, 0.32 respectively. However, unlike Eu(**6**)$_3$ where the white emission is bright, Eu(**8**)$_3$ white emission is very dim. Additionally, whilst the lack of monomer emission significantly improves white emission in solution, it does reduce the colour-tunable window, with only light blue emission capable at λ_{ex} above 290 nm and below 240 nm.

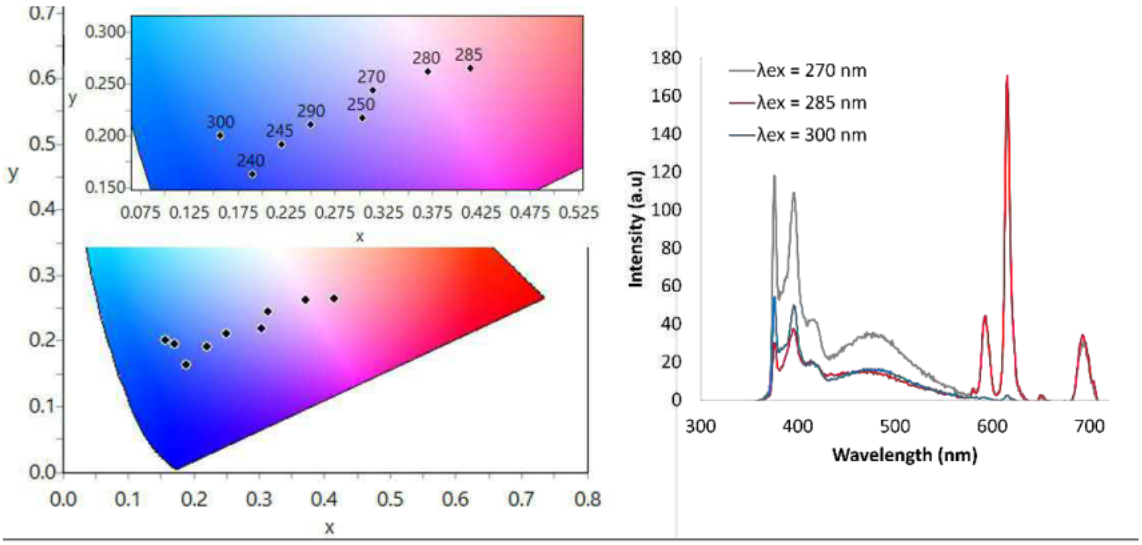

*Figure. 5.73.. CIE. 1931. chromaticity. diagram. with. different. overall. colours. capable. of. Eu(**8**)$_3$ in. 0.01. mM. MeOH. solution. dependent. on λ_{ex} and. fluorescence. spectra. of. important. λ_{ex}.. Calculated. CIE. coordinates:. 240. nm. x,y. =. 0.19,. 0.16;. 245. nm. x,y. =. 0.22,. 0.19;. 250nm. x,y =. 0.30,. 0.22;. 270. nm. x,y. =. 0.31,. 0.24;. 280. nm. x,y. =. 0.37,. 0.26;. 285. nm. x,y. =. 0.41,. 0.27;. 290. nm. x,y. =. 0.25,. 0.29. and. 300. nm. x,y. =. 0.16, 0.20..*

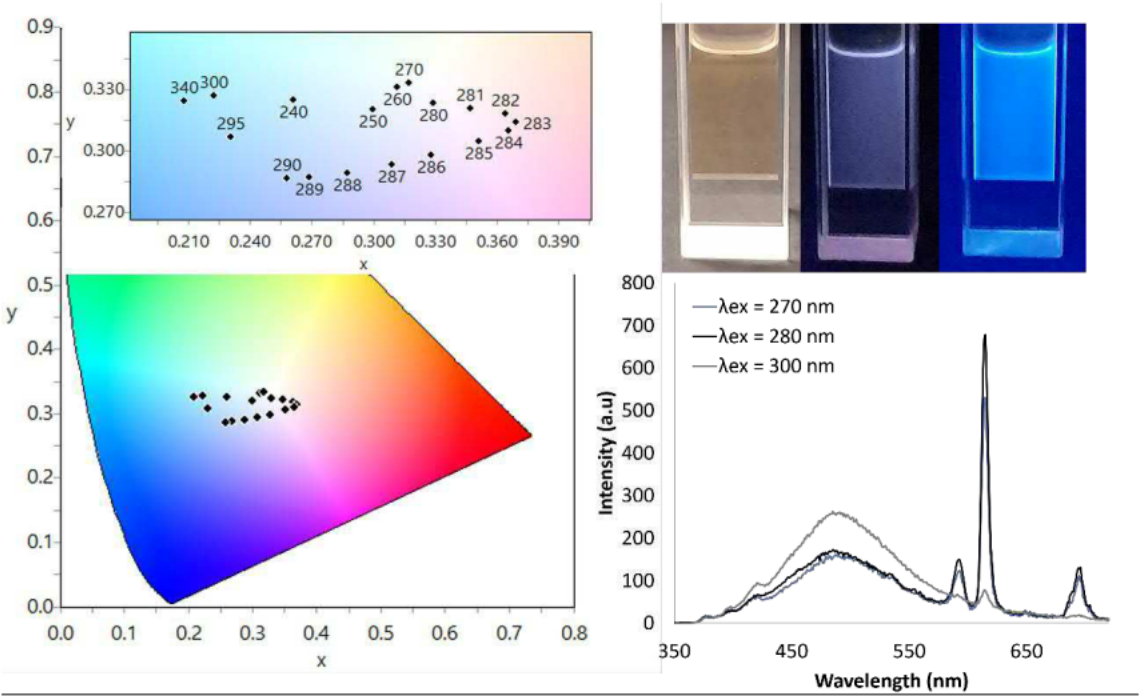

*Figure. 5.74.. CIE. 1931. chromaticity. diagram. with. different. overall. colours. capable. of. Eu(**8**)$_3$ in. 5. mM. MeOH. solution. dependent. on. λ_{ex} and. fluorescence. spectra. of. important λ_{ex}.. Calculated. CIE. coordinates:. 240. nm. x,y. =. 0.26,. 0.33;. 250. nm. x,y. =. 0.30,. 0.32;. 270. nm. x,y. =. 0.32,. 0.33;. 280. nm. x,y. =. 0.33,. 0.32;. 281. nm. x,y. =. 0.35,. 0.32;. 282. nm. x,y. =. 0.36,. 0.32;. 283. nm. x,y. =. 0.37,. 0.31;. 284. nm. x,y. =. 0.36,. 0.31; 285. nm. x,y. =. 0.32,. 0.30;. 286. nm. x,y. =. 0.33,. 0.30;. 287. nm. x,y. =. 0.31,. 0.29;. 288. nm. x,y. =. 0.29,. 0.29;. 282. nm. x,y. =. 0.27,. 0.28;. 290. nm. x,y =. 0.26,. 0.29;. 295. nm. x,y. =. 0.23,. 0.30;. 300. nm. x,y. =. 0.22,. 0.33;. and. 340. nm. x,y. =. 0.21,. 0.32.. Insert:. Eu(**8**)$_3$ solution. in. 5. mM. MeOH,. under ambient. light,. shortwave. UV. and. longwave. UV,. left. to. right..*

5.2.6.3 Terbium and Dysprosium Complexes

In terms of the other visibly emissive Ln^{3+} (Tb^{3+} and Dy^{3+}) emission was relatively disappointing, both in terms of intensity and the emission overlap with excimer emission. Tb(**6**)$_3$ fluorescence spectrum showed weak signs of Tb^{3+} centred emission (Figure 5.75) while [Tb(**7**)$_3$](CF$_3$SO$_3$)$_3$ showed no sign of Tb^{3+} centred emission (see Figure 8.3.80). In both cases, this was associated with the excimer emission practically overlapping the Tb^{3+} emission and concealing it. The presence of excimer emission in Tb(**6**)$_3$ however also indicated the formation of the complex as previously explained, with similar results observed in Dy(**6**)$_3$, La(**6**)$_3$, and La(**8**)$_3$ (see Section 8.3.5 for details). Additionally, for both Tb^{3+} complexes, instead of an increase in Φ_f a slight decrease was observed, which indicated a likely nr decay pathway was favoured in these systems, which could also be associated with the poor fluorescent emission of the terbium system.

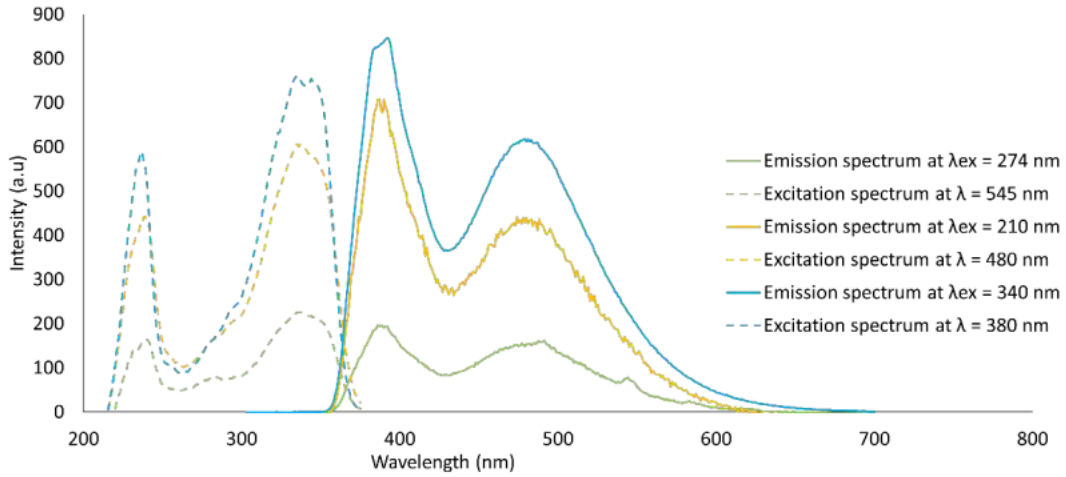

*Figure 5.75.. Fluorescence spectrum of Tb(**6**)$_3$. (0.01 mM, MeOH)..*

In contrast, in phosphorescence spectra Tb^{3+} centred emission is clearly present for both complexes (Figures 5.76 and 8.3.81), and effective population of the $^5D_4$ state was observed, with the subsequent deactivation to the ^7F_J (J = 3 – 6) states forming sharp emission bands centred at 490 nm ($^5D_4 \rightarrow {}^7F_6$), 545 nm ($^5D_4 \rightarrow {}^7F_5$), 587 nm ($^5D_4 \rightarrow {}^7F_4$), and 621 nm ($^5D_4 \rightarrow {}^7F_3$) for both systems. Lifetimes of the Tb^{3+} major transition $^5D_4 \rightarrow {}^7F_5$ were also measured and fit to a single exponential decay, indicative of a single species present, with average lifetimes of 0.363 and 0.794 ms for Tb(**6**)$_3$ and [Tb(**7**)$_3$](CF$_3$SO$_3$)$_3$ respectively (see Section 8.3.5). Excitation spectra of Tb^{3+} centred emission differed to the europium systems' excitation plots, with the Tb^{3+} excited state populated only from the pyridyl ring and energy transfer occurring from **NI**, unlike both europium systems. This was likely due to **NI** having better aligned T_1 for the europium $^5D_0$ state than terbium $^5D_4$ state.

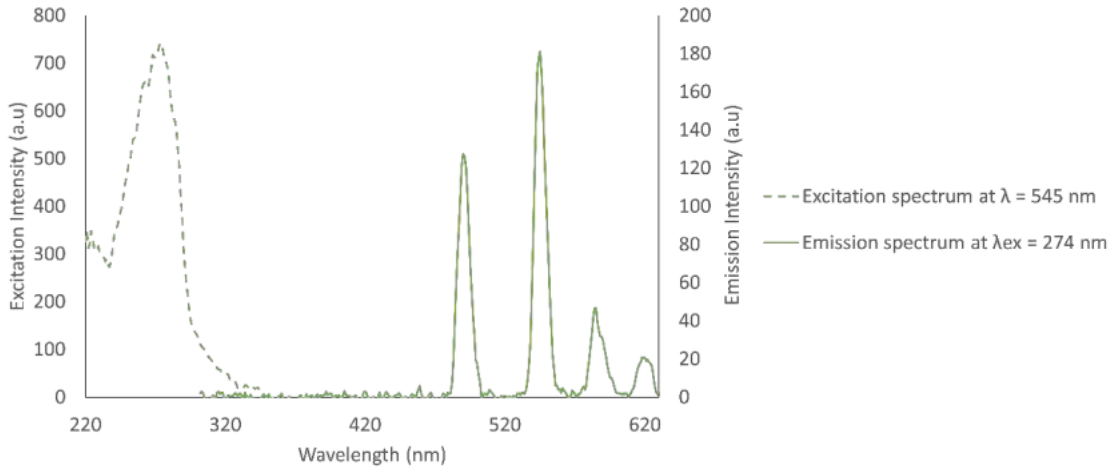

*Figure 5.76. Phosphorescence spectrum of Tb(**6**)$_3$ (0.01 mM, MeOH).*

In Dy(**6**)$_3$ the Ln^{3+} centred emission was slightly stronger than Tb(**6**)$_3$ (Figure 5.77), with Dy^{3+} emission peaks more easily assigned with both the blue 480 nm ($^4F_{9/2} \rightarrow {}^6H_{15/2}$) and yellow 575 nm ($^4F_{9/2} \rightarrow {}^6H_{15/2}$) bands distinctly present. However again Ln^{3+} centred emission was blended on top of the excimer emission. This caused [Dy(**7**)$_3$](CF$_3$SO$_3$)$_3$ to have no sign of Dy^{3+} emission (Figure 8.3.83). In the case of Dy(**6**)$_3$ emission was again only observed when excited at wavelengths associated with the pyridyl unit (λ_{ex} = 260 – 290 nm) and not the **NI**. Phosphorescence spectra showed no Dy^{3+} centred emission, as noted in chapter 4, likely due to the shorter lifetimes.

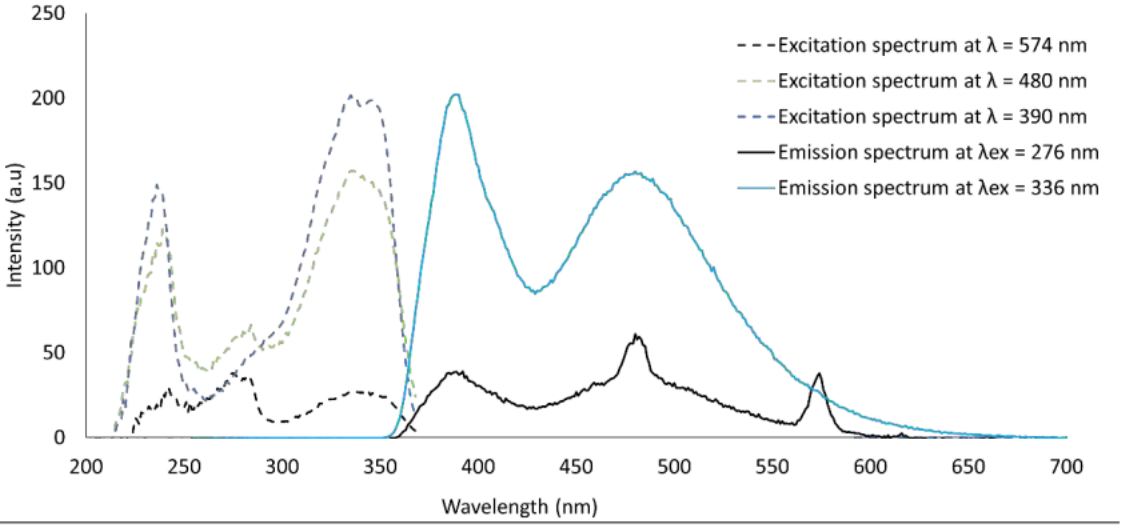

*Figure 5.77. Fluorescence spectrum of Dy(**6**)$_3$. (0.01 mM, MeOH).*

5.2.4.5 Lanthanide Photophysical Properties Closing Remarks

From these photophysical and characterisation studies, it became apparent which system was best suited for spin coating film formation. It was clear that ligands **6** and **8** were much better candidates than **7** as they clearly formed more stable complexes. In terms of lanthanides, it was clear that europium was the best match for these systems, with the best overall Ln^{3+} centred emission that was distinctly separated from the organic chromophore emission, which resulted in emission that was colour-tunable and white emissive in both solid and solution states. Overall, complex Eu(**6**)$_3$ was the clear winner, with its impressive colour-tunable range, and best overall **bright** white emission due to the much stronger quantum yields. Because of these factors, Eu(**6**)$_3$ was selected to continue to spin coating film formation.

5.2.7 Spin Coating and Film Formation

Unlike LB deposition utilized in chapter 4, spin coating requires more trial and error until the right film formation conditions are found for each system. Similar characterisation of film deposition which takes place *during* LB film formation does not occur with spin coating and films should ideally be characterised in terms of thickness, as well as roughness post film formation.

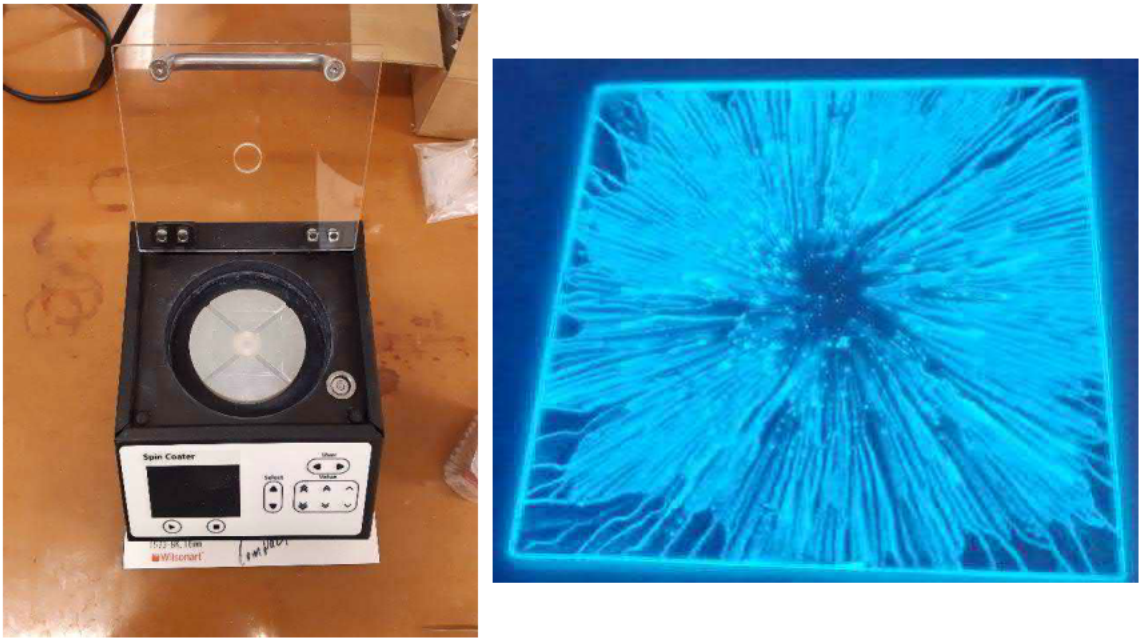

*Figure 5.78. (Left) Ossila spin coater, with white chuck in the centre of the spin coater. (Right) Initial spin coated film of Eu(**6**)$_3$ from DCM:MeOH (1:1) solution, max spin rate of 4000 rpm.*

The initial methodology utilized was based on the recommendations of the Ossila company which supplied the spin coater (Figure 5.78). Using a 10 mg/ml solution in a DCM:MeOH (1:1) (solvents selected for solubility), 100 µL of Eu(**6**)$_3$ was dynamically dispensed onto a 50 X 50 mm slide, with an initial 20 second 500 rpm (dynamic spin rate) and then spun up/off to 4000 rpm for 60 seconds. This methodology resulted in interesting looking coatings appearing with an almost flower like pattern (Figure 5.78). However, in terms of uniform coating the method was very poor. The quartz slides were unevenly coated with striation of Eu(**6**)$_3$. This defect is known to be caused by Marangoni instabilities, caused by the extreme volatility of the solvent combination.[80] Additionally the use of such large substrates was detrimental, as they required a significant amount of material to form a uniform film, and were only used as they fitted into the recesses of the sample chuck (Figure 5.78).

With the initial trial being discouraging, spin coating attempts moved away from the large substrates to smaller 15 x 20 mm glass substrates. The solvent was also changed to DMF (again chosen for solubility reasons), to overcome the Marangoni instabilities. With this method a 10 mg/ml solution was now syringe filtered twice to remove any undissolved material and spin coated using the same conditions, reducing the deposition volume to 50 µL. The results from this method were more encouraging, as seen in Figure 5.79, with films appearing uniform across the substrate. Although not always consistent, this gave much more reliable results, however due to the substrate composition (glass) UV-visible and luminescent measurements could not be obtained.

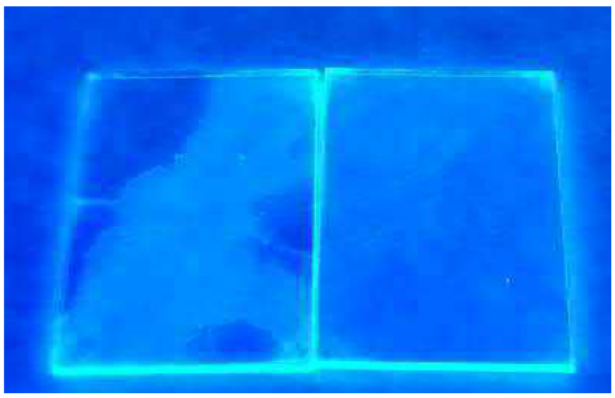

*Figure 5.79. Spin coated films of Eu(**6**)$_3$ (under longwave irradiation), fabricated from DMF solution. The spin coated film is made from Eu(**6**)$_3$ in a 10 mg/mL DMF solution, spun at 4000 rpm. Shown under shortwave UV irradiation (λ_{ex} = 254 nm).*

Because of the substrate issues, the decision was made to attach films using double sided tape, although this occasionally led to substrates breaking by being thrown off the chuck. Utilizing the previous method, uniform films of the Eu(**6**)$_3$ complex were formed, as seen in Figure 5.80, on 10 x 10 mm slides of UV grade quartz (broken from 50 x 50 mm slides) and silicon wafers (for AFM). The coating retained the impressive colour-tunable emission properties of Eu(**6**)$_3$, switching from white under shortwave to blue under longwave as previously observed. Fluorescence spectra of the coatings were very similar to that of the solid, with strong excimer emission. The colour-tunable window was similar, with both long- and short-wave irradiation resulting in blue emission, while white emission is achieved at λ_{ex} = 280 nm x,y = 0.34, 0.28 (Figure 5.81). Additionally, the absorption spectrum further indicated Eu(**6**)$_3$ within the coating, as it contained similar absorption bands as observed in solution measurements (Figure 5.81).

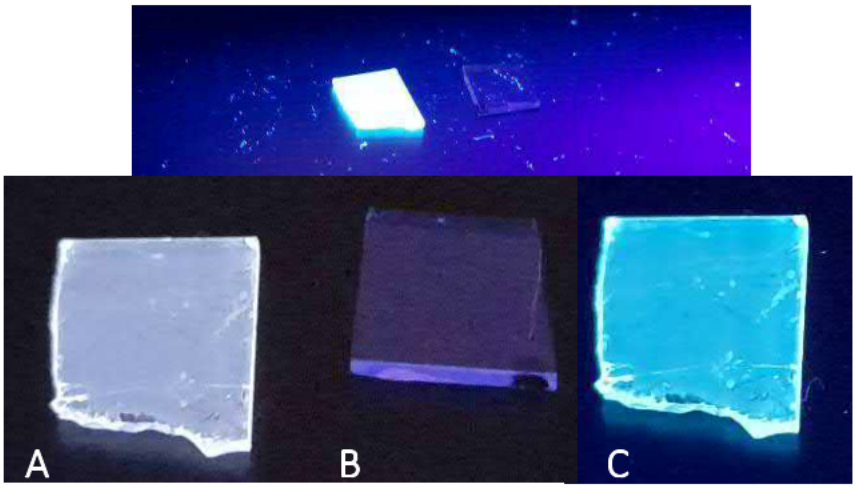

*Figure. 5.80.. (Top). Shows. the. brightness. of. the. spin. coated. film. under. shortwave. irradiation.. The. spin. coated. film. is. made. from. Eu(**6**)$_3$ in. a. 10. mg/mL. DMF. solution,. spun. at. 4000. rpm.. (Bottom). Spin. coated. film. deposited. on. a. quartz. slide. and. shown. under. short-. (A,. λ_{ex} =. 254. nm). and. long-. (C,. λ_{ex} =. 365. nm). wave. UV. irradiation. (≈10. x. 10. mm). (B). is. a. blank. under. shortwave. UV. light..*

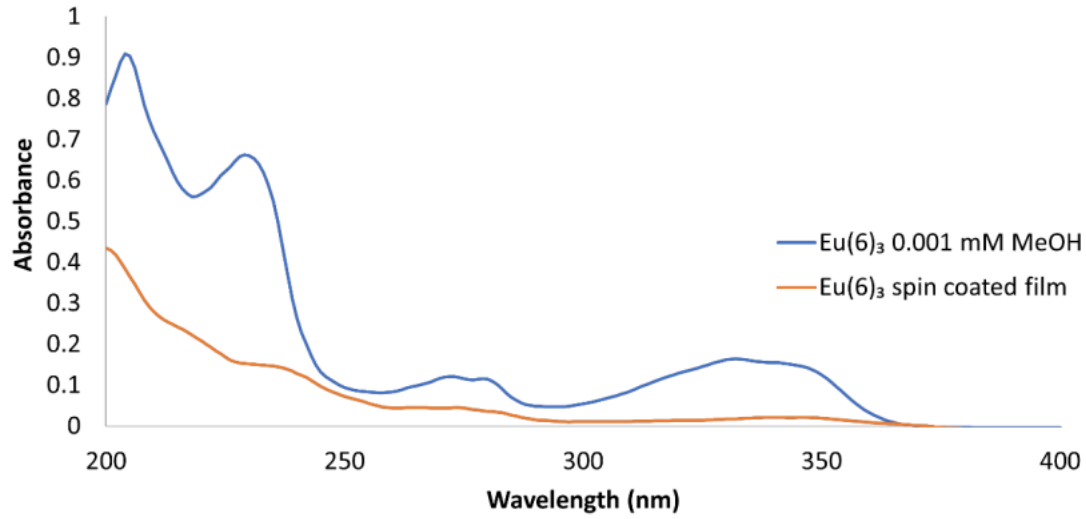

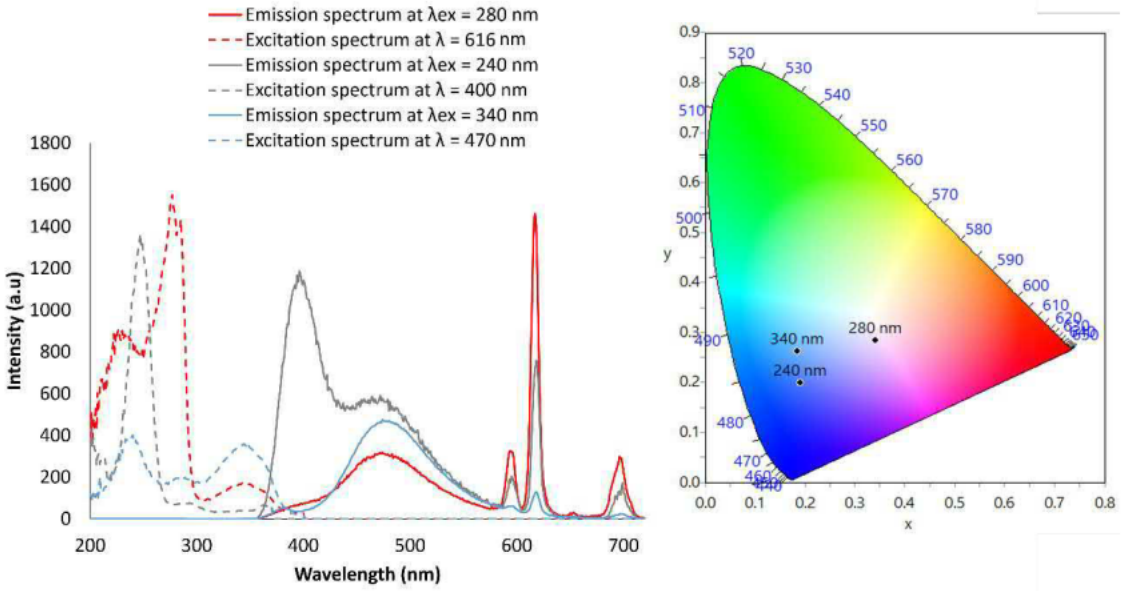

*Figure. 5.81.. (Top). UV-visible. absorption. spectrum. of. spin. coated. Eu(**6**)$_3$ film. and. 0.01. mM. MeOH. solution.. (Bottom. left). Fluorescence. spectrum. of. Eu(**6**)$_3$,. spin. coated. slide.. (Bottom. right). CIE. 1931. chromaticity. diagram. with. calculated. CIE. coordinates,. 340. nm. x,y. =. 0.19, 0.20;. 240. nm. x,y. =. 0.19. ,0.26. and. 280. nm. x,y. =. 0.34,. 0.28..*

With this methodology showing promising results, a range of different films were fabricated onto 10 x 10 mm silicon wafers, using a 10 mg/mL DMF solution and four different maximum speeds: 2000, 3000, 4000 and 5000 rpm. This was to determine how thick the coatings were but also to develop an understanding of how thickness may affect photophysical properties. Unexpectedly, only one film was able to be run, this being the thickest film spun at 2000 rpm. This was because all other spin speeds resulted in films too thin to be accurately measured by AFM. As seen in Figure 5.82 this film was relatively uniform bar the "comet" marks from dust particles on the surface. To determine thickness a cross section was scratched into the film before the AFM tip was run across the film (Figure 5.84). By comparing the height difference between the film and the scratch, the average film thickness was determined to be 10.6 nm. The film was also very rough on a nm scale (Figure 5.84) with the coating containing a large variation in peak height, with roughness calculated to be Ra ≈ 8 ± 2 nm over the whole film (large square in Figure 5.83), while in the area without large particles present (small square in Figure 5.83) Ra ≈ 5 ± 2 nm.

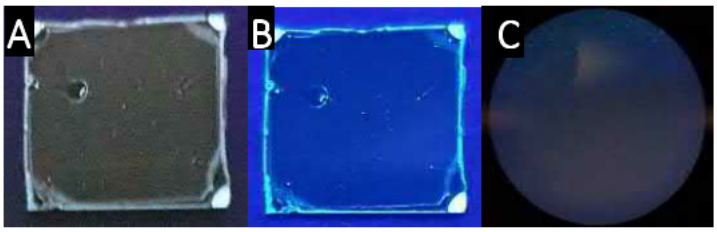

Figure 5.82.. Microscope images of the 10 mg/mL (2000 rpm) spin coated slides on silica wafers under short- (A, λ_{ex} = 254 nm) and long-wave (B, λ_{ex} = 365 nm) UV irradiation (≈10 x 10 mm). (C) is a 4x magnification into the centre of the film showing film smoothness to the eye in areas not affected by dust particles..

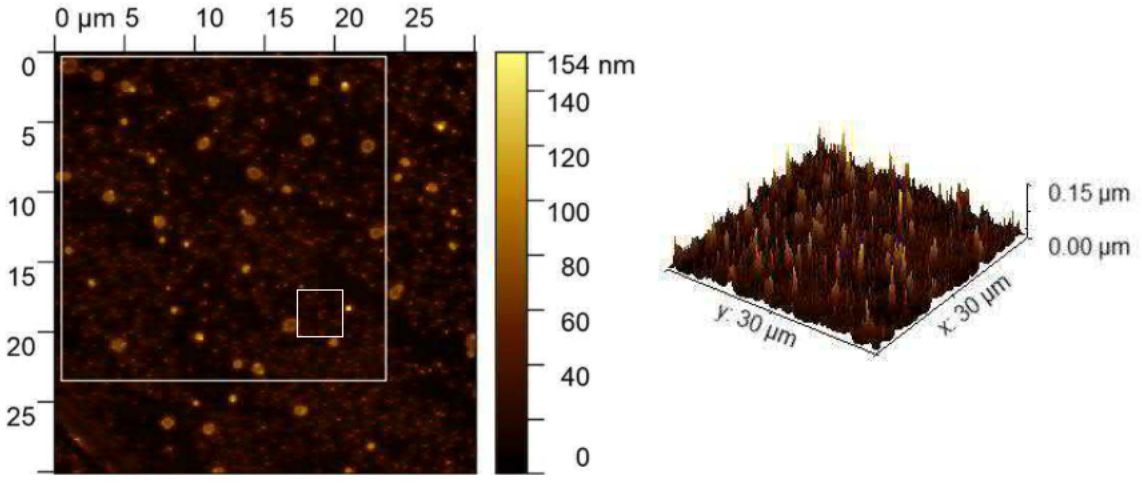

*Figure 5.83.. AFM measurement of spin coated film of Eu(**6**)$_3$ fabricated from 10 mg/mL DMF solution (2000 rpm) used to determine surface roughness.. (Left) Shows the area (white squares) from which the roughness was measured from, Ra ≈ 8.. ± 2 nm over the whole film (large square), 5. ± 2 nm in areas without large spots (small square).. (Right) Shows 3D representation of the films surface showing that the film is not uniform over a wide region..*

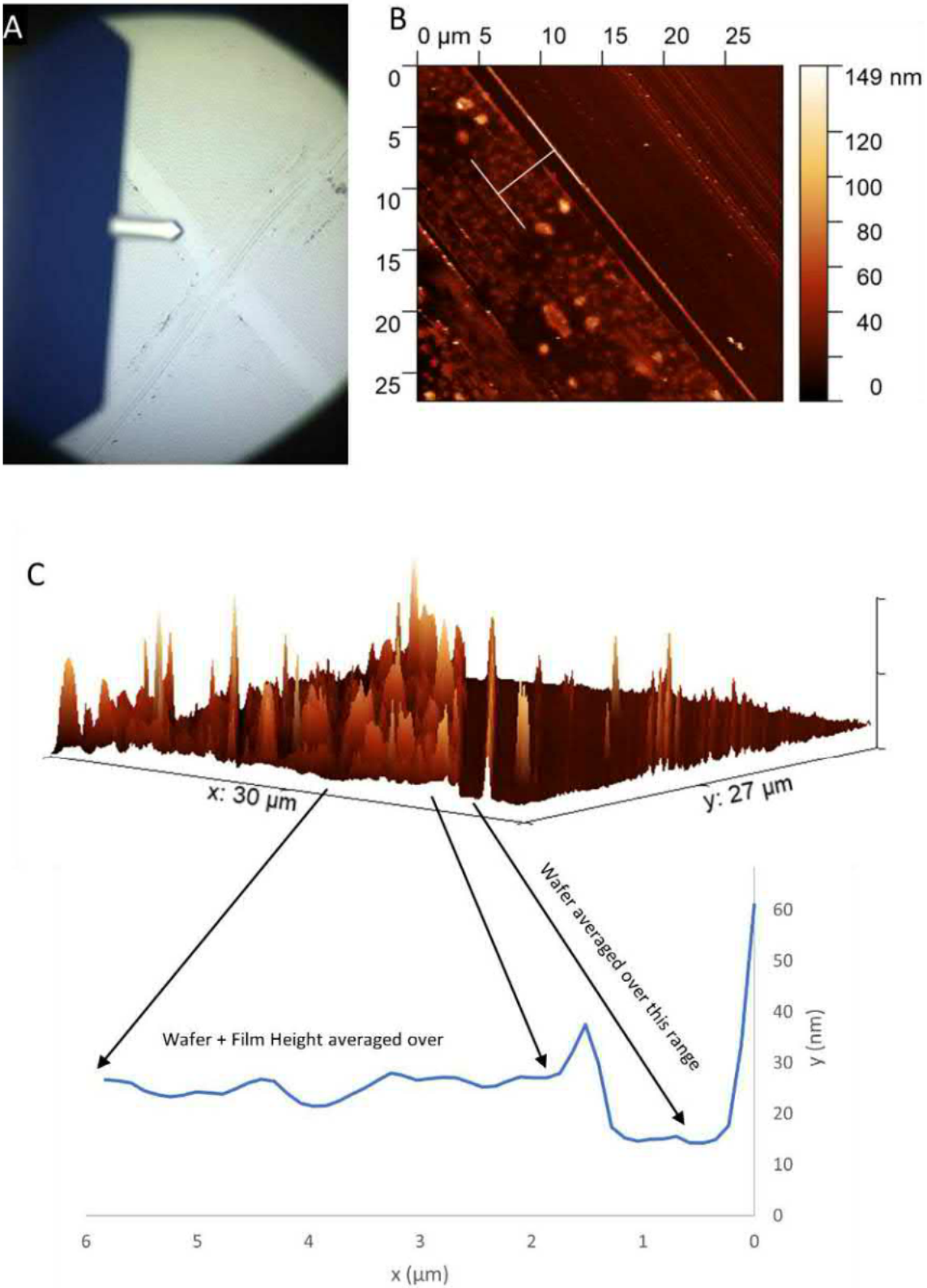

Figure. 5.84.. (A).. Microscope. image. of. scraped. film,. showing. a. clear. step. visible. to. the. eye. (even. without. a. microscope).. (B). AFM. map. of. scratch,. showing. clear. surface. difference. of. scratched. step. and. the. region. which. height. has. been. measured. in. C.. (C). 3D. AFM. image showing. height. difference. of. step. and. film,. below. being. the. average. height. over. the. region. in. B,. with. the. wafer. height. being. measured to. 14.81. nm,. wafer. +. film. =. 25.40. nm,. therefore. average. film. height. =. 10.60. nm..

Such thin films are indicative that the solution was not coating the surface very well. If the coating were to be used in an OLED device - a potential future application – thicker films would be required. To improve coating thickness, the solvent and injection volume was further investigated, as the main issue was suspected to be the non-volatile DMF being spun off before evaporation could occur. It is worth noting that again solvent selection was limited to what would fully dissolve the complex and would remain soluble at high concentrations.

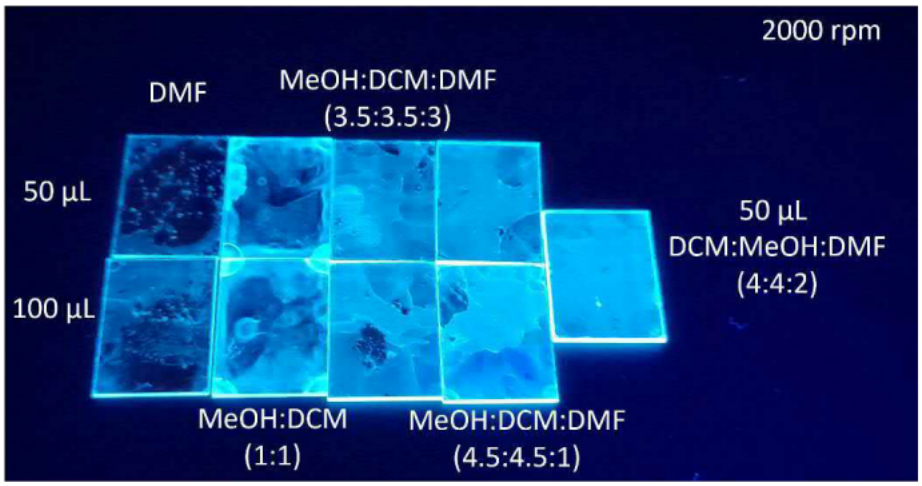

*Figure 5.85.. Different spin coated films of Eu(**6**)$_3$ on 15 x 20 mm glass slides.. Bottom row is 100 µL and top row is 50 µL deposition volumes.. From left to right solvents used to dissolve Eu(**6**)$_3$ into a 10 mg/ml solution are DMF,. MeOH:DCM (1:1), . MeOH:DCM:DMF (3.5:3.5:3), MeOH:DCM:DMF (4.5:4.5:1) and MeOH:DCM:DMF (4:4:2), all spun up to 2000 rpm..*

A range of Eu(**6**)$_3$ spin coated films were fabricated, now on 15 mm x 20 mm glass substrates, using the same methodology previously developed with 10 mg/ml solution of Eu(**6**)$_3$ injected onto the substrates with a now initial 10 second dynamic injection period (500 rpm) being spun up to 2000 rpm for 60 seconds. Deposition volume, either 50 or 100 µL, and different combinations of volatile and non-volatile solvents for which Eu(**6**)$_3$ is soluble were investigated for their affect on film uniformity (Figure 5.85). Using only DMF resulted in blotchy films, with coated and uncoated regions as the solution was clearly not evaporating in time and just being spun off. MeOH:DCM (1:1) solution resulted in films which were clearly thicker than the DMF solution, but non-uniform, suspected to be caused by films evaporating quickly before spin up stage is reached. Testing different combinations of the volatile MeOH:DCM mixture and non-volatile DMF solvent was seen to improve film coating, with the optimal coating mixture found to be MeOH:DCM:DMF (4:4:2) as seen in Figure 5.86. It was found that a 50 µL deposition volume resulted in more uniform films than 100 µL, as it led to a reduction in solvent beads seen in the corner of the slides, caused by excess solvent.

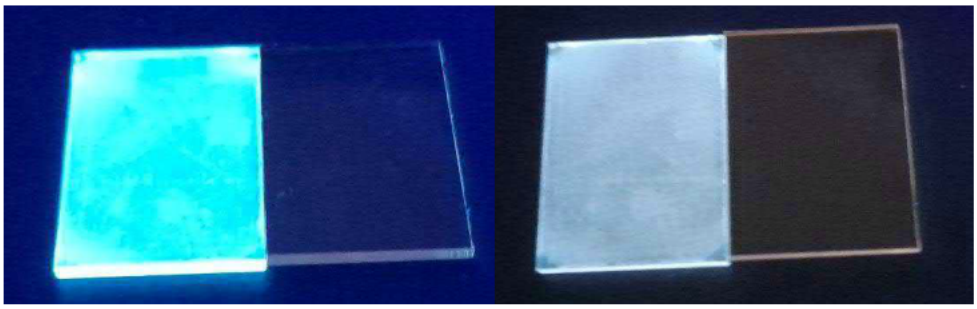

*Figure 5.86. Eu(**6**)$_3$ spin coated film (10 mg/ml, 5000 rpm) on 15 x 20 mm glass substrates. Left under longwave (λ_{ex} = 365 nm) and right under shortwave (λ_{ex} = 254 nm) irradiation.*

Using this solvent combination extremely uniform films (to the eye) were capable of being produced when the maximum spin rate was either 5000 rpm or 4000 rpm. Again, a range of different films were spin coated at 10 mg/mL with four different maximum speeds (2000, 3000, 4000 and 5000 rpm) on 30 x 30 quartz slides (see Section 5.4.3 for complete method). As seen in Figure 5.87, this gave four relatively uniform films (except for the beads that formed in the corner of the 2000 rpm film, caused by the slow spin rate), which under shortwave irradiation all appeared definitively white emissive while under longwave UV were light blue emissive.

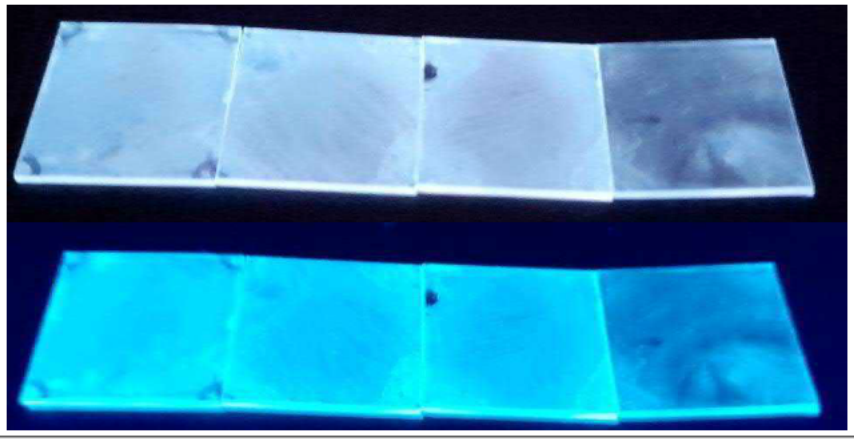

*Figure 5.87. Eu(**6**)$_3$ spin coated films at different spin rates, from left to right 2000, 3000, 4000 and 5000 rpm. Top image is under shortwave UV irradiation (λ_{ex} = 254 nm), bottom image is under longwave (λ_{ex} = 365 nm).*

Fluorescence measurements confirmed that indeed all four films retained Eu(**6**)$_3$ colour-tunable emission, with emission within the blue region when λ_{ex} is above approximately above 290 nm and below 260 nm. When λ_{ex} = 260 to 286 nm, emission is within the "white region" (see Figures 5.88-89, along with Table 5.16).

*Table 5.16. λ_{ex} which result in the closest to "pure-white" emission from the different spin coated films of Eu(**6**)$_3$*

Spin speed (rpm)	λ_{ex} (nm)	CIE coordinates
5000	277	x,y = 0.33, 0.28
4000	271	x,y = 0.33, 0.28
3000	270	x,y = 0.33, 0.28
2000	273	x,y = 0.33, 0.28

It can be seen that the different spin rates only have a slight effect on the photophysical properties of the films, as most films have a similar colour-tunable window and achieve relatively similar close to white emission. However as the film spin speed drops, and theoretically the film gets thicker (unfortunately due to COVID AFM of these films has not been measured to date) the difference between emission at λ_{ex} = 240 and 300 nm reduces. The v shaped "cone of emission" seen in the CIE diagram (Figures 5.88-89) gets smaller from 5000 to 2000 rpm, similar to that observed in the Eu(**6**)$_3$ concentration studies.

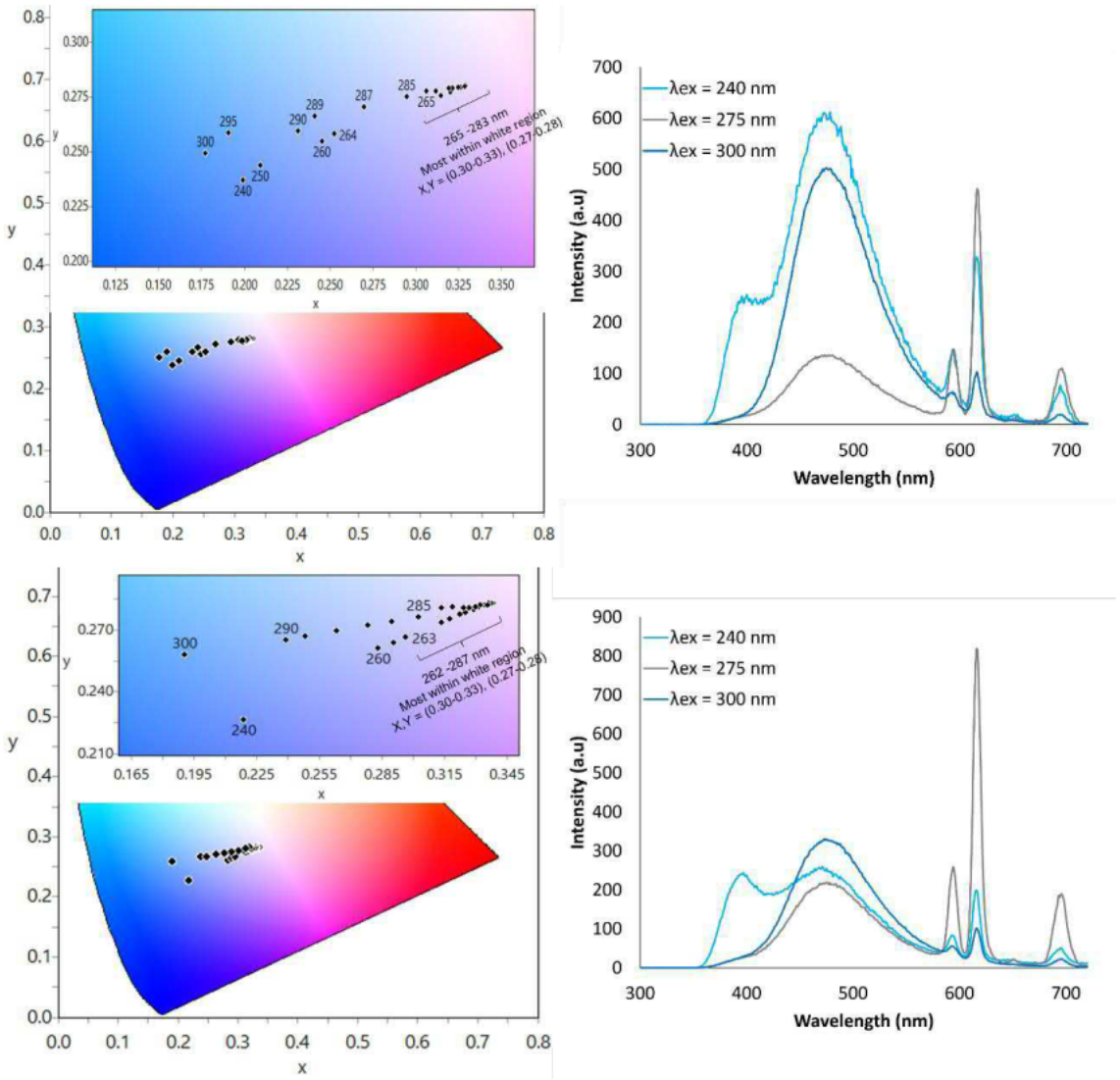

*Figure 5.88.. CIE 1931 chromaticity diagram with different overall colours capable of Eu(**6**)$_3$ in 2000 (Top) and 3000 (Bottom) rpm spin coated films dependent on λ_{ex} and fluorescence spectra of important λ_{ex}.. Calculated CIE coordinates for 2000 rpm:. 240 nm x,y = 0.21, 0.24;. 250 nm x,y = 0.20,. 0.24;. 260 nm x,y = 0.25,. 0.25;. 261 nm x,y = 0.29,. 0.27;. 264 nm x,y = 0.25,. 0.26;. 265-267 nm x,y = 0.31,. 0.28; 267-270 nm x,y = 0.32,. 0.28;. 271-277 nm x,y = 0.33,. 0.28;. 279-281 nm x,y = 0.32,. 0.28;. 283 nm x,y = 0.31,. 0.28;. 285 nm x,y = 0.29, 0.28;. 287 nm x,y = 0.27,. 0.27;. 289 nm x,y = 0.24,. 0.27;. 290 nm x,y = 0.23,. 0.26;. 295 nm x,y = 0.19,. 0.26 and 300 nm x,y = 0.18,. 0.25. Calculated CIE coordinates for 3000 rpm:. 240 nm x,y = 0.22,. 0.23;. 260 nm x,y = 0.28,. 0.26;. 261 nm x,y = 0.29,. 0.26;. 263 nm x,y = 0.30, 0.27;. 265 nm x,y = 0.31,. 0.27;. 266-267 nm x,y = 0.32,. 0.28;. 268-274 nm x,y = 0.33,. 0.28;. 272-278 nm x,y = 0.33,. 0.28;. 279-282 nm x,y = 0.33,. 0.28;. 283 nm x,y = 0.32,. 0.28;. 284nm x,y = 0.32,. 0.28;. 285 nm x,y = 0.30,. 0.28;. 286 nm x,y = 0.29,. 0.27;. 287 nm x,y = 0.28,. 0.27; 288 nm x,y = 0.26,. 0.27;. 289 nm x,y = 0.25,. 0.27;. 290 nm x,y = 0.19,. 0.27 and 300 nm x,y = 0.19,. 0.26..*

The cause of this was observed in the fluorescence spectra. While emission profiles remain relatively the same for λ_{ex} = 275 or 300 nm, at λ_{ex} = 240 nm monomer emission reduced as the spin speed reduced, while excimer emission increased. As previously stated, this occurs when there are increased π – π interactions between **NI**, suggesting that as the spin rate reduced the films became thicker, resulting in increased π – π interactions affecting the emission profile of the films, in line with the concentration study. Although the emission profiles of the spin coated films change slightly depending on film thickness, this study demonstrated that the colour-tunable properties of Eu(**6**)$_3$ can be transferred to the films. Furthermore, they are achieving a very close to "pure-white" emission as a solid film coating (CIE x,y = 0.33, 0.28), close to Yan and co-workers "pure-white" (CIE x,y = 0.34, 0.31) solid powder.

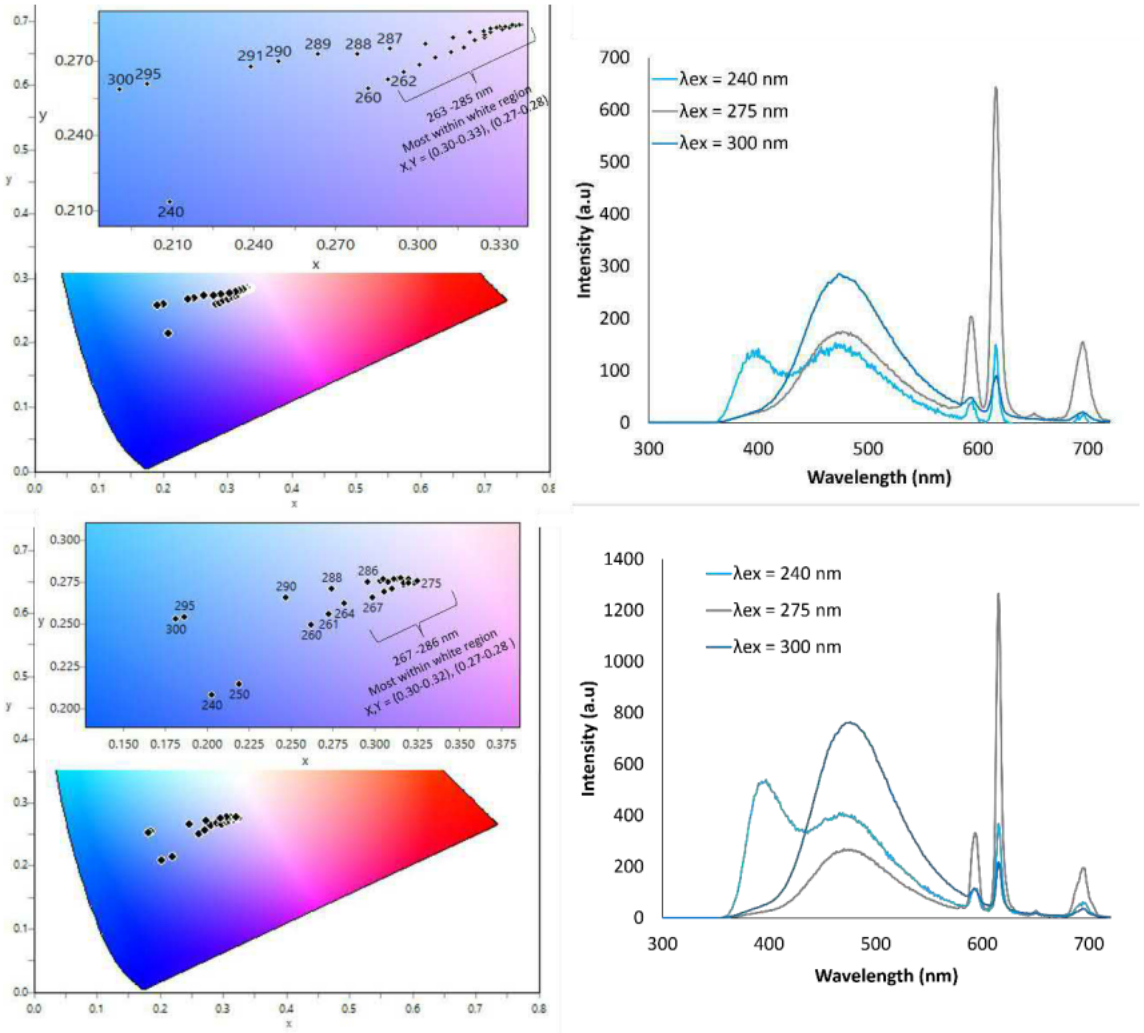

*Figure 5.89.. CIE 1931 chromaticity diagram with different overall colours capable of Eu(**6**)$_3$ in 4000 (Top) and 5000 (Bottom) rpm spin coated film dependent on λ_{ex} and fluorescence spectra of important λ_{ex}.. Calculated CIE coordinates for 4000 rpm: 240 nm x,y = 0.19, 0.21;. 260 nm x,y = 0.28,. 0.26;. 261 nm x,y = 0.29,. 0.26;. 262-263 nm x,y = 0.30,. 0.27;. 264 nm x,y = 0.31,. 0.27;. 265-266 nm x,y = 0.32, 0.28;. 267-273 nm x,y = 0.33,. 0.28;. 274-278 nm x,y = 0.34,. 0.28;. 279-283 nm x,y = 0.33,. 0.28;. 284-285 nm x,y = 0.32,. 0.28;. 286 nm x,y = 0.30,. 0.28;. 287 nm x,y = 0.29,. 0.27;. 289nm x,y = 0.26,. 0.27;. 290 nm x,y = 0.25,. 0.27;. 295 nm x,y = 0.20,. 0.26 and 300 nm x,y = 0.19, 0.. Calculated 1996 CIE coordinates for 5000 rpm:. 240 nm x,y = 0.20,. 0.21;. 250 nm x,y = 0.22,. 0.21;. 260 nm x,y = 0.26,. 0.25;. 261 nm x,y = 0.27,. 0.26;. 264 nm x,y = 0.28,. 0.26;. 267-270 nm x,y = 0.30,. 0.27;. 271 nm x,y = 0.31,. 0.27;. 272-273 nm x,y = 0.31,. 0.28;. 27 4nm x,y = 0.31,. 0.27;. 275 nm x,y = 0.32,. 0.27;. 276 nm x,y = 0.32,. 0.28;. 277 nm x,y = 0.33,. 0.28;. 278 nm x,y = 0.31,. 0.28;. 279nm x,y = 0.32,. 0.28; 280 nm x,y = 0.30,. 0.28;. 281 nm x,y = 0.32,. 0.28;. 281 nm x,y = 0.30,. 0.28;. 282 -283 nm x,y = 0.32,. 0.28;. 284 nm x,y = 0.30,. 0.28;. 285 nm x,y = 0.32,. 0.28;. 286 nm x,y = 0.30,. 0.28;. 286 nm x,y = 0.32,. 0.28;. 288 nm x,y = 0.28,. 0.27;. 290 nm x,y = 0.25,. 0.27;. 295 nm x,y = 0.19,. 0.25 and 300 nm x,y = 0.18,. 0.25..*

5.3 Conclusion

Herein three different ligands (**6 – 8**) have been successfully synthesised and 10 lanthanide complexes prepared. From our detailed investigation of these complexes, one complex was found to hold superior photophysical properties. This allowed for materials fabrication to focus its investigation on this system and not waste time on futile systems. This is an example of how the synthetic strategy allows for easy synthesis of a range of different lanthanide complexes which can easily be investigated prior to materials fabrication, allowing for the optimal systems to be carried forward to materials and application discoveries.

Three different ligands were successfully synthesised which incorporated **NI** or **PYR** chromophores into the PDC or PDA motif via the 1,2,3-triazole linker. These ligands were complexed with a range of visibly emissive Ln^{3+}, in most cases resulting in dual emissive complexes. From self-assembly titrations and complex characterisation, all form the 1:3 M:L complex as previous systems did. Out of the total 7 potential dual emissive complexes investigated, Eu(**6**)$_3$ was a prime example of a single component dual emissive system, with better quantum yields, a large colour-tunable window, and achieving white emission both as a solid or in solution. This system was used to coat the surface of different substrates forming a dual, colour-tunable, and white emissive film by spin coating technique. It is worth noting that this system has further promise as a potential oxygen sensor or OLED emitting layer, but to fully explore each application would require significantly more time. However, initial oxygen sensing has been explored and results are quickly discussed below. While OLED fabrication was planned, due to time constraints it was not tested. However HOMO and LUMO energy levels of Eu(**6**)$_3$ required for OLED layer fabrication were determined by cyclic voltammetry and DFT calculation (see Section 8.3.6 for details).

5.3.1 Oxygen Sensing

NI and **PYR** chromophores both contain a T_1 state with energy levels (18,500 cm^{-1} and 16,980 cm^{-1} respectively) which can be quenched in the presence of oxygen, thus quenching Ln^{3+} emission if the Ln^{3+} is being populated *via* that T_1 state.[32, 48, 57] Unfortunately, there was no sign the **PYR** antenna populating the Eu^{3+} excited state so this was unlikely to work. However, **NI** in both Eu(**6**)$_3$ and [Eu(**7**)$_3$](CF$_3$SO$_3$)$_3$ was seen to populate Eu^{3+} excited states and result in Eu^{3+} emission.

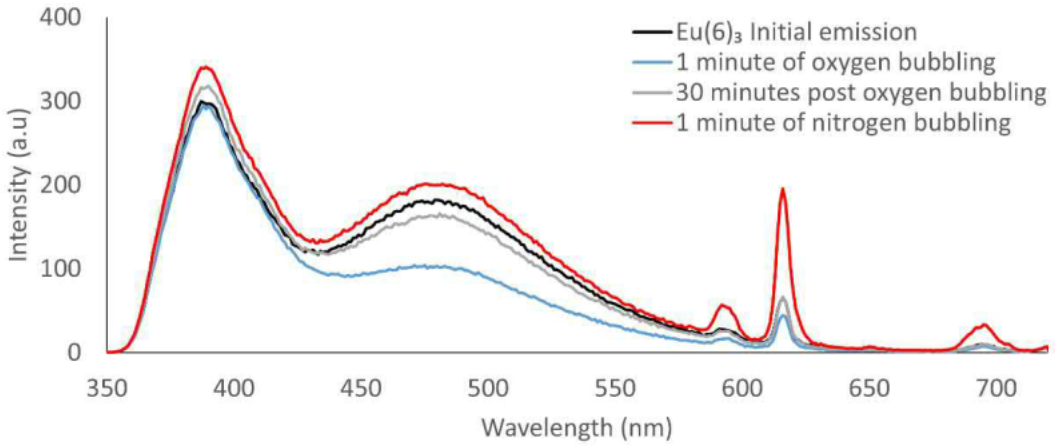

*Figure 5.90. Eu(**6**)$_3$ in 0.01 mM MeOH solution, pre and post bubbling with oxygen or nitrogen gas. (λ_{ex} = 340 nm).*

Eu(**6**)$_3$ was tested by bubbling either N_2 or O_2 into a 0.01 mM MeOH solution when exciting into the **NI** antenna at λ_{ex} = 340 nm. Upon bubbling O_2 into the solution for 1 minute, a major decrease was observed in the **NI** excimer emission (Figure 5.90), a change which had been noted previously in other systems.[81] Excimer emission intensity would then slowly increase to original emission intensity over a long period of time (≈ 30 minutes). Bubbling N_2 into the solution for 1 minute resulted in excimer emission becoming more intense than the original emission, likely a result of displacing all O_2. In terms of Eu^{3+} emission a similar change is observed but is likely connected with the changes observed in excimer emission, as the regions slightly overlap. However, the 1-minute N_2 bubbling does cause a significant increase in Eu^{3+} emission, potentially indicating quenching from oxygen present in solution. To fully explore this application both phosphorescent measurements (to observe Eu^{3+} emission without chromophore emission) and NIR measurements (for singlet oxygen generation) would be required.

5.4 Experimental

5.4.1 General Experimental Details

All reagents, solvents and starting materials were purchased from Sigma-Aldrich. NMR spectra were recorded using a Bruker Ultrashield 300, with chemical shifts recorded in parts per million (ppm) downfield from the standard. UV-visible spectra were recorded on a Shimadzu UV-1800, steady state fluorescence measurements were recorded on a Shimadzu RF-6000 Spectro fluorophotometer, with a ZJB380 UV filter 360 nm and time resolved phosphorescence measurements were carried out using an Agilent Technologies Cary Eclipse fluorescence spectrophotometer, with MeCN, CH_2Cl_3 and MeOH solvents in a capped 3.5 mL quartz cuvette with a 1 cm path length. Melting points were obtained on a Electrothermal IA9000 Series Melting Point Apparatus. FTIR of solids were recorded on a Bruker Alpha platinum-ATR. MS of ligands was carried out in HPLC grade solvents, on a Shimadzu LCMS-2020 for ligands and a Bruker Daltonics MicrOTOF™ Spectrometer for complexes. Single crystal X-ray diffraction data were collected on a Bruker D8 Venture equipped with an IμS DIAMOND microfocus with a Cu-Kα (λ = 1.54178) X-ray source with a PHOTON III detector, or a Bruker D8 quest with a Cu-Kα (λ = 1.54178) X-ray source with a PHOTON II detector.[29-31] Unit cell parameters were refined against all data and an empirical absorption correction applied on APEX3. Structures were solved by direct methods using SHELXS-2013[83] and refined by SHELXL-2013[83] using Olex2.[84] Spin coated films were developed on a Ossila spin coater. Atomic force microscopy (AFM) measurements were performed in tapping mode, on an Asylum Cypher ES. AFM tip parameters: 150 Hz budget sensor tip, with a set point at 80 % amplitude and measurements run in attractive mode. AFM measurements analysis and images generated in Gwyddion.[85] CIE plots were generated in OSRAM LED ColorCalculator software. Safety Note: low molecular weight organic azides are potential explosives, and care must be taken during their handling; however, no issues were encountered here.

5.4.2 Photophysical Measurements

The stock solutions of ligand or complex were prepared using a (1:1) ratio of CH_2Cl_2 and MeOH (spectroscopic grade). Emission (steady-state, time-resolved, and excitation) spectra and lifetimes were recorded at r.t. Phosphorescence lifetimes of the Eu^{3+} and Tb^{3+} excited states were measured in time-resolved mode, by monitoring the emission decay at 616 and 543 nm; these were carried out in triplicate and averaged.

5.4.2.1 Photophysical Self-Assembly Titrations

The formation of 1:1, 1:2 and 1:3 (M:L) species was monitored by measuring changes in the UV-visible absorption and fluorescence spectra of a solution of ligand (2×10^{-5} M in 3 mL volume in MeOH diluted from 0.001 M stock solution in DCM:MeOH (1:1)) when titrated with $Ln(CF_3SO_3)_3.xH_2O$ solution in MeOH (1 mM, 0 → 4.5 equivalents, with 3 μL additions for 0 to 1 equivalents, 6 μL additions for 1 to 2 equivalents, and 30 μL additions for 2 to 4.5 equivalents). In the case of **8** UV-visible absorption titration additions were reduced to 3 μL additions for 0 to 0.6 equivalents, 6 μL additions for 0.6 to 1 equivalents, 12 μL additions for 1 to 2 equivalents and 30 μL additions for 2 to 4 equivalents. Data was then fitted with ReactLab™ Equilibrium[68] for non-linear regression analysis.

5.4.2.2 Quantum Yield

Quantum yield measurements were determined by the dilute comparison method[86] using relative standards $Cs_3[Eu(DPA)_3]\cdot 8H_2O$ and quinine sulfate in 0.5 M H_2SO_4, complex in a 0.1 M Tris-HCl buffer solution (pH ≈ 7.45), with known quantum yields of Φ_r = 24 ± 2.5 % and Φ_r = 54.6 % respectively.[87, 88] $Cs_3[Eu(DPA)_3]\cdot 9H_2O$ was used for Eu(**L**)$_3$ and quinine sulfate was used for the organic based emissions. Instrument slit widths remained the same between measurements for different compounds with 1.5, 3 nm excitation and emission widths. Excitation wavelength was the same for all measurements with the standard 279 nm excitation wavelength being used for lanthanide standards/emissions and 366 nm for quinine sulfate/organic emissions. Complexes were dissolved in a 1:1 MeOH:CH_2Cl_2 and then diluted into MeOH or MeCN.

Estimated overall quantum yields $\Phi_{Ln}^{L} = \Phi_x$ were calculated according to the following equation 1. Here grad refers to the slope of plotted emission area vs absorbance (emission area was taken from specific emission peaks, Eu(**L**)$_3$ ($^5D_0 \rightarrow {}^7F_2$)), while chromophore emission (in some instances includes weak Ln^{3+} centred emission) was compared against quinine sulfate emission. Refractive index of n = 1.3295 was found for MeOH:CH_2Cl_2 solution and n = 1.3355 for MeCN solution.[89]

$$\boldsymbol{\Phi_x = \Phi_r\left(\frac{grad_x}{grad_r} \times \left(\frac{n_x{}^2}{n_r{}^2}\right)\right)} \quad \mathbf{(1)}$$

Other values such as observed lifetime (τ_{obs}), radiative lifetime (τ^{rad}), sensitisation efficiency (n_{sens}) and intrinsic quantum yield (Φ_{Ln}^{Ln}) were determined in the same manner as in chapter 3.

5.4.3 Spin Coating

10 mg of Eu(**6**)$_3$ was dissolved into 1 ml of DCM:MeOH:DMF (4:4:2) and the solution was heated to 60 °C to ensure that all material had dissolved. Once cooled the solution was syringe filtered (regenerated cellulose) twice to remove any particles. 30 x 30 mm quartz slides or 10 x 10 mm silicon wafers, which had been washed the day before by soaking in nitric acid and piranha solution for 30 minutes each and stored in milli-Q water overnight, were sprayed with MeOH and then wiped with lens tissues. The substrate was then attached to the spin coater chuck using double side tape and spun at 3000 rpm for 30 s. If there was any sign of particles left on the slide, they would be sprayed with nitrogen gas until no particles remained. Dynamic deposition was used, meaning the chuck was sped up to 500 rpm before depositing 50 µL of solution onto the substrate. This was done on a slight angle, ensuring the tip did not touch the substrate. The slide would then be sped up to its maximum spin speed for 60 s, and then left to dry for 60 s before being removed from the chuck.

5.4.4 Ligand Synthesis

5.4.4.1 Synthesis of N-(3-hydroxypropyl)-naphthalene-1,8-dicarboximide (F)

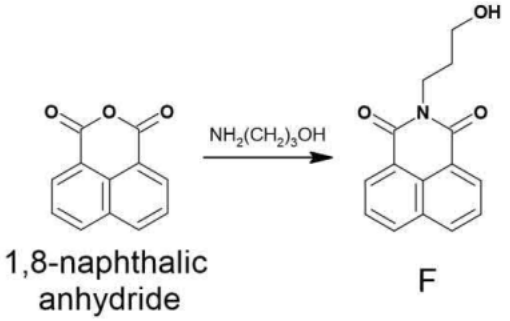

*Scheme 5.8. Synthesis of precursor **F**.*

1,8-naphthalic anhydride (1.963 g, 9.91 mmol) was combined with 0.758 mL of 3-amino-1-propanol in 20 mL of ethanol. The solution was refluxed for 24 hours, resulting in a translucent lime green solution. The solution was allowed to cool, and then reheated for 30 minutes, where upon a second cooldown a light yellow crystalline solid precipitated, which was filtered and washed with cold ethanol yielding **F** as a light-yellow crystalline material (1.583 g, 63 %). Melting point = 123.1 °C. LRMS *m/z* = 255.75 [**F** + H]$^+$ (calc. for $C_{15}H_{13}NO_3^+$, 256.10), 297.10 [**F** + K]$^+$ (calc. for $C_{15}H_{13}NO_3K^+$, 294.05). ^{1}H NMR (300 MHz, DMSO-d$_6$, ppm), δ = 8. 45 (m, 4H, **NI**-H), 7.85 (dd, J = 8.0, 7.0 Hz, 2H, **NI**-H), 4.52 (t, J = 5.5 Hz, 1H, O-H), 4.10 (m, 2H, N-**CH$_2$**), 3.50 (m, 2H, **CH$_2$**-OH) 1.78 (m, J = 6.0, 2H, CH$_2$-**CH$_2$**-CH$_2$); ^{13}C NMR (75 MHz, DMSO-d$_6$, ppm): δ = 163.9 (C=O), 134.7 (CH), 131.7 (C), 131.1 (CH), 127.8 (C), 127.7 (CH), 122.6 (C), 59.5 (CH$_2$), 38.0 (CH$_2$), 31.4 (CH$_2$). FTIR (cm^{-1}) 3454, 3169, 2946, 2860, 1690, 1648, 1620, 1583, 1511, 1441, 1386, 1361, 1336, 1275, 1233, 1169, 1146, 1073, 1051, 1024, 951, 922, 848, 800, 780, 739, 659, 541, 445, 412.

5.4.4.2 Synthesis of N-(3-bromopropyl)-naphthalene-1,8-dicarboximide (G)

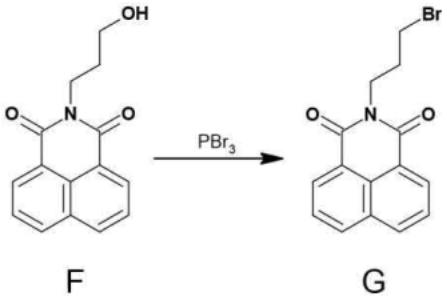

*Scheme 5.9. Synthesis of precursor **G**.*

F (1.583 g, 6.23 mmol) was dissolved in 20 mL of freshly dried ethyl acetate. 1.170 mL of PBr_3 was then added to the stirring solution dropwise and left to stir at r.t for 20 minutes, followed by heating to 75 °C for 3 hours. Water was then added to the solution causing a precipitate to form. This was filtered yielding **G** as an off-white solid (1.600 g, 81 %). Melting point = 140.3 °C. ^{1}H NMR (300 MHz, DMSO-d$_6$, ppm), δ = 8.45 (m, 4H, **NI**-H), 7.85 (dd, J = 8.0, 7.0 Hz, 2H, **NI**-H), 4.15 (t, J = 7.0 Hz, 2H, N-**CH$_2$**), 3.61 (m, J = 6.5, 2H, **CH$_2$**-Br), 2.19 (m, 2H, CH$_2$-**CH$_2$**-CH$_2$); ^{13}C NMR (75 MHz, DMSO-d$_6$, ppm): δ = 164.0 (C=O), 134.7 (CH), 131.7 (C), 131.1 (CH), 127.9 (C), 127.6 (CH), 122.6 (C), 39.2 (CH$_2$) 32.9 (CH$_2$), 31.4 (CH$_2$). FTIR (cm^{-1}) 2948, 1695, 1658, 1586, 1511, 1440, 1382, 1359, 1336, 1242, 1211, 1168, 1138, 1084, 1028, 1011, 887, 847, 800, 778, 740, 672, 620, 542, 483, 412.

5.4.4.3 Synthesis of N-(3-azidopropyl)-naphthalene-1,8-dicarboximide (H)

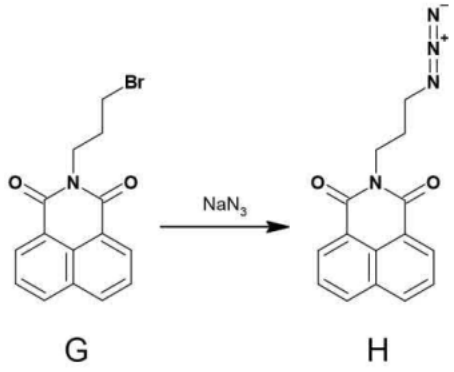

*Scheme 5.10.. Synthesis of precursor **H**..*

G (0.903 g, 2.84 mmol) was combined with NaN_3 (0.369 g, 5.68 mmol) in 30 mL of DMF. The yellow solution was heated to 80 °C for 24 hours. The product was then extracted with ethyl acetate, which was washed with 3 x 100 mL H_2O and then a final brine wash. The organic layer was dried by $MgSO_4$ and then removed under reduced pressure, yielding **H** as a bright green solid (0.652 g, 82 %). LRMS *m/z* = 281.05 [**H** + H]$^+$ (calc. for $C_{15}H_{12}N_4O_2^+$, 281.10). ^{1}H NMR (300 MHz, DMSO-d_6, ppm), δ = 8.46 (m, 4H, **NI**-H), 7.86 (dd, J = 8.0, 7.0 Hz, 2H, **NI**-H), 4.11 (t, J =7.0 Hz, 2H, N-**CH_2**), 3.44 (t, J = 6.5, 2H, **CH_2**-N_3), 1.90 (m, 2H, CH_2-**CH_2**-CH_2); ^{13}C NMR (75 MHz, DMSO-d_6, ppm): δ = 164.3 (C=O), 134.1 (CH), 131.6 (C), 131.4 (CH), 128.2 (C), 127.0 (CH), 122.5 (C), 49.2 (CH_2), 37.9 (CH_2), 27.5 (CH_2). FTIR (cm^{-1}) 2102 (N_3), 1693, 1650, 1624, 1584, 1512, 1439, 1388, 1366, 1341, 1272, 1232, 1176, 1150, 1075, 1055, 120, 893, 843, 798, 774.

5.4.4.4 Synthesis of N_2-bis((1-(N-(3-propyl)-naphthalene-1,8-dicarboximide)-1H-1,2,3-triazol-4-yl)methyl)-O_6-((benzyloxy)carbonyl)pyridine-2-carboxamide-6-carboxylate (I)

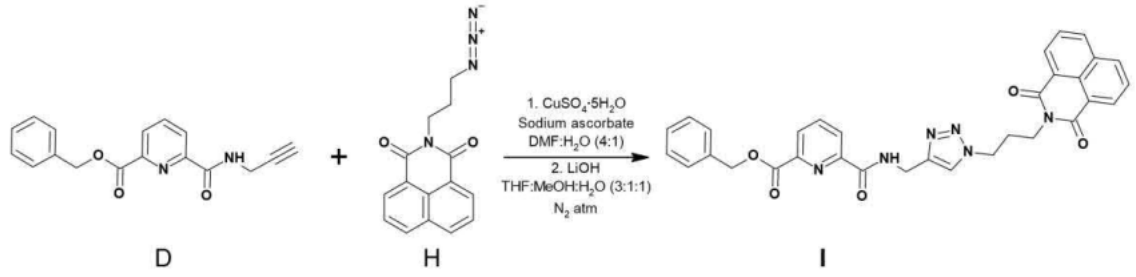

*Scheme 5.11.. Synthesis of intermediate **I**.*

D (0.400 g, 1.4 mmol) was combined with sodium ascorbate (0.269 g, 1.4 mmol), $CuSO_4 \cdot 5H_2O$ (0.170 g, 0.7 mmol) and **H** (0.381 g, 1.4 mmol) in 30 mL of DMF:H_2O (4:1). The solution was heated to 80 °C overnight, changing from a light yellow to a dark green. Water was slowly added to the solution until a cloudy precipitate was formed, which was filtered and then washed with (0.1 M) NaOH:(0.5 M) EDTA solution yielding **I** as an off-white solid (0.558 g, 71 %). Melting point = 143.3 °C. LRMS *m/z* = 575.15 [**I** + H]$^+$ (calc. for $C_{32}H_{27}N_6O_5^+$, 575.20). ^{1}H NMR (300 MHz, DMSO-d_6, ppm), δ = 9.04 (t, J = 6.0 Hz, 1H, NH), 8.49 (t, J = 7.0, 4H, **NI**-H), 8.27 (m, 3H, py-H), 8.05 (s, 1H, t-H), 7.89 (m, 2H, **NI**-H), 7.41 (m, 5H, Bn-H), 5.45 (s, 1H, CH_2-O), 4.59 (d, J = 5.5 Hz, 2H, CH_2-NH), 4.48 (t, J = 7.0 Hz, 2H, CH_2-), 4.15 (t, J = 7.0 Hz, 2H, CH_2-), 2.23 (m, 2.23, CH_2-**CH_2**-CH_2); ^{13}C NMR (75 MHz, DMSO-d_6, ppm): δ = 164.3 (C=O-py), 164.1 (C=O-Nap), 163.6 (C=O-py), 150.6 (CN-py), 146.9 (CN-py), 144.8 (C-tr), 140.0 (CH-py), 136.2 (C-Bn), 134.7 (CH-Nap), 131.7 (C-Nap), 131.1 (CH-Nap), 129.0 (CH-Bn), 128.7 (CH-Bn), 128.5 (CH-Bn), 127.9 (C-Nap), 127.9 (CH-py) 127.6 (CH-Nap), 125.9 (CH-py), 123.5 (CH-tr), 122.6 (C-Nap), 67.3 (CH_2-Bn), 48.0 (CH_2), 37.8 (CH_2), 35.2 (CH_2-NH), 29.0 (CH_2). FTIR (cm^{-1}) 1779, 1734, 1695, 1651, 1585, 1531, 1438, 1348, 1305, 1305, 1232, 1171, 1124, 1049, 1002, 907, 843, 773, 745, 675, 643, 541, 514.

5.4.4.5 Synthesis of N_2-((1-(N-(3-propyl)-naphthalene-1,8-dicarboximide)-1H-1,2,3-triazol-4-yl)methyl)pyridine-2-carboxamide-6-carboxylate (6)

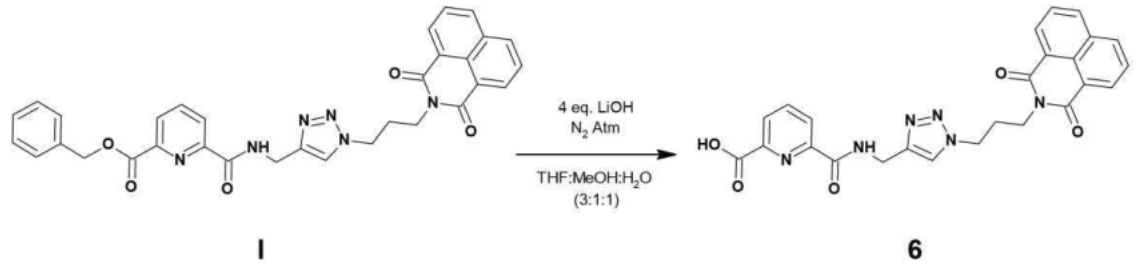

Scheme 5.12.. Synthesis of ligand ***6.***

I (0.858 g, 1.5 mmol) was combined with LiOH (0.143 g, 6.0 mmol) in 20 mL of THF:MeOH:H_2O (3:1:1). This was stirred overnight under an nitrogen atmosphere, where the solid slowly dissolved into a light yellow solution. The solvent was then removed until a residue remained, to which 1 M HCl was added causing an off-white precipitate to form, which was filtered and washed with water and then acetone to remove the 1,8-naphthalimide by-product, yielding **6** as an off-white solid (0.428 g, 59 %). Melting point = 148.2 °C. LRMS *m/z* = 485.10 [**6** + H]$^+$ (calc. for $C_{25}H_{21}N_6O_5^+$, 485.16) and *m/z* = 507.00 [**6** + Na]$^+$ (calc. for $C_{25}H_{20}N_6O_5Na^+$, 507.14). ^{1}H NMR (300 MHz, DMSO-d_6, ppm), δ = 9.72 (t, J = 6.0 Hz, 1H, NH), 8.47 (t, J = 6.0, 4H, **NI**-H), 8.25 (m, 3H, py-H), 8.05 (s, 1H, t-H), 7.85 (m, 2H, **NI**-H), 4.57 (d, J = 6.0 Hz, 2H, CH_2-NH), 4.45 (t, J =7.0 Hz, 2H, CH_2-), 4.11 (t, J = 7.0 Hz, 2H, CH_2-), 2.20 (m, 2H, CH_2-**CH_2**-CH_2); ^{13}C NMR (75 MHz, DMSO-d_6, ppm): 165.4 (C=O-py), 164.1 (C=O-Nap), 163.3 (C=O-py), 149.5 (CN-py), 146.4(CN-py), 144.8 (C-tr), 140.4 (CH-py), 134.8 (CH-Nap), 131.8 (C-Nap), 131.2 (CH-Nap), 127.9 (C-Nap) , 127.7 (CH-Nap), 127.1 (CH-py), 125.9 (CH-py), 123.6 (CH-tr), 122.8 (C-Nap), 48.0 (CH_2), 37.8 (CH_2), 34.9 (CH_2-NH), 29.0 (CH_2). FTIR (cm^{-1}) 3234, 3138, 2925, 2853, 2394, 1893, 1739 (py-COOH), 1695 (**NI**-COOH), 1657 (py-CONH), 1625, 1587, 1530, 1454, 1440, 1387, 1345, 1306, 1235, 1170, 1147, 1121, 1074, 1054, 1016, 1001, 963, 907, 880, 847, 801, 780, 765, 747, 682, 643, 628, 563, 546, 516, 489, 423.

5.4.4.6 Synthesis of N_2,N_6 -bis((1-(3-propyl)-naphthalene-1,8-dicarboximide)-1H-1,2,3-triazol-4-yl)methyl)pyridine-2,6-dicarboxamide (7)

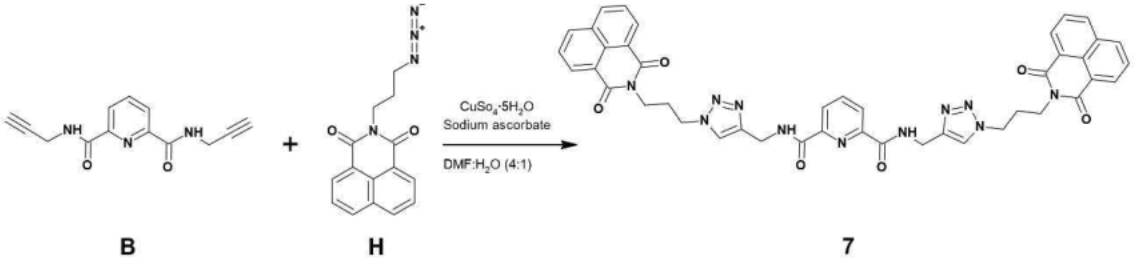

Scheme 5.13.. Synthesis of ligand ***7.***

B (0.253 g, 1.0 mmol) was combined with sodium ascorbate (0.35 g, 3.4 mmol), $CuSO_4$·$5H_2O$ (0.218 g, 1.7 mmol) and **H** (0.480 g, 1.7 mmol) in 30 mL of DMF:H_2O (4:1). The solution was heated to 80 °C overnight, changing from a bright yellow to a dark green. Water was slowly added to the solution until a cloudy precipitate was formed, which was filtered and then washed with (0.1 M) NaOH:(0.5 M) EDTA solution yielding **7** as an off-white solid (0.594 g, 70 %). Melting point = 265.7 °C. LRMS *m/z* = 824.40 [**7** + Na]$^+$ (calc. for $C_{43}H_{35}N_{11}O_6Na^+$, 824.40) and *m/z* = 840.20 [**7** + K]$^+$ (calc. for $C_{43}H_{35}N_{11}O_6K^+$, 840.24). ^{1}H NMR (300 MHz, DMSO-d_6, ppm), δ = 9.94 (t, J = 6.24 Hz, 1H, NH), 8.43 (m, 8H, n **NI**-H), 8.22 (m, 3H, py-H), 8.03 (s, 2H, t-H), 7.84 (m, 4H, **NI**-H), 4.60 (d, J = 6.09 Hz, 4H, CH_2-NH), 4.45 (t, J = 7.10 Hz, 4H, CH_2-) 4.10 (t, 4H, CH_2-) 2.19 (m, 4H, CH_2-**CH_2**-CH_2); ^{13}C NMR (75 MHz, DMSO-d_6, ppm): δ = 164.0 (C=O-Nap), 163.6 (C=O-Py), 149.0 (CN-Py), 145.2 (C-tr), 140.0 (CH-Py), 134.7 (CH -Nap), 131.7 (C-Nap), 131.1 (CH-Nap), 127.8 (C -Nap), 127.6 (CH-Nap), 124.9 (CH-Py), 123.5 (CH-tr), 122.6 (C-Nap), 48.0 (CH_2), 37.7 (CH_2), 34.9 (CH_2), 29.0(NH-CH_2). FTIR (cm^{-1}) 3339, 3139, 1693, 1672, 1650, 1623, 1586, 1539, 1439, 1386, 1344, 1306, 1235, 1200, 1170, 1147, 1132, 1057, 1047, 1003, 962, 906, 880, 844, 778, 738, 700, 630, 564, 542, 526, 501, 477.

5.4.4.7 Synthesis of 1-(4-Bromobutane)pyrene (J)

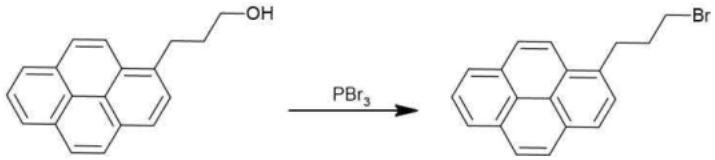

Scheme 5.14.. Synthesis of precursor ***J****.*

1-Pyrenebutanol (0.502 g, 1.8 mmol) was dissolved in 20 mL of dry ethyl acetate, to which 0.499 mL of PBr_3 was added dropwise. This was left to stir at room temperature for 20 minutes, causing the solution to turn a pale yellow; the solution was then refluxed for 12 hours. Ice cold H_2O was then added dropwise to the solution while stirring until solution went cloudy; the solution was then stored at 4 °C for 24 hours, causing a fine white precipitate, which was then filtered giving **J** as an off-white solid (0.573 g, 92 %). Melting point = 103.3 °C. LRMS *m/z* = 338.25 [**J** + H]$^+$ (calc. for $C_{20}H_{18}Br^+$, 338.26) and *m/z* = 360.25 [**J** + Na]$^+$ (calc. for $C_{20}H_{17}BrNa^+$, 360.24). ^{1}H NMR (300 MHz, $CDCl_3$, ppm), δ = 8.28 (d, J = 10.5 Hz, 1H, CH), 8.15 (m, 4H, **PYR**-H), 8.03 (s, 2H, **PYR**-H), 8.00 (t, 8.0 Hz, 1H, **PYR**-H), 7.78 (d, J = 8.0 Hz, 1H, **PYR**-H), 3.47 (t, J = 6.5 Hz, 2H, CH_2-Br) 4.10 (t, J = 7.0 Hz, 2H, CH_2-**PYR**) 2.19 (m, 4H, CH_2-**CH_2-CH_2**-CH_2); ^{13}C NMR (75 MHz, $CDCl_3$, ppm): δ = 136.1 (C), 131.4 (C), 130.9 (C), 129.9 (C), 128.6 (C), 127.5 (CH), 127.4 (CH), 127.2 (CH), 126.7 (CH), 126.7 (CH), 125.9 (CH), 125.1 (C), 125.0 (C), 124.9 (CH), 124.8 (CH), 124.8 (CH), 33.63 (CH_2), 32.6 (CH_2), 30.2 (CH_2). FTIR (cm^{-1}) 2948, 1695, 1658, 1586, 1511, 1440, 1382, 1359, 1336, 1242, 1211, 1168, 1138, 1084, 1028, 1011, 887, 847, 800, 778, 740, 672, 620, 542, 483, 412.

5.4.4.8 Synthesis of 1-(azidobutane)pyrene (K)

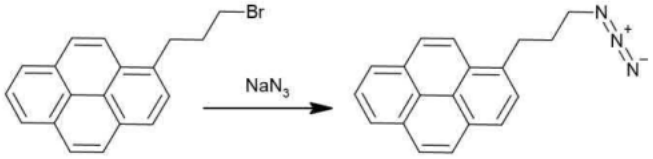

Scheme 5.15.. Synthesis of precursor ***K****..*

J (0.793 g, 2.3 mmol) was combined with NaN_3 (0.305 g, 4.6 mmol) in 20 mL of DMF and the colorless solution was heated to 80 °C for 24 hours. The solution was allowed to cool, and 20 mL of H_2O was added to the pale pink solution causing a white precipitate to form, which was redissolved into 30 mL of ethyl acetate. The organic layer was separated and then washed with 2 x 20 mL H_2O, then brine, and then dried with $MgSO_4$ before solvent was removed under vacuum, yielding **K** as a pale pink solid (0.624 g, 88 %). ^{1}H NMR (300 MHz, $CDCl_3$, ppm), δ = 8.26 (d, J = 9.5 Hz, 1H, **PYR**-H), 8.14 (m, 4H, **PYR**-H), 8.03 (S, 2H, **PYR**-H), 7.99 (t, J = 8.0 Hz, 1H, **PYR**-H), 7.86 (d, J = 8.0 Hz 1H, **PYR**-H), 3.36 (m, 4H, **PYR**-CH_2, N_3-CH_2), 1.95 (m, 1H, CH_2) 1.79 (m, 2H, CH_2); ^{13}C NMR (75 MHz, $CDCl_3$, ppm): δ = 136.1 9 (C), 131.4 (C), 130.9 (C), 129.9 (C), 128.6 (C), 127.5 (CH), 127.3 (CH), 127.2 (CH), 126.7 (CH), 125.8 (CH), 125.1 (C), 125.0 (C), 124.9 (CH), 124.8 (CH), 127.7 (CH), 123.2 (CH), 51.4 (CH_2), 33.0 (CH_2), 28.9 (CH_2), 28.8 (CH_2). FTIR (cm^{-1}) 3040, 2966, 2938, 2924, 2862, 2352, 2202, 2089 (N_3), 1806, 1600, 1582, 1506, 1485, 1464, 1455, 1428, 1414, 1366, 1351, 1332, 1306, 1295, 1278, 1245, 1208, 1182, 1098, 1070, 1049, 1017, 970, 892, 839, 816, 795, 777, 759, 747, 709, 679, 664, 607, 587, 552, 536, 517, 489, 434, 417.

5.4.4.9 Synthesis of N_2-((1-(1-butane)pyrene)-1H-1,2,3-triazol-4-yl)methyl)-O_6-((benzyloxy)carbonyl)pyridine-2-carboxamide-6-carboxylate (L)

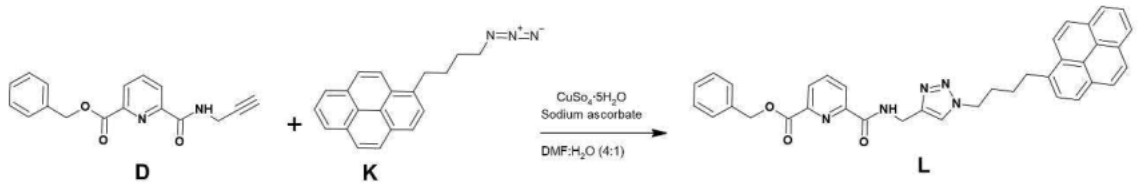

D K L

Scheme 5.16. Synthesis of intermediate ***L****.*

D (0.410 g, 1.4 mmol) was combined with sodium ascorbate (0.224 g, 1.4 mmol), $CuSO_4 \cdot 5H_2O$ (0.141 g, 0.7 mmol) and **K** (0.505 g, 1.4 mmol) in 30 mL of DMF:H_2O (4:1). The solution was heated to 80 °C overnight, changing from a light yellow to a brown. Water was slowly added to the solution until a cloudy precipitate was formed, which was filtered and then washed with (0.1 M) NaOH:(0.5 M) EDTA solution yielding a brown crystalline solid. The solid was redissolved into 10 mL DCM:MeOH (1:1) and washed with 2 x 50 mL H_2O. Solvent was then removed yielding **L** as a pale cream solid (0.363 g, 44 %). Melting point = 97.5 °C. LRMS m/z = 594.10 [**L** + H]$^+$ (calc. for $C_{37}H_{32}N_5O_3^+$, 594.68), *m/z* = 616.15 [**L** + Na]$^+$ (calc. for $C_{37}H_{31}N_5O_3Na^+$, 616.66) and *m/z* = 632.15 [**L** + K]$^+$ (calc. for $C_{37}H_{31}N_5O_3K^+$, 632.77). NMR (300 MHz, $CDCl_3$, ppm), δ = 8.68 (m, 1H, NH), 8.3 (dd, J = 8.0, 1.0 Hz, 1H, **PYR**-H), 8.20 -7.90 (m, 11H, pyr-H and **PYR**-H), 7.51 (s, 1H, t-H), 7.40 (m, 5H, Bn-H), 5.41 (s, 2H, CH_2-O), 4.72 (d, J = 6.0 Hz, 2H, CH_2-NH) 4.34 (t, J = 7.0, 2H, CH_2-N), 3.36 (t, J = 7.5 Hz, 2H, CH_2- **PYR**), 2.03 (m, 2H, **CH_2**-CH_2-N), 1.89 (m, 2H, **CH_2**-CH_2- **PYR**); ^{13}C NMR (75 MHz, $CDCl_3$, ppm): δ = 164.2 (C=O), 163.7 (C=O), 149.9 (CN), 146.6 (CN), 144.6 (C-t), 138.5 (CH), 131.4 (C), 130.8 (C), 130.0 (C), 128.7 (CH), 128.6 (CH), 128.6 (CH), 127.5 (CH), 127.5 (CH), 127.3 (CH), 126.8 (CH), 125.9 (CH), 125.4 (CH), 125.1 (C), 125.0 (CH), 124.8 (C), 124.8 (CH), 123.1 (CH), 122.4 (CH-t), 67.7 (CH_2), 50.3 (CH_2), 35.1 (CH_2), 32.7 (CH_2), 30.1 (CH_2), 28.5 (CH_2). FTIR (cm^{-1}) 3505, 3315, 3140, 3039, 2935, 2864, 1721, 1673, 1650, 1585, 1529, 1428, 1381, 1338, 1299, 1263, 1234, 1213, 1170, 1146, 1100, 1081, 1054, 1002, 985, 962, 938, 904, 843, 817, 783, 752, 730, 708, 691, 675, 650, 635, 585, 528, 488, 460, 428.

5.4.4.10 Synthesis of N_2-((1-(1-butane)pyrene)-1H-1,2,3-triazol-4-yl)methyl)pyridine-2-carboxamide-6-carboxylate (8)

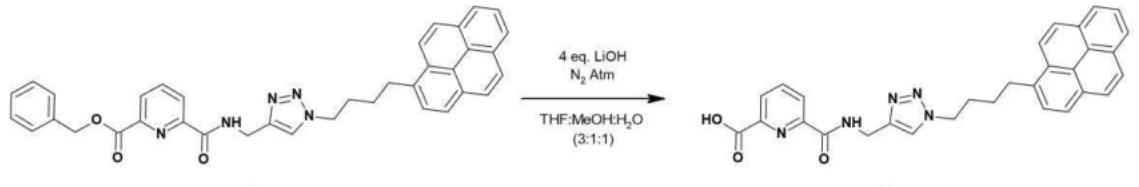

L 8

Scheme 5.17. Synthesis of ligand ***8****.*

L (0.380 g, 0.64 mmol) was combined with LiOH (0.061 g, 2.56 mmol) in 20 mL of THF:MeOH:H_2O (3:1:1), which was stirred overnight under a nitrogen atmosphere, where the solid slowly dissolved into a light yellow solution. The solvent was then removed until a residue remained. 1 M HCl was added to the solution causing an off-white precipitate to form, which was filtered and washed with water, yielding **8** as a brown solid (0.275 g, 86 %). Melting point = 115.9 °C. LRMS *m/z* = 502.1 [**8** - H]$^-$ (calc. or $C_{30}H_{24}N_5O_3^-$, 502.54).^{1}H NMR (300 MHz, DMSO-d_6, ppm), δ = 9.74 (t, J = 6.0 Hz, 1H, NH), 8.34- 7.91 (m, 13H, **PYR**-H, t-H and py-H), 4.61 (d, J = 6.0 Hz, 2H, CH_2-NH), 4.43 (t, J = 6.0 Hz, 2H, CH_2-N), 3.35 (t, J = 7.5 Hz, 2H, CH_2- **PYR**), 1.98 (m, 2H, **CH_2**-CH_2-N), 1.74 (m, 2H, **CH_2**-CH_2- **PYR**).^{13}C NMR (75 MHz, DMSO-d_6, ppm): δ = 165.2 (C=O), 163.3 (C=O), 149.6 (CN), 146.5 (CN), 144.9 (C-tr), 140.4(CH-Py), 137.0 (C-Py), 131.4 (C), 129.7 (C), 128.5 (C), 127.9 (C), 127.7 (CH), 127.1 (CH), 127.0 (CH), 126.6 (CH), 125.9 (CH-Py), 125.4 (CH), 125.2 (CH), 124.7 (C), 124.6 (C), 123.9 (C), 123.5 (CH-tr), 49.5 (CH_2), 34.9 (CH_2), 32.3 (CH_2), 30.2 (CH_2), 34.3 (CH_2), 28.8 (CH_2). FTIR (cm^{-1}) 3218, 3039, 2934, 2862, 2451, 2330, 2094, 1890, 1740, 1671, 1602, 1585, 1526, 1454, 1432, 1339, 1246, 1181, 1141, 1102, 1074, 1001, 842, 742, 721, 708, 678, 643, 618, 556, 505, 423.

5.4.5 Lanthanide Complexation

5.4.5.1 General procedure for complexation of 6, 7 and 8 with Ln^{3+}

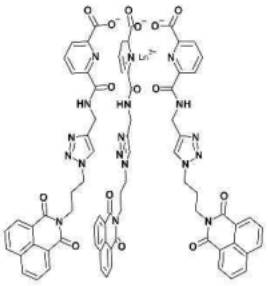

*Figure 5.91.. Ln(**6**)$_3$*

6 was dissolved in 5 mL of DCM:MeOH:$CHCl_3$ (3:3:2) and 1 equivalent of triethylamine was added followed by 0.33 equivalents of selected Ln^{3+} (added from a stock solution pre-dissolved in MeOH) yielding a clear yellow solution. If precipitation occurred upon Ln^{3+} addition more solvent was added to redissolve the precipitate. The solution was refluxed under microwave irradiation for 30 minutes and then subjected to vapour diffusion of diethyl ether at r.t until precipitation occurred and was then filtered.

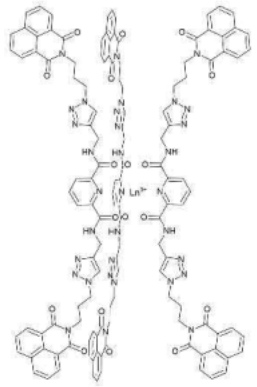

Figure 5.92.. $[Ln(\mathbf{7})_3]^{3+}$.

7 was suspended in 10 mL of DCE:EtOH (1:1) and heated to 150 °C until solution was a clear yellow. 0.33 equivalents of selected Ln^{3+} was then added from a stock solution pre-dissolved in EtOH. The solution was refluxed under microwave irradiation for 30 minutes and then subjected to vapour diffusion of diethyl ether at r.t until precipitation occurred and was then filtered.

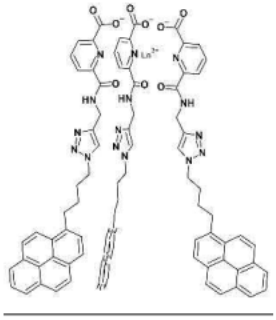

*Figure 5.93.. Ln(**8**)$_3$*

8 was dissolved in 5 mL of DCE:EtOH (1:1), and 1 equivalent of triethylamine was added followed by 0.33 equivalents of selected Ln^{3+} from a stock solution pre-dissolved in MeOH, yielding a clear brown solution. The solution was refluxed under microwave irradiation for 30 minutes and then subjected to vapour diffusion of diethyl ether at r.t until precipitation or film occurred and solvent was removed.

5.5.5.2 Synthesis of Eu(6)$_3$

6 (0.0640 g, 0.132 mmol) was combined with $Eu(CF_3SO_3)_3 \cdot 6H_2O$ (0.0308 g, 0.044 mmol) and 1 equivalent of triethylamine in 5 mL of DCM:MeOH:$CHCl_3$ (3:3:2). The complex precipitated as a white powder, which was filtered giving Eu(**6**)$_3$ as a white solid (0.058 g, 83 %). Melting point = 205 - 226 °C. HRMS *m/z* = 824.1980 $[Eu(\mathbf{6})_3 + 2Na]^{2+}$. (calc. for $(C_{75}H_{57}N_{18}O_{15}EuNa_2)^{2+}$, 824.1630), *m/z* = 1625.3545 $[Eu(\mathbf{6})_3 + Na]^+$ (calc. for $(C_{75}H_{57}N_{18}O_{15}EuNa)^+$, 1625.3367). FTIR ($cm^{-1}$) 3233, 3073, 2965, 1698, 1633, 1587, 1565, 1462, 1430, 1347, 1277, 1235, 1155, 1082, 1048, 1029, 1018, 890, 848, 801, 779, 761, 724, 687, 660, 637, 573, 540, 517, 410. Elemental analysis for $C_{75}H_{57}N_{18}O_{15}Eu \cdot 3.5H_2O \cdot 2.5CH_2Cl_2$ (1878.7389 $gmol^{-1}$) Calculated: C 49.55, H 3.70, N 13.42 %. Found C 49.74, H 4.00, N 13.45 %.

5.5.5.3 Synthesis of Tb(6)$_3$

6 (0.0617 g, 0.127 mmol) was combined with $Tb(CF_3SO_3)_3 \cdot 5H_2O$ (0.0293 g, 0.044 mmol) and 1 equivalent of triethylamine in 5 mL of DCM:MeOH:$CHCl_3$ (3:3:2). The complex precipitated as a white powder, which was filtered giving Tb(**6**)$_3$ as a white solid (0.036 g, 53 %). HRMS *m/z* = 827.1873 $[Tb(\mathbf{6})_3 + 2Na]^{2+}$. (calc. for $(C_{75}H_{57}N_{18}O_{15}TbNa_2)^{2+}$, 827.1644), *m/z* = 1631.3682 $[Tb(\mathbf{6})_3 + Na]^+$ (calc. for $(C_{75}H_{57}N_{18}O_{15}TbNa)^+$, 1631.3396). FTIR ($cm^{-1}$) 3247, 3078, 2969, 2337, 2318, 1697, 1624, 1587, 1566, 1436, 1347, 1277, 1235, 1156, 1083, 1049, 1029, 890, 847, 801, 778, 760, 725, 686, 660, 636, 573, 540, 516, 413. Elemental analysis for $C_{75}H_{57}N_{18}O_{15}Tb \cdot 4.5H_2O \cdot 4CHCl_3$ (2167.8951 $gmol^{-1}$) Calculated: C 43.77, H 3.25, N 11.63 %. Found C 43.50, H 3.32, N 11.95 %.

5.5.5.4 Synthesis of Dy(6)$_3$

6 (0.0273 g, 0.056 mmol) was combined with $Dy(CF_3SO_3)_3 \cdot 8H_2O$ (0.014 g, 0.019 mmol) and 1 equivalent of triethylamine in 5 mL of DCE:EtOH (1:1). The complex precipitated as a light yellow powder, which was filtered giving Dy(**6**)$_3$ as a light yellow solid (0.017 g, 56 %). LRMS *m/z* = 1636.50 $[Dy(\mathbf{6})_3 + Na]^+$ (calc. for $(C_{75}H_{57}N_{18}O_{15}DyNa)^+$, 1564.8678) and *m/z* = 824.16 $[Dy(\mathbf{6})_3 + 2Na]^+$ (calc. for $(C_{75}H_{57}N_{18}O_{15}DyNa2)^{2+}$, 824.16). FTIR ($cm^{-1}$) 3232, 3078, 2963, 1697, 1625, 1587, 1563, 1461, 1430, 1346, 1278, 1235, 1188, 1171, 1082, 1049, 1019, 891, 847, 801, 777, 724, 686, 661, 638, 572, 540, 416.

5.5.5.5 Synthesis of La(6)$_3$

6 (0.0622 g, 0.128 mmol) was combined with $La(CF_3SO_3)_3 \cdot 9H_2O$ (0.0317 g, 0.044 mmol) and 1 equivalent of triethylamine in 5 mL of DCM:MeOH:CHCl3 (3:3:2). The complex precipitated as a white powder, which was filtered giving La(**6**)$_3$ as a white solid (0.046 g, 68 %). HRMS *m/z* = 817.1818 $[La(\mathbf{6})_3 + 2Na]^{2+}$ (calc. for $(C_{75}H_{57}N_{18}O_{15}LaNa_2)^{2+}$, 817.1549). FTIR ($cm^{-1}$) 3270, 3080, 2967, 2337, 2318, 1697, 1624, 1587, 1566, 1436, 1347, 1275, 1235, 1169, 1084, 1049, 1030, 890, 847, 801, 778, 759, 723, 687, 637, 573, 540, 516, 407. Elemental analysis for $C_{75}H_{57}N_{18}O_{15}La \cdot 2CHCl_3$ (1860.0489 $gmol^{-1}$) Calculated: C 49.72, H 3.20, N 13.55 %. Found C 49.76, H 3.46, N 13.37 %.

5.5.5.6 Synthesis of Eu(7)$_3$

7 (0.0238 g, 0.030 mmol) was combined with $Eu(CF_3SO_3)_3 \cdot 6H_2O$ (0.063 g, 0.0098 mmol) and in 5 mL of DCE:EtOH (1:1) the solution was heated to 150 °C until dissolved. The solution was then microwaved for 30 minutes, and then subjected to vapour diffusion of diethyl ether once cooled. The complex precipitated as a light yellow powder, which was filtered giving Eu(**7**)$_3$ as a yellow solid (0.013 g, 57 %). FTIR (cm^{-1}) 3269, 3078, 2962, 1696, 1654, 1638, 1587, 1561, 1438, 1342, 1279, 1234, 1166, 1049, 1028, 906, 879, 845, 778, 739, 635, 572, 540, 516.

5.5.5.7 Synthesis of Tb(7)$_3$

7 (0.0265 g, 0.033 mmol) was combined with $Tb(CF_3SO_3)_3 \cdot 5H_2O$ (0.0076 g, 0.011 mmol) in 5 mL of DCE:EtOH (1:1) and was heated to 150 °C until dissolved. The solution was then microwaved for 30 minutes, and then subjected to vapour diffusion of diethyl ether once cooled. The complex precipitated as a light yellow powder, which was filtered giving Tb(**7**)$_3$ as a yellow solid (0.016 g, 62%). FTIR (cm^{-1}) 3306, 3138, 2961, 1695, 1649, 1640, 1587, 1563, 1545, 1526, 1439, 1384, 1342, 1280, 1233, 1167, 1050, 1028, 906, 879, 845, 778, 738, 636, 571, 541, 516.

5.5.5.8 Synthesis of Dy(7)$_3$

7 (0.0201 g, 0.025 mmol) was combined with $Dy(CF_3SO_3)_3 \cdot 8H_2O$ (0.062 g, 0.0083 mmol) in 5 mL of DCE:EtOH (1:1) and was heated to 150 °C until dissolved. The solution was then microwaved for 30 minutes, and then subjected to vapour diffusion of diethyl ether once cooled. The complex precipitated as a light-yellow powder, which was filtered giving Dy(**7**)$_3$ as a yellow solid (0.014 g, 74 %). FTIR (cm^{-1}) 3338, 3138, 2962, 2330, 2207, 1693, 1672, 1650, 1624, 1586, 1523, 1438, 1384, 1342, 1304, 1283, 1233, 1201, 1169, 1146, 1132, 1114, 1056, 1046, 1030, 1003, 961, 905, 879, 844, 777, 737, 698, 637, 564, 541, 524, 500, 476, 449 ,427.

5.5.5.9 Synthesis of La(7)$_3$

7 (0.0201 g, 0.033 mmol) was combined with $La(CF_3SO_3)_3 \cdot 9H_2O$ (0.0062 g, 0.0083 mmol) in 5 mL of DCE:EtOH (1:1) and was heated to 150 °C until dissolved. The solution was then microwaved for 30 minutes, and then subjected to vapour diffusion of diethyl ether once cooled. The complex precipitated as a light-yellow powder, which was filtered giving La(**7**)$_3$ as a yellow solid (0.012 g, 64 %). FTIR (cm^{-1}) 3338, 3139, 2961, 2330, 1695, 1650, 1587, 1539, 1439, 1385, 1343, 1280, 1233, 1168, 1048, 1028, 906, 879, 845, 777, 738, 636, 571, 540, 515, 427.

5.5.5.10 Synthesis of Eu(8)$_3$

8 (0.0312 g, 0.064 mmol) was combined with $Eu(CF_3SO_3)_3 \cdot 6H_2O$ (0.0148 g, 0.021 mmol) and 1 equivalent of triethylamine in 5 mL of DCE:EtOH (1:1). The brown solution was then subjected to vapour diffusion of diethyl either, yielding a brown film. The solution was decanted, and the brown film collected, yielding Eu(**8**)$_3$ as a brown solid (0.023 g, 70 %). LRMS *m/z* = 852.80 [Eu(**8**)$_3$ + 2Na]$^{2+}$ (calc. for $(C_{90}H_{72}N_{15}O_9EuNa_2)^{2+}$, 852.90) and *m/z* = 1682.35 [Eu(**8**)$_3$ + Na]$^+$ (calc. for $(C_{90}H_{72}N_{15}O_9EuNa)^+$, 1682.58). FTIR ($cm^{-1}$) 3268, 3040, 2943, 2342, 2330, 1632, 1588, 1564, 1463, 1431, 1390, 1278, 1240, 1223, 1157, 1084, 1060, 1028, 893, 843, 818, 800, 757, 722, 682, 660, 636, 573, 516, 411.

5.5.5.11 Synthesis of La(8)$_3$

8 (0.0125 g, 0.026 mmol) was combined with $La(CF_3SO_3)_3 \cdot 9H_2O$ (0.064 g, 0.009 mmol) and 1 equivalent of triethylamine in 5 mL of DCE:EtOH (1:1). The brown solution was then subjected to vapour diffusion of diethyl either, yielding a brown film. The solution was decanted, and the brown film collected, yielding La(**8**)$_3$ as a brown solid. (0.01 g, 72 %). LRMS *m/z* = 1669.65 [La(**8**)$_3$ + Na]$^+$ (calc. for $(C_{90}H_{72}N_{15}O_9LaNa)^+$, 1669.52). FTIR ($cm^{-1}$) 3253, 3040, 2942, 1633, 1588, 1566, 1464, 1432, 1391, 1279 ,1241, 1224, 1158, 1084, 1048, 1029, 892, 843, 818, 800, 757, 722, 682, 660, 636, 573, 516, 414.

5.5 Acknowledgements

I would like to acknowledge Jade Pope and Erin Moffet for aid in photography; Associate Professor Jenny Malmström and Dr Anaïs Chalard from Auckland University for teaching and running AFM measurements; Dr Jack Chen from Auckland University of Technology for allowing me access to the Agilent Technologies Cary Eclipse spectrophotometer for phosphorescent measurements; and Jenny Stockdell from Waikato University, for teaching me and allowing me to run Bruker Daltonics MicrOTOF™ Spectrometer for HRMS.

5.6 References

1. M. K. Bera, P. Pal and S. Malik, *J. Mater. Chem. C*, 2020, **8**, 788-802.
2. S. K. Behera, S. Y. Park and J. Gierschner, *Angew. Chem. Int. Ed.*, **60**, 22624-22638.
3. Y. Feng, J. Cheng, L. Zhou, X. Zhou and H. Xiang, *Analyst*, 2012, **137**, 4885-4901.
4. Y. Zhou and B. Yan, *J. Mater. Chem. C*, 2015, **3**, 9353-9358.
5. M. H. Lee, J. S. Kim and J. L. Sessler, *Chem. Soc. Rev.*, 2015, **44**, 4185-4191.
6. T. Sun, Y. Gao, Y. Du, L. Zhou and X. Chen, *Front. Chem.*, 2021, **8**, 2296-2646.
7. J. Wang, Y. Suffren, C. Daiguebonne, S. Freslon, K. Bernot, G. Calvez, L. Le Pollès, C. Roiland and O. Guillou, *Inorg. Chem.*, 2019, **58**, 2659-2668.
8. A. K. Gangwar, Kanika, G. Kedawat, G. S. Papanai and B. K. Gupta, *J. Mater. Chem. C*, 2019, **7**, 13867-13877.
9. M. A. Hernández-Rodríguez, C. D. S. Brites, G. Antorrena, R. Piñol, R. Cases, L. Pérez-García, M. Rodrigues, J. A. Plaza, N. Torras, I. Díez, A. Millán and L. D. Carlos, *Adv. Opt. Mater.*, 2020, **8**, 2000312.
10. D. Kim, K. Jeong, J. E. Kwon, H. Park, S. Lee, S. Kim and S. Y. Park, *Nat. Commun.*, 2019, **10**, 3089.
11. S. SeethaLekshmi, A. R. Ramya, M. L. P. Reddy and S. Varughese, *J. Photchem. Photobiol.*, 2017, **33**, 109-131.
12. T. Wang, P. Li and H. Li, *ACS Appl. Mater. Interfaces*, 2014, **6**, 12915-12921.
13. H. Liu, T. Chu, Z. Rao, S. Wang, Y. Yang and W.-T. Wong, *Adv. Opt. Mater.*, 2015, **3**, 1545-1550.
14. A. Sharma and T. D. Das, *Optik*, 2020, **221**, 165350.
15. S. Reineke, M. Thomschke, B. Lüssem and K. Leo, *RMP*, 2013, **85**, 1245-1293.
16. J. Moreira, A. C. Vale and N. M. Alves, *J. Mater. Chem. B*, 2021, **9**, 3778-3799.
17. J. Y. Na, B. Kang, D. H. Sin, K. Cho and Y. D. Park, *Sci. Rep.*, 2015, **5**, 13288.
18. K. Norrman, A. Ghanbari-Siahkali and N. B. Larsen, *Annu. Rep. Prog. Chem., Sect. C: Phys.*, 2005, **101**, 174-201.
19. N. Sahu, B. Parija and S. Panigrahi, *India J. Phys.*, 2009, **83**, 493-502.
20. M. Tyona, *Adv. Mater. Res.*, 2013, **2**, 195-208.
21. N. Chapman, M. Chapman and W. B. Euler, *Polymers*, 2021, **13**, 2184.
22. J.-H. Jou, S. Sahoo, D. K. Dubey, R. A. K. Yadav, S. S. Swayamprabha and S. D. Chavhan, *J. Mater. Chem. C*, 2018, **6**, 11492-11518.
23. J. Cordoba, M. Mera-Córdoba and C. A. Cordoba, *Rev*, 2017, **26**, 123.
24. M. Shibata, Y. Sakai and D. Yokoyama, *J. Mater. Chem. C*, 2015, **3**, 11178-11191.
25. C. J. Christopherson, D. M. Mayder, J. Poisson, N. R. Paisley, C. M. Tonge and Z. M. Hudson, *ACS Appl. Mater. Interfaces*, 2020, **12**, 20000-20011.

26. E. E. Rudebeck, R. P. Cox, T. D. M. Bell, R. Acharya, Z. Feng, N. Gueven, T. D. Ashton and F. M. Pfeffer, *Chem. Commun.*, 2020, **56**, 6866-6869.
27. Y. Yin, Z. Chen, C. Fan, G. Liu and S. Pu, *ACS Omega*, 2019, **4**, 14324-14332.
28. J. E. Elbert, S. Paulsen, L. Robinson, S. Elzey and K. Klein, *J. Photochem. Photobiol*, 2005, **169**, 9-19.
29. M. A. Alcala, C. M. Shade, H. Uh, S. Y. Kwan, M. Bischof, Z. P. Thompson, K. A. Gogick, A. R. Meier, T. G. Strein, D. L. Bartlett, R. A. Modzelewski, Y. J. Lee, S. Petoud and C. K. Brown, *Biomaterials*, 2011, **32**, 9343-9352.
30. C. S. Bonnet, M. Devocelle and T. Gunnlaugsson, *Org. Biomol. Chem.*, 2012, **10**, 126-133.
31. A. B. Carter, N. Zhang, I. A. Kühne, T. D. Keene, A. K. Powell and J. A. Kitchen, *ChemistrySelect*, 2019, **4**, 1850-1856.
32. K. R. Johnson and A. de Bettencourt-Dias, *Inorg. Chem.*, 2019, **58**, 13471-13480.
33. V. F. Plyusnin, A. S. Kupryakov, V. P. Grivin, A. H. Shelton, I. V. Sazanovich, A. J. H. M. Meijer, J. A. Weinstein and M. D. Ward, *Photochem. Photobiol. Sci.*, 2013, **12**, 1666-1679.
34. D. L. Reger, A. Leitner and M. D. Smith, *Cryst. Growth Des.*, 2015, **15**, 5637-5644.
35. D. L. Reger, A. P. Leitner and M. D. Smith, *Cryst. Growth Des.*, 2016, **16**, 527-536.
36. A. H. Shelton, I. V. Sazanovich, J. A. Weinstein and M. D. Ward, *Chem. Commun.*, 2012, **48**, 2749-2751.
37. J. Tang, H. Yang, J. Liu, Y. Wang, X. Yin, R. Wang, L. Huang and Z. Huang, *Opt. Mater.*, 2010, **32**, 1417-1422.
38. Z. Wang, N. Liu, H. Li, P. Chen and P. Yan, *Eur. J. Inorg. Chem.*, 2017, **2017**, 2211-2219.
39. J. Zhang, H. Li, P. Chen, W. Sun, T. Gao and P. Yan, *J. Mater. Chem. C*, 2015, **3**, 1799-1806.
40. M. de Sousa, M. Kluciar, S. Abad, M. A. Miranda, B. de Castro and U. Pischel, *Photochem. Photobiol. Sci.*, 2004, **3**, 639-642.
41. D. W. Cho and D. W. Cho, *New J. Chem.*, 2014, **38**, 2233-2236.
42. D. W. Cho, M. Fujitsuka, K. H. Choi, M. J. Park, U. C. Yoon and T. Majima, *J. Phys. Chem. B*, 2006, **110**, 4576-4582.
43. M. Licchelli, A. O. Biroli, A. Poggi, D. Sacchi, C. Sangermani and M. Zema, *Dalton Trans.*, 2003, 4537-4545.
44. S. Bhowmik, S. Banerjee and U. Maitra, *Chem. Commun.*, 2010, **46**, 8642-8644.
45. M. N. Bochkarev, *Chem. Rev.*, 2002, **102**, 2089-2118.
46. M. F. Ferreira, G. Pereira, A. F. Martins, C. I. O. Martins, M. I. M. Prata, S. Petoud, E. Toth, P. M. T. Ferreira, J. A. Martins and C. F. G. C. Geraldes, *Dalton Trans.*, 2014, **43**, 3162-3173.
47. T. M. George, S. Varughese and M. L. P. Reddy, *RSC Adv.*, 2016, **6**, 69509-69520.
48. R. Hueting, M. Tropiano and S. Faulkner, *RSC Adv.*, 2014, **4**, 44162-44165.
49. P. Kumar, S. Soumya and E. Prasad, *ACS Appl. Mater. Interfaces*, 2016, **8**, 8068-8075.
50. D. Lionetti, V. W. Day and J. D. Blakemore, *Dalton Trans.*, 2017, **46**, 11779-11789.
51. J. Park and M. Oh, *CrystEngComm*, 2016, **18**, 8372-8376.
52. S. J. A. Pope, *Polyhedron*, 2007, **26**, 4818-4824.
53. M. Poznik, U. Maitra and B. König, *Org. Biomol. Chem.*, 2015, **13**, 9789-9792.
54. N. M. Selivanova, A. T. Gubaidullin, K. A. Romanova and Y. G. Galyametdinov, *JSD*, 2017, **20**, 309-319.
55. T. A. Shakhverdov, V. N. Kalinin and R. Érgashev, *Theor. Exp. Chem.*, 1987, **23**, 281-288.
56. J. S. Sohna and F. Fages, *Tetrahedron Lett.*, 1997, **38**, 1381-1384.
57. A. Watkis, R. Hueting, T. J. Sørensen, M. Tropiano and S. Faulkner, *Chem. Commun.*, 2015, **51**, 15633-15636.
58. S. Bhattacharjee and S. Bhattacharya, *J. Mater. Chem.*, 2014, **2**, 17889-17898.
59. J. X. Li, Q. L. Guan, Y. Wang, Z. X. You, Y. H. Xing, F. Y. Bai and L. X. Sun, *New J. Chem.*, 2020, **44**, 1446-1454.
60. U. H. Sk and S. Bhattacharya, *Environ. Toxicol. Pharmacol.*, 2006, **22**, 298-308.

61. H. Ben El Ayouchia, L. Bahsis, H. Anane, L. R. Domingo and S.-E. Stiriba, *RSC Adv.*, 2018, **8**, 7670-7678.
62. Y. Zhao, J. Li, H. Gu, D. Wei, Y. C. Xu, W. Fu and Z. Yu, *Interdiscip Sci*, 2015, **7**, 211-220.
63. F. Grepioni, S. d'Agostino, D. Braga, A. Bertocco, L. Catalano and B. Ventura, *J. Mater. Chem. C*, 2015, **3**, 9425-9434.
64. S. Tsuzuki and A. Fujii, *Phys. Chem. Chem. Phys.*, 2008, **10**, 2584-2594.
65. J. Gawronski, K. Gawronska, P. Skowronek and A. Holmén, *J. Org. Chem.*, 1999, **64**, 234-241.
66. A. G. Crawford, A. D. Dwyer, Z. Liu, A. Steffen, A. Beeby, L.-O. Pålsson, D. J. Tozer and T. B. Marder, *J. Am. Chem. Soc.*, 2011, **133**, 13349-13362.
67. Y. Niko, Y. Hiroshige, S. Kawauchi and G.-i. Konishi, *Tetrahedron*, 2012, **68**, 6177-6185.
68. *ReactLabTM EQUILIBRIA (1.1), Jplus Consulting Multivariate Analytical Technologies, Kilaben Bay, Australia, 2022*.
69. O. Kotova, S. Blasco, B. Twamley, J. O'Brien, R. D. Peacock, J. A. Kitchen, M. Martínez-Calvo and T. Gunnlaugsson, *Chem. Sci.*, 2015, **6**, 457-471.
70. C. Lee, W. Yang and R. G. Parr, *Phys. Rev. B Condens. Matter*, 1988, **37**, 785-789.
71. P. J. Stephens, F. J. Devlin, C. F. Chabalowski and M. J. Frisch, *Phys. Chem.*, 1994, **98**, 11623-11627.
72. S. H. Vosko, L. Wilk and M. Nusair, *Can. J. Phys.*, 1980, **58**, 1200-1211.
73. R. Krishnan, J. S. Binkley, R. Seeger and J. A. Pople, *Chem. Phys.*, 1980, **72**, 650-654.
74. M. Dolg, H. Stoll, A. Savin and H. Preuss, *Theor. Chim. Acta*, 1989, **75**, 173-194.
75. M. Dolg, H. Stoll and H. Preuss, *Theor. Chim. Acta*, 1993, **85**, 441-450.
76. A. Weigand, X. Cao, J. Yang and M. Dolg, *Theor. Chem. Acc.*, 2010, **126**, 117-127.
77. *Gaussian 16, Revision C.01,* Frisch, M. J.; Trucks, G. W.; Schlegel, H. B.; Scuseria, G. E.; Robb, M. A.; Cheeseman, J. R.; Scalmani, G.; Barone, V.; Petersson, G. A.; Nakatsuji, H.; Li, X.; Caricato, M.; Marenich, A. V.; Bloino, J.; Janesko, B. G.; Gomperts, R.; Mennucci, B.; Hratchian, H. P.; Ortiz, J. V.; Izmaylov, A. F.; Sonnenberg, J. L.; Williams-Young, D.; Ding, F.; Lipparini, F.; Egidi, F.; Goings, J.; Peng, B.; Petrone, A.; Henderson, T.; Ranasinghe, D.; Zakrzewski, V. G.; Gao, J.; Rega, N.; Zheng, G.; Liang, W.; Hada, M.; Ehara, M.; Toyota, K.; Fukuda, R.; Hasegawa, J.; Ishida, M.; Nakajima, T.; Honda, Y.; Kitao, O.; Nakai, H.; Vreven, T.; Throssell, K.; Montgomery, J. A., Jr.; Peralta, J. E.; Ogliaro, F.; Bearpark, M. J.; Heyd, J. J.; Brothers, E. N.; Kudin, K. N.; Staroverov, V. N.; Keith, T. A.; Kobayashi, R.; Normand, J.; Raghavachari, K.; Rendell, A. P.; Burant, J. C.; Iyengar, S. S.; Tomasi, J.; Cossi, M.; Millam, J. M.; Klene, M.; Adamo, C.; Cammi, R.; Ochterski, J. W.; Martin, R. L.; Morokuma, K.; Farkas, O.; Foresman, J. B.; Fox, D. J. *Gaussian, Inc., Wallingford CT, 2016*.
78. K. T. Hua, J. Xu, E. E. Quiroz, S. Lopez, A. J. Ingram, V. A. Johnson, A. R. Tisch, A. de Bettencourt-Dias, D. A. Straus and G. Muller, *Inorg. Chem.*, 2012, **51**, 647-660.
79. K. Binnemans, *Coord. Chem. Rev.*, 2015, **295**, 1-45.
80. R. G. Larson and T. J. Rehg, in *Liquid Film Coating: Scientific principles and their technological implications*, eds. S. F. Kistler and P. M. Schweizer, Springer Netherlands, Dordrecht, 1997, pp. 709-734.
81. Y.-X. Yuan, H.-s. Peng, J.-T. Ping, X.-H. Wang and F.-T. You, *Biomed Res. Int.*, 2015, **2015**, 245031.
82. *LED ColorCalculator (7.77), OSRAM SYLVANIA Inc., 2022*.
83. G. Sheldrick, *Acta Crystallogr. A*, 2008, **64**, 112-122.
84. O. V. Dolomanov, L. J. Bourhis, R. J. Gildea, J. A. K. Howard and H. Puschmann, *J. Appl. Crystallogr.*, 2009, **42**, 339-341.
85. D. Nečas and P. Klapetek, *Open Physics*, 2012, **10**, 181-188.
86. G. A. Crosby and J. N. Demas, *J. Phys. Chem. A.*, 1971, **75**, 991-1024.
87. A. S. Chauvin, F. Gumy, D. Imbert and J. C. G. Bünzli, *Spectrosc. Lett*, 2004, **37**, 517-532.
88. A. S. Chauvin, F. Gumy, D. Imbert and J. C. G. Bünzli, *Spectrosc. Lett.*, 2007, **40**, 193-193.

6. Larger Assemblies

6.1 Introduction

Three ligands have been successfully synthesised (**9**, **10** and **11**, see Figure 6.1) for the development of multi-metal and mixed metal self-assembling systems. It is important to note that the research in this chapter is in the initial stages of development. Unfortunately, due to the impact of COVID, this topic has not been fully explored and thus this chapter will be a discussion on mainly ligand synthesis with some initial self-assembly studies. Nevertheless, it is worth noting that these systems have been developed and do demonstrate that our synthetic strategies can be used to easily develop ligands for multi-metal architectures.

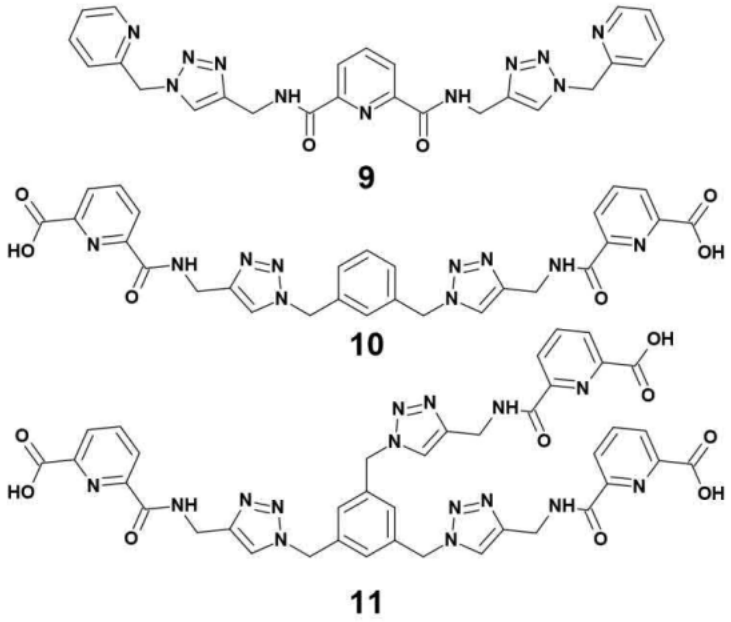

*Figure 6.1.. Ligands **9**, **10** and **11**.*

As showcased in Section 2.2.2, ligand architectures containing multiple PDA motifs are not uncommon. In the presence of Ln^{3+}, these ligand architectures can form multi-nuclear assemblies incorporating multiple Ln^{3+} within a single ligand thus improving lanthanide emission intensity. These ligand architectures take advantage of the predictable PDA coordination with Ln^{3+} and through proper design of both rigidity and length between PDA binding pockets, can lead to complex metallo-supramolecular architectures.[1]

The simplest version is the inclusion of two PDA motifs into a single ligand architecture. As discussed in Section 2.2.2, these in the presence of Ln^{3+} predominately form di-nuclear helicate assemblies ($Ln_2\mathbf{L}_3$),[2-6] but have also been shown to form complex tetrahedral ($Ln_4\mathbf{L}_6$) and cubic ($Ln_8\mathbf{L}_{12}$) cage assemblies by slightly modifying the spacer between the PDA binding pockets (Figure 6.2).[7, 8] Tris-PDA ligand systems predominantly form tetrahedral cage assemblies ($Ln_4\mathbf{L}_3$),[9-13] but also have been developed into encapsulating mono-nuclear Ln(**L**) complexes.[14-16] Systems additionally go beyond di- and tri-nuclear to form even more complex architectures, examples being the tetra-PDA ligand forming tetrahedral-helicate Eiffel towers ($Ln_5\mathbf{L}_3$)[17] and the hexa-PDA ligand which forms octa-nuclear expanded tetrahedral cage assemblies (Figure 2.14).[18]

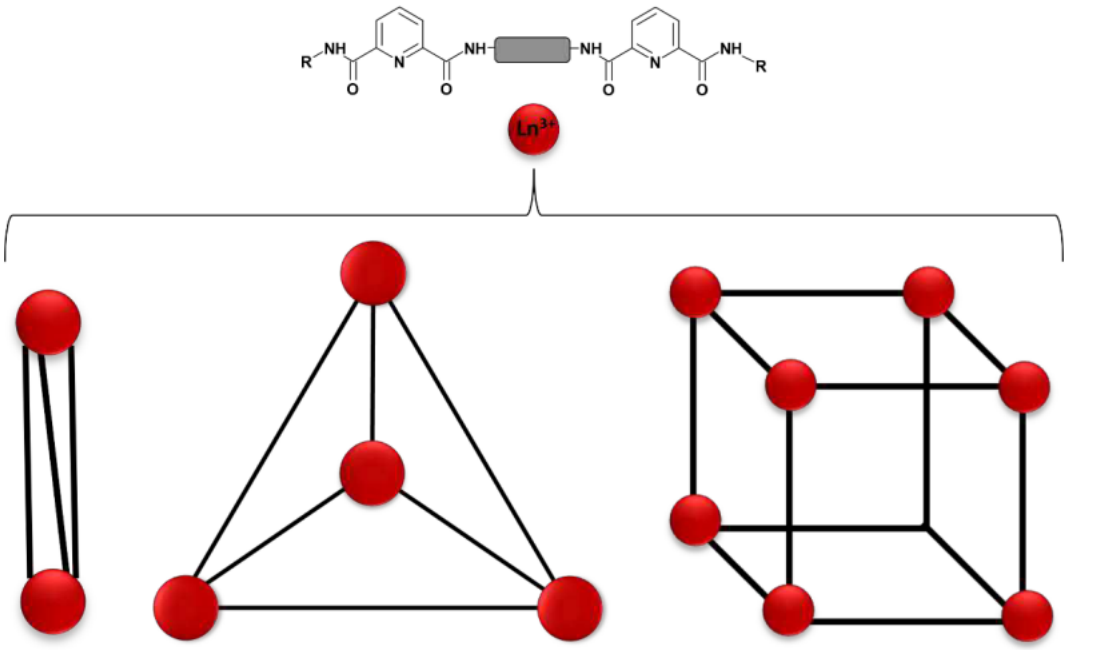

Figure 6.2.. Bis-PDA based ligands,. which in the presence of Ln^{3+}. can form helicate assemblies ($Ln_2\mathbf{L}_3$),. along with complex tetrahedral ($Ln_4\mathbf{L}_6$). and cubic ($Ln_8\mathbf{L}_{12}$). cages..

Multi-nuclear assemblies not only focus on the incorporation of multiple Ln^{3+}, but also mixed metal systems which incorporate both Ln^{3+} and *d*-block metals, however these are relatively rare for PDA based systems.[19-28] Incorporating *d*-block metals into the Ln^{3+} complex is commonly done for two main reasons, predictability and complexity. *d*-Block metal coordination is generally considered more predictable and well established, which allows for the predesign of complex 3D architectures and allows access to a range of different building blocks for 3D architecture not easily accessible to Ln^{3+}. Furthermore, certain combinations of *d*-block metals and Ln^{3+} can beneficially modify the photophysical and/or magnetic properties of Ln^{3+} or the transition metals.

Focusing on the more relevant Ln^{3+} photophysical properties, the incorporation of some *d*-block metals allows for new pathways to populate Ln^{3+} excited states. In most cases when Ln^{3+} are sensitized by *d*-block metals MLCT states normally take part. MLCT states are uncommon for Ln^{3+} but are very common for some *d*-block metals.[29, 32, 33] The use of *d*-block metals to populate lanthanide excited states can be ideal for a range of specific applications. Incorporation of *d*-block metals can shift the excitation absorption region into the visible, which is ideal for biological probe applications, removing the need for harmful UV irradiation. Furthermore MLCT state energy levels can be relatively low, ideal for population of NIR emitting lanthanides (which are more easily quenched by organic chromophores).[29, 33] In more specific systems, De Cola and co-workers were able to form a single component dual emissive Ir^{3+} and Eu^{3+} system (Figure 6.3). Excitation into the MLCT band of the Ir^{3+} results in both Ir^{3+} blue broad emission along with Eu^{3+} sharp red emission co-existing, resulting in white emission (CIE x,y = 0.28, 0.30).[34]

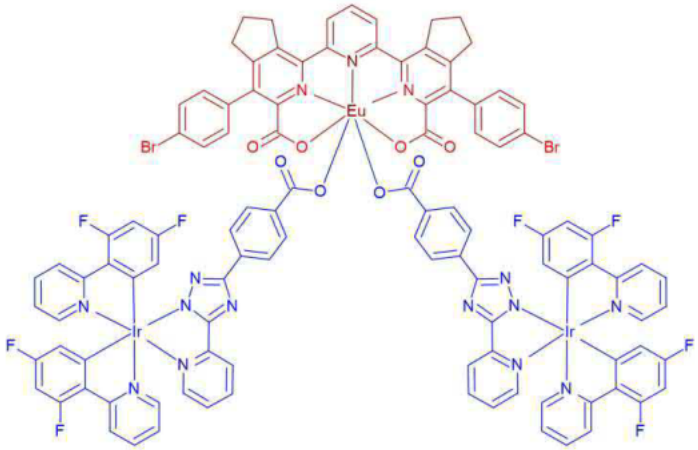

Figure 6.3.. De Cola and co-workers Ir^{3+} and Eu^{3+} complex capable of dual Ln^{3+} and d-block metal emission resulting in overall white emission..

Piguet and co-workers mixed metals system of Cr^{3+} / Er^{3+} / Cr^{3+} which formed a tri-metal triple stranded helicate (Figure 6.4) is a great example of how Ln^{3+} and *d*-block metal coexistence can lead to complex properties. The Cr^{3+} and Er^{3+} combination was shown to emit at 540 nm (green) associated with Er^{3+}. This emission is a result of excitation of both Cr^{3+} (λ_{ex} = 748 nm) which subsequently populates the Er^{3+} excited state, a complex up-conversion property ideal for solar waveguide applications.[35]

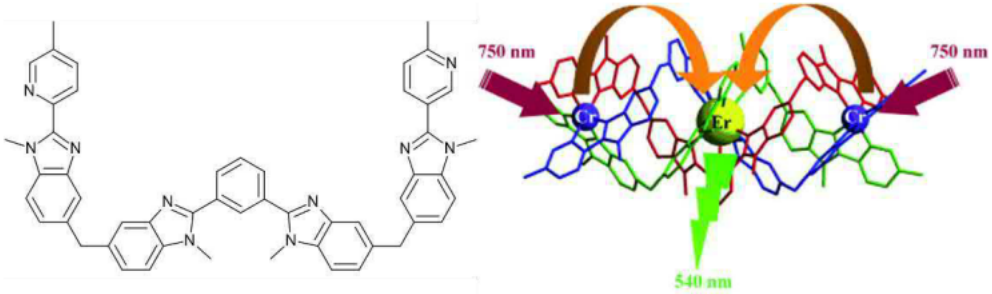

Figure 6.4.. Piguet and co-workers Cr^{3+}/Er^{3+}/Cr^{3+} tri-metal triple stranded helicate capable of UC.. Image adapted with permission from L.. Aboshyan-Sorgho,. C.. Besnard,. P.. Pattison,. K.. R.. Kittilstved,. A.. Aebischer,. J.-C.. G.. Bünzli,. A.. Hauser and C.. Piguet, Angew. Chem. Int. Ed.*,. 2011,. **50**,. 4108-4112.. Copyright 2022,. John Wiley and Sons..*

As stated Ln^{3+} and transition metal mixtures are relatively uncommon for PDA based systems. The majority of these cases focus on mixed metals systems for magnetism which is beyond the scope of this study,[19-25] and to the best of our knowledge few examples use them for photophysical or structure directing properties.[26-28] Sun and co-workers demonstrated how the combination of predictable coordination of PDA with Ln^{3+} combined with the predictable coordination of transition metals can be used to predesign and develop complex 3D metallo-supramolecular architectures.[26] In one instance they formed complex 3D trigonal bipyramidal cages (top of Figure 6.5), made from two building blocks, these being saddle-shaped dipalladium corners, which are connected to the end of a chiral PDA ligand.[27] Replacing the Pd^{2+} for Pt^{2+} they were able to form square macrocycles, utilizing the square planar geometry of Pt^{2+} coordinated to two PDA molecules *via* the back of the pyridyl antenna (bottom of Figure 6.5). This creates a ≈ 90 ° v-shaped coordination, such that in the presence of Eu^{3+} the metallo ligand forms a square macrocycle. It is worth noting that the quantum yield of this system when populated from the MLCT state of Pt^{2+} is 80 %, significantly higher than PDA based ligand systems.[26]

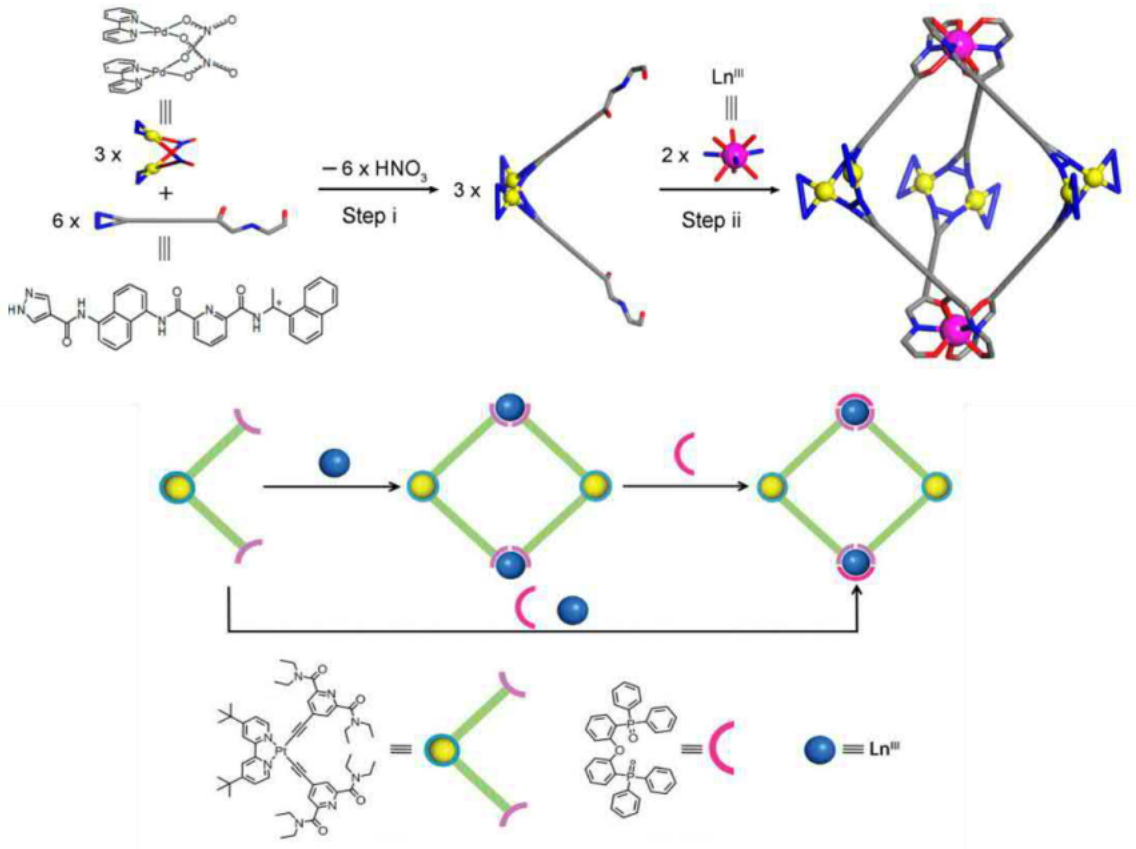

Figure 6.5.(Top). Sun. and. co-workers. 3D. trigonal. bipyramidal. cages.. Image. adapted. with. permission. from. Z.. Wang,. L.-P.. Zhou,. T.-H. Zhao,. L.-X.. Cai,. X.-Q.. Guo,. P.-F.. Duan. and. Q.-F.. Sun,. Inorg. Chem.*,. 2018,.* ***57****,. 7982-7992.. Copyright. 2022,. American. Chemical. Society. (Bottom). Sun. and. co-workers. square. like. macrocycle.. Image. adapted. with. permission. from. Q.-Y.. Zhu,. L.-P.. Zhou. and. Q.-F.. Sun,.* Dalton Trans.*,. 2019,.* ***48****,. 4479-4483.. Copyright. 2022,. Royal. Society. of. Chemistry..*

The design of **9** has the incorporation of a (2-pyridylmethyl)-1-H-1,2,3-triazole motif forming an N_2 pocket as a secondary binding pocket for *d*-block metals. It was hoped that this would lead to the formation of self-assembled tri-metal helicate architectures when in the presence of Ln^{3+} and *d*-block metals, as seen in Figure 6.6. Mixed helicate systems have been synthesised before but to the best of our knowledge not with the PDA motif.[35-38] This ligand was designed to ideally eventually mirror the UC properties of Piguet and co-workers Cr^{3+} / Er^{3+} / Cr^{3+} tri-metal triple stranded helicate, but initially Zn^{2+} was used, to simplify NMR characterisation.[29]

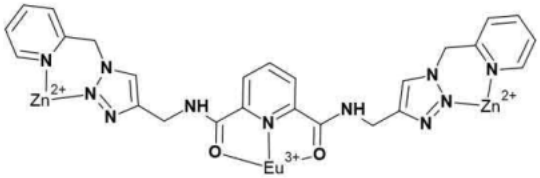

*Figure 6.6. **9** tridentate binding pockets in which would ideally form a triple stranded helicate.*

Ligand architectures containing multiple PDC motifs for lanthanide assemblies are relatively novel, with only three known examples (**L**[32], **L**[33] and **L**[35], Figures 2.15-16).[39, 40] As discussed in Section 2.3, Horrocks and co-worker developed two ligands (**L**[32] and **L**[33]) for the formation of neutral helicate assemblies (Ln_2L_3). From self-assembly titrations it is indicated that the helicate assemblies are forming in solution, but lanthanide complexes are not isolated and helicate assemblies were not confirmed.[39] In comparison, Bünzli, Piguet and co-workers tripodal ligand (**L**[35]) forms encapsulating nine-coordinated podates (Ln**L**[35]) in the presence of Ln^{3+} and was confirmed with a crystal structure (Figure 2.16), but the complex was found to be very insoluble.[40] Ligands **10** and **11** have been developed to further investigate the potential for ligand architectures which contain multiple PDC motifs (Figure 6.7). With similar design to the previous systems,[39, 40] **10** has been designed with the aim to develop helicate architectures, while **11** has been designed for the likely formation of encapsulating nine-coordinated podates or potential $Ln_4(L)_4$ cage formation.

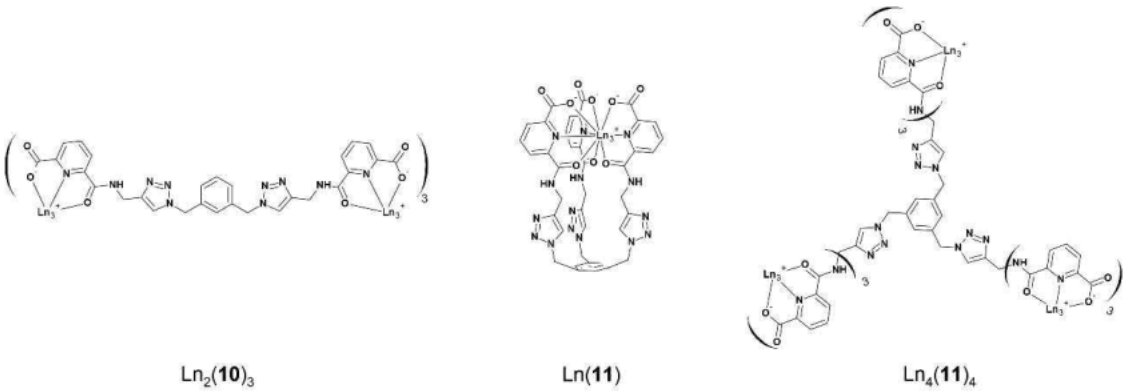

$Ln_2(\mathbf{10})_3$ $Ln(\mathbf{11})$ $Ln_4(\mathbf{11})_4$

*Figure 6.7. Potential complex formations of ligands **10** and **11**.*

6.2 Results and Discussion

6.2.1 Ligand Synthesis and Characterisation

Synthesis of **9** was relatively straight forward and followed the same one-pot multi-component CuAAC reaction and workup as developed in chapter 3. Bis-alkyne (**B**) underwent a $CuSO_4 \cdot 5H_2O$ catalysed cyclization in a DMF:H_2O (4:1) solvent mixture with 2-(azidomethyl)pyridine, which was formed *in situ* from NaN_3 and 2-(bromomethyl)pyridine hydrobromide. This reaction was high yielding (91 %).

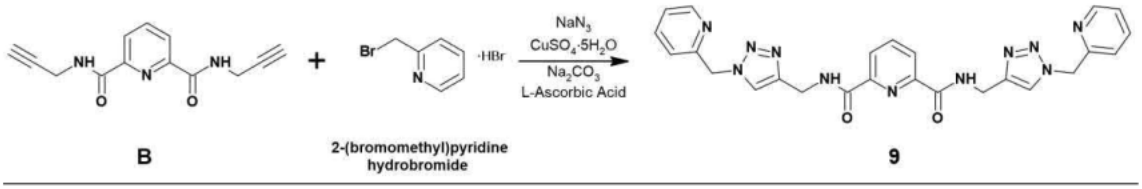

*Scheme 6.1. Synthesis of ligand **9**.*

In comparison syntheses of **10** and **11** was not as straight forward, but eventually they were successfully synthesised in a similar manner. In both cases, initial synthesis trials attempted to avoid making the azide separately by using the one-pot multi-component CuAAC reaction conditions, with α,α′-dibromo-m-xylene or 1,2,3-tris(bromomethyl)benzene respectively. This was because both azide precursors were above the relatively safe isolation ratio of $N_c/N_N \geq 3$, with α,α′-diazido-m-xylene and 1,2,3-tris(azidomethyl)benzene having a N_c/N_N ratio of 1.3 and 1 respectively.[41] Both azides have been isolated as solids before but for safety reasons they ideally would remain in solution.[42, 43] Unfortunately, the one-pot multi-component CuAAC reaction with the bromide precursors showed no indication of product formation. To overcome this, following a similar synthetic procedure in chapter 4 and 5, the azide would be pre-formed, only this time they would remain in solution and not be isolated, assuming 100 % theoretical yield.

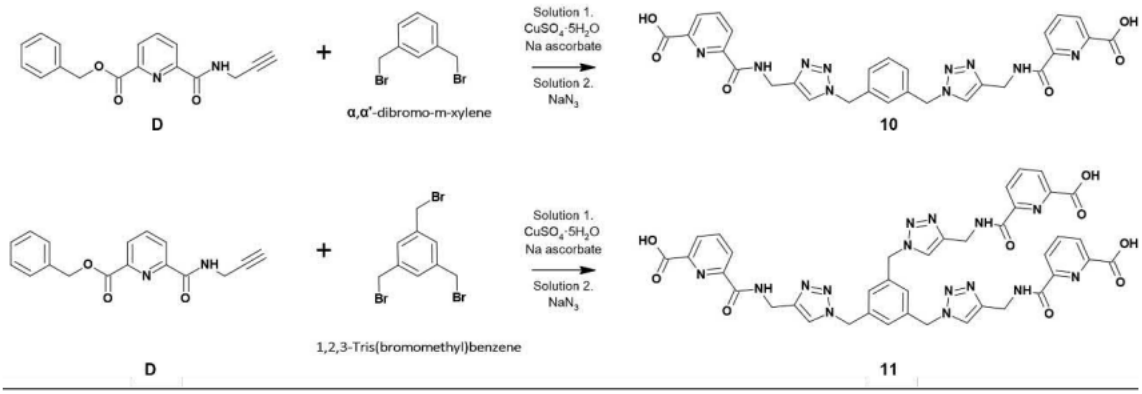

*Scheme 6.2. Synthesis of ligands **10** and **11**.*

As done with previous PDC systems, mono-alkyne (**D**) was stirred and heated in a DMF:H_2O solution, with $CuSO_4 \cdot 5H_2O$ catalyst and sodium ascorbate, pre-forming the Cu(I)-acetylide or π,σ-bis(Cu) intermediates prior to addition of azide,[44] indicated by a solution colour change to yellow or orange. To this the assumed azide, formed in solution, was added dropwise during which a notable darkening of the solution occurred. In both cases this indicated successful formation of **10** and **11** protected intermediates but were forming brown or green oils respectively that were not easily purified. This was solved by moving onto the next deprotection stage without further purification, using the same benzyl ester deprotection method used in chapter 4 and 5. Ligands **10** and **11** were successfully synthesised, but remained as oils. However, the addition of 2 M HCl caused the precipitation of both products leaving behind impurities. In the case of **11**, the solid required extensive stirring in 2 M HCl to remove excess copper, slowly changing the solid from green to off-white, leaving behind a green copper solution. Synthesis of **10** and **11** were relatively low yielding (32 % and 37 % respectively), likely a result of assumed 100 % azide formation.

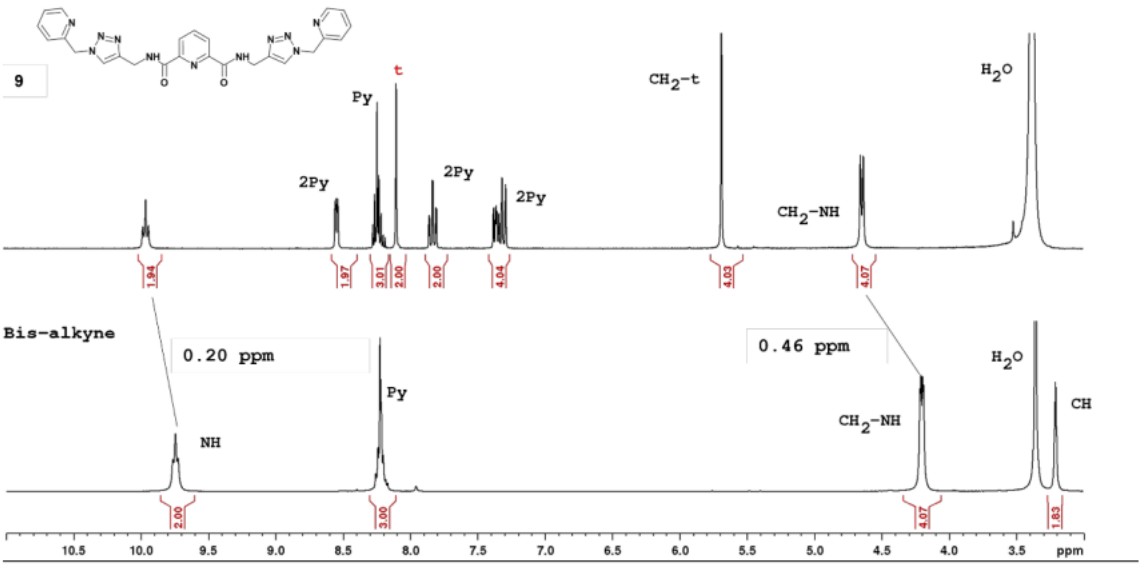

*Figure 6.8: ^{1}H NMR of **9** and bis-alkyne (**B**). Abbreviations: Py for PDA pyridine ring, 2Py for 2-pyridylmethyl and t for 1,2,3-triazole (300 MHz, DMSO-d_6).*

The successful synthesis of ligands **9**-**11** was confirmed by ^{1}H NMR, ^{13}C NMR, LRMS and FTIR (see Section 8.4). LRMS of ligands were found to match calculated peaks with *m/z* values of *m/z* = 510.15 [**9** + H]$^+$ (calc. for $C_{23}H_{24}N_{11}O_2^+$, 510.53), *m/z* = 595.15 [**10** - H]$^-$ (calc. for $C_{28}H_{23}N_{10}O_6^-$, 595.54) and *m/z* = 854.30 [**11** - H]$^-$ (calc. for $C_{39}H_{32}N_{15}O_9^-$, 854.77). ^{1}H NMR (Figure 6.8-9) for ligands showed the expected singlet signal at ≈ 8.1 ppm associated with the 1,2,3-triazole proton along with the associated downfield shifts in the NH (≈ 9.7 to 9.9 ppm for **9** and ≈ 8.9 to 9.7 ppm for **10** and **11**) and methylene linker (CH_2-NH, ≈ 4.1 to 4.6 ppm) signals, as well as the disappearance of the alkyne CH signal (3.2 - 3.1 ppm).

Ligands **10** and **11** also observed the disappearance of the benzyl ester proton signals (≈ 7.5 ppm), replaced by either a multiplet signal or a singlet signal at ≈ 7.3 ppm for **10** and **11** respectively. The signal associated with the benzyl linker is the only significant difference between the two similar ligands in ^{1}H NMR. ^{13}C NMR shows the expected number of carbon environments, along with the expected signals associated with the 1,2,3-triazole ring formation at 145 ppm and 123 ppm (Figure 6.10).

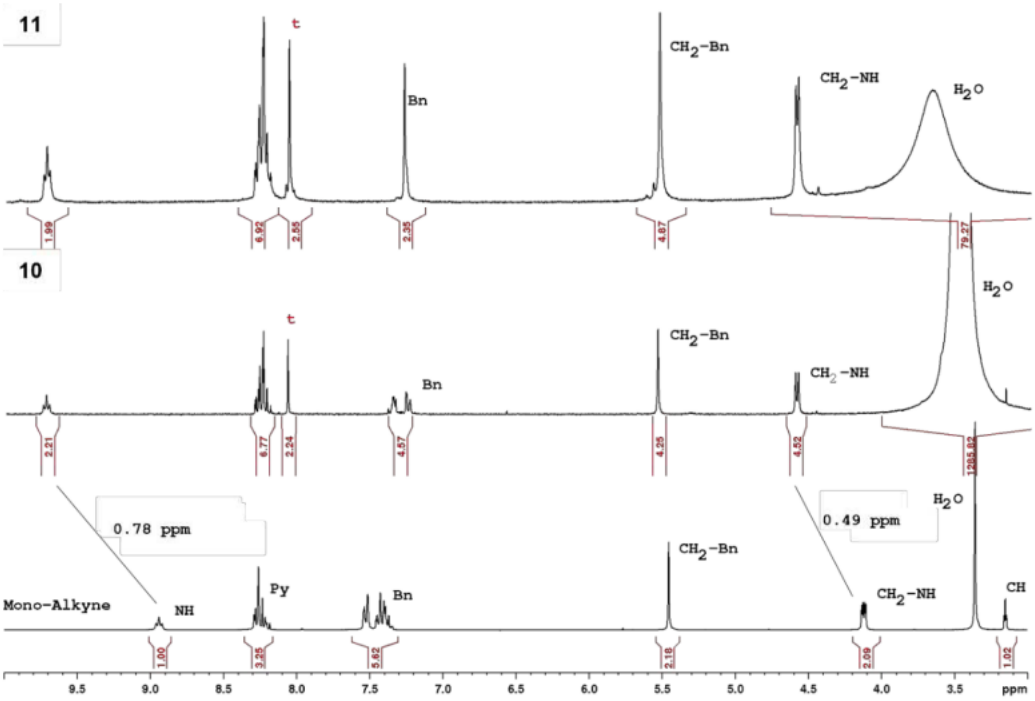

*Figure 6.9. ^{1}H NMR of **10**, **11** and mono-alkyne (**D**). Abbreviations: for PDA pyridine ring, Bn for benzyl ring and t for 1,2,3-triazole. (300 MHz, DMSO-d_6).*

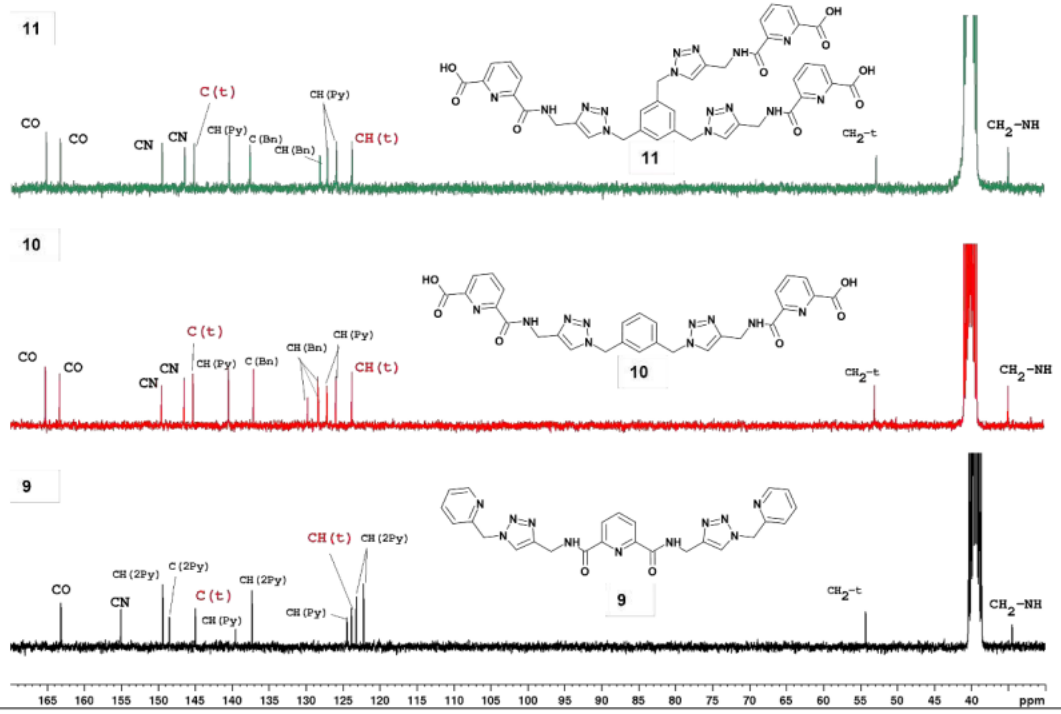

*Figure 6.10. ^{13}C NMR of **9-11** (75 MHz, DMSO-d_6). Abbreviations: Py for PDA pyridine ring, 2Py for 2-pyridylmethyl, Bn for benzyl ring and t for 1,2,3-triazole. CN for unsaturated carbons of PDA.*

6.2.2 Initial Complexation Results

As stated in the introduction (Section 6.1), lanthanide complexation studies for these systems are very limited, with only the initial trial complexation taking place. This is because from these initial results discussed below, early indications were noted that the ligands' designs would benefit from early modification rather than pursuing futile systems.

6.2.2.1 Ligand 9

9 was investigated for its potential formation of $[Ln(\mathbf{9})_3(Zn)_2]^{7+}$. This was carried out by a combination of computational calculations, *in situ* self-assembly titrations, and single crystal growth. From the combination of results, it was clear that although the system was indicated to be forming the $[Ln(\mathbf{9})_3]^{3+}$ species as previous bis-"clicked" systems had, formation of the mixed metal $[Ln(\mathbf{9})_3(Zn)_2]^{7+}$ was not definitive, with initial indications doubting the favoured formation of this mixed species. It is worth noting that a range of suspected $[Ln(\mathbf{9})_x(Zn)_x](CF_3SO_3)_3$ (where Ln = Eu^{3+}, Tb^{3+}, La^{3+}) were complexed, but unfortunately due to a combination of factors, obtaining definitive confirmation of molecular makeup has been elusive and thus will not be discussed here.

Computational Study

To gain insight into the potential structure of the desired complex, $[Eu(\mathbf{9})_3(Zn)_2]^{7+}$ was modelled in Spartan'18,[45] with a close to C_3 symmetry and a helical rotation of ligands (Figure 6.11). This model showed promise that the helicate or tri-metal complex could potentially be feasible; unfortunately optimization of this model in the Gaussian 16 software suite[46] indicated the opposite. It is worth noting that different variations of starting geometries and calculation

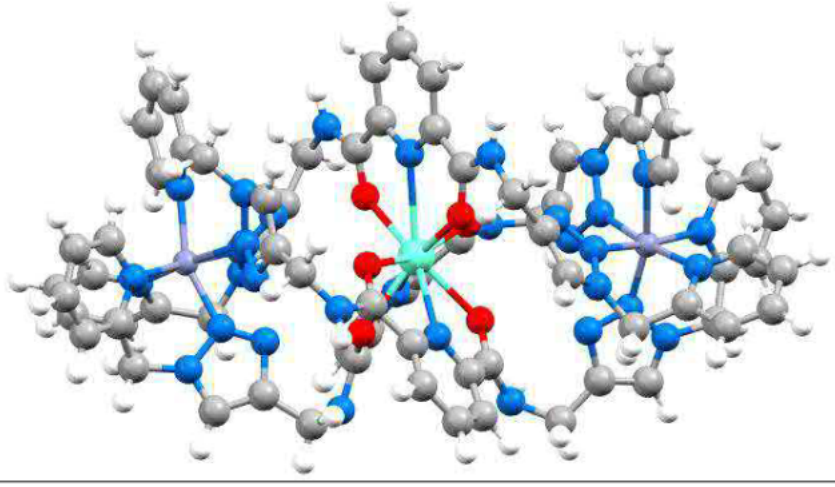

Figure 6.11.. Spartan model of $[Eu(\mathbf{9})_3(Zn)_2]^{7+}$.

conditions were tested, in most cases resulting in calculations which did not converge. However the resulting model could be subject to a molecular mechanics optimization, using an UFF[47] force field as parameters in the Gaussian 16 software suite.[46]

Table 6.1. Important bond lengths and angles of calculated $[Eu(\mathbf{9})_3(Zn)_2]^{7+}$ compared to calculated $[Eu(\mathbf{7})_3]^{3+}$.

Bond/Angle	Calculated $[Eu(9)_3(Zn)_2]^{7+}$	Calculated $[Eu(7)_3]^{3+}$
O – Eu^{3+}	2.250-2.35 Å	2.417 Å, 2.416 Å
N – Eu^{3+}	2.321, 2.281 & 2389 Å	2.652 Å
N-Eu^{3+}-N	142, 105 & ,112 °	120 °

The resulting mechanical optimized structure, as seen in Figure 6.12, shows that the structure no longer appears as a linear helicate complex, with the central PDC coordination being pushed out of line with the Zn(**9**)$_3$ coordination pockets. The tricapped trigonal prismatic geometry is distorted, and although the pyridyl rings appear to maintain a trigonal geometry, the bond angle between the N-Eu^{3+}-N is far from the expected 120° as seen in Table 6.1. The PDA unit is no longer planar, causing close proximity of carbonyl oxygens from opposing ligands, while Eu^{3+} - O and Eu^{3+} - N bond lengths are significantly shorter than the previously calculated structure. In terms of the Zn(**9**)$_3$ coordination sphere, both ends appear to be a distorted octahedral coordination sphere.

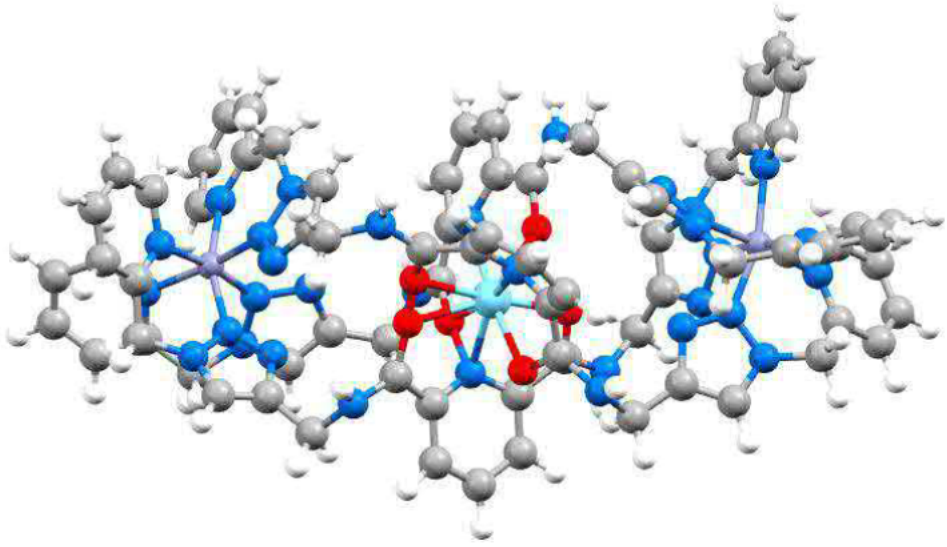

Figure 6.12. Mechanically optimized structure of $[Eu(\mathbf{9})_3(Zn)_2]^{7+}$.

Although the Spartan model is a promising indication that $[Ln(\mathbf{9})_3(Zn)_2]^{7+}$ may be feasible, the mechanically optimized calculated structure indicates the opposite, with the tricapped trigonal prismatic geometry being significantly distorted, in such a manner that it indicates formation is unlikely in the current state. Unfortunately, with higher levels of calculation failing to converge, initial modelling does not favour $[Ln(\mathbf{9})_3(Zn)_2]^{7+}$.

Self-Assembly Investigation

9 was also subjected to self-assembly studies and binding was investigated similar to ligands in chapter 3. La^{3+} (and now also Zn^{2+}) directed self-assembly and binding was investigated by analysing the changes in ^1H NMR spectra at r.t. This was carried out by monitoring changes in the ^1H NMR spectra of **9** in CD_3CN:CD_3OD:$CDCl_3$ (9.99:0.005:0.005, 1 mM) with the additions of either 0 to 2 equivalents of $La(CF_3SO_3)_3 \cdot 9H_2O$ or 0 to 2 equivalents of $Zn(CF_3SO_3)_2$. ^1H NMR spectra were recorded with 250 scan (30 minute) spectra between each addition. Spectra were calibrated to the CD_3CN peak at 1.94 ppm causing the resulting $CDCl_3$ peak at 7.58 ppm as seen in Figures 6.14-16.

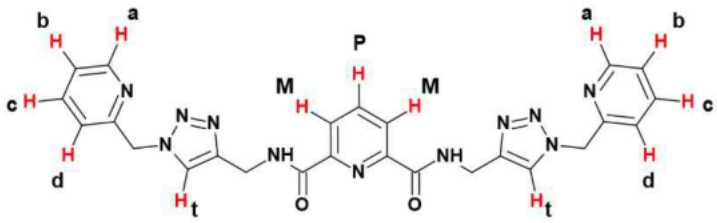

Figure 6.13.. Protons of interest in ^1H NMR titrations..

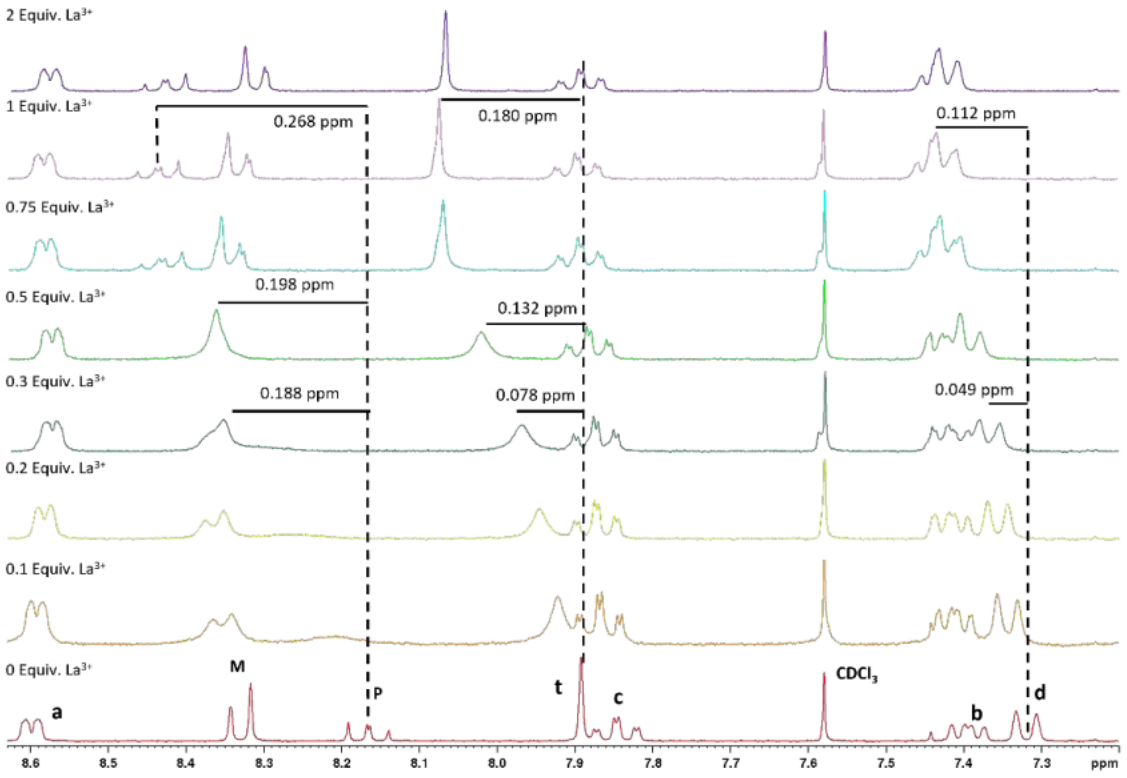

*Figure 6.14.. ^1H NMR spectra of **9** (0.001 M in CD_3CN,. 300 MHz) upon titrating with $La(CF_3SO_3)_3$ (0 – 2 equivalents)..*

Initially **9** was titrated with 0 to 2 equivalents of $La(CF_3SO_3)_3 \cdot 9H_2O$, as previously done in chapter 3 (Figure 6.14). Akin to what was observed in the bis-"clicked" ligands of chapter 3, upon the addition of La^{3+}, there is a significant downfield shift observed in the pyridyl *para* proton (**P**), merging with the pyridyl *meta* proton signal (**M**), indicative of the La^{3+} coordinating in the NO_2 pocket and formation of the $[La(\mathbf{9})_3]^{3+}$ species. Along with this, small downfield shifts were observed in the 1,2,3-triazole (**t**) proton signal as previously noted and the 2-pyridyl (**d**) proton doublet signal at 7.3 ppm. Upon further addition of La^{3+}, the **P** signal downfield shift continued until approximately 1 equivalent, separating from the **M** peak as previously observed. These shifts were indicative of the formation of lesser M:L species. Shifts observed in the **t** and **d** signals also continue to undergo a downfield shift until 1 equivalent is reached. The **d** signal shifting downfield does indicate that La^{3+} is also likely coordinating within the N_2 pocket. This shift, however, is notably not as significant as **P** at 0.3 equivalents but does become more significant as the titration progressed.

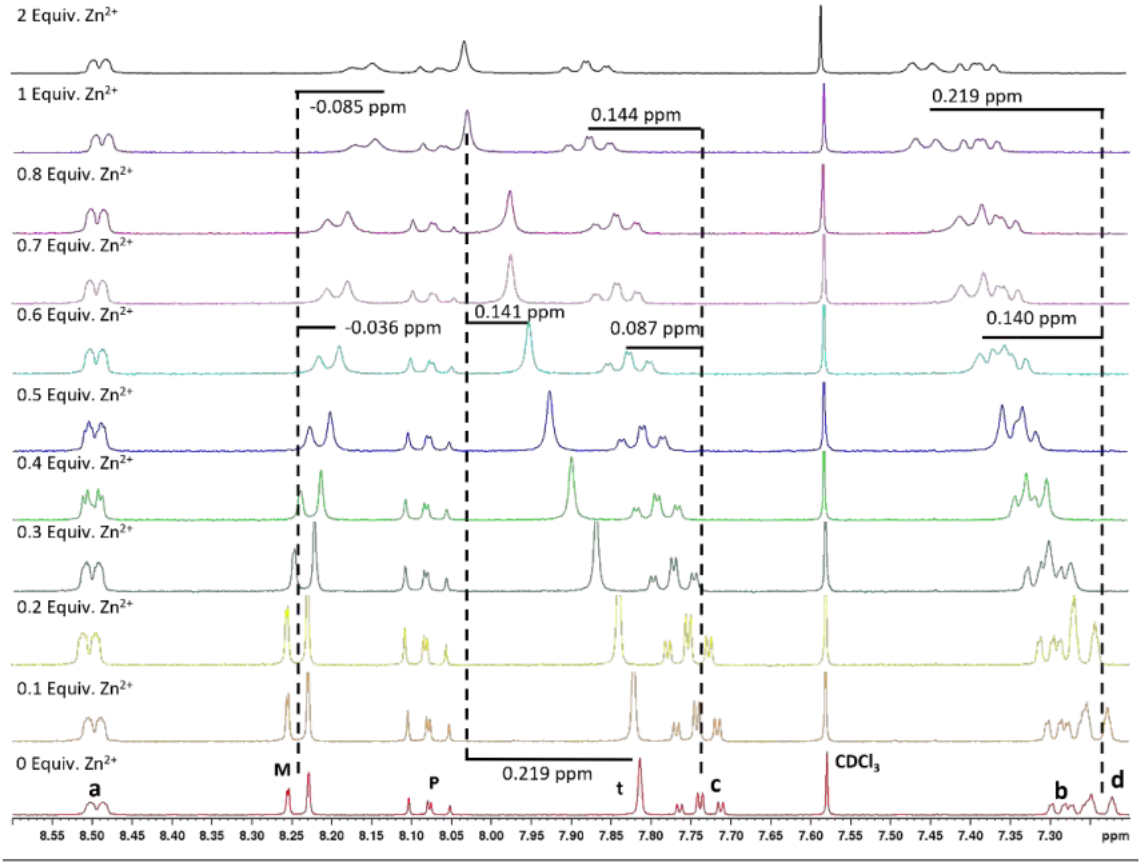

*Figure 6.15. ^{1}H NMR spectra of **9** (0.001 M in CD_3CN, 300 MHz) upon titrating with $Zn(CF_3SO_3)_2$ (0 – 2 equivalents).*

Titrations of **9** with 0 to 2 equivalents of $Zn(CF_3SO_3)_2$ as seen in Figure 6.15, resulted in significant downfield shifts in signals associated with the 2-pyridyl (**b** – **d**) and 1,2,3-triazole (**t**) from 0 to 1 equivalent of Zn^{2+}, with no further notable shifts observed from 1 to 2 equivalents. The downfield shifts observed are indicative of Zn^{2+} coordinating into the N_2 pocket as expected, but continuation of the downfield shift from 0.6 to 1 equivalent indicated that there are other M:L

species forming. Shifts in the **P** and **M** signals are relatively insignificant but there is a small upfield shift occurring throughout the titration. This shift is relatively insignificant until higher equivalents of Zn^{2+}, which could be due to a combination of factors, but because the shift is upfield it does not indicate that the Zn^{2+} is coordinating in the NO_2 pocket.

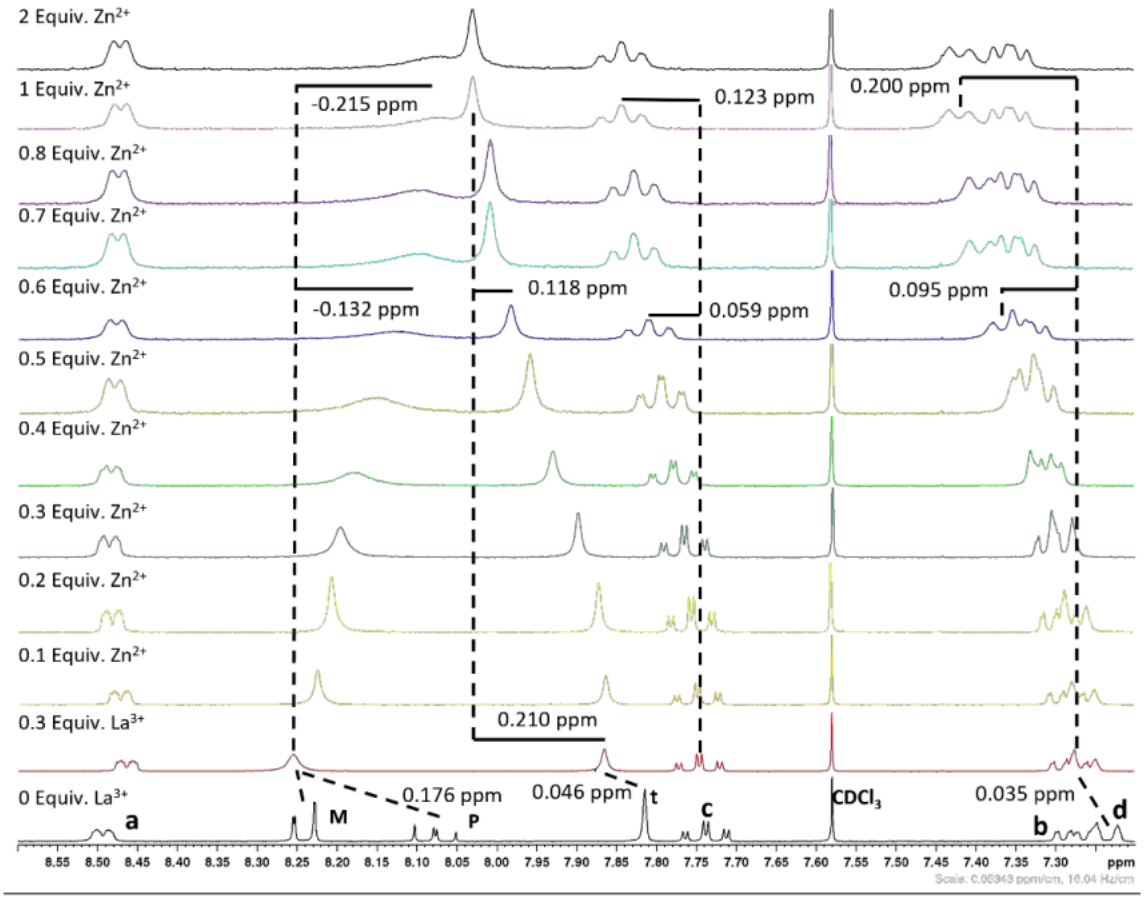

*Figure 6.16.. ^{1}H NMR spectra of **9** (0.001 M in CD_3CN, 300 MHz) upon titrating with 0.3 equivalents $La(CF_3SO_3)_3$ and then $Zn(CF_3SO_3)_2$ (0 – 2 equivalents)..*

Finally, **9** was titrated with 0.3 equivalents of $La(CF_3SO_3)_3 \cdot 9H_2O$, as seen in Figure 6.16, resulting in the expected merging of **P** and **M** proton signals. From here 0 to 2 equivalents of $Zn(CF_3SO_3)_2$ were titrated into the now assumed $[La(\mathbf{9})_3]^{3+}$ complex. Similar to the titration with $Zn(CF_3SO_3)_2$ significant downfield shifts in signals associated with the 2-pyridyl (**b – d**) and 1,2,3-triazole (**t**) from 0 to 1 equivalent of Zn^{2+} were observed, with no further notable shifts observed from 1 to 2 equivalents. Interestingly a more significant upfield shift is observed in the merged **P**/**M** signal until 1 equivalent of Zn^{2+} is reached. This could be associated with La^{3+} dissociating from the NO_2 pocket, but because there is no separation of the **P** & **M** signals, it could suggest that the La^{3+} remains coordinated within the NO_2 pocket. However, the lack of stagnation at 0.6/0.7 equivalents suggests the formation of species in solution other than the desired $[Ln(\mathbf{9})_3(Zn)_2]^{7+}$, making definitive confirmation of $[Ln(\mathbf{9})_3(Zn)_2]^{7+}$ formation difficult.

Monitoring species formation was also carried out by measuring changes in the fluorescence spectra of a solution of **9** (2×10^{-5} M) in MeCN (diluted from a stock solution of DCM:MeOH (1:1)) when titrated with specific aliquots of $Ln(CF_3SO_3)_3 \cdot xH_2O$ (where Ln = Eu^{3+} and Tb^{3+}) and $Zn(CF_3SO_3)_2$ from a 1 mM MeCN solution (see Section 8.4.4). Initially, upon the addition of 0 to 0.35 equivalents, Eu^{3+} and Tb^{3+} emission reaches peak intensity (Figure 6.17), indicative of $[Ln(\mathbf{9})_3]^{3+}$ formation. Excess Ln^{3+} addition results in the rapid decrease in Ln^{3+} centred emission intensity until 1 (Eu^{3+}) or 0.55 (Tb^{3+}) equivalent is reached leading to a plateau, indicative of the lesser M:L species formation as previously observed.

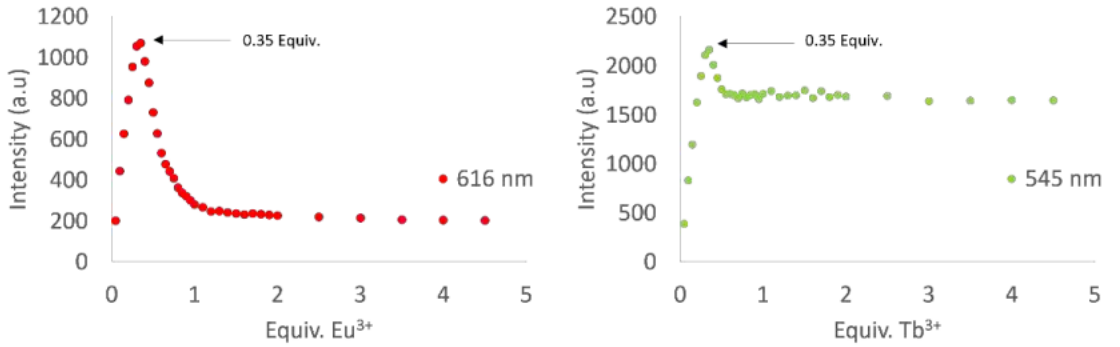

*Figure 6.17.. Fluorescence titration of **9** (0.02 M) with $Eu(CF_3SO_3)_3 \cdot 6H_2O$ (Left) and $Tb(CF_3SO_3)_3 \cdot 5H_2O$ (Right) from 0 to 4.5 equivalents, monitoring changes in intensity vs Ln^{3+} equivalents, at λ = 616 and 545 nm respectively..*

Similar to the ^{1}H NMR titrations, a solution of **9** was titrated with 0.35 equivalents of Eu^{3+} and Tb^{3+}, reaching a peak emission intensity. Upon the addition of $Zn(CF_3SO_3)_2$ both emissions are seen to significantly decrease upon every addition of $Zn(CF_3SO_3)_2$ until 3 equivalents is reached, where Ln^{3+} centred emission is completely quenched (Figure 6.18). This steady decline could be associated with the Zn^{2+} coordinating into the N_2 pocket, modifying the PDA antenna properties, but because there is no sign of a plateau occurring at any point it is more likely that the Ln^{3+} is displaced out of the NO_2 pocket upon the addition of Zn^{2+}.

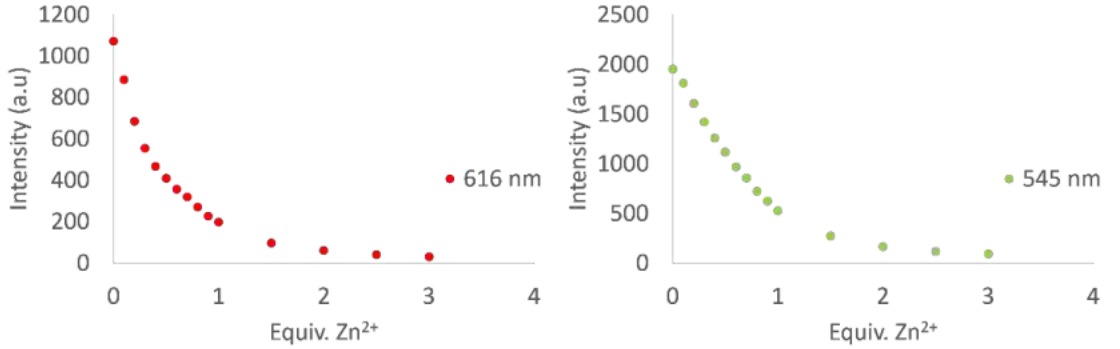

*Figure 6.18.. Fluorescence titration of **9** (0.02 M) with initial 0.35 equivalents of $Eu(CF_3SO_3)_3 \cdot 6H_2O$ (Left) and $Tb(CF_3SO_3)_3 \cdot 5H_2O$ (Right) and then $Zn(CF_3SO_3)_2$ from 0 to 3 equivalents, monitoring changes in intensity vs Ln^{3+} equivalents, at λ = 616 and 545 nm respectively..*

This in combination with ^{1}H NMR self-assembly results indicates that although the $[Ln(\mathbf{9})_3]^{3+}$ species is forming in the NO_2 pocket, and Zn^{2+} is likely coordinating in the N_2 pocket, the formation of $[Ln(\mathbf{9})_3(Zn)_2]^{7+}$ was unlikely and both indicate that the Ln^{3+} is being dissociated on addition of $Zn(CF_3SO_3)_2$.

Crystal Structure

The final indication that formation of the $[Ln(\mathbf{9})_3(Zn)_2]^{7+}$ was not favoured was the crystal structure obtained from a complexation of **9** with $Eu(CF_3SO_3)_3{\cdot}6H_2O$ and $Zn(CF_3SO_3)_2$. A solution of **9** was refluxed with 0.33 equivalents of $Eu(CF_3SO_3)_3{\cdot}6H_2O$ in MeOH:CH_2Cl_2 (1:1) for 30 mins under microwave irradiation. The solution appeared red emissive under shortwave UV irradiation indicative of Eu^{3+} coordination. 0.66 Equivalents of $Zn(CF_3SO_3)_3$ was then added to the assumed $Eu(\mathbf{9})_3(CF_3SO_3)_3$ solution and refluxed for a further 30 mins under microwave irradiation, remaining red emissive. The solution was then subjected to vapour diffusion of diethyl ether forming plate like colourless crystals. A structure of these single crystals was collected at low temperature (≈ 150 K) and revealed no presence of Eu^{3+} metal or helicate $Zn_2(\mathbf{9})_3(CF_3SO_3)_7$ molecule; rather it showed a metal coordination polymer made of repeating units of a zinc complex. The structure is represented in Figure 6.19 to show how **9** is coordinated with Zn^{2+}.

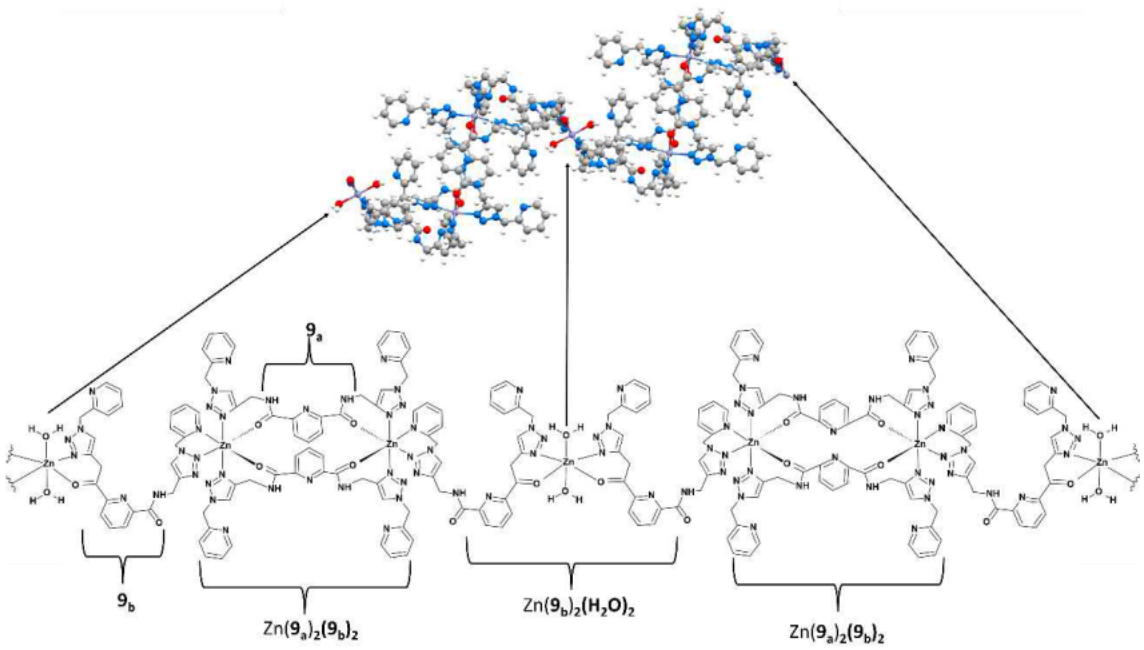

*Figure. 6.19.. (Top). Ball. and. stick. representation. of. the. metal. coordination. polymer. crystal. structure.. (Bottom). Drawn. scheme. of. the polymer. which. shows. how. **9**. are. coordinated. to. Zn^{2+}. and. the. two. different. octahedral. coordinations. which. form. the. polymer. like. chain. Note:. bond. lengths. and. angles. are. not. to. scale. in. scheme..*

The Zn^{2+} polymer network crystallised in triclinic space group $P\bar{1}$. The asymmetric unit contains two linked molecules of **9** via a Zn^{2+}. In one instance **9** is coordinated in the expected N_2 pocket, while the other molecule of **9** is coordinated through an unexpected 1,2,3-triazole and carbonyl pocket (NO) as seen in Figure 6.20. The asymmetric unit also contains a second Zn^{2+} (1/2 occupancy on a centre of inversion) coordinated to a single molecule of **9** also in the new NO pocket along with a coordinated molecule of water. There is also the presence of three $CF_3SO_3^-$ molecules and one MeOH solvent molecule in the asymmetric unit.

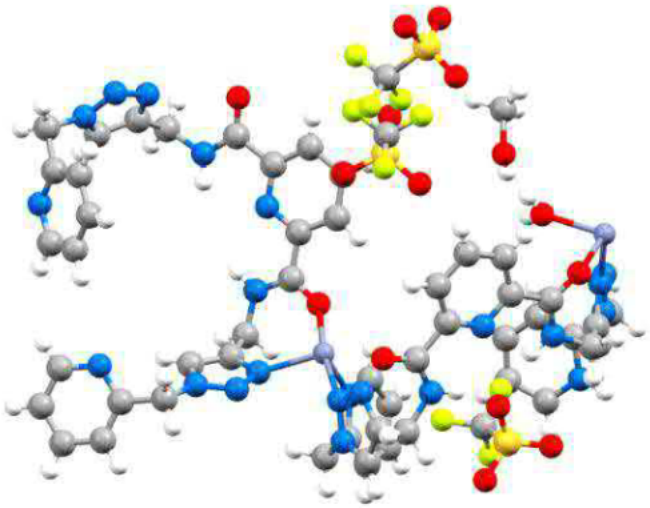

*Figure 6.20.. Asymmetric unit of Zn-**9** polymer network (ball and stick representation)..*

In the crystal packing there are two different instances of Zn^{2+} coordination which is repeated. In both instances they are forming octahedral coordination spheres, one is a filled octahedral "$Zn(\mathbf{9})_3$" coordination sphere while the other is also filled but with solvent - "$Zn(\mathbf{9})_2(H_2O)_2$". Since there are multiple instances of **9** coordinating to Zn^{2+}, it is easier to differentiate ligand **9** into $\mathbf{9}_a$ and $\mathbf{9}_b$ as seen in Figures 6.19, 21 and 22; this converts the octahedral coordination spheres into $Zn(\mathbf{9})_3 = Zn_2(\mathbf{9_a})_2(\mathbf{9_b})_2$ and $Zn(\mathbf{9})_2(H_2O)_2 = Zn(\mathbf{9_b})_2(H_2O)_2$.

The unit cell shows the "monomer" repeating unit which forms this metallo-polymer crystal packing. Two molecules of $\mathbf{9}_a$ are stacked in a sheet-like manner, with their central PDA motif forming an offset π-π interaction between the centroid of the PDA ring (see Section 8.4.3 for detail). Both ends of these molecules are coordinated to the same Zn^{2+} via the NO coordination pocket in an octahedral coordination sphere. The Zn^{2+} coordination sphere is then filled with a separate molecule of $\mathbf{9}_b$ coordinating via the N_2 pocket; this is the instance of the filled octahedral coordination sphere occurring twice in the unit cell between four molecules of **9,** forming $Zn_2(\mathbf{9_a})_2(\mathbf{9_b})_2$.

These molecules of **9b** which are coordinated to the Zn^{2+} via the N_2 pocket are also coordinated to a second Zn^{2+} at the other end via the NO pocket. This is the coordination which links the "monomer" units as this interaction is repeated from another molecule of **9b** (Figure 6.22).

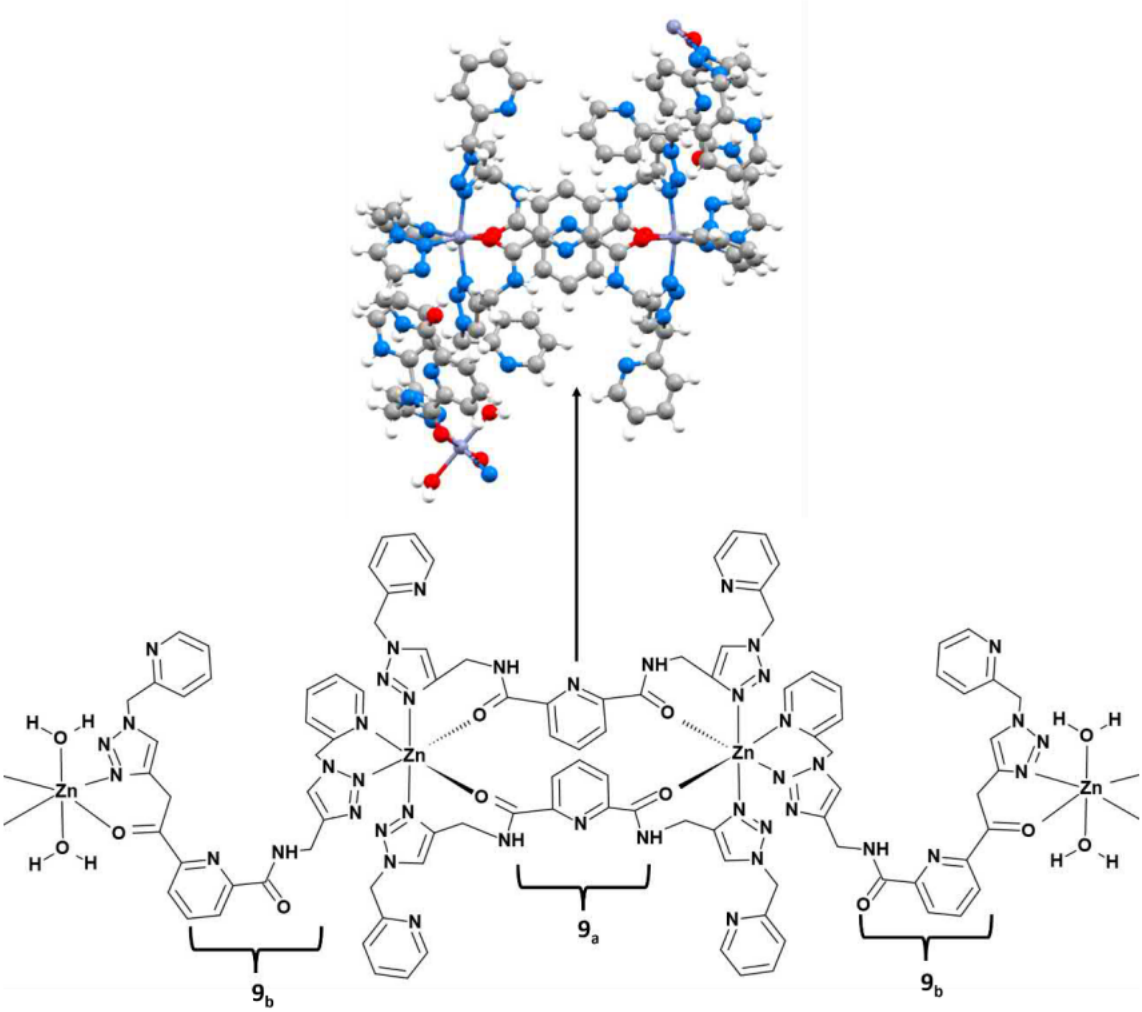

*Figure. 6.21.. (Top). The. unit. cell. "monomer". crystal. structure,. ball. and. stick. representation.. (Bottom). Drawn. scheme. of. the. unit. cell, which. show. how. **9**. are. coordinated. to. Zn^{2+}. and. the. two. different. octahedral. coordinations. which. form. the. polymer. like. chain.. Note: bond. lengths. and. angles. are. not. to. scale. in. scheme..*

It is important to note that this crystal does not comprehensively mean the $[Ln(\mathbf{9})_3(Zn)_2]^{7+}$ and $[Zn_2(\mathbf{9})_3]^{4+}$ does not form, rather indicating that it is unfavoured under these conditions, but with a combination of computational and self-assembly results, formation of the desired species is less promising. Furthermore, it is interesting to note that this unexpected NO coordination pocket formed between the Zn^{2+} and the carbonyl results in the rotation of the carbonyl group pointing the amides into the central PDC cavity. If this is also occurring in solution when Zn^{2+} is added during titrations, this would explain both the upfield shift observed in ^1H NMR and Ln^{3+} fluorescent emission quenching observed during titrations, as Ln^{3+} would be forced out of the NO_2 pocket.

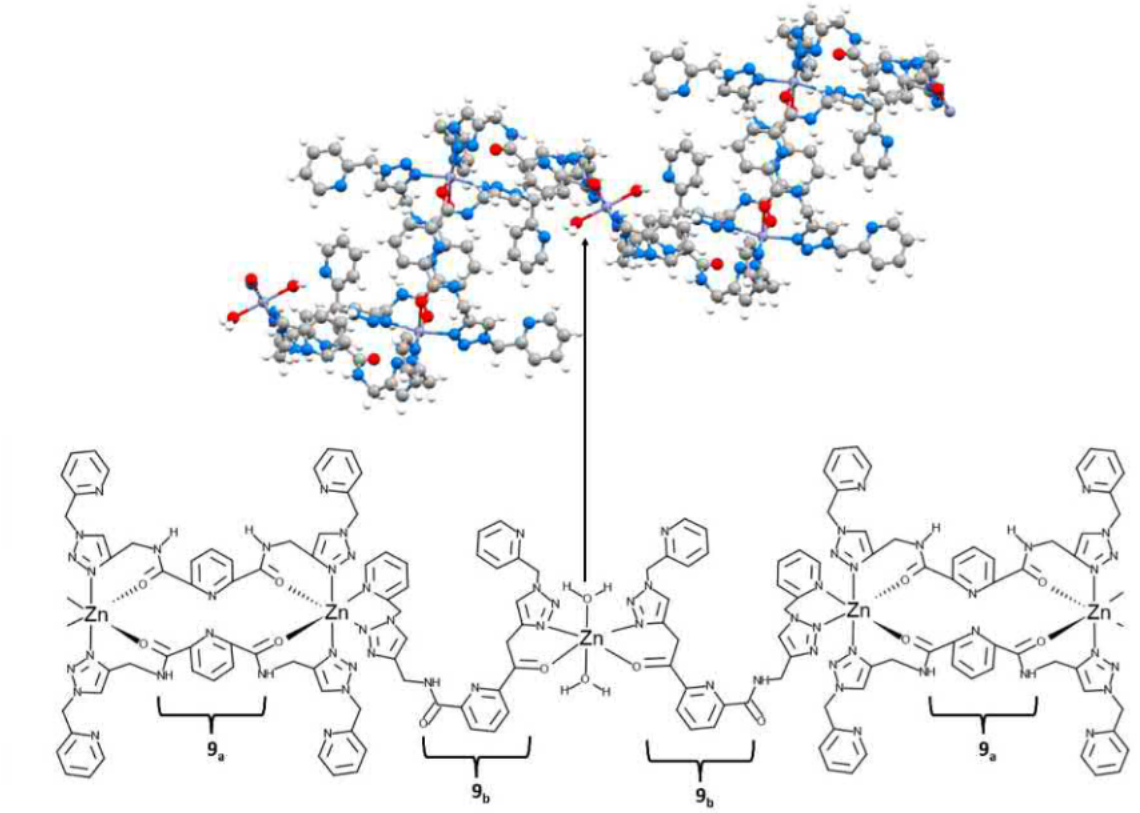

*Figure 6.22.. (Top). Zn(**9b**)2(H2O)2 linking two Zn(**9a**)2(**9b**)2, ball and stick representation.. (Bottom). Drawn scheme of the unit cell which show how. **9** are coordinated to Zn^{2+} and the two different octahedral coordinations which form the polymer like chain.. Note:: bond lengths and angles are not to scale in scheme..*

6.2.2.2 Ligands 10 and 11

Ligands **10** and **11** are the most recent ligands to be successfully synthesised, because of this lanthanide complexation studies are very limited and are only in the early stages of determining ideal solvents for complexation. It is worth noting that both systems are relatively insoluble, like the previous PDC tripodal ligand, which suggests that the carboxylic acid motifs are the cause of poor solubility due to the self-complementary H-bonding networks formed.[40] In most solvents tested the ligand can be dissolved in strongly polar solvents when deprotonated (with either Na_2CO_3 or NEt_3), but upon the addition of Eu^{3+} the solution instantly precipitates. **10** will dissolve in DCE:EtOH (1:1), along with 2 equivalents of NEt_3. Upon the addition of 0.6 equivalents of Eu^{3+}, the ligand and metal solution dissolve but only at high temperatures of 150 °C, and upon cooling the solid precipitates. In the case of **11** the precipitate would not redissolve. **11** has been found to dissolve in DMF with a few drops of water and remain soluble after addition of 3 equivalents of Na_2CO_3, but upon the addition of 1 equivalent of Eu^{3+} a solid would precipitate out within approximately 1 hour.

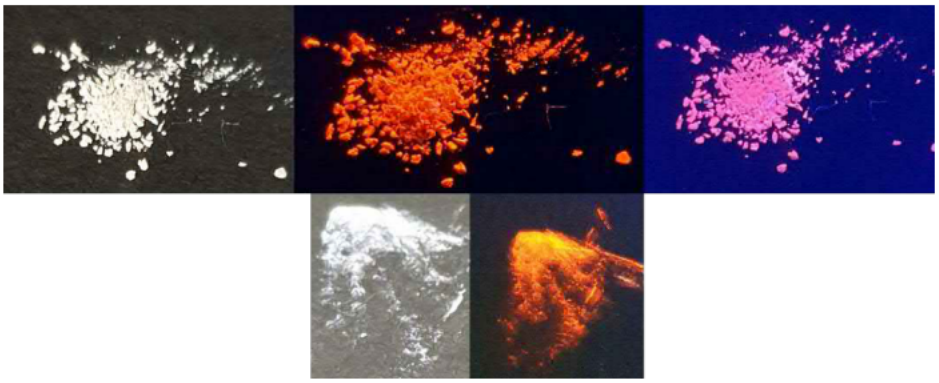

*Figure 6.23. (Top) Eu(**10**)$_x$ solid shown under ambient light, shortwave, and longwave irradiation from left to right. (Bottom) Eu(**11**)$_x$ solid, under ambient light and shortwave irradiation from left to right.*

The solids which do precipitate have been decanted, and as seen in Figure 6.23 the resulting solids are brightly emissive. To the eye these systems would easily be described as the brightest Eu^{3+} complexes in this thesis. Eu(**10**)$_x$ can be seen to appear both bright red and pink emissive under UV irradiation, while Eu(**11**)$_x$ is only bright red emissive. However, both complexes have been found to be very insoluble in a range of solvents including DMSO, making characterisation of the solid difficult. Apart from apparent Eu^{3+} centred emission, the only other indication of Eu^{3+} coordination is from FTIR spectrum of the solids, indicating that coordination has occurred in the NO_2 pocket, noting a classic shift observed in the carbonyl vibration from ≈ 1740 cm^{-1} (COOH) and ≈ 1666 cm^{-1} (CONH) to a merged band at ≈ 1635 cm^{-1} (see Figure 6.24 and Section 8.4.2). This also suggests that all PDC motifs present in the ligand architecture are coordinated to Eu^{3+}, as there is no sign of unshifted (or uncoordinated) carbonyl vibration present in the complex. Although it is true that solid fluorescence could be measured, without being able to determine the complex species formed, it was deemed unnecessary to perform fluorescence measurements at this stage.

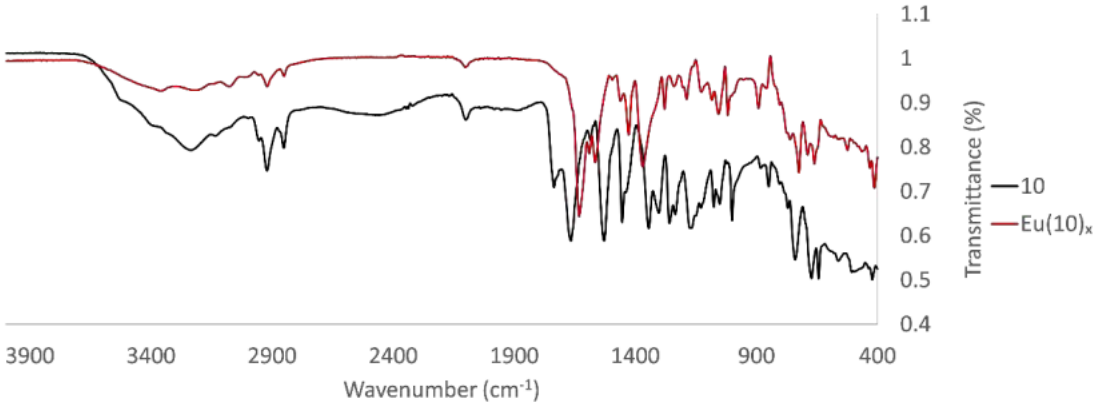

*Figure 6.24. Infrared spectra of **10** and Eu(**10**)$_x$(CF_3SO_3)$_x$.*

6.3 Conclusion

As stated throughout this chapter, these multitopic ligands have been successfully synthesised but are only at the very initial stages of lanthanide complexation investigation, and due to a combination of factors have not been fully explored. Initial studies for both suggest that the ligand systems would benefit from early modification (discussed below) rather than pursuing futile systems.

9 is indicated to be forming $Ln(\mathbf{9})_3CF_3SO_3$ assemblies as previously seen in chapter 3. However, formation of the mixed metal system $[Ln(\mathbf{9})_3(Zn)_2]CF_3SO_7$ could not be confirmed and attempts to obtain species confirmation by mass spectrometry were to no avail. From a combination of computational modelling, self-assembly titrations and crystal structure, there are indications that Zn^{2+} is likely coordinating into the N_2 pocket as designed, but also resulting in the potential dissociation of Ln^{3+} from the PDA pocket. To improve upon this system's chance of forming mixed metal assemblies, **9** would likely benefit from becoming a mono-"clicked" PDC ligand, improving Ln^{3+} binding while also reducing the complex charge from +7 to +2. Additionally, removal of the methyl linker between 1,2,3-triazole and the 2-pyridyl motif would benefit the octahedral coordination sphere of the Zn^{2+} as seen in other systems,[48-52] while alkyl linker length could be modified to optimize mixed metal formation, seen in Figure 6.25.

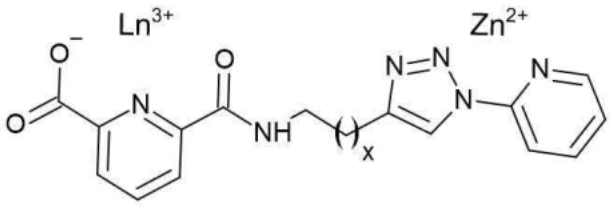

Figure 6.25.. Updated ligand design for mixed metal complexes..

The Ln^{3+} binding study of **10** and **11** indicated Ln^{3+} coordination. However, the poor solubility of these systems indicated that the complex may have formed an insoluble polymer network, as the rapid precipitation of the complexes does not allow for self-assembly in solution to an optimal arrangement. If future complexation studies were to be undertaken, water based solubilization would be investigated, which was found to be effective for previous PDC tripodal complexation although noted to still be relatively difficult. However, rapid precipitation and lack of solubility suggests that this system would likely benefit from being more labile, which could be easily achieved by converting the PDC motif to PDA, as seen in Figure 6.26, but at the detriment of novelty as discussed ligand systems which contain multiple PDA motifs are well studied in comparison to PDC motifs.

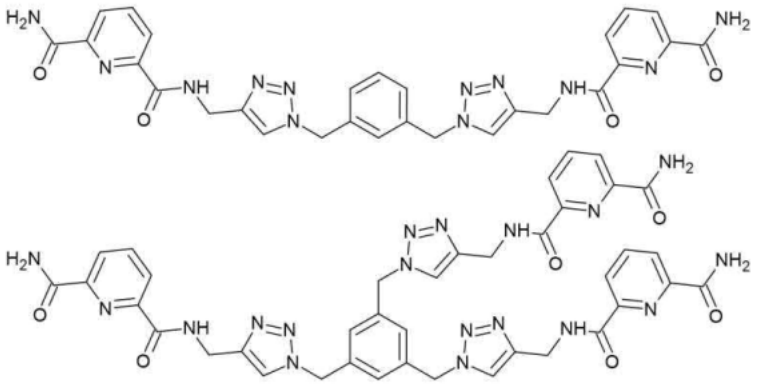

Figure 6.26.. Updated ligand design for multidentate complexes..

Unfortunately, due to time restrictions and COVID impact, these systems have not been fully investigated. However from this very small study it shows that the overall ligand designs are promising for the development of large assemblies and indicates that only a few minor modifications would be beneficial to the ligand design to overcome some of the initial issues encountered in the formation of large assemblies.

6.4 Experimental

6.4.1 General Experimental Details

All reagents, solvents and starting materials were purchased from Sigma-Aldrich. NMR spectra were recorded using a Bruker Ultrashield 300, with chemical shifts recorded in parts per million (ppm) downfield from the standard. FT-IR of solids were recorded on a Bruker Alpha platinum-ATR. MS of ligands was carried out in HPLC grade solvents, on a Shimadzu LMS 2020 with dual ionisation source. Fluorescence measurements were recorded on a Shimadzu RF-6000 Spectro fluorophotometer, with a ZJB380 UV filter 360 nm. Single crystal X-ray diffraction data were collected at 123 K on a Bruker D8 Venture equipped with an IμS DIAMOND microfocus with a Cu-Kα (λ = 1.54178) X-ray source with a PHOTON III detector. Unit cell parameters were refined against all data and an empirical absorption correction applied on APEX3. Structures were solved by direct methods using SHELXS-2013[53] and refined by SHELXL-2013[53] using Olex2.[54] Safety Note: low molecular weight organic azides are potential explosives, and care must be taken during their handling; however, no issues were encountered here.

6.4.1.1 Photophysical Self-Assembly Titrations

The formation of 1:1, 1:2 and 1:3 (M:L) species was monitored by measuring changes in fluorescence spectra of a solution of ligand (2×10^{-5} M, in 3 mL volume) in MeOH:DCM:MeCN (0.005:0.005:9.99) when titrated with $Ln(CF_3SO_3)_3.xH_2O$ or $Zn(CF_3SO_3)_2$ solution in MeCN.

6.4.1.2 ^{1}H NMR Self-Assembly Titrations

The (M:L) species formation was monitored by measuring changes in the ^{1}H NMR of a solution of ligand (1×10^{-3} M, ≈ 2 mL) in MeOD:$CDCl_3$:CD_3CN (0.005:0.005:9.99) when titrated with $La(CF_3SO_3)_3.9H_2O$ or $Zn(CF_3SO_3)_2$ solution in CD_3CN (10mM, 0→2 equivalents) taking 250 scans for each proton NMR.

6.4.2 Ligand Synthesis

6.4.2.1 Synthesis of N_2,N_6-bis((1-(2-pyridylmethyl)-1H-1,2,3-triazol-4-yl)methyl)pyridine-2,6-dicarboxamide (9)

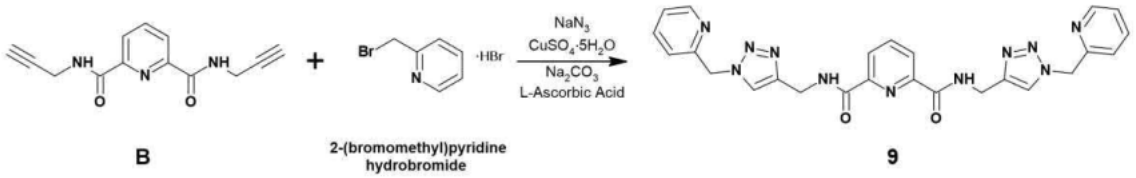

Scheme 6.3.. Synthesis of ligand ***9***.

B (0.497 g, 2.06 mmol) was combined with NaN_3 (0.321 g, 4.94 mmol), $CuSO_4 \cdot 5H_2O$ (0.206 g , 2.06 mmol), ascorbic acid (0.726 g, 4.12 mmol), Na_2CO_3 (1.310 g, 12.36 mmol) and 2-(bromomethyl)pyridine hydrobromide (1.042 g, 4.12 mmol) in 30 mL of DMF:H_2O (4:1). The solution turned instantly pink and slowly turned blood red over the course of 24 hours. Upon addition to (0.1 M) EDTA:NH_4OH a fluffy red precipitate formed; this was filtered and washed with water and diethyl ether yielding **9** as a white solid. (0.954 g, 91 %). LRMS *m/z* = 510.15 [**9** + H]$^+$ (calc. for $C_{23}H_{24}N_{11}O_2^+$, 510.53), 532.15 [**9** + Na]$^+$ (calc. for $C_{23}H_{23}N_{11}O_2Na^+$, 532.51) and 548.05 [**9** + K]$^+$ (calc. for $C_{23}H_{23}N_{11}O_2K^+$, 548.62).^{1}H NMR (300 MHz, DMSO-d_6 ,ppm), δ = 9.92 (m, 2H, NH), 8.51 (d , J = 3.5 Hz, 2H, 2py-H), 8.21 (m, 3H, central py-H), 8.07 (s, 2H, 1,2,3-triazole), 7.82 (t, J = 7.0 Hz, 2H, 2py-H), 7.33 (m, 2H, 2py-H), 7.28 (d, J = 8.0 Hz, 2H, 2py-H), 5.67 (s, 4H, CH_2-t), 4.62 (d, J = 5.5 Hz, 4H, CH_2-NH). ^{13}C NMR (75 MHz, DMSO-d_6, ppm): δ = 163.1 (C=O), 155.0 (CN), 149.4 (CH-2py), 148.5 (C-2py), 145.0 (C-t), 139.5 (CH-py), 137.3 (CH-2py), 124.4 (CH-py), 123.8 (CH-t), 123.2 (CH-2py), 122.2 (CH-2py), 54.2 (CH_2-t), 34.4 (CH_2-NH). FTIR (cm^{-1}) 3360, 3145, 3084, 3006, 2960, 2951, 1683, 1591, 1554, 1471, 1438, 1364, 1328, 1323, 1295, 1252, 1226, 1166, 1126, 1070, 1054, 1070, 1054, 1036, 992, 848, 828, 773, 752, 722, 671, 647, 593, 510, 457, 450.

6.4.2.2 Synthesis of N_2-bis((1-(m-xylene)-1H-1,2,3-triazol-4-yl)methyl)pyridine-2-carboxamide-6-carboxylate (10)

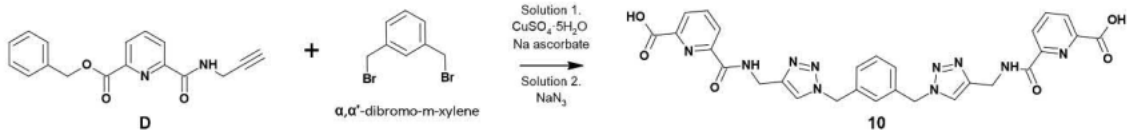

Scheme 6.4.. Synthesis of ligand ***10***.

D (0.214 g, 0.73 mmol) was combined with $CuSO_4 \cdot 5H_2O$ (0.091 g , 0.36 mmol) and sodium ascorbic acid (0.144 g, 0.73 mmol), in 16 mL of DMF:H_2O solution. The solution was stirred and heated to 60 °C for 30 minutes, in which the solution turned a pale orange. Alongside this another solution of α,α′-dibromo-m-xylene (0.096 g, 0.36 mmol) and NaN_3 (0.030 g, 0.46 mmol) in 5 mL of DMF was stirred and heated to 60 °C for 30 minutes, remaining clear throughout the heating. The solution of assumed α,α′-diazido-m-xylene was then added dropwise to copper catalysed solution. The solution was left to stir and heat for 24 hours changing to colour from a pale orange to a dark green. Once solution was cooled to r.t, the product was extracted with DCM and washed with water and (0.1 M) EDTA:NH_4OH. Solvent was removed by reduced pressure, resulting in a brown oil. Using theoretical 100 % yield, LiOH (0.035 g, 1.50 mmol) was combined with the brown oil and placed under an N_2 atmosphere. 10 mL of a mixed solvent solution THF:H_2O:MeOH (4:1:1) was added to the solution and was stirred for 24 hours, in which the brown oil slowly dissolved, resulting in a transparent yellow solution. The solvent was then removed by reduced pressure, resulting in a yellow residue. 2 M HCl was added to the yellow residue, causing a white precipitate to form. This was filtered yielding **10** as an off white solid (0.070 g, 32 %). LRMS *m/z* = 595.15 [**10** - H]$^-$ (calc. for $C_{28}H_{23}N_{10}O_6^-$, 595.54). ^{1}H NMR (300 MHz, DMSO-d_6, ppm), δ = 9.71 (m, 2H, NH), 8.23 (m, 6H, py-H), 8.07 (s, 2H, t-H), 7.34 (m, 4H, Bn-H), 5.53 (s, 4H, CH_2-t), 4.58 (d, J = 6.0 Hz, 4H, CH_2-NH). ^{13}C NMR (75 MHz, DMSO-d_6, ppm): δ = 163.4 (C=O), 159.6 (C=O), 149.5 (CN), 146.5 (CN), 145.2 (C-t), 140.5 (CH-Py), 137.0 (C-Bn), 129.7 (CH-Bn), 2x128.3 (CH-Bn), 127.2 (CH-Py), 125.9 (CH-Py), 123.7 (CH-t), 53.0 (CH_2-NH), 34.8 (CH_2-t). FTIR (cm^{-1}) 3231, 2922, 2852, 2491, 2100, 1923, 1720, 1664, 1586, 1530, 1454, 1344, 1302, 1258, 1237, 1163, 1128, 1077, 1051, 1000, 887, 848, 770, 741, 672, 643, 559, 503, 401.

6.4.2.3 Synthesis of 1,3,5-Tris((1-(methyl)-1H-1,2,3-triazol-4-yl)methyl)pyridine-2-carboxamide-6-carboxylate)benzene (11)

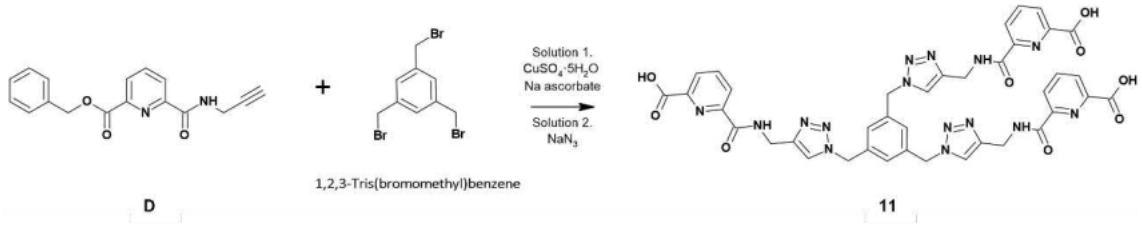

*Scheme 6.. 5.. Synthesis of ligand **11**.*

D (0.470 g, 0.16 mmol) was combined with $CuSO_4 \cdot 5H_2O$ (0.199 g , 0.80 mmol) and sodium ascorbic acid (0.316 g, 0.16 mmol), in 10 mL of DMF:H_2O solution. The solution was stirred and heated to 60 °C for 30 minutes, in which the solution turned a pale yellow. Alongside this another solution of 1,2,3-tris(bromomethyl)benzene (0.190 g, 0.53 mmol) and NaN_3 (0.111 g, 1.71 mmol) in 5 mL of DMF was stirred and heated to 60 °C for 2 hours, the solution remained clear throughout the heating. The solution of assumed 1,2,3-tris(azidomethyl)benzene was then added dropwise to copper catalysed solution. The solution was left to stir and heated for 24 hours changing to colour from a pale yellow to a dark orange. Water was then added to the solution causing a green precipitate, this was redissolved into DCM and (0.1 M EDTA):NH_4OH, H_2O and brine. The solvent was removed, yielding a green residue. Assuming theoretical 100 % yield, LiOH (0.051 g, 2.20 mmol) was combined with the green residue and was placed under an N_2 atmosphere. 10 mL of a mixed solvent solution THF:H_2O:MeOH (4:1:1) was added to the solution and was stirred for 24 hours, in which the green residue slowly dissolved, resulting in a transparent green solution. The solvent was then removed by reduced pressure, resulting in a green residue. 2 M HCl was added to the green residue, causing an off green precipitate to form, this was left to stir for 24 hours in 2 M HCl, until the precipitate appeared an off-white colour. This was filtered yielding **11** as an off-white solid (0.170 g, 37 %). LRMS *m/z* = 854.30 [**11** - H]$^-$ (calc. for $C_{39}H_{32}N_{15}O_9^-$, 854.77).^{1}H NMR (300 MHz, DMSO-d_6, ppm), δ = 9.72 (m, 3H, NH), 8.23 (m, 9H, py-H), 8.06 (s, 3H, t-H), 7.27 (s, 3H, Bn-H), 5.52 (s, 6H, CH_2-t), 4.58 (d, J = 6.0 Hz, 6H, CH_2-NH). ^{13}C NMR (75 MHz, DMSO-d_6, ppm): δ = 165.3 (C=O), 163.3 (C=O), 149.5 (CN), 146.5 (CN), 145.2 (C-t), 140.5 (CH-Py), 137.6 (C-Bn), 128.1 (CH-Bn), 127.1 (CH-Py), 125.9 (CH-Py), 123.8 (CH-t), 52.7 (CH_2-NH), 34.9 (CH_2-t). FTIR (cm^{-1}) 3236, 2920, 2098, 1900 ,1730 ,1667, 1586, 1530, 1454, 1433, 1347, 1302, 1172, 1074, 1001, 879, 847, 775, 743, 676, 643, 566, 509, 493, 455, 419.

6.5 References

1. J. A. Kitchen, *Coord. Chem. Rev.*, 2017, **340**, 232-246.
2. T. Zhang, G.-L. Zhang, L.-P. Zhou, X.-Q. Guo and Q.-F. Sun, *Tetrahedron: Asymmetry*, 2017, **28**, 550-554.
3. C.-T. Yeung, W. T. K. Chan, S.-C. Yan, K.-L. Yu, K.-H. Yim, W.-T. Wong and G.-L. Law, *Chem. Commun.*, 2015, **51**, 592-595.
4. F. Stomeo, C. Lincheneau, J. P. Leonard, J. E. O'Brien, R. D. Peacock, C. P. McCoy and T. Gunnlaugsson, *J. Am. Chem. Soc.*, 2009, **131**, 9636-9637.
5. L.-X. Cai, L.-L. Yan, S.-C. Li, L.-P. Zhou and Q.-F. Sun, *Dalton Trans.*, 2018, **47**, 14204-14210.
6. D. E. Barry, J. A. Kitchen, K. Pandurangan, A. J. Savyasachi, R. D. Peacock and T. Gunnlaugsson, *Inorg. Chem.*, 2020, **59**, 2646-2650.
7. X.-Z. Li, L.-P. Zhou, L.-L. Yan, D.-Q. Yuan, C.-S. Lin and Q.-F. Sun, *J. Am. Chem. Soc.*, 2017, **139**, 8237-8244.
8. L.-L. Yan, C.-H. Tan, G.-L. Zhang, L.-P. Zhou, J.-C. Bünzli and Q.-F. Sun, *J. Am. Chem. Soc.*, 2015, **137**, 8550-8555.
9. Q.-Q. Yan, L.-P. Zhou, H.-Y. Zhou, Z. Wang, L.-X. Cai, X.-Q. Guo, X.-Q. Sun and Q.-F. Sun, *Dalton Trans.*, 2019, **48**, 7080-7084.
10. J. Hamacek, A. Vuillamy, L. Peterhans, A. Homberg, D. Poggiali, M. W. Schneider and M. Mastalerz, *New J. Chem.*, 2018, **42**, 7803-7809.
11. B. El Aroussi, L. Guénée, P. Pal and J. Hamacek, *Inorg. Chem.*, 2011, **50**, 8588-8597.
12. S. Zebret, C. Besnard, G. Bernardinelli and J. Hamacek, *Eur. J. Inorg. Chem.*, 2012, **2012**, 2409-2417.
13. J. Hamacek, G. Bernardinelli and Y. Filinchuk, *Eur. J. Inorg. Chem.*, 2008, **2008**, 3419-3422.
14. J. Hamacek, C. Besnard, N. Mehanna and J. Lacour, *Dalton Trans.*, 2012, **41**, 6777-6782.
15. F. Renaud, C. Piguet, G. Bernardinelli, J.-C. G. Bünzli and G. Hopfgartner, *J. Am. Chem. Soc.*, 1999, **121**, 9326-9342.
16. G. Gil-Ramírez, S. Hoekman, M. O. Kitching, D. A. Leigh, I. J. Vitorica-Yrezabal and G. Zhang, *J. Am. Chem. Soc.*, 2016, **138**, 13159-13162.
17. B. E. Aroussi, S. Zebret, C. Besnard, P. Perrottet and J. Hamacek, *J. Am. Chem. Soc.*, 2011, **133**, 10764-10767.
18. S. Zebret, E. Vögele, T. Klumpler and J. Hamacek, *Chem. Eur. J.*, 2015, **21**, 6695-6699.
19. J. J. Jesudas, C. T. Pham, A. Hagenbach, U. Abram and H. H. Nguyen, *Inorg. Chem.*, 2020, **59**, 386-395.
20. L.-Z. Cai, W. Zhang, Z.-X. Zhu, J. Ru and M.-X. Yao, *J. Coord. Chem.*, 2019, **72**, 1097-1107.
21. J. Wu, L. Zhao, L. Zhang, X.-L. Li, M. Guo and J. Tang, *Inorg. Chem.*, 2016, **55**, 5514-5519.
22. J. Wu, X.-L. Li, M. Guo, L. Zhao, Y.-Q. Zhang and J. Tang, *Chem. Commun.*, 2018, **54**, 1065-1068.
23. J. Wu, L. Zhao, L. Zhang, X.-L. Li, M. Guo, A. K. Powell and J. Tang, *Angew. Chem. Int. Ed.*, 2016, **55**, 15574-15578.
24. J. Wu, M. Guo, X.-L. Li, L. Zhao, Q.-F. Sun, R. A. Layfield and J. Tang, *Chem. Commun.*, 2018, **54**, 12097-12100.
25. J. Wu, L. Zhao, M. Guo and J. Tang, *Chem. Commun.*, 2015, **51**, 17317-17320.
26. Q.-Y. Zhu, L.-P. Zhou and Q.-F. Sun, *Dalton Trans.*, 2019, **48**, 4479-4483.
27. Z. Wang, L.-P. Zhou, T.-H. Zhao, L.-X. Cai, X.-Q. Guo, P.-F. Duan and Q.-F. Sun, *Inorg. Chem.*, 2018, **57**, 7982-7992.
28. H. H. Nguyen, J. J. Jegathesh, A. Takiden, D. Hauenstein, C. T. Pham, C. D. Le and U. Abram, *Dalton Trans.*, 2016, **45**, 10771-10779.
29. J. C. G. Bünzli and S. V. Eliseeva, in *Comprehensive Inorganic Chemistry II (Second Edition)*, eds. J. Reedijk and K. Poeppelmeier, Elsevier, Amsterdam, 2013, vol. 8, pp. 339-398.
30. S. V. Eliseeva and J.-C. G. Bünzli, *Chem. Soc. Rev.*, 2010, **39**, 189-227.

31. A. D'Aléo, C. Andraud and O. Maury, in *Luminescence of Lanthanide Ions in Coordination Compounds and Nanomaterials*, 2014, pp. 197-230.
32. J.-C. Bünzli and S. Eliseeva, in *Lanthanide Luminescence*, ed. P. Hänninen, Härmä, Harri, Springer, Berlin, Heidelberg, 2010, vol. 7, pp. 1-45.
33. J.-C. G. Bünzli, *Chem. Rev.*, 2010, **110**, 2729-2755.
34. P. Coppo, M. Duati, V. N. Kozhevnikov, J. W. Hofstraat and L. De Cola, *Angew. Chem. Int. Ed.*, 2005, **44**, 1806-1810.
35. L. Aboshyan-Sorgho, C. Besnard, P. Pattison, K. R. Kittilstved, A. Aebischer, J.-C. G. Bünzli, A. Hauser and C. Piguet, *Angew. Chem. Int. Ed.*, 2011, **50**, 4108-4112.
36. M. Albrecht , O. Osetska, J.-C. G. Bünzli, F. Gumy and R. Fröhlich, *Chem. Eur. J.*, 2009, **15**, 8791-8799.
37. Y. Suffren, D. Zare, S. V. Eliseeva, L. Guénée, H. Nozary, T. Lathion, L. Aboshyan-Sorgho, S. Petoud, A. Hauser and C. Piguet, *J. Phys. Chem.*, 2013, **117**, 26957-26963.
38. D. Zare, Y. Suffren, H. Nozary, A. Hauser and C. Piguet, *Angew. Chem. Int. Ed.*, 2017, **56**, 14612-14617.
39. J. J. Lessmann and W. D. Horrocks, *Inorg. Chem.*, 2000, **39**, 3114-3124.
40. J.-M. Senegas, G. Bernardinelli, D. Imbert, J.-C. G. Bünzli, P.-Y. Morgantini, J. Weber and C. Piguet, *Inorg. Chem.*, 2003, **42**, 4680-4695.
41. S. Bräse, C. Gil, K. Knepper and V. Zimmermann, *Angew. Chem. Int. Ed.*, 2005, **44**, 5188-5240.
42. P. Ramírez-López, M. C. de la Torre, H. E. Montenegro, M. Asenjo and M. A. Sierra, *Org. Lett.*, 2008, **10**, 3555-3558.
43. F. Sander, U. Fluch, J. P. Hermes and M. Mayor, *Small*, 2014, **10**, 349-359.
44. H. Ben El Ayouchia, L. Bahsis, H. Anane, L. R. Domingo and S.-E. Stiriba, *RSC Adv.*, 2018, **8**, 7670-7678.
45. *Spartan'18, Wavefunction, Inc. Irvine, CA*.
46. *Gaussian 16, Revision C.01,* Frisch, M. J.; Trucks, G. W.; Schlegel, H. B.; Scuseria, G. E.; Robb, M. A.; Cheeseman, J. R.; Scalmani, G.; Barone, V.; Petersson, G. A.; Nakatsuji, H.; Li, X.; Caricato, M.; Marenich, A. V.; Bloino, J.; Janesko, B. G.; Gomperts, R.; Mennucci, B.; Hratchian, H. P.; Ortiz, J. V.; Izmaylov, A. F.; Sonnenberg, J. L.; Williams-Young, D.; Ding, F.; Lipparini, F.; Egidi, F.; Goings, J.; Peng, B.; Petrone, A.; Henderson, T.; Ranasinghe, D.; Zakrzewski, V. G.; Gao, J.; Rega, N.; Zheng, G.; Liang, W.; Hada, M.; Ehara, M.; Toyota, K.; Fukuda, R.; Hasegawa, J.; Ishida, M.; Nakajima, T.; Honda, Y.; Kitao, O.; Nakai, H.; Vreven, T.; Throssell, K.; Montgomery, J. A., Jr.; Peralta, J. E.; Ogliaro, F.; Bearpark, M. J.; Heyd, J. J.; Brothers, E. N.; Kudin, K. N.; Staroverov, V. N.; Keith, T. A.; Kobayashi, R.; Normand, J.; Raghavachari, K.; Rendell, A. P.; Burant, J. C.; Iyengar, S. S.; Tomasi, J.; Cossi, M.; Millam, J. M.; Klene, M.; Adamo, C.; Cammi, R.; Ochterski, J. W.; Martin, R. L.; Morokuma, K.; Farkas, O.; Foresman, J. B.; Fox, D. J. *Gaussian, Inc., Wallingford CT, 2016*.
47. A. K. Rappe, C. J. Casewit, K. S. Colwell, W. A. Goddard and W. M. Skiff, *J. Am. Chem. Soc.*, 1992, **114**, 10024-10035.
48. N. W. Kreofsky, M. D. Dillenburg, E. M. Villa and J. T. Fletcher, *Polyhedron*, 2020, **177**, 114259.
49. S. K. Vellas, J. E. M. Lewis, M. Shankar, A. Sagatova, J. D. A. Tyndall, B. C. Monk, C. M. Fitchett, L. R. Hanton and J. D. Crowley, *Molecules*, 2013, **18**, 6383-6407.
50. H. Crlikova, J. Malina, V. Novohradsky, H. Kostrhunova, R. A. S. Vasdev, J. D. Crowley, J. Kasparkova and V. Brabec, *Organometallics*, 2020, **39**, 1448-1455.
51. S. V. Kumar, W. K. C. Lo, H. J. L. Brooks and J. D. Crowley, *Inorg. Chim. Acta*, 2015, **425**, 1-6.
52. R. A. S. Vasdev, D. Preston, S. Ø. Scottwell, H. J. L. Brooks, J. D. Crowley and M. P. Schramm, *Molecules*, 2016, **21**, 1548.
53. G. Sheldrick, *Acta Crystallogr. A*, 2008, **64**, 112-122.
54. O. V. Dolomanov, L. J. Bourhis, R. J. Gildea, J. A. K. Howard and H. Puschmann, *J. Appl. Crystallogr.*, 2009, **42**, 339-341.

7. Conclusion

A range of luminescent self-assembled lanthanide-based supramolecular architectures and materials have been successfully developed utilizing the proposed synthetic strategy.

Chapter 3 developed the core synthetic strategy and procedure for incorporating the 1,2,3-triazole linker motif in the synthesis of ligands **1**-**4**, along with identifying that even with the introduction of the bulky and potentially competitive 1,2,3-triazole linker motif, the PDA based ligands retained the predictable coordination that was expected and desired, forming the $Ln(\mathbf{L})_3(CF_3SO_3)_3$ complexes (**L** = **1**-**3**). It also identified the flaws of the PDA motif, as although the 1:3 M:L species was forming, characterising this proved difficult, complexes were relatively unstable in competitive solvents and even though the substituents are distant from the central PDA motif, they can negatively impact Ln^{3+} centred emission as demonstrated by the aromatic naphthalene of **3** which exhibited poor Φ_{Ln}^{L}.

Taking these flaws of bis-"clicked" systems of **chapter 3** into account, the decision was made to focus synthesis on mono-"clicked" PDC systems for **chapter 4**, retaining one of the anionic carboxylates which was suspected to improve both stability and photophysical properties. With the new PDC based scaffold the amphiphilic ligand **5** was synthesised for LB film formation and was found to indeed improve complex stability and Φ_{Ln}^{L}, and were easier to characterize compared to previous PDA based ligands. Complexing **5** with a range of visible emissive Ln^{3+} resulted in very brightly emissive powders, solutions, and single layered LB films, which in the case of $Dy(\mathbf{5})_3$ resulted in overall emission which was within the "white" region. Mixing the different visibly emissive lanthanide complexes in solution resulted in emission from multiple Ln^{3+}, tuning the overall emission, a property which was retained on single layer LB film deposition.

With dual emission systems having such a wide variety of applications, there was an interest to improve upon the dual emission capability of lanthanide PDC systems which was so easily achieved by the mixed lanthanide systems of **chapter 4**. It was desired to develop single component dual emissive systems which incorporated both Ln^{3+} and organic chromophore centred emission, allowing for emission to be both colour-tunable and incorporate blue emission (for overall white emission). In **chapter 5,** blue emissive chromophores **PYR** and **NI** were attached via the 1,2,3-triazole linker forming two mono-"clicked" PDC ligand architectures

(**6** & **8**) and a single bis-"clicked" PDA ligand with **NI** (**7**, synthesised in case the single **NI** was too weak to achieve white emission). Complexing these ligand architectures with Eu^{3+} resulted in all cases in dual emissive systems which were colour-tunable. $Eu(\mathbf{6})_3$ was found to have the best overall photophysical properties, achieving very strong emission from both Eu^{3+} and **NI**, colour tunable emission which ranged from dark blue to bright red, crossing through the white emission region in both solution and solid form. These properties were also retained when spin coated onto quartz or glass slides, forming bright emissive films which could switch from bright blue to white.

Finally, although in the very initial stages of development, in **chapter 6** the synthetic strategy was used to synthesise multitopic ligand architectures. These multitopic ligand architectures were designed for either the incorporation of multiple Ln^{3+}, or incorporating a mixture of *d*-block metals and Ln^{3+}, as this can allow for the formation of complex supramolecular architectures along with improving Ln^{3+} photophysical properties. Unfortunately, initial complexation studies were discouraging, with mixed metal formation unfavoured, and the multi-PDA systems (**10** & **11**) were too insoluble. However, as discussed there are simple ligand modifications which have the potential to overcome some of these issues.

In conclusion, the synthetic strategy investigated streamlined the development of unique luminescent supramolecular assemblies and materials. Individually distinct but similar ligand architectures can be rapidly synthesised using similar methodologies (1,2,3-triazole "click" chemistry), allowing for systems to be quickly characterised and moved onto Ln^{3+} complexation. These simple ligand architectures in most cases predictably self-assemble in the presence of Ln^{3+} into complex unique luminescent supramolecular assemblies, credited to the predictable coordination of the PDA and PDC motifs. This allows for straightforward characterisation of the luminescent systems, from which the ideal candidates could then be moved into the final stages of material or application development as demonstrated in **chapters 4 and 5**, or if required can initially be modified to improve the systems properties before these final stages. Overall this "molecular toolbox" synthetic strategy led to the formation of a range of unique luminescent supramolecular assemblies and has the potential to be further used in the development of complex materials and applications as discussed below.

7.1 Future Studies

7.1.1 Future Applications and Improvements for Current Systems

The amphiphilic systems of **chapter 4**, mixed lanthanide LB films, currently could be used as luminescent bar codes, but a more specific and complex application which should be investigated is their use as solar waveguides. Solar cells (specifically silicon cells) currently can only absorb in certain regions, mainly the visible region, missing out on potential free energy from UV and IR light (Figure 7.1).[1-3] Solar waveguides are materials that have the potential to absorb light within these regions and convert it either by up conversion (UC) from NIR to visible or down conversion (DC) from UV to visible, which can then be absorbed by the solar cell.[1, 2] LB films have potential for this application, as they form ultra-thin films keeping the electronic devices small, requiring minimal material to fully coat the surface and films are near invisible and transparent (when not under UV irradiation) so they are not absorbing in the visible region taking away from the solar cell. Furthermore, LB films can be upscaled by the roller method allowing for use on an industrial scale.[4] A combination of UC and DC would account for approximately half of the irradiance from the sun and if both processes could be combined in a LB film effectively, both unutilized regions could be converted to usable visible light, increasing the efficiency of solar cells.[1, 2] The current Ln(**5**)$_3$ are ideal for the DC process as they absorbed in the UV region and DC into the visible region, as well as are already known to form LB films. In terms of UC, this could easily be achieved by UC nanoparticles, such as $NaYF_4$:Yb/Er

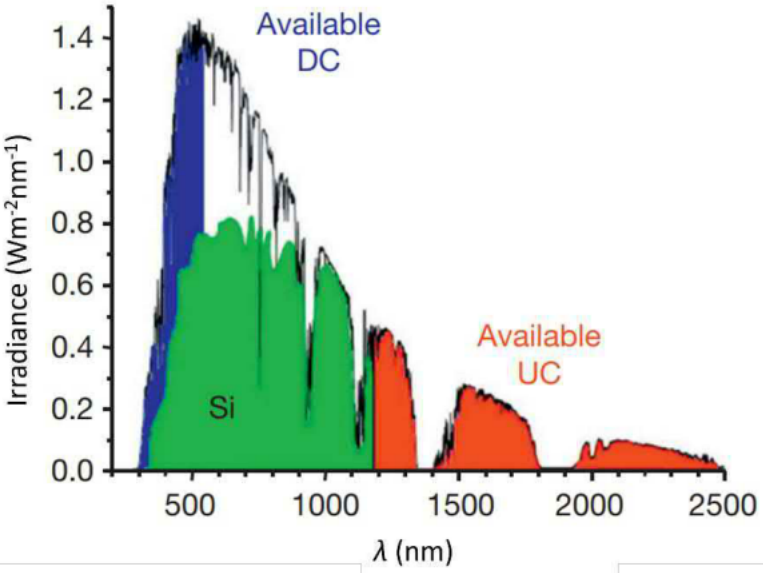

Figure. 7.1.. Solar. spectrum. showing. the. fractions. which. can. be. collected. by. silicon. cells. (green),. and. regions. which. DC. and. UC. could. take. place.. Image. adapted. with. permission. from. J.. C.. G.. Bünzli. and. S.. V.. Eliseeva,. in. Comprehensive. Inorganic. Chemistry. II. (Second Edition),. eds.. J.. Reedijk. and. K.. Poeppelmeier,. Elsevier,. Amsterdam,. 2013,. pp.. 339-398. and. B.. S.. Richards,. Sol. Energy Mater. Sol. Cells, *2006,.* ***90****,. 2329-2337.. Copyright 2022,. ELSEVIER..*

(purchasable at Sigma-Aldrich), which can be excited at ≈ 980 nm and result in Er^{3+} emission which ranges from ≈ 380 to 675 nm;[5, 6] additionally these nanoparticles have previously formed LB films and can also be encapsulated by amphiphilic chains which could potentially modify LB conditions to be better optimized with the Ln(**5**)$_3$ system.[7, 8]

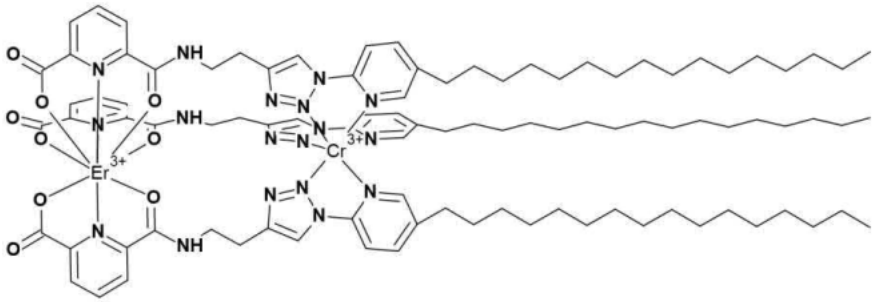

Figure 7.2. Potential ligand design for mixed d-transition metal and Ln^{3+} for UC or DC with Eu^{3+} and Zn^{3+}. It should be noted coordination spheres are not drawn to accuracy and are only there to give insight into how coordination may occur.

However, UC could also be achieved whilst retaining the PDC motif but utilizing the multidentate ligands of **chapter 6**. The multidentate ligands designed for mixed *d*-block metals and Ln^{3+} coordination were redesigned to be a mono-"clicked" PDC motif in the conclusion of **chapter 6** (Figure 6.25). If this system was more promising for the incorporation of both Ln^{3+} and *d*-block metals in the desired pockets, a Er^{3+} / Cr^{3+} system could be developed (which has previously resulted in UC with Er^{3+} emission).[9] The addition of a long chain off the 2-pyridyl motif would allow for LB film formation (Figure 7.2). Additionally, a Eu^{3+} / Zn^{3+} system could be made for DC, which would likely make Langmuir isotherms between the systems similar, making mixed LB film formation easier.

On the other hand, for the dual emissive systems of **chapter 5**, further investigation into both oxygen sensing and OLED applications would be beneficial. Initial oxygen sensing looks promising for Eu(**6**)$_3$ system in solution as shown in Section 5.3.1, and ideally Eu(**8**)$_3$ and spin coated films would also be investigated for similar properties. Oxygen sensing is not only an application as a sensor, but because the process generates $^1O_2$ the spin coated films could have photocatalyst,[10] biomedical,[11] and water purification[12] applications. As stated, to fully explore these applications phosphorescent measurements (to observe Eu^{3+} emission without organic chromophore emission) and NIR measurements (for singlet oxygen generation) would be required. Additionally, OLED fabrication could be explored with the Eu(**6**)$_3$ system. White light emissive systems are mainly utilized in displays and lighting applications;[2] as a consequence Eu(**6**)$_3$ white emission would ideally be maintained when excited by electrical current. As stated the HOMO and LUMO energy levels of the Eu(**6**)$_3$ emissive layer (EML) were determined (see Section 8.3.6), enabling suitable electron transport (ETL) and hole transport (HTL) layers to be

selected, these being PEDOT:PSS and bathocuproine (BCP) respectively.[13, 14] These layers could be spin coated/layered onto the anode (ITO) substrates and capped with the cathode (gallium-indium, Ga-In) see Figure 7.3, forming the OLED and potentially capable of electroluminescence and ideally white emissive. Although this seems simple on paper,[15, 16] this study alone would require extensive time beyond the scope of this thesis and equipment that is not easily accessible. OLED fabrication alone would require extensive studies in film thickness determination for each layer, determination into whether film layers were mixing, and fabrication would ideally be occurring in a dust free environment. While some characterising of electroluminescence could be carried out (such as fluorescent emission profiles), more specific characterising would require integration spheres which are not readily available.[17]

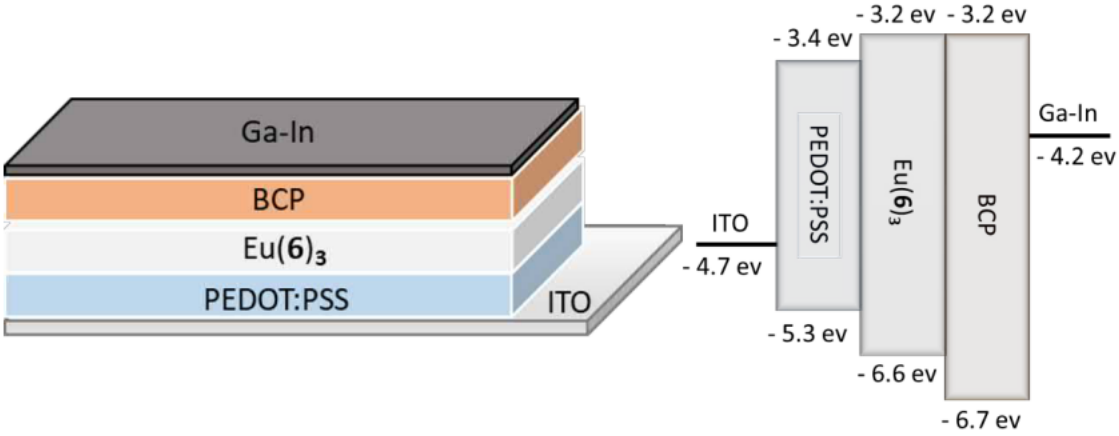

Figure. 7.3.. Potential. OLED. fabrication. design.. It. is. worth. noting. that. a. hole. blocking. layer. with. a. high. LUMO. level. to. block. electrons from. going. from. EML to. HTL would. likely. be. required.. HOMO. and. LUMO. energy. levels. obtained. from. Y.. He,. L.. Liu,. G.. Fu,. W.. Li,. X.. Lü,. H.. He. and. W.-Y.. Wong,. J.. Mater.. Chem.. C,. 2019,. 7,. 4800-4807.

7.1.2 Improved Ligand Scaffold

Finally in terms of new ligand architectures, the initial plan for this thesis was to only focus on the PDA motif, moving on from **chapter 3** to unsymmetrically modify the PDA motif, as seen in Figure 7.4. This unsymmetric approach would allow for one side of the PDA motif to focus on structure directing properties such as inclusion of long alkyl chains for LB films, strong hydrogen bonding groups for gels, or secondary coordination sites for MOFS or mixed metal systems. The other side could focus on applications substituents such as antenna property modifiers, molecular sensor sites, secondary emissive groups, or molecular machines like photo-switches. However, because of the poor stability and difficulty in characterisation of the PDA motif systems, the PDC motif has been favoured in this thesis and was shown to both improve stability and Ln^{3+} emissive properties.

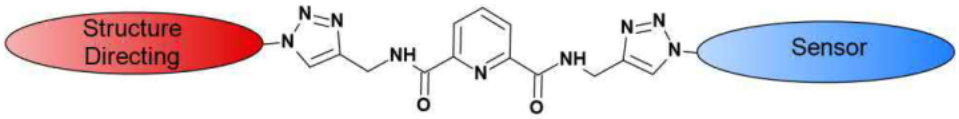

Figure. 7.4.. PDC.side.arms,. where.sensors.or.structure.directing.groups.can.be.simply."clicked".onto.the.scaffold..

However, the PDC motif does have the limitation of only allowing one of the anionic carbonyls to be replaced by the amide linker. As a result of this any attached substituent must contain either both structure directing and application properties desired as in **chapter 5** or only focus on one of the properties, limiting the complexity of any future PDC based system. To overcome this the PDC motif could additionally be modified off the back antenna using chelidamic acid, allowing for multiple substituents to be attached to the PDC scaffold while ideally retaining the better stability and emission properties of the PDC motif (Figure 7.5). For example, the simple modification of the *para* position phenol group to a range of different electron withdrawing and donating groups could modify the overall Ln^{3+} antenna property which could be used to make mixed LB films, which have different excitation wavelengths for different emission.

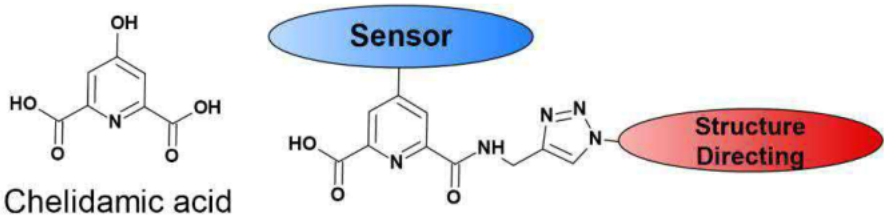

Figure. 7.5.. The.future. PDC.motif. with.dual.modification.allowing.for.multiple.substituents.with.different.properties.to.be.attached.to. the.binding.pocket..

In summary, the "molecular toolbox" synthetic strategy has developed a range of luminescent compounds and films, opening a pathway for many more simplistic ligand architectures to be designed from which complex lanthanide assemblies and materials can be developed.

7.2 References

1. S. V. Eliseeva and J.-C. G. Bünzli, *New J. Chem.*, 2011, **35**, 1165-1176.
2. J. C. G. Bünzli and S. V. Eliseeva, in *Comprehensive Inorganic Chemistry II (Second Edition)*, eds. J. Reedijk and K. Poeppelmeier, Elsevier, Amsterdam, 2013, vol. 8, pp. 339-398.
3. B. S. Richards, *Sol. Energy Mater. Sol. Cells*, 2006, **90**, 2329-2337.
4. M. Parchine, J. McGrath, M. Bardosova and M. E. Pemble, *Langmuir*, 2016, **32**, 5862-5869.
5. A. A. Ansari, R. Yadav and S. B. Rai, *RSC Adv.*, 2016, **6**, 22074-22082.
6. T. Rinkel, A. N. Raj, S. Dühnen and M. Haase, *Angew. Chem. Int. Ed.*, 2016, **55**, 1164-1167.
7. H.-P. Zhou, C. Zhang and C.-H. Yan, *Langmuir*, 2009, **25**, 12914-12925.
8. L. T. K. Giang, K. Trejgis, L. Marciniak, N. Vu and L. Q. Minh, *Sci. Rep.*, 2020, **10**, 14672.
9. Y. Suffren, D. Zare, S. V. Eliseeva, L. Guénée, H. Nozary, T. Lathion, L. Aboshyan-Sorgho, S. Petoud, A. Hauser and C. Piguet, *J. Phys. Chem*, 2013, **117**, 26957-26963.
10. Y. Nosaka and A. Y. Nosaka, *Chem. Rev.*, 2017, **117**, 11302-11336.
11. S. Monro, K. L. Colón, H. Yin, J. Roque, P. Konda, S. Gujar, R. P. Thummel, L. Lilge, C. G. Cameron and S. A. McFarland, *Chem. Rev.*, 2019, **119**, 797-828.
12. D. García-Fresnadillo, *ChemPhotoChem*, 2018, **2**, 512-534.
13. A. Boudrioua, M. Chakaroun and A. Fischer, in *Organic Lasers*, eds. A. Boudrioua, M. Chakaroun and A. Fischer, Elsevier, 2017, pp. 49-93.
14. S.-Y. Lu, S. Mukhopadhyay, R. Froese and P. M. Zimmerman, *J. Chem. Inf. Model.*, 2018, **58**, 2440-2449.
15. A. Banerji, M. W. Tausch and U. Scherf, *Educ. Quim.*, 2013, **24**, 17-22.
16. S. Vázquez-Córdova, G. Ramos-Ortiz, J.-L. Maldonado, A. Meneses and O. Garcia, *Rev. Mex. De Fis.*, 2008, **54**, 146-152.
17. Y. He, L. Liu, G. Fu, W. Li, X. Lü, H. He and W.-Y. Wong, *J. Mater. Chem. C*, 2019, **7**, 4800-4807.

8. Appendices

Table of Contents

8.1 Chapter 3 ..... ***275***

8.1.1 Ligand Characterisation Data 275
8.1.1.1 Intermediate **B** 275
8.1.1.2 Ligand **1** 276
8.1.1.3 Ligand **2** 278
8.1.1.4 Ligand **3** 280
8.1.1.5 Ligand **4** 282
8.1.2 Crystal Structure Data 283
8.1.3 Lanthanide Complex Data 284
8.1.3.1 Ln(**1**)$_3$(CF_3SO_3)$_3$ 284
8.1.3.2 Ln(**2**)$_3$(CF_3SO_3)$_3$ 290
8.1.3.3 Ln(**3**)$_3$(CF_3SO_3)$_3$ 295
8.1.4 Self-Assembly Titration Data 302
8.1.4.1 Self-Assembly Titration for **1** 302
8.1.4.2 Self-Assembly Titration for **2** 305
8.1.4.3 Self-Assembly Titration for **3** 308
8.1.4.4 Fitted Titration for **1** 313
8.1.4.5 Fitted Titration for **2** 313
8.1.4.6 Fitted Titration for **3** 314
8.1.5 Synthesis and Characterisation of hydroxymethyl-1,2,3-triazolylhexadecane 316

8.2 Chapter 4 ..... ***318***

8.2.1 Ligand Characterisation Data 318
8.2.1.1 Intermediate **C** 318
8.2.1.2 Intermediate **D** 319
8.2.1.3 Intermediate **E** 321
8.2.1.4 Ligand **5** 323
8.2.1.4 Precursor 1-azidohexadecane 326
8.2.2 Crystal Structure Data 326
8.2.3 Self-Assembly Titration Data 327
8.2.4 Lanthanide Complex Data 329
8.2.5 Langmuir Blodgett Data 336
8.2.5.1 Langmuir Isotherm Data 336
8.2.5.2 Langmuir Blodgett Deposition 337
8.2.6 Lanthanide Photophysics LB film and Solutions 340
8.2.6.1 Single Lanthanide Systems 340
8.2.5.2 MultiLayered LB Film. 342
8.2.6.3 Multilayered Eu(**5**)$_3$ Langmuir Blodgett Films 347
8.2.6.4 Lifetimes 348
8.2.6.5 Quantum Yields 353
8.2.7 X-Ray Photoelectron Spectroscopy (XPS) 355

8.3 Chapter 5 ..... *361*

8.3.1 Ligand Characterisation Data 361
8.3.1.1 Precursor **F** 361
8.3.1.2 Precursor **G** 362
8.3.1.3 Precursor **H** 364
8.3.1.4 Intermediate **I** 365
8.3.1.5 Ligand **6** 367
8.3.1.6 Ligand **7** 369
8.3.1.7 Precursor **J** 372
8.3.1.8 Precursor **K** 373
8.3.1.9 Intermediate **L** 375
8.3.1.10 Ligand **8** 377
8.3.2 Crystal Structure Data 379
8.3.3 Self-Assembly Titration Data 380
8.3.3.1 Self-Assembly Titration for **6** 380
8.3.3.2 Self-Assembly Titration for **7** 381
8.3.3.3 Self-Assembly Titration for **8** 382
8.3.4 Lanthanide Complex Data 383
8.3.5 Lanthanide and Chromophore Photophysics 386
8.3.5.1 Lifetimes 393
8.3.5.2 Quantum Yields 393
8.3.6 Electron Chemistry 399

8.4 Chapter 6 ..... *401*

8.4.1 Ligand Characterisation Data 401
8.4.1.2 Ligand **9** 401
8.4.1.2 Ligand **10** 402
8.4.1.2 Ligand **11** 404
8.4.2 Lanthanide Complex Data 405
8.4.3 Crystal Structure Data 406
8.4.4 Self-Assembly Titration Data 408

8.1 Chapter 3

8.1.1 Ligand Characterisation Data

8.1.1.1 Intermediate B

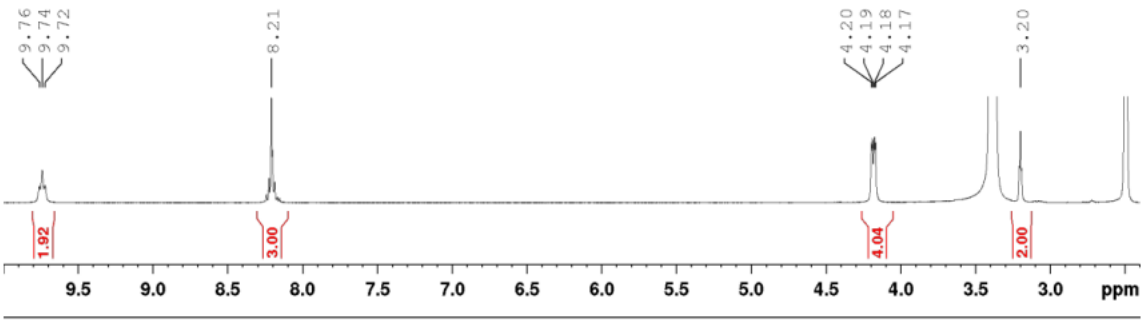

*Figure 8.1.1: ^{1}H NMR spectrum of **B** (300 MHz, DMSO-d_6).*

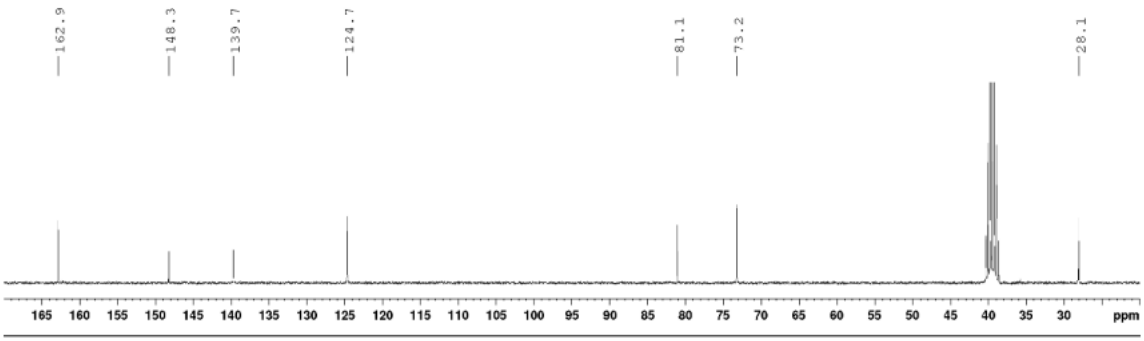

*Figure 8.1.2: ^{13}C NMR spectrum of **B** (75 MHz, DMSO-d_6).*

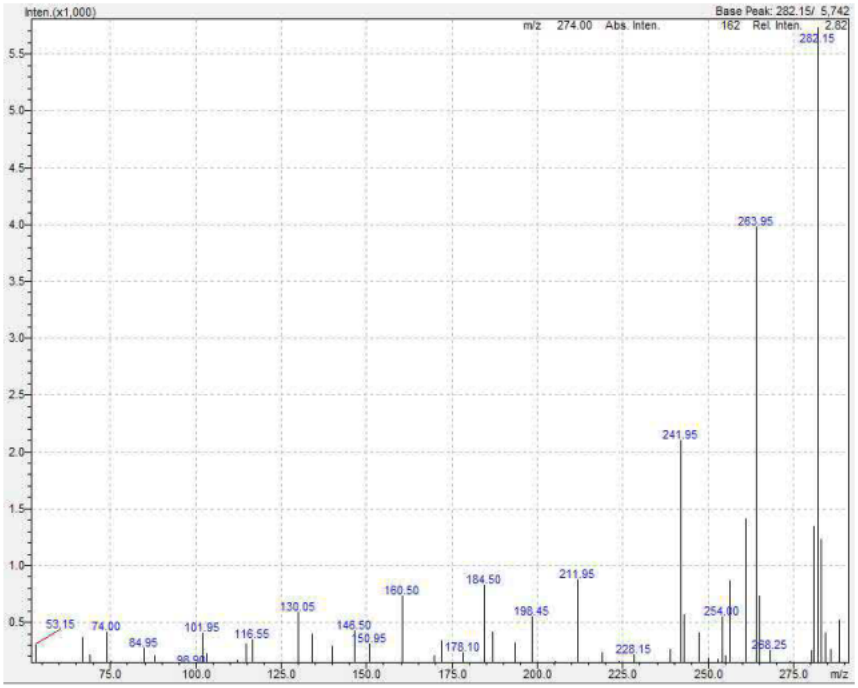

*Figure 8.1.3. LRMS m/z = 241.95 [**B** + H]$^+$ (calc. for $C_{13}H_{12}N_3O_2^+$, 242.09) and m/z = 263.95 [**B** + Na]$^+$ (calc. for $C_{13}H_{11}N_3O_2Na^+$, 264.07).*

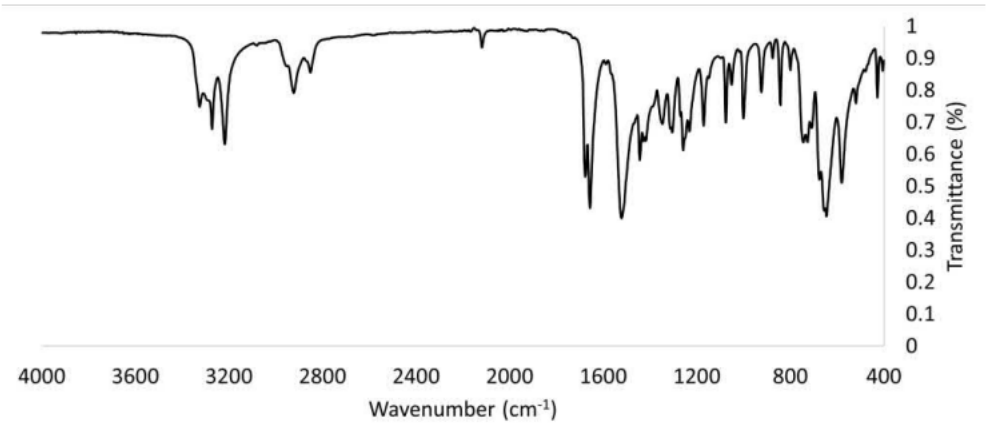

*Figure 8.1.4.. IR spectrum of **B**..*

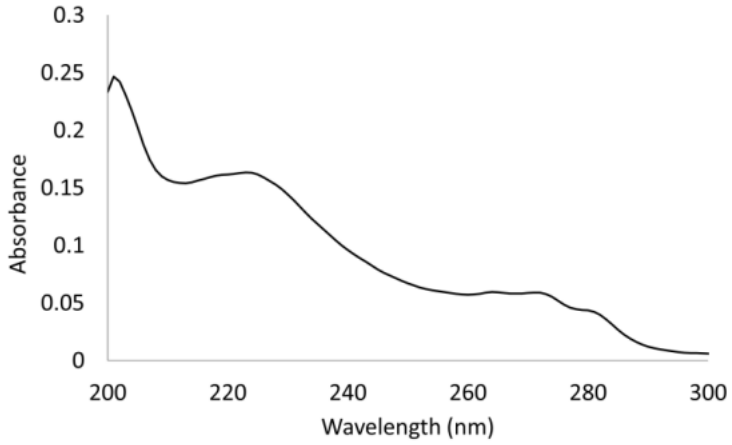

*Figure 8.1.5.. UV-visible absorption spectrum of **B** (0.01 mM, MeCN).*

8.1.1.2 Ligand 1

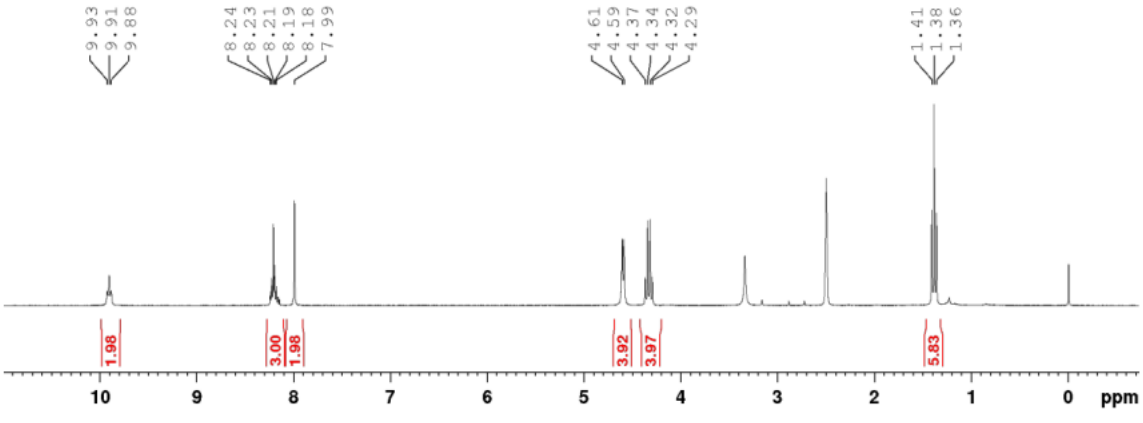

*Figure 8.1.6.·^{1}H NMR spectrum of **1** (300 MHz, DMSO-d_6)..*

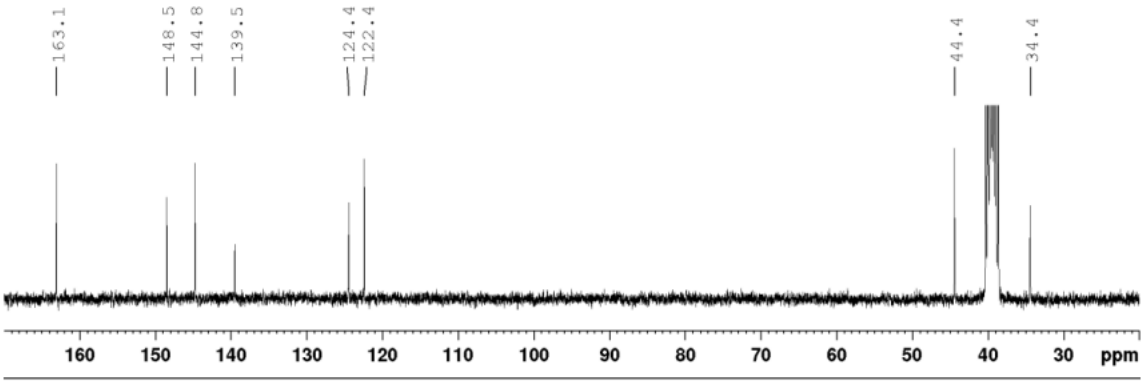

*Figure 8.1.7: ^{13}C NMR spectrum of **1** (75 MHz, DMSO-d_6).*

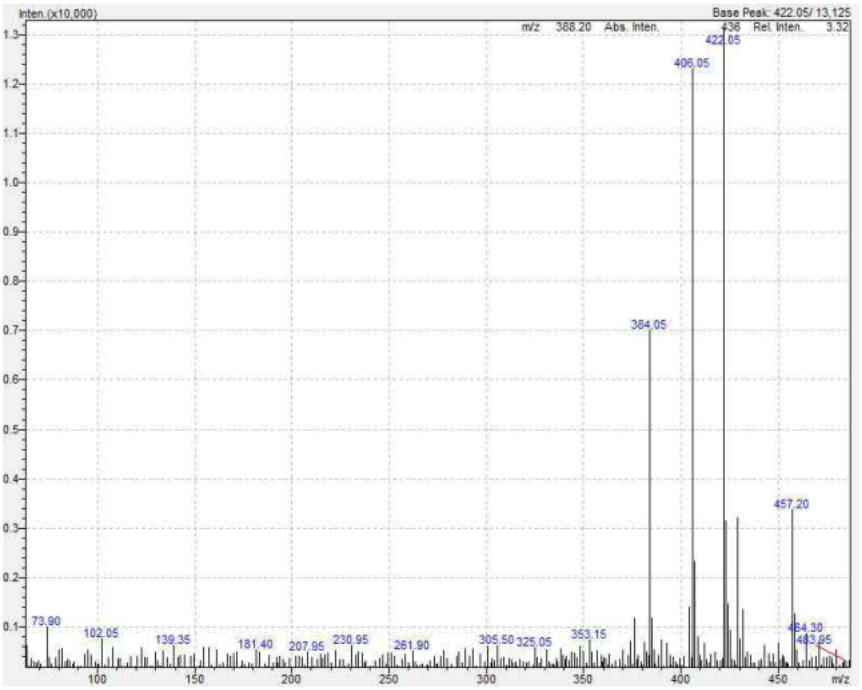

*Figure 8.1.8. LRMS m/z = 384.05 [**1** + H]$^+$ (calc. for $C_{17}H_{22}N_3O_2^+$, 384.19), m/z = 406.05 [**1** + Na]$^+$ (calc. for $C_{17}H_{21}N_9O_2Na^+$, 406.17) and m/z = 422.05 [**1** + K]$^+$ (calc. for $C_{17}H_{21}N_9O_2K^+$, 422.15).*

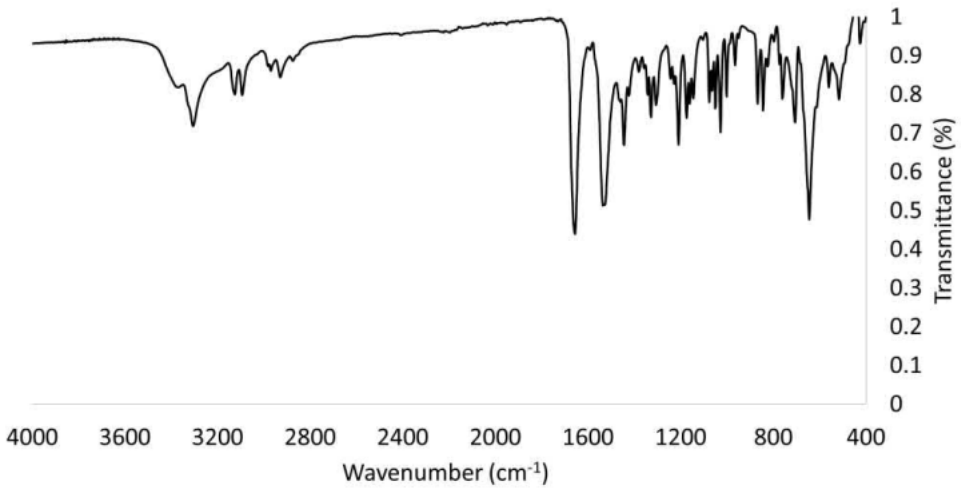

*Figure 8.1.9. IR spectrum of **1**.*

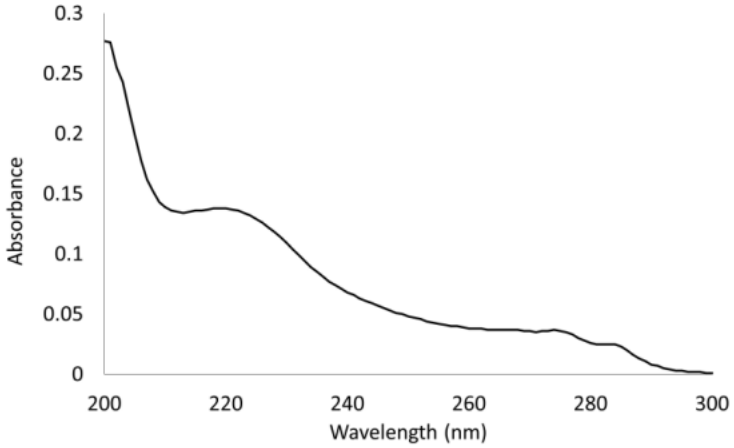

*Figure 8.1.10.. UV-visible absorption spectrum of **1** (0.01 mM,. MeCN).*

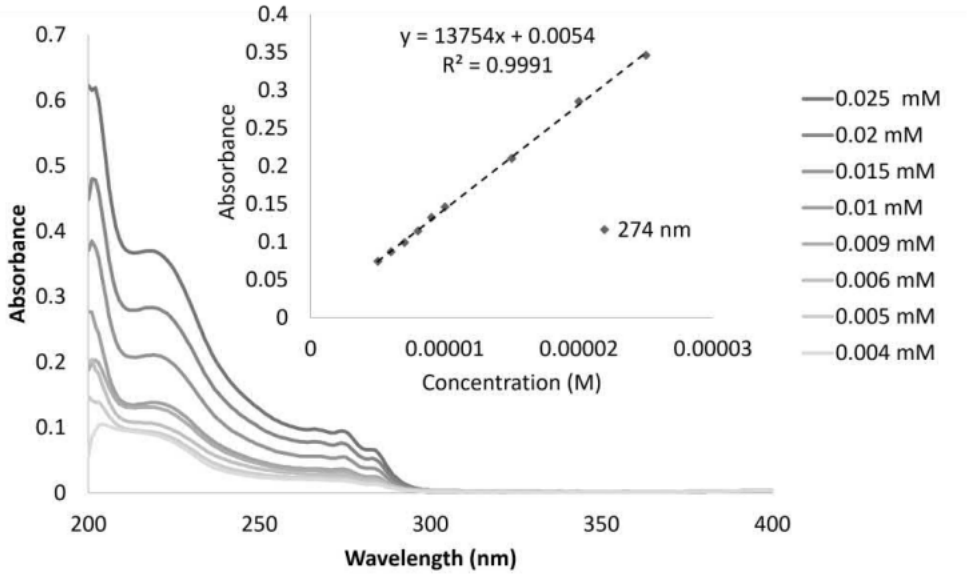

*Figure 8.1.11.. UV-visible absorption spectrum of **1**,. in MeCN.. Insert:. absorbance at 274 nm vs concentration..*

8.1.1.3 Ligand 2

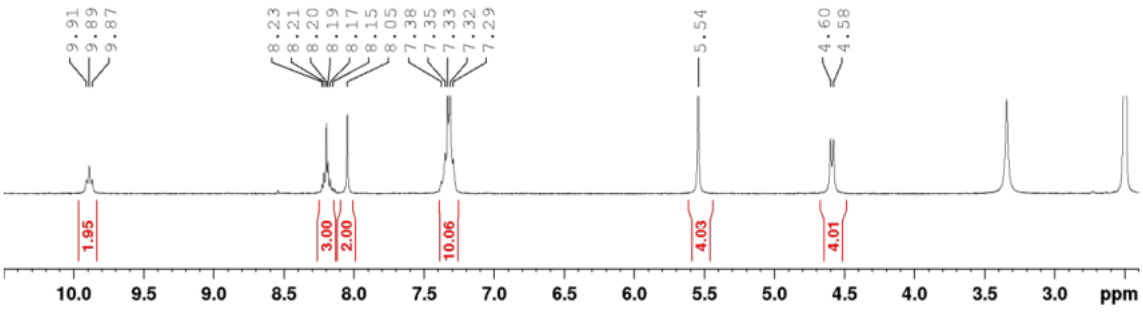

*Figure 8.1.12.. ^{1}H NMR spectrum of **2** (300 MHz,. DMSO-d_6)..*

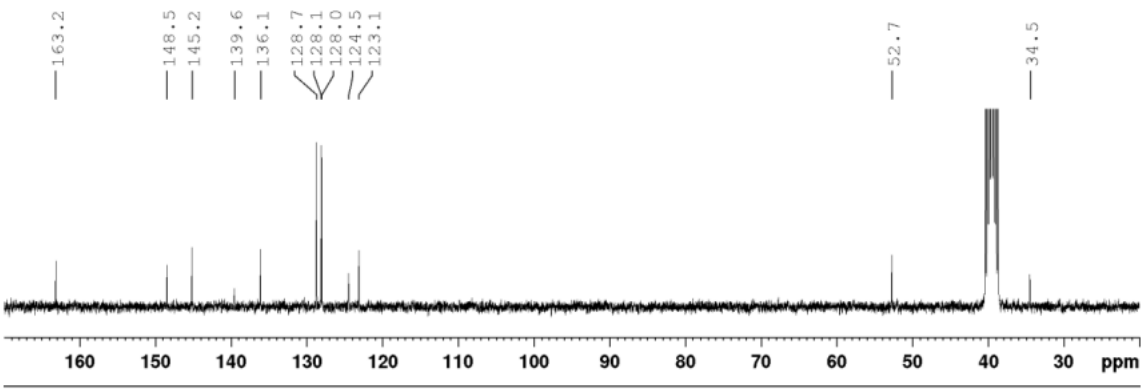

Figure.8.1.13.. ^{13}*C.NMR.spectrum.of.***2***.(75.MHz,.DMSO-d*$_6$*)..*

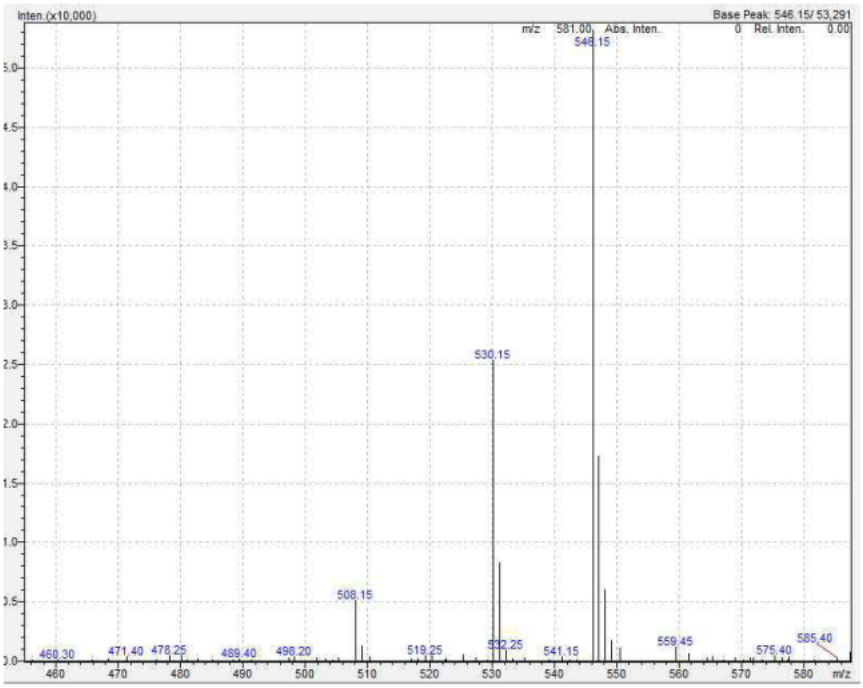

*Figure.8.1.14..LRMS.m/z.=.508.15.[***2***.+.H]*$^+$*.(calc..for.*$C_{27}H_{26}N_9O_2^+$*,508.22),.m/z.=.530.15.[***2***.+.Na]*$^+$*.(calc..for.*$C_{27}H_{25}N_9O_2Na^+$*,.530.20).and m/z.=.546.15.[***2***.+.K]*$^+$*.(calc..for.*$C_{27}H_{25}N_9O_2K^+$*,.546.18)..*

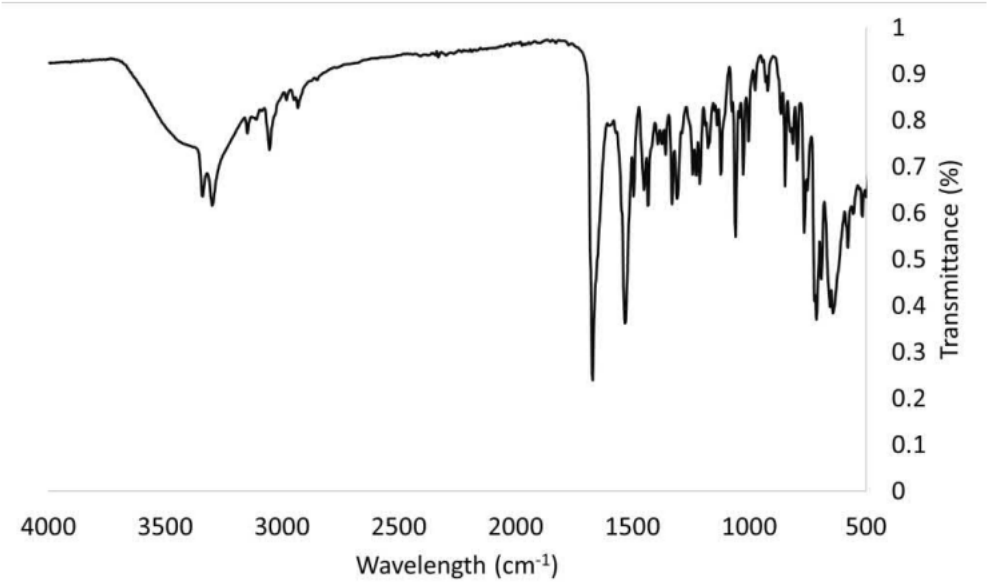

*Figure.8.1.15..IR.spectrum.of.***2***..*

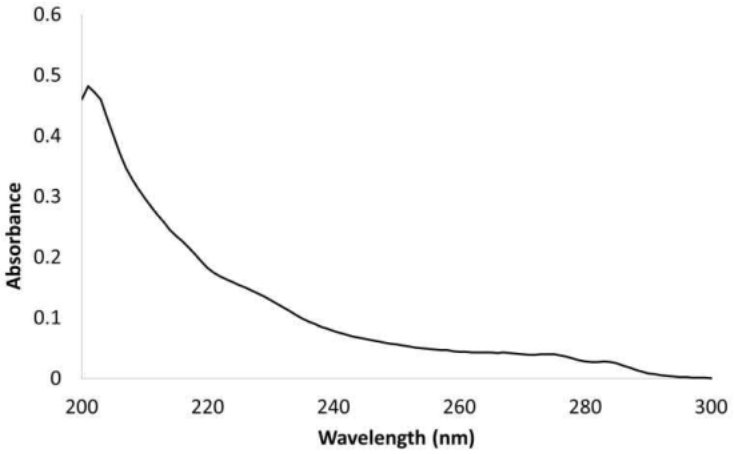

*Figure 8.1.16.. UV-visible absorption spectrum of **2** (0.01 mM, MeCN).*

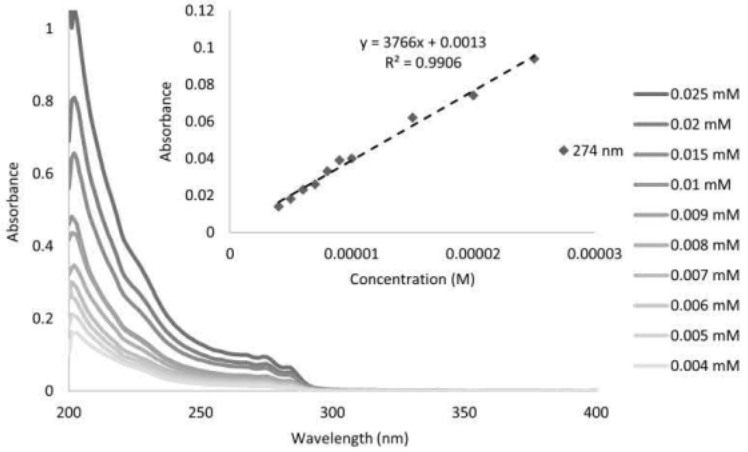

*Figure 8.1.17.. UV-visible absorption spectrum of **2**, in MeCN.. Insert: absorbance at 274 nm vs concentration..*

8.1.1.4 Ligand 3

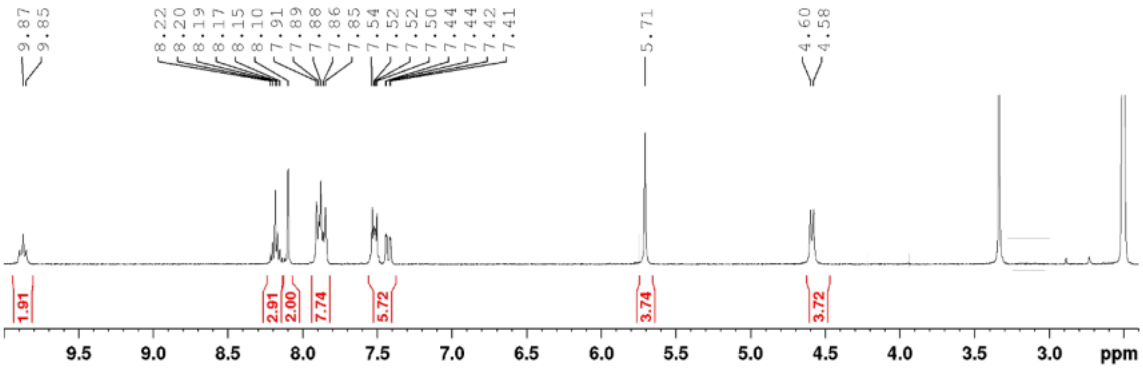

*Figure 8.1.18.. ^{1}H NMR spectrum of **3** (300 MHz, DMSO-d_6)..*

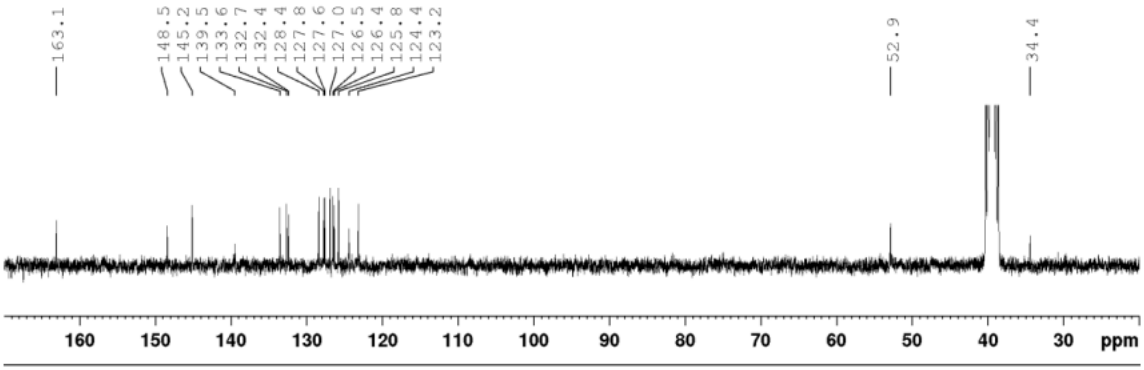

*Figure 8.1.19: ^{13}C NMR spectrum of **3** (75 MHz, DMSO-d_6).*

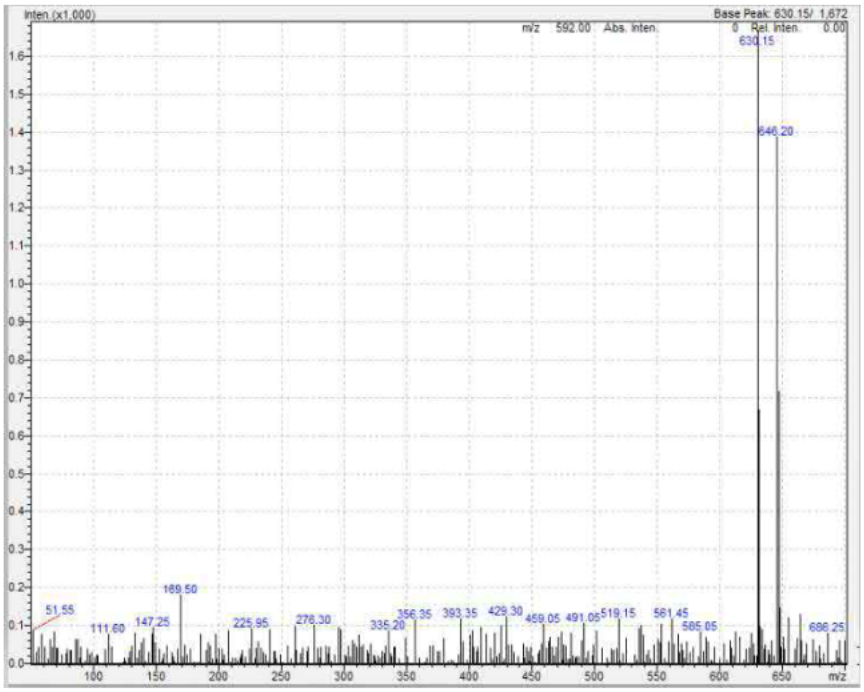

*Figure 8.1.20. LRMS m/z = 630.15 [**3** + Na]$^+$ (calc. for $C_{27}H_{25}N_9O_2Na^+$, 630.23) and m/z = 646.20 [**3** + K]$^+$ (calc. for $C_{27}H_{25}N_9O_2K^+$, 646.21).*

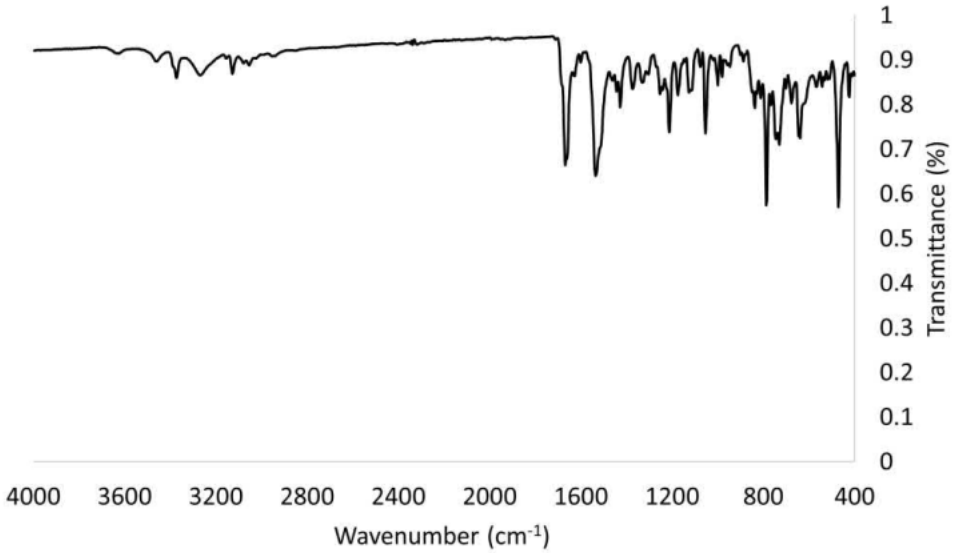

*Figure 8.1.21. IR spectrum of **3**.*

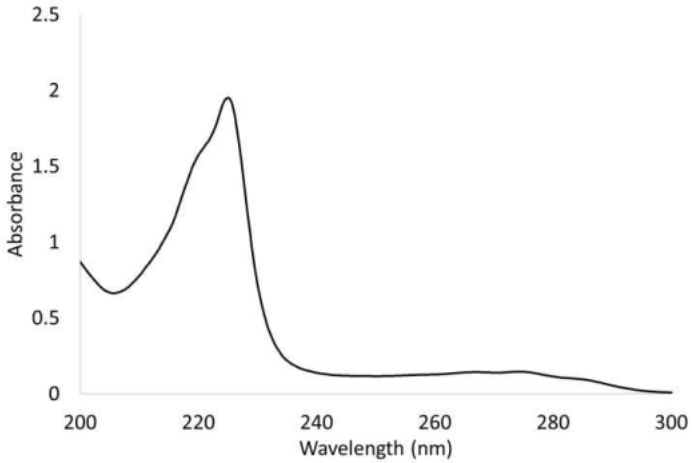

*Figure 8.1.22.. UV-visible absorption spectrum of **3** (0.01 mM,, MeCN).*

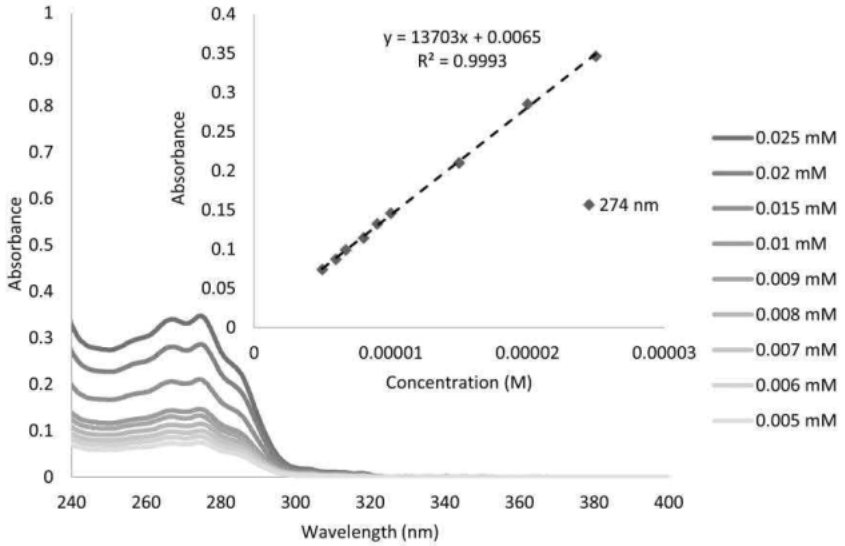

*Figure 8.1.23. UV-visible absorption spectrum of **3**,, in MeCN.. Insert:: absorbance at 274 nm vs concentration..*

8.1.1.4 Ligand 4

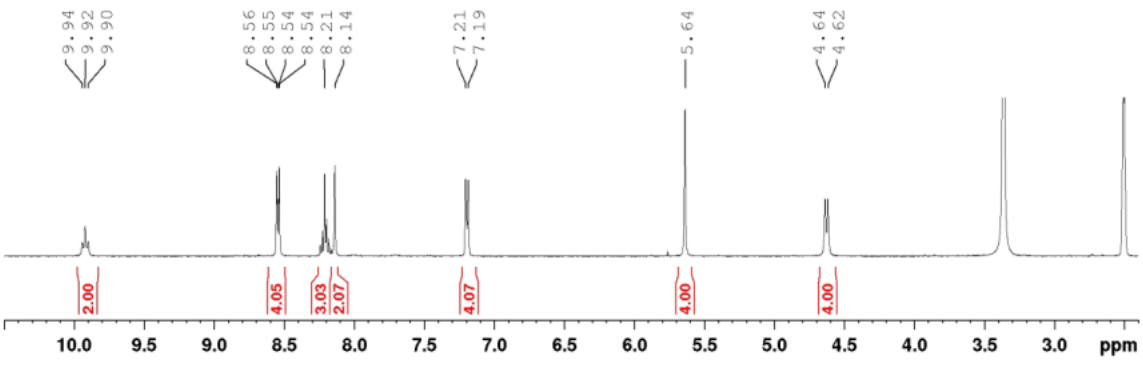

*Figure 8.1.24.. ^{1}H NMR spectrum of **4** (300 MHz,, DMSO-d_6)..*

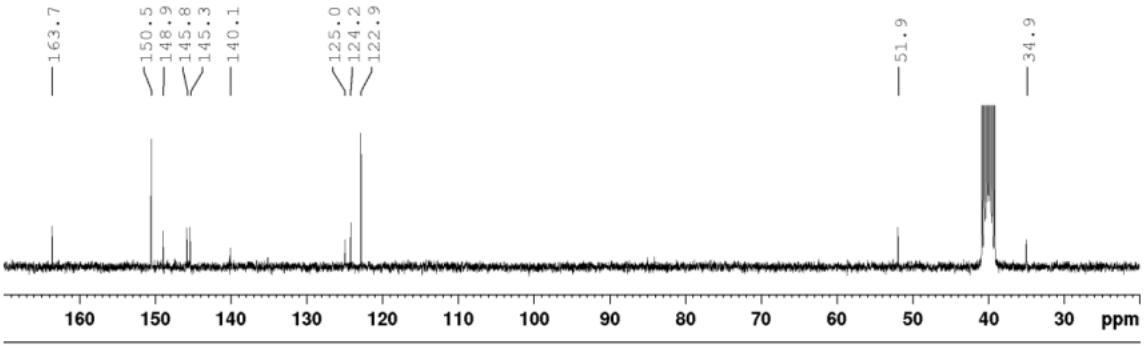

*Figure 8.1.25: ^{13}C NMR spectrum of **4** (75 MHz, DMSO-d_6).*

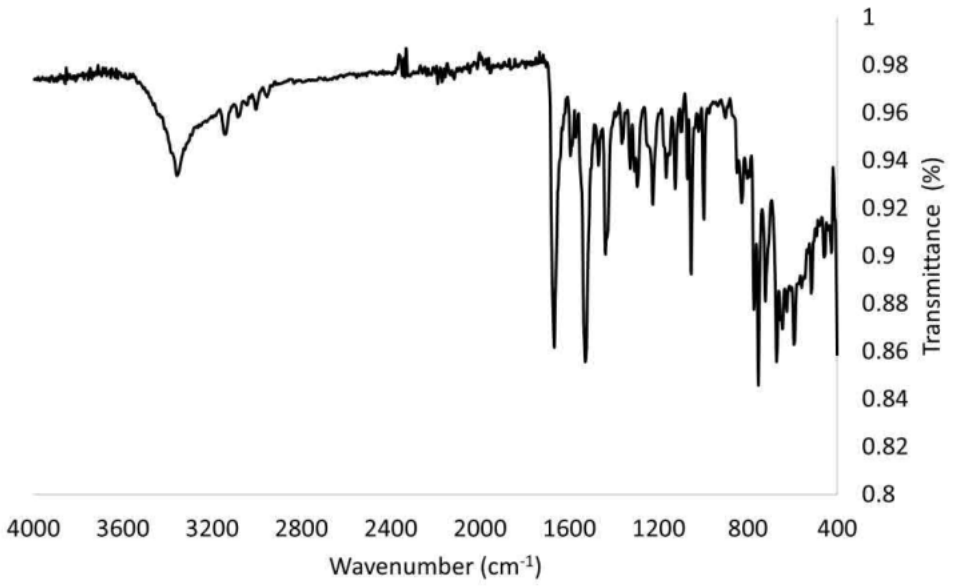

*Figure 8.1.26: IR spectrum of **4**.*

8.1.2 Crystal Structure Data

Crystal Data for **1**, $C_{17}H_{23}N_9O_3$ (*M* = 401.44 g/mol): monoclinic, space group $P2_1/c$ (no. 14), a = 25.2434(15) Å, b = 4.3553(2) Å, c = 18.5900(9) Å, β = 111.456(3)°, V = 1902.19(17) Å^3, Z = 4, T = 123.0 K, μ(CuKα) = 0.844 mm^{-1}, *Dcalc* = 1.402 g/cm^3, 21125 reflections measured (7.526° ≤ 2Θ ≤ 103.746°), 2081 unique (R_{int} = 0.0517, R_{sigma} = 0.0302) which were used in all calculations. The final R_1 was 0.0763 (I > 2σ(I)) and wR_2 was 0.2140 (all data).

Crystal Data for **2**, $C_{27}H_{25}N_9O_2$ (*M* = 507.56 g/mol): orthorhombic, space group $Pca2_1$ (no. 29), a = 19.0980(3) Å, b = 5.38450(10) Å, c = 48.5155(9) Å, V = 4989.00(15) Å^3, Z = 8, T = 100.00(12) K, μ(MoKα) = 0.091 mm^{-1}, *Dcalc* = 1.351 g/cm^3, 57300 reflections measured (5.986° ≤ 2Θ ≤ 51.998°), 9765 unique (R_{int} = 0.0536, R_{sigma} = 0.0399) which were used in all calculations. The final R_1 was 0.0561 (I > 2σ(I)) and wR_2 was 0.1255 (all data).

Crystal Data for **3**, $C_{35}H_{31}N_9O_3$ (*M* = 625.69 g/mol): monoclinic, space group $P2_1/c$ (no. 14), a = 33.248(3) Å, b = 4.8676(4) Å, c = 18.9440(14) Å, β = 105.693(5)°, V = 2951.6(4) Å^3, Z = 4, T = 123.0 K, μ(CuKα) = 0.764 mm^{-1}, *Dcalc* = 1.408 g/cm^3, 45388 reflections measured (2.76° ≤ 2Θ ≤ 100.864°), 3085 unique (R_{int} = 0.0499, R_{sigma} = 0.0256) which were used in all calculations. The final R_1 was 0.0605 (I > 2σ(I)) and wR_2 was 0.1638 (all data).

8.1.3 Lanthanide Complex Data

8.1.3.1 $Ln(1)_3(CF_3SO_3)_3$

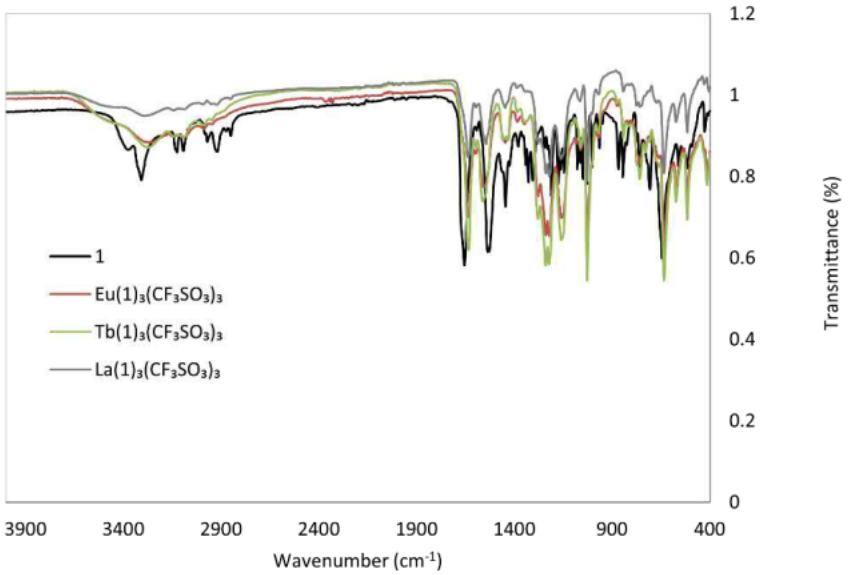

*Figure 8.1.27. IR spectra of **1**, $[Eu(1)_3](CF_3SO_3)_3$, $[Tb(1)_3](CF_3SO_3)_3$ and $[La(1)_3](CF_3SO_3)_3$.*

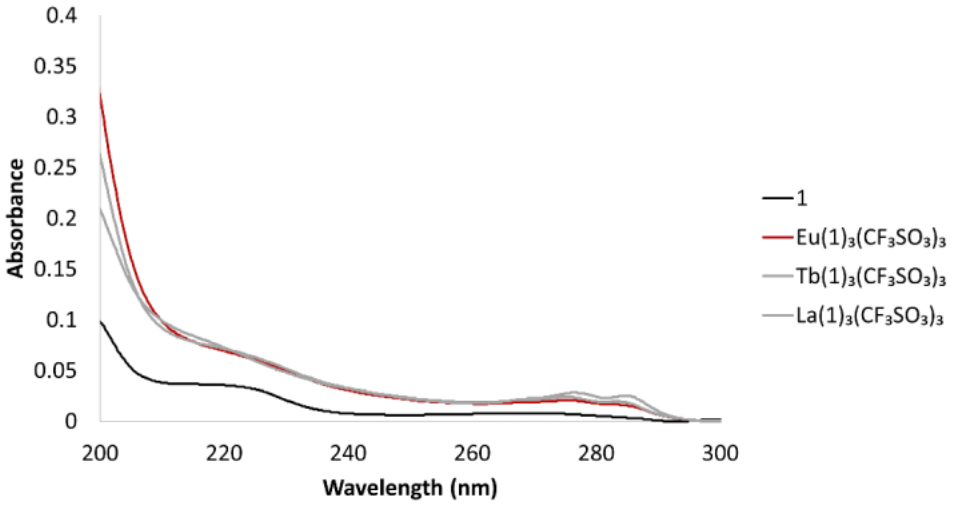

*Figure 8.1.28. UV-visible absorption of **1**, $[Eu(1)_3](CF_3SO_3)_3$, $[Tb(1)_3](CF_3SO_3)_3$ and $[La(1)_3](CF_3SO_3)_3$ (0.001 mM, MeCN).*

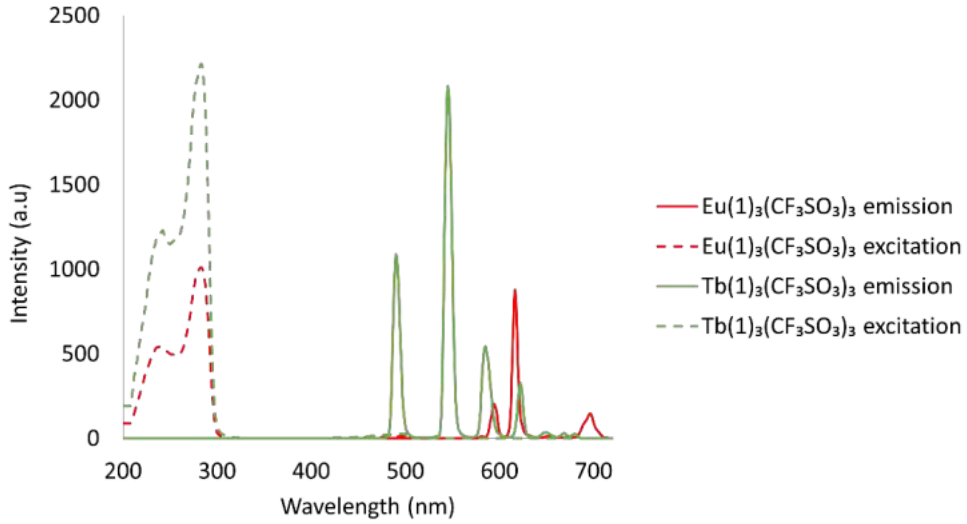

*Figure 8.1.29. Fluorescence spectra of **1**, [Eu(1)$_3$](CF$_3$SO$_3$)$_3$ and [Tb(**1**)$_3$](CF$_3$SO$_3$)$_3$ (0.01 mM, MeCN, $\lambda_{ex.}$ = 274nm). Excitation measured at wavelengths 616 nm for Eu^{3+} and 545 nm Tb^{3+}.*

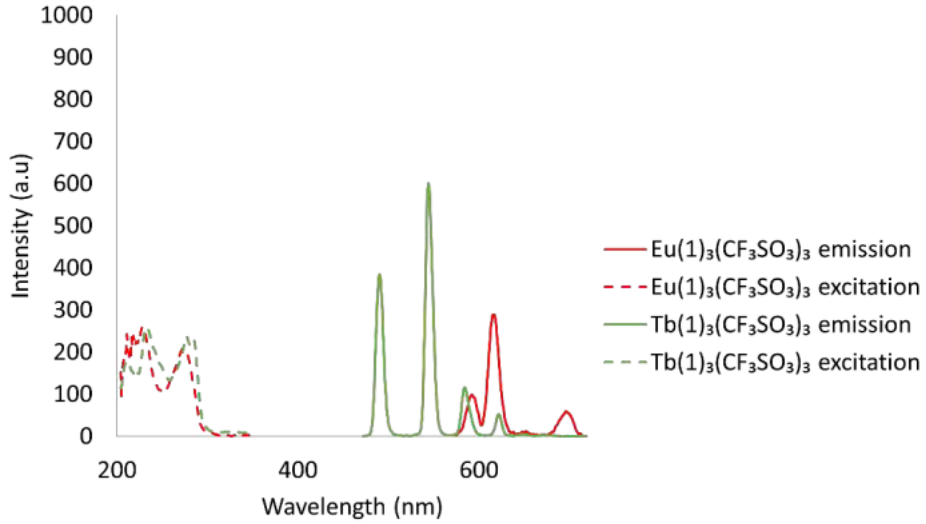

*Figure 8.1.30. Phosphorescence spectra of **1**, [Eu(**1**)$_3$](CF$_3$SO$_3$)$_3$ and [Tb(**1**)$_3$](CF$_3$SO$_3$)$_3$ (0.01 mM, MeCN, λex. = 274nm). Excitation measured at wavelengths 616 nm for Eu^{3+} and 545 nm Tb^{3+}.*

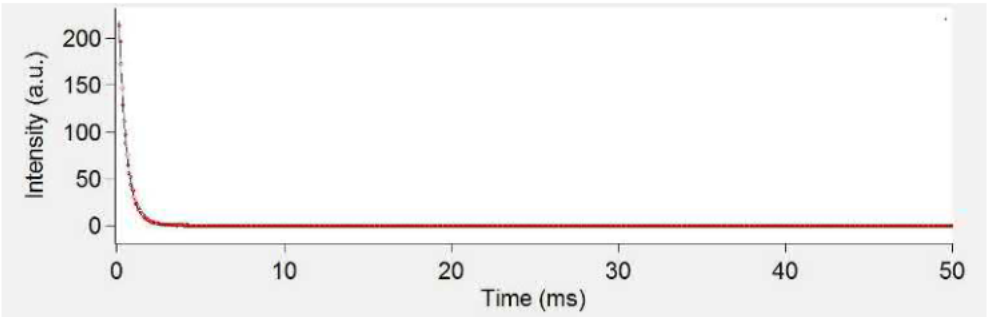

Figure 8.1.31. Lifetime measurement and single exponential fit for [Eu(1)$_3$](CF$_3$SO$_3$)$_3$ (0.01 mM, MeCN, $\lambda_{ex.}$ = 274nm, measured at 616 nm).

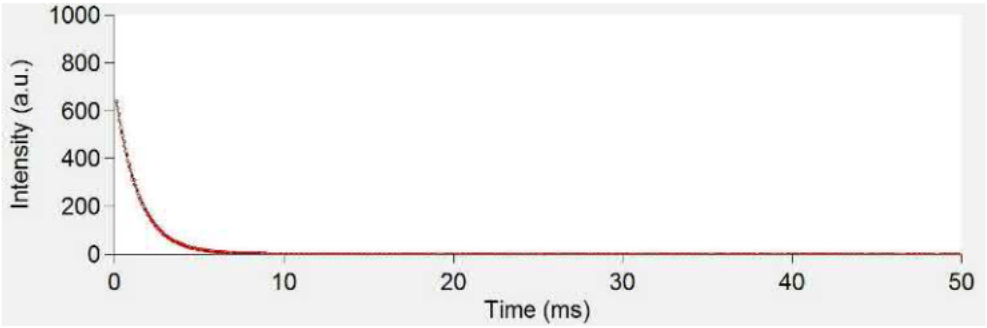

Figure 8.1.32. Lifetime measurement and single exponential fit for $[Tb(\mathbf{1})_3](CF_3SO_3)_3$ (0.01 mM, MeCN, λ_{ex} = 274nm, measured at 545 nm).

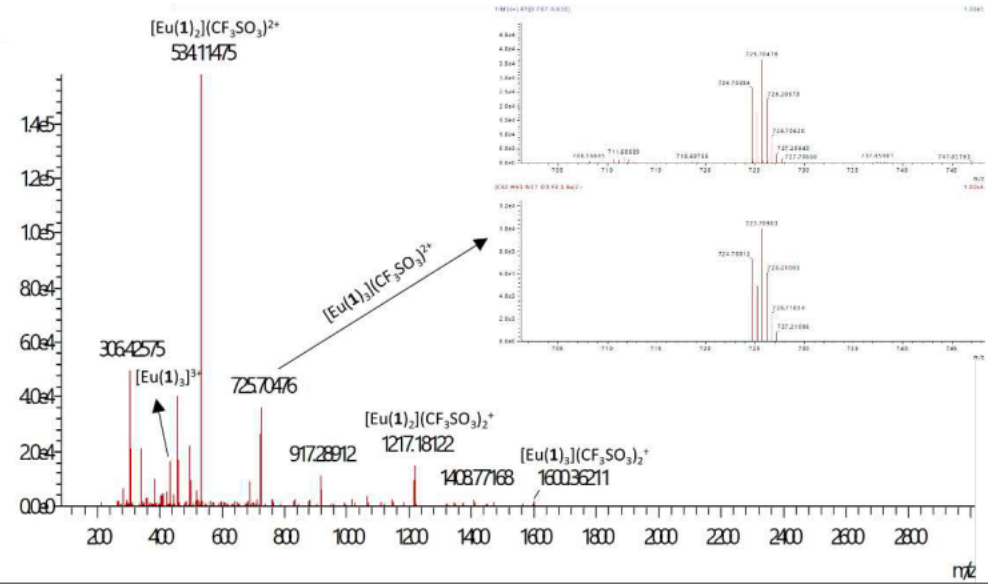

Figure 8.1.33. HRMS of $[Eu(\mathbf{1})_3](CF_3SO_3)_3$. Insert: zoom in of $[Eu(\mathbf{1})_3](CF_3SO_3)_2^+$ with isotopic simulation below, m/z = 725.7048 $[Eu(\mathbf{1})_3](CF_3SO_3)^{2+}$ calc. for $(C_{52}H_{63}N_{27}O_9SF_3Eu)^{2+}$, 725.7090.

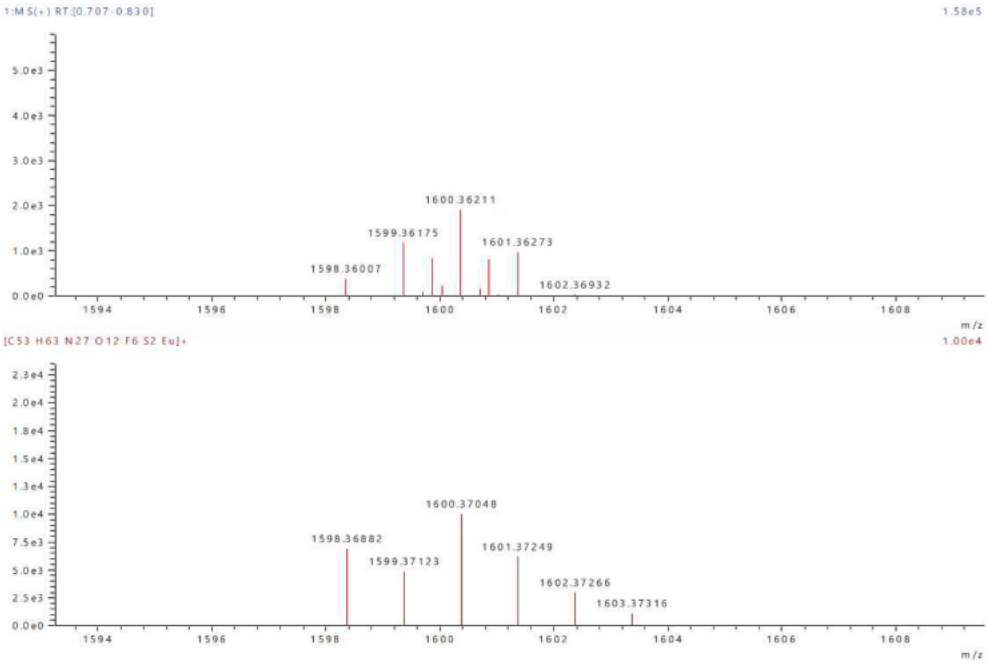

Figure 8.1.34. (Top) HRMS m/z = 1600.3621 $[Eu(\mathbf{1})_3](CF_3SO_3)_2^+$, (Bottom) calc. for $(C_{53}H_{63}N_{27}O_{12}S_2F_6Eu)^+$ 1600.3705.

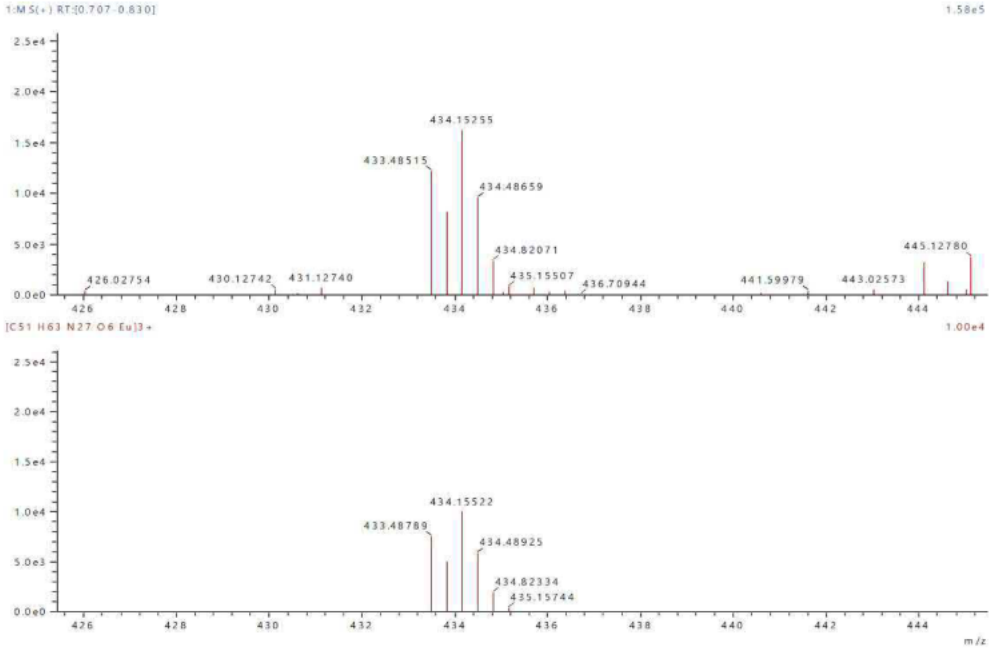

Figure. 8.. 1.. 35.. (Top). HRMS. m/z. =. 434.1526 [Eu(1)$_3$]$^{3+}$, (Bottom). calc.. for ($C_{51}H_{63}N_{27}O_6Eu$)$^{3+}$ 434.1552..

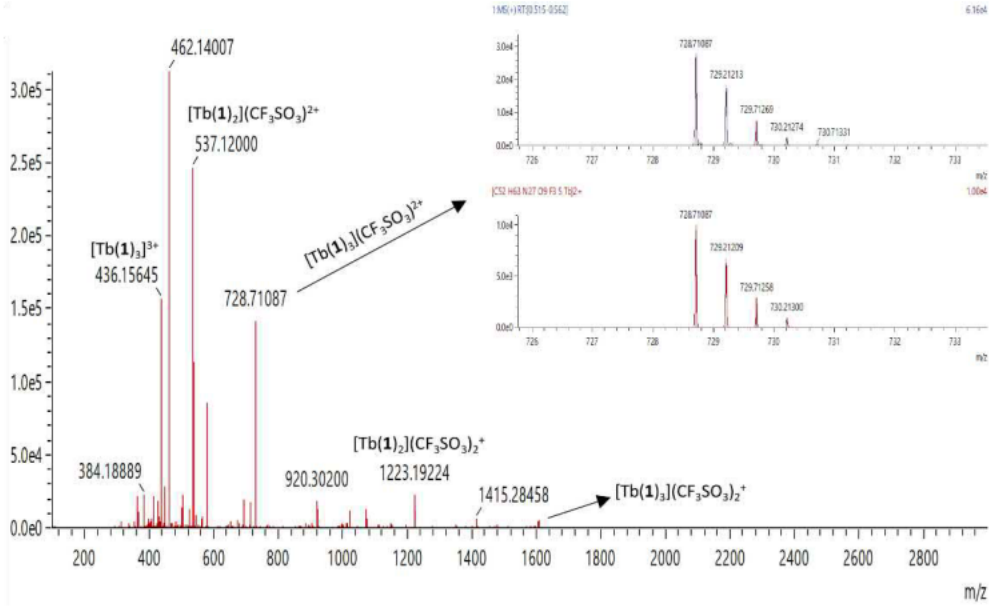

Figure. 8.. 1.. 36.. HRMS. of [Tb(1)$_3$](CF$_3$SO$_3$)$_3$, Insert:. zoom. in. of [Tb(1)$_3$](CF$_3$SO$_3$)$^{2+}$ with. isotopic. simulation. below,. m/z. =. 728.7109 [Tb(1)$_3$](CF$_3$SO$_3$)$^{2+}$ (calc.. for. ($C_{52}H_{63}N_{27}O_9SF_3Tb$)$^{2+}$ 728.7109)..

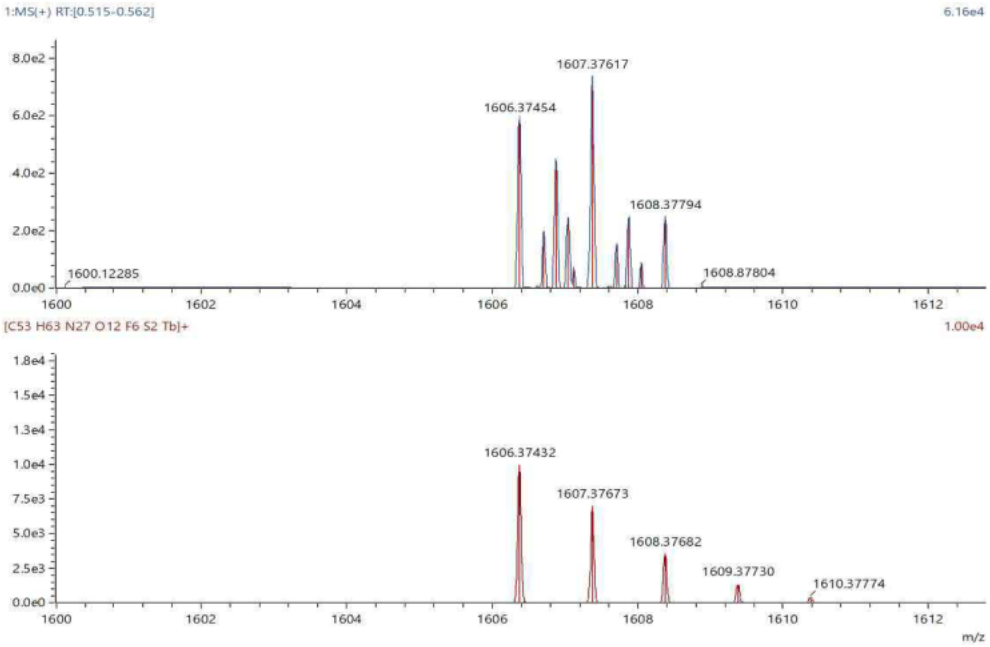

*Figure 8.1.37. (Top) HRMS m/z = 1606.3745 [Tb(**1**)$_3$](CF$_3$SO$_3$)$_2^+$, (Bottom) calc. for (C$_{53}$H$_{63}$N$_{27}$O$_{12}$S$_2$F$_6$Tb)$^+$ 1606.3743.*

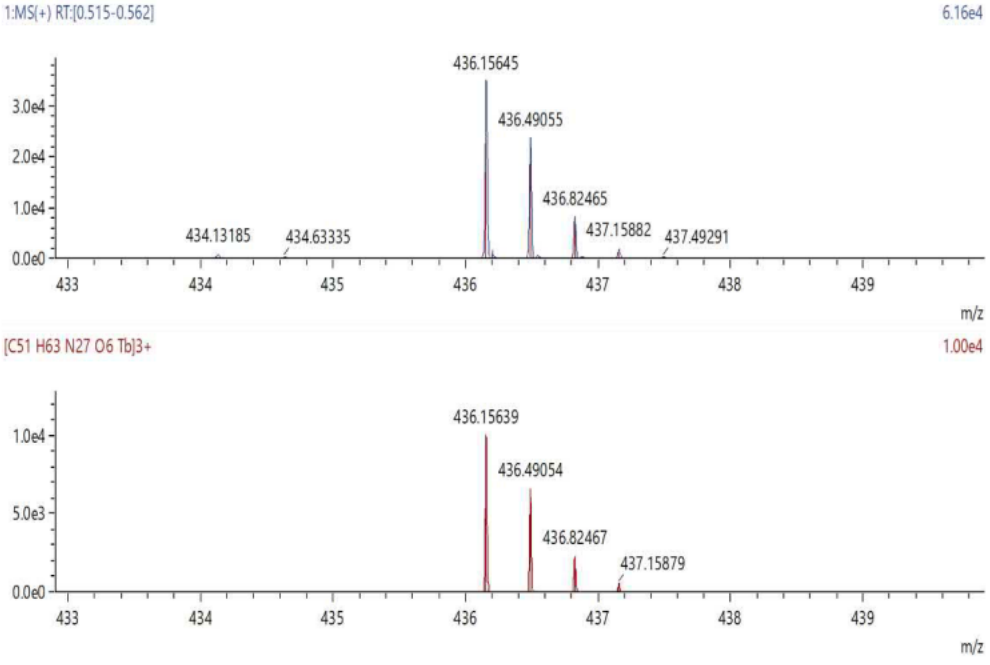

*Figure 8.1.38. (Top) HRMS m/z = 436.1565 [Tb(**1**)$_3$]$^{3+}$, (Bottom) calc. for (C$_{51}$H$_{63}$N$_{27}$O$_6$Tb)$^{3+}$ 436.1564.*

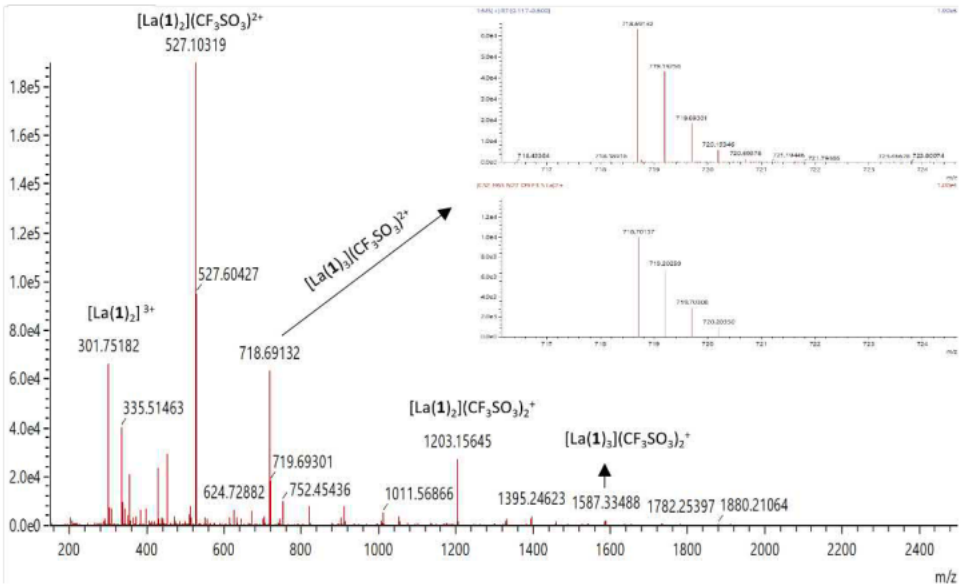

Figure. 8.1.39.. HRMS. of [La(1)$_3$](CF$_3$SO$_3$)$_3$, Insert:. zoom. in. of [La(1)$_3$](CF$_3$SO$_3$)$^{2+}$ with. isotopic. simulation. below,. m/z. =. 718.6913 [La(1)$_3$](CF$_3$SO$_3$)$^{2+}$ (calc.. for. (C$_{52}$H$_{63}$N$_{27}$O$_9$SF$_3$La)$^{2+}$,. 718.7014)...

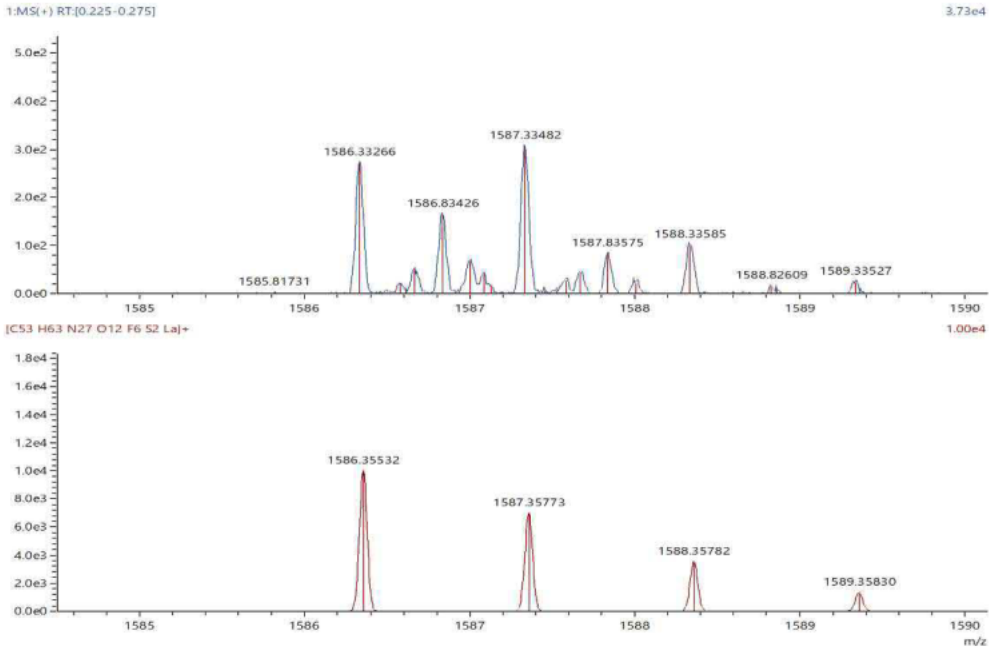

Figure. 8.1.40.. (Top). HRMS. m/z. =. 1586.3327 [La(1)$_3$](CF$_3$SO$_3$)$_2^+$, (Bottom). calc.. for (C$_{53}$H$_{63}$N$_{27}$O$_{12}$S$_2$F$_6$La)$^+$, 1586.3553..

8.1.3.2 Ln(2)$_3$(CF$_3$SO$_3$)$_3$

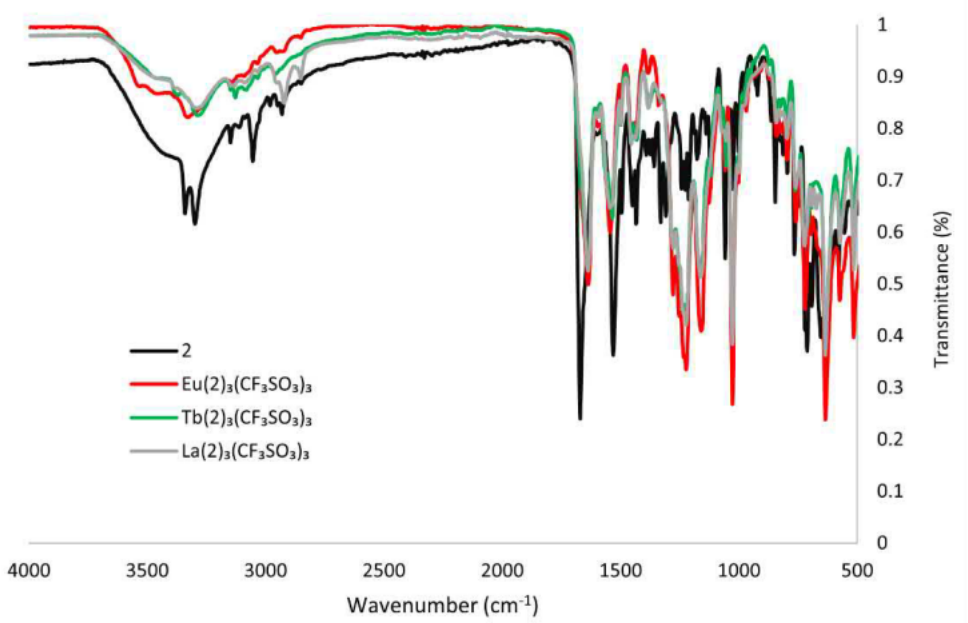

Figure 8.1.41. IR spectra of **2**, *[Eu(2)$_3$](CF$_3$SO$_3$)$_3$, [Tb(2)$_3$](CF$_3$SO$_3$)$_3$ and [La(2)$_3$](CF$_3$SO$_3$)$_3$.*

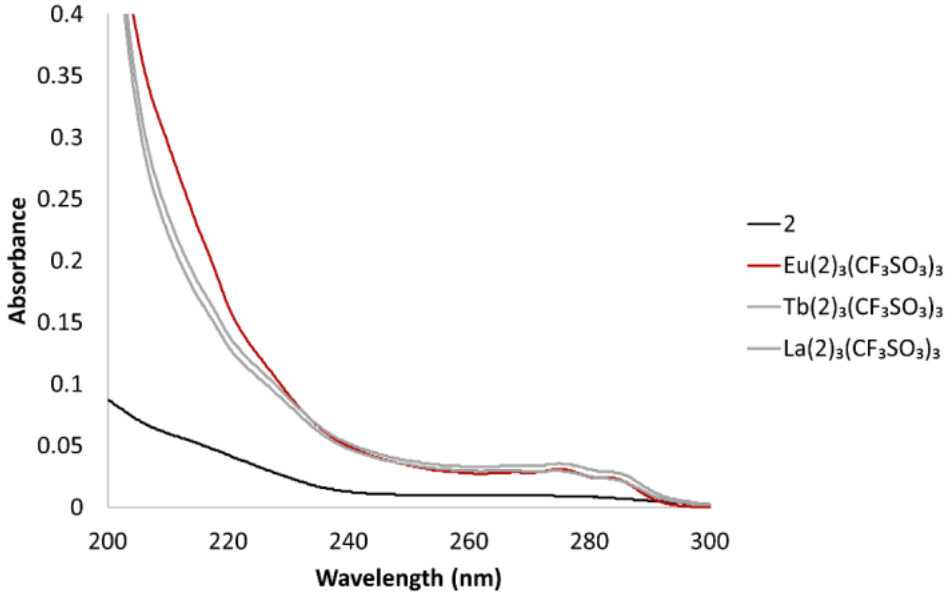

Figure 8.1.42. UV-visible absorption of **2**, *[Eu(2)$_3$](CF$_3$SO$_3$)$_3$, [Tb(2)$_3$](CF$_3$SO$_3$)$_3$ and [La(2)$_3$](CF$_3$SO$_3$)$_3$ (0.001 mM, MeCN).*

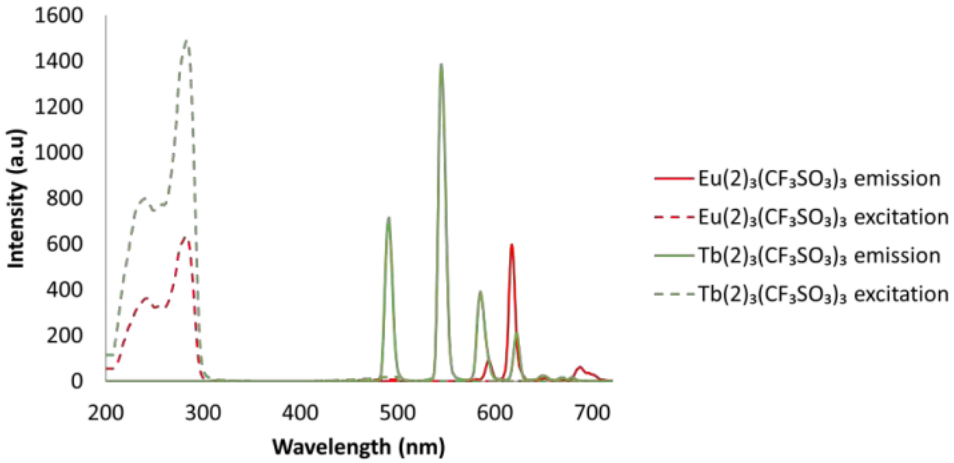

Figure. 8.1.43. Fluorescence. spectra. of. ***2****,. [Eu(2)$_3$](CF$_3$SO$_3$)$_3$,. [Tb(2)$_3$](CF$_3$SO$_3$)$_3$). (0.01. mM,. MeCN,. λ_{ex} =. 274nm),.. Excitation. measured at. wavelengths. 616. nm. for. Eu^{3+}. and. 545. nm. Tb^{3+}.*

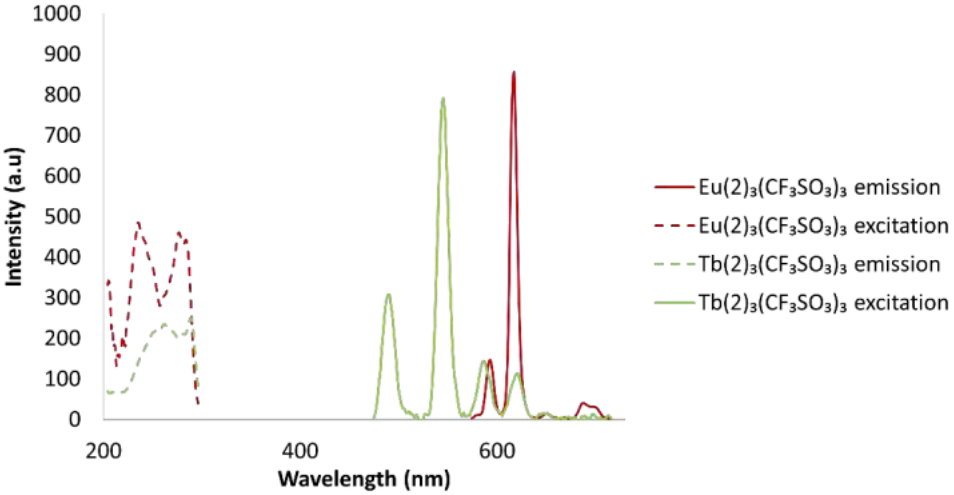

Figure. 8.1.44. Phosphorescence. spectra. of. ***2****,. [Eu(2)$_3$](CF$_3$SO$_3$)$_3$,. [Tb(2)$_3$](CF$_3$SO$_3$)$_3$ (0.01. mM,. MeCN,. λ_{ex} =. 274nm),.. Excitation measured. at. wavelengths. 616. nm. for. Eu^{3+}. and. 545. nm. Tb^{3+}.*

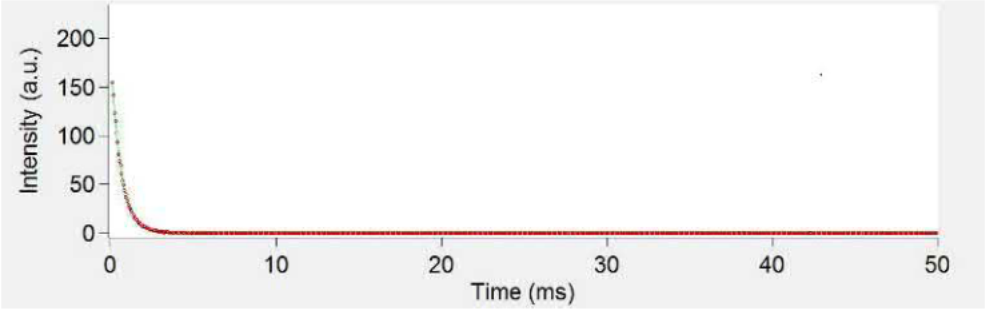

Figure. 8.1.45. Lifetime. measurement. and. single. exponential. fit. for,. [Eu(2)$_3$](CF$_3$SO$_3$)$_3$ (0.01. mM,. MeCN,. λ_{ex} =. 274nm,. measured. at. 616 nm)...

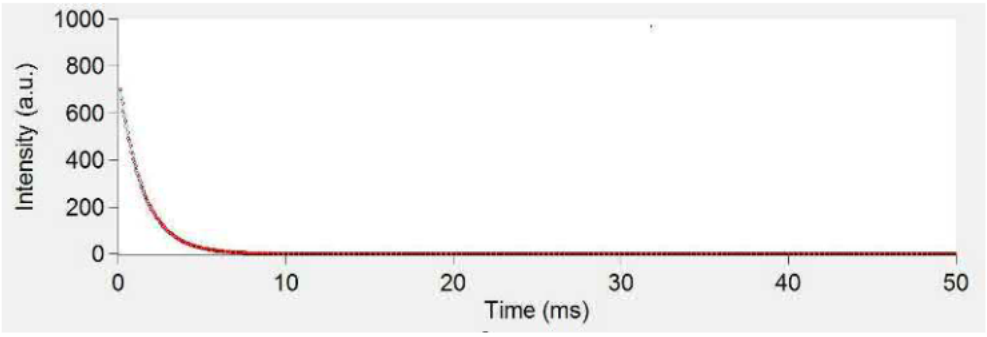

Figure 8.1.46. Lifetime measurement and single exponential fit for, [Tb(2)$_3$](CF$_3$SO$_3$)$_3$ (0.01 mM, MeCN, λ_{ex} = 274nm, measured at 545 nm).

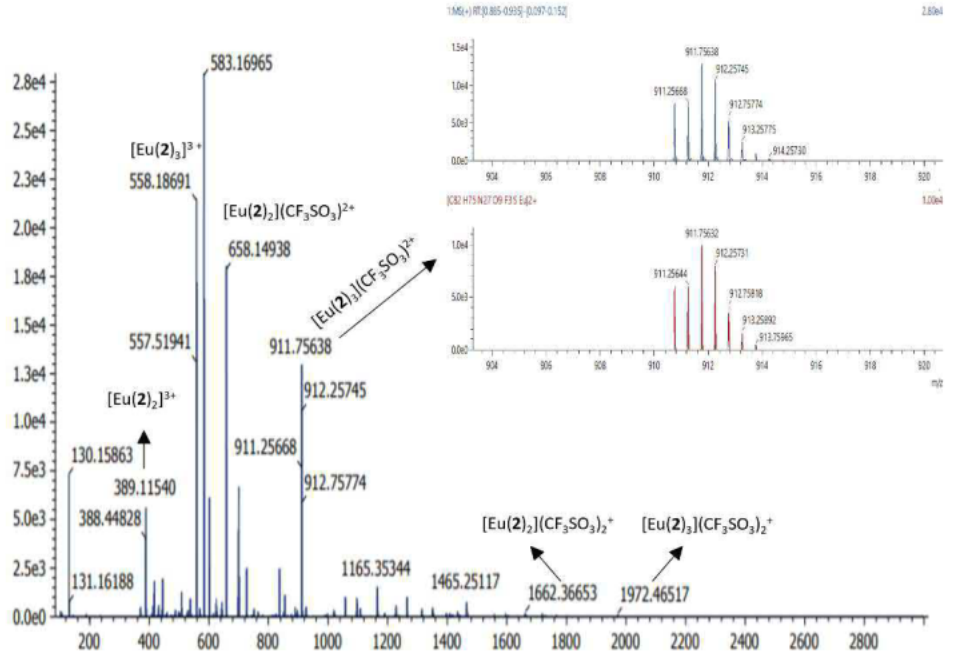

Figure 8.1.47. HRMS of [Eu(2)$_3$](CF$_3$SO$_3$)$_3$, Insert: zoom in of [Eu(2)$_3$](CF$_3$SO$_3$)$^{2+}$ with isotopic simulation below, m/z = 911.7564 [Eu(2)$_3$](CF$_3$SO$_3$)$^{2+}$ (calc. for (C$_{82}$H$_{75}$N$_{27}$O$_9$SF$_3$Eu)$^{2+}$, 911.7563).

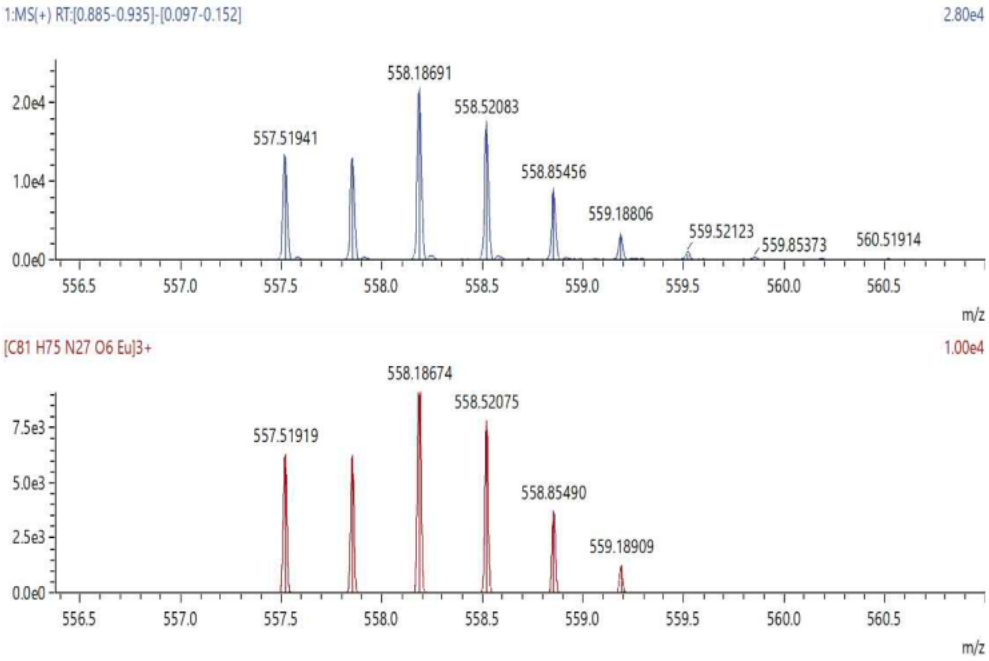

Figure 8.1.48. (Top) HRMS m/z = 558.1869 [Eu(2)$_3$]$^{3+}$ (Bottom) calc. for (C$_{81}$H$_{75}$N$_{27}$O$_6$Eu)$^{3+}$, 558.1867.

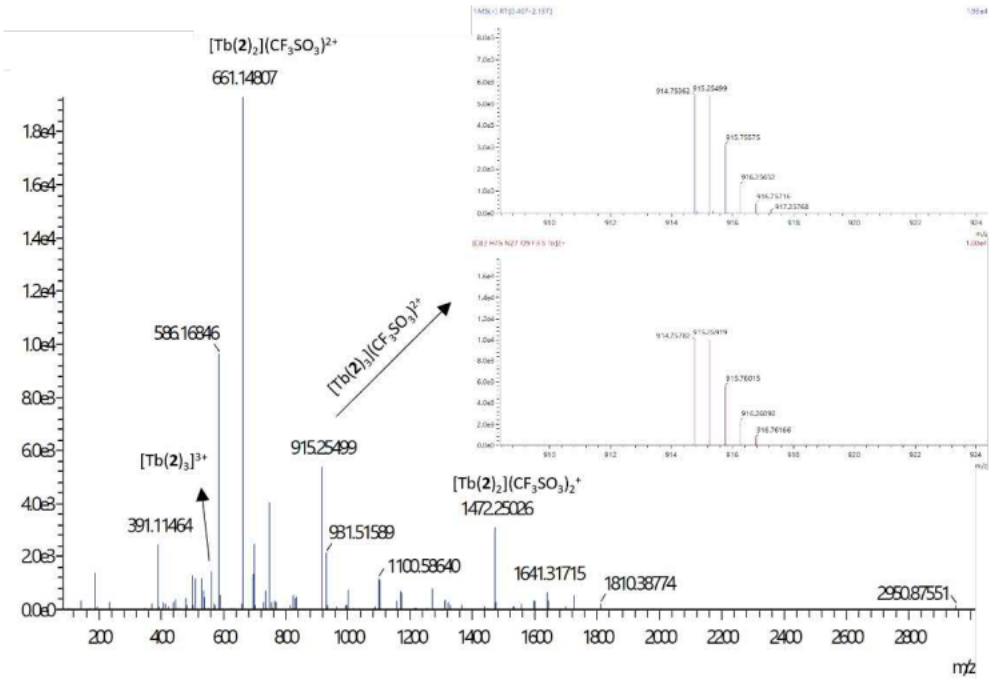

Figure. 8.1.49. HRMS. of [Tb(2)$_3$](CF$_3$SO$_3$)$_3$,. Insert:. zoom. in. of [Tb(2)$_3$](CF$_3$SO$_3$)$^{2+}$ with. isotopic. simulation. below,. m/z. =. 915.7536 [Tb(2)$_3$](CF$_3$SO$_3$)$^{2+}$ (calc..for (C$_{82}$H$_{75}$N$_{27}$O$_9$SF$_3$Tb)$^{2+}$,. 915.7578)..

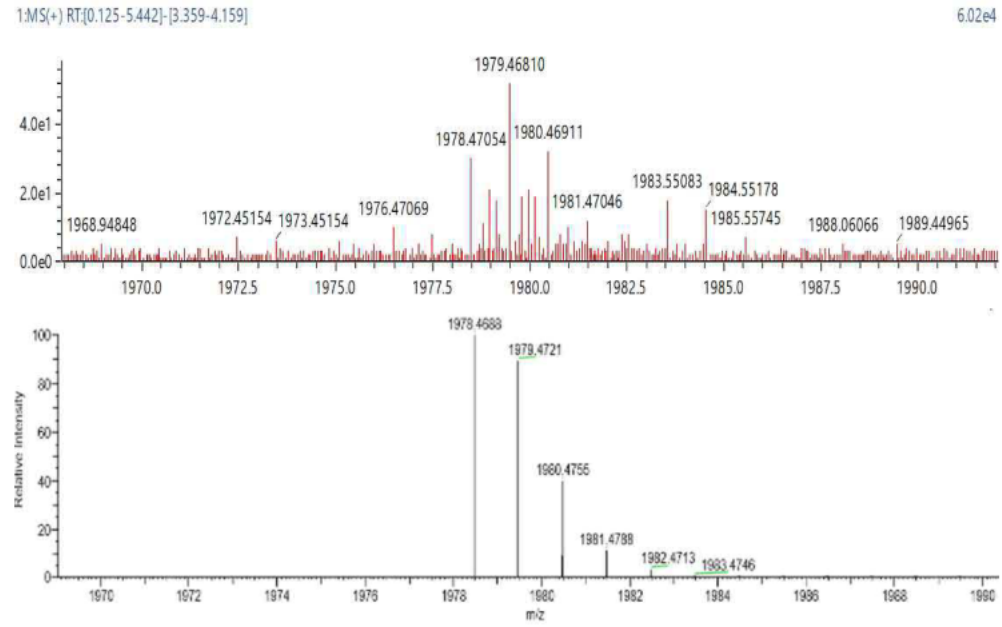

Figure. 8.1.50.. (Top). HRMS. m/z. =. 1978.4705 [Tb(2)$_3$](CF$_3$SO$_3$)$_2^+$ (Bottom). calc.. for (C$_{83}$H$_{75}$N$_{27}$O$_{12}$S$_2$F$_6$Tb)$^+$,. 1978.4688. .

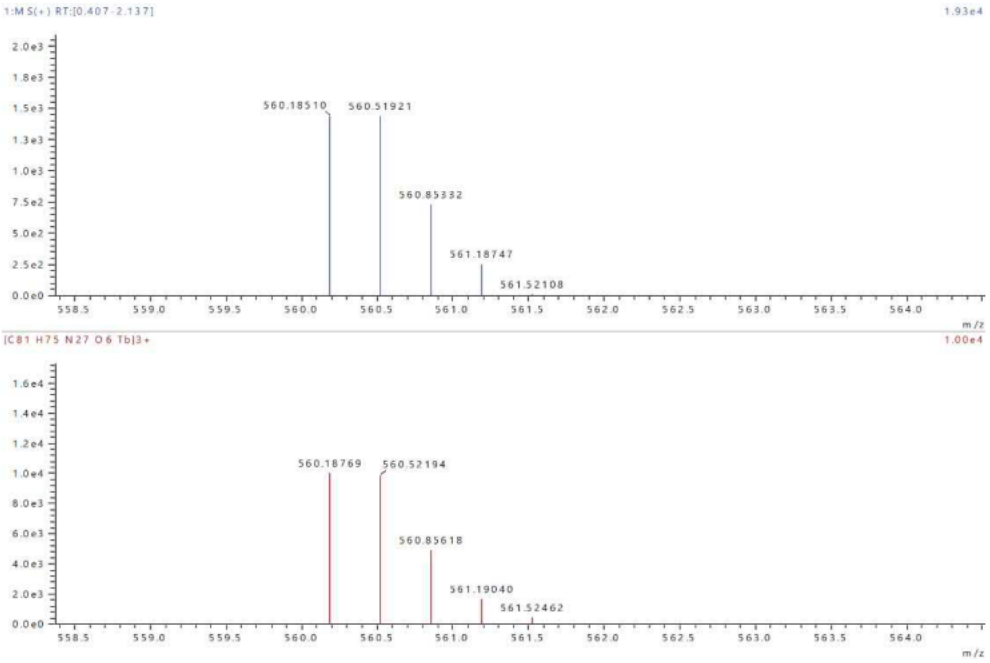

Figure 8.1.51. (Top) *HRMS m/z = 560.1851 [Tb(**2**)$_3$]$^{3+}$, (Bottom) calc. for (C$_{81}$H$_{75}$N$_{27}$O$_6$Tb)$^{3+}$, 560.1877.*

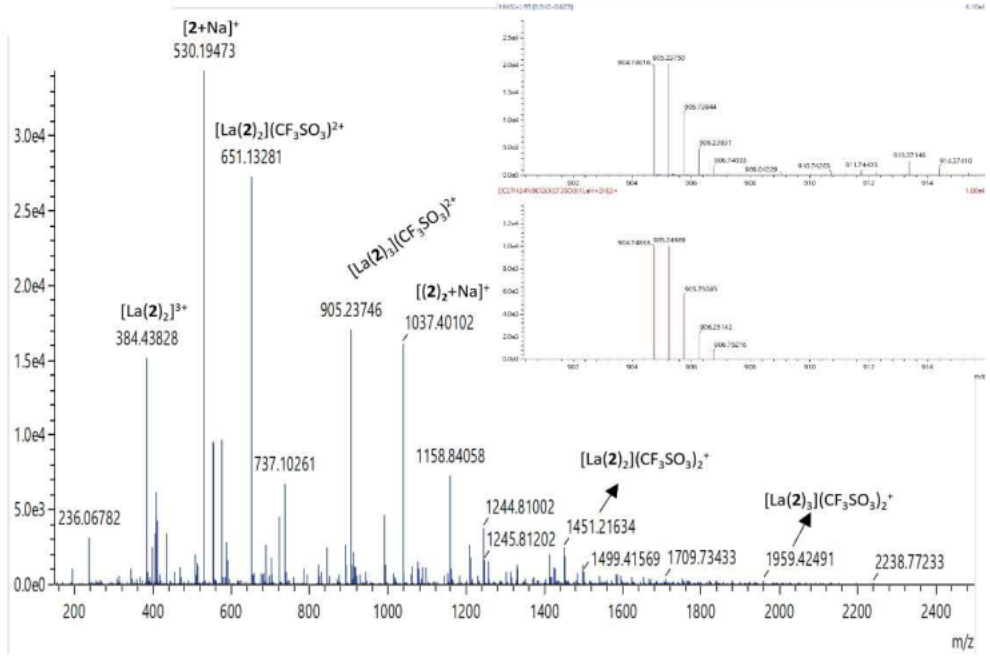

*Figure 8.1.52. HRMS of [La(**2**)$_3$](CF$_3$SO$_3$)$_3$. Insert: zoom in of [La(**2**)$_3$](CF$_3$SO$_3$)$^{2+}$ with isotopic simulation below, m/z = 904.7362 [La(**2**)$_3$](CF$_3$SO$_3$)$^{2+}$ (calc. for (C$_{82}$H$_{75}$N$_{27}$O$_9$SF$_3$La)$^{2+}$, 904.7483).*

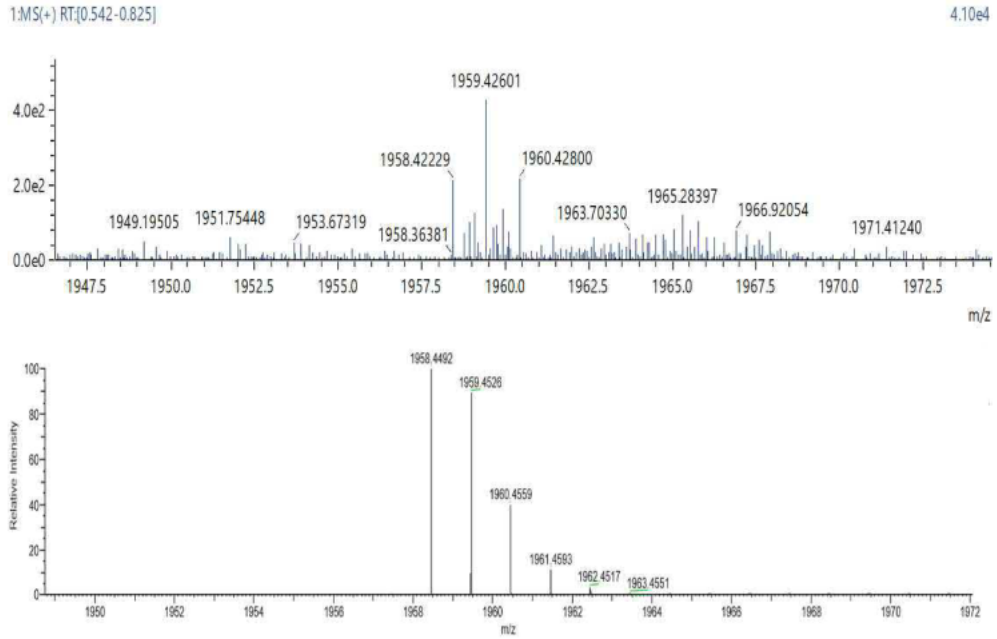

*Figure 8.1.53. (Top) HRMS m/z = 1958.4223 [La(**2**)$_3$](CF$_3$SO$_3$)$_2^+$, (Bottom) calc. for (C$_{83}$H$_{75}$N$_{27}$O$_{12}$S$_2$F$_6$La)$^+$, 1958.4492.*

8.1.3.3 Ln(3)$_3$(CF$_3$SO$_3$)$_3$

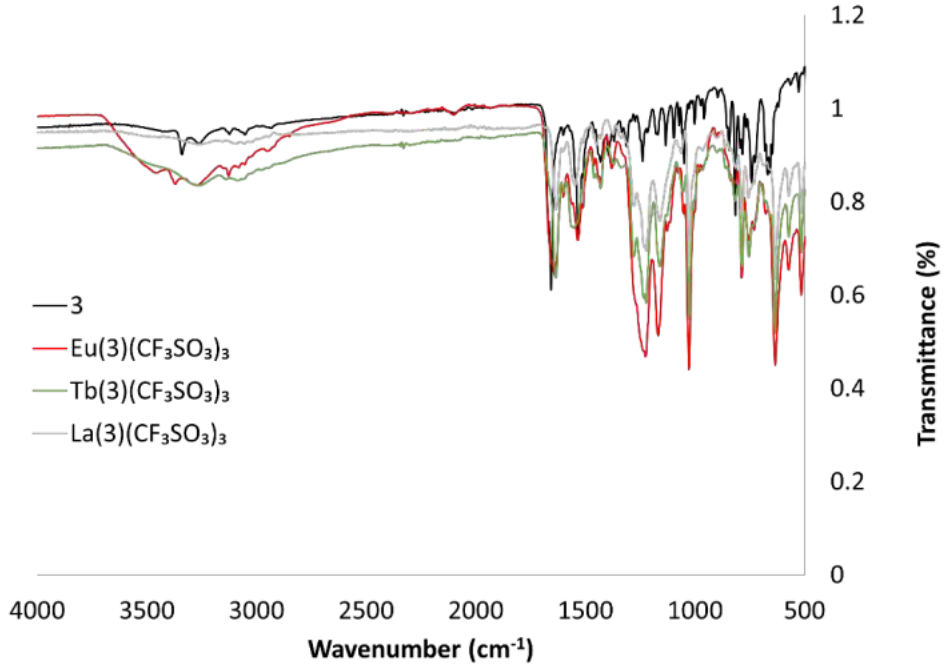

*Figure 8.1.54. IR spectra of **3**, [Eu(**3**)$_3$](CF$_3$SO$_3$)$_3$, [Tb(**3**)$_3$](CF$_3$SO$_3$)$_3$ and [La(**3**)$_3$](CF$_3$SO$_3$)$_3$.*

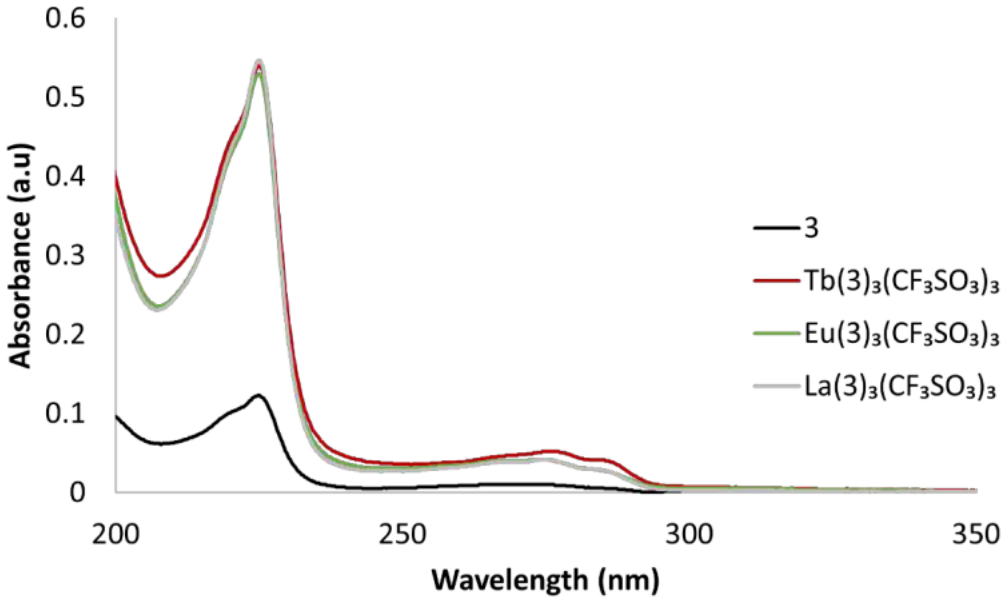

*Figure 8.1.55. UV-visible absorption of **3**, [Eu(**3**)$_3$](CF$_3$SO$_3$)$_3$, [Tb(**3**)$_3$](CF$_3$SO$_3$)$_3$ and [La(**3**)$_3$](CF$_3$SO$_3$)$_3$ (0.001 mM, MeCN).*

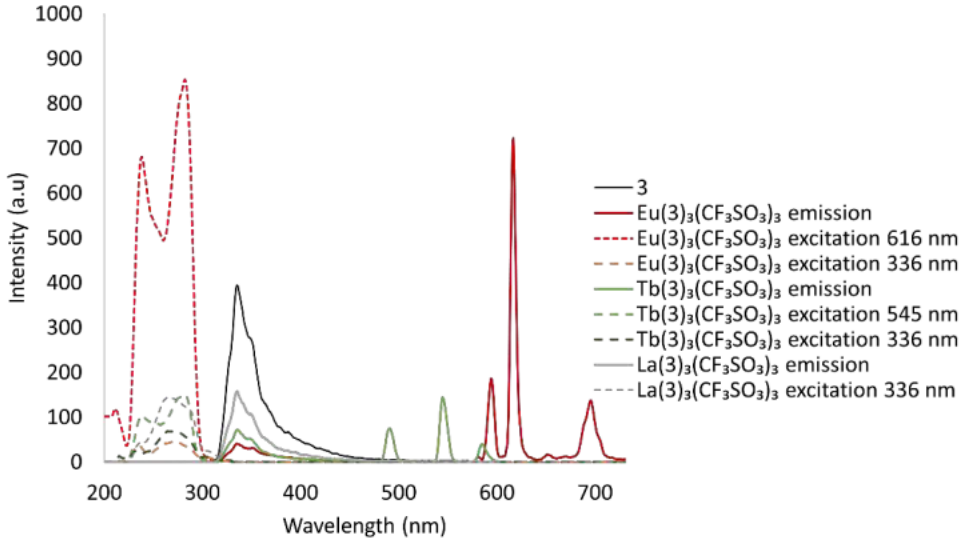

*Figure 8.1.56. Fluorescence spectra of **3**, [Eu(**3**)$_3$](CF$_3$SO$_3$)$_3$, [Tb(**3**)$_3$](CF$_3$SO$_3$)$_3$ and [La(**3**)$_3$](CF$_3$SO$_3$)$_3$ (0.01 mM, MeCN, $\lambda_{ex.}$ = 274nm). Excitation measured at wavelengths at 616 nm for Eu^{3+}, 545 nm Tb^{3+}, 336 nm for ligand centred emission.*

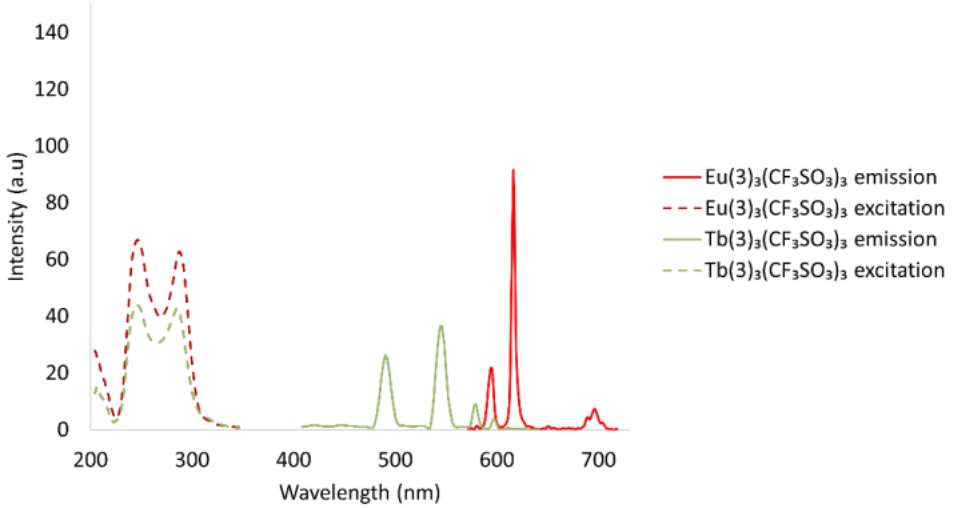

*Figure. 8.1.57. Phosphorescence. spectra. of. **3**,. [Eu(**3**)$_3$](CF$_3$SO$_3$)$_3$and. [Tb(**3**)$_3$](CF$_3$SO$_3$)$_3$ (0.01. mM,. MeCN,. λ_{ex} =. 274nm).. Excitation measured.at.wavelengths.at.616.nm.for.Eu^{3+}.and.545.nm.Tb^{3+}..*

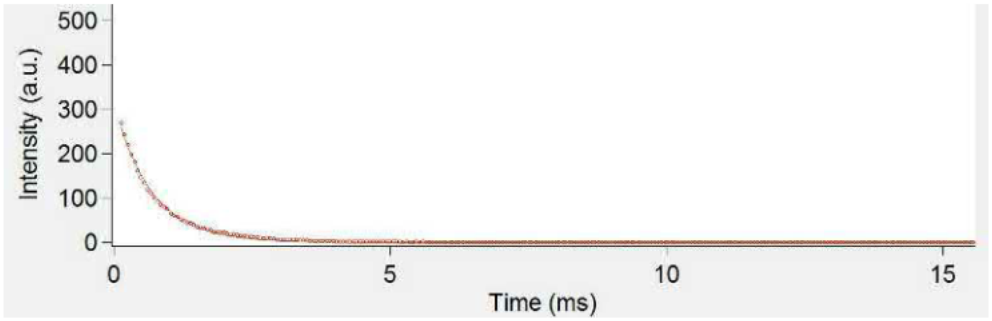

*Figure.8.1.58. Lifetime.measurement.and.single.exponential.fit.for,.[Eu(**3**)$_3$](CF$_3$SO$_3$)$_3$ (0.01.mM,.MeCN,.λ_{ex} =.274nm,.measured.at.616 nm)...*

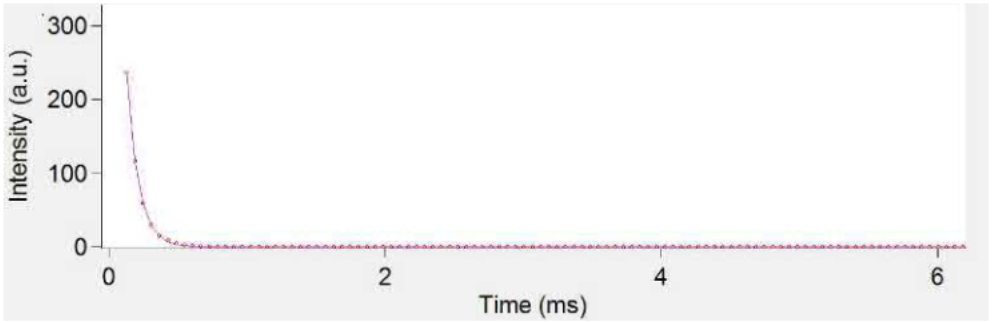

*Figure.8.1.59. Lifetime.measurement.and.single.exponential.fit.for.[Tb(**3**)$_3$](CF$_3$SO$_3$)$_3$ (0.01.mM,.MeCN,.λ_{ex} =.274nm,.measured.at.545 nm)...*

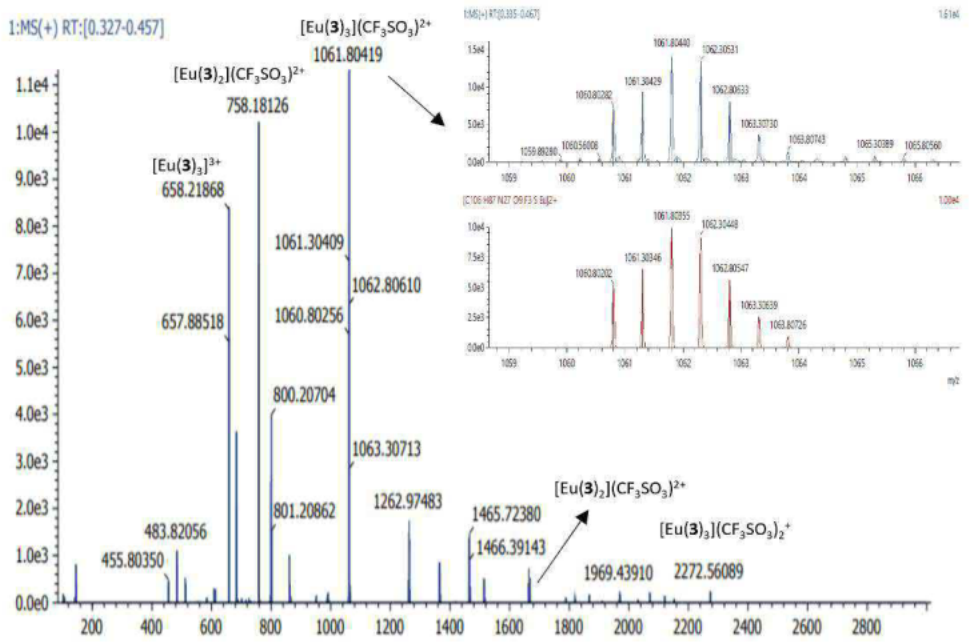

*Figure. 8.1.60.. HRMS. of [Eu(**3**)3](CF3SO3)3,. Insert:. zoom. in. of. [Eu(**3**)3](CF3SO3)2+. with. isotopic. simulation. below,. m/z =. 1062.3053 [Eu(**3**)3](CF3SO3)2+ (calc.. for (C106H87N27O9SF3Eu)2+,. 1062.3045)..*

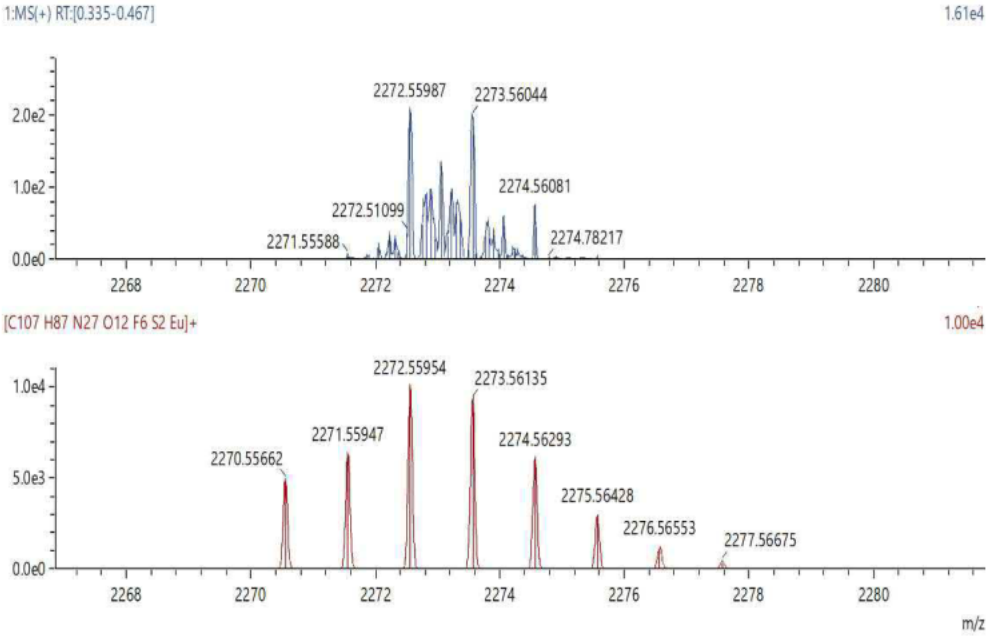

*Figure. 8.1.61.. (Top). HRMS. m/z. =. 2273.5604. [Eu(**3**)3](CF3SO3)2+,. (Bottom). calc.. for. (C107H87N27O12S2F6Eu)+,. 2273.5614..*

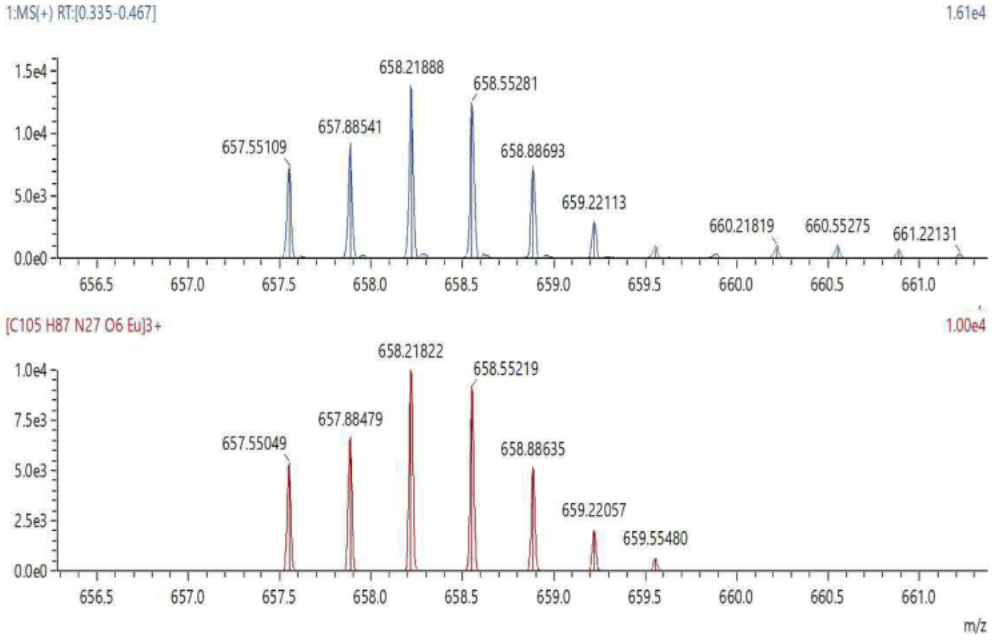

*Figure. 8.1.62.. (Top). HRMS. m/z. =. 658.5528 [Eu(**3**)$_3$]$^{3+}$, (Bottom). calc.. for ($C_{105}H_{87}N_{27}O_6Eu$)$^{3+}$,. 658.5522..*

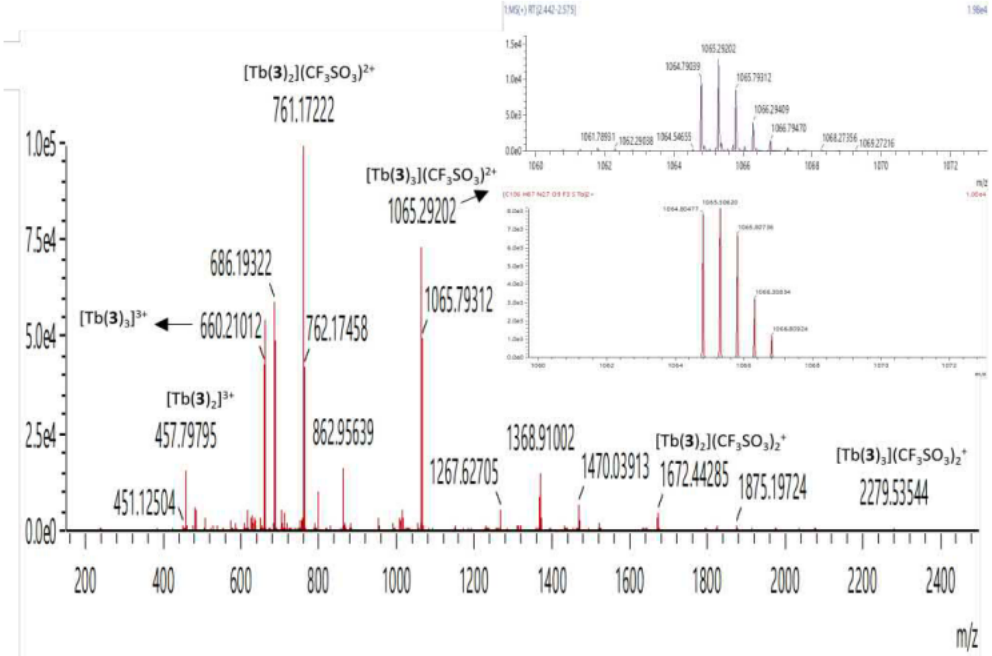

*Figure. 8.1.63.. HRMS. of. [Tb(**3**)$_3$](CF$_3$SO$_3$)$_3$,. Insert:. zoom. in. of. [Tb(**3**)$_3$](CF$_3$SO$_3$)$^{2+}$. with. isotopic. simulation. below,. m/z. =. 1065.2920 [Tb(3)$_3$](CF$_3$SO$_3$)$^{2+}$. (calc.. for. ($C_{106}H_{87}N_{27}O_9SF_3Tb$)$^{2+}$,. 1065.3062)..*

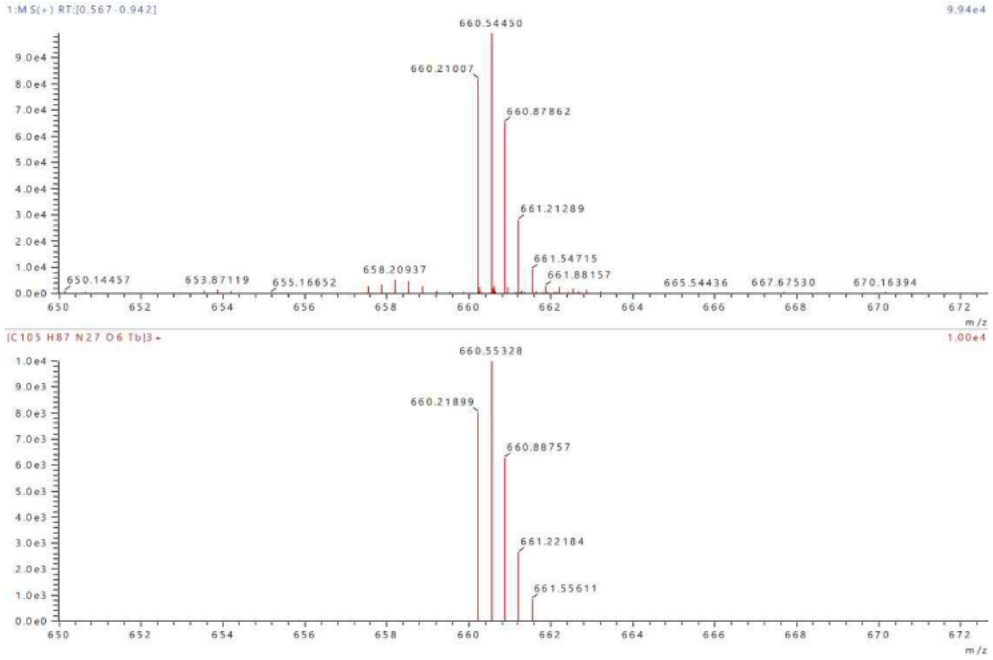

*Figure. 8.1.64.. (Top). HRMS. m/z. =. 660.5445 [Tb(**3**)$_3$]$^{3+}$, (Bottom) calc. for (C$_{105}$H$_{87}$N$_{27}$O$_6$Tb)$^{3+}$,. 660.5533..*

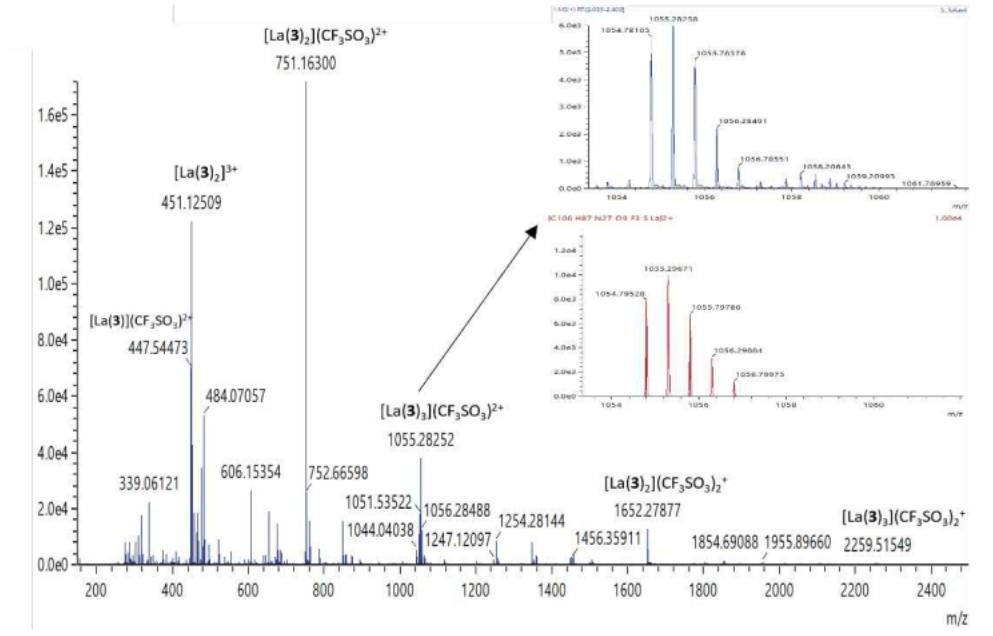

*Figure. 8.1.65.. HRMS. of. [La(**3**)$_3$](CF$_3$SO$_3$)$_3$,. Insert:. zoom. in. of. [La(3)$_3$](CF$_3$SO$_3$)$^{2+}$. with. isotopic. simulation. below,. m/z. =. 1055.2858 [La(3)$_3$](CF$_3$SO$_3$)$^{2+}$. (calc.. for. (C$_{106}$H$_{87}$N$_{27}$O$_9$SF$_3$La)$^{2+}$,. 1055.2967)..*

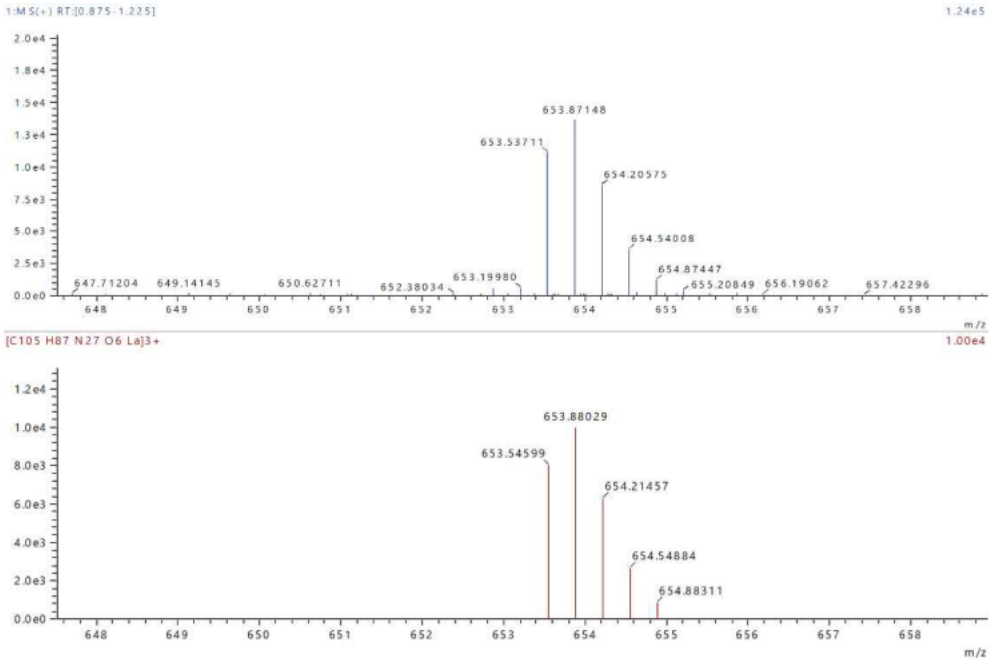

*Figure 8.1.66. (Top) HRMS m/z = 653.8715 [La(**3**)$_3$]$^{3+}$. (Bottom) calc. for (C$_{105}$H$_{87}$N$_{27}$O$_6$La)$^{3+}$, 653.8803.*

*Table 8.1.1. All [Ln(**L**)$_3$(CF$_2$SO$_3$)$_x$] ions observed in HRMS compared to their calculated m/z (Ln = Eu^{3+}, Tb^{3+} and La^{3+}; L = 1, 2, and 3 and x = 2, 1 and 0).*

Complex	Calculated *m/z*	Experimental *m/z*
[Eu(**1**)$_3$(CF$_3$SO$_3$)$_2$]$^+$	1600.3705	1600.3621
[Eu(**1**)$_3$(CF$_3$SO$_3$)]$^{2+}$	725.7090	725.7048
[Eu(**1**)$_3$]$^{3+}$	434.1552	434.1526
[Tb(**1**)$_3$(CF$_3$SO$_3$)$_2$]$^+$	1606.3743	1606.3745
[Tb(**1**)$_3$(CF$_3$SO$_3$)]$^{2+}$	728.7109	728.7109
[Tb(**1**)$_3$]$^{3+}$	436.1564	436.1565
[La(**1**)$_3$(CF$_3$SO$_3$)$_2$]$^+$	1586.3553	1586.3327
[La(**1**)$_3$(CF$_3$SO$_3$)]$^{2+}$	718.7014	718.6913
[Eu(**2**)$_3$(CF$_3$SO$_3$)$_2$]$^+$	1972.4651	1972.4652
[Eu(**2**)$_3$(CF$_3$SO$_3$)]$^{2+}$	911.7563	911.7564
[Eu(**2**)$_3$]$^{3+}$	558.1867	558.1869
[Tb(**2**)$_3$(CF$_3$SO$_3$)$_2$]$^+$	1978.4688	1978.4705
[Tb(**2**)$_3$(CF$_3$SO$_3$)]$^{2+}$	915.7578	915.7536
[Tb(**2**)$_3$]$^{3+}$	560.1877	560.1851
[La(**2**)$_3$(CF$_3$SO$_3$)$_2$]$^+$	1958.4492	1958.4223
[La(**2**)$_3$(CF$_3$SO$_3$)]$^{2+}$	904.7483	904.7362
[Eu(**3**)$_3$(CF$_3$SO$_3$)$_2$]$^+$	2273.5614	2273.5604
[Eu(**3**)$_3$(CF$_3$SO$_3$)]$^{2+}$	1062.3045	1062.3053
[Eu(**3**)$_3$]$^{3+}$	658.5522	658.5528
[Tb(**3**)$_3$(CF$_3$SO$_3$)$_2$]$^+$	2279.5655	2279.5354
[Tb(**3**)$_3$(CF$_3$SO$_3$)]$^{2+}$	1065.3062	1065.2920
[Tb(**3**)$_3$]$^{3+}$	660.5533	660.5445
[La(**3**)$_3$(CF$_3$SO$_3$)$_2$]$^+$	2259.5465	2259.5155
[La(**3**)$_3$(CF$_3$SO$_3$)]$^{2+}$	1055.2967	1055.2858
[La(**3**)$_3$]$^{3+}$	653.8803	653.8715

*Table 8.1.2. Lifetime measurements for Eu^{3+} and Tb^{3+} complexes with ligands **1**, **2** and **3**.*

Complex	1	Average Time (ms)	2	Average Time (ms)	3	Average Time (ms)
Eu(L)$_3$	0.458 ± 0.0 0.464 ± 0.0 0.458 ± 0.0	0.460 ± 0.0	0.548 ± 0.0 0.590 ± 0.0 0.592 ± 0.0	0.576 ± 0.0	0.678 ± 0.0 0.677 ± 0.0 0.674 ± 0.0	0.676 ± 0.0
Tb(L)$_3$	1.387 ± 0.0 1.377 ± 0.0 1.378 ± 0.0	1.381 ± 0.0	1.444 ± 0.0 1.445 ± 0.0 1.439 ± 0.0	1.443 ± 0.0	0.087 ± 0.0 0.087 ± 0.0 0.086 ± 0.0	0.087 ± 0.0

8.1.4 Self-Assembly Titration Data

8.1.4.1 Self-Assembly Titration for 1

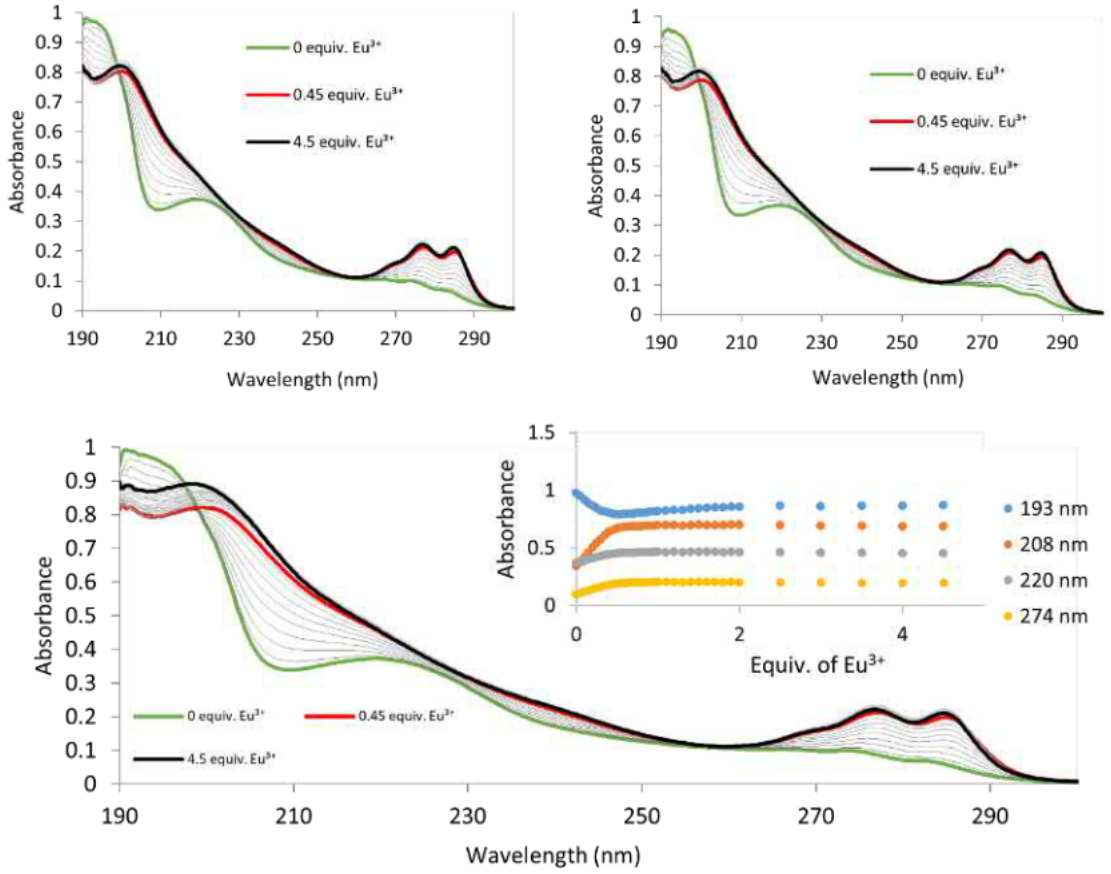

Figure 8.1.67. UV-visible absorption titration of **1** (0.02 M) with $Eu(CF_3SO_3)_3$ 0 to 4.5 equivalents, done in triplicate. Insert: monitoring changes in absorbance vs Ln^{3+} equivalents, at λ = 193, 208, 220 and 274 nm.

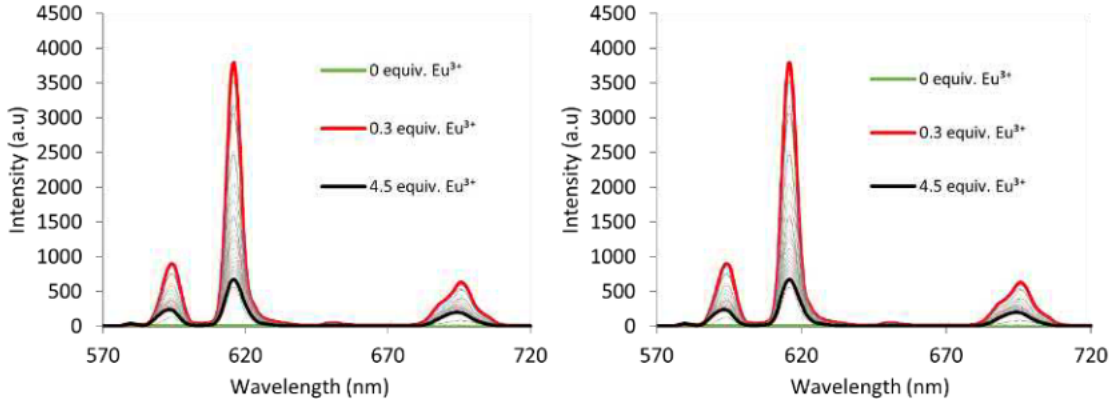

Figure 8.1.68. Fluorescence titration of **1** (0.02 M) with $Eu(CF_3SO_3)_3$ 0 to 4.5 equivalents, done in triplicate.

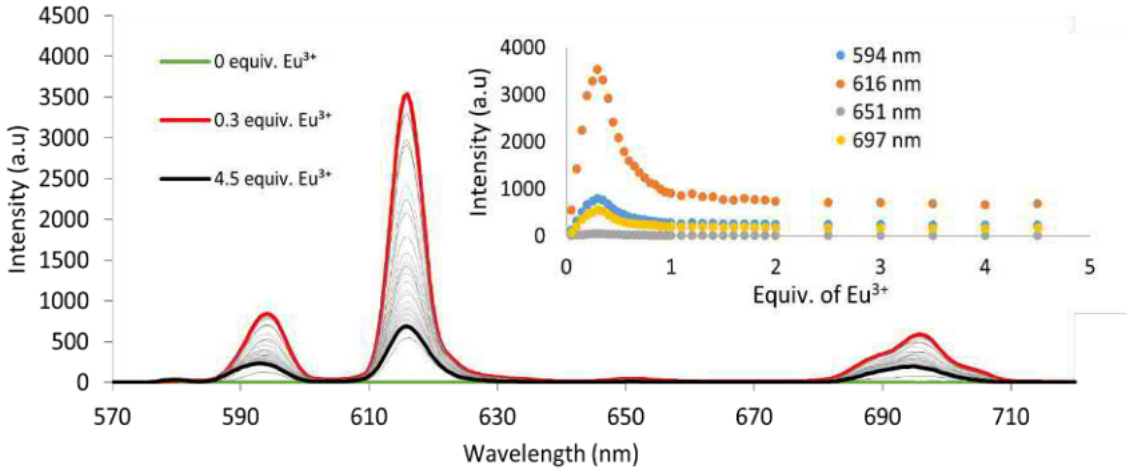

Figure.8.1.69. Fluorescence titration of **1** (0.02 M) with $Eu(CF_3SO_3)_3$ 0 to 4.5 equivalents, done in triplicate. Insert: monitoring changes in absorbance vs Ln^{3+} equivalents, at λ = 594, 616, 651 and 697 nm..

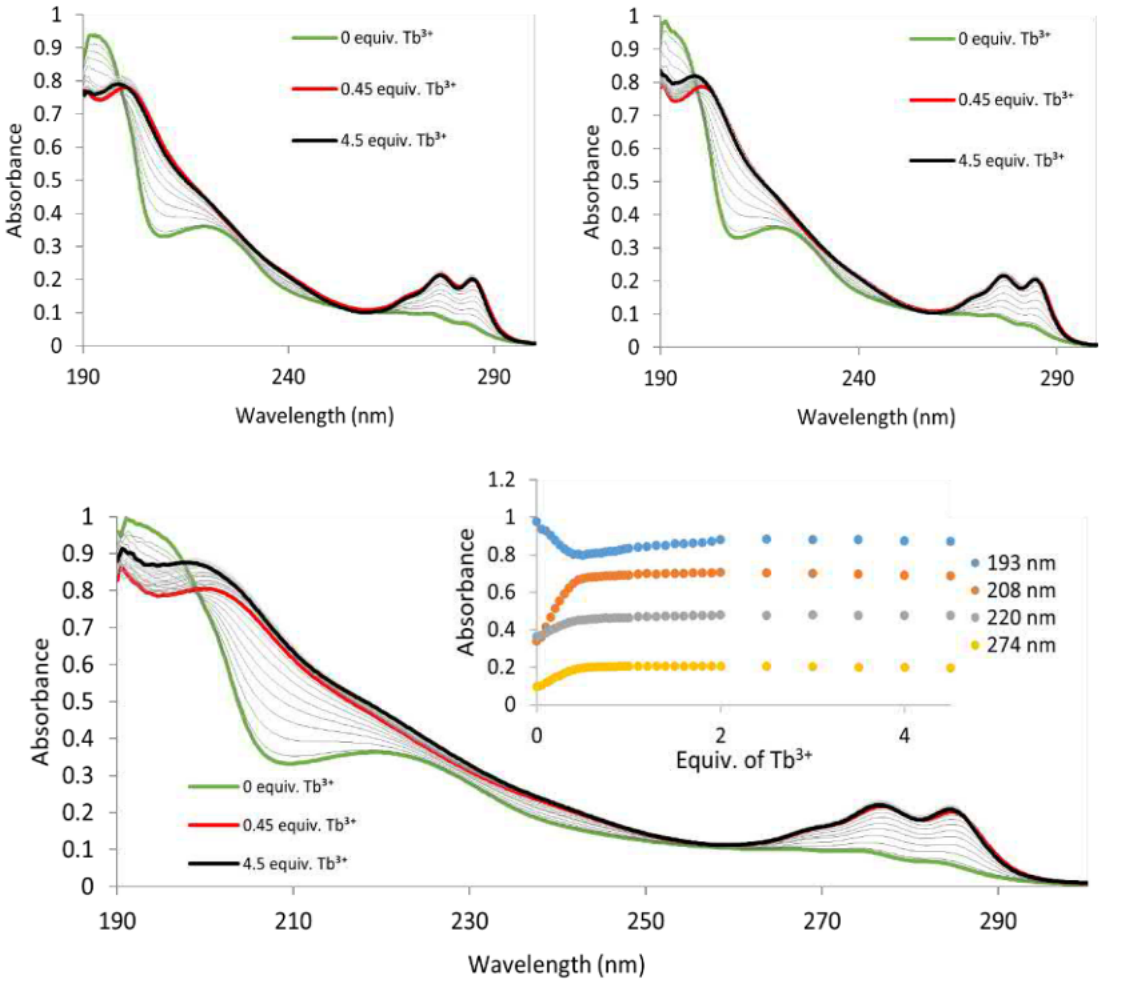

Figure.8.1.70. UV-visible absorption titration of **1** (0.02 M) with $Tb(CF_3SO_3)_3$ 0 to 4.5 equivalents, done in triplicate. Insert: monitoring changes in absorbance vs Ln^{3+} equivalents, λ = 193, 208, 220 and 274 nm..

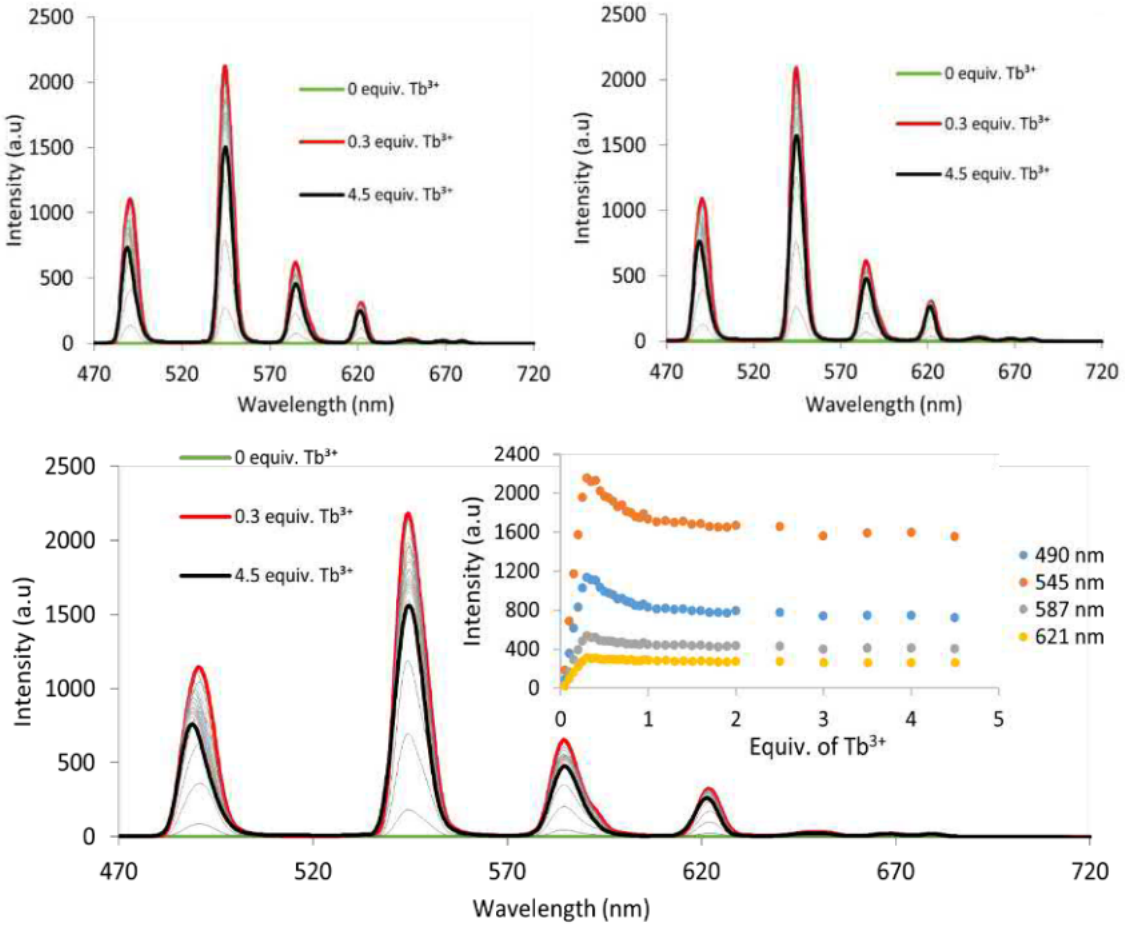

Figure.8.1.71. Fluorescence titration of **1** (0.02 M) with $Tb(CF_3SO_3)_3$ 0 to 4.5 equivalents, done in triplicate. Insert: monitoring changes in absorbance vs Ln^{3+} equivalents, at λ = 490, 545, 587 and 621 nm.

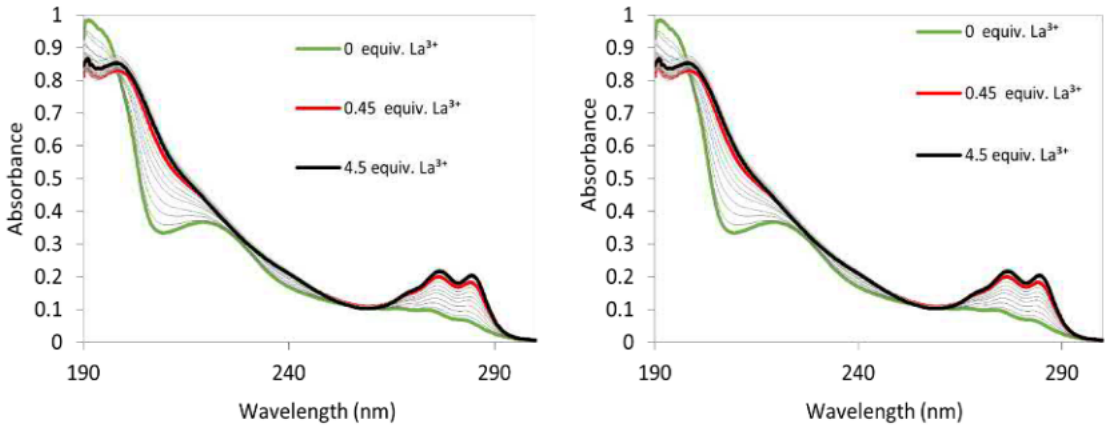

*Figure.8.1.72..UV-visible.absorption.titration.of.**1**.(0.02.M).with.La(CF₃SO₃)₃.0.to.4.5.equivalents,.done.in.triplicate..*

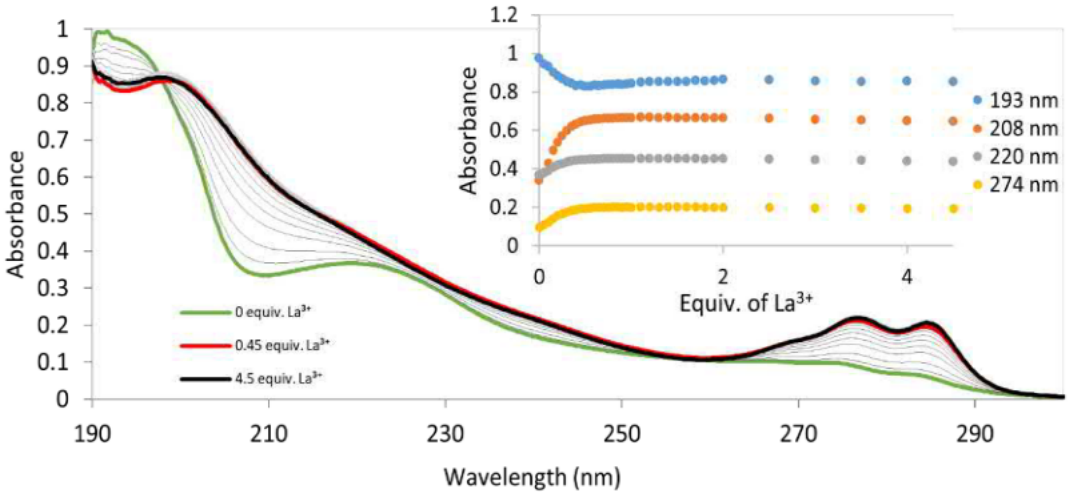

*Figure 8.1.73.. UV-visible absorption titration of **1** (0.02 M) with La(CF$_3$SO$_3$)$_3$ 0 to 4.5 equivalents,. done in triplicate.. Insert: monitoring changes in absorbance vs Ln^{3+} equivalents,. at λ = 193,. 208,. 220 and 274 nm..*

8.1.4.2 Self-Assembly Titration for 2

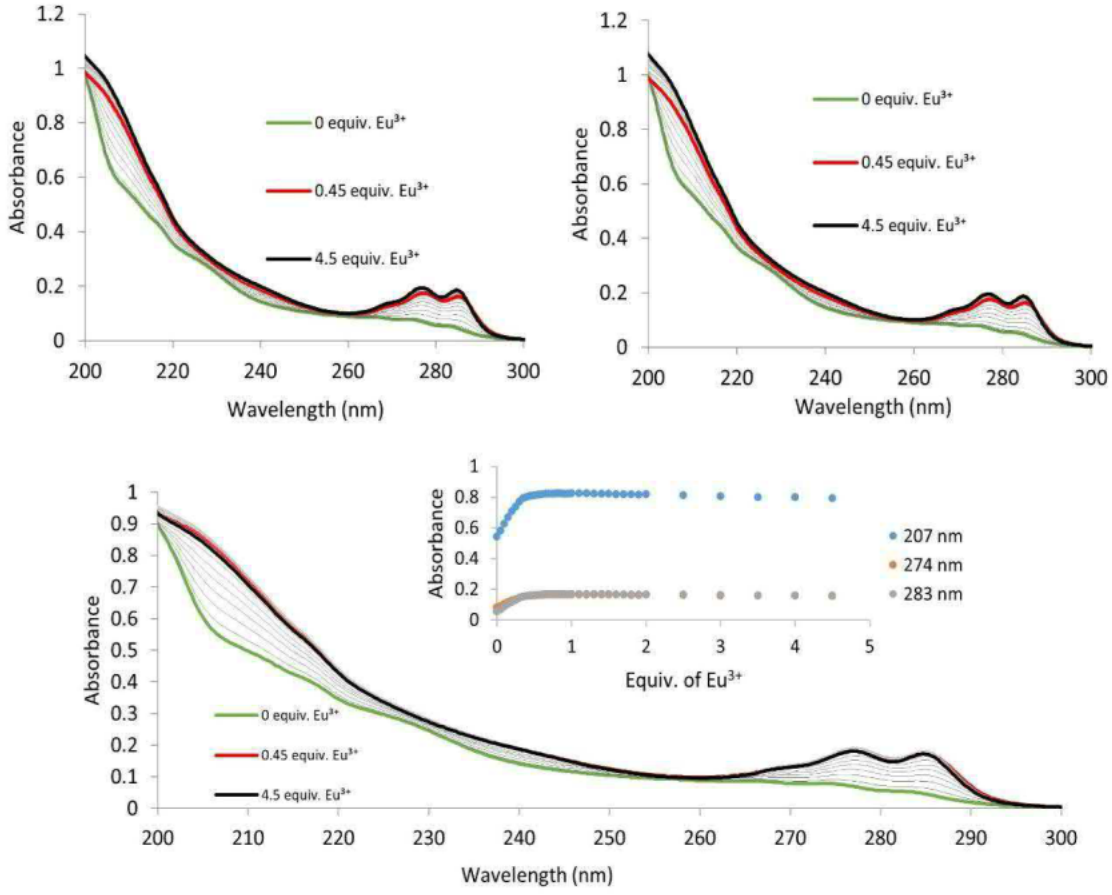

*Figure 8.1.74.. UV-visible absorption titration of **2** (0.02 M) with Eu(CF$_3$SO$_3$)$_3$ 0 to 4.5 equivalents,. done in triplicate.. Insert: monitoring changes in absorbance vs Ln^{3+} equivalents,. at λ = 207,. 274 and 283 nm..*

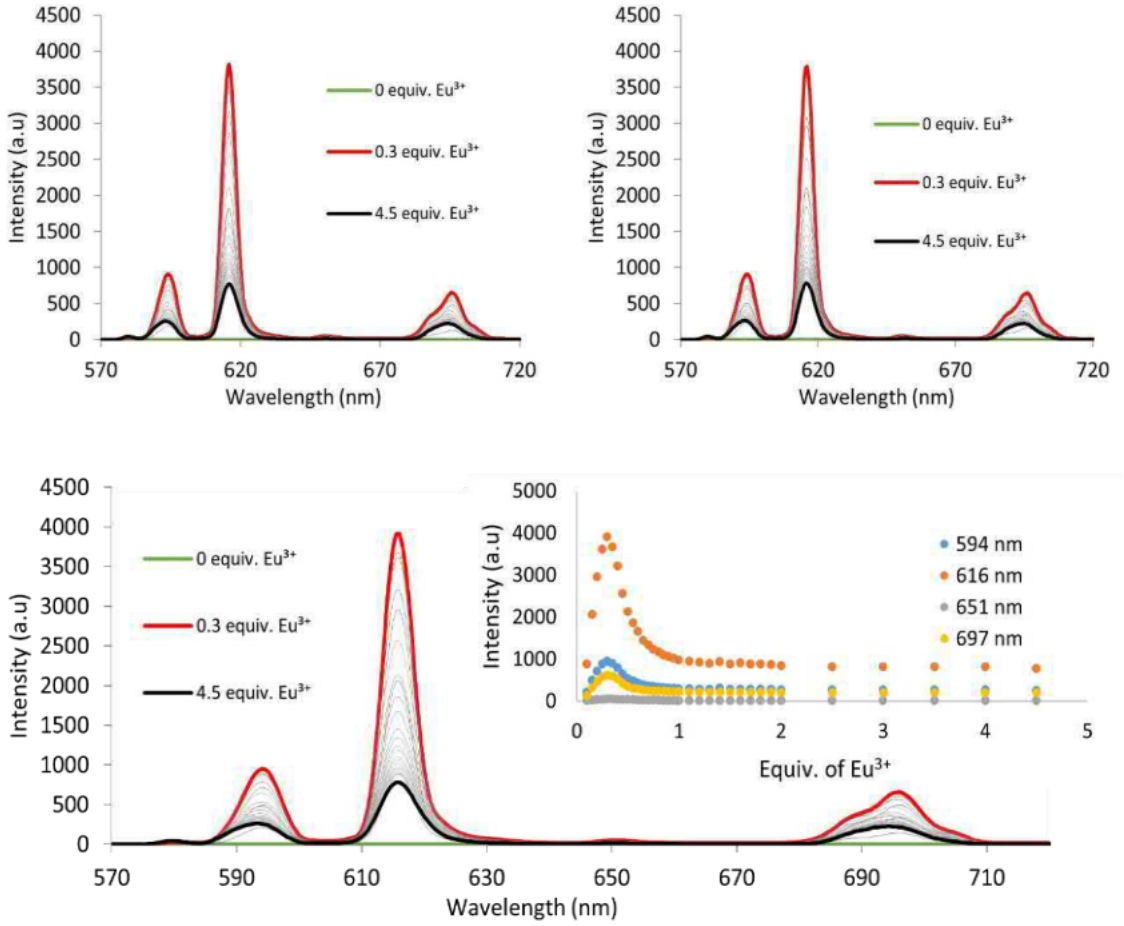

Figure.8.1.75.. Fluorescence.titration.of. ***2*** *(0.02.M).with.Eu(CF₃SO₃)₃.0.to.4.5.equivalents,.done.in.triplicate..Insert:.monitoring.changes in.absorbance.vs.Ln³⁺.equivalents,.at.λ =.594,.616,.651.and.697.nm..*

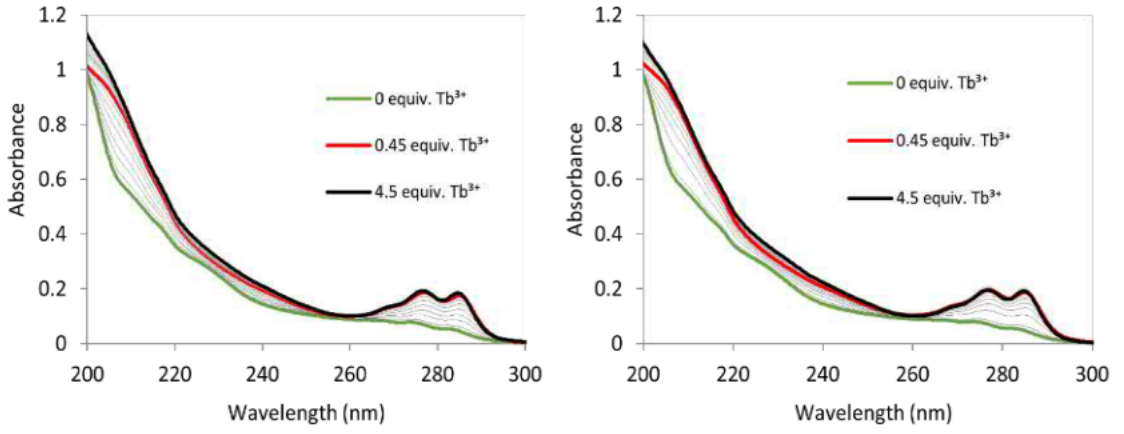

Figure.8.1.76.. UV-visible.absorption.titration.of. ***2*** *(0.02.M).with.Tb(CF₃SO₃)₃.0.to.4.5.equivalents,.done.in.triplicate..*

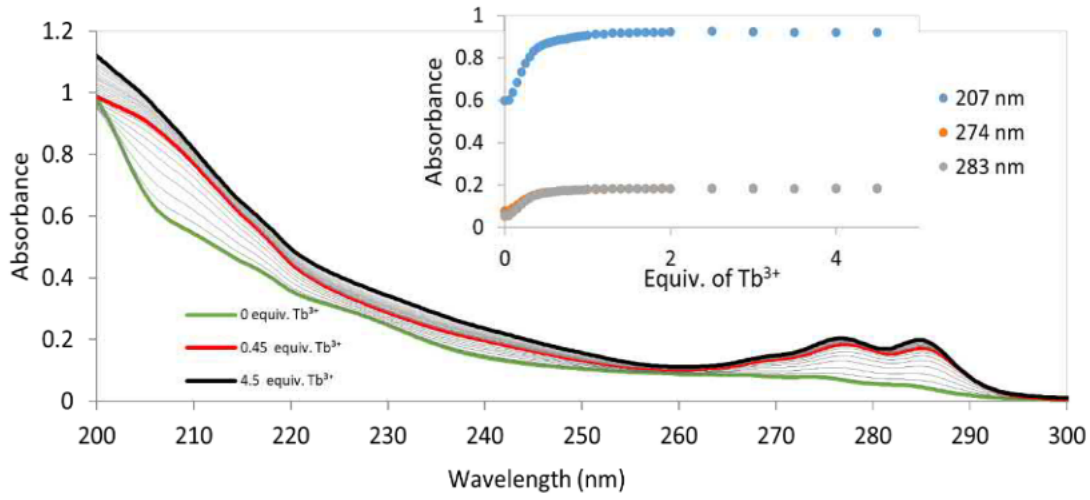

Figure 8.1.77. UV-visible absorption titration of **2** (0.02 M) with $Tb(CF_3SO_3)_3$ 0 to 4.5 equivalents, done in triplicate. Insert: monitoring changes in absorbance vs Ln^{3+} equivalents, at λ = 207 , 274 and 283 nm..

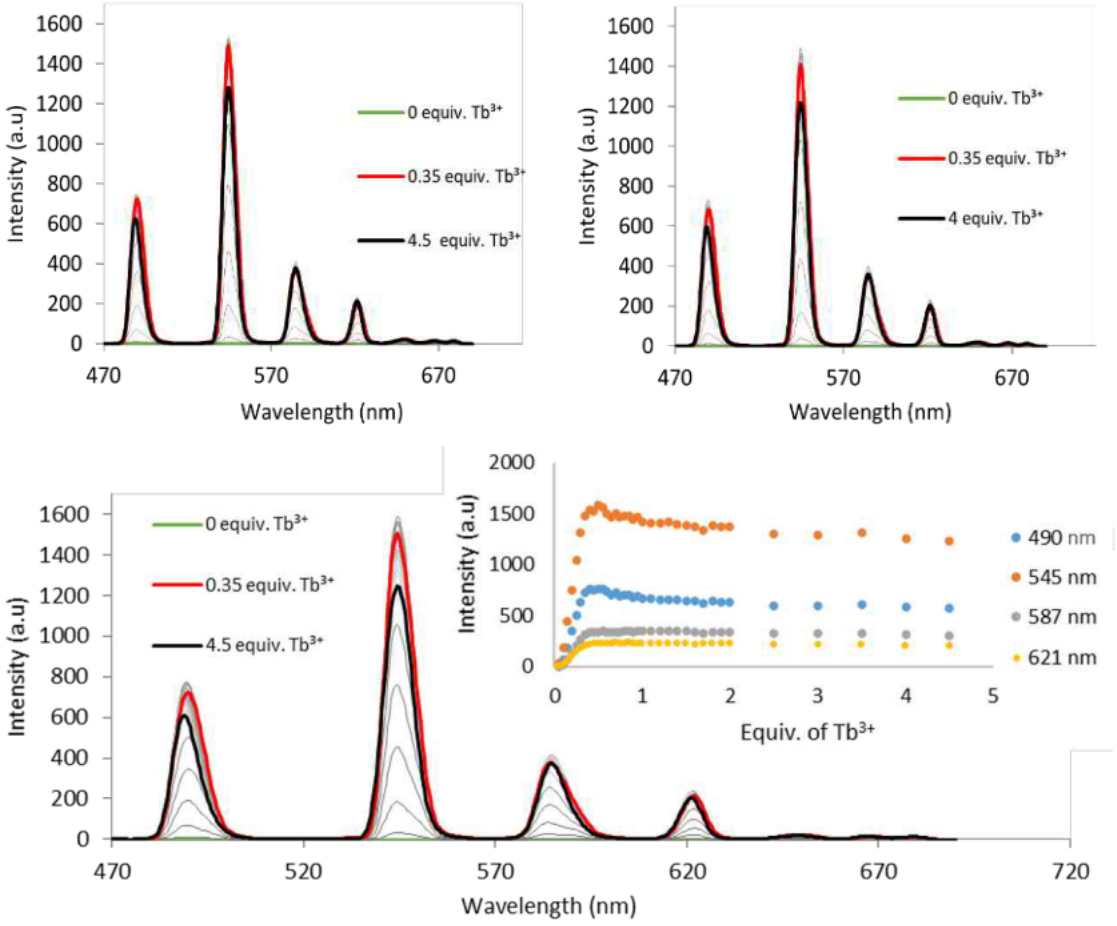

Figure 8.1.78.. Fluorescence titration of **2** *(0.02 M) with $Tb(CF_3SO_3)_3$ 0 to 4.5 equivalents,. done in triplicate.. Insert:. monitoring changes in absorbance vs Ln^{3+} equivalents,. at λ =. 490,. 545,. 587 and 621 nm..*

0

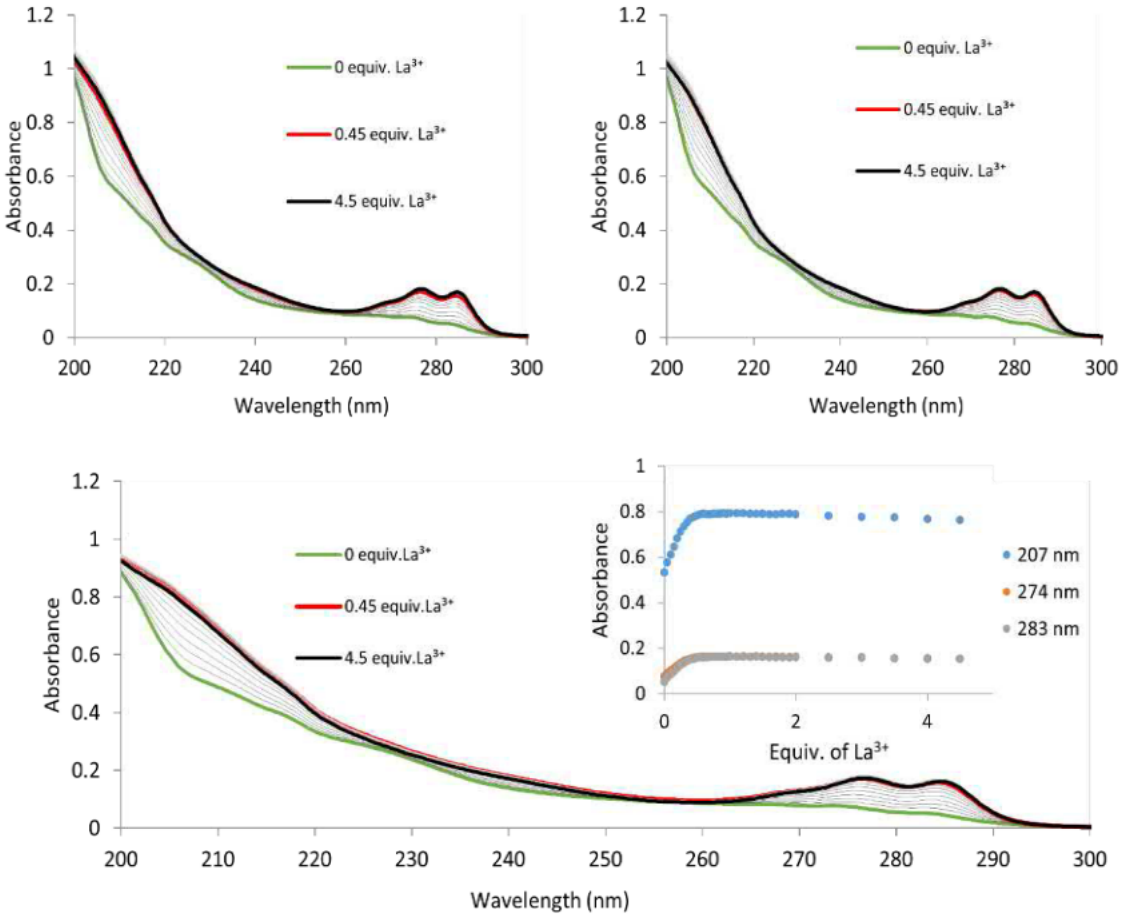

Figure.8.1.79.. UV-visible absorption titration of **2** (0.02 M) with $La(CF_3SO_3)_3$ 0 to 4.5 equivalents, done in triplicate. Insert: monitoring changes in absorbance vs Ln^{3+} equivalents, at λ = 207 , 274 and 283 nm

8.1.4.3 Self-Assembly Titration for 3

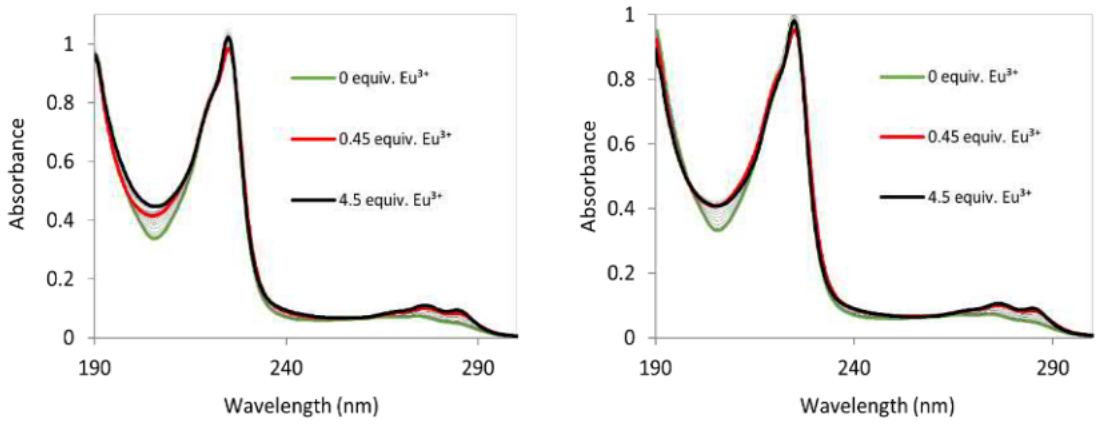

Figure.8.1.80. UV-visible absorption titration of **3** (0.005 M) with $Eu(CF_3SO_3)_3$ 0 to 4.5 equivalents, done in triplicate.

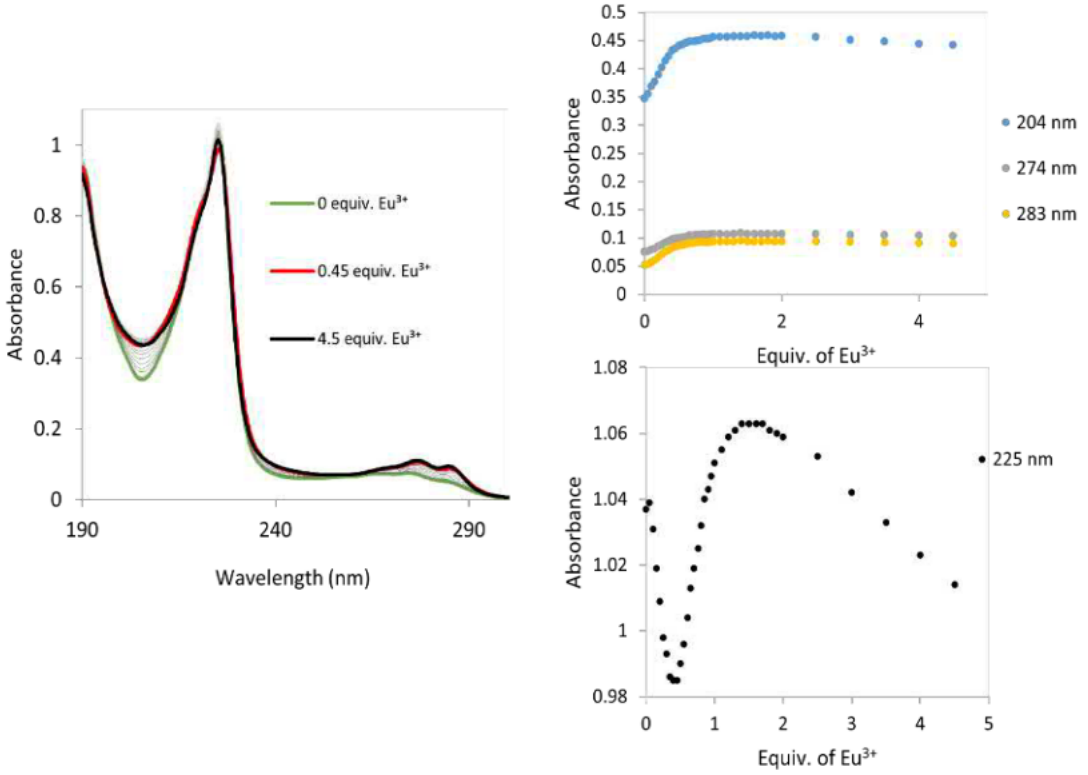

Figure 8.1.81.. (Left). UV-visible. absorption. titration. of. **3** *(0.005. M). with. $Eu(CF_3SO_3)_3$ 0. to. 4.5. equivalents,. done. in. triplicate.. (Right) Monitoring. changes. in. absorbance. vs. Ln^{3+}. equivalents. s. at. λ =. 204.,. 225,. 274. and. 283. nm..*

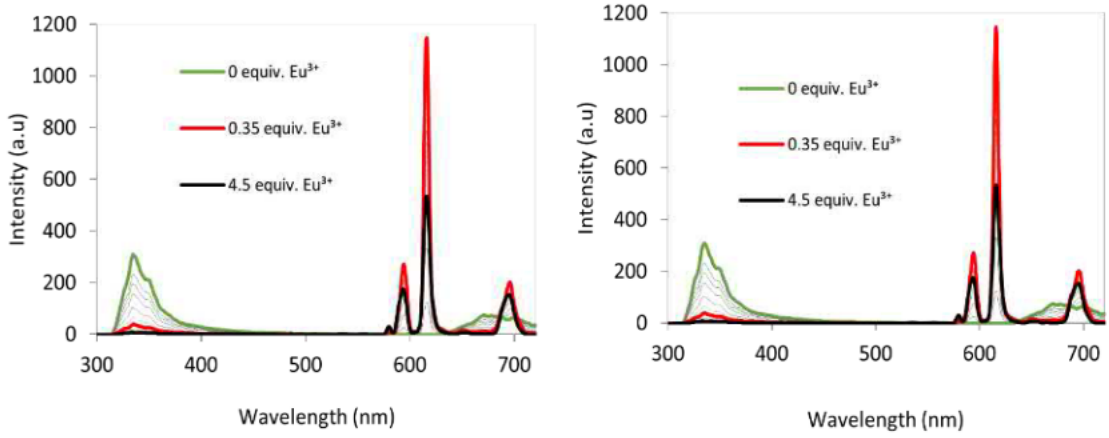

Figure 8.1.82. Fluorescence titration of **3** (0.02 M) with $Eu(CF_3SO_3)_3$ 0 to 4.5 equivalents, done in triplicate..

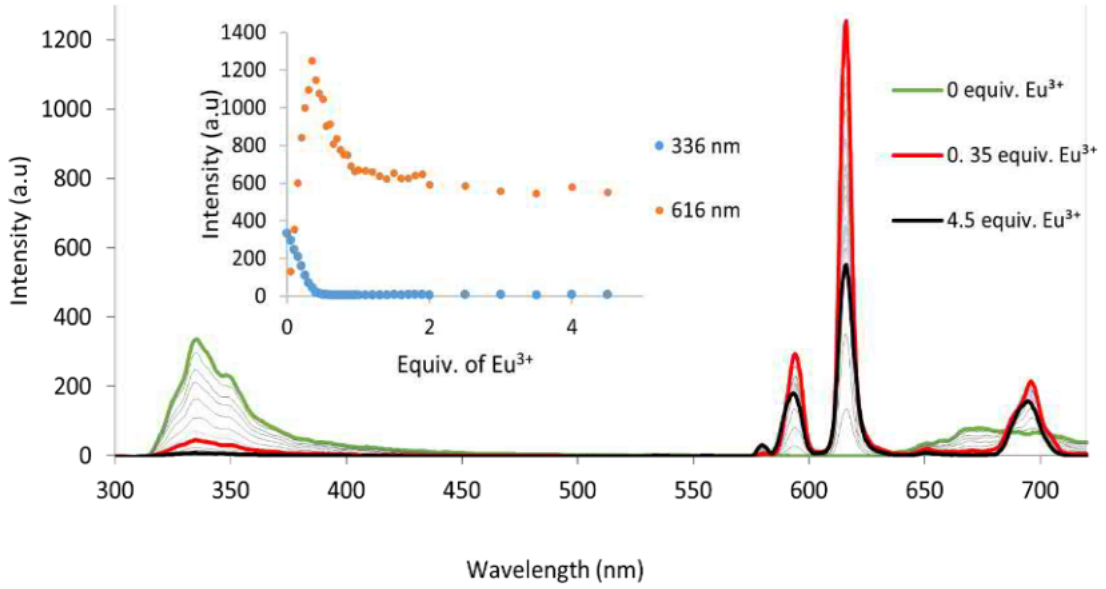

Figure. 8.1.83.. Fluorescence. titration. of. ***3*** *(0.02. M). with. Eu(CF3SO3)3. 0. to. 4.5. equivalents,. done. in. triplicate.. Insert:. monitoring. changes. in. absorbance. vs. Ln3+. equivalents,. at. λ. =. 336. and. 616. nm..*

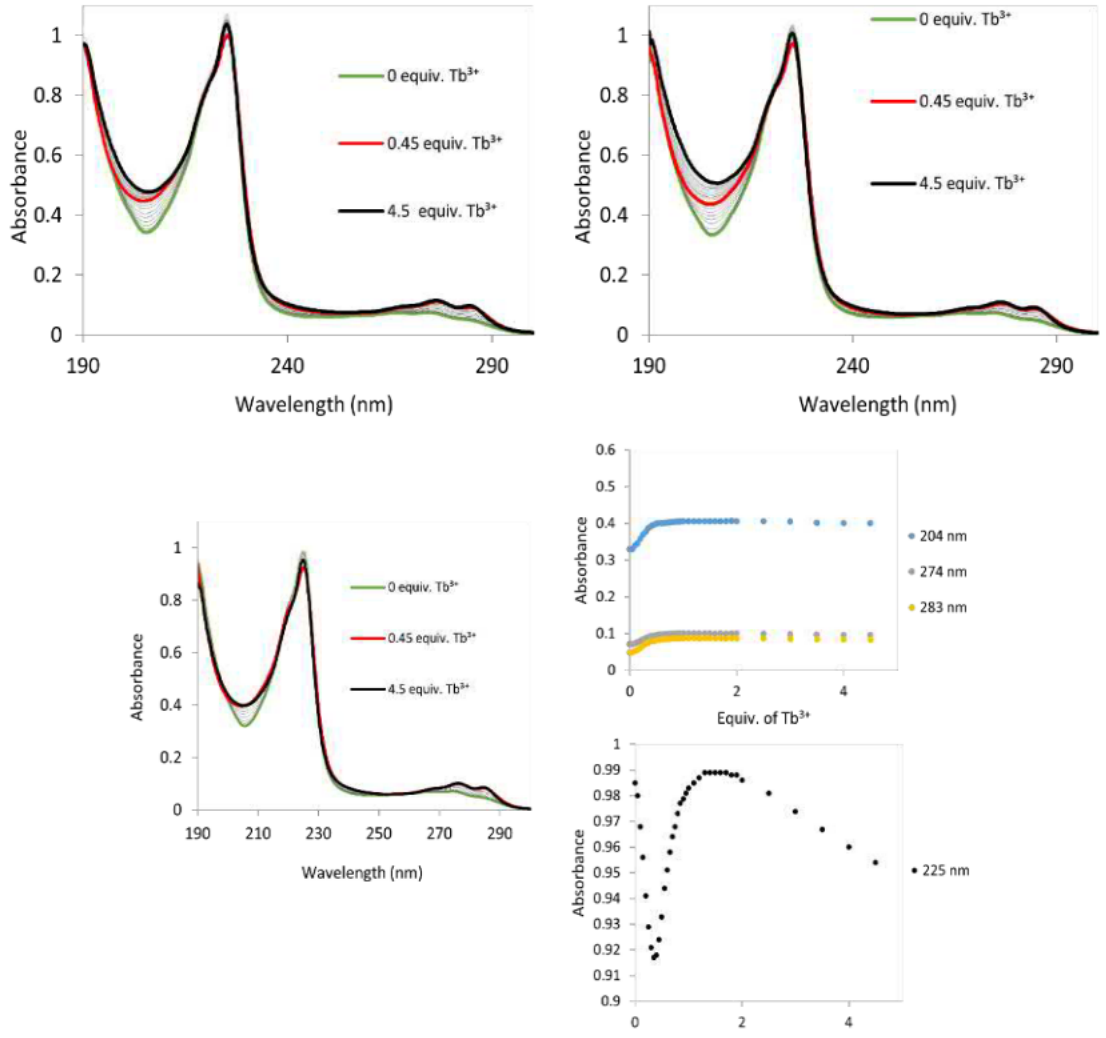

Figure. 8.1.84.. (Left). UV-visible. absorption. titration. of. ***3*** *(0.005. M). with. Tb(CF3SO3)3. 0. to. 4.5. equivalents,. done. in. triplicate.. (Right) Monitoring. changes. in. absorbance. vs. Ln3+. equivalents,. at. λ. =. 204.,. 225,. 274. and. 283. nm..*

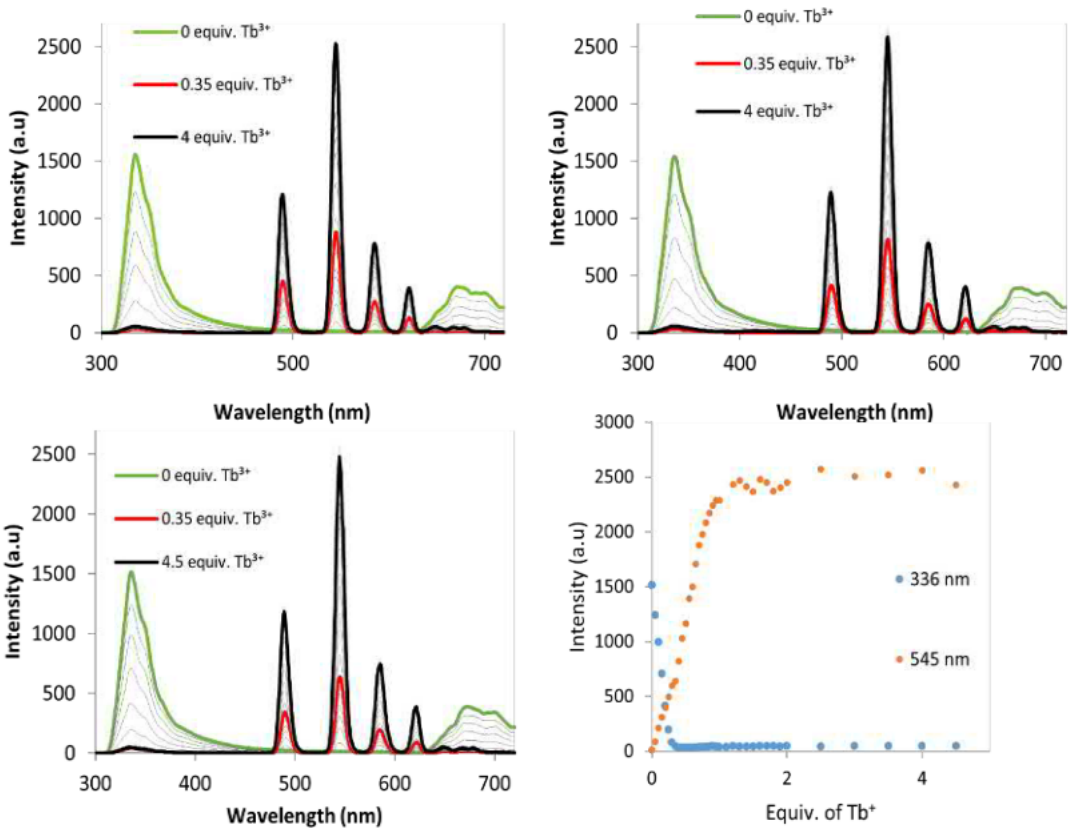

Figure.8.1.85. Fluorescence titration of **3** (0.02 M) with $Tb(CF_3SO_3)_3$ 0 to 4.5 equivalents, done in triplicate. (Right bottom) Monitoring changes in absorbance vs Ln^{3+} equivalents, at λ = 336 and 545 nm.

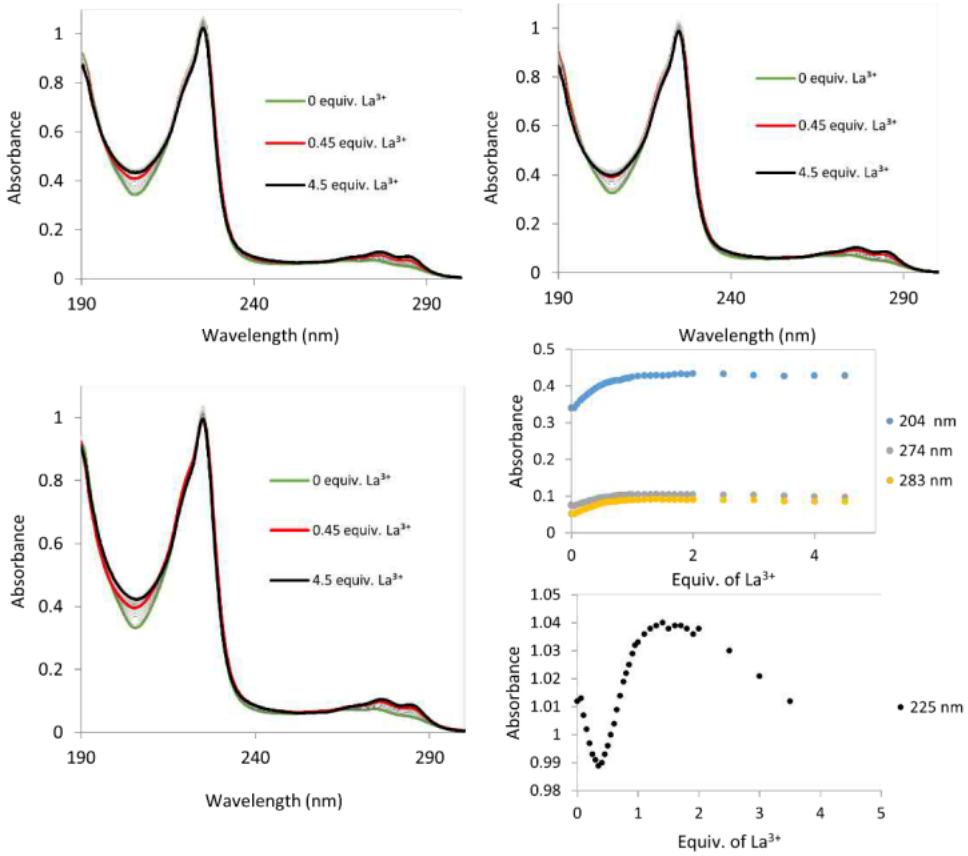

Figure. 8.1.86. (Left) UV-visible absorption titration of **3** (0.005 M) with $La(CF_3SO_3)_3$ 0 to 4.5 equivalents, done in triplicate. (Right) Monitoring changes in absorbance vs Ln^{3+} equivalents, at λ = 204 , 225, 274 and 283 nm.

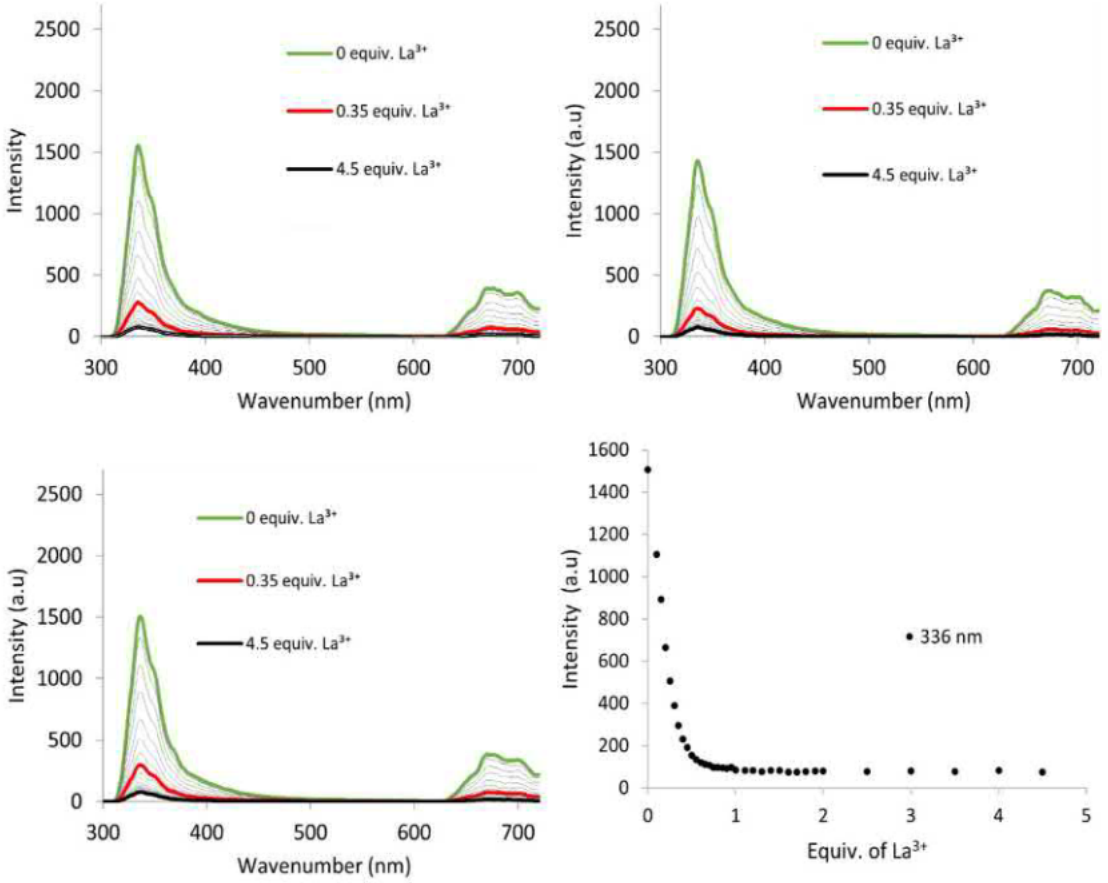

Figure 8.1.87. Fluorescence titration of **3** *(0.02 M) with $La(CF_3SO_3)_3$ 0 to 4.5 equivalents, done in triplicate. (Right bottom) Monitoring changes in absorbance vs Ln^{3+} equivalents, at λ = 336 nm.*

Table 8.1.3. Binding constants from fitting UV-visible absorption and fluorescence titrations data.

Ln(L)	UV-visible absorption			Fluorescent emission		
	Log $\beta_{1:1}$	Log $\beta_{1:2}$	Log $\beta_{1:3}$	Log $\beta_{1:1}$	Log $\beta_{1:2}$	Log $\beta_{1:3}$
Eu(**1**)	6.4 ± 0.02	13.1 ± 0.03	18.8 ± 0.05	6.6 ± 0.01	13.1 ± 0.01	18.9 ± 0.01
Eu(**2**)	7.1 ± 0.02	14.4 ± 0.02	21.5 ± 0.02	8.0 ± 0.04	15.3 ± 0.06	22.0 ± 0.08
Eu(**3**)	8.2 ± 0.03	15.3 ± 0.06	22.0. ± 0.10	8.4 ± 0.06	15.5 ± 0.10	21.8 ± 0.10
Tb(**1**)	6.6 ± 0.03	13.4 ± 0.06	19.8 ± 0.08	6.0 ± 0.03	12.6 ± 0.04	19.4 ± 0.03
Tb(**2**)	7.2 ± 0.08	14.7 ± 0.06	21.8 ± 0.24	8.2 ± 0.04	14.8 (fixed)	22.3 ± 0.03
Tb(**3**)	7.7 ± 0.05	15.1 ± 0.10	22.6 ± 0.15	-	-	-
La(**1**)	5.8 ± 0.02	11.5 ± 0.02	17.1 ± 0.02	-	-	-
La(**2**)	6.6 ± 0.03	13.0 ± 0.05	18.2 ± 0.06	-	-	-
La(**3**)	6.7 ± 0.02	12.6 ± 0.03	18.8 ± 0.06	7.5 ± 0.09	12.8 ± 0.09	18.8 ± 0.09

8.1.4.4 Fitted Titration for 1

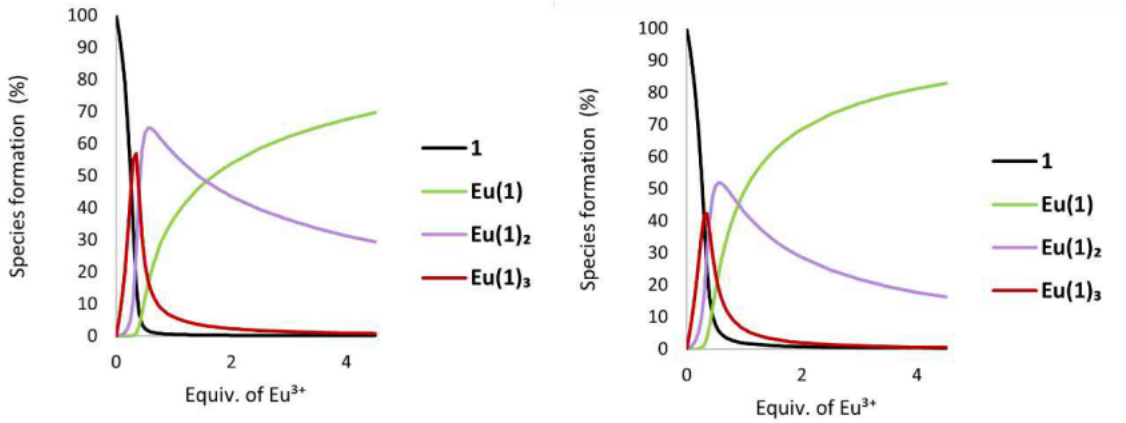

Figure.8.1.88.. UV-visible absorption (Left) fluorescence (Right). Speciation plots from fitted titration of **1** (0.02 M) with $Eu(CF_3SO_3)_3$ 0 to 4.5 equivalents.

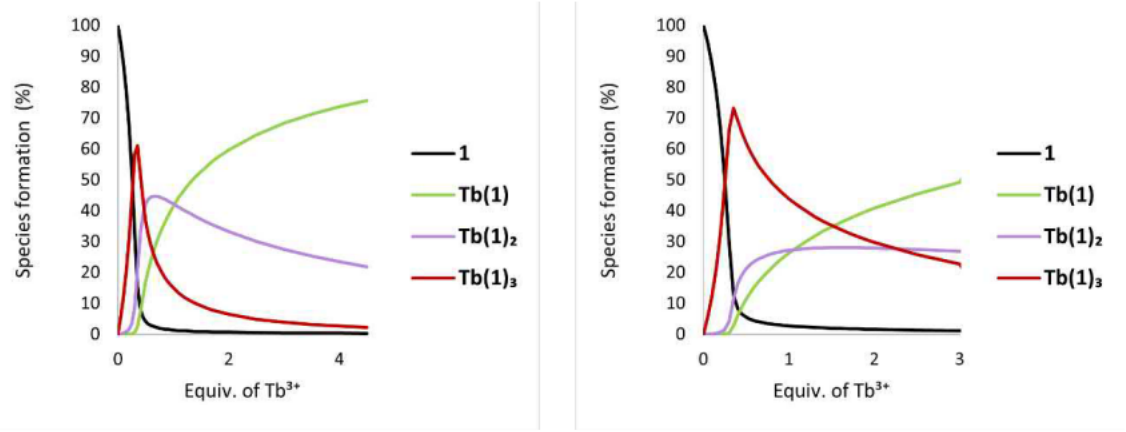

Figure.8.89.. UV-visible absorption (Left) fluorescence (Right). Speciation plots from fitted titration of **1** (0.02 M) with $Tb(CF_3SO_3)_3$ 0 to 4.5 equivalents.

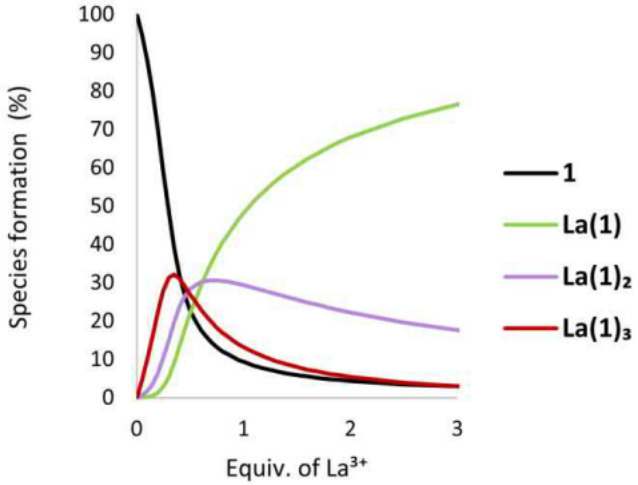

Figure.8.1.90. UV-visible absorption speciation plot from fitted titration of **1** (0.02 M) with $La(CF_3SO_3)_3$ 0 to 4.5 equivalents.

8.1.4.5 Fitted Titration for 2

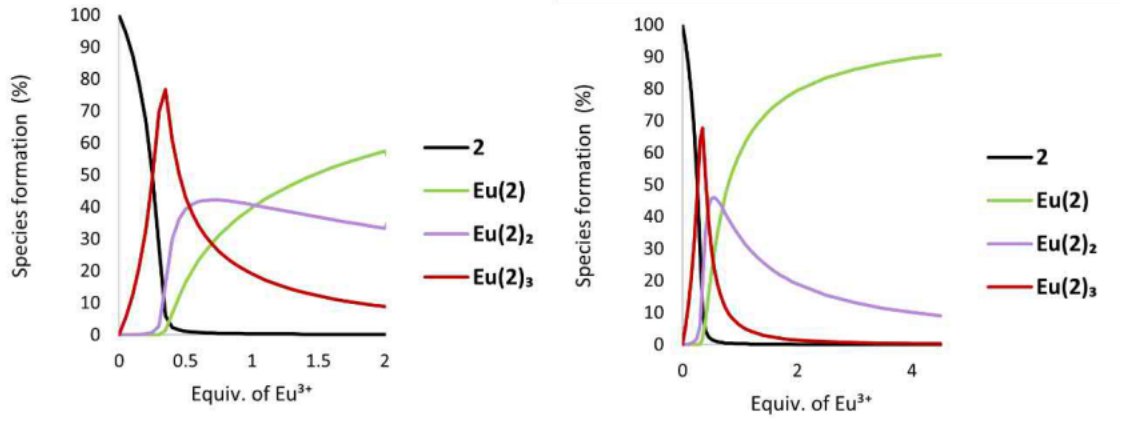

Figure 8.1.91. UV-visible absorption (Left) fluorescence (Right). Speciation plots from fitted titration of **2** (0.02 M) with $Eu(CF_3SO_3)_3$ 0 to 4.5 equivalents..

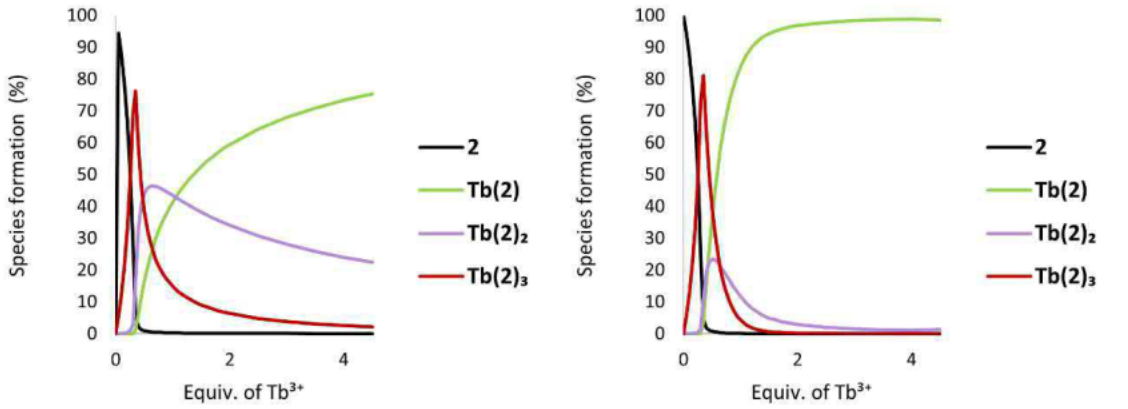

Figure 8.1.92.. UV-visible absorption (Left) fluorescence (Right). Speciation plots from fitted titration of **2** (0.02 M) with $Tb(CF_3SO_3)_3$ 0 to 4.5 equivalents.

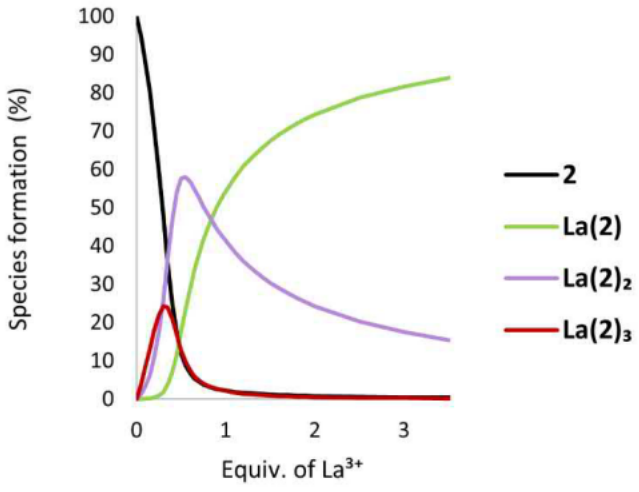

*Figure 8.1.93.. UV-visible absorption speciation plot from fitted titration of **2** (0.02 M) with $La(CF_3SO_3)_3$ 0 to 4.5 equivalents..*

8.1.4.6 Fitted Titration for 3

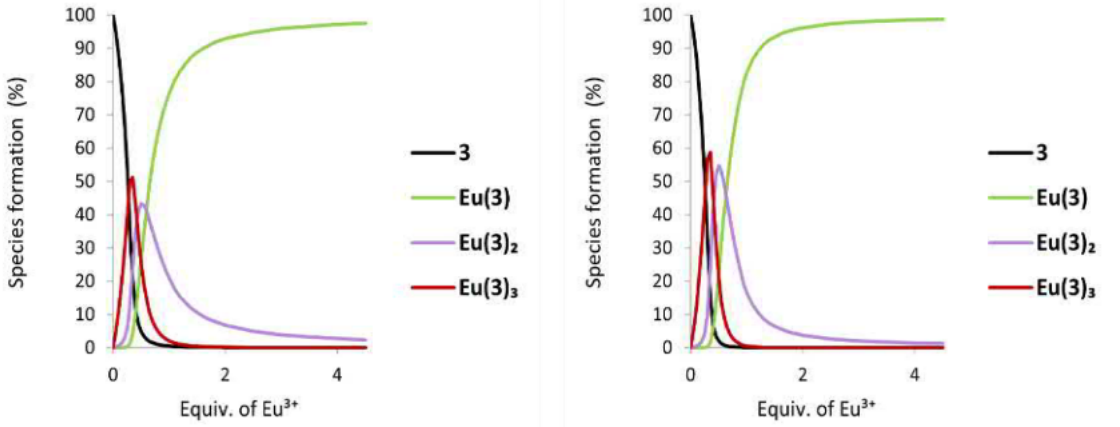

Figure. 8.1.94.. UV-visible. absorption. (Left). fluorescence. (Right).. Speciation. plots. from. fitted. titration. of. ***3****. with. $Eu(CF_3SO_3)_3$. 0. to. 4.5 equivalents.*

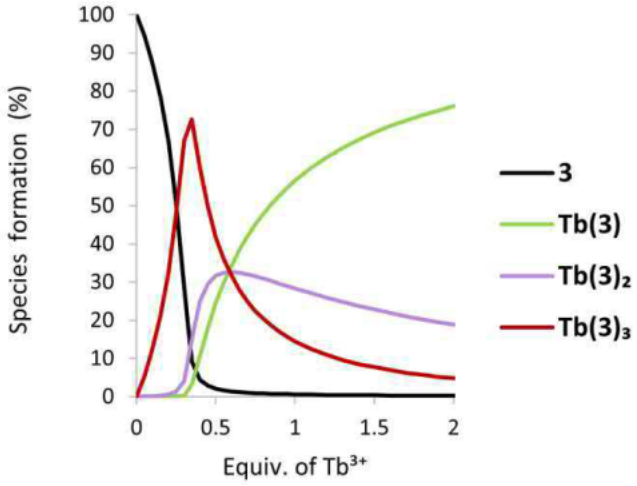

Figure. 8.1.95. UV-visible. absorption,. speciation. plot. from. fitted. titration. of. ***3*** *with. $Tb(CF_3SO_3)_3$ 0. to. 4.5. equivalents.*

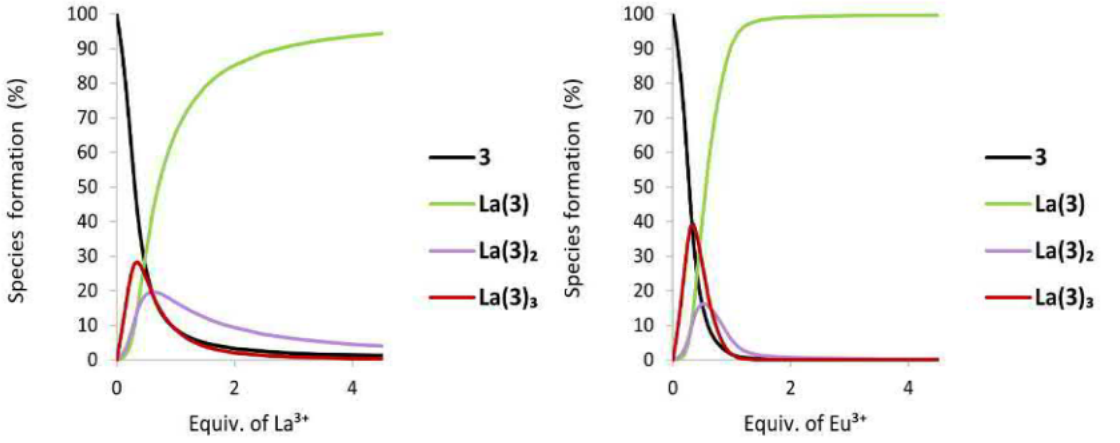

Figure. 8.1.96. UV-visible. absorption. (Left). fluorescence. (Right).. Speciation. plots. from. fitted. titration. of. ***3*** *(0.02. M). with. $La(CF_3SO_3)_3$ 0. to 4.5. equivalents.*

8.1.5 Synthesis and Characterisation of hydroxymethyl-1,2,3-triazolylhexadecane

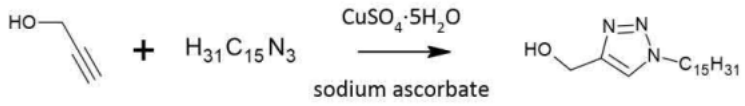

Figure 8.1.97.. Synthesis of hydroxymethyl-1,2,3-triazolylhexadecane

Propargyl alcohol (0.110 mL, 1.9 mM) was combined with $CuSO_4 \cdot 5H_2O$ (0.237 g, 0.95 mM) and sodium ascorbate (0.376 g, 1.9 mM) and stirred in DMF:H_2O (4:1, 10 mL) for 30 minutes, during which time the solution developed a light orange colour. 1-Azidohexadecane (0.507 g, 1.9 mM) was added to the solution and left to stir overnight resulting in a brown precipitate. The precipitate was filtered and washed with 1 M NaOH:EDTA solution and then redissolved in DCM and washed with 1 M HCl and water and then dried with $MgSO_4$. Solvent was removed by reduced pressure yielding a light brown solid (0.202 g, 32 %). Melting point = 82.5 °C. LRMS *m/z* = 324.15 [**L** + H]$^+$ (calc. for $C_{19}H_{38}N_3O^+$, 324.52). ^{1}H NMR (300 MHz, $CDCl_3$, ppm), δ = 7.51 (S, 1H, t-H), 4.80 (d, J = 5.5 Hz, 2H, **CH_2**-OH), 4.35 (t, J = 7.0 Hz, 2H,**CH_2**-$(CH_2)_{14}$-CH_3), 2.25 (m, 1H, **OH**), 1.90 (m, 2H, CH_2-**CH_2**-$(CH_2)_{13}$-CH_3), 1.29 (m, 26H, CH_2-CH_2-(**CH_2**)$_{13}$-CH_3), 0.88 (m, 2H, $CH_2)_{15}$-**CH_3**); ^{13}C NMR (75 MHz, $CDCl_3$, ppm): δ =147.4, 121.4, 56.7, 50.4, 31.9, 30.3, 29.7, 29.6, 29.5, 29.4, 29.0, 26.5, 22.7, 14.1. FTIR (cm^{-1}) 3293, 3133, 2955, 2914, 2872, 2847, 2329, 17700, 1533, 1469, 1377, 1337, 1209, 1150, 1099, 1050, 1018, 995, 861, 784, 719, 659, 468, 433.

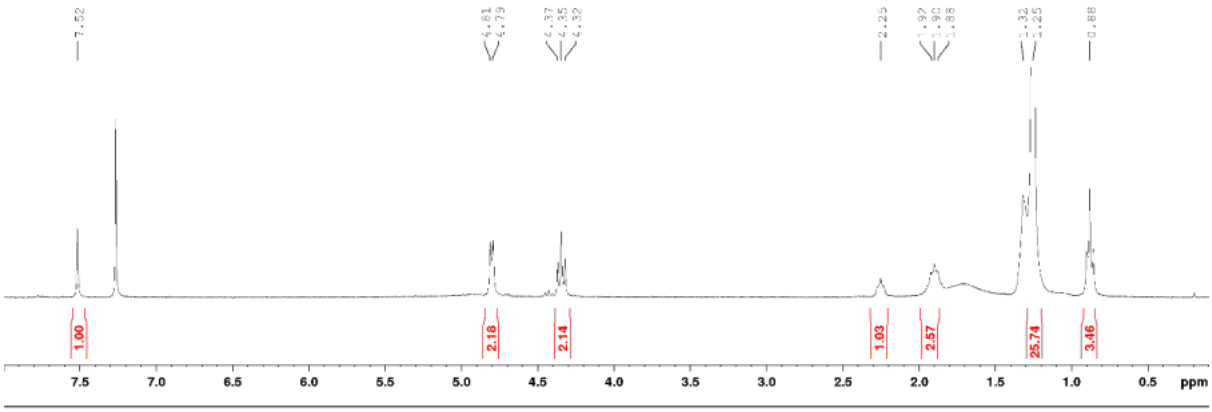

Figure 8.1.98.. ^{1}H NMR spectrum of hydroxymethyl-1,2,3-triazolylhexadecane (300 MHz, $CDCL_3$)..

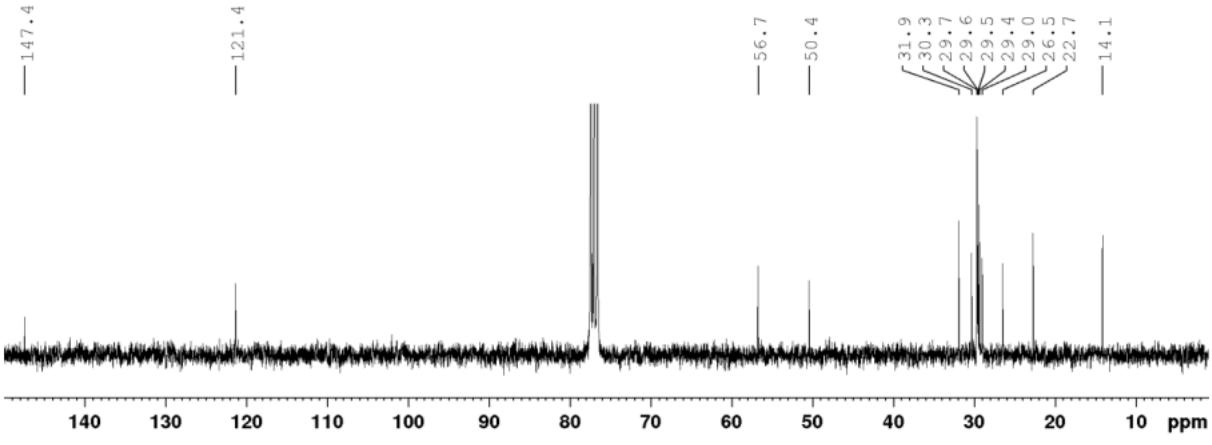

Figure 8.1.99.^{13}C NMR spectrum of hydroxymethyl-1,2,3-triazolylhexadecane.. (75 MHz, $CDCL_3$)..

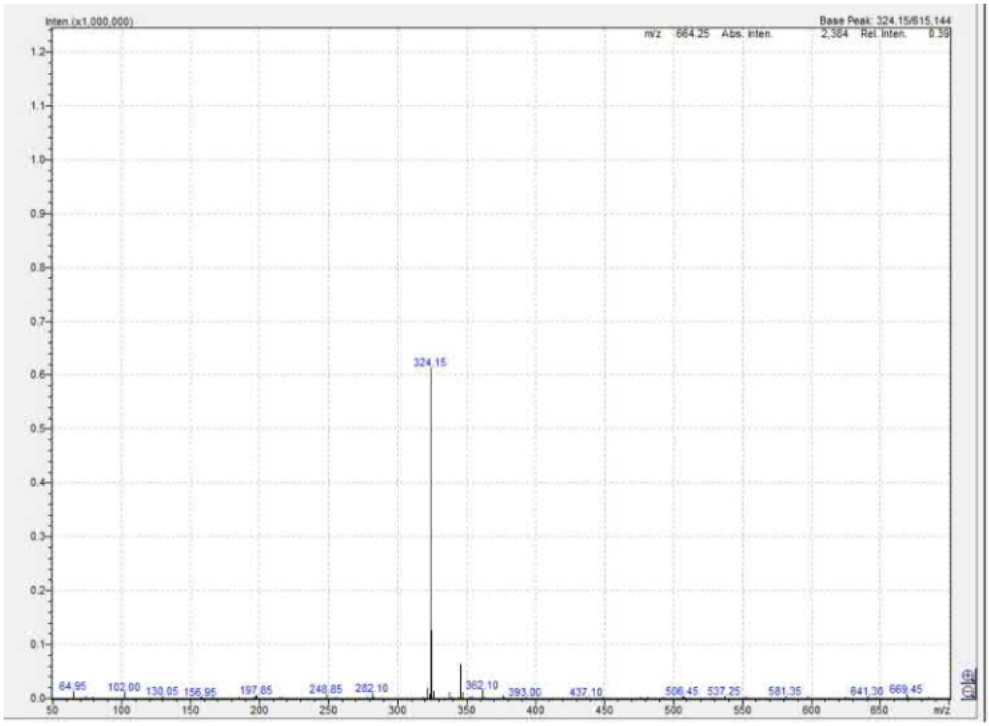

*Figure.8.1.100.. LRMS.m/z.=.324.15.[**L**+H]⁺.(calc..for.$C_{19}H_{38}N_3O^+$,.324.52)..*

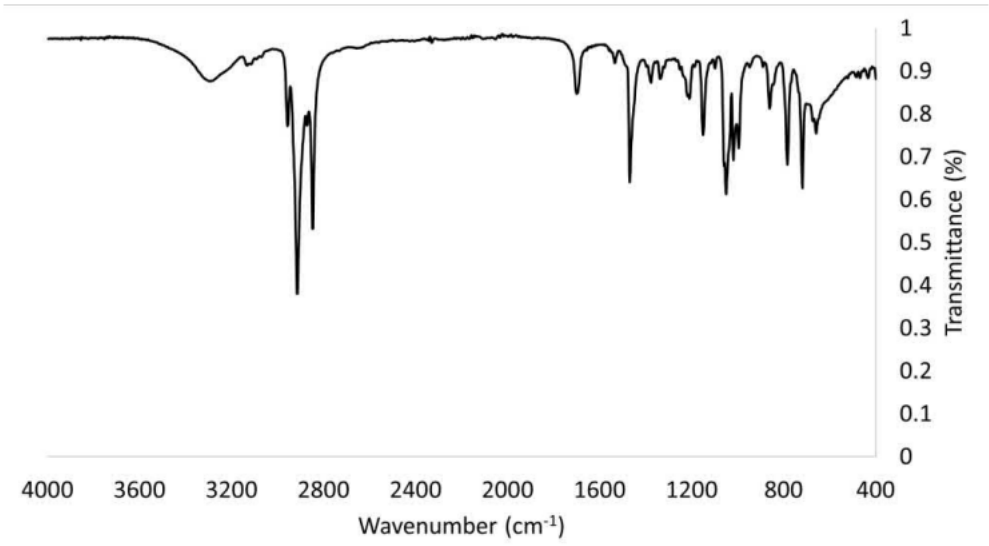

Figure.8.1.101.. IR spectrum.of.hydroxymethyl-1,2,3-triazolylhexadecane..

8.2 Chapter 4

8.2.1 Ligand Characterisation Data

8.2.1.1 Intermediate C

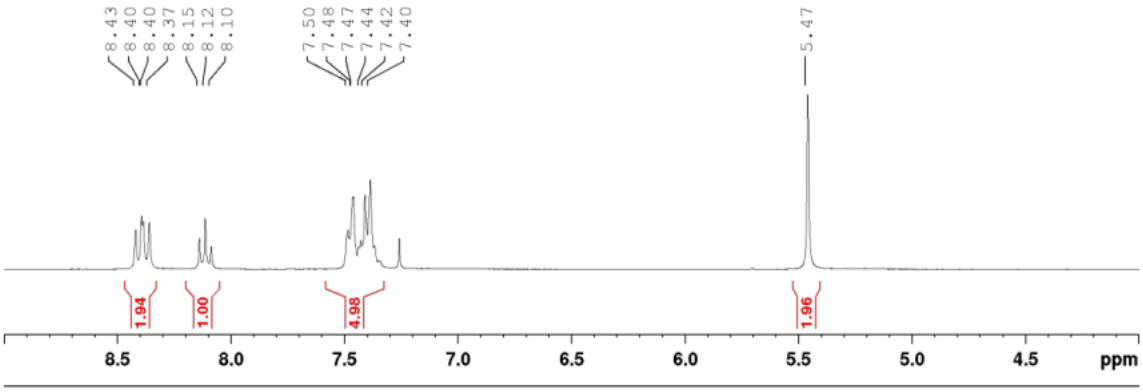

*Figure 8.2.1.. ^{1}H NMR spectrum of **C** (300 MHz, $CDCl_3$).*

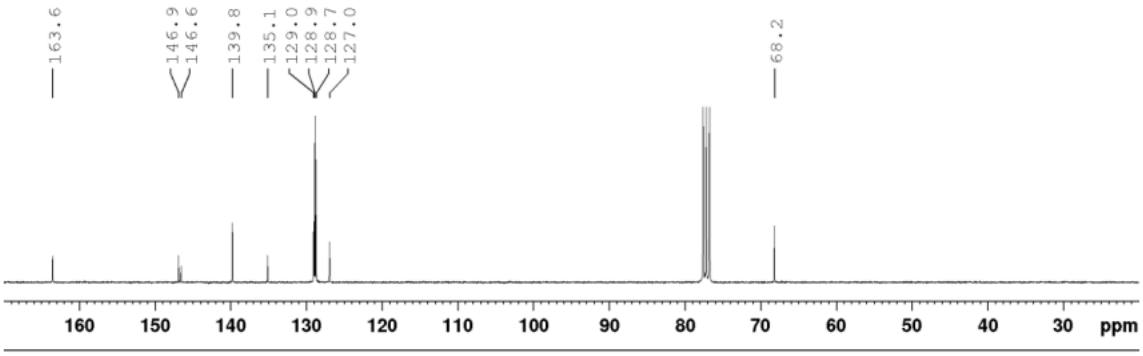

*Figure 8.2.2. ^{13}C NMR spectrum of **C** (75 MHz, $CDCl_3$).*

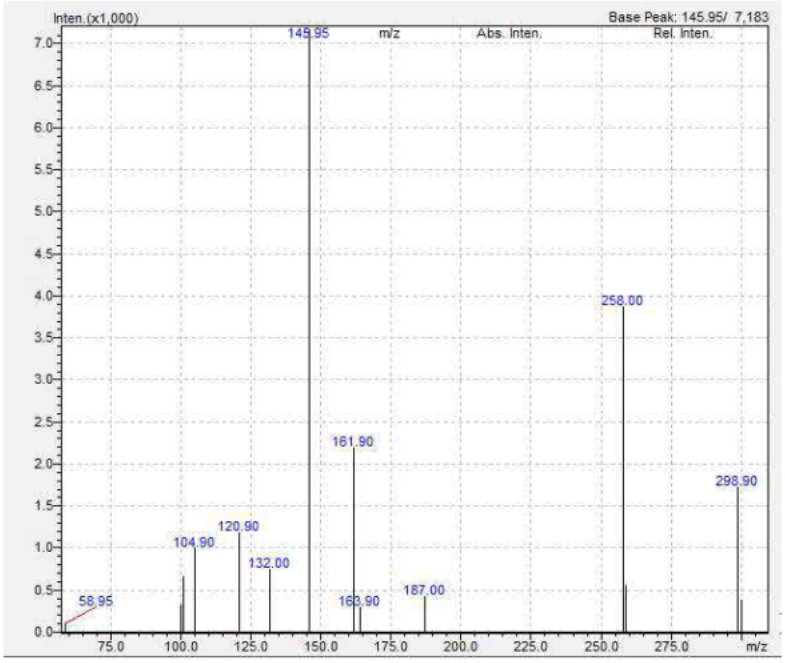

*Figure 8.2.3.. LRMS m/z= 258.00 [**C** + H]$^{+}$ (calc. for $C_{14}H_{12}NO_4^{+}$, 258.25).*

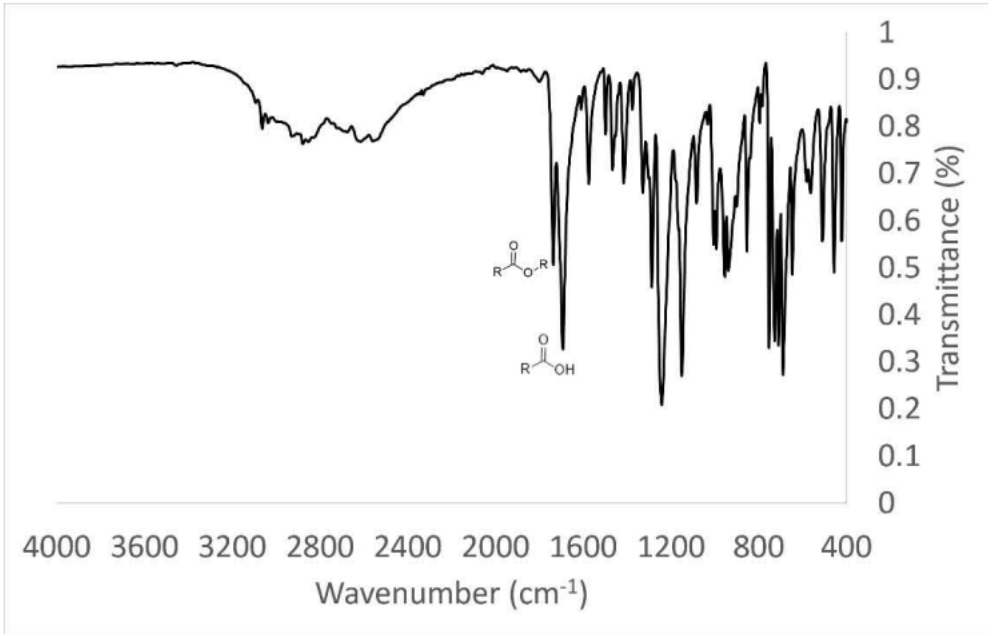

*Figure.8.2.4..IR.spectrum.of.**C**..*

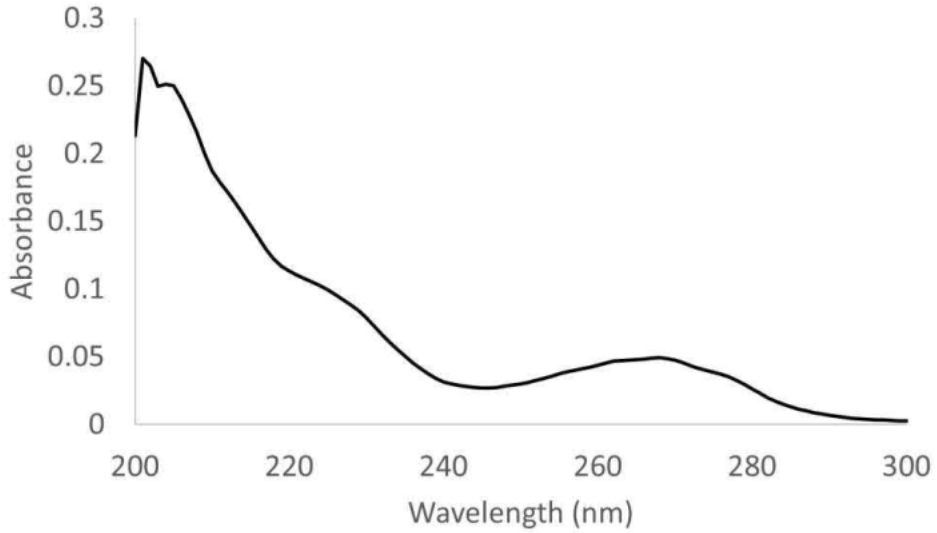

*Figure.8.2.5..UV-visible.absorption.spectrum.of.**C**.(0.01.mM,.MeCN)..*

8.2.1.2 Intermediate D

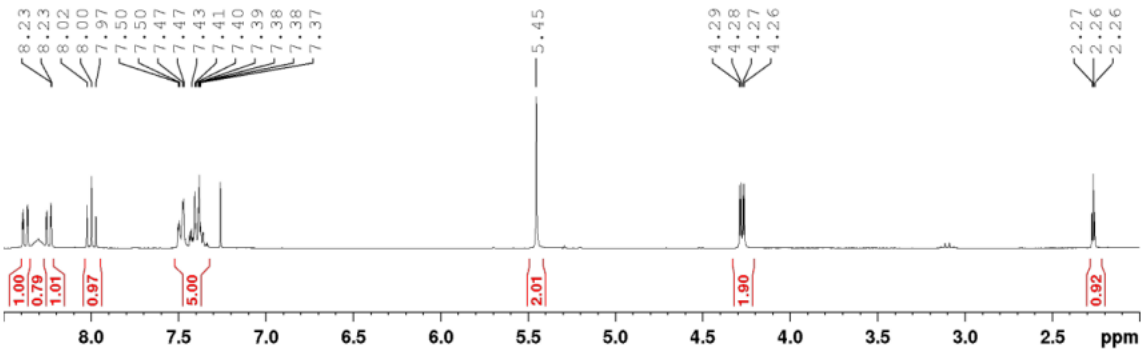

*Figure.8.2.6.:.^{1}H.NMR.spectrum.of.**D**.(300.MHz,.$CDCl_3$)..*

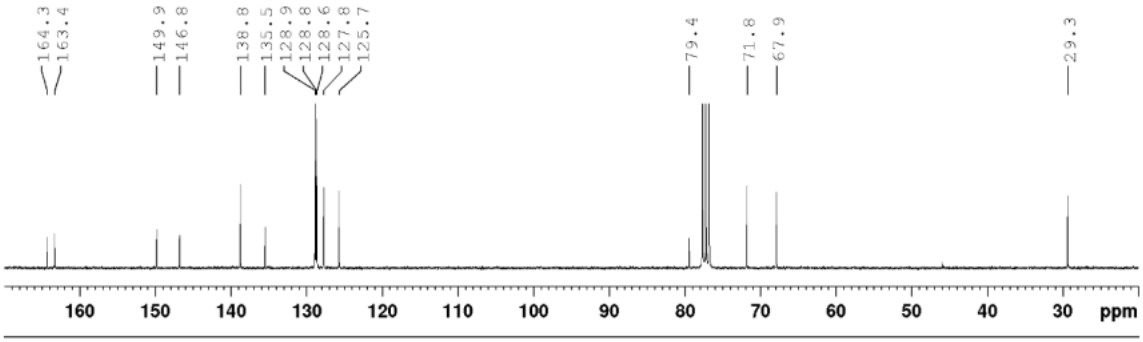

*Figure 8.2.7.. ^{13}C NMR spectrum of **D** (75 MHz, $CDCl_3$).*

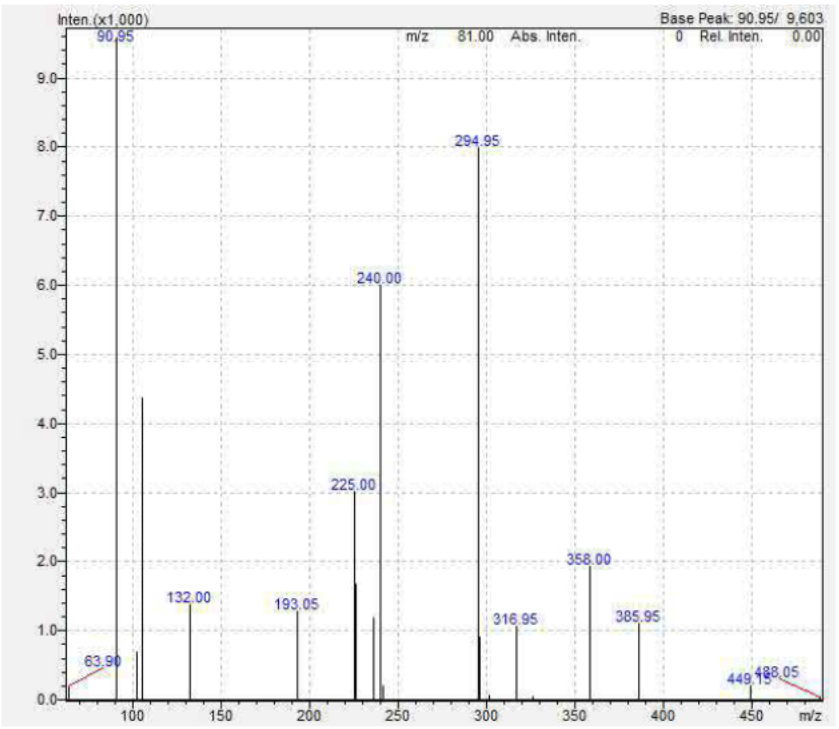

Figure 8.2.8.. LRMS m/z = 294.95 $[\mathbf{D}+H]^+$ (calc. for $C_{17}H_{15}N_2O_3^+$, 295.11), m/z = 316.95 $[\mathbf{D}+Na]^+$ (calc. for $C_{17}H_{15}N_2O_3^+$, 317.19).

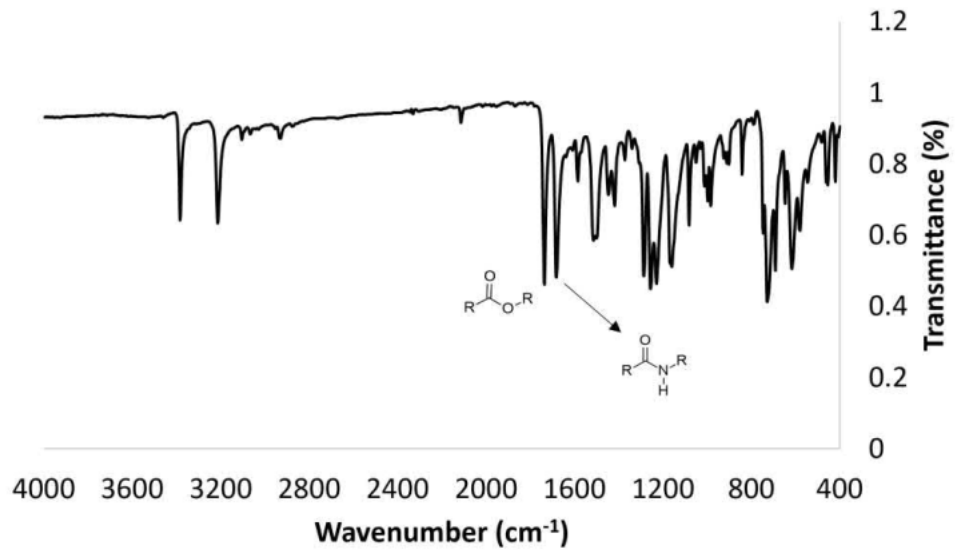

*Figure 8.2.9.. IR spectrum of **D**.*

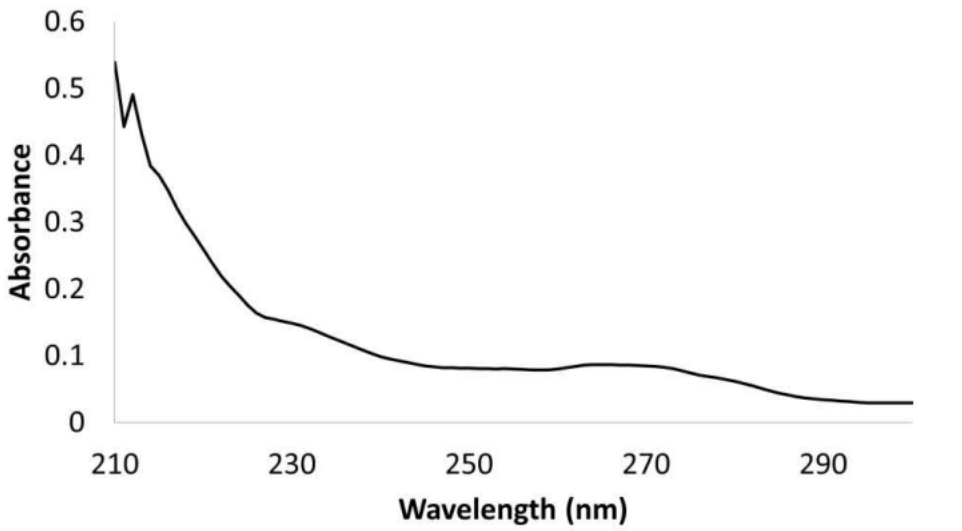

*Figure 8.2.10.. UV-visible absorption spectrum of **D** (0.01 mM,. MeCN).*

8.2.1.3 Intermediate E

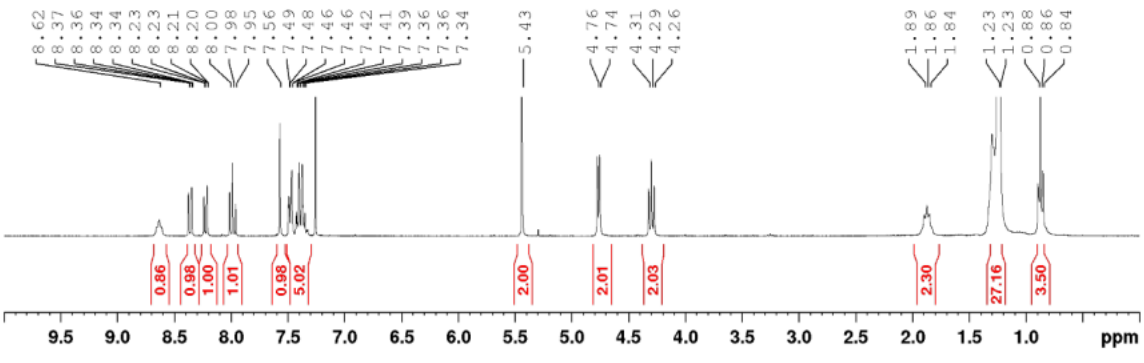

*Figure 8.2.11.. ^{1}H. NMR. spectrum. of. **E** (300. MHz,. $CDCl_3$)..*

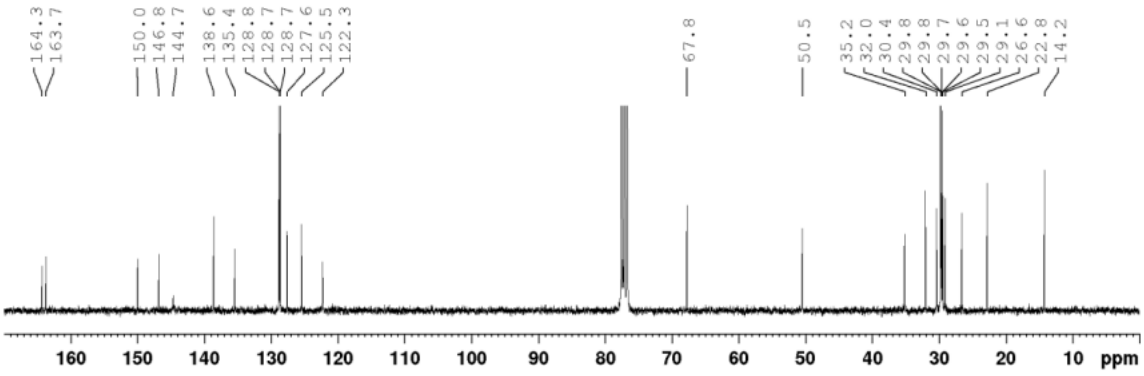

*Figure 8.2.12. ^{13}C. NMR. spectrum. of. **E** (75. MHz,. $CDCl_3$)..*

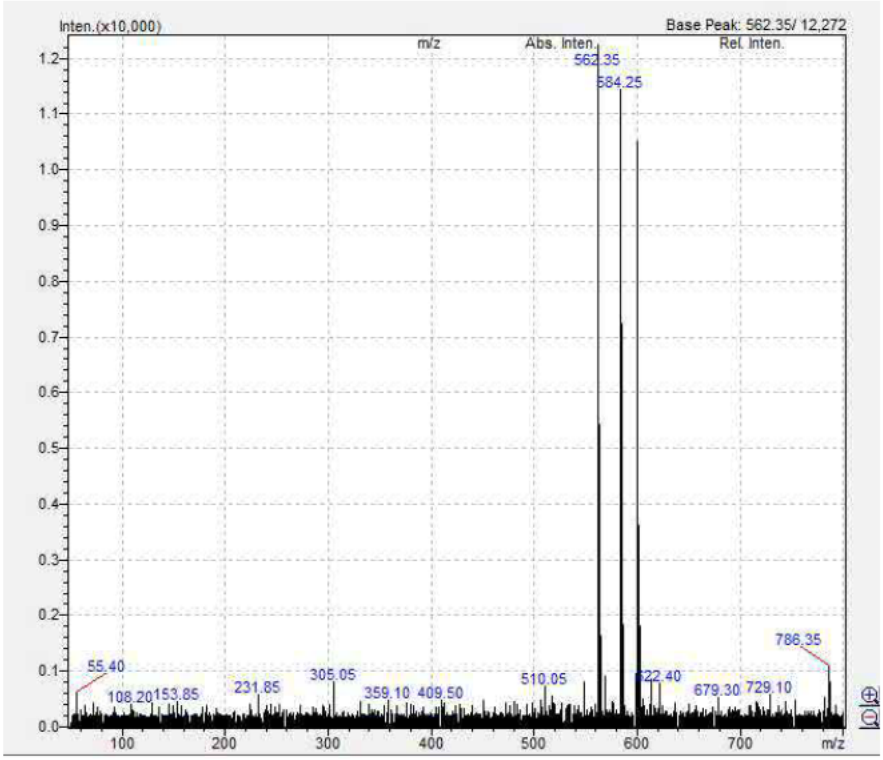

*Figure 8.2.13.. LRMS. m/z = 562.35. [**E** + H]$^+$. (calc.. for. $C_{33}H_{48}N_5O_3^+$, 562.38), m/z = 584.25. [**E** + Na]$^+$. (calc.. for. $C_{33}H_{47}N_5O_3Na^+$, 584.36), m/z = 600.25. [**E** + K]$^+$. (calc.. for. $C_{33}H_{47}N_5O_3K^+$, 600.20)..*

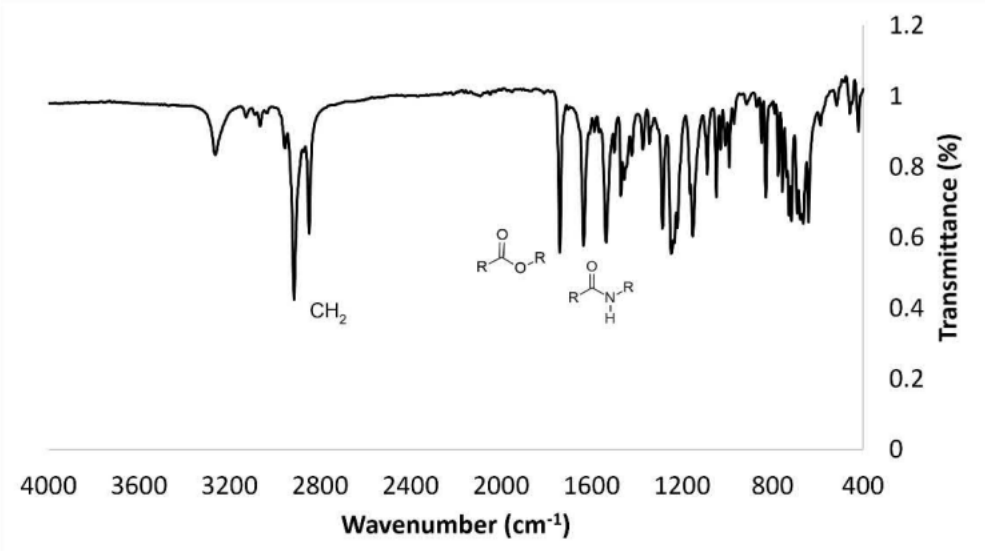

*Figure 8.2.14.. IR spectrum of **E**..*

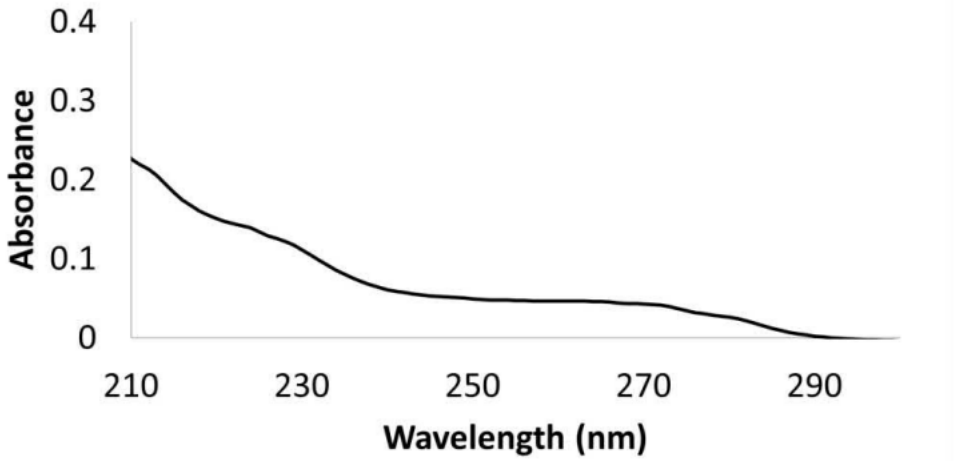

*Figure 8.2.15.. UV-visible absorption spectrum of **E** (0.01 mM, MeCN).*

8.2.1.4 Ligand 5

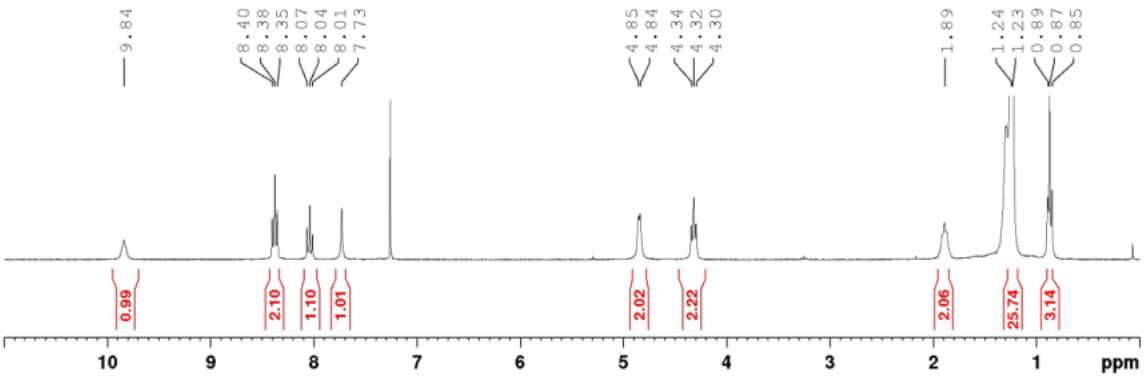

*Figure 8.2.16.. ^{1}H NMR spectrum of **5** (300 MHz, $CDCl_3$).*

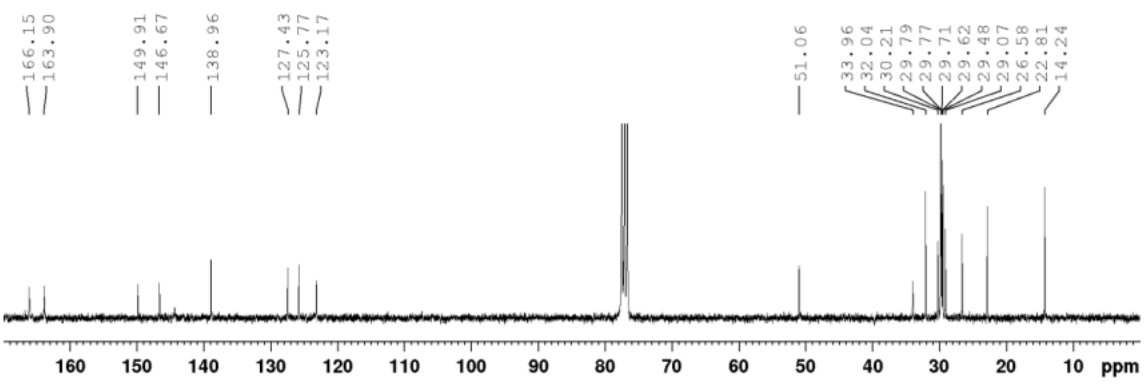

*Figure 8.2.17: ^{13}C NMR spectrum of **5** (75 MHz, $CDCl_3$).*

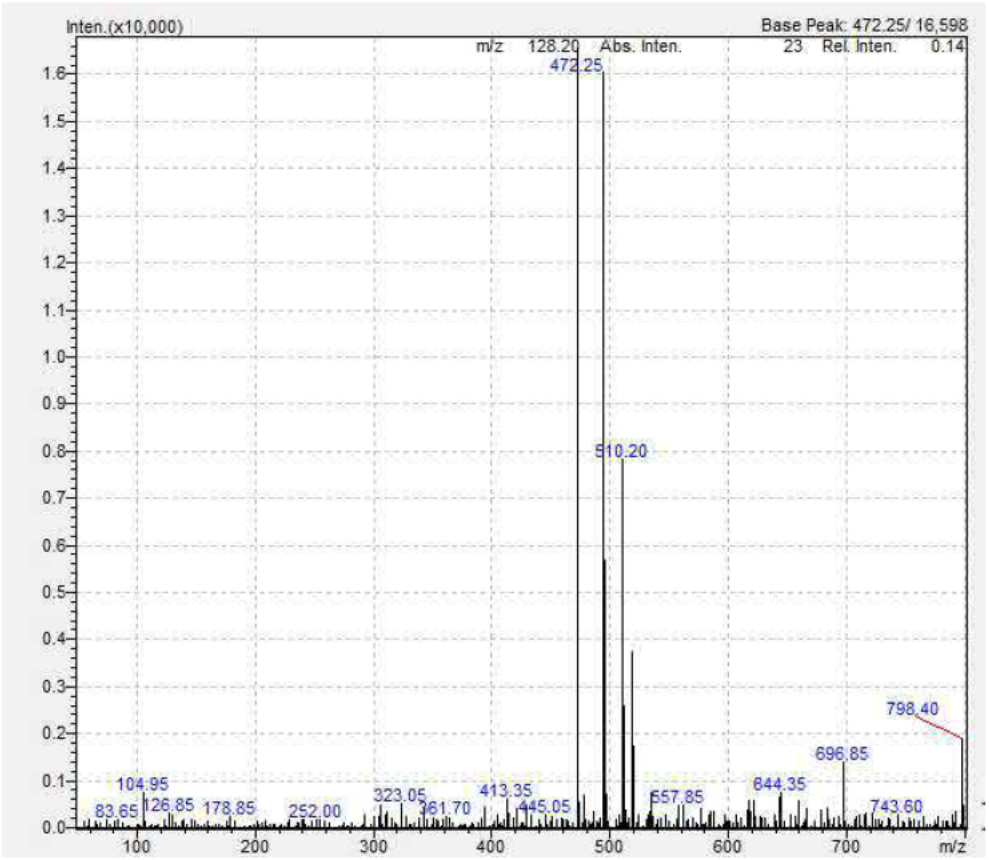

*Figure 8.2.18.. LRMS m/z = 472.25 [**5** + H]$^+$ (calc.. for $C_{26}H_{42}N_5O_3^+$, 472.33),. m/z =494.20 [5 + Na]$^+$. (calc.. for $C_{26}H_{41}N_5O_3Na^+$, 494.31) and m/z = 510.20 [**5** + K]$^+$ (calc.. for $C_{26}H_{41}N_5O_3K$+,. 510.28)..*

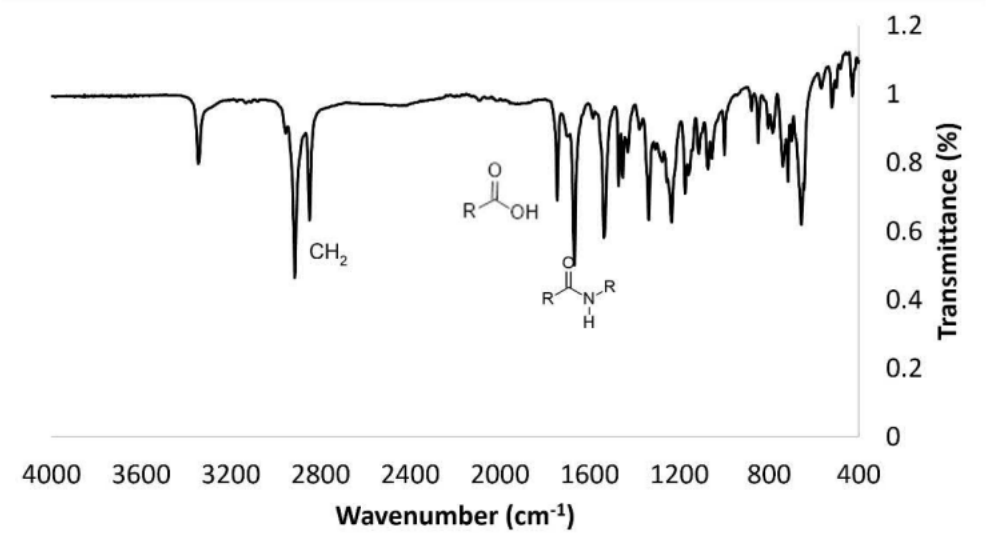

*Figure 8.2.19.. IR spectrum of **5**.*

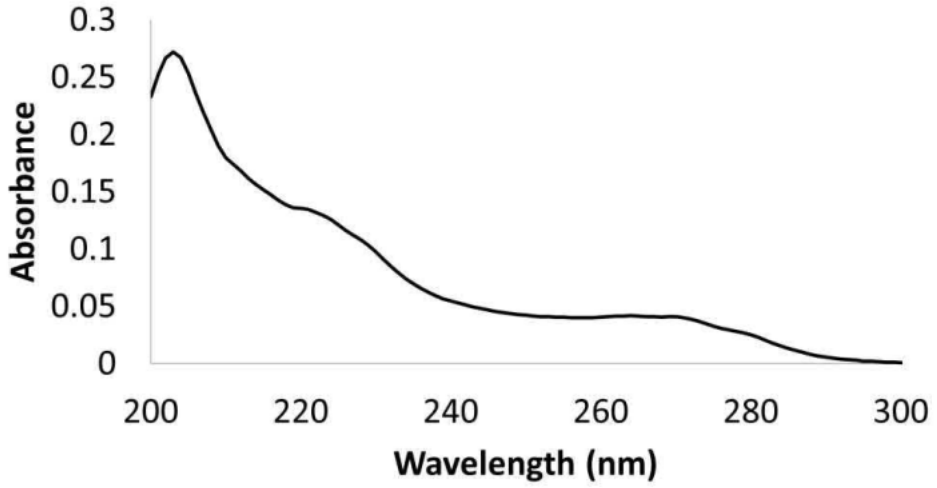

*Figure 8.2.20. UV-visible absorption spectrum of **5** (0.01 mM, MeCN).*

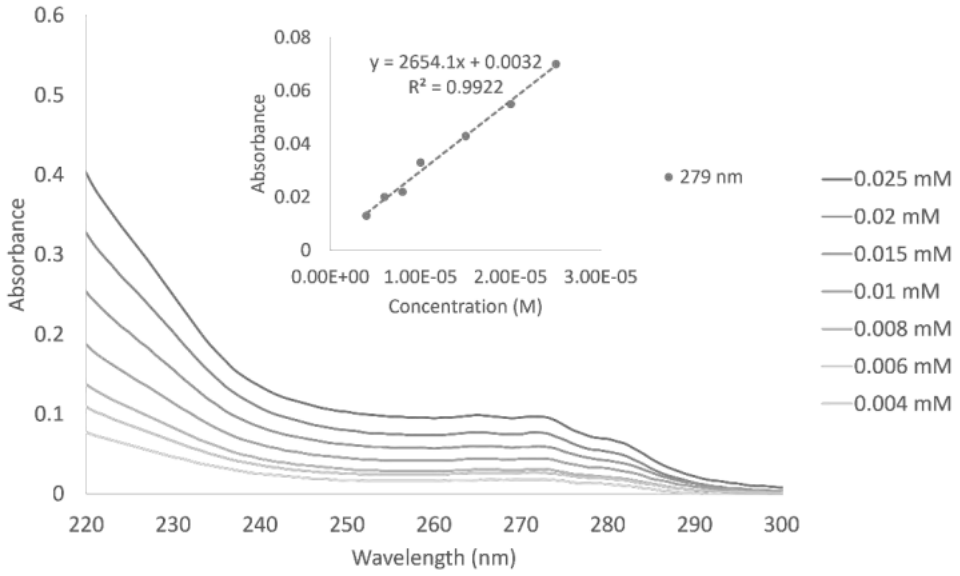

*Figure 8.2.21. UV-visible absorption spectrum of **5**, in MeCN. Insert: absorbance at 274 nm vs concentration.*

8.2.1.4 Precursor 1-azidohexadecane

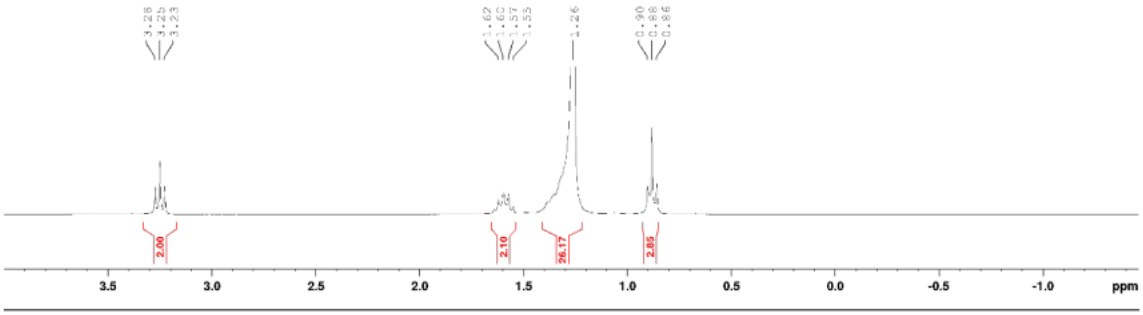

Figure. 8.2.22.. ^{1}H. NMR. spectrum. of. 1-azidohexadecane. (300. MHz,. $CDCl_3$).

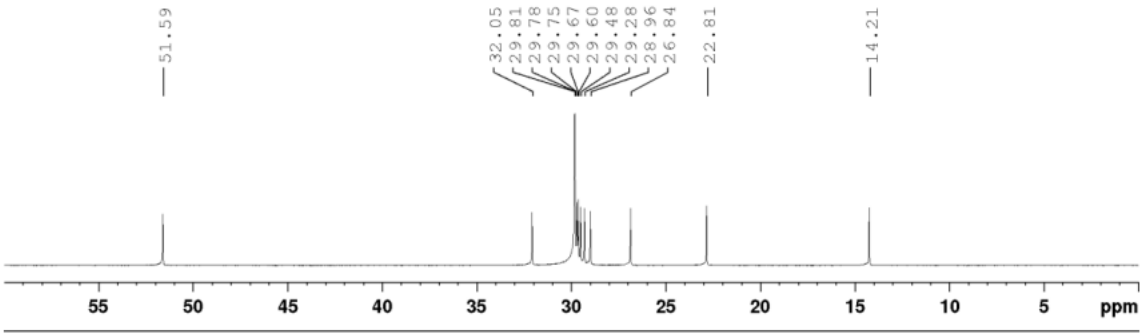

Figure. 8.2.23.. ^{13}C. NMR. spectrum. of. 1-azidohexadecane. (75. MHz,. $CDCl_3$)..

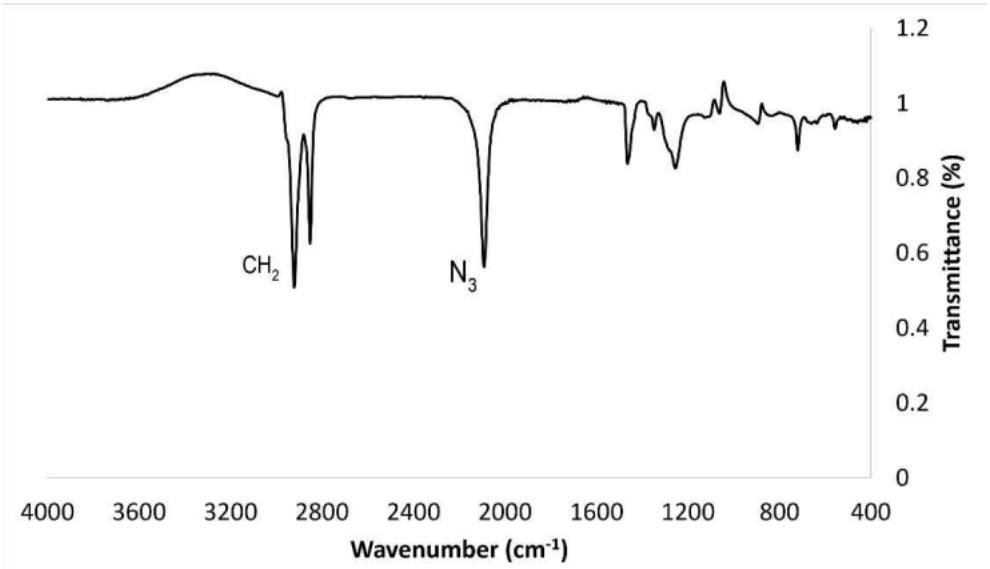

Figure. 8.2.24.. IR. spectrum. of. 1-azidohexadecane..

8.2.2 Crystal Structure Data

Crystal Data for **5**, $C_{28}H_{47}N_5O_4S$ (*M.*=549.76 g/mol): triclinic, space group *P*-1 (no. 2), *a* = 5.4939(6) Å, *b* = 9.5425(11) Å, *c* = 29.273(4) Å, *α* = 82.514(6)°, *β* = 87.742(6)°, *γ* = 84.220(6)°, *V.* = 1513.3(3) Å^3, *Z* = 2, *T* = 123.0 K, μ(CuKα) = 1.269 mm^{-1}, *Dcalc* = 1.206 g/cm^3, 25890 reflections measured (6.092° ≤ 2Θ ≤ 101.006°), 3130 unique (R_{int} = 0.0478, R_{sigma} = 0.0293) which were used in all calculations. The final R_1 was 0.0496 (I > 2σ(I)) and wR_2 was 0.1277 (all data). CCDC : 2046714

8.2.3 Self-Assembly Titration Data

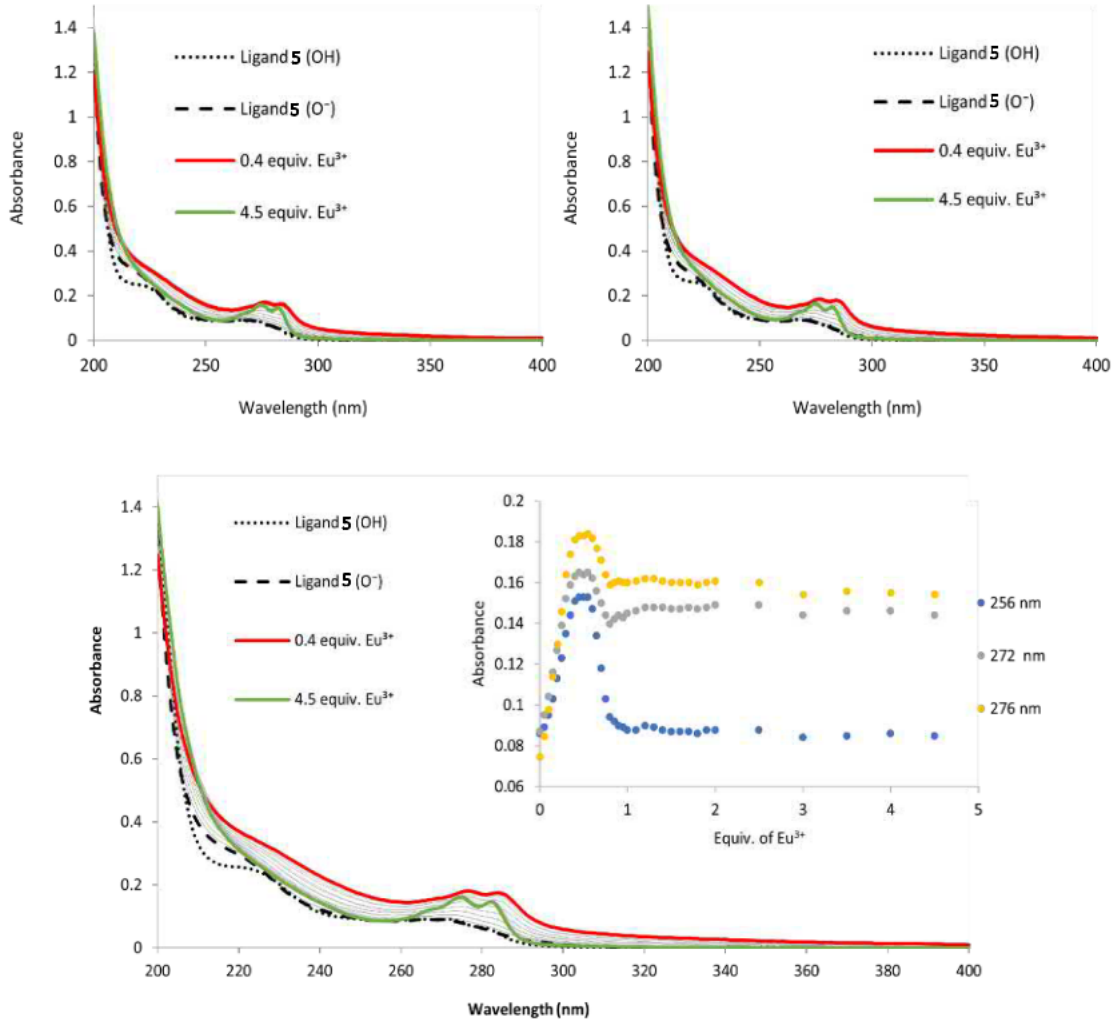

*Figure 8.2.25.. UV-visible absorption titration of **5** with $Eu(CF_3SO_3)_3$ 0 to 4.5 equivalents,. done in triplicate.. Insert:: Monitoring changes in absorbance vs Ln^{3+} equivalents at λ = 256,, 272 and 276 nm..*

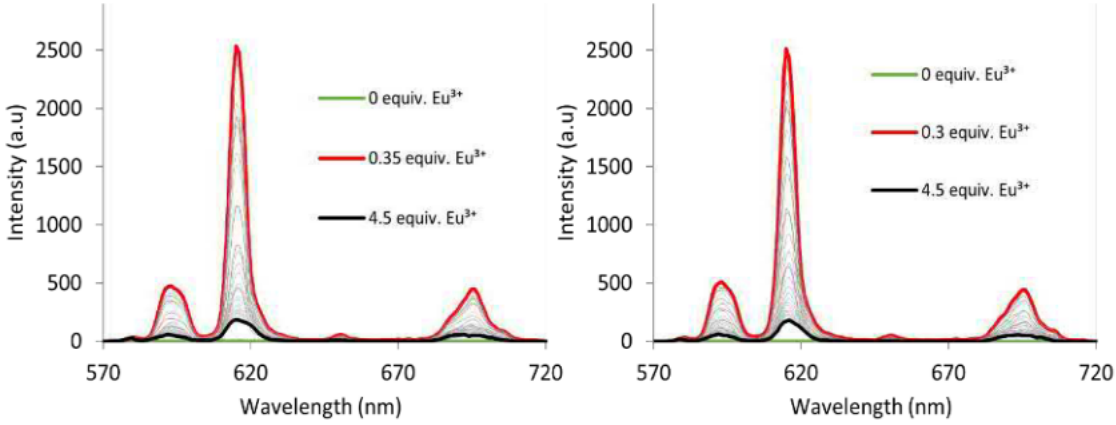

*Figure 8.2.26.. Fluorescence titration of **5** with $Eu(CF_3SO_3)_3$ 0 to 4.5 equivalents,. done in triplicate...*

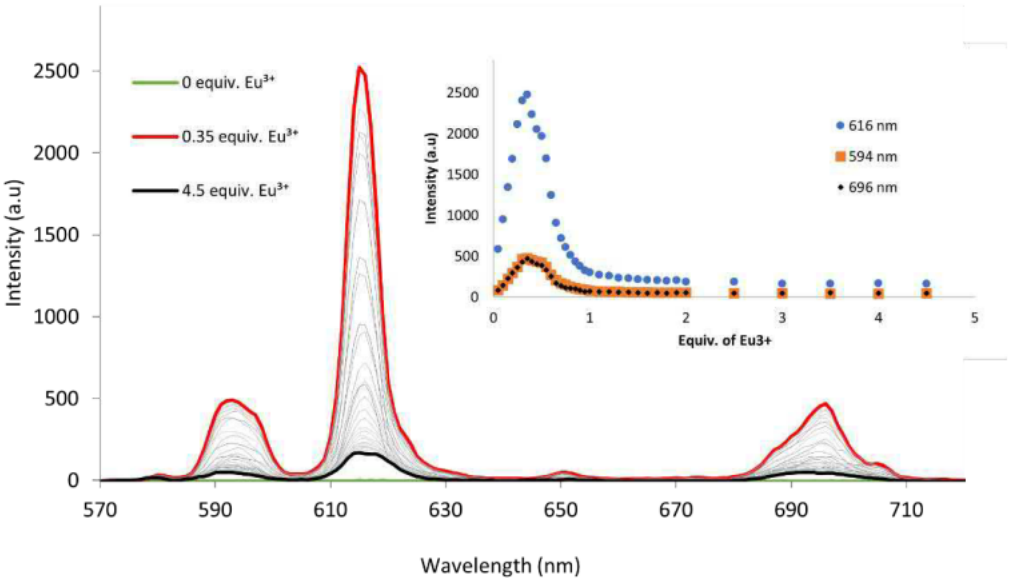

*Figure 8.2.27. Fluorescence titration of **5** with $Eu(CF_3SO_3)_3$ 0 to 4.5 equivalents, done in triplicate. Insert: Monitoring changes in emission vs. Ln^{3+} equivalents at λ = 594, 616 and 696 nm.*

8.2.4 Lanthanide Complex Data

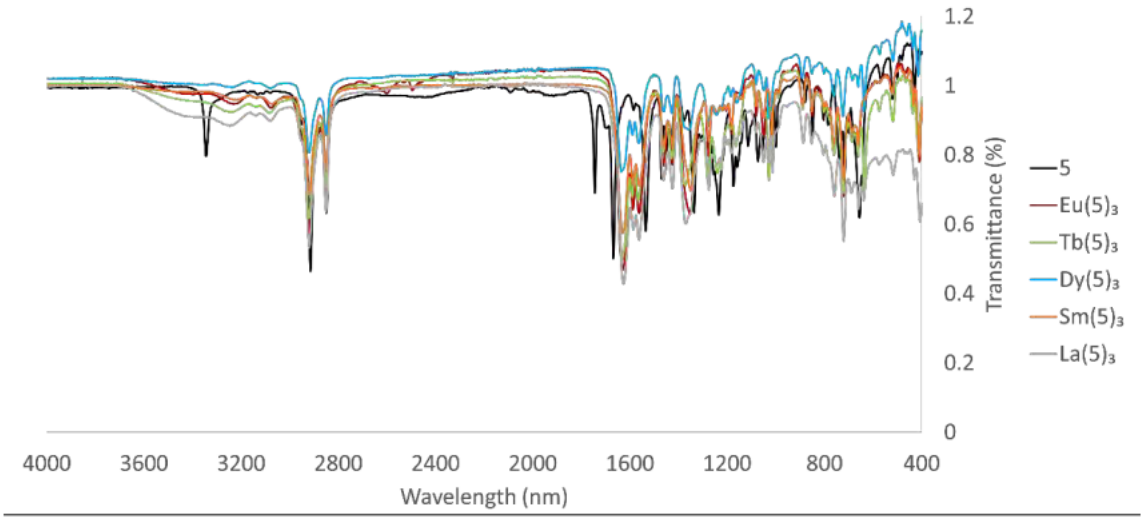

*Figure 8.2.28.. IR spectra of **5** and Ln(**5**)$_3$ where Ln. = Eu^{3+},. Tb^{3+},. Dy^{3+},. Sm^{3+},. and. La^{3+}..*

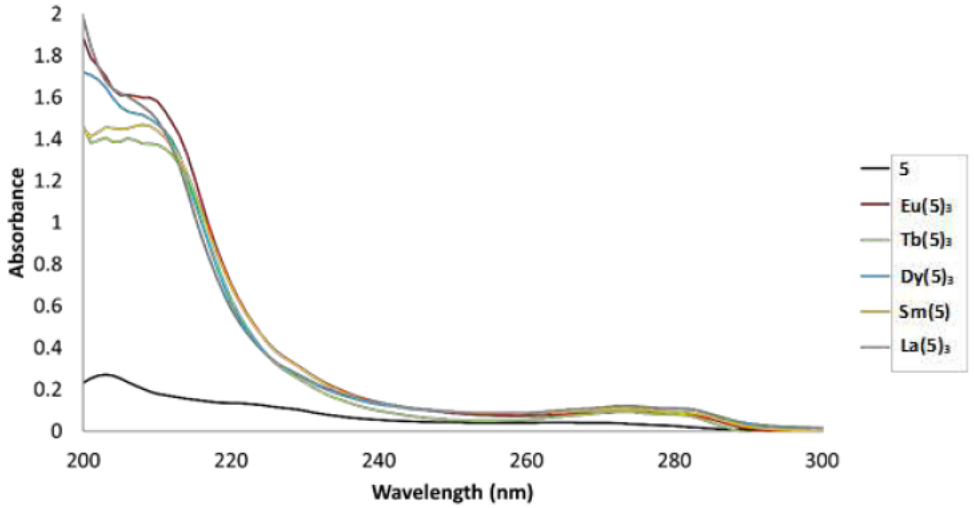

Figure 8.2.29. UV-visible absorption of **5** and Ln(**5**)$_3$ where Ln = Eu^{3+}, Tb^{3+}, Dy^{3+}, Sm^{3+} and La^{3+} (0.001 mM, MeCN)..

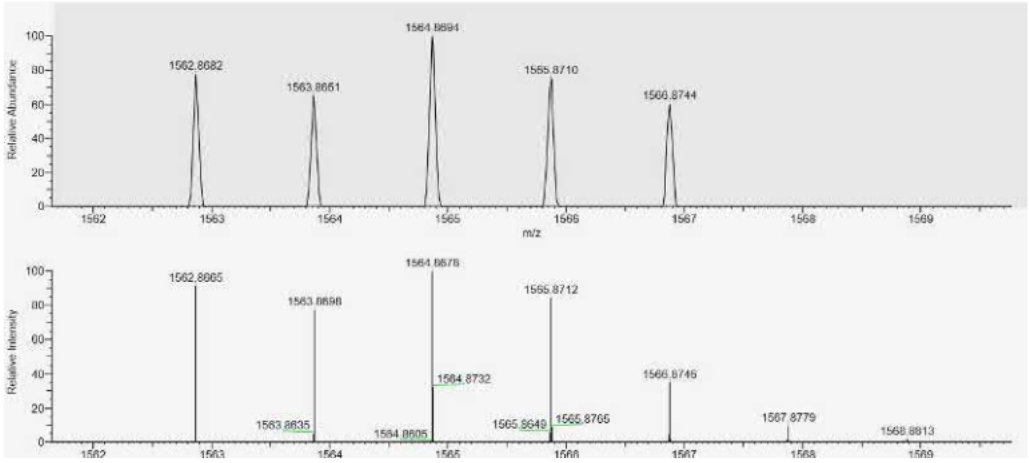

*Figure. 8.2.30. (Top). HRMS. m/z. =. 1564.8694. [Eu(**5**)$_3$ +. H]$^+$. :. (Bottom). Calc.. for. ($C_{78}H_{121}N_{15}O_9Eu$)$^+$,. 1564.8678.. Carried. out. on. ThermoFisher Q. Exactive. Focus. coupled. to. an. Ultimate™. 3000. RSLC..*

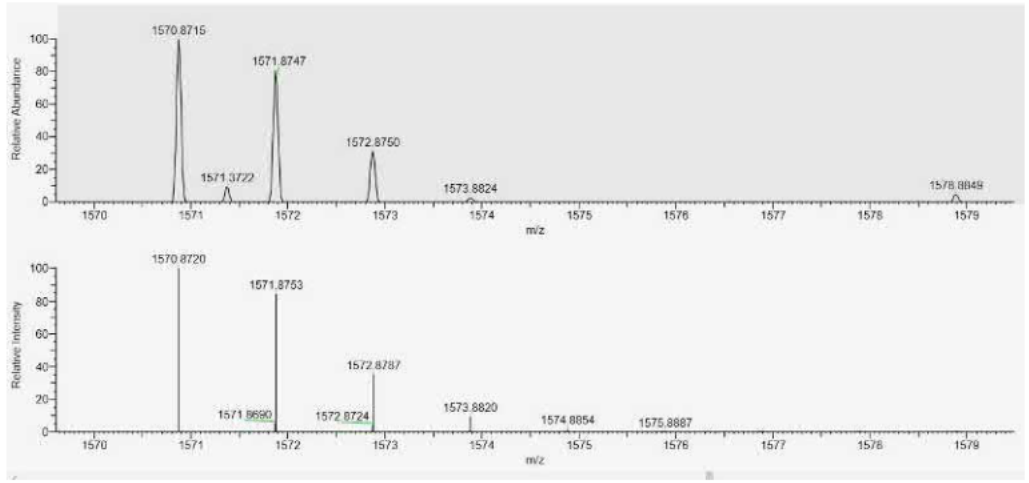

*Figure. 8.2.31.. (Top). HRMS m/z = 1570.8715 [Tb(**5**)$_3$ + H]$^+$. (Bottom) Calc. for ($C_{78}H_{121}N_{15}O_9Tb$)$^+$, 1570.8720.. Carried. out. on ThermoFisher. Q. Exactive. Focus. coupled. to. an. Ultimate™. 3000. RSLC..*

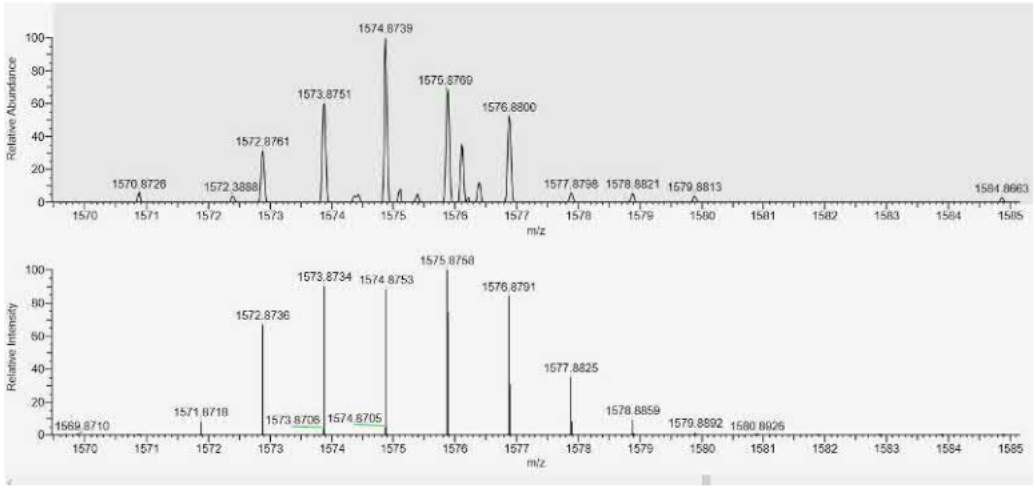

*Figure. 8.1.32.. (Top). HRMS. m/z. =. 1575.8769. [Dy(**5**)$_3$ +. H]$^+$.. (Bottom). Calc.. for. ($C_{78}H_{121}N_{15}O_9Dy$)$^+$,. 1575.8769.. Carried. out. on. ThermoFisher Q. Exactive. Focus. coupled. to. an. Ultimate™. 3000. RSLC..*

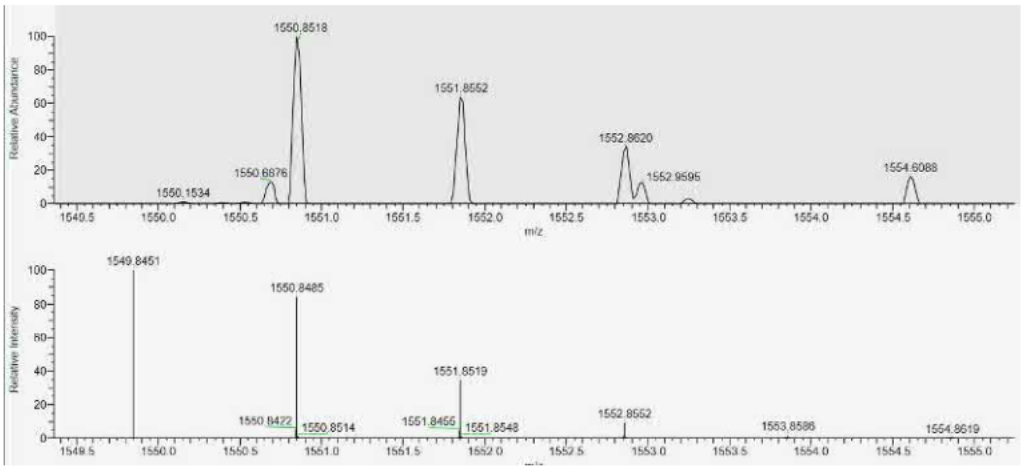

*Figure.8.2.33..(Top).HRMS.m/z.=.1550.8528.[La(**5**)$_3$.+.H]$^+$..(Bottom).Calc..for.($C_{78}H_{121}N_{15}O_9La)^+$,.1550.8530..Carried.out.on.ThermoFisher Q.Exactive.Focus.coupled.to.an.Ultimate™.3000.RSLC..*

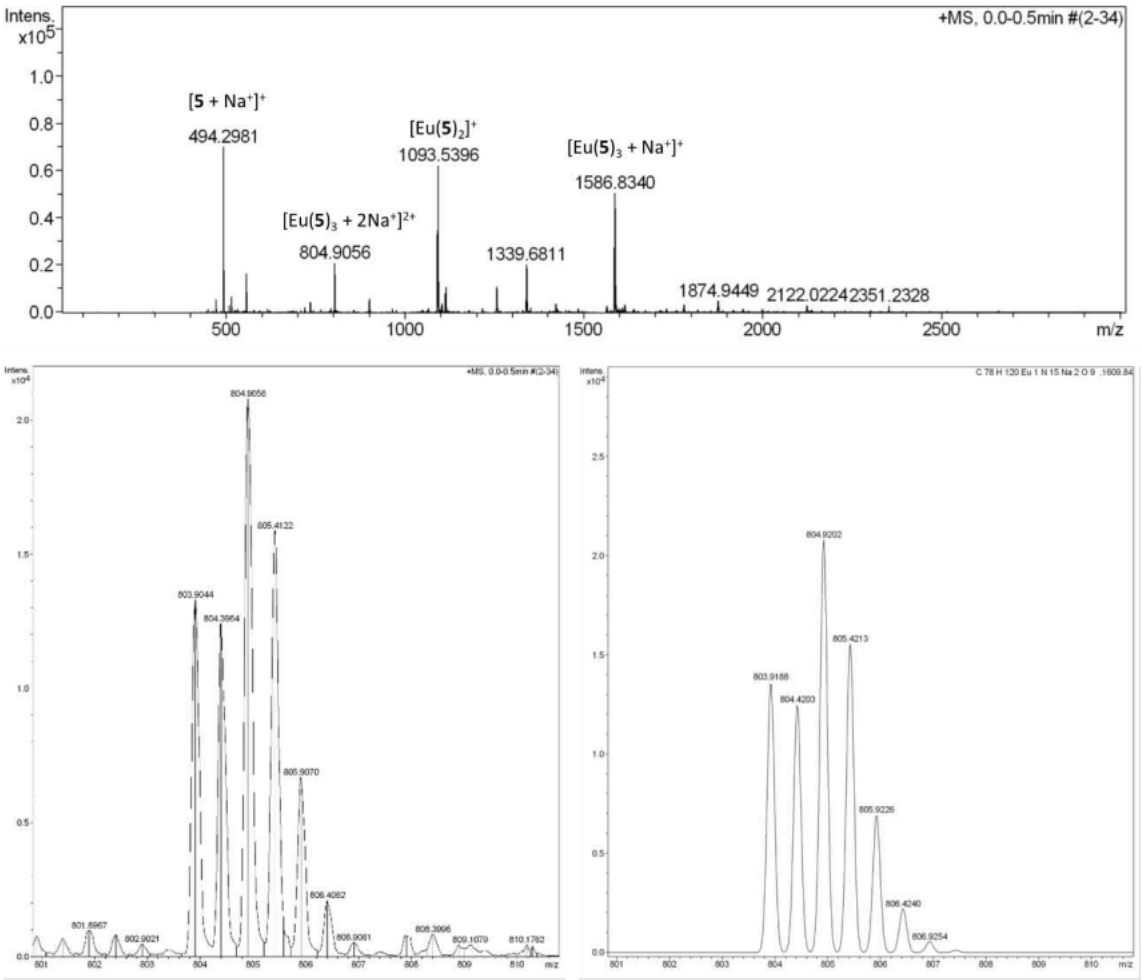

*Figure.8.2.34..HRMS.Eu(**5**)$_3$..(Top).Full.spectrum..(Bottom.Left).HRMS.zoom.in.of.m/z.=.804.9050.[Eu(**5**)$_3$.+.2Na]$^{2+}$..(Bottom.Right) Calc..for.($C_{78}H_{120}N_{15}O_9EuNa_2)^{2+}$,.804.9202..Carried.out.on.Bruker.Daltonics.MicrOTOF™.Spectrometer..*

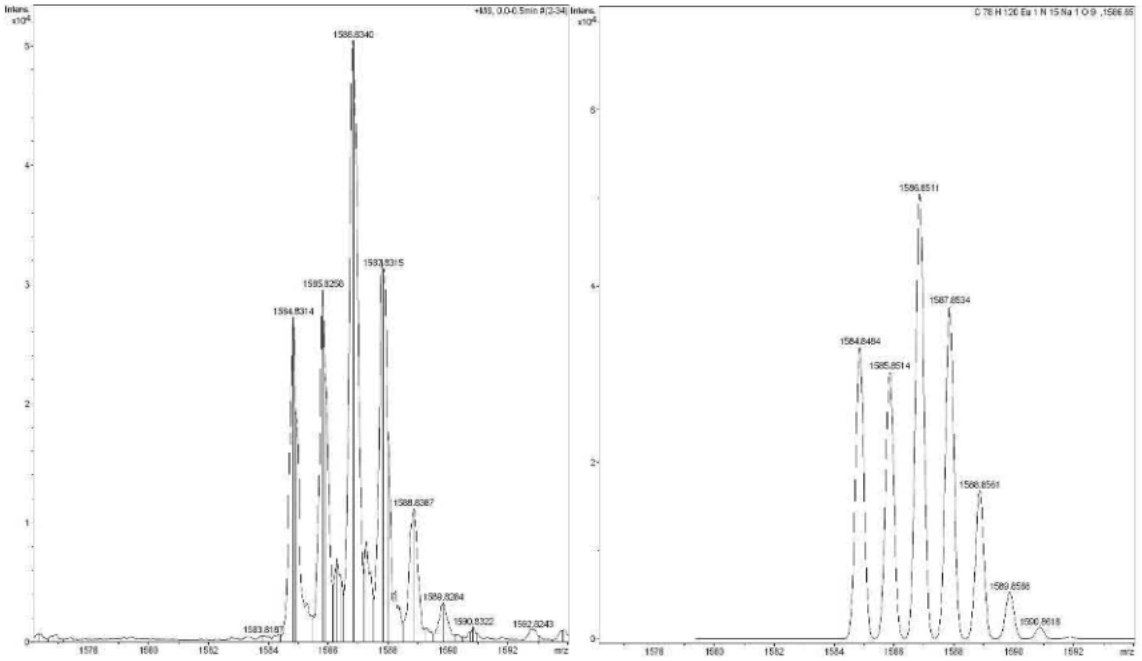

*Figure. 8.2.35.. (Left). HRMS zoom in of. m/z. =. 1586.8340. [Eu(**5**)$_3$ +. Na]$^+$. (Right). Calc.. for. ($C_{78}H_{120}N_{15}O_9EuNa$)$^+$,. 1586.8511.. Carried. out on. Bruker. Daltonics. MicrOTOF™. Spectrometer..*

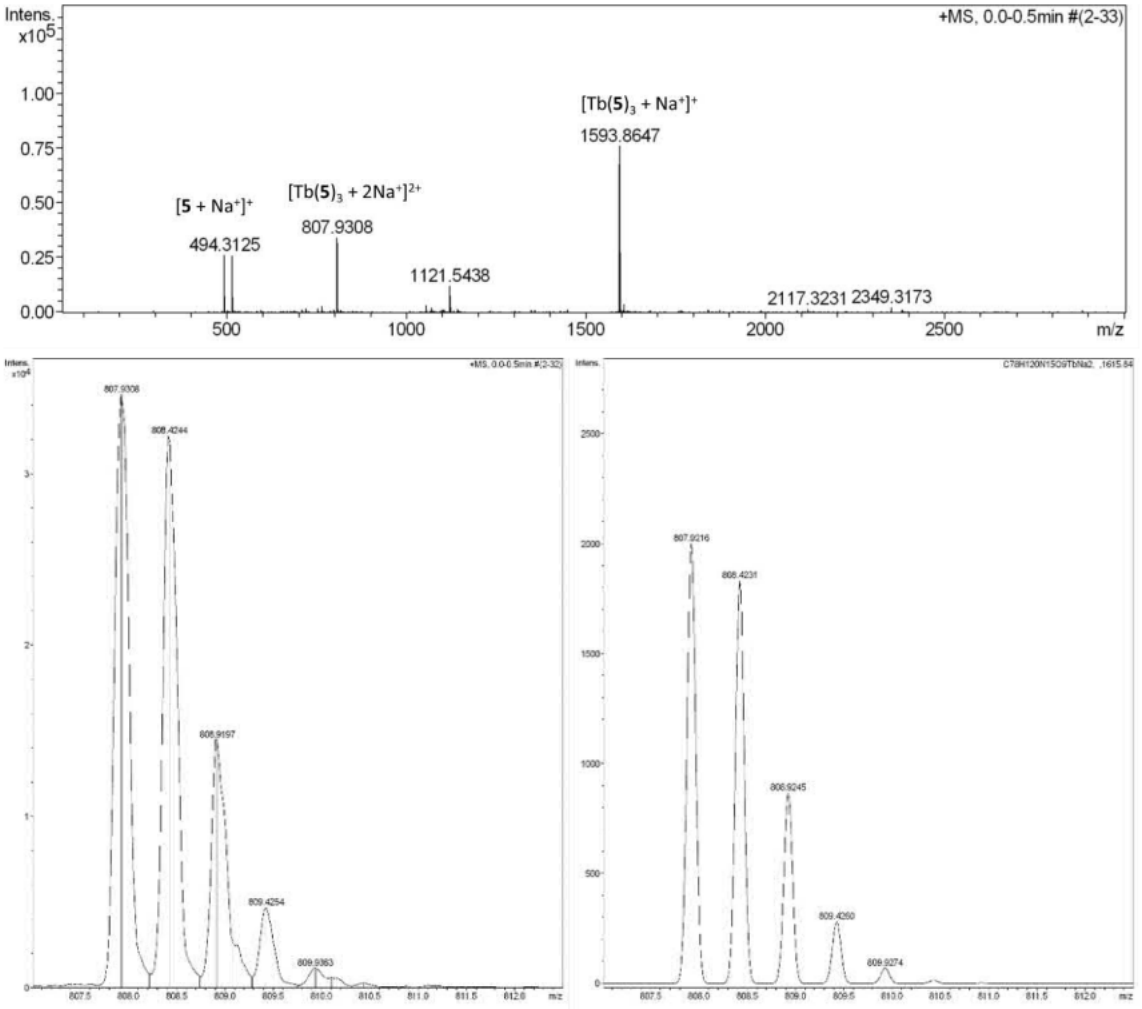

*Figure. 8.2.36.. HRMS. Tb(**5**)$_3$.. (Top). Full. spectrum.. (Bottom. Left) HRMS zoom in of. m/z = 807.9306 [Tb(**5**)$_3$ + 2Na]$^{2+}$. (Bottom Right) Calc. for ($C_{78}H_{120}N_{15}O_9TbNa_2$)$^{2+}$, 807.9216.. Carried. out. on. Bruker. Daltonics. MicrOTOF™. Spectrometer..*

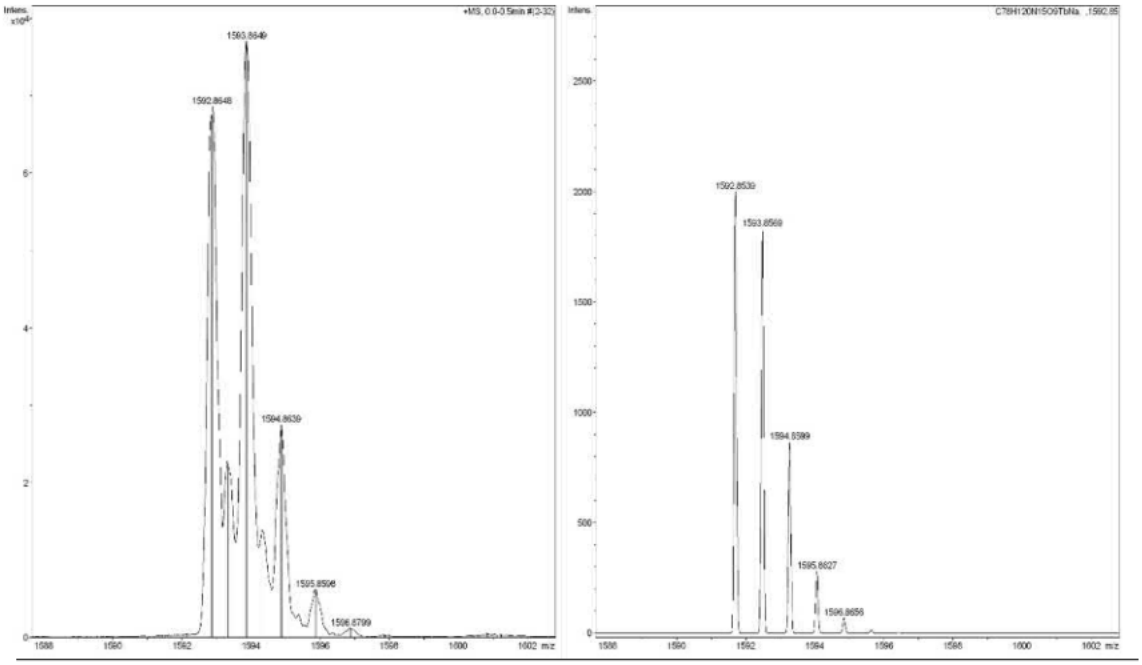

*Figure 8.2.37.. (Left). HRMS zoom in of m/z = 1592.8646 [Tb(**5**)$_3$ + Na]$^+$. (Right) Calc. for ($C_{78}H_{120}N_{15}O_9TbNa$)$^+$, 1592.8539.. Carried out on Bruker Daltonics MicrOTOF™ Spectrometer..*

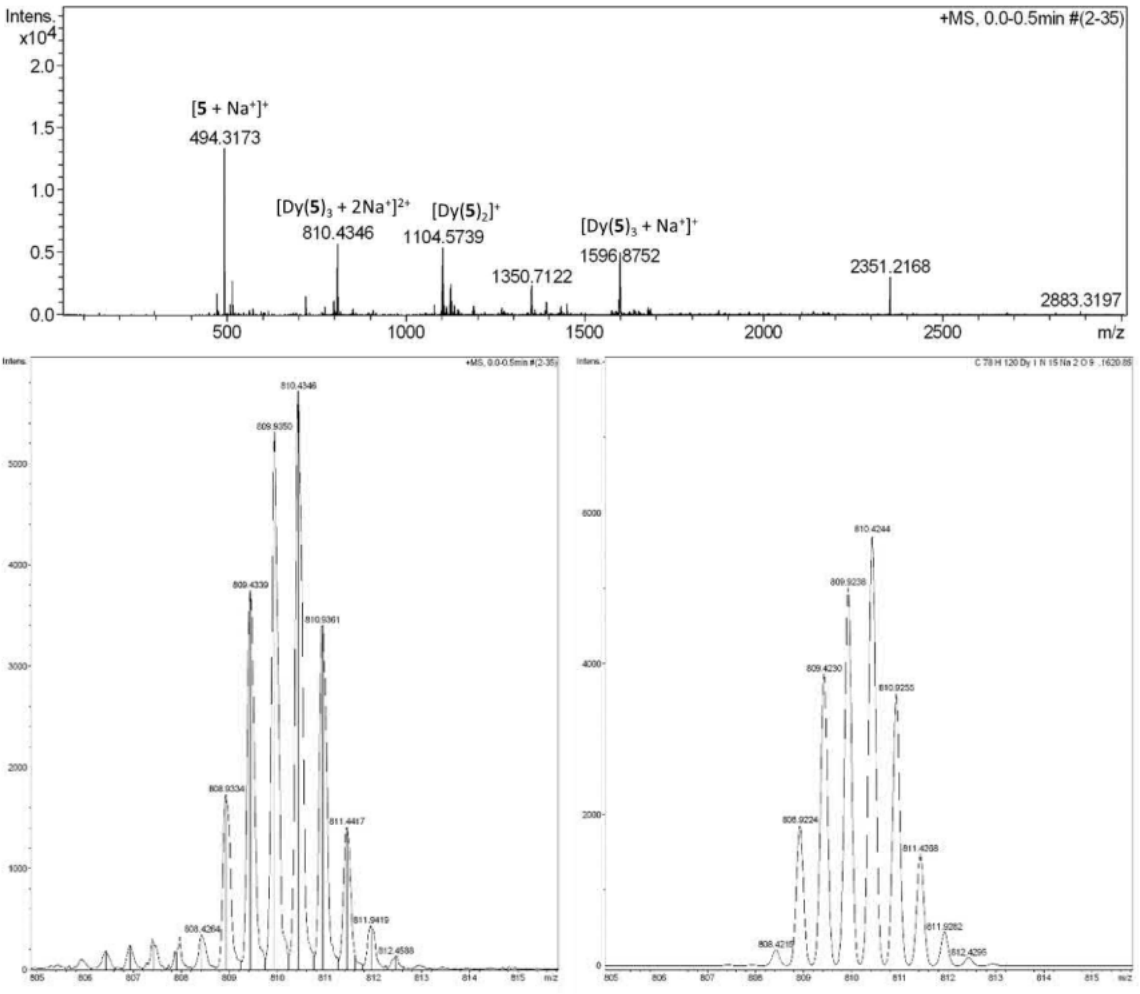

*Figure 8.2.38.. HRMS Dy(**5**)$_3$.. (Top). Full spectrum.. (Bottom Left). HRMS zoom in of m/z = 810.4346 [Dy(**1**)$_3$ + 2Na]$^{2+}$. (Bottom Right) Calc. for ($C_{78}H_{120}N_{15}O_9DyNa_2$)$^{2+}$, 810.4244.. Carried out on Bruker Daltonics MicrOTOF™ Spectrometer..*

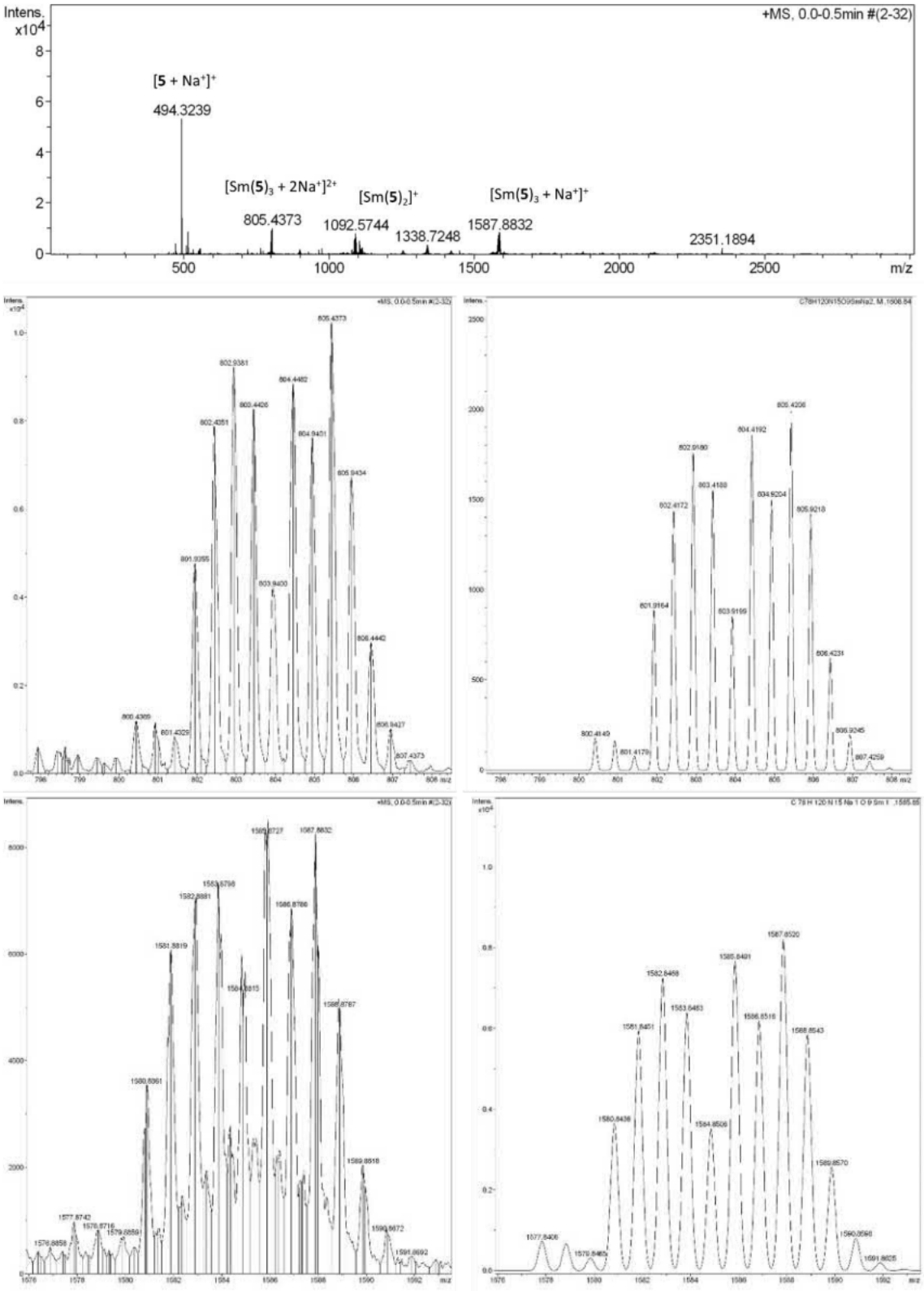

*Figure. 8.2.39.. HRMS. Sm(**5**)$_3$.. (Top). Full. spectrum.. (Middle. left). HRMS. zoom. in. of. m/z. =. 804.4482. [Sm(**5**)$_3$ +. 2Na]$^{2+}$.. (Middle. right). Calc.. for. ($C_{78}H_{120}N_{15}O_9SmNa_2$)$^{2+}$,. 804.4192.. (Bottom. left). HRMS. zoom. in. of. m/z. =. 1585.8727. [Sm(**5**)$_3$ +. Na]$^{+}$.. (Bottom. right). Calc.. for. ($C_{78}H_{120}N_{15}O_9EuNa$)$^{+}$,. 1585.8491.. Carried. out. on. Bruker. Daltonics. MicrOTOF™. Spectrometer..*

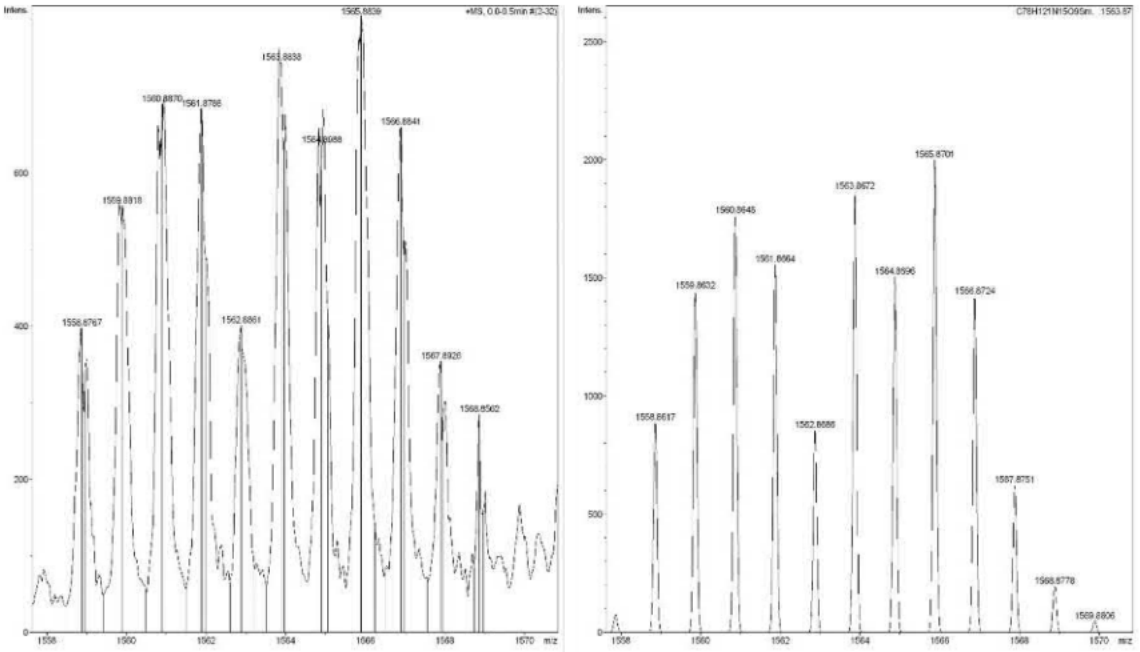

*Figure.8.2.40.. (Left).HRMS zoom in of m/z = 1563.8838 [Sm(**5**)$_3$ + H]$^+$. (Right) Calc. for ($C_{78}H_{121}N_{15}O_9Sm$)$^+$, 1563.8672.. Carried out on. Bruker. Daltonics. MicrOTOF™. Spectrometer..*

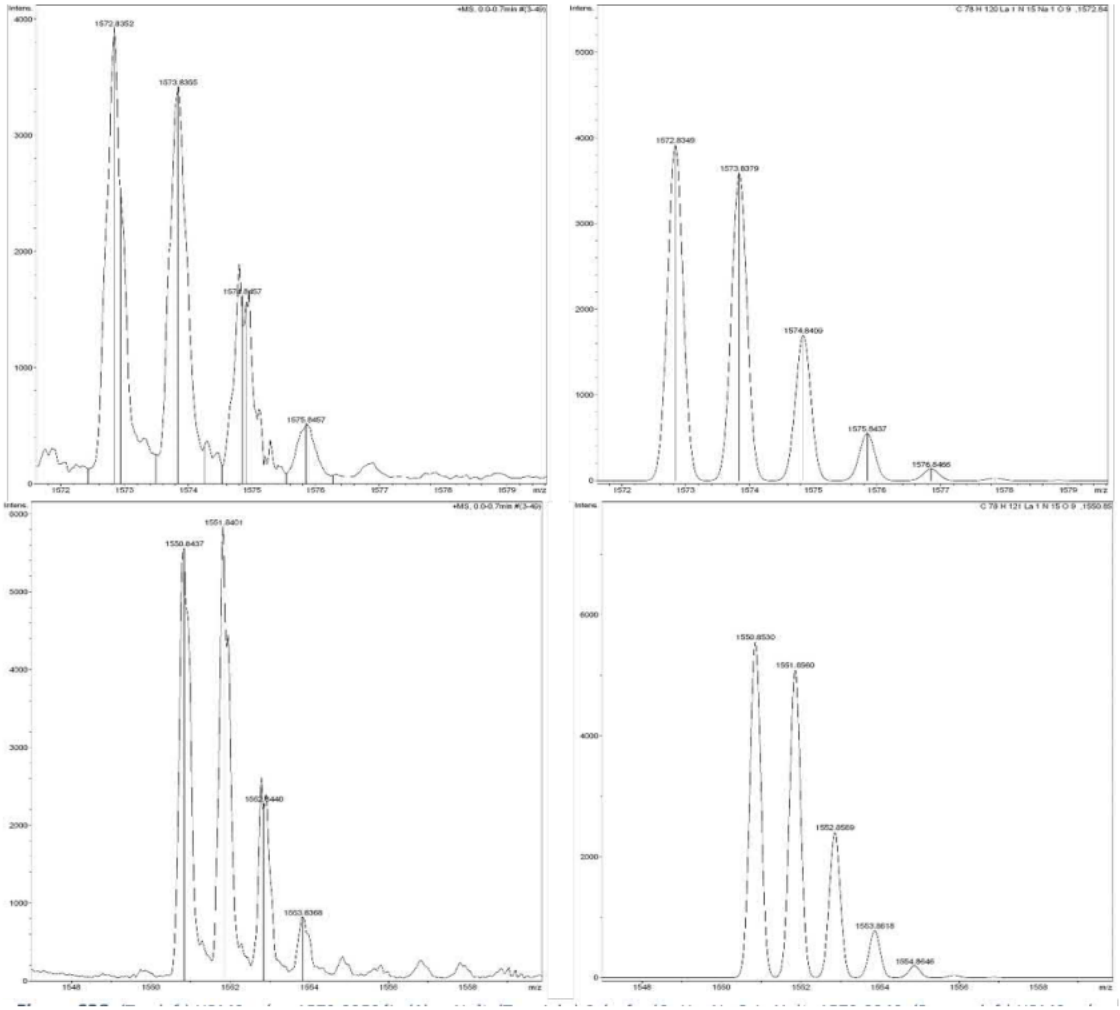

*Figure.8.2.41.. (Top.left).HRMS zoom in of m/z = 1572.8352 [La(**5**)$_3$ + Na]$^+$. (Top right) Calc. for ($C_{78}H_{120}N_{15}O_9LaNa$)$^+$, 1572.8349. (Bottom.left).HRMS zoom in of m/z = 1550.8437 [La(**5**)$_3$ + H]$^+$. (Bottom right) Calc. for ($C_{78}H_{121}N_{15}O_9La$)$^+$, 1550.8530.. Carried out on. Bruker. Daltonics. MicrOTOF™. Spectrometer..*

8.2.5 Langmuir Blodgett Data

8.2.5.1 Langmuir Isotherm Data

Table.8.2.1.. Langmuir.film.collapse.position.

Complex or Ligand	Surface-pressure at collapse (mN/m)	Area =(Å²/molecule)
5	53	20
Eu(**5**)$_3$	55	81
Tb(**5**)$_3$	56	78
Sm(**5**)$_3$	59	80
Dy(**5**)$_3$	57	78
Eu(**5**)$_3$: Tb(**5**)$_3$ (1:1)	58	82
Eu(**5**)$_3$: Tb(**5**)$_3$ (1:1)	56	82
Eu(**5**)$_3$: Tb(**5**)$_3$:Dy(**5**)$_3$ (1:1:1)	57	57
Eu(**5**)$_3$: Tb(**5**)$_3$:Dy(**5**)$_3$:Sm(**5**)$_3$ (1:1:1:1)	54	54

Table.8.2.2.. Transfer.ratios.of.mono.and.multilayer.LB.films..

Langmuir Blodgett Films	TR
Eu(**5**)$_3$	1.05
Eu(**5**)$_3$ Triple layered	1.09 (1^{st+}), 0.51 (2nd) & 1.06 (3rd)
Eu(**5**)$_3$ Five layered	1.15(1^{st+}), 0.43(2nd) , 1.20(3rd), 0.74(4th) & 1.01 (5th)
Eu(**5**)$_3$ Seven layered	1.03(1^{st+}), 0.33(2nd), 1.15(3rd), 0.63(4th) 1.07(5th) 0.68(6th) & 1.1(7th)
Tb(**5**)$_3$	1.04
Sm(**5**)$_3$	1.01
Dy(**5**)$_3$	1.01
Eu(**5**)$_3$Tb(**5**)$_3$ 1:1 mixture	1.12
Eu(**5**)$_3$Dy(**5**)$_3$ 1:1 mixture	0.93
Eu(**5**)$_3$Dy(**5**)$_3$ 1:10 mixture	0.99
Eu(**5**)$_3$Tb(**5**)$_3$Dy(**5**)$_3$ 1:1:1 mixture	1.01
Eu(**5**)$_3$Tb(**5**)$_3$Dy(**5**)$_3$ 1:1:10 mixture	1.02
Eu(**5**)$_3$Tb(**5**)$_3$Dy(**5**)$_3$Sm(**5**)$_3$ 1:1:1:1 mixture	1.08
Eu(**5**)$_3$Tb(**5**)$_3$Dy(**5**)$_3$Sm(**5**)$_3$ 1:1:10:10 mixture	1.02
Eu(**5**)$_3$Tb(**5**)$_3$Dy(**5**)$_3$Sm(**5**)$_3$ 1:1:10:50 mixture	1.05
Eu(**5**)$_3$:Tb(**5**)$_3$	1.07 (1^{st+}) & 1.16 (2nd)
Eu(**5**)$_3$:Dy(**5**)$_3$	1.01 (1^{st+}) & 1.03(2nd)
Eu(**5**)$_3$:Tb(**5**)$_3$:Dy(**5**)$_3$	1.04 (1^{st+}), 1.10 (2nd) & 1.05 (3rd)

8.2.5.2 Langmuir Blodgett Deposition

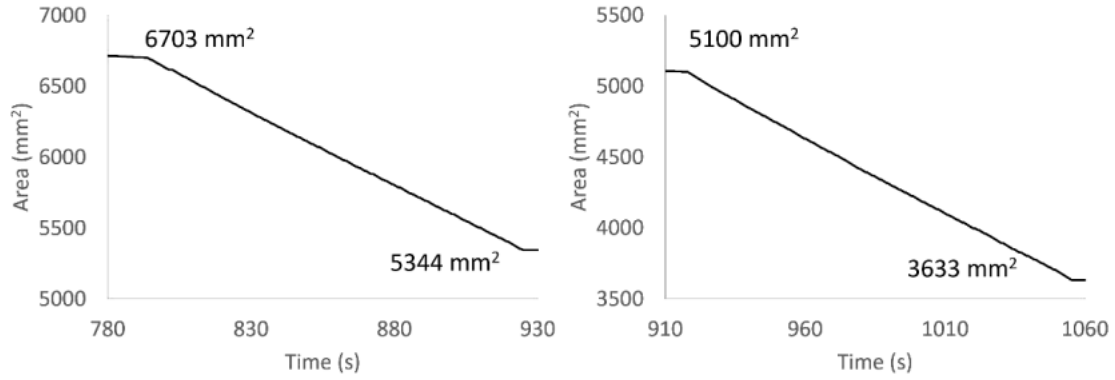

*Figure 8.2.42.. Zoomed in deposition plots of mixed multilayer Eu(**5**)₃:Tb(**5**)₃ (1:1) film.. Initial Eu(**5**)₃ (Left) and final Tb(**5**)₃ layer (Right)..*

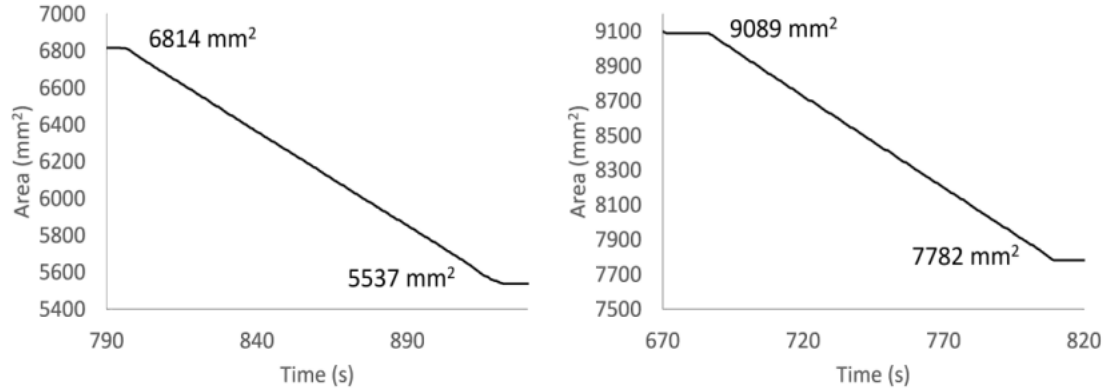

*Figure 8.2.43.. Zoomed in deposition plots of mixed multilayer Eu(**5**)₃:Dy(**5**)₃ (1:1) film.. Initial Eu(**5**)₃ (Left) and final Dy(**5**)₃ layer (Right)..*

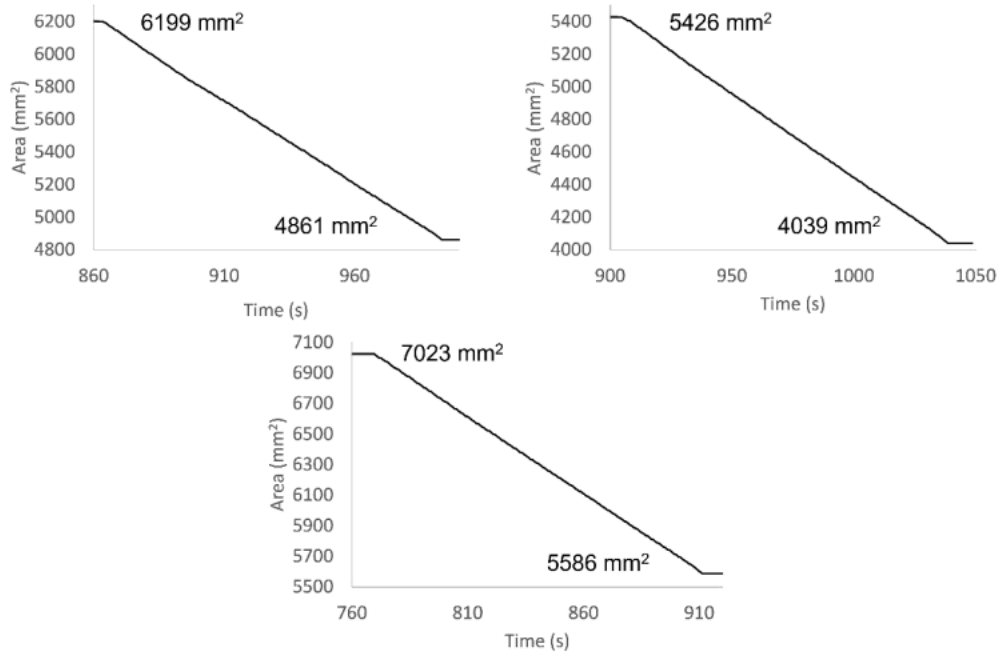

*Figure 8.2.44.. Zoomed in deposition plots of mixed multilayer Eu(**5**)₃:Tb(**5**)₃:Dy(**5**)₃ (1:1:1) film.. Initial Eu(**5**)₃ layer (. Top Left),. middle layer Tb(**5**)₃ (Top Right) and top layer Dy(**5**)₃ (Bottom)..*

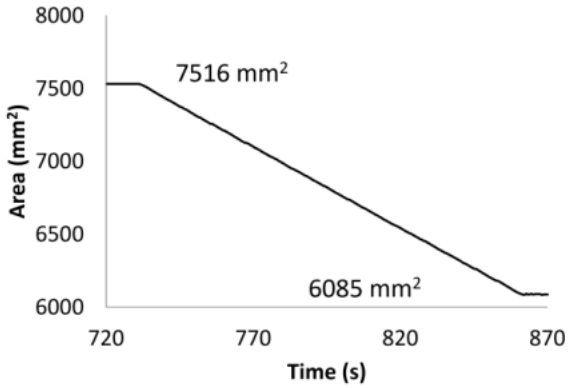

*Figure 8.2.45.. Zoomed in deposition plot of mixed multilayer Eu(**5**)$_3$:Tb(**5**)$_3$ (1:1) film..*

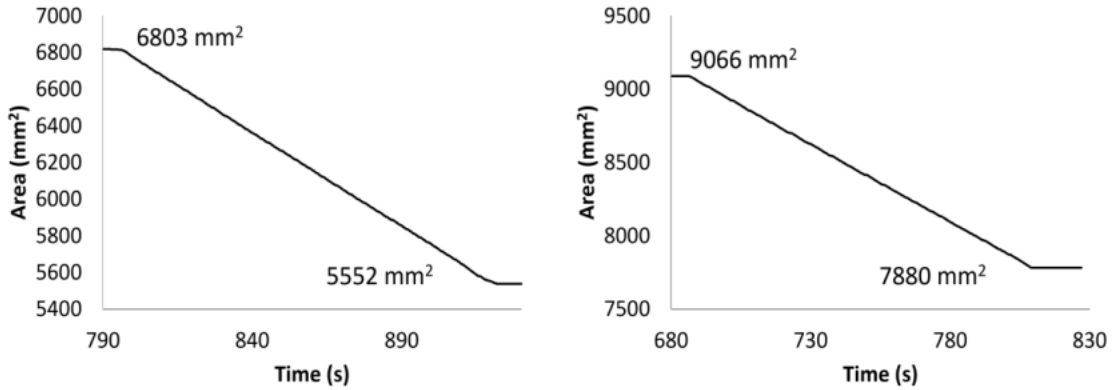

*Figure 8.2.46.. Zoomed in deposition plots of monolayer Eu(**5**)$_3$:Dy(**5**)$_3$ (1:1) (Right) and (Left) Eu(**5**)$_3$:Dy(**5**)$_3$ (1:10) films..*

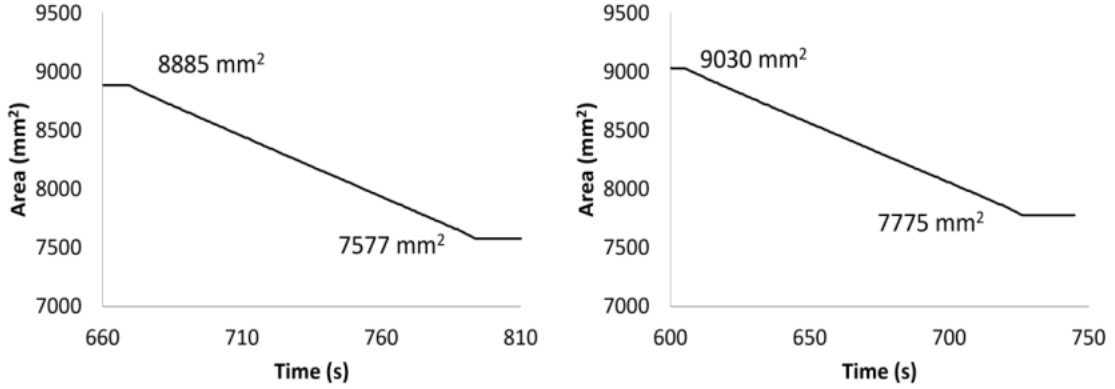

*Figure 8.2.47.. Zoomed in deposition plots of monolayer Eu(**5**)$_3$:Tb(**5**)$_3$:Dy(**5**)$_3$ (1:1:1) (Right) and (Left) Eu(**5**)$_3$:Tb(**5**)$_3$:Dy(**5**)$_3$ (1:1:10) films.*

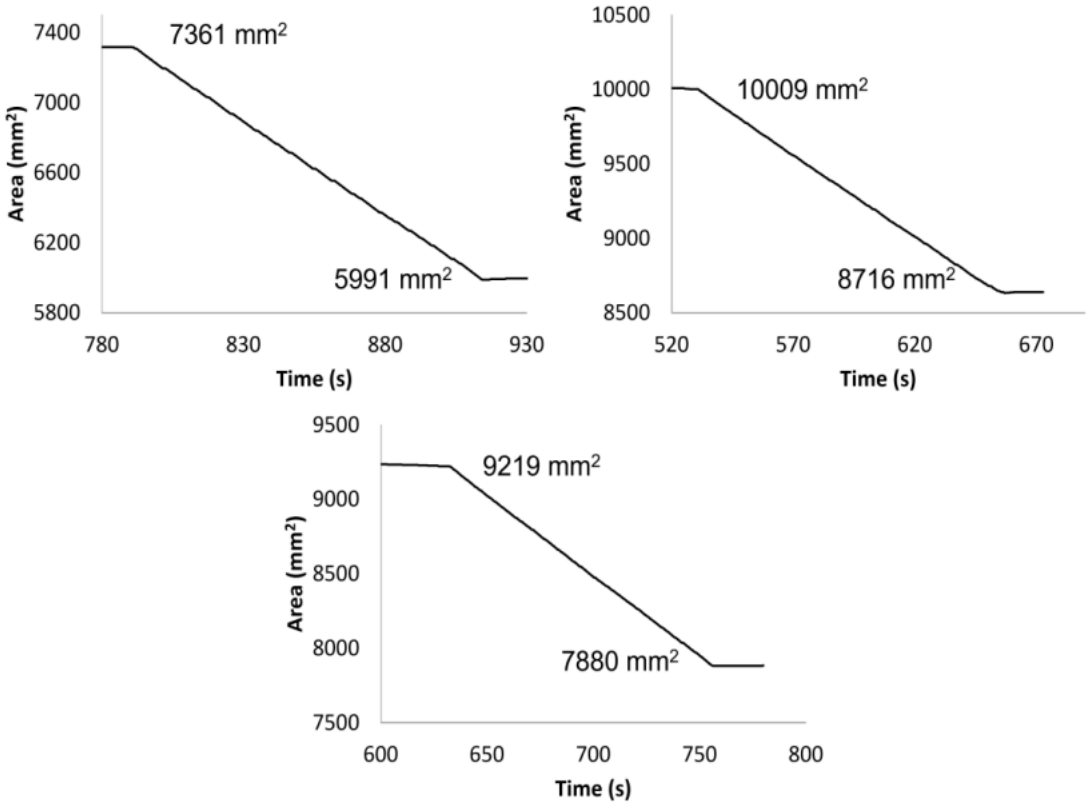

*Figure 8.2.48.. Zoomed in deposition plots of mixed multilayer Eu(**5**)$_3$:Tb(**5**)$_3$:Dy(**5**)$_3$:Sm(**5**) (1:1:1:1) (Top left),. Eu(**5**)$_3$:Tb(**5**)$_3$:Dy(**5**)$_3$:Sm(**5**) (1:1:10:10) (Top right) and Eu(**5**)$_3$:Tb(**5**)$_3$:Dy(**5**)$_3$:Sm(**5**)$_3$ (1:1:10:50) (Bottom) films..*

8.2.6 Lanthanide Photophysics LB film and Solutions

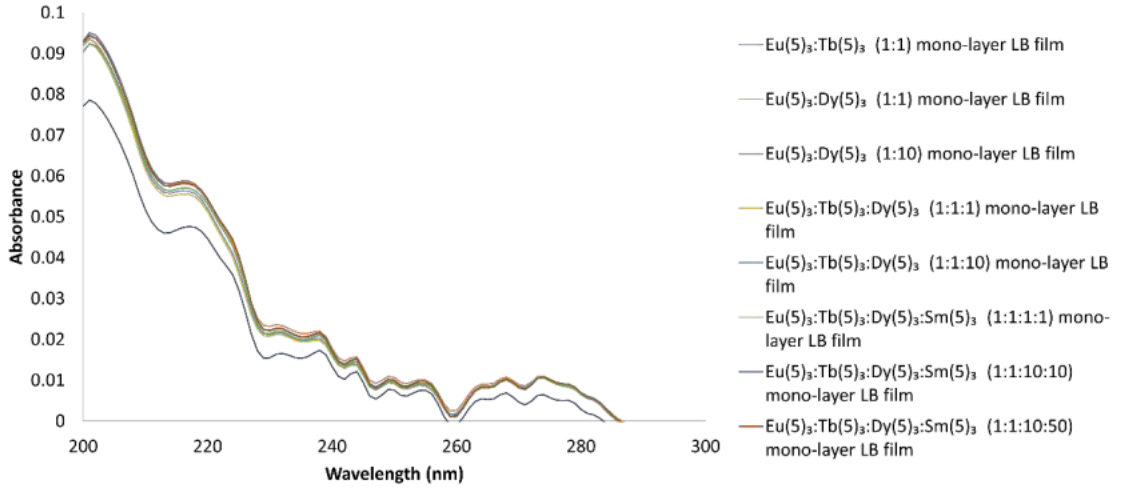

Figure 8.2.49.. UV-visible absorption of mixed monolayer LB films.

8.2.6.1 Single Lanthanide Systems

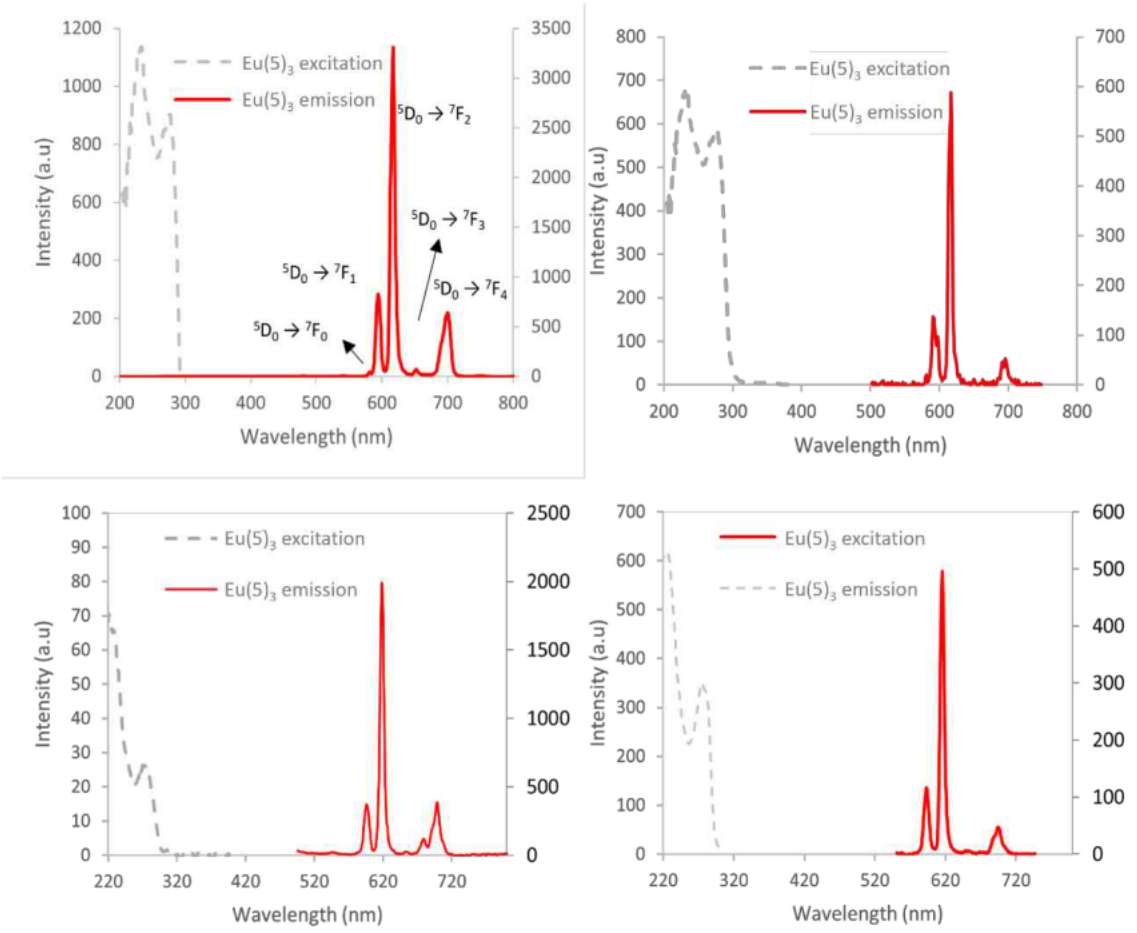

Figure 8.2.50.. (Top, left) *Fluorescence emission* and excitation spectra (monitoring 616 nm) of Eu(**5**)$_3$ (0.01 mM, MeCN). (Top, right). *Phosphorescence emission* and excitation spectra (monitoring 616 nm) of Eu(**5**)$_3$ (0.01 mM, MeCN). (Bottom, left) *Fluorescence emission and excitation spectra (monitoring 616 nm) of monolayer LB film of Eu(**5**)$_3$.. (Bottom,. right). Phosphorescence emission and excitation spectra (monitoring 616 nm) of monolayer LB film of Eu(**5**)$_3$.*

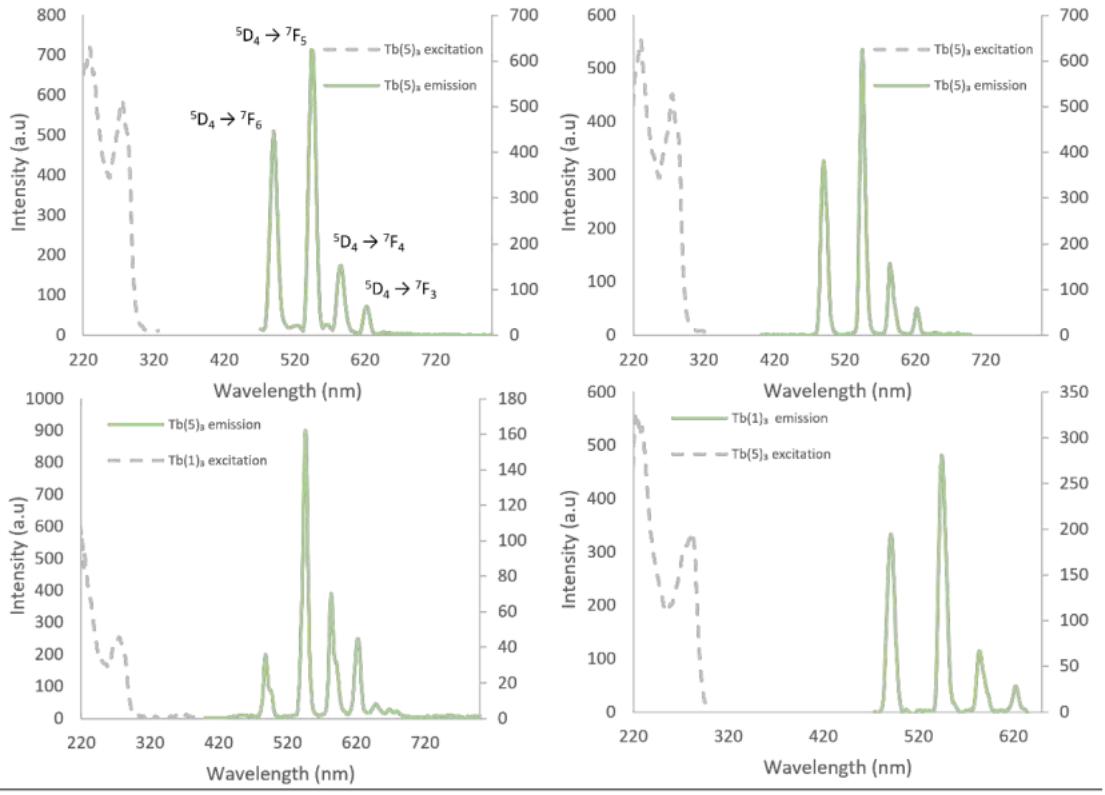

*Figure. 8.2.51.. (Top,. left). Fluorescence. emission. and. excitation. spectra. (monitoring. 545. nm). of. Tb(**5**)$_3$. (0.01. mM,. MeCN).. (Top,. right) Phosphorescence. emission. and. excitation. spectra. (monitoring. 545. nm). of. Tb(**5**)$_3$. (0.01. mM,. MeCN).. (Bottom,. left). Fluorescence emission. and. excitation. spectra. (monitoring. 545. nm). of. monolayer. LB. film. of. Tb(**5**)$_3$.. (Bottom,. right). Phosphorescence. emission. and excitation. spectra. (monitoring. 545. nm). of. monolayer. LB. film. of. Tb(**5**)$_3$..*

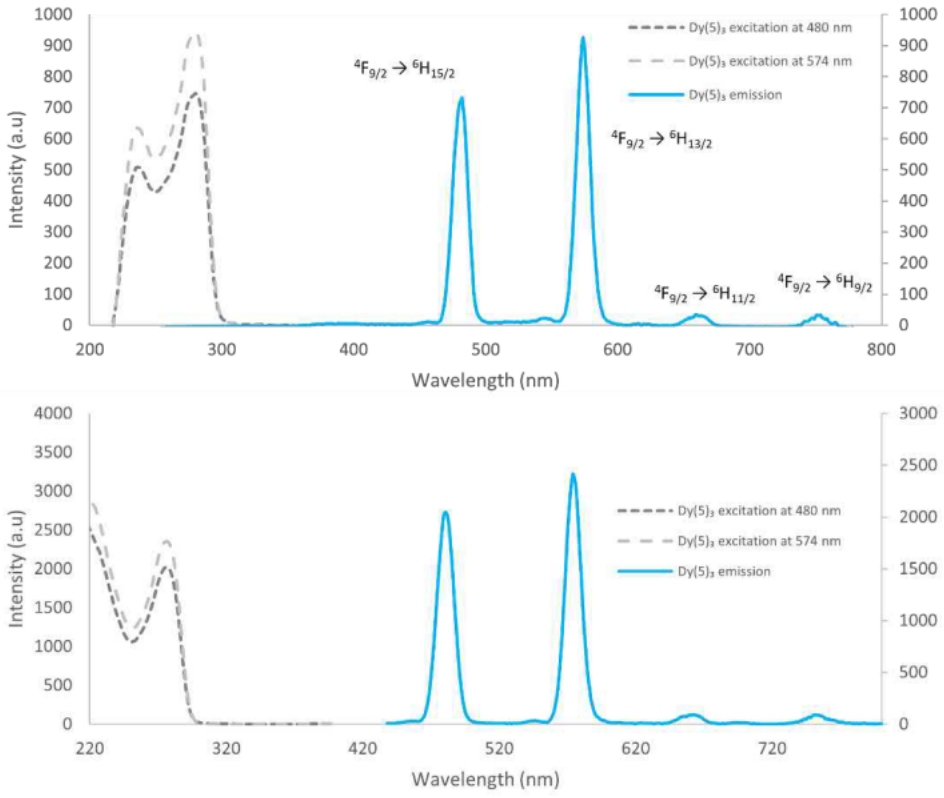

*Figure. 8.2.52.. (Top). Fluorescence. emission. and. excitation. plots. of. Dy(**5**)$_3$ (0.01. mM,. MeCN).. (Bottom). Fluorescence. emission. and excitation. plots. of. Dy(**5**)$_3$ monolayer. film..*

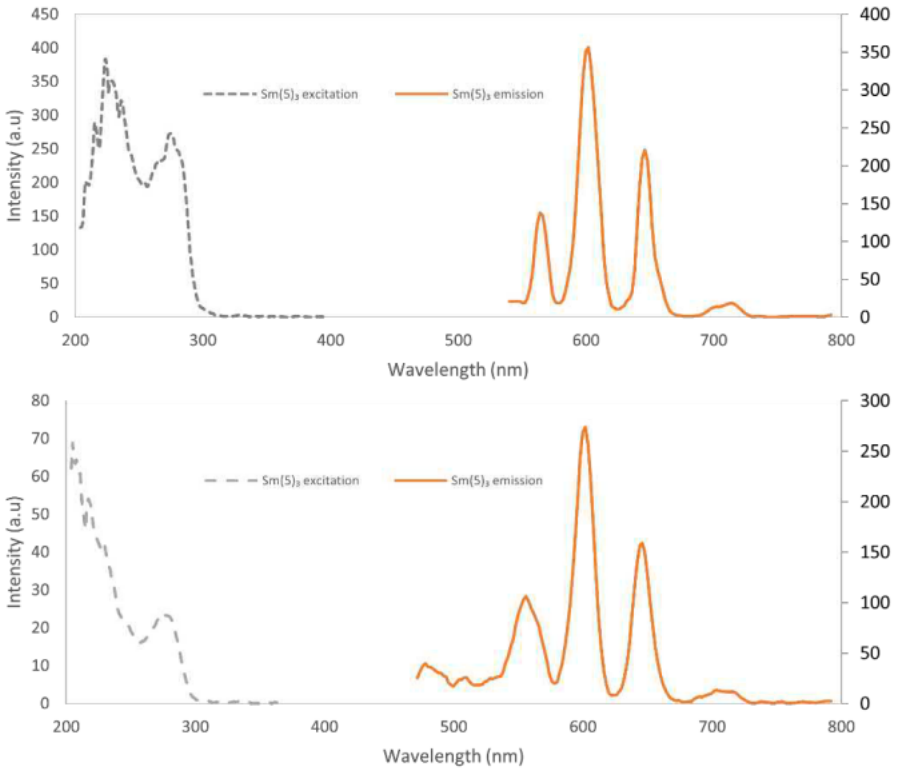

*Figure. 8.2.53.. (Top). Fluorescence. emission. and. excitation. spectra. (monitoring. 600. nm). of. Sm(**5**)₃ (0.01. mM,. MeCN).. (Bottom) Fluorescence.emission.and.excitation.spectra.(monitoring.600.nm).of.Sm(**5**)₃.monolayer.film..*

8.2.5.2 MultiLayered LB Film.

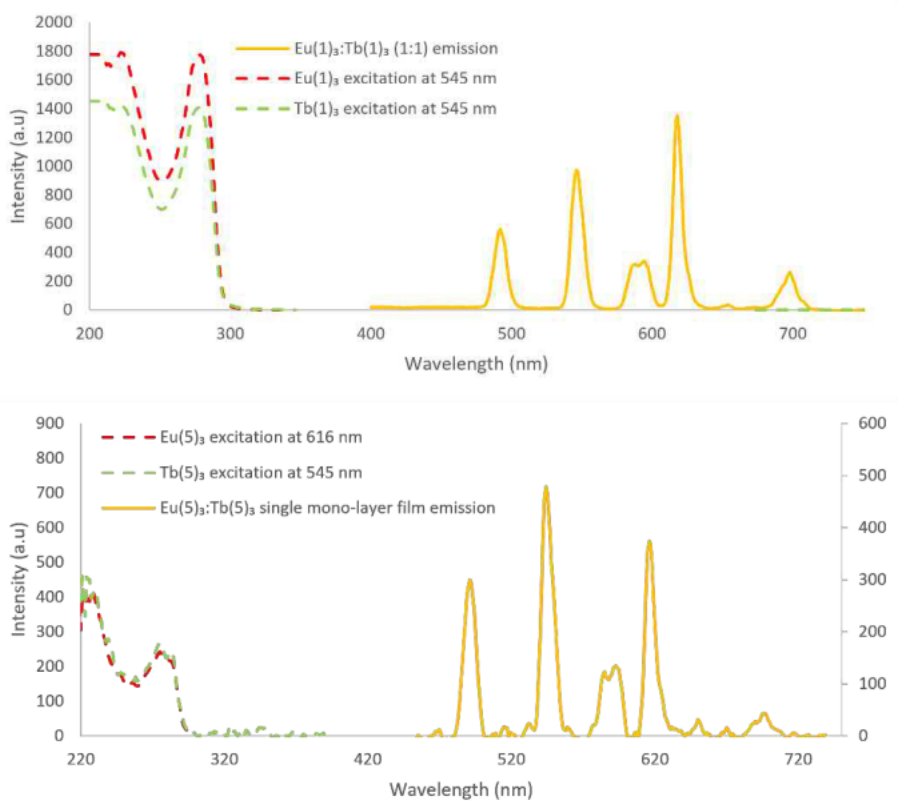

*Figure. 8.2.54.. (Top). Fluorescence. emission. and. excitation. plots. of. Eu(**5**)₃:Tb(**5**)₃ (1:1). in. monolayer. film.. (Bottom). Phosphorescence emission. and.excitation. plots. of. Eu(**5**)₃:Tb(**5**)₃ (1:1). in. monolayer. film..*

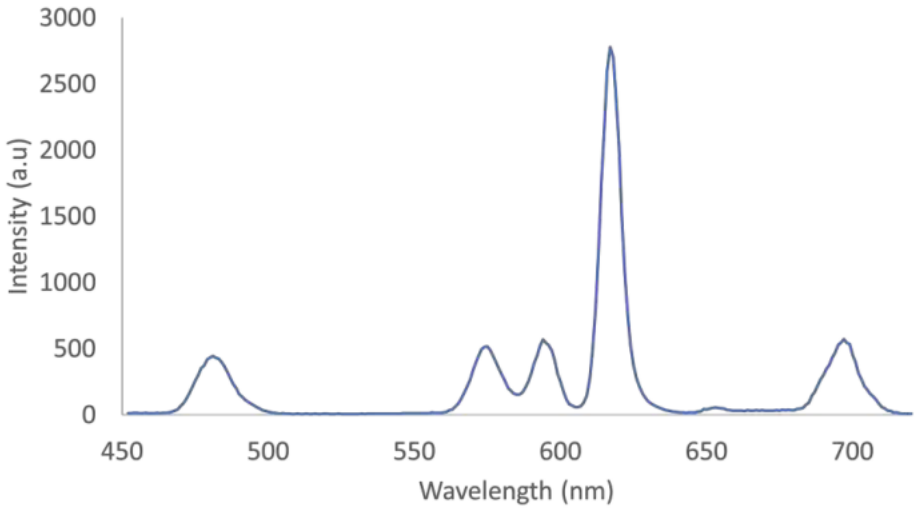

*Figure 8.2.55.. Fluorescence emission and excitation plots of Eu(**5**)$_3$:Dy(**5**)$_3$ (1:1) in monolayer film..*

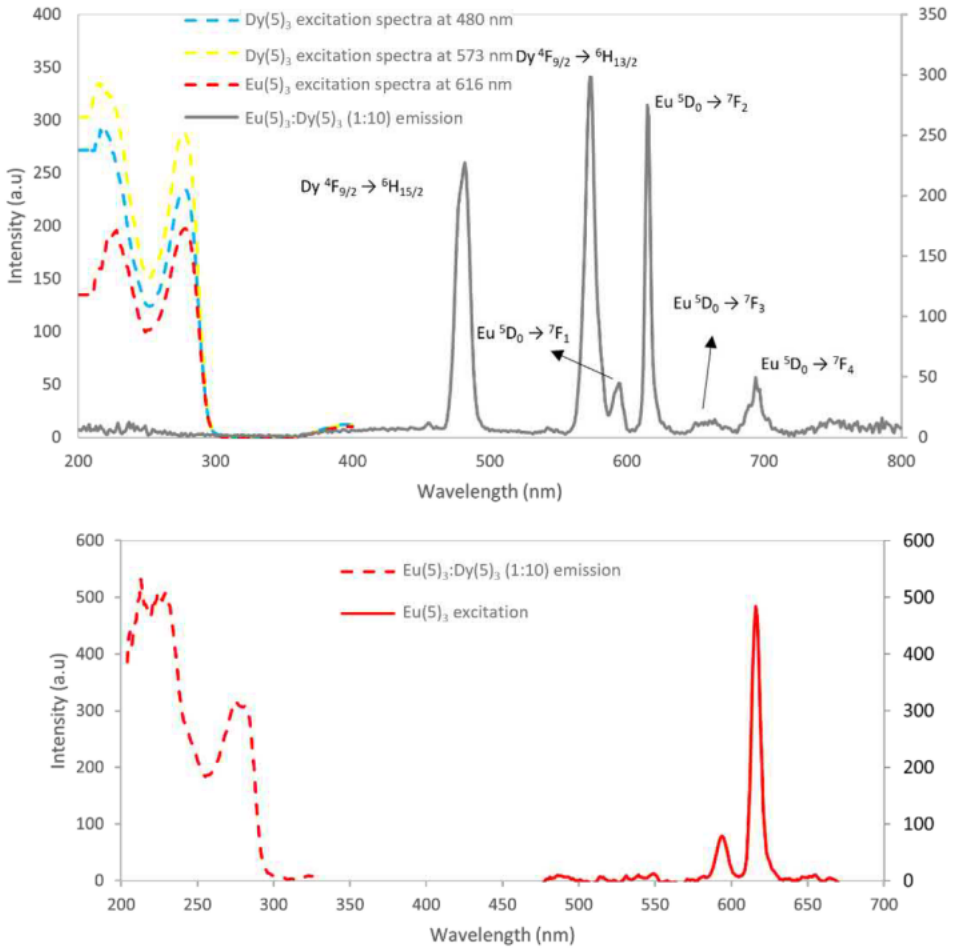

*Figure 8.2.56.. (Top) Fluorescence emission and excitation plots of Eu(**5**)$_3$:Dy(**5**)$_3$ (1:10) in a monolayer film.. (Bottom) Phosphorescence emission and excitation spectra (monitoring 616 nm) Eu(**5**)$_3$:Dy(**5**)$_3$ (1:10) in monolayer film..*

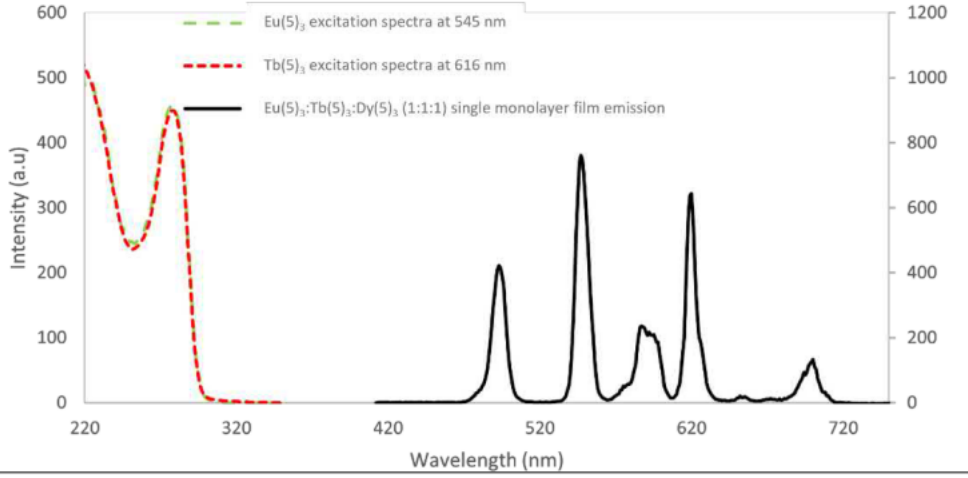

*Figure. 8.2.57.. Fluorescence. emission. and. excitation. plots. of. Eu(**5**)$_3$:Tb(**5**)$_3$:Dy(**5**)$_3$ (1:1:1). in. a. monolayer. film..*

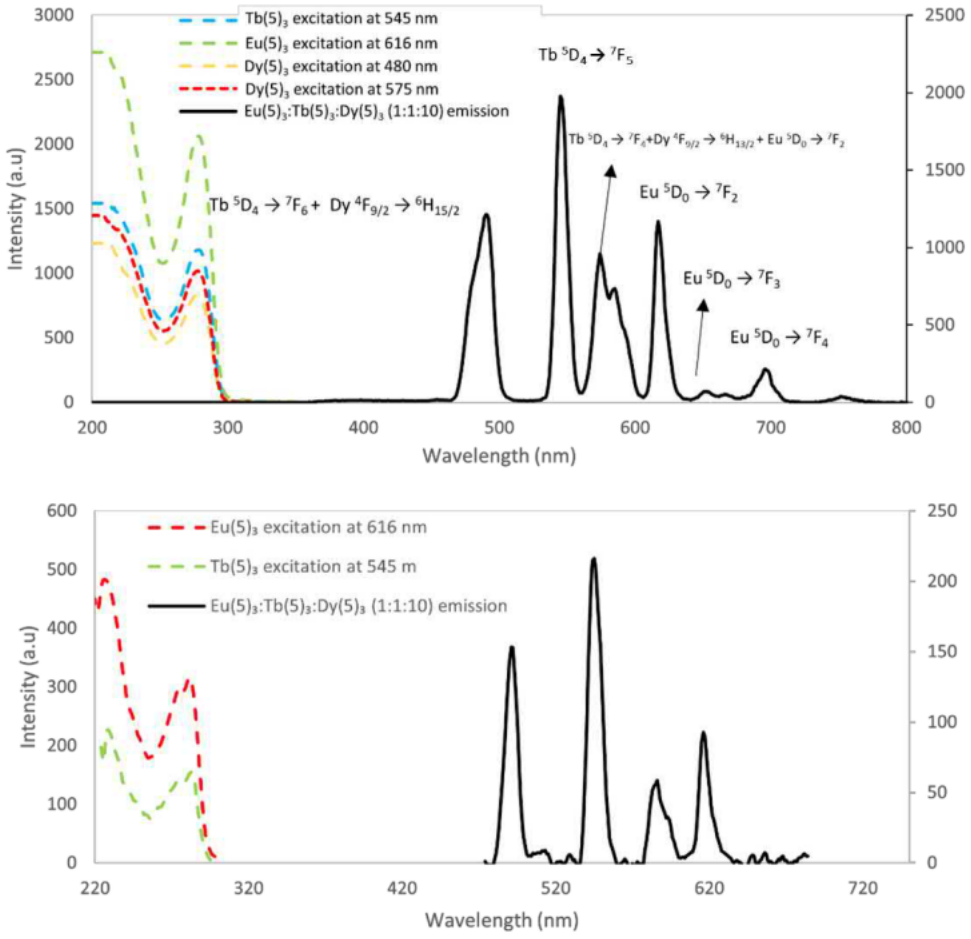

*Figure. 8.2.58.. (Top). Steady-state. emission. and. excitation. plots. of. Eu(**5**)$_3$:Tb(**5**)$_3$:Dy(**5**)$_3$ (1:1:10). in. monolayer. film.. (Bottom) Phosphorescence. emission. and. excitation. plots. Eu(**5**)$_3$:Tb(**5**)$_3$:Dy(**5**)$_3$ (1:1:10). in. monolayer. film..*

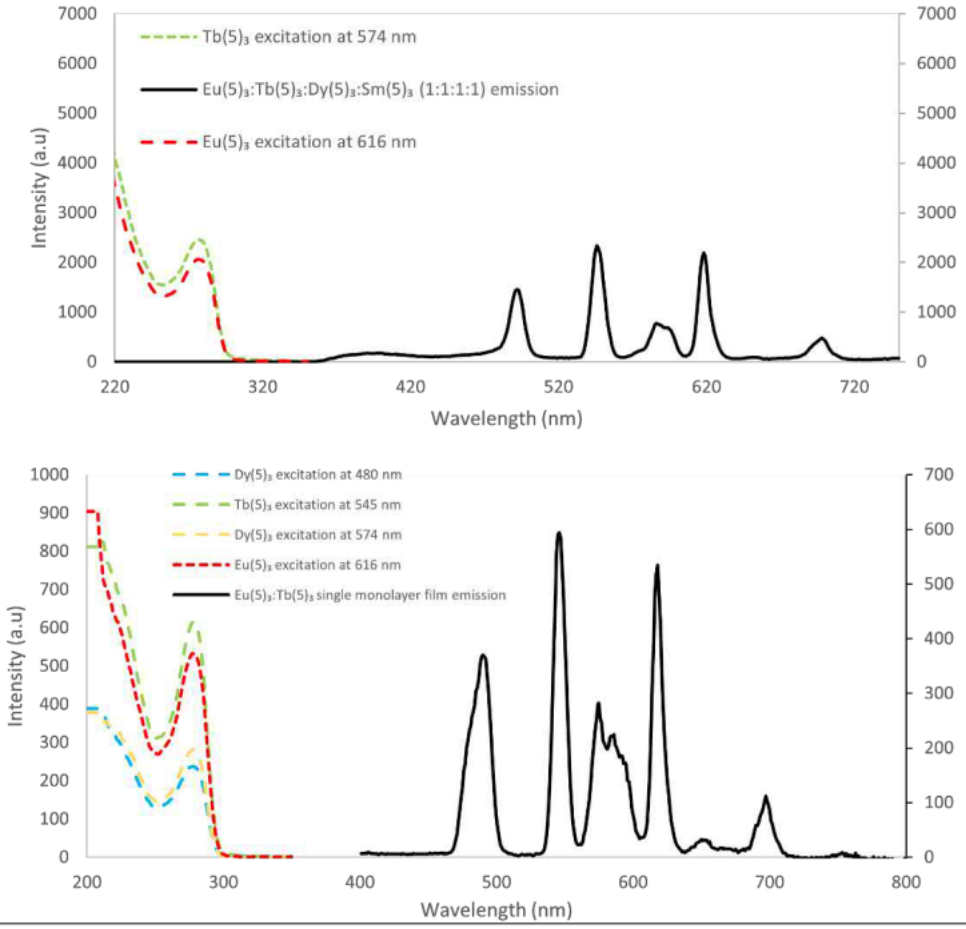

*Figure 8.2.59.. (Top). Fluorescence emission and excitation plots of Eu(**5**)₃:Tb(**5**)₃:Dy(**5**)₃Sm(**5**)₃ (1:1:1:1) in a monolayer film.. (Bottom). Fluorescence emission and excitation plots Eu(**5**)₃:Tb(**5**)₃:Dy(**5**)₃Sm(**5**)₃ (1:1:10:10) in a monolayer film..*

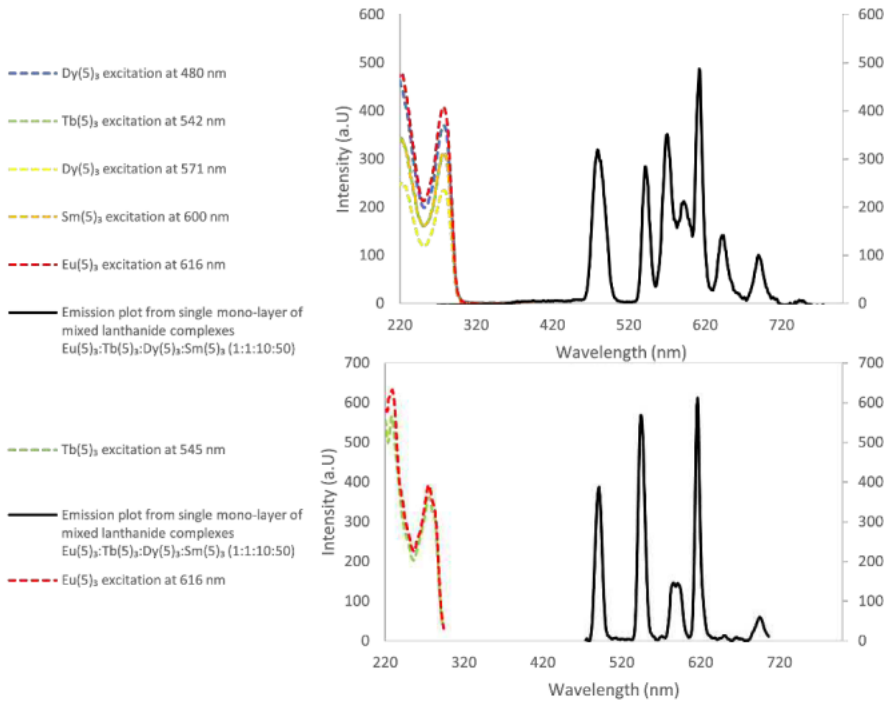

*Figure.8.2.60.. (Top). Fluorescence emission and excitation plots of Eu(**5**)₃:Tb(**5**)₃:Dy(**5**)₃Sm(**5**)₃ (1:1:10:50) in a monolayer film.. (Bottom) Phosphorescence emission and excitation plots of Eu(**5**)₃:Tb(**5**)₃:Dy(**5**)₃Sm(**5**)₃ (1:1:10:50) in a monolayer film..*

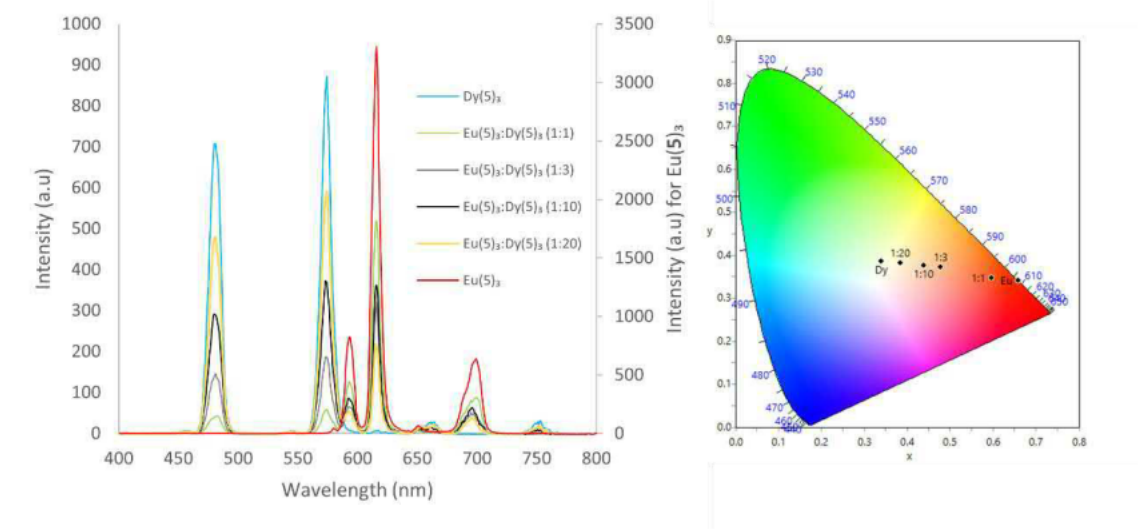

*Figure 8.2.61.. (Left) Fluorescence spectra of different ratios of Eu(**5**)$_3$:Dy(**5**)$_3$.. (Right) 1931 CIE chromaticity diagram with calculated CIE coordinates of Eu(**5**)$_3$:Dy(**5**)$_3$ ratios:. (0:1) x =. 0.33, y =. 0.38,. (1:0) x =. 0.67, y =. 0.34,. (1:1),. x=. 0.60, y =0.35,. (1:3) x =. 0.48, y=. 0.37,. (1:10) x =. 0.44, y =0.38,. and (1:20) x =0.38, y=. 0.38..*

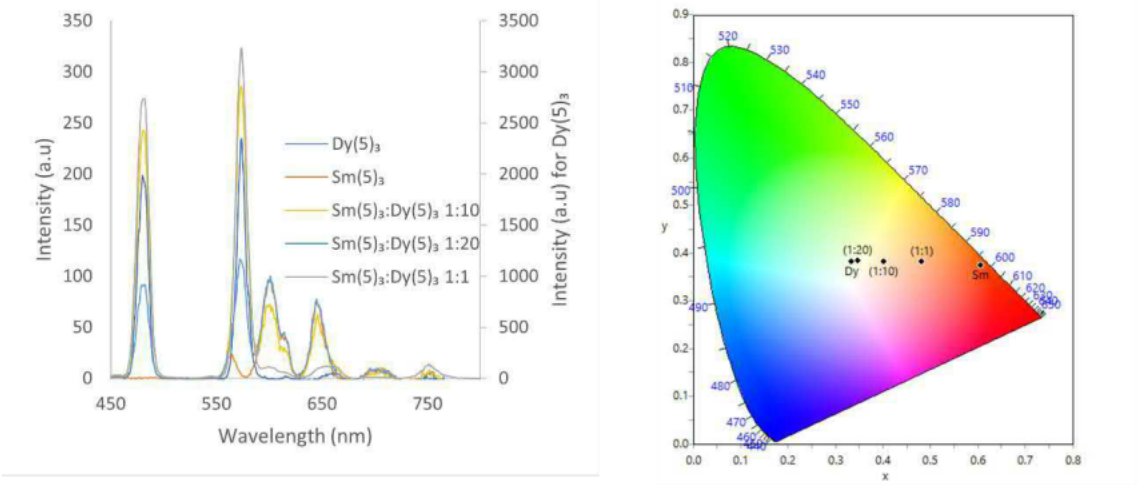

*Figure 8.2.62.. (Left) Fluorescence spectra of different ratios of Sm(**5**)$_3$:Dy(**5**)$_3$.. (Right) 1931 CIE chromaticity diagram with calculated CIE coordinates of Sm(**5**)$_3$:Dy(**5**)$_3$ ratios:. (0:1) x =. 0.33, y =. 0.38,. (1:0) x =. 0.61, y =. 0.38,. (1:1),. x=. 0.48, y =0.48,. (1:10) x =. 0.40 y=. 0.38,. and (1:20) x =0.35, y=. 0.38..*

8.2.6.3 Multilayered $Eu(5)_3$ Langmuir Blodgett Films

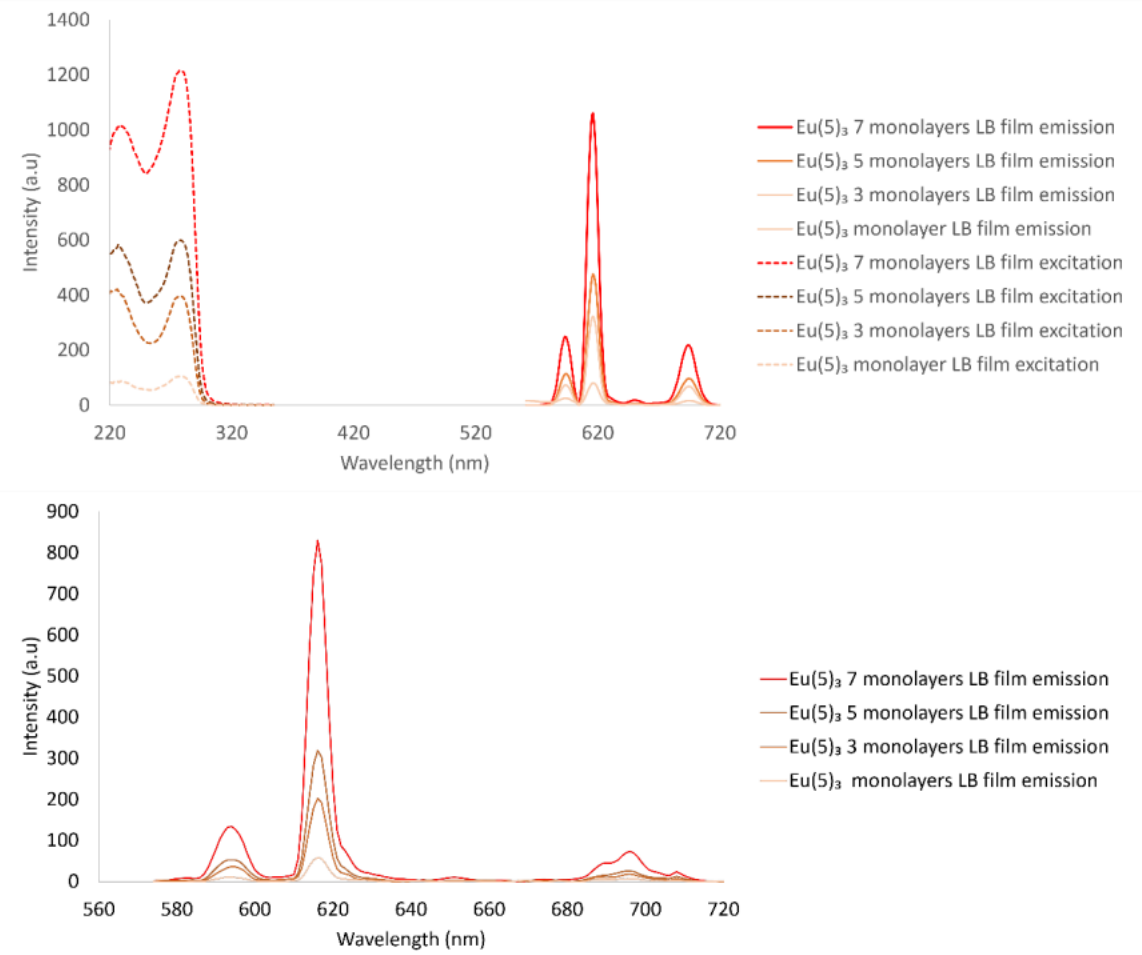

*Figure. 8.2.63.. (Top). Fluorescence. emission. and. excitation. spectra. (monitoring. 616. nm). of. Eu(**5**)₃ LB. films. with. 1,. 3,. 5. and. 7. layers.. (Bottom). Phosphorescence. emission. plots. of. Eu(**5**)₃ LB. films. with. 1,. 3,. 5. and. 7. layers..*

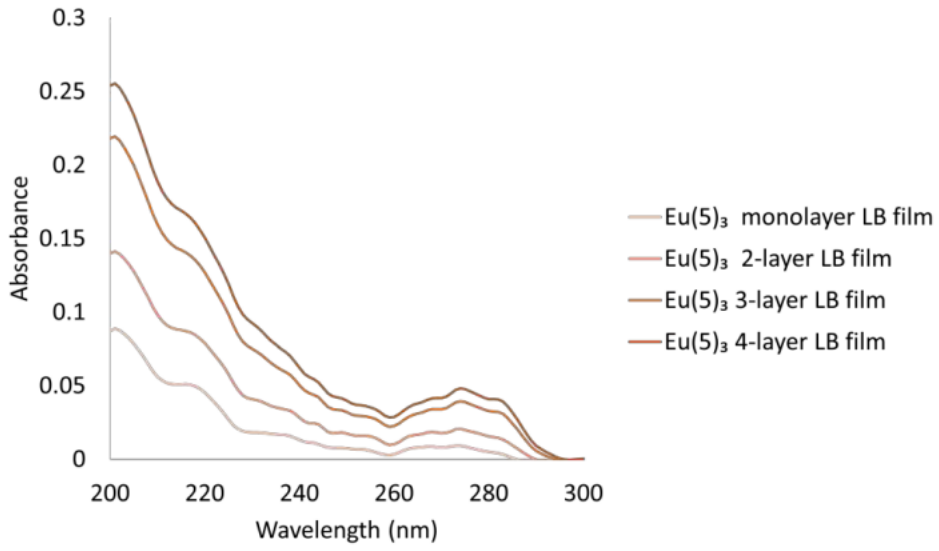

*Figure. 8.2.64.. UV-visible. absorption. Eu(**5**)₃ of. LB. films. with. increasing. layers..*

FT-IR

FT-IR measurements were taken on a multi-layered LB film (specifically an 8 layered film) of Eu(**5**)$_3$ deposited on a CaF_2 slide which was pre-washed by sonicating in $(CH_3)_2CO$, MeOH and finally with type 1 water.

*Table 8.2.3. IR stretch difference of solid ligand and Eu(**5**)$_3$ complex compared to on the CaF_2 slide.*

IR stretch	Solid 5	Solid Eu(5)$_3$	Film Eu(5)$_3$
CH_2	2919 and 2849 cm^{-1}	2919 and 2849 cm^{-1}	2945, 2918 and 2850 cm^{-1}
C=O	1744 and 1668 cm^{-1}	1640-1625 cm^{-1}	1638 cm^{-1}

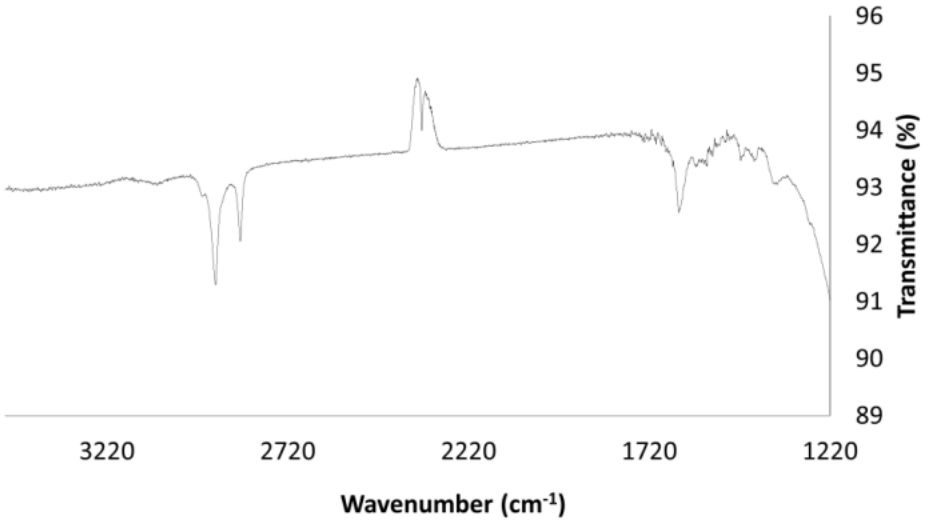

*Figure 8.2.65. IR spectra of Eu(**5**)$_3$ on a CaF_2 slide with 8 layers.*

8.2.6.4 Lifetimes

*Table 8.2.4. Single lifetimes of Eu(**5**)$_3$ and Tb(**5**)$_3$ complexes in solutions (0.01 mmol).*

Complex	Single Exponential	Average (ms)
Eu(**5**)$_3$ solution MeOH ($^5D_0 \rightarrow {}^7F_2$)	1.522	1.505
	1.512	
	1.481	
Eu(**5**)$_3$ solution MeOH ($^5D_0 \rightarrow {}^7F_1$)	1.426	1.442
	1.427	
	1.473	
Eu(**5**)$_3$ solution MeCN ($^5D_0 \rightarrow {}^7F_2$)	1.996	1.960
	1.936	
	1.947	
Eu(**5**)$_3$ solution MeCN ($^5D_0 \rightarrow {}^7F_1$)	1.899	1.888
	1.880	
	1.885	
Tb(**5**)$_3$ solution MeCN ($^5D_4 \rightarrow {}^7F_5$)	0.980	0.984
	0.988	
	0.983	

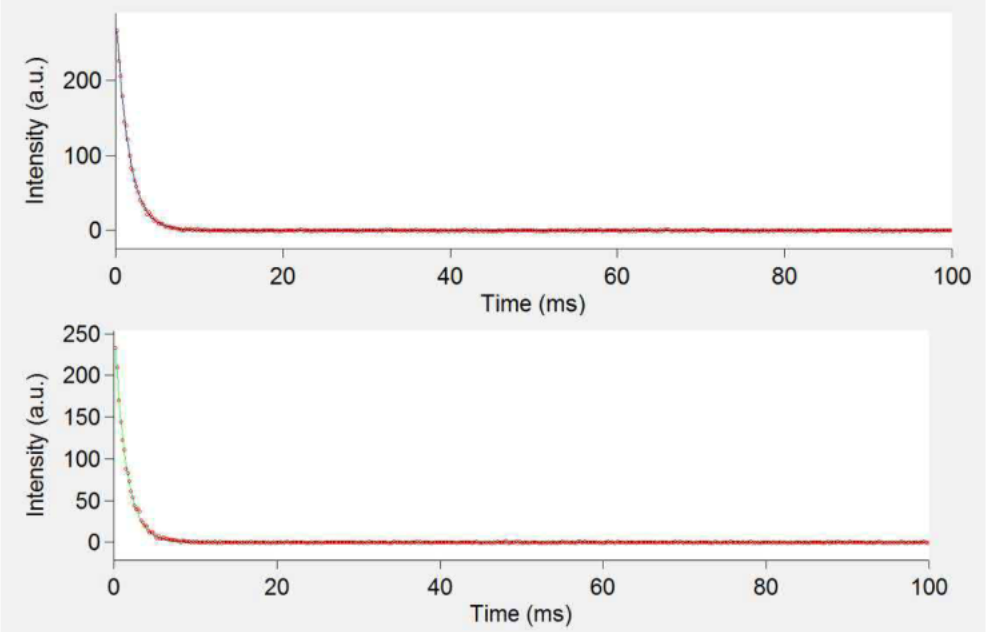

*Figure 8.2.66.. Lifetime of Eu(**5**)$_3$ complex in a solution of 0.01 mmol MeOH fit with a single exponential (Top) 616 nm and (Bottom) 594 nm..*

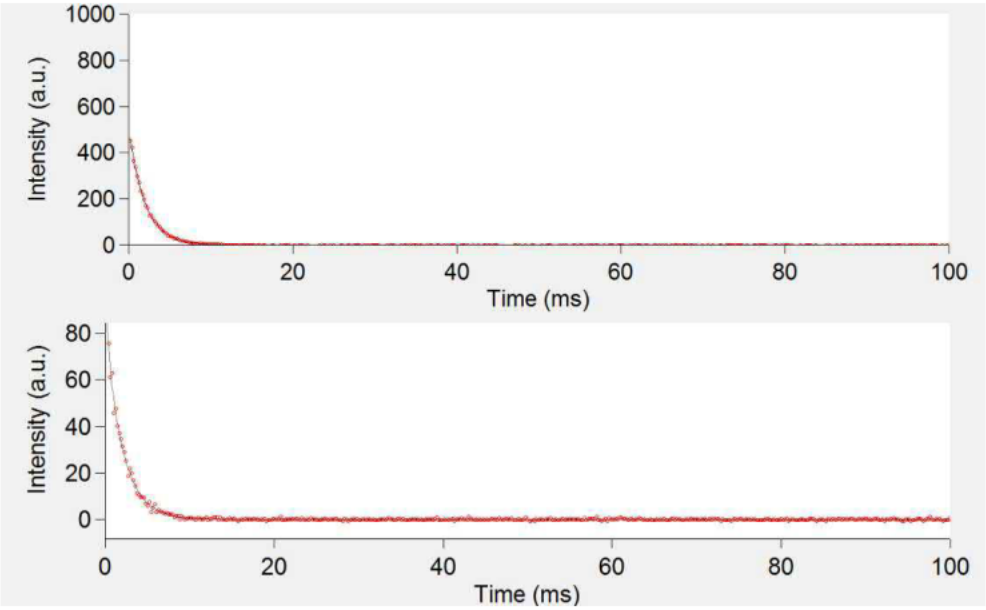

*Figure 8.2.67.. Lifetime of Eu(**5**)$_3$ complex in a solution of 0.01 mmol MeCN fit with single exponential (Top) 616 nm and (Bottom) 594 nm..*

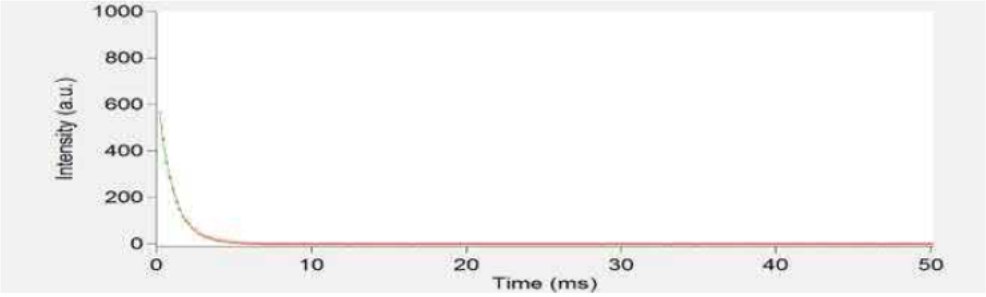

*Figure 8.2.68.. Lifetime of Tb(**5**)$_3$ complex in a solution of 0.01 mmol MeCN fit with single exponential (545 nm)..*

*Table. 8.2.5.. Single. and. double. exponential. lifetimes. of. Eu(**5**)$_3$ and. Tb(**5**)$_3$ complexes. on. LB. films.. Complex. in. bold. is. the. lifetime measured..*

Films	Single Exponential	Average (ms)
Eu(**5**)$_3$ monolayer film	1.412	1.396
	1.400	
	1.376	
Eu(**5**)$_3$ 3 layer film	1.457	1.439
	1.463	
	1.397	
Eu(**5**)$_3$ 5 layer film	1.359	1.374
	1.359	
	1.403	
Eu(**5**)$_3$ 7 layer film	1.535	1.569
	1.596	
	1.576	
Tb(**5**)$_3$ monolayer film	1.527	1.552
	1.568	
	1.562	
Eu(**5**)$_3$:Tb(**5**)$_3$ (1:1) monolayer film	1.516	1.551
	1.549	
	1.587	
Eu(**5**)$_3$:**Tb**(**5**)$_3$ (1:1) monolayer film	1.366	1.387
	1.473	
	1.321	
Eu(**5**)$_3$:Dy(**5**)$_3$ (1:10) monolayer film	0.899	0.882
	0.899	
	0.849	
Eu(**5**)$_3$:Tb(**5**)$_3$:Dy(**5**)$_3$:(1:1:10) monolayer film	1.077	1.059
	1.033	
	1.068	
Eu(**5**)$_3$:**Tb**(**5**)$_3$:Dy(**5**)$_3$:(1:1:10 monolayer film	1.712	1.748
	1.817	
	1.714	
Eu(**5**)$_3$:Tb(**5**)$_3$:Dy(**5**)$_3$:Sm(**5**)$_3$ (1:1:10:50) monolayer film	1.397	1.358
	1.361	
	1.317	
Eu(**5**)$_3$:**Tb**(**5**)$_3$:Dy(**5**)$_3$:Sm(**5**)$_3$ (1:1:10:50) monolayer film	1.136	1.135
	1.105	
	1.163	

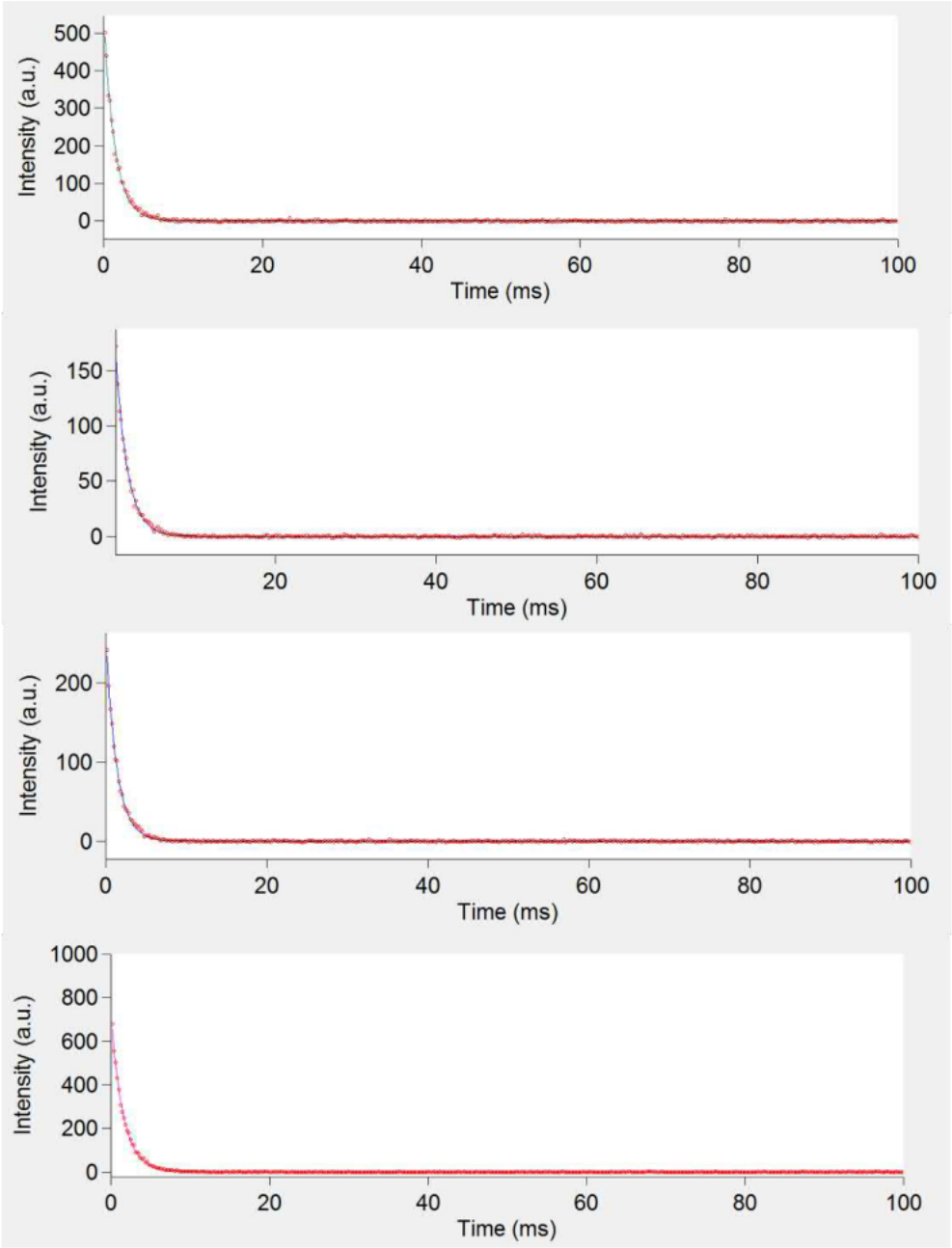

*Figure. 8.2.69.. Lifetime. of. LB. films. of. Eu(**5**)$_3$ complex.. From. top. to. bottom:. 1,. 3,. 5. and. 7. layers.. All. fit. to. a. single. exponential. and. monitoring. 616. nm. band..*

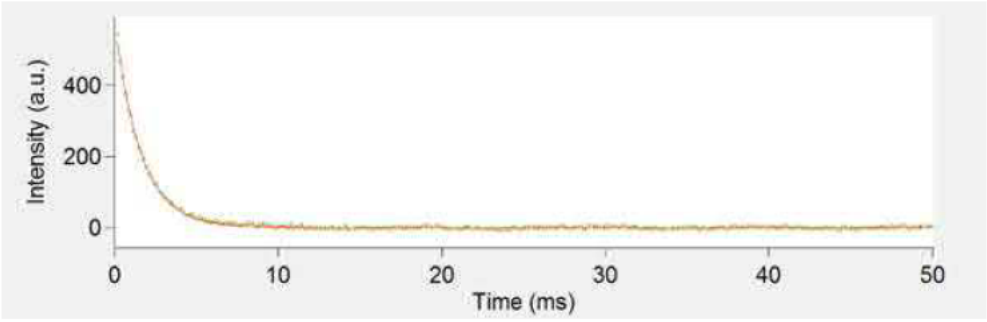

*Figure. 8.2.70.. Lifetimes. of. a. monolayer. LB. film. of. Tb(**5**)$_3$ complex,. fit. to. a. single. exponential. and. monitoring. 545. nm. band..*

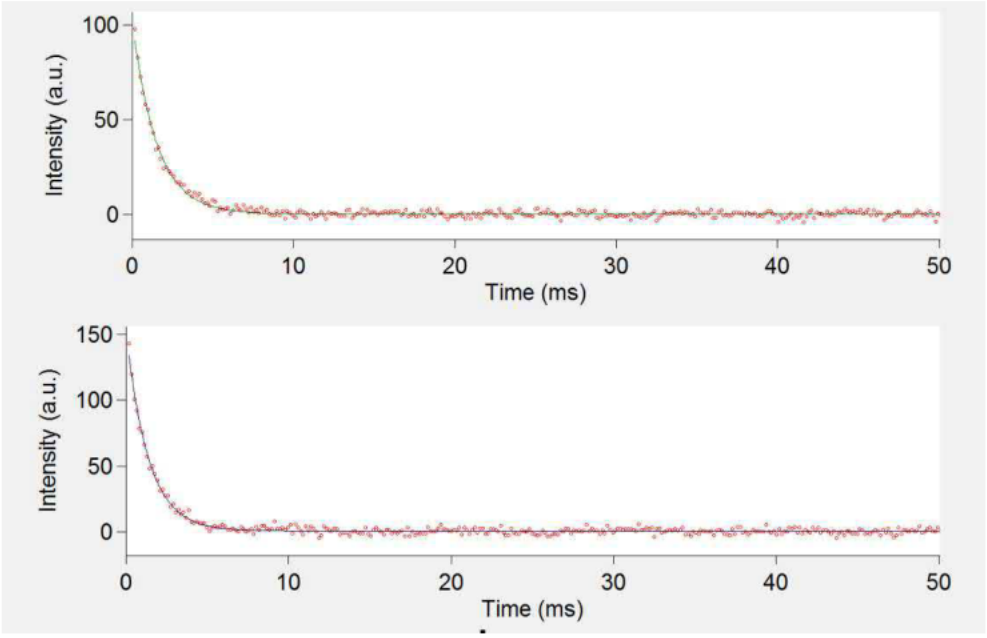

*Figure. 8.2.71.. Lifetime. of. a. monolayer. LB. film. of. Eu(**5**)$_3$:Tb(**5**)$_3$ complex,. fit. to. a. single. exponential. and. monitoring. (Top). 616. nm. and (Bottom). 545. nm. band..*

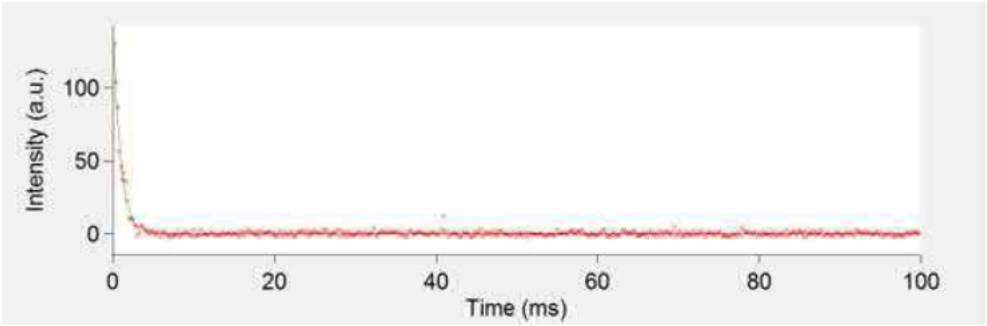

*Figure. 8.2.72.. Lifetime. of. a. monolayer. LB. film. of. Eu(**5**)$_3$Dy(**5**)$_3$ complex,. fit. to. a. single. exponential. and. monitoring. 616. nm..*

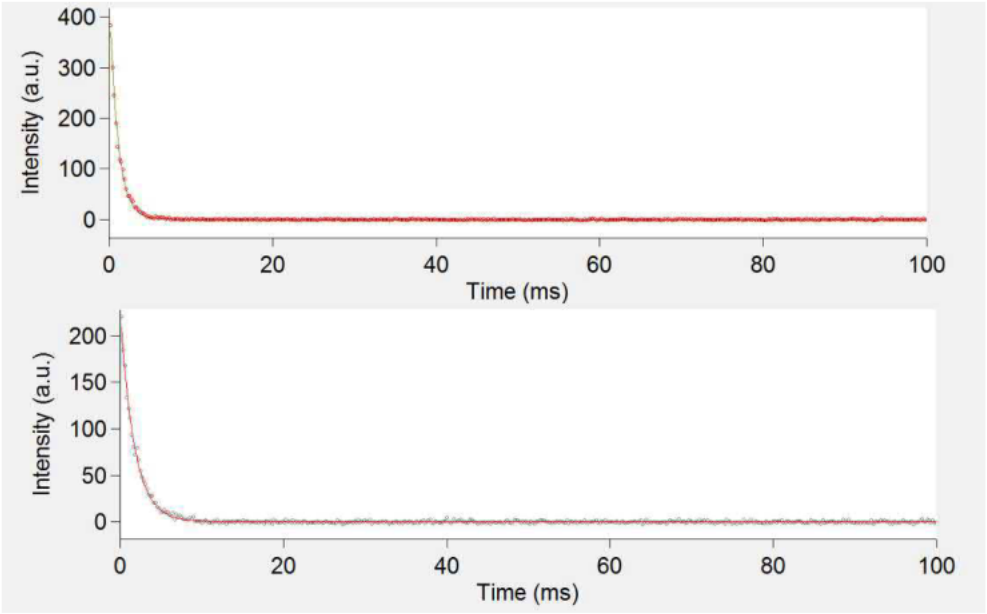

*Figure. 8.2.73.. Lifetime. of. a. monolayer. LB. film. of. Eu(**5**)$_3$:Tb(**5**)$_3$:Dy(**5**)$_3$ complex,. fit. to. a. single. exponential. and. monitoring. (Top). 616. nm and. (Bottom). 545. nm. band..*

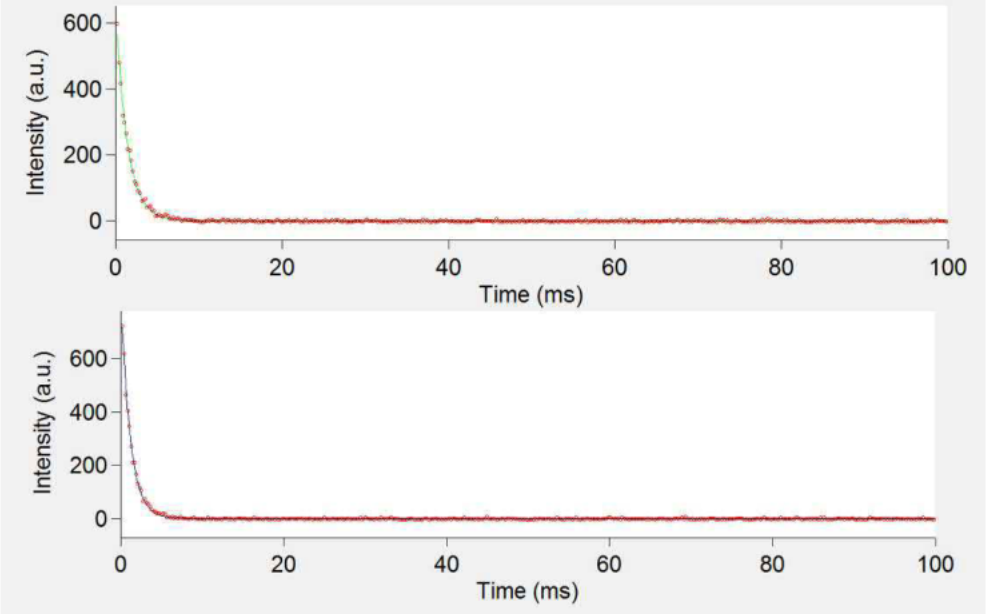

*Figure. 8.2.74.. Lifetime. of. monolayer. LB. film. of. Eu(**5**)$_3$:Tb(**5**)$_3$:Dy(**5**)$_3$:Sm(**5**)$_3$ (1:1:10:50). complex,. fit. to. a. single. exponential. and monitoring. (Yop). 616. nm. and. (Bottom). 545. nm. band..*

8.2.6.5 Quantum Yield

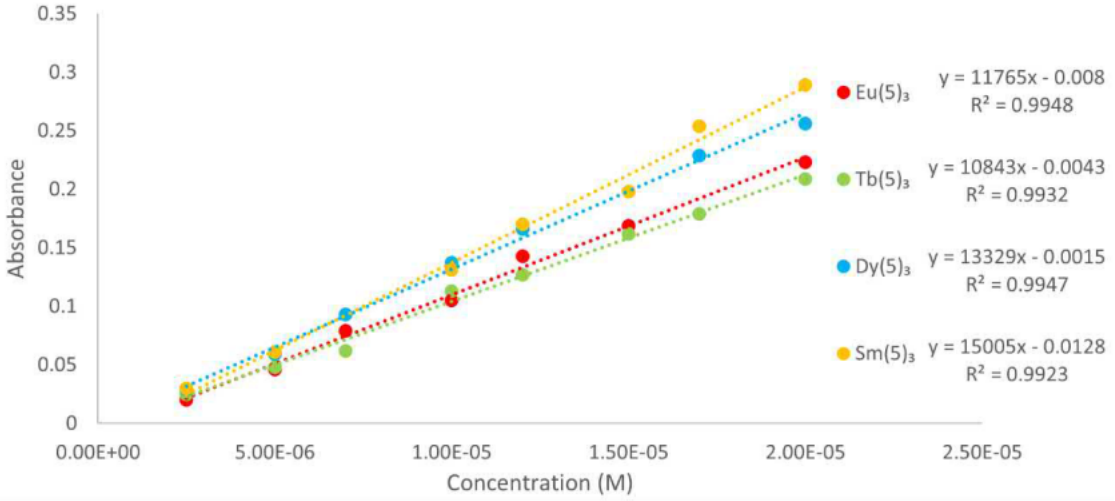

Figure. 8.2.75.. Concentration. vs. absorbance. of. lanthanide. complexes.

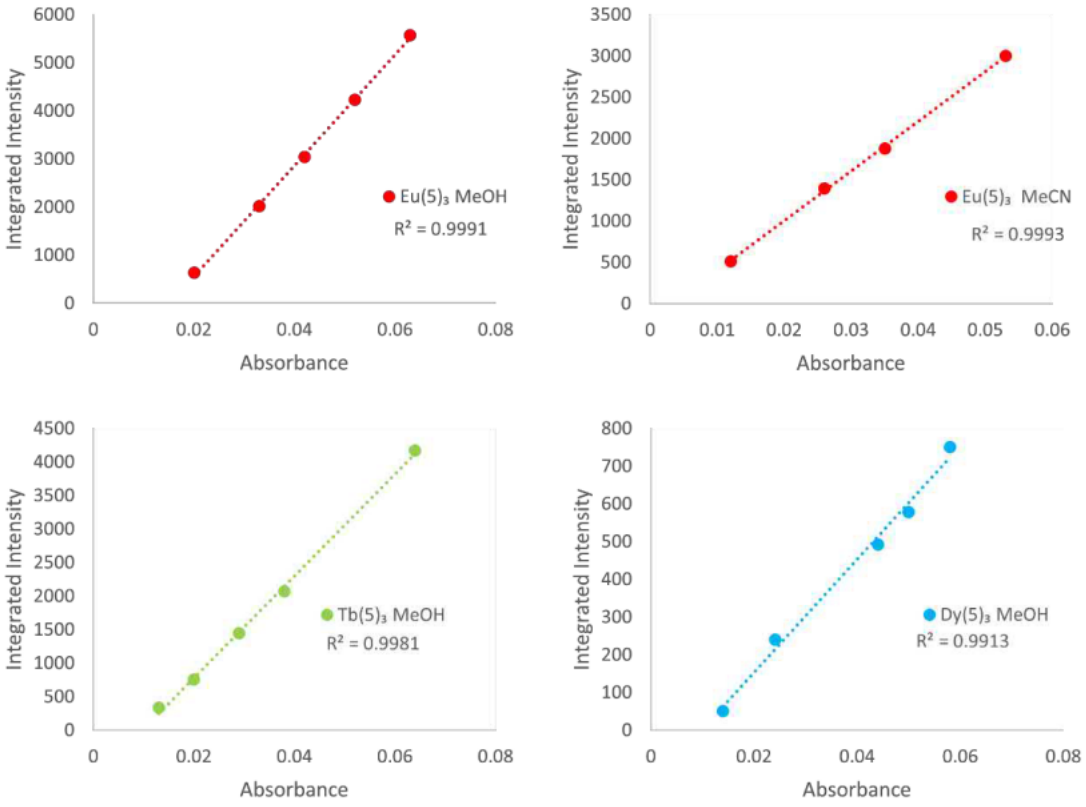

*Figure 8.2.76.. Absorbance vs. integrated intensity of lanthanide complexes in MeOH (and MeCN for Eu(**5**)₃), 1.5 and 3 nm excitation and emission widths..*

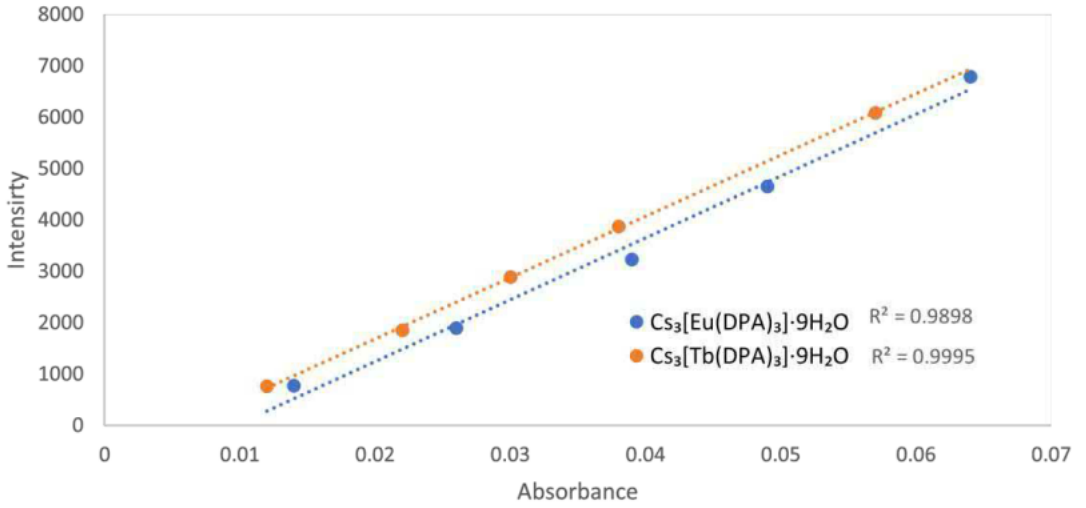

Figure 8.2.77.. Absorbance vs. integrated intensity of $Cs_3[Eu(DPA)_3]\cdot 8H_2O$ and $Cs_3[Tb(DPA)_3]\cdot 8H_2O$, 1.5 and 3 nm excitation and emission widths.

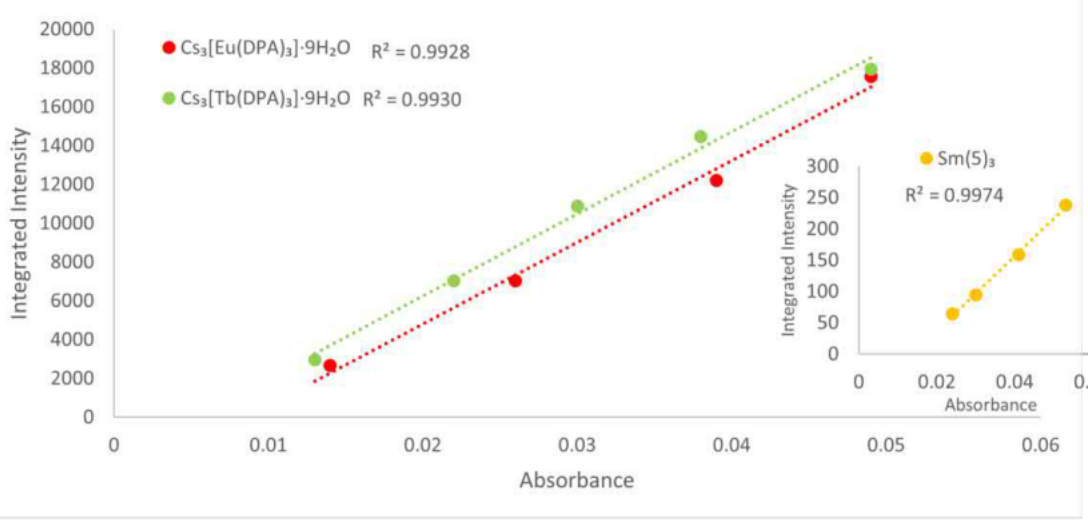

*Figure. 8.2.78.. Absorbance. vs. integrated. intensity. of. $Cs_3[Eu(DPA)_3]\cdot 8H_2O$. and. $Cs_3[Tb(DPA)_3]\cdot 8H_2O$,. 3. and. 3. nm. excitation. and. emission widths.. Insert. :. Absorbance. vs. integrated. intensity. of. Sm(**5**)$_3$..*

8.2.7 X-Ray Photoelectron Spectroscopy (XPS)

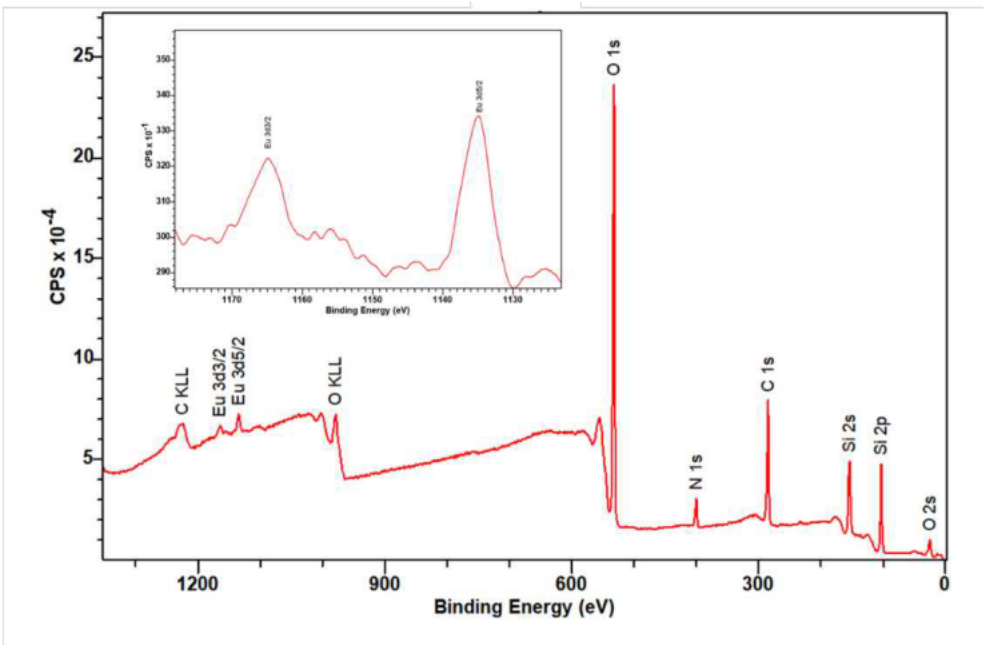

*Figure. 8.2.79.. Survey. scan. XPS. spectrum. of. Eu(**5**)$_3$ monolayer. LB. film.. Insert:. Enclosed. window. scan. of. Eu^{3+}. 3d. peaks. (a. total. of. 20 scans). with. Eu^{3+}. $3d_{3/2}$ =. 1135. and. $3d_{5/2}$ =. 1165. eV,. expected. being. 1166. and. 1135. eV. respectively..*

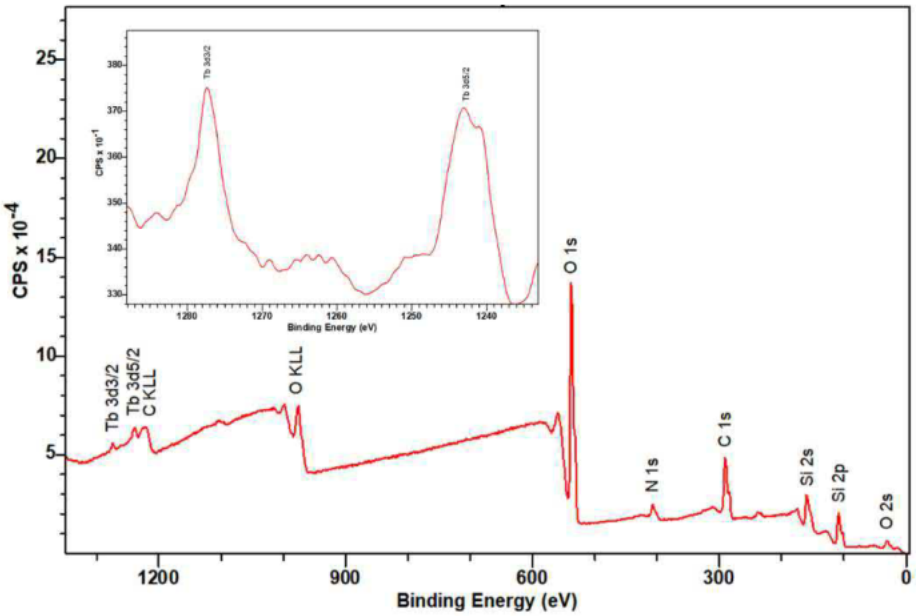

*Figure. 8.2.80.. Survey. scan. XPS. spectrum. of. Tb(**5**)$_3$. monolayer. LB. film.. Insert:. Enclosed. window. scan. of. Tb^{3+}. 3d. peaks. (a. total. of. 20. scans) with. Tb^{3+} $3d_{3/2}$ =. 1177. and. $3d_{5/2}$ =. 1142. eV,. expected. being. 1176. and. 1141. eV. respectively..*

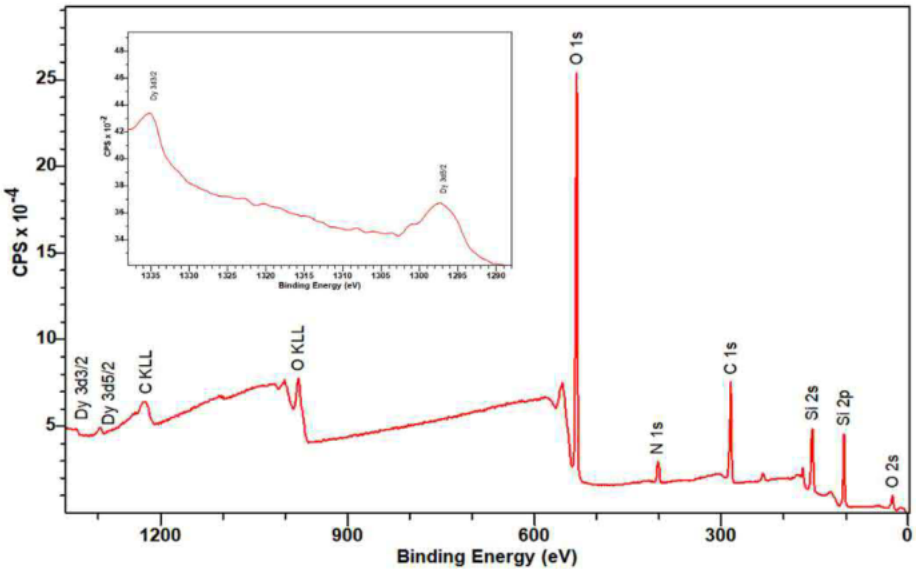

*Figure. 8.2.81.. Survey. scan. XPS. spectrum. of. Dy(**5**)$_3$. monolayer. LB. film.. Insert:. Enclosed. window. scan. of. Dy^{3+}. 3d. peaks. (a. total. of. 20 scans). with. Dy^{3+}. $3d_{3/2}$ =. 1334. and. $3d_{5/2}$ = 1297. eV,. expected. being. 1333. and. 1296. eV. respectively..*

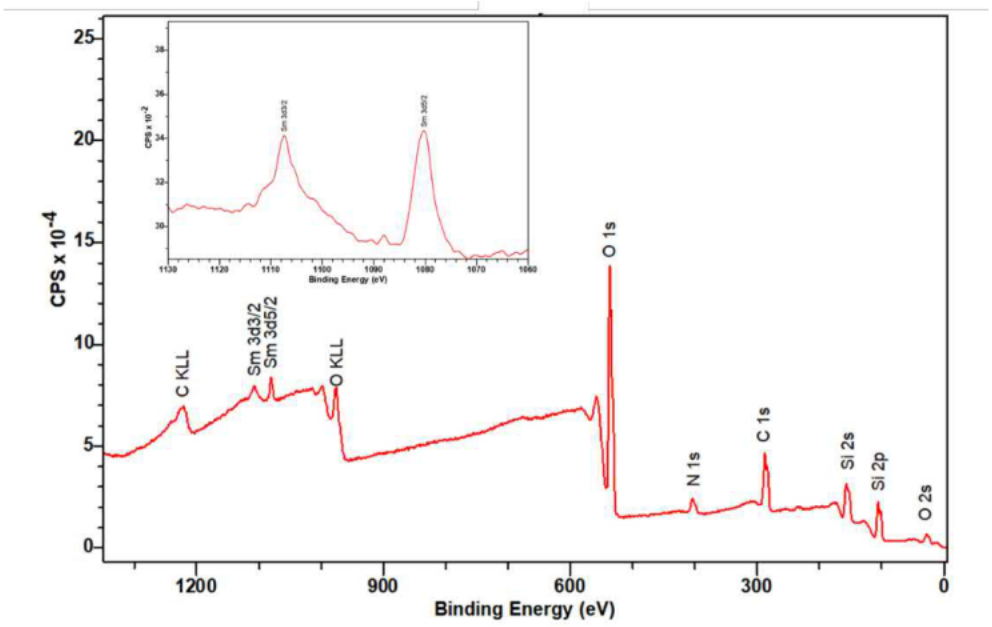

*Figure. 8.2.82.. Survey. scan. XPS. spectrum. of. Sm(**5**)$_3$ monolayer. LB. film.. Insert:. Enclosed. window. scan. of. Sm^{3+}. 3d. peaks. (a. total. of. 20 scans). with. Sm^{3+}. $3d_{3/2}$ =. 1107. and. $3d_{5/2}$ =. 1080. eV,. expected. being. 1108. and. 1081. eV. respectively..*

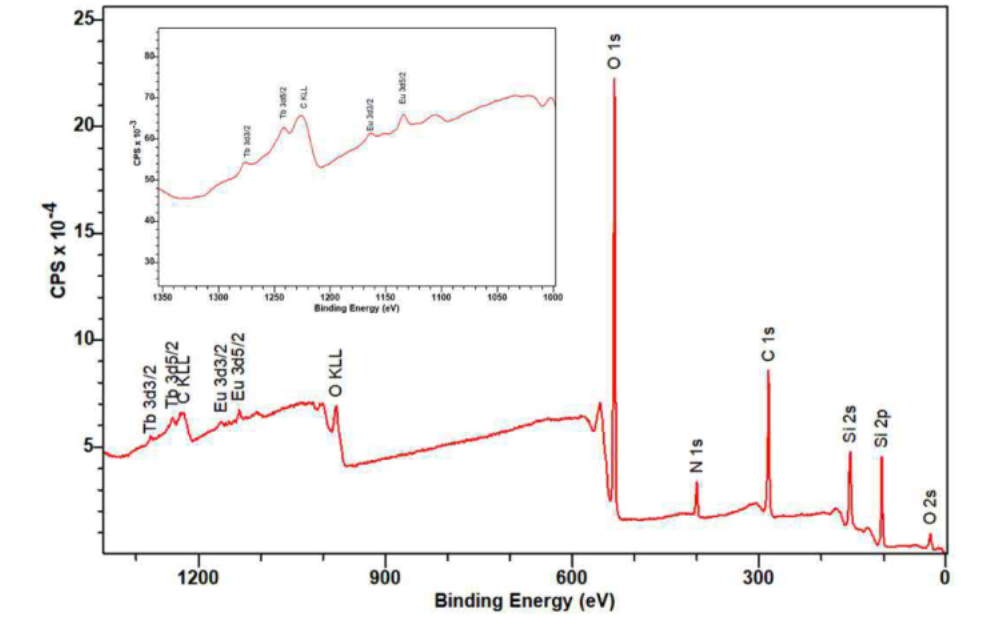

*Figure. 8.2.83.. Survey. scan. XPS. spectrum. of. Eu(**5**)$_3$:Tb(**5**)$_3$ (1:1). monolayer. LB. film.. Insert:. Smoothed. zoomed. in. survey. scan. of. Eu^{3+}. and Tb^{3+}. 3d. peaks,. with. Eu. $3d_{3/2}$ =. 1163. and. $3d_{5/2}$ =. 1135. eV,. expected. being. 1166. and. 1136. eV. respectively. and. Tb^{3+}. $3d_{3/2}$ =. 1177. and. $3d_{5/2}$ =. 1141. eV,. expected. being. 1176. and. 1141. eV. respectively..*

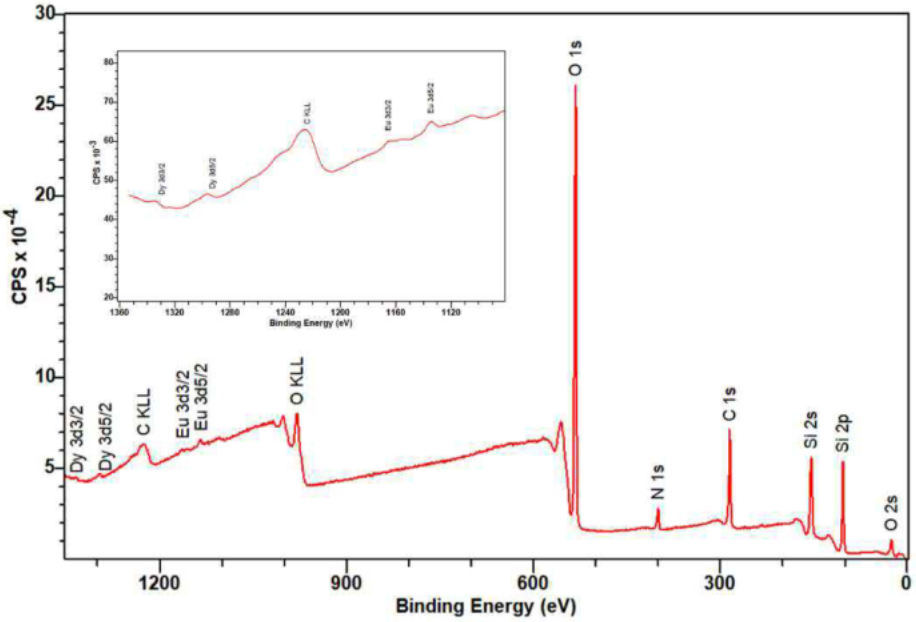

*Figure. 8.2.84.. Survey. scan. XPS. spectrum. of. Eu(**5**)$_3$:Dy(**5**)$_3$ (1:1). monolayer. LB. film.. Insert:. Smoothed. zoomed. in. survey. scan. of. Eu^{3+}. and Dy^{3+}. 3d. peaks,. with. Eu^{3+}. $3d_{3/2}$ =. 1165. and. $3d_{5/2}$ =. 1134. eV,. expected. being. 1136. and. 1166. eV. respectively[11]. and. Dy^{3+}. $3d_{3/2}$ =. 1334. and $3d_{5/2}$ =. 1296. eV,. expected. being. 1333. and. 1296. eV. respectively..*

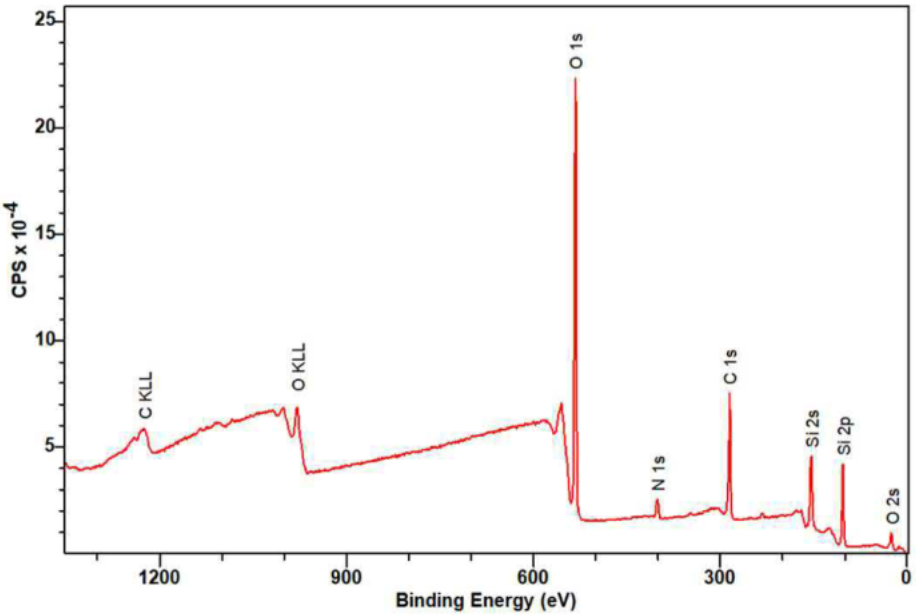

*Figure. 8.2.85.. Survey. scan. XPS. spectrum. of. Eu(**5**)$_3$:Tb(**5**)$_3$:Dy(**5**)$_3$:Sm(**5**)$_3$ (1:1:1:1). monolayer. LB. film.*

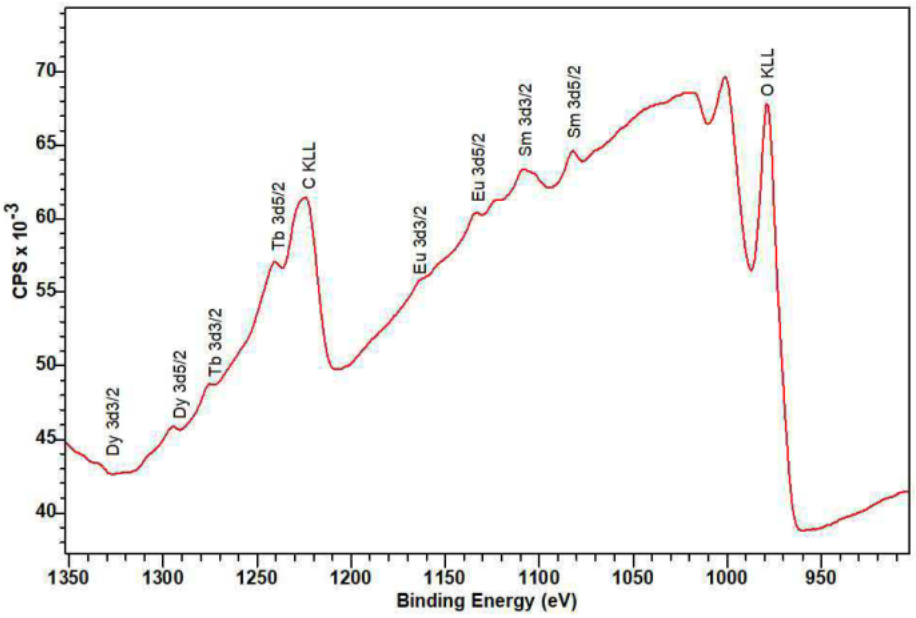

*Figure 8.2.86.. Enclosed window scan of Eu(**5**)$_3$:Tb(**5**)$_3$:Dy(**5**)$_3$:Sm(**5**)$_3$ (1:1:1:1) monolayer LB film (a total of 10 scans).. With Eu^{3+} $3d_{3/2}$ = 1164 and $3d_{5/2}$ = 1134 eV, expected being 1136 and 1166 eV respectively[11], Tb^{3+} $3d_{3/2}$ = 1175 and $3d_{5/2}$ = 1141 eV, expected being 1176 and 1141 eV respectively, Dy^{3+} $3d_{3/2}$ = 1334 and $3d_{5/2}$ = 1295 eV, expected being 1333 and 1296 eV respectivel[3] and with Sm^{3+} $3d_{3/2}$ = 1108 and $3d_{5/2}$ = 1082 eV, expected being 1108 and 1281 eV respectively..*

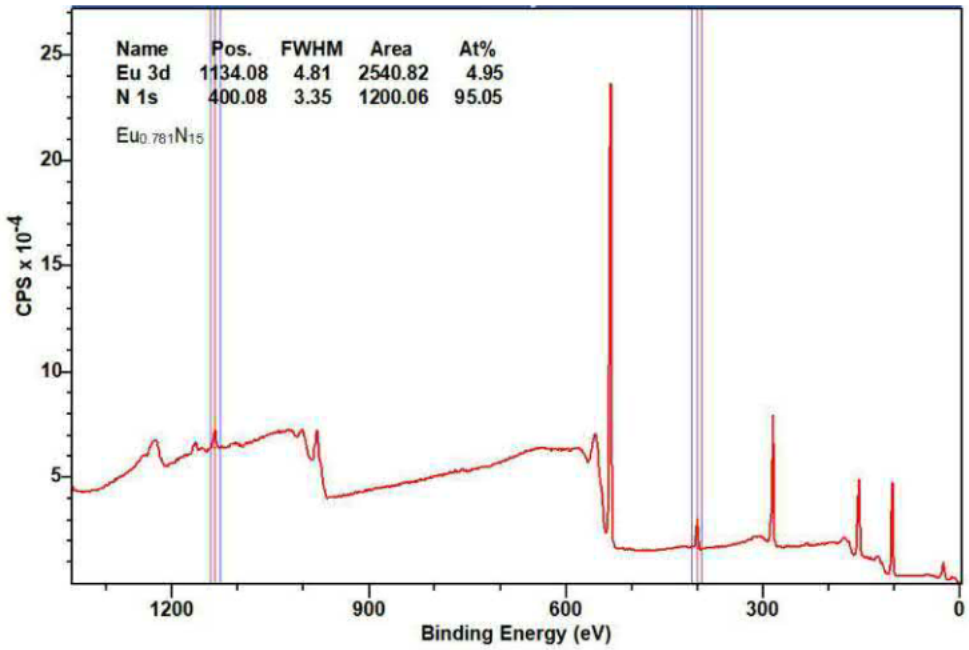

*Figure 8.2.87.. Survey scan XPS spectrum of Eu(**5**)$_3$ monolayer LB film, with ratios of N to Eu^{3+} compared, showing a close to 1:15 Eu^{3+}:N ratio as expected for the 1:3 metal to ligand complex $Eu(C_{26}H_{40}N_5O_9)_3$..*

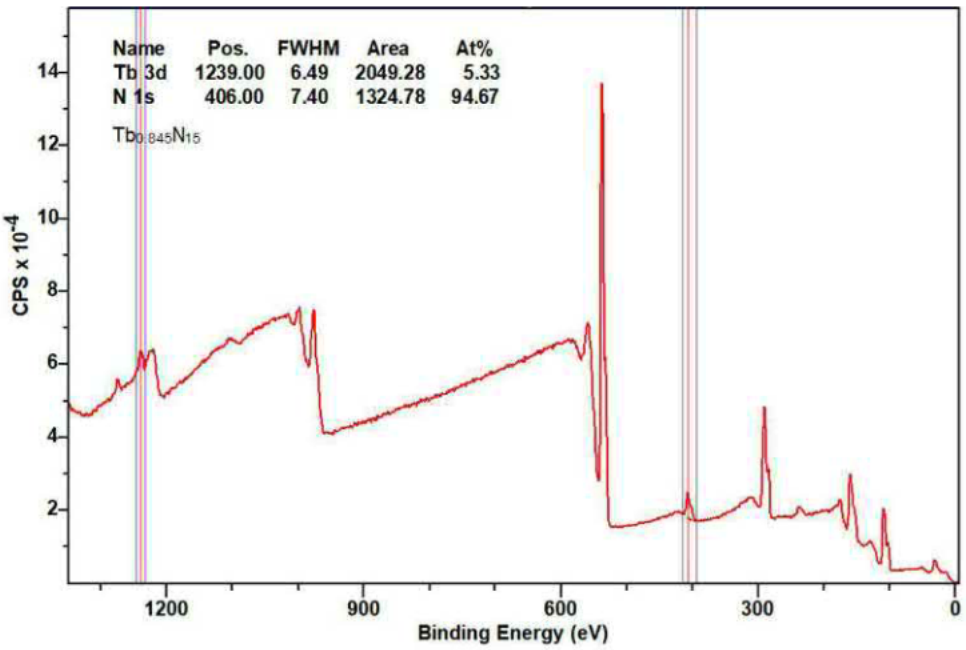

*Figure 8.2.88.. Survey scan XPS spectrum of Tb(**5**)$_3$ monolayer LB film,. with ratios of N to Tb^{3+} compared,. showing a close to 1:15 Tb^{3+}:N ratio,. as expected for the 1:3 metal to ligand complex $Tb(C_{26}H_{40}N_5O_9)_3$..*

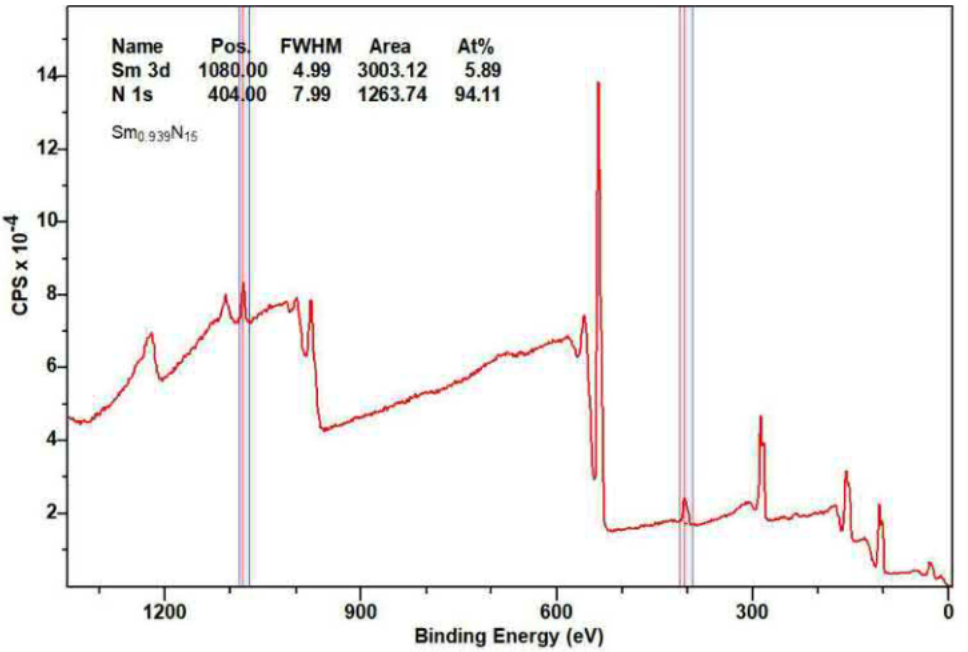

*Figure 8.2.89.. Survey scan XPS spectrum of Sm(**5**)$_3$ monolayer LB film,. with ratios of N to Sm^{3+} compared,. showing a close to 1:15 Tb^{3+}:N ratio,. as expected for the 1:3 metal to ligand complex $Sm(C_{26}H_{40}N_5O_9)_3$..*

8.3 Chapter 5

8.3.1 Ligand Characterisation Data

8.3.1.1 Precursor F

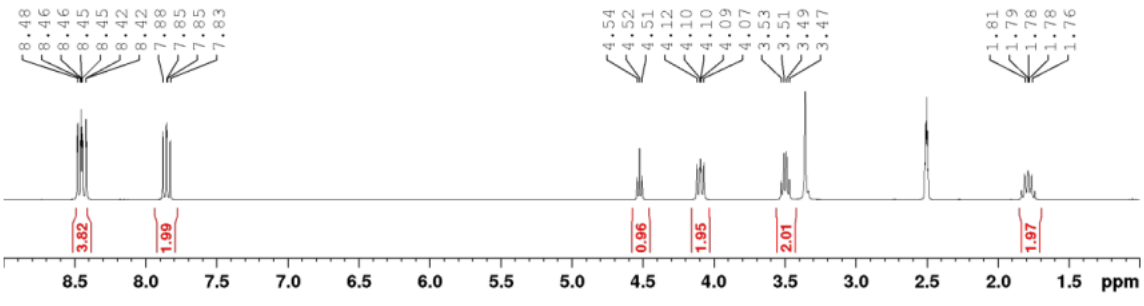

*Figure 8.3.1.. ^{1}H NMR spectrum of **F** (300 MHz, DMSO-d_6).*

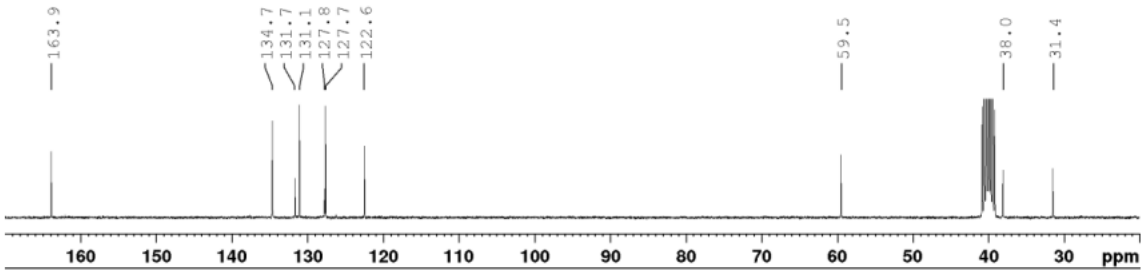

*Figure 8.. 3.. 2.. ^{13}C NMR spectrum of **F** (75 MHz, DMSO-d_6).*

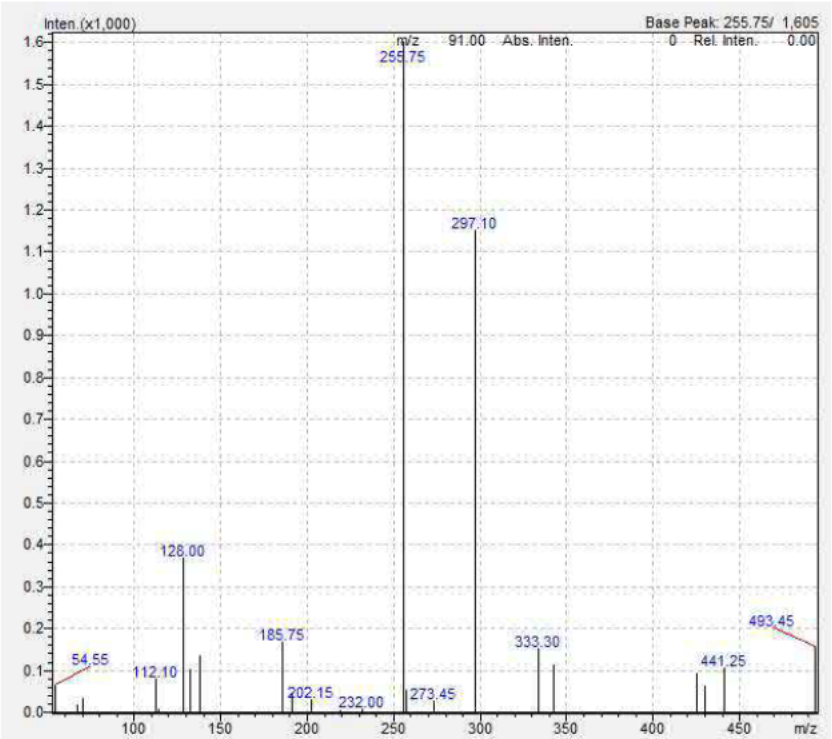

*Figure 8.3.3.. LRMS m/z = 255.75 [**F** + H]+ (calc.. for $C_{15}H_{13}NO_3^+$, 256.10), 297.10 [**F** + k]$^+$ (calc.. for $C_{15}H_{13}NO_3K^+$, 294.05)..*

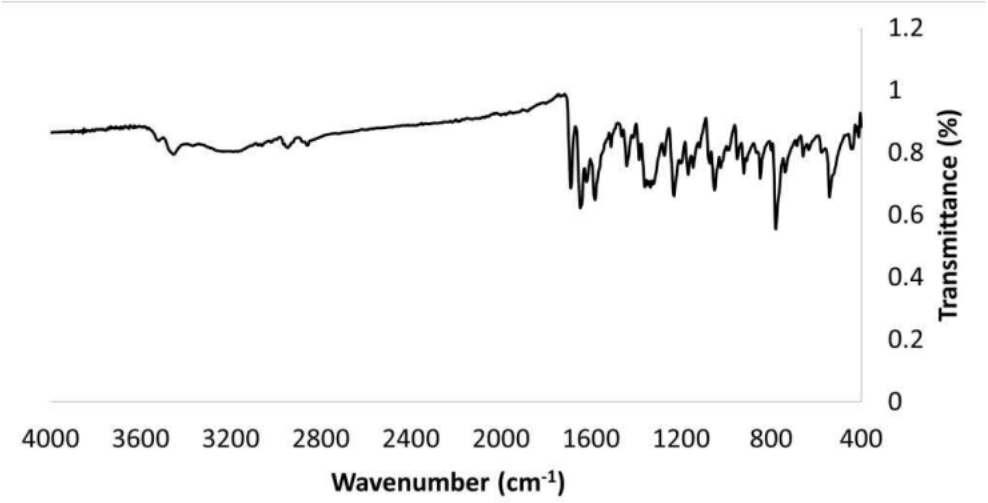

*Figure 8.3.4.. IR spectrum of **F**.*

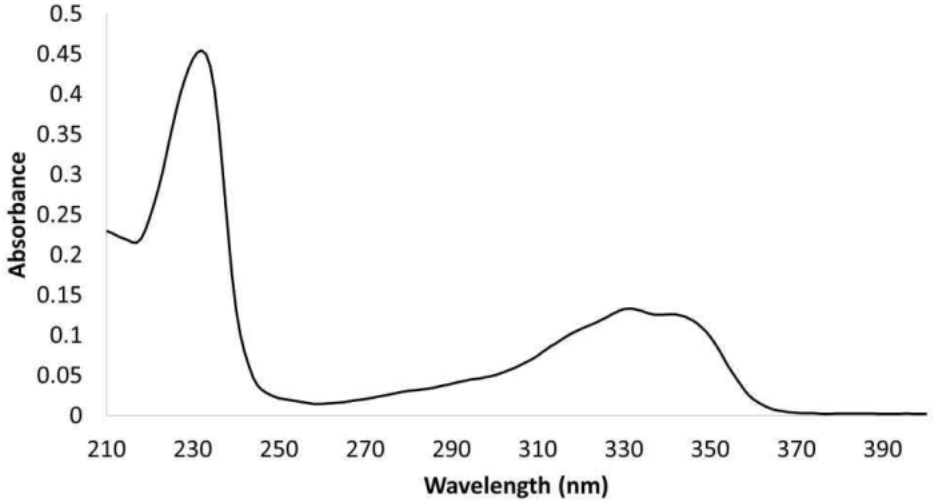

*Figure 8.3.5.. UV-visible absorption spectrum of **F**. (0.01 mM, MeOH).*

8.3.1.2 Precursor G

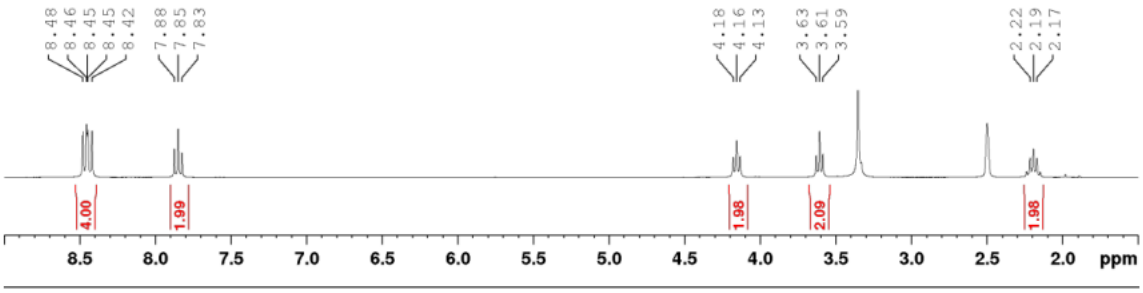

*Figure 8.3.6.. ^{1}H NMR spectrum of **G** (300 MHz, DMSO-d_6).*

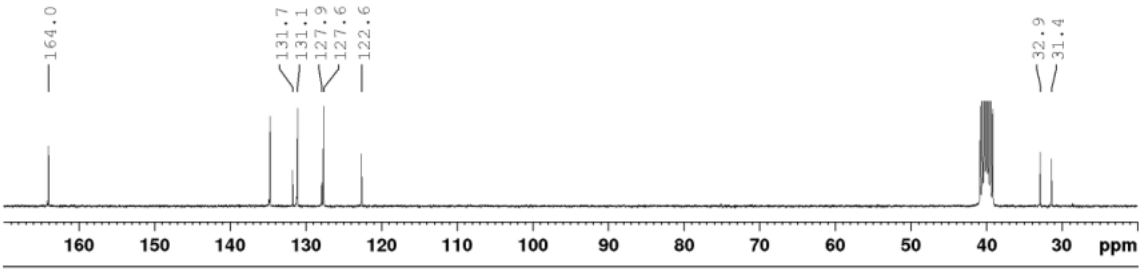

*Figure 8.3.7.. ^{13}C NMR spectrum of **G** (75 MHz, DMSO-d_6).*

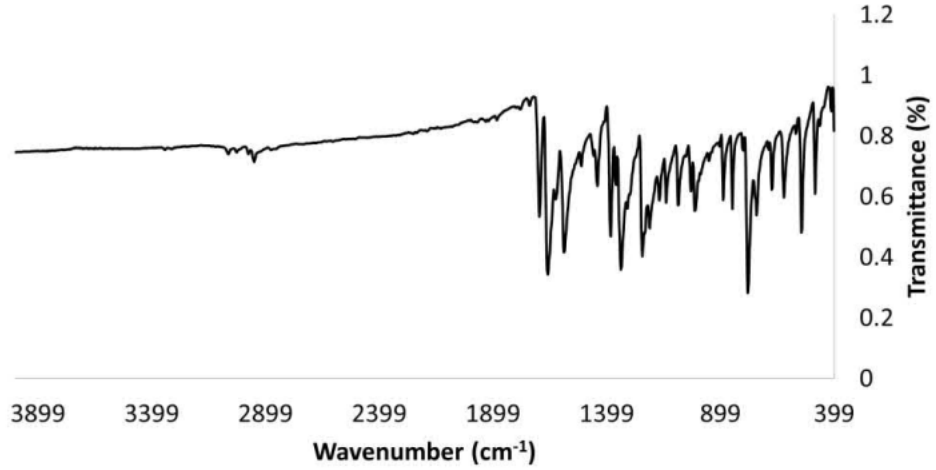

*Figure 8.3.8.. IR spectrum of **G**.*

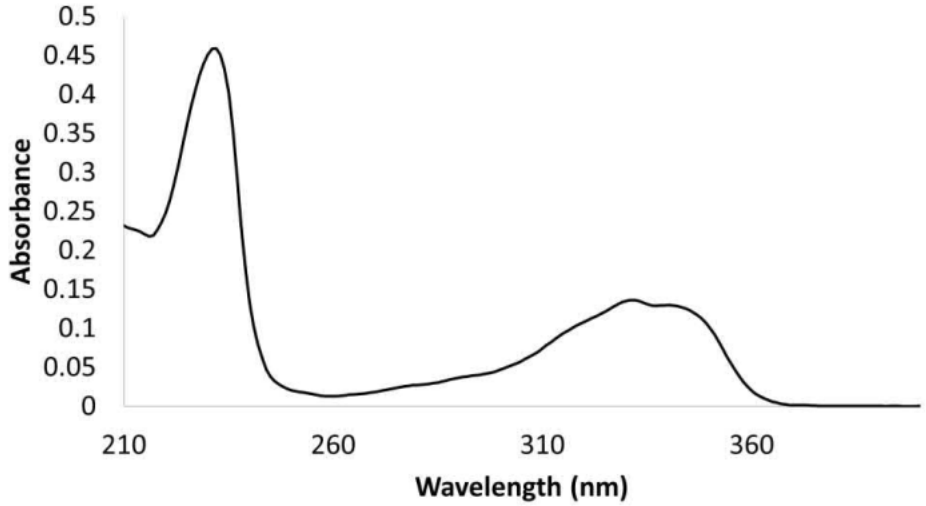

*Figure 8.3.9.. UV-visible absorption spectrum of **G** (0.01 mM, MeOH).*

8.3.1.3 Precursor H

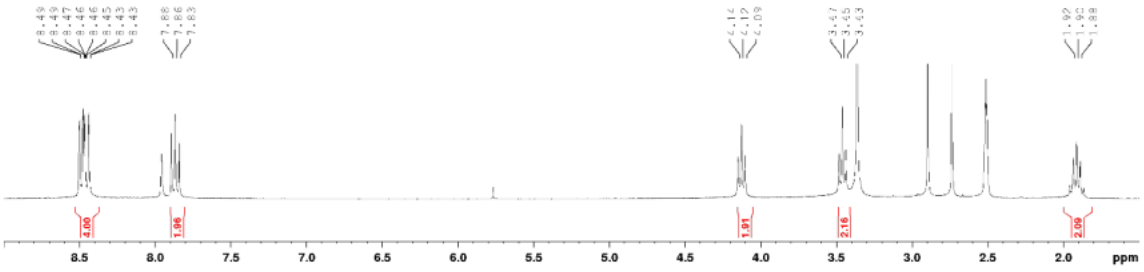

*Figure 8.3.10.. ^{1}H NMR spectrum of **H** (300 MHz, DMSO-d_6).*

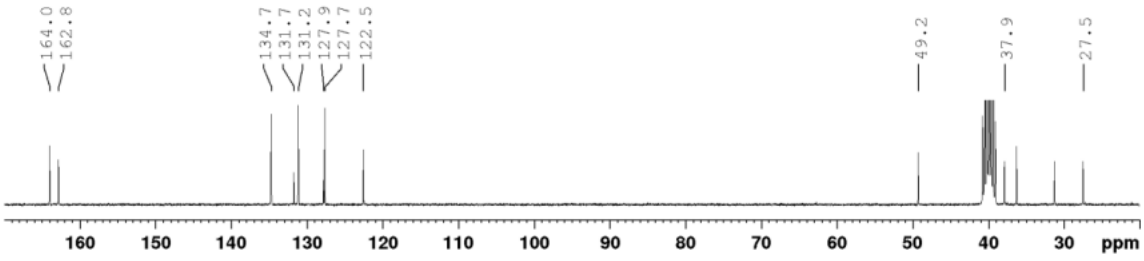

*Figure 8.3.11.. ^{13}C NMR spectrum of **H** (75 MHz, DMSO-d_6).*

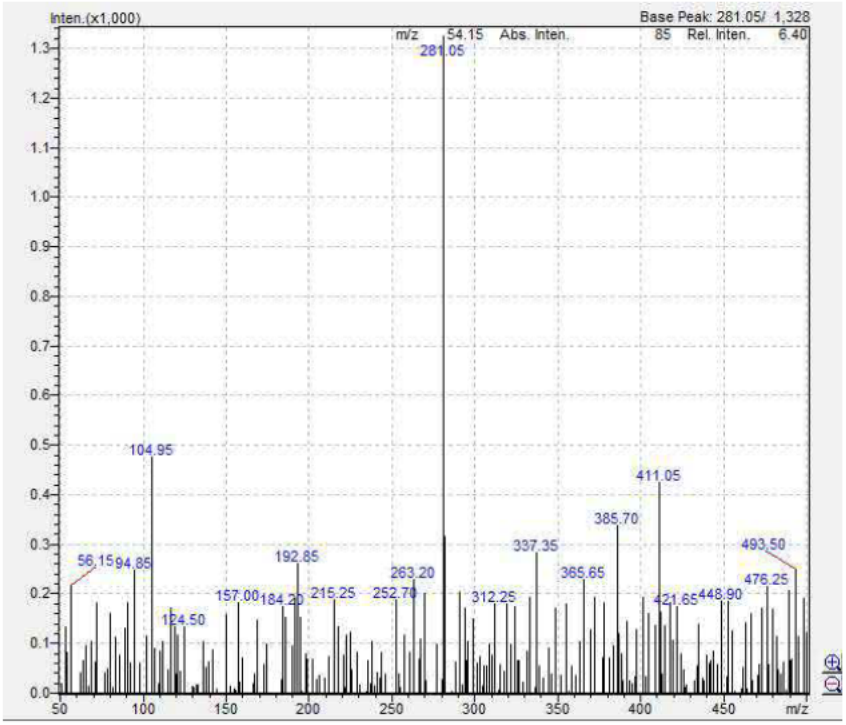

*Figure 8.3.12. LRMS m/z = 281.05 [**H** + H]$^{+}$ (calc.. for $C_{15}H_{12}N_4O_2^{+}$, 281.10).*

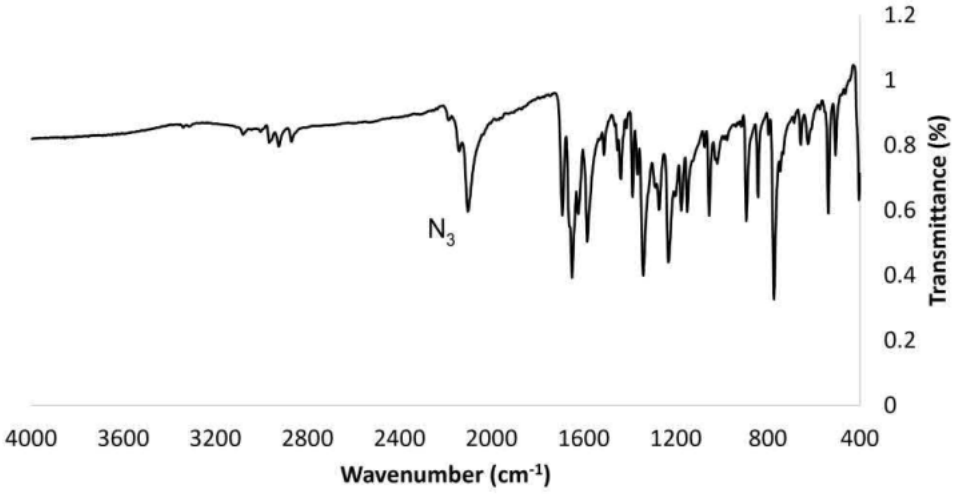

*Figure.8.3.13..IR.spectrum.of.**H**..*

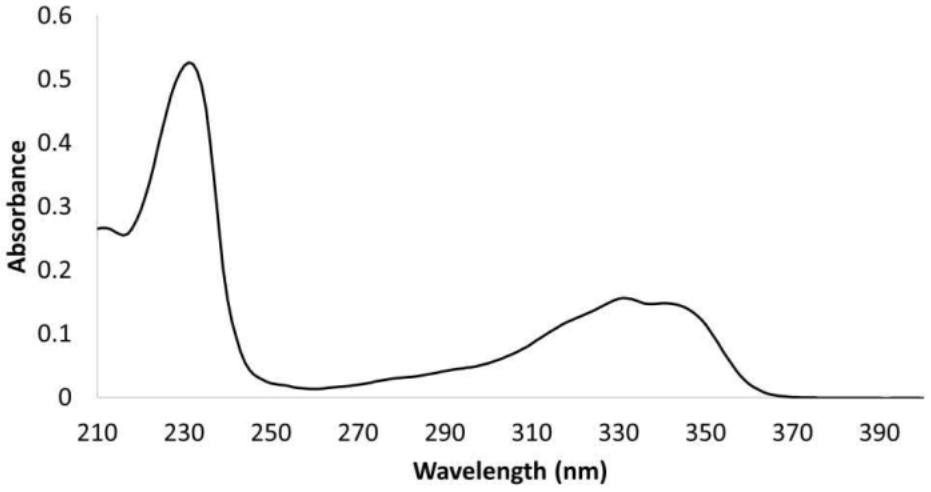

*Figure.8.3.14..UV-visible.absorption.spectrum.of.**H**.(0.01.mM,.MeOH)..*

8.3.1.4 Intermediate I

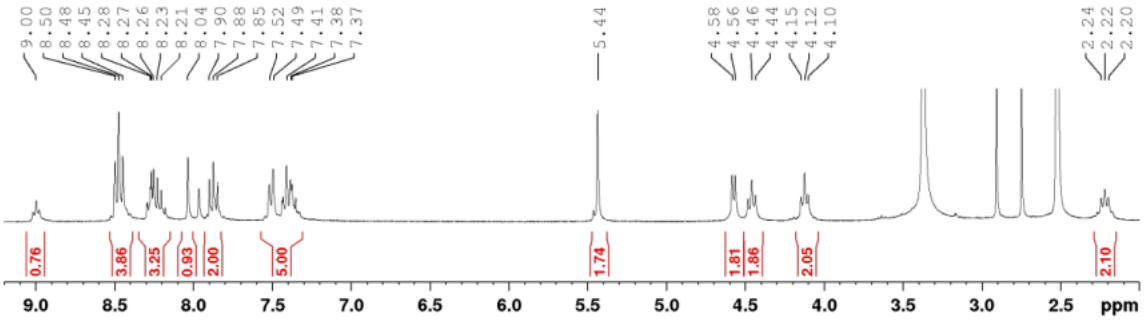

*Figure.8.3.15..[1]H.NMR.spectrum.of.**I**.(300.MHz,.DMSO-d_6).*

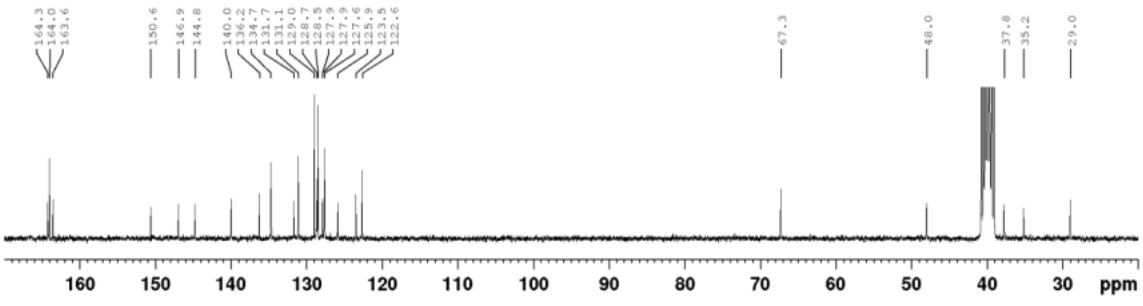

*Figure 8.3.16.. ^{13}C NMR spectrum of **I** (75 MHz, DMSO-d_6).*

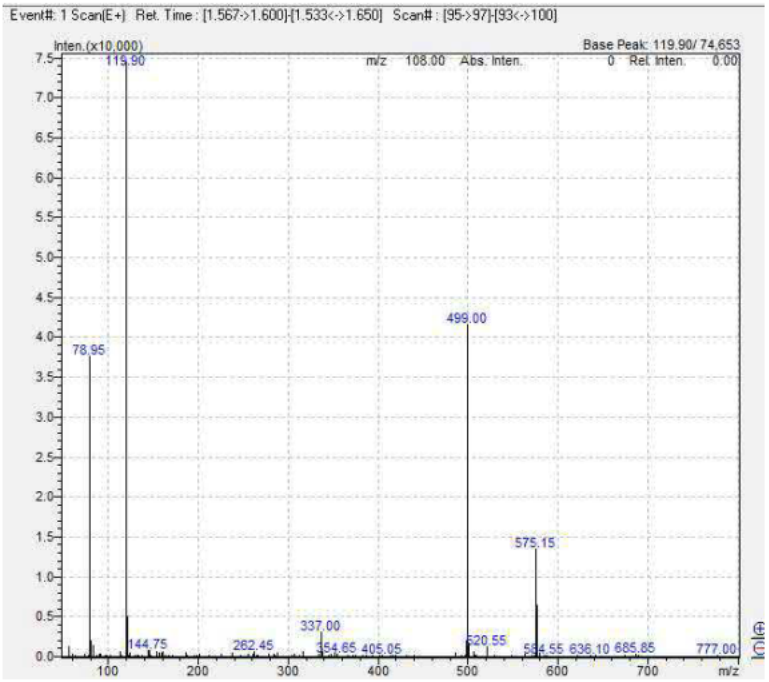

*Figure 8.3.17.. LRMS m/z = 575.15 ([**I** + H]$^+$ (calc. for $C_{32}H_{27}N_6O_5^+$, 575.20).*

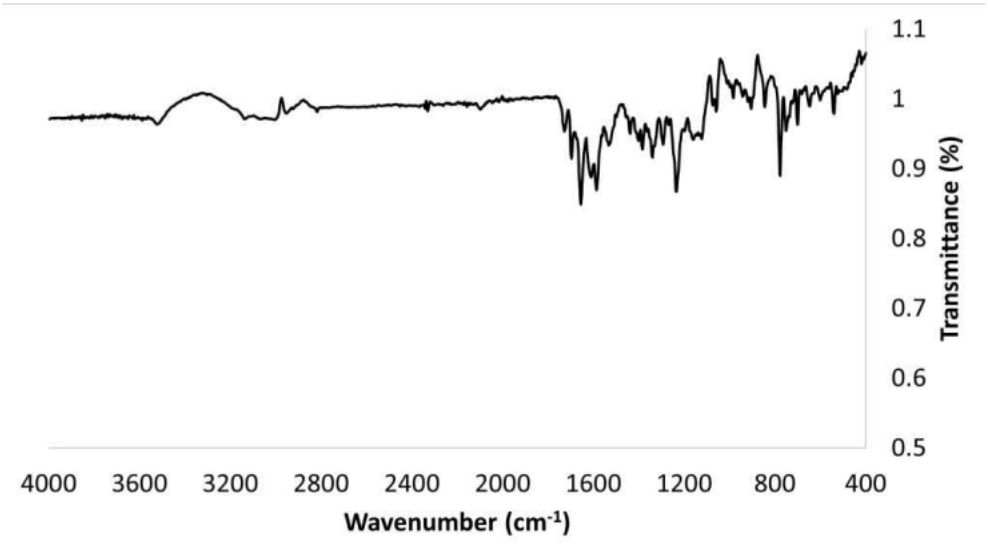

*Figure 8.3.18.. IR spectrum of **I**.*

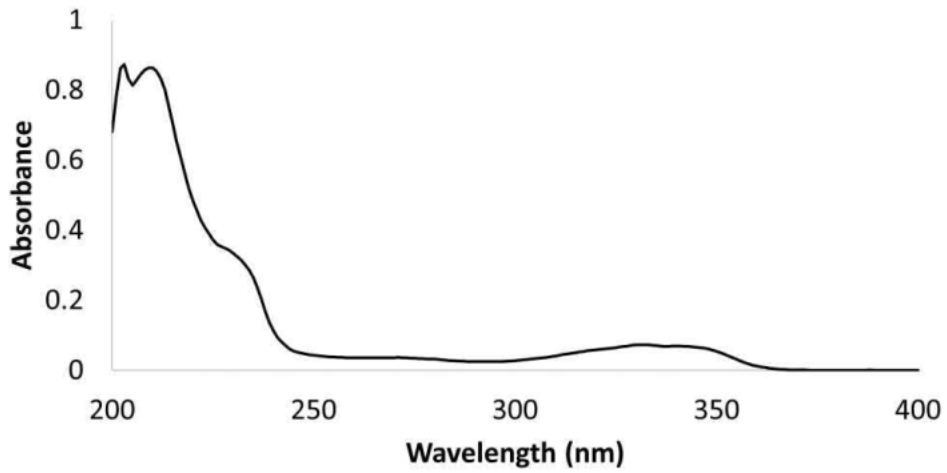

*Figure 8.3.19.. UV-visible absorption spectrum of **1** (0.01 mM, MeOH)..*

8.3.1.5 Ligand 6

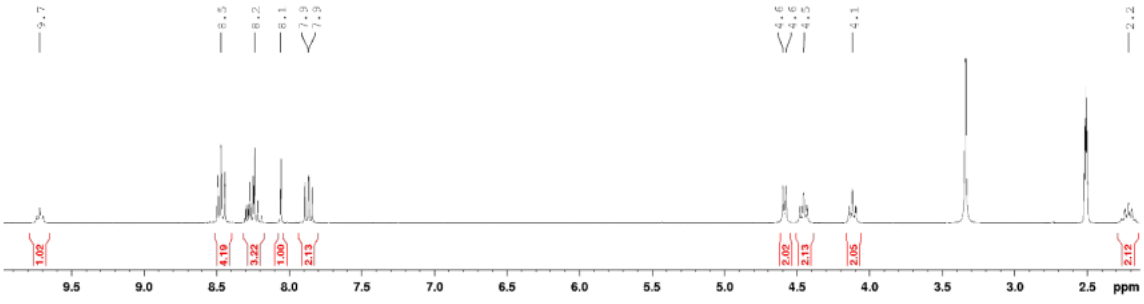

*Figure 8.3.20.. ^{1}H NMR spectrum of **6** (300 MHz, DMSO-d_6).*

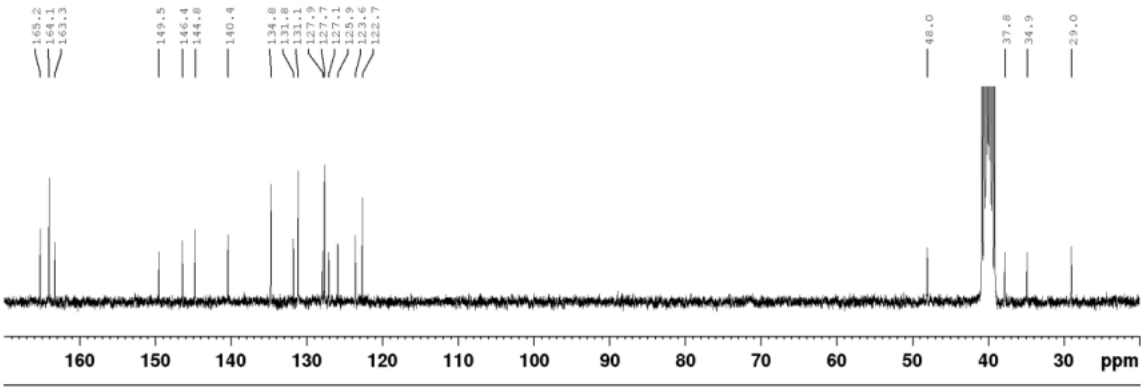

*Figure 8.3.21.. ^{13}C NMR spectrum of **6** (75 MHz, DMSO-d_6)..*

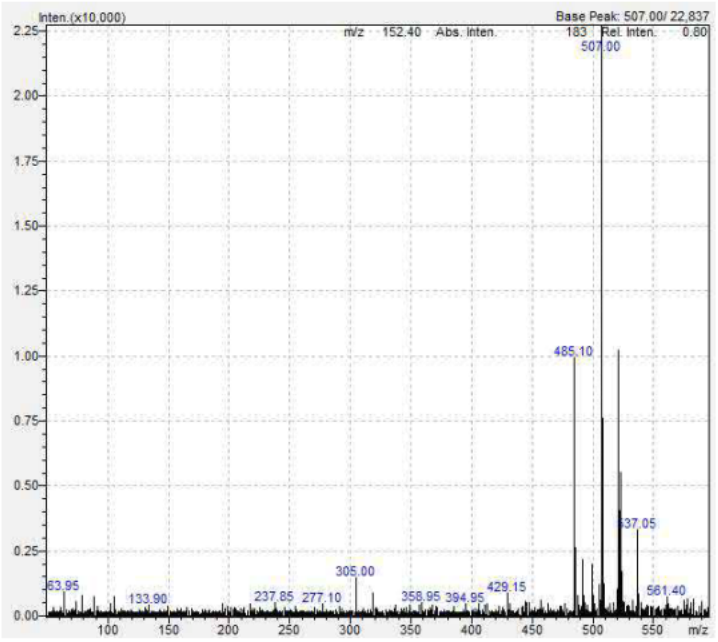

*Figure. 8.3.22.. LRMS. m/z =. 485.10. [**6** +. H]⁺. (calc.. for. $C_{25}H_{21}N_6O_5^+$,. 485.16). and. m/z =. 507.00. [**6** +. Na]⁺. (calc.. for. $C_{25}H_{20}N_6O_5Na^+$,. 507.14).*

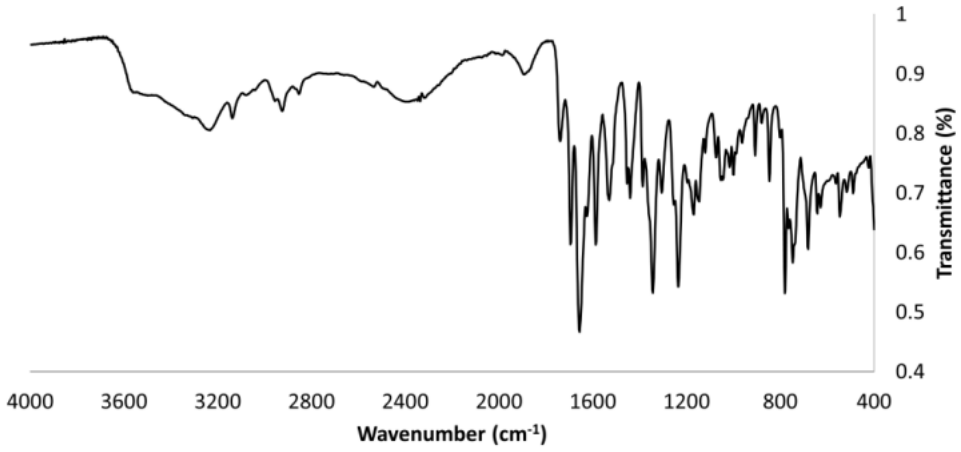

*Figure. 8.3.23.. IR. spectrum. of. **6**..*

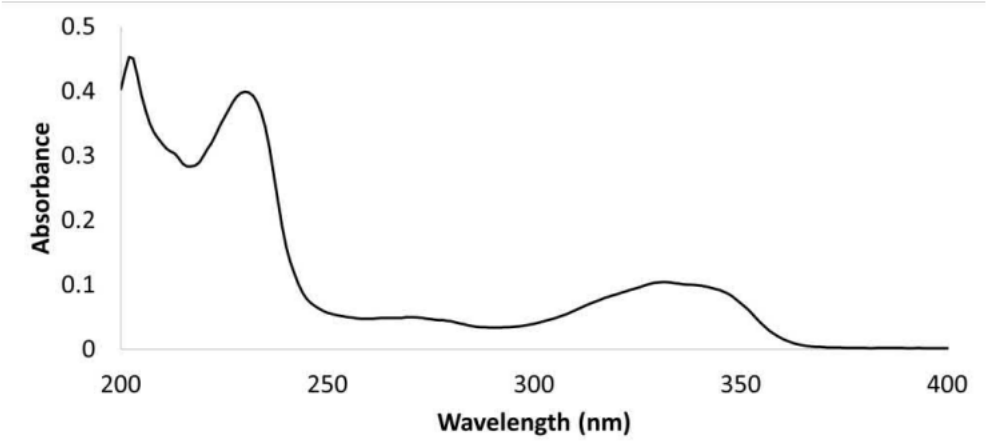

*Figure. 8.3.24.. UV-visible. absorption. spectrum. of. **6** (0.01. mM,. MeOH)..*

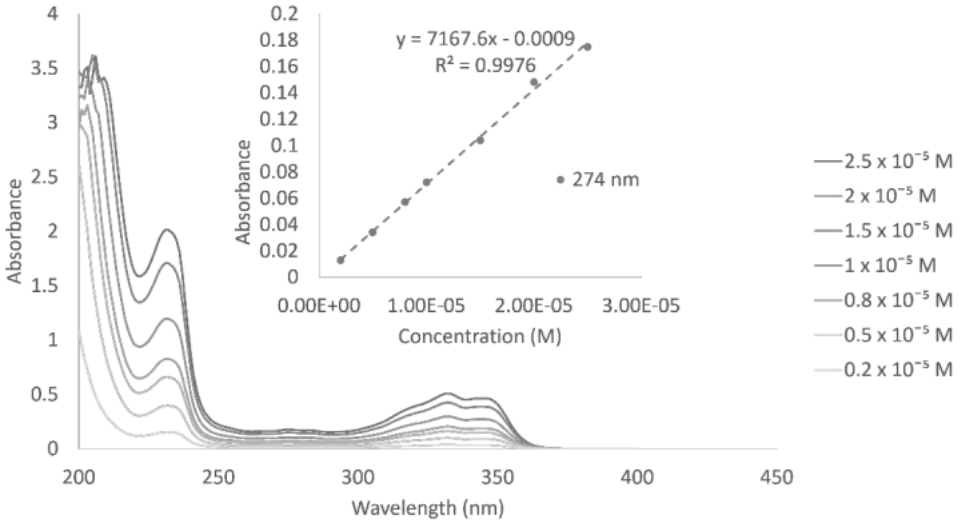

*Figure 8.3.25.. UV-visible absorption spectrum of **6**, in MeOH.. Insert: absorbance at 274 nm vs concentration..*

8.3.1.6 Ligand 7

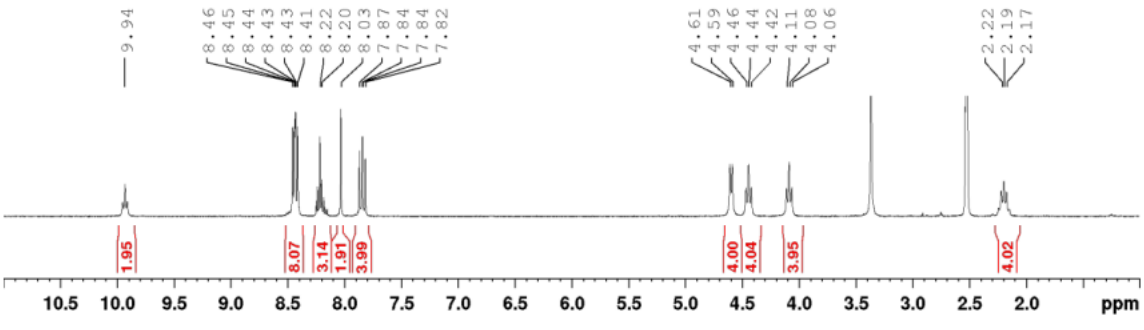

*Figure 8.3.26.. ^{1}H NMR spectrum of **7** (300 MHz, DMSO-d_6).*

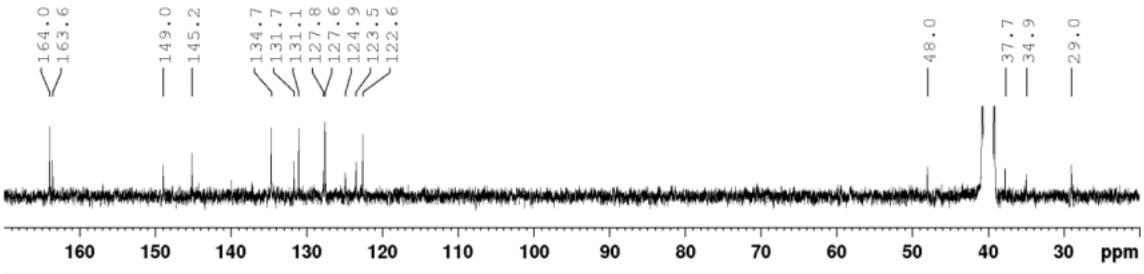

*Figure 8.3.27.. ^{13}C NMR spectrum of **7** (75 MHz, (DMSO-d_6).*

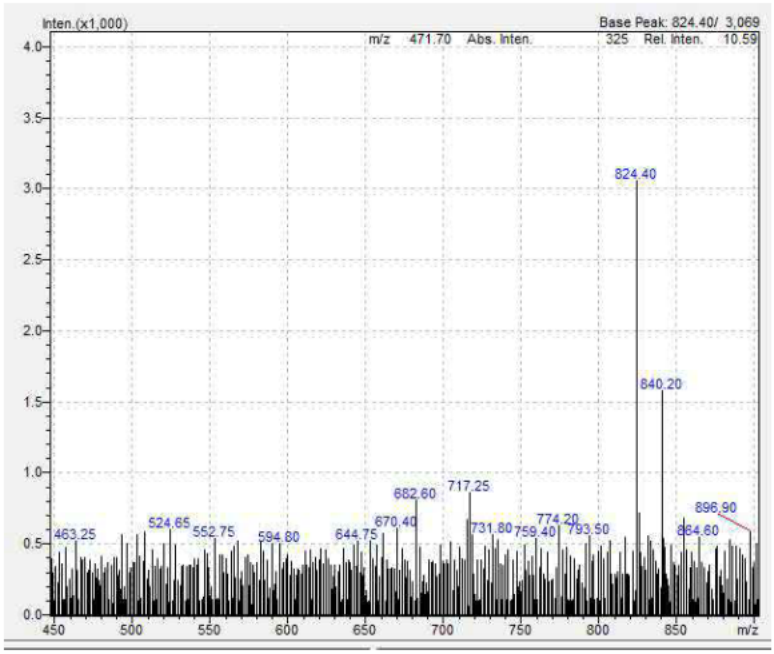

*Figure 8.3.28. LRMS m/z = 824.40 [**7**+Na]$^+$ (calc. for $C_{43}H_{35}N_{11}O_6Na^+$, 824.40) and m/z = 840.20 [**7**+K]$^+$ (calc. for $C_{43}H_{35}N_{11}O_6K^+$, 840.24).*

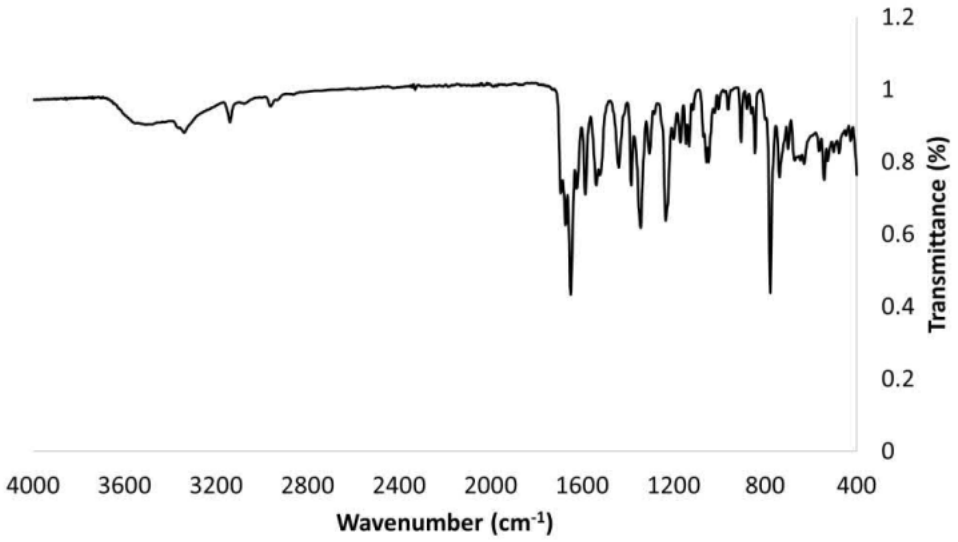

*Figure 8.3.29. IR spectrum of **7**.*

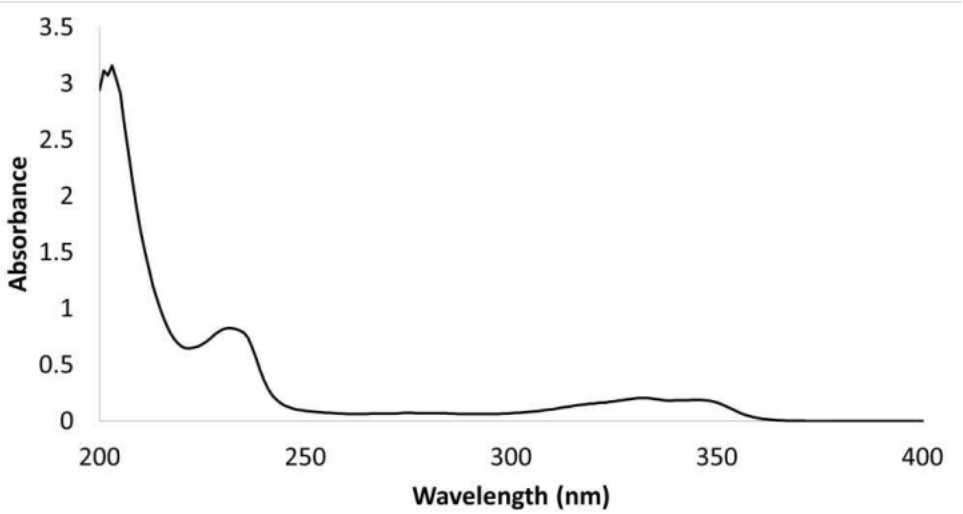

*Figure 8.3.30. UV-visible absorption spectrum of **7** (0.01 mM, MeOH).*

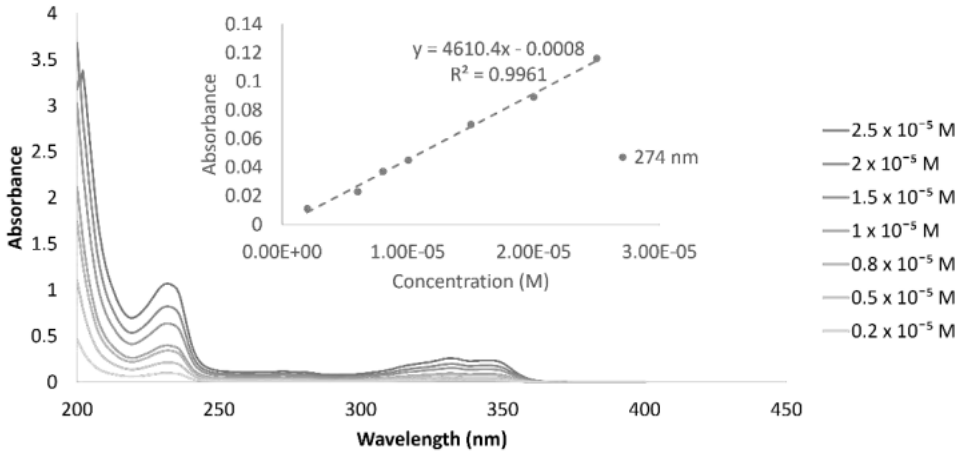

*Figure 8.3.31. UV-visible absorption spectrum of **7**, in MeOH. Insert: absorbance at 274 nm vs concentration.*

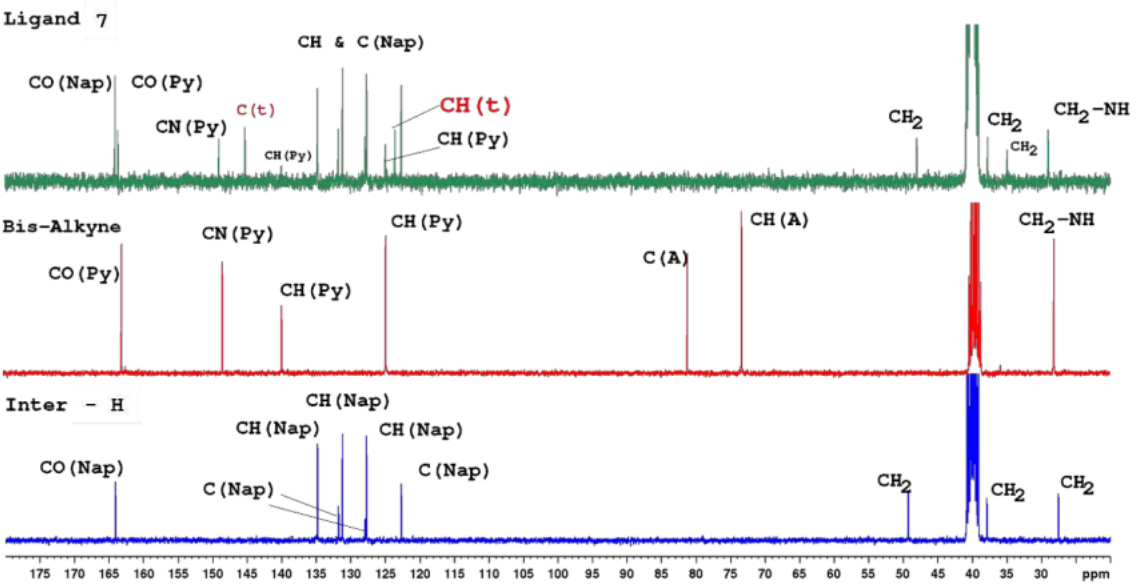

*Figure 8.3.32. ^{13}C NMR spectrum of **7** precursor **H** and bis-alkyne (**D**) (75 MHz, DMSO-d_6). Abbreviations: Py is for PDA pyridine ring, Bn is for benzyl ring, Nap is for 1,8-naphthalimide and t for 1,2,3-triazole.*

8.3.1.7 Precursor J

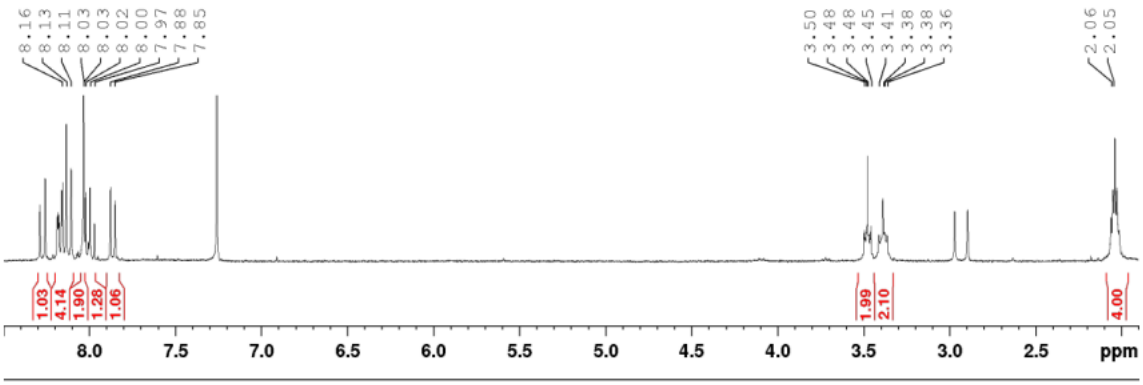

*Figure 8.3.33.. ^{1}H NMR spectrum of **J** (300 MHz, $CDCl_3$).*

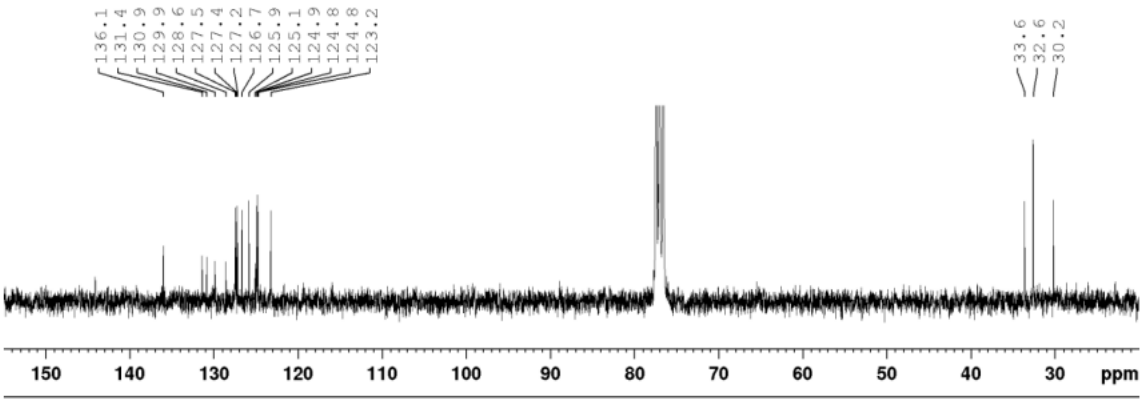

*Figure 8.3.34. ^{13}C NMR spectrum of **J** (75 MHz, $CDCl_3$).*

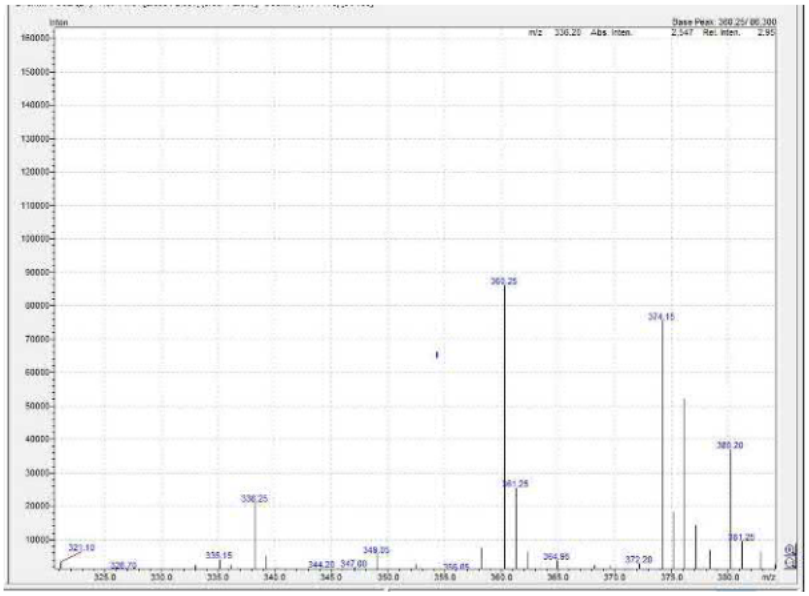

Figure 8.3.35.. LRMS m/z = 338.25 $[\mathbf{J} + H]^+$ (calc.. for $C_{20}H_{18}Br^+$, 338.26) and m/z = 360.25 $[\mathbf{J} + Na]^+$ (calc.. for $C_{20}H_{17}BrNa^+$, 360.24)..

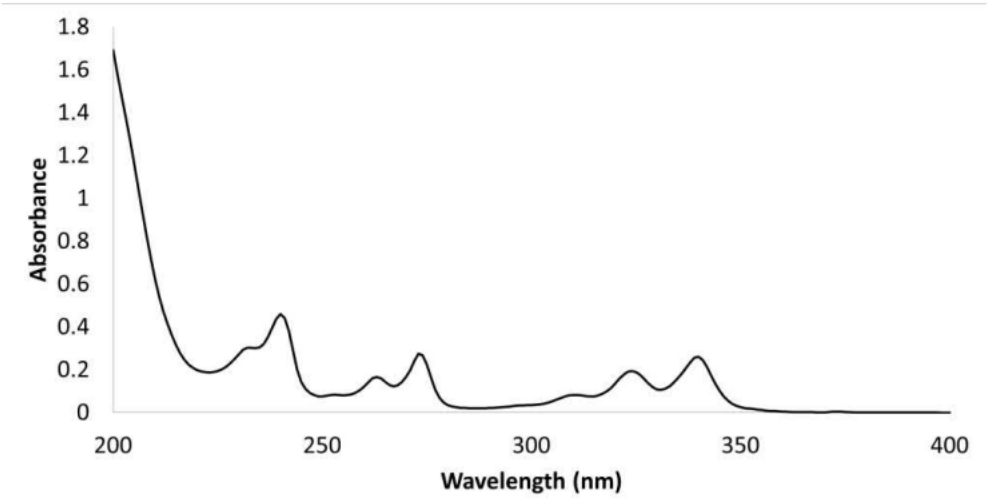

*Figure 8.3.36. UV-visible absorption spectrum of **J** (0.01 mM, MeOH).*

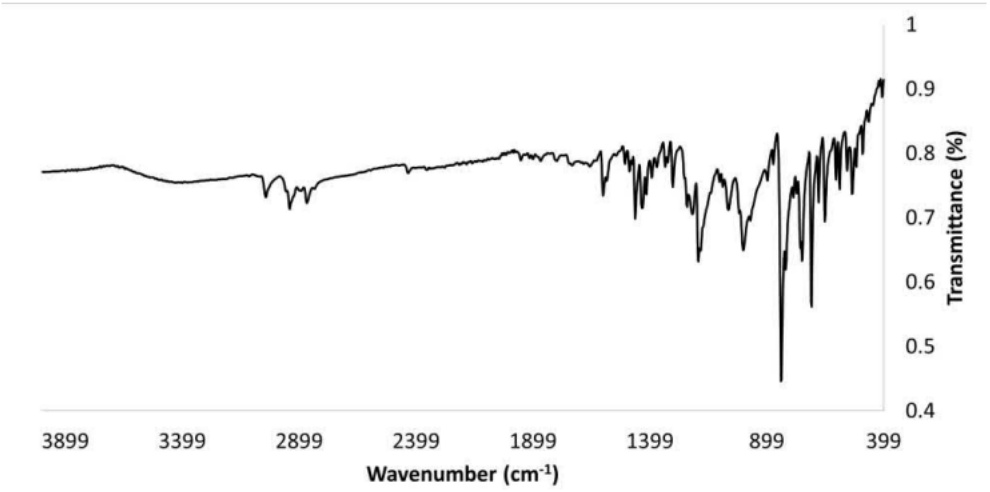

*Figure 8.3.37. IR spectrum of **J**.*

8.3.1.8 Precursor K

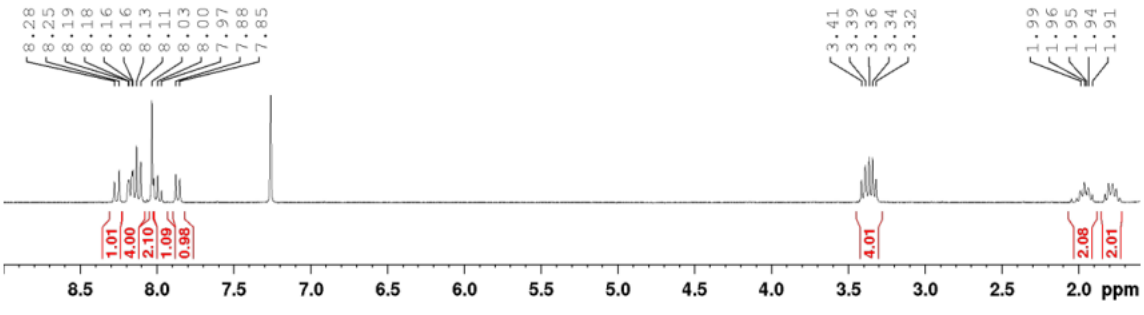

*Figure 8.3.38. ^{1}H NMR spectrum of **K** (300 MHz, $CDCl_3$).*

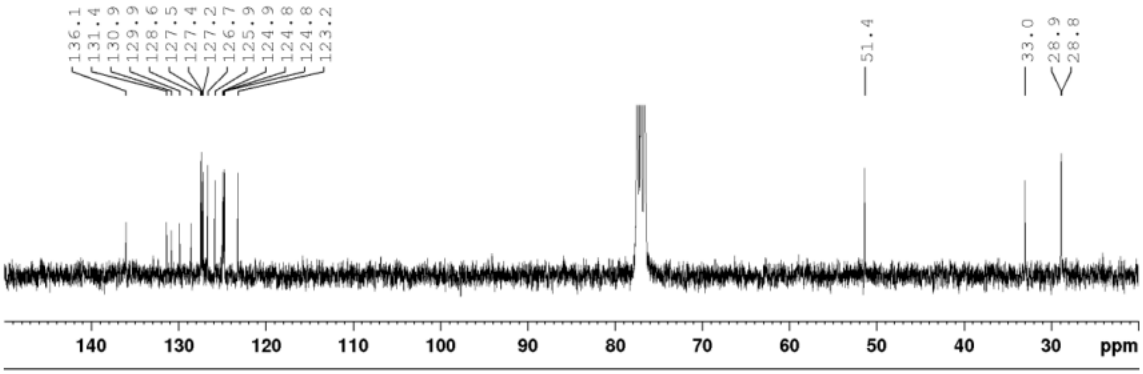

*Figure 8.3.39.. ^{13}C NMR spectrum of **K** (75 MHz, $CDCl_3$)..*

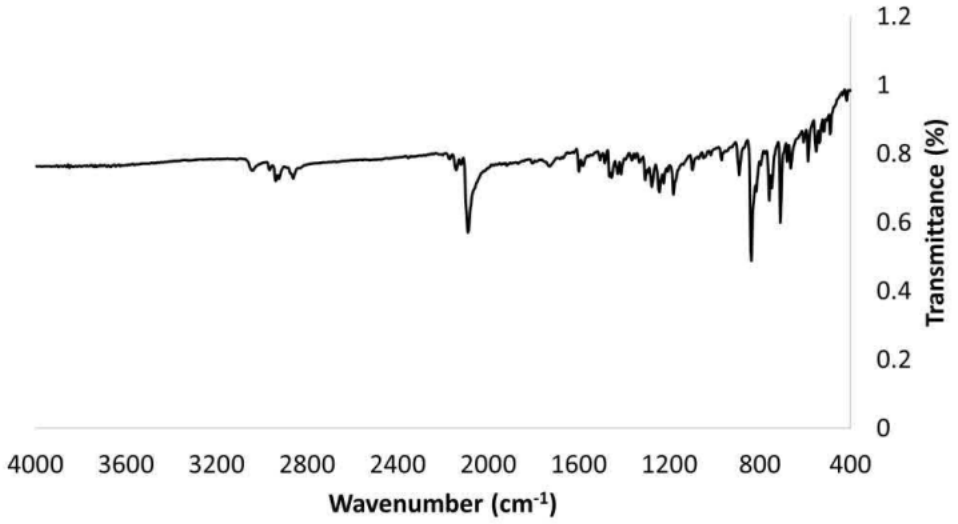

*Figure 8.3.40.. IR spectrum of **K**.*

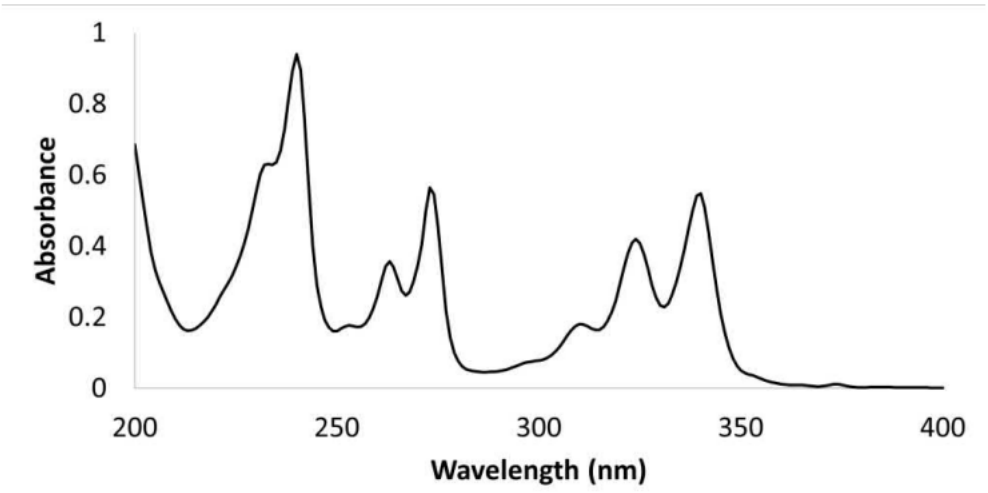

Figure 8.3.41.. UV-visible absorption spectrum of **K** (0.01 mM, MeOH).

8.3.1.9 Intermediate L

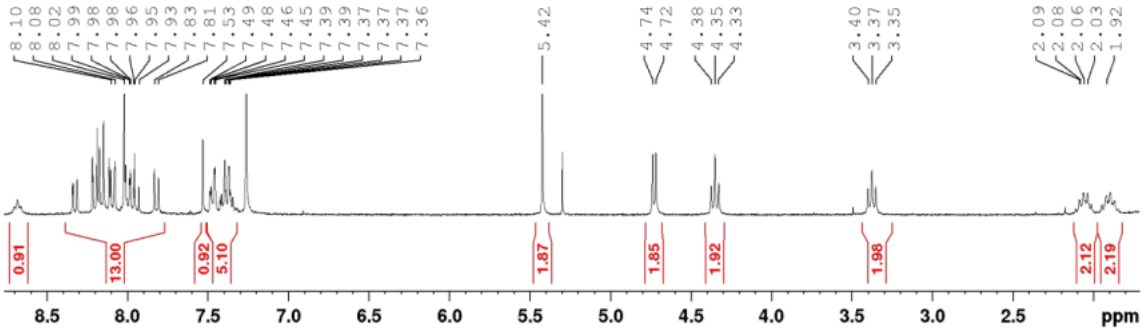

*Figure 8.3.42.. ^{1}H NMR spectrum of **L** (300 MHz, $CDCl_3$).*

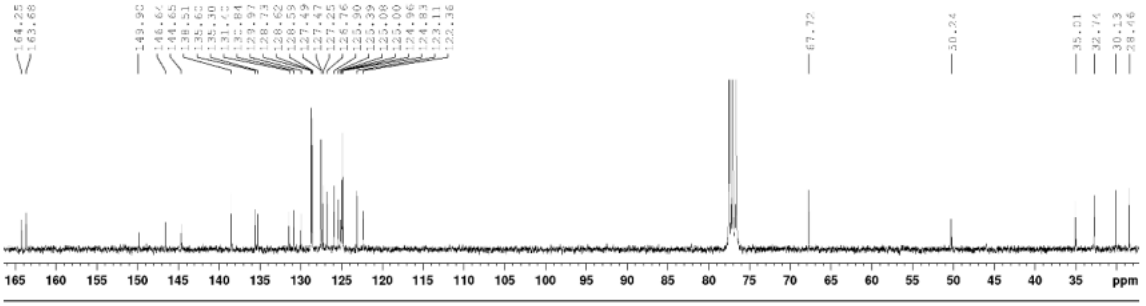

*Figure 8.3.43.. ^{13}C NMR spectrum of **L** (75 MHz, $CDCl_3$).*

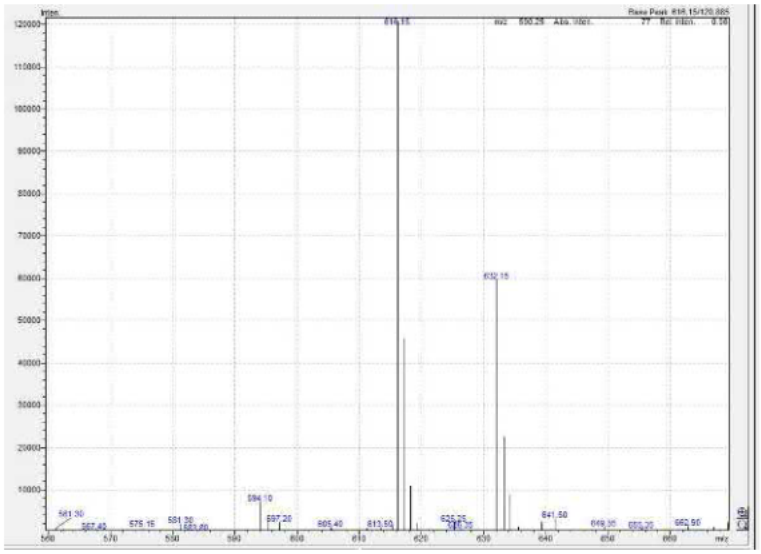

*Figure 8.3.44.. LRMS m/z = 594.10 [**L** + H]$^+$ (calc.. for $C_{37}H_{32}N_5O_3^+$, 594.68), m/z = 616.15 [**L** + Na]$^+$ (calc.. for $C_{37}H_{31}N_5O_3Na^+$, 616.66) and m/z = 632.15 [**L** + K]$^+$ (calc.. for $C_{37}H_{31}N_5O_3K^+$, 632.77)..*

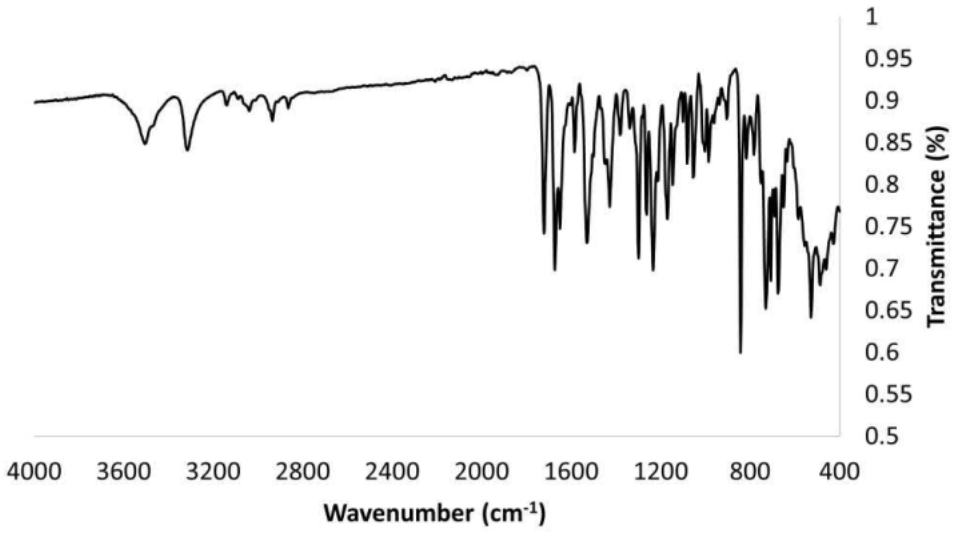

Figure 8.3.45. IR spectrum of **L**.

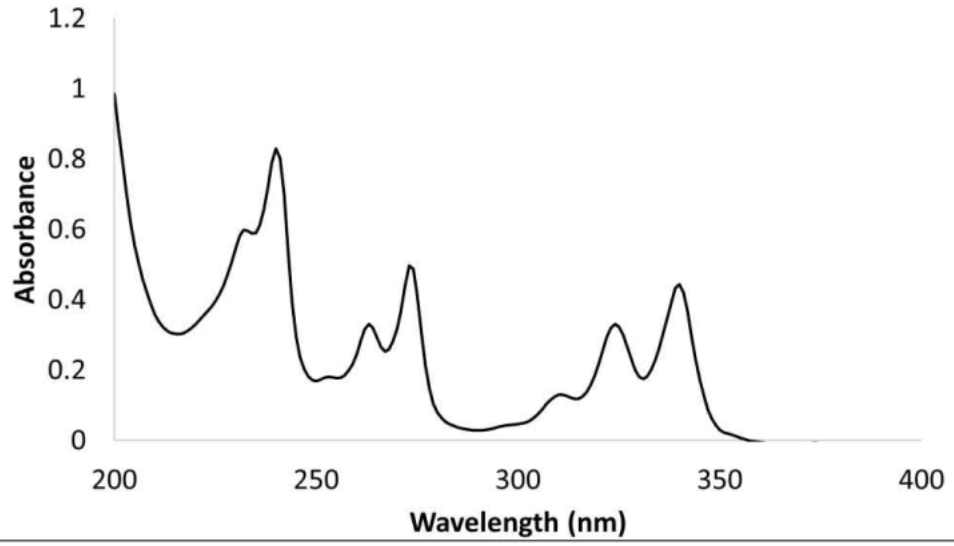

Figure 8.3.46.. UV-visible absorption spectrum of **L** *(0.01 mM, MeOH).*

8.3.1.10 Ligand 8

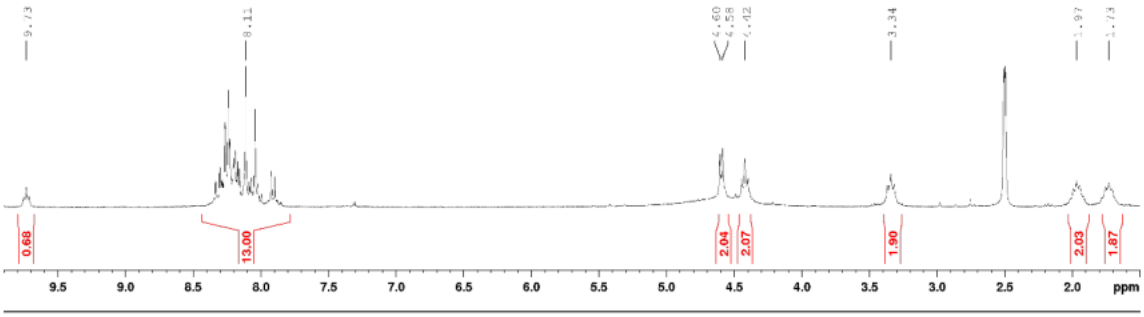

Figure. 8.3.47.. ^{1}H. NMR. spectrum. of. ***8****. (300. MHz,. DMSO-d_6)..*

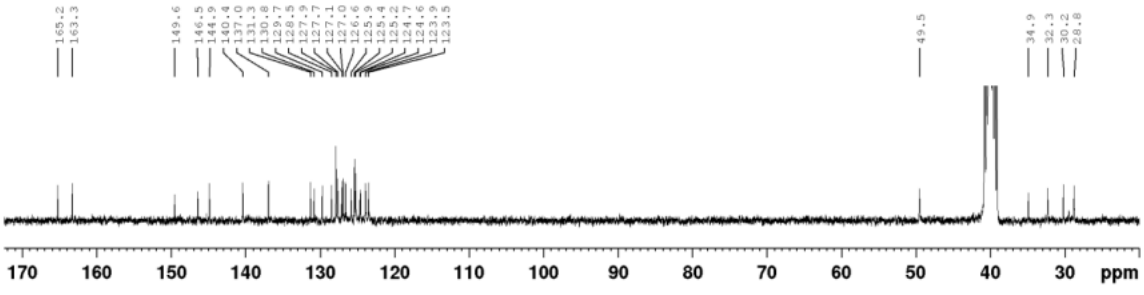

Figure. 8.3.48.. ^{13}C. NMR. spectrum. of. ***8****. (75. MHz,. DMSO-d_6)..*

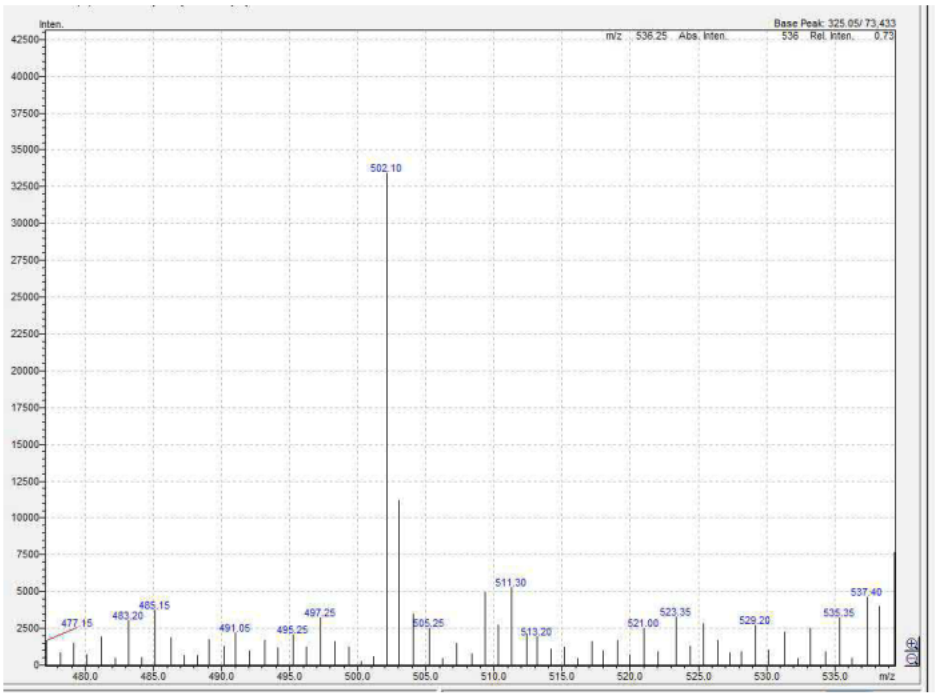

*Figure. 8.3.49.. LRMS. m/z. =. 502.1. [****8****. -. H]$^{-}$. (calc.. for. $C_{30}H_{24}N_5O_3^-$,. 502.54).*

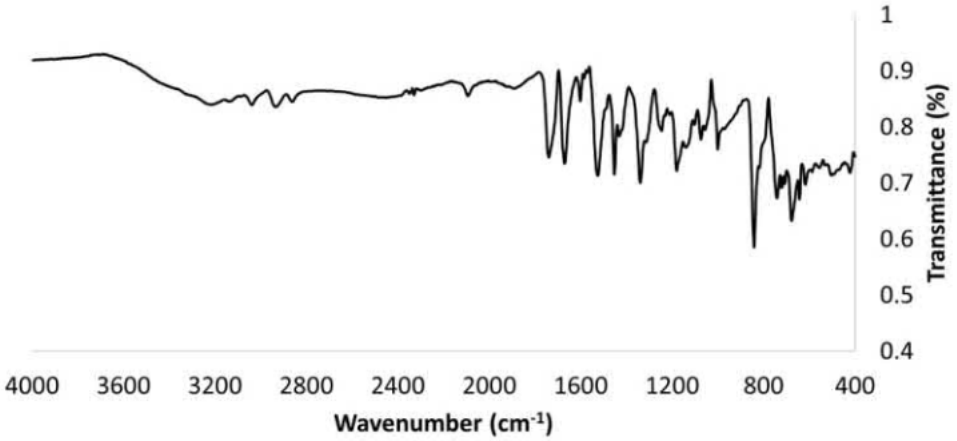

Figure. 8.3.50.. IR. spectrum. of. ***8.***

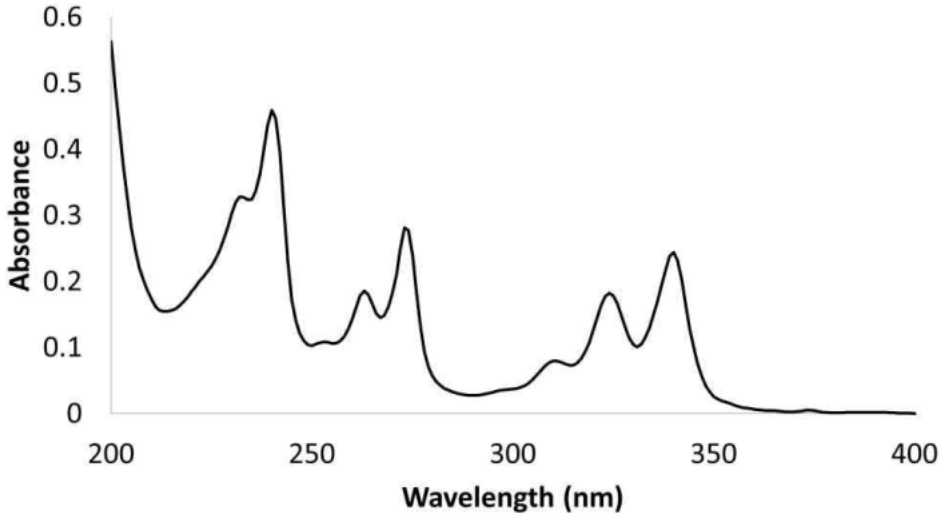

Figure. 8.3.51.. UV-visible. absorption. spectrum. of ***8*** *(0.01. mM,. MeOH)..*

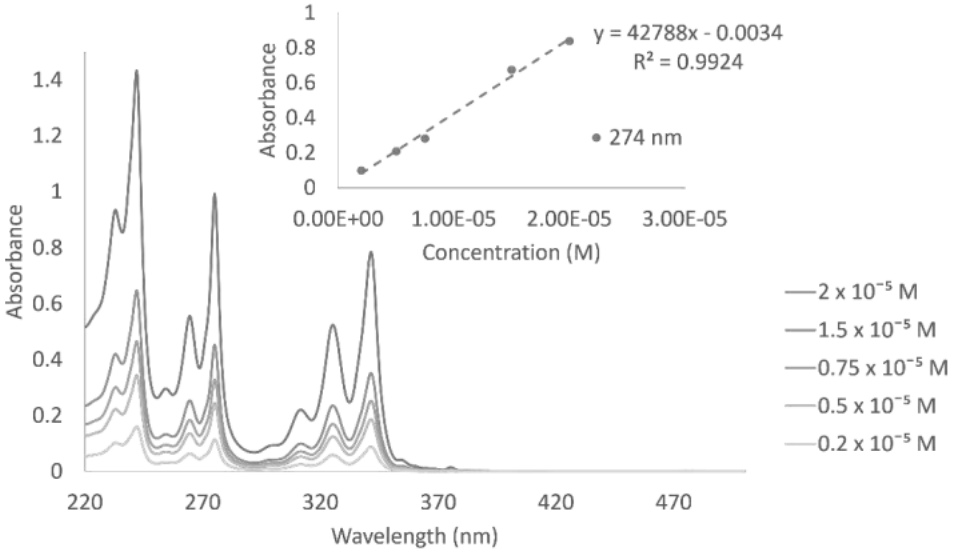

Figure. 8.3.52.. UV-visible. absorption. spectrum. of ***8****,. in. MeOH.. Insert:. absorbance. at. 274. nm. vs. concentration..*

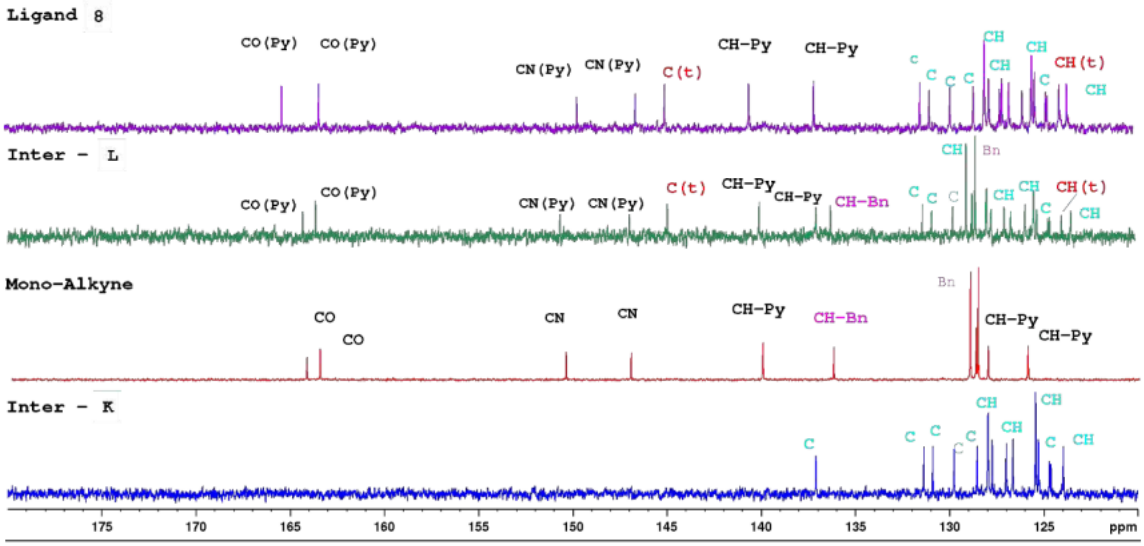

*Figure 8.3.53. ^{13}C NMR spectrum of **8** intermediate **L** and precursor **K** and mono-alkyne (**B**). (75 MHz, DMSO-d_6). Abbreviations: Py. is for pyridine ring, Bn. for benzyl ring and t. for 1,2,3-triazole.*

8.3.2 Crystal Structure Data

Crystal Data for **7** $C_{46}H_{42}N_{12}O_7$ (*M* =874.91 g/mol): monoclinic, space group $P2_1/n$ (no. 14), a = 14.986(2) Å, b = 15.682(2) Å, c = 17.566(4) Å, β = 102.28(2)°, V = 4033.7(13) Å^3, Z = 4, T = 293(2) K, μ(MoKα) = 0.101 mm^{-1}, *Dcalc* = 1.441 g/cm^3, 21954 reflections measured (6.998° ≤ 2Θ ≤ 49.998°), 7088 unique (R_{int} = 0.1942, R_{sigma} = 0.2181) which were used in all calculations. The final R_1 was 0.1716 (I > 2σ(I)) and wR_2 was 0.4263 (all data).

Crystal Data for **I** $C_{64}H_{52}N_{12}O_{10}$ (*M* =1149.17 g/mol): monoclinic, space group $P2_1/n$ (no. 14), a = 16.5986(17) Å, b =7.3891(9) Å, c = 21.913(2) Å, β = 92.242(6)°, V = 2685.6(5) Å^3, Z = 4, T = 123.0 K, μ(CuKα) = 1.624 mm^{-1}, *Dcalc* = 2.842 g/cm^3, 25883 reflections measured (6.558° ≤ 2Θ ≤ 101.122°), 2659 unique (*R*int = 0.1248, Rsigma = 0.1294) which were used in all calculations. The final R_1 was 0.1377 (I > 2σ(I)) and wR_2 was 0.2215 (all data).

Crystal Data for **L** $C_{18.5}H_{16.75}N_{2.5}O_{2.25}$ (*M* =310.09 g/mol): monoclinic, space group $P2_1/c$ (no. 13), a = 17.8961(7) Å, b = 5.5991(2) Å, c = 32.2637(12) Å, β = 92.649(2)°, V = 3229.4(2) Å^3, Z = 8, T = 150.0 K, μ(CuKα) = 0.691 mm^{-1}, *Dcalc* = 1.276 g/cm^3, 46848 reflections measured (4.942° ≤ 2Θ ≤ 129.192°), 5399 unique (R_{int} = 0.0675, R_{sigma} = 0.0403) which were used in all calculations. The final R_1 was 0.0439 (I > 2σ(I)) and wR_2 was 0.1114 (all data).

Crystal Data for **8** $C_{30}H_{25}N_5O_3$ (*M* =503.55 g/mol): monoclinic, space group $C2/c$ (no. 15), a = 39.784(4) Å, b = 7.7732(7) Å, c = 15.8074(14) Å, β = 96.632(3)°, V = 4855.7(7) Å^3, Z = 8, T = 296.15 K, μ(MoKα) = 0.092 mm^{-1}, *Dcalc* = 1.378 g/cm^3, 9275 reflections measured (5.188° ≤ 2Θ ≤ 52.196°), 4686 unique (R_{int} = 0.0688, R_{sigma} = 0.1282) which were used in all calculations. The final R_1 was 0.2038 (I > 2σ(I)) and wR_2 was 0.4638 (all data).

8.3.3 Self-Assembly Titration Data

8.3.3.1 Self-Assembly Titration for 6

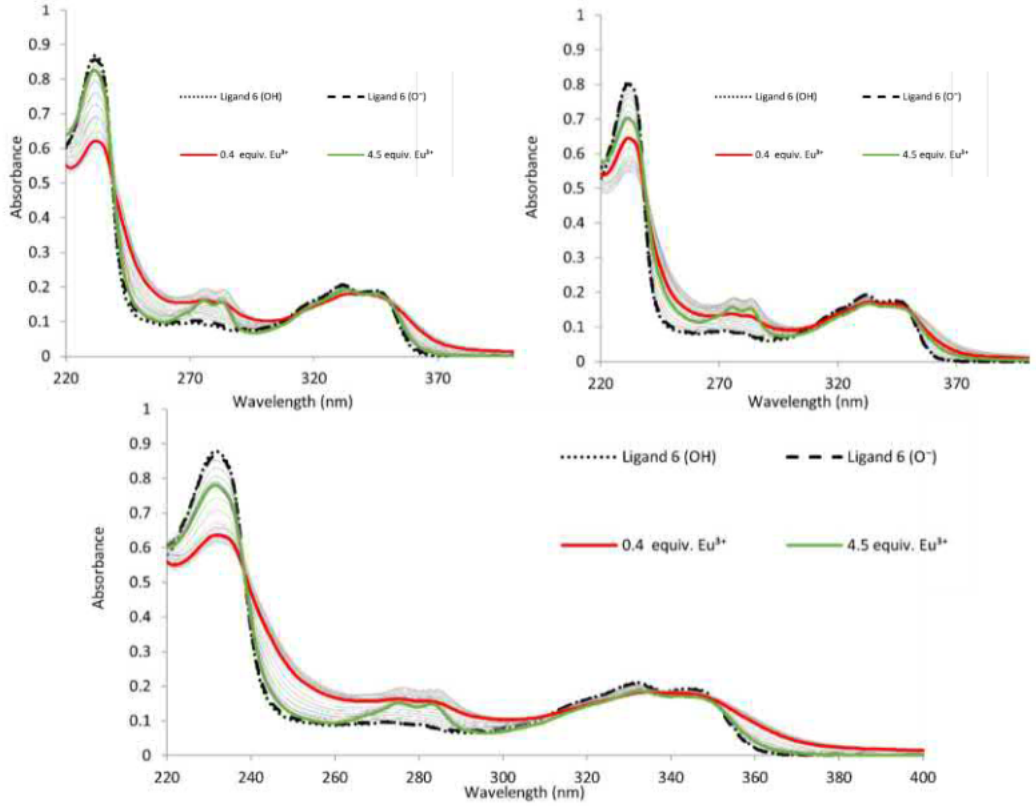

*Figure 8.3.54.. UV-visible absorption titration of **6** with $Eu(CF_3SO_3)_3$ 0 to 4.5 equivalents, done in triplicate (0.02 mM, MeOH)..*

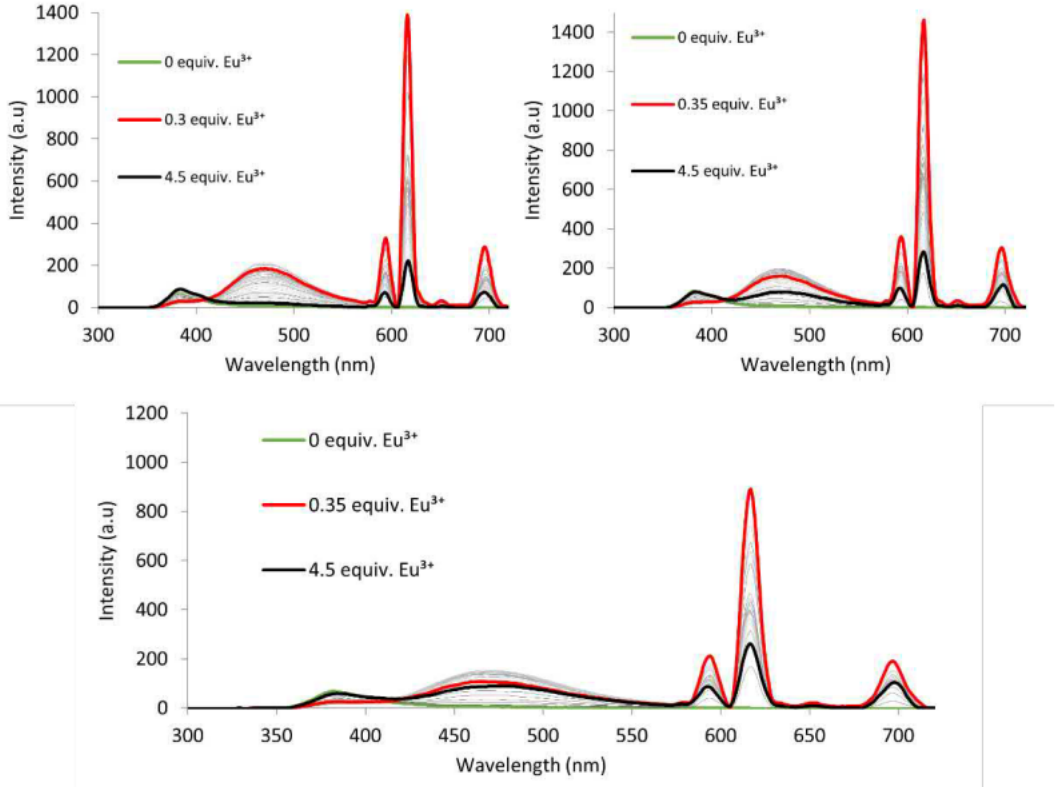

*Figure 8.3.55.. Fluorescence titration of **6** with $Eu(CF_3SO_3)_3$ 0 to 4.5 equivalents, done in triplicate (0.02 mM, MeOH)..*

8.3.3.2 Self-Assembly Titration for 7

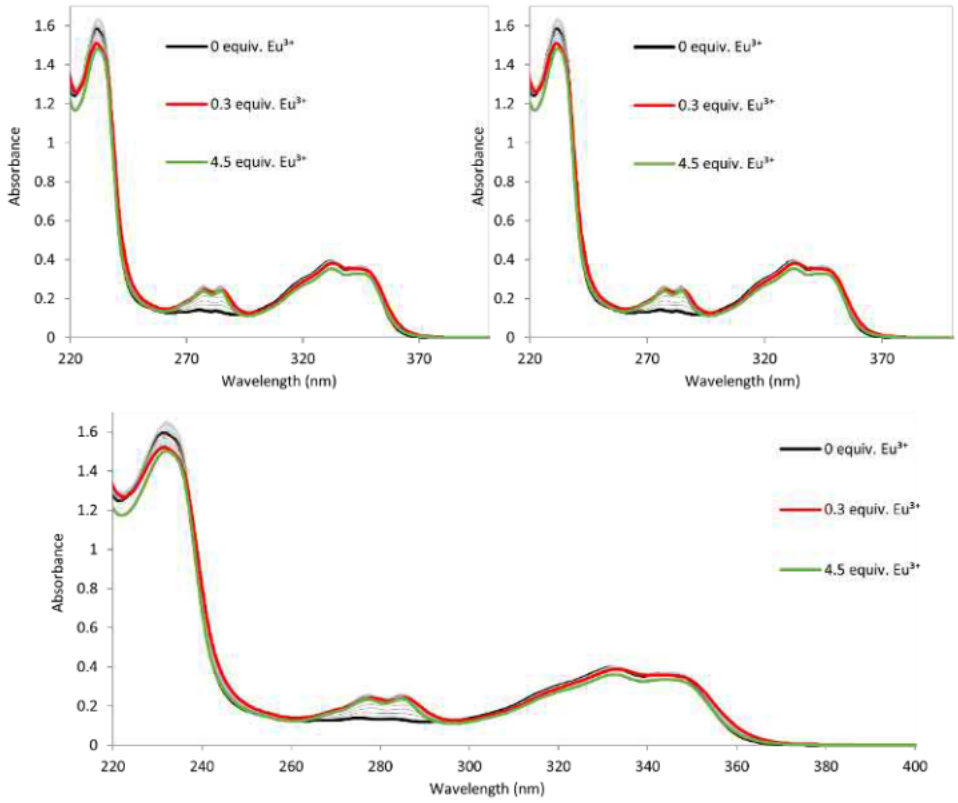

*Figure 8.3.56. UV-visible absorption titration of **7** with Eu(CF₃SO₃)₃ 0 to 4.5 equivalents, done in triplicate (0.02 mM, MeOH).*

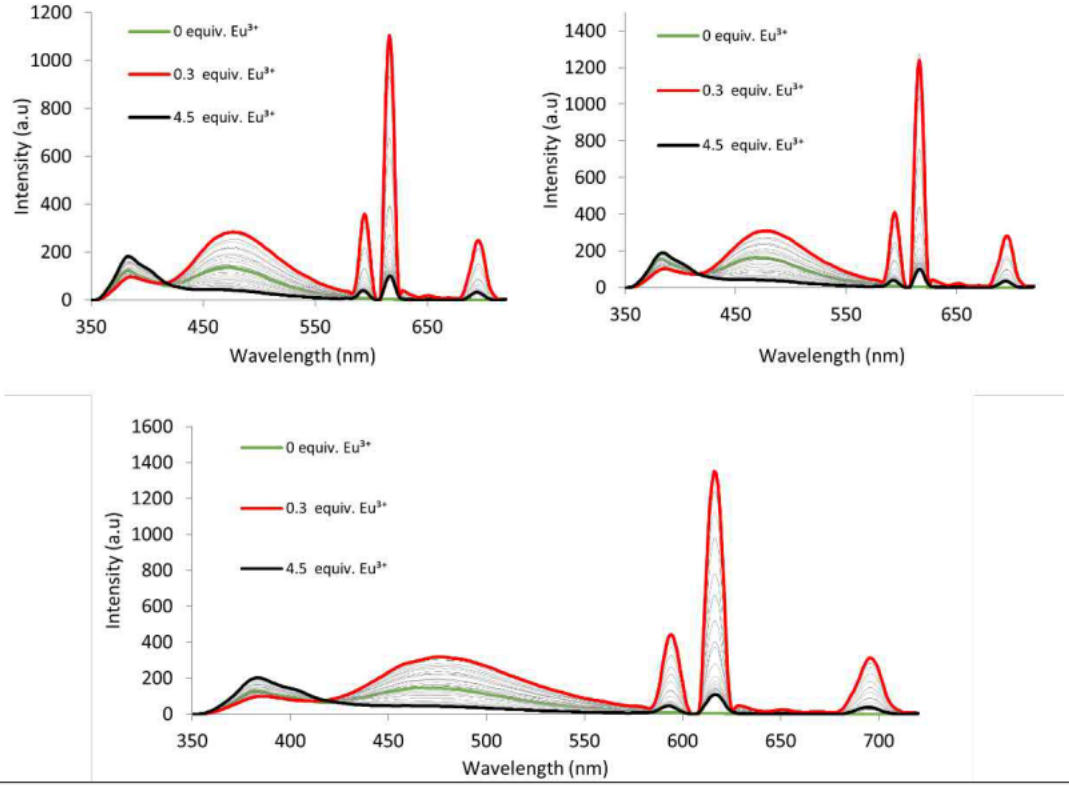

*Figure 8.3.57. Fluorescence titration of **7** with Eu(CF₃SO₃)₃ 0 to 4.5 equivalents, done in triplicate (0.02 mM, MeOH).*

8.3.3.3 Self-Assembly Titration for 8

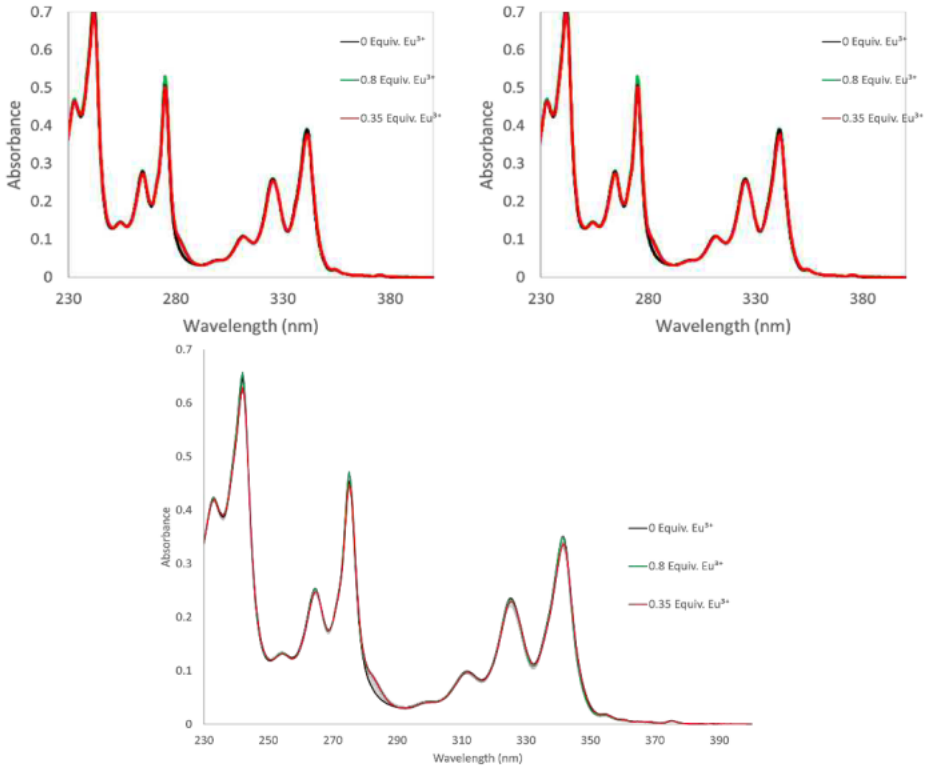

*Figure 8.3.58.. UV-visible absorption titration of **8** with $Eu(CF_3SO_3)_3$ 0 to 4.5 equivalents,. done in triplicate (0.02 mM,. MeOH)..*

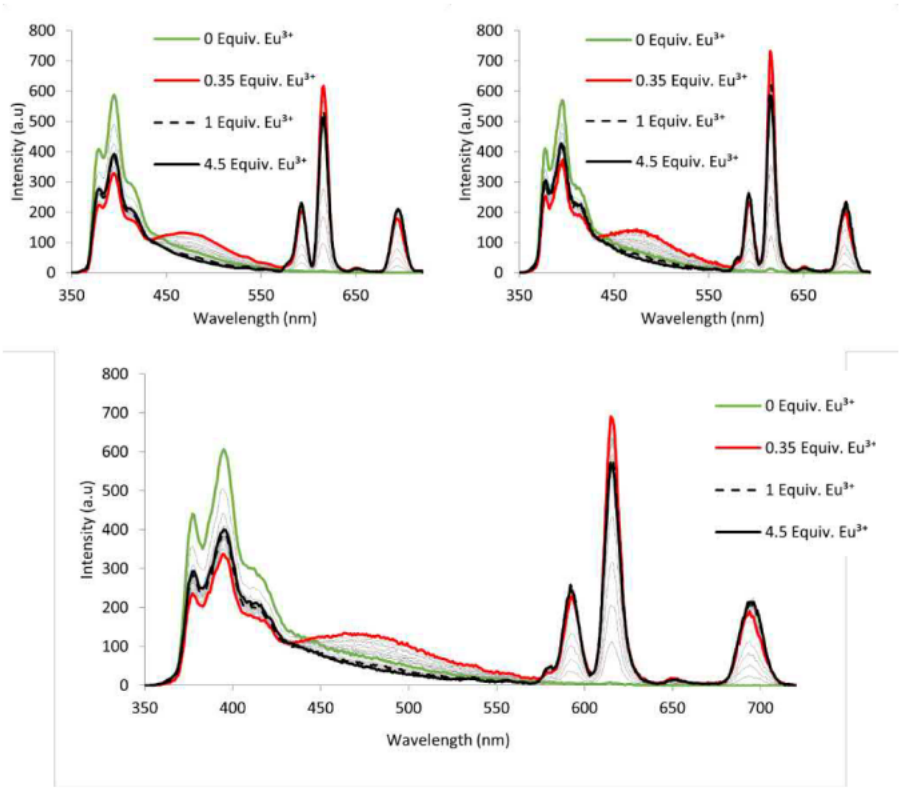

*Figure 8.3.59.. Fluorescence titration of **8** with $Eu(CF_3SO_3)_3$ 0 to 4.5 equivalents,. done in triplicate (0.02 mM,. MeOH)..*

8.3.4 Lanthanide Complex Data

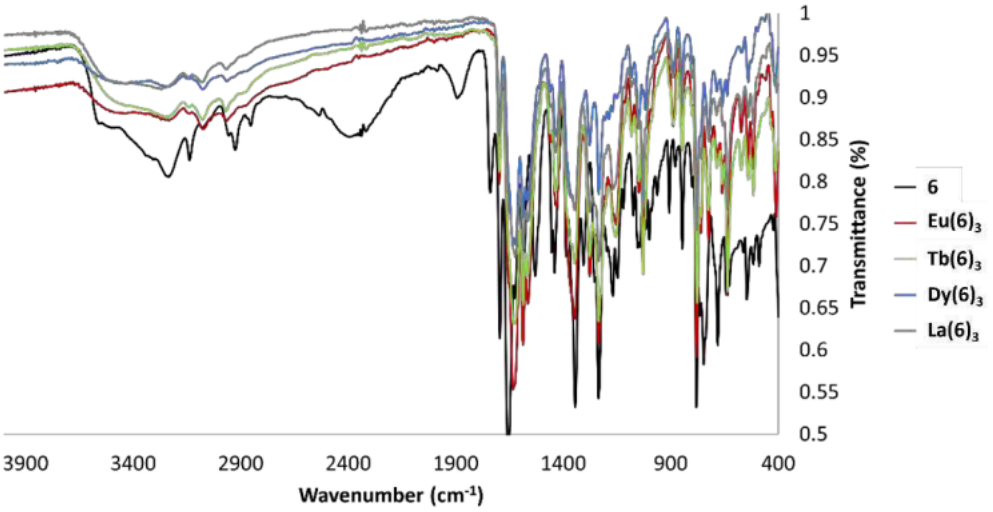

Figure. 8.3.60.. IR. spectra. of. ***6****. and. Ln(****6****)3. where. Ln. =. Eu3+,. Tb3+,. Dy3+,. and. La3+.. Shifts. can. be. seen. upon. complexation,. with. the. disappearance. of. the. COOH. at. 1739. cm.-1,. upfield. shift. of. CONH. from. 1656. cm-1. to. 1632. cm-1. and. no. shifts. noted. for. the. C=O. associated with. the. 1,8-naphthalimide. at. 1695. cm.-1..*

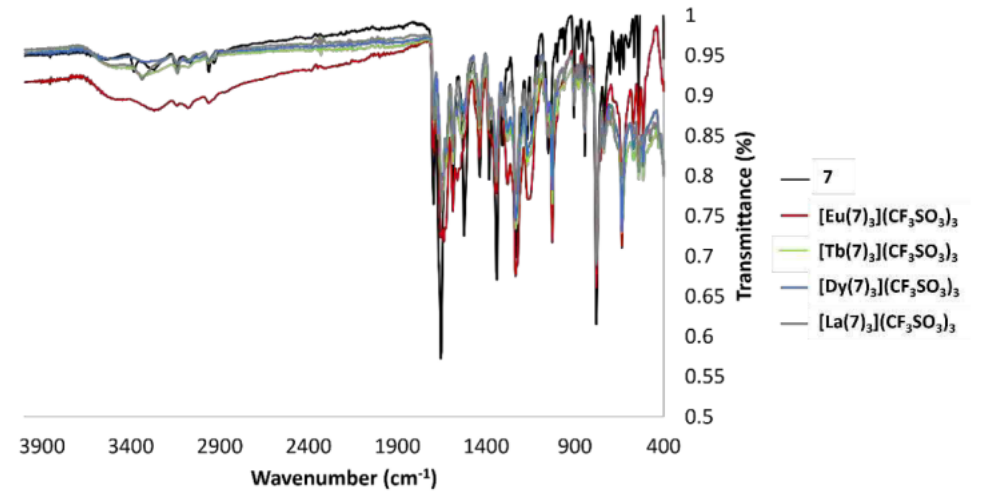

Figure. 8.3.61.. IR. spectra. of. ***7****. and. [Ln(****7****)3](CF3SO3)3. where. Ln. =. Eu3+,. Tb3+,. Dy3+,. and. La3+.. Shifts. can. be. seen. upon. complexation,. upfield shift. of. CONH. from. 1652. cm-1. to. 1638. cm-1. and. no. shifts. noted. for. the. C=O. associated. with. the. 1,8-naphthalimide. 1697. cm.-1.. Shifts for. triflate. anion. are. also. noted. in. the. complexes. and. not. the. ligand. with. 1281. cm.-1 assigned. to. SO3. and. 1168. cm-1. assigned. to. CF3.*

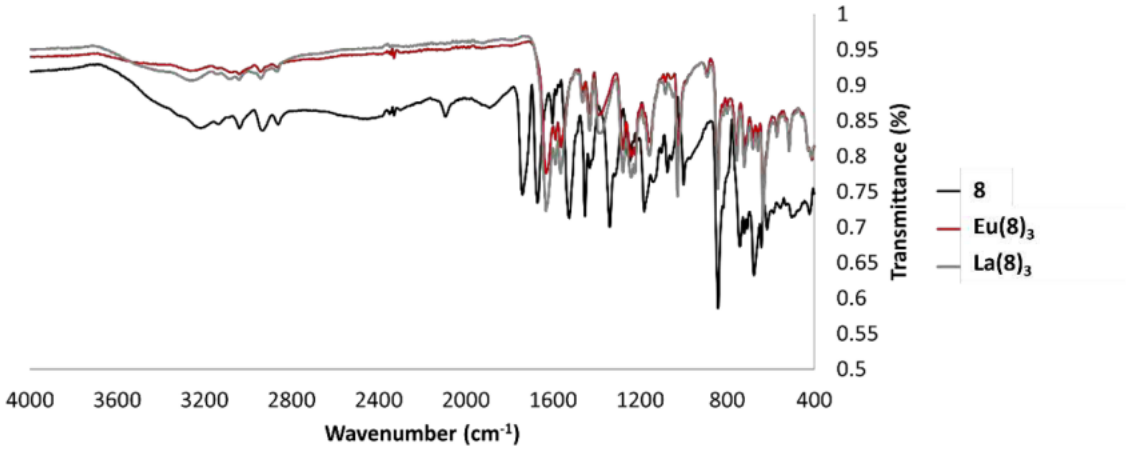

Figure. 8.3.62.. IR. spectra. of. ***3****. and. Ln(****3****)3 where. Ln. =. Eu3+. and. La3+.. Shifts. can. be. seen. upon. complexation,. with. the. disappearance. of. the COOH. at. 1742. cm.-1,. upfield. shift. of. CONH. from. 1672. cm-1. to. 1634. cm-1..*

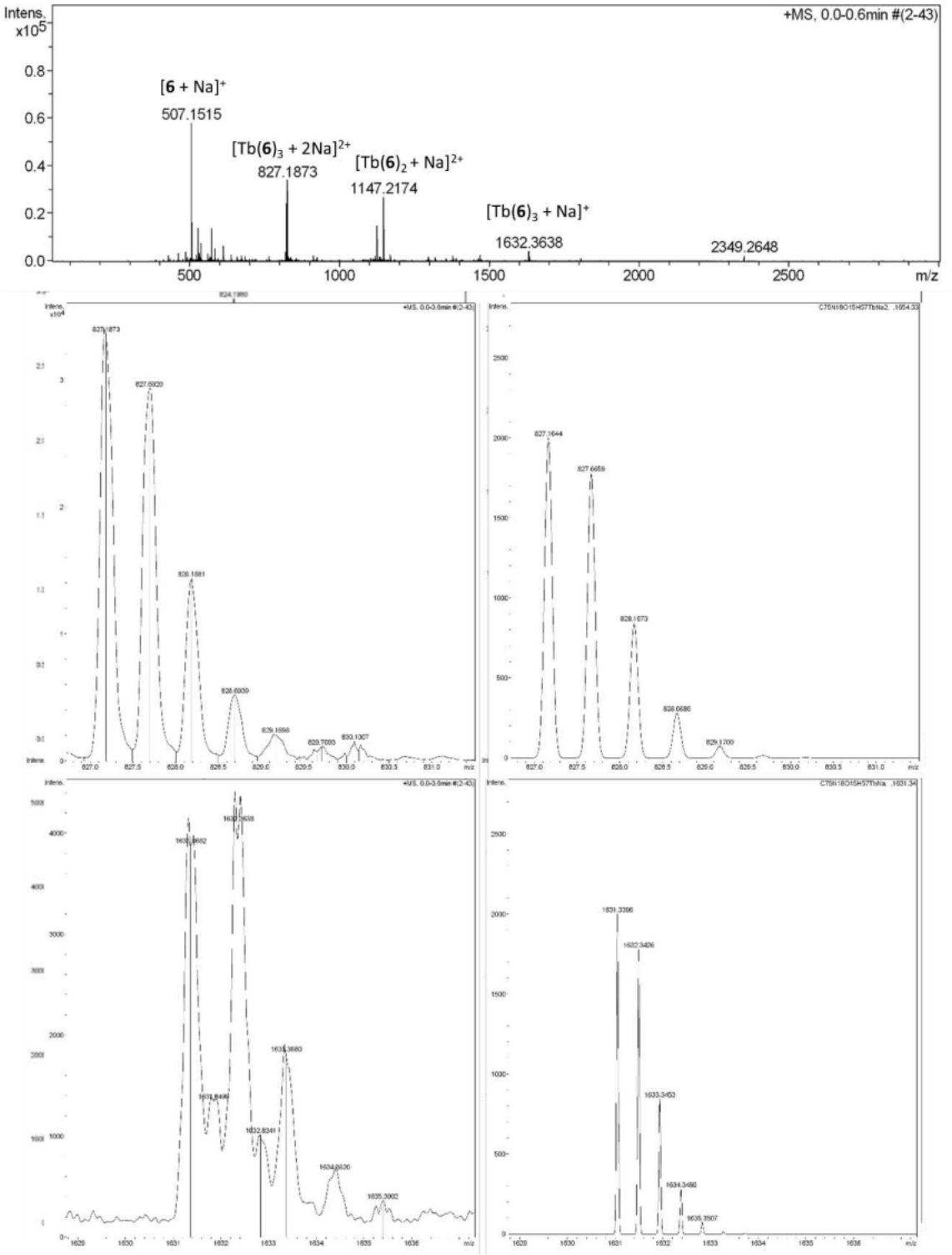

*Figure. 8.3.63.. HRMS. Eu(**6**)$_3$.. (Top). Full spectrum.. (Middle. Left). (HRMS m/z = 824.1980 [Eu(**6**)$_3$ + 2Na]$^{2+}$. (Middle right) Calc. for (C$_{75}$H$_{57}$N$_{18}$O$_{15}$EuNa$_2$)$^{2+}$, 824.1630.. (Bottom. left). HRMS m/z = 1625.3545 [Eu(**6**)$_3$ + Na]$^+$. (Bottom right) Calc. for (C$_{75}$H$_{57}$N$_{18}$O$_{15}$EuNa)$^+$, 1625.3367..*

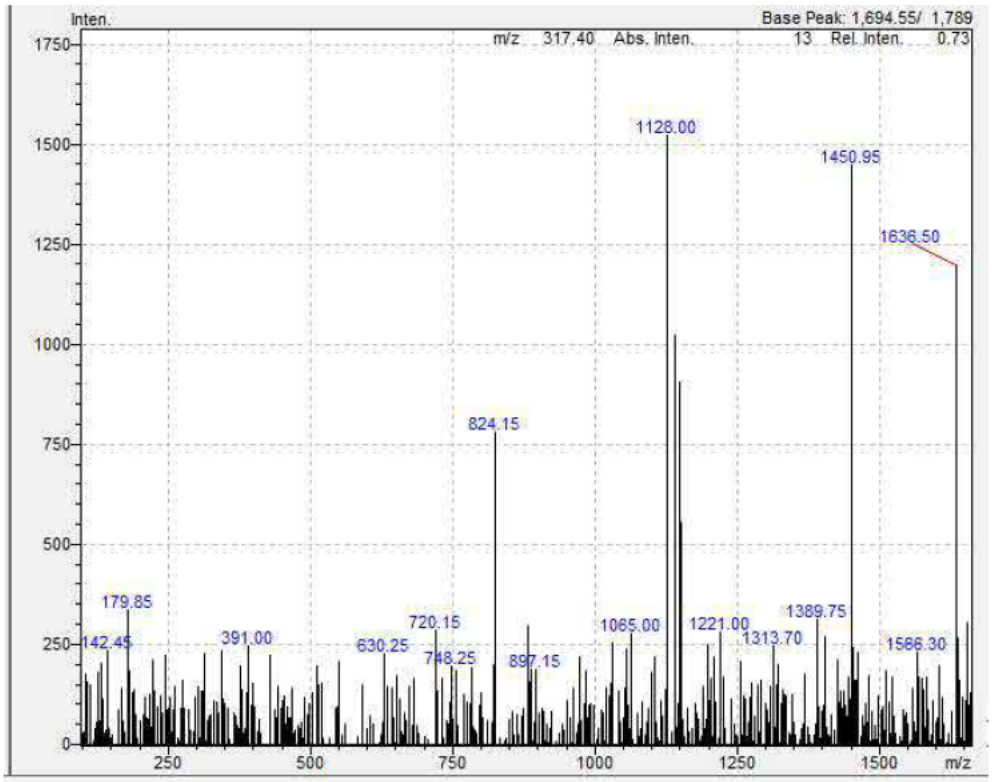

*Figure 8.3.64.. LRMS m/z = 824.15 [Dy(**6**)$_3$ + 2Na]$^{2+}$ Calc. for ($C_{75}H_{57}N_{18}O_{15}DyNa_2$)$^{2+}$, 824.16,. 1636.50 [Dy(**6**)$_3$ + Na]$^+$. Calc. for ($C_{75}H_{57}N_{18}O_{15}DyNa$)$^+$, 1635.85..*

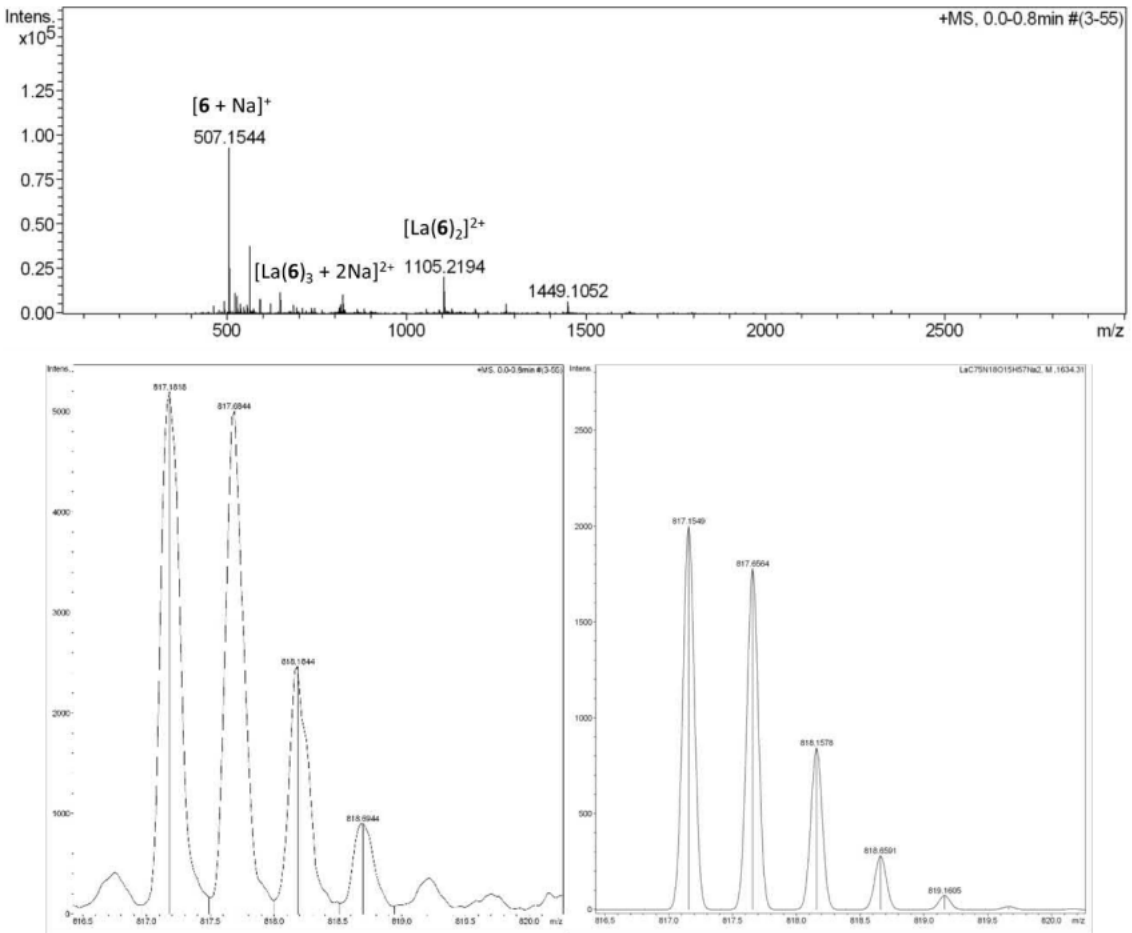

*Figure 8.3.65.. HRMS La(**6**)$_3$.. (Top). Full spectrum.. (Bottom left). HRMS m/z = 817.1818 [La(**6**)$_3$ + 2Na]$^{2+}$. (Bottom right) Calc. for ($C_{75}H_{57}N_{18}O_{15}LaNa_2$)$^{2+}$, 817.1549..*

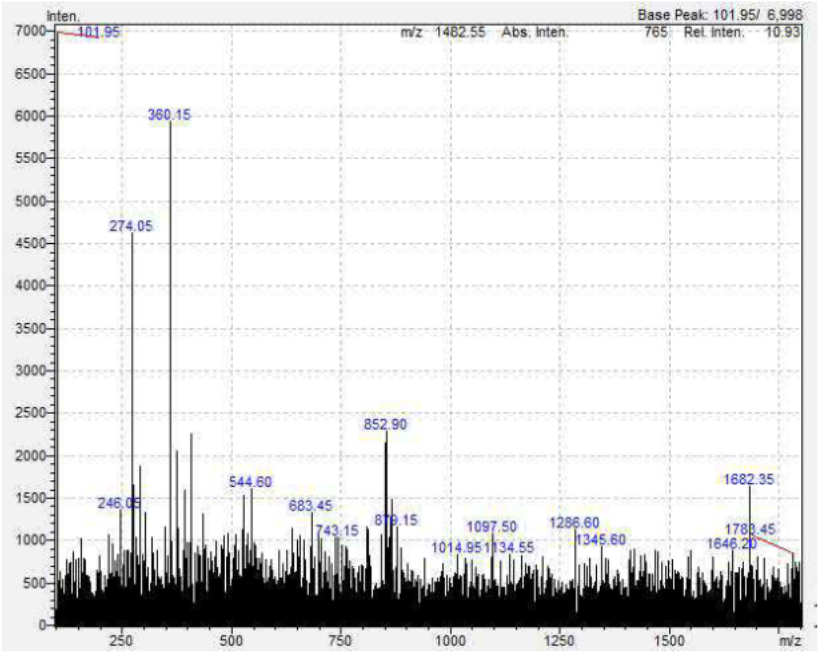

*Figure 8.3.66.. LRMS m/z = 852.80 [Eu(**8**)$_3$ + 2Na]$^{2+}$ Calc. for ($C_{90}H_{72}N_{15}O_9EuNa_2$)$^{2+}$, 852.90 and 1682.35 [Eu(**8**)$_3$ + Na]$^+$. Calc. for ($C_{90}H_{72}N_{15}O_9EuNa$)$^+$, 1682.58..*

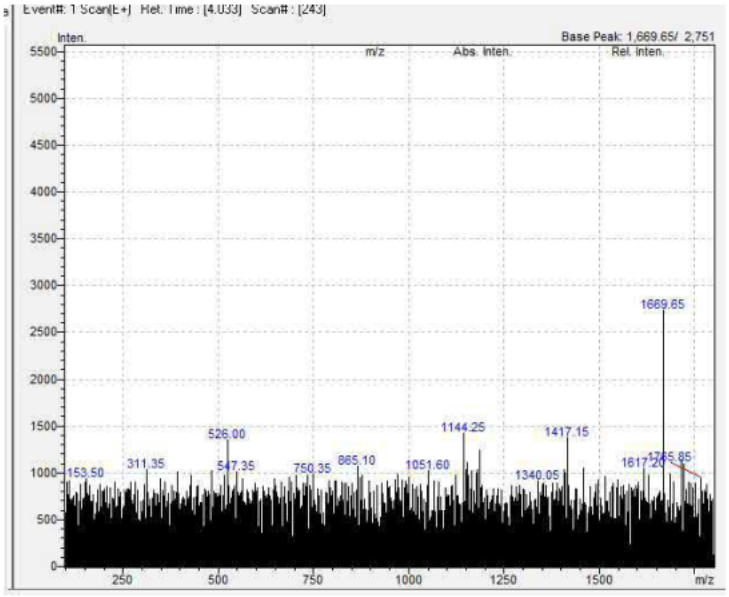

*Figure 8.3.67.. LRMS m/z = 1669.65 [La(**8**)$_3$ + Na]$^+$ Calc. for ($C_{90}H_{72}N_{15}O_9LaNa$)$^+$ 1669.52..*

8.3.5 Lanthanide and Chromophore Photophysics

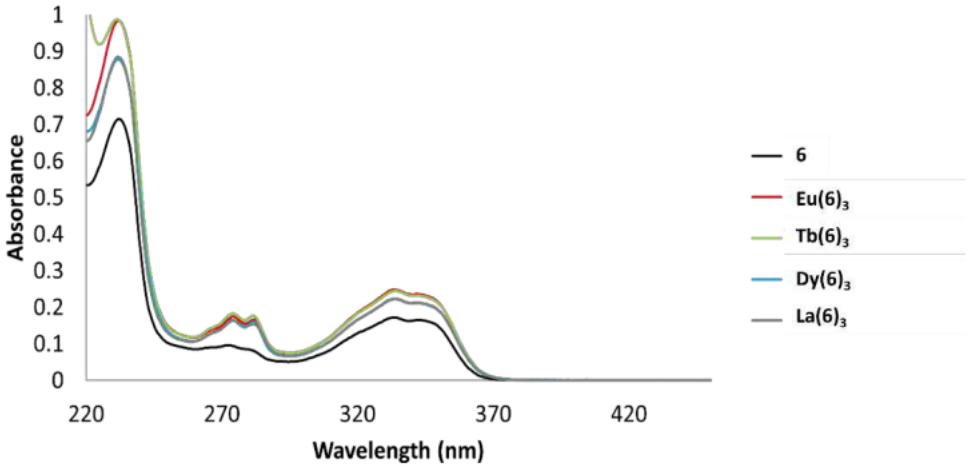

Figure 8.3.68.. UV-visible absorption of **6** *and Ln(***6***)₃ where Ln = Eu³⁺, Tb³⁺, Dy³⁺ and La³⁺ (0.01 mM, MeOH).. Alongside an absorbance increase associated with 3 ligands, there is also a classical slight red shift of the pyridyl broad shoulder π-π* transition at 270-280 nm associated with lanthanide coordination..*

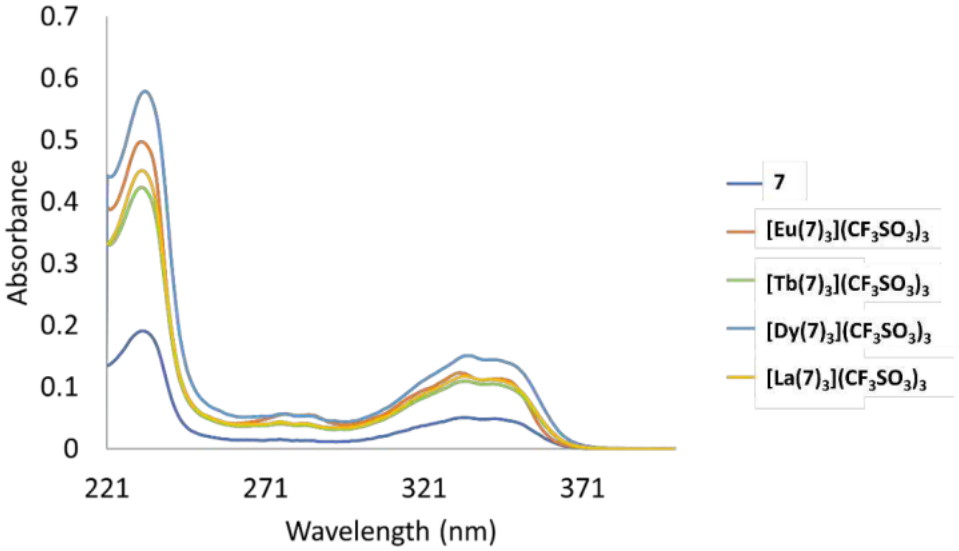

Figure 8.3.69.. UV-visible absorption of **7** *and Ln(***7***)₃](CF₃SO₃)₃ where Ln = Eu³⁺, Tb³⁺, Dy³⁺ and La³⁺ (0.002 mM, MeOH)..*

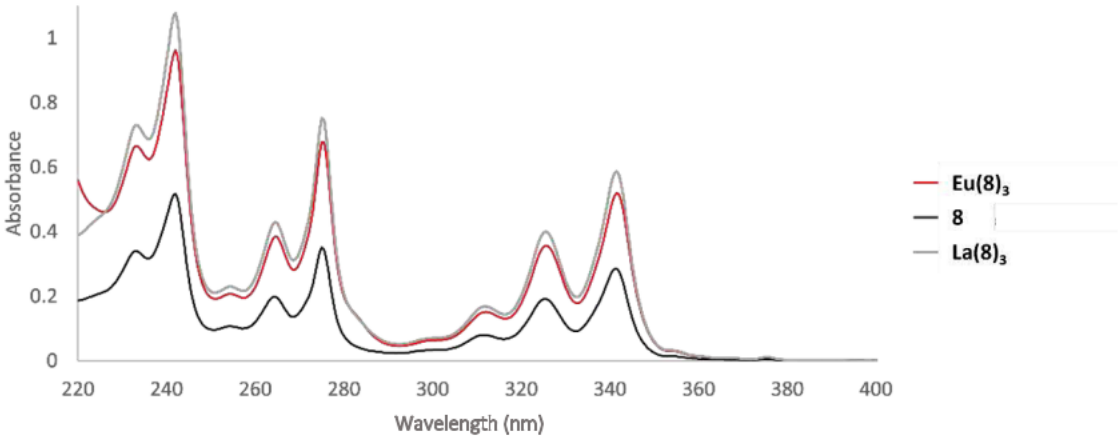

Figure 8.3.70.. UV-visible absorption of **8** *and Ln(***8***)₃ where Ln = Eu³⁺, and La³⁺ (0.005 mM, MeOH)..*

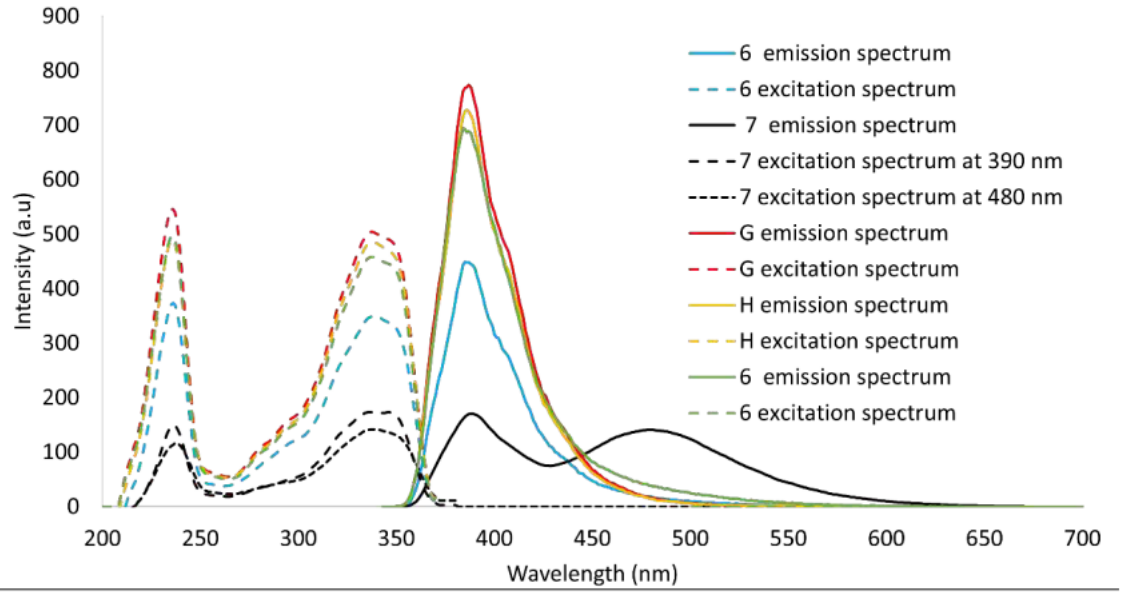

Figure 8.3.71. 1,8-Naphthalimide ligand centred emission.

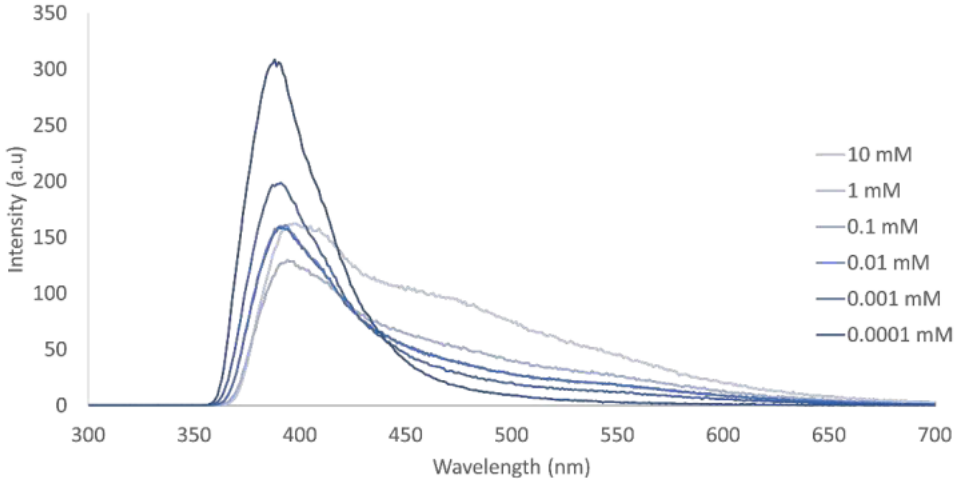

*Figure 8.3.72. Concentration study of **6** in MeOH excited at 340 nm.*

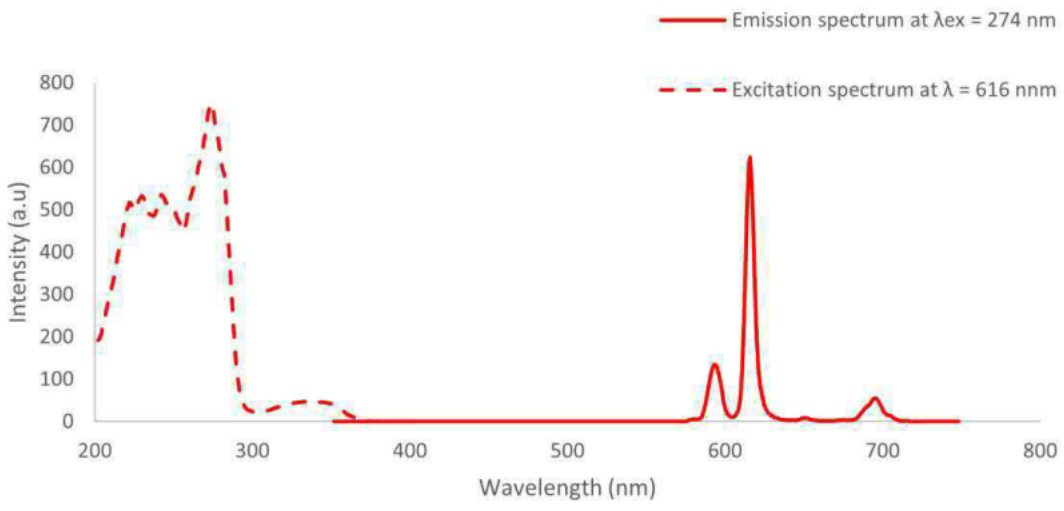

*Figure 8.3.73. Eu(**6**)$_3$ Phosphorescence spectra (0.01 mM, MeOH).*

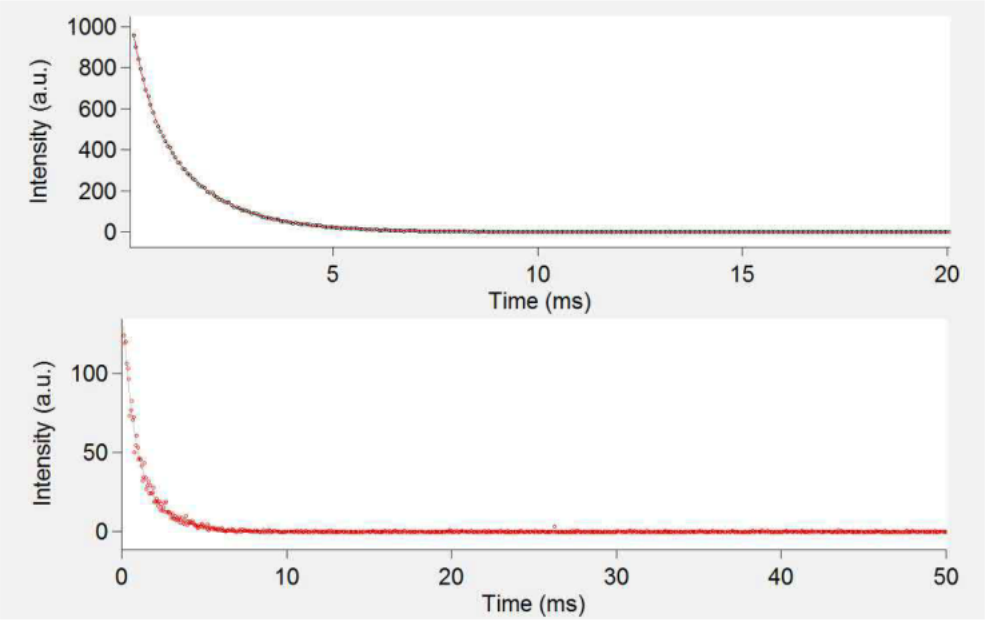

*Figure 8.3.74.. Lifetime of Eu(**6**)$_3$ complex (0.01 mmol,. MeOH) fit with single exponential (Top 616 nm and bottom 594 nm)..*

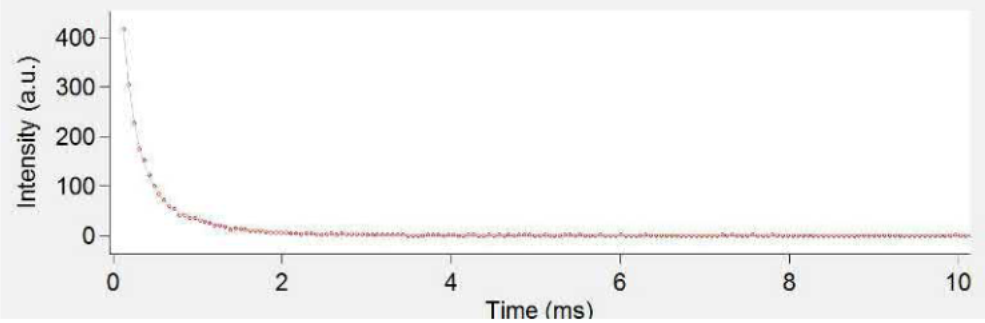

*Figure 8.3.75.. Lifetime of Tb(**6**)$_3$ complex (0.01 mmol,. MeOH) fit with single exponential (545 nm)..*

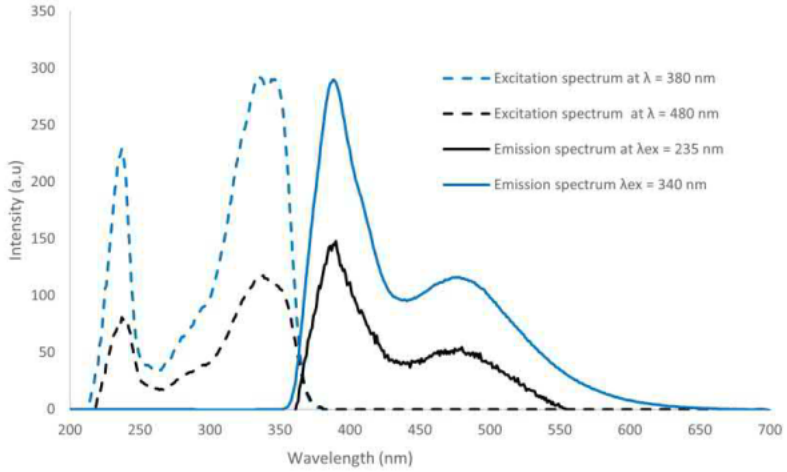

*Figure 8.3.76.. La(**6**)$_3$ fluorescence spectra (0.01 mM,. MeOH)..*

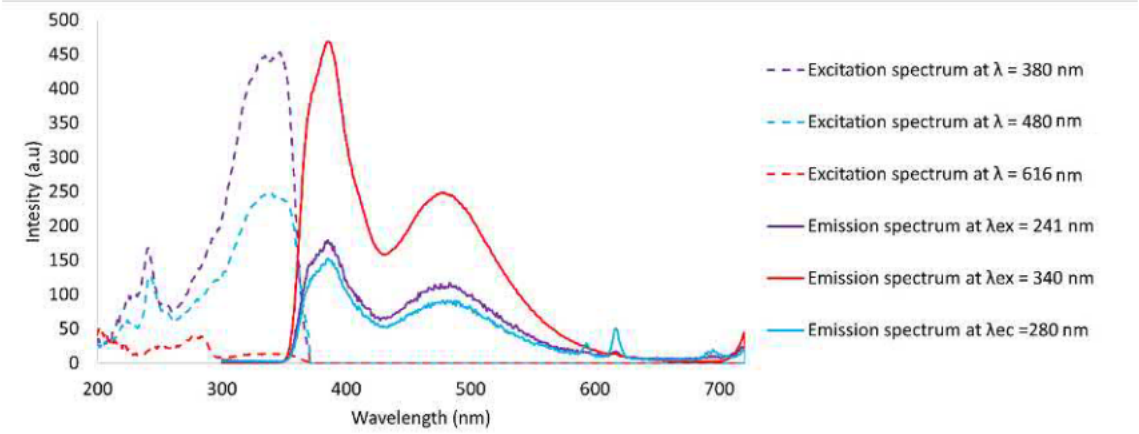

*Figure 8.3.77.. [Eu(**7**)$_3$](CF$_3$SO$_3$)$_3$ Fluorescence spectra in MeOH 0.01 mmol..*

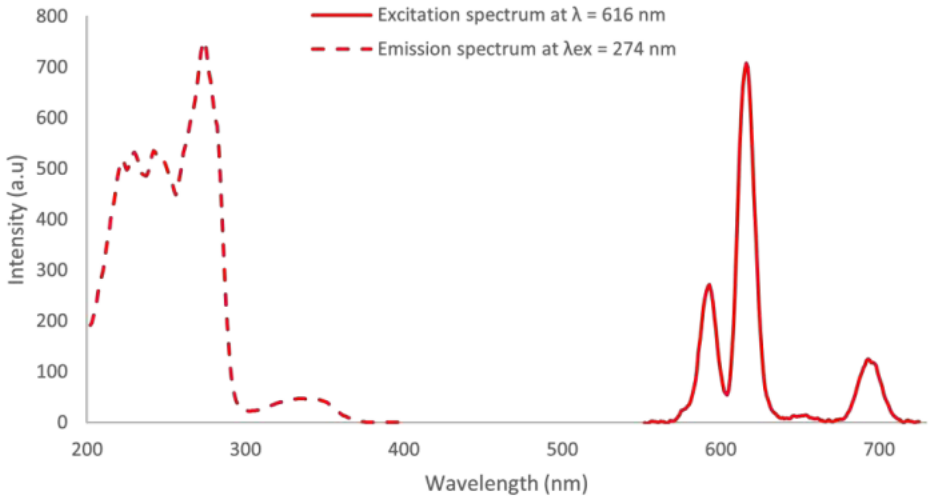

*Figure 8.3.78.. [Eu(**7**)$_3$](CF$_3$SO$_3$)$_3$ Phosphorescence spectra (0.01 mM, MeOH)..*

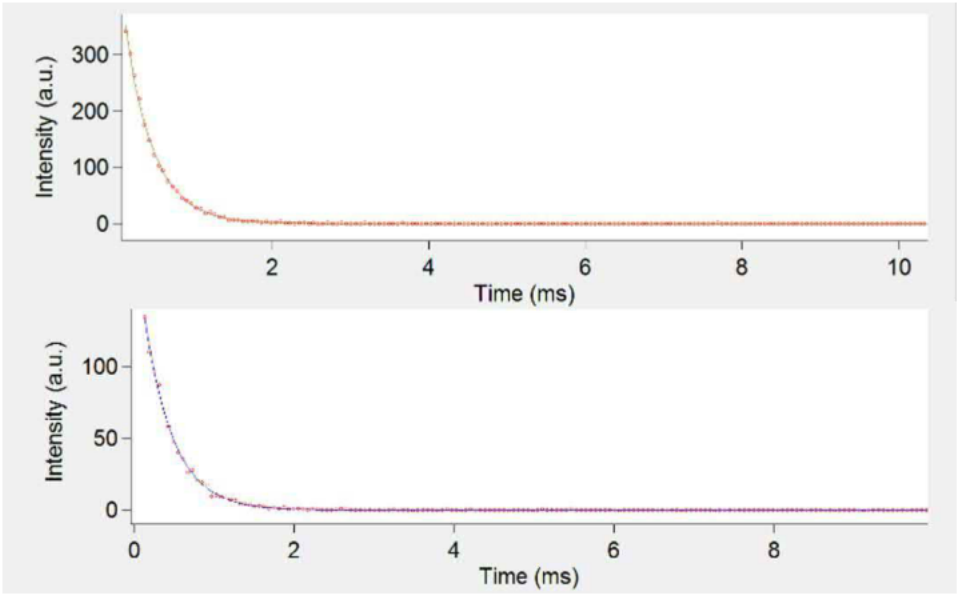

*Figure 8.3.79.. Lifetime of [Eu(**7**)$_3$](CF$_3$SO$_3$)$_3$ complex (0.01 mM, MeOH) fit with single exponential (Top 616 nm and bottom 594 nm)..*

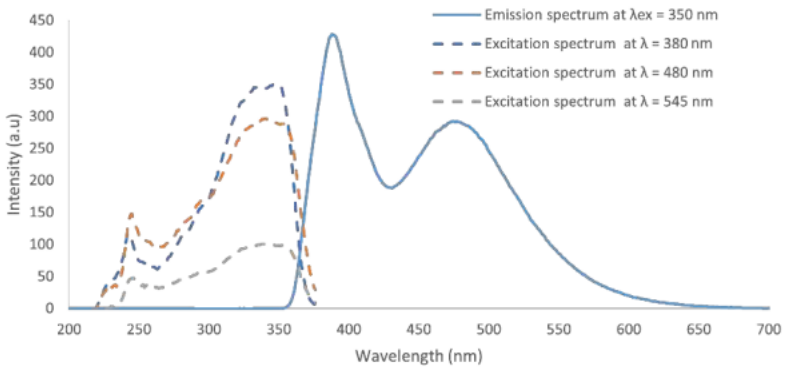

*Figure 8.3.80.. Tb(**7**)$_3$](CF$_3$SO$_3$)$_3$ Fluorescence spectra (0.01 mM, MeOH)..*

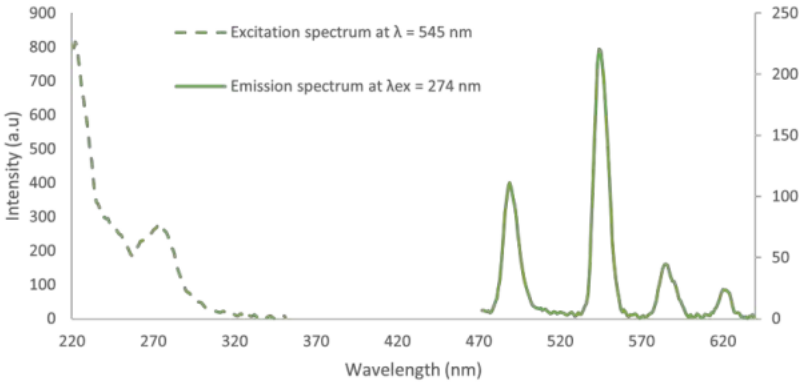

*Figure 8.3.81.. Tb(**7**)$_3$](CF$_3$SO$_3$)$_3$ Phosphorescence spectra (. 0.01 mM, MeOH)..*

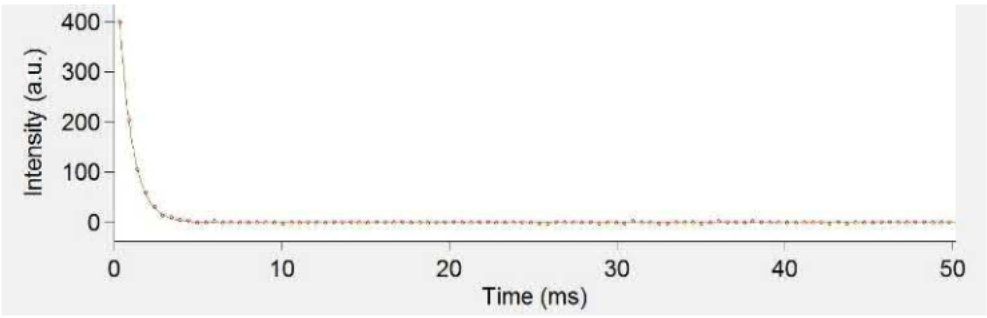

*Figure 8.3.82.. Lifetime of Tb(**7**)$_3$](CF$_3$SO$_3$)$_3$ complex (0.01 mM, MeOH) fit with single exponential..*

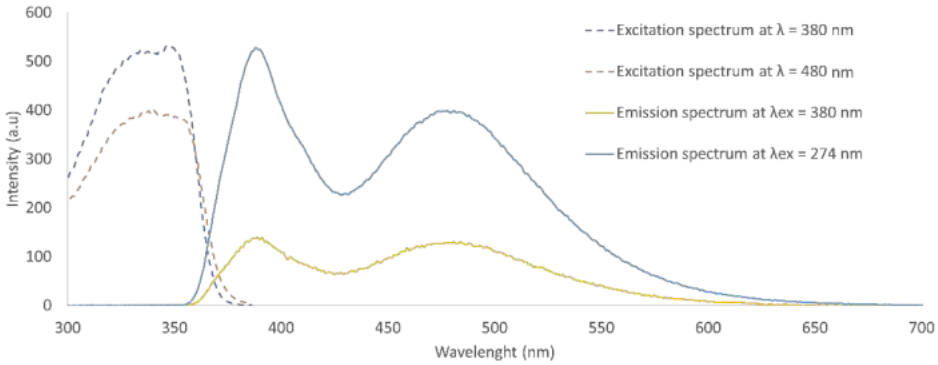

*Figure 8.3.83.. Dy(**7**)$_3$](CF$_3$SO$_3$)$_3$ Fluorescence spectra (0.01 mM, MeOH)..*

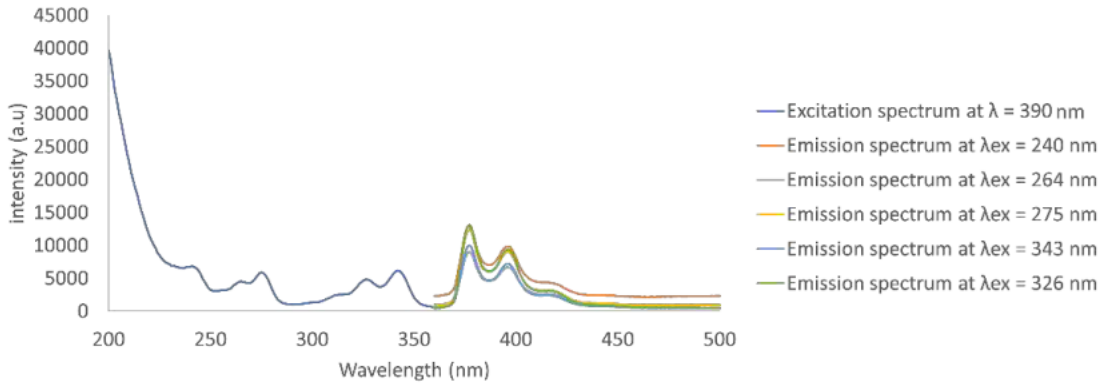

Figure 8.3.84. ***8*** *Fluorescence spectra (0.01 mM, MeOH).*

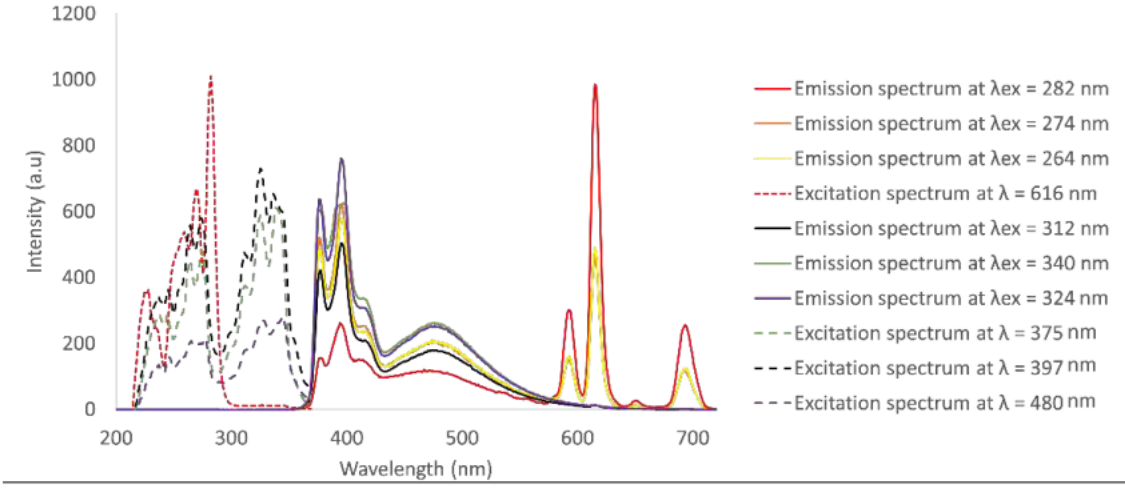

Figure 8.3.85. $Eu(\mathbf{8})_3$ *Fluorescence spectra (0.01 mM, MeOH).*

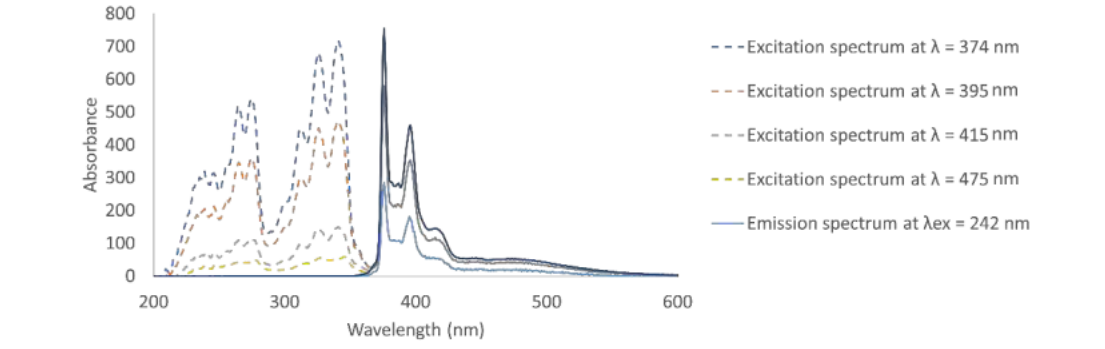

Figure 8.3.86. $La(\mathbf{8})_3$ *Fluorescence spectra. (0.01 mM, MeOH).*

8.3.5.1 Lifetimes

*Table 8.3.1 Single lifetimes of Eu(**6**)$_3$, [Eu(**7**)$_3$](CF$_3$SO$_3$)$_3$, Tb(**6**)$_3$, and [Tb(**7**)$_3$](CF$_3$SO$_3$)$_3$ complexes in solution (0.01 mmol).*

Complex	Single Exponential	Average (ms)
Eu(**6**)$_3$ solution MeOH ($^5D_0 \rightarrow {}^7F_2$)	1.177	1.175
	1.168	
	1.179	
Eu(**6**)$_3$ solution MeOH ($^5D_0 \rightarrow {}^7F_1$)	1.055	1.059
	1.063	
	1.059	
Tb(**6**)$_3$ solution MeCN ($^5D_4 \rightarrow {}^7F_5$)	0.275	0.281
	0.275	
	0.294	
[Eu(**7**)$_3$](CF$_3$SO$_3$)$_3$ solution MeOH ($^5D_0 \rightarrow {}^7F_2$)	0.359	0.363
	0.360	
	0.369	
[Tb(**7**)$_3$](CF$_3$SO$_3$)$_3$ solution MeOH ($^5D_4 \rightarrow {}^7F_5$)	0.807	0.794
	0.793	
	0.781	

8.3.5.2 Quantum Yield

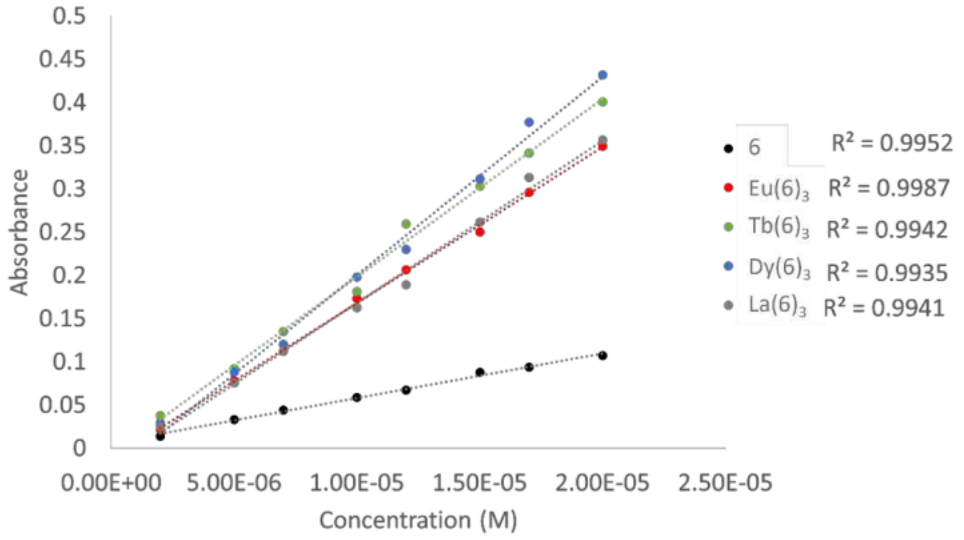

*Figure 8.3.87. Concentration vs absorbance for **6** and associated lanthanide complexes, in MeOH.*

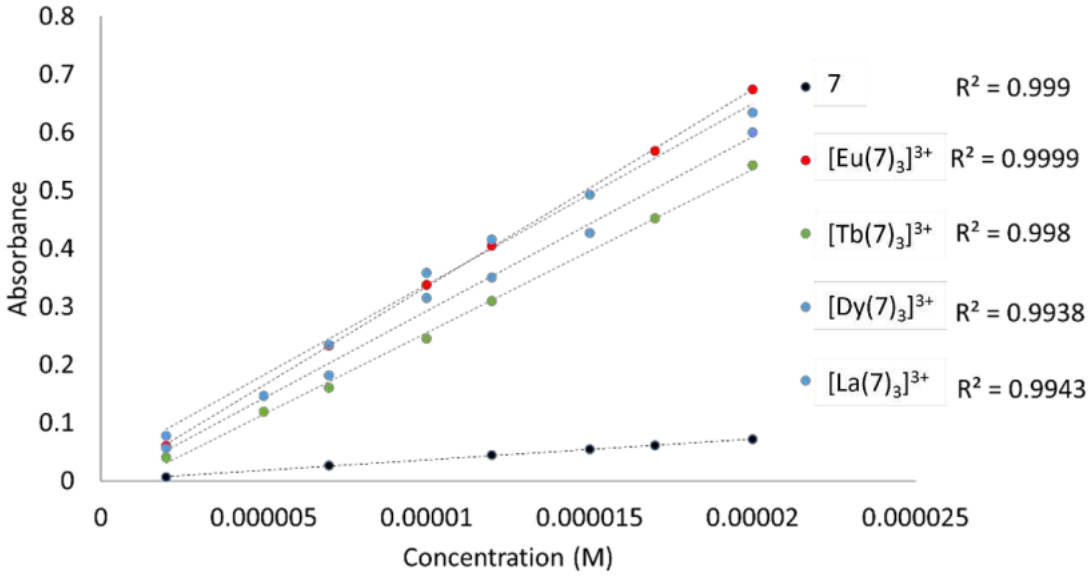

*Figure 8.3.88.. Concentration vs. absorbance for **7** and associated lanthanide complexes, in MeOH..*

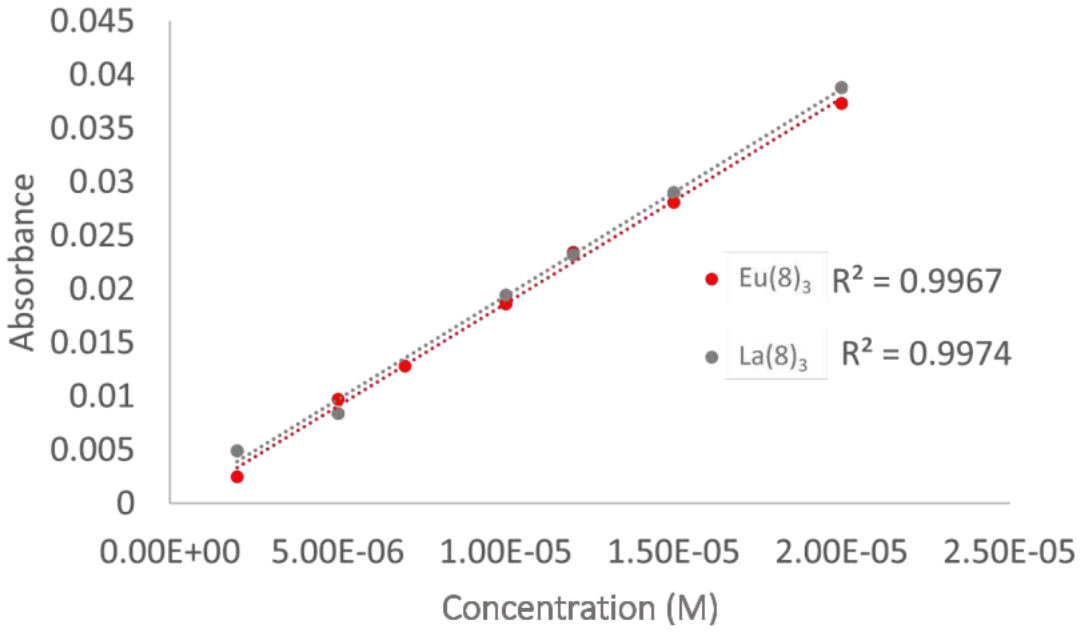

*Figure 8.3.89.. Concentration vs. absorbance for **8** and associated lanthanide complexes, in MeOH..*

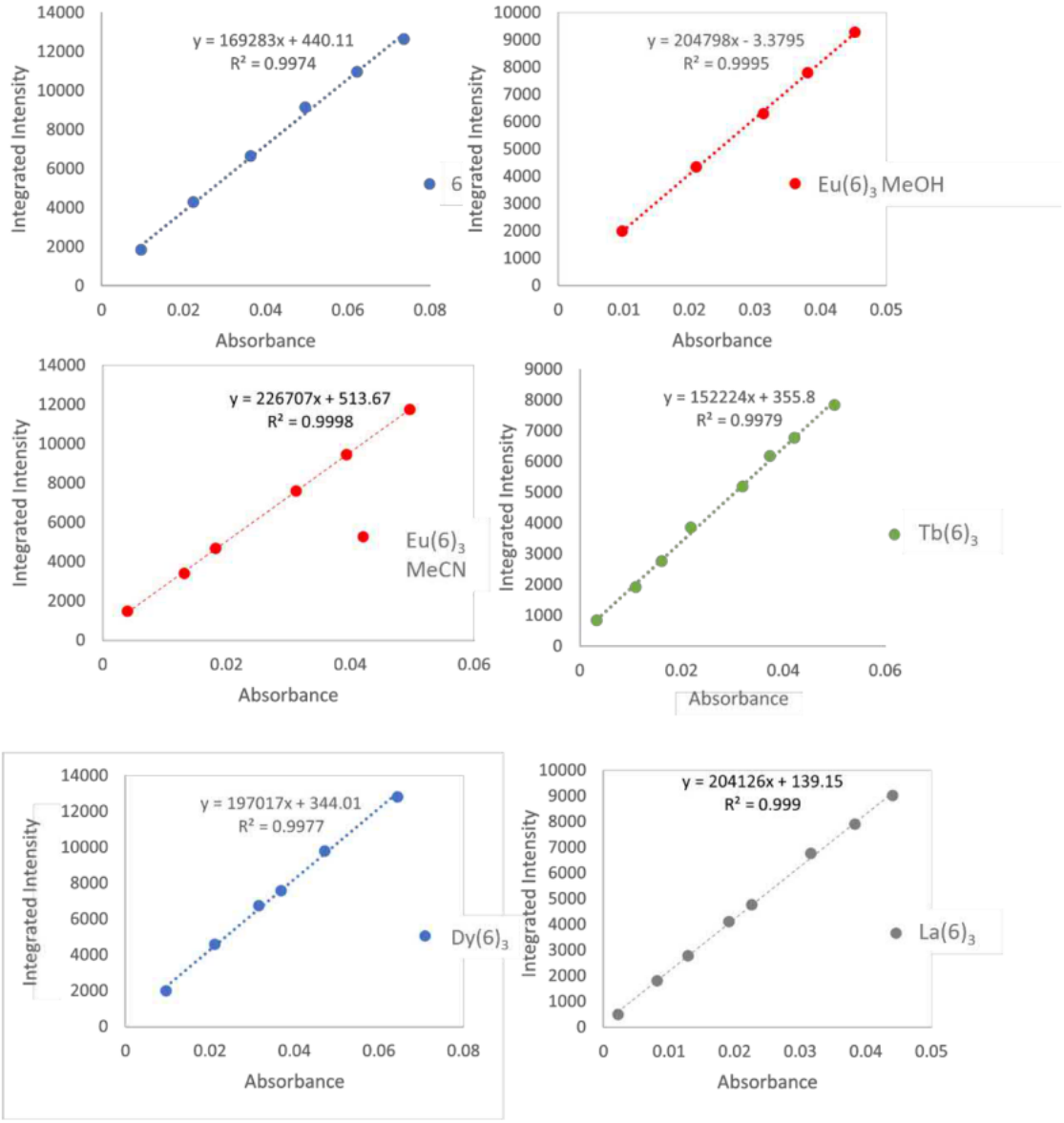

*Figure 8.3.90. Absorbance vs integrated intensity (organic chromophore emission) of **6** and associated lanthanide complexes Ln(**6**)$_3$ in MeOH (and MeCN for Eu(**6**)$_3$), 1.5 and 3 nm excitation and emission widths.*

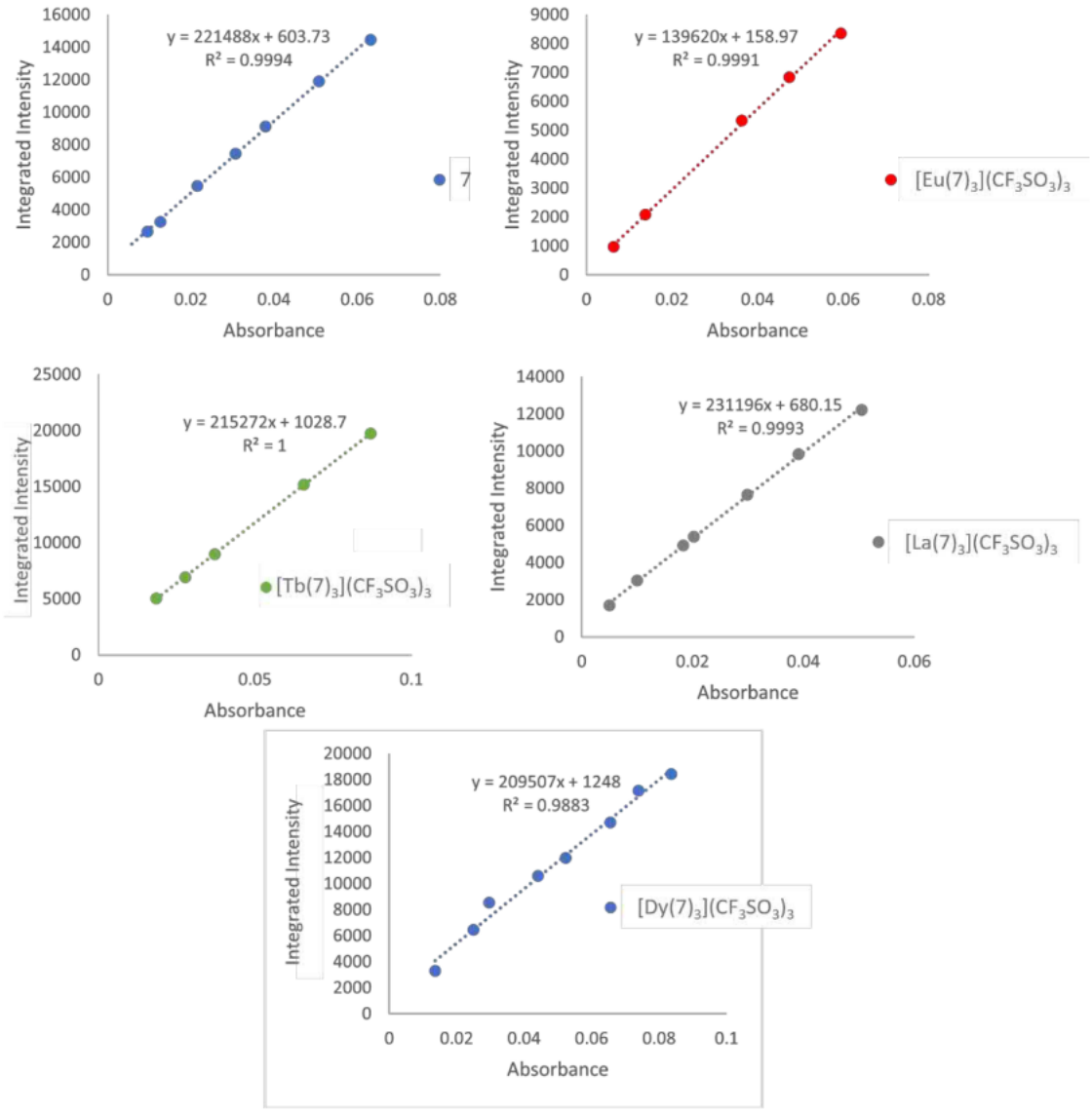

Figure. 8.3.91.. Absorbance. vs. integrated. intensity. (organic. chromophore. emission). of. ***7****. and. associated. lanthanide. complexes [Ln(****7****)3](CF3SO3)3. in. MeOH. ,. 1.5. and. 3. nm. excitation. and. emission. widths. ..*

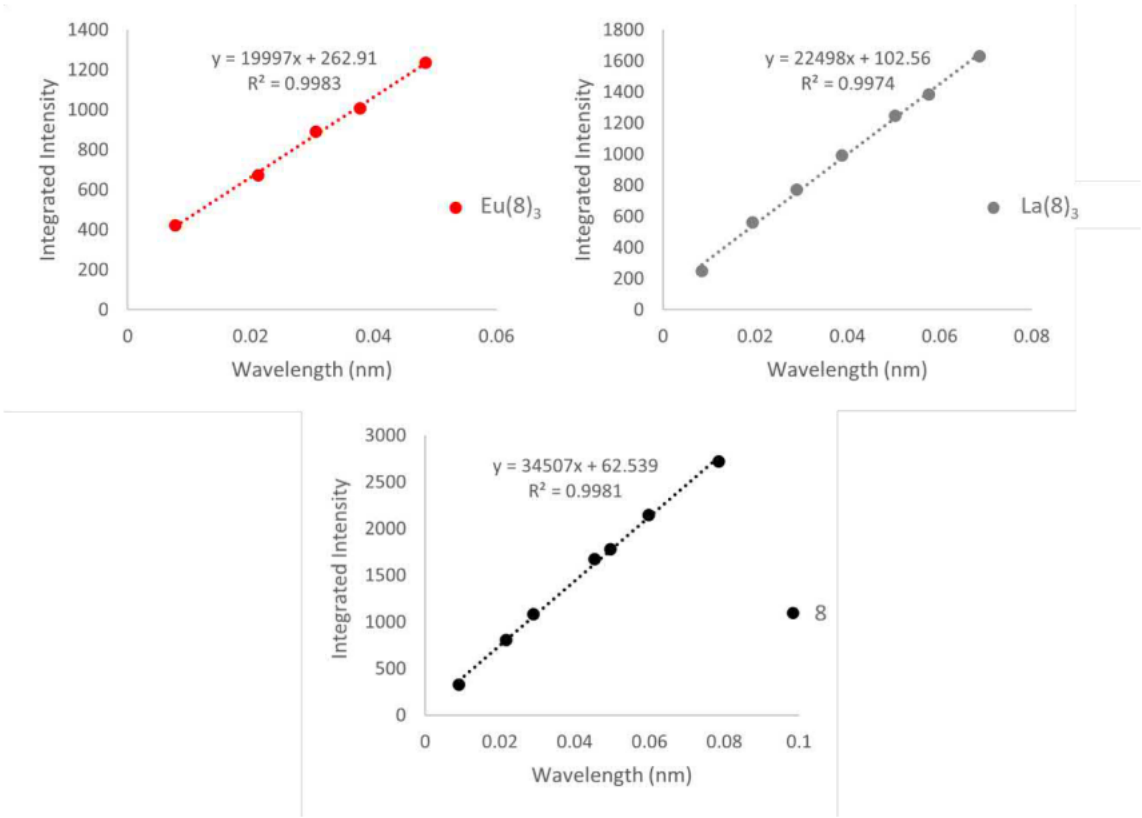

*Figure.8.3.92..Absorbance.vs.integrated.intensity.(organic.chromophore.emission).of.**8**.and.associated.lanthanide.complexes.Ln(**8**)₃.in MeOH,.1.5.and.3.nm.excitation.and.emission.widths.…*

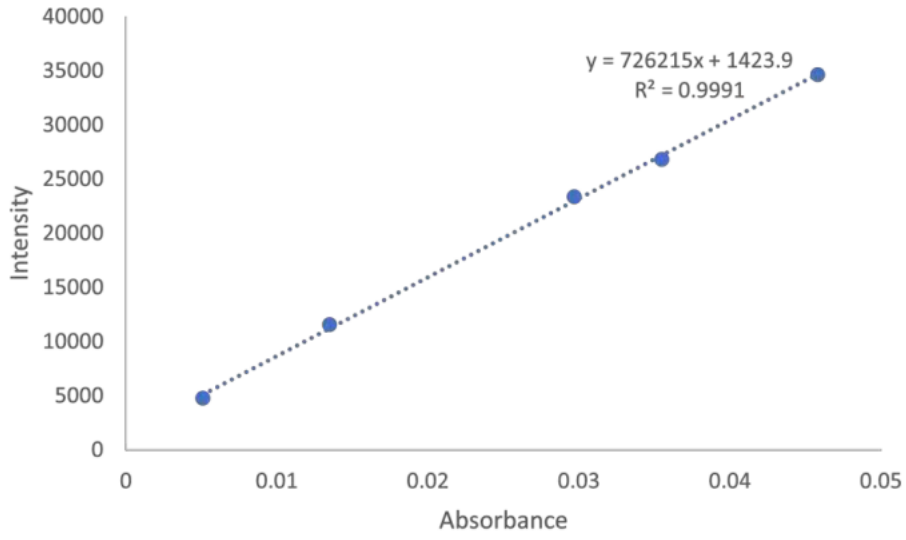

Figure.8.3.93..Absorbance.vs.integrated.intensity.of.quinine.sulfate.,.1.5.and.3.nm.excitation.and.emission.widths..

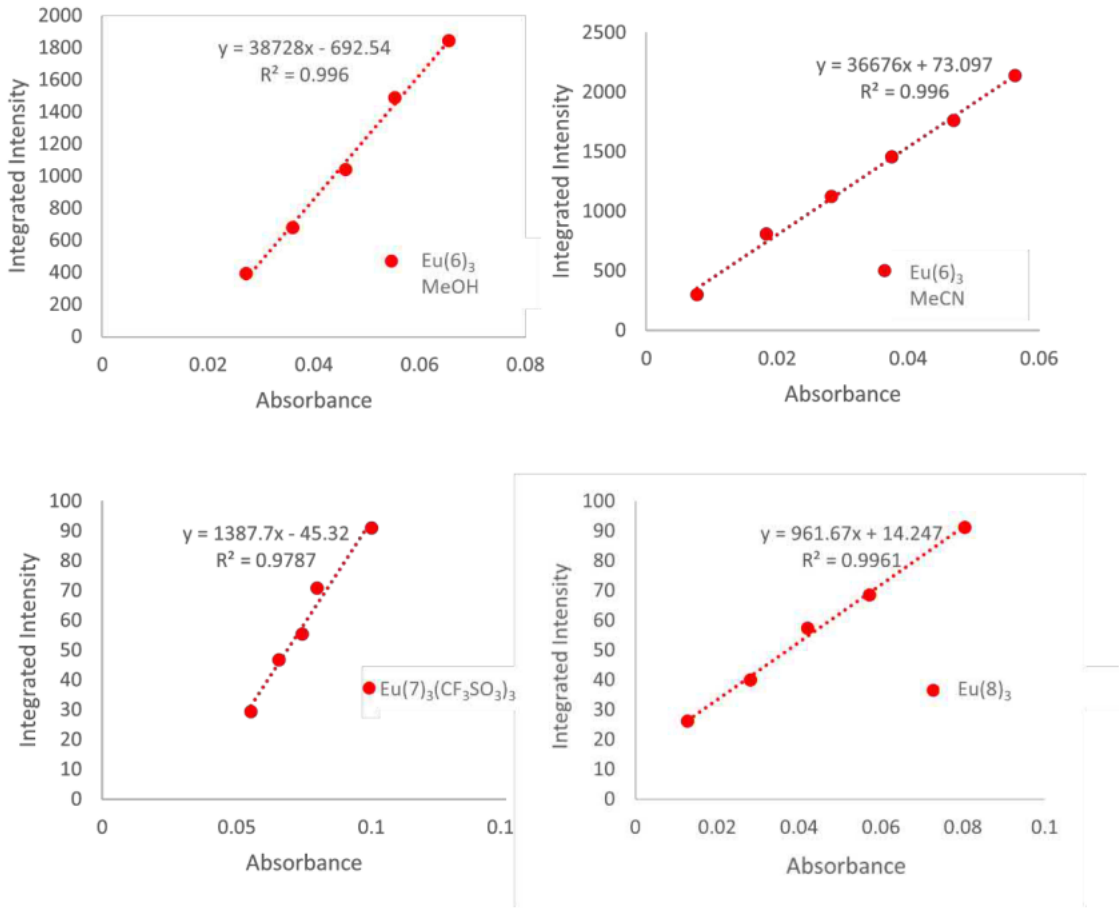

*Figure 8.3.94.. Integrated intensity vs absorbance of Eu(**L**)$_3$ MeOH and MeCN,. 1.5 and 3 nm excitation and emission widths..*

8.3.6 Electron Chemistry

In order to develop Eu(**6**)$_3$ from a solid state photoluminescent film to an electroluminescent OLED, the electrochemical properties were investigated and the HOMO and LUMO energy levels of the Eu(**6**)$_3$ complex were determined. These are required in order to make informed decisions on the electron transport layer (ETL) and the hole transport layer (HTL) for OLED design. These energy levels are determined experimentally by cyclic voltammetry (CV) (for LUMO) and optically (for HOMO determination) alongside theoretical determination by DFT optimization and frequency calculations for comparison the same Eu(**6**)$_3$ calculation.

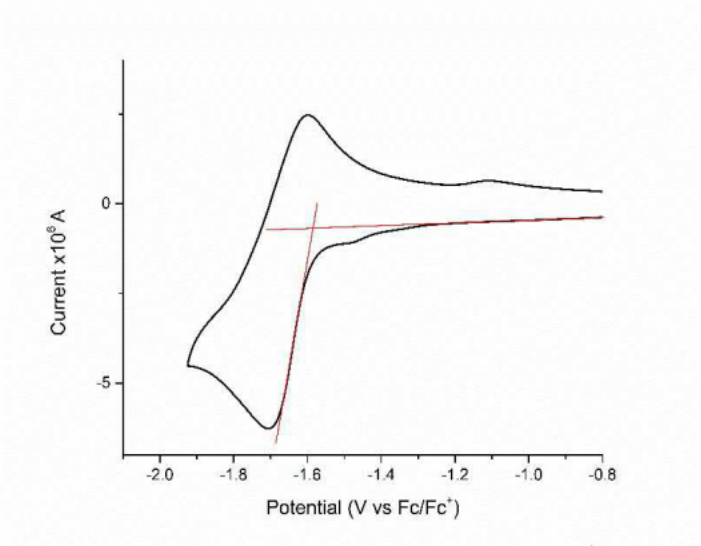

$$E_{LUMO} = -\text{IP V} = \{-E'_{red/onset} - IP(refrence)\}\, eV \quad \textbf{(1)}$$

$$= \{-E'_{red/onset} - E_{1/2}\,(\mathbf{Fc/Fc^+}) - (\mathbf{IP(FC)})\}\, eV \quad \textbf{(1-a)}$$

$$= \{-E'_{red/onset} - (\mathbf{IP(FC)})\}\, eV \quad \textbf{(1-b)}$$

*Figure. 8.3.95.. (Top). Cyclic. voltammogram. of. Eu(**6**)$_3$. in. DMF. (0.01. mM). showing. the. single. reversible. reduction. process. observed.. (Bottom). Equation. 1,. used. to. calculate. LUMO. energy. level. from. said. cyclic. voltammogram,. where. E_{LUMO} is. the. energy. of. the. LUMO. energy. level. $E'_{red/onset}$ is. onset. potential. of. the. first. reduction. wave. $E_{1/1}$(Fc/Fc$^+$). is. half-wave. potential. required. to. reference. to. Fc/Fc$^+$. and IP(FC). is. internal. standard. redox.. Equation. from. reference. 1..*

CV measurements of Eu(**6**)$_3$ were run in dried DMF (0.01 mM) solution and calibrated using decamethylferrocene and then referenced to ferrocene Fc/Fc$^+$, as commonly observed in literature. The cyclic voltammogram shown in Figure 8.3.97 shows that there are reversable reduction processes detected at E^0 = -1.67 V versus Fc/Fc$^+$, assigned to a NI reduction process, where no distinctive oxidation processes were identifiable. Ideally both the HOMO and LUMO can be derived from onset potentials in the first oxidation or reduction peaks. However, due to the lack of oxidation peaks present in CV results, only the LUMO could be derived from the onset potential of the first reduction peak using equation 1.[1]This is identical to the case in reference 1, since the CV results are reported vs Fc/Fc$^+$, the $E_{1/2}$(Fc/Fc$^+$) is already added, thus the equation reduces to (1-b). This leaves only the $E_{red/onset}$, which is the value of interaction between the line of baseline current and tangent of reduction curve seen in Figure 8.3.95, minus the internal standard redox of the system, represented as IP(Fc) and is taken to be 4.80.[1] This gave LUMO energy level to be -3.22 eV, where DFT calculation results found it to be -3.07 eV; these results are in good agreement with one another.

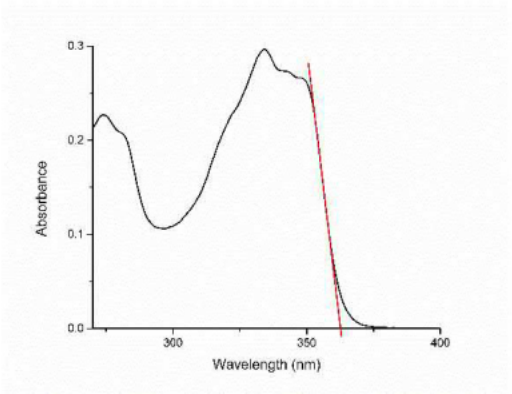

$$E_{gap,optical} = \frac{hc}{\lambda_{offset}} \quad (2)$$

$$E_{HOMO} = E_{LUMO} + E_{gap} \quad (3)$$

*Figure. 8.3.96.. (Left). UV-visible. absorbance. spectrum. of. Eu(**6**)$_3$ (0.01. mM,. DMF),. used. to. determine. the. wavelength. offset.. (Right) Equations. 2. and. 3. used. to. calculate. the. HOMO. energy. level.. Equation. from. reference. 2..*

The experimental HOMO can then be determined in two steps using the UV-visible spectrum of Eu(**6**)$_3$ (0.01 mM, DMF). First the $E_{gap,\ optical}$ is found using Planck-Einstein relationship in **equation 2**, where hc = 1240 eV ⋅ nm and λ_{offset} is obtained from the UV-visible spectrum of Eu(**6**)$_3$ (0.01 mM, DMF), which as seen in Figure 8.3.98 is the intersection of the baseline with absorption edge. From here, using the determined E_{LUMO} value from **equation 1** and the experimentally determined $E_{gap,\ optical}$ from **equation 2** the HOMO energy level can be determined from **equation 3**. **Equation 3** is under the assumption that the $E_{gap,\ electronic}$ = $E_{gap,\ optical}$ = E_{gap}, justified by theoretical calculations suggesting such a correlation.[1,2] This gave HOMO energy levels of -6.64 eV, which are slightly higher than the -5.70 eV found in the DFT calculation. Looking at the LUMO and HOMO orbitals calculated in Figure 8.3.98, the LUMO orbitals are found on the **NI** rings, where the HOMO orbitals are associated with the carboxylates of the pyridyl unit. This could be why there is a larger discrepancy in the HOMO energy levels but only a small one in the LUMO. For the LUMO energy levels, both the calculated (reduction peak) and experimental values are associated with the **NI** moiety of the complex, whereas the HOMO energy levels are experimentally determined (absorption edge) from the **NI** moiety but theoretically determined from the pyridyl moiety. In literature there is commonly quite a discrepancy between calculated and experimental associated with solvent effects and the large constraints made in calculations.

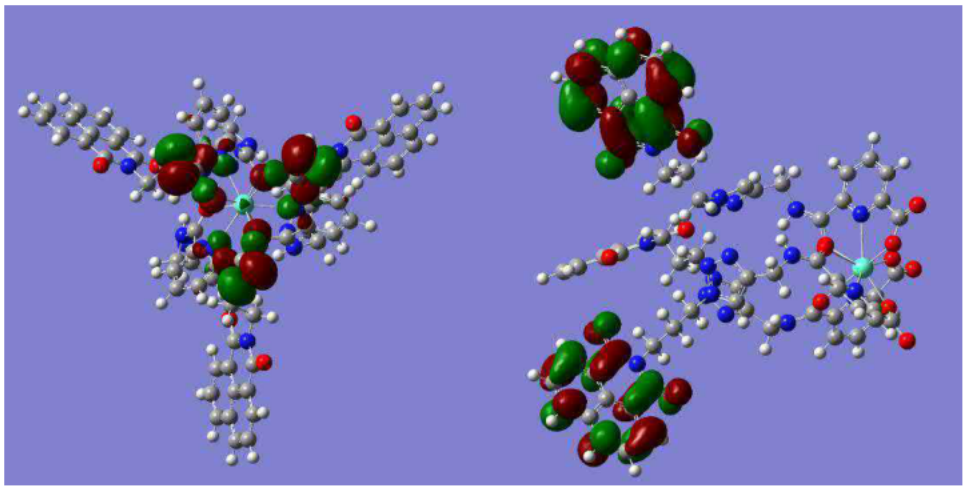

*Figure. 8.3.97.. Eu(**6**)$_3$ complex. calculated. HOMO. (Left). and. LUMO. (Right). orbitals,. produced. in. Gaussian. 16..*

1. A. A. Adeniyi, T. L. Ngake and J. Conradie, Electroanalysis, 2020, **32**, 2659-2668.
2. J. C. S. Costa, R. J. S. Taveira, C. F. R. A. C. Lima, A. Mendes and L. M. N. B. F. Santos, Opt. Mater., 2016, **58**, 51-60.

8.4 Chapter 6

8.4.1 Ligand Characterisation Data

8.4.1.2 Ligand 9

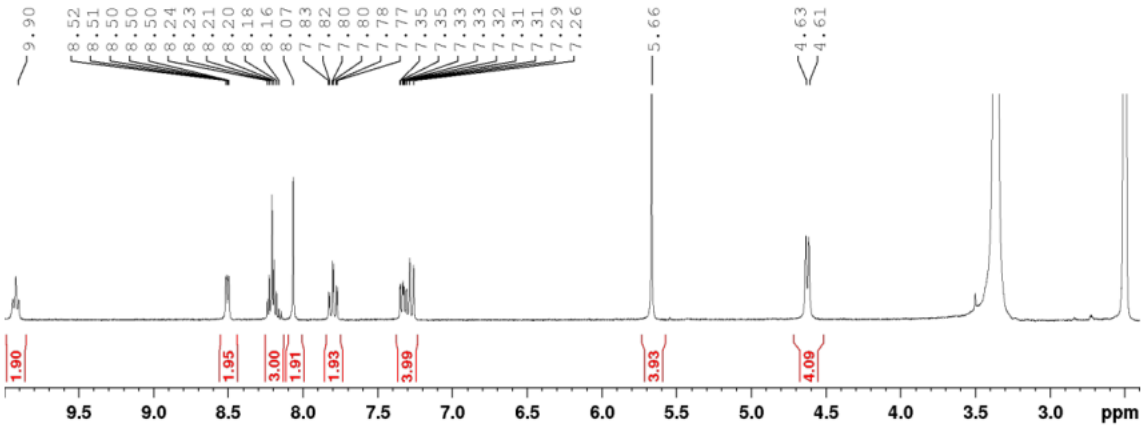

*Figure 8.4.1.. ^{1}H NMR spectrum of **9** (300 MHz, DMSO-d_6).*

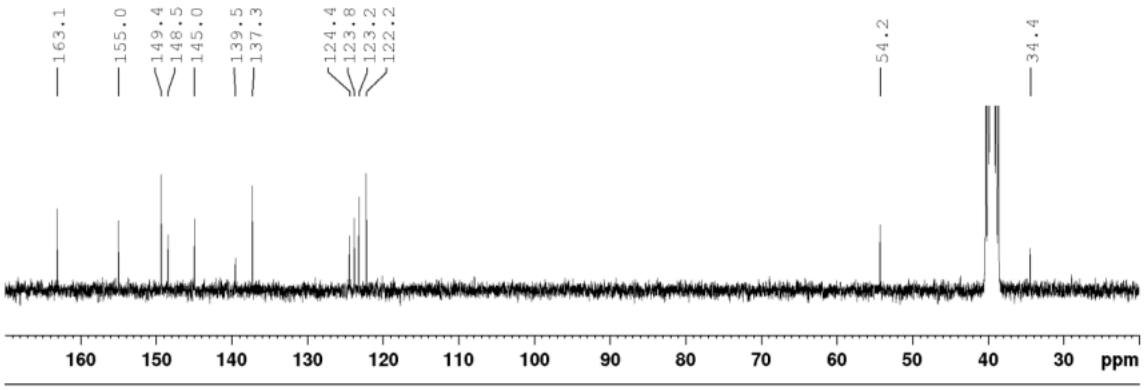

*Figure 8.4.2.. ^{13}C NMR spectrum of **9** (75 MHz, DMSO-d_6)..*

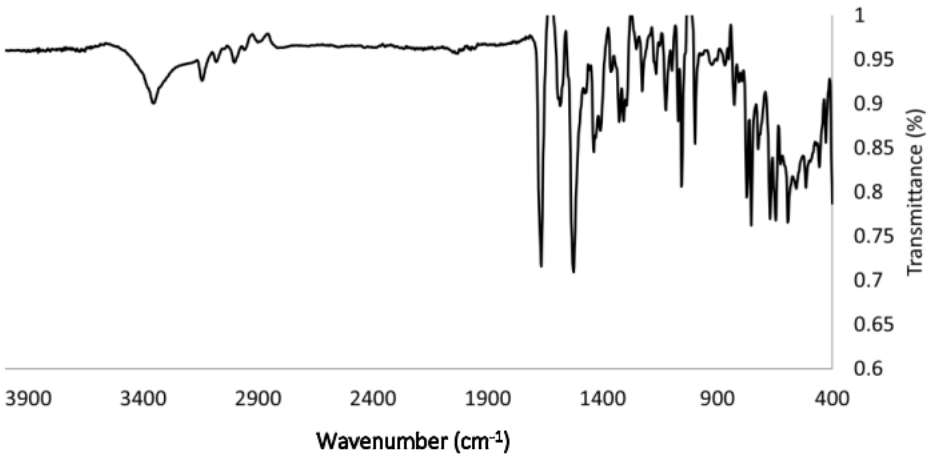

*Figure 8.4.3.. IR spectrum of **9**..*

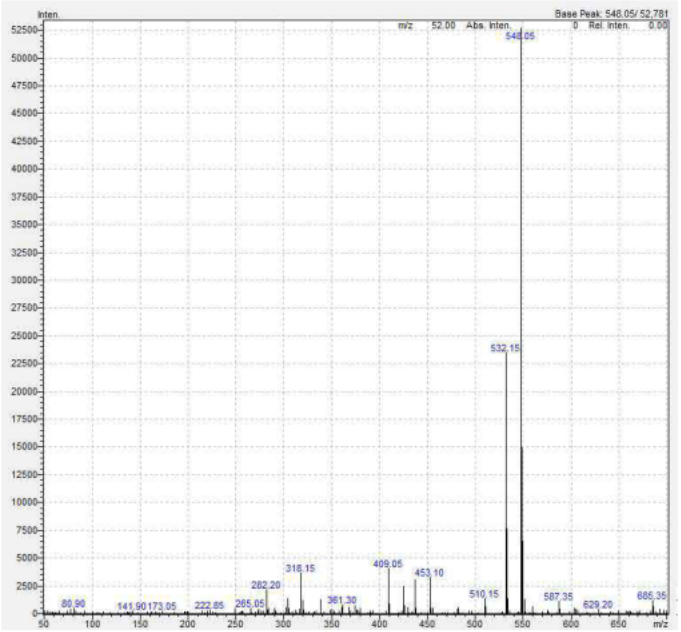

*Figure 8.4.4.. LRMS m/z= 510.15 [**9** + H]$^+$ (calc.. for $C_{23}H_{24}N_{11}O_2^+$, 510.53), 532.15 [**9** + Na]$^+$ (calc.. for $C_{23}H_{23}N_{11}O_2Na^+$, 532.51) and 548.05 [**9** + K]$^+$ (calc.. for $C_{23}H_{23}N_{11}O_2K^+$, 548.62)..*

8.4.1.2 Ligand 10

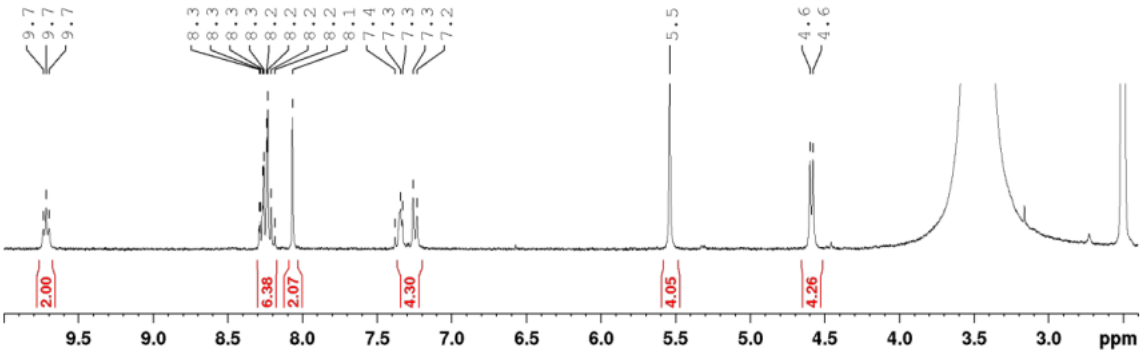

*Figure 8.4.5.. ^{1}H NMR spectrum of **10** (300 MHz, DMSO-d_6)..*

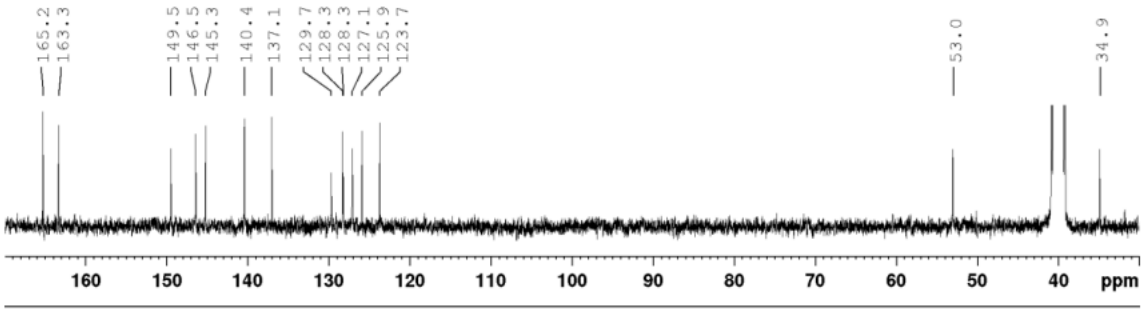

*Figure 8.4.6.: ^{13}C NMR spectrum of **10** (75 MHz, DMSO-d_6)..*

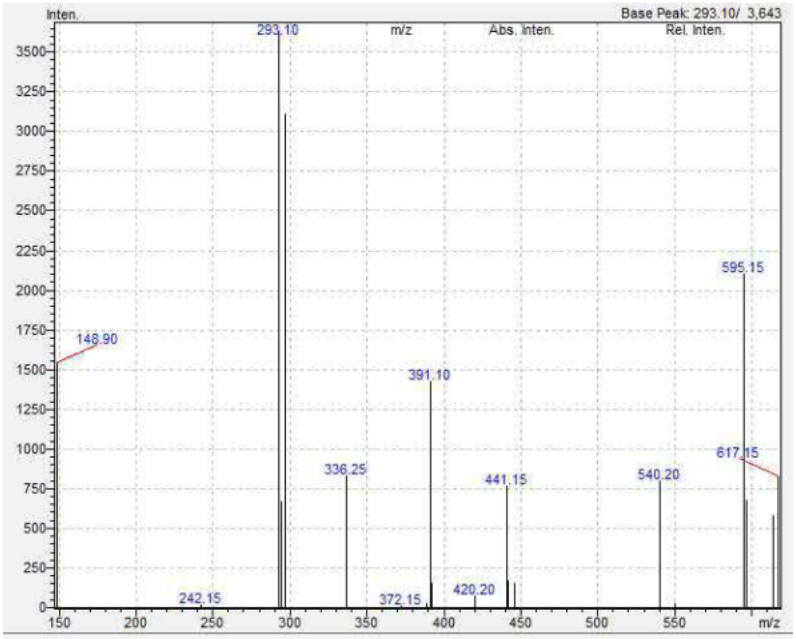

*Figure 8.4.7. LRMS m/z = 595.15 [**10** - H]⁻ (calc. for $C_{28}H_{23}N_{10}O_6^-$, 595.54).*

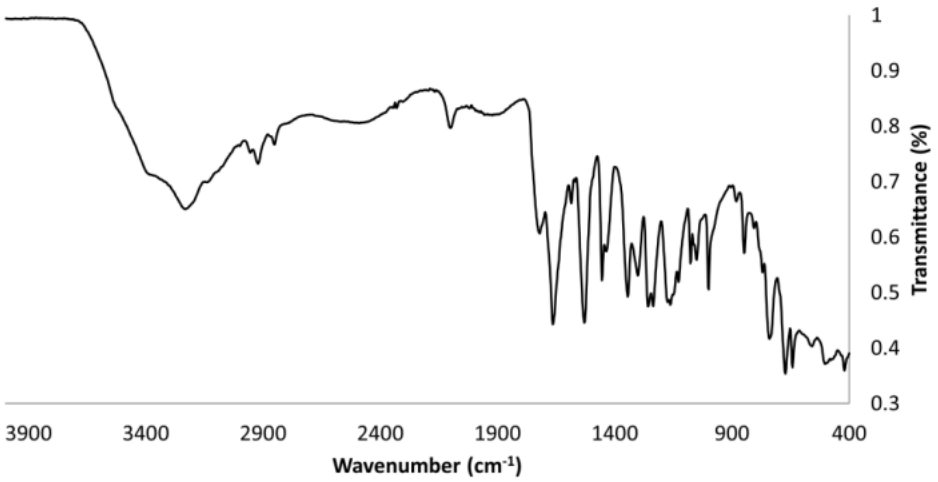

*Figure 8.4.8. IR spectrum of **10**.*

8.4.1.2 Ligand 11

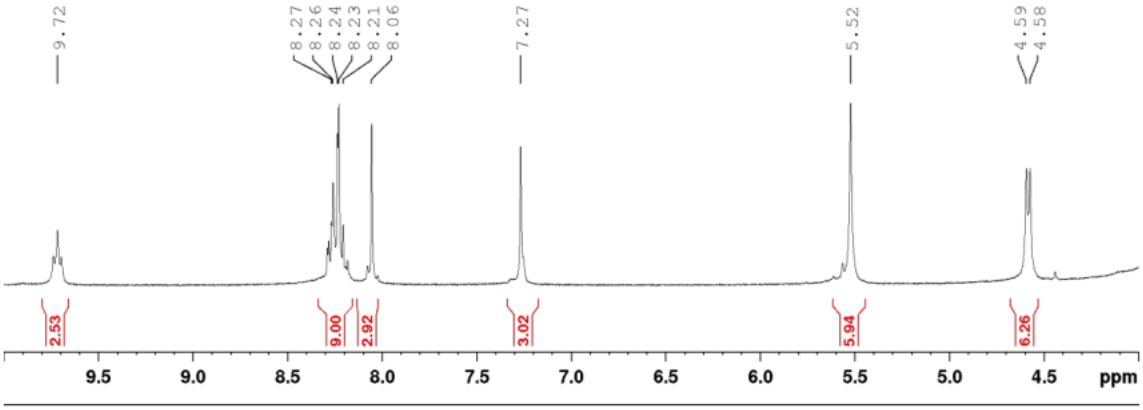

*Figure 8.4.9.. ^{1}H NMR spectrum of **11** (300 MHz, DMSO-d_6).*

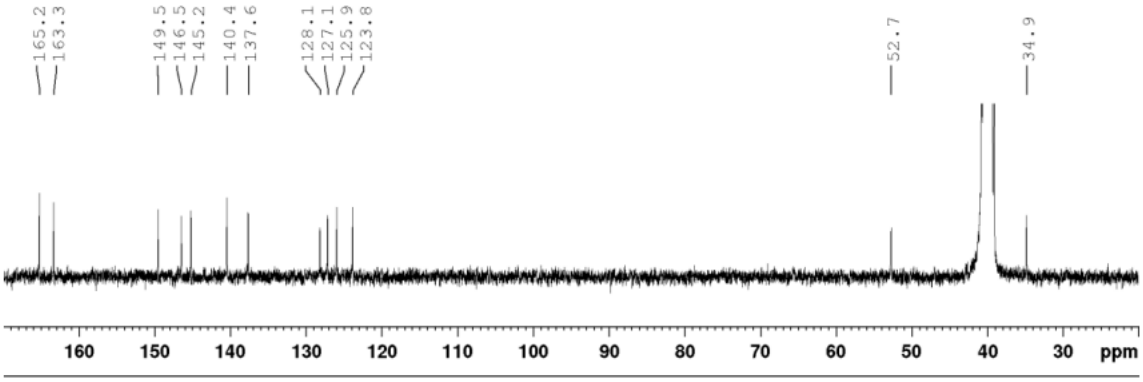

*Figure 8.4.10.. ^{13}C NMR spectrum of **11** (75 MHz, DMSO-d_6).*

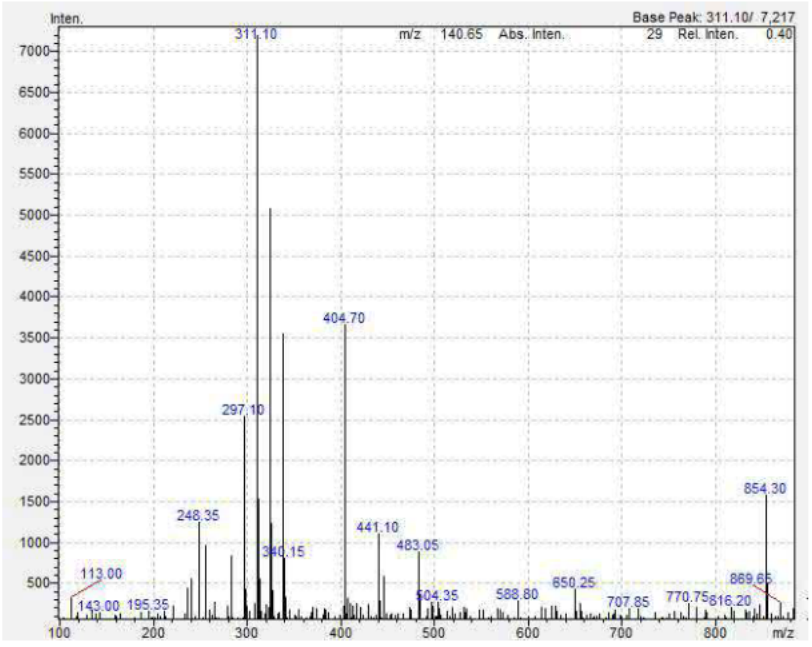

*Figure 8.4.11.. LRMS m/z= 854.30 [**11** - H]$^-$ (calc.. for $C_{39}H_{32}N_{15}O_9^-$, 854.77).*

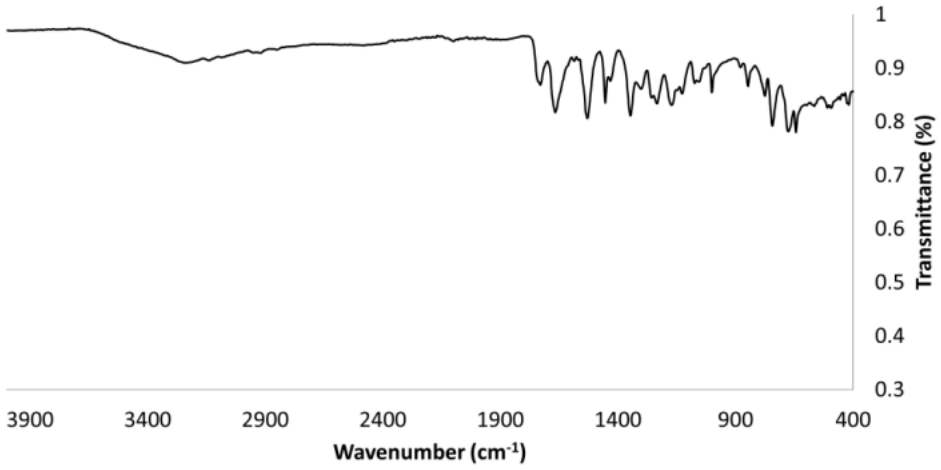

*Figure 8.4.12. IR spectrum of **11**.*

8.4.2 Lanthanide Complex Data

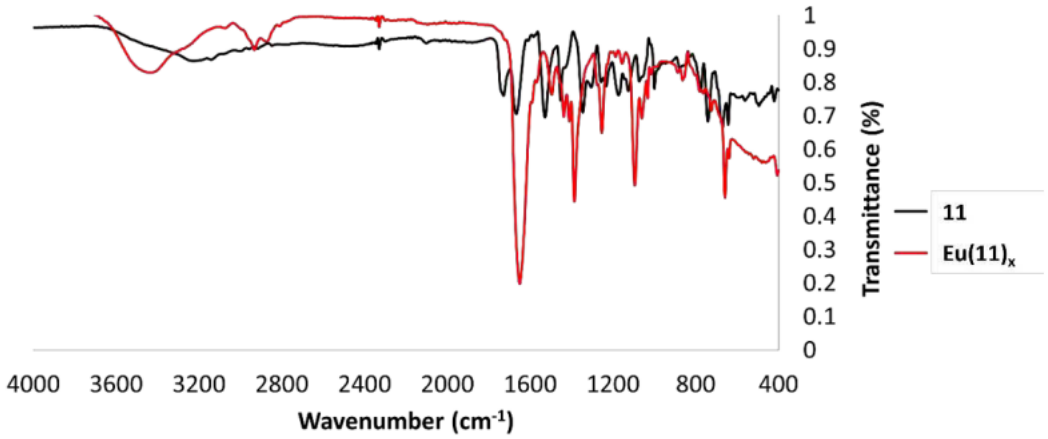

*Figure 8.4.13. Infrared spectra of **3** and $Eu(\mathbf{3})_x(CF_3SO_3)_x$.*

8.4.3 Crystal Structure Data

Crystal Data for $C_{54}H_{53}F_9N_{22}O_{15}S_3Zn_{1.5}$ (*M*.=1615.42 g/mol): triclinic, space group *P*-1 (no. 2), *a* = 11.5022(6) Å, *b* = 16.6768(9) Å, *c* = 21.5103(11) Å, *α* = 71.013(3)°, *β* = 76.945(3)°, *γ* = 82.557(3)°, *V*.= 3793.7(4) Å^3, *Z* = 2, *T* = 150.0 K, μ(CuKα) = 2.219 mm^{-1}, *Dcalc* = 1.414 g/cm^3, 25728 reflections measured (4.43° ≤ 2Θ ≤ 130.334°), 10301 unique (R_{int} = 0.0802, R_{sigma} = 0.1085) which were used in all calculations. The final R_1 was 0.0970 (I > 2σ(I)) and wR_2 was 0.2324 (all data).

*Table 8.4.1. π - π Stacking interactions occurring in the metallo coordinated polymer structure of Zn_x(**9**)$_x$*

π - π stacking **Interaction**	**Centroid distance**	**Shift distance**	**δ**	**Θ**
Offset *N1A···N1A*	3.7 Å	1.565 Å	87.85°	65.91°
Offset *N11B···N11B*	3.7 Å	1.563 Å	74.19°	65.76 °

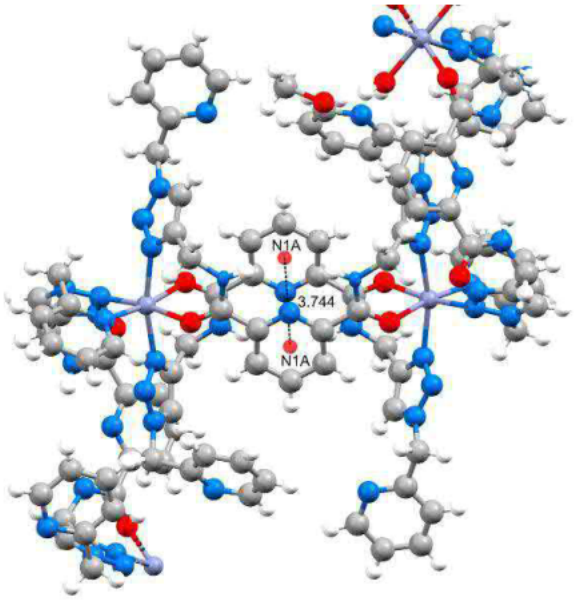

Figure 8.4.14. Offset π - π stacking interactions found by OLEX2 software and given centroid-centroid distances between N1A and N1A.

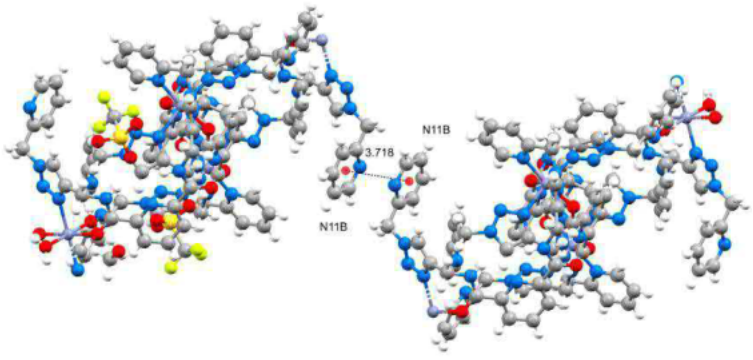

Figure 8.4.15. Offset π - π stacking interactions found by OLEX2 software and given centroid-centroid distances between N11B and N11B.

Table.8.4.1.. Hydrogen.bonding.interactions.between.stacking.molecules..

Interacting molecules	*Hydrogen bonding interactions*
***9**-CF_3SO_3*	O104···N2A' = 2.874 (9) Å and <(N2A-H2A··· O104') = 162° O104···N7A' = 2.904 (8) Å and <(N7A-H7A··· O104') = 164° O100···N7B' = 2.864 (9) Å and <(N7B-H7B··· O100') = 156° O100···N2B' = 2.897 (9) Å and <(N2B-H2B··· O100') = 151°

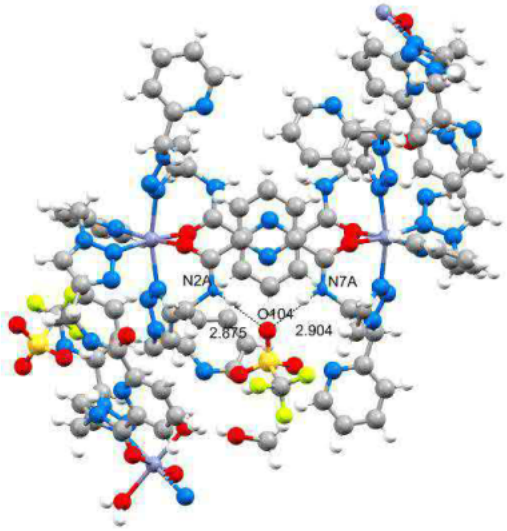

Figure.8.4.16.. Hydrogen.bonding.interactions.occurring.between.CF_3SO_3 and.**9_a**

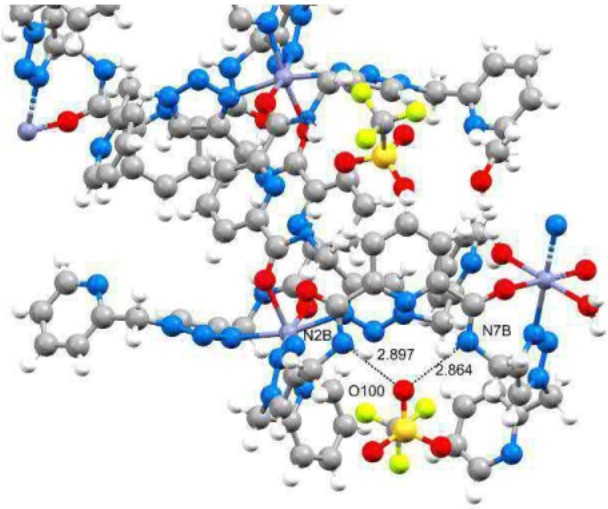

Figure.8.4.17.. Hydrogen.bonding.interactions.occurring.between.CF_3SO_3 and.**9_b**.

8.4.4 Self-Assembly Titration Data

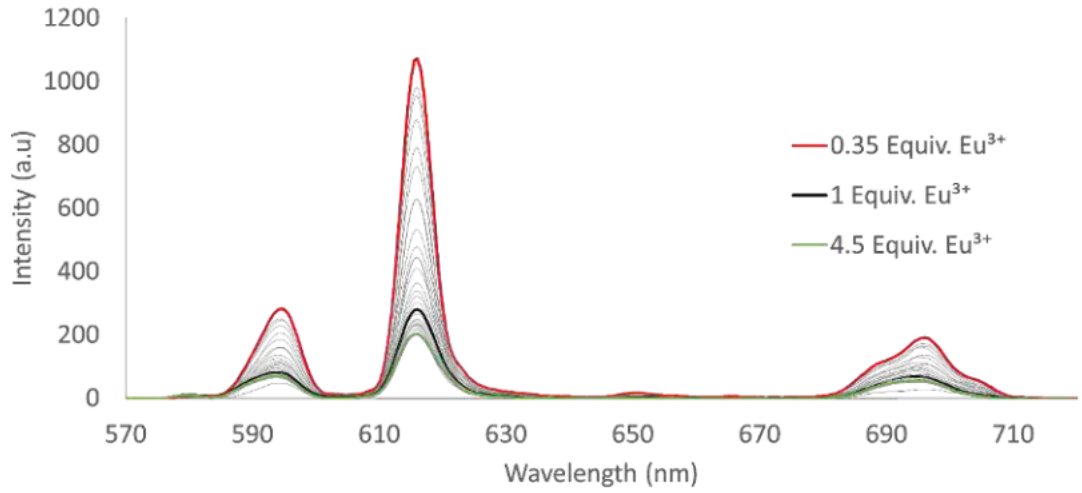

*Figure 8.4.16 – Fluorescence titration of **9** with $Eu(CF_3SO_3)_3$ 0 to 4.5 equivalents (0.02 mM, MeCN).*

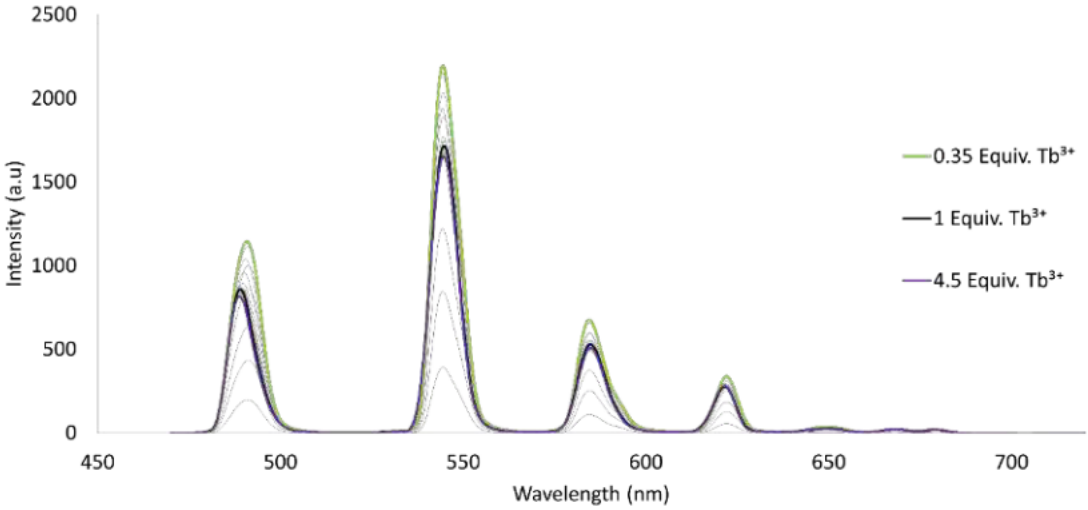

*Figure 8.4.17 – Fluorescence titration of **9** with $Tb(CF_3SO_3)_3$ 0 to 4.5 equivalents (0.02 mM, MeOH).*

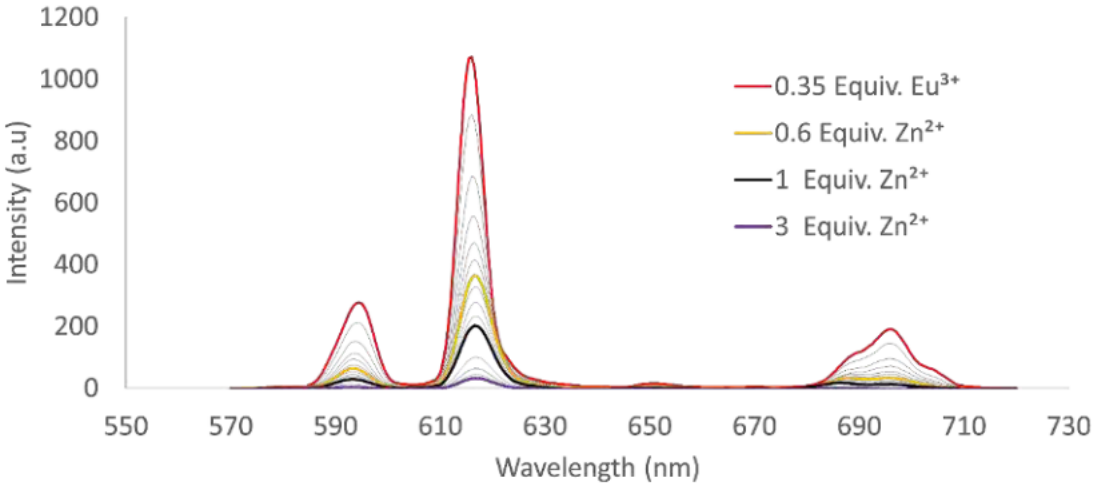

Figure. 8.4.18.. Fluorescence. titration. of. ***9****. with. initial. 0.35. equivalents. of. $Eu(CF_3SO_3)_3$ then. $Zn(CF_3SO_3)_2$ 0. to. 3. equivalents. (0.02. mM, MeCN)..*

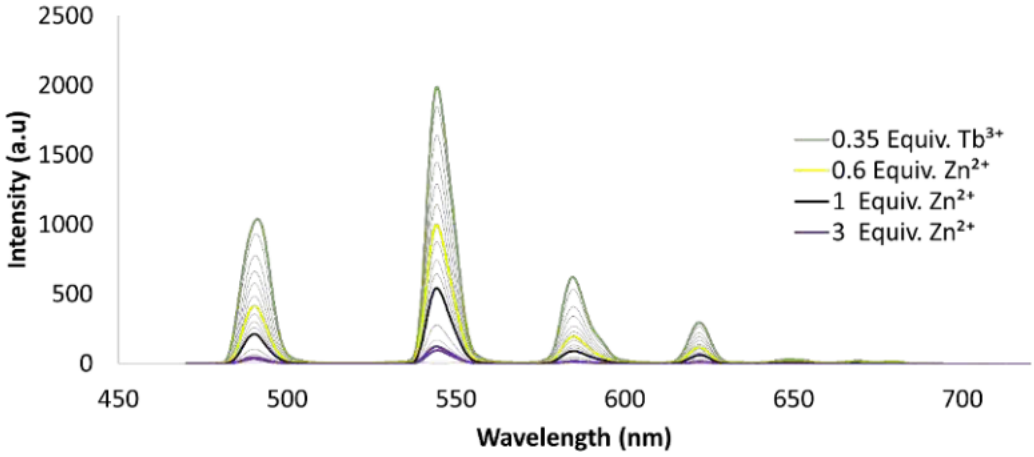

Figure. 8.4.19.. Fluorescence. titration. of. ***9****. with. initial. 0.35. equivalents. of. $Tb(CF_3SO_3)_3$ then. $Zn(CF_3SO_3)_2$ 0. to. 3. equivalents. (0.02. mM, MeCN).*

MASSEY UNIVERSITY
TE KUNENGA KI PŪREHUROA
UNIVERSITY OF NEW ZEALAND

GRADUATE RESEARCH SCHOOL

STATEMENT OF CONTRIBUTION
DOCTORATE WITH PUBLICATIONS/MANUSCRIPTS

We, the student and the student's main supervisor, certify that all co-authors have consented to their work being included in the thesis and they have accepted the student's contribution as indicated below in the Statement of Originality.

Student name:	Alex Thomas O'Neil
Name and title of main supervisor:	Associate Professor Jonathan Kitchen
In which chapter is the manuscript/published work?	Chapter 3
What percentage of the manuscript/published work was contributed by the student?	95%

Describe the contribution that the student has made to the manuscript/published work:

Alex completed all synthesis and characterisation of the compounds described in the manuscript One Xray dataset was collected by another author, however the data was solved and refined by Alex.

Please select one of the following three options:

- (●) **The manuscript/published work is published or in press**

  Please provide the full reference of the research output:

  A. T. O'Neil, N. Zhang, J. A. Harrison, S. M. Goldup and J. A. Kitchen. Synthesis, photophysical and assembly studies of novel luminescent lanthanide(III) complexes of 1,2,3-triazolyl pyridine 2,6-dicarboxamide based ligands, Supramolecular Chemistry Supramol Chem , 2021, 33, 160 173

- ( ) **The manuscript is currently under review for publication**

  Please provide the name of the journal:

- ( ) **It is intended that the manuscript will be published, but it has not yet been submitted to a journal**

Student's signature:	Alex O'Neil Digitally signed by Alex O'Neil Date: 2022.10.10 10:58:39 +13'00'	Main supervisor's signature:	Jonathan Kitchen Digitally signed by Jonathan Kitchen Date: 2022.10.07 09:25:50 +13'00'

This form should be placed at the beginning of each relevant thesis chapter.

MASSEY UNIVERSITY
TE KUNENGA KI PŪREHUROA
UNIVERSITY OF NEW ZEALAND

GRADUATE RESEARCH SCHOOL

STATEMENT OF CONTRIBUTION
DOCTORATE WITH PUBLICATIONS/MANUSCRIPTS

We, the student and the student's main supervisor, certify that all co-authors have consented to their work being included in the thesis and they have accepted the student's contribution as indicated below in the Statement of Originality.

Student name:	Alex Thomas O'Neil
Name and title of main supervisor:	Associate Professor Jonathan Kitchen
In which chapter is the manuscript/published work?	Chapter 4
What percentage of the manuscript/published work was contributed by the student?	100 %

Describe the contribution that the student has made to the manuscript/published work:

Alex carried out all synthesis and characterisation of the compounds in the published manuscript.

Please select one of the following three options:

- (●) **The manuscript/published work is published or in press**

  Please provide the full reference of the research output:

  A. T. O'Neil, J. A. Harrison and J. A. Kitchen. Ultra-thin films of amphiphilic lanthanide complexes: multi-colour emission from molecular monolayers Chem. Commun., 2021, 57, 8067 8070.

- ( ) **The manuscript is currently under review for publication**

  Please provide the name of the journal:

- ( ) **It is intended that the manuscript will be published, but it has not yet been submitted to a journal**

Student's signature:	Alex O'Neil Digitally signed by Alex O'Neil Date: 2022.10.10 10:59:02 +13'00'	Main supervisor's signature:	Jonathan Kitchen Digitally signed by Jonathan Kitchen Date: 2022.10.07 09:25:05 +13'00'

This form should be placed at the beginning of each relevant thesis chapter.

MASSEY UNIVERSITY
TE KUNENGA KI PŪREHUROA
UNIVERSITY OF NEW ZEALAND

GRADUATE RESEARCH SCHOOL

STATEMENT OF CONTRIBUTION
DOCTORATE WITH PUBLICATIONS/MANUSCRIPTS

We, the student and the student's main supervisor, certify that all co-authors have consented to their work being included in the thesis and they have accepted the student's contribution as indicated below in the Statement of Originality.

Student name:	Alex Thomas O'Neil
Name and title of main supervisor:	Associate Professor Jonathan Kitchen
In which chapter is the manuscript/published work?	Chapter 4
What percentage of the manuscript/published work was contributed by the student?	100 %

Describe the contribution that the student has made to the manuscript/published work:
Alex carried out all synthesis, characterisation and materials formation for this manuscript.

Please select one of the following three options:

○ **The manuscript/published work is published or in press**
Please provide the full reference of the research output:

◉ **The manuscript is currently under review for publication**
Please provide the name of the journal:
Journal: Chemistry MDPI

Lanthanide-based Langmuir-Blodgett Multilayers: Multi-Emissive,Temperature Dependent Thin Films.

○ **It is intended that the manuscript will be published, but it has not yet been submitted to a journal**

Student's signature:	Alex O'Neil Digitally signed by Alex O'Neil Date: 2022.10.10 10:59:19 +13'00'	Main supervisor's signature:	Jonathan Kitchen Digitally signed by Jonathan Kitchen Date: 2022.10.07 09:28:31 +13'00'

This form should be placed at the beginning of each relevant thesis chapter.

MASSEY UNIVERSITY
TE KUNENGA KI PŪREHUROA
UNIVERSITY OF NEW ZEALAND

GRADUATE RESEARCH SCHOOL

STATEMENT OF CONTRIBUTION
DOCTORATE WITH PUBLICATIONS/MANUSCRIPTS

We, the student and the student's main supervisor, certify that all co-authors have consented to their work being included in the thesis and they have accepted the student's contribution as indicated below in the Statement of Originality.

Student name:	Alex Thomas O'Neil
Name and title of main supervisor:	Associate Professor Jonathan Kitchen
In which chapter is the manuscript/published work?	Chapter 5
What percentage of the manuscript/published work was contributed by the student?	95 %

Describe the contribution that the student has made to the manuscript/published work:

Alex carried out all synthesis, characterisation and materials formation for this manuscript. AFM images were collected by another author.

Please select one of the following three options:

- ○ **The manuscript/published work is published or in press**
  Please provide the full reference of the research output:

- ◉ **The manuscript is currently under review for publication**
  Please provide the name of the journal:
  Journal: ChemComm, published by the Royal Society of Chemistry

  Single Component Colour-Tunable and White Light Emission from a Europium-1,8-Naphthalimide Thin Film

- ○ **It is intended that the manuscript will be published, but it has not yet been submitted to a journal**

Student's signature:	Alex O'Neil Digitally signed by Alex O'Neil Date: 2022.10.10 10:59:36 +13'00'	Main supervisor's signature:	Jonathan Kitchen Digitally signed by Jonathan Kitchen Date: 2022.10.07 09:30:08 +13'00'

This form should be placed at the beginning of each relevant thesis chapter.

MASSEY UNIVERSITY
TE KUNENGA KI PŪREHUROA
UNIVERSITY OF NEW ZEALAND

GRADUATE RESEARCH SCHOOL

STATEMENT OF CONTRIBUTION
DOCTORATE WITH PUBLICATIONS/MANUSCRIPTS

We, the student and the student's main supervisor, certify that all co-authors have consented to their work being included in the thesis and they have accepted the student's contribution as indicated below in the Statement of Originality.

Student name:	Alex Thomas O'Neil
Name and title of main supervisor:	Associate Professor Jonathan Kitchen
In which chapter is the manuscript/published work?	Chapter 5
What percentage of the manuscript/published work was contributed by the student?	95 %

Describe the contribution that the student has made to the manuscript/published work:

Alex carried out all synthesis, characterisation and materials formation of the compounds in the submitted manuscript Another authour assisted with Oxygen sensing studies

Please select one of the following three options:

- ○ **The manuscript/published work is published or in press**
  Please provide the full reference of the research output:

- ◉ **The manuscript is currently under review for publication**
  Please provide the name of the journal:
  Inorganic Chemistry Frontiers (RSC)

- ○ **It is intended that the manuscript will be published, but it has not yet been submitted to a journal**

Student's signature:	Alex O'Neil Digitally signed by Alex O'Neil Date: 2022.10.10 10:59:57 +13'00'	Main supervisor's signature:	Jonathan Kitchen Digitally signed by Jonathan Kitchen Date: 2022.10.07 09:28:02 +13'00'

This form should be placed at the beginning of each relevant thesis chapter.